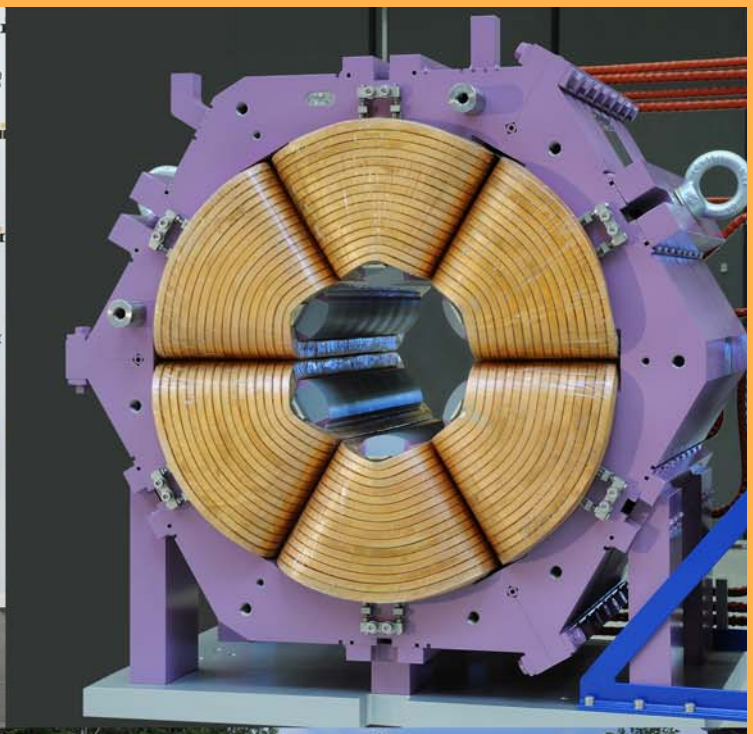
GSI Report 2018-1
November 2018

SCIENTIFIC REPORT 2017







GSI Helmholtzzentrum für Schwerionenforschung GmbH
Member of the Helmholtz Association

Cover picture:

The photograph in the upper left corner shows the joint GSI and FAIR management: J. Blaurock, U. Weyrich, and Prof. Dr. P Giubellino, who was inaugurated in March 2017. The new FAIR sextuple magnet build by a Danish company is visible in the upper right corner. Such type of magnets will be installed into each of the six segments of the FAIR synchrotron SIS100 and will be used for slow and continuous extraction of beams from SIS100. On the 4th of July 2017 the first sod was cut on the construction site northeast of the GSI for the FAIR synchrotron SIS100, which also marked the start of construction and civil engineering works for FAIR in 2017 (lower part of the cover).
All photographs by G. Otto/GSI.

GSI-FAIR Scientific Report 2017

GSI Report 2018-1

DOI:10.15120/GSI-2017-01856

ISSN: 2625-8692
and GSI Report 2018-1

Publisher: GSI Helmholtzzentrum für Schwerionenforschung GmbH,
Planckstr. 1, 64291 Darmstadt, Germany, <http://www.gsi.de>
GSI is a member of the Helmholtz association of national research centres <http://www.helmholtz.de>.
E-only-edition: DOI:10.15120/GSI-2017-01856
License CC BY 4.0

Editors: GSI Helmholtzzentrum für Schwerionenforschung GmbH, Darmstadt,
and Facility for Antiproton and Ion Research in Europe GmbH, Darmstadt Contact: gsilibrary@gsi.de, phone: +496159 712610.
Cover photographs: Gabi Otto.
Publication date: November 2018

For the production of this report templates and scripts of the JACoW collaboration (Joint Accelerator Conferences on Web <http://www.jacow.org>) were used.

/

Contents

Coordination NQM Nuclear and Quark Gluon Matter (Joachim Stroth) 1
Department CBM (head and editing: Peter Senger) . . . 1
RESEARCH-NQM-CBM-1 – Status of the Compressed Baryonic Matter (CBM) experiment at FAIR 1
RESEARCH-NQM-CBM-2 – The superconducting dipole magnet of the CBM experiment 5
RESEARCH-NQM-CBM-3 – CBM Micro Vertex Detector: Summary Report 6
RESEARCH-NQM-CBM-4 – Status of the Silicon Tracking System 7
RESEARCH-NQM-CBM-5 – stsDPB firmware development - preparations for CRI 10
RESEARCH-NQM-CBM-6 – Data transmission line for STS detector readout system 12
RESEARCH-NQM-CBM-7 – Summary Report of CBM RICH developments 13
RESEARCH-NQM-CBM-8 – Summary on the CBM-TRD project 14
RESEARCH-NQM-CBM-9 – Status of the CBM Time Of Flight system 17
RESEARCH-NQM-CBM-10 – The CBM FAIR Phase 0 project - eTOF at STAR 19
RESEARCH-NQM-CBM-11 – Development of muon detection system (MUCH) for the CBM experiment at FAIR 21
RESEARCH-NQM-CBM-12 – Preparation of a free-streaming DAQ system for mCBM@SIS18 . . 23
RESEARCH-NQM-CBM-13 – Status of the CBM physics performance studies 24
RESEARCH-NQM-CBM-14 – mCBM@SIS18 is on its way 30
RESEARCH-NQM-CBM-15 – D mesons Langevin propagation at SIS300-FAIR energies 35
RESEARCH-NQM-CBM-16 – CBM computing - progress, status and outlook 36
Department HADES (head: Joachim Stroth, editing: Romain Holzmann) . . . 39
RESEARCH-NQM-HADES-1 – HADES activities and status 2017 39
RESEARCH-NQM-HADES-2 – Performance of the plastic scintillator Time-of-Flight Wall of HADES in Au+Au collisions 44
RESEARCH-NQM-HADES-3 – Benchmarking new front-end electronics for the HADES drift chambers 45
RESEARCH-NQM-HADES-4 – The PaDiWa-AMPS2 TDC and QDC front-end electronics for the HADES Electromagnetic Calorimeter 46
RESEARCH-NQM-HADES-5 – Application of micron-size plasma for investigations of HADES Mini Drift Chamber (MDC) cells with an unique laser driven test facility 47
RESEARCH-NQM-HADES-6 – Machine learning for weak decay recognition in heavy-ion collisions 48
RESEARCH-NQM-HADES-7 – Strange meson production in pion-nucleus collisions at 1.7 GeV/c 49
RESEARCH-NQM-HADES-8 – A non-binomial model for efficiency corrections to particle number cumulants 50
RESEARCH-NQM-HADES-9 – π^0 and η production in π^- + PE collisions at 690 MeV/c beam momentum 51
RESEARCH-NQM-HADES-10 – Exclusive Λ analysis to study hyperon scattering in medium . . 52
RESEARCH-NQM-HADES-11 – Fit to transverse momentum spectra of dileptons measured by HADES 53
RESEARCH-NQM-HADES-12 – Understanding of transverse mass spectra of charged pions measured in Au+Au at 1.23 AGeV collisions with HADES 54
RESEARCH-NQM-HADES-13 – Protons and light nuclei in Au+Au collisions at 1.23A GeV measured with HADES 55
RESEARCH-NQM-HADES-14 – Λ polarization in Au+Au collisions at $\sqrt{s_{NN}}$ = 2.42 GeV investigated with HADES 56
RESEARCH-NQM-HADES-15 – Dilepton production in pion induced reactions with HADES . . 57
Department ALICE (head: Silvia Masciocchi, editing: Silvia Masciocchi, Ralf Averbeck) . . . 59
RESEARCH-NQM-ALICE-1 – Characterisation of a cascaded power supply for use with multi-GEM stacks 59

RESEARCH-NQM-ALICE-2 – Measurement of J/ψ production as a function of event multiplicity in pp collisions at $\sqrt{(s)}$ = 13 TeV with ALICE . . . 61
RESEARCH-NQM-ALICE-3 – Σ^0 baryon production in pp collisions at $\sqrt{s}$ = 13 TeV measured with the ALICE experiment . . . 62
RESEARCH-NQM-ALICE-4 – Baryon femtoscopy in p-Pb collisions at 5.02 TeV . . . 63
RESEARCH-NQM-ALICE-5 – Low-mass dielectron production in pp collisions at $\sqrt{s}$ = 13 TeV with ALICE . . . 64
RESEARCH-NQM-ALICE-6 – Production of electrons from semieptonic heavy-flavour hadron decays in proton-proton and heavy-ion collisions with ALICE at the LHC . . . 65
RESEARCH-NQM-ALICE-7 – Quality assurance of GEM-based readout chambers for the Time Projection Chamber of ALICE . . . 67
RESEARCH-NQM-ALICE-8 – Read-out electronics for the ALICE TPC upgrade . . . 69
RESEARCH-NQM-ALICE-9 – Nuclear modification factors in Xe-Xe collisions measured with ALICE . . . 71
RESEARCH-NQM-ALICE-10 – Measurement of the ^{3}He elliptic flow in Pb–Pb collisions with ALICE at the LHC . . . 72
RESEARCH-NQM-ALICE-11 – Optimization of the HV scheme for GEM-based detectors . . . 73
RESEARCH-NQM-ALICE-12 – dE/dx resolution studies of a pre-production read-out chamber with GEMs for the ALICE TPC . . . 75
RESEARCH-NQM-ALICE-13 – Systematic studies of correlations between different order flow harmonics in Pb-Pb collisions at $\sqrt{S_{nn}}$ = 2.76 TeV . . . 76
RESEARCH-NQM-ALICE-14 – Correction for secondary particles contamination in the charged particle yield measurement in Xe-Xe collisions by ALICE . . . 77
RESEARCH-NQM-ALICE-15 – Low-mass dielectron production in Pb-Pb collisions at $\sqrt{s_{NN}}$ = 5.02 TeV with ALICE . . . 78
RESEARCH-NQM-ALICE-16 – Proton-proton reference spectrum at $\sqrt{(s)}$=5.44 TeV . . . 79
RESEARCH-NQM-ALICE-17 – Production of antiparticles in p-Pb collisions at 5.02 TeV with ALICE . . . 80
RESEARCH-NQM-ALICE-18 – Neutral pion and η meson production in p-Pb and Pb-Pb collisions at the LHC . . . 81
RESEARCH-NQM-ALICE-19 – Inclusive and non-prompt J/ψ production in Pb-Pb collisions at $\sqrt{S_{NN}}$= 5.02 TeV measured at mid-rapidity with ALICE . . . 83
RESEARCH-NQM-ALICE-20 – Stability tests of ALICE TPC GEM chambers at the LHC . . . 85
RESEARCH-NQM-ALICE-21 – Report by the GSI-ALICE group . . . 86
RESEARCH-NQM-ALICE-22 – CATS - the modern tool for femtoscopy studies . . . 88

Coordination Hadron Physics (Klaus Peters) 89
Departments Hadron Spectroscopy (head: Klaus Peters, editing: Klaus Peters), Hadron Structure (head: Frank Maas, editing: Klaus Peter), and PANDA Detectors (head: Joachim Schwiening, editing: Klaus Peter) . . . 89
RESEARCH-PANDA-HAD-1 – Advanced performance measurements with microchannel-plate PMTs . . . 89
RESEARCH-PANDA-HAD-2 – The Barrel DIRC prototype in a beam experiment . . . 90
RESEARCH-PANDA-HAD-3 – Optical shape measurements of the Barrel DIRC radiator bars . . . 92
RESEARCH-PANDA-HAD-4 – Surface quality of the PANDA barrel DIRC prototype radiators . . . 93
RESEARCH-PANDA-HAD-5 – Geometrical Reconstruction for the DIRC PID at GlueX . . . 94
RESEARCH-PANDA-HAD-6 – First setup for the routine tests of the APFEL-ASIC rigid flex PCBs 95
RESEARCH-PANDA-HAD-7 – Measurement of cluster velocity distributions for PANDA . . . 96
RESEARCH-PANDA-HAD-8 – Cluster-jet beam and vacuum studies at the PANDA cluster-jet target . . . 97

Coordination NuSTAR / ENNA Nuclear Structue, Astrophysics and Reactions (Christoph Scheidenberger) 99
Department FRS / SFRS (head and editing: Christoph Scheidenberger) . . . 99
RESEARCH-NUSTAR-FRS-1 – New isotope search experiments at the FRS for FAIR phase-0 . . . 99
RESEARCH-NUSTAR-FRS-2 – Development of new ion-optical modes for NUSTAR FAIR Phase-0 experiments at the FRS . . . 101
RESEARCH-NUSTAR-FRS-3 – New opportunities at the border of nuclear and hadron physics using WASA at FRS: a status report . . . 102
RESEARCH-NUSTAR-FRS-4 – Search for η'-mesic nuclei with the ^{12}C(p,d) reaction . . . 106
RESEARCH-NUSTAR-FRS-5 – Observation of nuclear medium effects in the excitation of baryonic resonances . . . 107

DOI:10.15120/GSI-2017-01856

RESEARCH-NUSTAR-FRS-6 – Design of a double-sided silicon strip tracking system for hypernuclear spectroscopy at FRS & Super FRS . . . 108
RESEARCH-NUSTAR-FRS-7 – Λ hyperon reconstruction using the WASA cylindrical detector system for the FAIR-Phase 0 hypernuclear experiment S447 . . . 109
RESEARCH-NUSTAR-FRS-8 – Status of the FRS Ion Catcher . . . 110
RESEARCH-NUSTAR-FRS-9 – Reaction studies with the FRS Ion Catcher: A novel approach and universal method for the production, identification of and experiments with unstable isotopes produced in multi-nucleon transfer reactions with stable and unstable beams . . . 112
RESEARCH-NUSTAR-FRS-10 – Investigation of fusion in inverse kinematics with a target in the cryogenic stopping cell . . . 113
RESEARCH-NUSTAR-FRS-11 – A novel method for measuring β-delayed neutron emission . . . 114
RESEARCH-NUSTAR-FRS-12 – Detector tests with the prototype CSC for the Super-FRS and direct mass measurements of neutron-deficient nuclides below ^{100}Sn in FAIR Phase-0 . . . 115
RESEARCH-NUSTAR-FRS-13 – An upgrade to the RFQ beam line of the FRS Ion Catcher . . . 116
RESEARCH-NUSTAR-FRS-14 – Development of the stopping cell for the Low-Energy Branch of the Super-FRS . . . 117
RESEARCH-NUSTAR-FRS-15 – Combining the in-flight particle identification with high resolution mass spectrometry at the FRS . . . 118
RESEARCH-NUSTAR-FRS-16 – Mass measurements of neutron-rich Ti isotopes with the newly commissioned multiple-reflection time-of-flight mass spectrometer at TITAN, TRIUMF . . . 119
RESEARCH-NUSTAR-FRS-17 – Status of the EXPERT experiment . . . 120
RESEARCH-NUSTAR-FRS-18 – New isotopes ^{29}Ar and ^{28,30}Cl observed during the EXPERT pilot experiment . . . 124
RESEARCH-NUSTAR-FRS-19 – Tracking cosmic radiation by the NeuRad neutron detector prototype with multi-channel readout electronics . . . 125
RESEARCH-NUSTAR-FRS-20 – Measurements of proton and matter radii of neutron-rich isotopes 126
RESEARCH-NUSTAR-FRS-21 – Charge changing cross section measurement of cobalt isotopes . 127
RESEARCH-NUSTAR-FRS-22 – Energy-dependent total charge changing cross-sections of ^{12}C . 128
RESEARCH-NUSTAR-FRS-23 – Concept of a MUSIC detector for high Z-resolution measurements 129
RESEARCH-NUSTAR-FRS-24 – Improved accuracy of the code ATIMA for energy loss of heavy ions in matter . . . 130
RESEARCH-NUSTAR-FRS-25 – Implementation of ATIMA code in the GEANT4 transport model 132
RESEARCH-NUSTAR-FRS-26 – Accurate slowing-down measurements of heavy ions in gases and solids . . . 133
RESEARCH-NUSTAR-FRS-27 – Cherenkov radiation and half-wave crystal channeling as possible new mass/charge/velocity detectors of relativistic heavy ions . . . 134
RESEARCH-NUSTAR-FRS-28 – A new modular detector design as a possible TOF detector for the Super-FRS . . . 135
RESEARCH-NUSTAR-FRS-29 – Development of the dual time-of-flight detector system for ILIMA 136
Department Gamma Spectroscopy (head and editing: Juergen Gerl) . . . 137
RESEARCH-NUSTAR-GS-1 – Fast timing with FATIMA - From vBall at ALTO to DESPEC at GSI 137
RESEARCH-NUSTAR-GS-2 – Characterization of a Sunpower CryoTel CT cooling engine for DEGAS . . . 138
RESEARCH-NUSTAR-GS-3 – First spectroscopy of neutron-rich Sc isotopes using FAIR instrumentation in the third SEASTAR campaign . . . 140
RESEARCH-NUSTAR-GS-4 – Fuzzy Bayes Tracking - Experimental performance . . . 142
RESEARCH-NUSTAR-GS-5 – Position sensitive Ge detector . . . 143
RESEARCH-NUSTAR-GS-6 – Fast-timing lifetime measurement of ^{152}Gd with FATIMA-type $LaBr_3$ detectors . . . 144
RESEARCH-NUSTAR-SHE-1 – Activities in superheavy element research at SHIP and TASCA . 145
Department Nuclear Reactions (head: Thomas Aumann, editing: Aleksandra Kelic-Heil) . . . 149
RESEARCH-NUSTAR-KR-1 – Comparison of nuclear and electromagnetic breakup of ^{17}Ne . . . 149
RESEARCH-NUSTAR-KR-2 – Hypernuclei production within the new intranuclear cascade code INCL . . . 150
RESEARCH-NUSTAR-KR-3 – Experimental campaign using the NeuLAND demonstrator at SAMURAI . . . 151
RESEARCH-NUSTAR-KR-4 – A silicon vertex tracker for the SAMURAI19 experiment at RIKEN 156
RESEARCH-NUSTAR-KR-5 – Tests of CALIFA Barrel modules at CCB in Krakow . . . 158
RESEARCH-NUSTAR-KR-6 – Response and resolution measurements of CALIFA CsI(Tl) detectors 159
RESEARCH-NUSTAR-KR-7 – PMT saturation due to large dynamic range . . . 161
RESEARCH-NUSTAR-KR-8 – The quality assurance test stand for CALIFA APDs . . . 162

RESEARCH-NUSTAR-KR-9 – First measurement of isotopic fission-fragment yields with calorimetric low-temperature detectors . . . 163

Coordination APPA (Thomas Stoehlker) 165
Department Atomic Physics (head: Thomas Stoehlker, editing: Alexandre Gumberidze) . . . 165
RESEARCH-APPA-AP-1 – Optically Transparent Penning-trap electrodes for the ARTEMIS experiment . . . 165
RESEARCH-APPA-AP-2 – A scintillator-based ion detector for CRYRING@ESR . . . 166
RESEARCH-APPA-AP-3 – Atomic computations of hyperfine coupling constants . . . 167
RESEARCH-APPA-AP-4 – Elastic scattering of twisted light by hydrogenlike ions . . . 168
RESEARCH-APPA-AP-5 – The spin-polarised electron target PEGASUS . . . 169
RESEARCH-APPA-AP-6 – A third amplifier stage in the pulse system for laser cooling of relativistic ion beams at SIS100 . . . 170
RESEARCH-APPA-AP-7 – Auger cascade calculations in krypton supporting pump-probe experiments . . . 171
RESEARCH-APPA-AP-8 – Elliptical dichroism in two-photon atomic ionization . . . 172
RESEARCH-APPA-AP-9 – Towards a quantum standard for high voltage measurements . . . 173
RESEARCH-APPA-AP-10 – Towards a solution of the hyperfine puzzle of strong-field bound state-QED . . . 174
RESEARCH-APPA-AP-11 – Highly Charged Ions at the HILITE Penning trap experiment . . . 175
RESEARCH-APPA-AP-12 – First on-line applications of the LASPEC DAQ system . . . 176
RESEARCH-APPA-AP-13 – Cooling time constant of ions stored in Penning traps . . . 177
RESEARCH-APPA-AP-14 – Precision spectroscopy using a maXs microcalorimeter . . . 178
RESEARCH-APPA-AP-15 – The Transverse Electron Target for CRYRING@ESR . . . 179
RESEARCH-APPA-AP-16 – Status of a new laser ablation ion beam source for LASPEC . . . 180
RESEARCH-APPA-AP-17 – Experimental determination of electron capture into excited states of xenon projectiles . . . 181
RESEARCH-APPA-AP-18 – Towards laser spectroscopy of Mg^+ ions at CRYRING . . . 182
RESEARCH-APPA-AP-19 – Detectors and drives for UHV particle detection in CRYRING . . . 183
RESEARCH-APPA-AP-20 – Measurements of linear polarization of radiative electron capture . . . 184
RESEARCH-APPA-AP-21 – Ground-state ionization energies of boronlike ions . . . 185
RESEARCH-APPA-AP-22 – The spectral shape of the atomic two-photon transition in He-like ions 186
RESEARCH-APPA-AP-23 – First tests of x-ray crystal optics at the S-EBIT facilities . . . 187
RESEARCH-APPA-AP-24 – Status of the data analysis from proton capture reaction measurement with a UHV compatible DSSSD . . . 188
RESEARCH-APPA-AP-25 – Progress of a variable sensitivity resonant Schottky pick-up cavity . . . 189
RESEARCH-APPA-AP-26 – Excitation of helium-like uranium in relativistic collisions . . . 190
RESEARCH-APPA-AP-27 – Mode-dependent loading of resonant pick-up cavities . . . 191
RESEARCH-APPA-AP-28 – Excitation cross sections of hydrogenlike uranium in collisions with hydrogen and nitrogen targets . . . 192
RESEARCH-APPA-AP-29 – A status report on 2D Compton polarimeter development . . . 193
RESEARCH-APPA-AP-30 – Electron capture decay of hydrogen-like ^{142}Pm ions: status of data analysis . . . 194
Department Materials Research (head and editing: Christina Trautmann) . . . 195
RESEARCH-APPA-MF-1 – Grain size effects on irradiated CeO_2, ThO_2, and UO_2 . . . 195
RESEARCH-APPA-MF-2 – Radiation-induced disordering in compressed $A_2Zr_2O_7$ (A = Nd, Sm, & Er) . . . 196
RESEARCH-APPA-MF-3 – Similar local order in disordered fluorite and aperiodic pyrochlore structures . . . 197
RESEARCH-APPA-MF-4 – Effects of single swift heavy ions on H/Si(001) studied by means of STM . . . 198
RESEARCH-APPA-MF-5 – Effect of high-energy heavy ion irradiation on the nanoscale state of promising titanium alloys and ODS steel . . . 199
RESEARCH-APPA-MF-6 – Online monitoring of stress waves induced by short-pulsed 4.8 MeV/u $^{238}U^0$ beam in polycrystalline graphite . . . 200
RESEARCH-APPA-MF-7 – Impact response of high-performance carbon-based materials . . . 201
RESEARCH-APPA-MF-8 – Figures of merit of carbon materials for high power beam intercepting devices . . . 202
RESEARCH-APPA-MF-9 – Non-homogeneous ion beam induced modification of flexible graphite along the ion range . . . 203
RESEARCH-APPA-MF-10 – Ion-induced desorption and sputtering from frozen CO layers . . . 204
RESEARCH-APPA-MF-11 – Outgassing of gold-coated copper samples . . . 205

DOI:10.15120/GSI-2017-01856

RESEARCH-APPA-MF-12 – Radiolysis of polymers: temperature effect . . . 206
RESEARCH-APPA-MF-13 – In situ small angle x-ray scattering measurements of ion tracks in poly-carbonate . . . 207
RESEARCH-APPA-MF-14 – Ion sieving using nanoporous polymeric membranes . . . 208
RESEARCH-APPA-MF-15 – Etched ion tracks in SiO_2: dependence on ion energy and etching parameters . . . 209
RESEARCH-APPA-MF-16 – The iNAPO-project: Ion-track etched nanostructures in polymers as a base for ion conducting nanochannels for molecular sensing . . . 210
RESEARCH-APPA-MF-17 – Integration of ion-track etched membranes modified by atomic layer deposi-tion in microfluidic systems for biochemical sensing . . . 211
RESEARCH-APPA-MF-18 – Selective recognition of histamine with single nanofluidic pores . . . 212
RESEARCH-APPA-MF-19 – Translocation of polystyrene nanoparticles through track-etched nanopores . . . 213
RESEARCH-APPA-MF-20 – Cu_2O nanowire arrays photocathodes synthesized by electrodepo-sition and ion-track technology . . . 214
RESEARCH-APPA-MF-21 – Micro-probing of electronic components for space and high energy physics . . . 215
Department Plasma Physics / PHELIX (head: Vincent Bagnoud, editing: Andreas Tauschwitz, Diana Lang) . . . 217
RESEARCH-APPA-PP-1 – Activity report of the Plasma Physics department . . . 217
RESEARCH-APPA-PP-2 – X-ray Phase-Contrast Imaging for Laser-induced shock-wave . . . 220
RESEARCH-APPA-PP-3 – Ultra-high magnetic field generation in curved targets: A novel ap-proach to laboratory astrophysics and laser-based applications . . . 221
RESEARCH-APPA-PP-4 – Fourier transform spectral interferometry as plasma diagnostics . . . 222
RESEARCH-APPA-PP-5 – Relativistic interaction of mid-infrared laser pulses with nanowire targets: towards a novel laser-plasma interaction regime . . . 224
RESEARCH-APPA-PP-6 – X-ray generation by laser hole boring and channelling in dense plasma 225
RESEARCH-APPA-PP-7 – A pump-probe technique for laser-driven proton beam heating to warm, dense states with the PHELIX laser . . . 226
RESEARCH-APPA-PP-8 – Upgrade of back-reflection diagnostic based on frequency-resolved optical gating at PHELIX . . . 228
RESEARCH-APPA-PP-9 – Generation and transport of heavy ion beams at LIGHT . . . 230
RESEARCH-APPA-PP-10 – Final focussing of collimated proton beams with the laser-driven LIGHT beamline . . . 232
RESEARCH-APPA-PP-11 – Emittance measurement with the pepperpot measuring method at the LIGHT beamline . . . 234
RESEARCH-APPA-PP-12 – Ion acceleration with high laser energy using variable thickness liquid crystals . . . 235
RESEARCH-APPA-PP-13 – Ion acceleration using a flattop laser beam . . . 237
RESEARCH-APPA-PP-14 – Progress on the development of an actively cooled glass amplifier at PHELIX . . . 239
RESEARCH-APPA-PP-15 – Strecher simulations for temporal laser pulse optimization . . . 240
RESEARCH-APPA-PP-16 – Characterization of hard X-ray sources for radiographic purposes at the PHELIX laser . . . 241
RESEARCH-APPA-PP-17 – Application of a TLD-based ten channel system for the spectrometry of bremsstrahlung generated by laser-matter interaction . . . 242
RESEARCH-APPA-PP-18 – Optimisation of laser based sources of electrons and gammas for backlighting of high areal density targets at FAIR . . . 243
RESEARCH-APPA-PP-19 – Investigation of proton induced demagnetisation effects in Perma-nent Magnet Quadrupoles . . . 245
RESEARCH-APPA-PP-20 – On equation-of-state measurements at the binodal in ion-beam heated matter . . . 247
RESEARCH-APPA-PP-21 – Prospects of planetary physics research using intense ion beams at FAIR . . . 249
RESEARCH-APPA-PP-22 – Investigations on laser-based neutron sources for possible applications 250
RESEARCH-APPA-PP-23 – Moderation of laser-driven neutrons for Neutron Resonance Spec-troscopy . . . 252
RESEARCH-APPA-PP-24 – Construction, characterization and optimization of a plasma window for FAIR, status update . . . 254
RESEARCH-APPA-PP-25 – Study on a dense and high ionized plasma for ion beam stripping . . . 256
RESEARCH-APPA-PP-26 – Cone compression of a pulsed plasma sheath . . . 258
RESEARCH-APPA-PP-27 – Acceleration of plasma-propelled flyer plates . . . 260

Coordination Biophysics (Michael Scholz) **263**
Department Biohysics (heads: Michael Scholz, Corinna Kausch, editing: Michael Scholz) 263
RESEARCH-APPA-HEALTH-1 – Use of TC-Tag and ReAsH as a DNA DSB Marker in CLEM . . 263
RESEARCH-APPA-HEALTH-2 – Upgrade of the fluorescence lifetime imaging microscope for the measurement of metabolic changes linked to radiation damage and repair 264
RESEARCH-APPA-HEALTH-3 – Influence of sirtuin inhibitor nicotinamide on radiation-induced DNA damage repair 265
RESEARCH-APPA-HEALTH-4 – DNA end resection is decreased in RNF138 knockout cells upon irradiation 266
RESEARCH-APPA-HEALTH-5 – Early response of human neural stem cells to ionizing radiation 267
RESEARCH-APPA-HEALTH-6 – Generation of neural stem cells for the analysis of radiation-induced impairment of neurogenesis and neuroregeneration - BrainRadiationAssay . . . 268
RESEARCH-APPA-HEALTH-7 – Characterization of the cardiac cultures generated from human embryonic stem cells with distinct differentiation protocols 269
RESEARCH-APPA-HEALTH-8 – Persistence of translocations versus dicentrics after radiotherapy 270
RESEARCH-APPA-HEALTH-9 – A new approach for spike detection in a low signal-to-noise environment 271
RESEARCH-APPA-HEALTH-10 – Characterization of glioblastoma stem-like cells 272
RESEARCH-APPA-HEALTH-11 – Effect of extrusion-based bioprinting on neurospheres 273
RESEARCH-APPA-HEALTH-12 – Effect of reduced gravity on hematopoietic stem and progenitor cells and pe-ripheral blood lymphocytes - a pilot study 274
RESEARCH-APPA-HEALTH-13 – Pharmacological augmentation of heavy ion cancer therapy . 275
RESEARCH-APPA-HEALTH-14 – Substrate specific differentiation of osteoclasts in irradiation experiments 277
RESEARCH-APPA-HEALTH-15 – Senescence and inflammation in human endothelial cells . . . 279
RESEARCH-APPA-HEALTH-16 – Exposition of a mechanical lung model to radon gas 281
RESEARCH-APPA-HEALTH-17 – Characterisation of a psoriasis model system using cells grown on plasma treated boPET-foil 283
RESEARCH-APPA-HEALTH-18 – Influence of the LET distribution on the reliability of the dose-averaged LET as predictor for relative biological effectiveness 284
RESEARCH-APPA-HEALTH-19 – Towards modelling secondary cancer induction with the local effect model 285
RESEARCH-APPA-HEALTH-20 – Effect enhancement induced by micrometer focused particle beams 286
RESEARCH-APPA-HEALTH-21 – Physical dose enhancement by Au nanoparticles under ion beam irradiation 287
RESEARCH-APPA-HEALTH-22 – Contribution of dissolved molecular oxygen to the chemical ion track evolution 288
RESEARCH-APPA-HEALTH-23 – Towards a Space-TRiP: a space radiation version of the TRiP98 code 289
RESEARCH-APPA-HEALTH-24 – Applications for proton radiography in radiation oncology . 290
RESEARCH-APPA-HEALTH-25 – Treatment planning studies with ^{16}O beams for hypoxic tumors 292
RESEARCH-APPA-HEALTH-26 – Robust treatment planning with 4D intensity modulated particle therapy for multiple targets in stage IV non-small cell lung cancer 293
RESEARCH-APPA-HEALTH-27 – Measurement of cross section data relevant for PET range verification in proton therapy 294
RESEARCH-APPA-HEALTH-28 – Beam profile measurements with the MIMOSA28 pixel detector 296
RESEARCH-APPA-HEALTH-29 – Dose build-up effects in clinical proton Bragg curves 298
RESEARCH-APPA-HEALTH-30 – Programme report on IBER18 299
RESEARCH-APPA-HEALTH-31 – Flood fill segmentation for images from time-varying computed tomography 301

Departments Theory and WTA **303**
Department Theory (head: Bengt Friman, editing: Bengt Friman, Gabriel Martinez Pinedo) 303
RESEARCH-THEORY-1 – Low mass dileptons as fireball thermometer at HADES energies . . . 303
RESEARCH-THEORY-2 – The dark matter axion mass 304
RESEARCH-THEORY-3 – Transport coefficients of quark matter from the Kubo formalism . . . 305
RESEARCH-THEORY-4 – Influence of the axial anomaly on the decay $N(1535) \to N\eta$ 306
RESEARCH-THEORY-5 – Clustering in pre-compound nuclei in the TDDFT framework 307
RESEARCH-THEORY-6 – Dilepton production in carbon-carbon collision in comparison to HADES measurements 308
RESEARCH-THEORY-7 – Lattice QCD investigation of the structure of the $a_0(980)$ meson 310

DOI:10.15120/GSI-2017-01856

RESEARCH-THEORY-8 – Nucleosynthesis in neutrino-driven supernova ejecta: Influence of variations in the astrophysical conditions and of (α,n) reaction rates . . . 311
RESEARCH-THEORY-9 – Impact of spatial correlations among the proton constituents at LHC energies . . . 312
RESEARCH-THEORY-10 – Baryon number fluctuations in chiral effective models and their phenomenological implications . . . 313
RESEARCH-THEORY-11 – S-matrix approach to thermodynamics with structureless N-body scatterings . . . 314
RESEARCH-THEORY-12 – Single electrons from open heavy-flavors in relativistic heavy-ion collisions . . . 316
RESEARCH-THEORY-13 – Foundations of the Trojan-Horse method . . . 317
RESEARCH-THEORY-14 – Visualizing velocity field strengths with hyper-surfaces in spacetime 318
RESEARCH-THEORY-15 – Parton-Hadron-Quantum-Molecular Dynamics (PHQMD) - a novel microscopic N-body transport approach for heavy-ion dynamics and hypernuclei production . . . 319
RESEARCH-THEORY-16 – Production of light r-process elements in blue kilonova . . . 320
RESEARCH-THEORY-17 – Short-range and tensor correlations in back-to-back nucleon pairs . . 321
RESEARCH-THEORY-18 – Implementation of conservation laws at transition from hydrodynamics to microscopic transport in heavy ion collisions . . . 322
Departments WTA (heads and editing: Thorsten Kollegger, Christian Schmidt) . . . 323
RESEARCH-WTA-1 – DDS: the Dynamic Deployment System . . . 323
RESEARCH-WTA-2 – New release v6.3 of data acquisition framework MBS . . . 324
RESEARCH-WTA-3 – Progress in FairDB development . . . 325
RESEARCH-WTA-4 – Status of the ALICE Tier2 Centre at GSI and first prototype of an ALICE Analysis Facility . . . 327
RESEARCH-WTA-5 – Status of the R3BRoot framework . . . 328
RESEARCH-WTA-6 – Ongoing site specific XRootD related development . . . 330
RESEARCH-WTA-7 – Annealing studies of avalanche photodiodes irradiated with different gamma doses . . . 331
RESEARCH-WTA-8 – Development of a 128 channel ≤ 500 ps RMS TDC system for MBS DAQ . 332
RESEARCH-WTA-9 – An FPGA implementation of a 128-channel sub-nanosecond time-to-digital converter . . . 333
RESEARCH-WTA-10 – Monte Carlo simulations in FairMQ . . . 334
RESEARCH-WTA-11 – Advancing shared memory transport in ALFA . . . 335

Accelerator operations (head: Mai Bai, editorial board: Giuliano Franchetti, Winfried Barth, Wolfgang Geithner, Lars Groening, Petra Schuett) 337
General Developments (editorial board: Giuliano Franchetti, Winfried Barth, Wolfgang Geithner, Lars Groening, Petra Schuett) . . . 337
ACCELERATOROPERATIONS-GENERAL-1 – A prototype for a new 108 MHz CW RFQ for the HLI . . . 337
ACCELERATOROPERATIONS-GENERAL-2 – Upgrade of the HITRAP ion trap and charge breeding system . . . 338
ACCELERATOROPERATIONS-GENERAL-3 – First beam acceleration at the heavy-ion cw-Linac Demonstrator . . . 339
ACCELERATOROPERATIONS-GENERAL-4 – New results on development of 2.7 Hz operation for heavy elements from high current ion sources . . . 340
ACCELERATOROPERATIONS-GENERAL-5 – CW LINAC Advanced Demonstrator beam dynamics investigations . . . 342
ACCELERATOROPERATIONS-GENERAL-6 – Development and upgrade of the ECRIS facility 343
ACCELERATOROPERATIONS-GENERAL-7 – Shutdown report 2017 . . . 345
Machine UNILAC (editorial board: Giuliano Franchetti, Winfried Barth, Wolfgang Geithner, Lars Groening, Petra Schuett) . . . 347
ACCELERATOROPERATIONS-UNILAC-1 – UNILAC Upgrade Activities . . . 347
ACCELERATOROPERATIONS-UNILAC-2 – UNILAC status report . . . 349
ACCELERATOROPERATIONS-UNILAC-3 – Installation of the new HSI-LEBT Quadruplet . . . 351
ACCELERATOROPERATIONS-UNILAC-4 – Site acceptance tests of the new 108 MHz, 1.8 MW power amplifier prototype and status of the RF system modernisation at the UNILAC . . 353
ACCELERATOROPERATIONS-UNILAC-5 – Status of the new post-stripper DTL . . . 355
ACCELERATOROPERATIONS-UNILAC-6 – Cavity design activities for the UNILAC . . . 356
ACCELERATOROPERATIONS-UNILAC-7 – First measurements of the short CH-Cavities for the cw heavy Ion LINAC@GSI . . . 357

ACCELERATOROPERATIONS-UNILAC-8 – Prototyping for the new post-stripper DTL 358
ACCELERATOROPERATIONS-UNILAC-9 – Brilliance and error study for the new post-stripper DTL 360
ACCELERATOROPERATIONS-UNILAC-10 – First results at the pulsed gas stripper test stand . 361
ACCELERATOROPERATIONS-UNILAC-11 – Development of an IH-type linac for the acceleration of high current heavy ion beams 363
ACCELERATOROPERATIONS-UNILAC-12 – Investigations on KONUS beam dynamics using the pre-stripper drift tube linac at GSI 364
Machine ESR (editorial board: Giuliano Franchetti, Winfried Barth, Wolfgang Geithner, Lars Groening, Petra Schuett) 367
ACCELERATOROPERATIONS-ESR-1 – Low-Level RF for the ESR Barrier-Bucket System 367
ACCELERATOROPERATIONS-ESR-2 – Selection of β-decay daughters in the ESR 368
ACCELERATOROPERATIONS-ESR-3 – Resonant dynamics of particles in presence of space charge 369
Machine HEST (editorial board: Giuliano Franchetti, Winfried Barth, Wolfgang Geithner, Lars Groening, Petra Schuett) 371
ACCELERATOROPERATIONS-HEST-1 – HEST upgrade towards beam time 2018 371
Machine CRYRING (editorial board: Giuliano Franchetti, Winfried Barth, Wolfgang Geithner, Lars Groening, Petra Schuett) 373
ACCELERATOROPERATIONS-CRYRING-1 – Beam profile measurements and observation of beam cooling at CRYRING@ESR 373
ACCELERATOROPERATIONS-CRYRING-2 – CRYRING@ESR commissioning - ions stored, cooled, accelerated 375
ACCELERATOROPERATIONS-CRYRING-3 – Investigations of different types of current coupling for the new Cryogenic Current Comparator with eXtended Dimensions (CCC-XD) 376
ACCELERATOROPERATIONS-CRYRING-4 – A fluorescence detection system for laser-spectroscopy experiments at CRYRING@ESR 377
ACCELERATOROPERATIONS-CRYRING-5 – First electron cooled beam in CRYRING after electron cooler commissioning 378
ACCELERATOROPERATIONS-CRYRING-6 – Progress on the construction of the precision high voltage divider for the electron cooler at CRYRING 380

Future accelerators for FAIR (head and editing: Joerg Blaurock) **381**
General Developments (head and editing: Joerg Blaurock) 381
FAIRPROJECT-GENERAL-1 – Overview of the status of the FAIR Project 381
FAIRPROJECT-GENERAL-2 – The FAIR Sequencer : Semi-automation in view of accelerator commissioning and operation 392
FAIRPROJECT-GENERAL-3 – Development of optical beam profile monitors 394
FAIRPROJECT-GENERAL-4 – Prototype development of a Multipurpose Hardware Unit for deterministic bunch-to-bucket transfers between synchrotrons 395
FAIRPROJECT-GENERAL-5 – Characterization of the Cryogenic Current Comparator for FAIR . 396
FAIRPROJECT-GENERAL-6 – Bunch Shape Measurements at the GSI cw-Linac prototype 397
FAIRPROJECT-GENERAL-7 – RADHARD: a program for radiation damage to materials for FAIR 398
Future accelerators SIS100/SIS18 (project head and editing: Peter Spiller) 399
FAIRPROJECT-SIS100-SIS18-1 – The SIS100 laser cooling facility 399
FAIRPROJECT-SIS100-SIS18-2 – Current status of the phase calibration of synchrotron RF reference signals 400
FAIRPROJECT-SIS100-SIS18-3 – Fluorescence detector concept for laser cooling at the SIS100 . . 401
FAIRPROJECT-SIS100-SIS18-4 – Tuning rules for the digital filters of the SIS 100 longitudinal feedback system 402
FAIRPROJECT-SIS100-SIS18-5 – FLUKA/ANSYS study of the APPA beam dump for BIO-MAT experiment 403
FAIRPROJECT-SIS100-SIS18-6 – FLUKA/ANSYS study of the APPA beam dump for plasma physics experiment 404
FAIRPROJECT-SIS100-SIS18-7 – Exploitation of circulant symmetry in SIS18 orbit response matrix 405
FAIRPROJECT-SIS100-SIS18-8 – SIS100 Inspection robot - lane keeping and curved pipes 406
FAIRPROJECT-SIS100-SIS18-9 – Commissioning of the beam induced fluorescence monitor for the CERN e-lens 407
FAIRPROJECT-SIS100-SIS18-10 – Closed orbit feedback system for GSI SIS18 synchrotron 408
FAIRPROJECT-SIS100-SIS18-11 – Beamloading effects and their influence on cavity detuning in multi-cavity operation in SIS100 409
FAIRPROJECT-SIS100-SIS18-12 – Signal processing hardware for single-bunch manipulation . . 410

DOI:10.15120/GSI-2017-01856

Future accelerators Super-FRS (project head and editing: Haik Simon) . . . 411
FAIRPROJECT-SUPERFRS-1 – Developments and results of Dry-Runs at the fragmentseparator FRS . . . 411
FAIRPROJECT-SUPERFRS-2 – Recent developments for controls at the superconducting fragmentseparator S-FRS in the LHC software architecture LSA . . . 412
FAIRPROJECT-SUPERFRS-3 – Super-FRS design status report . . . 414
FAIRPROJECT-SUPERFRS-4 – Low cost interface for remote handling of insertions at the Super-FRS 416
FAIRPROJECT-SUPERFRS-5 – Design verification tests of the Super-FRS slit system . . . 417
FAIRPROJECT-SUPERFRS-6 – Tests of a SEETRAM prototype for the Super-FRS . . . 418
Future accelerators pLinac and pbar-target (project head and editing: Klaus Knie) . . . 419
FAIRPROJECT-PLINAC-1 – Status of the modulated 3 MeV 325 MHz Ladder-RFQ . . . 419
FAIRPROJECT-PLINAC-2 – Status of high power components for the FAIR Proton Linac RF systems . . . 420
FAIRPROJECT-PLINAC-3 – Commissioning of the proton injector for FAIR at CEA/Saclay . . . 421

Annex **423**
Lists and Organigram . . . 423
ANNEX-1 – Publications and dissertations in 2017 . . . 423
ANNEX-2 – Statutory organs and scientific advisory committees (2017) . . . 449
ANNEX-3 – GSI and FAIR organigram . . . 453

DOI:10.15120/GSI-2017-01856

Status of the Compressed Baryonic Matter (CBM) experiment at FAIR

N. Herrmann[1], for the CBM collaboration

[1]Physikalisches Institut, Univ. Heidelberg, Heidelberg, Germany

The exploration of the QCD phase diagram in the region of high baryon densities is the primary goal of the physics program of the Compressed Baryonic Matter (CBM) experiment at FAIR.

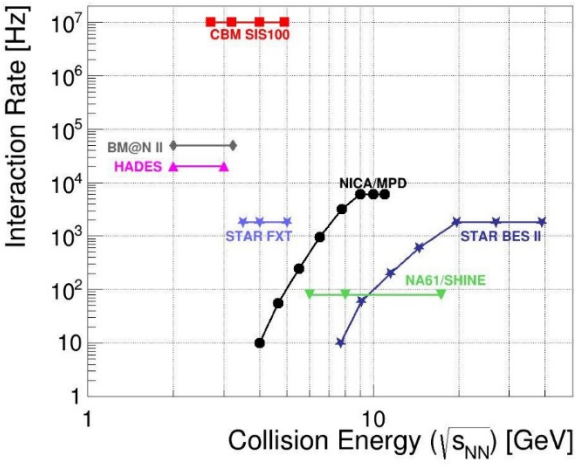


Figure 1: Rate capabilities as function of collision energy of existing experiments and experiments under construction.

In order to make substantial progress beyond existing data and currently running experiments the CBM experiment is designed to be operated at extremely high reaction rates of up to 10 MHz. This unprecedented rate capability allows to perform unique systematic measurements of multi-differential observables and at the same time the measurement of rare diagnostic probes. Figure 1 depicts a comparison of the interaction rates of existing and future heavy-ion experiments as function of collision energy.

The planned experimental setup shown in Fig. 2 is designed to address all observables that are currently employed in our research field to quantify QCD matter properties. Towards that goal CBM can be operated in various configurations, most notably two different base configurations are being prepared: i) the electron - hadron setup that allows the simultaneous measurement of electrons, positrons and charged hadrons, including all mother particles that have decay branches into these particles, and ii) the muon setup that focusses on the measurement of dimuon pairs originating from vector mesons including charmonium and the continuum exhibiting the same quantum numbers.

The key for high-rate operation are fast and radiation hard detectors, and a data acquisition and analysis concept that allows to enhance the rare probes to the level of significant results while keeping and characterising the accompanying features of the surrounding bulk matter. This will be achieved by a system without a traditional hardware based trigger system. All data items from the sensors will receive a time stamp and will be forwarded by the DAQ system in the so-called free streaming mode to a high performance computing cluster where event building and event selection occurs in real time.

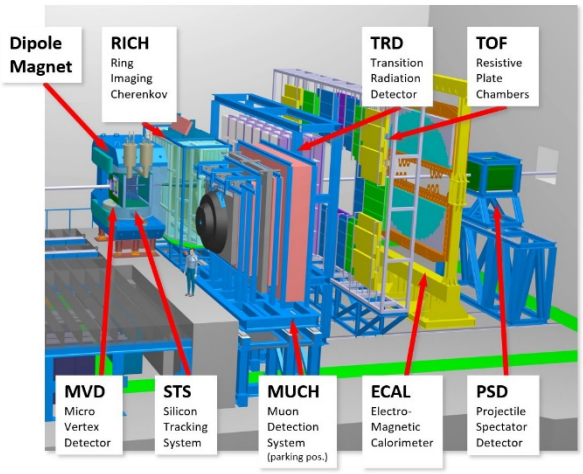


Figure 2: Overview of the CBM experimental setup. The experiment comprises high precision tracking by the MVD and STS detector systems in the magnetic field of a superconducting dipole magnet, event characterisation by a projectile spectator calorimeter (PSD) combined with two different detector arrangements for particle identification. Shown is the electron hadron setup in measuring and the muon setup in waiting position. For further details, see text.

The overall timeline for the construction and installation of the CBM experiment was adapted to the new FAIR baseline planning with the major milestones:

Dec 2021 - CBM building ready for infrastructural installations

Dec 2022 - CBM building ready for installation of components

Jun 2024 - First commissioning beam from SIS100 In the following recent developments of the overall CBM concept and its realisation are highlighted.

Detectors

On the detector side the Technical Design Report (TDR) for the last missing major component with large production time demands, the Transition Radiation Detector (TRD) was completed in 2017 and submitted to the FAIR ECE. A system of 4 layers of TRD chambers is

proposed that was shown to be efficient for achieving the physics goals:

i) electron - pion separation with a pion suppression factor of 20 at 90% electron efficiency in the momentum range beyond 5 GeV/c and ii) separation of nuclear charges e.g. for distinguishing deuterons from α - particles.

All other detector systems are as well on track to meet the FAIR timeline presented above.

Data Processing System

CBM is developing a high throughput data acquisition system that is based on the GBTx frontend ASIC developed at CERN. During the past year this system got further refined by shifting the long distance data transport task to commercial (Infiniband) components. Thus the former data processing board (DPB) and the FLES interface board are merged into a new component, the Common Readout Interface (CRI). The layout of the data processing system is shown in Fig.3.

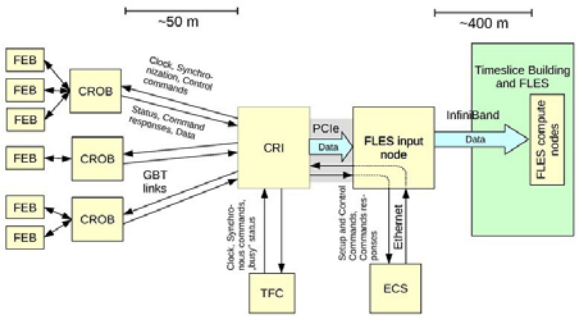


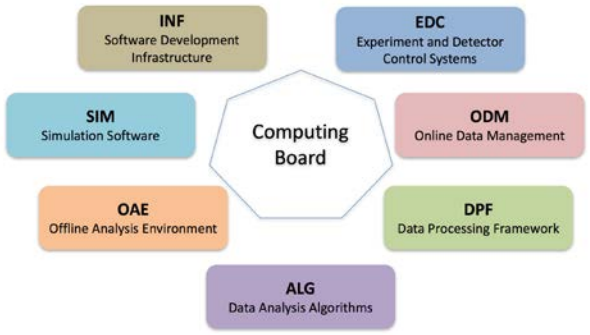
Figure 3: Schematics of the CBM data acquisition and pro- cessing system. Acronyms: FEB - Front End Board, CROB

- Common Readout Board, CRI - Common Readout Interface, TFC - Timing & Fast Control, ECS - Experiment Control System, FLES - First Level Event Selector

The CRIs will be placed into FLES input nodes that are part of the CBM experimental setup and are located in the counting house of CBM. The interface to the Online compute farm housed in the GreenCube of GSI/FAIR will be provided by a high performance Infiniband switch.

Computing

The execution of a high rate experiment like CBM that implements all data selection steps in software requires a software framework that is flexible, scalable and makes use of the latest hardware development. In order to accommodate the various tasks the computing effort within CBM was restructured and a Computing Board (COB) was installed.



Further details can be found in the corresponding chapter of this report.

Physics Performance

The physics goals of CBM encompass all relevant observables for studying the QCD equation of state, the signals for a possible phase transition, investigation of a possible critical point, chiral symmetry restoration at large baryon chemical potential and the search for rare (quasi) bound states of QCD. These observables are described in detail in the recent CBM publication [1].

The evaluation of the physics capabilities of the CBM experiment is being continued and extended e.g. with detailed studies of the reconstruction of neutral pions, weak decays with neutral daughter particles and evaluation of the accuracy of directed flow measurements.

FAIR Phase-0 Program

Due to the delay of the overall FAIR completion FAIR council has endorsed the usage of CBM detector components and the participation in running experiments, especially at the GSI site making use of the beams available from the SIS18 synchrotron.

Currently CBM groups are pursuing the following projects within the framework of FAIR phase-0:

1) Participate in the HADES experiment at SIS18 by providing an enhanced performance of the HADES RICH detector by employing a readout with CBM owned MAPMT photo sensors.

2) Participate in the Beam Energy Scan II (BES-II) campaign of the STAR experiment at the RHIC at BNL, USA by installing 10% of the final CBM - TOF modules as endcap time-of-flight system, significantly extending the phase space coverage of the experiment. [2]. In addition, CBM high performance tracking software will be used for elaborating efficient data processing.

3) Participate in the BM@N experiment at the Nuclotron accelerator of JINR with the installation of 4 STS tracking

DOI:10.15120/GR-2018-1

stations in order to enhance the momentum resolution of the setup and with the PSD detector for better event characterization.

4) Install and operate a CBM test facility (mCBM) at the SIS18 accelerator of GSI in order to develop and verify the full data acquisition and analysis chain of the CBM experiment (see next section).

The FAIR phase-0 programs will be terminated at latest in 2023, afterwards shifting the core activities to the preparation of running at SIS100. The experience gained during the phase-0 program will certainly help to minimize the commissioning time needed to get full CBM online.

mCBM

mCBM is a test installation of CBM in order to evaluate the performance of detector and data acquisition and analysis components for their full functionality under realistic load conditions at the SIS18 accelerator of GSI [3]. The conceptual design of the experiment is shown in Fig.5.

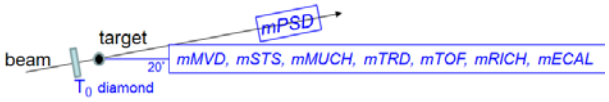


Figure 5: Conceptual layout of the mCBM experiment

mCBM is designed to explore the rate capability of all detector components arranged in a telescope like. Prototype and preproduction modules of MVD, STS, MUCH, TRD, TOF, RICH and ECAL will be placed under a scattering angle of about 20◦ with respect to the beam direction. In addition, one module of the PSD will be placed under the primary beam pipe at an angle of 5 degrees with respect to the beam direction. All detectors will be read out by a common triggerless data acquisition system. A dedicated link into the GreenIT cube to a mFLES cluster will be provided to exercise data transport and analysis.

The experiment is being prepared in the HTD area of the SIS18 experimental hall. No magnetic field will be available at the target spot.

One of the goals of mCBM is the validation of the CBM analysis concept that has to perform under real time conditions. The performance can and will be evaluated ma- king use of (sub)threshold Λ - baryon production in Ni + Ni (1.93A GeV) and Au + Au (1.24A GeV) collisions with cross sections available in literature. However, the unique and distinguishing feature of CBM, that has been worked out in the context of the proposal [3], is that spectra like the ones shown in Fig.7 have to be accumulated within 10s beam on target.

This report is also part of the CBM Progress Report 2017 (doi:10.15120/GSI-2018-00485)

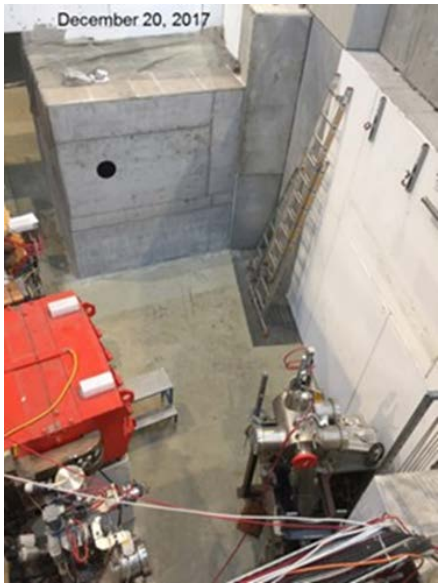


Figure 6: Cave of the mCBM experiment. A new beam dump surrounding the nominal beam position visible as a black circle had to be designed and constructed to enable the planned beam particle flux of 108 Au - ions per second at the highest SIS18 energy.

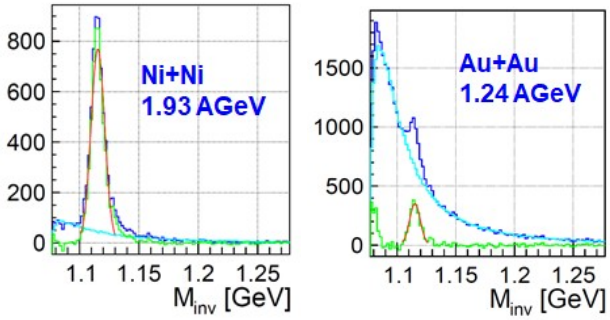


Figure 7: Benchmark observables for the mCBM experiment.

References

[1] T. Ablyazimov et al. (CBM Collaboration), “Challenges in QCD matter physics - The scientific programme of the Compressed Baryonic Matter experiment at FAIR”, Eur.Phys.J. A53 (2017) 60

[2] STAR and CBM - eTOF collaboration, “Physics Program for the STAR/CBM eTOF Upgrade”, arXiv:1609.05102v1 [nucl- ex]

[3] https://cbm-wiki.gsi.de/foswiki/bin/view/Public/Documents#mcbm 45proposal2GPAC 45fullVersion.pdf

Experiment beamline: SIS18-CaveC
Experiment collaboration: CBM
Experiment proposal: S471
Accelerator infrastructure: SIS18 / SIS100 / RHIC / Nuclotron
PSP codes: 1.1.1

Grants: see individual contributions
Strategic university co-operation with: Darmstadt / Frankfurt-M / Gießen / Heidelberg

 DOI:10.15120/GR-2018-1

The superconducting dipole magnet of the CBM experiment

P. Senger and the CBM collaboration

GSI, Darmstadt, Germany;

Magnet parameters

The magnet has a free aperture of 1.44 m vertically and 3.0 m horizontally in order to accommodate the STS detector system with a polar angle acceptance of 25 degrees and a horizontal acceptance of 30 degrees. The total length of the magnet is 1.5 m. The maximum magnetic field in the center of the magnet is 1.08 T, and the field integral within STS detector is BxL = 1.004 Tm. The fringe field downstream the magnet has values of the order of 50 to 100 Gauss at a distance of 1.6 m from the target at the position of the first RICH detector box. The field clamps are dismountable for the MUCH. The magnet can be operated as both polarities. The magnet is of the H-type with a warm iron yoke/pole and cylindrical superconducting coils. The wire has Nb-Ti filaments embedded into a copper matrix with a total Cu/SC ratio of about 7.1. The operating current and the maximal magnetic field in the coils are 686 A and 3.9 T, respectively. The coil case is made of stainless steel. The vertical force in the coils is about 250 tons. The cold mass is suspended from the room temperature vacuum vessel by six suspension links. Six cylindrical support struts compensate the vertical forces. The energy stored in the magnet is about 5 MJ.

Magnet design

The 3D magnetic field calculations were made with the Mermaid code, whereas the forces on the coils and the poles were calculated with the ANSYS 2D model. It was found that the calculated stresses in the coil structure and inside the windings are found to be well below acceptable stresses in stainless steel, copper, and the NbTi superconductor. The cross section of the iron yoke is shown in figure 1. The iron yoke serves as a construction frame for the magnet and systems of the detector. The total mass of the iron yoke is about 140 tons. It has special tools for adjusting its position in all directions. The yoke is assembled of iron blocks having masses in the range between 3 and 13.6 tons. The magnet comprises two separated superconducting coils symmetrically placed close at the top and bottom blocks of the iron yoke. The coils are placed around the cylindrical pole shoes of the magnet.

The lower coil is shown in figure 2. The main components of the coils are superconducting cables, the copper and the stainless steel cases. The copper case has a U-shape profile, and will serve as a bobbin during a winding procedure of the coil. The stainless steel case will be assembled around the copper case after finishing of the winding procedure. The parts of the stainless steel case will be bolted together. Each coil will be made of two pieces of superconducting cable each with a length of about 4.5 km. The splicing will be made during a winding procedure of one coil using soft soldering on a base of Sn-Ag alloy. The coils will cooled indirectly by a flow of liquid helium at 4.5 K through a tube which has an internal diameter 16 mm and wall thickness 2 mm. These tubes will be imbedded in the copper case such that the exit end of the tube is placed at a higher position than the inlet end of the tube (see figure 2). In this case the helium bubbles will accelerate the total helium flow along the tubes. If necessary, this thermosyphon cooling concept can be improved by additional heaters at the outlet of the tubes. The design includes the complete cryogenic system including the branch box, helium transfer line, the cryostat and the feed boxes, as well as the power supply and the quench detection and protection system. The magnet will be built by the Budker-Institute for Nuclear Physics (BINP) in Novosibirsk.

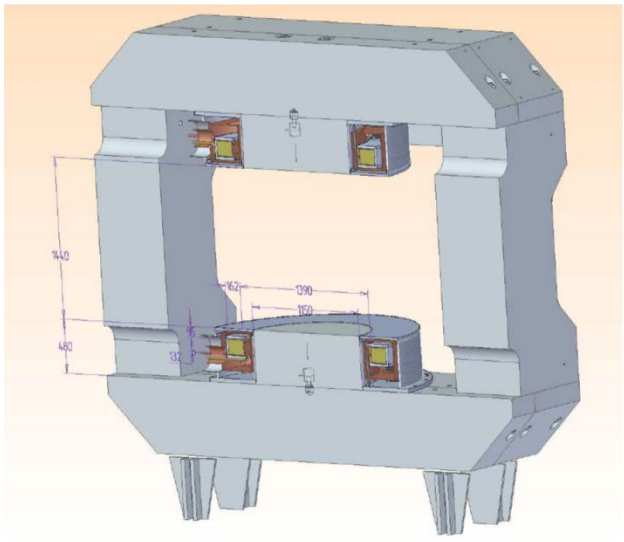


Figure 1: Cross section of the CBM superconducting dipole magnet.

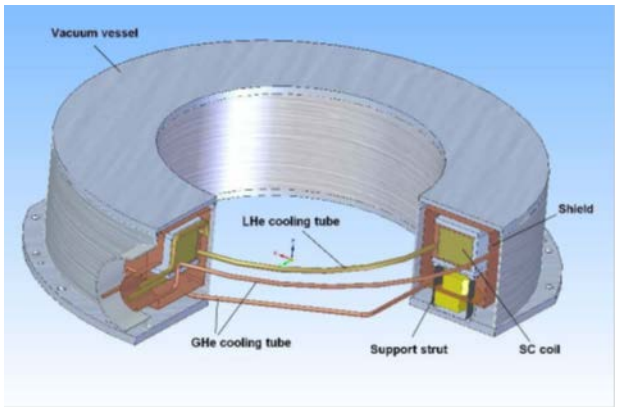


Figure 2: Total view of the lower coil of the CBM magnet (for explanation see text).

DOI:10.15120/GR-2018-1

CBM Micro Vertex Detector - Summary

C. Müntz, J. Stroth, and the CBM MVD working group

Goethe University Frankfurt, Germany; GSI, Darmstadt, Germany

The R&D carried out by the MVD team in 2017 focused on the design of the next generation pixel sensor MIMO- SIS and a review of the detector geometry. Moreover, the detector integration and slow control was studied in a dedicated research program. Radiation tolerance studies aimed to enable MAPS to resist the excessive radiation levels considered for a future MVD detector upgrade.

Sensor R&D and detector geometry review

Given the progress in sensor technology, is has recently decided to abandon the rolling shutter readout and to equip the MAPS sensors for CBM with the faster priority encoder readout, which was previously developed for the ALICE APIDE sensor. Among the benefits of the technology choice is an acceleration of the time resolution of the sensor by one order of magnitude, which turns into a proportional decrease of the detector occupancy and easier event reconstruction. Despite of this benefit, ALPIDE does not reach the radiation tolerance and data bandwidth needed for CBM. Therefore, a dedicated CBM sensor named MI- MOSIS is being developed. A first small size detector prototype MIMOSIS-0, which integrates updated pixel cells and priority encoders was designed at the IPHC Strasbourg and fabricated in 2017. Moreover, a dedicated test bench has been build. The necessary sensor tests will be carried out at the Goethe University Frankfurt and the IPHC Strasbourg in 2018.

The novel MIMOSIS sensor is projected to show different dimensions than the previously considered design. Therefore, an update of the MVD geometry and of the related simulation model was required. The updated model was build based on new scripting tools for CbmRoot. Two geometries, one optimized for vertexing and one optimized for low momentum tracking, were generated and their tracking performance was simulated. Preliminary results suggest that the tracking geometry provides indeed an improved tracking performance, namely in case the field of the CBM dipole magnet is reduced below its maximum intensity.

Sensor Integration and slow control

The integration of sensor into a full detector station was studied with the ”PRESTO” (PRototype of thE Second sTatiOn) prototype. The assembling of the prototype, which is formed from a TPG support holding two layers of MIMOSA-26 sensor, dedicated flex print cables and a TRBv3-based readout, has been completed.

The resulting sensor integration yield after sensor assembly is, though based on very limited statistics, not yet satisfactory. The wire bonding quality was excluded to cause the observed yield. Instead, ESD issues due to possibly low relative humidity during assembly in our laboratory are considered as origin of the observed sensor malfunction. At present, corrective measures are being implemented. Here- after, a second PRESTO module will be assembled in the hope to obtain a significantly improved integration yield.

The existing prototype is now being used as a test system for validating thermal management concept and the vacuum compatibility of the device. Doing long term in-vacuum tests requires to equip the prototype with robust slow control and protection system. A suited system based on EPICS was designed, implemented and commissioned.

Radiation Hardness

While the tolerance of present MAPS to non-ionizing radiation is sufficient to match the requirements of the CBM MVD, only few safety margin is remaining. Therefore, and in the prospective of a future MVD upgrade, options for a further improvement of this radiation tolerance was studied. The strategy consisted in fully depleting the active volume of the sensor, which was previously shown to improve the charge collection efficiency of the damaged device decisively. However, intense cooling was required to operate the irradiated sensors, which was initially not understood. Studies carried out in 2017 revealed that in- creasing the depleted zone of the photo diodes of the sensors comes with draw backs in terms of increased leakage currents, which were compensated by the cooling. An alternative solution to handle this issue suggests employing a faster shaping/readout mechanism, which is in any case required for a potential detector upgrade. Studying this effect more quantitatively is considered to provide valuable guidance for the next steps of sensor R&D.

This report is also part of the CBM Progress Report 2017 (doi:10.15120/GSI-2018-00485)

Experiment beamline: mCBM@SIS18
Experiment collaboration: CBM
Experiment proposal: S471
Accelerator infrastructure: SIS18 / SIS100
PSP codes: 1.1.1
Grants: BMBF 05P16VTFC1
Strategic university co-operation with: Frankfurt-M

Status of the Silicon Tracking System

H. R. Schmidt[1,2], J. M. Heuser[2], K. Agarwal[1], O. Bertini[2], A. Chaus[3], S. Das[1], M. Dogan[2,4], U. Frankenfeld[2], E. Friske[1], J. Hoffmann[2], M. Kis[2], K. Koch[2], P. Koczon[2], E. Lavrik[1], J. Lehnert[2], A. Lymanets[2], H. Malygina[2,6], O. Maragoto Rodriguez[2,6], S. Mehta[1,2], I. Momot[2,6], I. Panasenko[1,3], V. Pugatch[3], A. Rodriguez Rodriguez[2,6], Ch. Schmidt[2], C. Simons[2], M. Teklishyn[5], R. Visinka[2], O. Vasylyev[2], A. Weis[2], A. Wilms[2] for the CBM Collaboration

[1]Universität Tübingen, Germany, [2]GSI, Darmstadt, Germany, [3]KINR, Kiev, Ukraine, [4]Istanbul University, Turkey, [5]FAIR, Darmstadt, Germany, [6]Universität Frankfurt, IKF, Germany

The Silicon Tracking System (STS) of the CBM experiment will provide standalone charged-particle trajectory measurement and associated momentum determination, thus being the key detector in any phase of the CBM physics program, from the beginning of operation.

In this chapter of the Scientific Report, the STS work group teams from Germany, Poland, Russia and Ukraine give a cross section of the achievements made in the last year in the various fields of activities. On the chapter's title page, the depicted "mini STS" set-up for operation in the precurser project mCBM@SIS18 illustrates that the finalizing developments move from the component level to prototyping composite structures and their application in demonstration systems, prior to the start of series production of the CBM-STS parts after a number of readiness reviews in 2018.

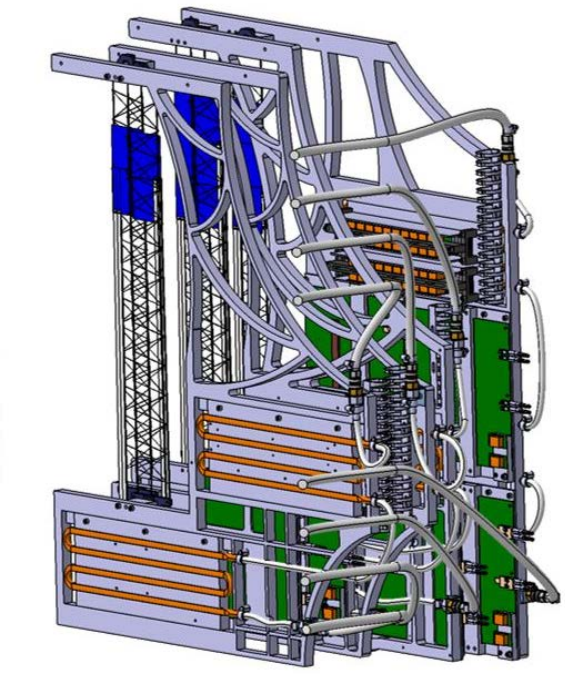


Figure 1: Sketch of the mSTS set-up planned for operation in the pre-curser project mCBM@SIS18.

The CBM Silicon Tracking System

The STS detector has been laid out to achieve the track reconstruction task (beam-target interaction rates up to 10 MHz, charged track multiplicities up to 700 per central Au+Au collision, momentum resolution of $dp/p \approx 1.8\%$, detection of strangeness by in-flight decays) with eight low-mass tracking layers in a 1 Tm dipole magnetic field covering the CBM aperture of $2.5^\circ < \theta < 25^\circ$, corresponding to rapidities ranging from mid rapidity to close to beam rapidity. The sensor technology is based on double-sided silicon wafers with microstrip segmentation. The readout strip pitch of 58 μm under 7.5° stereo angle realizes single-hit resolution of about 25 μm. The read-out is based on self-triggering front-end electronics streaming time-stamped data to a computing farm for on-line hit sorting, track identification, event forming and analysis. To minimize material budget in the acceptance region, the STS has been designed such that front-end read-out electronics, cooling and mechanical infrastructure are located outside of the physics acceptance. The detector modules employ ultra-thin microcables for separating those from the sensors. Four sensor variants (6.2 cm wide, 1024 strips per side, and 2.2/4.2/6.2/12.4 cm long, with the corresponding strip lengths matched to the hit densities at their respective positions) and different microcables up to 50 cm lengths result in 18 module variants to be constructed, 896 modules total. Eight or ten modules are integrated onto a detector ladder. The STS will comprise 106 detector ladders that are mounted on 18 mechanical units within the STS space frame, forming the tracking stations. The modules and ladders for the 4 upstream tracking stations are to be assembled at JINR VB-LEHP, those for the 4 downstream stations at GSI, where also the system assembly will be done. The detector's front-end and powering electronics will dissipate about 40 kW of power. Efficient heat removal through cooling plates circulating bi-phase CO_2 will be applied. The sensors will be operated at up to 500 V bias, at a temperature of around -5 °C to limit radiation damage induced leakage currents from the integrated lifetime fluence of up to 1×10^{14} cm^{-2} 1-MeV neutron equivalent in the regions close to the beam axis. The STS will thus be housed in a thermally insulating enclosure, incorporating feed-throughs for low and high voltage supply, optical and control links. A section of the vacuum beam pipe will cross the detector, made from 0.5 mm thick carbon fiber/foil layers, attaching to the target vacuum box on the beam upstream side and to

the downstream STS wall with further connection towards the RICH or MUCH detectors.

Progress with silicon microstrip sensor

The final prototypes of the STS silicon microstrip sensors have been developed. The four main variants with strip lengths matched to particle densities in the STS and the layout optimized for module assembly have been produced in small series with two vendors (CiS, Erfurt, Germany; Hamamatsu, Japan). The technical specifications and quality criteria are fixed. Radiation tolerance has been demonstrated in various tests on specimen irradiated up to twice the lifetime fluence. An internal sensor review was held in March, 2017, covering all aspects of required specifications, their realization, performance, quality assurance, capabilities of vendors. One open work item was identified: the demonstration of sensor performance (charge collection, signal-to-noise ratio, efficiency for track finding) in a realistic prototype module structure with the sensor tab-bonded to microcables and STS-XYTERv2.0 ASIC. This test took place in the in-beam test at COSY in February 2018. The production readiness review is planned for April 2018 and the call for tender in the second quarter of 2018

Progress with module assembly

The assembly of sensors, microcables and front-end electronics boards into the basic building block of the STS, the detector module, has been developed. The workflow for the double-sided handling has been established, assembly tools have been designed and manufactured, last improvements are being made for the modules to be assembled for the mSTS in 2018. The production site at GSI is equipped and ready for production. Likewise, at JINR where the module assembly with two daisy-chained sensors replacing the largest prototype has been studied. The specifications for the microcables with aluminum traces are almost fixed. Microcables with Copper traces have been ordered in industry and will be tested as an alternative. An internal production review is planned for July 2018.

Progress with ladder assembly

Ladders are the mechanical assemblies of detector modules onto carbon fiber support structures that will be attached to the mechanical units. Carbon fiber prototype structures with varying specifications have been produced with two companies in Germany and Switzerland; a third producer is to be tried. A work flow for ladder assembly has been established at GSI and the required module placement precision ± 35 μm demonstrated, using an optical survey machine installed there. The next iteration of the tools will address the ladders to be produced for mSTS. An internal review on ladder assembly will be held jointly with the module assembly review in July 2018.

Progress with front-end and read-out electronics

In preparation of the final STS front-end chip, STS-XYTERv2.1, detailed studies of the prototype v2.0 have been carried out. For the first time, hundreds of ASICs have been screened and the high production yield determined. Detailed insight into the performance of the analog and digital building blocks has been gained through dedicated measurements. Particular focus has been put on understanding the different loads and their influence on noise. Several substantial modifications to the analog front-end and to the digital back-end will be implemented for the submission in 2018. A first prototype of the front-end board holding 8 ASICs has been designed and produced at GSI. In a module, a left and a right-handed version are required. The prototypes are required for the mSTS modules in 2018. For the read-out of the FEB-8, the GBT protocol has to be used. A first prototype of the read-out board ("Common ReadOut Board", CROB) with GBTX ASICs and VersatileLink optical modules is under test. A prototype link cable for the transmission of data from the front-end to the read-out board has been produced and tested.

Progress with system integration and mSTS demonstrator

The system integration team has addressed various aspects of this wide topic. The STS CAD model is already quite detailed. Its finalization is ongoing, starting with a final confirmation of the sensor positions in a physics performance simulation study and subsequent freezing of all details of the module and ladder variants as well as the detailed dimensions of the mechanical units. A mechanical demonstrator of a quarter C-frame has been finished, allowing decisions regarding ladder mounting technology, mechanical precision, ladder installation, cabling in the detector. The routing of cables from the detector to the supplies in the CBM cave has been addressed. A cooling demonstrator under study addresses the feed-through panels in the thermal wall for HV/LV/data/control links, thermal interfaces for efficient cooling of the electronics, and cooling of the sensors. A first prototype of the STS beam pipe section has been produced and awaits vacuum stability tests. Simulation studies address detector alignment based on tracks to achieve higher-than-intrinsic mechanical precision of sensor positioning for physics measurements. Several aspects of system integration, as well as detector module operation and read-out ASIC performance, are to be demonstrated before production readiness with the "mini STS" (mSTS) in the "mini CBM" (mCBM) set-up. The primary purpose of mCBM is to prove data transport/event building in technical runs in 2018/2019, with potentially further physics runs in 2020/2021. As this requires realistic input from prototype CBM detector systems ("sectors"), the mSTS has been conceived, implementing two small tracking stations with two and three ladders (four and nine modules), on a somewhat simplified mechanical structure. Electronics cooling will be implemented and tested but the sensors will be operated non-cooled at ambient temperature as the radiation load will be non-critical. The mSTS specifications have been frozen and the design is close

 DOI:10.15120/GR-2018-1

to full detailing. Production of the components will start in March 2018

STS project plan

A detailed STS project plan has been established from the current pre-production phase, over test-experiments, production readiness reviews in 2018, the construction phase from 2019 to 2022 and readiness for STS installation into the CBM cave in 2023. It comprises milestones and is an official planning document within the FAIR project. The planning has been matched with a detailed cost assessment and spending profile, backed up by contracts between the participating project partners.

This report is also part of the CBM Progress Report 2017 (doi:10.15120/GSI-2018-00485)

Experiment beamline: mCBM@SIS18
Experiment collaboration: CBM
Experiment proposal: S471
Accelerator infrastructure: SIS18 / SIS100
PSP codes: 1.1.1
Grants: BMBF 05P16VTFC1
Strategic university co-operation with: Frankfurt-M

stsDPB firmware development - preparations for CRI

W.Zabołotny[1], A.Byszuk[1], M.Gumiński[1], G.Kasprowicz[1], K.Poźniak[1], R.Romaniuk[1]

[1]Institute of Electronic Systems, Warsaw University of Technology, Warszawa, Poland

New functionalities in the tester firmware

The firmware for the tester of MUCH-STS-XYTER 2 (SMX2) ASIC was further developed.

The implementation of the GBTX-based access to the SMX2 chip required serious rework of the SMX2 controller core. The GBT-IC/EC controller was delivered by the CERN GBT team and was integrated with the tester firmware. That allowed control of the phase of downlink clocks and delay of the uplink data via the optical link. Successful synchronization of e-Links and transmission of data was achieved. However, the I2C access to the GBTX chip is still needed for its initial configuration[1].

The support of ``time deterministic'' commands, needed for proper synchronization of the front-end ASICS has been added to the tester firmware and successfully tested.

Development of the stsDPB firmware

Even though the final solution for the CBM readout will be the Common Readout Interface (CRI) board, the Data Processing Boards (DPBs) are needed for development and test purposes. Therefore, the functionalities tested in the tester firmware were integrated into the stsDPB firmware initially developed by Junfeng Yang. Additionally, some new functionalities have been implemented directly in that firmware.

The tester firmware supports only a single SMX2. In the stsDPB, it was required to add support for multiple SMX2 chips.

That resulted in the reorganization of the firmware, modification of the block used to generate the phase-shifted downlink clocks, and modification of the Python procedures so that adjustment of one downlink does not corrupt state of the SMX2 ASICs connected to other downlinks. In particular, the downlink transmitter had to be completely stopped when the clock phase was adjusted. The Python procedures have also been refactored and supplemented with extensive logging functionalities.

Another task was the integration of the FLIM module with the stsDPB firmware. New functions for sorting and splitting the received data into microslices were added. A dedicated sorting system [1], shown in figure 1, was developed to merge multiple streams of sorted 32-bit data into a sorted output stream of 32-bit data at 320 MHz, without a necessity to operate complex sorters at so high clock frequency. The final sorter-merger performs the

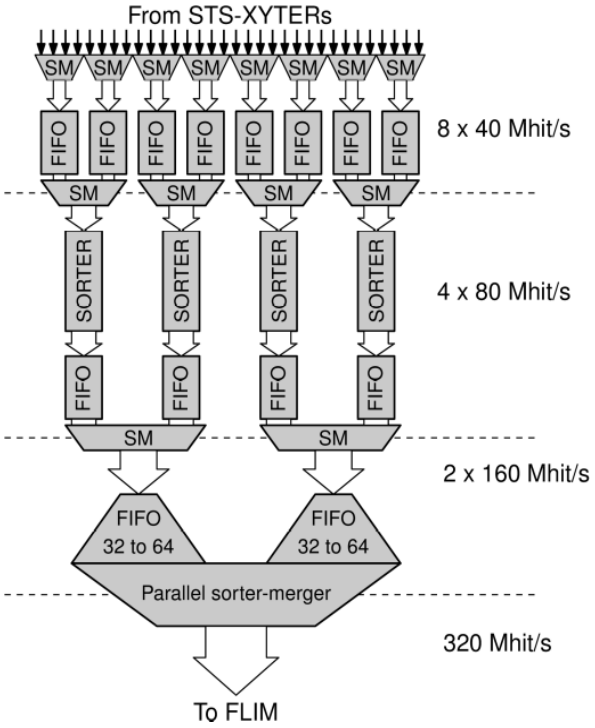


Figure 1: Structure of the data concentration system developed for stsDPB (SM - simple mergers).

comparison of 4 data words in parallel, selecting two oldest in a single 160 MHz clock cycle, producing the sorted stream of 32-bits words at 320 MHz.

The sorted data stream is split into Micro Slices and send via FLIM module to FLES.

Preparation for CRI

As a preparatory step for the development of the CRI boards, a review of available hardware solutions for the PCIe-based readout system was performed [2]. The results of this review allowed defining the viable configurations of the CRI boards and contributed to selection of the HTG-Z920 board as the first prototype of the CRI board.

1 The initial configuration of the GBTX provides settings needed to establish the connection via the optical GBT link. In the final setup the initial configuration will be read from e-Fuses. Because programming of e-Fuses is an irreversible operation, they could not be used at the development stage.

 DOI:10.15120/GR-2018-1

References

[1] M. Gumiński, “High-speed concentration of sorted data streams for HEP experiments”, presentation at Nica Days 2017

[2] W.M. Zabolotny et al., “Selection of hardware platform for CBM Common Readout Interface”, Proc. SPIE 10445 (2017) 1044549, doi:10.1117/12.2280938

Experiment beamline: none
Experiment collaboration: CBM
Experiment proposal: none
Accelerator infrastructure: none
PSP codes: none
Grants: Agreement between GSI and WUT “Development and implementation of a readout and control protocol between STS-XYTER and further data processing FPGA-based electronics for FAIR”
Strategic university co-operation with: none

Data transmission line for STS detector readout system

P.Koczon, J.Hoffmann[1], M.Kis, K.Koch[1], C.J.Schmidt, A.Weis

for the CBM collaboration FAIR@GSI and RBDL

[1] EEL GSI, Darmstadt, Germany

The silicon tracking detector STS for the CBM experiment @ FAIR/GSI in Darmstadt will consist of 900 double sided strip sensors and will register up to 10^7 events/sec of average multiplicity of 350. It will produce about 1 TB/s of data which has to be collected from 14000 front end ASICs (CBMxyter [1]) by a readout system based on the GBTx chip set [2]. The chips' specifications impose certain requirements on the quality of the data link between CBMxyter and GBTx which is proven for the concrete hardware realization in this work.

Test system for the link cable

The cable projected for the data transfer (Sumimoto Electric Interconnect) consists of 20 pairs of LVDS links and is 800 mm long and 20.5 mm wide. It has a strip pitch of 0.5 mm. These parameters were chosen to fulfil the STS@CBM specifications. Links are placed on one surface of a polyester supporting tape and shielded with aluminium foil along the entire length. The shielding can be grounded via extra pads at the cable ends. The cable ends are equipped with stiffening SUMI-CARDS fitting into 0.5 mm pitch horizontal ZIF FH41-40S-0.5SH(05) receptacle of Hirose. For the necessary data rate performance tests an adapter PCB with SMA connectors was constructed which allows to use high frequency LVDS signals produced by CLOSY2 [3]. Signals are fed via SMA- and ZIF [4]-connectors into the flat band cable of 20 LVDS link pairs. To avoid reflections 100 Ohm terminators were used on the end of the cable.

Test results

The signal propagation properties and the link quality of the link cable was proven through noise eye diagram measurement (Fig.1) and the cross talk measurements on side links (Fig.2). The horizontal opening of 1.25 ns of the very clean eye diagram obviously proves high quality of the cable under test to at least 800Mbit/s.

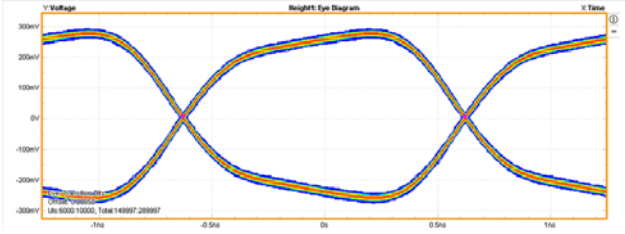


Figure 1. An eye diagram measured with DPO71254C Tektronix Oscilloscope at 400 MHz.

Fig. 2 shows very low cross talk between neighbouring links. Single ended signals are recorded on the end of the closest and second closest neighbour of an active LVDS link. The cross talk does not exceed 1% of the test signal height.

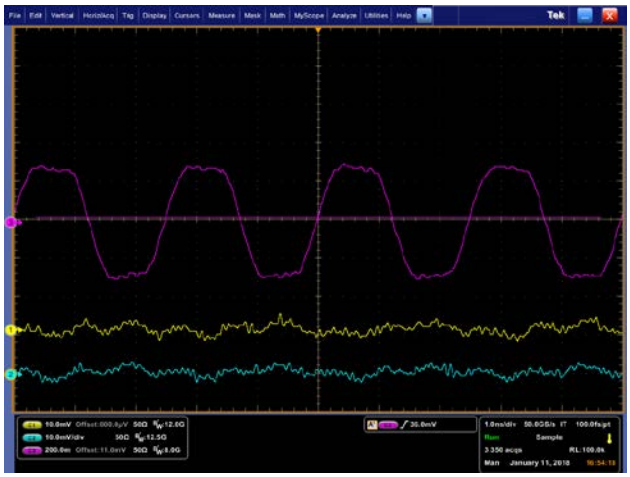


Figure 1. Crosstalk between one link carrying a *400 MHz LVDS signal and the neighbour*ing traces.

Conclusions

The symmetry of the eye diagram as well as the small RMS jitter of transitions together with very little crosstalk is a proof of high electrical quality of the tested LVDS cable. It seems that the cable can be used at still higher clock frequencies e.g. up to 800MHz and corresponding DDR rates of 1,6 Gbit/s, whereas 160 MHz (clk) and 320 Mbit/s is necessary for CBM.

References

[1] stacks.iop.org/1748-0221/11/i=11/a=C11018
[2] indico.gsi.de/event/3446/session/3/contribution/13/material/slides/0.pdf
[3] Helmholtz-berlin.de/media/media/spezial/events/sei/Desy10/koch_desy10_01.pdf
[4] hirose.com/product/en/products/FH41/FH41-40S-0.5SH%2805%29/

 DOI:10.15120/GR-2018-1

Summary Report of CBM RICH developments

J. Adamczewski-Musch[a], K.-H. Becker[b], S. Belogurov[c,f], J. Bendarouach[d], N. Boldyreva[e], C. Deveaux[d], V. Dobyrn[e], M. Dürr[d], J. Eschke[a], J. Förtsch[b], J. Heep[d], C. Höhne[d], K.-H. Kampert[b], L. Kochenda[e,f], P. Kravtsov[e,f], I. Kres[b], S. Lebedev[d], E. Lebedeva[d], E. Leonova[e], S. Linev[a], T. Mahmoud[d], J. Michel[g], N. Miftakhov[e], W. Niebur[a], J. Otto[d], E. Ovcharenko[c], V. Patel[b], C. Pauly[b], D. Pfeifer[b], G. Pitsch[d], S. Querchfeld[b], J. Rautenberg[b], S. Reinecke[b], Y. Riabov[e], E. Roshchin[e], V. Samsonov[e,f,h,] V. Schetinin[c], O. Tarasenkova[e], M. Traxler[a], C. Ugur[a], E. Vznuzdaev[e], M. Vznuzdaev[e], and A.A. Weber[d]

[a]GSI Helmholtzzentrum für Schwerionenforschung GmbH, Darmstadt, Germany;
[b]Department of Physics, University Wuppertal, Wuppertal, Germany;
[c]LIT JINR, Dubna, Russia;
[d]Institute of Physics II and Institute of Applied Physics, Justus Liebig University Giessen, Giessen, Germany;
[e]National Research Centre "Kurchatov Institute" B.P.Konstantinov PNPI, Gatchina, Russia;
[f]National Research Nuclear University MEPhI (Moscow Engineering Physics Institute), Moscow, Russia;
[g]Institut für Kernphysik, Goethe University Frankfurt, Frankfurt am Main, Germany;
[h]St. Petersburg State Polytechnic University (SPbSPU)

The CBM RICH project has made substantial progress in various fields in 2017 as will be presented in this report. First prototypes testing critical mechanical design issues of the RICH detector have been built. The RICH mirror wall is a sensitive part for the RICH detector as it has to combine high stability with low material budget. After discussing several conceptual ideas in 2015, an optimized design has been worked out in 2016 in which one pillar can support two rows of mirrors. In order to evaluate this design, a prototype pillar has been constructed in 2017 with 2 mm thick aluminum profile and successfully been tested for six months up to now with 150% of the expected load. The material budget of the small frames holding two mirrors each has been reduced by further 15-20% material budget. In parallel to ensuring highest stability from the mechanical part, software routines are in preparation in order to correct for any misalignment offline, should it happen to occur. In 2017 the full correction cycle was finally established showing that with software corrections remnant misalignments are on the level of 1 mrad which just fits to the specifications. Another critical design issue is the photodetector camera. A prototype ensuring a convenient construction of the cylindrical photodetector plane has been built and will be tested for stability, light and gas tightness in 2018. Unfortunately the shielding box of the photocamera remains to be an open design issue: The existing design could be adopted to the cylindrical photodetector plane, however partially blocks the acceptance of Cherenkov photons. In addition the redesign of the CBM magnet was not finished in 2017, the whole box has therefore to undergo a further iteration in 2018. The design of the RICH gas system was finalized and awaits the final approval. End of 2017 the last batch of the MAPMTs has been delivered by Hamamatsu. Within the first quarter of 2018 all 1100 MAPMTs will have been characterized. The RICH software underwent numerous changes to improve the realistic description, in particular quantum efficiency and sensitive area are now fully adopted to the chosen H12700 MAPMT. An important step forward was the implementation of an intermediate version of time-base RICH simulations. Within the next months this will be improved and tested 2019 with the participation of a mRICH detector in mCBM. A design of a mRICH prototype was developed and simulated reusing the testbox of the recent testbeam measurements at COSY. As radiator an aerogel tile will be used in order to enhance the pion-proton separation of mCBM.

The HADES RICH upgrade is running very well and driving the development of the RICH readout electronics. The first prototype of the RICH readout chain was available mid 2016, in 2017 an improved version was produced. This was tested in detail in the lab and could finally be fully verified in a testbeam experiment with proton beam at COSY. After initial problems with stability, the whole system was stable in the end and providing data with very low noise level. Automatic routines for threshold settings are available. First analysis of the data reveals that efficiencies are as expected from simulations, the time-over-threshold cut for noise suppression works successfully, and timing precision is on the order of 260 ps. Some MAPMTs were covered with WLS coating (p-terphenyl) in particular in order to measure timing properties. Results show a decay constant of 2.4 ns in agreement with time resolved fluorescence measurements. The previously increase of hit multiplicity of about 20 % was confirmed. Given these successful tests, the readout electronics was approved for mass production for the installation in HADES. The inner part of the photondetector will be coated with WLS films. Full installation is expected until the end of May 2018. The HADES RICH detector will then participate in the Ag+Ag beamtime of HADES in summer 2018 (FAIR phase 0) substantially enhancing the electron identification in HADES.

This report is also part of the CBM Progress Report 2017 (doi:10.15120/GSI-2018-00485).

Experiment beamline: mCBM@SIS18
Experiment collaboration: CBM
Experiment proposal: S471

Accelerator infrastructure: SIS18 / SIS100
PSP codes: 1.1.1
Grants: BMBF 05P15PXFCA, 05P15RGFCA, GSI
Strategic university co-operation with: Gießen

Summary on the CBM-TRD project

C. Blume[4,5], E. Bechtel[5], J. Beckhoff[8], A. Bercuci[1], N. Bialas[5], J. Book[5], V. Cătănescu[1], F. Fidorra[8], C. de J. García Chávez[8], S. Gläßel[5], M. Petrovivi[1], C. Şchiaua[1], S. Schreiber[5], H. Schuldes[5], D. Spicker[5], P. Kähler[8], L. Karalius[1,2], U. Kebschull[6], C. Klein-Bösing[8], M. Kohn[8], M. Krieger[7], A. Meyer-Ahrens[8], P. Munkes[8], I. Ouatu[1,3], F. Roether[5], R. Weihrich[5], the CBM collaboration, and the FAIR@GSI division

[1]National Institute for Physics and Nuclear Engineering (IFIN-HH), Bucharest, Romania; [2]Birmingham University, UK; [3]Oxford University, UK; [4]GSI, Darmstadt, Germany; [5]Institut für Kernphysik, Frankfurt am Main, Germany; [6]Infrastructure and Computer Systems for Data Processing (IRI), Frankfurt am Main, Germany; [7]ZITI, University of Heidelberg, Germany; [8]Institut für Kernphysik, Münster, Germany.

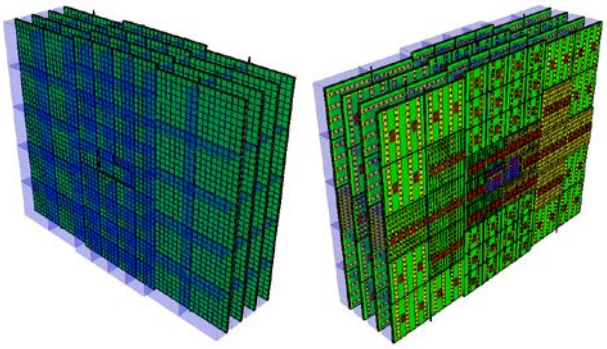


Figure 1: CBM-TRD geometry for SIS100, consisting of one station with four layers of detectors. Shown here is the implementation of the TRD geometry in the simulation framework. Visible are the ROCs with the radiator boxes in the front view (left), while the rear view (right) shows the backpanels of the ROCs together with the front-end electronics.

Introduction

The main task of the Transition Radiation Detector (TRD) is to identify electrons above momenta of 1 GeV/*c* and thus to extend the electron identification capabilities of the Ring Imaging CHerenkov (RICH) detector above momenta of $p \sim 5$ GeV/*c*. In this region the TRD should provide a pion suppression factor in the range of 10 – 20 at an electron efficiency of 90 %, in order to allow for a high quality measurement of dielectrons in the mass range from below the ρ and ω masses to beyond the J/ψ mass. Due to its capability to identify charged particles via their specific energy loss, the TRD in addition will provide valuable information for the measurement of fragments.

These requirements can be fulfilled with a Xe/CO_2 based Multi-Wire Proportional Counter (MWPC) detector in combination with an adequate radiator. The default MWPC design is composed of a symmetric amplification area of 3.5 + 3.5 mm thickness, complemented by a 5 mm drift region to enhance the TR-photon absorption probability in the active gas volume. This geometry provides also efficient and fast signal creation, as well as readout, with timescales below 200 µs per charged particle track. The performance of the detector is maximized by reducing the material budget between radiator and gas volume to a minimum.

The baseline design for the TRD at SIS100 will consist of one station, composed of four detector layers (see Fig. 1). It will be positioned between the RICH and the Time-Of-Flight (TOF) detector and thus will help to reduce the background in the TOF resulting from track mismatches by providing additional position information between RICH and TOF. The TRD will also be used as tracking station behind the last absorber of the MUCH detector in the muon configuration of CBM.

Technical design report

A first version of the Technical Design Report (TDR) for the TRD has been completed early in 2017. It was then scrutinized in an internal review in March 2017, which was performed by a committee of international experts on the various aspects of TRDs, electronics and the related physics topics. Based on the recommendations of the expert committee an extensive revision of the TDR and project was performed.

One major aspect of this process was the redesign of the TRD geometry with the aim of achieving an overall simplification. The new design, as shown in Fig. 1, now consists of only four (before six) different module types, two small ones (type 1 and 3, size 57cm × 57cm) and two large ones (type 5 and 7, size 99cm × 99cm). This facilitates the module production significantly and also allows for a simpler routing of service lines. Furthermore, many complications in the design of the readout system can now be avoided. E.g. only one type of Common ReadOut Board, namely C-ROB3, will now be required.

It was also decided to remove the chapter on alternative options from the TDR, such that the new version consistently describes a baseline solution for the whole TRD system. The innermost modules of the TRD, situated in the region of the highest hit rates, can still employ a different technology (i.e. pad planes with triangular pads and FASP readout), as being developed by the Bucharest group. This design will be described in an addendum to the existing TDR, which is currently under preparation.

The revised TDR has officially been submitted in Dec. 2017 to the ECE for the final approval.

Physics performance

The main physics cases for the TRD are the measurement of dielectrons in the intermediate mass range (i.e. between ϕ- and J/ψ-mass) and the identification of light nuclei. As a consequence of the TDR revision the corresponding physics performance studies had to be repeated with the

 DOI:10.15120/GR-2018-1

new TRD geometry and to be extended in order to address the referee comments. The results of the revised simulation studies are summarized in [7] (intermediate mass dielectrons) and [2] (identification of light nuclei). Both analyses were now done with three, four and five TRD layers in order to determine the optimal geometry for these physics observables. The results show that three layers would be insufficient, while an additional fifth layer is not needed to achieve the desired performance.

Front-end electronics

A test batch of the SPADIC 2.1 ASIC has been submitted. This version includes features suggested by the TDR referees, such as, e.g., an overload recovery and a running averaging for the baseline determination. It will have a BGA packaging in order to reduce the real estate occupied by the chip on the Front-End Boards (FEBs). This will allow to design FEBs which are small enough to fit flatly onto the backpanel of the TRD chambers, even for module type-1 which has the highest channel density.
The development of multi-ASIC FEBs is progressing well [3]. A first version of a quad-FEB, to be equipped with the SPADIC 2.0, is available and is intended to be used for mCBM.

Readout and feature extraction

The TRD readout has been upgraded for the connection of multiple SPADICS to a given AFCK board [4]. This implementation has been successfully tested at DESY and CERN-GIF and will be further extended for the quad-FEBs to be used for mCBM and for the GBTx-based C-ROBs.
An important part of the readout chain is the feature extraction stage, which will deliver event-filtered and bandwidth reduced data to the FLES. First performance studies on the online cluster reconstruction in terms of total cluster charge and position have been performed [5].

Laboratory and beam tests

Also in 2017 extensive test have been performed, both in the laboratory and at accelerators. The Bucharest group has set up a test stand equipped with a high intensity x-ray source, which allows to investigate the performance of prototypes under high counting rate conditions [6].
In Münster an automated calibration setup for the readout chambers using a Fe-source was build [7], which can be used for a quality assessment of newly produced readout chambers. This setup is currently also been used to study the multi-hit performance of the SPADIC [8].
A systematic test of four large prototypes with radiators was performed with electron beams at DESY [9]. These data allow for a detailed characterization of the radiators and will serve as a reference for the fine-tuning of the detector simulation.
In order to investigate the stability of the readout chambers and front-end electronics in a high rate environment a first test at the Gamma Irradiation Facility (GIF) at CERN was done [10].
The analysis of the test beam data of 2017 is currently still on-going. Several software developments on the software framework for the analysis of test beam data have been done [11], which now provide a unified environment for these studies.

Summary and outlook

With the finalization of the TDR the research and development phase for the TRD can almost be concluded. Ongoing activities mainly concern topics such as services, cooling and the gas system, while the design of the readout chambers themselves is essentially final. Four large chamber prototypes, which are already very close to this design and have already been operated at the CERN-SPS and DESY, will be available for mCBM. Also the development of the front-end electronics is progressing and final FEBs should be available by the end of 2018. Therefore, it is planned to start the production readiness review by the end of 2018 and to start mass production soon after that.

This report is also part of the CBM Progress Report 2017 (doi:10.15120/GSI-2018-00485).

References

[1] E. Bechtel et al., “Performance study on dielectron measurements in Au+Au collisions with the CBM-TRD”, CBM Progress Report 2017, p. 155.
[2] S. Gläßel et al., “Hadron identification via energy loss measurements with the TRD”, CBM Progress Report 2017, p. 156.
[3] F. Roether et al., “Front end board development for the CBM-TRD”, CBM Progress Report 2017, p. 86.
[4] C. de J. Garcia Chávez et al., “Status update of the TRD data acquisition chain during 2017”, CBM Progress Report 2017, p. 87.
[5] C. de J. Garcia Chávez et al., “Performance study of the feature extraction”, CBM Progress Report 2017, p. 88.
[6] A. Bercuci et al., “Laboratory tests of the TRD Bucharest prototype in close to realistic high counting rates (HCR) environment”, CBM Progress Report 2017, p. 89.
[7] J. Beckhoff et al., “Automated gain-table measurements for the CBM-TRD”, CBM Progress Report 2017, p. 91.
[8] M. Kohn et al., “Analysis of the SPADIC Multi-Hit feature”, CBM Progress Report 2017, p. 92.
[9] F. Roether et al., “Electron test beam campaign of the CBM-TRD at DESY”, CBM Progress Report 2017, p. 93.
[10] P. Kähler et al., “High-rate test of a CBM-TRD module at the CERN-GIF”, CBM Progress Report 2017, p. 94.

[11] P. Munkes et al., “A new in-beam-test data analysis framework for the CBM-TRD”, CBM Progress Report 2017, p. 95.

Experiment beamline: mCBM@SIS18
Experiment collaboration: CBM
Experiment proposal: S471
Accelerator infrastructure: SIS18 / SIS100
PSP codes: 1.1.1
Grants: BMBF-grants 05P15RFFC1 and 05P16PMF1, Romanian ANCSI/CAPACITATI Modul III Contract F04 and NUCLEU Project Contract PN 2018, Helmholtz-Alliance EMMI, HGS-HiRe.
Strategic university co-operation with: Frankfurt-M

Status on the CBM Time Of Flight system

I. Deppner[1], N. Herrmann[1], the CBM_TOF working group

[1]University of Heidelberg

We can look back, again, on a very successful year 2017. For the first time a trigger less readout system using close to final electronic components was operated successfully in the beamtime at SPS as well as in the cosmic setup in Heidelberg. Results concerning efficiency, time resolution and cluster size obtained in many beamtimes demonstrate that the counter development is far progressed and therefore in a very satisfactory situation. Along this line the mass production for the MRPC3a and MRPC3b counters [1] (foreseen for the FAIR phase 0 project at STAR and mCBM) started after the review readiness report in March 2017.

The main tasks for TOF in the last year were the following:

1) analysis of the data taken during the beamtime at ELBE in 2017 and at SPS in Nov. 2016,
2) operation of a free streaming cosmic stand in Heidelberg,
3) mass production of MRPC3a and MRPC3b counters for the FAIR Phase 0 projects at STAR and mCBM,
4) installation and conditioning of one eTOF sector in the STAR experiment at BNL.

Beamtimes are essential for testing high rate counters. At ELBE a mono-energetic single electrons beam of 30 MeV with pulse duration of 5 ps and a flux of $\leq$ 500 kHz/cm^2 is well suited to test the rate capability of single cell counters like the BFTC prototypes (active area is 4 cm^2) with ceramic resistive electrodes. However, since the beam has a diameter of only about 10 cm^2 only the spot response of counters larger than a few cm^2 can be tested. During the last year a beamtime at ELBE was carried out with the BFTC prototypes and results are reported in [2]. In order to achieve a full illumination on counters bigger than a few cm^2, beams with heavy ions impinging on lead targets like executed at CERN SPS is mandatory. The beamtime setup in Nov. 2016 (conf. Fig. 1), described in [3], consisted of about 500 read out channels distributed over 10 timing counters (including 2 layers of ceramic MRPCs) and one Bakelite resistive plate counter for the MUCH system from our Indian colleagues. For the first time a free streaming readout system was operated successfully and even synchronization with 2 GEM detectors (for the MUCH-subsystem) using FEBs with nXYTER (Rev-F) [4] could be demonstrated. During this campaign a Pb beam with an momentum of 156 AGeV/c was impinging on a 4 mm Pb target leading to high multiplicity events which are substantial to test the detector response under load. Occupancies higher than 50 % were reached. However, particle fluxes (measured by a plastic scintillator) above 1.5 kHz/cm^2 could not be reached even after adding 10 cm of iron to the target. As in the SPS beamtime in Nov. 2015 the radiation protection alarm was triggered and a reduction of beam intensity

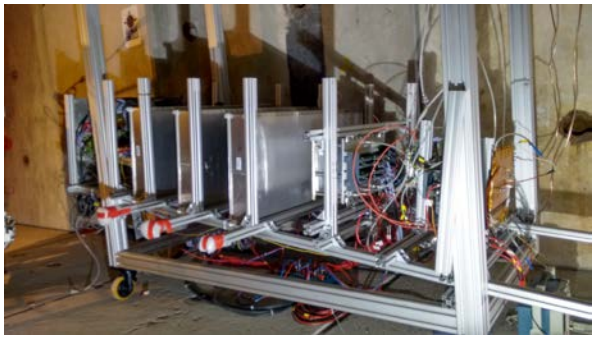


Figure 1: Photography of the CERN November 2016 setup. The beam enters the setup from the right side. The counters are arranged below the beam with an angle of 7◦.

was needed in order to continue the measurements. In conclusion the H4 beam line at SPS is not suited to deliver the anticipated rates for the inner part of the CBM TOF wall. Currently such high rates will only become accessible at the upcoming mCBM beamtimes at SIS 18 which shows the immense importance of this FAIR Phase 0 project not only in terms of DAQ integration tests but also as a test facility for high rate detectors. Nevertheless, during the beamtime at SPS more than 100 useful runs were taken which are right now still being analysed. First results for the MRPC1/2 prototypes [1] are presented in [5]. In order to adapt the MRPC1/2 prototypes to the front-end electronic and to minimize channel costs a redesign in the readout electrodes is currently ongoing where the number of channels is reduced from 40 to 32. The mechanical design for the inner TOF wall where these counters will be located is ongoing as well [6].

Equally important are counter tests with cosmic particles that have the advantage of being constantly available. A test stand for cosmics (see Fig. 2) was operated at Heidelberg during almost the full year. Per day about 100000 good tracks (in the acceptance of all counters) can be recorded and multi-dimensional analysis can be performed. On the left side of figure 3 an event with 2 tracks is shown that had hits in all 6 stations. Comparing 5 hit and 6 hit tracks, the efficiency as function of position in X and Y can be measured (see right plot in Fig. 3). Similar figures can be obtained for time resolution, cluster size, position resolution, time over threshold distributions and so on. In the cosmic setup counter time resolution of about 55 ps, X position resolution (across the strip) of about 2.5 mm and Y position resolution (along the strip) of about 5.5 mm was obtained. Beside resolution studies, the cosmic stand data also offer the opportunity to develop the software for calibration and reconstruction under clean conditions. In addition simulation with the same geometry can be performed and the counter response from realistic digitizer [7] as well as the analysis framework can be tested and compared to real data. However, this is not restricted only to cosmic data as shown in [8].

In the context of the CBM FAIR phase 0 programs for TOF the mass production of the MRPC3a and MRPC3b counter started in 2017. 73 MRPC3a counter with low

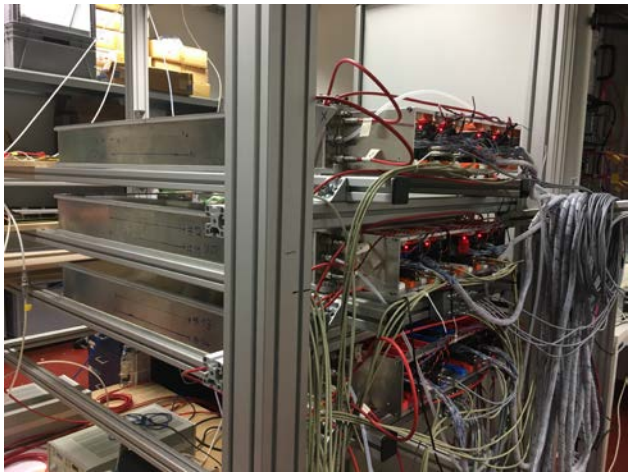


Figure 2: Photography of the Heidelberg cosmic setup. Three modules containing 2 counters each are placed on top of each other so that in total 6 counters can be tested simultaneously.

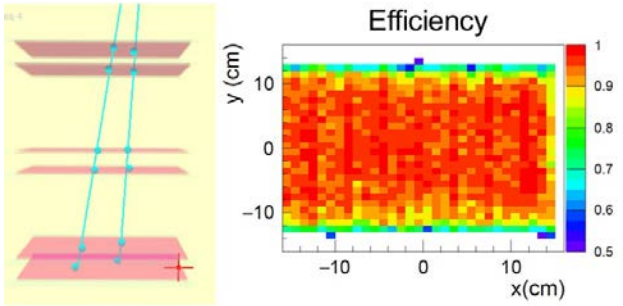


Figure 3: Left: cosmic setup with 6 MRPC stations. An event with 2 tracks with 6 hits each was found. Right: Efficiency of one MRPC as function of the X and Y coordinate.

resistive glass are produced at Nuctech in Beijing and most of them are tested and delivered to Heidelberg. The counter specs, the progress of the production, the test results as well as the QA procedure are described in [9]. It turned out that a conditioning time of about 120 hours is necessary in order to achieve stable operating conditions. 80 MRPC3b counter (float glass) are currently produced at USTC/Hefei. A short overview of the status and the QA procedure is given in [10]. The integration of the MRPC3a/b counters in modules will take place in Heidelberg. Currently 36 gas tight boxes for STAR and 5 boxes for mCBM are under construction in the mechanical workshop in Heidelberg. The module production for mCBM will be finished end of April while for STAR end of August. The plan is to test all modules extensively in the Heidelberg cosmic setup before the modules are delivered to GSI and to BNL.

Three modules for eTOF at STAR (see FAIR phase 0 program for TOF in [11] were produced last year, tested and shipped to Brookhaven National Laboratory. Figure 4 shows the three modules, forming one sector, mounted in the 6 o'clock position of the east-side end-cap of the magnet. The chambers are controlled remotely from Germany. Be- fore the RUN18 starts, cosmic data with the full STAR apparatus are taken and the data from eTOF are integrated in the data stream of STAR.

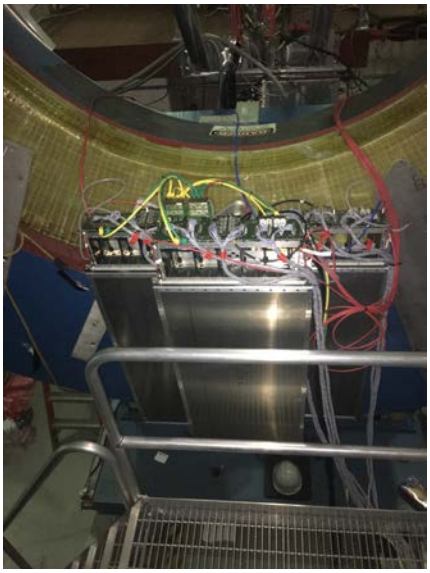


Figure 4: Sector consisting of 3 CBM-TOF modules moun- ted on the east pole tip of the STAR experiment.

This report is also part of the CBM Progress Report 2017 (doi:10.15120/GSI-2018-00485)

References

[1] N. Herrmann et al. "CBM-TOF Technical Design Report", http://repository.gsi.de/record/109024/files/, October 2014
[2] R. Sultanov et al., CBM Progress Report 2017 (2018)
[3] I. Deppner and N. Herrmann, CBM Progress Report 2016 (2017), S 124
[4] A. Kumar, CBM Progress Report 2016 (2017), S 88
[5] M. Petriș et al., CBM Progress Report 2017 (2018)
[6] L. Radulescu et al., CBM Progress Report 2017 (2018)
[7] C. Simon et al., CBM Progress Report 2017 (2018)
[8] Ph. Weidenkaff, CBM Progress Report 2017 (2018)
[9] P. Lyu et al., CBM Progress Report 2017 (2018)
[10] D. Hu et al., CBM Progress Report 2017 (2018)
[11] I. Deppner and N. Herrmann, CBM Progress Report 2017 (2018)

Experiment beamline: none
Experiment collaboration: CBM
Experiment proposal: none
Accelerator infrastructure: SIS100
PSP codes: 1.1.1.5
Grants: BNBF 05P15VHFC1
Strategic university co-operation with: Heidelberg

The CBM FAIR Phase 0 project - eTOF at STAR

I. Deppner[1], N. Herrmann[1], the CBM-TOF collaboration

[1]University of Heidelberg

The FAIR Phase 0 program of TOF comprises among other tasks the installation, commissioning and operation of 36 eTOF-modules, using 108 CBM-TOF MRPC3a/b counters [1], during the beam energy scan campaign II (BESII) of the STAR experiment at BNL. The modules will be grouped in 12 sectors and will be attached on the east side pole tip of the magnet (conf. Fig 1). During the last year a substantial progress regarding this project was made.

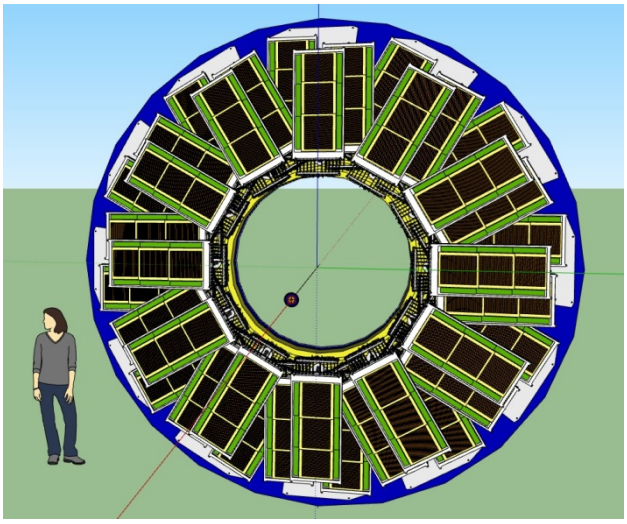


Figure 1: Conceptual design of the eTOF wall at STAR. The ”wheel” is composed of 36 module comprising 6912 readout channels.

The physical work of this project started with the installation of one module containing 2 MRPC3b counters at STAR in Jan. 2017 and operating it in the RUN17 (Mar. 17 - Jun. 17). The aim was to integrate our free streaming readout system in the trigger based readout system of STAR. It could be shown successfully that the first DAQ integration tests worked as expected (see last CBM Progress Report [2]). Currently software is developed in order to unpack the eTOF data and make them accessible to the STAR analysis framework. The test installation of the first module already delivered valuable information for a stable operation of our MRPC counters. After an accelerator intervention (un-planned beam loss event) one PADI FEE board stopped functioning pointing to the need for fast protection measures. After 2 month of operation both MRPC counters stopped working due to HV failure. This problem was analysed and cured by a modification in the design of the MRPC3b counter. These examples demonstrate the immense importance of the FAIR phase 0 programs in order to identify critical issues of the system under running conditions.

In the last year 3 modules for eTOF were produced. Two modules contain 3 MRPC3a counters each (with low resistive glass) manufactured at Nuctech in Beijing while 1 module is housing 3 MRPC3b counters build at USTC/Hefei. The module integration for the full wheel is carried out in Heidelberg. Figure 2 shows a photograph of the open module from the front side (left) and the back side (right). The 3 modules were shipped to BNL beginning of January 2018 and installed at the 6 o’clock position at the east pole tip (see Fig. 3). The readout system consists of the PADIX boards (inside the module box), a feed-through PCB, the TDC board with the GET4 V2.0 chip, a back-plane board distributing the power and the clock to the FEE cards, 5 AFCK boards sitting in a µTCA crate at 8 m distance from the modules and a FLIB board sitting in a rack mount PC located in the DAQ room about 50 m from the setup. The current connection between the back-plane board and the AFCK is copper cable (twisted pair) and will be re- placed with optical fiber after the RUN18. Then also the GBTx chip, sitting on the back-plane board, will be included in the readout chain. The connection between AFCK and FLIB is optical fiber.

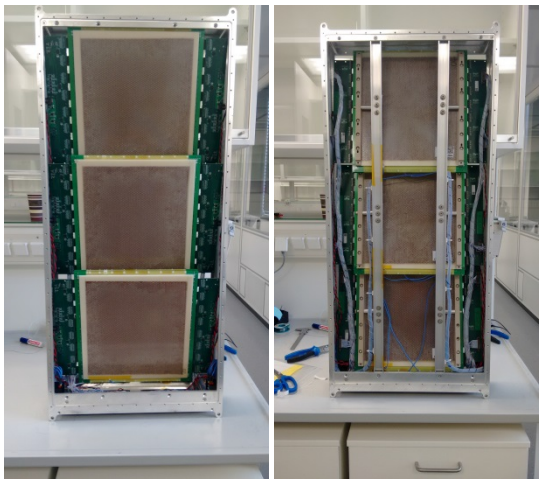


Figure 2: Open eTOF module - left: front side, right: back side.

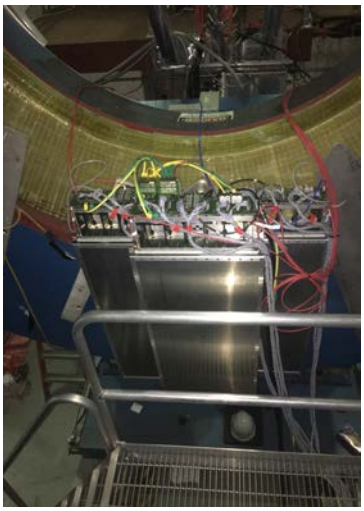


Figure 3: One sector mounted on the inner side of the pole tip.

In the meanwhile both institutes from China continued the mass production of the counters for the full eTOF wall (in total 150 counter). The production of the MRPC3a counters will be finished in March 2018 and 53 aut of 73 counters are shipped to Heidelberg. 25 of the MRPCa counters are devoted to the mCBM project. Figure 4 shows the production of MRPC3a counters in the clean room at Nuctech/Beijing. The clean room level is 100k. The production of the MRPC3b counter will be finished in July 2018. 5 counters are shipped to Heidelberg and integrated in the cosmic setup. The progress of the mass production as well as the QA procedure are summarized in [3, 4].



Figure 4: Mass production of MRPC3a counter in the clean room.

In order to coordinate and to discuss the progress as well as the open issues on the project two CBM-STAR meetings where organized during the last year. The first meeting took place at Darmstadt while the second meeting was carried out at Wuhan. Many fruitful discussion and solutions arises during these meetings. One example is the implementation of the eTOF geometry in the STAR simulation frame work (see Fig. 5).

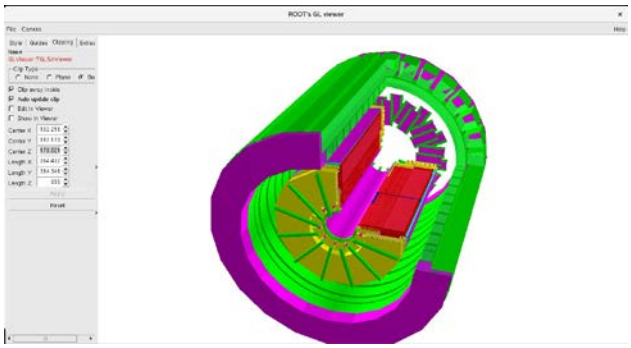


Figure 5: eTOF geometry included in the STAR simulation frame work.

The time line of the eTOF project is:
1) Jan 2018 - shipping and installation of one sector
2) Mar. - June 2018 - 2nd system integration test with one sector by participating in the Run18 beam time in STAR,
3) Mar. - Oct 2018 - Production and testing of 36 modules in Heidelberg
4) Sep 2018 - shipping of all 36 modules to BNL
5) Oct. - Feb. 2018 - Installation and commissioning of the eTOF syatem
6) 2019/2020 - Running in the BES II campaign
7) Summer 2021 - Decommissioning and shipping of all modules including infrastructure to FAIR

This report is also part of the CBM Progress Report 2017 (doi:10.15120/GSI-2018-00485)

References

[1] N. Herrmann et al. “CBM-TOF Technical Design Report”, http://repository.gsi.de/record/109024/files/, October 2014
[2] I. Deppner et al., TOF Summary, CBM Progress Report 2016 (2017)
[3] P. Lyu, CBM Progress Report 2017 (2018)
[4] D. Hu et al., CBM Progress Report 2017 (2018)

Experiment beamline: none
Experiment collaboration: CBM
Experiment proposal: none
Accelerator infrastructure: BNL-RHIC
PSP codes: 1.1.1.5
Grants: BNBF 05P15VHFC1
Strategic university co-operation with: Heidelberg

Development of muon detection system (MUCH) for the CBM experiment at FAIR

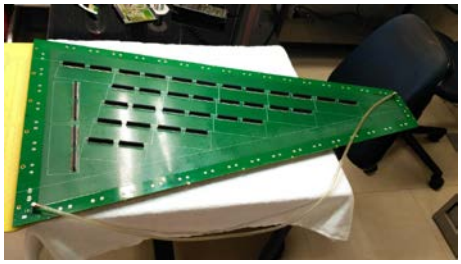
S. Chattopadhyay[1], A.K. Dubey[1], Z. Ahammed[1], J. Saini[1], P. Bhaduri[1], E. Nandy[1],V. Negi[1], M. Mandal[1],A. Kumar[1],C. Ghosh[1],S. Prasad[2], S. Biswas[2], S. Das[2], D. Emschermann[3], C. Schmidt[3], P. A. Loizeau[3], A. Senger[3],O. Singh[4], the CBM collaboration, and the FAIR@GSI division

[1]VECC, Kolkata, India; [2]Bose Institute, Kolkata, India; [3]GSI, Darmstadt, Germany,
[4]Aligarh Muslim University, Aligarh, India

The SIS-100 version of MUCH consists of five absorber segments with 4 detector stations sandwiched between them. While the first absorber is made of graphite, other absorbers are of iron. A gap of 10 cm houses the detector stations having 3 layers each consisting of varying number of chambers. The first and the second stations use GEM chambers to handle a hit rate of more than 400 KHz/cm^2. As the particle rate at the 3rd and 4th stations are considerably lower (maximum 5 KHz/cm^2 in Au+Au collisions at 10 AGeV), different technologies are being explored like high-rate RPC or straw tube chambers.

Two chambers fit to be placed in the 1st station are built at VECC-Kolkata and ready to be installed in the mini-CBM scheduled to take data in October 2018. The chambers (Fig. 1) use GEM foils from CERN custom-built for our configuration. Major features implemented in these chambers are (a) NS-2 technique for glue-less stretching (b) drift planes with opto-couplers connected to the HV line of each segment providing with a possibility of isolating the segment in case of any spark. This feature enables to use high-voltage segmentations using resistive chains thereby reducing the total cost of HV supply by a factor of 24 (the number of segments in each foil).

The readout planes of the chambers are having projective pads of varying sizes. Each pad covers 1 Degree in azimuth and equivalent radial distance. The chambers have been tested successfully with radioactive source (Fe-55, Sr-90) and ready to be installed in mini-CBM. A 1 cm thick Aluminium plate has been used to support the chamber and channels made inside the plate is being used for water-cooling. This setup has been tested to take data with Pb beam at SPS in November 2016.



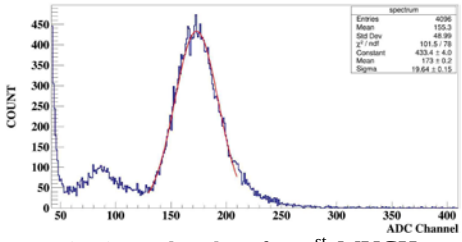


Fig.1 : (top) A chamber for 1st MUCH station (bottom) Fe-55 spectra

A low voltage distribution box (LVDB) has been developed to distribute LVs to the FEE boards. A FPGA-based system has been developed to control the operation of LVDB. A similar system has also been developed for the HV control. All components being used in the detector and supply systems have been tested with neutron and gamma sources to withstand a dose that is about a factor of two higher than estimated by FLUKA.

The MUCH system is being simulated using CBM-ROOT framework for measurement of LMVM and charmonia. The results obtained earlier have been found not to deteorirate using the most realistic geometry of the setup.

An ASIC called STS/MUCHXYTER have been developed for the MUCH readout and the version presently available has been connected to a GEM chamber for taking data with Sr-90 source. Even though the calibration is under progress, the readout shows clear source spot on the detector.

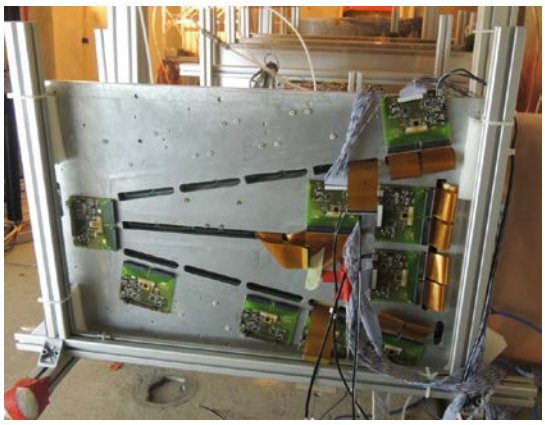


Fig.2: Al-plate for support and cooling of the GEM chambers. FEE boards are connected using small cables.

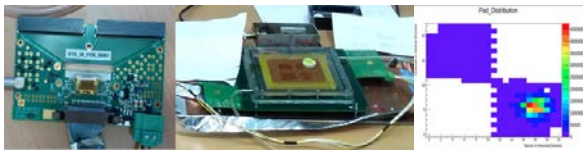


Fig.3: (left) STS-MUCHXYTER ASIC connected to a GEM chamber (right) beam spot seen online

A significant progress has been made on the mechanics of the MUCH system. Two major mechanical systems are absorbers and superframe to hold MUCH. Designs are in advanced stages and discussions are in progress with the prospective manufacturers.

One open area is to find a suitable technology for the 3rd and 4th stations of MUCH. Given the performance reported by ALICE muon chambers, two ALICE-muon RPCs have been tested with cosmics and with NINO and PADI electronics to provide >95% efficiency with cosmic muons. MUCH simulations using RPCs in the 3rd and 4th stations show good performance.

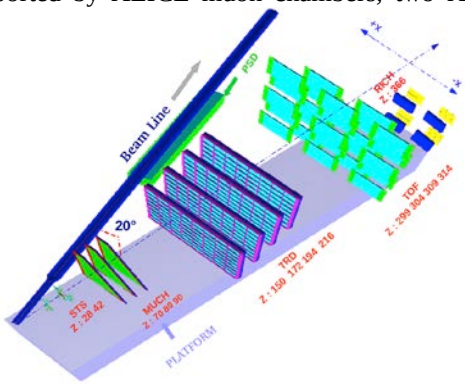


Fig. 4: 3 GEM chambers in miniCBM setup

Detailed setup has been developed to simulate the mini-iCBM setup including three GEM chambers. The digitization and formation of hits have been performed.

 DOI:10.15120/GR-2018-1

Preparation of a free-streaming DAQ system for mCBM@SIS18

D. Emschermann and C. Sturm for the CBM collaboration

The key objective of the Compressed Baryonic Matter experiment (CBM) at FAIR is to investigate the QCD phase diagram in the region of the highest net-baryon-densities by measuring nucleus-nucleus collisions. As a fixed-target experiment, CBM is consequently designed to cope with unprecedented collision rates up to 10 MHz which will allow studying extremely rare probes with high precision. To achieve the high rate capability, CBM will be equipped with fast and radiation hard detectors readout by a free-streaming data acquisition system transporting data with up to 1 TB/s to a large scale computer farm providing a first level event selection.

With mCBM@SIS18 we are presently constructing a CBM full-system test-setup at the GSI/FAIR host lab to study, commission and test the complex interplay of the different detector systems with the free-streaming data acquisition and the fast online event reconstruction and selection under realistic experiment conditions.

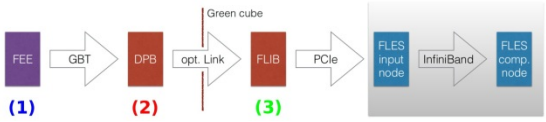


Figure 1: mCBM readout chain for the startup phase, based on DPB and FLIB. The mCBM subsystems are equipped with individual front-end electronics FEE (1). These front-ends are interfaced by the GBTx ASIC, which forwards the detector data via optical GBT link. All GBT links are received by the DBP layer located at 50 m distance in the DAQ container (2). The DPB is a FPGA based board which allows for subsystem specific pre-processing of the arriving data stream. A long optical link connects the DPB output to the FLIB board installed in the FLES input node in the Green IT Cube (3).

The detector stations will be equipped with final readout electronics containing ultra-fast and radiation-tolerant ASICs as front-end chips followed by CERN GBTx-based radiation-tolerant data aggregation units. Further down-stream, the data streams are handled by Data Processing Boards (DPB) containing powerful FPGAs and are forwarded via FLES Input Boards (FLIB), a PCIe based FPGA board, to a large-scale computer farm, the First-Level Event Selector (mFLES), which will perform on-line track and event reconstruction and selection, see Fig. 1.

The CBM detector front-ends are time-synchronized to the nanosecond level by the Timing and Fast Control (TFC) system. The detector front-end digitizes signals above threshold and assigns time stamps to hits. This data is then forwarded via an electrical connection to the GBTx readout board, where the electrical signals acquired through a large number of e-links are converted and merged into an optical GBT link operating at 4.48 Gbit/s. These GBT links are the detector interface to the Data AcQuisition (DAQ) chain.

On the road towards the full CBM DAQ system the mCBM DAQ system will be deployed in two phases. During phase I, the GBTx-based subsystems (mSTS, mMUCH, mTRD and mTOF) will be read out using already available readout chains based on existing prototype implementations of DPB and FLIB, see Fig. 1. As current prototype hardware, an AMC FMC Carrier Kintex (AFCK) board [1] is used for the DPB, a HiTech Global HTG-K700 PCIe board for the FLIB. Both boards are based on a Xilinx Kintex-7 FPGA. In phase II, DPB and FLIB will be replaced by a prototype of the Common Readout Interface (CRI) (see Fig. 2) in the FLES input stage, as it is foreseen for the CBM experiment. In addition, the mCBM subsystems (mRICH, mPSD) readout with FPGA TDCs chains will be added to the DAQ setup in 2019.

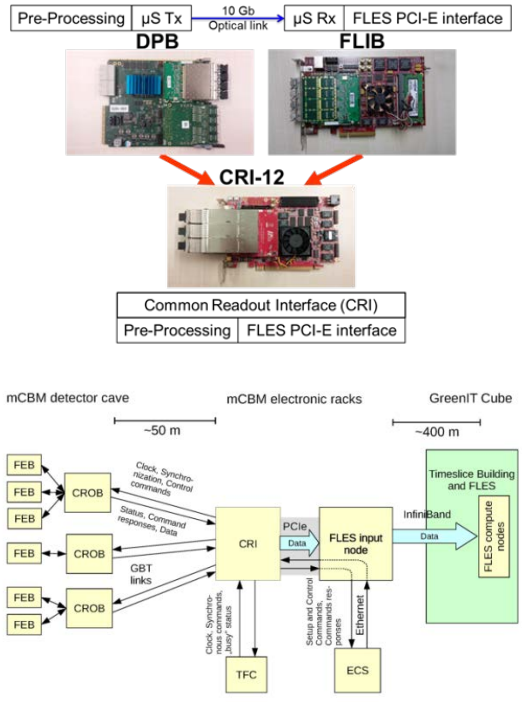


Figure 2: Upgrade of the mCBM DAQ in 2019, from two chained Kintex-7 devices to a single Ultrascale+ FPGA (top panel). This results to the final CBM DAQ scheme (bottom panel) [2].

References

[1] D. Hutter, J. de Cuveland, and V. Lindenstruth, Preparations for the mCBM FLES Setup, CBM Progress Report 2017, doi: 10.15120/GSI-2018-00485

[2] W.M. Zabołotny et al., Selection of hardware platform for CBM Common Readout Interface, Photonics Applications in Astronomy, Communications, Industry, and High Energy Physics Experiments 2017; 10445 (2017) 49, doi: 10.1117/12.2280938

Status of the CBM physics performance studies

I. Selyuzhenkov[1,2], I. Kres[3], C. Pauly[3], K.H. Kampert[3], M. Zyzak[1], I. Kisel[4], P. Kisel[1,5], I. Vassiliev[1], V. Klochkov[1,6], A. Senger[1], E. Bechtel[6], C. Blume[1,6], S. Glaessel[6], J. Book[6], H. Schuldes[6], M. Teklishyn[7], and H. Malygina[1] for the CBM collaboration

[1]GSI, Darmstadt, Germany; [2]MEPhI, Moscow, Russia; [3]Bergische Universität Wuppertal(BUW); [4]Frankfurt Institute for Advanced Studies(FIAS), Frankfurt, Germany; [5]JINR, Dubna, Russia; [6]Goethe-Universität Frankfurt, Frankfurt, Germany; [7]FAIR, Darmstadt, Germany

Introduction

The CBM experiment is designed to study the QCD phase diagram at high net-baryon densities and moderate temperatures with heavy-ion collisions at the high interaction rates. In this report we highlight the activities of the CBM Collaboration related to the physics performance studies.

π^0 reconstruction via double conversion

The produced heavy particles containing charm quarks, like J/ψ, and also rare vector mesons ω, ρ, φ can be detected via their leptonic decay ω/ρ/φ → e^+e^-. As leptons are insensitive to hadronic interaction with the dense medium, their leptonic decays offer a possibility to look into the early, dense phase of the fireball evolution. Due to their comparatively small production cross section, together with small branching ratio (BR) into e^+e^- a precise understanding of background is needed. A major source of background stems from decay of neutral pions into π^0 → γ+γ (BR 98.8%), aand π^0-Dalitz decays π^0 → e^++e^-+γ (BR 1.1%). Instead of measuring directly photons by using an electromagnetic calorimeter, the CBM-RICH detector is able to measure photons indirectly by detecting e^+e^--pairs stemming from conversion γ → e^+e^- in the target or in the material of the detectors. Two such reconstructed photons are then further combined to form a π^0.

The reconstruction efficiency for pions via double conversion is rather low (~ 10^{-4}), mainly due to the low conversion probability of the two photons. A precise acceptance and efficiency correction is required in order to quantitatively describe the π^0 background in dilepton studies. Two statistically independent Monte Carlo samples (each consists of 5 × 10^6 UrQMD events of central Au+Au collisions at 8 AGeV beam energy) are used to evaluate the analysis procedure. The first sample is used to derive a multi-dimensional (as a function of p_T and rapidity) acceptance and efficiency correction matrix. Using the fixed correction matrix, the data from the independent second sample (and also others in future) are analyzed. In Fig. 1 one can see the comparison between all generated (left panel) and reconstructed (middle panel) number of π^0 from the first simulated sample. The right plot shows their ratio, which determines the correction factors. These factors will be used for the realistic π^0 estimation from the second simulated sample. As can be seen from the different colors on the right plot of the Fig. 1, correction factors for different rapidity-p_T bins differ, therefore, the double conversion analysis has to be done for each rapidity-p_T bin separately, adding corresponding correction factors. Summing up all numbers of π^0 after the correction gives us the proper number of generated pions in the available acceptance.

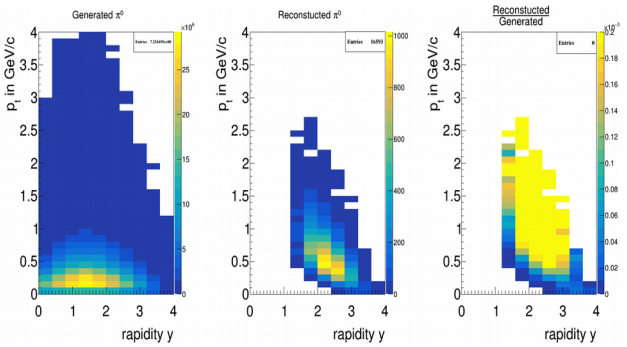


Figure 1: Phase-space coverage of all generated π^0 on the left plot, all reconstructed π^0 via conversion method on the middle plot, together with the their ratio on the right plot.

The corrected number of pions can be used for the temperature estimation of the emitting source. After summing up over rapidity to form 1-dimensional p_T distribution one can fit the resulting distribution and extract the corresponding temperature. In Fig. 2 one can see the comparison between reconstructed and generated p_T distributions together with the temperature fits.

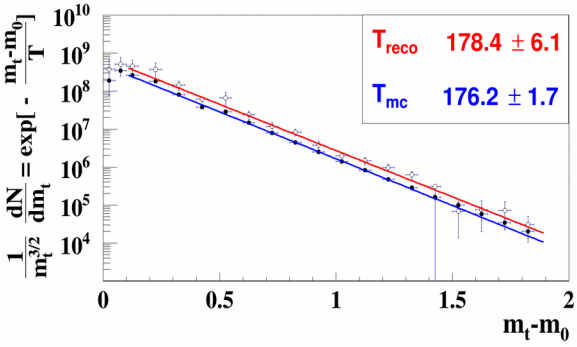


Figure 2: 1-dimensional p_T distributions of reconstructed π^0 after corrections (open circles) and simulated π^0.

Reconstruction of short-lived particles

The main goal of the short-lived particle analysis is to extract physics observables that characterize the system produced in a heavy-ion collision. One of such observables are particle yields as a function of momentum, rapidity, transverse mass, etc. In order to reconstruct short-lived particle spectra two methods were implemented in the KF Particle Finder package: side bands and background fit methods. The side bands method assumes that the back-

 DOI:10.15120/GR-2018-1

ground under the mass peak and around it has the same shape for all physics parameters. Under such assumption two kinds of spectra are collected for each parameter (p, rapidity, p_T, m_T) as well as two dimensional y-p_T and y-m_T spectra: signal+background within ±3σ of the peak and background in the region (3-6)σ around the peak. Then the background is normalized with respect to the integral of the background function in the region of ±3σ around the peak and subtracted from the signal+background spectra, that gives a reconstructed signal spectra.

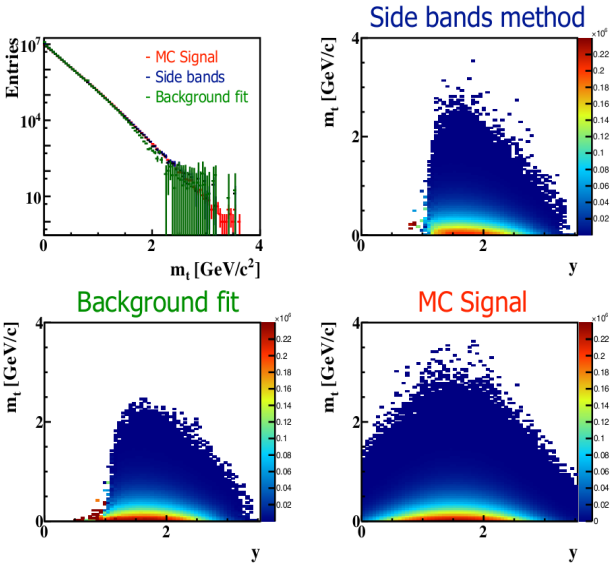


Figure 3: Efficiency corrected spectra of $K_s^0 \rightarrow \pi^+\pi^-$ decay as a function of m_t and y-m_t obtained by the side bands and background fit methods in comparison with the simulated Monte Carlo signal from 5M central Au+Au UrQMD collisions at 10 AGeV.

The second method which uses the background fit is implemented as follows: three dimensional histograms y-p_T -M and y-m_T-M are collected, where M is mass. Then the mass spectrum in each y-p_T or y-m_T bin is fitted with a signal+background function and the integral of the signal function provides the number of short-lived particles with given y and p_T or y and m_T respectively. The obtained number is filled to the corresponding bin of the signal spectra. Tools for collection of the efficiency plots were added to KF Particle Finder, that allow to reconstruct distributions of particles produced in the collision. Efficiency corrected m_T and y-m_T spectra obtained with both methods are shown in Fig. 3 for $K_s^0 \rightarrow \pi^+\pi^-$ decay in 5M central Au+Au UrQMD events at 10 AGeV. Reconstructed spectra are in a good agreement with each other and with the simulated Monte Carlo spectra.
The obtained m_T spectra can be further analyzed, for instance, in different rapidity bins, as it is shown in Fig. 4 - both reconstructed and simulated distributions are fitted with exponential functions, thus, providing the slope parameter. Under assumption, that produced particles are thermally distributed, the temperature can be extracted from the slope parameter.

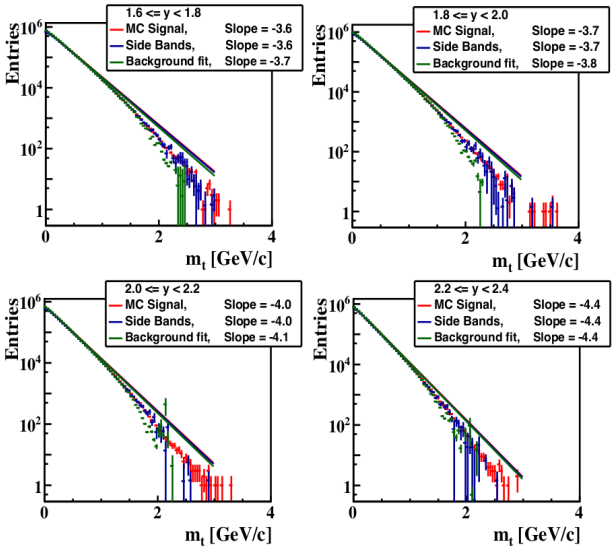


Figure 4: Reconstructed m_T signal in comparison to the simulated MC signal in different rapidity bins at an example of $K_s^0 \rightarrow \pi^+\pi^-$ obtained from 5M central Au+Au collisions.

Performance for directed flow measurement

The measurement of the anisotropic transverse flow is an important part of the CBM physics program. Due to the interaction among particles produced in a heavy-ion collision, the initial spatial asymmetry in the overlap region of the collision leads to the asymmetry in the direction of the particle's transverse momenta. This asymmetry can be measured via azimuthal distributions of produced particles with respect to the initial symmetry plane (reaction plane, RP) spanned by the impact parameter and the beam direction.
A sample of 5 million Au+Au collisions with beam momentum of 10 AGeV simulated with UrQMD event generator was used. Charge particles tracks were reconstructed using the Silicon Tracking System (STS) and Micro-Vertex Detector (MVD). The Projectile Spectator Detector (PSD) modules were grouped for analysis into three sets: central (PSD1), middle (PSD2) and outer (PSD3). Particle identification was done using Monte-Carlo information. Centrality determination was based on STS track multiplicity. The momentum asymmetry is quantified by constructing two-dimensional vectors q_n determined event-by-event from the STS tracks and calculated for three PSD module groups. Introducing a second harmonic vector helps to reduce non-flow correlations, such as contribution due to total momentum conservation. Imperfect acceptance and efficiency of the detector are biasing the azimuthal angle distribution of measured particles. A correction procedure for the q_n and Q vectors is implemented as a part of the QnCorrections framework.
Extracted values of the directed flow as a function of rapidity for negatively charged pions with reaction plane estimated from three different PSD subevents are shown in Fig. 5.

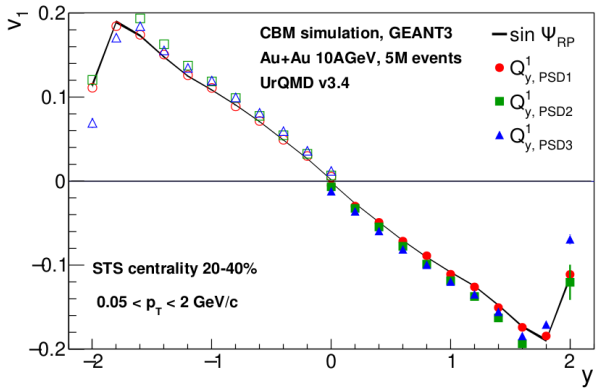


Figure 5: Directed flow of negatively charged pions for the 20-40% centrality class obtained using the y components of the PSD Q-vectors. Shaded area corresponds to v_1 calculated using MC-true reaction plane.

Di-muon measurement at low, intermediate and high invariant masses

The design of the CBM MUCH system consists of one absorber made of 60 cm carbon with additional Pb shielding around the beam pipe (5.7 degrees) and iron absorbers with thickness 20, 20, and 30 cm. Triplets of tracking detectors are mounted behind each absorber layer. Each tracking station behind the first and second absorber layer consists of 3 GEM detectors with high granularity in order to cope with the high particle density in these stations. The particle density behind the third and the fourth absorber is already significantly decreased, so that detectors with lower granularity could be used in order to reduce the number of channels.

The setup discussed above was optimized for measurements of the dimuon spectra in low invariant mass region. The Time-of-Flight (ToF) detector located 8 m downstream the target is used to suppress the background of protons and kaons. Figure 6 depicts the mass distributions for muons from ω (top) and for background (bottom) which are calculated using the time information. These simulations were performed for central Au+Au collisions at 8 AGeV generated with the UrQMD code assuming radial segmentation of 1 degree in stations 1 and 2, and 2 degrees in stations 3 and 4. The acceptance of the setup as a function of transverse momentum and rapidity is illustrated in the upper panel of Fig. 7.

An additional iron absorber of 1 m thickness behind the last detector station is required for measurements of the intermediate and high invariant mass regions. This study is devoted the investigation of the possibility to measure muon pairs over the full invariant mass spectrum. The simulations are based on the absorber system including the last absorber of 1 m thickness. In this case, the time measurements using the ToF detector are possible only for long tracks passing through all absorbers. Therefore, the soft muons are absorbed, and the acceptance of the reconstructed muons pairs will be shifted to forward rapidities (see central panel in Fig. 7). On the other hand, the signal-to-background ratio is very good, exceeding a value of 2 for omega mesons (see black histogram in Fig. 8). A possibility to shift the acceptance for dimuon signals back to midrapidity is to combine different types of tracks, for example long tracks with ToF information, and short tracks without ToF information. The acceptance for long-short and long-long combinations is shown in the lower panel of Fig. 7. The corresponding signal-to-background ratio is represented by the green histogram in Fig. 8.

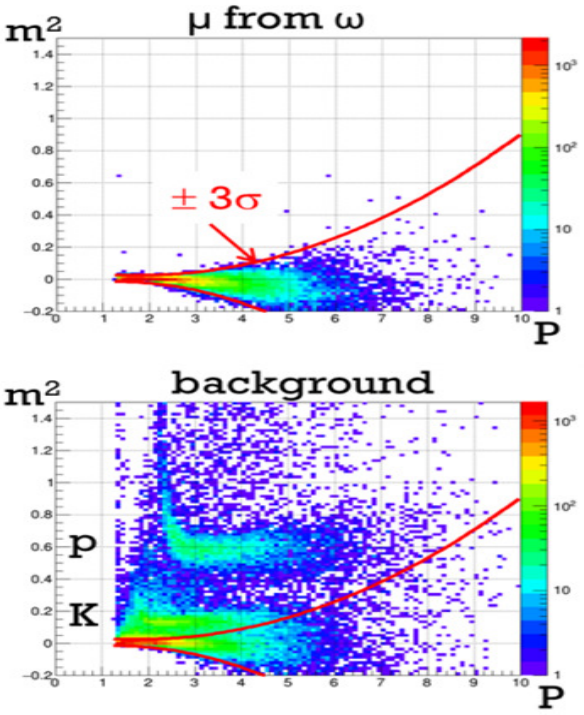


Figure 6: Mass squared versus momentum of muons distributions from omega meson decays (upper panel) and for protons, kaons and pions (lower panel) using ToF measurements. The red lines represent a 3 sigma selection of muon candidates by ToF.

In order to shift the acceptance further towards mid-rapidity, and simultaneously increase the signal-to-background ratio, one can consider an additional time-of-flight measurement in front of the last 1 m thick absorber. In this case, the contribution of short tracks to the background can be reduced, and all track combinations for muon pairs can be used: long-long, short-long, and short-short. Simulations have been performed with a ToF detector in station with a time resolution of 80, 200, 500 and 800 ps. Assuming a time resolution of 80 ps, the acceptance corresponds to the upper panel in Fig. 7, and the resulting signal-to-background ratio is represented by the red histogram in Fig. 8. For a much worse time resolution of 800 ps the signal-to-background ratio decreases by 35% only. When using only long-long and long-short track combinations together with the time measurement in station 4, the signal-to-background ratio improves further.

 DOI:10.15120/GR-2018-1

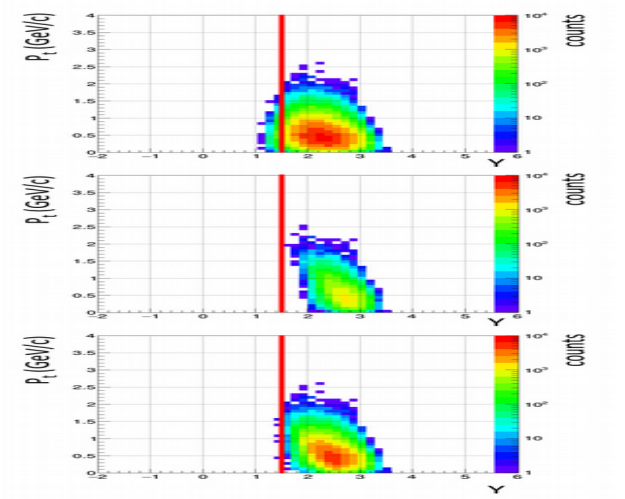


Figure 7: Acceptance for reconstructed muon pairs as a function of transverse momentum and rapidity. Upper panel: muon pairs from all muon track candidates. Middle panel: muon pairs from long tracks traversing 1 m iron absorber. Lower panel: muon pairs from short and long tracks. The red lines refer to mid-rapidity for 8 AGeV.

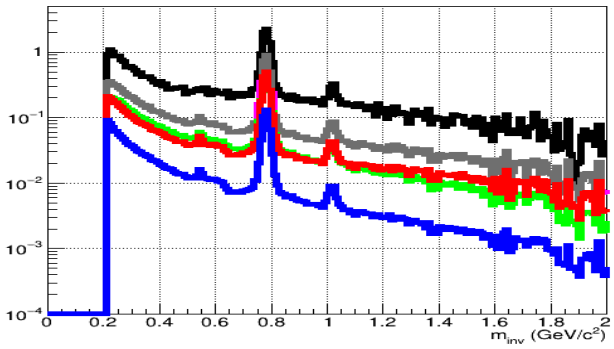


Figure 8: Signal-to-background ratio for muon pairs as a function of invariant mass for central Au+Au collisions at 8 AGeV. Black: muon pairs from long tracks with ToF information, Grey: muon pairs from long-long and long-short tracks, both with ToF information, Red: muon pairs from long-long, long-short, and short-short tracks, both with ToF information.

Dielectron measurements in Au+Au collisions

The measurement of dielectrons with sufficient signal-to-background ratio is essential for the CBM experiment. A good particle identification has to be provided in all momentum regions. For momenta below 6 GeV/c this can be done with the RICH detector. In the region of higher momenta the RICH loses its identification capabilities. The TRD can expand the particle identification and provide the necessary pion suppression to get access to the thermal radiation created in heavy-ion collisions.

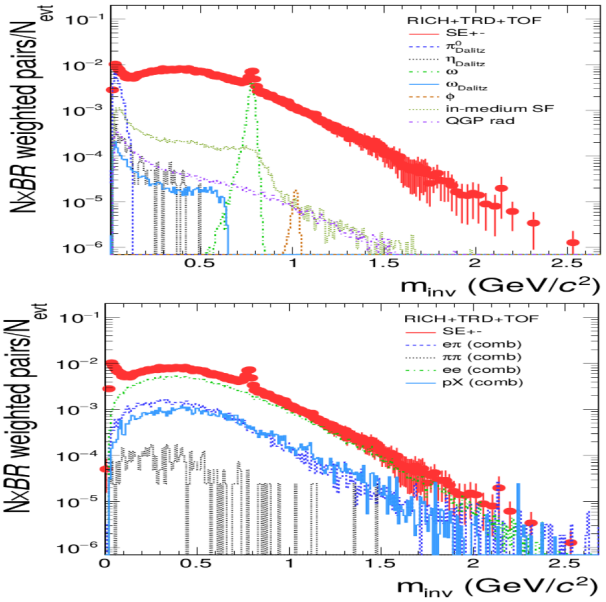


Figure 9: Invariant mass distribution for different unlike-sign pairs identified as electrons for central (10%) Au+Au collisions at 8 AGeV (red points), together with various signal channels (upper panel) and the combinatorial background contributions (lower panel). All contributions are weighted with their expected yield and branching ratio.

Figure 9 shows the invariant mass spectrum for different dielectron channels in the upper part. The simulation is done with 5 million Au+Au collisions at 8 AGeV beam energy for central (10%) events with the newest geometry of the TRD detector modules and four layers and a target thickness of 25 µm. A cocktail of low mass vector mesons (ρ, ω, ω dalitz and φ) as well as thermal radiation from the
hadronic and partonic medium is added via PLUTO generator. The electron identification for the RICH is done with the ANN output, tuned to a momentum independent efficiency of 90%, and for the TRD with the likelihood method tuned to 80% efficiency. The TOF identification uses β measurement to achieve an identification efficiency of ~ 90%. A p_T cut was used with a minimum of 0.2 GeV/c. The red points at the top panel of Fig. 9 show the total amount of reconstructed unlike-sign pairs which were identified as electrons. The signals of the in-medium and the QGP radiation are shown as violet and dark green dotted lines and can be accessed in the invariant mass range above 1 GeV/c^2 with a sufficient signal-to-background ratio. In the lower panel of Fig. 9 the corresponding background contributions are shown. The dotted green line presents the residual combinatorial dielectron pairs (e^+e^-) which are the most significant background contribution up to ~ 1.8 GeV/c^2. The other three lines consist of different hadronic combinations, which were misidentified as electrons but are strongly suppressed with respect to the e^+e^- component.

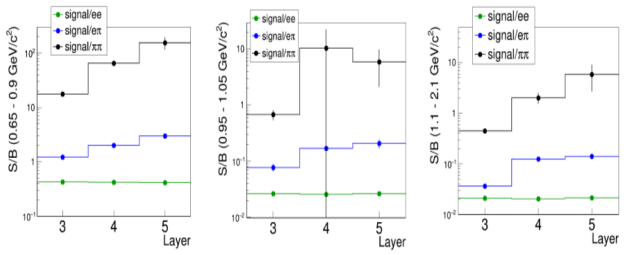


Figure 10: Total signal-to-background ratio in the range around the ω (0.65 − 0.9 GeV/c^2 - left), the φ (0.95 −1.05 GeV/c^2 - middle) and where the thermal radiation is expected to be dominant (1.1 − 2.1 GeV/c^2 - right).

To verify the best detector setup the simulation was also done for three and five TRD layers. Their performance can be quantified via the different signal-to-background ratios in the respective invariant mass regions as shown in Fig. 10. The four layer TRD setup shows a strong performance improvement in comparison to the three layer setup and provides sufficient identification for the requirements.

Hadron identification with the TRD

An important part of the CBM physics program is a high statistics measurement of double-Λ hypernuclei. Since up to now only very few double-Λ hypernuclei events have been identified, the measurement is considered to be a break-through in this field of physics. The Transition Radiation Detector (TRD) will significantly extend the number of hypernuclei states accessible within the program. For the identification of $^{6}_{\Lambda\Lambda}$He, which decays as $^{6}_{\Lambda\Lambda}$He → $^{5}_{\Lambda}$He+p+π and subsequently as $^{5}_{\Lambda}$He → ^{4}He+p+π , the separation of d and He is particularly important. The m/Z measurement of hadrons alone, as provided by the Time of Flight Detector (TOF), is not able to distinguish between the two different charge states. The TRD contributes to the separation of charged hadrons with a measurement of the specific energy loss. Fig. 11 shows how the identification of the light nuclei d and ^{4}He can be performed by combining TOF and TRD information.

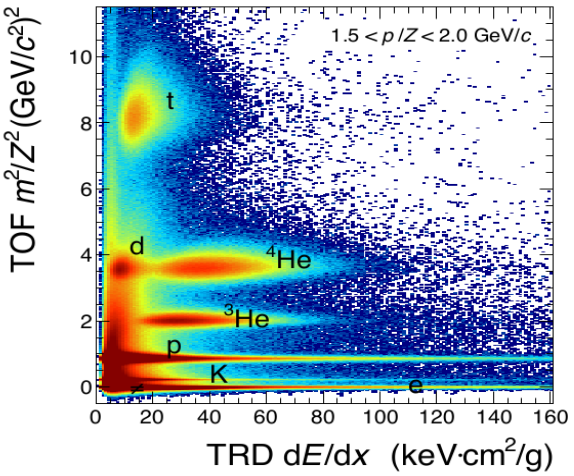


Figure 11: TOF versus TRD Mass squared distribution for 1.5 < *p/Z* < 2.0 GeV/c.

The distributions of the averaged energy loss signal *dE/dx* of d and ^{4}He, as reconstructed in the TRD for Au+Au collisions at 8 AGeV, are displayed in Fig. 12 for one momentum interval. A clear separation of d and ^{4}He is visible. The dE/dx distributions are fitted with a modified Gaussian, which includes the non-Gaussian tails of the distributions via the parameters α and β. Based on the corresponding energy loss resolution *σ(p/Z)/dE/dx(p/Z)*, the separation power can be determined for different particle species. The separation power for deuterons and ^{4}He for different detector geometries is shown in Fig. 13. A separation of d and ^{4}He on a level of σ ≥ 4 is achievable in the whole accessible momentum range with four TRD layers.

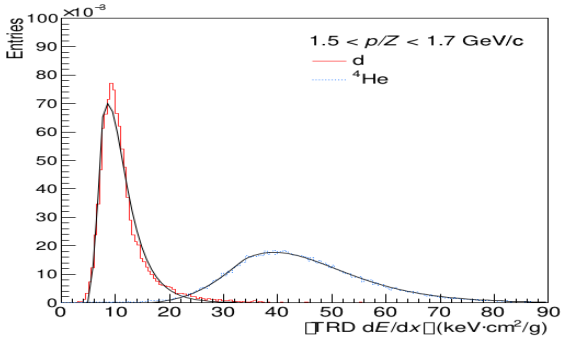


Figure 12: *dE/dx* distributions for d and ^{4}He, as reconstructed with the TRD, fitted with a modified Gaussian.

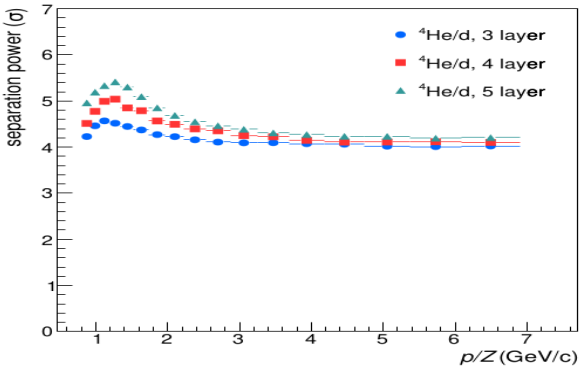


Figure 13: Separation power for d and ^{4}He as a function of momentum for setups with 3, 4 and 5 TRD layers.

Particle identification with the STS

Particle identification based on the energy loss in a thin absorber is a well-known technique in nuclear and particle physics. It can be naturally implemented in a tracking system by studying the energy loss Δ*E*/Δ*x* as function of the measured ratio of particle momentum and charge p/q. In the following we study the possibility of using the CBM-STS detector for particle identification in addition to the dedicated PID detectors (e.g., TOF). This way we expect to obtain a separation power for some particular cases such as low momentum particles not registered by the downstream detectors, decays inside the STS, and particles with the same m/Z ratio, e. g. ^{2}H and ^{4}He, which cannot be distinguished by means of a time-of-flight measurement alone. Since each track consists of several hits, each of which consists of two clusters, there are 2×N hits measurements of ΔE/Δx for a track. Each re-

 DOI:10.15120/GR-2018-1

constructed track has at least three hits in the STS. The chosen implementation for STS is based on the tracker geometry and readout electronics characteristics. The STS readout ASIC (STS-XYTER) has a dynamic range of 15 fC and a 5-bit flash ADC for each channel. These properties limit the implementation of the ΔE/Δx technique. If the charge in a given channel exceeds 15 fC (overflow), the energy loss measurement for the entire cluster (sum of all channels in the cluster) cannot be relied on.

For a proof of concept, we simulated 10^5 particles of various types (see Fig. 14) according to a thermal momentum distribution for Au+Au collisions at 10A GeV. A realistic detector response was involved in the simulation. An equivalent-noise charge of 1500e was used, which is 150−200% of the expected noise for a sensor connected to the readout electronics with a micro-cable; the threshold value was 3 × 1500 e = 4500e. Figure 1 shows that the energy loss measurement gives a reliable separation between single- and double-charged particles for the total momentum range, and separation between Hydrogen isotopes up to 2.5 GeV. The presence of clusters with overflow limits the application of the method in particular for heavy particles with low momentum. The efficiency is more than 99.99% for tritons and lighter particles, and 96.6% for the heaviest simulated particle ^{4}He (integrated over the whole momentum range). It is 100% for p > 2.5 GeV for all particles and drops for lower momenta.

The ΔE/Δx technique was tested on the example of ^{3}H reconstruction (see

Fig. 15). In this particular case it improves the signal-to-background ratio by a factor of 50 compared to using TOF alone for the identification of the decay products; the efficiency drops only by 0.3%. The method appears to be promising and shall be further developed for the implementation in the CBM software as one of the PID tools.

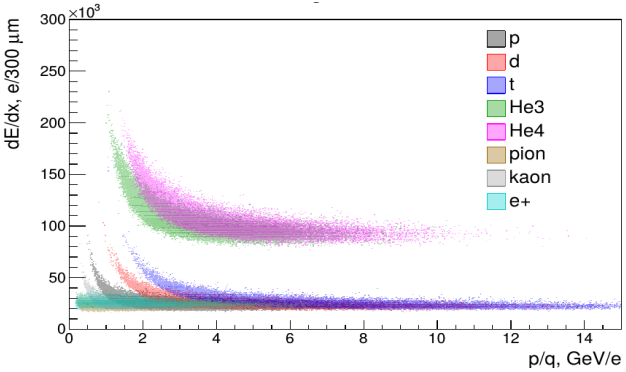


Figure 14: The reconstructed dE/dx normalized to the sensor thickness versus the reconstructed momentum-to-charge ratio from simulation of the CBM-STS.

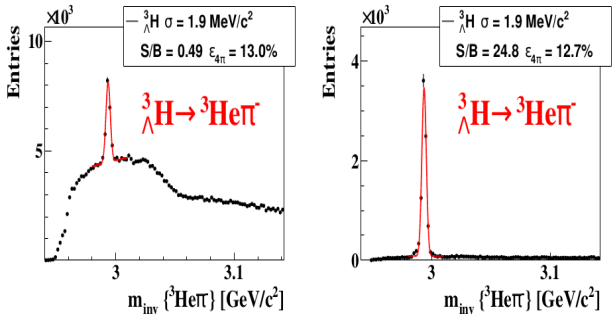


Figure 15: $^3_\Lambda$H reconstruction with TOF only (left) and with an additional PID from STS (right). 5×10^6 central Au+Au collisions at 10A GeV were simulated.

References

[1] [The CBM Collaboration], Chapter “Physics performance” in the CBM Progress Report 2017, DOI: 10.15120/GSI-2018-00485 (2018)

mCBM@SIS18 is on its way*

C. Sturm[1], D. Emschermann[1], J. de Cuveland[3], V. Friese[1], N. Herrmann[2], D. Hutter[3], P.-A. Loizeau[1], W. Niebur[1], A. Senger[1], F. Uhlig[1] , for the CBM collaboration

[1]GSI, Darmstadt, Germany; [2]Ruprecht-Karls-Universität Heidelberg, Germany, [3]Frankfurt Institute of Advanced Studies (FIAS), Frankfurt am Main, Germany.

The Compressed Baryonic Matter experiment (CBM) will explore the QCD phase diagram at the highest net-baryon densities by investigating nucleus-nucleus collisions in fixed-target mode at FAIR energies. The unique feature of CBM is its high-rate capability of up to 10^7 collisions per second, which will make it sensitive to extremely rare probes. In order to achieve these ambitious goals, CBM will employ fast and radiation-hard detectors as well as readout electronics. A novel, free-streaming data acquisition will be used, which aggregates the data sent by the self-triggered front-end electronics and pushes them to an online compute farm for data reconstruction and selection in real time.

By today, the design of the detector and electronics components for CBM is largely completed, and series production is going to start. The components were tested in the laboratory and in beam. Consequently, the next step is to test and optimize the operation of the full system of complex hard- and software components – from the detectors over the readout ASICs and the DAQ to on- and offline data processing and analysis – under realistic experiment conditions before the installation and commissioning of the full CBM detector setup. For this purpose we are presently installing a full-system test-setup for CBM at the GSI/FAIR host lab site under the name mCBM@SIS18 (”mini-CBM”, later shortened to mCBM). This test-setup will include detector modules from all CBM detector subsystems (MVD, STS, RICH, MUCH, TRD, TOF, ECAL and PSD see [1] - [6]) using prototypes or (pre-)series detector modules (mMVD, mSTS, mMUCH, mTRD, mTOF, mRICH, mECAL and mPSD).

Commissioning and running mCBM will complete our knowledge on proper functioning as well as on the performance of the CBM detector systems and their associated Front-End Electronics (FEE) before the final series production starts. The experiences gained during the complete mCBM campaign will significantly shorten the commissioning period for the full CBM experiment at SIS100.

Design of the test-setup

The mCBM test-setup will be positioned downstream a solid target under a polar angle of about 20° with respect to the primary beam, see Fig. 1 and 5. The present status of the mCBM engineering design is described in ref. [7]. mCBM does not comprise a magnetic field, and, therefore, will measure charged particles produced in nucleus-nucleus collisions traversing the detector stations following straight trajectories.

The tracking system comprises 2x STS (mSTS, see [8]), 3x MUCH (mMUCH) [9] and 4x TRD (mTRD) stations in total 9x tracking layers which provide redundant position information and allow to perform tracklet searches.

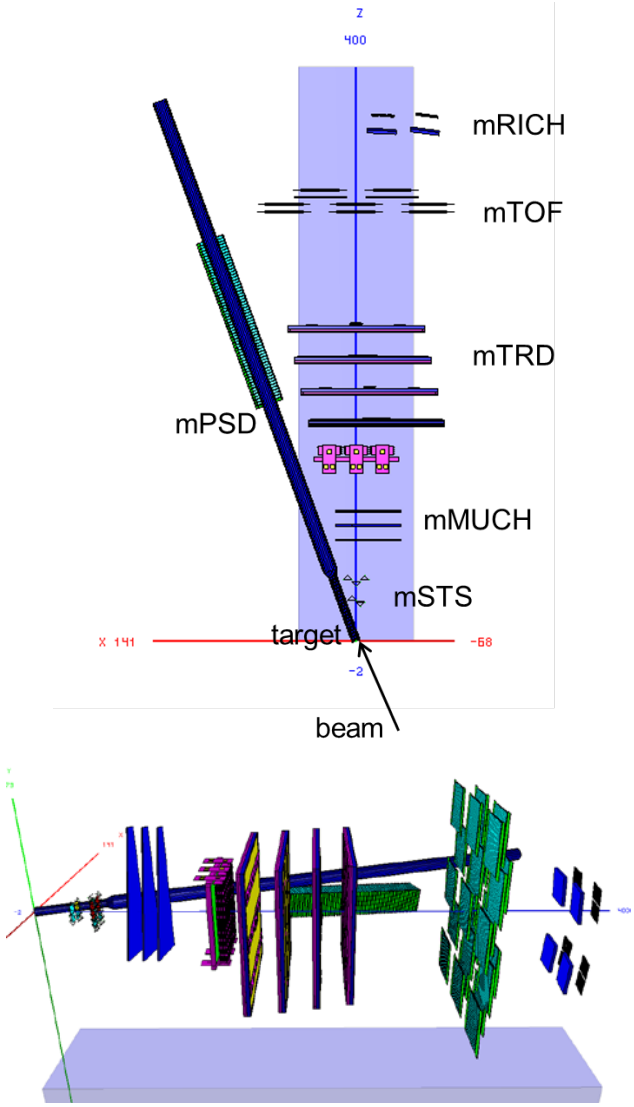


Figure 1: Top view (top panel) and side view (bottom panel) of the mCBM test setup (ROOT geometry) at the HTD cave. The detector stations are aligned at an emission angle of about θ_{lab}= 8° (beam pipe side, y = 0). Note, the GEM counters of the mMUCH subsystem are trapezoidal shaped (see lower panel), which is not visible in the top-view projection.

The setup will include a high-resolution time-of-flight system consisting of a fast and segmented diamond counter for time-zero (T_0) determination in front of the target as well as a TOF stop wall (mTOF) [10]. The mTOF detector modules are shown in Fig. 3 of [11]. An aerogel type RICH detector will be placed as the mRICH subsystem behind the mTOF detector and deliver a second measurement of the particle velocity in a selected ac-

 DOI:10.15120/GR-2018-1

ceptance window [12]. A small calorimeter (mECAL) will also be mounted behind the mTOF covering a reduced acceptance. Additionally, a PSD prototype-module (mPSD, see [13]) will be positioned directly under the beam pipe, 5° tilted relative to the beam axis while pointing to the target. In a later stage MVD stations (mMVD) will be added into the test-setup enabling a high-precision vertex reconstruction. However, the initial configuration of the mCBM test-setup is rather versatile and can be variably adapted according to the needs. Therefore, the detector stations are going to be mounted on sliders of a rail system on top of the mounting table.

The two mSTS stations and the 4^{th} layer of mTRD are centred in x and y. For tracks passing the active area of the mSTS, mMUCH, mTRD and mTOF subsystems the covered θ_{lab} range results to 8° – 32°. The overall acceptance is limited by the mSTS, which is located very close to the beam pipe [8] and cannot be moved further upstream.

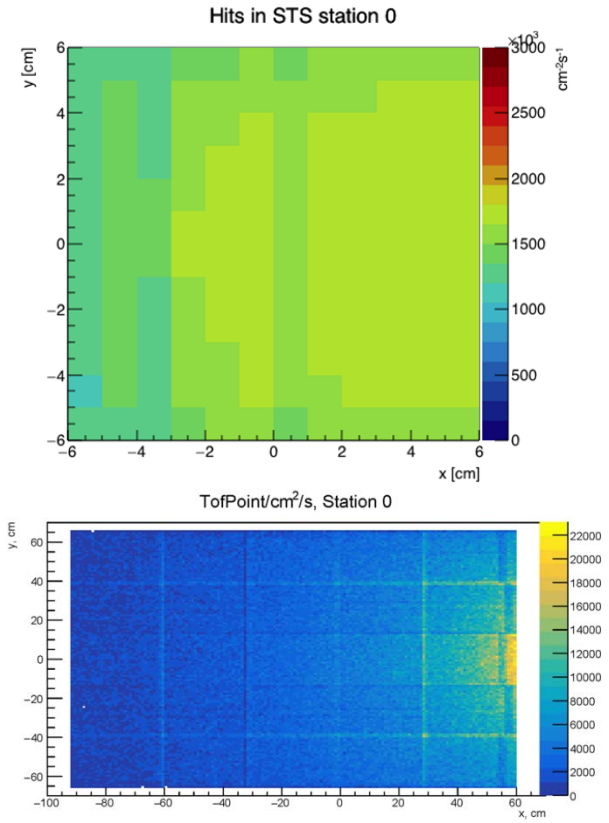


Figure 2: Hit rate within the first station of the mSTS (top panel) and of the mTOF (bottom panel). As input for the simulation, UrQMD events for minimum bias Au + Au col- lisions at 1.24 AGeV has been generated. δ-electrons have been taken into account.

Extensive Monte Carlo simulations have been performed to optimize the geometry of the setup. As input, events for minimum-bias Au+Au collisions at 1.24 AGeV have been generated with the UrQMD transport code. The complete mCBM geometry as shown in Fig. 1 has been implemented in CbmRoot and used for GEANT3 particle transport simulations taking δ-electrons into account. Within the mCBM acceptance an average charged-track-multiplicity yields to about 5 in minimum-bias and about 30 in central Au+Au collisions. In Fig. 2 hit rates normalized to 10^7 collisions per second (10^8 Au ions/s on a 10% interaction Au-target) are shown which have been obtained inside the first mSTS station (top panel) as well as in the mTOF stop wall (bottom panel). As shown, the hit rates result up to 1.8 MHz/cm^2 in the first mSTS station (mSTS0) and up to 22 kHz/cm^2 in the mTOF stop wall matching the design requirements of the CBM STS [1] as well as the CBM TOF [5] detector system. Here, δ-electrons enhance the hit rate within the first mSTS station by a factor of about 3.

The free-streaming DAQ system

The mCBM design focuses on the system performance aspect integrating existing (or currently under construction) prototype modules of all CBM detector subsystems into a common, high-performance free-streaming data acquisition (DAQ) system. The detector stations will be equipped with final readout electronics containing ultra-fast and radiation-tolerant ASICs as front-end chips followed by CERN GBTx-based radiation-tolerant data aggregation units. Further down-stream, the data streams are handled by Data Processing Boards (DPB) containing powerful FPGAs and are forwarded via FLES Input Boards (FLIB), a PCIe based FPGA board, to a large-scale computer farm, the First-Level Event Selector (mFLES, see [14]), which will perform on-line track and event reconstruction and selection, see Fig. 3.

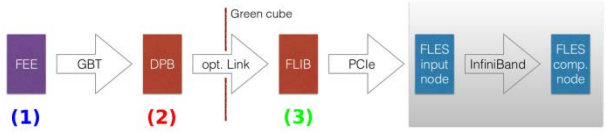


Figure 3: Envisaged mCBM readout chain for the startup phase, based on DPB and FLIB. The mCBM subsystems are equipped with individual front-end electronics FEE (1). These front-ends are interfaced by the GBTx ASIC, which forwards the detector data via optical GBT link. All GBT links are received by the DBP layer located at 50 m distance in the DAQ container (2). The DPB is a FPGA based board which allows for subsystem specific pre-processing of the arriving data stream. A long distance optical link connects the DPB output to the FLIB board installed in the FLES input node in the Green IT Cube (3).

The CBM detector front-ends are time-synchronized to the nanosecond level by the Timing and Fast Control (TFC) system. The detector front-end digitizes signals above threshold and assigns a time stamp to the hit. This data is then forwarded via an electrical connection to the GBTx readout board, where the electrical signals acquired through a large number of e-links are converted and merged into an optical GBT link operating at 4.48 Gbit/s. These GBT links are the detector interface to the Data AcQuisition (DAQ) chain.

On the road towards the full CBM DAQ system the mCBM DAQ system will be deployed in two phases. During phase I, the GBTx-based subsystems (mSTS, mMUCH, mTRD and mTOF) will be read out using already available readout chains based on existing prototype implementations of DPB and FLIB, see Fig. 3.

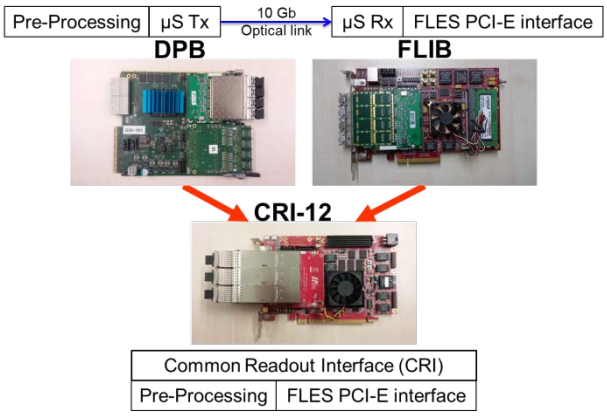


Figure 4: Upgrade of the mCBM DAQ in 2019.

As current prototype hardware, an AMC FMC Carrier Kintex (AFCK) board [15] is used for the DPB, a HiTech Global HTG-K700 PCIe board for the FLIB. Both boards are based on a Xilinx Kintex-7 FPGA. In phase II, DPB and FLIB will be replaced by a prototype of the Common Readout Interface (CRI) (see Fig. 4) in the FLES input stage, as it is foreseen for the CBM experiment. In addition, the mCBM subsystems (mRICH, mPSD) readout with FPGA TDCs chains will be added to the DAQ setup in 2019.

Reconstruction of the experimental area

The installation site for the mCBM test-setup is the detector test area named HTD in the GSI nomenclature (see Fig. 5) situated at the beam entrance of the experimental area cave-C (HTC) hosting the nuclear structure experiment R^3B. Although the space is very limited in the HTD area, the compact mCBM setup measuring a full length of about 4 m will fit into the HTD cave.

The arrangement of the HTD cave for the mCBM test-setup depends substantially on the incident angle of the beam as shown in Fig. 5. This also affects shielding measures which become necessary to make high-rate beam tests feasible up to CBM design collisions rates. Many iterations of radiation level simulations had been carried out using the FLUKA software package to fulfil the radiation safety requirements [16]. As one of the shielding measures, in particular to protect the R^3B experiment located in cave-C, a sandwich-like beam dump has been constructed consisting of 12x 12cm thick steel plates covered by 80 cm thick concrete blocks as visible in Fig. 6. A beam hole has been drilled up to the steel core (see Fig. 5) which will be blocked after irradiation.

Additional concrete blocks embedded into the chicane entrance have been placed directly in front of the R^3B target region (see Fig. 5 and 7). To block access into the HTD cave after high-rate beam-tests have taken place, a lockable entrance door is being installed. Up to four additional concrete layers with a thickness of 0.8 m each will be placed on top of the HTD cave ceiling.

As illustrated in Fig. 5, the incoming beam will be either transported to the R^3B experiment or deflected to the mCBM setup by a switching magnet (dipole magnet) mounted directly in front of cave-C carrying the name HTD MU1 in the GSI nomenclature. To date, beams had been deflected at an effective angle of 14.5° corresponding to an magnetic rigidity of Bρ = 10 Tm. Accordingly, the maximum kinetic energy for heavy projectiles like Au had been limited to 0.45 AGeV generating unrealistic conditions due to a large number of low-momentum fragments emitted during the collision. In order to exploit the full beam energy range of SIS18 we are going to exchange the vacuum chamber of the switching magnet by a spare chamber with vacuum outlets for 0° and 7.5°. With the given magnetic induction, beams will be bend on a radius of ρ = 11.25 m at top SIS18 energy which results to an effective deflection angle of 8.0°.

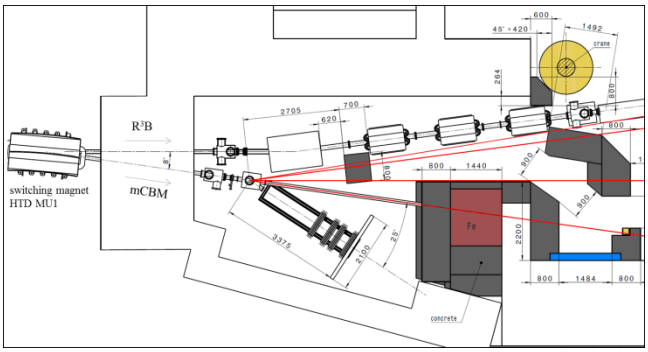


Figure 5: The modified mCBM cave (HTD) at the SIS18 facility of GSI/FAIR (as of August 31, 2017).



Figure 6: The Iron core of the beam dump is prepared for concrete pouring.



Figure 7: Chicane entrance to the mCBM cave (HTD).

 DOI:10.15120/GR-2018-1

Benchmarking the mCBM test-setup

To verify the performance of the CBM data taking concept the mCBM setup will be used to reconstruct physics observables that can be compared to published data. A feasibility study with the mCBM setup was performed using the Λ production probability in heavy-ion collisions as a benchmark observable. At SIS18 beam energies Λ baryons are produced close to or below the free NN production threshold. Thus their production probability is rather small posing a CBM-like challenge to the reconstruction and se- lection task.

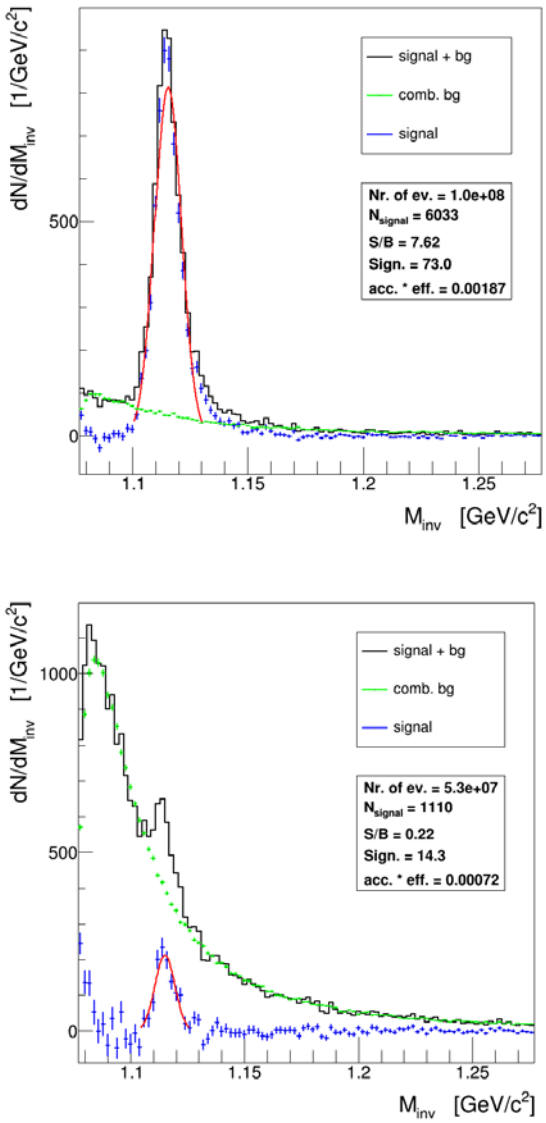


Figure 8: Λ-identification in minimum bias UrQMD events in Ni+Ni collisions at 1.93 AGeV (top) and in Au+Au at 1.24 AGeV (bottom). Invariant mass distributions are shown for (π-p) pair combinations (combinatorics) within events (black line, signal + bg), for pair combinations from mixed events (green symbols, comb. bg) and for the resulting distribution after subtraction (blue symbols, signal). Statistics information is obtained from a Gaussian fit to the subtracted distribution (red line).

Since mCBM does not include a magnetic field for momentum measurement, the reconstruction has to be done via time-of-flight (TOF) and track topology, assuming the pion and proton mass for (π-p) pair candidates. For simplicity, only STS and TOF hits are considered for the reconstruction algorithm. As geometry, the most recent mCBM setup has been used within the MC simulation as it is depicted in Fig. 1. Fig. 8 demonstrates that the limited information available is sufficient for Λ reconstruction. Improvements are certainly possible by tuning the selection cut values. As simulation input, 10^8 minimum bias events of the reactions Ni+Ni at an incident energy of 1.93 AGeV and $5.3 \cdot 10^7$ minimum bias events of Au+Au collisions at 1.24 AGeV have been generated with the UrQMD transport model [17]. The corresponding phase space coverage (efficiency in z-direction) for Ni+Ni collisions at 1.93 AGeV is shown in Fig. 9 demonstrating that the acceptance of mCBM is limited to a small angular range close to mid-rapidity.

For both benchmark collision systems published data from the FOPI collaboration are available in [18] as well as from the HADES collaboration in [19] that the mCBM results can be quantitatively compared to. It is worth noting that the technical goal and challenge is to reconstruct the invariant mass distributions shown in Fig. 8 within a time period of about 10 s data taking at SIS18, assuming 10^7 nucleus-nucleus collisions per second (10^8 ions per second bombarded on a 10 % interaction target).

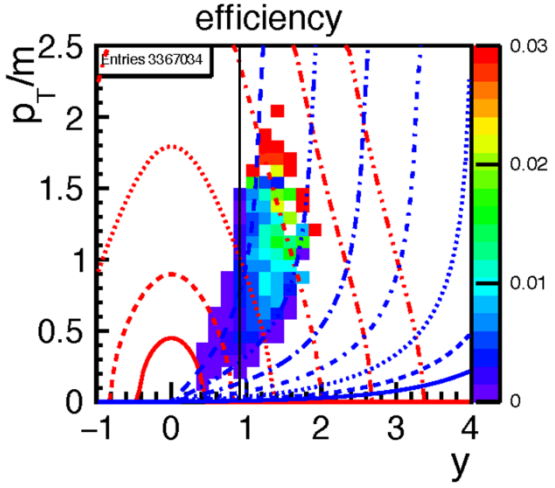


Figure 9: Efficiency of reconstructed Λ - baryons with mCBM produced in Ni+Ni collisions at 1.93 AGeV (input: events generated with UrQMD). Red and blue lines indicate constant laboratory momenta and laboratory polar angles, respectively. The black line marks mid-rapidity.

mCBM beamtime

Mid of 2017 a beamtime proposal had been submitted to the General Program Advisory Committee of GSI/FAIR (G-PAC) for the year 2018 (”development & commissioning”) with the focus on data transport, the data analysis as well as detector tests, and for the year 2019 (”approaching full performance”) implying the completion of subsystems, the high-rate data transport and data processing incl. online reconstruction. The applied beamtime has been fully granted by the G-PAC in September 2017.

All the background rejection strategies necessary to reconstruct rare probes with CBM at SIS100 can be prepared and exercised with mCBM. In addition, if the technical goals of mCBM are achieved, a measurement of the Λ production excitation function should become feasible. This was not yet measured in the SIS18 beam energy range thus offering a unique opportunity to contribute to world data, although the covered phase space is limited and therefore systematic errors become large when extrapolating to unmeasured regions.

The successful implementation and demonstration of the technical capabilities would also open the road to more relevant physics observables like the measurement of light hypernuclei. The beam time request for more physics oriented observables will be placed in the next beamtime period from 2020 – 2021, once the preliminary results are supporting the high expectations.

References

[1] J. Heuser, W. F.J. Müller, V. Pugatch, P. Senger, C.J. Schmidt, C. Sturm and U. Frankenfeld, Technical Design Report for the CBM Silicon Tracking System (STS),GSI-2013-05499, http://repository.gsi.de/record/54798

[2] S. Chattopadhyay, Y. P. Viyogi, P. Senger, W. F.J. Müller and C. J. Schmidt, Technical Design Report for the CBM: Muon Chambers (MuCh), GSI-2015-02580, https://repository.gsi.de/record/161297

[3] C. Höhne et al., Technical Design Report for the CBM Ring Imaging Cherenkov Detector (RICH), GSI-2014-00528, http://repository.gsi.de/record/65526

[4] C. Blume et al., Technical Design Report for the CBM Transition Radiation Detector (TRD), to be published

[5] N. Herrmann et al., Technical Design Report for the CBM Time-of-Flight System (TOF), GSI-2015-01999, https://repository.gsi.de/record/109024

[6] F. Guber and I. Selyuzhenkov, Technical Design Report for the CBM Projectile Spectator Detector (PSD), GSI-2015-02020 , https://repository.gsi.de/record/109059

[7] L. Radulescu, D. Emschermann, and A. Bercuci, CAD integration of the mCBM subsystems, CBM Progress Report 2017, 2018, DOI 10.15120/GSI-2018-00485

[8] O. Vasylyev et al., Progress with the integration of the mCBM Mini Silicon Tracking System, CBM Progress Report 2017, 2018, DOI 10.15120/GSI-2018-00485

[9] C. Ghosh et al., Development of a MUCH Cooling system for mCBM, CBM Progress Report 2017

[10] I. Deppner , N. Herrmann , and the CBM TOF working group, Time Of Flight Detector - Summary, CBM Progress Report 2017, 2018, DOI 10.15120/GSI-2018-00485

[11] The CBM eTOF working group, The TOF FAIR Phase 0 project - eTOF at STAR, CBM Progress Report 2017, 2018, DOI 10.15120/GSI-2018-00485

[12] G. Pitsch , S. Lebedev, and C. Höhne, Monte-Carlo Simulations of a mRICH detector with aerogel radiator in mCBM, CBM Progress Report 2017, 2018, DOI 10.15120/GSI-2018-00485

[13] F. Guber, mPSD at mCBM, CBM Progress Report 2017, 2018, DOI 10.15120/GSI-2018-00485

[14] D. Hutter , J. de Cuveland , and V. Lindenstruth, Preparations for the mCBM FLES Setup, CBM Progress Report 2017

[15] W.M. Zabołotny and G. Kasprowicz, "Data processing boards design for CBM experiment", Proc. SPIE 9290 (2014) 929023, doi:10.1117/12.2073377

[16] A. Senger et al. (CBM Collaboration), Concrete shielding and beam dump for mCBM, CBM Progress Report 2017, 2018, DOI 10.15120/GSI-2018-00485

[17] M. Bleicher et al., Relativistic Hadron-Hadron Collisions in the Ultra-Relativistic Quantum Molecular Dynamics Model, J. Phys. G: Nucl. Part. Phys. 25 (1999) 1859-1896

[18] M. Merschmeyer et al. (FOPI collaboration), K0 and Λ production in Ni+Ni collisions near threshold, Phys. Rev. C 76 (2007) 024906

[19] H. Schuldes et al. (HADES collaboration), Studying Strangeness Production with HADES, Web of Conferences 171, 01001 (2018), SQM2017

Experiment beamline: mCBM@SIS18
Experiment collaboration: CBM
Experiment proposal: S471
Accelerator infrastructure: SIS18 / HEST
PSP codes: 1.1.1
Grants:
GSI Helmholtzzentrum für Schwerionenforschung GmbH
Facility for Antiproton and Ion Research,
Helmholtz Gemeinschaft,
BMBF No. 05P12VHFC7, 05P2015, 05P15PXFCA, 05P15RGFCA, 05P12RGFCG, 05P15RFFC1, 05P12VTFCE, 05P15VHFC1, 05P15PMFC1, 05P16VTFC1, 05P16PMF1, 05P16PMFC1, 05P15ZAFC1,
HIC for FAIR Helmholtz International Center,
HGS-HIRe for FAIR,
Hessian Initiative for Excellence (LOEWE),
Cremlin - Connecting Russian and European Measures for Large-scale Reasearches Infrastructure,
European Union's Horizon 2020 research and innovation programme under grant agreement No.654166 and 654168, Helmholtz-YIG grant No.VH-NG-823,
Humboldt foundation, Germany
Strategic university co-operation with:
Darmstadt, Frankfurt-M, Gießen, Heidelberg

* This report is also part of the CBM Progress Report 2017, 2018, DOI 10.15120/GSI-2018-00485

D mesons Langevin propagation at SIS300-FAIR

G. Inghirami [1,2,3,4], H. Van Hees[1,2], S. Endres[1,2], J. Torres-Rincon[5] and M. Bleicher[1,2,3,4]

[1]FIAS, Frankfurt am Main, DE; [2]Goethe-Universität, Frankfurt am Main, DE; [3]GSI, Darmstadt, DE;
[4]J. von Neumann Institute for Computing, Jülich, DE; [5]Stony Brook University, Stony Brook, New York, USA

Heavy quarks represent an excellent tool to probe the properties of the medium which is supposed to form in relativistic heavy ion collisions, because they are produced in the very initial stages after the collision and their number is conserved until the hadrons they form decay by weak interaction, long time after the kinetic freezeout. Since their masses are considerably larger than the light quark masses, we can model their propagation into the medium by adopting a Langevin approach. In this work we perform the Langevin propagation of c and anti-c quarks in fixed target Au-Au collisions, with 25 AGeV beam energy, in the range of the future FAIR facility. In our simulations we neglect the back reaction of charm quarks and D mesons on the medium, allowing for the simultaneous propagation of many charm quarks at the same time, whose initial momentum distribution is computed by using Pythia 8.2. We compute the evolution of the background medium using both the UrQMD/hybrid [1] and the UrQMD/coarse graining [2] approaches, running simulations at fixed impact parameters b = 3 fm and b = 7 fm. We perform the hadronization by adopting an instantaneous coalescence model [3] in momentum space combined with Peterson fragmentation. We consider only the formation of D^+, D^0 mesons and their antiparticles. We take into account the effects of the finite baryon chemical potential on the values of the transport coefficients through a fugacity factor. The drag and diffusion coefficients in the partonic phase are computed within a resonance model [4], while the description of how the coefficients are derived in the case of D mesons can be found in ref. [5]. We study how variations in the centrality class and in the conditions for charm quark hadronization influence the elliptic flow and the nuclear modification factor of the final D and anti-D mesons.

We find that most of the final elliptic flow of D and anti-D mesons is built during the partonic phase, while the subsequent hadronic interactions seem to have a limited influence. Moreover, we find that the model of the dynamics of the medium and the hadronization procedure have a large impact on the magnitude and on the transverse momentum dependence of the elliptic flow and of the nuclear modification factor.

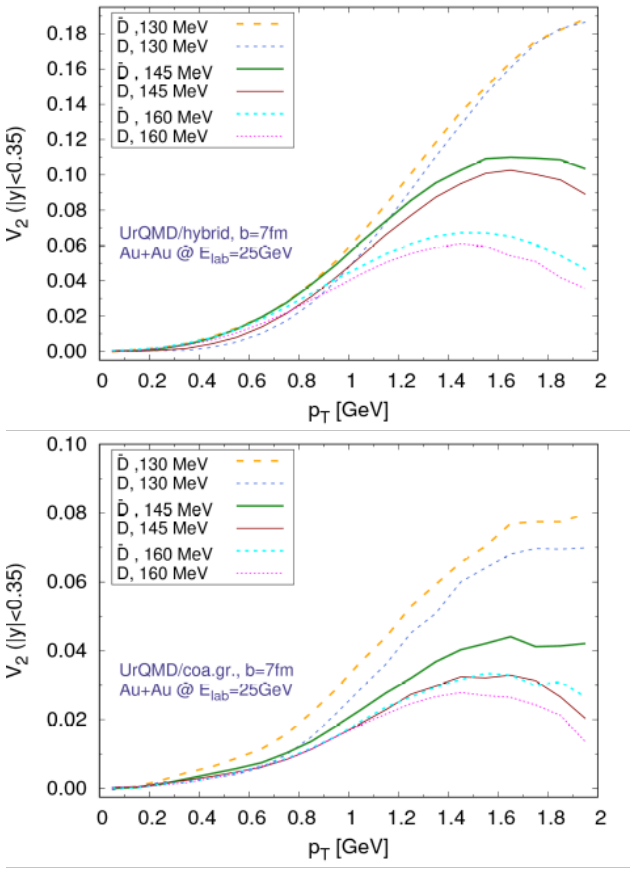


Figure 1: Elliptic flow of D and anti-D mesons (|y| < 0.35) within the UrQMD/hybrid (top) and UrQMD/coarse graining (bottom) approaches. Here we show the dependence on the hadronization temperature in Au+Au collisions at Elab = 25 AGeV at a fixed impact parameter b = 7 fm.

References

[1] H. Petersen, J. Steinheimer, G. Burau, M. Bleicher and H. Stöcker, Phys. Rev. C 78, 044901 (2008)

[2] S. Endres, H. van Hees, J. Weil and M. Bleicher, Phys. Rev. C 92, 014911 (2015)

[3] V. Greco, C. M. Ko and R. Rapp, Phys. Lett. B 595, 202 (2004)

[4] H. van Hees and R. Rapp, Phys. Rev. C 71, 034907 (2005)

[5] L. Tolos and J. M. Torres-Rincon Phys. Rev. D 88, 074019 (2013)

Grants: COST Action CA15213 (THOR)

Strategic university co-operation with: Frankfurt-M

CBM computing – progress, status and outlook

J. de Cuveland[1], V. Friese[2], P.-A. Loizeau[2], F. Uhlig[2], M. Zyzak[2]
for the CBM Computing Working Group

[1]FIAS, Frankfurt, Germany; [2]GSI, Darmstadt, Germany

The development of CBM software has, over the years, concentrated on simulation of nuclear collision events in the CBM detector setup, and reconstruction and analysis of the simulated data. The corresponding tools were widely used for studying the physics performance of the CBM detector.

With the advent of mCBM, which will start taking data in August 2018, new challenges appeared, which have to be met on a rather short timescale. mCBM will allow to test the entire data chain, from the front-end electronics through the DAQ chain to online and offline processing of experiment data on CPU. This will allow to scrutinise existing software concepts, but also enforces to accelerate the process of moving simulation and reconstruction from the event-by-event case to the handling of free-streaming data, corresponding to the real situation for CBM and mCBM. Moreover, issues not addressed so far, like the software needed to set-up, run and control the experiment, and, most of all, a framework concept of processing data in real-time, suddenly become very urgent.

To meet these challenges organisationally, the CBM software activities were structured and defined in a project-like manner, with the aim to distribute responsibilities, assess manpower, planning, timelines and milestones, and identify critical items and shortage of workforce. The following Computing Projects were defined (see Fig. 1):

- Experiment and Detector Control Systems (EDC): tools to configure and monitor detectors and DAQ
- Online Data Management (ODM): software to operate the online computing farm, receive data from the experiment, build time slices and deliver them to the compute nodes
- Data Processing Framework (DPF): the environment for data processing both online and offline
- Data Analysis Algorithms (ALG): algorithms for event reconstruction and common data analysis
- Simulation Software (SIM): enable detector simulation on the same level as real experiment raw data
- Offline Analysis Environment (OAE): develop strategies and tools for the offline analysis of large-scale data
- Software Development Infrastructure (INF): provide and maintain tools for collaborative software development and maintenance

The platform for coordination of and communication between the projects is the newly established Computing Board. In the following, we briefly report on the status and progress following the project structure.

Experiment and Detector Control system

The detector control was until now driven by beam-time activities and therefore mostly concerned systems with single detector type [1-3]. Following the establishment of the Computing Board, work is ongoing to define the tasks, interfaces and general specifications of the slow-control, detector-control and central experiment control systems. Prototypes of these systems will help for the operation of mCBM phase I and are necessary for efficient data taking with mCBM phase II.

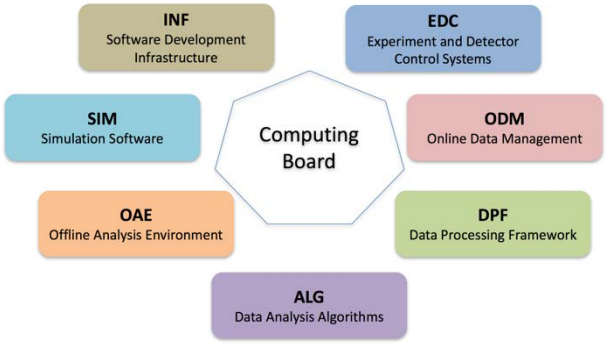


Figure 1: Computing project structure

Online Data Management

A demonstrator software that implements time slice building as well as the interfaces to detector links and online processing has been available for several years. This software, named *FlesNet* has already been used for online data taking in various CBM detector test setups and beam tests. It is still evolving, with recent work focusing on operational improvements for small and medium-sized setups. This includes the addition of a ZeroMQ-based transport complementing the existing RDMA-based transports [4].

With regard to the full SIS-100 setup, the scalability of the time slice building has been improved, including the demonstrator implementation of a new data-flow scheduler [5]. The work of the near future will cover additional features and tools that will also be beneficial to the upcoming operation of mCBM.

Data Processing Framework

The ROOT-based software framework employed by CBM for many years now allows to simulate, reconstruct and analyse physics events in an integrated environment. It, however, provides no inherent mechanism to parallelise the execution of tasks and thus make full use of the available computing architectures. This strongly limits its applicability for real-time data processing on the CBM compute nodes. First studies to introduce parallelism schemes into *CbmRoot* were undertaken [6, 7], but showed little performance gain owing to the structure of the reconstruction processing graph. In the future, the possibility to use the message-queue based *FairMQ* scheme, developed by the Scientific Computing group of GSI as extension to *FairRoot*, will be investigated.

 DOI:10.15120/GR-2018-1

Databases for various purposes (configuration, conditions, components) will be important ingredients to the framework. *FairDB* is currently used for managing the hardware component properties in several detector systems and may also be usable for other purposes [8].

Data Analysis Algorithms

The core reconstruction algorithm, the track finding in the STS, was already enabled to operate on free-streaming data. The event-building procedure from reconstructed STS tracks is also available and was tested with physics analysis [9]. The proper time-based input from cluster and hit finding, however, is currently only available for the STS and MUCH systems [7, 10]. Thus, current efforts are devoted to extend the existing time-based reconstruction to the downstream detectors (global tracking). Progress was made for tracking in the muon system [11, 16] and in the TRD [12]. In addition, the particle identification potential for light nuclei, relevant for the study of e.g., hyper-nuclei production, was investigated using the energy loss in the STS [13] and in the TRD [14]. Moreover, a first version of track finding in mCBM, which differs from the full CBM in the track model, was made available [15].

Development of the time-based procedure for reconstruction of global tracks is in progress. Two approaches are being considered at the moment: based on the *littrack* and the CA track finder algorithms. The *littrack* method is the current standard, and addition of the time measurement to the reconstruction scheme is a straightforward solution. However, it is based on the track following algorithm using STS tracks as seeds, which makes it complicated to be applied for the detector alignment task. In its turn, the CA track finder in STS is already fully adapted for time-based reconstruction and expansion of the method to the downstream detectors is currently being implemented [16]. The task of the time-based global track finder requires realistic description of the time response of cluster and hit finding algorithms, which will be addressed in the nearest future. Based on this realistic input, the existing solutions for global tracking will be compared w.r.t. performance in order to arrive at an optimal solution.

Simulation Software

The two major ingredients for simulations are the description of the detector geometry and a model for the detailed detector response (digitizer). The detector geometries for CBM were consolidated; by now, all detector systems deliver the geometry in the ROOT *TGeoManager* format as agreed on for standalone visualisation and management through a database (see [17-19]). Geometry descriptions for all detector system participating in mCBM are also available. In order to manage the increasing number of geometry versions for the detector system for different contexts / setups and provide them in a controlled and user-friendly way, the development of a Geometry Database was continued; a prototype is now available for testing [20].

Time-based version of all digitizers were provided (see [18, 21]), which is of particular importance for the modelling of the actual data stream from both mCBM and CBM. Together with a (simplified) software representation of the time-slice building, the simulation output is now logically equivalent to the raw data expected from the data acquisition. It is, however yet on the *digi* (ROOT) level and does not include all details of the time slice building (e.g., micro-slice sub-structure). Similarly, not all relevant features (e.g., data loss due to pile-up from different events) are yet included in all digitizers; this will be the task for the immediate future.

The next issues to be addressed by simulation software are thus: the proper treatment of inter-event pile-up in the digitizers, the inclusion of not event-correlated background sources into the simulations (see [22, 23]) and the description of the data stream in the actual raw data format.

Offline Analysis Environment

Considerations to organise the offline analysis of the huge amount of data CBM will archive when starting operations in 2024 have not started yet in earnest. A strategy will be developed in close cooperation with the other FAIR experiments, in particular with PANDA as the other data-intensive experiment, and with FAIR/GSI-IT. First steps to develop a common FAIR computing model, of which the CBM computing model will be one part, will be taken in 2018, with the aim to arrive at a Technical Design Report in 2020.

Software Development Infrastructure

The basic tools to enable an effective and collaborative software development are in place and operational since several years.

- Software distribution: *CbmRoot*, comprising simulation, reconstruction and analysis software, is distributed through a *subversion* repository hosted on a GSI server. Several packages (*KFParticle*, *KFParticleFinder*, *FlesNet*), are hosted separately on *git* servers and are integrated into *CbmRoot* in the build process. The movement of the entire CBM software to a *git* repository is one of the tasks for the next future.
- Build system: We use *CMake* to build *CbmRoot*, which takes also care of the integration of external packages. Shell scripts for the installation of external packages and of *FairRoot* are provided. The installation is supported on all Linux flavours as well as for OS X.
- Documentation: By convention, documentation is provided in-code in *Doxygen* format. The documentation is generated nightly on a GSI server, which provides a browser-based output [24]. Additional requirements on documentation are to be defined by the Computing Projects.
- Software integrity management: the possibility to perform regular tests (nightly or on commit) is provided through a *CDash* system. Tests are to be defined by the Computing Projects. The test results are furnished on a web server [25].
- Project management and communication: The collaborative platform for software development in

CBM is a *Redmine* instance [26]. It integrates a browser front-end to the repository, systems for issues, news, forum and Wiki, and project planning facilities. The *Redmine* system is also used for some hardware projects.

The development tools and the deployment of servers are subject to constant maintenance and further development following the needs of the Computing Projects.

This report is also part of the CBM Progress Report 2017 (doi:10.15120/GSI-2018-00485).

References

[1] P. Klaus et al., *The Detector Control System for the MVD prototype PRESTO*, CBM-PR2017*, p. 12

[2] J. Bendarouach and C. Höhne, *Design of a control and monitoring system for the mirror alignment of the CBM RICH detector*, CBM-PR2017, p. 59

[3] V. Negi, J. Saini and S. Chattopadhyay, *Design and development of error resilient control system of Low Voltage Distribution Board for CBM-MUCH detector*, CBM-PR2017, p. 79

[4] J. de Cuveland et al., *A FLESnet transport using ZeroMQ*, CBM-PR2017, p. 129

[5] F. Salem et al., *Data-flow scheduling for a scalable FLESnet*, CBM-PR2017, p. 130

[6] M. Prokudin, *Parallelization of CbmRoot at task level*, CBM-PR2017, p. 132

[7] V. Singhal et al., *Parallelization of cluster and hit finding for the CBM-MUCH*, CBM-PR2017, p. 144

[8] D. Bertini and E. Lavrik, *Progress with FairDB development*, CBM-PR2017, p. 133

[9] V. Akishina et al., *Reconstruction of time-slices in CBM at high interaction rates*, CBM-PR 2017, p. 145

[10] V. Friese, *Time-based cluster finding in the CBM-STS detector*, CBM-PR2017, p. 143

[11] A. Zinchenko and V. Ladygin, *Application of the vector finding-based track reconstruction method for the CBM muon setup*, CBM-PR2017, p. 146

[12] O. Derenoskaya, T. Ablyazimov and V. Ivanov, *Towards $J/\psi \to e^+e^-$ triggering with the CBM-TRD*, CBM-PR2017, p. 148

[13] H. Malygina et al., *Investigation into the particle identification potential of the CBM-STS*, CBM-PR2017, p. 160

[14] S. Gläßel et al., *Hadron identification via energy loss measurements with the TRD*, CBM-PR2017, p. 156

[15] T. Ablyazimov, V. Friese and V. Ivanov, *Using the binned tracker in mCBM*, CBM-PR2017, p. 189

[16] V. Akishina, I. Kisel and M. Zyzak, *Kalman Filter track fit for the CBM STS and MUCH detector systems*, CBM-PR2017, p. 147

[17] P. Klaus et al., *Update on the CBM MVD geometry*, CBM-PR2017, p. 135

[18] L. Lebedev, E. Ovcharenko and C. Höhne, *RICH software status*, CBM-PR2017, p. 138

[19] O. Singh et al., *Description of the CBM-MUCH geometry in ROOT format*, CBM-PR2017, p. 140

[20] E. Akishina et al., *Geometry database for the CBM experiment*, CBM-PR2017, p. 142

[21] A. Bercuci et al., *Time-based CbmRoot simulations of the Bucharest TRD prototype for mCBM*, CBM-PR2017, p. 186

[22] V. Friese, *Implementation of electronic noise in the simulation of the CBM-STS*, CBM-PR2017, p. 137

[23] A. Senger, *Time-based track reconstruction in STS with δ-electrons*, CBM-PR2017, p. 136

[24] http://cbmroot.gsi.de/cbm-doc/daily/html/index.html

[25] https://cdash.gsi.de/index.php?project=CbmRoot

[26] https://redmine.cbm.gsi.de/projects/cbmroot

.

* I. Selyuzhenkov and A. Toia (eds.), CBM Progress Report 2017, Darmstadt 2018, ISBN 978-3-9815227-5-4, doi:10.15120/GSI-2018-00485

HADES activities and status 2017

The HADES collaboration

GSI Helmholtzzentrum für Schwerionenforschung

Introduction

The main goal of the HADES experiment is to explore the microscopic structure of dense baryonic matter. HADES experiments performed in the last years in nucleus-nucleus and proton-nucleus reactions have shown the important role played by the propagation of far off-shell ρ mesons due to their coupling to baryonic resonances in hadronic matter, visible as an excess radiation of the e^+e^- production above conventional sources for invariant masses below the vector meson poles. To provide a reference to these medium effects and to study the electromagnetic structure of the baryonic resonances an important programme has been developed by the HADES collaboration to investigated elementary reactions like pp, quasi-free ′n′p and recently πp.

Studying reactions with proton and pion beams on proton (liquid H_2 or polyethylene) targets is indeed an important element of the HADES program. Besides measurements of production cross sections, which provide an essential reference for heavy-ion collisions, also the elementary reaction mechanisms are studied. In particular, the role of baryonic resonances is investigated in both strangeness and dielectron production.

Recent physics results

Results from 2012 Au+Au run

The time-of-flight (TOF) resolution of HADES has been improved by using additional information in the calibration procedure and by assessing the quality of the TOF detector and its readiness for the upcoming experimental runs at SIS18 (see contribution of G. Kornakov).

We have also improved our analysis techniques of weakly decaying hadrons, like neutral kaons and hyperons, by applying machine learning techniques to the recognition of the decay topologies. To train such algorithms high statistics signal and background samples are needed. In our analysis the signal sample is obtained from a simulation, while the background sample is generated by combining tracks from different real events. Figure 1 shows a comparison between the resulting invariant-mass spectra when either using the hard topology cuts from [1] or when using a trained neural network. It is evident that the neural network based approach provides a gain of up to 200% in the yield of reconstructed Λ hyperons, when optimized for significance of the signal.

In addition, we have started to refine the analysis of protons and light nuclei, with a specific emphasis on the amount of thermalization of the created system and the nucleon coalescence parameter.

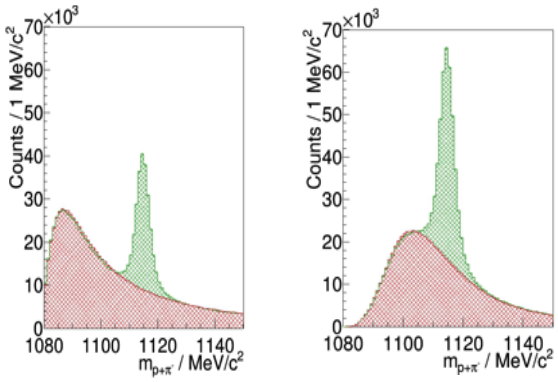


Figure 1: Reconstructed Λ mass spectrum in Au+Au collisions obtained with hard cuts [1] (left) and using a neural network (right). The signal is shown in green and the uncorrelated background in red.

Because of their self-analysing nature, weak decays can be used to measure the average spin orientation of the mother particle and interpret this as a signal of a possible global spin polarization. We have analyzed a significant Λ sample and extracted the centrality dependence of the polarisation parameter (see report of F. Kornas).

We have furthermore made a step forward towards understanding the transverse momentum spectra of charged pions in terms of their production from the thermalized system (see report of M. Gumberidze).

The studies on directed (v_1) and elliptic (v_2) flow of identified particles have been further extended. In addition to the multi-differential analysis for protons and pions (see 2016 GSI reports by B. Kardan and M. Gumberidze), now also the v_1 and v_2 of deuterons and tritons have been investigated as a function of transverse momentum and rapidity. After normalizing p_t and v_2 with the mass number A, the elliptic flow of p, d and t exhibits a clear scaling at mid-rapdity, as expected within a simple nucleon coalescence picture. Furthermore, higher moments of proton flow, v_3 and v_4, with respect to the first order reaction plane have been investigated.

First results on two-pion HBT correlations have been obtained as well. A special algorithm for the reduction of the effect of close track pairs had to be implemented for this analysis. The study was performed for negatively charged pions and allowed to extract the radius parameters R_{long}, R_{out}, and R_{side} as a function of pair momentum k_t and collision centrality. A significant k_t-dependence of the radius parameters is observed, in line with the expectation for a radially expanding source as it is also visible in the mass dependence of the p_t-spectra of identified single particles.

We have finally performed a comprehensive dilepton analysis for the Au+Au data and were able to extract significant medium modifications of hadron properties,

based on an established NN reference spectrum [2,3]. The excess yield has been quantitatively understood as thermal radiation emitted from the hot and dense fireball. Above an invariant mass of 0.4 GeV/c, the observed spectral shape of the excess radiation for the 40% most central collisions, corrected for the acceptance of the spectrometer, exhibits an almost exponential shape, consistent with an average temperature of the transient fireball of around 72 MeV. The absence of a bump in the vector meson pole mass region indicates a "melting" of the ρ meson in the medium.

We have extracted the multi-differential pattern of dilepton emission, including transverse mass, rapidity, helicity and azimuthal anisotropy distributions, for several centrality bins (see report of S. Harabasz).

Results from 2014 pion beam run

In 2014 a pioneering campaign investigating pion-nucleus collisions (π + C, W) at an incident momentum of 1.7 GeV/c was carried out with HADES at the GSI pion beam facility. This allowed to investigate in-medium effects on the strange mesons K^-, K^+, and ϕ in cold nuclear matter.

Previous studies indicated a moderately repulsive KN potential for kaons (K^+, K^0), while the antikaons (K^-) are expected to propagate in an attractive potential with a considerable imaginary part. Antikaon absorption processes in nuclear matter mediated by strangeness exchange reactions on one (KN $\rightarrow$ πY) or more nucleons (KNN $\rightarrow$ YN) contribute sizeably. A similar study pf the phi meson is also of considerable interest. And this concerns not only the significant feed-down into the K^- as observed in sub-threshold Au+Au collisions and elementary p+p reactions close to the ϕ production threshold. Of even more importance is the ϕ absorption in cold nuclear matter, resulting in a widening of the ϕ natural width.

Yet another interesting topic that can be addressed with pion-nucleus reactions is the study of hyperon propagation within nuclear matter. In the discussion of the equation of state of neutron stars the properties of the Λ are of considerable interest as its interacton with one or several nucleons enters various theoretical models. Since pion-induced reactions happen mostly on the nuclear surface, the lambda is also produces there and subsequently traverses the nucleous where it can rescatter on a nucleon. A measurement of the exclusive channel π^-+p $\rightarrow$ K + Λ with an additional recoil proton offers the opportunity to study the ΛN interaction in nuclear matter through a comparison of the data with transport models. A preliminary analysis of the HADES data shows that this process can indeed be isolated experimentally.

Production of e+e- pairs was measured in another run using the GSI pion beam at a lower momentum of 0.685 GeV/c impinging on polyethylene (PE) and carbon targets.

To allow for a more direct study of the baryonic contributions to the pair spectrum, we performed an exclusive analysis by applying invariant-mass and missing-mass cuts.

We have selected 1500 events corresponding to the free or quasi-free pi-p $\rightarrow$ ne^+e^- reaction. The comparison to model predictions is on-going. Using the Partial Wave Analysis (PWA) of the two-pion production measured in an energy scan in the same experiment, this excess can be interpreted as an off-shell contribution, consistent with the Vector Meson Dominance model (see report of F. Scozzi).

A parametrization of the angular distributions using the spin density formalism was also performed, allowing for the first time to get important information on the helicity structure of baryon electromagnetic transitions in the time like region.

The neutral pion and eta contributions were reconstructed in pi-PE reactions at 0.685 GeV/c using the photon conversion method. The preliminary extracted cross sections fit well to the world data (see repport of J.-H. Otto).

Status of the upgrade projects

With the start of FAIR Phase-0, most of the HADES detector systems will have reached an age of over 15 years. In order to keep the detector operational, an upgrade program has been started: For reasons of better photon detection efficiency, (1) the UV detector of the RICH has been replaced by MAPMTs, and (2) the Pre-Shower detector (polar angle coverage from 18 to 45 degree) has been replaced by a full-fledged electromagnetic calorimeter (ECAL). Moreover, the success of the experimental program addressing elementary reactions motivated the instrumentation of the acceptance region between polar angles of 0.5 to 6.5 degree with a straw-tube tracker. Most of these upgrade projects profit by close synergies with instrumentation projects of other FAIR collaborations (PANDA and CBM).

Electromagnetic Calorimeter

The addition of an electromagnetic calorimeter (ECAL) to HADES will moreover allow to study by photon measurements new reaction channels involving e.g. the production of neutral mesons, as well as neutral Λ(1405) or Σ(1385) resonances in elementary and heavy-ion reactions. Another advantage is the resulting improvement of the electron-to-pion separation at large momenta. ECAL is based on 978 lead glass modules recycled from the OPAL experiment. It is divided into 6 sectors, and it covers forward angles of $16^\circ < \theta < 45^\circ$ and almost the full azimuthal angle. The Technical Design Report had already been approved in 2014 by the FAIR ECE. The project is carried out by groups from Rez, Krakow, Moscow, Bratislava, Frankfurt, Darmstadt, Munich and GSI.

The readout of the detector is based on PaDiWa AMPS boards [4] (charge-to-width measurement) developed especially for the calorimeter and connected to a TRB3 [5] setup. The second generation of the 8-channel PaDiWa-AMPS front-end boards was assembled at GSI EE, tested in the laboratory and meanwhile the four completed sectors of the ECAL have been equipped (see report of A. Rost). A dedicated optical monitoring system has been de-

 DOI:10.15120/GR-2018-1

veloped for the ECAL. It is based on a laser LED and a microlens array with optical fibers which allows to send light pulsed of defined intensity into each single ECAL module for calibration purposes.

In the current funding concept, photomultipliers of two different types are installed. The limited budget forces the HADES collaboration, other than recommended by the ECE, to partly reuse 1.5" EMI 9903KB photomultipliers recovered from the MIRAC (WA98) detector; for the rest, new 3" Hamamatsu R6091 photomultipliers have been purchased.

RICH Photon Detector

The MWPC based gaseous RICH VUV photon detector with its CsI photon converter is currently being replaced by an arrangement of multi-anode photo multiplier tubes (MAPMTs, Hamamatsu H12700C) with blue-enhanced high quantum efficiency photo cathodes. The detector modules composed of 6 MAPMTs and integrated together with all required readout electronics on a backplane are developed together with CBM and will also be used as UV photon detectors in the CBM RICH. The pixel size (5.8×5.8 mm^2) of these devices perfectly matches the pad geometry of the old MWPC detector and guarantees reasonable position resolution of single photon hits and efficient ring image recognition on the 0.92 m^2 sensitive area. The MAPMTs are arranged on two aluminum carrier frames such as to fit as close as possible to the focal surface of the RICH mirror. Altogether 428 MAPMTs (27392 readout channels in total) arranged on 74 super-modules with 3×2 individual MAPMTs each will be mounted inside the existing gas tight detector chamber and flushed with nitrogen. A schematic view of the new RICH configuration and the design of the new photon detector device is depicted in Fig. 2.

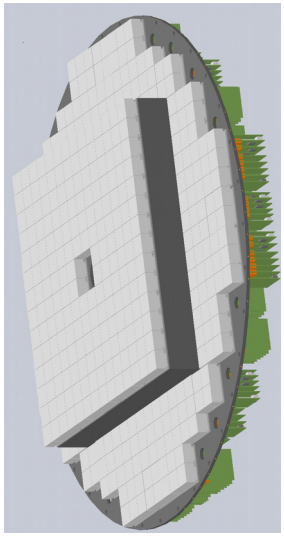


Figure 2: Schematic view of the redesigned HADES RICH photon detector and read-out configuration.

The newly developed readout front-end (DiRich) comprises pulse amplification, discrimination, time-to-digital conversion and time-over-threshold measurement for single photon signals from each individual MAPMT pixel. Twelve densely packed DiRich cards serve six MAPMTs and are arranged on a super-module backplane together with a power- and combiner card providing connection to the TRBnet of the HADES data acquisition system. Laser measurements with MAPMTs and final DiRICH prototypes show the expected performance with respect to single photo electron detection efficiency and rate capability.

The high quantum and single photo electron detection efficiency, low cross talk probability, and a new versatile ring finder algorithm lead to an expected superb single e^+/e^- identification efficiency across the whole detector area, in spite of the very short radiator length at small polar angles. In particular, the ring finder allows to efficiently discriminate overlapping rings even for very close e^+e^- pairs with opening angles down to $\delta\Omega \simeq 3^\circ$. Simulations done with conservative detector parameters promise a significant reduction of the misidentified combinatorial e^+e^- pair background also in heavy-ion reactions.

The new RICH photon detector will be ready for the 2018 beam times.

New Forward Detector System

To extend the acceptance of the HADES Spectrometer towards lower polar angles, 0.5° – 6.5°, a dedicated Forward Detector is being constructed. This detection system consists of two tracking stations placed 3.1 and 4.6 m downstream of the target and is based on straw tubes. It is followed by a high precision time-of-flight wall based on RPC technology and a high granularity scintillator based hodoscope. As this detector will operate in a field-free region the particle identification has to be performed based on dE/dx and time-of-flight measurements. Additionally, the straw tube tracking stations will be used for reconstruction of off-vertex decays.

The two stations of the Forward Tracking Detector are each composed of 8 layers of self-supporting straw tubes with 10 mm diameter. The layers are built from vertical straws rotated by 0, 90, 0, 90 and 0, 90, −45, 45 degree around the beam axis. The position resolution of the detector amounts to around 150µm which, for the given detector geometry, provides track reconstruction with angular resolution of $\sigma_\theta = 0.5$ mrad for 2 GeV protons. The Straw Trackers are currently assembled by the Krakow and FZ Juelich teams, based on developments for the PANDA Forward Tracker. LIP Coimbra is producing the Forward RPC.

The increase of acceptance will play a significant role in studies of N (π) + N and p + A reactions where this detector is essential for exclusive channel reconstruction and PWA analyses of hyperon production and for studies of decays like $\Lambda \rightarrow p\pi^-$, Λ^* (Σ^*) $\rightarrow \Lambda e^+ e^-$ (hyperon transition form-factors) and $\Xi^- \rightarrow \Lambda\pi^-$. For heavy-ion reactions the Forward Detector will consist only of an highly granular plastic scintillator (the other two components will be removed). The detector will then focus on reaction plane reconstruction and precise centrality measurements.

Start Detector Upgrade

For experiments with HADES, a radiation hard and fast beam detector is required. The detector is placed directly in the beam either close in front of the target (START) and in some configurations also at the exit of the RICH detector (VETO). To properly handle the rates the detector has to be segmented and radiation hard. The time resolution of the START should be so good (time-zero measurement with $\sigma_{t0} < 50$ ps) that the time-of-flight measurement is not deteriorated by it. While this is mandatory for proton- and pion-beam induced reactions, in case of heavy-ion collisions, the time-zero determination is further improved by taking the average of a properly corrected stop measurements of all charged particles in the acceptance. These requirements can in general be fulfilled by utilizing single-crystal Chemical Vapor Deposition (scCVD) diamond based detectors. High counting rate capability of the diamond detector (up to 107 ions/s/mm^2) has been shown in the Au+Au run. The measured radiation damage to the diamond material by Au ions has been quantified and it has been shown that while the energy resolution of a degraded detector is reduced significantly, its timing properties are, however, worsened only slightly. A similar concept for T0 measurement will be used during the 2018 Ag+Ag run.

The detection of minimum-ionizing particles remains challenging since one has to deal with very small amounts of induced charge carriers while the expected high rates require special emphasis on the read-out electronics. A read-out concept for diamond detectors for minimum ionising particles will be based on the already well established TRB3 (Trigger and readout board - version 3) platform developed at GSI. The board provides 260 high precision (RMS < 12 ps) multi-hit FPGA-TDC channels and serves as a flexible data acquisition system (DAQ). The available comprehensive software package allows on-line monitoring capabilities including basic analysis. A large variety of front-end electronics is available in order to extend its functionality.

MDC FEE Upgrade

The about 27.000 sense wires of the HADES drift chambers are currently read out by means of dedicated front-end electronics mounted on the frames of the detectors. The analog section is based on the ASD-8 ASIC featuring amplification, shaping and discrimination with a common threshold per 8 channels and a typical integration time of 7 – 8 ns. A semi-customized ASIC for time digitization provides both, drift time and valuable time-over-threshold information. Built nearly 20 years ago, the system suffers from an increasing number of dead channels and the data transfer bandwidth turned meanwhile out to be a limiting factor of the DAQ. Moreover, in high-rate applications it is recommended to employ multi-hit capability of the read-out to avoid efficiency losses due to occupied channels fired by random coincidences (notably δ electrons). Also, a higher detection sensitivity is desirable to increase the stability of the detector under high load by lowering the gas gain. Besides that, the HADES tracking algorithms would accept slightly worse spatial resolution while profiting from an improved noise immunity.

Pursued by groups from Frankfurt and GSI, state-of-the-art solutions based on available ASICs (the ASD-8 is no longer on the market) and time digitization realized in FPGAs are being studied in order to replace the old FEE in the near future. A promising replacement candidate is the PASTTREC ASIC, developed at the Jagiellonian University, Krakow, for reading out straw tubes of the PANDA experiment and future forward tracking in HADES. This chip is currently at the focus of our investigations. It is supplemented by a high precision FPGA-based TDC, implemented on a TRB3 board. In parallel, a cost-efficient and lightweight, but coarsely binned (500 ps) FPGA-based prototype TDC was successfully tested and is now foreseen to replace the currently used dedicated TDC ASICs. To arrive at conclusive performance results, the tests are being conducted under realistic conditions in direct comparison to the present ASIC. To do so, a spare drift chamber is employed and both signal-to-noise and dE/dx, as well as time resolution are systematically characterized with radioactive sources and cosmic rays. Furthermore, a test beam time took place at the Jülich Cooler Synchroton COSY in October 2017.

One key issue is the compatibility of the present flex-based signal routing and the PASTTREC ASIC mounted on a customized board, which significantly affects the noise immunity together with determining the optimum parameter settings of the PASTTREC chip. Due to the arrangement of two stereo angle layers, it is possible to assess the drift time (and spatial) resolution by correlating adjacent drift cells. This study, together with beam tests, will help to answer the other key question on the possibility of assigning an ASIC optimized for straw tube signals – which deliver more charge (operation at 2 bar and longer track path in a straw tube cell) – to read out the mini (cell) drift chambers of HADES. The final decision on the replacement of the existing electronics is foreseen to take place in the first half of 2018. A new MDC read-out is then scheduled to be available for the year 2020.

 DOI:10.15120/GR-2018-1

References

[1] T. Scheib, "*Λ and K^0 Production in Au+Au collisions at 1.23A GeV"*, Ph. D. thesis, U. Frankfurt (2017).
[2] P. Sellheim, "*Reconstruction of the low-mass dielectron signal in 1.23A GeV Au+Au collisions"*, Ph. D. thesis, U. Frankfurt (2017).
[3] S. Harabasz, "*Reconstruction of virtual photons from Au+Au collisions at 1.23 GeV/u*", Ph. D. thesis, TU Darmstadt and Jagellonian U. Krakow (2017).
[4] A. Rost et al., "A flexible FPGA-based QDC and TDC for the HADES and the CBM calorimeters", Jinst 12, C02047 (2017).
[5] C. Ugur et al., "*264 Channel TDC Platform applying 65 channel high precision FPGA-based TDCs*", in IEEE Nordic Mediterranean Workshop on Time-to-Digital Converters, IEEE NoMe TDC 1 (2013).

Experiment beamline: HADES
Experiment collaboration: HADES
Experiment proposals: S333, S407, S447
Accelerator infrastructure: SIS18
PSP codes: 1.1.2
Grants: BMBF 05P12CRGHE HZDR Dresden; BMBF 05P12RGGHM, U. Gießen; BMBF 05P15PXFCA, U. Wuppertal; BMBF 05P15WOFCA, TU München; Helmholtz Alliance HA216/EMMI; HIC for FAIR (LOEWE).
Strategic university co-operations with: Darmstadt, Dresden, Frankfurt am Main, Giessen, TUM, Wuppertal

Performance of the plastic scintillator Time-of-Flight Wall of HADES during the Au+Au run

G. Kornakov[1] for the HADES Collaboration

[1] TU Darmstadt, Germany.

The performance of the HADES TOF plastic scintillator wall [1] has been studied in great detail. This study had a twofold purpose: The first one was an attempt to improve the time-of-flight resolution by including additional information in the calibration procedure. The second one was to assess the quality of the detector and its readiness for the upcoming experiments.

The adoption of a TRB [2] based data acquisition scheme required new front-end electronics. The new boards based on the NINO chip [3] encode into the leading edge and width of a digital pulse the arrival time and (integral) charge of the signal read out on both sides of the scintillator coupled to Photo-Multipliers (PMTs). A consequence of these changes is a position dependent relation between the arrival time and the width of the TRB signal. Therefore, the goal of the new calibration strategy was to incorporate to the sequence of procedures the local dependence between the measured charge and time, the so-called "walk correction". For such a purpose the time-charge relation was studied in 20 equally long sections (bins) along the scintillator rods. Figure 1 shows such a correlation for a single bin of one rod. The reference time was calculated using the measured momentum and flight distance of particles identified in the tracking detector using the specific energy loss. With this, the dependence can be modelled by a linear combination of exponential and power-law functions, which are used during the calibration procedure to remove the walk effect from the data.

The measured time-of-flight and position along the rod can be reconstructed using the half-sum and half-difference of both times multiplied by the light group-velocity in the scintillator. Following previous works, the timing could be improved if instead of the half-sum a weighted average is used [4].

The result of these procedures is shown for minimum ionizing particles in Figure 2. Timing precisions of the order of 130 ps where achieved for the shortest rods of 1475 mm, degrading slightly to 160 ps due to signal attenuation in the longest rods of 2365 mm.

This result confirms the excellent time capabilities of the TOF Wall and its readiness for the upcoming experiments with both heavy and light beams.

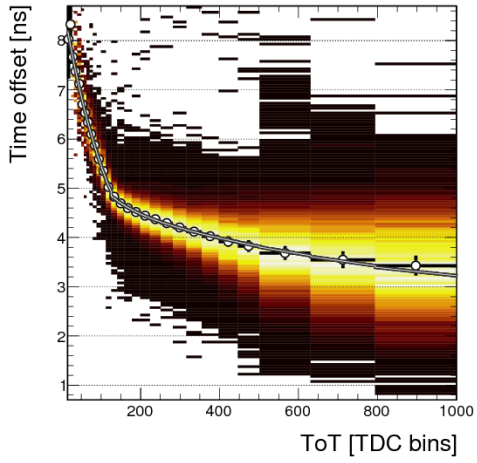


Figure 1: Example of a time-charge dependence measured in one longitudinal bin of a scintillator rod. The white circles correspond to the median of the distribution and the line is a fit consisting of a linear combination of exponential and power-law functions.

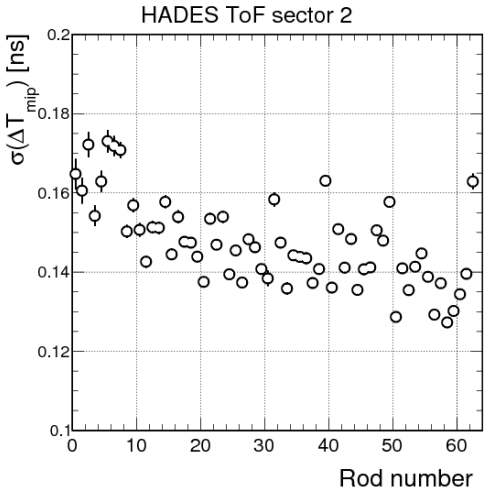


Figure 2: Timing performance for minimum ionizing particles of one of the sectors of the scintillator wall.

References

[1] C. Agodi et al., Nucl. Instrum. Meth. A 492 (2002) 14.
[2] I. Fröhlich et al., IEEE Trans. Nucl. Sci. 55 59. (2008)
[3] F. Anghinolfi et al., Nucl. Instrum. Meth. A 533 (2004) 183-187.
[4] M. Kurata et al., Nucl. Instrum. Meth. A 349 (1994)

Experiment beamline: HADES
Experiment collaboration: HADES
Experiment proposal: S407
Accelerator infrastructure: SIS18
PSP codes: none
Grants: VH-NG-823, Helmholtz Alliance HA216/EMMI
Strategic university co-operation with: Darmstadt

 DOI:10.15120/GR-2018-1

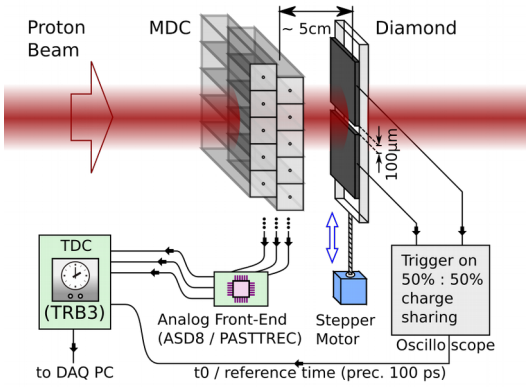
Benchmarking new front-end electronics for the HADES drift chambers

M. Wiebusch[1], C. Wendisch[2], J. Pietraszko[2], C. Müntz[1], J. Stroth[1,2] for the HADES Collaboration

[1] Goethe Universität, Frankfurt, Germany, [2] GSI, Darmstadt

Upgrading the digital part of the HADES MDC read-out system in preparation for SIS-100 requests a re-design of the analog part as well. Instead of re-using the ASD8 ASICS we want to benchmark a modern amplifier-shaper-discriminator chip, the PASTTREC ASIC [1], developed by JU Krakow, w.r.t. to precision in time and energy loss measurement.

Figure 1:



Sketch of the COSY beam test set-up to assess timing precision of the joint system comprising a drift chamber and different read-out electronics.

The timing precision, being the most crucial performance parameter of the joint system of detector and read-out electronics, was assessed during a beam test at the COSY accelerator in Juelich using a proton beam with a momentum of 2.7 GeV/c. As shown in figure 1, a diamond detector [2] served to provide trigger, reference time and position of protons in a narrow slice (<100 µm) of the beam, parallel to the sensing wire, and thus allows to select perpendicular tracks at any position within a drift cell.

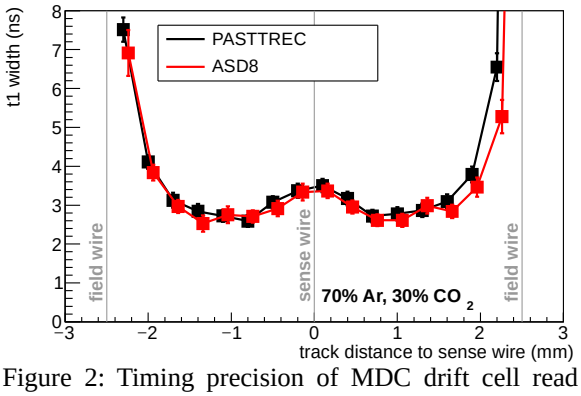


Figure 2: Timing precision of MDC drift cell read out with ASD8 and PASTTREC ASIC as a function of track position within the cell. Shown is the sigma of a gaussian fit of the coincidence time spectrum.

The resulting time precision is illustrated in figure 2. Within the error bars, PASTTREC (when walk correction is applied to the data) can achieve a similar, though slightly worse, timing precision as ASD8, i.e. ~3 ns in the inner regions of the cell. These results improve upon earlier measurements at the GSI Detector Lab via tracking of cosmic muons, because access to higher statistics allowed for finding better ASIC settings.

Concerning energy loss measurement precision, both ASICs were tested with a ^{55}Fe X-ray source irradiating a drift chamber operated at various high voltages. The pulse charge spectrum (figure 3) was derived from the recorded time-over-threshold spectrum by applying a calibration function which was recorded by means of a programmable pulse generator. In contrast to ASD8, PASTTREC was able to separate the main X-ray peak from the argon escape peak at and even below the HV working point.

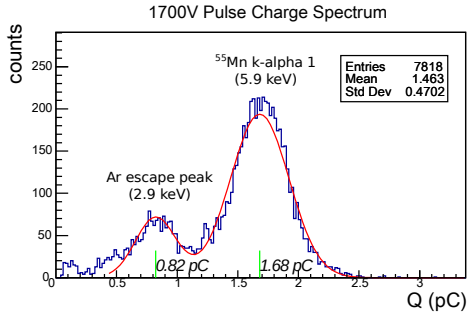


Figure 3: Calibrated charge spectrum (derived from TOT distribution) of MDC irradiated with a ^{55}Fe X-ray source and recorded with PASTTREC.

References

[1] G. Korcyl et al., "Readout electronics and data acquisition for gaseous tracking detectors," in IEEE Transactions on Nuclear Science, vol. PP, no. 99, pp. 1-1. doi: 10.1109/TNS.2017.2786464

[2] J. Pietraszko et al., doi:10.15120/GR-2015-1-MU-NQM-HADES-28

Experiment beamline: HADES
Experiment collaboration: HADES
Experiment proposal: S477
Accelerator infrastructure: SIS18
PSP codes: 1.1.2
Grants: GSI strategic partnerships (FuE), HIC for FAIR, BMBF(05P15RFFCA)
Strategic university co-operation with: Frankfurt-M

The PaDiWa-AMPS2 TDC and QDC front-end electronics for the HADES Electromagnetic Calorimeter

A. Rost[1], I. Fröhlich[2], T. Galatyuk[1,3], H. Kayan[3], J. Michel[2], A. Prozorov[4], M. Traxler[3] for the HADES collaboration

[1]TU Darmstadt, Darmstadt, Germany; [2]Goethe Universität, Frankfurt am Main, Germany; [3]GSI, Darmstadt, Germany; [4]Nuclear Physics Institute of ASCR, Rez, Czech Republic

The second generation of the 8 channel PaDiWa-AMPS front-end board was assembled at GSI department for Experiment Electronics (GSI EE). The board implements precise TDC and QDC measurements optimized to read out the 978 PMTs of the HADES-electromagnetic calorimeter (ECAL) [1]. The measurement principle [2] is to integrate the signals and to encode the results in the width of the digital output pulses. High precision is achieved by implementing a modified Wilkinson-ADC method, so actively discharging the integrated signal results in a fast crossing of the threshold. The lengths of the digital pulses are measured by the well-established TRB3 (General Purpose Trigger and Readout Board - version 3) platform [3].

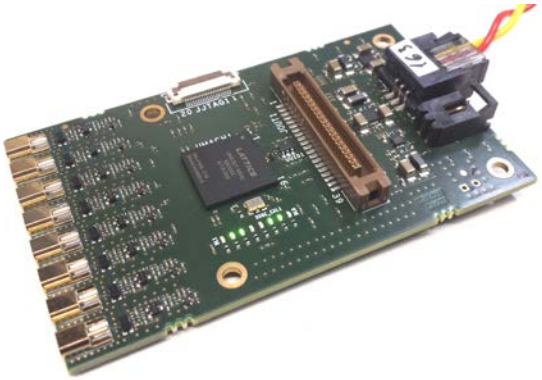


Figure 1: Photography of the PaDiWa-AMPS2 front-end board.

The circuitry of the front-end board is based on the Come&Kiss1 principle, where analogue electronics is used only for the amplification stage and integration, while other tasks, e.g. discrimination, threshold settings, delay generation for discharging and the LVDS drivers are implemented in a field-programmable gate array (FPGA). The second version of the PaDiWa-AMPS2 front-end board is shown in Fig. 1.

Because of the new layout in combination with a smaller package size, the routing of the signal lines have been optimized for better timing precision and reduced crosstalk. The concept of using a transformer in the input stage in order to galvanically isolate the ground was carefully tested. In laboratory measurements it has been shown that the transformer improved the signal to noise ratio. The charge measurement precision (resolution of the system defined as sigma/mean of the charge distribution) as a function of the measured charge has been determined with a pulse-generator. The results are shown in Fig. 2. A time precision of 20 ps and a relative charge precision below 0.5% (for ECAL PMT pulses >1 V) was reached.

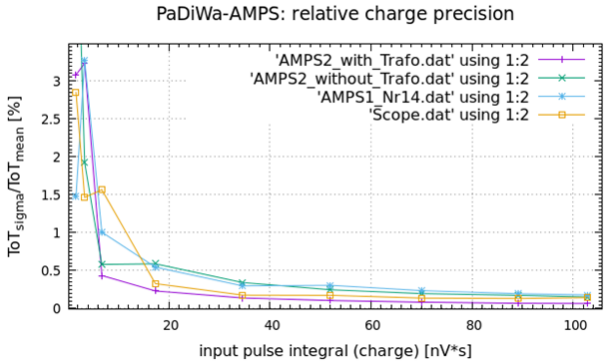


Figure 2: Relative charge precision of the PaDiWa-AMPS2 board compared to PadiWa-AMPS1 and a Oscilloscope reference measurement.

The HADES ECAL detector is currently under construction. The mass production of 150 PaDiWa-AMPS2 front-end boards was done by the GSI EE. The read-out electronics will be installed by end of spring 2018 and fully commissioned with cosmic muons and LED signals. A production beam time with the HADES spectrometer is planned in August 2018. Four sectors of the ECAL will be in place for the 2018 beam time to enable the photon measurement.

References

[1] W. Czyzycki et al., Electromagnetic Calorimeter for HADES, [1109.5550]

[2] A. Rost et al., 2017, “A flexible FPGA based QDC and TDC for the HADES and the CBM calorimeters”, JINST 12 C02047

[3] M. Traxler et al., “A Precise Multi-Channel QDC FEE utilizing FPGAs as Discriminators and Delay Elements Based on the TRB3 as TDC and Readout Platform”, GSI Scientific Report 2013

Experiment beamline: HADES
Experiment collaboration: HADES
Experiment proposal: none
Accelerator infrastructure: SIS18
PSP codes: none
Grants: Work supported by the DFG through GRK 2128 and VH-NG-823.
Strategic university co-operation with: Darmstadt

1 use commercial elements & keep it small and simple

 DOI:10.15120/GR-2018-1

Application of micron-size plasma for investigations of HADES Mini Drift Chamber (MDC) cells with an unique laser driven test facility

X. Fan[1], L. Naumann[1], M. Siebold[1], D. Stach[1], C. Wendisch[2], M. Wiebusch[3]

[1] HZDR, Dresden, [2] GSI, Darmstadt, [3] Goethe Universität, Frankfurt, Germany

To investigate the electron drift and amplification in gaseous detectors a high precision laser driven detector test facility has been developed at the Helmholtz-Zentrum Dresden-Rossendorf, using a pulsed UV laser beam with 257 nm wavelength, 10^{-2} to 10^{5} Hz frequency and 10^{11} to 10^{13} W/cm^2 energy density [1]. A multi-photon ionization process generates electrons and ions in micron-size beam envelope within radii of $r_{x,y} = 10$ µm and Debye length $l_z = \pm 100$ µm. An adaptable drift chamber detector (s. fig.1) has been designed to create the real electric field topology of each of all six different Mini Drift Detector cells of the MDC II plane of the HADES spectrometer [2]. Due to the anode wire alignment of ±40°, ±20° and ±0° (with respect to the cathode wires in adjacent wire layer), in each different drift cell type a different anomalous radial electrical field distribution is formed. With an increased precision in knowledge of the local field topology, we assume to increase the track reconstruction quality of the HADES spectrometer, and for the future, improve in optimizing cell geometries. The laser beam is focused into the detector with a well-defined 3D position, start time and number of primary electrons.

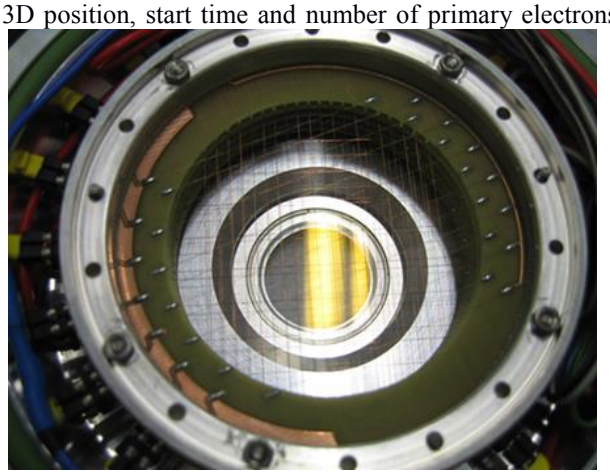


Figure 1: Drift chamber inside the opened gas tight box.

The start time signal, taken from the laser pulse has a resolution of 2 ps (FWHM). This signal triggers the data acquisition (DAQ) of five readout channels, on which read-out electronics with ASD-8 and PASTTREC [3] ASICs have been tested. 2D and 3D drift velocity distributions have been measured for different counting gas mixtures of Ar/CO_2. Figure 2 shows the nearly perfect radial symmetry in the +0° cell with exception of the four corners, which are defined by the shortest distance between field wires and cathode layers. Electrons generated in the corners were delayed there due to the gas properties and low electrical field strength. The Electron drift-velocity is constant over a wide range of more than 70% of the drift cell (see fit in fig.3) and amounts to (62±0.3) µm/ns.

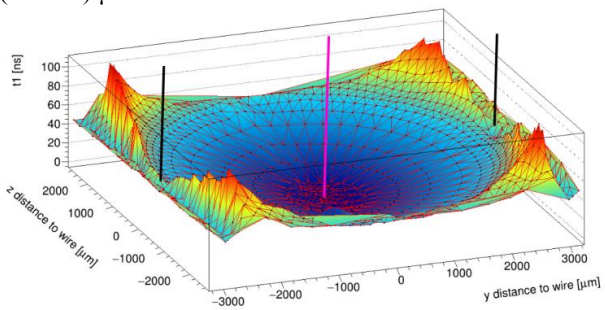


Figure 2: Mean drift time (t1) as function of the laser ionization point inside a drift cell, (1290 data points, each contains 8000 events) measured on an area orthogonal to the (+0°) anode wire (pink), between two field wires (black) and two cathode layers at z = ±2500 µm.

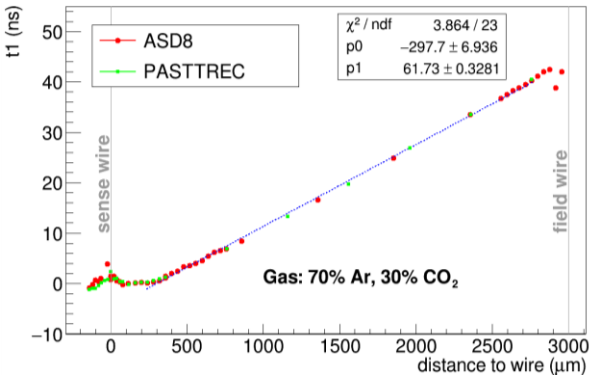


Figure 3: Measured mean drift time (t1) as a function of the distance perpendicular to sense wire, obtained for both amplifier ASICs at z=0, $U_{field} = U_{cathode} = -1.7$ kV.

Close to the anode wire the Debye length of the plasma disturbs the measurement. The drift time distribution has a standard deviation of 0.5 to 1.0 ns, this allows in case of a laser induced point source to deduce the spatial resolution of 30 to 60 µm for the HADES-MDC II with the used ASICs.

References

[1] L. Naumann et al., JINST 9 (2014) C10009
[2] G. Agakishiev et al.,Eur.Phys.J. A 41(2009) 243
[3] G. Korcyl et al., IEEE TNS, V. PP,N. 99 (2017)

Experiment beamline: HADES
Experiment collaboration: HADES
Experiment proposal: S477
PSP codes: 1.1.2.
Grants: HGS-HIRe**,** GSI strategic partnerships (FuE), HIC for FAIR, BMBF(05P15RFFCA)
Strategic university co-operation with: Frankfurt-M

Machine learning for weak decay recognition in heavy-ion collisions

S. Spies[1] and M. Lorenz[1] for the HADES collaboration

[1]Goethe-University, Frankfurt

The production of quark flavor is one of the most important observables in heavy-ion collisions. At SIS 18 energies this corresponds mainly to the production of strangeness. In contrast to hadron production in elementary N+N collisions, in heavy-ion reactions additional multi-step processes do occur and the production of e.g. strange hadrons below their free N+N threshold is possible by accumulation of energy. Therefore, the investigation of sub-threshold strangeness production is one of the most promising probes, as it contains newly produced quarks, it is sensitive to the amount of energy provided from the created system [1].

The recent experimental observations challenge the understanding of sub-threshold strangeness production: The first simultaneous measurement of K^- and Φ mesons in central heavy-ion collisions below a kinetic beam energy of 10A GeV by HADES revealed that the Φ/ K^- multiplicity ratio is found to be surprisingly high with a value of 0.52±0.16. Consequently, the different slopes of the K^+ and K^- transverse-mass spectra can be explained solely by feed-down, which substantially softens the spectra of K^- mesons. Hence, the different slopes do not imply diverging freeze-out temperatures of these two mesons caused by unequal coupling to baryons, as suggested commonly [2].

Yet, any detailed understanding of strangeness production and propagation in heavy-ion reactions requires information on all production channels of all particles with open or hidden strangeness. Therefore, the analysis is extended to further particles carrying strangeness such as K^0 mesons and Λ hyperons. They decay via the weak interaction and can be reconstructed through their decay products. Data on these hadrons in central Au+Au collisions at kinetic beam energies below 2A GeV have never been published before. Due to their decay via the weak interaction, these particles have a characteristic decay topology, which can be used to suppress combinatorial background. As most of the particles produced in heavy-ion collisions result from strong processes and are hence emitted from the interaction point of the two colliding ions, the latter one can be reconstructed from the intersection point of all reconstructed charged particle trajectories in the detector. Due to the weak decay, a fraction of e.g. Λ hyperons decay a few centimeter away from their creation point (cτ=7.89 cm). Hence, one can search for trajectories which meet in space (secondary vertex) separated by a given distance from the reaction vertex. Applying such selection criteria the combinatorial background of random pion proton combinations is more strongly suppressed than the signal of truly correlated pion-proton pairs. The drawback of this method is the low efficiency, usually of a few per mill.

Machine learning methods e.g. based on artificial neural networks are a very promising tool to overcome this shortcoming. Such algorithms can be trained to recognize specific correlations, resulting in higher reconstruction efficiencies compared to a series of hard cuts. We applied the methodology of machine learning for the recognition of weak decay topologies for the first time for heavy-ion collision data within HADES. For the training of such algorithms high statistic signal and background samples are needed. For the signal sample, we use a simulation, while the background sample is generated by combining tracks from different events, which are by definition uncorrelated.

Analysis results

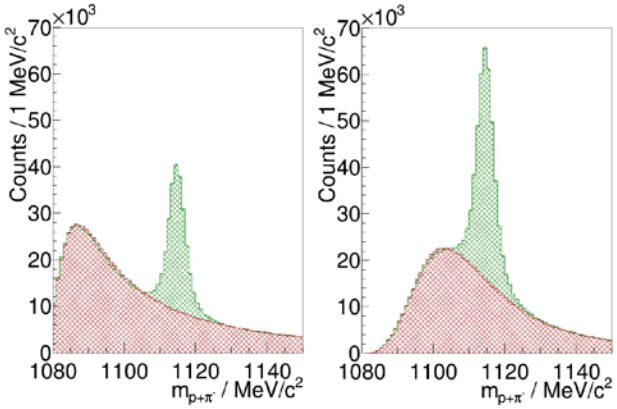


Figure 1: Λ mass spectrum from data with hard cuts from [3] (left) and using a neural network (right), signal is shown green and combinatorial background red.

Figure 1 shows a comparison between the resulting invariant mass spectra using only the hard topology cuts from [3] and with the use of a neural network. The analysis based on the neural network provides a gain of about 200% in the amount of reconstructed Λ hyperons, when optimized for significance of the signal.

References

[1] S. Weissenborn, D. Chatterjee and J. Schaffner-Bielich, Nucl. Phys. A 881 (2012) 62.

[2] J. Adamczewski-Musch et al. [HADES Collaboration], Physics Letters B 778 (2018) 403-407.

[3] T. Scheib, Λ and K^0_s Production in Au+Au Collisions at 1.23A GeV, Ph.D. thesis U. Frankfurt, 2017

Experiment beamline: HADES
Experiment collaboration: HADES
Experiment proposal: none
Accelerator infrastructure: UNILAC / SIS18
Grants:
Strategic university co-operation with: Frankfurt-M

 DOI:10.15120/GR-2018-1

Strange meson production in pion-nucleus collisions at 1.7 GeV/c

J. Wirth[1,2], L. Fabbietti[1,2], A. Scordo[3] and the HADES collaboration

[1]Excellence Cluster Universe, Technische Universität München, Garching, Germany; [2]Physik Department, Technische Universität München, Garching, Germany; [3]INFN Laboratori Nazionali di Frascati, Frascati, Italy

The production of strange mesons in pion-nucleus reactions allows for a quantitative study of in-medium effects such as re-scattering and absorption processes at a well-defined density (ρ_0). In 2014 the versatile HADES setup at the GSI pion beam facility [1] provided a worldwide unique opportunity to study open and hidden strange mesons (K^+, K^- and ϕ) in cold nuclear matter generated in pion-nucleus reactions ($\pi^- + A,\ A = C,\ W$) at an incident pion beam momentum of 1.7 GeV/c.

In the case of the kaons (K^+, K^0) several hints for the existence of a moderately repulsive KN potential for the kaons (K^+, K^0) exist [2]. On the contrary, the antikaons (K^-) are expected to propagate in an attractive potential with a considerable imaginary part. Antikaons can be absorbed in nuclear matter via strangeness exchange processes on one ($K^-N \rightarrow Y\pi$) or more nucleons ($K^-NN \rightarrow YN$). Furthermore, the study of the ϕ meson production and absorption ($\phi \rightarrow K^+K^-, BR = 48.9 \pm 0.5\%$ [3]) of light (C) and heavy (W) nuclei is essential. Since, the absorption of the ϕ meson in cold nuclear matter has been interpreted as a proof of the widening of the ϕ natural width [4]. Besides, ϕ decays may substantially affect the observed K^- abundance. In subthreshold 1.23 AGeV $Au + Au$ collisions a surprisingly high ϕ/K^- ratio with a value of 0.52 ± 0.16 was obtained [5]. Also in elementary $p + p$ close to threshold the ϕ meson is a sizeable source for the K^- production [6].

Both charged kaons are identified by means of the time-of-flight (Target T0 Detector/RPC/TOF) and momentum measurements with the drift chambers (MDCs) combined with the toroidal magnet field. To enhance the signal to background ratio, both kaons are pre-selected by their specific energy loss in the MDCs.

Figure 1 shows the mass distribution of the K^- in the polar angle and momentum interval of $15.0 \leq \theta[°] < 27.5$ and $430 \leq p\ [MeV/c] < 500$ in the RPC detector. The neutral ϕ meson is reconstructed in terms of the invariant mass of K^+K^- pairs as shown in Fig. 2 in the polar angle and momentum interval of $15.0 \leq \theta[°] < 27.5$ and $500 \leq p\ [MeV/c] < 1250$.

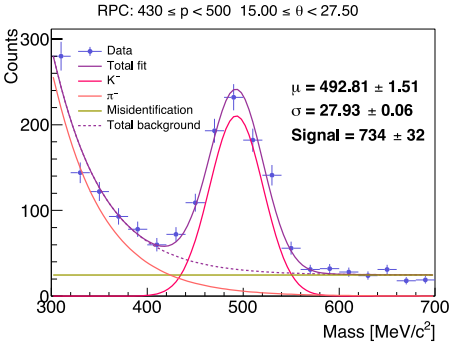


Figure 1: Reconstructed K^- mass spectrum in a specific $p - \theta$ region (see legend) for the RPC in $\pi^- + C$ collsions. The K^- signal is represented by a Gaussian (magenta line). The background is composed of an exponential function for the pions (pink line) and a polynomial (green line).

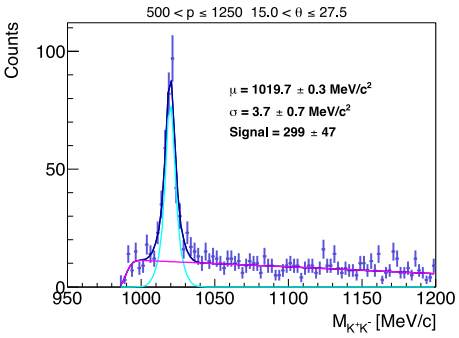


Figure 2: Invariant mass distribution of K^+K^- pairs in a specific $p - \theta$ region (see legend) in $\pi^- + C$ collsions.

References

[1] J. Adamczewski-Musch et al. [HADES Collaboration], Eur. Phys. J. A 53 (2017) 188
[2] G. Agakishiev et al. [HADES Collaboration], Phys. Rev. C 90 (2014) 054906
[3] C. Patrignani et al. [Particle Data Group Collaboration], Chin. Phys. C 40 (2016) 100001
[4] D. Cabrera et al., Nucl. Phys. A 733 (2004) 130
[5] J. Adamczewski-Musch et al. [HADES Collaboration], Phys. Lett. B 778 (2018) 403
[6] Q. J. Ye et al. [ANKE Collaboration], Phys. Rev. C 85 (2012) 035211

Experiment beamline: HADES@SIS18
Experiment collaboration: HADES
Experiment proposal: S333
Grants: SFB Sonderforschungsbereich 1258 “Neutrinos und Dunkle Materie in der Astro- und Teilchenphysik (NDM)“, GSI F&E TMLFRG1316 CBM-RICH
Strategic university co-operation with: none

A non-binomial model for efficiency corrections to particle number cumulants

R. Holzmann[1], and the HADES collaboration

[1]GSI, Darmstadt, Germany

Fluctuations of conserved quantities (e.g. baryon number, strangeness, charge) are considered among the most promising probes of the QCD phase diagram [1]. Fluctuations are usually quantified in terms of the cumulants of the observed particle distributions and detector efficiency corrections are applied in order to obtain the true cumulants. This is generally done [2] assuming the efficiency to be of binomial type, i.e. assuming that the detection processes of multiple particles in any given event are independent.

In the binomial model, the probability of detecting p out of M emitted particles in an event can be written:

$$P_p^M = C_M^p \epsilon^p (1-\epsilon)^{M-p} . \quad (1)$$

By expanding the $(1-\epsilon)^{M-p}$ term in Eq. (1) and averaging P_p^M over all events one finds a relationship between the average probability to observe p particles and the so-called factorial moments $\langle F_n \rangle$ of the true particle distribution:

$$P_p = \sum_{m=p}^{\infty} (-1)^{m-p} \frac{\langle F_m \rangle}{m!} C_m^p \epsilon^m . \quad (2)$$

Using Eq. (2) one retrieves the well-known relation between measured and true factorial moments [3]:

$$\langle f_n \rangle = \epsilon^n \langle F_n \rangle . \quad (3)$$

Real-life detectors are commonly designed with a finite occupancy: they can register only a limited number of particles per given event and consequently their detection efficiency decreases with increasing particle number. This effect can be studied in simulations and for HADES the efficiency drop was found to be of order 10% - 15%.

We therefore propose a new, fully analytical, non-binomial model which naturally incorporates efficiency losses resulting from an increasing particle number. Our model strictly applies to detectors segmented into a finite number N of modules of given solid angle Ω such that the total solid angle covered (or total efficiency) is $\varepsilon = N\Omega$. Any given module can fire when hit by a particle, but only once, i.e. multiple hits of a module are not distinguishable from single hits. Following [3, 4], the detection probability in Eq. (1) transforms into:

$$P_{Np}^M = C_N^p \sum_{l=0}^{p} (-1)^{p-l} C_p^l \left[1 - \frac{(N-l)}{N}\epsilon\right]^M , \quad (4)$$

and the factorial moments relation of Eq. (3) into:

$$\langle f_n \rangle = \sum_{m=n}^{N} \langle F_m \rangle \frac{(-1)^m}{m!} \frac{\epsilon^m}{N^m} \sum_{k=n}^{m} C_N^k k(k-1)\cdots \cdots (k-n+1) \sum_{l=0}^{k} (-1)^k C_k^l (N-l)^m . \quad (5)$$

Figure 1 below illustrates the influence of the detector segmentation on the drop of efficiency with multiplicity.

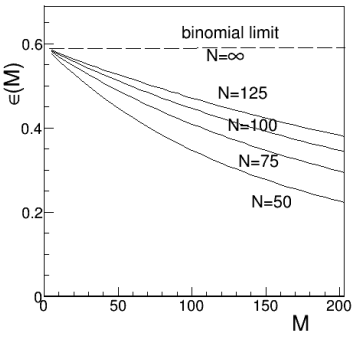


Figure 1: Non-binomial efficiencies as function of the particle multiplicity M for ε = 0.59 and N = 50 – 125.

For a "continuous" detector like HADES a strict hardware segmentation into N distinct modules is not realized, but an effective segmentation $\tilde{N}$ can still be introduced, with $\tilde{N}$ and ε adjusted to describe the observed (or simulated) efficiency behavior $\epsilon = \epsilon(M)$.

References

[1] M. Asakawa and M. Kitazawa, Prog. Part. Nucl. Phys. 90 (2016) 299.
[2] A. Bzdak and V. Koch, Phys. Rev. C 91, (2015) 027901.
[3] S.Y. Van der Werf, Nucl. Inst. Meth. 153 (1978) 221.
[4] G. Bellia et al., Nucl. Inst. Meth. 226 (1984) 424.

Experiment beamline: HADES
Experiment collaboration: HADES
Experiment proposals: S407, S447
Accelerator infrastructure: SIS18
PSP codes: 1.1.2
Grants: none
Strategic university co-operation with: none

 DOI:10.15120/GR-2018-1

π^0 and η production in π^-+PE collisions at 690 MeV/c beam momentum

J. Otto[1] for the HADES collaboration

[1]Justus-Liebig Universität, Gießen, Germany

In this work we present the analysis of neutral mesons (π^0 and η) in π^- + *polyethylene (PE, [-CH_2-CH_2-]$_n$)* data at a beam momentum of *p = 690 MeV/c* taken by HADES in summer 2014. As HADES does not employ an electromagnetic calorimeter, detection is performed via conversion of decay photons *(π^0 / η → γγ / γγ*→ $e^+e^+e^-e^-$).*

First, lepton identification is performed with rather soft cuts on the particle sample: To do so we require the momentum to be smaller than *1 GeV/c*, an energy loss in the MDCs of less than *12 MeV*, a reconstructed mass *m < 100 MeV/c^2* and *0.8 < β < 1.2*. Since di-leptons originating from conversion are characterized by small opening angles, we allow for hit sharing in the inner MDCs. Accordingly we cut on opening angles smaller than 10° when reconstructing unlike-sign lepton-pairs to reduce combinatorial background. Simulation shows that π^0 (η) mesons produced at our energies mainly decay into 2γ with opening angles *15° < θ_{lab} < 45°* (*115° < θ_{lab} < 145)*. After the formation of lepton-quadruplets from our pair sample we cut on the specified ranges of opening angles between two photon candidates. Clear signals of π^0 and η production with background contribution at the percent level are observed. Figure 1 shows the reconstructed invariant mass spectrum after all cuts. 632 entries in the π^0 mass range and 93 entries in the η mass range are counted.

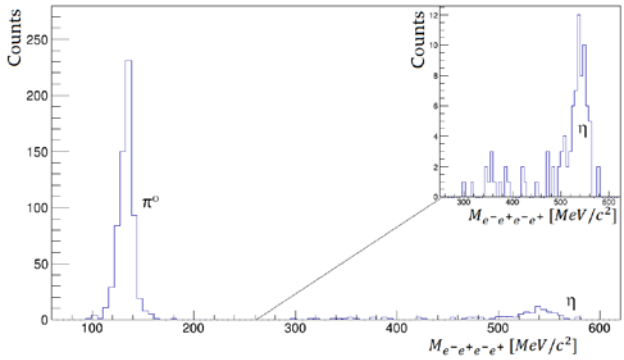


Figure 1: Reconstructed invariant mass spectrum of two detected di-lepton pairs after cuts.

In order to extract π^0 and η cross sections, raw data have to be corrected for detector inefficiency, geometrical acceptance and be properly normalized. We performed an efficiency correction in p_t-y bins based on PLUTO simulations of the $\pi^-p \rightarrow \pi^0/\eta + n$ reactions and subsequent decay as $\pi^0/\eta \rightarrow \gamma\gamma/\gamma\gamma^*$.

We derived integrated efficiencies of

$$\epsilon_{\pi^0} = (4.80 \pm 0.22) \cdot 10^{-6}$$

$$\epsilon_{\eta} = (2.60 \pm 0.05) \cdot 10^{-5}$$

These values include the conversion probability in the target region of HADES, geometrical acceptance and reconstruction efficiency with all cuts applied. Errors shown are statistical only.

Normalizing on elastic scattering [1,2] we can derive cross sections for π^0 and η production in π^- + *PE*

$$\sigma_{\pi^0} = \frac{\sigma_{el}}{N_{ev}^{el}} \cdot \frac{N_{\pi^0}}{\epsilon_{\pi^0} \cdot N_{ev}^{\pi^0}} = (12.68 \pm 1.08)\, mb$$

$$\sigma_{\eta} = \frac{\sigma_{el}}{N_{ev}^{el}} \cdot \frac{N_{\eta}}{\epsilon_{\eta} \cdot N_{ev}^{\eta}} = (0.836 \pm 0.105)\, mb$$

using $\frac{\sigma_{el}}{N_{ev}^{el}} = 0.88 \cdot 10^{-7} mb$ [1,2]

HADES has also measured the reaction π^- + *C*. Analysing this data accordingly we are able to subtract the carbon fraction in our data and derive a cross section for π^0 production in π^- +*p* (for the η, statistics is too small):

$$\sigma_{\pi^0}^{\pi^-+p} = \frac{\sigma_{el}}{N_{ev}^{el}} \cdot < \pi^0 >_p = (14.39 \pm 2.73)\, mb$$

with $< \pi^0 > = \frac{N_{\pi^0}}{\epsilon_{\pi^0} \cdot N_{ev}^{\pi^0}}$

and $< \pi^0 >_{PE} = < \pi^0 >_p + \frac{2}{3} < \pi^0 >_C$ [1,2]

In literature we find values for the π^0 and η production in π^- +*p* collisions at *690 MeV/c* beam momentum listed as:

$$\sigma_{\pi^0}^{\pi^-+p} = 16.5\, mb \text{ [3]}$$

$$\sigma_{\eta}^{\pi^-+p} = 0.5\, mb \text{ [4]}$$

Our result for the π^0 cross section in π^- +*p* is in agreement with literature. For the η we can not compare directly as our cross section is related to π^- +*PE*. Besides the statistical errors shown, our analysis has systematic errors which are being estimated. Those mainly originate from missing production processes in our simulation with three particles in the final state leading to significant differences in the momentum distribution in experiment and simulation, and therefore influence our efficiency.

References

[1] F. Scozzi [HADES collab.], EPJ Web Conf. 137 (2017) 05023

[2] W. Przygoda [HADES collab.], EPJ Web Conf. 130 (2016) 01021

[3] Landolt-Börnstein Database, values received from P. Salabura.

[4] D. Rönchen et al., Coupled-channel dynamics in the reactions πN → πN, ηN, KΛ, KΣ, EPJA49(2013)44.

Experiment beamline: HADES
Experiment collaboration: HADES
Accelerator infrastructure: SIS18
Grants: GSI strategic partnership
Strategic university co-operation with: Gießen

Exclusive Λ analysis to study hyperon scattering in medium

S. Maurus[1], L. Fabbietti[1], for the HADES collaboration

[1]Excellence Cluster Universe, Technische Universität München, Boltzmannstr. 2, D-85748, Garching, Germany

Since several years the study of the Λ, the lightest hyperon, is of special interest in several topics, like the equation of state. In vacuum, the elastic interaction between the proton and the Λ-p already has been measured in scattering experiments, constraining theoretical models. [1].

Still, the in-medium properties of the Λ-p system lacks any data point from the experimental side.

In July 2014 a dedicated secondary pion beam campaign was performed with the HADES detector setup impinging on a tungsten (W) and carbon (C) target with an incident beam-momentum of 1.7 GeV/c. As pion reactions are happening close to the surface [2], also the lambdas are created here, traversing the whole nucleus and therefore they form an ideal system to study the lambda in-medium properties.

Our approach is to use the exclusive channel $\pi^- + p \rightarrow K^0 + \Lambda$ where the Λ eventually can interact elastically with its surrounding ($\Lambda + \mathrm{p} \rightarrow \Lambda + \mathrm{p}$). This may provide information on lambda proton scattering and shed light on the in medium properties of the lightest hyperon.

This channel is isolated by searching for a matching charge pattern ($K^0 \rightarrow \pi^+ + \pi^-, \Lambda \rightarrow \mathrm{p} + \pi^-, p$) with 3 positive and 2 negative charged particle candidates.

Further, the particle identification of these particle candidates is based on their characteristic energyloss in the MDCs and their velocity β, measured in the time of flight sub-detector system in combination with the momentum.

In addition, a mass cut further reduces the chance of a wrong identification of these candidates, reducing the background.

Caused by the multiple appearance of particles (p, π^-) in the final state, an event hypothesis is necessary, to assign these particles to their correct mother (K^0, Λ). The best combination is found when both invariant masses (p, π^-) and (π^+, π^-) are best matching to their nominal value (Λ, K^0). The invariant mass of (π^+, π^-) vs. (p, π^-) for the best combination is illustrated in Fig. 1, subtracted by their PDG mass.

To be sensitive to the in-medium behaviour of the Λ an angle difference is extracted, which is constructed as follows:

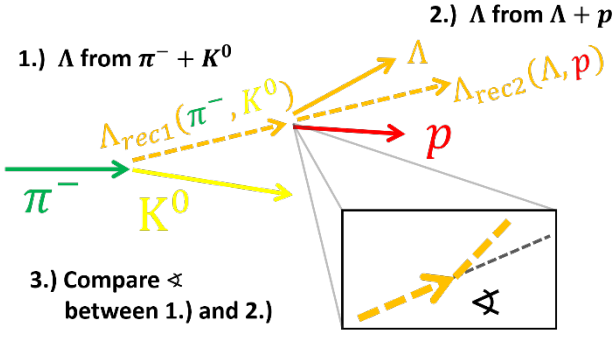


Fig.2 Construction of the observable.

Based on the incident π^- beam in combination with the measured K^0, the Λ momentum can be inferred (Λ_{rec1}) right after its creation. Now this Λ is reconstructed from the measured Λ in the detector in combination with the measured proton. If we assume a single reaction, the sum of the measured Λ and p gives us the Λ before the reaction (Λ_{rec2}). Now the angle between (Λ_{rec1}) (Λ_{rec2}) is evaluated, as sketched in Fig. 2. In theory they should be perfectly aligned. As both protons have an unknown start momentum, arising from the fermi-momentum and we are facing limited resolution, this distribution will be shifted and smeared. Nevertheless, these effects are included in the simulation framework.

The next step in this analysis will include the creation of templates for all different production channels and scenarios which can happen inside the nucleus.

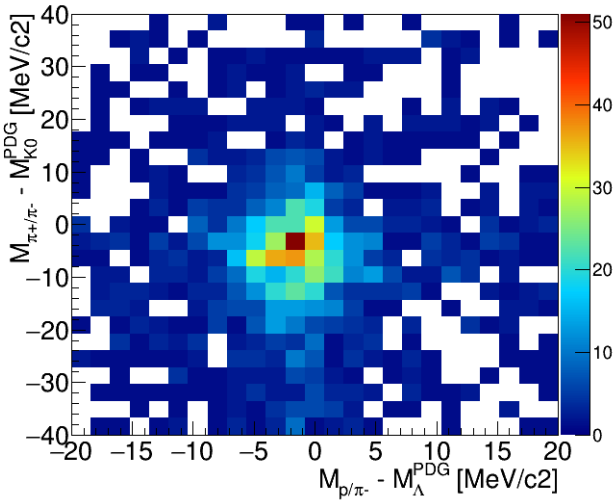


Fig.1 Invariant mass of (π^+, π^-) vs inv. mass of (p, π^-), subtracted by the nominal mass of K^0 and Λ, respectivley. Only the best combination is shown. Details see text.

References

[1] J. Haidenbauer et al., Nucl. Phys. A 915 (2013)24
[2] Benabderrahmane et al. Phys. Rev. Lett. 102, 182501 (2009)

Experiment beamline: HADES
Experiment collaboration: HADES
Experiment proposal: S333
Grants: BMBF HADES: "Verbundprojekt 05P2015", GSI F&E TMLFRG1316 CBM-RICH

 DOI:10.15120/GR-2018-1

Fit to transverse momentum spectra of dileptons measured by HADES

S. Harabasz[1] for the HADES collaboration

[1]Technische Universität Darmstadt, Germany

Virtual photons are penetrating probes emitted throughout the whole evolution of the fireball formed in collisions of heavy ions and therefore they are well suited for studying the properties of strongly interacting matter at extreme conditions.

The analysis of Au+Au collisions at $\sqrt{s_{\mathrm{NN}}} = 2.42$ GeV measured by HADES showed [1] that the invariant mass distribution of dileptons has a Boltzmann shape, which leads to the conjecture, that the temperature of the emitting source, at least the one averaged over the evolution of the system, can be read out from the inverse slope of the mass spectrum.

To do this in a proper way, it is essential to understand which probability density function of invariant mass corresponds to a thermal phase-space distribution. The derivation quoted e.g. in [2] shows that the correct parametrization is

$$\frac{\mathrm{d}N}{\mathrm{d}M} \propto V\tau \frac{\mathrm{Im}\Pi_{\mathrm{em}}(M;T)}{M^2} 4\pi M^2 T\, K_1\left(\frac{M}{T}\right),$$

where V, τ and T are the volume, lifetime and temperature of the fireball, respectively, $\mathrm{Im}\Pi_{\mathrm{em}}$ is the vector meson spectral function, and K_1 is a modified Bessel function of the second kind. This form is obtained after integrating out rapidity. Moreover, the fit has to be made in the range of invariant masses high enough such that the shape of the spectrum is governed by the Boltzmann distribution (Bessel function) and not by the spectral function, so that the latter one can be treated as approximately proportional to M^2. Therefore, the fraction in the above formula is a constant. While at SPS and RHIC energies the temperature can be extracted from the spectra above 1.2 GeV/c^2, at SIS18, where the expected temperature is about four times lower, the fit starting at 0.3 GeV/c^2 would yield a slope parameter that could be compared on the same footing [3]. In addition, in this mass range the argument of the Bessel function can be treated as large enough to justify its known approximation by $K_1(x) \underset{x\to\infty}{\longrightarrow} \sqrt{\pi/2x}\exp(-x)$, which leads to:

$$\frac{\mathrm{d}N}{\mathrm{d}M} \propto V\tau(2\pi MT)^{3/2}\exp\left(-\frac{M}{T}\right)$$

and one gets the well-known representation (cf. [4]):

$$\frac{\mathrm{d}N}{\mathrm{d}M} \propto M^{3/2}\exp\left(-\frac{M}{T}\right)$$

On the other hand, starting from a Boltzmann distribution, and assuming that the spectral function varies little with transverse momentum, one can arrive, by nearly identical mathematical reasoning, to the parametrization:

$$\frac{1}{p_t}\frac{dN}{dp_t} \propto m_t K_1\left(\frac{m_t}{T}\right) \qquad (1)$$

which is exact and does not require any approximation, especially that $m_t \gg T$ is certainly not fulfilled in the low part of the transverse momentum spectra for low invariant masses.

These arguments can be tested with HADES data. The transverse momentum distributions, together with fits of Eq. (1) are shown in Fig. 1. The rather good description of the spectra is visible, which confirms the assumption of the thermal radiation. Particularly, the approximate exponential fit would not reproduce properly the convexity of the spectra. The slope parameters from the fit are shown as well.

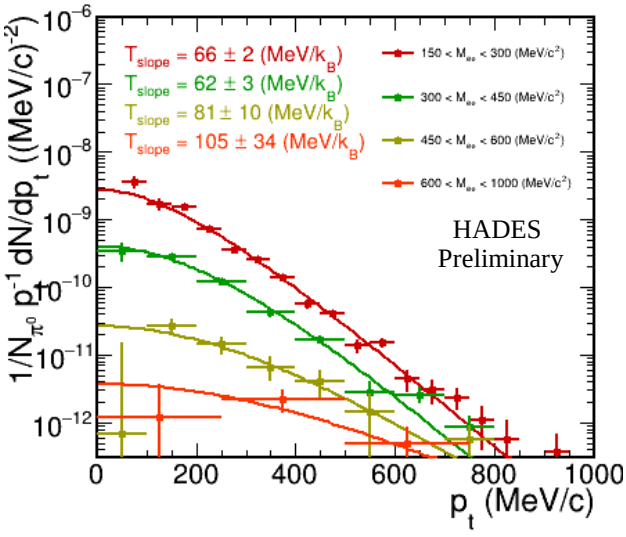


Figure 1. Transverse momentum distributions of dileptons measured by HADES in different invariant mass bins together with fits of Eq. (1).

Another necessary condition is the consistency between the slope parameter extracted from the fit to the invariant mass and the one from the transverse momentum fits, extrapolated to mass zero. This will be tested and discussed in a future publication.

References

[1] P. Sellheim, PhD thesis, Goethe-Universität Frankfurt am Main, 2017, S. Harabasz, PhD thesis, Technische Universität Darmstadt and Jagiellonian University in Cracow, 2017

[2] F. Seck, Master's thesis, Technische Universität Darmstadt, 2015

[3] T. Galatyuk et al., Eur.Phys.J. A52 (2016) 131

[4] H.R. Schmidt and J. Schukraft, J.Phys. G19 (1993) 1705

Experiment beamline: HADES
Experiment collaboration: HADES
Experiment proposal: S407
Accelerator infrastructure: SIS18
PSP codes: none
Grants: VH-NG-823, Helmholtz Alliance HA216/EMMI
Strategic university co-operation with: Darmstadt

Understanding the transverse mass spectra of charged pions measured in Au+Au at 1.23 AGeV collisions with HADES

M. Gumberidze[1] for the HADES collaboration

[1]Technische Universität, Darmstadt, Germany

It is well established that hadron abundances in ultra-relativistic heavy-ion collision can be described with a statistical partition function with fitted temperature T and baryon chemical potential μB. It is interesting to validate if also the spectra of particles at low energies are consistent with thermal production at chemical freeze-out. For such a study Therminator [1] has been used as Monte Carlo event generator. Therminator was previously designed for studying particle production in relativistic heavy-ion collisions performed at different experimental facilities, e.g. SPS, RHIC and LHC.

Therminator assumes that the fireball freezes out at a predefined hypersurface in space-time at given temperature- and bayro-chemical potential. While the program accepts any boost-invariant flow profile, two common flow profiles, the Blast Wave and the Cracow model are already implemented. At this single freeze-out particles abundances are determined by the temperature and baryon chemical potential via the Cooper-Frye formalism.

The parameters used for the Blast Wave model calculations T = 53 MeV, μB = 803 MeV were taken from [2]. This assumes that the collision system investigated by HADES freezes out along the “universal freeze-out line”. This curve can be parameterized by <E>/<N> approximately equal to 1 GeV. A collective expansion velocity (β) on the order of 0.36 has been extracted from the same HADES data sample [3] using blast-wave parameterization.

In Fig. 1 mid-rapidity transverse mass spectra of negative and positive pions for the 5% most central collisions are shown in comparison to a cocktail of various sources of pion production obtained from Therminator. Since Therminator simulates also the decays of resonances, the final spectra contain primordial and secondary contributions (the primordial particles are emitted directly from the fireball, while the secondary particles come from resonance decays). Simulated spectra have been scaled up by a factor of 0.7 and 0.5 for negative and positive pions respectively in order to compare slope of the spectra.
We observe good agreement between the data and the model results for low transverse mass region (mT < 400 MeV/c2). On the other hand, the model results underpredict the data for higher transverse masses. This can be interpreted as contribution from decays of higher lying resonances produced in hot/dense matter [4]. This conjecture is presently being checked with transport models.

References

[1] A.Kisiel, T.Taluc, W.Broniowski and W. Florkowski, Comput. Phys. Commun., 174: 669-687 (2006).
[2] J.Cleymans et.al., Phys. Rev. C73 (2006) 034905
[3] H.Schuldes (HADES Coll.) ”Studying Stramgeness Production with HADES” proceedings SQM2017
[4]. C. Muentz et. al. Z. Phys. A 357(1997) 399

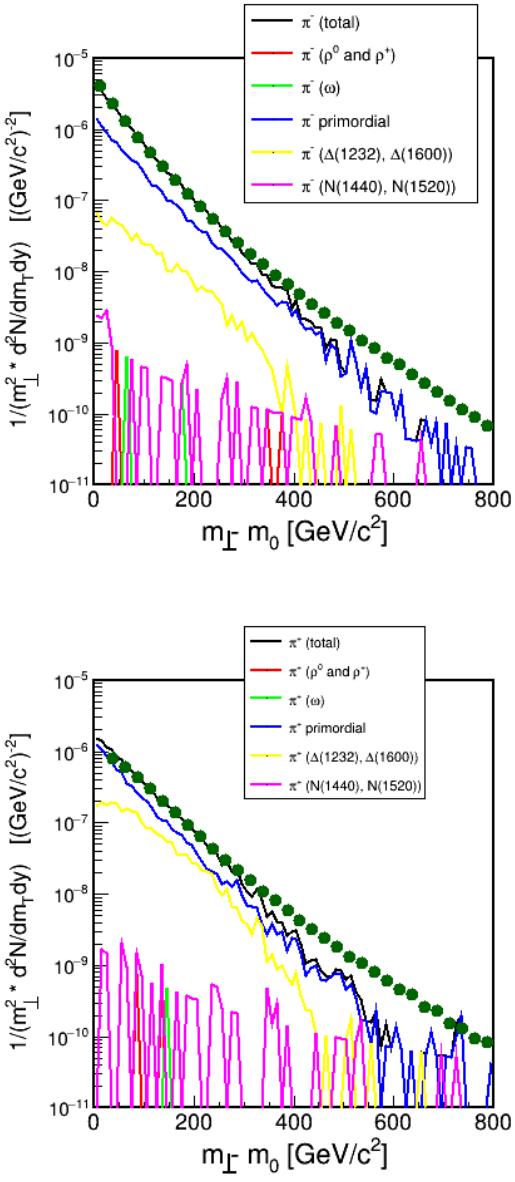


Figure 1. Transverse mass spectrum for negative (upper) and positive pions (lower) compared to the model.

Experiment beamline: HADES
Experiment collaboration: HADES
Experiment proposal: S407
Accelerator infrastructure: UNILAC / SIS18
Grants: VH-NG-823, Helzholtz Alliance HA216/EMMI
Strategic university co-operation with: TU Darmstadt

 DOI:10.15120/GR-2018-1

Protons and light nuclei in Au+Au collisions at 1.23A GeV measured with HADES

M. Szala[1] for the HADES collaboration

[1]Goethe-Universität Frankfurt, Germany

By varying the collision system and the beam energy of heavy ion collisions one can access broad areas of the phase diagram of strongly interacting matter.
We have carried out a detailed moment analysis of proton multiplicity distributions of Au+Au collisions with 1.23A GeV [1]. As the fully conserved quantity investigated here is the baryon number, further investigations will focus on including protons bound in the light nuclei formed in Au+Au collisions to the analysis.
A first estimate of the produced nuclei can be made using the β versus momentum correlation, which is used for particle identification (see Fig. 1). It turns out that the created system is a baryonic dominated system and the ratio between proton and deuteron multiplicity is approximately 0.3. Hence, indeed a significant contribution of protons is indeed bound in deuterons and light nuclei.

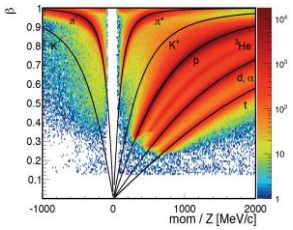


Figure 1: Correlation between measured time-of-flight β and particle momentum. Black lines correspond to the expected values of the different particles.

Furthermore by studying the light nuclei, one can also estimate the degree of thermalization of the system by comparing e.g. transverse rapidity distributions to longitudinal rapidity distributions. Also the mechanism for the production of the nuclei can be examined in detail and confronted with phenomenological models, e.g. formation of coalescence versus thermal production.
In order to calculate the count rate of protons, in this analysis the phase space is divided into cells along the rapidity and transverse mass axis. These cells were chosen to cover an interval of 0.09 < y < 1.59 in 0.1 steps for rapidity and 0-1000 MeV/c^2 in 25 MeV/c^2 steps along m_t-m_0. For every reduced transverse mass bin the mass spectra is plotted and the proton countrate is extracted using a multi-gaussian fit.
The resulting transverse mass spectra extracted for various rapidities are subsequently corrected for detector acceptance and efficiency. The resulting corrected number of counts is divided by m_t^2 in order to easily compare to a thermal distribution and a blast wave.
From these spectra, information about the freeze-out in form of the kinetic freeze-out temperature T_{kin} and characteristics of the radial flow in form of the radial expansion velocity β_r can be derived.

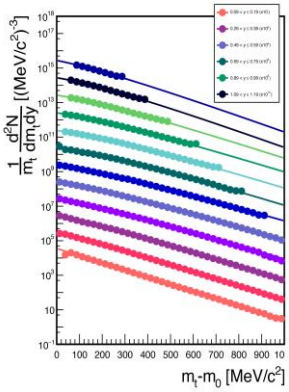


Figure 2: Corrected transverse mass spectra of protons for the 0-40% most central events, scaled by 1/m_t. Each spectrum is multiplied by a power of 10 and fitted using a blast wave function.
To estimate the multiplicities, the spectra have to be extrapolated to full phase space. One approach for extrapolation is by using blast wave functions fitted to the data:

$$\frac{1}{m_t}\frac{d^2N}{dm_t dy} = \int_0^R A m_t K_1\left(\frac{m_t \cosh(\rho)}{T_{kin}}\right) I_0\left(\frac{p_t \sinh(\rho)}{T_{kin}}\right) r dr$$

with A being a constant, $\rho(r) = tanh^{-1}(\beta_r(r))$, K_1 and I_0 are two modified Bessel functions ans the transverse geometric radius of the source is denoted by R.
The transverse velocity field $\beta_r(r))$ can be derived as

$$\beta_r(r) = \beta_s \left[\frac{r}{R}\right]^n \text{, with n = 1.}$$

According to formula a blast wave was fitted to the data (shown in Fig. 2). For this β and T are extracted in a global χ^2 scan over all data points.
Further steps in the analysis will be the centrality dependend analysis and the extension to the analysis of light nuclei in order to reconstruct the complete kinematics of participating baryons.

References

[1] GSI Scientific Report 2016, [10.15120/GR-2017-1] (p. 108)
[2] H. Schuldes, PhD thesis, Frankfurt (2016)

Experiment beamline: HADES
Experiment collaboration: HADES
Experiment proposal: S407
Accelerator infrastructure: SIS18
PSP codes: 1.1.2.
Grants: GSI strategic partnerships (FuE), HIC for FAIR, BMBF(05P15RFFCA)
Strategic university co-operation with: Frankfurt-M

Λ polarization in Au+Au collisions at $\sqrt{s_{NN}} = 2.42$GeV investigated with HADES

F. Kornas[1] for the HADES collaboration

[1]TU Darmstadt, Darmstadt, Germany

Λ hyperons can be used as a probe for possible vortical effects in the early stages of heavy-ion collisions since their weak decays preserve information about their polarization due to parity violation [1,2].

A good candidate to search for such an effect is the Λ hyperon with its decay channel $\Lambda \to p + \pi^-$. The polarization can be described by proton azimuthal angle in the Λ frame ϕ_p^* with respect to the total orbital angular momentum L [3]. Since L is always perpendicular to the reaction plane Ψ_{RP}, the reconstructed event plane Ψ_{EP} can be used as a measure for L, taking into account its resolution R_{EP}:

$$P_\Lambda = \frac{8}{\pi \alpha_\Lambda} \frac{\langle \sin(\Psi_{EP} - \phi_p^*) \rangle}{R_{EP}} \qquad (1)$$

Here $\alpha_\Lambda = 0.642 \pm 0.013$ [4] is the corresponding decay parameter and the brackets denote the average over all Λs and events.

Previous measurements by the STAR collaboration indicate an enhancement of the Λ and $\bar{\Lambda}$ polarization in Au+Au collisions towards lowest collision energy, $\sqrt{s_{NN}} = 7.7$ GeV [5] while there is no polarization found at the highest collision energy, $\sqrt{s_{NN}} = 200$ GeV [3].

At a center-of-mass energy of $\sqrt{s_{NN}} = 2.42$ GeV, seven billion events of Au+Au collisions were recorded with HADES in april 2012. After event selection and track reconstruction, the decay daughters of Λ candiates were selected first using a cut on their mass times charge of $0.3\ GeV/c^2 < m \cdot q/e < 1.3\ GeV/c^2$ for the proton and $-0.3\ GeV/c^2 < m \cdot q/e < 0\ GeV/c^2$ for the pions. All identified protons and pions in one event are combined to Λ candidates. Possible Λ candidates are selected by the parameters of the decay topology: the offset of both daughter tracks to the event vertex, the closest distance of these tracks as a possible decay vertex, the distance of the Λ track to the event vertex and the flight distance of the Λ with a lifetime of $c\tau \sim 8\ cm$. The distributions of these variables from simulated thermal Λs embedded into UrQMD [6] are handed to the TMVA to train a neural network to distinguish between signal and background. The mixed-event method is used to generate the background. This results in one cut parameter, the discriminant which is a weighted sum of all the input parameters. In the current analysis, various cuts are applied to the Λ candidates in order to guarantee a high purity sample after the TMVA is performed.

The discriminant is optimised on the significance which results in $\sim 3 \cdot 10^5 \Lambda$s remaining for $0 - 40\%$ centrality which is enough statistics to perform this analysis. The results of this sample of Λs for 10% centrality classes is shown in Figure 1 for three different mass bins. For the sidebands the $2 - 4\sigma$ range around the fitted Λ peak is taken, while for the Λs the 2σ region around the mean value is used as an input. The signal-to-background ratio in this region is 3.7 for the most peripheral bin and drops down to 1.3 in the most central case. The significance is in the range of $sig \sim 200$.

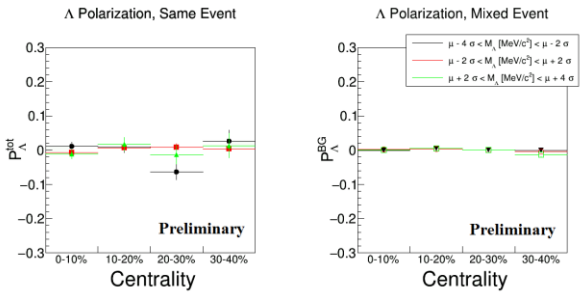


Figure 1: Λ Polarization in Au+Au collisions at $\sqrt{s_{NN}} = 2.42$ GeV in comparison to the sideband of the mass spectrum as a function of the centrality of the collision. In the left panel, the results are shown for the same event while in the right panel the results from the mixed-event are shown.

As a proof of principle the Λs from the mixed-event are not polarized. Yet for the same-event analysis the measured polarization is comparable to zero. For sure, one has to be aware of the effects of a limited detector acceptance. The results shown here are integrated values over rapidity and transverse momentum. The p_t and rapidity dependent analysis will be performed in the near future. Nevertheless, one has to correct for the finite geometrical coverage of the detector. The effects of the limited detector acceptance are discussed in [7] and will be investigated for the case of HADES.

References

[1] Z.-T. Liang and X.-N. Wang, Phys. Rev. Lett. 94, 102301 (2005).
[2] Z.-T. Liang and X.-N. Wang, Phys. Lett B 629, 20 (2005).
[3] B. I. Abelev et. al. (STAR Collaboration), Phys. Rev. C 77, 061902(R) (2008).
[4] Review of Particle Physics, Chin. Phys. C 38, 090001 (2014).
[5] L. Adamczyk et. al. (STAR Collaboration), Nature 548, 62 (2017).
[6] S. A. Bass et. al., Prog. Part. Nucl. Phys. 41 (1998) 255-369.
[7] S. Lan et. al., arXiv:1710.03895 (2017).

Experiment beamline: HADES
Experiment collaboration: HADES
Experiment proposal: S407
Accelerator infrastructure: UNILAC/SIS 18
PSP codes: none
Grants: VH-NG-823, Helmholtz Alliance HA216/EMMI
Strategic university co-operation with: Darmstadt

 DOI:10.15120/GR-2018-1

Dilepton production in pion induced reactions with HADES

F. Scozzi[1,2] for the HADES collaboration

[1]TU Darmstadt, Germany; [2]Institut de Physique Nucleaire Orsay, CNRS-IN2P3, Univ. Paris-Sud, Paris

The HADES experimental program on pion-beam induced reactions was recently started at GSI [1,2]. The π-nucleon reaction is an ideal probe to study baryon resonances. In particular, the dilepton (e^+e^-) production is used to investigate baryon resonance Dalitz decays ($R \to Ne^+e^-$), which provides access to the time-like electromagnetic structure of baryon transitions.

The e^+e^- production was measured in a test experiment using the GSI pion beam at a momentum of 0.685 GeV/c impinging on polyethylene and carbon targets [3]. The standard algorithm to identify leptons (**ring finder**) is based on finding ring patterns induced by the Cherenkov photons in the RICH detector. In addition, a matching between the reconstructed ring centre and a lepton track candidate is required. In case of small number of reconstructed photons per ring the efficiency of the lepton reconstruction can be improved using another method, the so-called **backtracking**. Here, one starts from lepton candidate tracks extrapolated to the RICH and searches for corresponding hits with looser constraints than in the ring finder method. After a careful tuning of the simulated RICH response, a realistic description of the RICH observables and of the efficiencies of the reconstruction algorithms in the simulation could be achieved. This is demonstrated in Fig.1, where the dilepton invariant mass spectra obtained for each algorithm after efficiency corrections are compared. The backtracking algorithm reaches an efficiency about factor 3 three higher, which is important, in particular when considering the low e^+e^- yield in the invariant mass region above π^0.

To allow for a more direct study of the baryonic contributions, events from the π^0 and η Dalitz decays present in the inclusive spectra can be efficiently rejected by applying conditions on invariant mass ($M_{ee} > 140\ MeV/c^2$and missing mass ($M_{miss} > 1040\ MeV/c^2$). In this way, about 1500 events corresponding to free or quasi-free $\pi^- p \to ne^+e^-$ reaction were selected, with a contribution of about 66% of pion carbon events. The comparison to model predictions is on-going, but it is already clear that a significant excess above expected contributions assuming point-like baryon Dalitz decays is present in the dilepton invariant mass distribution. Based on a Partial Wave Analysis (PWA) of the two-pion production measured in an energy scan in the same experiment, this excess can be interpreted as an off-shell ρ contribution, consistent with the Vector Dominance Model (VDM). These studies have a direct impact on the modelling of the emissivity of strongly interacting matter, which is based on VDM [4].

A parametrization of the angular distributions using the spin density formalism was also performed. It allows for the first time to extract important information on the helicity structure of baryon electromagnetic transitions in the time like region [5].

In future, we propose to extend these measurements to the third resonance region ($\sqrt{s} \sim 1.7\ GeV$), with higher statistics, taking advantage of the foreseen improvement of the beam intensity and of the upgraded HADES detector, including in particular the new Electro Magnetic Calorimeter and a new Forward Detector.

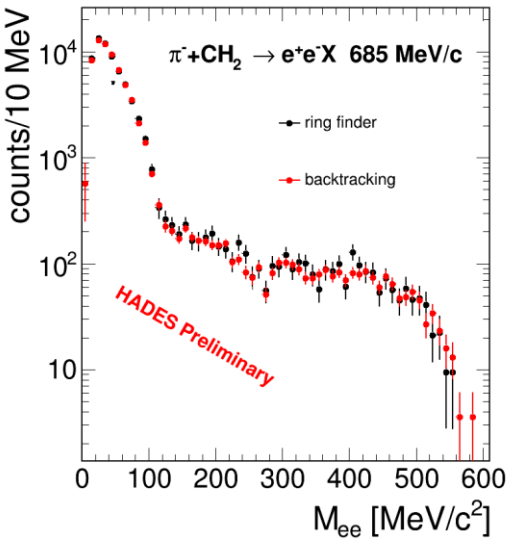


Figure 1: Efficiency corrected yield e^+e^- pairs reconstructed using the ring finder (black dots) and the backtracking algorithm (red dots). The data was taken for a pion beam at a central momentum of 0.685 GeV/c impinging on a polyethylene target.

References

[1] J. Adamczewski-Musch *et al.*, (HADES collaboration) Eur. Phys. J. A53 (2017) 188
[2] J. Diaz *et al.*, Nucl.Instrum.Meth. A478 (2002)
[3] F. Scozzi *et al.*, (HADES collaboration) EPJ Web Conf. 137 (2017) 05023
[4] R. Rapp and J. Wambach, Adv.Nucl.Phys. 25 (2000)
[5] E. Speranza *et al.*, Phys.Lett. B764 (2017)

Experiment beamline: HADES
Experiment collaboration: HADES
Experiment proposal: S333
Accelerator infrastructure: SIS18
PSP codes: 1.1.2
Grants: VH-NG-823 TU Darmstadt and CNRS/IN2P3 IPN Orsay
Strategic university co-operation with: Darmstadt

 DOI:10.15120/GR-2018-1

Characterisation of a cascaded power supply for use with multi-GEM stacks

P. Gasik[1,2], L. Fabbietti[1,2] and the ALICE Collaboration

[1]Physik Department E62, TU München, 85748 Garching, Germany;
[2]Excellence Cluster 'Origin and Structure of the Universe', 85748 Garching, Germany

The ALICE Collaboration will undertake a major upgrade of the detector apparatus in view of the LHC Runs 3 and 4 (2021 to 2029). In particular, new readout chambers will be installed in the TPC, replacing currently used Multi Wire Proportional Chambers with Gas-Electron-Multiplier-(GEM)-based detectors. New chambers employ stacks of four GEM foils, which require a High-Voltage system with eight HV power channels. This can be realised by employing a passive voltage divider (resistor chain), eight independent HV channels (each referring its potential to ground) or a novel system of eight "cascaded" HV channels that sit on top of each other (each referring its potential to the channel below) generating a cascade of high voltages.

In the first scenario, all fields and GEM voltages are defined by the resistor values and cannot be changed easily during the detector operation. Independent HV channels give full flexibility in choosing GEM voltages, however, the potential differences between subsequent channels may increase substantially in case of a spark discharge event or emergency shutdown of all channels caused by a power supply trip. Measurements performed at the Technical University of Munich have shown that the time difference between switching subsequent HV channels off may reach several hundreds of milliseconds. This can easily result in large potential differences across GEMs causing their irreversible damage.

The cascaded PS system was characterised in terms of its reaction on a discharge event and different tripping modes. Measurements were performed with a prototype delivered by ISEG GmbH. All tests were done using a GEM-PCB Simulator [1], an equivalent of a ~0.17 m^2 large quadruple GEM stack of an ALICE Inner Readout Chamber. Measurements included realistic cable lengths and protection resistor values. Differential voltages on the HV channels were monitored with 1:10 and 1:100 scope test probes via decoupling capacitors. Self-made 1:1000 probes were used to monitor absolute voltages on a long-timescale.

A discharge event is induced using a Gas Discharge Tube connected across a capacitor representing a single GEM segment (~5 nF). We do not measure any significant over-voltages across GEM foils and GEM segments other than the sparking one. Small voltage variations observed in the subsequent GEMs are due to the capacitive coupling of the foils and may cause increase of the potential difference across a GEM at a single-volts level.

The time-characteristics of the cascaded power supply is measured for different tripping modes after detection of an overcurrent:

- turn channel off with ramp,
- turn channel off without ramp,
- turn all channels off without ramp.

A relay is used to create a short across a single GEM segment and trigger a trip.

In case of the single-channel reaction, we do not observe any significant voltage increase across non-tripping GEMs. Occasional few-volts increase due to the capacitive coupling of the subsequent foils does not pose a threat to the GEMs. It is worth to mention that in case no software delay is specified between an overcurrent detection and turning the HV channel off, the intrinsic system delay varies between 10 and 20 ms. This means that the voltage across GEM may be reduced immediately after spark detection, before the nominal potential difference is reached (the typical re-charging time of a 100 cm^2 segment, powered via 10 MΩ protection resistor, is ~200 ms).

The most crucial issue is a measurement of the last tripping mode, when all channels are switched off without ramp (emergency shutdown of the PS). By construction, no overvoltage is expected across any of GEMs, as the HV channels of the cascaded PS are stacked in a row as in case of the passive voltage divider. The latter is confirmed in our tests where we measure time delays between switching off subsequent channels. In a series of measurements where the emergency shut down is triggered in different HV channels, we observe that all channels are switched off at the same moment (see Fig. 1) and no overvoltage is created across any of the GEMs in the stack.

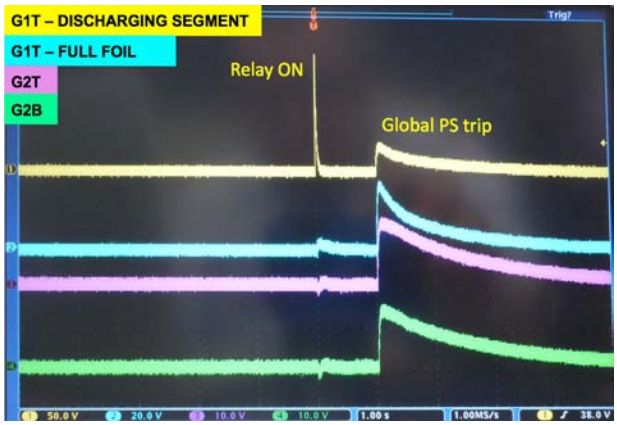


Figure 1: Reaction of the cascaded PS to an overcurrent detected in one of the channels (Relay ON). All channels are switched off at the same moment (within <1 ms). A one-second reaction-delay was set in the PS software.

In summary, the measurements presented in this report assure safe operation of GEM-stacks with the cascaded power supplies that are considered as a baseline PS system for the ALICE TPC upgrade.

References

[1] P. Gasik, "Quadruple GEM-PCB Simulator", GSI Scientific Report 2016, doi:10.15120/GR-2017-1.

Experiment beamline: none
Experiment collaboration: CERN-ALICE
Experiment proposal: none
Accelerator infrastructure: CERN-LHC
PSP codes: none
Grants: Excellenzcluster Universe 'Origin and Structure of the Universe' DFG EClust 153, BMBF ALICE 'Verbundprojekt 05P2015'
Strategic university co-operation with: none

 DOI:10.15120/GR-2018-1

Measurement of J/ψ production as a function of event multiplicity in pp collisions at √s = 13 TeV with ALICE*

S. Weber[1,2], for the ALICE collaboration

[1]GSI, Darmstadt, Germany; [2]TU Darmstadt, Germany

The event multiplicity dependent production of charmonium gives insight into QCD processes and particularly the interplay between the hard and soft mechanisms in particle production. ALICE has performed multiplicity dependent measurements of inclusive J/ψ production at mid and forward rapidity in pp collisions at √s = 7 TeV [1], reaching multiplicities of about 4 times the mean value. The results are consistent with a stronger than linear increase with multiplicity, similar to results for open-charm hadrons and J/ψ originating from beauty-hadron decays ("non-prompt" J/ψ) [2].

A new measurement of J/ψ production as a function of event multiplicity was performed with the ALICE detector [3] in pp collisions at √s = 13 TeV. Using a trigger on high event multiplicities, based on a large deposited charge in the ALICE V0 scintillator arrays at forward and backward rapidity, mid-rapidity multiplicities of about 7 times the mean value in minimum bias collisions were reached. High p_T J/ψ (p_T > 8 GeV/c) were obtained from data triggered by the EMCAL electromagnetic calorimeter. The signal was extracted from the dielectron decay channel in the ALICE central barrel. Particle identification was performed with the TPC detector, for high p_T ,together with the EMCAL PID information.

Figure 1 shows the self-normalized J/ψ yield as a function of charged-particle multiplicity in four p_T bins. A stronger increase for higher p_T is observed, in qualitative agreement with predictions from the PYTHIA8 model [4]. Within this model, the increase of J/ψ production can be understood from production in multi-parton interactions (MPI).

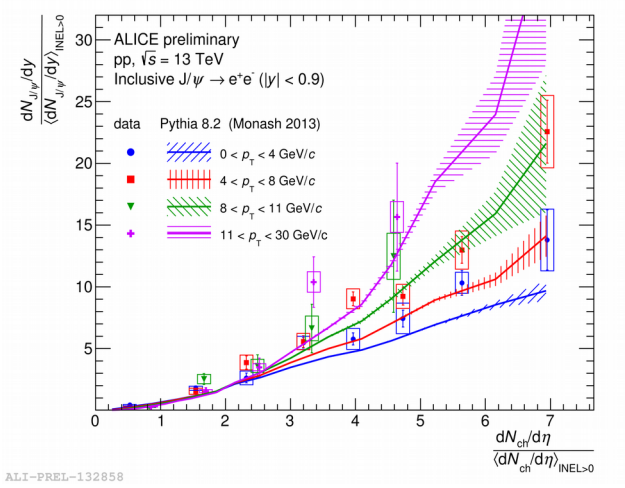


Figure 1: Multiplicity dependence of inclusive J/ψ production at mid-rapidity at √s = 13 TeV in four transverse momentum bins, comparison to PYTHIA8.

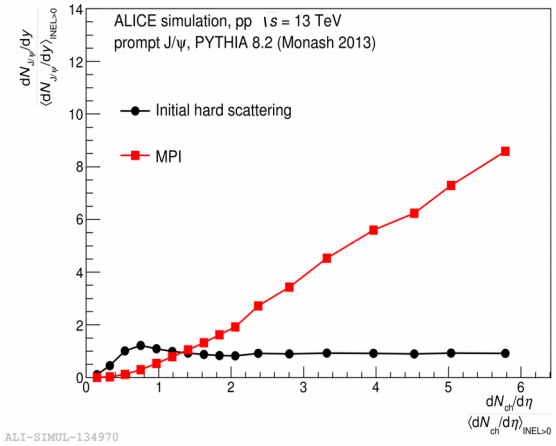


Figure 2: PYTHIA8 prediction for multiplicity dependence of prompt J/ψ production from initial hard scatterings and from MPI in pp collisions at √s = 13 TeV.

Figure 2 shows the PYTHIA8 prediction for the self-normalized yield of prompt J/ψ (excluding beauty-hadron decays) as a function of charged-particle multiplicity for J/ψ produced in the initial hard scattering of the event, and for J/ψ produced in subsequent ones from the MPI framework. It can be seen that initially produced J/ψ are independent of the charged-particle multiplicity, so the contribution of J/ψ from MPI is vital for the understanding of the data.

References

[1] B. Abelev, et al., Phys. Lett. B712 (2012) 165–175.
[2] J. Adam, et al., JHEP 09 (2015) 148.
[3] K. Aamodt, et al., JINST 3 (2008) S08002.
[4] T. Sjostrand, S. Mrenna, P. Z. Skands, Comput. Phys. Commun. 178 (2008) 852–867.

*Work supported by BMBF, GSI, HGS-HIRe, HIC4-FAIR, H-QM, TU Darmstadt

Σ^0 baryon production in pp collisions at $\sqrt{s}$ = 13 TeV measured with the ALICE experiment*

A. Mathis[1,2] and L. Fabbietti[1,2], for the ALICE collaboration

[1]Technische Universität München, Physik Department E62, Garching, Germany
[2]Excellence Cluster 'Origin and Structure of the Universe', Garching, Germany

To present day, only very little is known about the interaction between Σ baryons and nucleons (Σ-N). This is due to the fact that up to now, Σ hypernuclei have not been observed yet and moreover, scattering data for Σ hyperon beams are scarce. Hence, the Σ-N interaction remains to be probed. For other hyperons, the situation is somewhat better, in particular for the case of the Λ. Recently, much progress has been made for the case of the Λ-N interaction by employing femtoscopy as a complementary method compared to scattering data. In the context of femtoscopic measurements, it is also interesting to quantify the feed-down from the Σ^0 which decays almost exclusively into a Λ baryon and a photon [1] to the final state of interest containing a Λ. At low collision energies close to the NN threshold, the production cross-sections $\sigma_\Lambda/\sigma_\Sigma \approx 10$ [2] suggest a feed-down of ~ 10%. For larger energies, however, according to isospin considerations, the ratio is expected to approach 1/3 [3] as the Λ is represented in an isospin singlet state while the Σ^0 belongs to an isospin triplet representation. Hence, if sufficient energy is available in the reaction, three different Σ states can be excited but only one Λ state.

A study of the Σ-N, and the hyperon-nucleon interaction in general is also of interest in the context of the study of the content of neutron stars. Even though, as recently demonstrated, gravitational wave observations of binary neutron star mergers are a powerful tool to determine the neutron star equation of state (EOS), the latter still remains a puzzle. In particular, for the description of such a system in the presence of hyperons a thorough understanding of the hyperon-nucleon interaction is mandatory.

As a first step, we measure the production of the Σ^0 baryon at an unprecedented high energy of $\sqrt{s}$ = 13 TeV in pp collisions with the ALICE detector. For the analysis, all available data are employed, which account to about 1×10^9 events collected with a minimum-bias trigger. For the reconstruction of the Σ^0 the dominant decay channel $\Sigma^0 \rightarrow \Lambda\ \gamma$ is exploited. The Λ is then subsequently identified via its decay into a charged pion and a proton (BR ~ 63.9 % [1]) employing the dE/dx information provided by the ALICE Time Projection Chamber. The energy of the photon is typically too low to allow for the employment of ALICE's electromagnetic calorimeter. Instead, the photon conversion method is used which relies on the identification of the dielectron pair produced in the conversion of a photon in the detector material, $\gamma \rightarrow e^+e^-$. For the case of ALICE, the corresponding probability is about 8 %. The four-momentum vector of the Λ is then combined with a dielectron pair and the resulting invariant mass is depicted in Fig. 1. The background is described by a forth-order polynomial (dotted line) and the signal is parametrized by a single Gaussian.

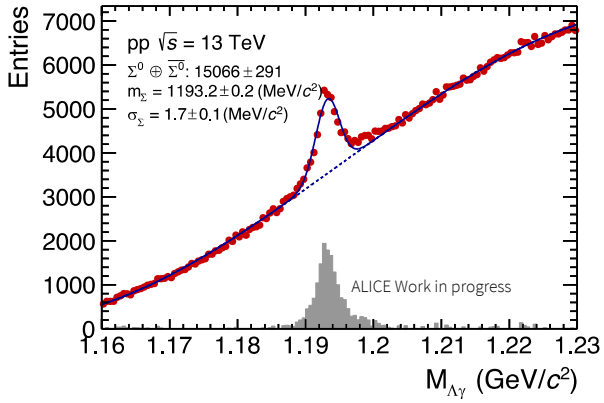


Figure 1: Invariant mass of the Λ and a dielectron pair. The dotted line depicts the combinatorial background and the signal is parametrized by a Gaussian. The grey histogram displays the signal after subtraction of the background.

A global fit of the spectrum yields in total about 15,000 Σ^0 baryons candidates at a signal-to-noise ratio of about 0.2. After correcting the spectra for acceptance and efficiency, this analysis will yield the Σ^0 production cross-section and the Σ^0/Λ ratio at an unprecedented high energy of $\sqrt{s}$ = 13 TeV together with a comparison to event generators such as PYTHIA [4]. Moreover, with more data being reconstructed, the feasibility of p-Σ^0 femtoscopy will be checked, possibly allowing to constrain the Σ-N interaction for the first time. Additionally, with the available statistics, a study of all relevant decay channels ($\Sigma^0 \rightarrow \Lambda\ \gamma$, $\Sigma^0 \rightarrow \Lambda\ \gamma\ \gamma$ and $\Sigma^0 \rightarrow \Lambda\ e^+e^-$ [1]) may be at hand and the feasibility will be explored, which for the first time would allow for a relative measurement of the corresponding branching ratios.

References

[1] K.A. Olive *et al.*, Chin. Phys. C, 38, 0900001 (2014).
[2] P.Kowina *et al.*, Eur. Phys. J. A 22, 293-299 (2004).
[3] H.Landolt, R.Börnstein, Landolt-B.12, (1988).
[4] T. Sjöstrand, S. Mrenna, and P. Skands, Journal of High Energy Physics 2006 no. 05, (2006) 026.

*) Work supported by the DFG Excellenzcluster Universe, "Origin and Structure of the Universe" (DFG EClust 153), BMBF ALICE „Verbundprojekt 05P2015" and the Collaborative Research Center "Neutrinos und Dunkle Materie in der Astro- und Teilchenphysik (NDM)" (SFB 1258).

 DOI:10.15120/GR-2018-1

Baryon Femtoscopy in p–Pb Collisions at 5.02 TeV

B. Hohlweger[1,2] and L. Fabbietti[1,2], for the ALICE collaboration

[1]Technische Universität München, Physik Department E62, Garching Germany,[2]Excellence Cluster `Origin and Structure of the Universe`, Garching, Germany

Understanding the interaction of hyperons at finite densities is fundamental in order to understand the role of strange degrees of freedom in the Equation of State (EoS) of neutron stars. Scattering data for hyperons does not allow to discriminate between models of baryon-hyperon interaction. Therefore, femtoscopy has been proposed to study the interaction of these pairs. The observable in femtoscopic analysis is the two-particle correlation function, defined as

$$C(\boldsymbol{p}_1,\boldsymbol{p}_2) = \frac{P(\boldsymbol{p}_1,\boldsymbol{p}_2)}{P(\boldsymbol{p}_1)P(\boldsymbol{p}_2)} = C(k) = \int S(\boldsymbol{r},k)|\psi(\boldsymbol{r},k)|^2 d\boldsymbol{r}, \quad (1)$$

where $P(\boldsymbol{p}_1,\boldsymbol{p}_2)$ is the conditional probability of finding a particle pair with a momentum $\boldsymbol{p}_1$and $\boldsymbol{p}_2$ in the same event, while $P(\boldsymbol{p}_i)$ is the single particle probability of independently finding the particles with momentum $\boldsymbol{p}_i$. This quantity can also be viewed as a function of the relative momentum k in the pair center of mass frame and is related to the product of source function $S(\boldsymbol{r},k)$ and wave function $\psi(\boldsymbol{r},k)$ [2]. The sensitivity to the interaction arises from the wave function, which is obtained by solving the Schrödinger equation incorporating the interaction potential of a given pair. The source is typically described by a Gaussian distribution and is assumed to be the same for all baryon pairs.

In a recent study in p–Nb collisions at √s = 3.5 GeV [1] and in pp collisions at √s = 7 TeV it has been shown that the correlation function for p-Λ pairs develops a sensitivity to different scattering parameters. It was however apparent that more statistics would allow for stronger constraints on different models and for this purpose, the analysis was extended to data from p–Pb collisions at $\sqrt{s_{NN}}$ =5.02 TeV. After applying event selection criteria, around 600 million events are available to analyse pairs of p-Λ and p-Ξ. The Λ hyperon is identified via its decay into a charged pion and proton (BR ~63.9%), which subsequently are identified by the dE/dx measurement in the Time Projection Chamber (TPC). The resulting sample has a purity of around 96%. The Ξ hyperon is identified via its decay into a Λ and a pion (BR ~99.9%). A first signal of Ξ's in the invariant mass distribution is depicted in Fig. 1, where a purity of around 87% is reached. The experimental correlation function for p-p, p-Λ and p-Ξ pairs is then obtained by constructing the relative momentum distribution from pairs in the same event $N_{SE}(k)$ and of uncorrelated pairs $N_{ME}(k)$ where each particle is from a different event. The correlation function is obtained by dividing the $N_{SE}(k)$ by $N_{ME}(k)$.

The Correlation Analysis Tool using the Schrödinger Equation (CATS) [3] framework has been employed in the calculation of the proton-hyperon interaction. For p-Λ pairs the interaction has been described by χ_{EFT} potentials at LO and NLO. In the case of p-Ξ pairs a preliminary local potential from the HAL Lattice QCD collaboration [4] has been adopted. The correlation function, as shown in Eq. (1), depends both on the source size and the undergoing potential. Studying the source with p-p pairs, where the interaction potential is well known, allows to reduce the uncertainty arising from the size of the emitting source and permits to set tighter constraints on the strong potential of more exotic pairs as baryon-hyperon or hyperon-hyperon. In the p–Pb system the size of the source depends on the impact parameter and its variations are expected to be larger than in the elementary collisions. The geometry of the emitting source can be studied by using the p-p correlation function binned in several multiplicity classes. The results of this study will provide the necessary input to perform a final combined fit of baryon-baryon pairs in the p–Pb collision system and to ultimately constrain the interaction potentials for baryon-hyperon pairs.

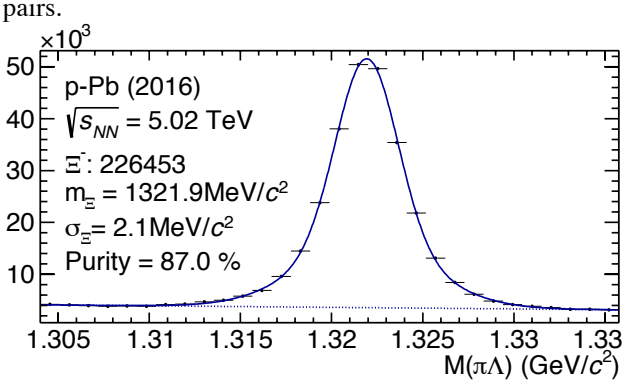


Figure 1: Ξ – Signal reconstructed in the $\Lambda\pi$ channel from p-Pb Data at $\sqrt{s_{NN}}$ =5.02 TeV.

References

[1] HADES Collaboration, Λp interaction studied via Femtoscopy in p+Nb recations at $\sqrt{s_{NN}}$=3.18 GeV, Phys. Rev. C, 94, 025201 (2016)

[2] Michael Annan Lisa and Scott Pratt et al, Femtoscopy in Relativistic Heavy Ion Collisions: Two Decades of Progress, Annual Review of Nuclear and Particle Science, 55, 357-402 (2005)

[3] D.L. Mihaylov, V. Mantovani Sarti et. al, A femtoscopic Correlation Analysis Tool using the Schrödinger equation (CATS), arXiv:1802.08481

[4] Kenji Sasaki, Sinya Aoki et. al, Baryon interactions from lattice QCD with physical masses -- S=−2 sector, arXiv:1702.06241

Experiment collaboration: CERN-ALICE
Accelerator infrastructure: CERN-LHC
Grants: SFB: Sonderforschungsbereich 1258 "Neutrinos und Dunkle Materie in der Astro- und Teilchenphysik (NDM)"
Strategic university co-operation with: TU München

Low-mass dielectron production in pp collisions at $\sqrt{s}$ = 13 TeV with ALICE*

I. Vorobyev[1,2], A.Dashi[1,2], O. Vazquez Doce[1,2], T. Dahms[1,2], for the ALICE collaboration

[1]Excellence Cluster Universe, Technische Universität München, Garching, Germany;
[2]Physik Department, Technische Universität München, Garching, Germany

Electron–positron pairs (dielectrons) are a unique experimental tool to investigate the hot and dense medium created in ultra-relativistic heavy-ion collisions. Such pairs are produced during all stages of the collision and do not interact strongly. Therefore, they carry information about the medium properties and the whole space-time evolution of the system.

Measurements of dielectron production in minimum-bias proton–proton (pp) collisions provide an important vacuum reference for any modifications observed in heavy-ion collisions. Moreover, the measurement of e^+e^- pairs from semileptonic decays of correlated heavy-flavour hadrons in the intermediate-mass region ($1.1 < m_{ee} < 2.9$ GeV/c^2) allow further studies and understandings of the primordial heavy-flavour production. Recent studies of pp collisions with high charged-particle multiplicities showed interesting results similar to the observations previously made in heavy-ion collisions. Measurements of low-mass dielectrons could provide further insight into the underlying physics processes.

The dielectron analysis is performed in the central barrel spectrometer of ALICE [1]. For both multiplicity classes the collision events are triggered on by the V0 detector. Charged particle tracks are reconstructed with the Inner Tracking System (ITS) and the Time Projection Chamber (TPC) in the kinematic range $|\eta_e| < 0.8$ and $p_{T,e} > 0.2$ GeV/c. Specific energy loss in the TPC and the time-of-flight information from the TOF detector are used for the electron identification.

All electron and positron candidates are paired considering the combinations with opposite but also same charge. The combinatorial background is estimated via the geometric mean of same-sign pairs within the same event. Conversions of real photons in the detector material are removed from the raw signal by their orientation relative to the magnetic field. The resulting raw dielectron spectra in high-multiplicity and minimum-bias events are shown in Fig. 1.

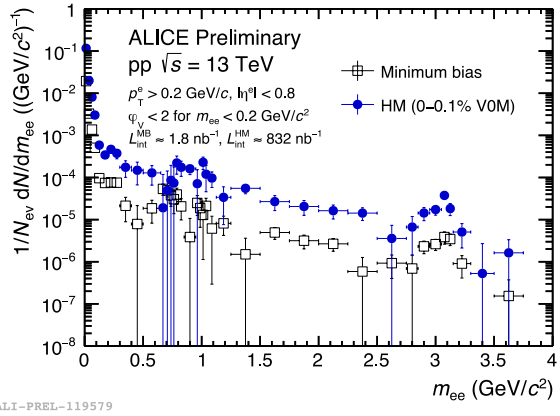


Figure 1: Raw dielectron spectra in minimum-bias (black) and high-multiplicity (blue) events.

The current work focuses on the analysis of approximately 5 times more pp collision data from 2016. The raw dielectron spectra will be corrected for the reconstruction efficiencies using detailed Monte Carlo simulations. The results will be compared to the expectations from all known hadronic sources, i.e. the hadronic cocktail, contributing to the dielectron spectrum in the ALICE central barrel acceptance. For the high-multiplicity cocktail, the light-flavour hadron p_T distributions are adjusted according to the measured modification of charged hadron p_T spectra [2]. The contribution of correlated semileptonic decays of open charm and bottom mesons is estimated with PYTHIA and POWHEG simulations. For the multiplicity dependence, the results on D-meson production as a function of p_T and multiplicity [3] are used to weight the open charm and bottom contributions. In the intermediate mass range the data will be fitted with PYTHIA and POWHEG templates of open charm and bottom production, which will allow us to extract the heavy-flavour cross sections. Finally, assuming the equivalence between the fraction of real direct photons and the fraction of virtual direct photons at zero mass, the former can be extracted from the dielectron spectrum measured at small invariant mass.

* Work supported by Excellence Cluster “Origin and Structure of the Universe”, DFG EClust 153 and BMBF ALICE: “Verbundprojekt 05P2015”

References

[1] ALICE Collaboration, JINST3 (2008) 08002
[2] ALICE Collaboration, Phys. Lett. B 753, 319 (2016)
[3] ALICE Collaboration, JHEP 09, 148 (2015)

 DOI:10.15120/GR-2018-1

Production of electrons from semileptonic heavy-flavour hadron decays in proton-proton and heavy-ion collisions measured with ALICE at the LHC*

C. de Conti[1], A. Dubla[2,3], M. Faggin[5], S. Hornung[2,3], S. P. Rode[4], for the ALICE collaboration

[1]Universidade de Sao Paulo, Brasil; [2]GSI, Darmstadt, Germany; [3]Heidelberg university, Germany; [4]Indian Institute of Technology Indore, India; [5]University of Padova

The transverse momentum (p_T) spectra and the nuclear modification factor (R_{AA}) of electrons from semileptonic heavy-flavour hadron decays is measured in Pb-Pb collisions at $\sqrt{s_{NN}}$ = 5.02 TeV and in Xe-Xe collisions at 5.44 TeV. The modification of the p_T spectra is studied at mid-rapidity (|y| < 0.8) in the p_T interval 0.5-6 GeV/c. The R_{AA} is calculated using the proton-proton (pp) reference cross-section measured in the same p_T interval and at the same center-of-mass energy as for the Pb-Pb measurement. For the Xe-Xe R_{AA} the pp reference was obtained using an interpolation procedure. In addition, the production cross-section was also measured in pp collisions at $\sqrt{s}$ =7 TeV and $\sqrt{s}$ = 13 TeV.

Introduction

In ultra-relativistic heavy-ion collisions at the Large Hadron Collider (LHC) a strongly-interacting matter, characterised by high energy density and temperature, is produced. Under these conditions, the formation of a deconfined state of quarks and gluons, the Quark-Gluon Plasma (QGP), is predicted by Quantum ChromoDynamic (QCD) calculations on the lattice. The production of heavy quarks, i.e. charm (c) and beauty (b) is characterised by a timescale shorter than $1/(2*m_{c,\,b})$, where m is the mass of the quark. This timescale (e.g. ~ 0.08 fm/c for charm) is expected to be smaller than the QGP thermalization time (~ 0.6-1 fm/c). Heavy quarks interact with the QGP and suffer energy loss while propagating through it. The modification of the p_T spectra in heavy-ion collisions with respect to those in pp collisions at the same centre-of-mass energy is quantified by the nuclear modification factor R_{AA}, defined as:

$$R_{AA} = \frac{(dN_{AA}/dp_T)}{(d\sigma_{pp}/dp_T)\cdot\langle T_{AA}\rangle}, \quad (1)$$

where dN_{AA}/dp_T is the measured yield in heavy-ion collisions and $d\sigma_{pp}/dp_T$ is the corresponding cross-section in pp collisions.

* Work supported by GSI, BMBF, DST-DAAD and HGS-HIRe and ISOQUANT.

The average nuclear overlap function, $\langle T_{AA}\rangle$, is estimated via Glauber model calculations and is proportional to the average number of binary nucleon-nucleon collisions in nucleus-nucleus (AA) collisions in a given centrality class.

Low-p_T heavy-flavour measurements are very important to test the binary scaling of the heavy-quark production in heavy-ion collisions. In addition, they allow to extract information about possible influences from the initial state effects, like the modification of the parton distribution functions at the LHC energies. They also carry information about different hadronisation mechanisms, namely the fragmentation in the vacuum and the coalescence in the medium. At high-p_T heavy quarks are sensitive to the medium energy density, through the mechanism of parton energy loss.

Results

The p_T-differential cross section for electrons from heavy-flavour hadron decays at mid-rapidity in pp collisions at $\sqrt{s}$ = 5.02, 7 and 13 TeV using the photonic-electron tagging are shown in the left, middle and right panel of Figure 1, respectively. The statistical uncertainties are shown as vertical bars and the systematic uncertainties as empty boxes. The dashed line indicate the central value of the FONLL calculation [1]. The full systematic band of the model originates from the variation of the factorization and normalization scale as well as the heavy-quark masses and the uncertainty of the parton distribution function (PDF) used. In the lower panels of Figure 1 the ratios of the experimental measurements with the central value of the FONLL calculations are shown. Within the systematic uncertainties of the measurement and the calculation, the theoretical calculation is in good agreement with the data. The measured cross sections are close to the upper edge of the FONLL uncertainty band.

Figure 2 shows the R_{AA} of electrons from heavy-flavour hadron decays at mid-rapidity (|y| < 0.8) as a function of p_T in Pb-Pb collisions at $\sqrt{s_{NN}}$ = 5.02 TeV for the 0-10% centrality class. The new low p_T measurement is shown together with the high p_T results obtained using the TPC+EMCal detectors to identify the electron (orange closed marker) [2].

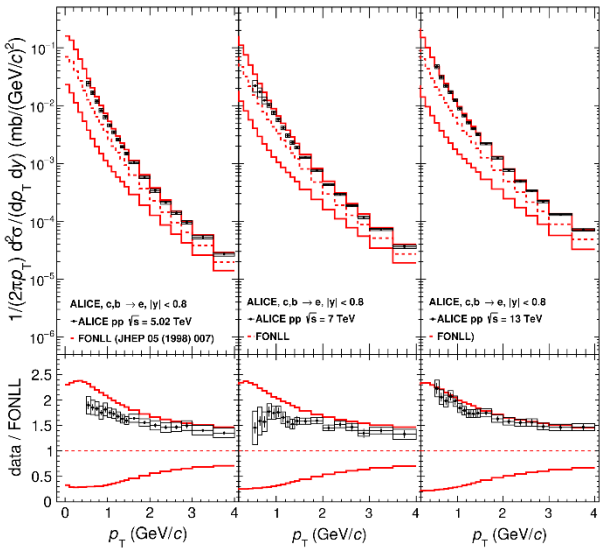


Figure 1: p_T-differential cross section of electrons from heavy-flavour hadron decays at mid rapidity in pp collisions at $\sqrt{s}$ = 5.02 TeV, 7 TeV and 13 TeV compared to pQCD calculations.

The statistical and systematic uncertainties of the spectra in Pb-Pb and pp were propagated as independent uncertainties. The uncertainty on the normalisation (3%) is the uncertainty on $\langle T_{AA} \rangle$ and it is represented by a filled box at R_{AA} = 1. At high p_T, the R_{AA} is below unity, showing a suppression of the yield of electrons from heavy-flavour hadron decays with respect to pp due to the energy loss of heavy quarks in the QCD medium.

For p_T < 1.5 GeV/c, the data is compatible with unity

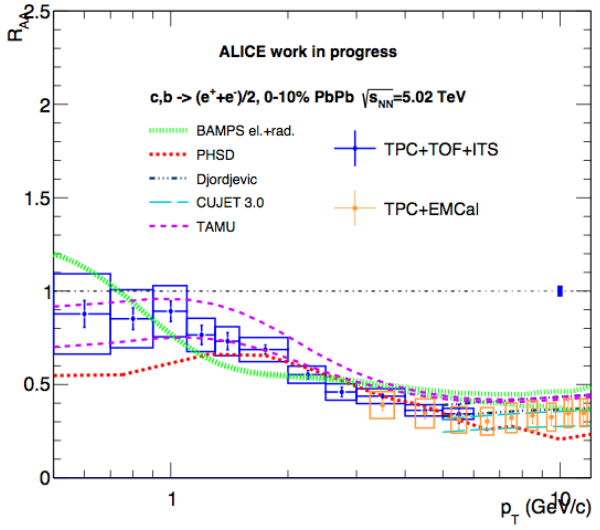


Figure 2: Heavy-flavour hadron decay electron RAA at mid-rapidity as a function of pT in central Pb-Pb collisions at $\sqrt{s_{NN}}$ = 5.02 TeV compared to models [3-6].

within systematic uncertainties. Models which include shadowing, like TAMU [4], predict an R_{AA} smaller than one even at low p_T and are in good agreement with the experimental measurement.

In Figure 3 the R_{AA} of electrons from heavy-flavour hadron decays at mid-rapidity ($|y|$ < 0.8) as a function of p_T in Xe-Xe collisions at $\sqrt{s_{NN}}$ = 5.44 TeV is shown in the 0-20% centrality interval. The measurement is important to further study and constrain the energy loss dependence of the heavy quarks with respect to the size of the colliding nuclei. In addition, the modification of the parton distribution functions using a similar centre-of-mass collision energy but different nuclei can be investigated. Also in this case the uncertainty on the normalisation (9%) is the uncertainty on $\langle T_{AA} \rangle$ and it is represented by a filled box at R_{AA} = 1. When compared with the R_{AA} in Pb-Pb collisions an indication of a smaller suppression in Xe-Xe collision is observed.

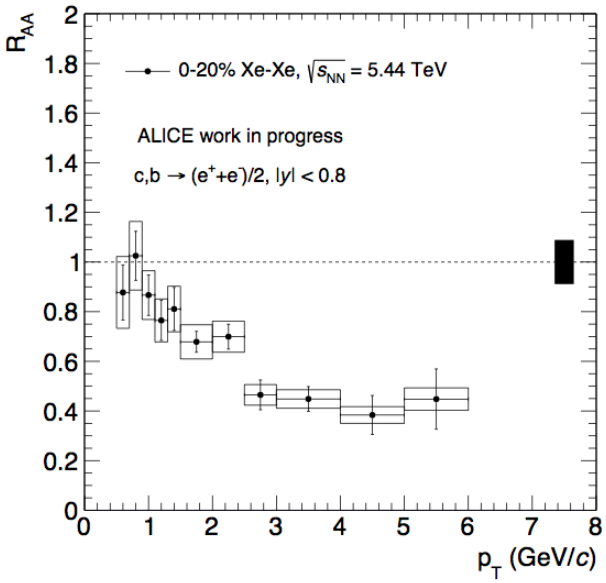


Figure 3: Heavy-flavour hadron decay electron R_{AA} at mid-rapidity as a function of p_T in the 0-20% centrality class in Xe-Xe collisions at $\sqrt{s_{NN}}$ = 5.44 TeV.

References

[1] M. Cacciari et al., JHEP 05 (1998) 007
[2] ALICE Collaboration, Nucl. Phys. A 967 (2017)
[3] J. Uphoff et al., J.Phys.Conf.Ser. 509 (2014) 012077
[4] M. He et al., Phys.Lett. B735 (2014) 445–450
[5] W. Cassing et al., Phys.Rev. C78 (2008) 034919
[6] J. Xu, J. Liao et al. Chin. Phys. Lett. 32 no. 9, (2015)

 DOI:10.15120/GR-2018-1

Quality assurance of GEM-based readout chambers for the Time Projection Chamber of ALICE

L. Kreis[1,2], M. Habib[1,3], A. Harlenderová[1,2], S. Hornung[1,2], J. Hehner[1], S. Masciocchi[1,2], D. Miśkowiec[1], T. Rudzki[1,2], B. Voss[1], the ALICE Collaboration

[1]GSI, Darmstadt, Germany; [2]Ruprecht-Karls-Universität Heidelberg, Germany; [3]Technische Universität Darmstadt, Germany

In the upcoming long shutdown period of the LHC, ALICE will be upgraded to be able to record Pb–Pb collisions at an event rate of 50 kHz. The current readout chambers of the Time Projection Chamber (TPC) are multiwire proportional chambers, which limit the event rate to 3 kHz. A new readout based on gas electron multipliers (GEM) is currently under construction. A stack of four GEMs is used, where two large pitch foils are sandwiched between two standard pitch foils.

These new readout chambers will allow continuous data-taking during LHC Run 3 and 4. The ALICE TPC readout chambers come in two sizes: the inner readout chambers and the outer readout chambers (OROC) with one stack and three GEM stacks, respectively. The TPC upgrade project is distributed between different institutes. GSI is responsible for the framing of GEMs from the largest stack and for the OROC assembly.

After the assembly, several parameters are measured to guarantee a stable operation of the chambers at the LHC, while maintaining the performance of the current setup [1]. The ion backflow (defined as the ratio of the cathode current and the current on the pad plane $IBF = I_{cathode} / I_{pads}$ at an effective gas gain of 2000 has to be below 1%. The local energy resolution measured with an 55Fe source at the same operating point must be below 12%.

The chambers are transferred onto a 2D scanning device. The gas tightness is evaluated by flushing the chamber while monitoring the oxygen content. The voltage settings for an effective gain of 2000 are determined for each GEM stack. These settings are used in the following tests. The energy resolution is measured for each GEM stack at one point with an 55Fe source. The resolution is determined by a Gaussian fit to the spectrum. Gain uniformity and ion backflow are measured with x-ray irradiation at each point using the 2D scanner. A chamber passes the test if the gain uniformity is better than 20%. An example of the ion backflow is shown in Fig. 1.

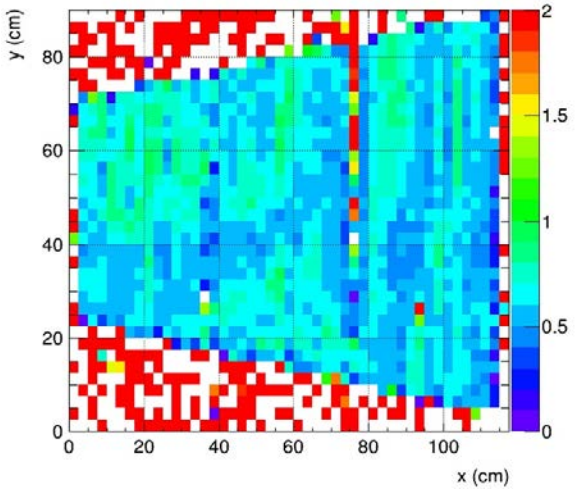


Figure 1: Two-dimensional scan of the ion backflow showing the uniformity of the chamber OROC/6.

Each solder joint of the high voltage connections and the GEM foils is irradiated for 15 minutes to check for possible defects which may cause discharges. After the 2D scans, the chamber load exceeding the anticipated LHC Run 3 and Run 4 conditions is simulated in a shielding box. During this six-hour-long full area irradiation the chamber is monitored for possible discharges. Subsequently the leakage current for each GEM is measured to be able to exclude any possible short circuits. If a chamber passes all the tests, it is moved into a transportation box in which it will be sent to CERN.

The work at the GSI detector lab is progressing well. The first two chambers were already shipped to CERN. The final assembly of the TPC will take place in 2019.

Work supported by BMBF and GSI.

References

[1] The ALICE Collaboration, “Upgrade of the ALICE Time Projection Chamber”, CERN,

October 2013, https://cds.cern.ch/record/1622286

 DOI:10.15120/GR-2018-1

Read-out electronics for the ALICE TPC upgrade

C. Lippmann[1] and the ALICE collaboration

[1]GSI, Darmstadt, Germany

The front-end electronics for the upgrade of the ALICE Time Projection Chamber (TPC) is based on the 32-channel SAMPA ASIC and a radiation-hard data and control link (CERN GBT). The SAMPA ASIC incorporates for each channel a charge-sensitive amplifier, a shaper, and a 10-bit ADC. The TPC uses the SAMPA (5 per Front-End Card, FEC) in direct-serialization mode, where all ADC values are sent via electrical links to the GBTx multiplexer ASIC (2 per FEC) and through the optical read-out links without compression. In this way, the data can be corrected for the Common Mode Effect in the FPGA-based read-out card, the ALICE Common Readout Unit (CRU), with high precision. The Common Mode Effect is a systematic, common baseline shift expected at high occupancies.

Beamtest results

A pre-production Inner Readout Chamber (IROC) has been tested together with 6 prototype versions of the TPC FEC with SAMPA chips of version 'v2' at the CERN Proton Synchrotron with electrons and pions at 1 to 6 GeV/c. Since CRUs were not yet available the Read-Out Receiver Card (RORC) of the current ALICE experiment was fitted with a custom firmware (T-RORC) implementing the 12 bi-directional GBT links necessary for communicating with the 6 FECs.

The SAMPAs on the 6 FECs are synchronised with dedicated control signals. They synchronously sample the detector signals on 960 channels. Triggers from the beam scintillators are received on the T-RORC and open a time window of 0.1 ms length, where the ADC data are stored to disk.

The particle identification achieved at 1 GeV/c is shown in Fig. 1. The separation power is compatible with the value expected at this short track length (63 pad rows). For a full TPC sector the deposited charge information from 152 pad rows will be used, and the separation power will improve accordingly.

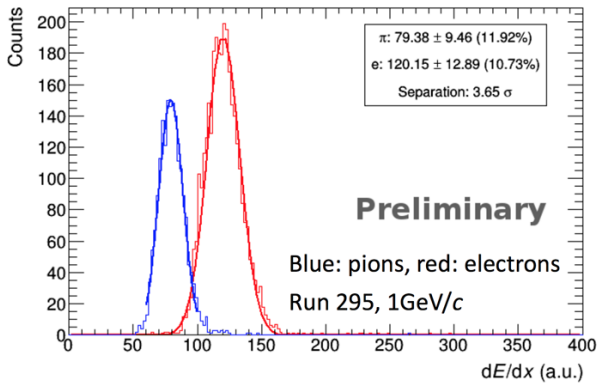


Figure 1: Particle separation power (electrons and pions) measured with a TPC pre-production IROC.

The read-out system was running stable for the full beam time over many days. No issues with synchronisation between the SAMPAs have been seen. During and after the beam test the data decoded, reconstructed and analysed with software based on the official ALICE online-offline package.

Noise results

The TPC FEC connects to the detector via flexible signal cables (in order to decouple the weight from the FEE from the read-out chambers and drift field cage). The Printed Circuit Board (PCB) for the final version is based on rigid flex technology where the flexible cables are realized as one layer of the PCB (see Fig. 2).

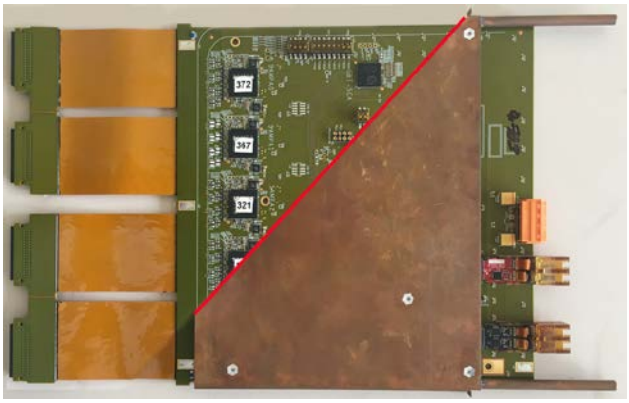


Figure 2: Overlay of 2 images showing a TPC Front-End Card (FEC) with and without its copper cooling envelope. The 4 flexible signal cables, the input protection network and the SAMPA ASICs are visible on the left, the power and optical connectors on the right.

FECs of this revision ('1a') and equipped with the different versions of the SAMPA (v2, v3 and v4) have been tested on the IROC after the beamtest. A noise distribution for 6 FECs is shown in Fig. 3. The mean noise in this particular detector region is 0.93 LSB. The targeted noise value is 1 LSB, corresponding to an equivalent noise charge (ENC) of 670 electrons.

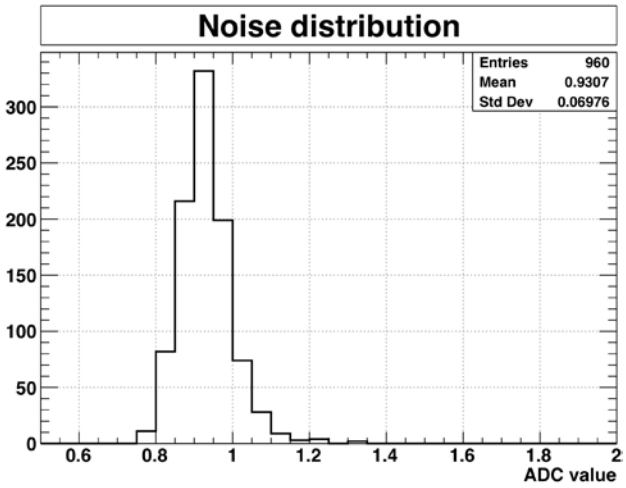


Figure 3: Noise distribution on 960 channels using 6 revision '1a' FECs.

The revision ‘1a’ of the FEC with SAMPA v4 will go into production. The SAMPA production readiness review (PRR) was successfully held on 20 February 2018. The PRR for the TPC FEC is planned for Spring 2018.

*Work supported by BMBF and GSI.

 DOI:10.15120/GR-2018-1

Nuclear modification factors in Xe-Xe collisions measured with ALICE*

J. Gronefeld[1] for the ALICE collaboration
[1]GSI, Darmstadt

The suppression of charged particle yields in heavy-ion collision compared to a superposition of independent nucleon-nucleon collisions at RHIC was one of the first indications of the creation of a deconfined medium[1, 2]. This observation is related to parton energy loss in the hot and dense QCD matter created in the collision of heavy ions, leading to a modification of transverse-momentum (p_T) distributions of the resulting particles, as initially suggested by Bjorken in 1982 [3].

Results from ALICE [4, 5] show that hadron yields at high p_T in central Pb–Pb collisions at LHC are suppressed even stronger than at RHIC, indicating a hotter and denser medium.

The suppression is quantified in terms of the nuclear modification factor:

$$R_{AA} = \frac{dN_{AA}/dp_T}{\langle T_{AA} \rangle \, d\sigma_{pp}/dp_T}$$

Here, dN_{AA}/dp_T represents the p_T-differential charged-particle yield in nucleus-nucleus (AA) collisions, while $d\sigma_{pp}/dp_T$ stands for the p_T-differential cross section in proton-proton (pp) collisions. The average nuclear overlap function $\langle T_{AA} \rangle$ is determined by Glauber Monte-Carlo calculations for each class of centrality.

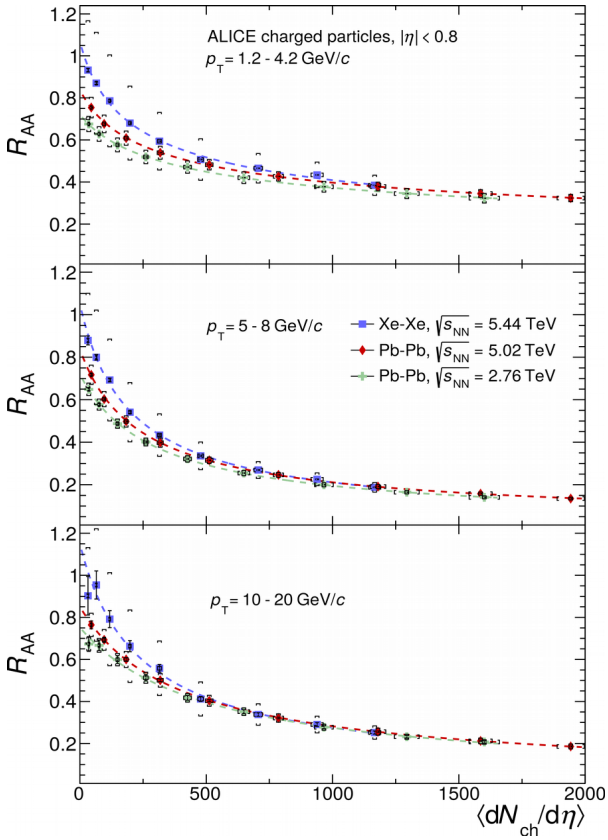
In absence of medium effects, the nuclear modification factor will be equal to unity, while $R_{AA} < 1$ indicates a suppression of charged-particle yields.

To obtain the primary charged-particle yield as a function of p_T, corrections are made for tracking efficiency and acceptance and for contamination by secondary particles. These correction factros are obtained from Monte-Carlo simulations that are reweighted to account for differences in the particle composition of event generators and the data. In addition the distribution is corrected for p_T resolution .

The charged particle nuclear modification factor for Xe-Xe and Pb-Pb collisions at two different center-of-mass energies is shown as a function of the charged particle multiplicity per unit of rapidity for three ranges in p_T. All systems exhibit a similar trend, showing an increase in suppression for events with a increased charged particle production.

For high charged particle densities we observe the same R_{AA} for all collision systems and for all energies at high p_T where parton energy loss is believed to play a dominant role (lower panel). This shows that a deconfined medium is created in heavy-ion collisions that exceeds a charged particle density of 400 per unit of rapidiy independently of the collision system.

At low p_T (top panel) a energy dependence of the R_{AA} is observed, which is attributed to the inceased particle production with higher collision energy.



The charged particle R_{AA} as a function of charged particle density.

[1] PHENIX Collaboration, Phys. Rev. Lett. 88, (2002) 022301.
[2] STAR Collaboration, Phys. Rev. Lett. 89, (2002) 202301.
[3] J. Bjorken, Preprint FERMILAB-PUB-82-059-THY (1982).
[4] ALICE Collaboration, Phys. Lett. B 746, (2015).
[5] ALICE Collaboration, arXiv: 1802.09145 (2018).

* Work supported by GSI, TU Darmstadt and HGS-HIRe

Measurement of ^{3}He elliptic flow in Pb-Pb collisions with ALICE at the LHC

A. Caliva[1], the ALICE collaboration

[1]GSI, Darmstadt, Germany

The elliptic flow coefficient (v_2) of (anti-)^{3}He is measured as a function of p_T in Pb-Pb collisions at $\sqrt{s_{NN}}$ = 5.02 TeV for different centrality ranges using the Event Plane (EP) method [1].

This measurement provides an important contribution to the understanding of collectivity effects for loosely bound nuclear systems, complementing the picture obtained from the v_2 of (anti-)deuterons [2] and (anti-)protons [3], and puts additional constraints to the coalescence approach and other hadronization models that describe the elliptic flow of light (anti-)nuclei in heavy-ion collisions.

Analysis strategy

In Pb-Pb collisions with non-zero impact parameter, the hot and dense partonic matter is created with an initial spatial asymmetry with respect to the reaction plane, defined by the impact parameter and the beam direction.

This initial geometrical anisotropy produces a non-uniform azimuthal distribution of particles with respect to the reaction plane, due to the different pressure gradients “in-plane” and “out-of-plane”.

The elliptic flow coefficient (v_2) is defined as the asymmetry between the numbers of particles emitted in-plane and out-of-plane:

$$v_2 = \frac{\pi}{2R_2}\frac{N_{\text{in-plane}}(p_T) - N_{\text{out-of-plane}}(p_T)}{N_{\text{in-plane}}(p_T) + N_{\text{out-of-plane}}(p_T)}$$

The centrality of the collision is determined from the charged particle multiplicity measured by two forward detectors (V0A and V0C).

Pileup rejection is applied to select single Pb-Pb collisions and all events are required to have a reconstructed vertex within 10 cm from the geometric centre of the ALICE experiment in order to ensure a uniform response of the detectors in the central barrel.

All reconstructed tracks are required to fulfil a set of track quality criteria. The ^{3}He candidates are identified by requiring that their specific energy loss dE/dx in the TPC is within 3σ from the expected mean for ^{3}He calculated from the Bethe-Bloch formula, being σ the resolution in the dE/dx measurement.

The contribution from secondary ^{3}He produced by spallation in the detector material is suppressed by selecting tracks with transverse distance-to-closest approach (DCA) to the primary vertex smaller than 0.1 cm.

The systematic uncertainties due to tracking, particle identification, occupancy effects in the TPC, event selection and feed-down from weak decays of hyper-triton, are in the range 6-8%.

Results

The elliptic flow of ^{3}He measured in Pb-Pb collisions at 5.02 TeV, shown in Fig.1, has a clear centrality dependence and a slower rise with p_T compared to other particle species due to the larger mass of ^{3}He [3].

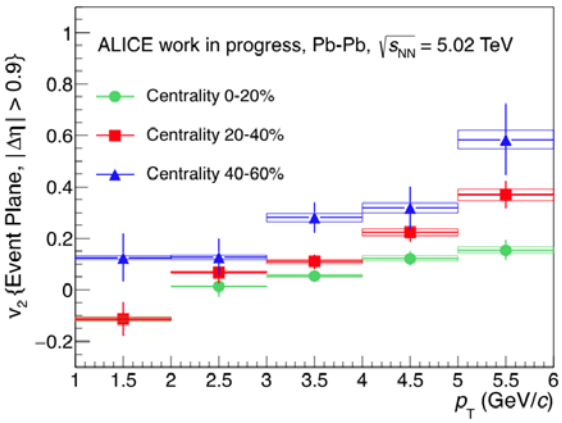


Figure 1: Elliptic flow coefficient (v_2) of ^{3}He as a function of p_T measured in Pb-Pb collisions at $\sqrt{s_{NN}}$ = 5.02 TeV for different centrality classes.

References

[1] A. Bilandzic et al., Phys. Rev. C 83, 014909 (2011).

[2] S. Acharya et al., The ALICE Collaboration, Eur. Phys. J. C77, 658 (2017).

[3] B. Abelev et al., The ALICE Collaboration, JHEP 06, 190 (2015).

Experiment collaboration: CERN-ALICE
Accelerator infrastructure: CERN-LHC

Work supported by GSI

 DOI:10.15120/GR-2018-1

Optimization of the HV scheme for GEM-based detectors

L. Lautner[1,2], P. Gasik[1,2], L. Fabbietti[1,2] and the ALICE TPC collaboration

[1]Physik Department E62, TU München, 85748 Garching, Germany; [2]Exellence Cluster `Origin and Structure of the Universe´, 85748 Garching, Germany

Gas Electron Multiplier (GEM) [1] - based detectors are widely used in many experiments (COMPASS, LHCb, TOTEM) and future upgrades (ALICE, CMS). Electrical discharges that may occur during operation of those detectors can damage them permanently in form of increased leakage currents or electric short circuits that render the detector e ectively blind. Initital discharges, caused by high charge densities obtained in a single GEM hole [2] may trigger a propagated (secondary) discharge between two GEMs in a stack or between the last GEM and the readout anode. The latter is especially dangerous - as the front-end electronics can be severely a ected by high energy released in a discharge event. The behaviour of the electric eld in the gap between GEM foils or a GEM foil and the readout anode after an initial spark cannot explain the appearance of the propagated discharges whose nature is still not fully understood. However, the thorough optimization of the HV scheme in terms of its RC characteristics allows to mitigate (or even avoid) the appearance of these potentially harmful events.

In this report we present our measurements on the in uence of the RC components on the propagated discharge probability. The study has been conducted with a single 10×10 cm^2 GEM foil in Ar-CO_2 (90-10) and Ne-CO_2-N_2 (90-10-5) mounted at a 2 mm distance to the readout anode (induction gap) and a drift gap, between the cathode and the GEM, of 19.5 mm. A mixed (^{239}Pu, ^{241}Am, ^{244}Cm) source is placed on top of the cathode, emitting alpha particles perpendicular to the GEM. The voltage di erence across the GEM was set su ciently high to increase the primary discharge probability.

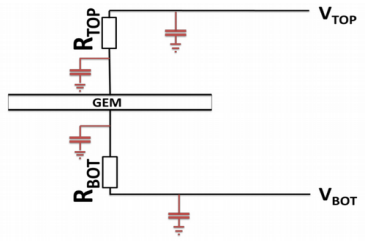


Figure 1: HV scheme of the system with all considered RC elements

Figure 1 presents the RC elements of the HV scheme used in the measurements. Each cable in the system introduces a parasitic capacitance marked in red in the scheme. R_{TOP} and R_{BOT} are the decoupling resistors installed on the top and the bottom side of the GEM, respectively. Particular attention should be paid to R_{BOT} as it has a signi cant in uence on the secondary discharge probability as shown in Fig. 2.

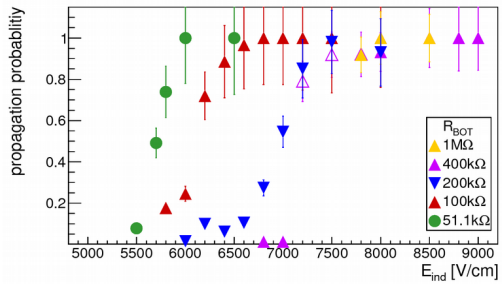


Figure 2: Secondary discharge probability for di erent values of the decoupling resistor R_{BOT} as a function of the induction eld in Ar-CO_2 (90-10)

A large resistance on the GEM bottom electrode increases the potential of that electrode after a primary discharge and thus also the induction eld which should make propagation more likely. In contrary, however, the measured onset of the propagted discharges increases with the increasing value of the induction eld. This points to a development of a current in the induction gap which, as a consequence, induces a current across the R_{BOT} resistor. The latter results in a potential drop (thus the decrease of the induction eld) and quenching of a propagated discharge. Therefore, a clear recommendation for $R_{BOT} > 0$ can be given. In the course of this study, a set of recommendations for the stable operation of GEM detectors has been derived. The Cable length between decoupling resistors and GEM electrodes should be minimized as additional capacitances may keep E_{IND} high after primary discharges. As the cable length between the power supply and the decoupling resistors does not in uence the propagation probability for su ciently large values of R_{BOT} and R_{TOP}, those can be freely choosen. For $R_{BOT,}$ a value greater than 100 kΩ has been proven acceptable. The measurements presented in this report may serve as a baseline for the HV scheme optimization of mulit-GEM based detectors.

References

[1] F. Sauli, NIM A 386 (1997) 531-534

[2] P. Gasik, A. Mathis & L. Fabbietti, NIM A 870 (2017) 116-122

Experiment beamline: none
Experiment collaboration: CERN-ALICE
Experiment proposal: none
Accelerator infrastructure: none
PSP codes: none
Grants: GSI F&E TMLFRG1316 CBM-RICH
Strategic university co-operation with: none

 DOI:10.15120/GR-2018-1

d*E*/d*x* resolution studies of a pre-production read-out chamber with GEMs for the ALICE TPC

T. Klemenz[1], P. Gasik[1], A. Mathis[1], H. Schulte[2], J. Wiechula[2]

[1]Physik Department E62, Technische Universität München, Germany; [2]IKF, Goethe Universität Frankfurt am Main, Germany

The ALICE Collaboration is planning a major upgrade of its central barrel detectors to be able to cope with the increased LHC luminosity beyond 2020 [1]. In order to record at an increased interaction rate of up to 50 kHz in Pb-Pb collisions, the TPC will be operated in an ungated mode with continuous read-out [2]. This demands for a replacement of the currently employed gated Multi-Wire Proportional Chambers by GEM-based (Gas Electron Multiplier) read-out chambers without compromising the performance, in particular in terms of particle identification capabilities via the measurement of the specific energy loss. A stack of 4 GEMs, where two large pitch foils are sandwiched between two standard pitch foils, has proven to meet the requirements when powered with a proper High voltage (HV) configuration. These are an ion back flow (IB) < 1% and an energy resolution for a ^{55}Fe source ($\sigma(^{55}\mathrm{Fe})$) < 12%. The increase in interaction rate and the requirements of a continuous read-out not only demand for significant modifications of the read-out chambers, but also the front-end cards and the corresponding software framework.

To validate the performance of a 4-GEM Inner Read-Out Chamber (IROC) from the pre-production phase of the project, the dE/dx resolution was evaluated with a beam of electrons and pions at the Proton Synchrotron at CERN. The detector was equipped with the newly developed front-end electronics based on the SAMPA ASICs [3], sampling the signal with 5 MHz. Throughout the measurements, 11 HV configurations, corresponding to different values of the local energy resolution and IB, were used to power the IROC. The online and offline data analysis was conducted with O^2, the new software framework for reconstruction, simulation and analysis in ALICE.

For the data analysis, only events with single tracks were selected in order to make use of the particle identification provided by a threshold Cherenkov counter as a reference. Local gain variations in the GEM stack and channel-by-channel variations of the front-end electronics may cause variations of the gain. These were measured and corrected for on a pad-by-pad level. With a width of 6.3% these gain variations are very well within the specifications of < 10%. At 1 GeV/c, a dE/dx resolution for pions (11.92%) and electrons (10.73%) as well as the corresponding separation power (3.65 σ), defined as

$$S_{AB} = \frac{\left|\langle dE/dx\rangle_A - \langle dE/dx\rangle_B\right|}{0.5\left(\sigma(dE/dx)_A + \sigma(dE/dx)_B\right)} \quad (1)$$

for two particle species A and B, is obtained.

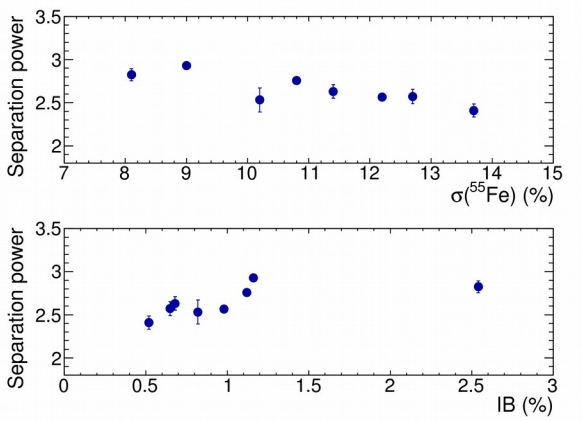


Figure 1: Separation power of electrons and pions as a function of ^{55}Fe resolution (top) and ion back flow (bottom) at a beam momentum of 2 GeV/c

In Fig. 1 the separation power as a function of the ^{55}Fe resolution (top) and the ion back flow (bottom) is shown. The data points represent different HV configurations. One can see that the separation power has only a shallow dependency on those parameters and therefore the separation power does not set any tight constraints on the choice of the final HV configuration for the IROC.

The new read-out system for the TPC upgrade has been tested at the CERN Proton Synchrotron. The read-out chamber, front-end electronics and software framework all work as intended. Currently, the project is in the final production phase. All read-out chambers are scheduled to be assembled until 2019, when the LS2 is supposed to start. The installation and commissioning of the read-out chambers will last until the end of 2020.

References

[1] B.Abelev et al. [ALICE Collaboration], "Upgrade of the ALICE Experiment: Letter of Intent", CERN-LHCC-2012-012 (2012), https://cds.cern.ch/record/1475243

[2] B.Abelev et al. [ALICE Collaboration], "Technical Design Report for the Upgrade of the ALICE Time Projection Chamber", CERN-LHCC-2013-020 (2014), https://cds.cern.ch/record/1622286

[3] S.H.I. Barboza et al., SAMPA chip: a new ASIC for the ALICE TPC and MCH upgrades, 2016 JINST 11 C02088.

Grants: Excellenzcluster Universe, Origin and Structure of the Universe DFG EClust 153; BMBF ALICE: „Verbundprojekt 05P2015"

Systematic studies of correlations between different order flow harmonics in Pb-Pb collisions at $\sqrt{s_{NN}}$ = 2.76 TeV

A. Bilandzic[1,2], L. Fabbietti[1,2], and the ALICE Collaboration

[1]Physik Department E62, Technische Universität München, 85748 Garching, Germany; [2]Excellence Cluster 'Origin and Structure of the Universe', 85748 Garching, Germany

Systematic studies, comprising the centrality dependence of correlations between the higher order harmonics (the quadrangular v_4 and pentagonal v_5 flow) and the lower order harmonics (the elliptic v_2 and triangular v_3 flow), as well as their transverse momentum dependences, have been recently measured by the ALICE Collaboration, using new flow observables dubbed Symmetric Cumulants. These results provide further constraints on the properties of quark-gluon plasma produced in ultra-relativistic heavy-ion collisions.

Introduction

The main emphasis of the ultrarelativistic heavy-ion collision programs at the Relativistic Heavy Ion Collider (RHIC) and the Large Hadron Collider (LHC) is to study the deconfined phase of strongly interacting nuclear matter, the quark-gluon plasma (QGP). Difference in pressure gradients and the interactions among matter constituents produced in the spatially anisotropic overlap region of the two colliding nuclei result in anisotropic transverse flow in the momentum space. The large values of measured flow harmonics demonstrated that the shear viscosity to the entropy density ratio (η/s) of the QGP in heavy-ion collisions at RHIC and LHC energies is close to a universal lower bound 1/4π [1].

New constraints on η/s of QGP and on initial conditions in heavy-ion collisions

The newly developed flow observables, Symmetric Cumulants (SC), have provided the first experimental constraints on the temperature dependence of η/s of the QGP produced in heavy-ion collisions [2,3]. In these measurements only the centrality dependence of few lower order SC observables have been reported. The next step in this direction came with the recent measurement of centrality dependence of higher order SC observables and of their transverse momentum dependence [4].

The comparisons to theoretical models show that all the models with large η/s, regardless of the initial conditions, fail to describe the centrality dependence of higher order correlations. Based on the tested model parameters, the data favor small η/s values and the initial conditions obtained from the AMPT model [4].

When it comes to the differential measurements, it was found that SC observables exhibit moderate p_T dependence in midcentral collisions. This might be an indication of possible viscous corrections to the equilibrium distribution at hadronic freeze-out [4].

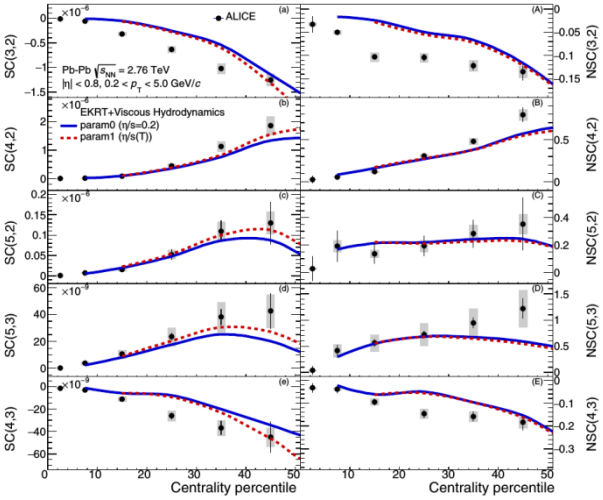


Figure 1: The centrality dependence of SC (left) and normalized SC observables (right) in Pb-Pb collisions at $\sqrt{s_{NN}}$ = 2.76 TeV. Results are compared to the event-by-event EKRT+viscous hydrodynamic calculations [5]. The lines are hydrodynamic predictions with two different parametrizations for temperature dependence of η/s.

The calculations for the two sets of parameters which describe the lower order harmonic correlations best are compared to the data in Fig. 1.

Together with the measurements of individual harmonics, these new results for SC observables can be used to further optimize model parameters and put better constraints on the initial conditions and the transport properties of nuclear matter in ultrarelativistic heavy-ion collisions.

References

[1] P. Kovtun, D. T. Son, A. O. Starinets, Phys. Rev. Lett. 94 (2005) 111601.
[2] A. Bilandzic et al, Phys. Rev. C 89, 064904 (2014).
[3] ALICE Collaboration, Phys. Rev. Lett. 117, 182301 (2016).
[4] ALICE Collaboration, Phys. Rev. C 97, 024906 (2018).
[5] H. Niemi, K. J. Eskola, and R. Paatelainen, Phys. Rev. C 93, 024907 (2016).

 DOI:10.15120/GR-2018-1

Correction for secondary particles contamination in the charged particle yield measurement in Xe-Xe collisions by ALICE*

M. Habib for the ALICE collaboration
TU Darmstadt and GSI

Introduction

During the LHC operation in 2017 with Xe beams the ALICE experiment has recorded a sample of Xe-Xe collisions with a energy (per nucleon pair, $\sqrt{s_{NN}}$) of 5.44 TeV. A measurement of the primary charged particle transverse momentum (p_T) yield for this collision system is ongoing [1]. The measurement requires precise knowledge about the contamination by particles originating from interaction with the detector material or secondary decays with a lifetime $\tau > 1$ cm/c.

This contamination is usually determined from Monte Carlo (MC) simulations. However, most of the models under predicts the production of secondaries from weak decays. To correct for this phenomena a data driven method based on template fits to the distance to closest approach (DCA), defined as the smallest distance between particle trajectory and the collision vertex, is applied.

Method

Using a MC sample we construct DCA templates for primaries, secondaries originating from decays and interaction with the detector material. The DCA distributions generated with MC have a well known and distinguishable shapes which are shown in the Fig. 1 (upper panel).

A linear combination of the templates can describe the reconstructed data while it gives access to the composition of the measured data sample. However non-physical results were observed showing a lager contribution of secondaries from material than from decay products, which originates due to the fit procedure. To overcome this problem, we assume the relative amount of secondaries form material to be well described in MC and redo the template fit fixing its fraction to the MC prediction. The fit result still describes the data while showing the expected trend. The scaled MC DCA distributions and the ratio of the fit to the measurement are shown in the Fig.1.

Systematic Uncertainty

The ratio deviates from unity by less than 5 %, which is used to assign a corresponding systematic uncertainty on the fit quality.

A second systematic uncertainty is estimated from the fit with two templates only distinguishing between secondaries and primaries. The comparison to the standard method leads to an additional relative uncertainty of roughly 10 % on the reweighting factor.

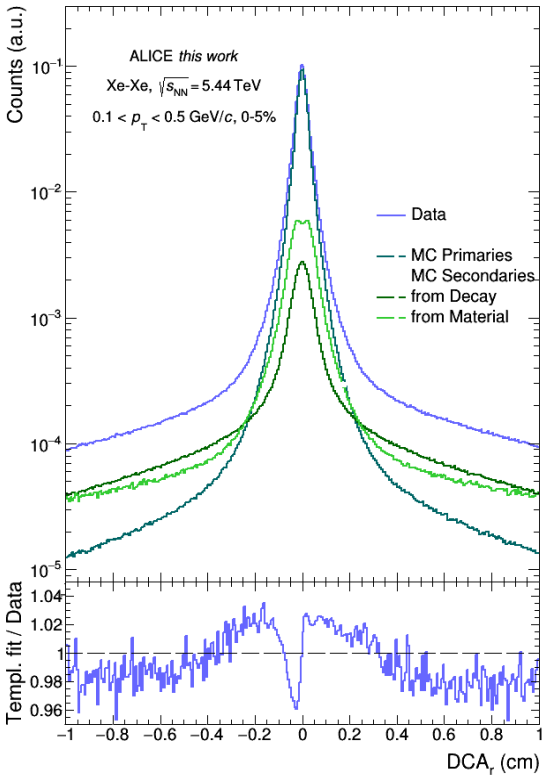


Figure 1: DCA distribution for data and three different MC templates (primaries, secondaries from decay and material) and the ratio of the fit to data.

Result

The fit results show that the secondary particles in the MC are underestimated by 20 - 60 %.

A corresponding reweighting factor is introduced to rescale the secondaries contribution for the primary charged particle yield measurement.

This data driven correction has a significant effect in the small p_T (< 1 GeV) region, while overall having a relative small uncertainty below 3 %.

References

[1] J. Gronefeld, GSI Scientific Report 2017, contribution 112

* Work supported by GSI, TU Darmstadt and HGS-HIRe

Low-mass dielectron production in Pb-Pb collisions at $\sqrt{s_{NN}} = 5.02$ TeV with ALICE

C. Klein[1] and the ALICE Collaboration

[1]IKF, Goethe Universität, Frankfurt, Germany

The ALICE experiment at the CERN-LHC was designed to understand the properties of the strongly interacting quark-gluon plasma (QGP) produced in ultrarelativistic heavy-ion collisions. The production of electron-positron pairs (dielectrons) demonstrated to probe the QGP. Dielectrons only interact electromagnetically and are therefore not affected by the strong force in the hot and dense QGP matter. They are produced in all stages of the collision and therefore give access to the complete spacetime evolution of the system. Whereas proton-lead collisions help to disentangle cold- from hot-medium effects, the dielectron measurement in proton-proton collisions serves as a baseline. With dielectron measurements in lead-lead collisions one can extract directly the temperature of the QGP and can investigate in-medium modifications of the ρ-meson which are associated to a predicted chiral-symmetry restoration [1].

The data set in this study was recorded in 2015 during LHC Run 2 and consists of approximately 84 million events in the centrality class of 0-80% measured in the ALICE central barrel at a center of mass energy of $\sqrt{s_{NN}}$ = 5.02 TeV. Electron and positron identification is based on their specific energy loss in the Inner Tracking System (ITS) and in the Time Projection Chamber (TPC). Additionally, the Time Of Flight (TOF) detector helps to reject heavier hadrons. This identification scheme results in a high electron identification efficiency while rejecting most of the hadronic contamination.

To extract dielectron spectra, in every event electrons and positrons are paired forming the so-called unlike-sign spectrum (ULS). The ULS consists of the dielectron signal and additional correlated and combinatorial background. To estimate this background, in each event like-sign pairs are created to form the like-sign spectrum (LS). The dielectron signal is then obtained by subtracting LS from ULS.

Due to a very low signal to background ratio, efficient background rejection is crucial. The major contribution to the combinatorial background originates from real-photon conversions in the detector material and in the beam pipe around the collision vertex. Real-photon conversions dominate at very low invariant masses m_{ee} < 0.02 GeV/c² of the signal spectrum, see Fig. 1.

Since photons have zero mass, the electron and positron from a photon conversion are emitted in the same direction. This property is used in two different ways. The first conversion rejection method is exploiting the fact that dielectrons with zero opening angle are very close to each other in the detector. Those two tracks are not distinguishable in a given silicon layer of the ITS: they share an ITS cluster. Selecting only tracks with zero shared clusters in the ITS leads to a reduction of conversion dielectrons by a factor of 98.5% while keeping 68% of the dielectron signal.

The second method takes advantage of the pair orientation of conversion dielectrons ϕ_V relative to the magnetic field which is given only by the magnetic field of the ALICE solenoid magnet. This property allows to separate them from dielectrons from hadronic decays where the pair orientation is random. While charge-ordered conversion pairs show a peak at higher ϕ_V, signal pairs have no angular correlation. Remaining conversion pairs can be rejected by choosing only pairs with $\phi_V < 2$ and correcting for the cut. These two conversion rejection methods, higher statistics and better understanding of the detector lead to an improved performance of the Pb-Pb dielectron analysis compared to the Run 2 analysis at $\sqrt{s_{NN}}$ = 2.76 TeV [2].

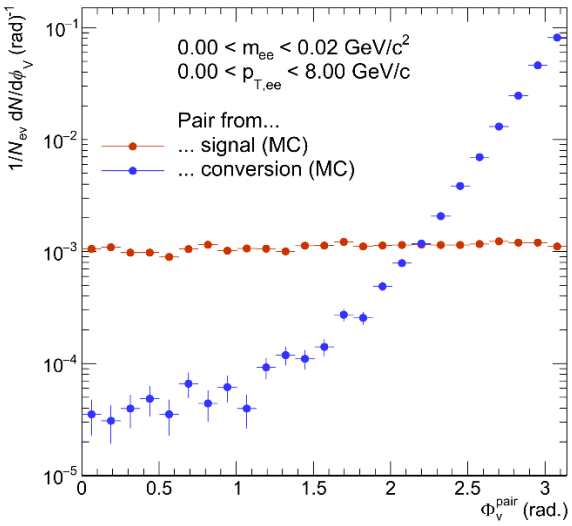


Figure 1: Dielectron signal pairs (red) and conversion pairs (blue) at very low mass m_{ee} < 0.02 GeV/c². Selecting tracks with zero shared ITS clusters reduces the conversion contribution by 98.5% while keeping 68% of the total signal. A subsequent selection on pairs with $\phi_V < 2$ reduces remaining contribution by conversions pairs.

References

[1] Rapp, Chanfrey, Wambach. (1995). Medium Modifications of the Rho Meson at CERN/SPS Energies. Phys.Rev.Lett. 76 (1996) 368-371

[2] Calivà, Alberto. (2017). Measurement of dielectrons in pp, p–Pb and Pb–Pb collisions with ALICE at the LHC. Journal of Physics: Conference Series. 779. 012052.10.1088/1742-6596/779/1/012052

Work supported by: BMBF and Helmholtz Association

 DOI:10.15120/GR-2018-1

Proton-proton reference spectrum at √s = 5.44 TeV

E. Perez Lezama[1] for the ALICE collaboration

[1]GSI, Darmstadt, Germany

Particle production at high energies is often described as a result of the interplay of perturbative (hard) and non-perturbative (soft) QCD processes. Therefore, the measurements of transverse momentum spectra in pp collisions are important to provide a baseline for calculations in perturbative QCD and constraints for a better tuning of models and event generators. In addition, they constitute a valuable reference to study nuclear effects in nucleus-nucleus and proton-nucleus collisions, in particular allowing one to measure the nuclear modification factors.

In order to calculate the nuclear modification factor, a pp reference for the same collision energy is required. Since the Xe–Xe data was taken at $\sqrt{s_{NN}}$ = 5.44 TeV, and there is no pp measurement available at this energy, we construct the pp reference using measured data at √s = 2.76 TeV, √s = 5.02 TeV [2] and √s = 7 TeV. We have implemented two different methods:

- Scaling the √s = 5.02 TeV pp spectrum up using the PYTHIA 8 Monash tune event generator, as shown in equation 1.
- Interpolation between the data at √s = 5.02 TeV and √s = 7 TeV assuming a power law behaviour as a a function of √s .

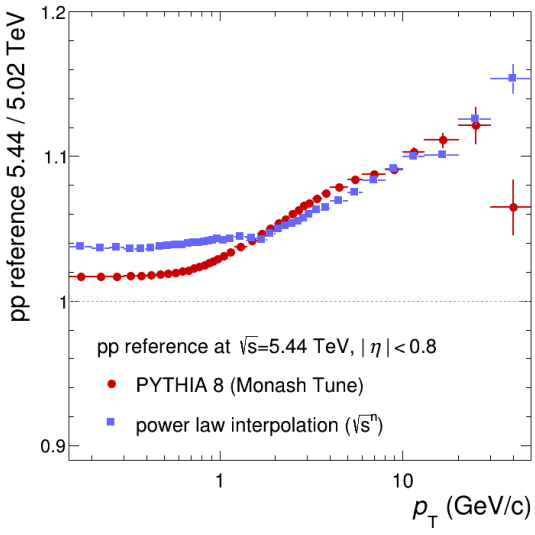
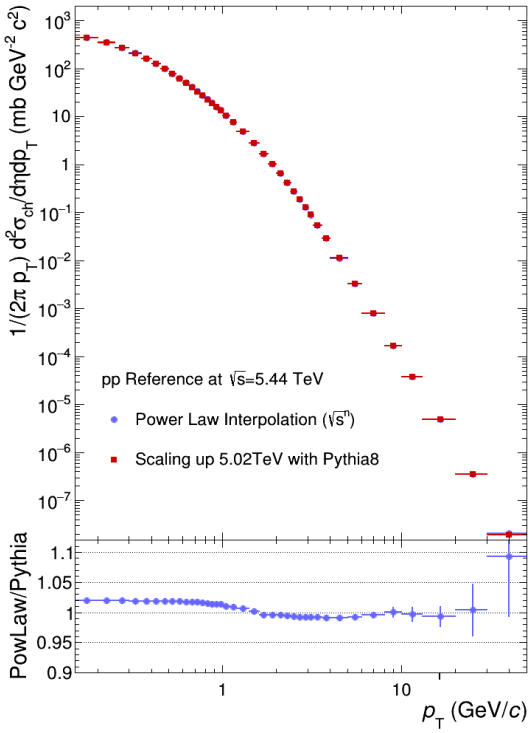


Figure 1: Ratio of generated p_T-differential cross section in pp at √s = 5.44 TeV to the measured one at √s = 5.02 TeV.

The ratio of the pp reference spectra at √s = 5.44 TeV and √s = 5.02 TeV from the power-law extrapolation is shown in figure 1 together with results obtained with the alternative method. The systematic uncertainty of the pp reference at √s = 5.44 TeV has two contributions which are added quadratically. For each p_T interval, we take the systematic uncertainty of the pp references at √s = 5.02 TeV and √s = 7 TeV and interpolate them by a power-law fit to √s = 5.44 TeV. Figure 2 shows the interpolated reference spectrum compared to the reference constructed using PYTHIA-scaling.



$$\frac{d\sigma}{d\eta dp_T} = \frac{\left(\frac{d\sigma}{d\eta dp_T}\right)^{Measured}_{\sqrt{s}=5.02\,TeV} \times \left(\frac{d\sigma}{d\eta dp_T}\right)^{MC}_{\sqrt{s}=5.44\,TeV}}{\left(\frac{d\sigma}{d\eta dp_T}\right)^{MC}_{\sqrt{s}=5.44\,TeV}} \quad (1)$$

Figure 2: p_T-differential cross section in pp at √s = 5.44 TeV and the measured one at √s = 5.02 TeV. Bottom panel shows the ratio of the two cross sections.

References

[1] arXiv:1802.09145
[2] Eur. Phys. J. C 73 (2013) 2662

Work supported by GSI and HGS-HIRe.

Production of antiparticles in p-Pb collisions at 5.02 TeV with ALICE

L.Córdova[1], B.Hohlweger[1], L.Fabbietti[1,2], for the ALICE collaboration

[1]Technische Universität München, Physik Department E62, Garching Germany; [2]Excellence Cluster `Origin and Structure of the Universe`, Garching, Germany

Under the assumption that dark matter particles can annihilate to form standard model particles, the indirect search for dark matter looks for these annihilation products. Cosmic-ray particles and antiparticles can often be challenging to detect due to a high background originating from the high-energy cosmic ray propagation through the interstellar medium. Low-energy antideuterons, however, have an ultra-low astrophysical background. The predicted flux of antideuterons originating from the annihilation of various viable dark matter candidates exceeds the background flux by more than two orders of magnitude in the kinetic energy range below 0.25 GeV/n. For that reason, low-energy antideuterons could be a unique probe for indirect searches for dark matter [1].

Hence, for the indirect dark matter search it is important to understand how antideuterons interact with matter. The ALICE detector allows to identify and track antideuterons from its creation in the collision or from decays. Since the ALICE Transition Radiation Detector (TRD) has a high material budget, the interaction probability of antideuterons with this detector can be investigated by analyzing the products with the next detector layer, the ALICE Time Of Flight detector (TOF). The basic principal of the measurement is shown in Figure 1.

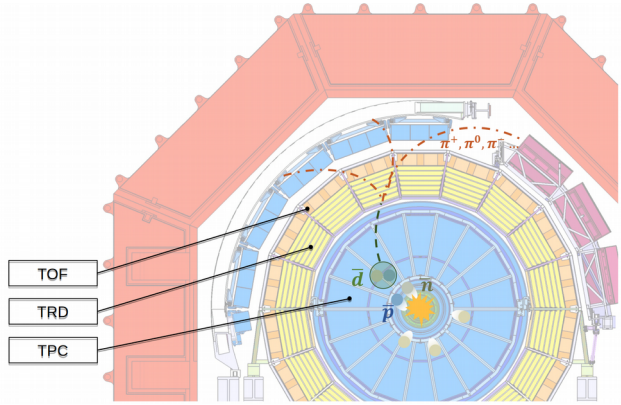


Figure 1: Cross section of the ALICE detector. Schematic representation of an antideuteron that interacts with the TRD material and produces a pion shower, which can be analyzed with the TOF.

In order to have a baseline in the antideuteron analysis, beside (anti-)deuterons, also (anti-)protons are identified in a first step.

During the analysis, a kink at the momentum region p ~ 1.0 GeV/c was found in the (anti-) proton spectrum. By looking at the mass hypothesis for the energy loss correction in the ALICE Time Projection Chamber the source of this irregularities was found. In the region p ~ 1.0 GeV/c an electron mass was assumed to correct protons and this led to a wrong energy loss correction. The correction was obtained with a fit to the data and implemented to correct the momentum track-by-track.

In a next step the track cuts implemented in the analysis need to be optimized in order to measure the production and extract the absorption cross sections of protons, deuterons and their corresponding antiparticles. Especially the Monte Carlo data of (anti-) deuteron needs further investigation.

The Monte Carlo productions with injected nuclei, which are necessary for the (anti-)deuteron analysis, have an entirely different statistical background than the data and cannot be applied as templates for the yield of primaries and secondaries. At the moment, when calculating the purity of (anti-) deuterons, we get a result of almost 100% in the whole momentum range, which means that there are too many nuclei injected. This is why the yields of the Monte Carlo data first need to be rescaled according to a fit that best describes the experimental sample. Further, it must be considered that scattering data for (anti-) deuterons is very limited but required as an input for the simulation in GEANT for the propagation of (anti-) deuterons through the detector and the resulting detector signals[2].

Finally, the analysis can focus on the conversions of antiparticles when interacting with the TRD material. Since the lower limit of the energy range of identified (anti-) deuterons is given by the surrounding magnetic field, for low energetic (anti-) deuterons an analysis with a lower magnetic field could be done in the future.

References

[1] T. Aramaki, S. Boggs et al. Review of the theoretical and experimental status of dark matter identification with cosmic-ray antideuterons, Physics Reports, 618, 1-37 (2016).

[2] ALICE Collaboration. Production of light nuclei and anti-nuclei in pp and pb-pb collisions at lhc energies, Phys. Rev. C 93, 024917 (2015).

 DOI:10.15120/GR-2018-1

Neutral pion and ηmeson production in p-Pb and Pb-Pb collisions at the LHC*

A. Marin[1], F. Bock[2], P. González-Zamora[3], Y. Kharlov[4], L. Leardini[5], A. Morreale[6], T. Okubo[7], A. Passfeld[8], D. Peresunko[9], K. Reygers[5], M. Sas[10], J. Stachel[5], for the ALICE collaboration

[1]GSI Helmholtzzentrum für Schwerionenforschung GmbH, Darmstadt, Germany; [2]CERN, Geneva, Switzerland, [3]Benemérita Universidad Autónoma de Puebla, Puebla, Mexico, [4]NRC "Kurchatov institute"-IHEP, Protvino, Russia, [5]Physikalisches Institut, Ruprecht-Karls-Universität Heidelberg, Heidelberg, Germany, [6]SUBATECH, IMT Atlantique, Université de Nantes, CNRS-IN2P3, Nantes, France, [7]Hiroshima University, Hiroshima, Japan, [8]Institut für Kernphysik, Westfälische-Wilhelms-Universität-Münster, Münster, Germany, [9]NRC "Kurchatov Institute", Moscow, Russia [10]Institute for Subatomic Physics of Utrecht University, Utrecht, The Netherlands

Neutral pion and η meson production has been measured in p-Pb collisions at $\sqrt{s_{NN}}$ = 5.02 TeV [1] and Pb-Pb collisions $\sqrt{s_{NN}}$ = 2.76 TeV [2] with the ALICE experiment at the CERN LHC. The measured η/π^0 ratio deviates from m_T scaling for p_T < 3 GeV/c in both systems. At high p_T, a large suppression of the same magnitude for π^0 and η meson production is observed in central Pb-Pb collisions with respect to the scaled pp reference, while the π^0 and η R_{pPb} ratios are consistent with unity above a p_T of 2 GeV/c. These results support the interpretation that high p_T particle suppression in Pb-Pb collisions is due to parton energy loss in the hot QCD medium.

Results

The measurement of neutral pions and η mesons in a broad p_T range in Pb-Pb collisions can provide information on the energy loss mechanisms in the hot QCD medium. Their measurement in p-Pb collisions is needed to disentangle initial and final-state effects.

Photons are reconstructed in ALICE using two complementary techniques: the photon conversion method (PCM), and electromagnetic calorimeters (PHOS and EMCal). Neutral mesons are reconstructed in the two-photon decay channel and additionally in the Dalitz decay channel for the p-Pb system. Neutral pions and η mesons are identified as peaks at their corresponding rest mass in two-photon invariant mass distributions. The invariant differential yields are measured independently in each method and then combined using the Best Linear Unbiased Estimate.

The invariant yields of π^0, and, for the first time at the LHC, of η mesons have been measured for central and semi-central Pb-Pb collisions at $\sqrt{s_{NN}}$ = 2.76 TeV, as well as for non-single diffractive (NSD) p-Pb collisions at $\sqrt{s_{NN}}$ = 5.02 TeV up to 20 GeV/c, and compared to different theoretical model predictions [1, 2]. The measured η/π^0 ratio in p-Pb (Fig. 1) and Pb-Pb collisions reaches a plateau value for p_T > 3 GeV/c of 0.483±0.015*stat*±0.015*sys* and 0.457±0.013*stat*±0.018*sys*, respectively. For p_T < 3 GeV a deviation from m_T scaling is observed in both collisions systems. Decay of heavier resonances into π^0 and presence of radial flow even for the p-Pb system are among the possible explanations. The large radial flow in central Pb-Pb collisions gives rise to the enhancement of the η/π^0 ratio at p_T ~ 2-4 GeV/c, as similarly observed for $K^{\pm}/\pi^{\pm}$. The nuclear modification factor of π^0 or η in Pb-Pb collisions quantifies particle production suppression at high p_T in heavy-ion collisions. For π^0 and η mesons a large suppression factor of ~ 8-9 is observed at p_T = 7 GeV/c in central 0-10% Pb-Pb collisions (Fig. 2), with increasing trend at higher p_T. The π^0 suppression is stronger than the one observed at lower center-of-mass energies. The π^0 and η R_{pPb} are consistent with unity for p_T > 2 GeV/c in p-Pb collisions. These results support the interpretation that π^0 and η meson high p_T suppression in central Pb-Pb collisions is due to parton energy loss in the hot QCD medium.

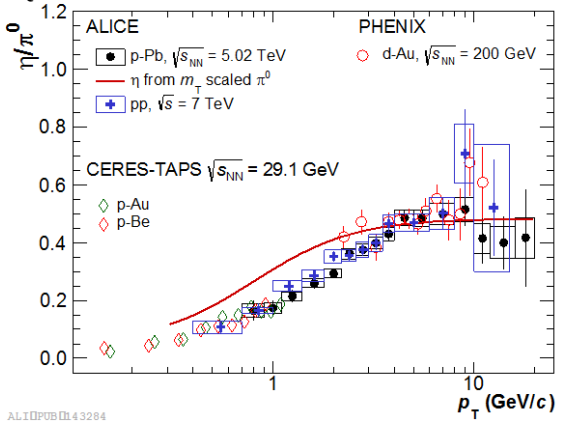


Figure 1: η/π^0 ratio measured in p-Pb collisions compared to m_T scaling and to existing measurements.

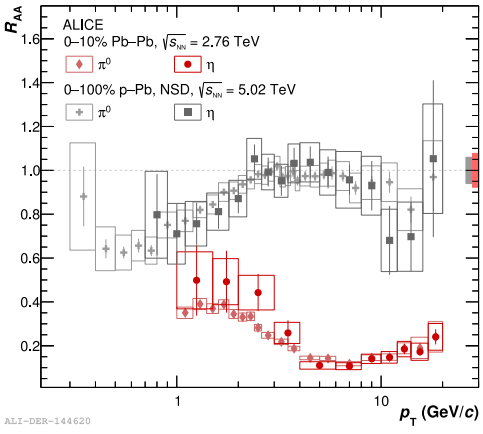


Figure 2: Measured π^0 and η meson R_{AA} in 0-10% central Pb-Pb collisions and in NSD p-Pb collisions.

References

[1] ALICE Collaboration, S. Acharya *et al.*, "Neutral pion and η meson production in p-Pb collisions at $\sqrt{s_{NN}}$ = 5.02 TeV ", arXiv: 1801.07051.

[2] ALICE Collaboration, S. Acharya *et al.*, "Neutral pion and η meson production at mid-rapidity in Pb-

Pb collisions at $\sqrt{s_{NN}}$ = 2.76 TeV", arXiv: 1803.05490.

*Work supported by BMBF, GSI, and University of Heidelberg

 DOI:10.15120/GR-2018-1

Inclusive and non-prompt J/ψ production in Pb-Pb collisions at $\sqrt{s_{NN}}$ = 5.02 TeV measured at mid-rapidity with ALICE

R.T.Jimenez Bustamante[1,2], L.Layer[1,2], D.Weiser[2], S.Masciocchi[1,2], A.Andronic[1,3], I.Arsene[4], M.Köhler[2],

and the ALICE collaboration

[1]GSI, Darmstadt; [2]Universität Heidelberg,[3] Universität Münster; [4]University of Oslo

Introduction

Quarkonium and open heavy-flavor production plays a crucial role as a probe of the hot deconfined medium created in heavy ion collisions. The suppression of charmonium production induced by the color screening of quarks was proposed more than 30 years ago as a probe of the formation of the Quark Gluon Plasma (QGP) [1]. At LHC collision energies, the average number of charm-anticharm quark pairs per event exceeds the average number of charm-anticharm quark pairs per event at RHIC by one order of magnitude. Two different approaches [2,3] suggested new production mechanisms playing a role at LHC collision energies, leading to a charmonium enhancement in the most central A-A collisions. The inclusive J/ψ nuclear modification factor R_{AA} measured by ALICE [4,5] at $\sqrt{s_{NN}}$ = 2.76 TeV, showed a striking enhancement in central collisions compared to the measurements at lower energies [6,7], supporting the models including (re)generation. The transport and comovers models assume the creation of the charmonium states due to continuous dissociation and regeneration throughout the lifetime of the medium [8,9,10]. On the other hand the statistical hadronization model [11] assumes creation of charmonium at the phase boundary. Due to the increase of the initial number of charm-anticharm pairs relative to the total number of quarks, an increase of the R_{AA} with the collision energy is predicted by the models. The statistics gathered by ALICE during LHC Run 2 measurement at $\sqrt{s_{NN}}$ = 5.02 TeV provides essential information for the suppression and regeneration picture.

The determination of the non-prompt J/ψ fraction gives access to the physics of B-hadrons. Since the mass of heavy quarks is large compared to the temperature of the medium, they are produced in the early stage of the collision and thus experience the entire space-time evolution of the system [12]. While there is a strong experimental indication for a thermalization of charm quarks in the medium, beauty quarks are not expected to fully thermalize, since their lifetime is larger than the lifetime of the plasma [13]. Therefore they carry information starting form the beginning of the collision. Experimentally at RHIC and at the LHC a strong suppression of the nuclear modification factor R_{AA} has been observed [12]. From a theoretical point of view, the large masses of the heavy quarks make the computation of the transport coefficients, which characterize transport properties of the medium, feasible directly from first principle QCD calculations [13]. Measurements of the nuclear modification factor R_{AA} and the flow coefficient v_2 of heavy-flavour hadrons are an essential observable to constrain phenomenological models that build a bridge between experiment and first principle QCD calculations.

Inclusive J/ψ production

The ALICE experiment [14] allows to measure J/ψ mesons at mid-rapidity (|y| < 0.8) in the dielectron decay channel. Two main detectors are used for the electron reconstruction. The Inner Tracking System (ITS), consisting of six layers of silicon detectors located around the interaction point, is used for tracking, vertex determination and triggering. The Time Projection Chamber (TPC) is the main tracking detector and is also used for particle identification via the measurement of the specific energy loss in the detector gas (dE/dx). The electrons are identified using the TPC information, and the invariant mass distribution is constructed using opposite sign pairs.

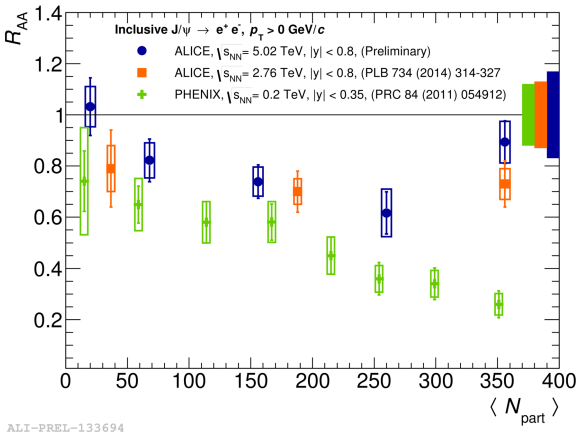


Figure 1: Nuclear modification factor of inclusive J/ψ as a function of centrality at different energies.

Work supported by: GSI, CONACYT, University of Heidelberg

The analysis of the inclusive and non-prompt J/ψ production presented here is based on 75 million minimum bias events in Pb-Pb collisions at $\sqrt{s_{NN}}$ = 5.02 TeV. This allows to measure the inclusive J/ψ production in 5 different centrality classes: 0-10%, 10-20%, 20-40%, 40-60% and 60-90%.

Figure 1 shows the inclusive R_{AA} at $\sqrt{s_{NN}}$ = 5.02 TeV as a function of centrality compared to the ALICE measurement at $\sqrt{s_{NN}}$ = 2.76 TeV at mid-rapidity [7]. The centrality dependence is similar at the two energies. However, a slight increase is observed in the most central collisions. Within the uncertainties the results at both energies are compatible. The measurement by PHENIX at $\sqrt{s_{NN}}$ = 0.2 TeV [9] clearly shows a stronger suppression of the R_{AA} values in central collisions compared to ALICE measurements.

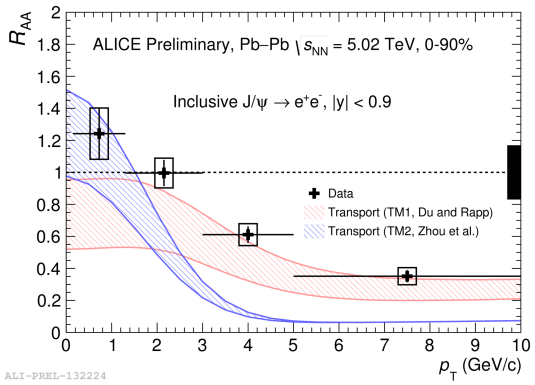


Figure 2: Nuclear modification factor of inclusive J/ψ as a function of transverse momentum.

The inclusive R_{AA} at $\sqrt{s_{NN}}$ = 5.02 TeV is also measured as a function of transverse momentum in the centrality classes 0-90%, 0-20%, 20-40% and 40-90%. In figure 2 the results for the 0-90% centrality class is shown. The increase of the R_{AA} towards low momentum is consistent with the (re)generation scenario and in agreement within uncertainties with the model calculations.

Non-prompt J/ψ production

The non-prompt J/ψ fraction coming from the decay of B-hadrons is determined by decomposing the inclusive J/ψ yield into its prompt and non-prompt components via a 2-dimensional log-likelihood fit to the invariant mass and the pseudo-proper decay length of the J/ψ. The distribution of the pseudo-proper decay length of the non-prompt J/ψ mimics the proper decay length of B-hadrons and thus can be used as a discriminative variable. The same selections as for the inclusive J/ψ analysis are applied. Additionally, machine learning techniques are used to calculate a variable based on the PID and kinematics of the electron candidates in order to enhance the signal-to-background ratio and the significance of the measurement. Figure 3 shows the results for the nuclear modification factor R_{AA} at $\sqrt{s_{NN}}$ = 5.02 TeV for the non-prompt J/ψ. The results are shown together with the results of CMS at $\sqrt{s_{NN}}$ = 2.76 TeV at mid-rapidity [15] and various models are overlaid [16,17,18]. The measurement of ALICE extends the measurement of CMS towards lower transverse momentum. A strong suppression of the nuclear modification factor is observed for intermediate and high transverse momenta. Qualitatively, the models are in agreement with the measurement.

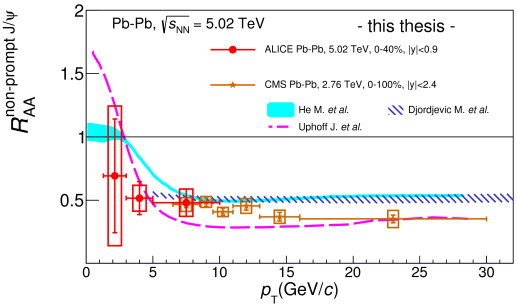


Figure 3: Nuclear modification factor of non-prompt J/ψ as a function of transverse momentum.

References

[1] T.Matsui, H.Satz, Phys Lett B.178 (1986) 416
[2] P. Braun-Munzinger, J. Stachel, Phys. Lett. B 490, (2000) 196–202
[3] R. L. Thews, M. Schroedter, J. Rafelski, Phys. Rev. C 63, (2001) 054905.
[4] ALICE Coll., Phys.Rev.Lett. 109 (2012) 072301
[5] ALICE Coll., Phys. Lett. B 734 (2014) 314–327.
[6] NA 50 Coll., Eur. Phys. J. C 39, 335 (2005)
[7] PHENIX Coll.Phys. Rev. C 84, 054912 (2011).
[8] X Zhao, R. Rapp, Nucl. Phys. A 859 (2011) 114–125.
[9] K. Zhou et al, Phys. Rev. C 89 5, 459 (2014) 054
[10] E.G. Ferreiro, Phys. Lett. B 731 (2014) 57–63
[11] A.Andronic, P. Braun-Munzinger, J. Stachel, Phys. Lett. B 652 (2007) 259-261
[12] A. Andronic and others, Eur. Phys. J. C76 (2016)
[13] Aarts, G. and others, Eur. Phys. J. A53 (2017)
[14] ALICE Coll., Int. J. Mod. Phys. A 29 (2014) 1430044
[15] CMS Coll., Eur. Phys. J. C77 (2017)
[16] Djordjevic, Magdalena and Djordjevic, Marko, Phys. Lett. B734 (2014)
[17] Uphoff and others, Phys. Lett. B717 (2012)
[18] He and others, Phys. Lett. B735 (2014)

Work supported by: GSI, CONACYT, University of Heidelberg

 DOI:10.15120/GR-2018-1

Stability tests of ALICE TPC GEM chambers at the LHC

C. Garabatos[1], K. Schweda[1], Robert Münzer[2], Renato Negrao[3], and Rainer Renfordt[2]

[1]GSI, Darmstadt, Germany; [2]Goethe University, Frankfurt, Germany; [3]University of São Paulo, Brazil

The current multi-wire proportional chambers of the ALICE TPC are replaced by new chambers composed of quadruple stacks of GEMs as detectors for the forthcoming LHC Run 3, in 2020.

The production of these 80 (72 plus spares) detectors is ongoing. As ultimate test for the stability of these micro-pattern devices against discharges under the harsh condition of the LHC, a subset of the final detectors are sequentially operated in the ALICE cavern at the LHC itself.

Sets of two detectors (one Inner and one Outer Readout Chamber) are placed close to the LHC beam pipe at about 10 m from the interaction point at the ALICE cavern, where particle densities are about one order of magnitude higher than those expected in the TPC chambers in Run 3 with 50 kHz Pb-Pb collision rate. Figure 1 shows one OROC under the beam pipe at the ALICE experiment.

The detectors are included in the TPC gas circuit and are thus operated with the same gas mixture. They are powered with a HV system which includes the final, cascaded power supplies especially designed for GEM operation, protection resistor networks close to the detector, and a set of high precision, high bandwidth picoammeters. A custom-made Labview application allows for a safe operation of the HV system, including automatic ramping according to the LHC modes, such that the HV is on only when there is no beam or stable beams. The voltages and currents are thus monitored and recorded, potential current excursions analysed, and a tripping mechanism is put is place.

All pads of each readout plane are connected together into a digital oscilloscope, located in the cavern, which is remotely controlled and readout. Thus, the operator can control and monitor the detectors from the surface, since there is no access to the cavern while beams are on the machine.

The HV powering scheme is a crucial aspect for the safe operation of these detectors, since the voltage in each electrode of the GEM stack is closely coupled to the voltages in the neighbouring electrodes. Thus, if a spark in a given place leads to an overvoltage between any two electrodes, further sparking may result into irreversible damage of the GEM foils.

Operation of first prototypes in this manner showed instabilities and damage due precisely to the sub-optimal HV configuration strategy. Further improvements – adequate choice of protection resistor networks, cascading scheme, tripping mechanism, decoupling resistors – lead to success.

Final production chambers were thus exposed to the LHC conditions at forward rapidity under nominal gas and HV conditions without any trips for several weeks of operation. Minor discharges were recorded during this period. Operation included special ALICE tests where the particle rates expected in Run 3 were reproduced in the experiment, which resulted in about one order of magnitude higher doses in the forward location of the Upgrade GEM detectors.

Plans for 2018 are to periodically install in the ALICE cavern two sets of detectors with four readout chambers in total – two inner readout chambers and two outer ones-, operate them for several weeks, and then replace them during technical stops or other suitable opportunities, in order to qualify a meaningful subset of the full production.

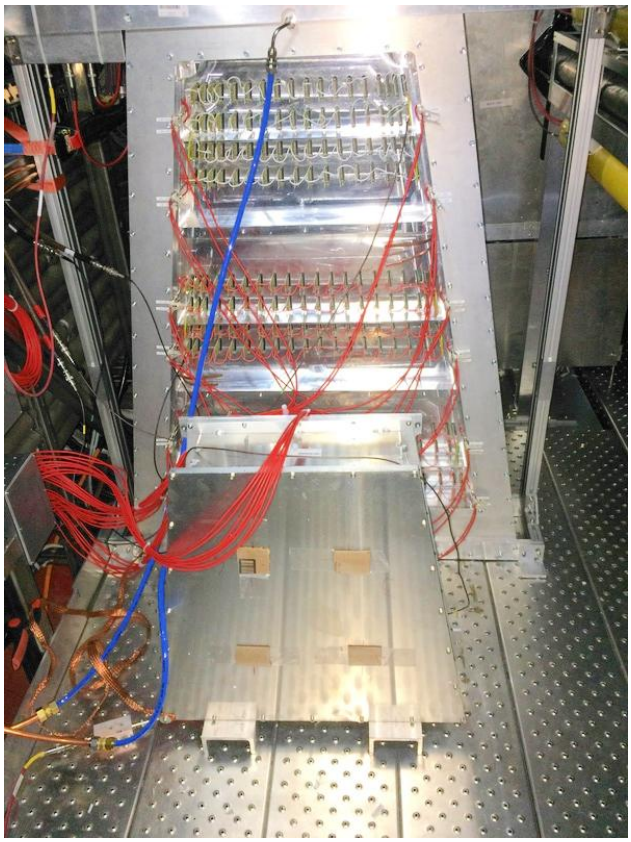


Figure 1: Set of two chambers placed close to the LHC beam pipe in the ALICE cavern ready to be operated with beams.

Experiment collaboration: CERN-ALICE
PSP codes: none
Strategic university co-operation with: Frankfurt-M / Heidelberg / Munich / Bonn / Budapest / Bucharest / Helsinki / New Haven / Oakridge / Detroit

*Work supported by BMBF, GSI.

Report by the GSI-ALICE group

K. Schweda[1], for the ALICE collaboration

[1]GSI, Darmstadt, Germany

ALICE is currently engaged in the Run-2 period of the LHC operation at CERN that started in 2015. Collisions of lead nuclei (Pb) at the highest energy ever reached in the laboratory were recorded in 2015, and a second Pb-Pb run will take place at the end of 2018. During the heavy-ion period in autumn 2016, proton-lead collisions were recorded which do not only provide a reference for the Pb-Pb system but are also interesting in their own right. Collisions were recorded at two collision energies: a first period was devoted to 5.02 TeV per nucleon pair to match the energy of the Pb-Pb run and to increase the statistics of the p-Pb data sample recorded in 2013 with a new minimum bias data sample. Collisions at the highest reachable energy of 8 TeV were recorded in a second period at high interaction rate, with triggers from the muon system, the calorimeters and the transition radiation detector.

The LHC produced for the first time collisions of xenon nuclei at a center-of-mass energy of 5.44 TeV during a pilot run with 6 hours of stable beams in October 2017. The remaining time was dedicated to proton-proton collisions at 13 TeV in order to collect a high-statistics data sample with a reach up to highest transverse momenta. A high-multiplicity trigger enables the study of features of events that resemble aspects typical of heavy-ion collisions.

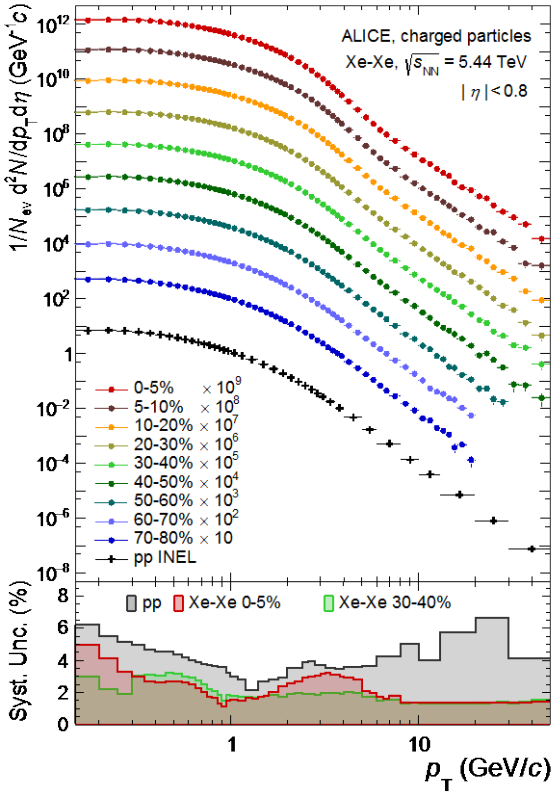


Figure 1: Transverse momentum spectra of charged particles in Xe-Xe collisions at 5.44 TeV together with an interpolated pp reference spectrum (top panel) and systematic uncertainties (bottom panel).

Until April 2018, ALICE has published 198 peer reviewed scientific papers, with an average of 93 citations each.

The GSI ALICE group is deeply involved in Run-2, starting from the responsibility to continuously operate the Time-Projection-Chamber (TPC) and the participation in the mandatory shifts to operate the experiment at CERN, up to the calibration and analysis of the recorded data and the publication of the results.

The GSI ALICE group is engaged in the analysis of data from all collisions systems and, recently, made public several results of high scientific impact. All relevant results are discussed individually in contributions to this GSI Scientific Report. Here, a brief overview is given.

Transverse momentum spectra and the nuclear modification factor of electrons from semileptonic heavy-flavour hadron decays were measured in Pb-Pb collisions at 5.02 TeV, in Xe-Xe collisions at 5.44 TeV, and in pp collisions at 7 and 13 TeV. At high momenta, the nuclear modification factor is below unity, exhibiting a substantial suppression of the yield of electrons from heavy-flavour hadron decays with respect to pp collisions due to the energy loss of heavy quarks in the QCD medium. Models including shadowing of parton distributions predict a nuclear modification factor below unity even at low momentum and are in better agreement with the data than models without shadowing.

Inclusive and non-prompt production of J/ψ and its centrality dependence was measured in Pb-Pb collisions at 5.02 TeV. Non-prompt J/ ψ production originates from the decay of B mesons. Thus both measurements give access to transport coefficients of heavy quarks in the QCD medium. The inclusive measurement confirms the observation in Pb-Pb collisions at 2.76 TeV of a reduced suppression in central collisions when compared to lower energies.

The Xe-Xe data allow for studying the dependence of particle production on the collision system size where xenon neatly bridges the gap between existing data from pp, p-Pb and Pb-Pb collisions with atomic mass numbers of A=129 for xenon, and A=208 for lead. Figure 1 shows the transverse momentum spectra of charged particles in Xe-Xe collisions at 5.44 TeV in nine centrality classes together with an interpolated pp reference spectrum (top panel) and systematic uncertainties (bottom panel).

 DOI:10.15120/GR-2018-1

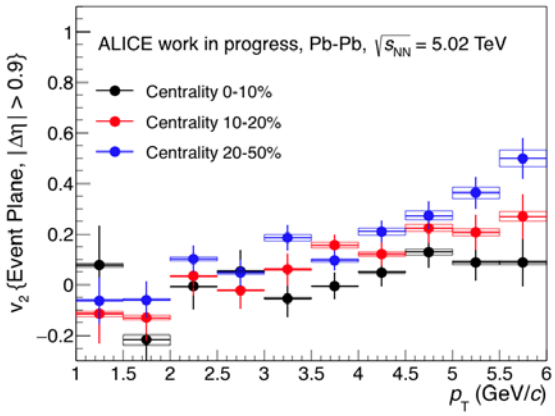


Figure 2: Elliptic flow coefficient (v2) of 3He in Pb-Pb collisions at 5.02 TeV.

The elliptic flow coefficient (v2) of (anti-)3He was measured versus transverse momentum in Pb-Pb collisions at 5.02 TeV for different centrality ranges using the Event Plane method, see Fig. 2. This measurement decisively adds to the picture obtained from the v2 of (anti-) deuterons and (anti-)protons and poses a serious challenge to the coalescence approach and other hadronization models that describe the elliptic flow of light anti-nuclei in heavy-ion collisions.

The GSI ALICE group is centrally involved in the preparation of the experiment upgrades, to be completed until the end of 2020. These upgrades will allow ALICE to fully exploit the improved performance of the LHC in Run-3, when Pb nuclei will collide with a rate of 50 kHz.

The construction of new readout chambers for the ALICE TPC, equipped with Gas Electron Multiplier (GEM) foils is at full swing.

A pre-production GEM-based Inner Readout Chamber (IROC) has been tested together with 6 prototype versions of the TPC front-end card based on SAMPA version ‘v2’ at the CERN Proton Synchrotron with electrons and pions at 1 to 6 GeV/c.

The measured noise and separation power in particle identification meet the design specifications. Groups of two detectors, i.e. one Inner and one Outer Readout Chamber (OROC), are placed close to the LHC beam pipe at about 10 m from the interaction point in the ALICE cavern, where particle densities are about one order of magnitude higher than those expected in the TPC chambers in Run-3 at a 50 kHz Pb-Pb collision rate. Figure 3 shows one OROC being positioned below the beam pipe at the ALICE experiment.

Final production chambers were thus exposed to the LHC conditions at forward rapidity under nominal gas and high voltage conditions without any trips during several weeks of operation. However, minor discharges were observed.

Plans for 2018 are to periodically install in the ALICE cavern sets of four readout chambers – two inner readout chambers and two outer ones-, operate them for several weeks, and then replace them during technical stops or other suitable opportunities, in order to qualify a meaningful sub-set of the full production for the final installation for Run-3 operations at the LHC.

*Work supported by BMBF, GSI.

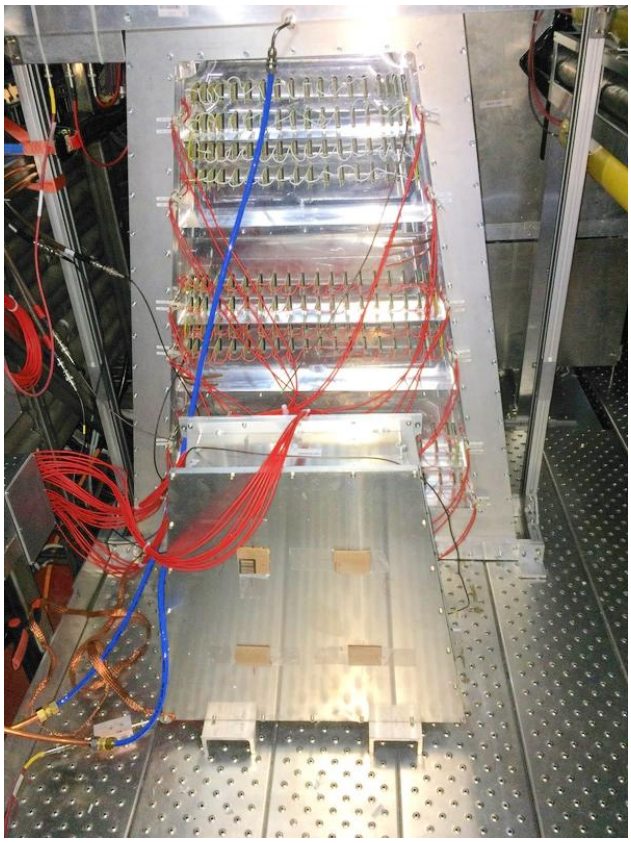


Figure 3: Four chambers (two inner and two outer readout chambers) placed close to the LHC beam pipe in the ALICE cavern ready to be operated with beams.

CATS - the modern tool for femtoscopy studies

V. Mantovani Sarti[1], D.L. Mihaylov[1] and L.Fabbietti[1,2]

[1]Physics Department E62, TUM, Garching, Germany; [2]Excellence Cluster Universe, Garching, Germany

Femtoscopy relates the correlation function $C(k)$ between particle pairs to their emission source $S(r,k)$ and the wave function $\Psi(r,k)$. The latter is obtained by solving the Schrödinger equation (SE) for an interaction potential $V(r)$.

Investigating small collision systems, such as proton-proton, has the advantage of probing the inner part of the interaction potential. However, modelling the correlation function for small sources requires an exact determination of the wave function, which is not provided by the common femtoscopic tools developed for investigating correlations in heavy-ion collisions. For this reason, we have developed a new "Correlation Analysis Tool using the Schrödinger equation" (CATS) [1] capable of modelling $C(k)$ exactly using a numerical solution to the SE.

CATS was used to fit the ALICE experimental results for p-p and p-Λ correlations in pp collisions at $\sqrt{s} = 7TeV$. The source was assumed to be Gaussian and the size was extracted from a combined fit of the p-p and the p-Λ correlations. Both systems show the presence of a linear baseline, which is not reproduced by transport models. Thus, the fit is performed by multiplying C(k) with a linear function. The result is show in fig. 1.

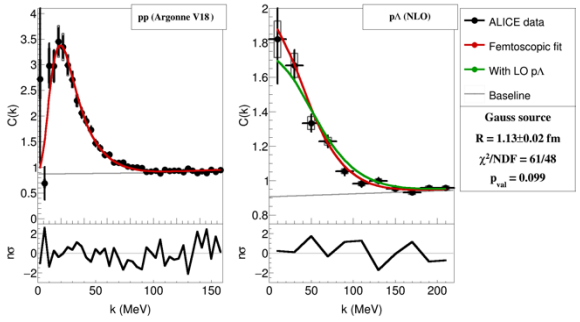


Figure 1: The ALICE preliminary, pp at $\sqrt{s} = 7TeV$ [2] was fitted using CATS to model the p-p correlation function. The p-Λ interaction was evaluated with the Lednický model [3] using the scattering parameters of a next to leading order (NLO) chiral effective theory calculation [4].

For more exotic pairs, such as hyperon-hyperon or hyperon-nucleon in the $S = -2$ sector, the correlation function $C(k)$ permits to gain access to the underlying strong interaction, which so far has not been fully constrained by scattering or hypernuclei data. We expect to be able to use the ALICE pp data at $\sqrt{s} = 13TeV$ to get an insight into the Λ-Λ and p-Ξ⁻ correlations (fig. 2). For this purpose, we established collaborations with theory groups working on chiral effective field theory and lattice calculations, allowing us to probe the most modern potentials for different particle species and make predictions about the feasibility to study those pairs experimentally.

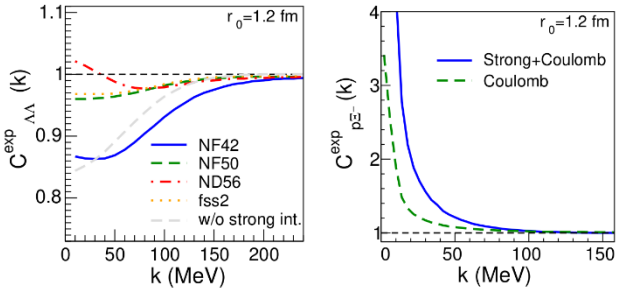


Figure 2: The predicted experimental correlation function for Λ-Λ (left) and p-Ξ⁻ (right), including momentum resolution and feed-down effects expected in pp collisions at LHC energies.

In the left panel of Fig. 2 we compare the Λ-Λ correlation functions for different attractive (NF50, ND56 and fss2) potentials and one potential (NF42) which allows for a bound state [5]. The binding potential (NF42) is well separated from the attractive ones, which implies that a high statistics experimental data sample can differentiate between those cases. For the p-Ξ⁻ (right) we use a preliminary lattice local potential from the HAL QCD collaboration [6]. We see a significant modification of $C(k)$ due to the strong interaction, which should be possible to detect experimentally.

To get better constraints on the investigated interaction potentials, we are working on a CATS based analysis framework capable of performing global fits over all available femtoscopic data.

The work on CATS and the complementary studies are in preparation for publication and currently to be found on arXiv [1].

This work is supported by SFB1258.

References

[1] D. L. Mihaylov, V. M. Sarti, O. W. Arnold, L. Fabbietti, B. Hohlweger and A. M. Mathis, arXiv:1802.08481 [hep-ph].

[2] O.Arnold [for the ALICE collaboration], poster at the QM2017 conference.

[3] R. Lednicky and V. L. Lyuboshits, Sov. J. Nucl. Phys. 35 (1982) 770 [Yad. Fiz. 35 (1981) 1316].

[4] J. Haidenbauer, S. Petschauer, N. Kaiser, U.-G. Meissner, A. Nogga and W. Weise, Nucl. Phys. A 915 (2013) 24 doi:10.1016/j.nuclphysa.2013.06.008 [arXiv:1304.5339 [nucl-th]].

[5] A. Ohnishi, K. Morita, T. Furumoto, JPS Conf. Proc. 17 (2017) 031003 doi:10.7566/JPSCP.17.031003 [arXiv:1512.08444 [nucl-th]].

[6] T. Hatsuda, K. Morita, A. Ohnishi and K. Sasaki, Nucl. Phys. A 967 (2017) 856 doi:10.1016/j.nuclphysa.2017.04.041 [arXiv:1704.05225 [nucl-th]].

 DOI:10.15120/GR-2018-1

Advanced performance measurements with microchannel-plate PMTs

A. Lehmann[1], M. Böhm[1], R. Frytz[1], S. Krauss[1], D. Miehling[1], M. Pfaffinger[1], and S. Stelter[1]

[1]Physikalisches Institut IV, Universität Erlangen-Nürnberg, Erwin-Rommel-Str. 1, D-91058 Erlangen

The Cherenkov photons of the PANDA DIRC detectors will be read out by 300 microchannel-plate (MCP) PMTs. Our on-going long-term measurements show that the lifetime of these devices has recently increased by more than a factor of 50 with the best PHOTONIS model reaching >15 C/cm2 integrated anode charge without any quantum efficiency (QE) loss [1]. This is safe for >10 years of operation within the PANDA high rate environment.

For quality assurance (QA) measurements of the MCP-PMTs we have assembled a semi-automatic setup consisting of a large copper-cladded dark box combined with a pico-second laser pulser, a 3D-stepper for accurate position scans of the active tube area, and a PADIWA/TRB DAQ system for the parallel readout of all anode pixels. It is planned to simultaneously measure with a surface scan the main performance parameters gain, time resolution, darkcount rate (DCR), crosstalk and afterpulsing for each MCP-PMT being built into the PANDA DIRC detectors. For each tube QE, surface and wavelength scans and rate capability tests will be performed, as well as for sample MCP-PMTs accelerated lifetime measurements and gain characterisations inside a strong magnetic field of >1 T.

The PADIWAs are equipped with multi-hit TDCs with adjustable thresholds that produce a time stamp and time-over-threshold for each hit anode pixel. In the TRBs this information and the number of hits are permanently written to a ring buffer and are read out in an adjustable time window around a trigger pulse that in our case is the laser trigger. The available information for this time window is the laser x- and y-position, and the hits of direct photo-electrons, darkcount, recoil electron and crosstalk events.

Among others the first scans with the new QA setup demonstrated a unique capability in terms of quantifying the DCR and the fraction of events followed by an ion afterpulse as a function of the anode pixels, and other unwanted effects like distributions of electrons recoiling from the MCP surface and crosstalk among the anode pixels induced by charge sharing and electronics.

The left plot in Fig. 1 shows the DCR of the different anode pixels for a new hiQE MCP-PMT from PHOTONIS indicating that the overall DCR is dominated by individual pixels at the corners and borders of the tube. This is a new finding and was observed also in other MCP-PMTs. The reason of this effect is currently unknown. In the right plot of Fig. 1 the afterpulsing TOF distribution of the same tube is presented suggesting that ~0.3% of the single photon events are followed by afterpulse background induced by light and heavy ions from H to Pb.

In Fig. 2 (upper-left) the xt-distribution of pixel x3-y6 of the before mentioned MCP-PMT is shown indicating the regions where charge sharing crosstalk and recoil electrons are expected. By pointing the laser to different x- and y-positions we find that the read out pixel may be also hit by events which stem from laser positions outside the pixel area (red region) and later (>100 ns) than expected for prompt laser photons. The xy-distributions of the charge sharing crosstalk and recoil electron events can be further studied and quantified. The recoil electrons reach into an area of more than twice the pixel diameter and arrive up to 5 ns later than a direct photo electron. Crosstalk mainly takes place between adjacent pixels. The width of the red strips in Fig. 2 (lower right) allows the estimation of the size of the charge cloud arriving at the anode pixel. We find about 1 mm for the tube shown here.

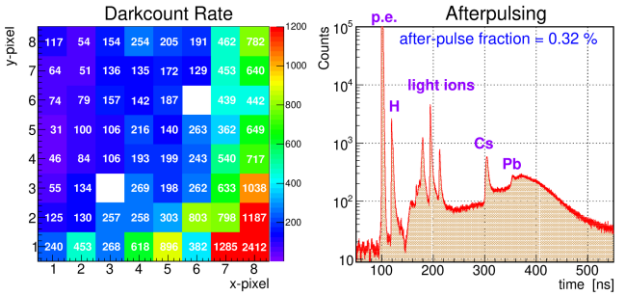


Figure 1: DCR (left) as a function of the anode pixel and afterpulsing TOF distribution (right) for the hiQE MCP-PMT PHOTONIS XP85112 (9002085) with 10 µm pores.

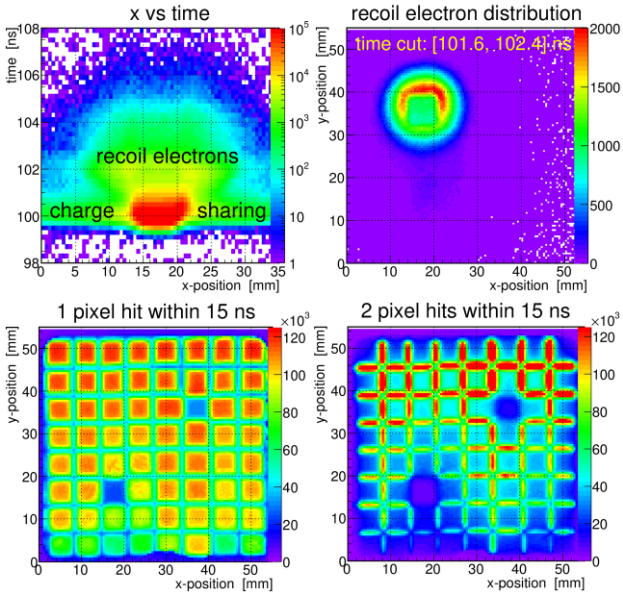


Figure 2: xy-distributions of recoil electrons (upper-right) and charge sharing crosstalk events (lower-right) for the MCP-PMT as in Fig. 1. The xt-distribution of pixel x3-y6 (upper-left) indicates the regions where events populated by recoil electrons and charge sharing are expected.

References

[1] A. Lehmann, et al., 2018 JINST 13 C02010

Experiment collaboration: PANDA
PSP codes: 1.4.1.5
Grants: GSI strategic partnership (FuE): ERANTO1419, EREYRI1416

The Barrel DIRC prototype in a beam experiment

C. Schwarz[1], A. Ali[1,2], A. Belias[1], R. Dzhygadlo[1], A. Gerhardt[1], M. Krebs[1,2], D. Lehmann[1], K. Peters[1,2], G. Schepers[1], J. Schwiening[1], and M. Traxler[1]

[1]GSI, Darmstadt, Germany; [2]Goethe Universität Frankfurt, Germany

A beam time in August/September 2017 in the T9 beamline of the CERN PS was used to evaluate the performance of a PANDA Barrel DIRC [1] prototype in a mixed hadronic beam at several energies. Protons and pions were tagged by a time of flight system. Aspects of the PANDA Barrel DIRC (radiator bars) and of the future DIRC in the Electron-Ion-Collider (EIC) project (radiator plates) were tested.

A picture of the prototype in a configuration with a narrow bar is shown in Fig. 1. The radiator bar, made from synthetic fused silica, is coupled via a prism to an array of 12 PHOTONIS XP85012 Microchannel-Plate (MCP) PMTs. Different focusing elements were placed between the radiator bar and the prism. Figure 1 shows a cylindrical lens, designed for the EIC DIRC and made from a layer of LaK33 glass embedded between two fused silica adapter pieces.

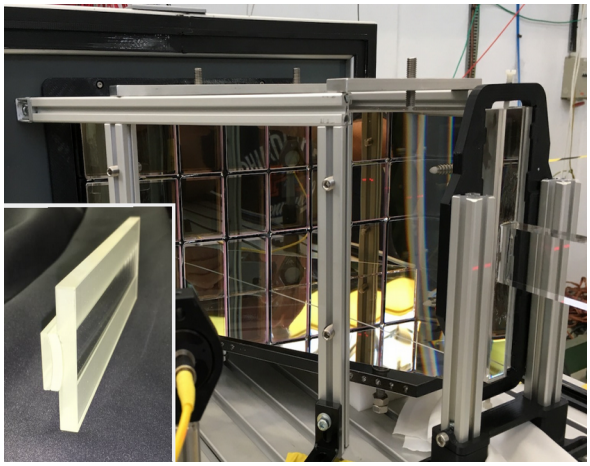


Figure 1: Photograph of the Barrel DIRC prototype at CERN. The insert shows details of the cylindrical lens.

The primary goal of this experiment was to test a compact prism with an opening angle of 33°, the cylindrical lens, and 12 new readout modules, each comprising one MCP-PMT with a high-voltage divider and four PADIWA discriminator cards, actively cooled by pressurized air. The position of the beam on the radiator bar or plate, as well as both the polar and azimuthal angle between the radiator and the beam, were adjustable to evaluate the particle identification (PID) performance of the prototype in various configurations for the entire phase space of kaons in PANDA.

Experiment beamline: CERN-T9
Experiment collaboration: PANDA
Experiment proposal: PANDA

Figure 2 shows the accumulated hit pattern for tagged pions with 7 GeV/c momentum at a polar angle of 25°. Although the spherical lens produces a sharper image than the cylindrical lens for the narrow bar, the quality of the image from the cylindrical lens agrees well with detailed Geant simulations. This is an important result for the possible use of wide plates as radiators, as one of the designs of the DIRC for the EIC detector foresees, since spherical lenses will no longer an option for wide plates and cylindrical focusing will be required.

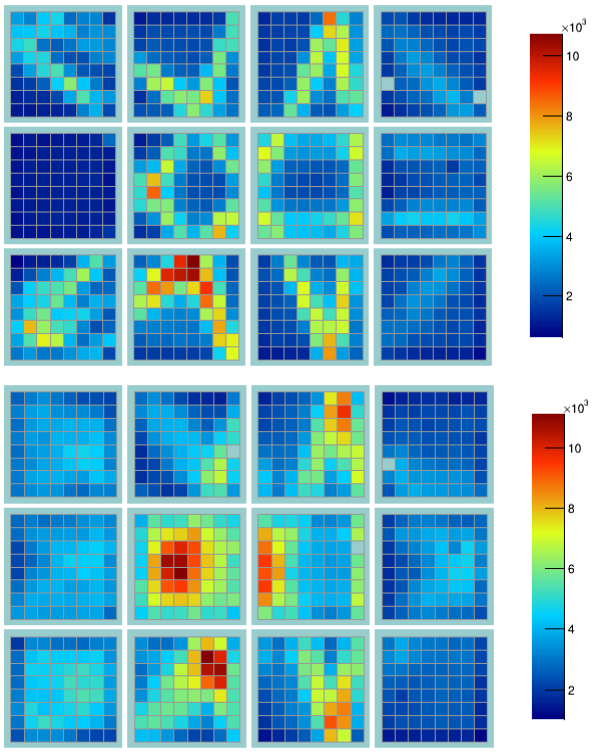


Figure 2: Cherenkov image from many events produced in a narrow bar for 7 GeV/c pions at a polar angle of 25° for a spherical lens (top) and a cylindrical lens (bottom).

References

[1] PANDA Collaboration, Technical Design Report for the PANDA Barrel DIRC detector, https://arxiv.org/pdf/1710.00684.pdf

Accelerator infrastructure: HESR
PSP codes: 1.4.1.5

 DOI:10.15120/GR-2018-1

Grants: ERANTO1419**, eRD14 (future Electron Ion-Collider)**
Strategic university co-operation with: Frankfurt-M / Erlangen

Optical shape measurements of the Barrel DIRC radiator bars

J. Rieger[1,3], G. Schepers[1], M. Krebs[1,2], K. Peters[1,2], and J. Schwiening[1]

[1]GSI, Darmstadt, Germany; [2]Goethe Universität Frankfurt, Germany; [3]TU Darmstadt, Germany

The radiator bars for the PANDA Barrel DIRC are made of synthetic fused silica. Since the bars also act as light guides for the Cherenkov photons, whose angular distribution has to be conserved in many internal reflections, the bars have to meet tight specifications. The maximum deviation from a rectangular cross section must not exceed 0.25 mrad along the full length of the bar and the end faces must not differ from an ideal shape by more than 0.5 mrad. Prototype bars from different vendors have been tested to see if they fulfil those requirements.

Autocollimator Setup

The setup consists of a Nikon 6D LED autocollimator, a Nikon pentaprism and two supports to mount the bars, as shown in figure 1. The supports are wrapped with cleanroom cloth to protect the bars from scratches.

The autocollimator is a telescope-like instrument that focuses a reticle of light to infinity. It is reflected by the object surfaces back into the autocollimator, focused and observed. Reflections originating from different surfaces can be seen simultaneously as reticles through the ocular. Their distance can be measured and corresponds to the angle included by the surfaces. In order to measure the downwards-facing bar side, a pentaprism is used to deflect some autocollimator rays by 90°. The big advantage of this setup is that only relative alignment is important and that it is contact-free, so the highly polished bar surfaces are not touched.

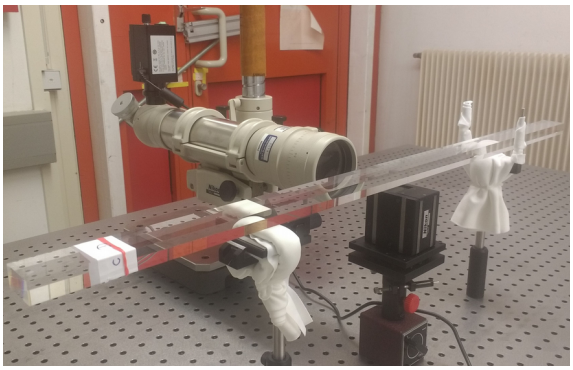


Figure 1: The measuring setup, including the autocollimator, the pentaprism, and a prototype bar mounted on two adjustable supports.

Measuring accuracy

In order to determine the optimal measuring accuracy, the positioning of the bar supports has been optimized and the precise alignment of prism and bar has been checked before each measurement. The measuring accuracy is 0.02 mrad for parallelism measurements and 0.05 mrad if the pentaprism is used [1].

Results

A comparison of results for all measured prototype bars are shown in figure 2. Due to challenges in producing single prototype bars, the quality of the end faces did not always meet the specification. This is not expected to be an issue for mass production.

The most important specification for the PANDA Barrel DIRC, the squareness and parallelism of the faces and sides, was met by two of the four vendors, InSync and Zeiss. Although a few of the parallelism measurements for the Zygo bar were marginally outside the specification, this vendor is considered validated for the mass production as well.

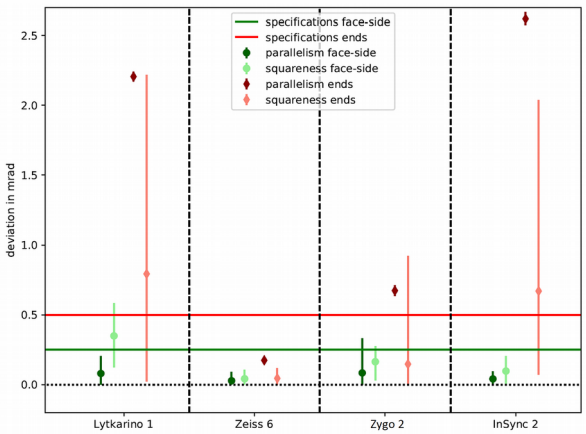


Figure 2: Comparison of the prototype bars from four different vendors, adapted from [1]. The displayed values are the mean of all measured ones, and the error bars indicate the range of the measured values. The horizontal lines show where the production specifications are.

References

[1] J.Rieger, “Optical Shape Measurements of the Radiator Bars for the PANDA Barrel DIRC”, Bachelor Thesis, TU Darmstadt, Febuary 2018

Experiment collaboration: PANDA
PSP codes: 1.4.1.5
Strategic university co-operation with: Darmstadt / Frankfurt-M
Grants: HGS-HIRe for FAIR

 DOI:10.15120/GR-2018-1

Surface quality of the PANDA barrel DIRC prototype radiators

M. Krebs[1,2], K. Peters[1,2], J. Rieger[1,3], G. Schepers[1], C. Schwarz[1], J. Schwiening[1]

[1]GSI, Darmstadt, Germany; [2]Goethe University Frankfurt, Germany; [3]TU Darmstadt, Germany

A DIRC (Detection of Internally Reflected Cherenkov light) detector will provide charged Particle Identification (PID) in the target spectrometer of the PANDA experiment. The Barrel DIRC uses rectangular bars made from synthetic fused silica as radiators. Cherenkov photons are trapped inside while they propagate through the radiator by total internal reflection until they exit towards the readout end to be measured by the photon sensors. The Cherenkov angle can be calculated from the observed hit pattern to identify the particle that traversed the radiator. Since the Cherenkov photons can undergo several hundred reflections until they reach the photon sensors, the radiators have to meet very strict optical and geometrical requirements. To ensure high transport efficiency the radiator surfaces need to be smoothly polished.
The determination of surface quality of radiators is done by using a fully automated motion-controlled laser setup, measuring critical values, such as bulk attenuation and coefficients of total internal reflection (Figure 1).

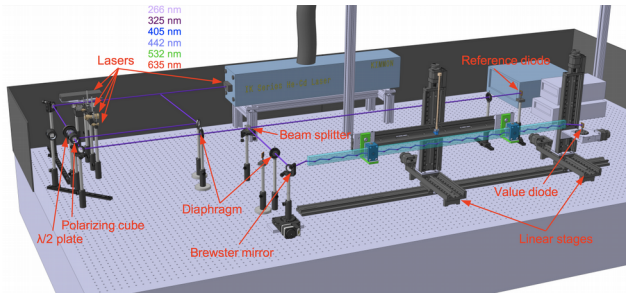


Figure 1: PANDA Barrel DIRC optics lab setup accommodating a radiator plate for an internal reflection measurement.

The attenuation length is measured by coupling the laser straight into the radiator, determining the intensity loss inside the bulk material.
For the internal reflection measurement the laser beam is coupled into the radiator at Brewster angle. Depending on the length and orientation of the radiator, the beam is internally reflected from the faces (wide sides) up to 53 times, until it exits to be measured by the (value) photodiode. An additional reference photodiode is used to correct for laser intensity fluctuations. The fraction of light lost during all internal reflections is translated into the coefficient of total internal reflection, which in turn can be related to the surface roughness via the scalar scattering theory. An extensive prototype radiator program had been started several years ago, resulting in a total of 30 prototype radiators produced by various manufacturers. Using different types of fused silica and polishing techniques, the optical quality of these prototype radiators was evaluated at GSI to qualify vendors for the mass production of DIRC bars. Upgrading the Barrel DIRC optical setup by adding a HeCd laser (325 nm and 442 nm), lead to an increase in sensitivity of measuring possible production technique related sub-surface damage inside the material. A full set of measurements for all vendors that produced prototypes is now available.

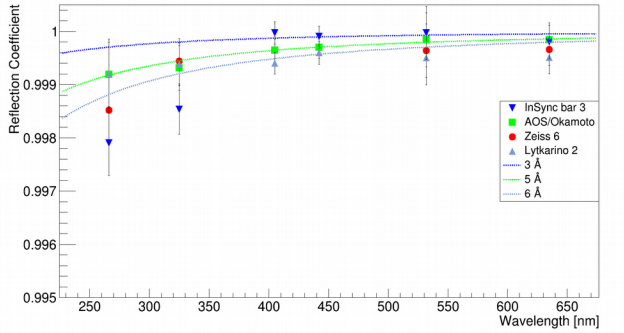


Figure 2: Reflection coefficients for four different prototype bars from AOS/Okamoto, InSync Inc., Carl Zeiss GmbH, and Lytkarino. The dashed lines show the expected reflection coefficients from theory for a given surface roughness.

Figure 2 shows results for four prototype bars. The measured reflection coefficient values are found to be in good agreement with data from the vendors.
On the basis of this data the call for tender is expected to be issued in the summer of 2018 to collect offers from manufacturers proven to be able to deliver the optical quality required for the PANDA Barrel DIRC.
The radiator production is expected to start in early 2019.

Experiment collaboration: PANDA
Experiment proposal: PANDA
Accelerator infrastructure: none
Grants: HGS-HIRe
Strategic university co-operation with:
Goethe University Frankfurt

References

[1] PANDA-Collaboration, Technical Design Report for the PANDA Barrel DIRC, arXive:1710.00684

Geometrical reconstruction for the DIRC PID at GlueX

R. Dzhygadlo[1], A. Ali[1,2], K. Peters[1,2], C. Schwarz[1], and J. Schwiening[1]

[1]GSI, Darmstadt, Germany; [2]Goethe Universität Frankfurt, Germany

The particle identification (PID) capability of the GlueX experiment will be enhanced by the upgrade with a Detector of Internally Reflected Cherenkov light (DIRC) [1]. It will be a compact and robust PID system utilizing optical components from the decommissioned BaBar DIRC detector [2] and a new expansion volume based on the SuperB FDIRC prototype [3]. A clean π/K separation for forward angles ($\theta < 11^{O}$) and momenta up to 4 GeV/c is expected based on the BaBar performance.

Three different reconstruction approaches are in development to evaluate the PID performance of the detector: kernel density estimation, time imaging, and geometrical reconstruction. The first two are based on probability density functions of the spatial distribution and the arrival time of the detected photons [4,5]. The 3rd method is based on look-up tables (LUTs), and was previously used for the BABAR DIRC.

The geometrical reconstruction is the first of those methods to be implemented in the current GlueX analysis framework. In this approach the direction of a detected photon is approximated by the three-dimensional vector between the centers of the bar and the hit pixel. LUTs are produced by simulating optical photons at the end of the bar, covering all possible angles, and storing direction vectors for all photons that hit a given pixel. Those direction vectors are then combined with the particle momentum vector available from the tracking system to determine the Cherenkov angle θ_C.

Figure 1 shows the reconstructed single photon Cherenkov angle distribution for 1000 pions (blue) and kaons (red) simulated by GEANT4 at 4 GeV/c and a polar angle of $\theta = 4^{O}$.

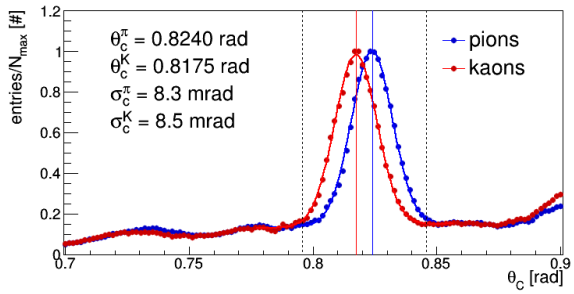


Figure 1: Reconstructed single photon Cherenkov angle distribution for 1000 pions (blue) and kaons (red). Solid vertical lines indicate the values of the expected Cherenkov angle.

A fit of a Gaussian plus a linear function gives a good description. The background is primarily caused by combinatorial reconstruction ambiguities, which are the result of the various possible photon paths inside the expansion volume. This background can be efficiently suppressed by applying selection on time difference between measured propagation time of the detected photons and the time determined from the LUT. The averaged number of the detected photons per particle after selection is 57±4.

The mean of the Gaussian fit determines the θ_C of the corresponding particle species, while the sigma of the fit gives the resolution of the reconstructed angle which is important indicator of the performance. The dashed vertical lines shows the range where an unbinned likelihood test is used to perform the PID. Figure 2 shows the resulted log-likelihood difference, giving a π/K separation power of 4.5±0.2 s.d at 4 GeV/c and 4^{O} polar angle.

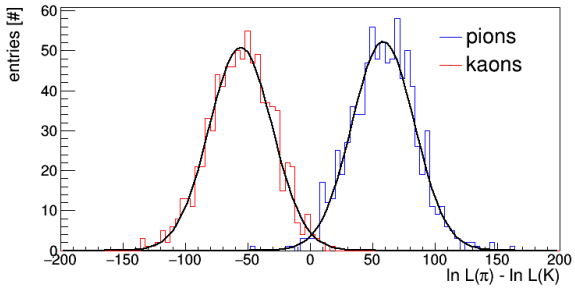


Figure 2: Pion-kaon log-likelihood difference distribution for 4 GeV/c and 4^{O} polar angle.

The reconstruction of the tracks from the full phase space of the GlueX DIRC yields photon multiplicity in a range of 30-60 photons providing π/K separation power of 3.0-4.5 s.d. at 4 GeV/c.

References

[1] J. Stevens, et al., J. Instrum. 11 (07) (2016) C07010.
[2] I. Adam et al. Nucl. Instr. Meth. A, 538:281, 2005.
[3] D.A. Roberts et al. Nucl. Instr. Meth. A, 766, 2014.
[4] J. Hardin, M. Williams, arXiv:1608.01180.
[5] R. Dzhygadlo et al., Nucl. Instr. and Meth. Phys. Res A 766 (2014) 263.

Experiment beamline: none
Experiment collaboration: other: GlueX
Experiment proposal: none
Accelerator infrastructure: other: CEBAF
PSP codes: none
Grants: HGS-HIRe
Strategic university co-operation with: Frankfurt-M

 DOI:10.15120/GR-2018-1

First setup for the routine tests of the APFEL-ASIC rigid flex PCBs

P. Wieczorek[1], S. Löchner[1] and J. Adamczewski-Musch[1]

[1]GSI, Darmstadt, Germany

Introduction

For the first slice of the PANDA-EMC-Barrel the required rigid flex PCBs with the APFEL-ASIC [1] were ordered in 2016. With the delivery of these rigid flex PCBs the developed setup for the characterisation was finalised and totally 900 PCBs are measured in functionality and analogue performance. The routine tests are done with a dedicated mainboard, developed at GSI. An external current meter is connected to the mainboard and provides the current. For the data readout the GSI 16 channel sampling ADC board FEBEX [2] and the GSI data aquisition system MBS [3] are used. Based on the MBSPEX device driver software a graphical control and operating tool (APFEL GUI) has been developed. By means of various automatic tests sequences it allows to show a positive or negative decision concerning the quality of rigid flex PCBs immediately on the GUI.

Test Procedure

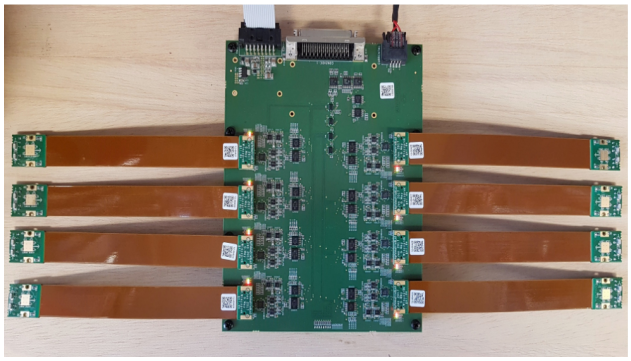


Figure 1: Mainboard overview with 8 rigid flex PCBs.

To record all dependent parameters the mainboard shown in figure 1 has been designed. Up to 8 rigid flex PCBs can be connected to the mainboard and measured successively. The test sequence is divided in a functionality test and a performance measurement. The functionality of the electronics, respectively power consumption and short connections between power, high voltage and ground potential, is specified with the current meter. Other properties like Chip ID scan or DAC access values to an on-chip register are also verified.

To define the analogue performance of the electronics the noise and the amplitude of the output signal as a function of input charge is measured. All values are saved to an ASCII file and stored into a database.

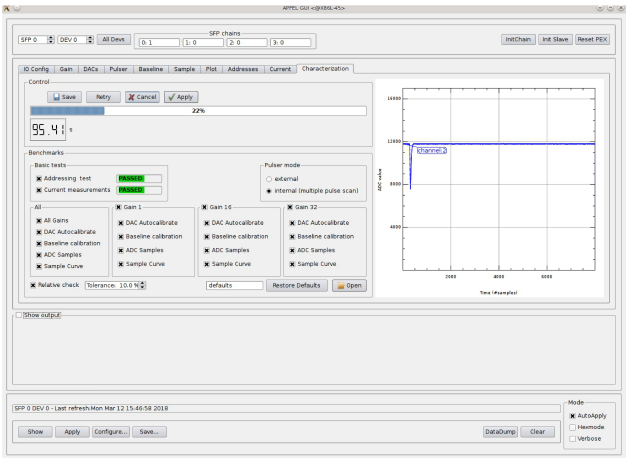


Figure 2: APFEL GUI.

In figure 2 a screenshot of the APFEL GUI is shown. This tool allows to operate the routine test without technical background of the tested electronics. For the choosen characterisation in the GUI sequences are defined to be executed like gain settings, DAC programming or sending a test pulse. The online results are displayed in the GUI as well as the final overview of the test results.

Summary and Outlook

The 900 rigid flex PCBs with the APFEL-ASIC for the first slice of the PANDA-EMC-Barrel were characterised successfully. 68 of the rigid flex PCBs have failed the requirements and are sorted out. Since the ASICs and PCBs were not tested before, the yield of over 90% is an excellent result. The first beam and cosmic tests for the slice prototype are forseen for 2018.

References

[1] P. Wieczorek and H. Flemming, “Low Noise Preamplifier ASIC for the PANDA EMC”, IEEE Nuclear Science Symposium 2010, Knoxville, USA, NSS-N47-74, Published in NSS/MIC, 2010 IEEE

[2] www.gsi.de/daqhardware

[3] J. Adamczewski-Musch, N. Kurz and S. Linev, “New Release v6.3 of data acquisition of the Framework MBS”, GSI Report 2017

DOI:10.15120/GR-2018-1

Measurement of Cluster Velocity Distributions for PANDA

S. Grieser[1], D. Bonaventura[1], B. Hetz[1], and A. Khoukaz[1], the PANDA collaboration

[1]Institut für Kernphysik, Westfälische Wilhelms-Universität Münster, Germany

Cluster-jet targets are highly suited as internal targets for storage ring experiments, like the PANDA experiment at FAIR. Such targets provide by the expansion of pre-cooled gases through fine Laval nozzles a high and constant beam thickness that is additionally adjustable over several orders of magnitude. The PANDA cluster-jet target prototype, designed and built up at the University of Münster, is successfully in operation for years and achieves thicknesses of more than 2×10^{15} atoms/cm² in a distance of 2.1 m from the nozzle. The geometry of the nozzles strongly influences the production of the clusters and their characteristics. Therefore, an advanced production process of Laval nozzles was developed at the University of Münster and important investigations on the cluster beam properties are performed [1].

An essential property is the velocity distribution of the clusters, which determines directly the thickness. Therefore, detailed studies on the velocity distribution with a newly produced nozzle were realised. A spherical joint, a feature of the PANDA cluster-jet target prototype and also of the final PANDA cluster-jet target [2], offers the possibility to tilt the nozzle with angles up to ± 3.5° in horizontal and vertical direction with the narrowest diameter of the nozzle as point of rotation (see Fig. 1). The following orifice, the skimmer, only extracts a small and well defined part of the cluster beam. This allows for measurements of cluster beam characteristics from different cluster beam parts.

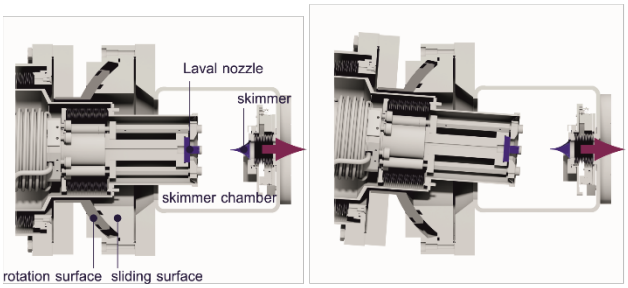


Figure 1: Spherical joint of the PANDA cluster-jet target prototype. Left: Zero position corresponds to 0°. Right: Tilting of the nozzle allows for studies of different cluster beam parts [3].

The PANDA cluster-jet target prototype offers the possibility to determine the velocity distribution of the clusters by time of flight measurements. For this purpose, a pulsed electron gun is used to ionise the clusters and to mark the start time. At the end of the beam dump and after a flight path of around 4 m, a channeltron detects the clusters and stops the measured flight time.

Studies on the velocity and thickness distribution in dependency of the tilting angle of the spherical joint show in the case of gaseous hydrogen in front of the nozzle as expected a symmetric distribution. Decreasing the temperature or increasing the pressure of the gas leads to liquid or supercritical hydrogen in front of the nozzle. As consequence, the thickness is not symmetric any more and cluster beam structures are observed (see Fig. 2). Additionally, the velocity distribution indicates the same compositions within the cluster beam. Moreover, a high thickness corresponds to a small velocity and the other way around.

To describe the velocity distributions simulations developed in the framework of the thesis of A. Täschner [4] were performed. Therein, van der Waals gas is used to characterize the velocities including a variable z parameter. This z parameter corresponds to the distance from the narrowest point of the nozzle where a decoupling of clusters from the surrounding gas is assumed. Calculations of the velocities with varied z parameter based on these results are also included in figure 2.

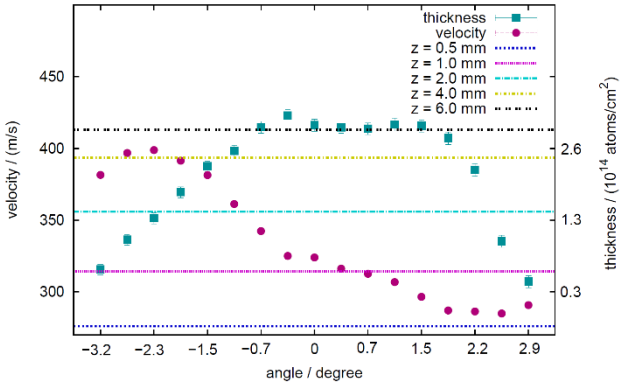


Figure 2: Thickness and velocity distribution in dependency of the spherical joint tilting angle with hydrogen at 17 bar and 22 K in front of the nozzle. The thicknesses and velocities show structures within the cluster beam. The coloured lines show the simulations with varied z parameter.

These new results expose a highly complex cluster formation process within the nozzle if a liquid or supercritical fluid is used as target material. Consequently, further studies on this topic are of highest interest to get a deeper insight into the cluster production process within the nozzle and offer the possibility to optimize the nozzle geometry towards highest thicknesses.

References

[1] S. Grieser, GSI Scientific Report 2014 (2015).
[2] B. Hetz, GSI Scientific Report 2017 (2018).
[3] E. Köhler, PhD Thesis, University of Münster, 2015, Germany.
[4] A. Täschner, PhD Thesis, University of Münster, 2012, Germany.

Experiment collaboration: PANDA
Experiment proposal: none
Accelerator infrastructure: HESR
PSP codes: 1.4.1.02
Grants: FuE: MSKHOU1720
Strategic university co-operation with: Darmstadt

 DOI:10.15120/GR-2018-1

Cluster-jet beam and vacuum studies at the PANDA cluster-jet target

B. Hetz[1], D. Bonaventura[1], S. Grieser[1], and A. Khoukaz[1], the PANDA collaboration

[1]Institute of Nuclear Physics, Westfälische Wilhelms-Universität Münster, Germany

The internal cluster-jet target build up in close to PANDA geometry at the University of Münster will be the phase one target for the upcoming PANDA experiment at the antiproton storage ring HESR at FAIR. It is by now successfully set into operation, including the final vacuum and beam monitor systems for the PANDA experiment. Furthermore, the final PANDA cluster-jet beam dump, developed by the INFN Genova, is installed at the Münster laboratory offering the possibility to study the cluster-jet beam vacuum performance with next to PANDA conditions (cf. figure 1).

Thicknesses of more than 1.4×10^{15} atoms/cm^2 directly measured at the upcoming PANDA interaction point distance of 2.25 m away from the cluster-jet nozzle demonstrate the great performance of the PANDA cluster-jet target for a high luminosity 4π experiment. The given thickness was measured using a recently installed absolute thickness monitor system at PANDA interaction point distance. Further jet beam optimization studies are expected to yield even higher thicknesses, as already demonstrated by the PANDA cluster-jet prototype with thicknesses of more than 2.0×10^{15} atoms/cm^2 at PANDA interaction point distance [1]. Also the ongoing research of new nozzle production processes and cluster-jet beam velocity distribution studies at the PANDA cluster-jet target prototype will advance the Münster PANDA cluster-jet target performance [2].

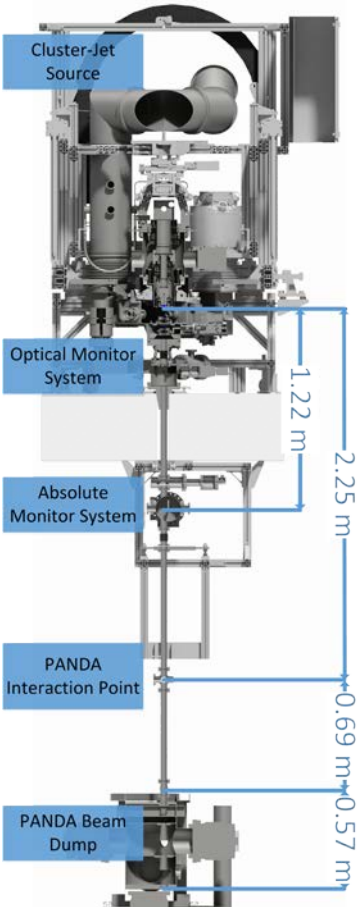


Figure 1: The PANNDA cluster-jet target setup in next to PANDA geometry at the WWU Münster.

The PANDA setup at the HESR/FAIR will be equipped with an optical monitor system due to other detector module acceptance reasons. This setup yields relative jet beam thickness information by measuring the scattered light intensity of a laser from the cluster-jet beam without influencing the jet beam itself.

Recent studies showed that the response of the optical monitor system is directly proportional to the absolute measured thickness (cf. figure 2). This matching of the optical thickness to the absolute measured jet beam target thickness makes the optical monitor highly suited for the later PANDA activities at HESR/FAIR.

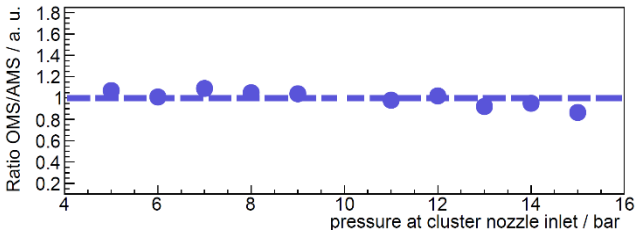


Figure 2: Scaled ratio of the relative thickness measured by the optical monitor system (OMS) and the absolute thickness monitor system (AMS) showing a proportional response.

PANDA cluster-jet target beam and vacuum studies at the COSY accelerator

The PANDA cluster-jet target beam thickness and vacuum conditions are constantly optimized at the WWU Münster setup using specialized collimators, orifices and other means. Having reached highest thicknesses with the PANDA cluster-jet target at the WWU Münster the next step will be to perform direct accelerator beam - jet beam interaction studies.

For this reason a directly PANDA related beam time at the COSY accelerator in Jülich was approved for August 2018. Thus the PANDA cluster-jet target will be moved from the WWU Münster to Jülich and be installed at COSY in June 2018.

During the August 2018 beam time the PANDA cluster-jet target will interact with the COSY proton beam and the influence of the jet target beam on the accelerator beam quality and lifetime in conjunctions with the measurement of the accelerator vacuum conditions will be performed. Furthermore the investigation of the COSY cooling systems (2 MeV electron cooler, stochastic cooling) and its barrier bucket system is from highest interest for later PANDA experiments.

References

[1] E. Köhler, PhD Thesis, University of Münster, 2015, Germany.

[2] S. Grieser et al., Measured Velocity Distribution for Determining the Cluster Beam Thickness, GSI scientific report 2017.

Experiment beamline: none
Experiment collaboration: PANDA
Experiment proposal: none
Accelerator infrastructure: HESR
PSP codes: 1.4.1.02
Grants: FuE: MSKHOU1720
Strategic university co-operation with: Darmstadt

 DOI:10.15120/GR-2018-1

New isotope search experiments at the FRS for FAIR phase-0

S. Pietri[1], A.M. Bruce[2], T. Grahn[3,4], W.R. Plass[1,5], C. Scheidenberger[1,5], T. Dickel[1,5], A. Kelić-Heil[1], H. Geissel[1,5], H. Weick[1], F. Ameil[1], L. Audouin[6], J. Aysto[3,4], S. Bagchi[1,5,7], M. Bai[1], J. Benlliure[8], G. Benzoni[9], C. Bruno[10], D. Cortina[8], T. Davisson[10], J. Gerl[1], M. Gorska[1], E. Haettner[1], O. Hall[10], L. Harkness-Brennan[11], A. Heinz[12], A. Helert[13], J.P. Hucka[1,14], A. Jokinen[3,4], A. Kankainen[4], D. Kahl[10], B. Kindler[1], I. Kojuharov[1], D. Kostyleva[1,5], N. Kuzminchuk[1], M. Labiche[15], C. Lederer-Woods[11], B. Lommel[1], G. Matinez-Pinedo[14], G. Münzenberg[1], I. Mukha[1], R. Page[12], M. Pfutzner[16], Zs. Podolyak[17], A. Prochazka[1], S. Purushotaman[1], C. Rappold[1,5], P. Regan[17], M.V. Ricciardi[1], S. Rinta-Antila[4], S. Saha[1], T. Saito[1,5,18], H. Schaffner[1], F. Schirru[1], J. Simpson[15], H. Simon[1], P. Spiller[1], J. Stadlmann[1], J. Taieb[19], Y. Tanaka[1], I. Tanihata[20,21], J. Vesic[1], B. Voss[1], P.M. Walker[17], P.J. Woods[10], J. Winfield[1], M. Winkler[1].

for the Super-FRS Experiment Collaboration, in collaboration with the DESPEC Collaboration

[1]GSI Helmholzzentrum für Schwerionenforschung GmbH, Darmstadt, Germany ;[2]University of Brighton, UK;[3]Helsinki institute of Physics, Finland;[4]University of Jyväskylä, Finland;[5]Justus-Liebig-Universität Gießen, Germany; [6]IPNO, Université de Paris-Saclay, CNRS/IN2P3, Orsay, France; [7]St Mary's University, Halifax, Canada;[8]Universidad de Santiago de Compostela, Spain;[9]INFN sezione di Milano, Italy;[10]University of Edinbourg, UK;[11]University of Liverpool, UK;[12]Chalmers University of Technology, Göteborg, Sweden;[13]FAIR Darmstadt, Germany ;[14]Technische Universität Darmstadt, Germany;[15]SFTC Daresbury Laboratory, UK;[16]University of Warsaw, Poland;[17]University of Surrey, UK;[18]Iwate University Morioka ;[19]CEA DAM Bruyères-le-Châtel;[20]Beihang University, Beijing, China;[21]Osaka University, Japan

The region "south" of ^{208}Pb nuclei along the N=126 line has been identified as a region of key interest for the NUSTAR Collaboration at GSI/FAIR; generally it is of high interest for nuclear structure studies and nuclear astrophysics applications. A proposal has been submitted and accepted to the GSI PAC to perform an exploratory study; it aims to extend the frontiers of known isotopes and to obtain nuclear structure data on gross properties. It is expected to simultaneously identify over 28 new isotopes. Using new detector equipment from different NUSTAR sub-collaborations jointly and using the same FRS settings that are used very successfully in the identification of new isotopes permits to obtain 26 news masses and 47 new lifetimes together with spectroscopic investigations on isomeric decay properties. Furthermore, the experiment will study the production of (new) isotopes "south" of the primary-beam isotones, i.e., measure their production cross sections and momentum distributions.

Today this region can best be studied at "FAIR phase-0" using fragmentation of the intense ^{208}Pb beam and in-flight separation of the neutron-rich projectile fragments. The crossing of the N=126 line "south" of ^{201}Re will be accomplished by the higher intensities of ^{238}U beam and the Super-FRS beams at "FAIR phase-1".

The current experiment is, moreover, presented as a benchmark of the NUSTAR "FAIR phase-0" facility proving the worldwide competitiveness of the current facility in this mass region, it will help planning further other NUSTAR "FAIR phase-0" experiments and serve for testing of new NUSTAR devices (AIDA, Cryogenic Stopping Cell….) and data acquisition together.

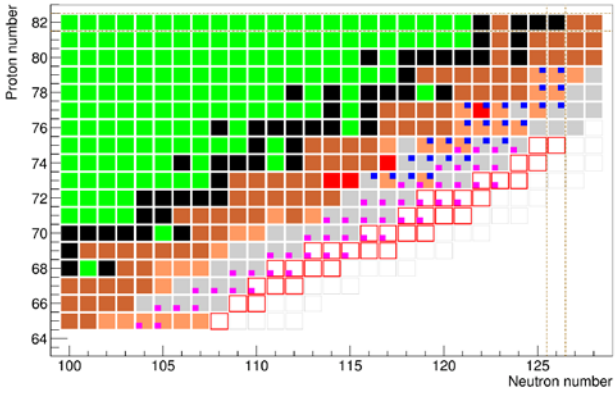


Figure 1: The region of interest in the chart of nuclei for the coming experiment. Black: stable nuclei; green: neutron deficient nuclei; dark brown: isotopes with known half-lives and masses; salmon: nuclei with known half-lives; red: nuclei with known mass; grey: already discovered isotopes; red borders: new isotopes from this proposal; pink square: proposed halve-lives measurements; blue squares: proposed masses measurements.

This will be achieved by extraction of a 1000 A·MeV ^{208}Pb^{67+} primary beam from the SIS-18 and focusing it on the production target at the entrance of the FRS. A target of 2.5 g/cm^2 Be with a 223 mg/cm^2 Nb backing will be used to produce the isotopes of interest via projectile fragmentation. The thickness of the target was estimated as an optimum between the number of produced isotopes (which would call for a thicker target) and transmission through the separator (which suffers when target thickness and momentum spread are too large). The high beam energy, together with the Nb backing, assures that more than 90% of the ions emerging from the target will be

fully stripped, which is important for high transmission and unambiguous identification by the Bρ-ΔE-ToF method. In order to optimize the efficient use of the beam time overall, only one target will be used for all settings.

The FRS is equipped with its standard instrumentation for beam tracking, separation and particle identification. Some of the MUSIC or TPC detectors will be replaced by their upgraded versions planned for the Super-FRS when available.

The 1000 A·MeV primary beam assures that all fragments penetrate the MUSIC detectors at the final focus of the FRS with at least 600 A·MeV. At this energy for the worst case (Re) a 13% chance exists to pick up an electron inside the active volume of the MUSIC detector. Using two MUSICs and a stripper foil in between means incorrectly identified elements are in the 1.6% range. As mentioned earlier the higher energy primary beam assures a more forward focus of the fragments thus a higher transmission. Aluminum degraders at the first focal plane and in the middle focal plane will assure separation of the ions of interest and eliminate unwanted contaminants.

The mean energy loss in the degrader is independent of the ionic charge state of the emerging fragments. This information can help in addition to identify the element number and the few-electron ions.

New NUSTAR equipment, constructed for FAIR, and already available – at least as prototypes or "start versions" – for experiments in phase-0, will be used. In the FRS, new TPC- and MUSIC-detectors will be used for beam monitoring and particle identification. At the final focus (F4 area), the FRS Ion Catcher and detectors of the DESPEC collaboration (AIDA, FATIMA) will be used for the first time for experiments. It is the combined use of these novel instruments, which allows for these pioneering studies and the rich nuclear data harvest in short time. The overall experimental setup is shown in figure 2.

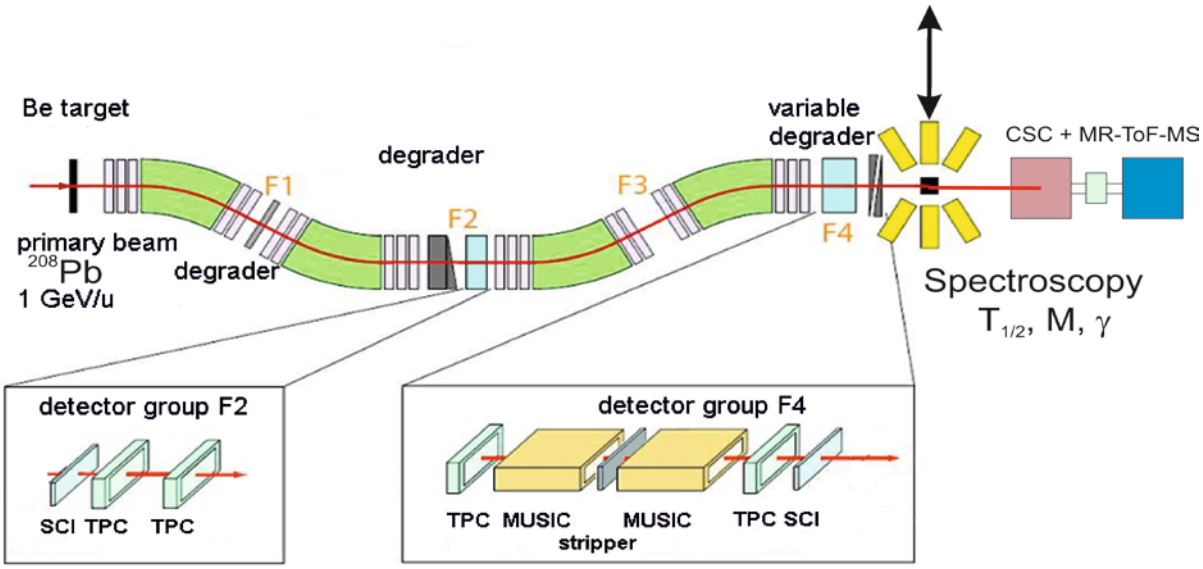


Figure 2: Schematic view of the two FRS final focal-plane setups planned for this experiment. The FRS detectors for particle identification in-flight are indicated. At the final focal plane F4 two experimental setups can be used alternatively (black arrow), a spectroscopy setup with LaBr3 gamma detectors viewing the silicon implantation detector and the cryogenic stopping cell (CSC) coupled to the multiple reflection time-of-flight mass spectrometer (MR-ToF-MS).

Outlook

The project presented here is part of the topic 1 of the Super-FRS Experiment Collaboration (SEC), which aims at similar experiment in phase 1 looking for new isotopes and studying their gross properties. In parallel to this the topic 1 of SEC together with performing nuclear reaction studies using the combination of the FRS Ion Catcher with standard DESPEC equipment to perform isomeric ratio measurements over a wide life time range[1].

Experiment beamline: FRS
Experiment collaboration: NUSTAR-SuperFRS-Experiments/ NUSTAR-DESPEC-HISPEC
Experiment proposal: S468
Accelerator infrastructure: UNILAC / SIS18 / FRS /
Strategic university co-operation with: Giessen, Darmstadt

References

[1] Ubbi Sauerwine, summer student report 2015

 DOI:10.15120/GR-2018-1

Development of new ion-optical modes for NUSTAR FAIR Phase-0 experiments at the FRS

E. Haettner[1], T. Dickel[1,2], K. Dort[2], H.Geissel[1,2], N. Iwasa[3], W. R. Plaß[1,2], C. Scheidenberger[1,2], Y. Tanaka[1], S. Terashima[4], H. Weick[1], J. S. Winfield[1], M. Winkler[1], M. Yavor[5], and the Super-FRS Experiment collaboration

[1]GSI, Darmstadt, Germany; [2]University of Giessen, Giessen, Germany; [3]Tohoku University, Sendai, Japan; [4]Beihang University, Beijing, China; [5]Institute of Analytical Instrumentation, Russian Academy of Science, St Petersburg, Russia

The in-flight separator and spectrometer for short-lived exotic nuclei Fragment Separator FRS [1,2] is a central instrument in the NUSTAR collaboration. The FRS consists of four stages with various diagnostic equipment and shaped matter in between. This makes the FRS flexible; transmission, resolution, separation, focal plane conditions, achromatism are example of properties that have to be optimized for each category of experiments.

Experiments and tests with the FRS Ion Catcher [3] have so far used an ion-optical mode [4] with a monoenergetic degrader [1,5,6] installed at the mid-focal plane. In principle, this particular experiment setup can, because of its own mass tagging capabilities [7] and separation by range selection, tolerate less identification and separation quality of the FRS. However, the resolving power also determines the energy bunching quality, thus it should not be reduced below approximately 800 (ε_x=13.5 π mm mrad, x_0=1.5 mm). Furthermore, the degrader itself, even without presence of possible inhomogenities, limits the achievable resolution to the order of 0.1%, due to unavoidable energy loss straggling. Figure 1 shows the optical transmission of the mode used so far in these experiments as well as of two modified optic settings with lower resolving power. The transmission (evaluated with a phase space filling an ellipsoid with parameters as indicated in the figure) can be improved by about a factor of 2-3. The development is of advantage for all NUSTAR experiments that do not need the ion optical resolution of the mode used so far, either because the nuclide of interest is still separated and identified, or the experiment provides its own identification and/or benefits from a cocktail beam.

Similarly, other experiments need optimization and development of ion-optical modes. An example is an experiment that investigates the influence of the tensor force as a part of the nuclear force [8]. In a pilot experiment the population of ground and excited states in the ^{16}O(p,d) reaction for various beam energies was measured. This only possible due to the development of an ion optical mode where the resolving powers of the four dispersive dipole magnet stages were added such that a momentum resolving power of 16,500 (x_0=0.5mm, realized by sharp focusing, $B\rho_{max}$=13.8 Tm) was achieved.

A third example is the atomic collision experiment [9], where precise heavy ion energy-loss measurements as well as charge-state distributions behind different targets will be measured. The atomic-collision target is placed at the dispersive mid-focal plane of the FRS. The charge-state distribution will be measured via position sensitive detectors at the subsequent focal plane and the energy-loss distribution at the final focal plane which is achromatic with respect to the entrance of the FRS. The optics has been adapted to the requirement of the mounted setups of other NUSTAR experiments and the need to minimize the matter thickness.

These described new ion-optical developments are essential for successful completion of the FAIR phase-0 experiments of the NUSTAR collaboration.

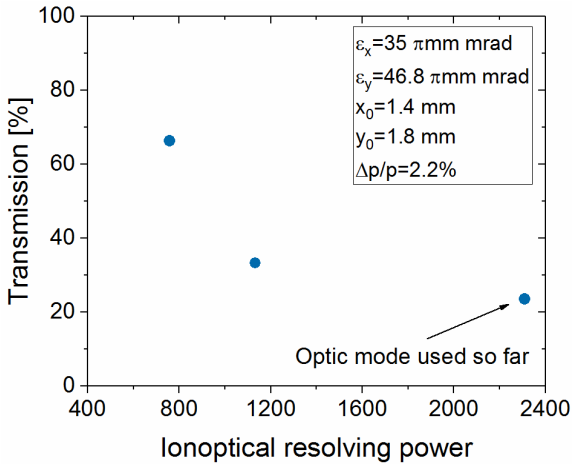


Figure 1: Simulated transmission as a function of resolving power (see text for details) of three different ion-optical modes.

References

[1] H. Geissel et al., Nucl. Inst. Meth. A 282 (1989) 247.
[2] H. Geissel et al., Nucl. Inst. Meth. B 70 (1992) 286.
[3] W. R. Plaß et al., Nucl. Inst. Meth. B 317 (2013) 457.
[4] H. Irnich, PhD Thesis, JLU Giessen (1995).
[5] H. Weick et al., Nucl. Inst. Meth. B 164-165 (2000) 168.
[6] Ch. Scheidenberger et al., Nucl. Inst. Meth. B 204 (2003) 119.
[7] C. Hornung et al., GSI Sci. Rep. 2016 (2017) p. 175.
[8] H. J. Ong et al., Phys. Lett. B 725 (2013) 277.
[9] S. Purushothaman et al., GSI Sci. Rep. 2017, this issue.

Experiment beamline FRS
Experiment collaboration: NUSTAR-SuperFRS-Experiments
Experiment proposal: S436, S469, S474
Accelerator infrastructure: UNILAC / SIS18
PSP codes: none
Grants: BMBF (05P16RGFN1), HMWK (LOEWE Center HICforFAIR)
Strategic university co-operation with: Gießen

New opportunities at the border of nuclear and hadron physics using WASA at FRS: a status report

K.-H. Behr[1], J. Benlliure[2], T. Blatz[1], H. Calen[3], M. Gleim[1], F. Goldenbaum[4], K. Itahashi[5], C. Rappold[1,6], J. Ritman[4], J.L. Rodrigues-Sanchez[1,2], T.R. Saito[1,7], V. Serdyuk[4], S. Schadmand[4], C. Scheidenberger[1,6], B. Szczepanczyk[1], Y. Tanaka[1,6], M. Wolke[3], for the WASA-at-FRS collaboration, the S447 collaboration, the S457 collaboration, the S463 collaboration, and the Super-FRS Experiment collaboration

[1]GSI, Darmstadt, Germany; [2]USC, Santiago de Compostela, Spain; [3]Uppsala Univ., Uppsala, Sweden; [4]Forschungszentrum Juelich, Juelich, Germmany; [5]RIKEN, Wako, Japan; [6]Giessen Univ, Giessen, Germany; [7]HIM, Mainz, Germany

Introduction

Study of the nature of hadrons inside sub-atomic nuclear systems has recently become more important in the fields of nuclear and hadron physics. In particular, with heavy ion- and proton-beams at GSI, several results on light Λ-hypernuclei, η'-nucleus and baryon resonances in nuclei have recently revealed. These experiments have revealed interesting phenomenon as discussed in the following sections in this report. However, the results have also shown that resolution and sensitivity of these experiment were not yet sufficient for the results to be conclusive. Therefore, we are introducing a new technique at GSI.

To improve resolution and sensitivity, we have proposed a novel technique for measuring light charged particles and photons from exotic nuclei at the mid-focal plane of the FRS, S2, in coincidence with decay residues detected by the second half of the FRS. As a target spectrometer at S2, the WASA central detector (WASA CD), currently at COSY in Juelich, will be implemented. With the setup of WASA CD at FRS, as shown in Figure 1, three experimental programs on hypernuclear spectroscopy, η'-nucleus and baryon resonances in nuclei have been proposed, as discussed below.



Figure 1: Layout of the FRS. The WASA CD will be mounted at the mid-focal plane S2.

The WASA central detector at FRS

The 4π detector WASA (Wide Angle Shower Apparatus) was designed for studies of production and decays of light mesons at CELSIUS in Uppsala, Sweden. Pions and η-mesons were produced in proton-proton and proton-deuteron interactions. In 2005, WASA was moved to the Cooler Synchrotron COSY at Juelich, Germany, where the forward detection and the data acquisition were upgraded. A detailed description of the WASA is found in [1].

The WASA central detector consists of an inner mini-drift chamber (MDC) of straw tubes, thin plastic scintillators in a cylinder geometry (PS), a super-conducting solenoid, and a CsI calorimeter. The general idea is to use WASA for measuring light particles from the decay of exotic nuclei produced in front of or inside the WASA CD with a large acceptance, while decay residues are measured by the second half of the FRS with an excellent momentum resolution. Figure 2 shows a side view of the WASA CD at S2 of FRS. The production target of nuclei of interest for experiments of hypernuclei and baryon resonances in nuclei will be in front of the WASA CD, while that for the η'-nucleus experiment will be mounted behind the MDC.

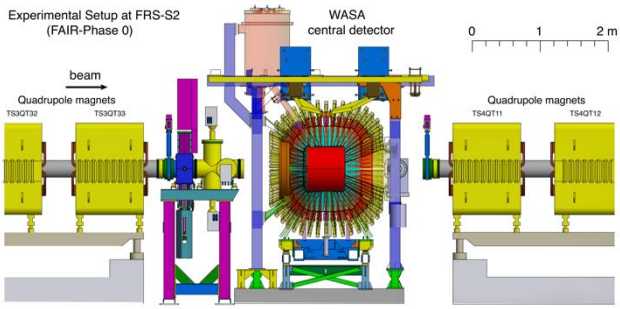


Figure 2: A side view of the WASA CD installed at S2 of FRS.

Physics case

Three projects are in preparation; S447 for hypernuclei, S457 for η'-mesic nucleus and S463 for baryon resonances in nuclei. These proposals were discussed in the G-PAC at GSI in 2017. Other new experiments are also under preparation.

Hypernuclei

Hypernuclei, subatomic nuclei with strange quark(s), have been studied in order to understand baryon interactions under the flavored-SU(3) symmetry. Conventional ways to produce hypernuclei are with the use of secondary meson- and primary electron beams, mainly with the missing mass spectroscopy or/and emulsion techniques. Ultra-relativistic heavy ion collisions at RHIC and LHC have also been employed to study light hypernuclei with mass values of A<4. Recently, the hypernuclear physics has entered a new era by the success of the HypHI Phase 0 experiment at GSI [2]. It has demonstrated feasibility of hypernuclear spectroscopy with heavy ion beams bombarding a fixed target by employing invariant mass tech-

 DOI:10.15120/GR-2018-1

nique. The HypHI Phase 0 experiment was performed with ^{6}Li beams at 2 A GeV and the graphite target, and it successfully produced and identified hypernuclei with A=3 and 4 [2].

One of the striking but also surprising results of HypHI Phase 0 is the observation of signals that may be related to the existence of an extremely exotic neutral hypernucleus, two neutrons together with a Λ-hyperon, (nnΛ), which has been observed in the d+π^- and t+π^- invariant mass distributions [3]. However, there are no theoretical calculations that can reproduce such a bound state [4,5,6,7]. Therefore, the existence of the nnΛ bound state is under debate and will be studied in forthcoming experiments.

Another striking result of the HypHI Phase 0 experiment is the observation of unexpected short lifetime of $^{3}_{\Lambda}$H, 183^{+42}_{-32} ps, for the first time, which is significantly shorter than that of the free Λ-hyperon (263.2 ps) [2]. This contradicts the current understanding of the structure of the lightest hypernucleus $^{3}_{\Lambda}$H, which is understood as Λ attached to a deuteron core with a binding energy of only 130 keV. With such a small binding energy, the lifetime of $^{3}_{\Lambda}$H has been expected to be similar to that of free Λ-hyperons. So far, none of the theoretical calculations can reproduce such short lifetime of $^{3}_{\Lambda}$H. Very recently, the STAR and ALICE collaborations also observed significantly shorter lifetime of $^{3}_{\Lambda}$H than Λ respectively to be 155^{+25}_{-22} ps [8] and 181^{+54}_{-39} ps [9].

Though the results of the HypHI Phase 0 experiment have revealed interesting and new mysterious observations, the achieved sensitivity and resolution of the hypernuclear spectroscopy with heavy-ion beams does not allow for detailed conclusions. Also, with the previous setup, further studies on unknown and exotic hypernuclei will not be feasible.

In contrast to the results of the HypHI experiment, with the proposed experiment with WASA at FRS, negative charged pions will be measured with a large angular and momentum coverage, therefore, observed signals will be well separated by a broad background distribution. The invariant mass resolution will be improved due to the excellent momentum resolution of FRS. Furthermore, the statistics will be largely increased due to the large acceptance of the WASA detector for measuring negative charged pions and the new possibility to simplify the trigger to the DAQ system because of reasonably small geometrical and momentum acceptance of FRS.

Additional detectors for measuring decay vertexes of hypernuclei and position and time information of decay residues will be installed in front of and behind the WASA CD. According to Monte Carlo simulations, the resolutions and statistics will be improved by factors of approximately 3 and 10, respectively. Therefore, the results of the proposed experiments will contribute further to solve the two puzzles discussed above. Furthermore, $^{4}_{\Lambda}$H will also be studied in the same experiment.

η'-mesic nuclear bound state

The possible existence of η'-mesic nuclei, i.e., bound states of an η' meson in nuclei, has recently attracted strong interests related to UA(1) quantum anomaly and partial restoration of chiral symmetry in QCD. The η' meson has an exceptionally large mass of 958 MeV/c^2, which is considered as a consequence of the anomaly effect under presence of spontaneous breaking of chiral symmetry [10]. In finite nuclear density, where chiral symmetry is partially restored, reduction of the η' mass is predicted [11, 12]. Such an in-medium mass reduction would induce an attractive potential between an η' meson and a nucleus, suggesting the possible existence of η'-mesic nuclei [13].

The first experiment to search for η'-mesic nuclei was performed with the FRS at GSI in 2014 by missing mass spectroscopy of the ^{12}C(p,d) reaction at an incident proton energy of 2.5 GeV [14, 15]. The proton beam extracted from SIS-18 impinged on a carbon target installed at the target area of the FRS. The momentum of the ejected deuterons at forward 0 degrees was analyzed by the FRS, operated as a high-resolution spectrometer.

High statistical sensitivity was achieved in the measured spectra to search for relatively narrow and small peak structures in the continuous background due to quasi-free meson production processes. However, no significant peak structure related to the formation of the η'-mesic states was observed, and thus upper limits on the formation cross section of the bound states as well as constraints on the η'-nucleus interaction were deduced [14, 15]. The experimental sensitivity was limited mainly by the continuous background, which had in total >100 times larger cross section than expected formation cross sections of the bound states.

For FAIR Phase 0, a semi-exclusive measurement of the ^{12}C(p,dp) reaction is planned to aim at increasing the experimental sensitivity [16]. In coincidence with the ejected deuteron from the (p,d) reaction, decay particles from η'-mesic nuclei are detected and identified for event selection. The continuous background dominating the spectra of the previous experiment can be suppressed by tagging the decay particles. Expected major decay modes of the η'-mesic nuclei are one- and two-nucleon absorption processes: η'N → η'N, η'N → π'N, and η'NN → NN [17]. In particular, the two-nucleon absorption process emits a proton (or neutron) with relatively high kinetic energy of about 500 MeV [18].

The experimental setup with the WASA-CD at FRS-S2 is an ideal configuration for the planned measurement. The carbon target will be installed at the downstream side of the WASA-CD to maximize the angular acceptance for the detection of the backward emitted proton. The ejectile deuteron will be measured with the S2-S4 section of the FRS, and the decay proton with the WASA-CD. By tagging high-energy protons in the backward angular range (θ lab > 90deg) by WASA-CD, we expect that the signal-to-background ratio will be improved by two orders of magnitude compared to the previous experiment [18].

S463: Baryon resonances in nuclei

Resonances are largely produced in relativistic heavy-ion collisions and could appear in the core of neutron stars at densities around 2 or 3 times the nuclear matter saturation density [19]. Nucleon resonances also play a

significant role in the understanding of three-body nuclear forces or the quenching of the Gamow-Teller strength [20]. For instance, the Δ-resonance is a ΔS =1; ΔI =1 spin- and isospin-flip intrinsic excitation of the nucleon. As such it is a partner of the corresponding ΔS=1; ΔI=1 excitation of the nuclear medium, known as the Gamow-Teller resonance.

Studies with the Super-FRS present unique possibilities to study the Delta(Δ)- and other baryon resonances in stable and in exotic nuclei by using isobaric charge-exchange reactions in relativistic heavy-ion collisions. Pilot experiments have already been performed with the FRS and reveal that the high resolution of the spectrometer makes it possible to identify in the missing energy spectra of the forward-emitted ejectiles the in-medium excitation of Delta and Roper resonances [21].

These measurements are expected to contribute to open up a new field linking subnucleonic and nucleonic degrees of freedom through the production of resonant nuclear matter. In particular, these experiments will help to constrain the in-medium NΔ and NR potentials above the 400 MeV range covered by electron-nucleus and pion-nucleus scattering experiments and to address the possible in-medium mass modification of nuclear resonances. These reactions may also provide an opportunity to study two Δ's in nuclei and provide a chance to study ΔΔ interactions and the recently observed d*(2380) resonance. Moreover, the use of relativistic nuclei far off stability will allow exploring the isospin degree of freedom enlarging in this way our present knowledge of the properties of isospin-rich nuclear systems. Particularly, one could also take advantage of the peripheral character of these reactions to probe the relative abundances of protons and neutrons at the nuclear periphery and constraint the density derivative of the symmetry energy.

The proposed experiments can be realized by using the FRS with its standard tracking detector systems measuring the momentum distribution of the isobaric projectile residues created via charge-exchange reactions. In addition, measuring the charged pions emitted in the decay of the nucleon resonances in coincidence with the WASA CD detector will allow to separate resonance excitations in the projectile and target nuclei remnants. The use of a liquid hydrogen target will also contribute to isolate the excitation of particular resonances.

Status of the project

Green light from the WASA-at-COSY collaboration to transport the WASA CD to GSI was given in August 2017. In November 2017, the Joint Scientific Council of GSI/FAIR approved the WASA-at-GSI project, stating the goodness of the physics cases. Three experimental proposals have been discussed with the G-PAC in 2017, and two of them, S447 and S457, have been approved. Allocated shifts will be 27 shifts for S447 and 18 shifts for S457, with 18 parasitic shifts for commissioning the detectors. Preparations are on-going to perform the two experiments in the second half of 2019.

Design work for the holding structure of the WASA CD at S2 of FRS is in progress and manufacturing will begin in 2018. The MDC together with electronics, slow control and gas controlling systems have been transported to GSI. Currently, we are preparing laboratory space for WASA CD and the superconducting magnet with its cryogenic system. Subdetectors of the WASA CD will be tested and commissioned with cosmic rays and radioactive sources by the end of 2018. In the beginning of 2019, the WASA CD will be mounted at S2 of FRS to be ready for commissioning.

In the meantime, Monte Carlo simulations for the optimization of the detection and analysis methods are in progress. Furthermore, the development of the online/offline analysis software is to be completed.

References

[1] nucl-ex/0411038.
[2] C. Rappold et al., Nucl. Phys. A 913 170 (2013).
[3] C. Rappold et al., Phys. Rev. C 88 041001(R) (2013).
[4] A. Gal and H. Garcilazo, Phys. Lett. B 736 93 (2014).
[5] E. Hiyama et al., Phys. Rev. C 89 061302R (2014).
[6] H. Garcilazo and A. Valcarce, Phys. Rev. C 89 057001 (2014).
[7] J.M. Richard et al., Phys. Rev. C 91 014003 (2015).
[8] STAR Collaboration, Proc. 12th Int. Conf. on Hypernuclear and Strange Particle Physics (HYP2015) JPS Conf. Proc. 021005 (2017).
[9] ALICE Collaboration, Phys. Lett. B 754 360 (2016).
[10] D. Jido et al., Phys. Rev. C85,032201(R) (2012).
[11] P. Costa, M. C. Ruivo, C. A. de Sousa, and Y. L. Kalinovsky, Phys. Rev. D 71, 116002 (2005).
[12] H. Nagahiro, M. Takizawa, and S. Hirenzaki, Phys. Rev. C 74, 045203 (2006).
[13] H. Nagahiro and S. Hirenzaki, Phys. Rev. Lett. 94, 232503 (2005).
[14] Y. K. Tanaka et al., Phys. Rev. Lett. 117, 202501 (2016).
[15] Y. K. Tanaka et al., Phys. Rev. C97, 015202 (2018).
[16] K. Itahashi et al., Experimental Proposal for FAIR Phase 0, S457 (2017).
[17] H. Nagahiro, Nucl. Phys. A 914, 360 (2013).
[18] Y. Higashi, Master's thesis, Nara Women's University (2015).
[19] A. Drago et al., Phys. Rev. C 90, 065809 (2014).
[20] H. Lenske et al. Prog. Nucl. Part. Phys. 98, 118 (2018).
[21] J. Vargas et al., Nucl. Instrum. Methods A 707, 16 (2013).

 DOI:10.15120/GR-2018-1

Experiment beamline: FRS
Experiment collaboration: NUSTAR-SuperFRS-Experiments
Experiment proposal: S447, S457, S463
Accelerator infrastructure: SIS18

Search for η′-mesic nuclei with the ^{12}C(*p*,*d*) reaction

Y. K. Tanaka[1], K. Itahashi[2], H. Fujioka[3] for the η-PRiME/Super-FRS Experiment collaboration

[1]GSI, Darmstadt, Germany; [2]RIKEN, Wako, Japan; [3]Kyoto University, Kyoto, Japan.

We investigate η′-meson nucleus bound states (η′-mesic nuclei) by missing-mass spectroscopy of the ^{12}C(*p*,*d*) reaction [1]. Such bound states are expected to provide a unique and direct probe for studying in-medium properties of the η′ meson, which are closely related to chiral symmetry and axial $U_A(1)$ anomaly in QCD [2].

In 2014, we performed an inclusive measurement of the ^{12}C(*p*,*d*) reaction to measure the excitation spectrum of ^{11}C near the η′-meson production threshold. A carbon target was irradiated with a 2.5 GeV proton beam accelerated by SIS-18 to produce η′-mesic nuclei via the ^{12}C(*p*,*d*)η′⊗^{11}C reaction. Deuterons emitted at 0° were momentum-analyzed by the FRS used as a high-resolution spectrometer. Details of the experimental method are described in Ref. [3, 4].

Figure 1 (top) presents the obtained excitation spectrum around the η′ production threshold. Data sets with seven scaling factors (f = 0.980–1.020) for the central magnetic rigidity of the FRS have been combined, as indicated in the figure. The spectrum exhibits a continuous increase in the measured region and is fitted well with a polynomial function, as shown by the gray curve and the residual plot (bottom). This continuous component is consistent with estimated cross sections of quasi-free meson production processes, $p + N \rightarrow d + X$ ($X = 2\pi$, 3π, 4π, ω).

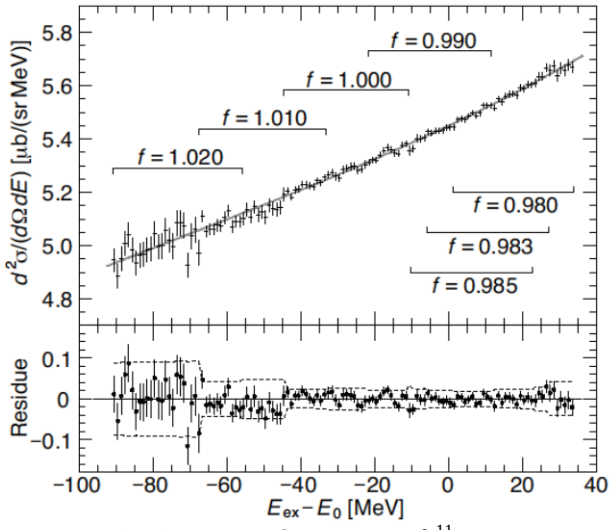


Figure 1: (Top) Measured spectrum of ^{11}C excitation energy (E_{ex}) relative to the η′ production threshold (E_0 = 957.78 MeV). The spectrum was obtained by combining data at seven momentum settings (f = 0.980–1.020) of the FRS. The gray curve displays a third-order polynomial fitted to the spectrum. (Bottom) Residual plot of the polynomial fit. Envelopes of two standard deviations are shown by the dashed lines. This figure is adopted from Ref. [4].

No prominent structures associated with the formation of η′-mesic nuclei are observed, although a very high statistical sensitivity at a level of < 1% has been achieved in the spectrum. We have evaluated upper limits on the formation cross section of η′-mesic nuclei to be ~20 nb/(sr MeV) at the production threshold for assumed Lorentzian width of Γ = 5–15 MeV. Furthermore, a comparison with theoretical calculations [5] has set a constraint on the η′-nucleus interaction, as depicted in Fig. 2 [3, 4].

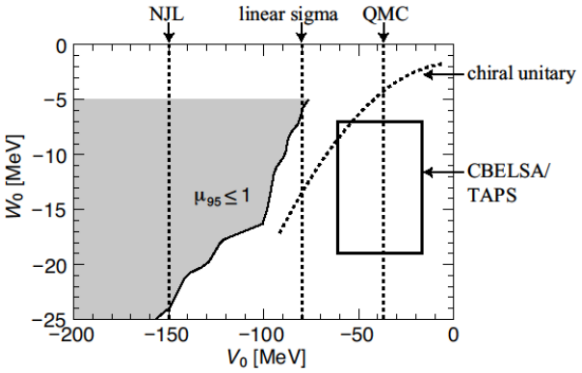


Figure 2: Evaluated constraint on the η′-nucleus potential ($V_0 + iW_0$) at normal nuclear density. The shaded region ($\mu_{95} \leq 1$) is excluded by the analysis of this experiment. Other theoretical and experimental information is displayed as well. See Ref. [4] for further details.

In FAIR Phase-0, we plan a semi-exclusive measurement of the ^{12}C(*p*,*dp*) reaction aiming at achieving higher experimental sensitivity [6]. The continuous background, dominating the inclusive (*p*,*d*) spectrum, can be efficiently reduced by simultaneously measuring the forward emitted deuteron and decay particles from η′-mesic nuclei. In particular, by tagging high-energy protons emitted in the two-nucleon absorption process (η′*NN*→*NN*), the signal-to-background ratio is expected to be enhanced by a factor ~100 compared with the inclusive measurement. The WASA central detector combined with the FRS is an ideal setup for this experiment, and its preparation is in progress.

References

[1] K. Itahashi *et al.*, Prog. Theor. Phys. 128, 601 (2012).
[2] D. Jido *et al.*, Phys. Rev. C 85, 032201(R) (2012).
[3] Y. K. Tanaka *et al.*, Phys. Rev. Lett.117, 202501 (2016).
[4] Y. K. Tanaka *et al.*, Phys. Rev. C 97, 015202 (2018).
[5] H. Nagahiro *et al.*, Phys. Rev. C 87, 045201 (2013).
[6] K. Itahashi, Y. K. Tanaka *et al.*, Experimental Proposal for FAIR Phase-0, S457 (2017).

Experiment beamline: FRS
Experiment collaboration: NUSTAR-SuperFRS-Experiments
Experiment proposal: S437, S457
Accelerator infrastructure: SIS18 / FRS

 DOI:10.15120/GR-2018-1

Observation of nuclear medium effects in the excitation of baryonic resonances

J. L. Rodríguez-Sánchez[1,2], J. Benlliure[2], H. Alvarez-Pol[2], J. Atkinson[1], T. Aumann[1], Y. Ayyad[2], S. Beceiro-Novo[2], K. Boretzky[1], E. Casarejos[2], D. Cortina-Gil[2], P. Dıaz Fernández[2], A. Estrade[1], H. Geissel[1,3], K. Itahashi[4], A. Kelić-Heil[1], Yu. A. Litvinov[1], C. Paradela[2], D. Pérez[2], S. Pietri[1], A. Prochazka[1], T. R. Saito[1], S. Schadmand[5], C. Scheidenberger[1,3], M. Takechi[1], Y. Tanaka[1,3], J. Vargas[2], I. Vidaña[6], H. Weick[1], and J. S. Winfield[1]

[1]GSI, Darmstadt, Germany; [2]USC, Santiago de Compostela, Spain; [3]Giessen Univ, Giessen, Germany; [4]RIKEN, Wako, Japan; [5]IKP, Jülich, Germany; [6]Università di Catania, Catania, Italy

The in-medium properties of baryonic resonances are not well understood. Up to now, the in-medium e ects of Δ-isobars have been studied in heavy-ion collisions at kinetic energies above the production threshold using nuclear reactions at small impact parameters [1], where there is not a good control over the production of residual fragments and thus over the number of interactions during the collision. Further investigations were performed at SATURNE using isobar charge-exchange reactions, in which the Δ resonance is excited at the surface of the nucleus [2]. These experiments provided the missing energy distributions of the (p,n) and (n,p) charge-exchange reactions induced by projectiles of ^{20}Ne at 0.95*A* GeV. The measurements were performed using di erent targets and the analysis showed a clear deviation of 50 - 70 MeV in the average value of the Δ peak between the target of protons and the others. This shift was understood as an in-medium e ect due to the Fermi motion [3] and/or di erences beetwen target and projectile excitations [4].

In this work we report on the results obtained from an experiment carried out at GSI using the fragment separator FRS, which provides unique conditions to perform measurements of isobar charge-exchange reactions with high quality, allowing us to identify the (n,p) and (p,n) charge-exchange reactions from the determination of the atomic and mass numbers of the residual fragments. Here, we measure the Δ excitation in isobar charge-exchange reactions of stable projectiles of ^{112}Sn impinging on carbon and proton targets of around 100 mg/cm^2, placed at the experimental area S0. In Fig. 1 we display the missing-energy spectrum for the isobar charge-exchange reactions C(^{112}Sn, ^{112}In)X and p(^{112}Sn, ^{112}In)X at 1*A* GeV, together with the results obtained at SATURNE for the reaction p(^{20}Ne,^{20}F)X at 0.95*A* GeV [5].

The peak close to zero corresponds to the quasi-elastic channel, while the peak around -300 MeV represents the inelastic contribution due to the excitation of the Δ resonance. Thanks to the thin targets, we obtained these spectra with a bin width of about 12 MeV, improving the resolution by a factor two with respect to experiments performed at SATURNE.

In the gure, one can see that for the reactions in the proton target the Δ peak is around -350 MeV, while for the reaction in the carbon target the peak is around -300 MeV, resulting in a shift of ~50 MeV. Therefore, these new measurements con rm the results obtained in previous experiments at SATURNE [2,5].

New measurements are planned for the phase 0 of the Super-FRS experiments, in which the isobar charge-exchange reactions will be studied in coincidence with the pions emitted from the Δ decay using the WASA@FRS setup, introducing more constraints in the analysis that will help to go further in the understanding of this e ect.

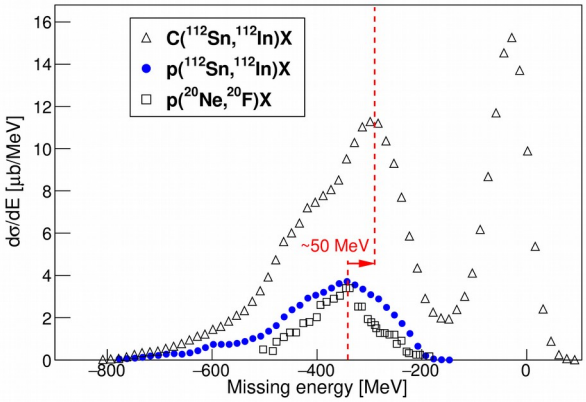


Figure 1: Missing energy distribution for ^{112}Sn and ^{20}Ne induced charge-exchange reactions in a target of protons. For comparison, the distribution of p(^{20}Ne,^{20}F)X was scaled by a factor four (for clarify of the display).

References

[1] S.B. Kaufman et al., Phys. Rev. C 20 (1979) 2293.
[2] D. Bachelier et al., Phys. Lett. B 172 (1986) 23.
[3] T. Hennino et al., Phys. Lett. B 283 (1992) 42.
[4] E. Oset et al., Nuclear Phys. A 468 (1987) 631.
[5] M. Roy-Stephan et al., Nucl. Phys. A 488 (1988) 178.

Experiment collaboration:
NUSTAR-SuperFRS Experiments

Grants: This work has been supported by the Department of Education, Culture and University Organization of the Regional Government of Galicia under the program of postdoctoral fellowships

Design of a double-sided silicon strip tracking system for hypernuclear spectroscopy at FRS & Super FRS

C. Rappold[1,2,3], S. Horta Muñoz[1], M.C. Serna Moreno[1], T. Saito[2], C. Scheidenberger[2,3]

[1]University of Castilla La-Mancha, ETSII, Ciudad Real, Spain; [2]GSI, Darmstadt, Germany; [3]Justus-Liebig-Universität Giessen, Germany

The feasibility of hypernuclear spectroscopy by means of heavy ion beam induced reactions was demonstrated by the results obtained in the first experiment of the HypHI collaboration. A ^{6}Li beam at 2*A*GeV impinged on a stable ^{12}C target. The main results of the experiment showed the measurements of Λ hyperon and $^{3}_{\Lambda}$H, $^{4}_{\Lambda}$H. Results on the invariant masses, lifetime and production cross-sections were published [1, 2, 3]. For the FAIR-Phase 0 beam-time a new hypernuclear spectroscopy experiment was approved by the G-PAC in order to assess the possible existence of the nnΛ bound state. This novel experiment will take place at the FRS fragment separator utilizing the WASA central detector that will be moved and installed in the S2 focal plane of the FRS.

An additional detector system is proposed to improve the measurements of the primary and secondary vertex. The primary vertex corresponds to the initial interaction point between the beam and the target, where the nuclear collision happens. The secondary vertexes correspond to the weak decay of produced hyperons or hypernuclei that will occur behind the target area thanks to their respective Lorentz boost. The purpose of creating such a detection system is to improve the hypernuclear identification by a more precise vertex position measurement. By improving the decay vertex position determination, the lifetime of the hypernucleus of interest will be improved twofold, by increasing the purity of the hypernuclear identification and the position precision. The concept considered for such a device is to use four stations of thin silicon trackers as micro vertex detector. The detector stations will be placed few centimetres behind the target area where particles and fragments from the mid-rapidity and the projectile rapidity are expected to be measured.

The optimization of the design of the detector is based on Monte Carlo simulations that includes the nuclear interactions, the radiation rate and the particle-matter interactions; it has been achieved within the GEANT4 simulation framework. The holding structure of the detector was designed by means of SolidWorks. The design of the mechanical structure of a double-sided silicon strip tracking system was accomplished in collaboration with members of the research group COMES of the university of Castilla-La Mancha.

A light structure with low cross sections was designed to accommodate the silicon tracker planes with a pitch of 1 cm. Light and rigid material for the support was selected for minimizing the possible interaction with the outgoing particles. A schematic view of the final design is shown in Figure 1. Industrial production of the holding structure has been considered and the plan for manufacturing of the different pieces and the procedure for their assembly have been studied and reported.

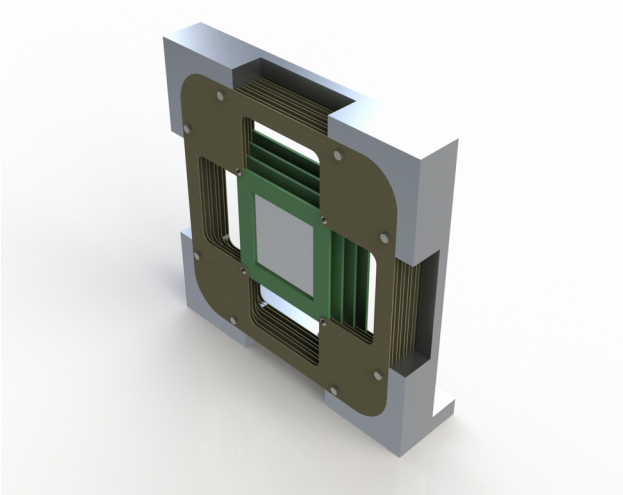


Figure 1: Assembly view of the mechanical holding structure of a double-sided silicon strip detector system. The silicon trackers are silver and green plates. The overall dimensions of the holding structure are 32 cm x 32 cm x 4 cm. The brown plates are made on a fibre-reinforced-polymer based composite. Its low density is optimal for minimizing nuclear interaction. The external frame is made of aluminium for its mechanical properties and light mass.

References

[1] C. Rappold *et al.*, Nucl. Phys. A **913**, 170 (2013).
[2] C. Rappold *et al.*, Phys. Rev. C **88**, 041001 (2013).
[3] C. Rappold *et al.*, Phys. Lett. B **747**, 129 (2015).

Experiment beamline: FRS
Experiment collaboration: NUSTAR-SuperFRS-Experiments / HypHI
Experiment proposal: S447
Accelerator infrastructure: SIS18
Grants: co-funded program of the University of Castilla-La Mancha “Ayudas para estancias de investigadores invitados en la UCLM para el año 2017” and FEDER 2014-2020.
Strategic university co-operation with: JLU - Giessen

 DOI:10.15120/GR-2018-1

Λ hyperon reconstruction using the WASA cylindrical detector system for the FAIR-Phase 0 hypernuclear experiment S447

C. Rappold[1,2], T. Saito[1], C. Scheidenberger[1,2]

[1]GSI, Darmstadt, Germany;[2]Justus-Liebig-Universität Giessen, Germany

For the FAIR-Phase 0, the accepted experiment S447, has proposed to assess the existence of the nnΛ possible bound state. This experiment will be performed at the fragment separator FRS with the WASA central detector. The WASA central detector will be moved from COSY, Juelich, and installed in the S2 area of the FRS.

In addition to the measurement of the nnΛ bound state, $^{3}_{\Lambda}$H and $^{4}_{\Lambda}$H will be measured in order to demonstrate the efficiency of the novel experimental setup, combining a solenoid magnet for the detection of light hadrons from the mid- and forward rapidity and the S2-S4 forward spectrometer of FRS for the precise measurement of the forward decay fragments: d, ^{3}He and ^{4}He from the hypernuclear decay [1, 2].

The performance of the reconstruction and calibration of the magnetic field, tracking detectors and reconstruction algorithms will need an independent physical probe of the FRS setup. For this purpose, the reconstruction of the Λ hyperon within the WASA central detection system will be crucial.

In the heavy ion collisions, the Λ hyperon is produced in the mid-rapidity of the collision. Part of the mid-rapidity phase-space overlaps with the forward rapidity, inducing some Λ hyperons to be forward-Lorentz boosted. With the WASA central detection system placed 1 meter behind the hypernuclear production target, the Λ hyperon can be reconstructed from its decay particules, $\Lambda \rightarrow p + \pi^-$.

A detailed GEANT4 simulation of this specific production and decay has been performed. The analysis of the simulated events involved the analysis framework developed for the future experiment. Track reconstruction, particle identification and vertex reconstruction was realistically performed, including realistic position and time resolution. The differential acceptance efficiencies for the decay proton and π^- is shown in Fig. 1, with an overall acceptance efficiency of 61% and 57% for π^- and proton, respectively. The resulting Λ event reconstruction is shown in Fig 2. The invariant mass resolution is about 3.6 MeV.

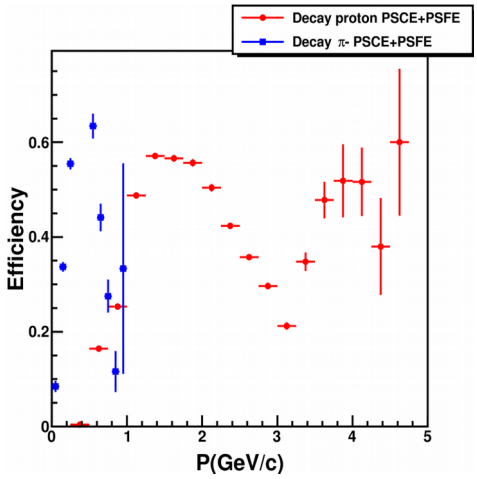


Figure 1: Differential acceptance efficiency for the decay π^- (blue) and proton (red) as a function of its momentum from Λ hyperon within the central plastic barrel, PSCE, and plastic hodoscope wall, PSFE, of the WASA central detector.

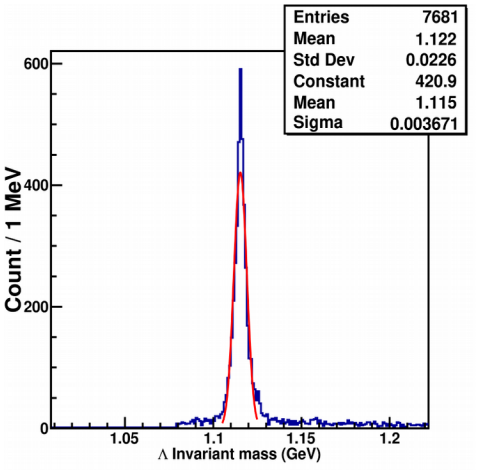


Figure 2: Invariant mass reconstruction of Λ hyperon from the decay $\Lambda \rightarrow p+\pi^-$ within the WASA central detection system. The invariant mass resolution is about 3.6 MeV.

References

[1] C. Rappold *et al.*, GSI Scientific Report 2016 [GSI Report 2017-1] (2017) p. 177.

[2] C. Rappold *et al.*, GSI Scientific Report 2016 [GSI Report 2017-1] (2017) p. 178.

Experiment beamline: FRS

Experiment collaboration: NUSTAR-SuperFRS-Experiments / HypHI

Experiment proposal: S447

Accelerator infrastructure: SIS18

Strategic university co-operation with: JLU - Giessen

Status of the FRS Ion Catcher

W. R. Plaß[1,2], T. Dickel[1,2], D. Amanbayev[1], S. Ayet[1,2], J. Äystö[3], D. Balabanski[4], S. Beck[1,2], J. Bergmann[1], O. Cheriviakova[5], P. Constantin[4], T. Eronen[6], H.Geissel[1,2], T. Grahn[6], F. Greiner[1], E. Haettner[2], C. Hornung[1], J.-P. Hucka[2], A. Jokinen[6], A. Kankainen[6], I. Mardor[7,8], I.Miskun[1,2], I. Moore[6], S. Pietri[2], A. Pikthtelev[9] , I. Pohjalainen[6], S. Purushothaman[2], Z. Patyk[5], M. P. Reiter[1,2,10], A.-K. Rink[1], S. Rinta-Antila[6], C. Scheidenberger[1,2], A. Spataru[4], H. Weick[2], J. Winfield[2], M. Yavor[11] for the Super-FRS experiment collaboration

[1]JLU, Gießen, Germany; [2]GSI, Darmstadt, Germany; [3]Helsinki Institute of Physics, Helsinki, Finland; [4]IFIN-HH/ELI-NP, Magurele, Romania; [5]National Centre for Nucl. Res., Warszawa, Poland; [6]University of Jyväskylä, Jyväskylä, Finland; [7]TAU, Tel-Aviv, Israel; [8]Soreq NRC, Yavne, Israel; [9]BINEP, RAS, Chernogolovka, Russia; [10]TRIUMF, Vancouver, Canada; [11]Institute for Analytical Instrum., RAS, St. Petersburg, Russia

At the FRS Ion Catcher [1] precision experiments with thermalized exotic nuclei can be performed. The fragments are produced by projectile fragmentation or fission at relativistic energies, separated in-flight and energy-bunched in the FRS [2]. With the FRS Ion Catcher (figure 1) these fragments are then slowed down and thermalized in a cryogenic stopping cell (CSC) [3]. A multiple-reflection time-of-flight mass spectrometer (MR-TOF-MS) is used to perform direct mass measurements and to provide an isobarically clean beam for further experiments, such as mass-selected decay spectroscopy [4]. A versatile RF quadrupole transport and diagnostics unit guides the ions from the CSC to the MR-TOF-MS, provides differential pumping, ion identification and includes reference ion sources. The FRS Ion Catcher serves as a test facility for the Low-Energy Branch (LEB) of the Super-FRS and already now enables a variety of new precision experiments in FAIR Phase-0.

The FRS Ion Catcher has been commissioned and its components have been characterized. For the first time, a stopping cell for exotic nuclei was operated on-line at cryogenic temperatures. Using a gas density almost three times higher than ever reached before for a stopping cell with RF ion repelling structures, various ^{238}U projectile and fission fragments were thermalized and extracted with very high efficiency. A combined ion stopping, survival and extraction efficiency of up to 30% and an extraction time of about 25 ms have been measured [5]. The rate capability of the CSC has been investigated [6]. Direct mass measurements of several short-lived fragments (e.g. ^{220}Ra with a half-life of 17.8 ms) have been performed with the MR-TOF-MS. In total for more than 40 short-lived nuclei the ground state masses have been determined and 15 isomeric states have been measured. A data evaluation procedure for MR-TOF-MS data has been developed that allows achieving high accuracies even for low statistics and overlapping peaks. As a part of this work a new mathematical function has been developed to describe the peak shapes in MR-TOF-MS spectra [7]. The error budget of the measurement with the MR-TOF-MS has been made. Mass accuracies down to 10^{-7} have been achieved. Furthermore, the FRS Ion Catcher is the ideal device to search for long lived isomers (> 10 ms), because it is universal, i.e. element and decay mode independent, faster than other mass spectrometry techniques (e.g. SMS, TOF-ICR), very sensitive (non-scanning), has high mass resolving power (>> 10^5), high dynamic range (> 10:1) and is broadband in nature, i.e. can measure all isobars and isomers of several mass units in parallel. Moreover, the isomers can be spatially separated from the ground state and an isomerically clean beam can be provided to experiments, such as decay spectroscopy [8].

In an experiment in 2016 the integration of the Ion Catcher in the FRS DAQ has been started [9]. The aim of this work is to make the data from the FRS Ion Catcher available as a part of the standard FRS particle identification (PID). This enables the use of the system as a mass tagger [10] for the FRS PID or to use high-accuracy mass measurement as the only information for PID, instead of the standard PID [11]. This has been successfully tested even under challenging conditions (with fission and projectile fragments with Z > 70 produced at a primary beam energy of 300 MeV/u). Furthermore the operation of the CSC with argon as stopping gas has been investigated and first tests to use the stopping gas as a reaction target for fusion studies were performed [12].

Recently, the FRS Ion Catcher has been upgraded in several aspects. In particular, (i) in the CSC the electrode structure and the connections have been revised to increase the operational reliability and to allow for higher extraction field strengths and thus shorter extraction times. (ii) A new pre-pump allows operation of the turbo-molecular pumps on the RFQ beamline (first differential pumping stage after the CSC) at higher pressures. (iii) An extension of the RFQ beamline has been developed and commissioned [13]. (ii) and (iii) in combination will allow the operation (for heavy ions) of the CSC at higher areal densities up to 10 mg/cm².

The FRS Ion Catcher is part of four approved experiment proposals for FAIR Phase-0. These experiments cover a wide variety of nuclear physics questions, from detector tests and novel concepts for higher yields (very thick targets) [14] over mass measurements in different regions of the nuclear chart (N=126 [15] and N=Z [14]) to reaction studies on multi-nucleon transfer [16] and measurements of beta-delayed neutron emission probabilities [17]. These experiments will make use of recently developed new ion optical modes of the FRS, that will allow higher transmission and FRS performance tailor-made for these experiments [18].

 DOI:10.15120/GR-2018-1

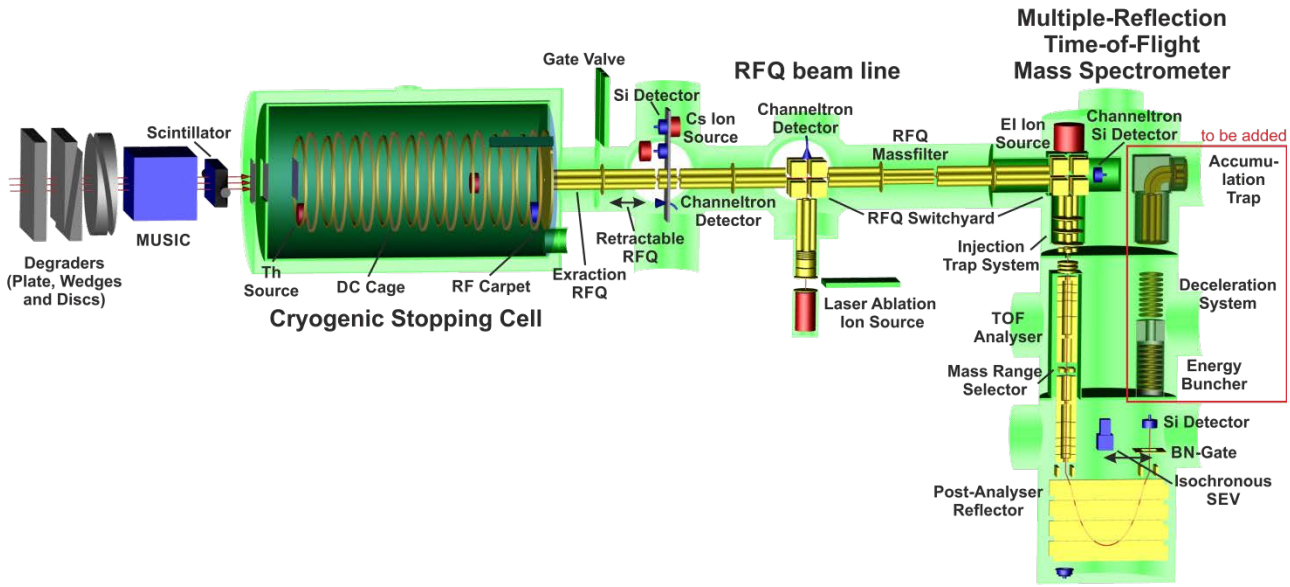


Figure 1: Schematic view of the setup of the FRS Ion Catcher at the final focal plane of the FRS. The beam enters the setup from the FRS from the left and passes the detectors for the PID of the FRS and the variable degrader to adjust the range of the ions. Then the ions are thermalized in the CSC, extracted and transmitted through the RF quadrupole transport and diagnostics unit to the MR-TOF-MS.

For the LEB of the Super-FRS a new **H**igh **A**real **D**ensity **O**rthogonal extraction CSC (HADO-CSC) is under development [19,20]. It will feature significantly improved performance characteristics, including higher rate capability, stopping efficiencies and active area, matching the requirements for beams at the LEB. The LEB stopping cell will be a key device for the research with thermalized projectile and fission fragments that will be performed with the experiments MATS and LaSpec [21]. The development and operation of the stopping cells of the FRS Ion Catcher and of the LEB are performed in the context of the Super-FRS Experiment Collaboration. The HADO-CSC is also the basis for the development of stopping cells at ELI-NP [22] and SARAF [23].

The MR-TOF-MS will be part of MATS and perform mass measurements of very short-lived and rare nuclei complementary to measurements with the Penning trap system of MATS. At the same time it can be operated as isobar and isomer separator for MATS and LaSpec, and it will be an essential tool to perform diagnostics and PID at the LEB. The MR-TOF-MS has been the basis for spin-off developments for analytical mass spectrometry [24] and a system for the TITAN experiment at the ISOL facility ISAC at TRIUMF [25].

References

[1] W.R. Plaß et al., NIM B 317 (2013) 457.
[2] H. Geissel et al., NIM B 70 (1992) 286.
[3] M. Ranjan et al., NIM A 770 (2015) 87.
[4] T. Dickel et al., NIM A 777 (2015) 172.
[5] S. Purushothaman et al., EPL 104 (2013) 42001.
[6] M.P. Reiter et al., NIM B 376 (2016) 240.
[7] S. Purushothaman et al., IJMS 421 (2017) 245.
[8] T. Dickel et al., PLB 744 (2015) 137.
[9] E. Haettner et. al., this issue.
[10] M.P. Reiter, PhD thesis, JLU Gießen (2015).
[11] C. Hornung et al., GSI Sci. Rep. 2016 (2017) 175.
[12] I. Miskun et al., this issue.
[13] C. Hornung et al., this issue.
[14] W.R. Plaß et al., this issue.
[15] S. Pietri et al., this issue.
[16] T. Dickel et al., this issue.
[17] I. Mardor et al., this issue.
[18] E. Haettner et al., this issue.
[19] D. Amanbayev et al., this issue.
[20] T. Dickel et al., NIM B 376 (2016) 216.
[21] D. Rodriguez et al., EPJ Special Topics 183 (2010) 1.
[22] D. L. Balabanski et al., Rom. Rep. Phys. 68 (2016) 621.
[23] I. Mardor et al., arXiv:1801.06493v2.
[24] T. Dickel et al., NIM B 317 (2013) 779.
[25] M.P. Reiter et al., this issue.

Experiment beamline: FRS
Experiment collaboration:
NUSTAR-Super-FRS-Experiments / FRS Ion Catcher
Experiment proposal: S411, S468, S472, S474, S475
Accelerator infrastructure: SIS18
PSP codes: 1.2.1.2; 1.2.3.13; 2.4.11.2.7; 2.4.11.2.8
Grants: BMBF (05P12RGFN8, 05P16RGFN1), HMWK (LOEWE Center HICforFAIR), HGS-HIRe, Helmholtz Association of German Research Centers (NAVI VH-VI-417)
Strategic university co-operation with: Gießen

Reaction studies with the FRS Ion Catcher: A novel approach and universal method for the production, identification of and experiments with unstable isotopes produced in multi-nucleon transfer reactions with stable and unstable beams

T. Dickel[1,2], P. Constantin[3], J. S. Winfield[2], S. Ayet[1,2], S. Bagchi[1,2,4], D. Balabanski[3], S. Beck[1,2], H. Geissel[1,2], F. Greiner[1], E. Haettner[2], S. Heinz[1,2], C. Hornung[1], A. Kankainen[5], A. Karpov[6], D. Kostyleva[1,2], N. Kuzminchuk[2], B. Kindler[2], B. Lommel[2], I. Mardor[7,8], I. Miskun[1], I. Mukha[2], G. Münzenberg[2], S. Pietri[2], Z. Patyk[9], G. Martinez-Pinedo[10], W. Plaß[1,2], A. Prochazka[1], S. Purushothaman[2], C. Rappold[1,2], V. Saiko[6], T. Saito[2,11,12], C. Scheidenberger[1,2], Y. Tanaka[1,2], H. Weick[2] and the Super-FRS experiment collaboration

[1]JLU, Gießen, Germany; [2]GSI, Darmstadt, Germany; [3]IFIN-HH/ELI-NP, Magurele, Romania; [4]Saint Mary's University, Canada; [5]University of Jyväskylä, Jyväskylä, Finland; [6]JINR, Dubna, Russia; [7]TAU, Tel-Aviv, Israel; [8]Soreq NRC, Yavne, Israel; [9]National Centre for Nucl. Res., Warszawa, Poland; [10]TU Darmstadt, Darmstadt, Germany; [11]Helmholtz Institut Mainz, Mainz, Germany; [12]Iwate University Morioka, Japan

Experiments with radioactive ion beams at Coulomb-barrier energies represent a new field for reaction studies which will contribute to a better understanding of multi-nucleon transfer, deep inelastic, fusion-fission and complete fusion reactions. One of the main goals of these experiments is to access new neutron-rich heavy and super heavy isotopes, not reachable in fission or fragmentation reactions [1].

Slowed-down rare ion beams of all chemical elements, including refractory elements, independent of their chemical properties, are available at the FRS and Super-FRS. Their optimum use requires a new philosophy for experiments and instrumentation [2]. For instance multi-nucleon transfer (MNT) reactions inside the cryogenic stopping cell (CSC) of the FRS Ion Catcher is a unique and novel method that is very sensitive, clean, universal and has a high angular acceptance for the reaction products. It is planned to mount targets (e.g., Dy, Pt, U) on a wheel will be installed in the stopping volume of the CSC. The identification and quantification of the reaction products will be performed by a high resolution and broadband mass spectrometer, which allows to identify the reaction products completely by their mass-to-charge ratio. This will pave the way for broad range measurements with primary and secondary beams. The concept is based on the uniqueness of the beams and experimental setups of GSI/FAIR and their combination.

In a first experiment we will perform MNT reaction studies with a 500 MeV/u ^{238}U primary beam slowed-down to Coulomb barrier energies impinging on different targets. We expect to measure in 12 approved shifts more than 150 cross sections (figure 1) and 15 new masses of neutron-rich isotopes. The cross-sections will be used to benchmark reaction models. The proposed nuclei are important for the rare earth abundance peak in the r-process as well as for the understanding the properties of fissioning nuclei involved in the r-process.

This is the first step towards future broad range reaction studies with secondary beams at the (LEB of the Super-)FRS.

References

[1] V. Zagrebaev and W. Greiner, PRL 101, 2–5 (2008).
[2] G. Münzenberg et al., EXON-2014 Proc. (2014).
[3] A.V. Karpov, et al PRC 96 (2017) 024618.

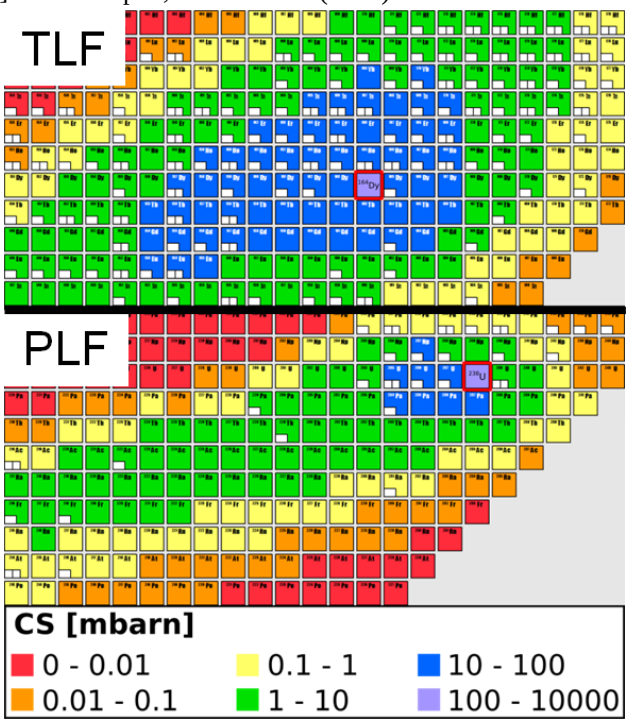


Figure 1: Calculated production cross-sections [3] for ^{238}U on ^{164}Dy. Upper panel: target-like fragments (TLF); lower panel: projectile-like fragments (PLF). The estimated sensitivity limit will be about 0.1 mbarn.

Experiment beamline: FRS
Experiment collaboration:
NUSTAR-SuperFRS-Experiments / FRS Ion Catcher
Experiment proposal: S475
Accelerator infrastructure: SIS18
PSP codes: none
Grants: BMBF (05P12RGFN8 & 05P16RGFN1), HMWK (LOEWE Center HICforFAIR), HGS-HIRe
Strategic university co-operation with: Gießen

 DOI:10.15120/GR-2018-1

Investigation of fusion in inverse kinematics with a target in the cryogenic stopping cell

I.Miskun[1], T. Dickel[1,2], S. Ayet[1,2], S. Bagchi[1,2,3], J. Bergmann[1], J.Ebert[1], A.Finley[4,5], H.Geissel[1,2], F. Greiner[1], E. Haettner[2], C. Hornung[1], S. Kaur[3], W. Lippert[1], J.-H. Otto[1], S. Pietri[2], W. R. Plaß[1,2], S. Purushothaman[2], A.-K. Rink[1], C. Scheidenberger[1,2], Y. Tanaka[1,2], H. Weick[2], J. S. Winfield[2], the FRS Ion Catcher collaboration and for the Super-FRS experiment collaboration

[1]Justus-Liebig-University of Giessen, Giessen, Germany; [2]GSI, Darmstadt, Germany; [3]Saint Mary's University, Canada; [4]TRIUMF, Vancouver, Canada; [5]UBC, Vancouver, Canada

Radioactive ion beams at Coulomb barrier energies will open a wide field for the study of deep-inelastic reactions of heavy nuclei and their application for the synthesis of new exotic heavy and super-heavy nuclei [1]. The slowing-down of heavy-ion fragment beams from relativistic production energies to near Coulomb barrier energies has been done for many years for the stopping cell experiments and tests [2] at the FRS [3].

In experiments with the FRS Ion Catcher secondary beams are stopped inside the cryogenic stopping cell (CSC), extracted and their properties are measured. If a thin reaction target is installed in the CSC and the energy of the secondary beams is adjusted to be close to the Coulomb barrier, fusion products will be generated, which can be stopped, measured and identified with the MR-TOF-MS of the FRS Ion Catcher. Also, the stopping gas itself can be used as reaction target. This is of special interest if heavier noble gases (e.g. argon) are used. This allows the study of fusion reactions in inverse kinematics with low intensity beams (e.g., exotic secondary beams) and high sensitivity. The advantages of inverse kinematics are (i) that the range distribution of the impinging beam is small, so the products will be produced over a narrow depth in the target and (ii) the range of the products is larger, which allows the release over a wider depth of the target. Because of these effects the effective target thickness is much larger, especially for secondary beams, in inverse than in normal kinematics reactions. (iii) For a given areal weight, the target has more reaction centers in inverse kinematics than a target in normal kinematics, since in inverse kinematics the mass number of the target atoms is smaller. If the stopping gas itself is used as a target these advantages are maximized, because one can have very thick targets for fusion reactions (~10 mg/cm²), while having 100% release efficiency from the target. The disadvantages of this concept are the need for very high density stopping cells and the limitation in the available targets/stopping gases, He, Ne, Ar and maybe carbon (methane). For heavier gases the repelling RF electrode structure (RF-carpet), which ensure high efficient ion extraction from the stopping gas, will not work. The CSC was operated with up to 20 mg/cm² neon [2].

Here we report the first tests with more than 10 mg/cm² argon (figure 1). One can see that the extraction efficiency was limited by the available RF carpet electronics. A first test under this non-optimal conditions was done, in an experiment with the FRS in 2016. For this experiment a natural titanium target was installed inside the CSC and the CSC was operated with argon as stopping gas (13 mg/cm²).

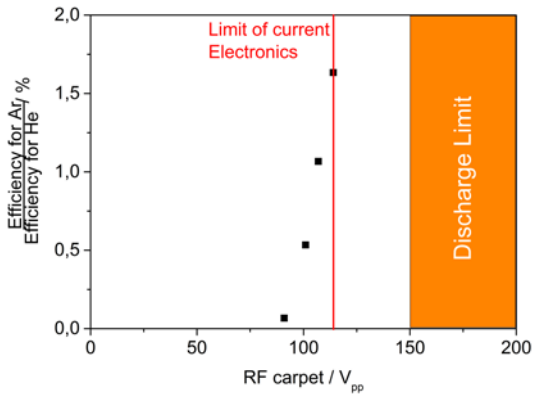


Figure 1: Measured relative extraction efficiency for $^{220}Rn^{+}$ vs. RF voltage on the RF carpet for argon as stopping gas (12 mg/cm²) as compared to operation of the CSC with helium.

A primary beam of $2 \cdot 10^5$ ^{124}Xe/spill with 600 MeV/u was transported to the CSC and slowed down to Coulomb barrier energies in the target and stopping gas. The search for fusion products in the mass spectra was not conclusive. However, it was demonstrated that under the conditions of the experiment the background is very low, such that in the future 10 detected fusion products will be sufficient for an unambiguous identification. An upgraded RF carpet electronics has been developed and is now ready to overcome the limits of past experiments.

In FAIR phase 0 an experiment built on these results has been approved by the G-PAC and will focus on multi-nucleon transfer reactions [4].

References

[1] W. Loveland, Phys. Rev. C 76 (2007) 014612
[2] P. Reiter, PhD JLU Giessen (2015).
[3] H. Geissel et al., NIM B 70 (1992) 286
[4] T. Dickel et al., this issue

Experiment beamline: FRS
Experiment collaboration:
NUSTAR-SuperFRS-Experiments / FRS Ion Catcher
Experiment proposal: S475
Accelerator infrastructure: SIS18
PSP codes: none
Grants: BMBF (05P12RGFN8 & 05P16RGFN1), HMWK (LOEWE Center HICforFAIR), HGS-HIRe
Strategic university co-operation with: Gießen

A novel method for measuring β-delayed neutron emission

I. Mardor[1,2], T. Dickel[3,4], S. Ayet[3], S. Bagchi[5,3,4], S. Beck[3,4], H. Geissel[3,4], F. Greiner[4], E. Haettner[3], C. Hornung[4], D. Kostyleva[3,4], N. Kuzminchuk[3], B. Kindler[3], B. Lommel[3], G. Martínez-Pinedo[6], I. Miskun[4], I. Mukha[3], E. Piasetzky[1], S. Pietri[3], W. R. Plaß[3,4], I. Pomerantz[1], A. Prochazka[3], S. Purushothaman[3], C. Rappold[3,4], T. Saito[3,7,8], C. Scheidenberger[3,4], Y. Tanaka[3,4], H. Weick[3], J. S. Winfield[3], and the Super-FRS Experiment Collaboration

[1]Tel Aviv University, Tel Aviv, Israel, [2]Soreq NRC, Yavne, Israel, [3]GSI, Darmstadt, Germany, [4]Justus-Liebig-Universität, Gießen, Germany, [5]Saint Mary's University, Halifax, NS, Canada, [6]Technische Universität Darmstadt, Darmstadt, Germany, [7]Helmholtz Institute Mainz, Mainz, Germany, [8]Iwate University, Morioka, Japan

β-delayed single- or multi-neutron emission is possible when a mother nucleus β-decay Q-value (Q_b) is larger than the daughter nucleus one- or x-neutron separation energy (S_{1n} or S_{xn}). The probability for β-delayed neutron emission (P_{xn} for x emitted neutrons) increases with neutron number per isotope. Measured P_{xn} values provide important input to the astrophysical r-process, nuclear structure models, and control of nuclear reactors [1].

P_{xn} data is scarce, especially for multi-neutron emission. For present and near-future accessible isotopes, less than 10% of multi-neutron emission candidates have been measured [2]. Moreover, in the fission-product region, the most relevant for the r-process and nuclear reactors, there is published P_{2n} data for only four nuclides.

Therefore, there are several world-wide campaigns to bridge this data gap, mostly by counting β-delayed emission n-β coincidence events [3]. In this method, efficiency decreases with x (higher number of coincident neutrons), β and n detector efficiencies depend on prior energy spectra measurements or models, and the measurement includes neutron background from the beam and cosmic rays. Other proposed methods count the recoil nuclides via gamma spectra [4], time-of-flight [5], or mass measurements, in a series of stopping cells and MR-TOF-MSs (RIKEN) [6], or in the ESR (GSI) [7]. These methods are less efficient and/or prone to systematic errors, especially for multi-neutron emission.

Given the above, we propose a complementary and independent method for measuring P_{xn} at the FRS Ion Catcher, which circumvents the drawbacks of existing methods [8]. Obtain separated isotopes with the FRS, contain them in the Cryogenic Stopping Cell (CSC) for periods long enough for decay, and identify and count the precursor and recoil isotopes with the Multiple-Reflection Time-of-Flight Mass-Spectrometer (MR-TOF-MS).

The required n-rich isotopes will be produced via in-flight fission of ^{238}U primary beam from the SIS18. The areal density of the CSC (10 mg/cm^2) provides another separation stage, ensuring that only the required precursors are stopped in it.

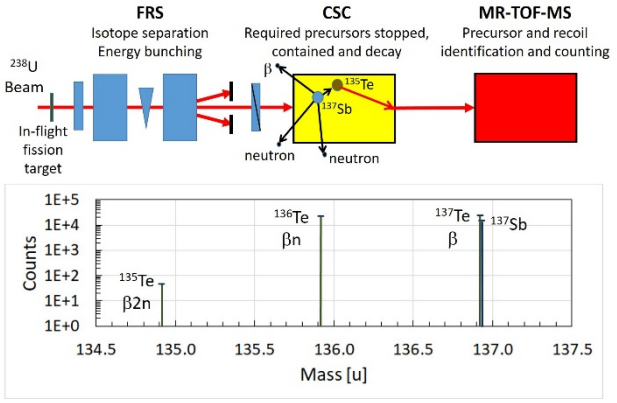


Figure 1: Top - Scheme of the proposed method. A β2n decay of ^{137}Sb in the CSC is depicted. Bottom - expected spectrum in the MR-TOF-MS, when containing the precursors in the CSC for two ^{137}Sb half-lives.

For P_{xn} extraction, the masses of the precursor and all recoils are measured simultaneously at the MR-TOF-MS with accuracy that enables their unambiguous identification. Ratios between the recoil isotopes infer P_{xn} for all x (x=0 is regular β-decay) (Fig. 1). Concurrently, the method will provide measurements of mass, Q-values (precursor-recoil mass difference) and half-lives (precursor to all recoils ratio). The method has the same efficiency for all x, is independent of nuclear models, has practically no background, and is sensitive to isomers.

The proposal has been approved for FAIR Phase-0, pending beam availability. First planned measurements are of P_{xn} of $^{135\text{-}137}$Sb and ^{142}I, the heaviest and highest Z β2n precursor measured yet, setting the stage for a survey of β-delayed neutron emission, including the N~126 region.

References

[1] M.R. Mumpower et al., PRC 94, 064317 (2016)
[2] I. Dillmann et al., AIP Conf. Proc. 332, 1594 (2014)
[3] A. Tarifeño-Saldivia et al., JINST 12 P04006 (2017)
[4] J. A. Winger et al., PRL 102, 142502 (2009)
[5] R. M. Yee et al., PRL 110, 092501 (2013)
[6] P. Schury, Fragment Separator Expert Meeting, Grand Rapids (2016)
[7] A. Evdokimov et al., PoS (NIC XII) 115 (2012)
[8] I. Mardor et al., NUSTAR Week 2017, Ljubljana, (2017)

Experiment beamline: FRS
Experiment collaboration: NUSTAR-SuperFRS-Experiments / FRS Ion Catcher
Experiment proposal: S472
Accelerator infrastructure: SIS18
PSP codes: none
Grants: BMBF (05P12RGFN8 & 05P16RGFN1), HMWK (LOEWE Center HICforFAIR), HGS-HIRe, Israel Ministry of Energy Research Grant
Strategic university co-operation with: Gießen

 DOI:10.15120/GR-2018-1

Detector tests with the prototype CSC for the Super-FRS and direct mass measurements of neutron-deficient nuclides below ^{100}Sn in FAIR Phase-0

W. R. Plaß[1,2], T. Dickel[1,2], S. Ayet San Andrés[1,2], S. Bagchi[1,2,3], S. Beck[1,2], P. Constantin[4], T. Eronen[5], H. Geissel[1,2], F. Greiner[1], E. Haettner[2], C. Hornung[1], A. Jokinen[5], A. Kankainen[5], B. Kindler[2], D. Kostyleva[1,2], N. Kuzminchuk[2], B. Lommel[2], I. Mardor[6,7], I. Miskun[1], I. D. Moore[5], I. Mukha[2], Z. Patyk[8], S. Pietri[2], A. Prochazka[2], S. Purushothaman[2], C. Rappold[1,2], S. Rinta-Antila[4], T. Saito[2,9,10], C. Scheidenberger[1,2], Y. Tanaka[1,2], H. Weick[2], J. S. Winfield[2], J. Äystö[11], and the Super-FRS Experiment Collaboration

[1]Justus-Liebig-Universität Gießen, Germany; [2]GSI, Darmstadt, Germany; [3]St Mary's University, Halifax, Canada; [4]IFIN-HH / ELI-NP, Magurele, Romania; [5]University of Jyväskylä, Jyväskylä, Finland; [6]Tel Aviv University, Israel; [7]Soreq NRC, Yavne, Israel; [8]National Centre for Nucl. Res., Warszawa, Poland; [9]Helmholtz Institute Mainz, Germany; [10]Iwate University Morioka, Japan; [11]Helsinki Institute of Physics, Helsinki, Finland

In the context of the experiment proposal S474, detector tests with the prototype of the cryogenic stopping cell (CSC) for the Low Energy Branch (LEB) of the Super-FRS and direct mass measurements will be performed at the FRS with the FRS Ion Catcher [1] in FAIR Phase-0. The detector tests include (i) the commissioning of the CSC with an areal density of 10 mg/cm^2 and with higher DC fields (doubling the stopping efficiency and reducing the extraction time), (ii) the on-line test of the pumping and He recycling unit and the gas purification techniques to be used with the LEB stopping cell, (iii) the control of charge states of ions thermalized in the CSC for increased stopping and extraction efficiencies of multiply-charged ions, (iv) the on-line commissioning of the upgrade of the RFQ beamline of the FRS Ion Catcher [2], (v) the test of the new large aperture precision degrader system and the scintillator for the Super-FRS Ion Catcher and (vi) the integration of the FRS Ion Catcher in the FRS data acquisition system. In addition the use of a very thick target (>>4 g/cm^2; d/R>0.5 where d is the thickness and R the range) will be investigated, which should increase yields by multi-step fragmentation reactions and enable access to more exotic nuclides at the FRS Ion Catcher and the LEB of the Super-FRS [3].

After many years of R&D and tests, direct mass measurements of rare neutron-deficient nuclides under challenging realistic conditions can be performed and shall demonstrate the overall performance of the system. Projectile fragments in the range from Zr to Rh produced by projectile fragmentation of ^{124}Xe and ^{107}Ag are ideal to perform these measurements. They are refractive and can therefore be ideally produced and separated in-flight. Furthermore, depending on the ionization potentials of the various elements, the ions are expected to be thermalized in different charge states (+1 and +2). The controlled manipulation of charge states can thus be tested with these fragments. The mass measurements aim at N=Z and N=Z+1 nuclides in the element range from Y to Ag and will provide experimental mass values for many of these nuclides for the first time (Fig. 1). These nuclides are of high interest because of their impact on the rp process, isospin symmetry as well as pairing and the Wigner energy, the region of nuclear deformation in the vicinity of ^{80}Zr [4], and the high-spin isomer in ^{94}Ag [5,6].

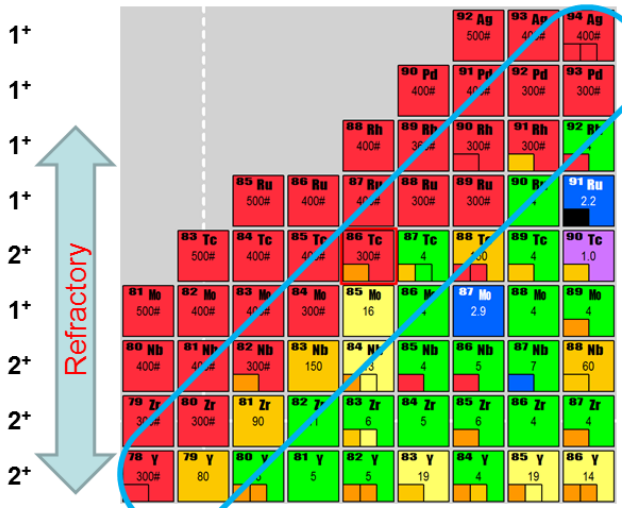


Figure 1: Section of the chart of the nuclides showing the region of interest for the experiment proposal and the uncertainty of mass values in the elemental range from Y to Ag (in keV). For nuclides shown in red the mass has not been measured yet [7]. Left: Expected charge states of the ions extracted from the CSC and range of refractory elements in this region.

References

[1] W.R. Plaß et al., Nucl. Instrum. Methods B 317 (2013) 457.
[2] C. Hornung et al., this issue.
[3] E. Haettner et al., this issue.
[4] C. J. Lister et al., Phys. Rev. Lett. 59 (1987) 1270.
[5] I. Mukha et al., Nature 439 (2006) 298.
[6] A. Kankainen et al., PRL 101, (2008) 142503.
[7] M. Wang et al., Chin. Phys. C 41 (2017) 030003.

Experiment beamline: FRS
Experiment collaboration: NUSTAR-Super-FRS-Experiments / FRS Ion Catcher
Experiment proposal: S474
Accelerator infrastructure: SIS18
PSP codes: 1.2.1.2; 1.2.3.13; 2.4.11.2.7; 2.4.11.2.8
Grants: BMBF (contract No. 05P16RGFN1), HMWK (LOEWE Center HICforFAIR), HGS-HIRe
Strategic university co-operation with: Gießen

An upgrade to the RFQ beam line of the FRS Ion Catcher

C. Hornung[1], D. Amanbayev[1], S. Ayet[1,2], J. Bergmann[1], T. Dickel[2], H. Geissel[1,2], F. Greiner[1], L. Gröf [1], W. R. Plaß[1,2], A.-K. Rink[1], and C. Scheidenberger[1,2]

[1]JLU, Gießen, Germany; [2]GSI, Darmstadt, Germany

At the FRS Ion Catcher the cryogenic stopping cell (CSC) and the MR-TOF-MS are connected via an RFQ beam line. To achieve highest mass accuracies with the MR-TOF-MS it is necessary to have calibrant ions over a broad mass range at a high repetition rate (≈ 100 Hz) in order to match the repetition rate of the MR-TOF-MS. These requirements can be fulfilled by the laser ablation carbon cluster ion source (LACCI) [1], which is a part of the upgrade of the RFQ beam line [2] of the FRS Ion Catcher. An overview of the FRS Ion Catcher setup including main features of the RFQ beam line is shown in fig. 1.

LACCI is equipped with a x-y-movable target table, which enables a fast (≈ s) change of targets and a permanent 2D movement of the targets during ion production. In the 2D movement the targets are scanned by a horizontal and vertical meander, in which the step size and the velocity can be adjusted. This allows long-term stable operation (>10 hours), even at high repetition rates (≈ 100 Hz, two orders of magnitude higher than with systems used at other facilities world-wide). A first proof-of-principle demonstrating the long-term stability of LACCI is shown in fig. 2 for erbium ions.

In order to couple LACCI to the existing RFQ beam line an RFQ based switchyard [3] is used. An RFQ switchyard is a novel device which acts like six gas-filled RFQs leading away from a central point along three perpendicular axes. Modes with input or output along multiple axes at once are possible, allowing for beam splitting or merging, and switching between input/output configurations during operation.

The upgrade of the RFQ beam line improves differential pumping between the CSC and the MR-TOF-MS. This will enable a higher helium gas pressure in the CSC, while keeping the pressure in the MR-TOF-MS low, to avoid collisional losses during the TOF measurement. A decoupling of the pressure in the CSC and the MR-TOF-MS enables to operate the MR-TOF-MS with optimum performance even with the highest pressure in the CSC.

A dedicated RFQ mass filter will be added to the existing beam line. The expected mass resolution (<1 u) will be high enough to perform a pre-separation of ions accordingly to their mass numbers in the beam line in front of the MR-TOF-MS. The extension of the RFQ beam line also enables an improved operation of the collision induced dissociation inside the RFQ beam line [4], by including several activation stages. This provides a higher suppression of molecular background.

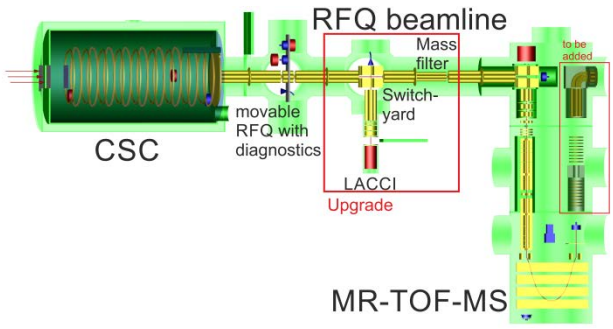


Figure 1: Schematic view of the FRS Ion Catcher with the CSC, the upgraded RFQ based beam line, including diagnostics tools, LACCI, a dedicated RFQ mass filter, and the MR-TOF-MS (from the left to the right).

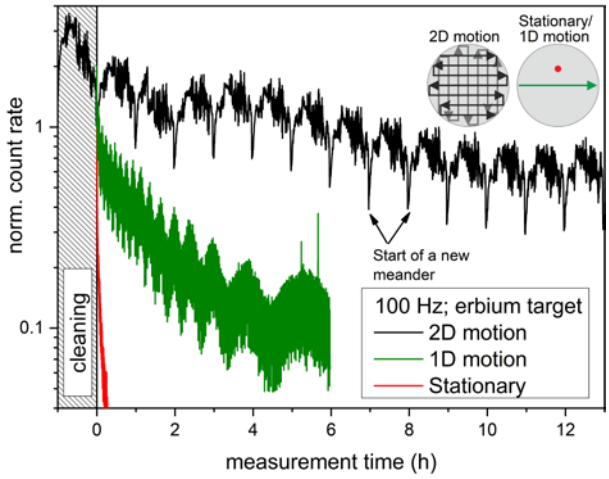


Figure 2: Measurement of the long-term stability of the count rate for erbium ions produced in laser ablation in LACCI with a repetition rate of 100 Hz. The count rate vs. time with a 2D motion of the movable target is compared to a stationary target and 1D motion. The latter is the established state-of-the-art technique for similar laser ion sources. The data are normalized to the count rate after cleaning of the target surface, since it was seen that the first target layer has different properties than the following layers.

References

[1] C. Hornung et al., GSI Sci. Rep. 2013 (2014) 105.
[2] L. Gröf, Bachelor thesis, JLU Gießen, 2017.
[3] W. Plaß et al., Phys. Scr. T166 (2015) 014069.
[4] F. Greiner, Master thesis, JLU Gießen, 2017.

Experiment beamline: FRS
Experiment collaboration:
NUSTAR-SuperFRS-Experiments / FRS Ion catcher
Experiment proposal: S474
Accelerator infrastructure: SIS18
PSP codes: none
Grants: BMBF (05P12RGFN8 & 05P16RGFN1), HMWK (LOEWE Center HICforFAIR), HGS-HIRe
Strategic university co-operation with: Gießen

 DOI:10.15120/GR-2018-1

Development of the stopping cell for the Low-Energy Branch of the Super-FRS

D. Amanbayev[1], S. Ayet San Andrés[1,2], T. Dickel[1,2], H. Geissel[1,2], F. Greiner[1], I. Miskun[1], S. Purushothaman[2], W. R. Plaß[1,2], A.-K. Rink[1], C. Scheidenberger[1,2] for the FRS Ion Catcher Collaboration and for the Super-FRS Experiment Collaboration

[1]Justus-Liebig-Universität Gießen, Germany; [2]GSI, Darmstadt, Germany

The technical design of the cryogenic stopping cell (CSC) for the Low-Energy Branch (LEB) of the Super-FRS [1] has been developed. The CSC will thermalize exotic nuclei, which have been produced in the Super-FRS at relativistic energies, and make them available to the experiments MATS and LaSpec. A prototype of the stopping cell has been successfully commissioned as a part of the FRS Ion Catcher at GSI and enabled an access to short-lived exotic nuclei, providing high areal densities of up to 6.3 mg/cm^2, short extraction times of 25 ms, a rate capability of more than 10^4 ions/s and total efficiencies of up to 30% [2].

The CSC for the LEB will be a high areal density orthogonal extraction CSC (HADO-CSC). It will use the techniques of cryogenic operation to ensure a high purity of the stopping gas and high-density operation enabled by using an RF carpet with a small electrode structure size, which have been successfully applied in the prototype CSC. In addition it will implement several novel concepts, which will result in important performance advantages compared to conventional stopping cells, such as very high stopping efficiencies, short extraction times and high rate capability [1]. The CSC consists of two chambers (Fig 1.). The outer chamber provides the insulation vacuum for the inner chamber, which is operated at a temperature of 70 K. The inner chamber contains a stopping volume with high buffer gas pressure and an extraction volume with low pressure and is pumped differentially. The beam is injected horizontally into the CSC and stopped in the buffer gas. Using electric fields the termalized ions are transported in vertical direction onto an array of RF carpets, which focusses the ions to several nozzles. The ions are swept out by the gas flow from the stopping volume to the extraction volume and there they are transported on a low-pressure RF carpet to the extraction nozzle and into an extraction RFQ.

Detailed simulations of the CSC have been performed. The RF carpet in the stopping volume will have a density of 6 electrodes/mm and be operated at frequencies up to 15 MHz. The stopping volume has a length of 2 m, and the maximum areal density will amount to 30 mg/cm^2. In parallel to the simulation studies, experiments with the prototype of the CSC have been performed at the FRS Ion Catcher to investigate the operation of the CSC at the high field strengths (>> 10 V/cm) planned for the CSC of the LEB [3]. From these, extraction times of 10 ms can be projected. The rate capability of the CSC will exceed 10^7 ions/s. The cryogenic system of the CSC will use electrically driven cryo-coolers. The pumping system of the CSC will include a helium recovery unit (HRU) [4] that allows the helium stopping gas to be re-circulated and continuously purified.

The HADO-CSC is also the basis for the development of stopping cells at ELI-NP [5] and SARAF [6].

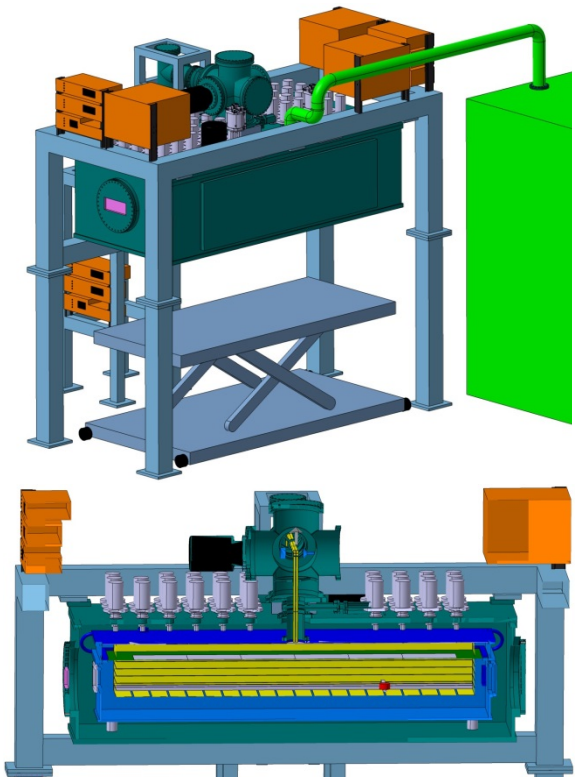


Figure 1: Digital mock-up of the stopping cell system for the LEB. Upper panel: Overview showing the stopping cell (dark green), HRU (light green), frames (grey) and electronics (brown). Lower panel: Cut along the longitudinal direction, showing the inner cryogenic chamber (blue) with the stopping volume (lower) and extraction volume (upper), the electrode system (yellow), the outer vacuum chamber (dark green), the extraction RF quadrupole, and the cryo-coolers (grey).

References

[1] T. Dickel et al., NIM B 376 (2016) 216.
[2] S. Purushothaman et al., EPL 104 (2013) 42001.
[3] A.-K. Rink, PhD thesis, JLU Gießen (2017).
[4] T. Sonoda et al., Rev. Sci. Instr. 87 (2016) 065104.
[5] D. L. Balabanski et al., Rom. Rep. Phys. 68 (2016) 621.
[6] I. Mardor et al., arXiv:1801.06493v2.

Experiment beamline: FRS / Super-FRS
Experiment collaboration: NUSTAR-Super-FRS-Experiments / FRS Ion Catcher
Experiment proposal: none
Accelerator infrastructure: none
PSP codes: 1.2.1.2; 1.2.3.13; 2.4.11.2.7; 2.4.11.2.8
Grants: BMBF (contract No. 05P16RGFN1), HMWK (LOEWE Center HICforFAIR), HGS-HIRe
Strategic university co-operation with: Gießen

Combining the in-flight particle identification with high resolution mass spectrometry at the FRS

E. Haettner[1], A. Spataru[1,2], S. Ayet[1,3], S. Bagchi[1], J. Bergmann[3], T. Dickel[1,3], J. Ebert[3], A. Finlay[4], H.Geissel[1,3], C. Hornung[3], S. Kaur[5], W. Lippert[3], I.Miskun[3], J.-H. Otto[3], S. Pietri[1], W. R. Plaß[1,3], A. Prochazka[1], S. Purushothaman[1], C. Rappold[1,3], A.-K. Rink[3], C. Scheidenberger[1,3], Y. Tanaka[1], H. Toernqvist[1], H. Weick[1], J. S. Winfield[1], the FRS Ion Catcher collaboration, and the Super-FRS Experiment collaboration

[1]GSI, Darmstadt, Germany; [2]University of Bucharest, Romania; [3]Justus Liebig University Giessen, Germany; [4]TRIUMF, Vancouver, Canada; [5]Saint Mary's University, Halifax, Canada.

The mass resolving power of the multiple-reflection time-of-flight mass spectrometer (MR-TOF-MS) [1], which is a part of the FRS Ion Catcher [2], can be as high as 600000 [1]. Thus it can provide an unambiguous identification by mass [3] of the various exotic ions produced and separated at the FRS [4]. This method of identification is independent on the standard identification scheme at the FRS which relies on measurement of magnetic rigidity, velocity, and nuclear charge at high velocity. In particular, identification by mass becomes valuable if the energies are not high enough to keep the ions of interest fully ionized, then a mixture of charge states appears which obscures the standard identification scheme of FRS. Moreover, the method allows the identification and counts long-lived isomers which are not possible with the standard PID of the FRS.

In an experiment, the time-of-flight signals from the MR-TOF-MS were fed into the FRS data acquisition system. A common clock gives the time for each ion passing the scintillation detector in front of the CSC and each ion detected by the MR-TOF-MS. This makes a correlation between particles passing the FRS and particles identified in the MR-TOF-MS possible for the first time. It was shown [5], that the particles of interest could be identified unambiguously by their mass-to-charge ratio also in the time-of-flight spectrum measured with the FRS DAQ.

In an experiment with ^{124}Xe fragments, the measured distributions in time of all particles passing in front of and ^{109}In ions behind the CSC were evaluated [5]; an example showing the time distribution during the spills is shown in Fig. 1. This comparison has applicability in several ways: (i) As a monitor of the efficiency of the setup as a function of the time. Thus it enables a more efficient optimization of the experiment and also serves as a monitor of the CSC performance during the experiment, e.g. detect losses during beam on time due to build-up of space charge. (ii) It is a measurement of the average extraction time of the ions from injection into the CSC to detection in the MR-TOF-MS. This information is crucial in experiments were correction for decay losses are needed, e.g. production cross section mesaurements or measurement of probability for β-delayed neutron emission [6]. Finally, the time of each event recorded in the MR-TOF-MS were compared to the time signal for beam on and beam off. This was successfully used to suppress background from the mass spectrum.

In future, the method will be developed as standard techniques to allow a more efficient setup of experiments with the FRS Ion Catcher, e.g. range adjustment. In purposive experiments even mass tagging by event-by-event correlation of the ions in front of and behind the CSC at an incoming rate of approximately 100Hz will be possible. This will for example allow measuring the ground-to-isomer ratio in dependence of the momentum transfer in the production, and thus, will give important insights to the production and population of exotic isotopes and their isomers [7].

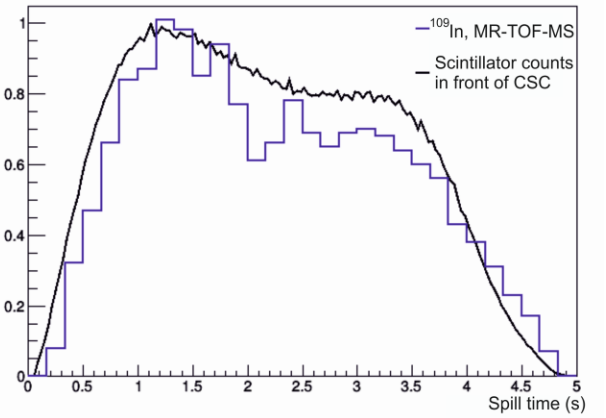


Figure 1: Measured time distribution of fragments passing the scintillation detector in front of the CSC (black) and ^{109}In ions detected by the MR-TOF-MS (blue).

References

[1] T. Dickel et al., Nucl. Inst. Meth. A 777 (2015) 172.
[2] W. R. Plaß et al., Nucl. Inst. Meth. B 317 (2013) 457.
[3] C. Hornung et al., GSI Sci. Rep. (2016) (GSI Report 2017-1) p. 175.
[4] H. Geissel et al., Nucl. Inst. Meth. B 70 (1992) 286.
[5] A. Spataru, Master thesis (2017), University of Bucharest, Romania.
[6] I. Mardor et al., this issue.
[7] U. Sauerwein, GSI Summer student report 2015.

Experiment beamline: FRS
Experiment collaboration:
NUSTAR-SuperFRS-Experiments / FRS Ion Catcher
Experiment proposal: S474
Accelerator infrastructure: UNILAC / SIS18
PSP codes: none
Grants: BMBF (05P12RGFN8 & 05P16RGFN1), HMWK (LOEWE Center HICforFAIR), HGS-HIRe
Strategic university co-operation with: Gießen

 DOI:10.15120/GR-2018-1

Mass measurements of neutron-rich Ti isotopes with the newly commissioned multiple-reflection time-of-flight mass spectrometer at TITAN, TRIUMF

M. P. Reiter[1,2], S. Ayet San Andres[1,3], C. Hornung[1], J. Bergmann[1], T. Dickel[1,3], J. Dilling[2,4], A. Finlay[2,4], H. Geissel[1,3], C. Jesch[1], A. A. Kwiatkowski[2], E. Leistenschneider[2,4], W. R. Plaß[1,3], D. Short[2], C. Scheidenberger[1,3], C. Will[1] and the TITAN collaboration

[1]JLU-Giessen, Giessen, Germany; [2]TRIUMF, Vancouver, Canada; [3]GSI, Darmstadt, Germany; [4]UBC, Vancouver, Canada;

TRIUMF's Ion Trap for Atomic and Nuclear science (TITAN) [1] is a multiple ion trap system capable of performing high-precision mass measurements and in-trap decay spectroscopy. In particular TITAN has specialised in fast Penning trap mass spectrometry of short-lived exotic nuclei using its Measurement Penning Trap (MPET). In order to reach the highest possible precision, ions can be charge bred into higher charge states by an Electron Beam Ion Trap (EBIT), reducing the required measurement time for a needed precision. Using highly charged ions, TITAN is capable of performing mass measurements of short-lived heavy species with very high precision. Although the Isotope Separator and Accelerator (ISAC) facility at TRIUMF, Vancouver, Canada can deliver high yields even for some of the most exotic species, some measurements suffer from a strong isobaric background. This background often prevents the high precision measurement of the exotic species of interest. To overcome this limitation an isobar separator based on the Multiple-Reflection Time-Of-Flight Mass Spectrometry (MR-TOF-MS) technique has been developed at the JLU-Giessen [2] and installed recently at TITAN (Fig. 1). The MR-TOF-MS is based on the design of the MR-TOF-MS developed for MATS [3,4] which is currently in use at the FRS Ion Catcher [5]. In contrast to this system, mass selection is achieved using dynamic re-trapping of the ions of interest after a time-of-flight analysis in an electrostatic isochronous reflector system [6]. Use of this novel technique allowed installation of the MR-TOF-MS with minimal impact on the existing TITAN beam line and also provides cooled and clean isobaric beams for downstream ion traps. Additionally the MR-TOF-MS enables mass measurements of very short-lived nuclides that are weakly produced, complementing TITAN's existing mass measurement program of short-lived exotic nuclei.

After a first online commissioning with stable beam from ISAC in early 2017 the MR-TOF-MS was employed in a measurement campaign trying to investigate the evolution of the N = 32 neutron shell closure around Ca-52. This shell closure forms several neutrons away from stability and has been established in neutron-rich K, Ca and Sc isotopes, where as in the higher Z elements, V and Cr, no shell effects had been found, leaving the intermediate Ti isotopes as the ideal test case for state-of-the-art ab-initio shell model calculations.

High-precision mass measurements with TITAN's MPET and the new MR-TOF-MS were able to prove the existence of a weak shell closure in Ti and were able to challenge four of the most successful modern ab-initio theories, which all over predict the strength of the weak N=32 shell closure [7]. The unexpected reduction in shell strength will be used to refine the aforementioned and forthcoming nuclear models.

Being able to detect all isobars at the same time, the new MR-TOF-MS has become a routine device during TITAN beam times, being used for real-time determination of the radioactive beam composition and optimization of the ISAC mass separator, for precision mass measurements and in the near future for isobar separation. The experiences gained at TITAN go hand in hand with further developments of the MR-TOF-MS system used at GSI as part of the FRS Ion Catcher and for future experiments with MATS and LaSpec at the Low-Energy Branch of the Super-FRS at FAIR.

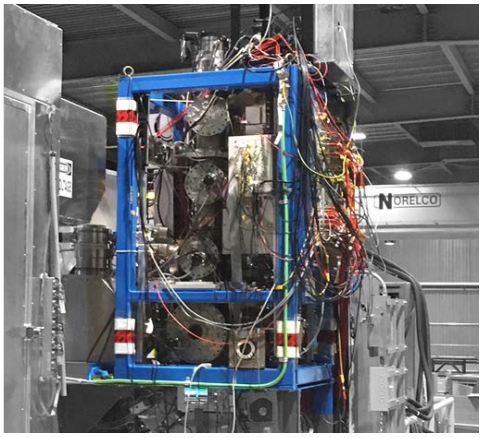


Figure 1: The new TITAN MR-TOF-MS system coupled to the existing TITAN beam line at TRIUMF.

References

[1] J. Dilling et al., IJMS 251, 198 (2006)
[2] C. Jesch et al., Hyperfine Interact. 235, 97 (2015)
[3] W. R. Plaß et al., NIM B 266, 4560 (2008)
[4] Dickel et al., NIM A 777, 172 (2015)
[5] W. R. Plaß et al., IJMS 349-350, 134 (2013)
[6] T. Dickel et al., JASMS 28, 1079 (2017)
[7] E. Leistenschneider et al., PRL. 120, 062503 (2018)

Experiment beamline: not applicable
Experiment collaboration: FRS Ion Catcher
Experiment proposal: not applicable
Accelerator infrastructure: not applicable
PSP codes: 1.2.3.13
Grants: NSERC, NRC, CNPq (249121/2013-1), Helmholz (VH-VI-417), HMWK (LOEWE), US-NSF (PHY-1419765), DFG (FR 601/3-1), BMBF (05P15RDFN1, 05P12RGFN8), NRC
Strategic university co-operation with: Gießen

Status of the EXPERT experiment

V. Chudoba[1,2], O. Kiselev[3], I. Mukha[3], L.V. Grigorenko[1,4,5], C. Scheidenberger[3,6], H. Geissel[3,6], S.G. Belogurov[1], A.A. Bezbakh[1,2], W. Dominik[7], V.B. Dunin[8], V. Eremin[9], I. Eremin[9], S.N. Ershov[10], N. Fadeeva[9], A.S. Fomichev[1,11], M.S. Golovkov[1,11], A.V. Gorshkov[1], Z. Janas[7], G. Kaminksi[1,12], A.G. Knyazev[1,13], Y.N. Kopach[14], A.A. Korsheninnikov[5], D. Kostyleva[6], E. Kozlova[3], S.A. Krupko[1], E.A. Kuzmin[5], Ch. Mazzocchi[7], I.A. Muzalevsky[1,2], E.Yu. Nikolskii[1,5], Y.L. Parfenova[1], M. Pfützner[7], S. Pietri[3], S.A. Rymzhanova[1], V. Schetinin[15], P.G. Sharov[1], S.I. Sidorchuk[1], H. Simon[3], R.S. Slepnev[1], G.M. Ter-Akopian[1,11], E. Terukov[9], Yu. Tuboltsev[9], E. Verbitskaya[9], H. Weick[3], X. Xu[16], and the Super-FRS Experiment collaboration

[1] Flerov Laboratory of Nuclear Reactions, JINR, Dubna, Russia; [2] Institute of Physics, Silesian University, Opava, Czech Republic; [3] GSI, Darmstadt, Germany; [4] University MEPhI, Moscow, Russia; [5] Kurchatov Institute, Moscow, Russia; [6] II. Physikalisches Institut, Justus-Liebig-Universität, Gießen, Germany; [7] Faculty of Physics, University of Warsaw, Poland; [8] Veksler and Baldin Laboratory of High Energy Physics, JINR, Dubna, Russia; [9] Ioffe Physical-Technical Institute, St.-Petersburg, Russia; [10] Bogolyubov Laboratory of Theoretical Physics, JINR, Dubna, Russia; [11] State University DUBNA, Dubna, Russia; [12] Heavy Ion Laboratory, Warsaw University, Warszawa, Poland; [13] Physics Department, Lund University, Lund, Sweden; [14] Frank Laboratory of Neutron Physics, JINR, Dubna, Russia; [15] Laboratory of Information Technologies, JINR, Dubna, Russia; [16] School of Physics and Nuclear Energy Engineering, Beihang University, Beijing, China.

The EXPERT (EXotic Particle Emission and Radioactivity by Tracking) setup is a part of the Super-FRS Experiment Collaboration [1]. Prototype detectors of EXPERT are being used in pilot experiments at the FRS in the FAIR Phase-0 (S443, S459).

Physics program and methods

The EXPERT experiments aim at studies of exotic nuclear systems in the most-remote part of the nuclear landscape close to the proton and neutron drip lines [2]. Nuclear decays with very small decay energies emitting proton(s) or neutron(s) in-flight, i.e., proton radioactivity and neutron radioactivity, can be studied by tracking the trajectories of the decay fragments and reconstructing their decay vertices. This technique allows for investigations of nuclei with short half-lives down to 10^{-12} s. Also proton–proton and neutron–neutron correlations, even in case of multiple proton or neutron decays, can be studied by tracking charged particles and neutrons. Complementarily, two-proton radioactivity will be studied by using an Optical Time-
Projection Chamber (OTPC) placed at the final focus of the (Super-)FRS, where exotic nuclei are first implanted into the OTPC and then decay. These two detection schemes of EXPERT may utilize the same radioactive beam simultaneously and therefore efficiently. Together they cover half-life ranges from 10^{-12} to 10^{-7} s (with the in-flight decay technique) and from 10^{-7} to 1 s (with the implantation-decay method). Such a combination has successfully been demonstrated at the FRS [3].

The EXPERT modular detector assembly consists of 5 subsystems sketched in Fig.1, whose locations at the future Super-FRS are shown in Fig.2. The silicon (Si) beam-detector subsystem consists of the Si-strip timing detectors SSD, the tracking module (double-sided Si microstrip detectors), the γ-ray detector GADAST (128 CsI(Tl) and 32 LaBr3(Ce) crystals), the neutron detector NeuRad (~10000 scintillator fibers), and the implantation detector on the basis of OTPC.

The SSD detectors should provide timing information of the heavy ions up to U with the precision of 50 ps and for lighter ions of 100 ps. In addition, hit coordinates of the ions need to be measured with a precision of 0.3 mm and the deposited ionisation energy with a precision of 5%.
The microstrip Si tracking detectors should deliver proton-hit coordinates with an accuracy of 30 μm. The energy-deposition measurement should identify ions with Z < 28 at counting rates up to 10^4 s^{-1}.

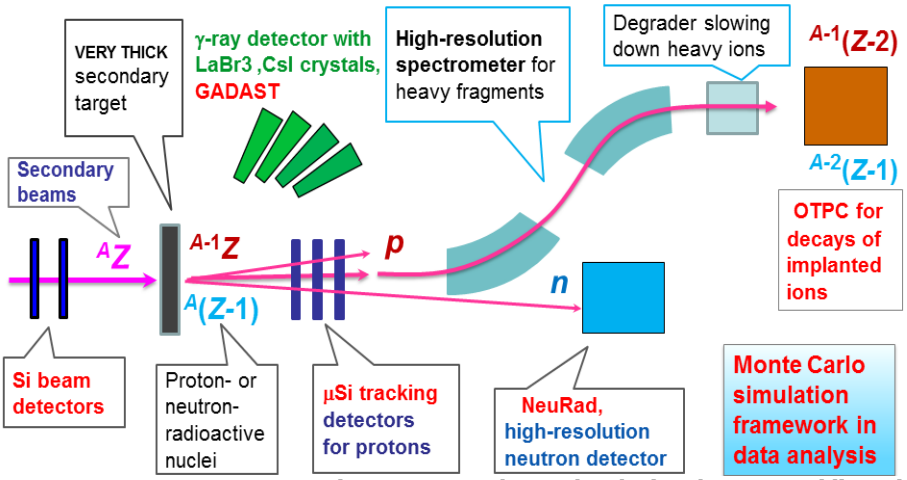


Figure 1. The EXPERT main components and experiment scheme sketched at the FRS middle and final focal planes.

 DOI:10.15120/GR-2018-1

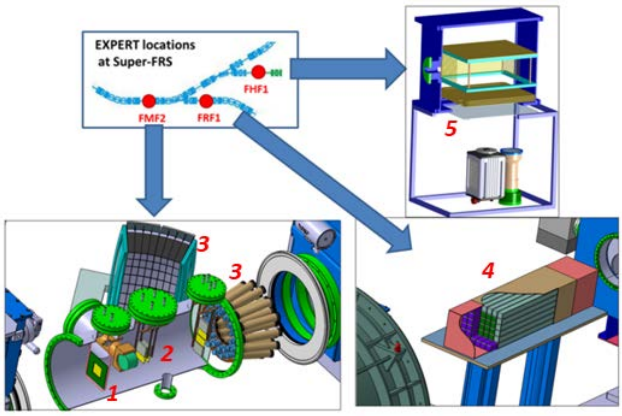


Figure 2: Locations of the EXPERT detectors at the Super-FRS middle and final focal planes (upper-left panel). Itemized instrumentation: 1 – Si beam detectors, SSD; 2 – microstrip Si tracking detectors; 3 – γ-ray detectors GADAST; 4 – neutron detector NeuRad; 5 – optical time-projection chamber OTPC.

The energy resolution of the γ-ray detector GADAST should be ~5% at 3 MeV. GADAST should work at a flux up to 1000 cm^{-2} s^{-1} of γ-rays and charged particles.

The OTPC should provide 3D reconstruction of implanted multi-particle decays of fragments and measure the charge, energy and emission angle of the decay products. With respect to the existing device the size needs to be increased by 20-30%, and the angular and energy resolution to be improved by a more advanced digital photo camera.

The angular resolution of the neutron detector NeuRad must be below of 0.2 mrad. The detection threshold for the energy deposited after one interaction of a neutron should not exceed 1 MeV and the time resolution of 0.5 ns. The total angular range covered by the detector is supposed to be 12 mrad. The planned size and location of the detector as well as its high granularity shall allow for distinguishing multiple neutron interactions as well.

EXPERT technical status

The technical feasibility of EXPERT has been proven by two successful experiments with the exotic ion beams performed at GSI and several test experiments at GSI and JINR, which resulted in a dozen publications (see e.g., Refs. [3,4]). The most recent result is the observation of previously-unknown isotopes ^{29}Ar, ^{28}Cl, ^{30}Cl and the first spectroscopy of ^{31}Ar. The data have been obtained as a by-product of the main objective ^{30}Ar (see the recent article [4]) during the pilot EXPERT experiment S388 in 2012. The corresponding contribution by D. Kostyleva et. al. follows this report.

The parameters of the different subsystems are proven by testing the prototypes or using final detectors during the pilot experiments at GSI. Prototypes of all components have shown good functionality in high-precision tracking and time measurements of light and heavy ions simultaneously; in neutron detection with the highest spatial resolution; in tagging of the radioactive decays with fine structure by using a segmented γ-ray detector GADAST with efficiency of 10% of 4π; and in implantation-decay measurements with OTPC. The EXPERT Technical Design Report has been approved by the ECE/FAIR in 2017 [5].

Tests in 2017

The NeuRad timing properties have been tested with a 20 cm long, 16x16 bundle of scintillation fibers BCF-12, two multi-anode PMTs H9500 and a 128-channel readout system based on TOFPET ASICs [6]. A new updated version of this system is under investigation. The first results on performance of such a NeuRad prototype have been obtained by detecting tracks produced by cosmic radiation, which is presented in the contribution by D. Kostyleva et. al.

Several Si microstrip detectors have been refurbished in order to use new front-end ASICs IDE1140 from IDEAS. The detectors have been tested in the laboratory and are ready for GSI-beam tests in 2018. Lower noise level, better linearity and higher dynamic range allow for a better resolution in tracking and identification of ions and protons.

A new readout system for the TOF Si detectors has been assembled and tested. It uses the last version of the front-end amplifier/discriminator ASIC PADI-X and FPGA TDC providing the highest time resolution down to 11 ps per channel. This system is prepared for beam tests of the new Si TOF detectors at GSI in 2018.

For GADAST, newly purchased LaBr3(Ce) crystals have been tested at the INP Krakow, Poland. GADAST has been prepared for commissioning as a detector for heavy charged particles in experiments at JINR in 2018.

The day-0 experiments with EXPERT in 2018/2019

The EXPERT components (new Si timing and Si tracking detectors) are planned to be tested during the beamtime assigned to the experiments S443 (Search for four-proton decay of Mg-18) and S459 (Two-proton radioactivity of unobserved S-26). In total, 4+4 shifts of beamtime in parasitic and main-user modes have been granted. The allocated beamtime is sufficient for testing the developed EXPERT instrumentation. For this purpose, in-flight detection of two-proton (^{12}O) or four-proton (^{8}C) decay precursors has been proposed, which is possible with primary beams ^{16}O or ^{12}C, respectively. The scheme of such test experiment is shown in Figure 3.

The proposed experiment allows for testing all components of EXPERT (except the neutron detector NeuRad) by using the known decay schemes and levels of 2p/4p emitters ^{12}O/^{8}C [7,8] whose decay energies will be re-measured by registering ^{9}C+p+p or ^{4}He+p+p+p+p coincidences, respectively. Such a calibration is feasible within the granted beam-time because of sufficiently high production rates of the nuclei of interest at FRS.

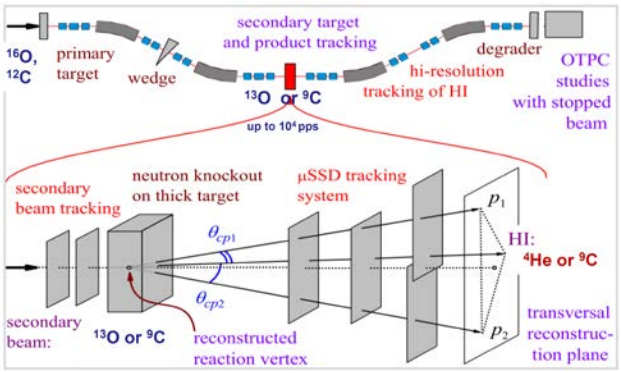


Figure 3. Sketch of the EXPERT test experiment at FRS. Beams of $^{16}O/^{12}C$ are fragmented in a primary target, and a secondary $^{13}O/\ ^{9}C$ beam is selected and focused on the middle focal plane in achromatic ion-optics mode. Nuclei of interest $^{12}O/^{8}C$ are produced in the secondary target in one-neutron knock-out reaction. Heavy-ion decay products $^{9}C/^{4}He$ are identified by their energy-loss and time-of-flight as well as the magnetic rigidity by using the standard FRS beam detectors. At the final focal plane of FRS, the studies of beta-delayed proton radioactivity of the stopped $^{13}O/\ ^{9}C$ ions will be performed by using the implantation-decay method with OTPC. The lower inset shows the EXPERT decay-in-flight detectors located downstream the secondary target, where the trajectories of incoming ions as well as the trajectories of the decay products $^{9}C/^{4}He$ and protons p1, p2 are measured.

References

[1] J. Aysto et al., Nuclear Instruments and Methods in Physics Research B **376**, 111 (2016).
[2] H. Geissel et al., Proc. Int. Symposium on Exotic Nuclei (EXON2014), World Scientific, 2015, ISBN 978-981-4699-45-7, p. 579.
[3] I. Mukha et al., Phys. Rev. Lett. **115**, 202501 (2015).
[4] X. Xu et. al., Phys. Rev. C **97**, 015202 (2018).
[5] Technical Design Report of the EXPERT setup for FAIR, 2017, https://edms.cern.ch/document/1865700.
[6] D. Kostyleva et al., GSI Scientific Report 2016, DOI:10.15120/GR-2017-1, p.171.
[7] M.F. Jager et al., Phys. Rev. C **86** (2012).
[8] R.J. Charity et al., Phys. Rev. C **84** (2011).

Experiment beamline: FRS

Experiment collaboration: NUSTAR-SuperFRS-Experiments

Experiment proposal: S443, S459

Accelerator infrastructure: UNILAC / SIS18 / FRS /

PSP codes: 1.2.10.7

Grants: HRS-HIREe / BMBF GSI-JINR grant /

Strategic university co-operation with: Darmstadt / Gießen /

New isotopes ^{29}Ar and ^{28,30}Cl observed during the EXPERT pilot experiment

D. Kostyleva[1], I. Mukha[2], L.V. Grigorenko[3,4,5], L. Acosta[6], E. Casarejos[7], A.A. Ciemny[8], W.Dominik[8],J. Duénas-Díaz[9], V. Dunin[10], J.M. Espino[11], A. Estradé[12], F. Farinon[2], A. Fomichev[3], H. Geissel[1,2],A. Gorshkov[3], Z. Janas[8], G. Kaminski[3,15], O. Kiselev[2], R. Knöbel[2], S. Krupko[3], M. Kuich[8],Yu.A. Litvinov[2], G. Marquinez-Durán[9], I. Martel[9], C. Mazzocchi[8], C. Nociforo[2], A. K. Ordúz[9],M. Pfützner[8], S. Pietri[2], M. Pomorski[8], A. Prochazka[2], S. Rymzhanova[3], A.M. Sánchez-Benítez[9],C. Scheidenberger[1,2], P. Sharov[3], H. Simon[2], B. Sitar[13], R. Slepnev[3], M. Stanoiu[14], P. Strmen[13], I. Szarka[13],M. Takechi[2], Y.K. Tanaka[15], H. Weick[2], M. Winkler[2], J.S. Winfield[2], X. Xu[1,16], and M.V. Zhukov[17]

[1]II. PhysikalischesInstitut, Justus-Liebig-Universität, Gieβen, Germany; [2]GSI, Darmstadt, Germany; [3]Flerov Lab of Nuclear Reactions, JINR, Dubna, Russia; [4]University MEPhI, Moscow, Russia; [5]Kurchatov Institute, Moscow, Russia; [6]Instituto de Física, Universidad Nacional Autónoma de México, Mexico; [7]University of Vigo, Spain; [8]Faculty of Physics, University of Warsaw, Poland; [9]Department of Applied Physics, University of Huelva, Spain; [10]Veksler and Baldin Lab of High Energy Physics, JINR, Dubna, Russia; [11] Department of Atomic, Molecular and Nuclear Physics, University of Seville, Spain; [12]University of Edinburgh, UK; [13]Faculty of Mathematics and Physics, Comenius University, Bratislava, Slovakia; [14]IFIN-HH, Bucharest, Romania;[15]Heavy Ion Laboratory, University of Warsaw, 02-093 Warszawa, Poland; [16]School of Physics and Nuclear Energy Engineering, Beihang University, Beijing, China; [17]Department of Physics, Chalmers University of Technology, Göteborg, Sweden

The EXPERT pilot experiment S388 has been performed at FRS in 2012. Here we report the preliminary results of the data analysis indicating an observation of previously-unknown isotopes ^{29}Ar, ^{28}Cl, ^{30}Cl and the first spectroscopy of ^{31}Ar [1]. The data have been obtained as a by-product of the main objective, ^{30}Ar [2,3].

EXPERT pilot experiment at FRS. The proton-unbound argon and chlorine isotopes were detected by measuring trajectories of their decay-in-flight products by using a tracking technique with micro-strip detectors.

The primary ^{36}Ar beam hit a thick target, and a secondary beam of ^{31}Ar was selected and focused on the middle focal plane, where nuclei of interest ^{31}Ar*,^{29}Ar were produced in the secondary target in reactions of in-elastic scattering and two-neutron knock-out. Decay products ^{27,30}S were identified by their energy-loss and time-of-flight as well as the magnetic rigidity by using the standard beam detectors of FRS. The proton (1p) and two-proton (2p) emission processes have been identified in the measured angular correlations of decay products, heavy ions (HI) with protons, HI+p and HI+p+p, respectively.

Monte-Carlo simulations. The ground states of the previously unknown isotopes ^{30}Cl and ^{28}Cl have been discovered, providing the 1p-separation energies of about 0.48(2) and 1.60(8) MeV, respectively, see [1] for details. In order to interpret the angular spectra quantitatively and precisely identify the 1p and 2p decay energies, one has to perform detailed Monte-Carlo simulations of the setup response. Such simulations were performed by using the GEANT-based program which was calibrated on the known 2p-decay pattern of ^{19}Mg [2]. The states of interest were fit by varying the assumed values of their 1p-decay energies. Each simulated spectrum was then compared with the corresponding experimental angular correlation. The simulated distribution and experimental data were tested for compatibility by applying the Kolmogorov-Smirnov algorithm, see details in [3]. This test provides a probability that the data and simulation distributions have the same shape. The probability plotted as a function of decay energy provides the best-fit decay energy and its uncertainty. For example, on Fig.1, one can see the distribution of probability obtained for different 1p-decay energy of the ^{30}Cl first excited state. The derived 1p-decay

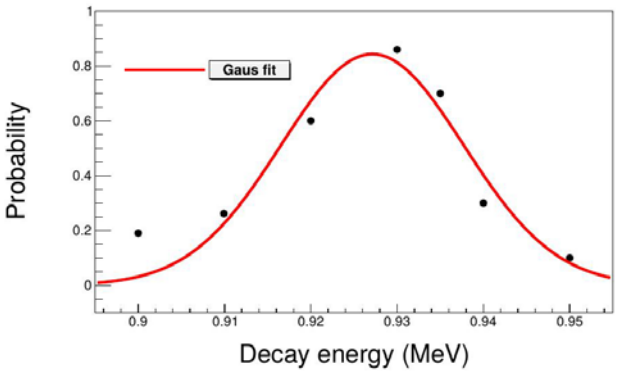


Figure 1:Probability that the ^{30}Cl data are reproduced by the respective simulations as a function of 1p-decay energy.

energy of the first excited state of ^{30}Cl is about 0.93(3) MeV. In a similar way, the observed excited states of ^{31}Ar allow to infer 2p-separation energy of 6(34) keV for its ground state. Moreover, one level was observed in ^{29}Ar. The observed state in ^{29}Ar with the derived 2p-decay energy of 5.50(18) MeV may be identified either as a ground or an excited state depending on the systematics applied in analysis. The relevant systematics of 1p and 2p separations energies have been studied theoretically in the HI+p and HI+p+p cluster models.

References

[1] I. Mukha, L.V. Grigorenko, D. Kostyleva et al., arXiv:1803.10951 [nucl-ex] (2018).
[2] I. Mukha et al., Phys. Rev. Lett. **115**, 202501 (2015).
[3] X. Xu et. al., Phys. Rev. C **97**, 015202 (2018).

Experiment beamline: FRS
Experiment collaboration: SuperFRS Experiments
Experiment proposal: [S338]
Accelerator infrastructure: SIS18 / FRS / Super-FRS /
PSP codes: 1.2.10.7
Grants: HRS-HIREe/BMBF GSI-JINR grant /
Strategic university co-operation: Darmstadt/Gießen/

 DOI:10.15120/GR-2018-1

Tracking cosmic radiation by the NeuRad neutron detector prototype with multi-channel readout electronics

D. Kostyleva[1], A.A. Bezbakh[2,3], V. Chudoba[2,3], A.S. Fomichev[2], A.V. Gorshkov[2], O. Kiselev[4], S.A. Krupko[2], I. Mukha[4], I.A. Muzalevskii[2,3], C. Scheidenberger[1,4] for the Super-FRS Experiment collaboration

[1] II.PhysikalischesInstitut, Justus-Liebig-Universität, Gießen, Germany; [2]Flerov Laboratory of Nuclear Reactions, JINR, Dubna, Russia; [3] Institute of Physics, Silesian University, Opava, Czech Republic; [4]GSI, Darmstadt, Germany.

The NeuRad (Neutron Radioactivity) detector for high-energy neutrons belongs to the EXPERT (EXotic Particle Emission and Radioactivity by Tracking) setup which is a part of the Super-FRS Experiment Collaboration [1]. NeuRad is constructed out of ~10^4 scintillation fibers, and it is aimed at high-precision measurements of the angular correlations between the neutrons and heavy fragments stemming from exotic neutron decays. Due to a high granularity, an important feature of the NeuRad is the ability to track trajectories of the recoil protons produced by incident neutrons. The results of the tests of NeuRad tracking properties measured with cosmic radiation are presented in this report.

The first tests of NeuRad prototype. The first test of the timing properties of the NeuRad detector prototype has been performed at FLNR JINR and later on at GSI [2]. The demonstrator, consisting of a 16x16 bundles of BCF-12 scintillation fibers (each fiber is 25 cm long and has 3x3 mm^2 cross section) coupled with two PMT's H9500, has been irradiated by a ^{60}Co gamma-ray source. The time uncertainty between two opposite PMT channels was determined to be ~ 1 ns (sigma). The reference measurement with a BC-420 0.4 cm thick scintillator and two H9500 PMTs showed the time resolution of 0.5-0.7 ns.

PETsys TOFPET2 ASIC readout chip. The next test of the NeuRad prototype has been done with the multi-channel electronics. For this purpose, the readout system provided by the PETsys Electronics has been chosen. This system is based on the high performance TOFPET2 ASIC, which is a new 64-channel chip combining a current amplifier, discriminator, TDC and QDC. It is developed for the readout and digitization of signals from fast photon detectors in applications where high data rates and fine time resolution are required [3]. In order to test the TOFPET2 performance, the PETsyscompany provided an Evaluation Kit which includes two LYSO crystals of 3x3x5 mm^3 viewed by two KETEK SiPM PA3325-WB-0808 arrays mounted on a board that plugs into the TOFPET2 ASIC test board. The kit has been tested with a standard ^{22}Na source. The time resolution, obtained with the kit, is ~95 ps, see Fig. 1(a), or ~67 ps per channel.

The NeuRad prototype test with TOFPET2 ASIC. The NeuRad prototype module (see above for the details) has been tested with the PETsys e-kit using cosmic radiation. H9500 MAPMTs were coupled to the electronics via special connectors, so the signals from only 64 fibers on each side were measured. The data acquisition was set in a coincidence mode, i.e. only the events creating signals on both PMTs with a time difference less than 20 ns were recorded. Precise timing of the signals in each channel (fiber) allowed for restoration of the track of the cosmic particle crossing the NeuRad prototype. In Fig.1(b) one can see a typical track from a cosmic-ray particlepresented in the transverse cross-section of the prototype. The presented event has the time resolution 0.5(3) ns.

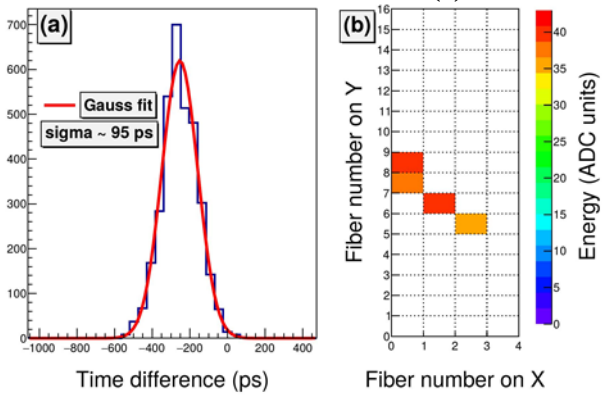


Figure 1: (a) Time resolution with LYSO crystals, SiP-Mphotosensors and TOFPET2 ASIC. (b) The track of a cosmic-ray particle in a transverse cross-section of the NeuRad prototype. Both sides of 4 x 16 fibers are readout by the PMTs and TOFPET2 system. The measured light intensity (due to ionization energy loss in a fiber) is shown in colours.

The measurement has shown that the tracks of minimum-ionizing cosmic-ray particles can be determined within each fiber of the NeuRad detector prototype by using the TOFPET2 ASIC electronics.

The day-0 experiments with NeuRad/EXPERT in 2018/2019. The NeuRad prototype will be tested at FRS during the beam-time assigned to the experiments S443 and S459.

References

[1] Technical Design Report of the EXPERT setup for FAIR, 2017, https://edms.cern.ch/document/1865700.

[2] D. Kostyleva et al., GSI Scientific Report 2016, DOI:10.15120/GR-2017-1, p.171.

[3] http://www.petsyselectronics.com

Experiment beamline: FRS
Experiment collaboration: NUSTAR-SuperFRS-Experiments
Experiment proposal: [S443, S459]
Accelerator infrastructure: SIS18 / FRS / Super-FRS /
PSP codes: 1.2.10.7
Grants: HRS-HIREe / BMBF GSI-JINR grant /partial support by RSF (project No.17-12-01367) / FAIR-Russia Research Center/
Strategic university co-operation: Darmstadt / Gießen

Measurements of proton and matter radii of neutron-rich isotopes

S. Bagchi[1,2,3], Y. Tanaka[1,2,3], R. Kanungo[1,4], H. Geissel[2,3], C. Scheidenberger[2,3], K. -H. Behr[2], A. Prochazka[2] and the S395 and the NP1412-RIBF132 Collaborations

[1]Saint Mary's University, Halifax, Canada; [2]GSI, Darmstadt, Germany; [3]JLU, Giessen, Germany; [4]TRIUMF, Canada.

Recent trends in nuclear physics research are moving towards studies with radioactive ions or rare isotopes where the neutron-to-proton ratio is quite exotic. Since the discovery of exotic nuclei, characterized by halos and skins, interaction cross section measurements and high-resolution momentum measurements have played a key role to identify nuclei with new properties due to extended spatial distributions of the valence nucleons [1]. The proton distribution radius is crucial for determining the neutron-skin thickness if the matter radius is known. The proton radius is also necessary to understand the spatial correlation between the halo and the core. The experiments based on high-energy electron scattering, atomic hyperfine structure or isotope shift have limitations for very short-lived nuclei available with low beam intensity. On the other hand, charge changing cross section measurements are a versatile tool which can be applied very well for stable nuclei as well as for exotic nuclei far from the β-stability line.

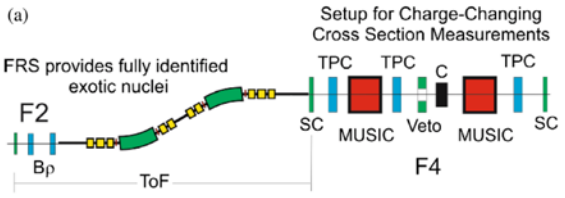


Figure 1: Schematic view of the second half of the FRS spectrometer at GSI with the detector setup to measure the charge changing cross section.

The exotic nuclei facility at GSI is unique in having energies up to 1*A* GeV. Experiments for precise radii measurements are best suitable at this energy as a wide variety of isotopes of interest is fully ionized. It is also possible to perform such studies for light nuclei at beam energies around 200-300 MeV/u that are available at RIKEN. In Fig. 1, second half of the fragment separator at GSI [2] is shown along with the detector configuration at the final focus of the FRS. Details of the experimental setup and methodology is mentioned in Refs.[3-5].

To obtain the proton radii from the measured σ_{cc}, finite-range Glauber model framework is used. For stable isotopes (e.g. ^{10}B, $^{12-14}$C, ^{14}N), the obtained proton radii are in good agreement with the electron scattering data [3-5]. Together with information on the matter distribution radii from interaction cross section measurements, a very thick neutron-skin has been obtained for ^{22}N [5].

Extending these investigations of halo and shell evolution to the neutron-rich fluorine isotopes, in this context we also mention our recent experiment at the BigRIPS [6] and ZeroDegree Spectrometer (ZDS) facilities at the RIKEN RI Beam Factory. The interaction cross section, charge changing cross section and longitudinal momentum distribution measurements were performed. The details on the experiment and the detector setup can be found in Ref.[7].

A carbon reaction target placed at the F8 focus was surrounded by the DALI2 gamma detector array [8] to detect excited states of the nucleus and/or the fragment. The analysis of the work is in progress.

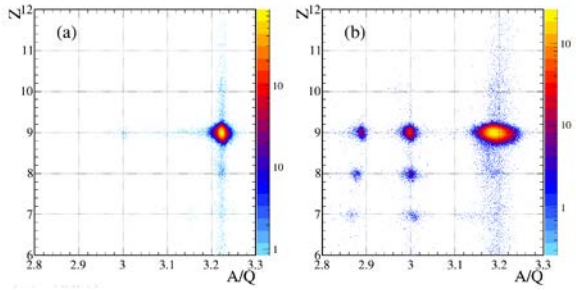


Figure 2: Particle identification spectrum using the ZDS spectrometer set for (a) ^{29}F and (b) ^{27}F

References:

[1] I. Tanihata et al., PRL 55, 2676 (1985).
[2] H. Geissel et al.,Nucl. Instrm. Meth. B 70, 286 (1992).
[3] A. Estrade et al., PRL 113, 132501 (2014).
[4] R. Kanungo et al., PRL 117, 102501 (2016).
[5] S. Bagchi et al., submitted for publication.
[6] T. Kubo et al., Nucl. Instrm. Meth. B 204, 97 (2003).
[7] R. Kanungo et al.,RIKEN Accel. Prog. Rep. 50 (2017).
[8] S. Takeuchi et al.,Nucl. Instrm. Meth. A 763, 596 (2014).

Experiment beamline: FRS
Experiment collaboration: NUSTAR-SuperFRS-Experiments
Experiment proposal: S395
Accelerator infrastructure: SIS18 / FRS
PSP codes:
Grants: (experiment) NSERC, Canada; PR China government and Beihang University under the Thousand Talent program

Strategic university co-operation with: Saint Mary's University, JLU Gießen, Hokkaido University, University of Tennessee, Nihon University, Santiago de Compostela University, Comenius University, Dalhousie University, Osaka University, Beihang University, University of Tokyo.

 DOI:10.15120/GR-2018-1

Charge changing cross section measurement of cobalt isotopes

S. Kaur[1,2], R. Kanungo[1,4], S. Bagchi[1,3], S. Ayet[3,5], J. Bergmann[5], T. Dickel[3,5], J. Ebert[5], A. Finley[4,6], H. Geissel[3,5], E. Haettner[3], C. Hornung[5], W. Lippert[5], I. Miskun[5], J.-H. Otto[5], S. Pietri[3], W. R. Plaß[3,5], S. Purushothaman[3], A.-K. Rink[5], C. Scheidenberger[3,5], Y. Tanaka[3,5], H. Weick[5], J. Winfield[3] and the Super FRS experiment Collaboration

[1]Saint Mary's University, Halifax, Canada; [2]Dalhousie University, Halifax, Canada; [3]GSI, Darmstadt, Germany; [4]TRIUMF, Vancouver, Canada; [5]JLU, Giessen, Germany; [6]UBC, Vancouver, Canada

The charge radius is an important bulk property of a nucleus for investigating nuclear structure. The knowledge of proton radii is crucial for understanding halo and skin formation and also the shell evolution in unstable nuclei. The proton radii also serve as a test of newly developed structure models including those based on ab-initio theory. Electron scattering measurements are ideal for probing the distribution but so far not applicable to short-lived unstable nuclei. Isotope shift measurements allow us to precisely deduce the charge (proton) radius for some unstable nuclei. The measurement of the charge-changing cross sections (σ_{CC}) is a potential method that can be used to extract the proton radius for stable nuclei and as well as for exotic nuclei far from the β-stability line. The proton radii of light unstable nuclei have been successfully determined from the σ_{CC} measurements using the Glauber Model framework in ref. [1-3].

We report here the charge-changing cross section measurements of $^{57-59}$Co that were performed to investigate the application of this new tool to extract proton radii of medium mass projectiles at intermediate energy. The test measurement was performed at the fragment separator (FRS) [4] at GSI, Germany. Beams of $^{57-59}$Co were produced by fragmentation of a ^{124}Xe beam at 600 MeV/u, on a 1612 mg/cm^2 thick Be target. The isotopes of interest were separated in flight and identified through the magnetic rigidity (Bρ) - time of flight (TOF) - energy loss (ΔE) method. In Fig. 1(a), the second half of the FRS is shown along with the detector configuration at the final focus of the FRS. The TOF of the incoming beam was measured from the intermediate focal plane F2 to F4 using plastic scintillators. The event-by-event Bρ of the incoming particles was determined from the horizontal position of particles, measured with a scintillator detector at F2 and time-projection chambers (TPC) at F4. Multisampling ionization chambers provided the energy loss (ΔE) measurements (Fig.1b). A 2.5 g/cm2 thick carbon reaction target was placed at F4. A veto scintillator with a central aperture placed in front of the target rejected beam events incident on the edges of the target scattered by matter upstream and the multi-hit events. The σ_{CC} is measured using the transmission technique, where the σ_{CC} is obtained from the relation:

$$\sigma_{CC} = \frac{1}{t} ln\left(\frac{R_{out}}{R_{in}}\right)$$

Here $R_{in(out)}$ = N_{sameZ}/N_{in} is the transmission ratio with (without) the target and t denotes the target nuclei per cm^2. In this method, the number (N_{in}) of incident nuclei ^{A}Z before the reaction target are identified and counted. After the target, we only require to identify and count the nuclei with the same charge Z (Fig.1c). The losses due to interactions with non-target materials are accounted by taking the measurements without the target in the setup.

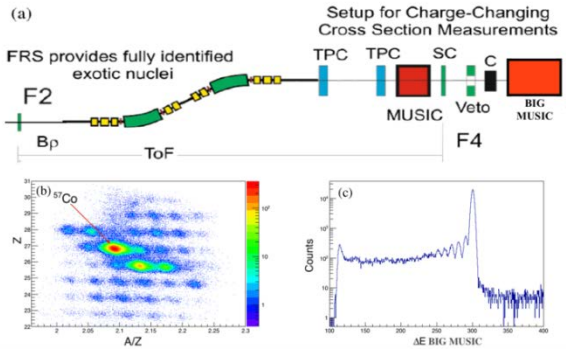


Figure 1: (a) Schematic view of the second half of the FRS spectrometer. (b) Particle identification spectrum before the C reaction target. (c) The energy loss spectrum in MUSIC after the reaction target with ^{57}Co incident beam.

The point proton radii (protons considered as point particles) will be determined from the measured σ_{CC} using the Finite-range Glauber model. This technique has been successfully applied to determine the proton radii of B, C and N isotopes where proton radii of stable isotopes (^{10}B, $^{12-14}$C, ^{14}N) agree very well with the electron-scattering experiments [1-3]. The measured σ_{CC} of ^{59}Co will be used to compare to known proton radii from electron scattering.

References:

[1] A. Estrade et al., Phys. Rev. Lett. 113, 132501 (2014).
[2] R. Kanungo et al., Phys. Rev. Lett. 117, 102501 (2016).
[3] S. Bagchi et al., submitted to journal.
[4] H. Geissel et al., Nucl. Instrum. Methods Phys. Res., Sect. B 70, 286 (1992).

Experiment beam line: FRS
Experiment collaboration: NUSTAR-SuperFRS-Experiments
Experiment proposal:
Accelerator infrastructure: SIS18 / FRS
PSP codes:
Grants: NSERC, Canada.
Strategic university co-operation with: Saint Mary's University / University of Giessen / Dalhousie University

Energy-dependent total charge changing cross-sections of ^{12}C

A. Prochazka[1], S. Bagchi[1,2], H. Geissel[1,2], E. Haettner[1], C. Hornung[2], S. Pietri[1], S. Purushothaman[1], C. Scheidenberger[1,2], Y. Tanaka[1,2], H. Weick[1] , J. Winfield[1], X. Xu[1] and the Super-FRS Experiment Collaboration

[1]GSI, Darmstadt, Germany; [2]Justus-LiebigUniversität, Gießen, Germany

Charge changing reactions are used to determine the root mean square radius of the nucleus proton distribution. In this work we measured total charge changing cross-sections of ^{12}C ions in carbon, polyethylene and lead targets at 350, 450 and 600 MeV/u. The measurements were done at the FRS using the transmission method as described in [1]. The experimental setup shown in Figure 1 was located at the final focal plane of the FRS. The incoming beam was identified in mass and charge using the FRS spectrometer, TPC tracking detectors, time-of-flight detectors and the multiple sampling ionization chamber MUSIC [2] in front of the target on event-by-event basis. The reaction rate was measured using the second MUSIC detector placed behind the reaction target.

The goal of the measurement was to measure total charge changing cross sections at intermediate energies where previous partly contradicting experimental values exist. Multiple data sets are compared in Figure 2, where it can be seen that the data measured in [3] and [6] are not in agreement with the data published in [1],[4],[5] and [7]. The preliminary cross sections measured at the FRS from this work (shown by red points in Figure 2) support the group of measurements with higher cross-section values.

Glauber model type calculations are used to describe the charge changing cross sections and relate them to effective proton radii. Two Glauber Model calculations reproducing the same experimental effective charge radius of ^{12}C (2.47 fm) are show in Figure 2. The blue line corresponds to the optical limit zero range calculation corrected by the empirical energy dependent scaling as described and used in [8] which reproduces the ^{28}Si charge changing cross sections. The orange line corresponds to optical limit finite range calculations as used in [3].

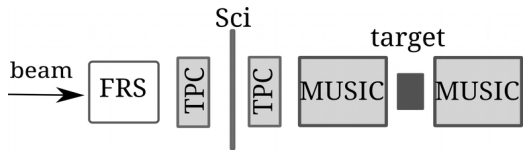


Figure 1: Experimental setup at S4 focal plane of the FRS.

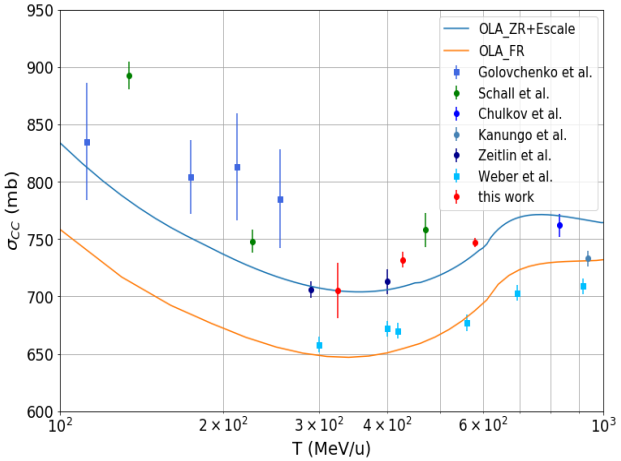


Figure 2: Experimental total charge changing cross-sections of ^{12}C ions on C targets as a function of energy. The data from this work (red points) are compared to the other experimental data shown by green and blue squares. Glauber Model calculations are shown by solid lines.

Using the two different models the same radius leads to cross sections which differ by ~5%. Therefore we aim to develope a model which reproduces the measured total charge changing and also total reaction cross-section data with the same time and without empirical corrections. As a first attempt we extended the models used in [3] and [8] by correction to the residual nucleus evaporation after one- and multi-neutron removals. The development is ongoing and the code will be published as an open source.

References

[1] L.V. Chulkov et al., Nuclear Physics A 674 (2000) 330-342
[2] MUSIC manual: https://www-win.gsi.de/frs/technical/FRSsetup/detectors/music80/music80_manual.pdf
[3] R. Kanungo et al., Phys.Rev.Lett.117(2016) 102501
[4] A.N. Golovchenko et al., Phys. Rev. C66, 014609
[5] I. Schall et al., NIM B117 (1996) 221-234
[6] W.R. Weber et al., Phys. Rev. C41 (1990)
[7] C. Zeitlin et al., Phys. Rev. C76 (2007) 014911
[8] T. Yamaguchi et al., Phys. Rev. C82 (2010) 014609

Experiment beamline: FRS
Experiment collaboration: NUSTAR-SuperFRS-experiments
Experiment proposal:
Accelerator infrastructure: SIS18
PSP codes:

 DOI:10.15120/GR-2018-1

Concept of a MUSIC detector for high Z-resolution measurements

S. Bagchi[1,2,3], B. Voss[2], C. Scheidenberger[2,3], R. Kanungo[1,4], K-H. Behr[2] and the Super-FRS Experiment Collaboration

[1]Saint Mary's University, Halifax, Canada; [2]GSI, Darmstadt, Germany; [3]JLU, Giessen, Germany, [4]TRIUMF, Canada

Research in nuclear physics is now moving towards studies with radioactive ions or exotic isotopes far from the line of stability. Facilities like FRS at GSI, Darmstadt, Germany, BigRIPS at RIKEN, Tokyo, Japan and NSCL, USA produce the extensive part of the exotic nuclei in the nuclear landscape. In order to identify the exotic nuclei after production Bρ-ΔE-TOF technique is used. Energy loss measurements give the Z identification of the products since $\Delta E \propto Z^2$. The nuclear charge Z of the secondary ion is obtained by measuring the energy loss in MUltiple-Sampling Ionization Chamber (MUSIC) [1, 2].

Here we report on the concept of compact portable detector for high-resolution Z measurements for experiments at GSI and possibly other RI beam facilities worldwide. The main goal of this MUSIC detector is to measure the Z for light to medium heavy nuclei, i.e., having a larger dynamic range. A sketch of the experimental set-up is shown in Fig. 1 after a fragment separator. The MUSIC detector before the secondary target is to allow Z identification and the one after the secondary target is for nuclear reaction studies.

The MUSIC detector should be able to stand with the 10^5-10^6 particle counts per second. Working pressure inside the active volume of the detector is 1 atm. The outer dimension of the detector is 440 (X) x 240 (Y) x 400 (Z) mm^3 while the volume of the active area is 220 (X) x 100 (Y) x 300 (Z) mm^3. There will be 8 segmented anodes for charge collection.

The main idea is to fabricate a MUSIC detector whose Z resolution is as good as the SOFIA Twin-MUSIC. The design will be similar as the prototypes that are developed in GSI since 2010 [3-5]. The energy-loss resolution for SOFIA Twin-MUSIC is measured to be σ(ΔE)/E = 0.34% with P25 gas[3]. In Fig. 2, the charge distribution for electromagnetically exited fission using SOFIA Twin-MUSIC is shown. Fine adjustment of drift time inside the active volume with the help of position sensitive detector must lead to the position resolution of single anode of the order of μm.

Newly developed preamplifiers (MUSAMP/CEA made) that are with low noise, high rate capability and very short rise time will be used. In addition, a new VME read-out module from MESYTEC (MDPP-16) will be adopted. It has low noise analogue input stage coupled to a high sensitivity digitizer; multi hit ADC, TDC; pileup tagging; adjustable shaper and online processing. These detectors are the central part of a compact, movable setup for the complementary measurements of charge-changing cross section at various facilities mentioned above in the coming years. See also the contribution by A. Prochazka et al. to this report.

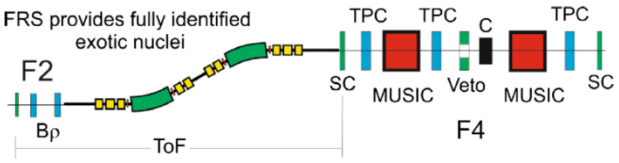


Figure 1: Experimental setup to identify the exotic nuclei and for nuclear reaction study. The MUSIC detectors provide the full Z identification of exotic nuclei.

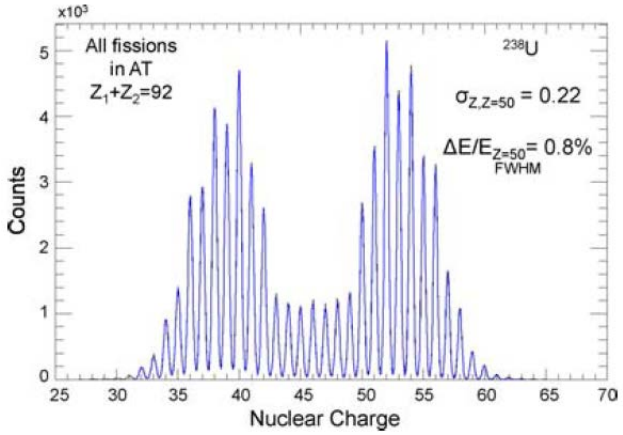


Figure 2: Nuclear charge distribution for electromagnetic exited fission using SOFIA Twin-MUSIC [3].

References:

[1] A. Stolz et al., Phys. Rev. C 65, 064603 (2002).
[2] R. Schneider and A. Stolz, Technical manual Ionization Chamber MUSIC80.
[3] I. Kaufeld, M. Takechi, and B. Voss, GSI Scientific Report 2013,GSI Report 2014-1 (2014) p.345.
[4] B.Voss et.al., GSI Scientific Report 2012,GSI Report 2013-1 (2013) p.204.
[5] B. Voss et al., GSI Scientific Report 2010, GSI Report 2011-1 (2011) p.223.

Experiment beamline:
Experiment collaboration: NUSTAR (R&D)
Experiment proposal: none
Accelerator infrastructure:
PSP codes:
Grants:
Strategic university co-operation with: Giessen, Saint Mary's University

Improved accuracy of the code ATIMA for energy loss of heavy ions in matter

H. Weick[1], H. Geissel[1,2], N. Iwasa[3], C. Scheidenberger[1,2], J. L. Rodriguez Sanchez[1], A. Prochazka[1], S. Purushotaman[1], for the Super-FRS experiment collaboration

[1]GSI, Darmstadt, Germany; [2]Justus-Liebig Universität Gießen, Germany, [3]Tohoku University, Sendai, Japan

The precise knowledge of the energy loss of heavy ions penetrating through layers of matter is essential for experiments, heavy ion therapy, separation of projectile fragments and many more accelerator applications. The program ATIMA (ATomic Interaction with MAtter) predicts the energy loss, energy-loss straggling and angular scattering of ions penetrating matter. Its predictions compared to data measured at the fragment separator FRS have demonstrated that an accuracy of ~1% in the stopping force (dE/dx) can be achieved. This has been accomplished for bare ions by using the LS-theory [1], whereas the pure Bethe theory deviates up to 10% [2] and by up to a factor of two in energy-loss straggling for high projectile atomic number (Z_1) ions at 1 GeV/u [3]. However, for ions with a few or many electrons the simple charge formula of Pierce and Blann [4] used in the ATIMA up to version 1.3 is not accurate [5], because it is not dependent on the target material. The experimental data also show that with an improved projectile mean charge description a good agreement can be achieved for high Z_1 ions (Au-U) down to 100 MeV/u where the K and L shells are partially filled.

Compared to the many mean charge formulas, theory-based analytical cross sections work best at sufficiently high velocity, as theory distinguishes correctly between the various electron capture and ionization processes. Yet for lower velocities the involved perturbation theory shows significant deviations. Based on the large amount of measured data with the FRS, a simple correction to the results from the GLOBAL program [6] with only three parameters was derived. The calculated mean charge depends on the velocity, the projectile (Z_1) and the target material (Z_2). This new description implemented in ATIMA, works for the entire range of projectile and target combinations down to 40 MeV/u.

Figure 1 shows the mean charge state prediction of uranium projectiles compared to our experimental data. The predicted mean charge varies considerably with Z_2, from <q>=86.2 in Be down to <q>=79.6 in Pb at 30 MeV/u. For even lower energies down to 10 MeV/u a pure fit formula [7] is used. For smoothening in the transition region a weighted average is used.

Unlike most other programs, in ATIMA we use the mean charge as it can be observed directly in experiments, whereas often an effective charge is used in stopping-power predictions to adjust for many effects. All other contributions to dE/dx are described by separate formulas such as the Barkas effect, shell corrections, and the Fermi-density effect [8]. With this approach we can gain a deeper understanding and improve the theoretical descriptions.

The accuracy of our new description has been tested with experimental data of projectiles with many electrons and different materials. The experimental data have been collected with the FRS in the last decades. This is an independent test as none of these measured data was used as a parameter in ATIMA 1.4 except for the mentioned mean charge. The data include U, Bi, Pb, Au, Xe, Kr, Ni projectiles on mainly solid targets ranging from Z_2=4 to 82 with energies from 1000 MeV/u down to 45 MeV/u.

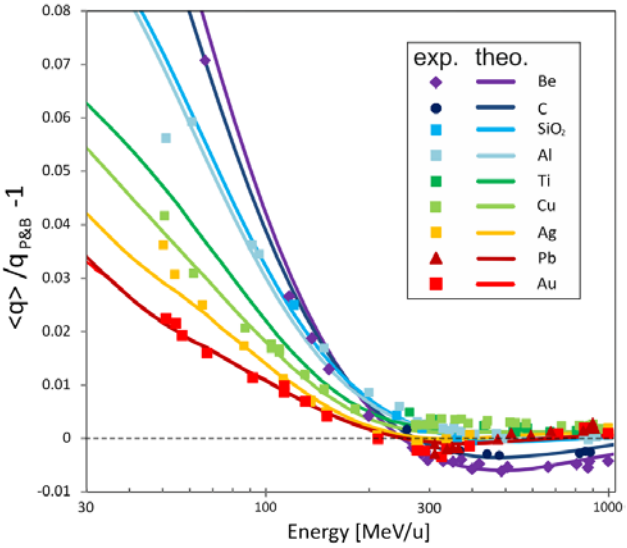


Figure 1: New predictions for the mean charge states of uranium ions after penetration of different target materials as function of energy are compared with experimental data. The comparison is normalized to the simple mean charge formula [4] used in the previous ATIMA versions.

Figure 2 shows a comparison of measured and predicted stopping forces in the energy range with the biggest differences to the previous ATIMA. The improvement is clearly demonstrated. In a limited energy range other programs, based on fits to measured data [9, 10], are better than the previous ATIMA version, but they fail for higher energies due to the simple effective charge approach and missing fully relativistic theory. At high energies for bare ions the results of ATIMA are accurate and remain unchanged.

The comparison of ATIMA 1.4 with experimental data includes all the available measured dE/dx values above 30 MeV/u. Table 1 shows the average standard deviations to theory from five experiments with the FRS. For the listed average relative standard deviations, the differences were weighted with the experimental errors. Of course the accuracy of the comparison is limited by the experimental errors.

For the data of ref. [11] up to 1 GeV/u with mainly bare ions ATIMA 1.4 naturally yields only a small improvement, but theories based only on perturbation theory show large deviations. The data of ref. [12] for Au-Bi ions in the range of 110 to 880 MeV/u with projectiles carrying a few electrons can be described better with ATIMA1.4. The same holds for the data of ref. [13] for Xe ions in the

 DOI:10.15120/GR-2018-1

energy range of 60 to 290 MeV/u. The new yet unpublished Uranium data down to 80 MeV/u with many electrons require ATIMA1.4. In this case the remaining deviations are only as small as the experiment errors themselves, while ATIMA1.3 - and other formulas even more - deviate significantly. At even lower energies (ref. [14]) the charge prediction and also the Barkas and shell corrections become less accurate, which explains the larger remaining deviation to ATIMA 1.4. Here the simple charge formula of ATIMA1.3 is not useful anymore as could already be seen in the comparison of Figure 1. Still ATIMA 1.4 is slightly better or is as good as the fit formulas.

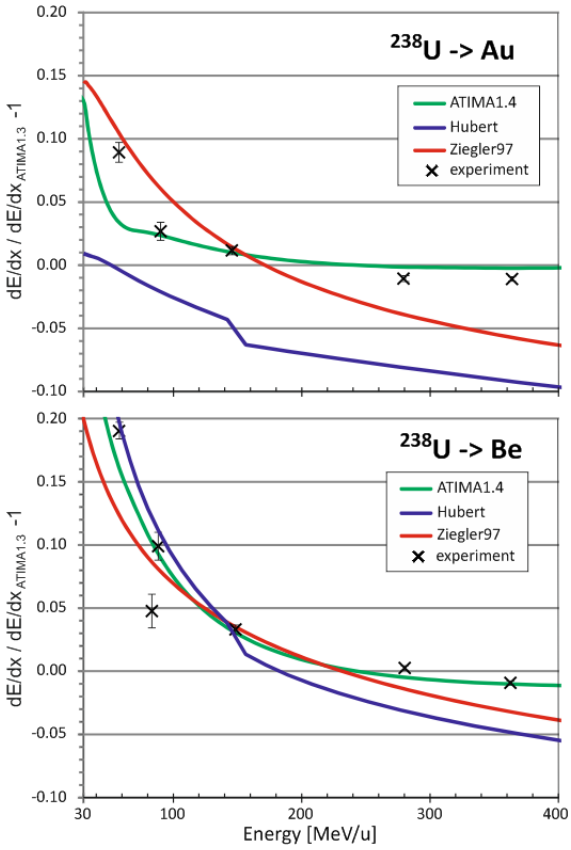


Figure 2: Comparison of new experimental dE/dx values of uranium ions in Au and Be targets to different formulas.

References

[1] J. Lindhard, A.H. Sørensen, Phys. Rev. A53 (1996) 2443.
[2] C. Scheidenberger et al., Phys. Rev. Lett. 73 (1994) 50.
[3] C. Scheidenberger et al., Phys. Rev. Lett. 77 (1996) 3987.
[4] T.E. Pierce, M. Blann, Phys. Rev. 173, 390 (1968).
[5] H. Weick et al., Nucl. Instr. Meth. B164 (2000) 168.
[6] C. Scheidenberger, et al., Nucl. Instr. Meth. B 142 (1998) 441.
[7] J. Winger et al., Nucl. Instr. Meth. B70 (1992) 380.
[8] C. Scheidenberger, H. Geissel, Nucl. Instr. Meth. B 135 (1998) 25.
[9] F. Hubert, R. Bimbot, H. Gauvin, Atomic and Nuclear Data Tables 46 (1990) 1.

Table 1: Comparison of experimental data for different projectiles (Z_1) and number of data points (N) with different theories: ATIMA1.3 ATIMA 1.4, Hubert [9], and Ziegler97 [10]. Listed are the average relative experimental errors and the average deviations of the theory from experimental data.

			[%]	[%]	[%]	[%]	[%]
Ref.	Z_1	N	exp.	A1.3	A1.4	Hub.	Z97
[10]	8-92	31	1.9	0.88	0.84	8.6	6.7
[11]	79-83	41	1.1	1.8	1.3	8.1	6.1
[12]	54	21	0.84	2.6	1.5	3.4	2.7
[13]	92	21	2.2	10.0	3.6	4.6	3.3
new	92	23	0.78	1.5	0.78	5.0	1.8

In the energy region much below 100 MeV/u the gas-solid difference in stopping powers of heavy ions makes the description more difficult. The gas-solid difference has been discovered at GSI about 40 years ago and has been confirmed in many experiments [15]. New experiments (approved proposal S469) are planned in different gaseous or solid targets.

Presently, below 10 - 30 MeV/u the region where direct theory becomes unreliable fit formulas with an effective charge as a variant of Ziegler's code [10] are applied in ATIMA and in addition a calculation for the contribution by elastic atomic collisions.

Since ATIMA version 1.3 the calculation includes projectiles up to Z_1=120 and targets up to Z_2=99 based on extrapolations. On the higher energy side ATIMA 1.4 calculates up to 450 GeV/u and also includes the then important nuclear size effect of the projectile [1, 8].
Integration of ATIMA into other programs such as MOCADI [16], PHITS [17], GEANT4, or ion optical codes has been done or is in progress. For an easy application, we provide a program as an interface to pre-calculated tables, as well as an online calculator [18].

[10] J.F. Ziegler, J.B. Biersack, U. Littmark, "The Stopping and Range of Ions in Solids", Vol.1, Pergamon Press (1985).
[11] C. Scheidenberger, PhD thesis, University of Giessen, 1994.
[12] H. Weick, PhD thesis, University of Giessen, 2000.
[13] M. Maier, PhD thesis, University of Giessen, 2004.
[14] A. Fettouhi, PhD thesis, University of Giessen, 2006.
[15] H. Geissel et al., Nucl. Instr. Meth. B195 (2002) 3.
[16] N. Iwasa et al., Nucl. Instr. Meth. B126 (1997) 284.
[17] T. Sato et al., J. Nucl. Sci. and Tech. (2018).
[18] ATIMA web page, http://web-docs.gsi.de/~weick/atima

Experiment beamline: FRS
Experiment collaboration: NUSTAR-SuperFRS-Experiments
Experiment proposal: S469
Accelerator infrastructure: SIS18 / FRS / Super-FRS
PSP codes:
Grants: SATNURSE EU project number 654002
Strategic university co-operation with: JLU Gießen

Implementation of ATIMA code in the Geant4 transport model

J. L. Rodríguez Sánchez[1,2], H. Weick[1], C. Scheidenberger[1], H. Geissel[1], N. Iwasa[3], A. Prochazka[1], S. Purushotaman[1]

[1]GSI, Darmstadt, Germany; [2]USC, Santiago de Compostela, Spain; [3]Tohoku University, Sendai, Japan

Geant4 [1] is a toolkit for Monte Carlo particle transport simulation in a wide range of applications, based on the object oriented technology. *Geant4* contains different models to compute the scattering and energy loss of the propagated particles and ions in matter. A great effort was carried out to improve and to validate the transport of γ-rays, leptons, mesons, and hadrons [2] as well as ions at low kinetic energies [3]. However, in *Geant4* there are few improvements concerning the transport of heavy ions at high energies (>400 MeV/u) [3]. Fortunately, in this energy range it was demonstrated that ATIMA code provides a precise description of the stopping power and angular scattering of ions when passing through matter [4]. For this reason, we will implement this code in *Geant4*. The first step was already performed translating the ATIMA code, written in Fortran language, to C++.

In this report, we present the benchmark of ATIMA [5] and *Geant4* for the stopping power of medium and heavy projectiles impinging on different targets. The experimental data were obtained with an accuracy around 1% at FRS-GSI during the last 30 years [5].

The stopping power of fast ions moving through matter is mainly due to the process of ionisation and excitation in target atoms. In *Geant4*, stopping power (dE/dx), range and inverse-range tables are constructed only for proton, antiproton, muons, pions, and kaons. The energy loss of other particles like ions is computed from these tables. The mean value of the energy loss is given by the Bethe-Bloch formula, in which the energy loss is calculated as a function of the ion velocity. For light particles like protons, the Bethe-Bloch formula provides an accuracy better than 1% [2], while deviations up to 9% are observed for heavy ions. According to this formula the energy loss of any fast ion can be expressed via the energy loss of another ion by using scaling factors. Therefore, the stopping power of an ion (ΔE_i) is proportional to the energy loss of a proton with a scaled velocity, such as: $\Delta E_i(T) = Z^2_i \Delta E_p(T_{scaled})$, where Z_i is the charge of the ion and ΔE_p is the stopping power of a proton with the scaled velocity, which corresponds to the so-called scaled kinetic energy: $T_{scaled} = T\ M_{proton}/M_i$, where T and M_i are the kinetic energy and the mass of the ion, respectively, and M_{proton} is the proton mass. As shown in Fig. 1, this model underestimates the stopping power around 7% at high kinetic energies (E_{kin}>400 MeV/u), while for lower energies the standard deviation is of about 3%. In the same figure, we can also see that ATIMA model predicts better results, for instance, ATIMA-1.2 provides a standard deviation around 1.8% while ATIMA-1.4 leads to deviations of about 1.3%.

Therefore, in order to improve the stopping power predictions in *Geant4*, we are implementing the ATIMA code according to the common structure based on the interfaces *G4VEmModel* and *G4VEnergyLossProcess* [6]. The first steps will be submitted to the *Geant4* repository at the end of May 2018.

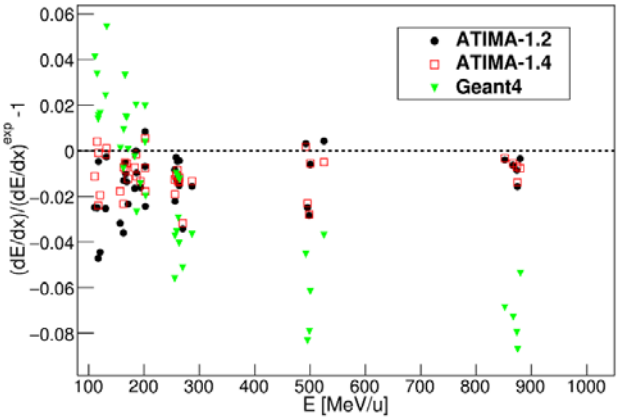


Figure 1: Comparison of the stopping power predicted by *Geant4* and different versions of ATIMA with experimental data taken from Ref. [5].

References

[1]S. Agostinelli et al., Nucl. Inst. Meth. A 506 (2003) 250.
[2]V. N. Ivanchenko et. al., J. Phys: Conf. Ser. 219 (2010) 032045.
[3]A. Lechner et al., Nucl. Inst. Meth. B 268 (2010) 2343.
[4]C. Scheidenberger et al., Phys. Rev. Lett. 73 (1994) 50.
[5]H. Weick et al., "Improved accuracy of the code ATIMA for energy-loss of heavy ions in matter", GSI Scientific Report 2017.
[6]J. Apostolakis et al., Rad. Phys. Chem. 78 (2009) 859.

Experiment collaboration: NUSTAR-SuperFRS-Experiments
Grants: SATNURSE EU project number 654002. This work has been also supported by the Department of Education, Culture and University Organization of the Regional Government of Galicia under the program of postdoctoral fellowships
Strategic university co-operation with: JLU Gießen

 DOI:10.15120/GR-2018-1

Accurate slowing-down measurements of heavy ions in gases and solids

S. Purushothaman[1], H. Geissel[1,2], H. Weick[1], S. Bagchi[1], T. Dickel[1,2], P. Egelhof[1], T. Grahn[3], E. Haettner[1,], A. Jokinen[3], B. Kindler[1], S. Kraft-Bermuth[2], N. Kuzminchuk-Feuerstein[1], B. Lommel[1], C. Montanari[4], Z. Patyk[5], S. Pietri[1], Y. Pivovarov[6], W.R. Plaß[1,2], A. Prochazka[1], C. Scheidenberger[1,2], V.P. Shevelko[7], D. Severin[1], P. Sigmund[8], A. Sørensen[9], T. Stöhlker[1], Y. K. Tanaka[1], M. Tomut[1], B. Voss[1], J.S. Winfield[1], M. Winkler[1]
and the Super-FRS Experiment Collaboration

[1]GSI Helmholtzzentrum für Schwerionenforschung GmbH, Darmstadt, Germany; [2]Justus-Liebig-Universität Gießen, Germany; [3]University of Jyväskylä, Finland; [4] Institute of Astronomy and Space Physics, Buenos Aires, Argentina; [5]National Centre for Nuclear Research, Warszawa, Poland; [6]Tomsk Polytechnic University, Tomsk, Russia; [7]P.N.Lebedev Physical Institute, Moscow, Russia; [8]University of Southern Denmark, Odense M, Denmark; [9]University of Aarhus, Aarhus C, Denmark

Accurate knowledge of heavy-ion slowing down in matter is crucial for a variety of scientific disciplines [1, 2]. Material science, heavy-ion therapy, astronautics, and accelerator physics are some of the examples. In the context of FRS experiments [3] at GSI and Super-FRS [4] at the future FAIR facility, the atomic interaction of heavy ions has to be known with high accuracy over the full energy range down to thermalization for efficient spatial isotope separation, energy-bunching and implantation experiments for spectroscopy or with gas-filled chambers. For kinetic energies close to the stopping power maximum the theoretical descriptions and widely used computer programs still fail to reproduce the experimentally observed gas-solid difference of stopping-powers and energy loss straggling [1, 5]. In the upcoming beam time at GSI in 2018-19 the stopping powers and charge-state distribution of xenon, lead and uranium ions penetrating amorphous monoatomic solids and gases of neighbouring proton numbers in the range of specific kinetic energies from 30 to 300 MeV/u will be measured. The main goal of this experiment is to obtain precision data and develop a valid description of this density effect, especially to observe where it vanishes at the higher velocities. This will also depend on the atomic number of the slowing down medium.

The absolute mean energy of the SIS beam is known with a relative accuracy of better than 10^{-3}. The FRS will be operated as a high-resolution magnetic spectrometer. A thin foil will be mounted at the entrance of FRS to prepare the desired charge-state population which will impinge on the atomic collision targets placed at the dispersive central focal plane.

The overall ion-optical mode of the FRS in these measurements will be achromatic to be independent of beam energy fluctuations from the accelerators which is a basis for high-resolution energy straggling measurements. We plan to use a microcalorimeter to enhance the precision for low ion energies. A schematic setup is shown in Figure 1

References

[1] P. Sigmund, Particle Penetration and Radiation Effects, Vol. 179. Springer Berlin, 2014.
[2] H. Geissel, et al., Nucl. Instr. Meth. B 195 (2002) 3.
[3] H. Geissel, et al., Nucl. Instr. Meth. B 70 (1992) 286.
[4] H. Geissel, et al., Nucl. Instr. Meth. B 204 (2003) 71.
[5] J. F. Ziegler, et al., Nucl. Instr. Meth. B 268 (2010) 1818.
[6] N. Iwasa, H. Weick, H. Geissel, Nucl. Instr. Meth. B269 (2012) 752

Experiment beamline: FRS
Experiment collaboration: NUSTAR-SuperFRS-Experiments
Experiment proposal: S469
Accelerator infrastructure: UNILAC / SIS18 / FRS
Strategic university co-operation with: Justus-Liebig-Universität Gießen

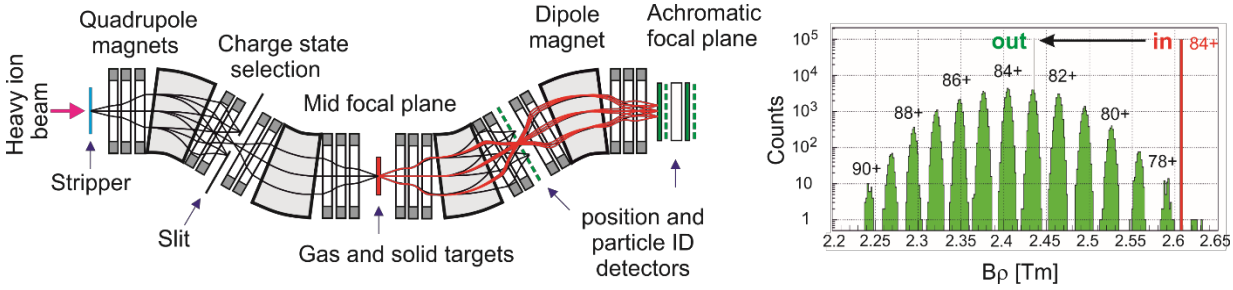


Figure 1: Experimental scenario for atomic collision experiments at the magnetic spectrometer FRS. The 4 dipole magnet stages are displayed with the focusing multipole magnets. The experimental detector setup at the focal planes will be used to measure the charge-state and energy-loss distributions. Simulated (MOCADI) charge state distribution and energy loss of an example case of 238U ions with (green) and without (red) a titanium target are shown in the inset [6].

Cherenkov radiation and half-wave crystal channeling as possible new mass/charge/velocity detectors of relativistic heavy ions

Yu. L. Pivovarov [1], O. Bogdanov[1], A. Bräuning-Demian[2], N. Kuzminchuk-Feuerstein[2], H. Geissel[2], S. Purushothaman[2], E. I. Rozhkova[1], C. Scheidenberger[2], T. A. Tukhfatullin[1], and the Super-FRS Experiment collaboration

[1]National Research Tomsk Polytechnic University, Russia; [2]GSI, Darmstadt, Germany.

Several basic atomic physics experiments are integral part of the scientific program of the Super-FRS Experiment Collaboration [1], including the study of Cherenkov radiation in liquid [2] and solid radiators [3] and channeling in thin half-wave crystals (HWC) [3] and the application of these effects as charge/mass/velocity detectors of relativistic heavy ions (RHI).

According to recent models [2, 3, 4] the slowing-down of the ions in the radiator at Super-FRS energies leads to broadening and complicated diffraction structures of the spectral and angular distributions (see in Fig.1).

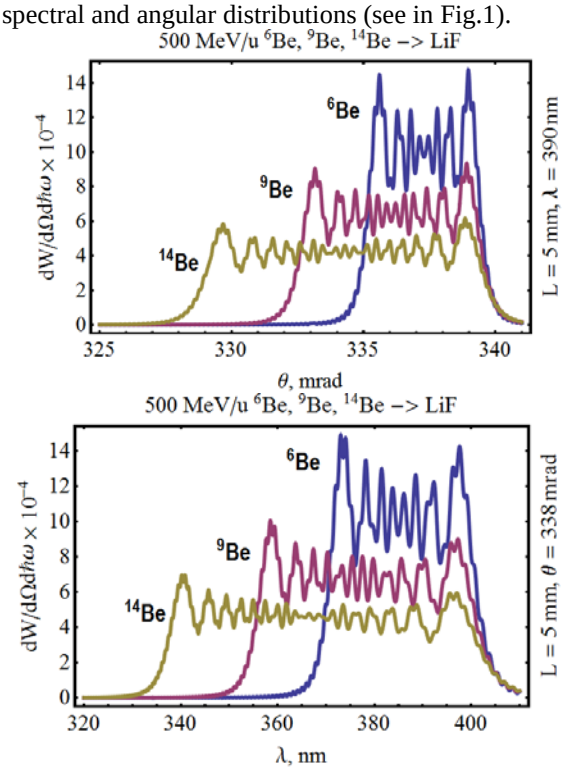


Figure 1. Angular (upper panel) and spectral (lower panel) distributions of Cherenkov Radiation from 500-MeV/u ^{6}Be, ^{9}Be, ^{14}Be isotopes in a LiF radiator of thickness L = 5 mm.

These distributions are very sensitive to the charge and velocity of RHI, and to the radiator thickness [2, 3, 4], thus the experiments with the Super-FRS will contribute to a detailed understanding of ChR from RHI ions and will lay the ground for improved and novel detector developments, like charge/mass/velocity detectors [3]. This topic is also discussed in Refs. [5, 6].

The FRS research collaboration has already performed channeling experiments at the FRS [7], the necessary equipment exists and can be used to continue these experiments at the FRS and later Super-FRS. We suggest to include studies of RHI channeling in a half-wave crystal into experimental program, which is a very recent trend in high-energy physics [8]. According to simulations, the achievable deflection angle through the mirror effect is of the order of critical channeling angle θc (see, in Fig. 2). Important is that the critical channeling angle depends both on the charge and mass of RHI.

The effect of HWC channeling can be used as effective beam deflector and even as charge/velocity selector.

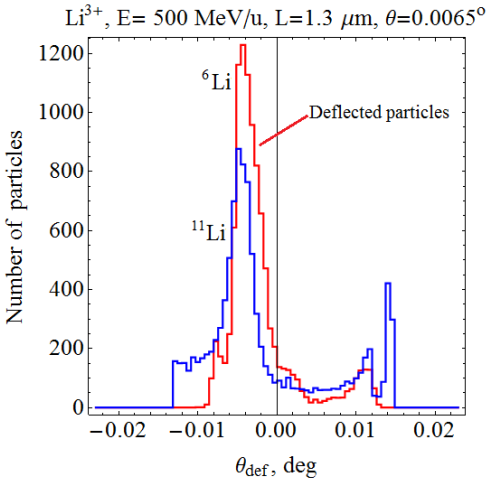


Figure 2. Deflection of 500 MeV/u Li isotopes by a (100) tungsten half-wave crystal. The critical channeling angle is θc = 0.0178° for ^{6}Li and θc = 0.0132° for ^{11}Li.

References

[1] CDR for the Scientific Program of the Super-FRS Experiment Collaboration (2016) DOI: 10.15120/GSI-2016-03763.
[2] H. Geissel et. al., GSI Scientific Report 2016, 179.
[3] E. I. Fiks et. al., Phys. Lett. A 380 (2016), 2386.
[4] O.V. Bogdanov et. al., Journ. Instr. Vol. 13 C02015 (2018) 7.
[5] T. Yamaguchi et. al., Nucl. Instrum. Methods A 766 (2014) 123.
[6] M. Machida et. al., POS (INPC2016) 084.
[7] D. Dauvergne et. al., Phys. Rev. A 59 (1999) 2813.
[8] W. Scandale et. al., Phys. Lett. B 734 (2014) 1.

Experiment beamline: FRS
Experiment collaboration: APPA / NUSTAR-SuperFRS-Experiments
Experiment proposal:
Accelerator infrastructure: UNILAC / SIS18 / FRS / SIS100 / Super-FRS
PSP codes:
Grants
Strategic university co-operation with: Tomsk Polytechnic University, Russia

 DOI:10.15120/GR-2018-1

A new modular detector design as a possible TOF detector for the Super-FRS

N. Kuzminchuk-Feuerstein[1], A. Neeb[2], E. Rozhkova[3], C. Scheidenberger[1], R. Siegert[4], B. Voss[1], and the Super-FRS collaboration

[1]GSI, Darmstadt, Germany; [2]Frankfurt University of Applied Science; [3]National Research Tomsk Polytechnic University, Russia; [4]RheinMain University of Applied Sciences, Rüsselsheim.

A high performance Time-of-Flight (TOF) detector is one of the key detectors in sub-atomic physics experiment to measure the velocity and mass of particles. Aiming to develop a TOF detector with a precision down to about 50 ps in time and resistant to a high radiation rate of relativistic ions of up to 10^7per spill a liquid medium, e.g. an Iodine Naphthalene ($C_{10}H_7I$) liquid radiator, was proposed for investigation of using Cherenkov radiation as a diagnostic tool for relativistic heavy ions [1], [2], [3].

The first-proof-of principle experiment with a TOF prototype detector using a $C_{10}H_7I$ radiator was performed at the SIS facility at GSI in April 2014 with nickel beam at 300-1500 MeV/u and ion beam intensities of up to 4×10^6 ions/spill [1]. Recently (2016), TOF measurements were performed with xenon ions at 600 MeV/u and a timing resolution of 63 ps (σ) was achieved [4].

To achieve the required time resolution and not to limit the application to a certain material we have initiated a development of a new design based on modular TOF detector employing Cherenkov or fast-plastic scintillator light emitted media (see Fig. 1).

The active media is a disk of 1 to 50 mm in thickness and a diameter of 18 cm. The system is designed with the possibility of quick exchange of the active media. The light is read out by 16 PMTs (ø 15 mm) of type Photonis XP1918, which are placed around the circumference of the disk. The time difference detected by two opposite PMTs (e. g. t_1 and t_9) are constant at a given ion position on a disk. As all PMTs are of the same type and show similar time characteristics the full detector time resolution is assumed to be equal to the average time accuracy of each PMT pair. In particular, in the TOF measurements between two detectors with 16 PMTs each time difference is expected to average out.

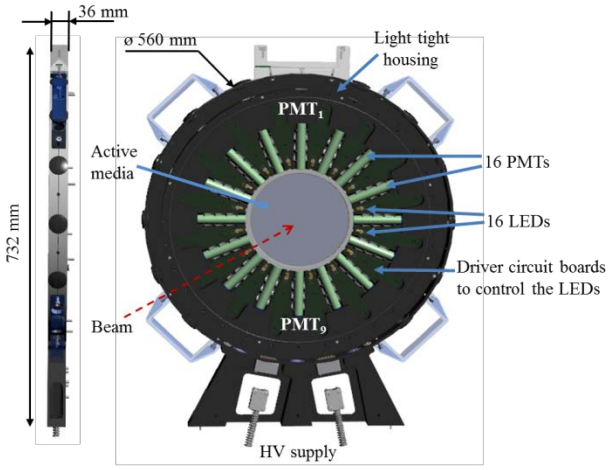


Figure 1: Conceptual design of the modular TOF detector with exchangeable active media. Arrangement of 16 PMTs and LEDs are shown.

The calibration system is based on short-pulsed LEDs placed around the active media between PMTs. The photons created in the media by the emitted light from LEDs can be detected by opposite placed PMTs. For the operation of LEDs, an avalanche generator was developed, based on the avalanche effect in a transistor [5]. With an avalanche transistor it is possible to generate needle pulses of less than 1 ns duration. The view of the setup used for test of LEDs is shown in Fig. 2. To trigger the LED's the driver circuit board has to be developed.

In-beam test of the detector design as well as of the data acquisition including VFTX-TDC are necessary and will be performed at GSI in 2018.

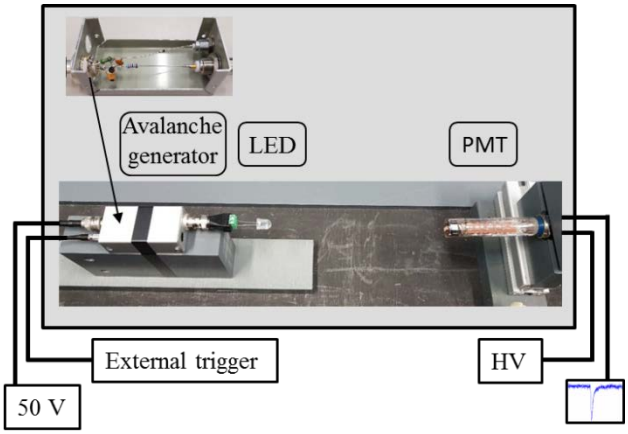


Figure 2: View of the setup used for measurements of the LEDs pulse duration with an avalanche generator [5].

References

[1] CDR for the Scientific Program of the Super-FRS Experimental Collaboration (2016). DOI: 10.15120/GSI-2016-03763

[2] N. Kuzminchuk-Feuerstein et. al., Nucl. Instrum. Methods A 821 (2016) 160-168.

[3] N. Kuzminchuk-Feuerstein et. al., GSI Scientific Report 2013, 141.

[4] N. Kuzminchuk-Feuerstein et. al., GSI Scientific Report 2016, 173.

[5] R. Siegert, "Entwicklung einer Treiberschaltung für Kurzpuls-LEDs", Bachelor Thesis, Hochschule RheinMain (2018).

Experiment beamline: FRS
Experiment collaboration: NUSTAR-R&D / FRS / SuperFRS /
Experiment proposal:
Accelerator infrastructure: SIS18 / SIS100 / Super-FRS

Development of the dual time-of-flight detector system for ILIMA

N. Kuzminchuk-Feuerstein[1], S. Ayet San Andreas[1], T. Dickel[1,2], M. Diwisch[2], O. Dolinskyy[1], H. Geissel[1,2], O. Gumenyuk[1], R. Knöbel[1], S. Litvinov[1], Y. A. Litvinov[1], W. R. Plaß[1,2], C. Scheidenberger[1,2], M. Steck[1], B. Sun[1,2], H. Weick[1], and the ILIMA collaboration

[1]GSI, Darmstadt, Germany; [2]Justus-Liebig-Universität, Gießen, Germany.

The Isomeric Beams LIfetimes and MAsses (ILIMA) collaboration will exploit heavy-ion storage rings at FAIR for the study of exotic nuclei. The CR is designed to allow for the operation in the isochronous ion-optical mode, a prerequisite for Isochronous Mass Spectrometry (IMS) with nuclei with lifetimes as short as several tens of µs, and for an acceptance many orders of magnitude larger than previous isochronous storage ring ESR. The masses of exotic nuclei can be deduced from a precise revolution time measurements by a TOF detector [1]. When the ions penetrate the thin detector foil, secondary electrons (SEs) are emitted from both surfaces and transported by perpendicular superimposed electric and magnetic fields to two microchannel plate (MCP) detectors (see Fig.1).

In the CR, we are aiming at in-ring measurement of the velocity of each particle in addition to its revolution time to correct for a wide mass-to-charge range in the mass measurement. Two TOF detectors with a distance of 16.9 m on a straight section are planned in the CR layout [2]. In this case the timing accuracy measured between the two detectors can be estimated from the resolution for a single passage of $\sigma_t = 35$ ps and averaging over many turns. Over a distance of 16.9 m at $\gamma_t = 1.67$ the TOF is 70 ns. Then the accuracy of measurement of one turn by two detectors is equal to $dt/t = (0.035 \cdot \sqrt{2})/70\ \text{ns} = 7 \cdot 10^{-4}$. Already after 10 turns this can be improved to $dt/t < 1 \cdot 10^{-4}$, which allows for correcting Bρ through dedicated velocity measurement. The design of new TOF detectors is based on the proven concept implemented in the present ESR-TOF detector [3].

The new CR will accept more intense stored beams with an acceptance of ΔBρ/Bρ=±0.5% and a transverse emittance of ε = 100 mm mrad, which results in larger beam diameters on the detector. Furthermore, the ring will run at a higher magnetic rigidity of up to Bρ = 13 Tm and a higher ion optical transition point (up to γ_t=1.84). The choice of the detector foil size (ø=80 mm) increases the area by a factor of four and the phase space acceptance by a factor of 16. It is motivated by the large emittance of the CR. The main challenge was to incorporate a larger diameter foil into the design and thus, to develop a larger construction with optimized fields.

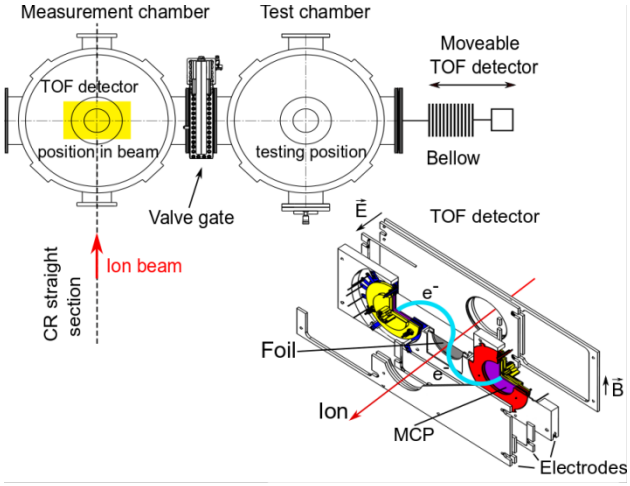


Figure 1: The overall setup of new TOF detector with vacuum chambers at measurement and test position as it will be installed twice on the straight section in the CR.

The dual time-of-flight detector system consists of two separated TOF detectors. Two vacuum chambers will be installed in the CR for each TOF detector. The movement of the detector into the beam line and back will be done using a long bellow, rails and stepper motors. The mounting and the offline tests of the detector will be done inside the test chamber, separated from the measurement chamber with a valve gate, which will be opened only after having reached sufficient UHV condition not to deteriorate the vacuum in the CR.

An optimized electrode system with only three electrode plates has been developed based on the results of simulations [4]. The pole-shoe and outer diameter of the dipole magnet are equal to 900 mm and 1000 mm. The preliminary design, checked with a manufacturer, foresees about 320 windings and applied current of 5.2 A.

Recently, a method of data analysis, using a correlation-matrix (first developed for Schottky) for the combined data set from different experiments, was adapted and used to determine new mass values [5] [6].

The TDR was submitted to FAIR through the NUSTAR collaboration board in December 2017 and currently is under review.

References

[1] N. Kuzminchuk-Feuerstein et. al., Nucl. Instrum. Methods A 821 (2016) 160-168.
[2] N. Kuzminchuk-Feuerstein et. al., TDR of the dual TOF - detector system for ILIMA (2017). https://edms.cern.ch/document/1896955
[3] J. Trötscher PhD Thesis, JLU Gießen (1993).
[4] M. Diwisch, PhD Thesis, JLU Gießen (2015).
[5] R. Knöbel et. al., Eur. Phys. J. A (2016) 52:138.
[6] R. Knöbel et. al., Phys. Lett. B 754, 288 (2016).

Experiment beamline: CR
Experiment collaboration: NUSTAR-ILIMA
Experiment proposal:
Accelerator infrastructure: SIS18 / SIS100 / CR / Super-FRS /
PSP codes: 1.2.6.4, 1.2.6.6
Grants: BMBF (Contract no.05P09RGFN9, 05P16RGFN1)
Strategic university co-operation with: Gießen

 DOI:10.15120/GR-2018-1

Fast timing with FATIMA - From νBall at ALTO to DESPEC at GSI

P.-A. Söderström[1,2], M. Rudigier[3], T. Arici[2], S. Bottoni[4], M. Brunet[3], R. Canavan[3], N. Cieplicka-Oryńczak[5], S. Courtin[6], D. Doherty[3], J. Gerl[2], M. Gorska[2], K. Hadyńska-Klęk[3], M. Heine[6], Ł. W. Iskra[5], N. Jovančević[7], V. Karayonchev[8], A. Kennington[3], I. Kojouharov[2], P. Koseoglou[1,2], M. Lebois[7], N. Kurz[2], C. Lizarazo[1,2], G. Lorusso[3,9], G. Lotay[3], M. Nakhostin[3], C.R. Niță[10], S. Oberstedt[11], N. Pietralla[1], S. Pietri[2], Zs. Podolyák[3], L. Qi[7], P.H. Reagan[3,9], J.-M. Régis[8], S. Saha[1,2], H. Schaffner[2], R. Shearman[3], J. Vesić[2], J. Wilson[7], W. Witt[1,2]

[1]TU-Darmstadt, Darmstadt, Germany; [2]GSI, Darmstadt, Germany; [3]University of Surrey, Guildford, U.K.; [4]University of Milano, Milano, Italy; [5]Institute of Nuclear Physics, PAN, Kraków, Poland; [6]IPHC, Strasbourg, France; [7]IPN, Orsay, France; [8]Universität zu Köln, Köln, Germany; [9]NPL, Teddington, UK; [10]IFIN-HH, Magurele, Romania; [11]European Commission, Geel, Belgium

Lifetime measurements of excited states using fast $LaBr_3$ scintillators is a strongly emerging field within nuclear physics that has gained significant popularity in recent years. Most of the experiments performed to date have taken place using γγ-coincidences at stable beam facilities [1]. With the upcoming generation of high-intensity radioactive ion beam facilities, this technique is becoming increasingly used to study the structure of more exotic nuclei [2]. For example, in one of the recent experiments at RIKEN, βγ-coincident fast-timing with $LaBr_3$ and plastic scintillators have been very successful [3,4]. This type of experiment will be one of the foci of the upcoming DESPEC beam times.

Implementing FATIMA with νBall

In November 2017 the first experiment with the new mixed EUROBALL HPGe and FATIMA $LaBr_3$ spectrometer, νBall, was performed in Orsay. It's aim was to measure the lifetime of the low-lying states in ^{166}Dy as well as to search for a predicted 4^- isomer. The experiment was performed using a pulsed ^{18}O beam from the ALTO tandem to induce two-neutron transfer reactions on a ^{164}Dy target as well as fusion-evaporation reactions to reach high-spin states in ^{178}W. One of the key features in this experimental setup is the possibility to use the high resolution pulsed beam to extract lifetimes from beam radiofrequency-γ coincidences. A typical example of the spectra obtained is shown in Figure 1. Within the data from this experiment the transitions of interest in ^{166}Dy were clearly observed in singles and in γγ-coincidences, the lifetime of the first excited state in the Coulex of ^{164}Dy was well reproduced, and γ rays originating from the decay of the high-spin isomers of ^{178}W could also be identified. The full data from this experiment is currently under analysis. However, the data already shows stable operation and a high quality of the output data from FATIMA.

Experiments within DESPEC in 2018

For the DESPEC campaign the FATIMA detectors will be moved to GSI in spring 2018. One of the proposed experiments at GSI is the study of neutron-rich Hf, W, and Os isotopes. The advanced implantation detector AIDA will be used as an active stopper consisting of three layers of silicon detectors. AIDA will be complemented by thin plastic scintillators for electron tagging and these will be read out via regular or silicon photomultipliers. FATIMA will be configured into three rings upstream, and for high-resolution spectroscopy an array of HPGe detectors will be installed; currently proposed as seven DEGAS triple-clusters. The proposed readout of FATIMA will consist of 10-bit resolution and 1 GS/s V1751 8-channel digitizers, and V1290 16-channel multihit TDCs. These electronic units will be integrated into the GSI readout system MBS via a RIO4 CPU, TRIVA trigger module, and a VULOM4b VME universal logic module. The results and experience from these experiments will be crucial for future implementation of NUSTAR at FAIR.

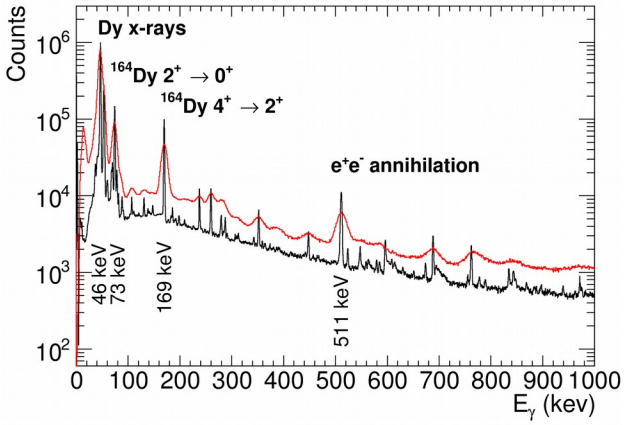


Figure 1: Example spectra of γ rays detected in the HPGe (black) and $LaBr_3$ (red) detectors. The most intense features are labelled.

References

[1] N. Mărginean, et al., Eur. Phys. J. A 46 (2010) 329
[2] P. H. Regan, et al., EPJ Web Conf. 63 (2013) 01008
[3] F. Browne, et al., Phys. Lett. B 750 (2015) 448
[4] F. Browne, et al., Phys. Rev. C 96 (2017) 024309

Characterization of a Sunpower CryoTel CT cooling engine for DEGAS

W. Witt[1,2], P. Koseoglou[1,2], P.-A. Söderström[1,2], E. Adamska[3], J. Gerl[2], I. Kojouharov[2], N. Pietralla[1]

[1]TU Darmstadt, Darmstadt, Germany; [2]GSI, Darmstadt, Germany; [3]University of Warsaw, Warsaw, Poland

As one of the four experimental pillars of the FAIR project the NUSTAR collaboration aims at investigating exotic beams provided by the accelerator through the Super-FRS. This includes the decay spectroscopy setup DESPEC, which is to be located at the low-energy branch of the facility. To obtain maximum output from DESPEC, new detector systems for high-efficiency measurements are being developed and adapted to the facility's requirements. One of the key instruments is the DEGAS germanium-array, which, due to its compact design, makes the standard liquid nitrogen cooling impossible. Therefore, new technology based on compact electrical coolers of the type Cryotel CT by Sunpower is under development [1].

One of the main obstacles in the application of electrical cooling are the vibrations originating from the Stirling engine, which transfer directly to the Ge-crystal to be cooled and affect its energy resolution. To characterize the thermal properties of the cooler and, in particular, to quantify the vibrations and explore possible countermeasures, several measurements were performed at the Helmholtz-Institut Mainz during summer 2017. The purpose of this measurements was to observe time-dependent temperature and acceleration developments at the cooling point during the cooling-down process and the effect of different mechanical holding structures on the oscillations.

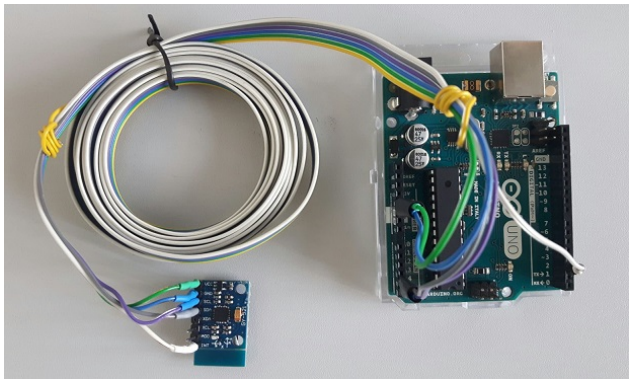


Figure 1: The MPU6050 sensor connected to an Arduino Uno Board for readout.

The thermal measurement performed with a PT-100 sensor showed a gradual cooling-down process towards the operating temperature of 77K, which was achieved within 150 minutes. The power consumption did not exceed 170 W and remained at 60 W at 77K. These properties met the expectations and requirements for the DEGAS cooling.

The accelerometry was performed using an Arduino Uno Board and a MPU6050 sensor [2], as shown in Fig. 1. The MPU6050 sensor is equipped with an accelerometer and a gyroscope and the Arduino Uno board was programmed to read the values from the sensor and stream them to a computer at 500 kbps. The effective sampling frequency was determined globally for the full setup by the sampling frequency of the sensor, and the internal clocks of the sensor and the Arduino board. The maximum sampling frequency of the MPU6050 sensor's accelerometer is 1 kHz and the highest sampling frequency reached during these measurements was around 600 Hz. The acceleration measuring range was set to ±16 G.

The obtained data were analysed using a three-dimensional Fast Fourier Transform (FFT), including a low-pass filter. One main product of these measurements can be seen in Fig. 2. showing the vibration frequency as a function of time during 30 minutes of the cooling-down phase. Besides lower-intensity vibrational features four strong bands are dominant, which coincide with the frequency of the cooler's gear (60 Hz) [3] and it's harmonic modes (120 Hz, 180 Hz, 240 Hz).

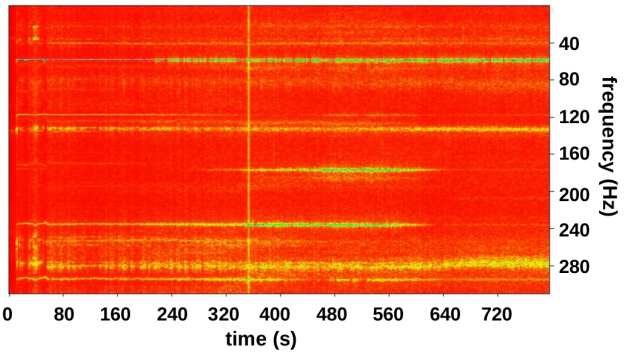


Figure 2: Typical frequency-time spectrum of oscillations at the cooling point of the Cryotel CT during the cool-down process.

In previous tests of the cooler [1], the malfunction or wrong setting of the AVC (active vibration cancellation, a mechanical attachment to the cooler to perform anti-phase oscillations for a net-zero vibration of the cooler) remained unclear. This was ruled out in this work. The AVC was shown to work correctly and dampen the oscillations slightly.

Furthermore, accelerometry was performed after changing the properties of the cooler's holding structure (damping legs, Styrofoam, additional weight on top), cp. Fig. 3. The structure variation proved to have a potentially damping effect on the measured oscillations and, hence, the adaption of the holding structure in terms of mechanical decoupling of the cooler from the cooling point, e.g. employed in [4], was persued.

 DOI:10.15120/GR-2018-1

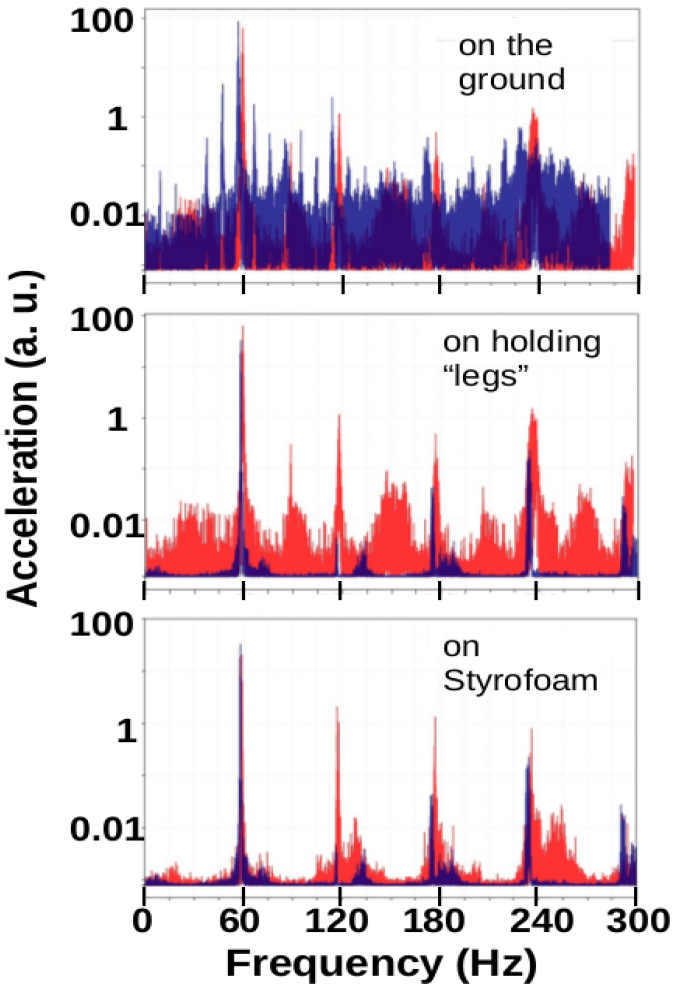


Figure 3: Variation of the cooler oscillations with changing holding structure and with (blue) /without (red) lead on top.

The design and manufacture company Ortec could be convinced to design and produce such adapted holding structure. A first draft of the design based on vacuum bellows and flexible copper rods for the decoupling is shown in Fig. 4. The production is planned to be finished in April 2018.

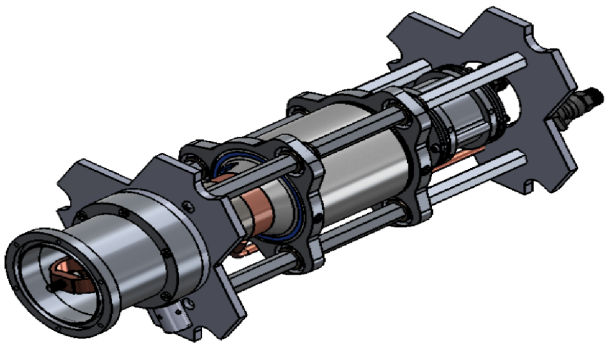


Figure 4: New Cryotel CT holding structure as designed by Ortec employing oscillation-decoupling mechanics.

Further tests will show the efficiency of the modifications. Should the oscillations prove to be sufficiently reduced, the electrical Cryotel CT coolers will be used in the DEGAS array as foreseen starting Fall 2018 with the FAIR-0 DESPEC experiments.

This work was supported by HGS-HIRe and the German ministry for education and research (BMBF) within the project NUSTAR R&D under grant no. 05P15RDFN1.

References

[1] W. Witt et al., GSI Scientific Report 2016, 186 (2017)
[2] http://www.arduino.cc/ accessed in September, 2017
[3] Sun Power CryoTel User Manual V.7 (2012)
[4] G. Raskin et al., Compact Stirling cooling of astronomical detectors, Instr. and Meth. for Astrophys. (2013)

First spectroscopy of neutron-rich Sc isotopes using FAIR instrumentation in the third SEASTAR campaign

P. Koseoglou[1,2], V. Werner[1], P.-A. Söderström[1,2], M. Lettmann[1], N. Pietralla[1], P. Doornenbal[3], A. Obertelli[1,4,3], N. Achouri[4], H. Baba[3], F. Browne[3], D. Calvet[4], F. Château[4], S. Chen[5,6,3], N. Chiga[3], A. Corsi[4], M. L. Cortés[3], A. Delbart[4], J-M. Gheller[4], A. Giganon[4], A. Gillibert[4], C. Hilaire[4], T. Isobe[3], T. Kobayashi[7], Y. Kubota[3,8], V. Lapoux[4], H. Liu[4,9], T. Motobayashi[3], I. Murray[3,10], H. Otsu[3], V. Panin[3], N. Paul[4], W. Rodriguez[11,3], H. Sakurai[3,12], M. Sasano[3], D. Steppenbeck[3], L. Stuhl[8], Y. L. Sun[4], Y. Togano[13,3], T. Uesaka[3], K. Wimmer[12,3], K. Yoneda[3], O. Aktas[9], T. Aumann[1], L. X. Chung[14], F. Flavigny[10], S. Franchoo[10], I. Gasparic[3,15], R.-B. Gerst[16], J. Gibelin[17], K. I. Hahn[18], D. Kim[18], T. Koiwai[12], Y. Kondo[19], J. Lee[6], C. Lehr[1], B. D. Linh[14], T. Lokotko[6], M. MacCormick[10], K. Moschner[16], T. Nakamura[19], S. Y. Park[18], D. Rossi[1], E. Sahin[20], D. Sohler[21], S. Takeuchi[19], H. Törnqvist[1], V. Vaquero[22], V. Wagner[1], S. Wang[23], X. Xu[6], H. Yamada[19], D. Yan[23], Z. Yang[3], M. Yasuda[19] and L. Zanetti[1].

[1]Institut für Kernphysik, Technische Universität Darmstadt; [2]GSI Helmoltzzentrum für Schwerionenforschung GmbH; [3]RIKEN Nishina Center; [4]IRFU, CEA, Université Paris-Saclay; [5]School of Physics, Peking University; [6]Department of Physics, The University of Hong Kong; [7]Department of Physics, Tohoku University; [8]Center for Nuclear Study, the University of Tokyo; [9]Department of Physics, Royal Institute of Technology; [10]Institut de Physique Nucléaire Orsay, IN2P3-CNRS; [11]Universidad Nacional de Colombia; [12]Department of Physics, University of Tokyo; [13]Department of Physics, Rikkyo University; [14]Institute for Nuclear Science & Technology, VINATOM; [15]Rudjer Boskovic Institute, Zagreb; [16]Institut für Kernphysik, Universität zu Köln; [17]LPC Caen, ENSICAEN, Université de Caen; [18]Ewha Womans University; [19]Department of Physics, Tokyo Institute of Technology; [20]Department of Physics, University of Oslo; [21]MTA Atomki; [22]Instituto de Estructura de la Materia, CSIC; [23]Institute of Modern Physics, Chinese Academy of Sciences.

Recent results for the level structure of ^{54}Ca have shown evidence for the existence of a new magic neutron number N=34 [1]. At the same time there might not be a corresponding shell gap in Ti isotopes [2, 3]. Scandium isotopes lie between calsium and titanium. In scandium isotopic chain the valence proton occupies the $\pi f_{7/2}$ orbital, interacting with the $\nu f_{5/2}$ orbital in $^{55-61}$Sc. The evolution of the proton orbitals of these isotopes can reveal the nature of both the magic number N=34, recently proved to vanish in ^{55}Sc [4], and the N=40 *pf*-shell closure.

Gamma-ray spectroscopy of the neutron-rich $^{55-61}$Sc isotopes was performed at the Radioactive Isotope Beam Factory (RIBF) in Wako-shi, Japan, as part of the third SEASTAR campaign [5]. A ^{70}Zn beam at 345 MeV/u, delivered from the RIBF accelerator complex, produced a cocktail of secondary radioactive beams by impinging on a 10-mm-thick ^{9}Be target. The secondary beams, that were identi ed and separated by the BigRIPS fragment separator [6], produced the isotopes of interest by knock-out reactions in the MINOS target system [7], consisting of a 150-mm-thick LH_2 target surrounded by an active TPC. The emitted gamma-quanta of the isotopes produced were measured by the DALI2+ array [8], consisting of 226 NaI(Tl) detectors, surrounding MINOS. The reaction products were reconstructed event-by-event in SAMURAI [9] using two drift chambers and a hodoscope plastic-scintillator array. Additionally, NeuLAND [10] and NEBULA [11] were used for neutron detection. The experimental set-up is shown in Figure 1.

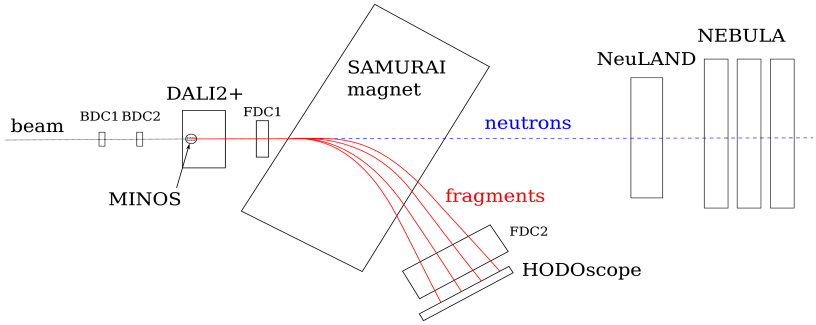


Figure 1: Experimental set-up of the 3rd SEASTAR campaign at RIBF.

 DOI:10.15120/GR-2018-1

The γ transitions reported previously for ^{55}Sc in Ref. 4 have been already identified in the current early state of our data analysis from the neutron knock-out reaction, ^{56}Sc(p,pn)^{55}Sc. The analysis for $^{55\text{-}61}$Sc is on-going. Figure 2 shows the particle identification in BigRIPS after gating on $^{55\text{-}61}$Sc nuclei in SAMURAI.

The large number of detectors together with the BigRIPS fragment separator and the SAMURAI magnet formed a complex experimental set-up similar to the planned NUSTAR HISPEC/DESPEC experiments at FAIR.

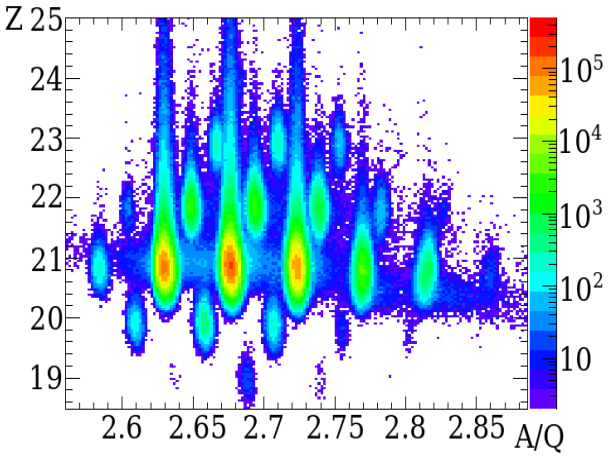


Figure 2: The particle identification in BigRIPS after gating on $^{55\text{-}61}$Sc in SAMURAI.

The first author would like to thank the Helmholtz Graduate School for Hadron and Ion Research (HGS-HIRe) for FAIR for its support though the HGS-HIRe abroad program.

References

[1] D. Steppenbeck, et al., Nature **502**, 207-210 (2013).
[2] D.-C. Dinca, et al., Phys. Rev. C **71**, 041302(R) (2005).
[3] S. N. Liddick, et al., Phys. Rev. Lett. **92**, 072502 (2004).
[4] D. Steppenbeck, et al., Phys. Rev. C **96**, 064310 (2017).
[5] P. Doornenbal and A. Obertelli, RIKEN Proposal for Scientific Program (2013).
[6] T. Kubo, et al., Prog. Theor. Exp. Phys. 2012, 03C003 (2012).
[7] A. Obertelli, et al., Eur. Phys. J. A **50**, 8 (2014).
[8] S.Takeuchi, et. al., Nucl. Instr. and Meth., A **763** (2014) 596-603.
[9] T. Kobayashi, et. al., Nucl. Instr. and Meth., B **317** (2013) 294-304
[10] NeuLAND-TDR, https://edms.cern.ch/document/1865739.
[11] T. Nakamura, Y. Kondo, Nucl. Instr. Meth. B **376**, 1 (2015).

Fuzzy Bayes Tracking – Experimental results

P. Napiralla[1,2], H. Egger[3], P. R. John[1], N. Pietralla[1], M. Reese[1], and C. Stahl[1]

[1]Institut für Kernphysik, Technische Universität Darmstadt, Darmstadt, Germany; [2]GSI, Darmstadt, Germany;
[3]AG Numerik und wissenschaftliches Rechnen, Technische Universität Darmstadt, Darmstadt, Germany

The Advanced GAmma Tracking Array AGATA [1] will be the key instrument for nuclear structure investigations in the upcoming HISPEC and DESPEC experimental campaigns at the Facility for Antiproton and Ion Research FAIR. Due to its germanium shell without any Compton-shielding, γ-ray tracking algorithms are essential for experiments with high reaction rates.
Based on the mathematical framework of the *Bayes-Tracking* (see [2]), the Fuzzy Bayes Tracking (FBT) adds a geometrical clustering algorithm into the framework. This clustering algorithm is based on a *Fuzzy c-means* algorithm (see [4]), which forms simple geometrical clusters via a minimization process. These clusters are then either physically confirmed or torn further by the Bayesian analysis of the tracking algorithm, if a higher amount of clusters is more likely. This is achieved by comparing all possible sub-combinations of observed clusters via *marginalization* [3]

$$P(cluster) = \sum_{n=1}^{N} P(cluster|n)\,P(n)$$

where n is the number of possible sub-clusters and N is the number of observed interaction points. For each sub-cluster, the probability $P(cluster|n)$ is calculated using known cross sections of Compton scattering and photo-electric absorption. In addition, the plausibility of the resulting photon paths are considered by comparing geometrical scattering angles with energetic Compton scattering angles under the metrological restraints of the AGATA detectors. Comparing all possible probabilities $P(cluster|n)$, the most probable sub-clusters are chosen and their respective total deposited energies are set as the tracked energies.

Using ^{60}Co source data from the AGATA-Demonstrator experiment 09.08 conducted at LNL in 2011, a first benchmark test of the Fuzzy Bayes Tracking can be made. The achieved performance of the Fuzzy Bayes Tracking can be seen in Figure 1. By suppressing cluster formation with very low probabilities (mostly belonging to escaped photons), the tracked spectrum can be cleaned significantly (see Fig. 1).

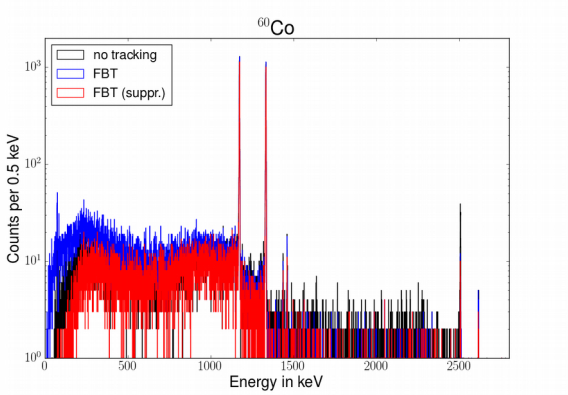


Figure 1: Performance of the Fuzzy Bayes Tracking on a ^{60}Co spectrum. Black is without any tracking, blue the tracked spectrum without suppression and red with suppression.

Comparing the Peak-to-Total ratios with and without the Fuzzy Bayes Tracking yields:

- no tracking: 38 %
- FBT: 31 %
- FBT with suppression: 43 %

To improve the Fuzzy Bayes Tracking further, future work will focus on merging FBT's methods with the reconstruction methods mentioned in [2]. In addition, further improvements of the geometrical clustering process will be made.

References

[1] A. Akkoyun *et. al.*, AGATA – Advanced Gamma Tracking Array, Nuclear Instruments and Methods in Physics Research A, 668:26-58, 2012.
[2] P. Napiralla *et. al.*, Bayes-Tracking – A novel approach to γ-ray tracking, GSI Scientific Report 2016, 2016.
[3] D. Sivia and J. Skilling, Data Analysis – A Bayesian Tutorial, volume 2, Oxford University Press, Oxford, 2006.
[4] M.S. Yang and Y. Nataliani, Robust-learning fuzzy c-means clustering algorithm with unknown number of clusters, Pattern Recognition, 71:45-49, 2017.

Experiment beamline: none
Experiment collaboration: NUSTAR-DESPEC-HISPEC
Experiment proposal: none
Accelerator infrastructure: none
PSP codes: 1.2.2.8
Grants: BMBF 05P15RDFN1, BMBF 05P15RDFN9
Strategic university co-operation with: Technische Universität Darmstadt

 DOI:10.15120/GR-2018-1

Position sensitive Ge detector

T. Arici[1], I. Kojouharov[1], J. Gerl[1]

[1]GSI, Darmstadt, Germany

Position sensitivity of gamma-ray detection is required for a wide range of applications. In order to achieve good position sensitivity, segmentation of the contacts of the crystal must be applied. Recently, segmentation of HPGe has been applied to coaxial crystals, such as the AGATA detectors, results in a position resolution of 3-5 mm with a high energy resolution [1]. Despite the impressive results obtained by these detectors, the demand for increased position resolution of 1 mm requires focusing on segmented planar detectors. Nevertheless, having a superior position resolution, the physics of the operation and the feasible technical solutions resulted in a large dead volume in the crystal and large insensitive space around it, which affects negatively the performance of a planar detectors array. To solve the problem, a new geometry, namely the semi-planar detector geometry, which severely minimizes this layer, has been proposed.

Detector Test

The project proposed is aimed at development of semi-planar detector with point contacts as a segmentation tool. This includes a detailed study by numerically simulating the electric field and the charge transport inside the detection crystal and a search for the optimal geometry.
The crystal processing is supposed to be carried out by an industrial partner and the detector to be scanned by the GSI Detector Scanner. The main idea is to make several point read-outs on a planar crystal which are sensitive to certain area. The distribution and number of these points can be estimated by performing simulations taking the electric field and charge transportation into account. In this framework, semi-planar HPGe detector with a single point contact read-out was studied in order to characterize the behaviour of such a novel contact technology replacing the segmentation of the crystal. A non-segmented p-type HPGe crystal with a dimension of 33.2x33.2x15.5 mm^3 and Carrier concentration of 3.3x109 atom/cm^3 was used for the test purposes. The charge signal was extracted from the p+ electrode. The detector was operated at 100 V and 1.2 pA leakage current was observed. Sudden increase of the leakage current when increasing the bias voltage caused the saturation of the pre-amplifier which is related to the type of the coupling used for the signal read-out. Detector was tested using ^{57}Co and ^{60}Co sources in order to cover the low and high energy regions. For each source different shaping times were tested. Experimental data was fitted using an exponentially modified Gaussian function and the results for two different shaping times are given in Figure 1 for ^{60}Co source. Using the ^{57}Co source, 2.1 keV and 2.3 keV energy resolutions at 122 keV line was obtained respectively for 3 µs and 6 µs shaping times. While with ^{60}Co source, 4.5 keV and 4.3 keV energy resolution was obtained for the 1332 keV transition respectively for 3 µs and 6 µs shaping times.

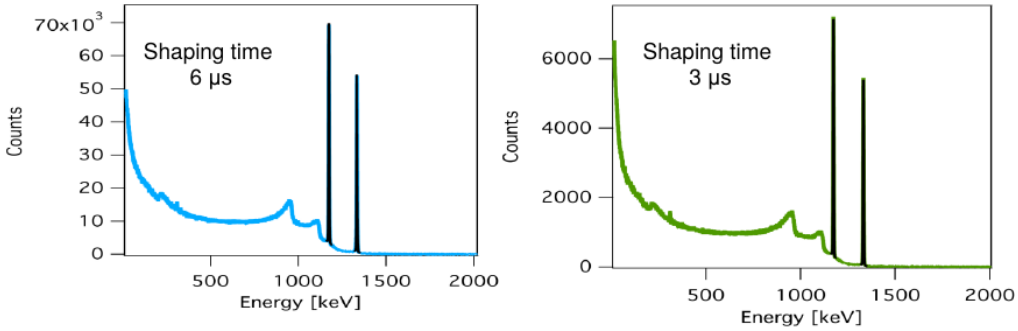


Figure 1: The observed energy spectrum with ^{60}Co source. The spectrum on the left side was recorded using 6 µs shaping time while the one on the right side obtained with 3 µs shaping time.

References

[1] S. Akkoyun and A. Algora, "AGATA – Advanced Gamma Tracking Array", NIM volume 668, 26-58 2012

Experiment beamline: Gamma-Spectroscopy
Experiment collaboration: NUSTAR-DESPEC-HISPEC
Grants: ENSAR2

Fast-timing lifetime measurement of ^{152}Gd with FATIMA-type $LaBr_3$ detectors

J. Wiederhold[1], R. Kern[1], C. Lizarazo[1,2], W. Witt[1,2], V. Werner[1], N. Pietralla[1], D. Bucurescu[3], N. Florea[3], D. Ghita[3], T. Glodariu[3], R. Lica[3], N. Marginean[3], R. Marginean[3], C. Mihai[3], R. Mihai[3], I.O. Mitu[3],A. Negret[3], C. Nita[3], A. Olacel[3], S. Pascu[3], L. Stroe[3], S. Toma[3], A. Turturica[3]

[1]Institut für Kernphysik,TU Darmstadt, Germany; [2]GSI, Darmstadt, Germany, [3]IFIN-HH, Bucharest, Romania

In preparation of the upcoming DESPEC campaign at FAIR with the Fast TIMing Array (FATIMA), experiments were performed at the 9-MV FN Tandem of the National Institute for Physics and Nuclear Engeneering Horia Hulubei in Bucharest. The experimental setup at IFIN-HH for γ-ray spectroscopy uses the RoSphere Array [1] consisting of 11 FATIMA-type $LaBr_3$ detectors and 14 HPGe detectors, which is similar to the planned setup for the upcoming DESPEC campaign in 2018/19 with the DEGAS and FATIMA detectors.

Fast electronic scintillation timing (FEST)

The lifetime of an excited nuclear state is determined using FEST by measuring the time di erence between a start and a stop signal. The respective time signals originate from the detection of γ quanta from nuclear transitions feeding and depopulating the state of interest. The resulting time-di erence distribution is a convolution of the prompt response of the experimental setup and the exponential decay of the excited nuclear state. Lifetimes in the range of dozens of ps can be determined by measuring the centroid shift of the time-di erence distribution after a correction for the energy dependent time-walk of the experimental setup is applied. A more detailed overview of the experimental technique and the setup can be found in [1-3].

Lifetimes of ^{152}Gd

The region around neutron number N=90 is a well-known example for a rather rapid change in structure as a function of the nucleon number, i.e., a rst order quantum phase transition (QPT) [4]. Excited states of ^{152}Gd (N=88 neutrons) were populated via the ^{149}Sm(α,n)^{152}Gd reaction and lifetimes were measured using FEST. In particular, the lifetime of the second 0^+ was investigated, searching for a possible new signature of a QPT [5]. Figure 1 shows the obtained energy spectrum of the HPGe detectors. Many transitions of ^{152}Gd can be identi ed.

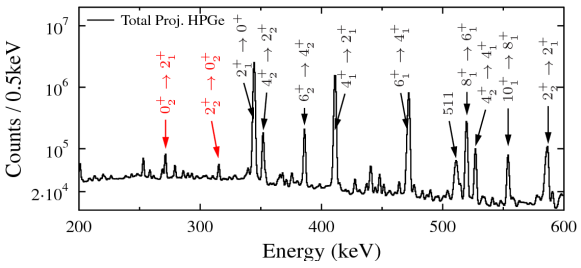


Figure 1: Partial energy spectrum of the HPGe detectors.

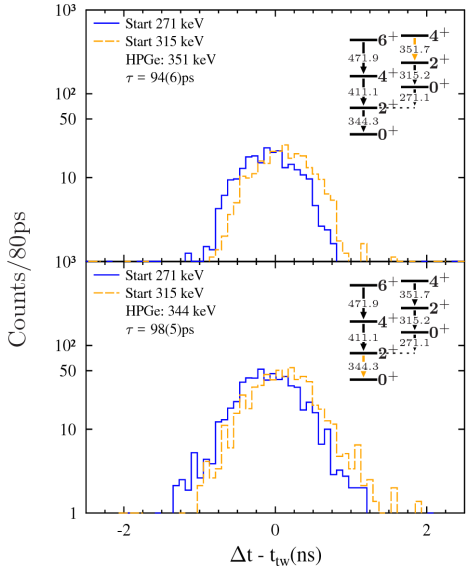


Figure 2: Time-di erence spectra for the combination of gates on the 2^+_2 0^+_2 and 0^+_2 2^+_1 transitions of ^{152}Gd.

Figure 2 shows the nal time-di erence spectrum for the combination of gates on the populating (315 keV) and decaying (271 keV) transitions of the second 0^+ state of ^{152}Gd. Additional gates were set in the pulse-height spectra from the HPGe detectors, selecting the cascade of interest and eliminating background contributions.

The newly determined mean lifetime of the second 0^+ state of ^{152}Gd of τ=96(6) ps [5] turned out to be nearly two times larger than the literature value of 53(12) ps [6] with direct implications for the charaterization of the QPT in the Gd isotopic chain [5].

Supported by the BMBF under the grants 05P15RDFN1 and 05P15RDFN9 and by HIC for FAIR.

References

[1] D. Bucurescu *et al.*, Nucl. Instrum. Methods Phys. Res. A **837**, 1 (2016).
[2] N. Marginean *et al.*, Eur. Phys. J. A **46**, 329 (2010).
[3] J.-M. Régis *et al.*, Nucl. Instrum. Methods. Phys. Res. A **726**, 191 (2013).
[4] R. Casten, Nature Physics **2**, 811 (2006).
[5] J. Wiederhold *et al.*, Phys. Rev. C **94**, 044302 (2016).
[6] N. R. Johnson *et al.*, Phys. Rev. **C** 26, 1004 (1982).

 DOI:10.15120/GR-2018-1

Activities in superheavy element research at SHIP and TASCA

H. David[1], Ch.E. Düllmann[1,2,3], M. Götz[1,2,3], S. Götz[1,2,3], E. Jäger[1], J. Khuyagbaatar[1,3], J. Krier[1], L. Lens[1,2], A. Di Nitto[1,2], V. Pershina[1] , J. Runke[1,2], B. Schausten[1], A. Yakushev[1,3,] for the SHE Chemistry department and the TASCA Collaboration,

M. Block[1,2,3], P. Chhetri[4,1], M. Eibach[5,1], F. Giacoppo[1,3], F. P. Hessberger[1,3], O. Kaleja[2,6], M. Laatiaoui[2,3], J. Maurer[1], A. K. Mistry[1,3], T. Murböck[1], S. Raeder[1,3] for the SHE Physics department and the SHIP/SHIPTRAP Collaborations.

[1]GSI, 64291 Darmstadt, Germany; [2]Universität Mainz, 55099 Mainz, Germany [3]Helmholtz Institut Mainz, 55099 Mainz, Germany; [4]Technische Universität Darmstadt, 64289 Darmstadt, Germany; [5] Universität Greifswald, 17489 Greifswald, Germany; [6]MPIK Heidelberg, 69117 Heidelberg, Germany

In the year 2017, efforts of the Superheavy Element Chemistry department focused on analysis of data obtained in the past UNILAC beamtime period. Major modifications to the experimental setups were performed: i) an upgrade of the cave X8 (TASCA) to install improved shielding, ii) the installation of a new, more flexible TASCA detector chamber, iii) a relocation of the TASCA control room in anticipation of major refurbishment of the SE building, which currently houses the control room, and iv) the design and implementation of a next generation TASCA Control System. Thus, best use was made of the extended shutdown period at GSI.

Selected experiments were performed at other facilities, including the Cyclotron Institute at Texas A&M University, College Station, USA.

'For the superheavy element physics department the activities concentrated on the analysis of data obtained in the past UNILAC beamtime period and preparations of the different experimental setups for the planned experiments in the beamtime period 2018 at GSI.

In parallel, several technical developments were advanced, for example, the completion of the decay spectroscopy system COMPASS, the construction of the single-ion mass measurement setup SHIPTRAP-2, and the design of a novel setup for gas-jet laser spectroscopy.

The specific activities are discussed briefly in the following sections.

Nuclear reaction studies

The drastic reduction of fusion-evaporation cross sections for reactions that form the heaviest elements cannot be understood without knowledge of the competing quasifission (QF) process, which hinders the fusion. Generally, this competition is studied by measuring fission fragments originating from QF and fusion-fission (FF). However, quantitative descriptions of experimental results become complex as many degrees of freedoms are involved and observables for FF and QF can overlap significantly. In collaboration with the Australian National University (ANU), Canberra, Australia, several experiments have been carried out in recent years at ANU's Heavy Ion Accelerator Facility (HIAF). Here, a large range of beam-target configurations was examined in order to investigate how QF/FF competition evolves with changes in entrance channels, taking advantage of the wide angular range available for fission-fragment detection with the CUBE detector setup. These data, together with data on fusion-evaporation reactions (e.g., measured at TASCA and SHIP), provide a comprehensive dataset for describing the QF and FF [Khu17]. In particular, measurements of varying QF probabilities in the ^{48}Ti+^{204,208}Pb and ^{50}Ti+^{206,208}Pb reactions have shed light on the strong influence of nuclear structure on the fusion process. Observed differences for ^{48}Ti+^{208}Pb and ^{50}Ti+^{206}Pb, providing distinct experimental evidence that even reactions that form the same compound nucleus and share the same charge product ($Z_p \cdot Z_t$) can exhibit different levels of QF, cannot be explained by current theories. In addition, data collected using beams of ^{48}Ca, ^{50}Ti, ^{54}Cr, ^{58}Fe and ^{64}Ni incident on actinide targets has yielded a clear systematic picture of a strong dynamical evolution when moving from ^{48}Ca to heavier beams. The data are currently under final analysis. To obtain a conclusive picture concerning the choice of the most preferable beam-target combination for the synthesis of new elements beyond Z=118, fusion-evaporation cross-section measurements of ^{50}Ti-induced reactions on any actinide is suggested. Such measurements are planned to be performed, e.g., at RIKEN, Japan and Dubna, Russia.

Nuclear Structure

Construction of the novel ALpha-BEta-GAmma (ALBEGA) multi-coincidence spectroscopy setup for chemically separated samples [DiN15] continued. Advanced prototypes of the two ALBEGA core detectors, whose inner surfaces are covered with a thin Al and SiO_2 layer, respectively, have been tested. They were developed to provide i) improved energy resolution and sensitivity to low energy signals produced by electrons, ii) higher photon detection efficiency, and iii) better mechanical stability against pressure differences. The tests performed with several radioactive sources including ^{241}Am (α particles) and ^{133}Ba (conversion electrons) confirmed performance according to specifications, including the uniformity and desired very thin thickness of the dead layers, as well as the sensitivity to the low energy signals. In a next step, the detectors will be mounted in a sandwich configuration to produce the final version of the ALBEGA core detector that will be characterized in 2018.

Nuclear decay spectroscopy data collected in parasitic ^{48}Ca beamtime was examined as part of the commissioning of the new Compact Decay Spectroscopy Setup (COMPASS) [Ack18] detection system at SHIP. Initially, the upgrade of using a higher granularity implantation

detector in the form of a double-sided silicon strip detector was assessed, with long correlation times from the decay ^{254}No→^{250}Fm (~30 min) →^{246}Cf measured [Mis18]. In addition, the ability to perform α-γ coincidences was successful, with excited states in ^{249}Fm populated following the decay of ^{253}No. Secondly, with the use of new digital electronics (FEBEX3A) [Hof12], the heavy neutron deficient region around *Z*=92-94 was explored. The use of such a fast timing system (20 ns time resolution) enables full chains to be acquired from a region of fast decaying nuclei, where with a conventional analogue system chain members could not be recorded due to dead time of the electronics system. A successful product of this investigation was synthesis of the previously unconfirmed isotope ^{225}Np. Development work on improvements to the detector system included upgrading to FEBEX4A (10 ns timing resolution) and enhancements to the escape 'box' detectors to maximize efficiency.

Mass measurements for nuclear structure studies

The nuclear structure studies by direct mass spectrometry with SHIPTRAP will be further extended to heavier and more exotic nuclides in the next beamtime period at GSI in 2018. Facing the challenge of ever-lower production rates, it has been worked on measures for a further increase in efficiency and sensitivity. To this end in the recent years, a cryogenic gas cell for SHIPTRAP has recently been built. In the commissioning beamtime in 2015 an increase of the overall efficiency by almost one order of magnitude was achieved [Kal15]. In 2017, additional offline studies were performed with radioactive sources. We studied the extraction of different elements from the gas cell and to optimize the transport of ions to the SHIPTRAP Penning traps following the 2016 relocation of the complete setup [Gia17]. The phase imaging (PI-ICR) measurement technique [Eli13] was further optimized at SHIPTRAP studying systematic uncertainties, exploring the achievable mass resolving power and improving the long-term stability for measurements with lowest yield. The PI-ICR technique has become the new standard for on-line mass measurements of radionuclides worldwide. However, challenges for direct mass spectrometry of the heaviest elements remain. In the next measurement campaign at GSI the identification of low-lying isomeric states in No-, Lr-, and Rf-isotopes is planned. In this mass region the various types of isomeric states are known, many of which have low excitation energies and similar half-lives to the ground state rendering their identification by means of conventional nuclear spectroscopy difficult. The high mass resolving power of the PI-ICR method makes it an ideal choice for this. A mass resolving power of about 100,000 for only 100 ms measurement time has also been reached for heavy ions.

Atomic Physics

The pioneering laser spectroscopy work on nobelium performed at the GSI in recent years led to the observation of more than 30 atomic states in the nobelium atom, among them several Rydberg states [Laa16]. From the convergence of the observed Rydberg series, we eventually obtained the ionization potential based on a two-step laser ionization scheme with high accuracy. However, the presence of buffer gas collisions led to the population of long-lived metastable states below the $^1P_1$ state that was directly excited by the first-step laser. The second laser excitation had sufficient energy to ionize the nobelium atoms from either of the two states. Thus, the identification of the different series was crucial for the IP determination. This was accomplished based on the delayed ionization signal obtained when the second step laser was delayed compared to the first one. In the case of the $^1P_1$ state that features a lifetime of only about 2 ns this signal decayed rapidly, whereas a longer-lived component with a lifetime of tens of ns was observed indicating the population of the lower-lying metastable state. In 2017, the data analysis was completed, and a rate equation model was developed that allowed us to describe the experimental data for nobelium as well as corresponding data for the homolog ytterbium perfectly [Chh17]. Consequently, the first ionization potential of nobelium was determined two orders of magnitude more accurately than before [Chh18].

The analysis of the hyperfine spectroscopy data for ^{253}No was supported by three different sets of atomic structure calculations that provided the mass shift and field shift constants as well as the hyperfine parameters. The results support the ground state spin and parity assignment of $9/2^-$, previously derived from in-beam gamma spectroscopy, and furthermore provide the magnetic and quadrupole moment of this odd-*A* nucleus accurately. Recently, state-of-the-art density functional calculations reproduced the differential charge radii of lighter actinides [Mar14, Rei17]. These calculations are also in excellent agreement with the nobelium data on differential charge radii. This confirms the theoretical prediction of maximum deformation in the nobelium isotopic chain around neutron number N = 152. It also substantiates the claim of a sizeable central depression in the proton distribution of ^{254}No, a feature that is only found in superheavy nuclei and originates from their strong Coulomb repulsion. The hyperfine spectroscopy results have been submitted for publication [Rae18].

Chemistry

In the past beamtime periods, experiments to study the chemical behavior of Fl and Nh in comparison with Hg, Tl, Pb, and Rn were performed at TASCA [Blo16]. In addition, the volatility and reactivity of these elements towards surfaces like SiO_2 and Au were measured. The comprehensive analysis of these results was continued. For Nh, experimental results [Blo16, Aks17] indicate a reduced volatility and enhanced reactivity compared to Cn and Fl. To render assistance to these gas-phase experiments, calculations of the adsorption energies of these elements and their lighter homologs on a Au(111) surface have been performed using a periodic ADF BAND code. Such periodic calculations of adsorption energies have been performed for the first time for superheavy element systems adsorbing on gold. The results have shown that Cn should indeed be the most volatile element out of

 DOI:10.15120/GR-2018-1

those under consideration. In addition, Fl should interact with gold at room temperature. Nh, should very strongly interact with gold. Such a different adsorption behavior allows for a good separation between all of these elements using a combination of quartz and gold surfaces [Per17a]. In addition, molecular properties of group-13 hydroxyls (of Tl and Nh) needed for predictions of their reactivity with quartz and gold have been calculated with the use of most advanced relativistic methods. In difference to the conclusion from the earlier predictions, NhOH is expected to be less volatile than TlOH [Per18]. To study Nh under improved conditions, advanced setups for optimized transport of the element under study to the detection setup are under development also allowing investigation of less volatile species. One such approach involves the direct connection of the existing COMPACT detection array [Yak14] to the TASCA Recoil Transfer Chamber (RTC). Another possibility involves the coupling of COMPACT to a recoil separator by employing a buffer-gas stopping cell instead of a classical RTC. First studies of the extraction efficiency of ^{219}Rn ions obtained from a ^{223}Ra recoil ion source installed in the SHIPTRAP buffer gas stopping cell [Neu06] into a COMPACT detector array were measured in off-line experiments at GSI. A first on-line experiment with such a setup was performed at the Cyclotron Institute, Texas A&M University, College Station, USA. The buffer gas stopping cell was coupled to the Momentum Achromat Recoil Spectrometer (MARS) [Fol12]. The isotopes ^{182,183}Hg and ^{199,200}At were produced in the reactions ^{40}Ar + ^{147}Sm and ^{40}Ar + ^{165}Ho, isolated in MARS, thermalized in the buffer gas stopping cell, and extracted into the COMPACT by using electric fields. The final analysis of the obtained extraction efficiencies and transport times is currently ongoing.

The studies related to volatile transition metal carbonyl complexes with short-lived isotopes have been continued. Currently, the method of choice is the isolation of the studied isotopes in a recoil separator, followed by their thermalization in an RTC that is flushed with CO-containing carrier gas [Eve14]. As the fusion-evaporation products of asymmetric fusion reactions needed for the productions of sufficiently long-lived isotopes of the elements of interest like Sg, Bh, and Hs, have a relatively large angular and energy spread, transmission efficiencies through a recoil separator like TASCA or GARIS at RIKEN are rather moderate, around 10-15%. Thus, the overall efficiency for the synthesis of carbonyl complexes in combination with physical preseparation is rather low. Therefore, possibilities for the chemical investigation of these compounds without a physical preseparator are currently explored. First experiments performed at the Tandem accelerator at JAEA Tokai, Japan, suggested that the successful synthesis of Os and W carbonyl complexes is feasible if the thermalization of the evaporation residues is spatially decoupled from the chemical synthesis. In that way it is needed, that the formation of the carbonyl complexes takes place in the absence of the beam, which is a strict requirement [Wan14]. In experiments with fission products at the research reactor TRIGA Mainz, the partial efficiencies for the flush-out transfer of non-volatile products from the thermalization chamber into the chemical synthesis chamber were measured and confirm that such an approach allows obtaining higher efficiencies than with preseparation. To support gas-phase experiments on studies of the stability and volatility of carbonyls of the heaviest elements, calculations of the electronic structures and properties of group-6 carbonyls [Ili17] and group-7 carbonyls, including those of Bh, were performed using the most advanced relativistic quantum-chemical methods (ADF BAND, X2c-DFT, DIRAC). The work considers all possible formation reaction scenarios of the single species that do not exist in macrochemistry. The formation mechanisms have been found and the volatile species that should form at the experimental conditions are suggested. Accordingly, the detailed properties of the $M(CO)_5H$ species (M= Tc, Re and Bh) have been calculated, including radicals $M(CO)_5$. Volatilities of these species and first bond dissociation energies have been predicted [Per17b].

Further activities, including those centered at the Helmholtz Institute Mainz, are described in more detail in the contribution to the Annual Report 2018 of the Helmholtz Institute Mainz [HIM18].

References

[Ack18] D. Ackermann, A.K. Mistry, F.P. Hessberger et al., Nucl. Instrum. Meth. A, accepted, in publication (2018).
[Aks17] N.V. Aksenov et al., Eur. Phys. J. A 53, 158 (2017).
[Blo16] M. Block et al., GSI Sci. Rep. 2016, p. 197-199, RESEARCH-NUSTAR-SHEP-1.
[Chh17] P. Chhetri et al., Eur. Phys. J. D 71,195 (2017).
[Chh18] P. Chhetri et al., in preparation (2018).
[DiN15] A. Di Nitto et al., GSI Sci. Rep. 2014, p. 184, MU-NUSTAR-SHE-C-06 (2015).
[Eli13] S. Eliseev et al., Phys. Rev. Lett. 100, 082501 (2013)
[Eve14] J. Even et al., Science 345, 1491 (2014).
[Fol12] C.M. Folden III et al., NIMA 678, 1 (2012).
[Gia17] F. Giacoppo et al., Acta Phys. Pol. B 48, 423 (2017).
[HIM18] SHE section of the 2017 HIM Annual Report (2018).
[Hof12] J. Hoffmann et al., GSI Scientific Report 2011, 253, (2012).
[Ili17] M. Iliaš and V. Pershina, Inorg. Chem. 56, 1638 (2017).
[Kal15] O. Kaleja et al., xxx
[Khu17] J. Khuyagbaatar, EPJ Web Conf., 163, 00030 (2017).
[Laa18] M. Laatiaoui et al., Nature 538, 495 (2016).
[Mar14] J. A. Maruhn et al., Comput. Phys. Commun. 185, 2195 (2014).
[Mis18] A. K. Mistry et al., Acta Phys. Pol., accepted, in publication (2018).
[Neu06] J.B. Neumayr et al., NIMB 244, 489 (2006).
[Per17a] V. Pershina, Relativistic Quantum Chemistry for Chemical Identification of the Superheavy Elements, In: Handbook of Relativistic Quantum Chemistry, Ed. W. Liu, Springer, (2017) pp. 857-899.

[Per17b] V. Pershina and M. Iliaš, J. Chem. Phys. 146, 184306 (2017).
[Per18] V. Pershina and M. Ilias, Chem. Phys. Lett. 694, 107 (2018).
[Rae18] S. Raeder et al., in publication (2018).
[Rei17] P.-G. Reinhard and W. Nazarewicz, Phys. Rev. C 95, 064328 (2017).
[Wan14] Y. Wang et al., Radiochim. Acta 102, 69 (2014).
[Yak14] A. Yakushev et al., Inorg. Chem. 53, 1624 (2014).

Experiment beamline: SHIP-SHIPTRAP / TASCA
Experiment collaboration: NUSTAR-SHE / NUSTAR-LASPEC / NUSTAR-MATS
Experiment proposal:
[U259,U288,U295,U308,U312,U313,U314]
Accelerator infrastructure: UNILAC
Grants: [EU H2020 contract No. 654002 / TNA]
Strategic university co-operation with: JGU Mainz

 DOI:10.15120/GR-2018-1

Comparison of nuclear and electromagnetic breakup of ^{17}Ne

F. Wamers[1,2], J. Marganiec[1,2,3], T. Aumann[2,1], L.V. Chulkov[4,1], M. Heil[1], B. Jonson[5], R. Plag[1], H. Simon[1], and the R^{3}B collaboration

[1]GSI, Darmstadt, Germany; [2]TU Darmstadt, Darmstadt, Germany; [3]EMMI@GSI, Darmstadt, Germany; [4]NRC Kurchatov Institute, Moscow, Russia; [5]Chalmers Tekniska Högskola, Göteborg, Sweden

In previous years we have reported on various aspects of the structure of and reactions with the proton dripline nucleus ^{17}Ne, as observed in the S318 experiment [1-4].

Here we highlight our recent study of ~500 MeV/u ^{17}Ne reactions on light (carbon and CH_2) vs. heavy (lead) targets, with a focus on electromagnetic breakup to the ^{15}O+2p continuum [5].

Momentum Distributions

We have analysed channels with one heavy fragment, ^{15}O or ^{14}O, and one or two coincident beam-like protons as forward-focused reaction residues. While, e.g., ^{15}O+1p produced from light targets (H, C) show a narrow fragment momentum distributions (142 MeV/c, 152 MeV/c), produced mainly via *1p knockout* on ^{17}Ne, on the Pb target such a 1p knockout is taking place inside the target's strong Coulomb field causing the ^{15}O momentum distribution is about 3 times wider (430 MeV/c). The fragment momentum distributions in the ^{15}O+2p channels are generally wider (C: 301 MeV/c, Pb: 285 MeV/c), since the reaction mechanisms at work here are mainly *inelastic scattering* and *diffraction dissociation* (plus *electromagnetic dissociation* for Pb), which typically transfer momentum to more than just one nucleon in the projectile nucleus. For the H target and the ^{15}O+2p channel, however, the observed ^{15}O momentum distribution exhibits an even larger width (365 MeV/c); the reaction mechanism here is still unclear, since the three mentioned above should typically be negligible for a proton target.

Electromagnetic Dissociation

Because of the nuclear astrophysics interest for the ^{15}O(2p,g)^{17}Ne reaction rate, we have distilled the pure electromagnetic fraction of the Pb-target based ^{15}O+2p differential cross section, by subtracting the equivalent C-target distribution (scaled by 1.84). Figure 1 shows a comparison of this E_{f2p}-differential cross section (blue filled diamonds) with three theoretical calculations (solid lines = raw, dashed lines = broadened by the experiment resolution). First, the blue line represents a calculation based on a ^{15}O+2p three-body model [6] in which the weight s^2 configuration of the ^{17}Ne g.s. was at P(s^2) = 5%. The calculation result was scaled by 0.5 in order to get a better agreement with the experimental data. Results obtained for larger P(s^2) within this model require an even stronger downscaling; e.g., for P(s^2) = 48% the required scaling is 0.25. Second, the red curve stems from a different three-body model, with P(s^2) = 16%, [7]. Third, the magenta curve shows an RQPRPA based Hartree-Bogoliubov calculation [8]. Generally, the three models produce ^{15}O+2p internal energy spectra that strongly differ between each other. We observe that the calculation resulting from the model of [7] matches the experimental data better than the others, in particular in absolute numbers, and at energies E_{fpp} > 5 MeV. It is interesting to note in particular the difference between [6] and [7], since they are both based on a ^{15}O+2p three-body model. Furthermore, all three calculations feature E1-only dissociation, whereas the experimentally observed population of the $5/2_1^-$ excited state at 830 keV above threshold suggests a non-negligible contribution of E2 strength to the electromagnetic dissociation of ^{17}Ne. We find that yet none of the theoretical models on the market match the entire experimental spectrum in a satisfactory way. However, our data may help to validate models of the ^{17}Ne structure and of dissociation processes in the future.

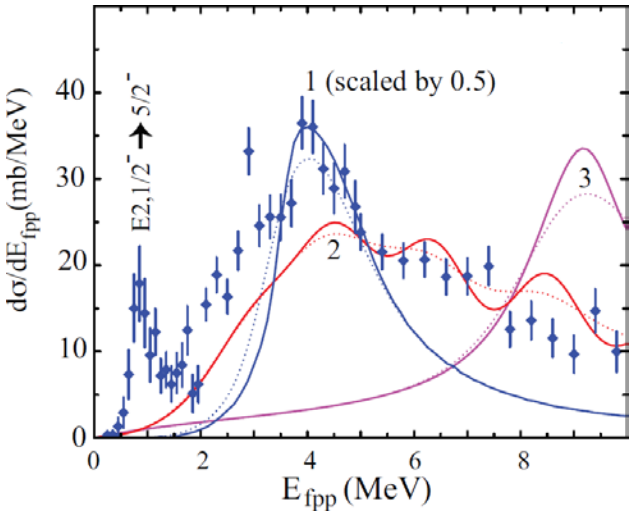


Figure 1: Comparison of our experimental Pb-target electromagnetic dissociation cross section (blue filled diamonds) with theoretical models (solid lines - raw; dotted lines - broadened by experimental resolution). Lines "1": blue [6]; lines "2": red [7]; lines "3": magenta [8].

References

[1] J. Marganiec et al., GSI Scientific Report 2013
[2] J. Marganiec et al., GSI Scientific Report 2014
[3] F. Wamers et al., GSI Scientific Report 2014
[4] J. Marganiec et al., GSI Scientific Report 2015
[5] F. Wamers et al., PRC 97, 034612 (2018)
[6] L. Grigorenko et al., PLB 641, 254 (2006)
[7] T. Oishi et al., PRC 84, 057301 (2011)
[8] Z.Y. Ma, Y. Tian, Sc. Ch. Ph., M. Astr. 54, 49 (2011)

Experiment beamline: R3B
Experiment collaboration: NUSTAR-R3B
Experiment proposal: S318
Accelerator infrastructure: UNILAC / SIS18 / FRS
PSP codes: none
Grants: NAVI, GSI-TU Darmstadt cooperation, HIC for FAIR, EMMI, BMBF, DFG (through grant SFB1245)
Strategic university co-operation with: Darmstadt

Hypernuclei production within the new intranuclear cascade code INCL

J. L. Rodríguez-Sánchez[1,2], J.-C. David[3], J. Cugnon[4], J. Hirtz[3], A. Kelic-Heil[2], S. Leray[3], and D. Mancusi[3].

[1]GSI, Darmstadt, Germany; [2]USC, Santiago de Compostela, Spain; [3]CEA, Saclay, France; [4]Univ. of Liège, Belgium.

In this work, we study the production of hypernuclei in spallation reactions using intranuclear-cascade models (INC) coupled to de-excitation codes by means of a two-step process [1]: the collision itself, where part of the nucleons contained in the target nucleus are removed or modi ed and some excitation energy and angular momenta are gained by the remnant; and subsequent de-excitation processes by evaporation of particles or, if applicable, by ssion. Here, INC models are considered as a Monte Carlo method to solve numerically the dynamic transport equations describing the hadron-nucleus collision. The nature of INC models is essentially classical, being assumed that nucleons are perfectly localised in phase space and that they are bound by a potential. In this approach, the nuclear collision is treated as successive relativistic binary hadron-hadron collisions separated in time, where the positions and momenta of hadrons are followed as time evolves. It is also assumed that hadrons move along straight trajectories until they undergo a collision with another hadron or until they reach the surface, where they could eventually escape. Cross sections are determined from a set of collision events taken at di erent impact parameters and for which nucleon positions and momenta are initially sampled for each participant nucleus.

Recently, the Liege intranuclear-cascade model (INCL) [2,3] has been extended towards high energies (~15 GeV) including multipion production [4], production of η and ω mesons [5], and strange particles like kaons and hyperons [6]. This new version permits us to predict the formation of hyperremnants and their characterization in atomic, mass, and strange numbers together with their excitation energies and angular momenta.

In the new version of INCL, elementary cross sections related with the production and interaction of strange particles (such as K, $\overline{\text{K}}$, Σ, and Λ) were implemented using sophisticated parametrizations of available experimental data as well as their characteristics: angular distributions, momenta, and charge repartition of the particles in the associated nal states. These new ingredients made INCL become in a powerful tool to study the production of strange particles in nuclear matter and to go further in the understanding of hypernuclei formation.

For modeling the de-excitation stage, we use the ABLA07 code [7] developed at GSI, which describes the de-excitation of a nucleus emitting γ-rays, neutrons, light-charged particles, and intermediate-mass fragments according to Weisskopf's formalism. For a more realistic description of this process, the separation energies are taken from the atomic mass evaluation of 2003 and the emission barriers for charged particles are determined with the Bass potential. Fission is also considered according to Ref. [8]. This model has been also extended by us to account for the emission of Λ particles and the production of cold Λ-hypernuclei following Ref. [9].

The coupling of these codes allows us to predict the production of Λ-hypernuclei in spallation reactions, as shown in Fig. 1. In addition, both codes are available in GEANT4 after an important e ort, which will provide a reliable input to design and optimize new experimental setups for the investigation of hypernuclei and strange particles. The benchmark of these models with available experimental data on the production of strange particles will be published soon with promising results.

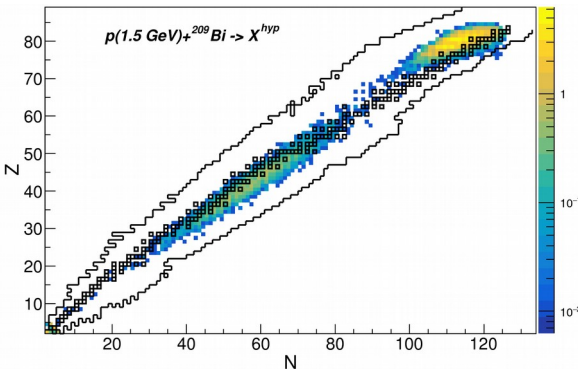


Figure 1: Cross section (in b) of cold Λ-hypernuclei produced in the spallation reaction ^{209}Bi + p at 1.5A GeV.

References

[1] J.-C. David, Eur. Phys. J. A 51 (2015) 68.
[2] D. Mancusi et al., Phys. Rev. C 90 (2014) 054602.
[3] J.L. Rodríguez et al., Phys. Rev. C 96 (2017) 054602.
[4] D. Mancusi et al., Eur. Phys. J. A 53 (2017) 80.
[5] J.-C. David et al., submitted to Eur. Phys. J. Plus.
[6] J. Hirtz et al., submitted to Eur. Phys. J. Plus.
[7] A. Kelic et al., arXiv:0906.4193v1.
[8] B. Jurado et al., Nucl. Phys. A 747 (2005) 14.
[9] A.S. Botvina et al., Phys. Rev. C 94 (2016) 054615.

Grants: This work has been supported by the Department of Education, Culture and University Organization of the Regional Government of Galicia under the program of postdoctoral fellowships

 DOI:10.15120/GR-2018-1

Experimental campaign using the NeuLAND demonstrator at SAMURAI

J. Kahlbow[1], K. Boretzky[2], N.L. Achouri[3], D.S. Ahn[4], H. Al Falou[5], G. Alkhazov[6], M. Assie[7], L. Atar[1], T. Aumann[1,2], H. Baba[4], D. Beaumel[7], D. Bemmerer[8], M. Böhmer[9], M. Caamano[3], C. Caesar[2], D. Calvet[10], H. Chae[11], S. Chen[4], M.I. Cherciu[12], N. Chiga[4], L. Chulkov[13], A. Corsi[10], M.L. Cortes[4], D. Cortina[14], T.E. Cowan[8,15], H.L. Crawford[16], F. de Oliveira Santos[17], F. Delaunay[3], A. Delbart[10], G. Dentinger[1], Q. Deshayes[3], Z. Dombradi[18], P. Doornenbal[4], C.A. Douma[19], F. Dufter[9], Z. Elekes[18], J. Enders[1], P. Fallon[16], J. Feng[20], B. Fernandez[14], F. Flavigny[7], U. Forsberg[21], N. Fukuda[4], Z. Fülöp[18], D. Galaviz Redondo[22], I. Gasparic[23], Z. Ge[4], R. Gernhäuser[9], J.-M. Gheller[10], J. Gibelin[3], A. Gilibert[10], K. Göbel[24], N. Gruzinsky[6], Z. Halasz[18], F. Hammache[7], M.N. Harakeh[19], T. Heftrich[24], M. Heil[2], A. Heinz[25], A. Hirayama[26], C.R. Hoffman[27], M. Holl[1], A. Horvat[1], A. Horvath[28], J.W. Hwang[29], N. Inabe[4], T. Isobe[4], H.T. Johansson[25], B. Jonson[25], N. Kalantar-Nayestanaki[19], S. Kawase[30], A. Kelic-Heil[2], S. Kim[29], D. Kim[31], K. Kisamori[4], R. Kissel[1], M. Knösel[1], T. Kobayashi[32], Y. Kondo[26], D. Körper[2], P. Koseoglou[1,2], S. Koyama[33], N.G. Kozlenko[6], D. Kresan[2], T. Kubo[4], Y. Kubota[4], I. Kuti[18], V. Kuznetsov[6], C. Langer[24,2], V. Lapoux[10], C.S. Lee[34], C. Lehr[1], P.J. Li[35], S. Lindberg[25], Y. Liu[20], B. Löher[1], Y. Maeda[36], F.M. Marques[3], S. Masuoka[34], Y. Matsuda[32], M. Matsumoto[26], A. Matta[3], J. Mayer[37], K. Miki[38], M. Miwa[4], B. Monteagudo[3], T. Murakami[39], I. Murray[4], M.A. Najafi[19], T. Nakamura[26], K. Nakano[30], N. Nakatsuka[39], T. Nilsson[25], G.H. Nyman[25], A. Obertelli[10], N.A. Orr[3], H. Otsu[4], T. Ozaki[26], V. Panin[4], S. Park[31], M. Parlog[3], S. Paschalis[1,21], N. Paul[10], M. Petri[21], S.G. Pickstone[37], M. Pohl[24], P.-M. Potlog[12], S. Reichert[9], R. Reifarth[24], S. Reinicke[8], A. Revel[3,17], C. Rigollet[19], D.M. Rossi[1], A.T. Saito[26], T. Saito[33], S. Sakaguchi[30], M. Sako[4], H. Sakurai[4], M. Sasano[4], H. Sato[4], Y. Satou[29], D. Savran[40], H. Scheit[1], F. Schindler[1], P. Schrock[34], M. Shikata[26], Y. Shimizu[4], S. Shimoura[34], H. Simon[2], D. Sohler[18], O. Sorlin[17], E. Stan[12], S. Storck[1], L. Stuhl[4,34], T. Sumikama[4], Y.L. Sun[10], H. Suzuki[4], D. Symochko[1], I. Syndikus[1], H. Takeda[4], S. Takeuchi[26], J. Tanaka[1], M. Tanaka[41], M. Thoennessen[38], Y. Togano[26], T. Tomai[26], H.T. Törnqvist[1], J. Tscheuschner[1], J. Tsubota[26], T. Uesaka[4], L. Uvarov[6], S. Volkov[6], V. Wagner[1], A. Wagner[8], H. Wang[4], K. Wimmer[33], H. Yamada[26], Z. Yang[4], B. Yang[20], L. Yang[34], M.Yasuda[26], K. Yoneda[4], L. Zanetti[1], J. Zenihiro[4], A. Zilges[37], K. Zuber[15]

(R^3B-NeuLAND-SAMURAI Collaboration)

[1]Technische Universität Darmstadt, Institut für Kernphysik, Darmstadt, Germany; [2]GSI Helmholtzzentrum für Schwerionenforschung, Darmstadt, Germany; [3]LPC Caen, Caen, France; [4]RIKEN Nishina Center for Accelerator-Based Science, Wako, Saitama, Japan; [5]Lebanese-French University, Deddeh, Lebanon; [6]Petersburg Nuclear Physics Institute Gatchina, Leningrad district, Gatchina, Russia; [7]IPN Orsay, Orsay, France; [8]Helmholtz-Zentrum Dresden-Rossendorf, Institute of Radiation Physics, Dresden, Germany; [9]Technische Universität München, Garching, Germany; [10]CEA Saclay, Gif-sur-Yvette, France; [11]IBS, South Korea; [12]Institute of Space Sciences, Magurele, Romania; [13]NRC Kurchatov Institute pl. Akademika Kurchatova, Moscow, Russia; [14]Universidade de Santiago de Compostela, Santiago de Compostela, Spain; [15]Technische Universität Dresden, Institut für Kern- und Teilchenphysik, Dresden, Germany; [16]Lawrence Berkeley National Laboratory, Berkeley, United States of America; [17]GANIL, Caen, France; [18]MTA Atomki, Debrecen, Hungary; [19]KVI - Center for Advanced Radiation Technology, Groningen, Netherlands; [20]Peking University, Beijing, China; [21]Department of Physics, University of York, United Kingdom; [22]Laboratory for Instrumentation and Experimental Particle Physics, Lisbon, Portugal; [23]RBI Zagreb, Zagreb, Croatia; [24]Johann Wolfgang Goethe-Universität Frankfurt, Frankfurt am Main, Germany; [25]Chalmers University of Technology, Göteborg, Sweden; [26]Tokyo Institute of Technology, Tokyo, Japan; [27]Argonne National Laboratory, Lemont, United States of America; [28]Eötvös Lorand University, Budapest, Hungary; [29]Seoul National University, Seoul, South Korea; [30]Kyushu University, Fukuoka, Japan; [31]Ewha Womans University, Seoul, South Korea; [32]Tohoku University, Sendai, Japan; [33]University of Tokyo, Tokyo, Japan; [34]Center for Nuclear Study, Tokyo, Japan; [35]Hongkong University, Hongkong; [36]Miyazaki University, Miyazaki, Japan; [37]Universität zu Köln, Institut für Kernphysik, Köln, Germany; [38]Michigan State University, East Lansing, United States of America; [39]Kyoto University, Kyoto, Japan; [40]Extreme Matter Institute, Darmstadt, Germany; [41]Osaka University, Osaka, Japan

NeuLAND – an introduction

The Large Area Neutron Detector NeuLAND [1] as part of the R^3B setup at FAIR is a neutron time-of-flight spectrometer aiming at detecting fast neutrons (0.2 to 1 GeV) from nuclear reactions. The detector concept is based on detection of hadronic interactions within the fully-active detector volume, made from organic scintillator material. The design goals comprise a spatial

Year	*Experiment*	*Spokespersons*
2015	ImPACT campaign (transmutation studies)	H. Sakurai (RIBF)
	1n efficiency measurement at 110 MeV & 250 MeV	H. Otsu (RIBF)
	^{28}O & ^{27}O spectroscopy	Y. Kondo (TITech)
2016	Sπrit TPC – EOS experiment	T. Isobe (RIBF) / W. Lynch (NSCL) / T. Murakami (U Kyoto) / B. Tsang (NSCL)
	^{31}Ne Coulomb breakup & knockout	N. Kobayashi (RCNP) / Y. Togano (TITech)
	Search for ^{22}C (2^+) and ^{21}B: Structure at and beyond the N=16 subshell closure	N.A. Orr (LPC)
	Lifetime of ^{26}O ground state	C. Caesar (TU Darmstadt/GSI)
2017	Dipole response of n-rich Ca isotopes	Y. Togano (TITech) / T. Kobayashi (U Tohoku)
	SEASTAR-3 (n-rich isotopes in K – V region)	P. Doornenbal (RIBF) / A. Obertelli (CEA)
	Dipole response of light, dripline nuclei (^{6,8}He)	T. Aumann (TU Darmstadt)
	Study of tetraneutron system using ^{8}He(p,pα)4n	D. Rossi (TU Darmstadt) / S. Paschalis (U York) / S. Shimoura (CNS)
	Study of tetraneutron system using ^{8}He(p,2p)^{7}H	F.M. Marques (LPC) / Z. Yang (RIBF)

Table 1: Overview over the experiments using the NeuLAND demonstrator at the SAMURAI setup at RIKEN during 2015-2017.

resolution of $\sigma_{x,y,z} \approx 1$ cm and a time resolution of $\sigma_t < 150$ ps. The once finished detector will have a front size of 250x250 cm^2 and a depth of 3 m, thus enabling a high neutron-detection efficiency of more than 90%. Due to its calorimetric properties, NeuLAND has also a large multi-neutron recognition capability, aiming for the unambiguous detection of up to 5 neutrons simultaneously. Together with the long flight path of about 35 m between target and detector, available in the high-energy cave at FAIR, a resolution of about $\sigma_E \approx 20$ keV at 100 keV above threshold will be obtained. NeuLAND consists of scintillator bars arranged in double planes. Each double plane comprises one horizontal and one vertical layer of 50 scintillator bars (250x5x5 cm^3). The production of double-planes is underway at GSI, and 13 out of the final 30 double-planes will be used in the phase-0 campaign at GSI, starting from 2018.

Experimental campaign at RIKEN

After successful tests of the first 4 double-planes, the so-called NeuLAND demonstrator, with beams at GSI in 2014, this demonstrator was transported to the RI Beam Factory (RIBF) at the RIKEN Nishina Center (Japan) in the beginning of 2015. There it complemented the neutron detection system NEBULA [2,3] at the SAMURAI setup [4] for a two-year experimental campaign [5].

Figure 1 displays a schematic view of the SAMURAI experimental setup including the NeuLAND demonstrator. At SAMURAI, experiments with radioactive beams with a large-acceptance spectrometer are performed. In a kinematically complete measurement also the fast neutrons need to be detected.

The combination of the neutron detection systems leads to a significant increase in total efficiency and invariant-mass resolution, thus allowing for the detection of four simultaneously emitted neutrons, their tracking and the determination of their individual four-momenta.

In total, 12 experiments were performed, covering a wide spectrum of nuclear physics from nuclear breakup reactions with very exotic light systems, and the dipole response of neutron-rich nuclei to the study of the

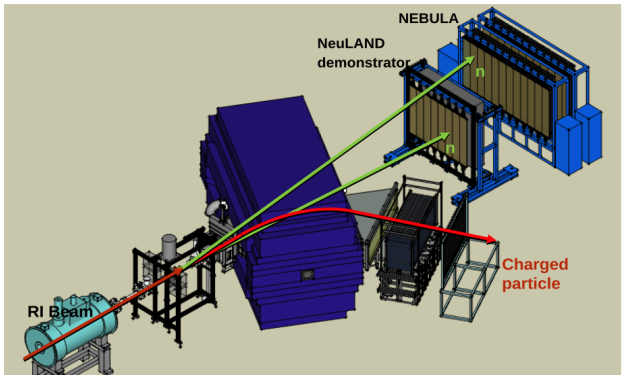


Figure 1: Schematic view of the SAMURAI experimental setup with its target region at the left hand side, the SAMURAI large-acceptance superconducting dipole magnet in the center and at the zero degree line the NeuLAND demonstrator, complemented with a VETO wall, in front of the NEBULA arrays. At deflection angles around 60 degrees a charged particle detection system is located.

equation-of-state (EOS) of nuclear matter in central collisions. These are summarized in Table 1. In the

 DOI:10.15120/GR-2018-1

following, we give an overview about the experiments in this campaign and highlight selected experiments.

One-neutron detection efficiency study

In one of the first experiments a key quantity of the NeuLAND demonstrator, namely the one-neutron detection efficiency, was determined. In the charge-exchange reaction ^{7}Li(p,n)^{7}Be(g.s.+430 keV) quasi-monoenergetic neutrons at 106.8 MeV and 250.5 MeV were produced from a high-intensity proton beam and detected by NeuLAND [6,7]. Preliminary results for the 1n-detection efficiency give (27.8±1.2)% and (26.6±1.1)% for neutrons at energies of 106.8 MeV and 250.5 MeV, respectively. These results are essential to extract cross sections from experiments using NeuLAND at SAMURAI.

Once NeuLAND was successfully commissioned at SAMURAI, the physics program started. We describe the experiments in the following, starting with experiments focussing on multi-neutron decays beyond the dripline.

Spectroscopy of ^{28}O

The combined neutron detection system of NeuLAND and NEBULA allows for the first time the detection and tracking of four coincident neutrons, in particular the spectroscopy of the neutron-unbound nuclei ^{28}O and ^{27}O. The neutron dripline is established at mass number 24 for the oxygen isotopic chain; heavier oxygen isotopes are not bound. A sudden change in the binding is observed by adding one more proton to oxygen – fluorine can bind at least six more neutrons. It is crucial to understand the shell evolution for these most neutron-rich isotopes. The spectroscopy of the one- and two-neutron decay channels ^{25}O and ^{26}O has already been performed in a previous experiment at SAMURAI [8].

The unbound system ^{28}O was populated by a proton knockout reaction on a ^{29}F beam at 235 MeV/u (before target). Since the neutron-reconstruction efficiency is still low for three and four neutrons a liquid hydrogen target of 15 cm length was used to increase the luminosity. The target was surrounded by a time-projection chamber to reconstruct the reaction-vertex position. Including this information the invariant mass can be determined precisely. For details on the setup see [9]. After the reaction, the ^{28}O system decays in-flight into the heavy fragment ^{24}O and four neutrons. The challenge is the unambiguous identification of the four neutrons in NeuLAND and NEBULA to reconstruct the invariant-mass of the decaying system.

In this experiment also other reaction channels were investigated, in particular proton-knockout reactions on neon isotopes. Thus, also spectroscopy of the heaviest fluorine can be performed. Here, γ-rays are measured in addition to neutrons. With this information, excitation energies are obtained, which provide insight into the shell structure and its evolution.

In order to benchmark the performance of the detection system a reference channel, the invariant-mass of the ^{24}O fragment, and only one neutron from the 4n decay channel is investigated, see Figure 2. Known intermediate resonances from sequential decays are identified, in particular the broad ground-state resonance of ^{25}O at 749 keV and the ground state of ^{26}O which is located at only 18 keV above threshold [8]. The sharp peak close to the decay threshold in this preliminary analysis indicates the good resolution of the detection system where the narrow ^{26}O(g.s.) resonance is well resolved.

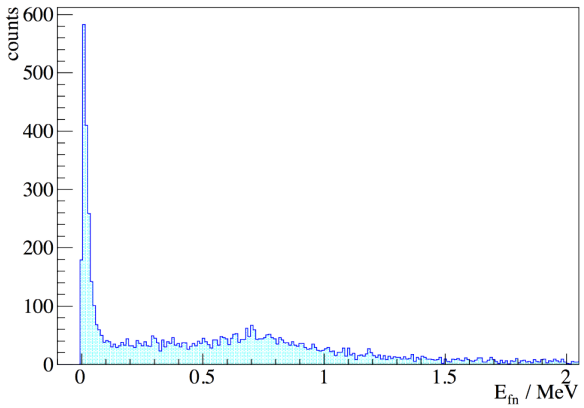


Figure 2: Preliminary invariant-mass spectrum of ^{24}O+1n from the reaction ^{29}F(p,2p). The narrow ^{26}O(g.s.) resonance at 18 keV is clearly seen.

Lifetime of the ^{26}O ground state

Another experiment along the oxygen-chain aimed specifically at investigating the properties of ^{26}O. Besides the spectroscopic information of ^{26}O, the ground state of this nucleus might have an unusually long lifetime [10] where the two-neutron decay is hindered by the angular momentum barrier for *d*-wave valence neutrons. We have developed a new method to determine lifetimes in the (sub-)picosecond range of systems which decay via neutron emission [11]. The method is based on the idea that the ^{26}O nuclei, which are produced by proton removal on a ^{27}F beam, decay with a larger fraction outside the reaction target the longer their lifetime is. This can be observed in the velocity difference between the decay-neutrons and the ^{24}O fragment. The characteristic shape of this velocity-difference spectrum allows to extract the lifetime. A stack of targets of dense material and of high nuclear charge was used to decelerate the ^{26}O ions and thereby increase the sensitivity of the method. The neutron velocity is determined from the time-of-flight and position measured with NeuLAND and NEBULA. For further details on the setup see [12].

Search for a tetraneutron system

The possible existence of a four-neutron system as well as its properties has been a long lasting question in nuclear physics starting in the mid-1960s [13]. A recent experiment carried out at the SHARAQ spectrometer at RIKEN uncovered four candidate events for a low-lying four-neutron ground-state resonance with a 4.9σ significance level, generated in a ^{4}He(^{8}He,^{8}Be) reaction

[14]. This measurement triggered new efforts to finally uncover direct evidence for the existence of this system.

To this end, we have performed an experiment to investigate the four-neutron system via a new method, i.e., the measurement of ^{8}He(p,pα)4n at large momentum transfer, using a secondary ^{8}He beam at an energy of 156 MeV/u, impinging on a liquid-hydrogen target of 5 cm thickness [15]. The ^{8}He nucleus is expected to be a suitable environment to form the four-neutron system in a ground-state resonance. The reaction process described above allows for a very clean investigation of its properties due to the fact that final-state interactions between the tetraneutron and the outgoing charged particles are basically absent.

The four-neutron energy-spectrum will be deduced from the momenta of all charged particles, i.e. the ^{8}He projectile, the knocked-out ^{4}He, and the target proton via the missing-mass technique to identify the possible resonance and to determine its energy and width. The neutron measurement will allow for a kinematically complete investigation of the reaction and the study of the four-neutron decay properties with lower but sufficient statistics in addition.

Complementary insight into the system of interest will be achieved by a ^{8}He(p,2p)^{7}H measurement, namely the investigation of the ^{7}H ground state and its decay into a triton and four neutrons, performed within the same experimental campaign [16].

Dipole response of n-rich nuclei

In 2017, two experiments were carried out, using Coulomb excitation in inverse kinematics to investigate the dipole response of neutron-rich nuclei. One experiment focused on the low-lying dipole strength of the two- and four-neutron halo nuclei ^{6}He and ^{8}He [17]. After electromagnetic excitation these nuclei mainly decay via two- and four-neutron emission. The ^{6}He breakup has been measured previously at GSI up to around 7 MeV excitation energy [18], while nothing is known so far about the ^{8}He 4n-breakup channel. In this experiment the multi-neutron decay of ^{6}He and ^{8}He, after heavy-ion induced electromagnetic excitation up to increased excitation energies of approx. 15 MeV, has been measured in complete kinematics. The unique combination of the neutron detector NEBULA, the NeuLAND demonstrator, and the high beam intensities available at RIBF made the measurement of the 4n-breakup channel of ^{8}He possible for the first time. A primary ^{18}O beam with an energy of 220 MeV/u was used to produce secondary beams of ^{6}He and ^{8}He with 180 MeV/u. The dipole-strength distribution dB(E1)/dE and the photo-absorption cross section will be obtained from the differential cross section for the E1 excitation dσ(E1)/dE where the excitation energy is reconstructed from the invariant mass. To excite ^{6}He and ^{8}He electromagnetically, a Pb target was used. Additionally, a series of targets covering a wide range of nuclear charges, namely CH_2, C, Ti and Sn, was used to enable a precise study of the nuclear contribution to the cross section. This is especially important for high excitation energies, where the contribution of electromagnetic excitation might not be dominant.

The Coulomb excitation method to study the dipole response of neutron-rich nuclei was also utilized to study ^{50}Ca and ^{52}Ca [19] in an experiment carried out during spring 2017. This experiment is motivated by theoretical predictions, indicating a strong rise of the pygmy dipole resonance strength from ^{48}Ca to ^{54}Ca and its firm correlation with the density dependence of the symmetry energy term of the EOS of neutron matter.

Sπrit TPC – EOS experiment

During 2016, NeuLAND was moved from 0° to 30° with respect to the beamline to measure light charged particles, neutrons and γ-rays from central collisions of neutron-rich and neutron-deficient Sn-isotope systems in experiments studying the nuclear EOS by its proton/neutron and triton/^{3}He yield ratios and flows. The VETO detector in front of NeuLAND played an essential role for distinguishing charged and neutral particles in contrast to other experiments, where neutrons are expected to be dominant and the VETO serves for background discrimination only [5,20].

Structure of n-rich nuclei

It is known that shell structure evolves substantially for nuclear systems with large isospin asymmetry. For bound and unbound systems well known shell closures disappear and new sub-shell closures may appear.

One of the experiments aimed to study the most neutron-rich B and C isotopes, namely ^{21}B and ^{22}C, to establish their level scheme. It is predicted that the sub-shell closure at N=14, which is confirmed in case of the oxygen isotopes, disappears but the increased energy gap at N=16 remains. This can be seen as the origin of the halo character of ^{22}C. In the experiment, the one- and two-proton removal reactions of ^{23}N on a carbon target are analysed. Excitation energies of excited states in both, ^{22}C and ^{21}B, will be reconstructed from the 2n-decay channels to ^{19}B and ^{20}C. Further details about the experiment can be found in [21].

Another experiment from the same campaign investigates neutron-rich neon isotopes. ^{31}Ne is a strongly deformed nucleus located in the so-called island of inversion. In addition, it is also seen as one of the heaviest halo nuclei, which is in particular formed by a dominant p-wave neutron orbiting around the core. Here, ^{31}Ne was studied with exclusive methods at the SAMURAI setup, for details see [22]. The inelastic scattering reaction on a C target, ^{31}Ne(C,X)^{30}Ne+n, and the one-neutron removal reaction on ^{32}Ne were employed to study the neutron-unbound excited states. In addition, the Coulomb breakup reaction was studied in terms of the invariant-mass analysis.

Nuclear shell-structure information is also deduced from spectroscopy of bound excited states. The “Shell Evolution And Search for Two-plus energies At RIBF”

 DOI:10.15120/GR-2018-1

(SEASTAR) project studies new 2^+ excitation energies in a wide range of the neutron-rich nuclei. The 3rd campaign in 2017 focused on the medium-mass nuclei around neutron-rich Ca isotopes and many reaction channels were observed. The combination of the NeuLAND demonstrator and NEBULA allows to construct the invariant-mass above the neutron-decay thresholds.



Figure 3: The NeuLAND demonstrator (oversize silver box) and its electronics (blue box) arriving at GSI after being transported back from RIKEN, Japan.

Summary

During this very fruitful experimental campaign the NeuLAND demonstrator with its 800 read-out channels showed a very good reliability in operation and excellent performance, exhibiting its design goals. While the analysis of the data is underway, the demonstrator was delivered back to GSI in autumn of 2017, see Figure 3. It is now being integrated into the NeuLAND startup version for the experimental campaign at GSI in 2018/19.

Acknowledgments

We would like to thank the RIBF accelerator and BigRIPS teams for the excellent beam-preparation work.

References

[1] NeuLAND@R3B: A Fully-Active Detector for Time of Flight and Calorimetry of Fast Neutrons, NeuLAND Technical Design Report, https://edms.cern.ch/document/1865739/1
[2] T. Nakamura and Y. Kondo, Large acceptance spectrometers for invariant mass spectroscopy of exotic nuclei and future developments, NIM B 376 (2016) 156–161
[3] Y. Kondo et al., Calibration methods of the neutron detector array NEBULA, RIKEN Accel. Prog. Rep. 45, 131 (2012)
[4] T. Kobayashi et al., SAMURAI spectrometer for RI beam experiments, NIM B 317, 294 (2013)
[5] K. Boretzky et al., NeuLAND – from the demonstrator to the start version, GSI Scientific Report 2016 (2017) p.207-210, 10.15120/GR-2017-1
[6] J. Kahlbow et al., RIKEN Accel. Prog. Rep. 49 (2017)
[7] J. Kahlbow et al., Efficiency study of the NeuLAND demonstrator, GSI Scientific Report 2016 (2017) p.211, 10.15120/GR-2017-1
[8] Y. Kondo et al., Phys. Rev. Lett. 116, 102503 (2016)
[9] Y. Kondo et al., RIKEN Accel. Prog. Rep. 49 (2017)
[10] Z. Kohley et al., Phys. Rev. Lett. 110, 152501 (2013)
[11] J. Kahlbow et al., NIM A 866 (2017) 265-271
[12] C. Caesar et al., RIKEN Accel. Prog. Rep. 50 (2017)
[13] D.R. Tilley et al., Nucl. Phys. A 541, 1104 (1992)
[14] K. Kisamori et al., Phys. Rev. Lett. 116, 052501 (2016)
[15] F. Schindler et al., Investigation of the tetraneutron by quasi-free α-knockout from ^{8}He, submitted to RIKEN Accel. Prog. Rep. 51 (2018)
[16] F. M. Marqués, Z. Yang et al., Many-neutron systems: search for superheavy ^{7}H and its tetraneutron decay, submitted to RIKEN Accel. Prog. Rep. 51 (2018)
[17] C. Lehr et al., Low-energy dipole response of the halo nuclei ^{6,8}He, submitted to RIKEN Accel. Prog. Rep. 51 (2018)
[18] T. Aumann et al., Phys. Rev. C 59, 1252 (1999)
[19] Y. Togano et al., Electric dipole responses of ^{50}Ca and ^{52}Ca, submitted to RIKEN Accel. Prog. Rep. 51 (2018) and references therein
[20] I. Gasparic et al., RIKEN Accel. Prog. Rep. 50 (2017)
[21] N. Orr et al., RIKEN Accel. Prog. Rep. 50 (2017)
[22] T. Tomai et al., RIKEN Accel. Prog. Rep. 50 (2017)

Experiment beamline: other: RIBF, RIKEN
Experiment collaboration: other: R3B-NeuLAND-SAMURAI
Experiment proposal: none at GSI
Accelerator infrastructure: other: RIBF, RIKEN
PSP codes: 1.2.5.1.2.5
Grants: This work was supported by the Deutsche Forschungsgemeinschaft through Grant No. SFB 1245, the BMBF Verbundforschung contracts NuSTAR.DA 05P15RDFN1, 05P15PKFNA and 05P15RFFN1, the Croatian Science Foundation (CSF) project SR-ETNo, HIC for FAIR, and NN114454 (NKFIH)
Strategic university co-operation with: Darmstadt, Frankfurt-M

A silicon vertex tracker for the SAMURAI19 experiment at RIKEN

F. Dufter[1], T. Aumann[2], M. Böhmer[1], R. Gernhäuser[1], S. Paschalis[2,3], S. Reichert[1], D. Rossi[3], M. Sasano[4] for the R³B-NeuLAND-SAMURAI collaboration

[1]Physik-Dept., Technische Universität München, Germany; [2]Physics-Dept., Technische Universität Darmstadt, Germany;[3]University of York, United Kingdom;[4]RIKEN, Nishina Center for Accelerator-Based Science, Japan

The SAMURAI19 [1,2] experiment at the RIKEN RIBF aims for producing *4n* ground-state resonances with the ^{8}He(p,pα)4n quasi-free scattering reaction at large momentum transfers at beam energies of 156 *A*MeV. A 5 cm long liquid-hydrogen target (MINOS) with a diameter of 4 cm was used to achieve a luminosity of ~ 10^{28} cm^{-2}s^{-1}. For missing-energy reconstruction, the momenta of all particles are measured with high accuracy.

To get the best energy and track reconstruction using such a thick target, a silicon vertex tracker was developed by TUM and RIKEN. The tracker is placed in a vacuum chamber (49 cm x 36 cm x 29 cm) and records the hits of charged particles in six layers of silicon detectors, allowing to track the produced particles, their opening angle and the position of the vertex. The chamber was drilled from a single aluminium block to reach a vacuum of 10^{-4} Pa. It features in total six data feedthroughs, a newly designed connection to the LH_2 target and a 125 µm thick kapton window for the beam exit. The chamber is mounted on a rail system for fast and easy setup.

The detector system with X and Y readout capabilities consists of six single sided silicon strip detectors (AC coupled) with an active area of 5x8 cm^2 each and a thickness and pitch size of 100 µm developed in a RIKEN cooperation with Hamamatsu. Two SSD's each were combined in three water-cooled stations at distances of 0.6 cm, 12.6 cm and 24.6 cm with respect to the end of the target cell. A detector station is depicted in Fig. 1. The Y and X sectors are closely placed with a distance of 3 mm only on top of each other to optimize the spatial resolution.

The 3708 detector segments are all individually read out by 60 ASIC APV25S1 chips [3]. The multiplexed analog data are then digitalized by an ADCM module developed at TUM. The digital data are collected through a single TRB3 board developed at GSI [4]. Synchronization with the BABIRL-DAQ is done with a 40 MHz time stamp distribution, which is used for other parts of the experiment.

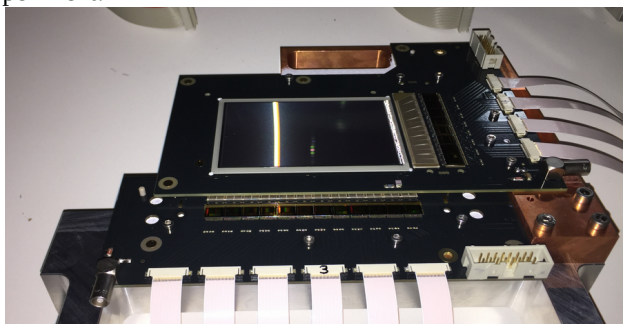


Figure 1: One detector station with attached data cables. The Y layer is placed on top of the X layer, both are mounted on the same cooling frame.

As a first step in the analysis, the detectors are calibrated with proton and ^{6}He calibration beams. Due to the typical electronics-noise figure of ENC ~ 7 keV a single-channel energy threshold of 38 keV was used to reduce event multiplicities. The average energy loss of a proton from the reaction of interest in the detector is in the order of 60 keV per silicon layer only while signals from α-particles may exceed the ASIC's analogue range, which is limited to about 8 MIPs (Minimum ionizing particle) only. To separate α-particles from the reaction from ^{8}He projectiles, which pass all detector planes at a high rate, a sophisticated pulse-shape algorithm is applied.

The ADCM samples the shaper signals of triggered events with three samples in 150 ns and allows therefore to improve the data purity [5]. In Fig. 2 the relations among the three consecutive samples are compared with each other. Unaffected events should appear on the lower right quadrant.

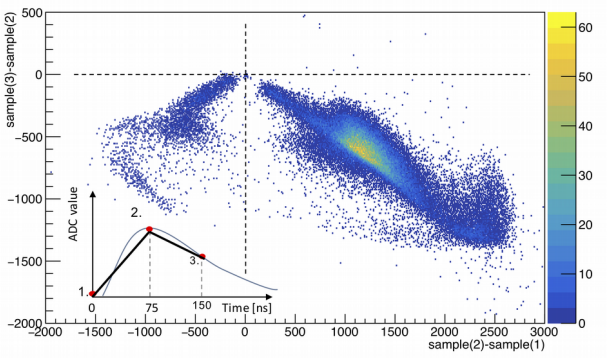


Figure 2: Comparison between the sample differences from shaper signals. Events with an ADC-value < 30 channels are neglected. Events in the lower left quadrant are influenced by beam particles. The inset depicts a shaper signal while the marked points resemble points of sampling schematically.

Hits in all three detector stations are sorted by their energy and combined to identify particles and their tracks. Events with two particle tracks are used to determine a reaction vertex. We deduced an average transverse vertex resolution of $\sigma_{x,y}$ ~ 60 µm. The resolution along the beam direction is σ_z ~ 1 mm due to the small opening angle of the reaction residues.

As a next step, we will further investigate the detection efficiency, hit multiplicities, transverse momenta and the tracking towards the SAMURAI detectors.

We especially thank Michael Traxler and Jan Michel from the TRB3 team of GSI for their continuous help and support of this work.

 DOI:10.15120/GR-2018-1

References

[1] S. Paschalis, S. Shimoura et al.: RIBF Proposal NP1406-SAMURAI19
[2] F. Schindler et al. RIKEN Accel. Prog. Rep. 50, 2017
[3] M.J. French et al. NIM A 466/2 359-365, 2001
[4] M. Traxler et al.: TRB3 Documentation, "https://hades-wiki.gsi.de/cgi-bin/view/DaqSlowControl/TDCReadoutBoardV3"
[5] F. Dufter et al. RIKEN Accel. Prog. Rep. 50, 2017

Experiment beamline: other, RIBF, RIKEN
Experiment collaboration: other: R3B-NeuLAND-SAMURAI
Experiment proposal: none at GSI, RIBF Proposal NP1406-SAMURAI19
Accelerator infrastructure: other: RIBF, RIKEN
PSP codes:
Grants: DFB grant SFB 1245, BMBF 05P15WOFNA
Strategic university co-operation with: contract Nr. TMLFRG1316

Tests of CALIFA Barrel modules at CCB in Kraków

J. Park[1], B. Heiss[2], A.-L. Hartig[3], H. Alvarez-Pol[4], G. Bruni[5], E. Casarejos[6], J. Cederkäll[1], D. Cortina-Gil[4], P. Díaz Fernández[5], D. Galaviz[7], R. Gernhäuser[2], P. Golubev[1], A. Heinz[5], H. T. Johansson[5], P. Klenze[2], A. Knyazev[1], T. Kröll[3], T. Nilsson[5], A. Perea[8], H.-B. Rhee[3], O. Tengblad[8], P. Teubig[7], M. Zieblinski[9], for the CALIFA working group of the R[3]B collaboration

[1]Lund University, [2]TU München, [3]TU Darmstadt, [4]University of Santiago de Compostela, [5]Chalmers University of Technology, [6]Universidade de Vigo, [7]LIP Lisbon, [8]CSIC Madrid, [9]IFJ PAN Kraków

CALIFA (CALorimeter for In-Flight gamma-ray and pArticle detection) [1] is dedicated to the detection, tracking and energy determination of light charged particles and γ rays emerging from R^{3}B experiments. Significant progress has been made on the Barrel section [2] of CALIFA, which consists of ~2000 CsI(Tl) scintillator crystals that provide a high angular resolution needed for effective Doppler corrections.

For the Phase-0 experiments at GSI in 2018, a substantial part of the CALIFA Barrel detectors will be installed and operated in the Demonstrator [3] configuration. An extensive preparatory work in detector performance, stability and data acquisition is required to provide a sound and effective experimental campaign at GSI. To that end, in-beam tests at the Bronowice Cyclotron Center (CCB) at IFJ PAN in Kraków were carried out. The cyclotron at CCB provided proton beams with energies up to 225 MeV, which enabled experiments for (p,2p) quasifree scattering (QFS) reactions on stable targets.

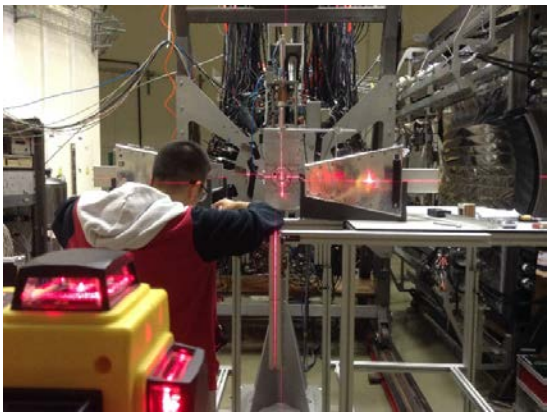


Figure 1: Detectors seen during mounting at CCB for the (p,2p) experiment. Three CALIFA Barrel petals (one placed below the target later), two DSSSD tracking detectors, and one CEPA4 detector were tested.

The experimental setup at CCB is shown in Fig. 1. Two petals were positioned on a horizontal plane with a polar angular coverage of 25° < θ < 58° to detect the scattered particles. One petal was deployed at its nominal CALIFA position (43° < θ < 82°) to detect γ rays. Two double-sided silicon strip detectors (DSSSDs) were also employed as particle trackers. A CEPA4 [4] prototype detector for the CALIFA Forward Endcap was placed at θ ~ 11° for its performance test. Data from the petals and the DSSSD trackers were read out with the MBS system featuring FEBEX3B cards [5]. The calibration data from a ^{60}Co γ-ray source was analysed with the UCESB/R^{3}BRoot software [6].

A laminar water jet, with a small diameter of 0.46 mm was used to provide well-defined tracking correlations for the reactions at the target, and give an energy straggling below the expected resolution limit for the total energy reconstruction of the scattered protons with CALIFA. Other targets such as graphite, polypropylene, ^{112,124}Sn and ^{208}Pb were also irradiated. The proton beam energy was 200 MeV for over 95% of the total beam time. Other beam energies ranged from 70 to 225 MeV.

A preliminary analysis of (p,2p) data from the water target revealed a γ-ray peak at 6.3 MeV (see Fig. 2), corresponding to the known transition from the first excited 3/2$^-$ state to the 1/2$^-$ ground state in ^{15}N. More sophisticated energy calibration, event selection cuts and simulations are being developed to refine and extend the analysis to the data from other targets. We acknowledge the local support at CCB with logistics and beam delivery.

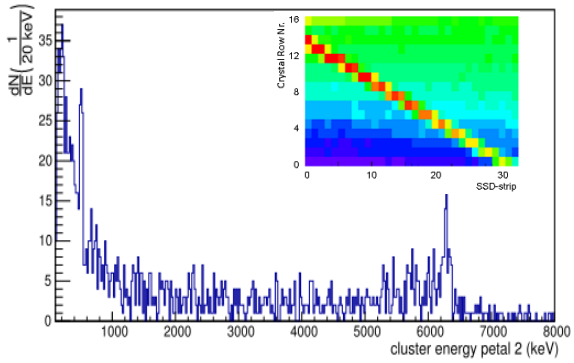


Figure 2: γ-ray energy spectrum following (p,2p) reactions on the water target. The 6.3-MeV transition in ^{15}N is clearly visible. The inset shows the proton tracking data from a DSSSD-petal pair used in the event selection cut.

References

[1] D. Cortina-Gil et al., NDS 120 (2014) 99.
[2] H. Alvarez-Pol et al., NIM A 767 (2014) 453.
[3] B. Pietras et al., NIM A 814 (2016) 56.
[4] E. Nacher et al., NIM A 769 (2015) 105.
[5] T. Le Bleis et al., GSI Scientific Report (2013) 201.
[6] D. Bertini, J. Phys. Conf. Ser. 331 (2011) 032036.

Experiment beamline: none
Experiment collaboration: NUSTAR-R3B
Experiment proposal: none
Accelerator infrastructure: CCB at IFJ PAN in Kraków
PSP codes: none
Grants: EU H2020 contract No. 654002, BMBF 05P15WOFNA
Strategic university co-operation with: none

 DOI:10.15120/GR-2018-1

Response and resolution measurements of CALIFA CsI(Tl) detectors

A. Knyazev[1], J. Park[1], H. Alvarez-Pol[2], G. Bruni[3], E. Casarejos[4], J. Cederkäll[1], D. Cortina-Gil[2], P. Díaz Fernández[3], D. Galaviz[5], R. Gernhäuser[6], P. Golubev[1], A.-L. Hartig[7], A. Heinz[3], B. Heiss[6], H. T. Johansson[3], P. Klenze[6], T. Kröll[7], T. Nilsson[3], A. Perea[8], H.-B. Rhee[7], O. Tengblad[8] and P. Teubig[5] for the CALIFA working group of the R3B collaboration

[1]Lund University, [2]University of Santiago de Compostela, [3]Chalmers University of Technology, [4]Universidade de Vigo, [5]LIP Lisbon, [6]TU München, [7]TU Darmstadt, [8]CSIC Madrid

A test bench has been constructed for acceptance test of CsI(Tl) detector elements for the CALIFA calorimeter [1] for R^{3}B. A detector module consists of an APD and a long tapered CsI(Tl) crystal wrapped in ESR foil. The geometry is a consequence of the requirement to have high granularity, to achieve the necessary angular resolution for Doppler correction, and the need to be able to register high-energy charged particles that emerge from the reactions.



Figure 1: The test bench for CALIFA Barrel crystals in the Lund university detector laboratory. Batches of up to 32 crystals can be scanned per test with a rate of 5.2 detectors per hour.

An inherent challenge with such a geometry is that the combined effects of absorption and focusing of optical photons influence the scintillation light output, and thus the signal amplitude for events occurring at different depths in the crystal. In order to ensure that these effects do not influence the overall resolution of the detector module, it is necessary to measure the response to ionizing radiation along the crystal axis.

To accomplish this, a test stand consisting of an insulated dark box, in which up to 32 crystals can be mounted for performance tests, has been constructed. The temperature in the enclosed volume of the setup can be regulated with the help of a Peltier element and a temperature sensor feedback loop. The crystals are scanned using two separate scanning heads mounted on a commercial XY-table using a collimated ^{137}Cs source for light output non-linearity tests, or alternatively an uncollimated ^{22}Na source for energy resolution measurements. Dedicated software has been developed to operate the XY-table, the temperature regulation, the bias supply and to automatically analyse the registered spectra to extract the resolution and light output nonlinearity (LON) along the crystal axis.

Readout of the signals from the modules is done using the standard readout chain planned for CALIFA. The chain comprises a Mesytec MPRB-32 preamplifier, with integrated detector bias supply, and a FEBEX3B sampling digitizer [2]. The data from from the digitizer is fed to an acquisition system based on the Multi Branch System (MBS).

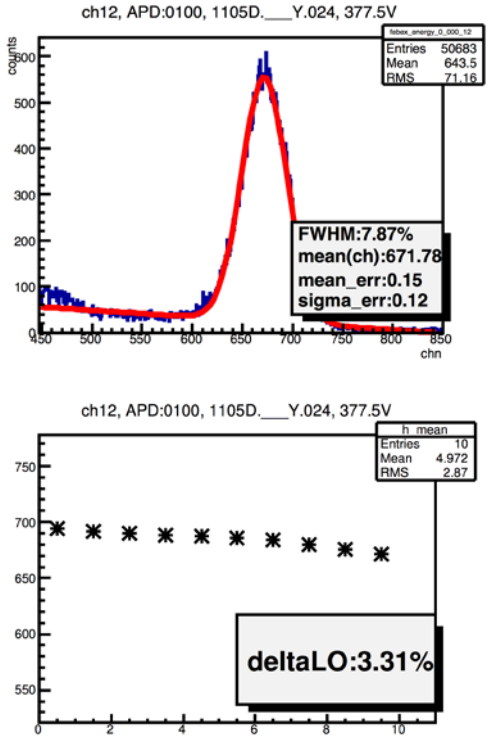


Figure 2: Typical response of a test scan showing, in the top panel, an automatically fitted response of the 662 keV gamma ray from ^{137}Cs source and the change in position of the centroid of this peak as a function of the source position.

The typical crystal scanning rate is 5.2 detectors per hour for a non-linearity test, using 10 points along the crystal axis and 2 minutes per measurement point; and 13.8 detectors per hour for resolution measurements. To date ca 600 crystals have been tested using the test bench, corresponding to nine CALIFA petals of 64 crystals, that can be used in Phase-0 experiments in the fall of 2018.

References

[1] D. Cortina-Gil et al., NDS 120 (2014) 99.
[2] Bendel, M., Gernhäuser, R., Henning, W.F. et al. Eur. Phys. J. A (2013) 49: 69.

Experiment beamline: R3B
Experiment collaboration: NUSTAR-R3B
Experiment proposal: none
Accelerator infrastructure: FRS
PSP codes: 1.2.5.1.2.3.1.1.5.
Grants: VR-822-2012-4550**,** BMBF 05P15WOFNA
Strategic university co-operation with: none

 DOI:10.15120/GR-2018-1

PMT saturation due to large dynamic range

G. Bruni[1], P. Díaz Fernández[1], H.T. Johansson[1], A. Heinz[1], T. Nilsson[1], O. Tengblad[2], H. Alvarez-Pol[3], J. Cederkäll[5], E. Casarejos[6], D. Cortina Gil[3], D. Galaviz Redondo[7], R. Gernhäuser[4], B. Heiss[4], P. Klenze[4], P. Golubev[5], A.-L. Hartig[8], A. Knyazev[5], T. Kröll[8], J. Park[5], A. Perea[2], H.-B. Rhee[4], P. Teubig[7], M. Zieblinski[9], for the CALIFA /R³B working group.

[1]Chalmers Tekniska Högskola, Göteborg, Sweden; [2]Instituto de Estructura de la Materia, CSIC, Madrid, Spain, [3]University of Santiago de Compostela, Santiago de Compostela, Spain;[4]Technische Universität München, Garching, Germany;[5]Lund University, Lund, Sweden; [6]University of Vigo, Vigo, Spain;[7]FCU Lisbon, Lisbon, Portugal;[8]Technische Universität Darmstadt, Darmstadt, Germany;[9]Institute of Nuclear Physics, Kraków, Poland.

Phoswich detectors, composed of optically coupled $LaBr_3$ and $LaCl_3$ scintillating crystals will be used at the most forward angles in the CALIFA calorimeter at the R³B setup [1]. These crystals offer ideal conditions for detection of gamma radiation, as well as for charged particles at relativistic energies, with high efficiency, and excellent energy and time resolution [2-5].

The goal of this study is to verify the performance of the CEPA4 prototype, consisting of four phoswich crystals with individual photo-multiplier tubes (PMTs) for readout, attached to the $LaCl_3$. A particular challenge, especially for the PMTs and read-out electronics, is the large dynamic range needed to cope with signals from gamma radiation (up to 20 MeV) and charged particles (up to 270 MeV). The TDR [5] specifies the use of the Hamamatsu R7600U-200 PMTs. These tests have been performed using the commercial digitisers CAEN DT5751 and DT5730.

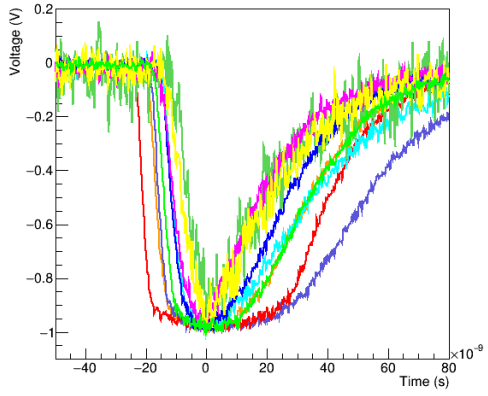
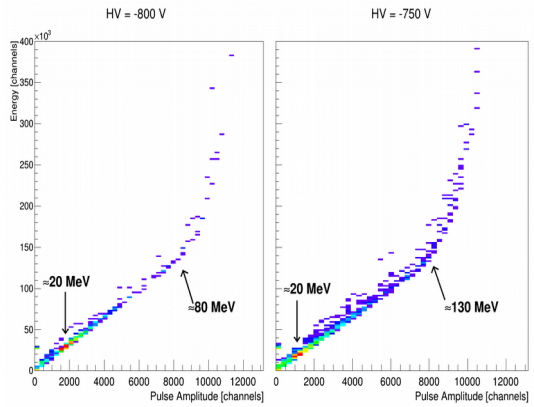


Figure 1: Photomultiplier tube signals of cosmic muons, normalized to the maximum amplitude, showing saturation.

The investigations performed with the crystals revealed a good energy and time resolution for both gammas and muons. While it is relatively easy to obtain good energy resolution for either gamma rays or protons by selecting an appropriate bias voltage, it was not possible to find a bias voltage, which allowed for a good resolution for both, because the PMTs displayed clear signs of saturation already around 20 MeV of deposited energy (see Figure 1). As a first attempt at improving this situation, a new base was used for the R7600U-200 PMTs, providing also a second lower-gain signal from the last dynode in addition to the anode readout (with a gain ratio of ~2.5). This was not sufficient. Therefore, a new PMT, R11187, has been tested. Results are shown in Figure 2, where the saturation starts at the same pulse amplitude independently of the applied bias voltage. This indicates that saturation occurs in the final stages of the PMT.

Figure 2: Energy versus pulse amplitude for two high voltages. The degradation of the signals starts at about the same signal amplitude, indicating that saturation occurs in the final stages of the PMT.



To cope with the large dynamic range we want to implement an improved double read-out with a higher gain ratio between the two branches [6].

References

[1] Technical Design Report for the Design, Construction and Comissioning of the CALIFA Endcap, (2015).
[2] O. Tengblad et al., Nucl. Instr. Meth. Phys. Res. A 704, 19 (2013).
[3] E. Nácher et al., Nucl. Instr. Meth. Phys. Res. A 709, 105 (2015).
[4] M. Mårtensson, Master thesis, Chalmers Univ. Tech. (2013).
[5] G. Bruni, Master thesis, Chalmers Univ. Tech. (2017).
[6] Hongkui Lv et al., Nucl. Instr. Meth. Phys. Res. A 781, 34-38 (2015).

Experiment collaboration: NUSTAR-R3B.
PSP codes: 1.2.5.1.2.3.2
Grants: supported by the Swedish Research Council, ENSAR2 (project Nr. 654002) and BMBF (contract Nr. 05P15WOFNA)
Strategic university co-operation with: contract Nr. TMLFRG1316

The quality assurance test stand for CALIFA APDs

H.-B. Rhee[1], A.-L. Hartig[1], H. Alvarez-Pol[2], G. Bruni[3], E. Casarejos[4], J. Cederkäll[5], D. Cortina-Gil[2], P. Díaz Fernández[3], D. Galaviz[6], R. Gernhäuser[7], P. Golubev[5], A.Heinz[3], B. Heiss[7], H. Johansson[3], P. Klenze[5],A. Knyazev[5], T. Kröll[1], T. Nilsson[3], J. Park[5], A. Perea[8], O. Tengblad[8], P. Teubig[6] , for the CALIFA working group of the R3B collaboration

[1]TU Darmstadt,[2]University of Santiago de Compostela, [3]Chalmers University of Technology, [4]Universidade de Vigo, [5]Lund University, [6]FCU Lisbon,[7]TU München, [8]CSIC Madrid

The quality assurance test stand for the CALIFA APDs aims to prove the functionality of the APDs and to characterize them. It ensures controlled temperature and bias voltage for the APDs during the test [1].
Particularly, the bias voltage of the APDs is readjusted with respect to the temperature to keep the gain constant during the experiment. The main goal of this project is to obtain the temperature coefficients of the tested APDs.

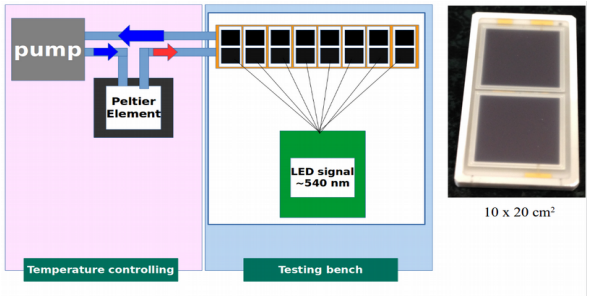


Figure 1: Left: Schematic view of the quality assurance test stand. Right: CALIFA APD (Hamamatsu S8664 series).

Fig. 1 shows a schematic view of the quality assurance test stand. It is divided into two parts: temperature controlling (left) and testing bench (middle). The Mesytec MPRB-16, which is a preamplifier and bias voltage supply for APDs, is chosen to maintain consistency with the electronics of CALIFA. The output of the APDs and the temperature are read by FEBEX3b.
The temperature of the test bench is kept constant by circulating water heated or cooled by peltier units. The temperature of the system is monitored with a NTC thermistor. The testing bench can test 8 APDs simultaneously. The APDs were tested with a pulsed green LED signal (λ_{max} = 520 nm), which is chosen to mimic signals of the CsI(Tl) scintillator.
The test temperature spans the range from 15°C to 25°C. This range includes the working condition required for the CALIFA APDs: 18 ± 1°C. For each temperature step, the gain curve of the APDs as a function of bias voltage is obtained. Fig. 2 shows an example of the gain curve and the energy resolution of the APD for the LED wavelength. In addition, a temperature stability check is necessary to confirm for reliability of the measured data (Fig. 3).
The APDs have a reference voltage for a nominal gain 50. It is the bias voltage that corresponds to gain 50 at 25°C.

Experiment collaboration: NUSTAR-R3B
PSP codes: 1.2.5.1.2.3.1
Grants: BMBF(05P15RDFN1), HIC for FAIR

Fig. 4 shows the comparison between the nominal voltage provided by the manufacturer and the measured one.

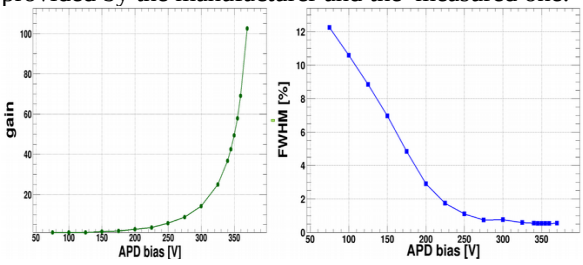


Figure 2: Left: APD gain curve. Right: APD energy resolution for LED signal.

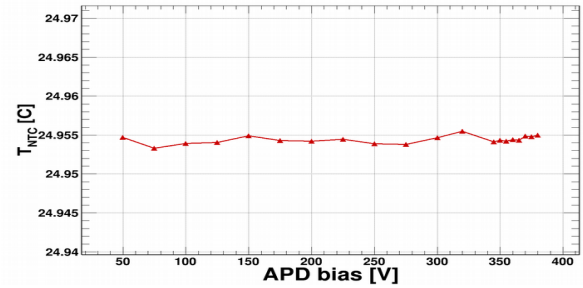


Figure 3: Measured temperature. The temperature of the system is stable within 0.002°C over 20 min. ($T_{peltier}$ = 25°C)

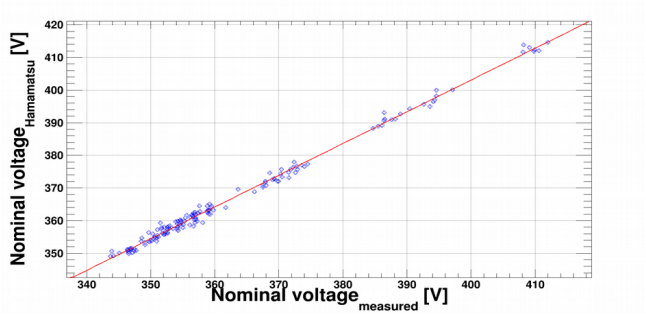


Figure 4: Correlation between the nominal voltage provided by the manufacturer with respect to the measured value.

References

[1] R.S. Gilmore et al., "Avalanche photodiodes as proportional particle detectors", Nucl. Instr. and Meth. A 388, 79 (1997).

Strategic university co-operation with: TU Darmstadt

 DOI:10.15120/GR-2018-1

First measurement of isotopic fission-fragment yields with calorimetric low-temperature detectors

S. Dubey [1,2], A. Echler[1,2], P. Egelhof[1,2], M. Mutterer[1], P. Grabitz[1,2], W. Lauterfeld[2], S. Stolte[2], A. Blanc[3], U. Köster[3], S. Kraft-Bermuth[4], P. Scholz[4], S. Bishop[5], J.M. Gomez-Guzman[5], and F. Gönnenwein[6]

[1]GSI, Darmstadt, Germany; [2]University of Mainz, Germany; [3]Institut Laue-Langevin, Grenoble, France; [4]University of Giessen, Germany; [5]Technical University Munich, Germany; [6]University of Tübingen, Germany

For thermal-neutron induced fission, precise data on fission-fragment yields in terms of mass, nuclear charge, and kinetic energy are of great interest for a better understanding of the fission process, and also required at several stages of the fuel cycle in nuclear reactors. Since more than 3 decades, the recoil mass spectrometer LOHENGRIN at the ILL Grenoble has been a leading instrument for fission fragment studies. Fission fragments emerging from a thin fissile target located close to the high-flux reactor core are separated according to the ratios of E/q and A/q (A = mass of fragment, q = ionic charge) and registered with silicon detectors or ionization chambers. For determining isotopic fragment yields a fairly universal method is the passive absorber technique exploiting the nuclear charge dependent energy loss of fission fragments in an energy degrader [1]. Due to its perfect mass resolution, LOHENGRIN has contributed more complete data sets on mass, nuclear-charge and energy distributions than any other method, with the resolving power for isotopic yields being restricted to the group of light fragment masses. Hitherto, cumulative yields of specific radioactive isotopes in the heavy fragment group have been tackled with the aid of gamma spectroscopy or, formerly, determined by radiochemical methods.

In the present work we have applied a new experimental approach to determine isotopic yields at LOHENGRIN by the passive absorber method using an array of calorimetric low-temperature detectors (CLTDs) instead of an ionization chamber for the residual energy measurement. Due to their principle of operation, CLTDs provide good energy linearity and resolution for the spectroscopy of heavy ions at low energies [2] and are, thus, predestined for measuring heavy fission fragments after degradation of a large proportion of kinetic energy. Furthermore, for the first time, stacks of commercially available silicon nitride (SiN) membranes were used as degrader material, favourably replacing the previously used Parylene-C plastic foils.

The detector array used in the present experiment is built-up from 25 individual pixels, made of sapphire chips of 430 µm thickness, with a total active area of 15x15 mm^2, operated at 1.5 K temperature in a windowless 4He-bath cryostat. The SiN absorber stacks of 16 x 10 mm^2 area were positioned closely in front of the CLTDs by a rotatable sample changer with six positions for SiN stacks of various thicknesses (Figure 1). This arrangement was intended to optimize the setup with respect to transmission, resolution and flexibility for measurements in different mass and energy ranges.

During a measuring period of about 4 weeks we investigated fragment yields in various fragment mass regions

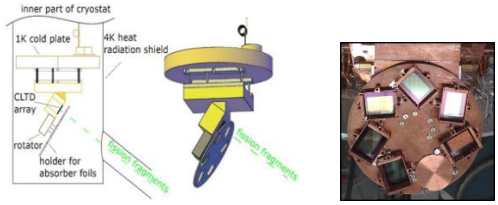


Figure 1: Schematic view of the detector cryostat with CLTD's as residual-energy detector and rotatable sample changer for silicon nitride absorber stacks (right).

for ^{235}U(n$_{th}$,f), ^{239}Pu(n$_{th}$,f) and ^{241}Pu(n$_{th}$,f). As a first topic, we have gained first ever LOHENGRIN data on fractional Z yields in the light-mass group of ^{241}Pu fission. A second topic was the study of light-fragment yields towards mass symmetry, up to A = 112 (113) in $^{241(239)}$Pu(n$_{th}$,f). This permits to elucidate how the local proton odd-even effect develops towards mass symmetry, which is of high interest for the nuclear model description near scission. A further issue was accurately measuring the isotopic fission yields of ^{92}Rb and ^{96}Y from ^{235}U(n$_{th}$,f), ^{239}Pu(n$_{th}$,f) and ^{241}Pu(n$_{th}$,f) since the decay of these isotopes is a main contributor to the integral reactor antineutrino spectra above 4 MeV that are important for the quantification of the so-called antineutrino anomaly and the postulation of sterile neutrinos. A final topical issue was to elaborate our novel technology for an accurate determination of isotopic yields for the first time also in the heavy fragment group, for selected masses in ^{239}Pu(n$_{th}$,f) up to A = 137. For the heavy fragments, the obtained Z-resolution did not permit to fully resolve individual peaks in the residual energy spectra, but to reliably retrieve fractional isotopic yields by constrained fitting of the overlapping peaks. Figure 2 shows, as example, residual energy spectra and fit results for A = 128 to 130 at 88 MeV, assuming up to three Z constituents. The increasing dominance of the magic proton shell Z = 50 towards symmetry is obvious.

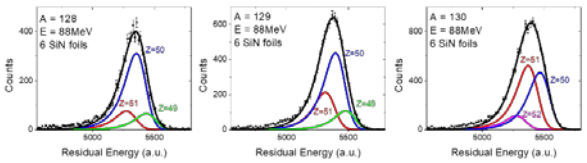


Figure 2: Residual energy spectra of heavy-fragment masses at 88 MeV energy in ^{239}Pu(n$_{th}$,f) from A = 128 to A = 130, with their individual Z constituents.

References

[1] U. Quade et al., Nucl. Phys. A 487, 1 (1988).
[2] S. Kraft-Bermuth, et. al., Rev. Sci. Instr. 80, 103304 (2009).

 DOI:10.15120/GR-2018-1

Optically Transparent Penning-trap electrodes for the ARTEMIS experiment

M. Voge1[1], G. Birkl[2], M. Ebrahimi[1], Z. Guo[1], N. Stallkamp[1] and W. Quint[1]

[1]GSI, Darmstadt, Germany; [2]Institut für Angewandte Physik, TU Darmstadt, Germany

We have conceived, built, and operated a cryogenic Penning trap with an electrically conducting yet optically transparent solid electrode [1,2]. The trap, dedicated to spectroscopy and imaging of confined particles under large solid angles in the ARTEMIS experiment [3,4] at HITRAP is of 'half-open' design, with one open endcap and one closed endcap that mainly consists of a glass window coated with a highly transparent conductive layer. This arrangement allows for trapping of externally or internally produced particles, yields flexible access for optical excitation and efficient light collection from the trapping region. At the same time, it is electrically closed and ensures long-term ion confinement under well-defined conditions. With its superior surface quality and its high and homogeneous optical transmission, the window electrode is an excellent replacement for partially transmissive electrodes that use holes, slits, metallic meshes and such.

Penning traps are valuable tools for precision spectroscopy of confined particles, largely owing to the multitude of available techniques for ion confinement and cooling. Confinement of internally or externally produced ions leads to a localisation of the species of interest in a small volume of space for long times. Cooling of these ions reduces shifts and transition line broadenings due to the Doppler effect, giving access to spectroscopy with high resolution and precision. To this end, a multitude of cooling techniques have been developed, which either require conducting surfaces close to the ions, good optical access, or both.

Our design is a so-called 'half-open' cylindrical Penning trap with the favourable electrical properties of a compensated open-endcap Penning trap, while at the same time surpassing its solid angle of optical access by more than an order of magnitude [3]. It features a window with transparent yet conductive coating, which has been characterized in a series of measurements, particularly with regard to its use in cryogenic Penning trap experiments.

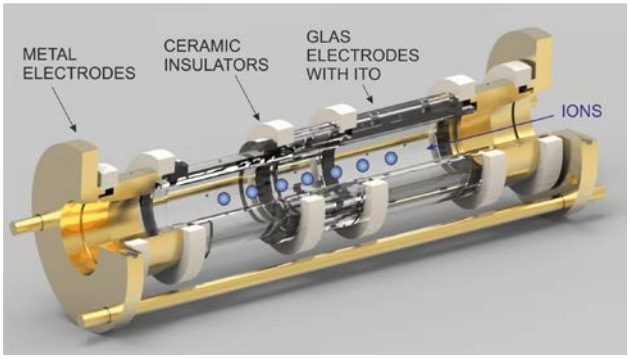


Figure 1: Artist's view of a possible further application of transparent electrodes with ITO coating on the inside, in a cylindrical Penning trap for spectroscopy of confined ions.

To the end of obtaining an optically transparent yet electrically closed electrode, a glass with an interior coating of ITO has been used. ITO is a doped n-type semiconductor with a bandgap of around 4 eV and is hence largely transparent in the visible part of the spectrum. It typically consists of about 75% indium (In), 17% oxygen (O2) and 8% tin (Sn) coated on a substrate. Several coating techniques are in use, including sputtering, spray coating and vapour deposition, all of which allow to fully coat or to produce 2D structures on the substrate surface, including bent substrates. ITO has a sheet resistance of around 80 Ohm/sq at a layer thickness of 125 nm. We have shown it to withstand cryogenic temperatures of down to 4 K, operation in a magnetic field of up to 7 Tesla, and resilience to impinging highly charged ions of keV kinetic energies per charge, while at the same time delivering a well-defined and stable electrostatic potential with a maximum surface roughness of few tens on nanometers, which is several orders of magnitude better than polished metal surfaces.

With this work we have introduced a novel realisation of Penning traps for precision spectroscopy, in which one endcap is made of a window with an electrically conductive yet optically transparent coating. This allows for a stable confinement of charged particles under well-defined conditions and efficient optical access to the confined particles under a large solid angle. This arrangement lends itself towards demanding applications such as optical precision spectroscopy of confined ions requiring efficient light collection. We have shown stable confinement of highly charged ions in such a trap and have studied the resilience and durability of an ITO-coated window used as an electrode in a cryogenic Penning trap environment.

References

[1] M. Wiesel, G. Birkl, M.S. Ebrahimi, A. Martin, W. Quint, N. Stallkamp, and M. Vogel, Rev. Sci. Inst. 88, 123101 (2017);

[2] L. Cockbill, Novel Penning trap design delivers optical access for precise spectroscopy, Scilight, DOI: 10.1063/1.5017839;

[3] D. von Lindenfels, M. Vogel, G. Birkl, W. Quint and M. Wiesel, Hyp. Int. 227, 197 (2014);

[4] D. von Lindenfels, M. Wiesel, W. Quint, D. Glazov, V.M. Shabaev, G. Birkl and M.Vogel, Phys. Rev. A 87, 023412 (2013)

Experiment beamline: HITRAP
Experiment collaboration: APPA-SPARC
Experiment proposal:
Accelerator infrastructure: SIS18, ESR
PSP codes:
Grants:
Strategic university co-operation with: Darmstadt

A scintillator-based ion detector for CRYRING@ESR*

C. Hahn[1,2,3], P. Pfäfflein[1,2,4], E. Menz[1,2], G. Weber[1,3] and Th. Stöhlker[1,2,3]

[1]HI Jena, Jena, Germany; [2]FSU, Jena, Germany; [3]GSI, Darmstadt, Germany; [4]DESY, Hamburg, Germany

The realization of the novel FAIR accelerator and storage ring complex achieved a major milestone with the commissioning of the CRYRING facility in late 2017. To fully exploit the multifaceted field of research thus made accessible, robust and reliable ion detectors are of fundamental importance [1]. These sensors will need to cope with MHz count rates of ions with energies ranging from sub-MeV/u to 15 MeV/u, and have to withstand the radiation damage imparted by the energetic ions. Given these restrictions, a detector system based on the YAP:Ce crystal scintillator provides an attractive approach, utilizing a material that is both comparatively affordable and endowed with a significant degree of radiation hardness [2].

A UHV-capable sensor design was devised and implemented as a collaborative effort of HI Jena, the University of Jena's Institute for Optics and Quantum Electronics, and the GSI Helmholtz Center. Figure 1 shows a cutaway view of the detector head: to accommodate the low end of the expected ion energy spectrum, the detector is essentially windowless, placing the scintillator material directly inside the vacuum. A light guide coupled to a fused silica window then channels the luminescence generated by the impinging ions to a photomultiplier tube (PMT) for conversion into an electrical signal. To facilitate the vacuum capability, this PMT – and all subsequent electronics – are kept on the atmospheric side of the window, and are installed only after the mandatory baking procedure is completed.

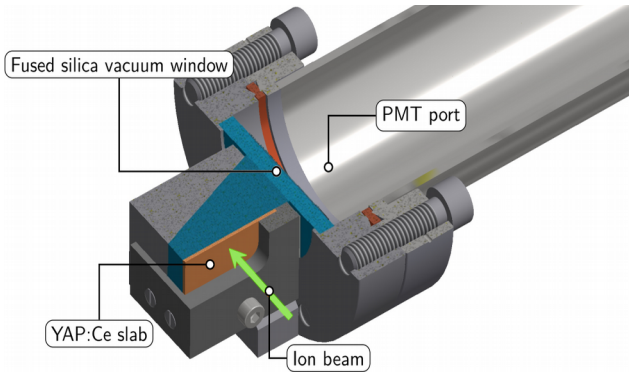


Figure 1: Schematic drawing of the detector head design. The ion beam hitting the scintillator induces light pulses which are registered by a photomultiplier tube attached to the atmospheric side of a UV-transparent vacuum window.

To gauge the assembly's sensitivity and long-term durability, a characterization measurement of this system, without the light guide prism, was conducted at the 3 MV tandem accelerator JULIA operated by the Institute of Solid State Physics at the University of Jena. Using hydrogen, oxygen and iodine ions at energies varying from 0.1 MeV/u to 2.4 MeV/u, the evolution of the PMT output signal was traced through increasing fluences of ion deposition inside the scintillator material, as illustrated by Figure 2. A marked decrease of the pulse height was found with proliferating damage: eventually, the output signal amplitude falls below the level of random noise pulses emitted by the PMT, at which point "true" events, i.e. pulses originating from incident ions, can no longer be reliably discerned by a simple pulse height threshold. This establishes a critical fluence, usually on the order of 10^{13} cm^{-2}, upon which the scintillator material has to be replaced. The exact magnitude of this fluence depends largely on the mass of the impinging ions; their kinetic energy plays only a minor role. On the other hand, the accumulating substrate damage does not appear to lead to an increase of the output pulse length past the initial value of about 50 ns, ensuring a uniform rate capability even after prolonged ion irradiation [3].

Building on the results of this successful proof-of-concept measurement, the final detector setup will be installed at CRYRING in early 2018.

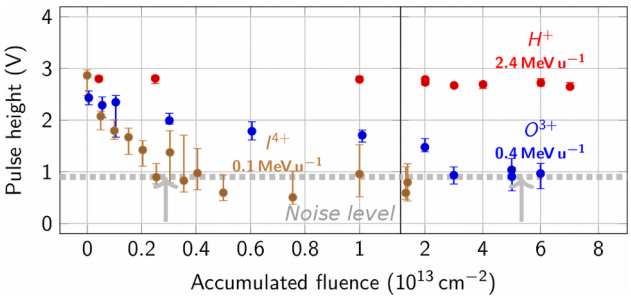


Figure 2: The average observed peak height for different ion species, at increasing accumulated fluences. Once the peak height reaches about 1 V, pulses originating from impinging ions can no longer be easily distinguished from random noise.

References

[1] M. Lestinsky et al., European Physics Journal Special Topics 225 (2016) 797
[2] M. Tokman et al., Physica Scripta 2001 (2001) 406
[3] P. Pfäfflein, "Entwicklung und Aufbau eines Teilchendetektors für erste Experimente am Ionenspeicherring CRYRING", Masterarbeit, Friedrich-Schiller-Universität Jena (2017)

Experiment beamline: CRYRING
Experiment collaboration: SPARC
Experiment proposal: none
Accelerator infrastructure: CRYRING
PSP codes: none
Grants: none
Strategic university co-operation with: none

*This report is also part of the HI Jena Scientific Report 2017.

 DOI:10.15120/GR-2018-1

Atomic computations of hyperfine coupling constants *

R. Beerwerth[1,2] and S. Fritzsche[1,2]

[1]Helmholtz Institute Jena, Germany; [2]Theoretisch-Physikalisches Institut, Friedrich Schiller University Jena, Germany

Precise spectroscopic measurements of hyperfine structures and isotope shifts allow to extract information about the nucleus under investigation, such as mean squared charge radii, deformation, nuclear spin and nuclear moments [1]. With the help of isotope separator online facilities that allow the production of atomic beams for large chains of isotopes one can probe these quantities for many short-lived nuclei. Recent advances [2] now open the perspective to extend these studies also into the region of superheavy elements, such as nobelium and in the near future lawrencium in order to probe possible regions of increased stability.

The hyperfine coupling constants A and B relate the nuclear magnetic dipole μ and electric quadrupole moments Q to the magnetic field and electric field gradients generated by the electrons at the site of the nucleus, respectively. Both of these quantities can be determined experimentally by measuring the same transition in different isotopes, if the nuclear moments are known for one of these isotopes. Alternatively, both hyperfine coupling constants can be computed from atomic many-body theory such as the multi-configuration Dirac-Fock (MCDF) method [3]. For iron, the only stable odd mass isotope ^{57}Fe with nuclear spin ½ does not have a quadrupole interaction, and consequently no quadrupole moment was known so far. In order to extract the nuclear quadrupole moment of ^{53}Fe, we performed extensive MCDF calculations of the hyperfine constants for the $3d^6 4s^2\ ^5D_4$ ground level and the $4s4p\ ^5F_5$ excited level [4]. Since the nuclear dipole moment and its coupling constants are well known, the A values for both levels were used as a benchmark to test the computations. Our result for B was subsequently used to extract Q.

Several independent model calculations were performed to provide an estimate of the theoretical uncertainty. Each model computation was performed in a systematically enlarged configuration space, which was generated by virtual single and double excitations of the valence electrons. Especially the magnetic dipole interaction of the ground level was strongly influenced by core effects. To account for these effects, single excitations from the core orbitals had to be incorporated into the generation of the atomic basis and lead to an agreement between experiment and theory at the 10% level.

Our computed results are shown in Fig. 1, where every circle marks the result of one model calculation of the hyperfine coupling constants for the ground or excited level. The results clearly show that the A-factor for the ground level deviates significantly from experiment when no core effects are considered. This effect does not happen for the excited level, since here the main contribution to the hyperfine interaction comes from the uncoupled *s*-electron and hence core effects are much less significant. The *B*-factors for both levels scatter much less, which, together with the good agreement of the *A*-factors with the experimental values, leads to the conclusion that an uncertainty of 15%, shown as coloured bar, for the computed values seems reasonable. The black lines denote the experimentally determined coupling constants with additional input from nuclear theory, whose error bars are not shown here.

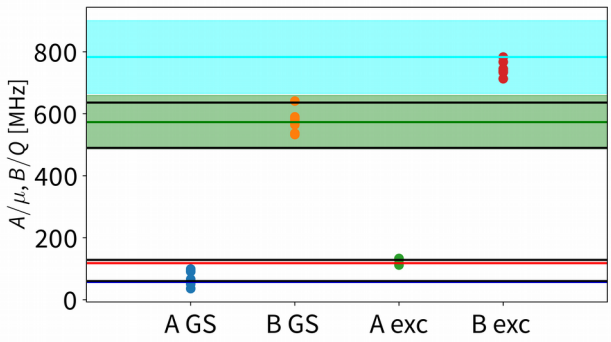


Figure 1: Computed hyperfine coupling constants A and B for the $^5D_4$ ground (GS) and $^5F_5$ excited Level of neutral ^{53}Fe from different model computations (circles). The black lines denote experimental values, the coloured lines the adopted values from our computations and the coloured bars the computational uncertainty.

In summary, atomic computations can provide valuable input in interpreting experimental data and in this case helped to extract nuclear properties. The combination of independent model calculations and systematically enlarged configuration spaces can provide estimates of theoretical uncertainties.

References

[1] M. Block, Hyperfine Interact. 238 (2017), 40
[2] M. Laatiaoui et al., Nature 538 (2016), 495-498
[3] P. Jönsson et al., Comput. Phys. Commun. 177 (2007), 597622
[4] A. J. Miller et al., Phys. Rev. C 96 (2017), 054314

* Also part of the Annual Report 2017, Helmholtz Institute Jena

Elastic scattering of twisted light by hydrogenlike ions*

A. A. Peshkov[1], A. V. Volotka[1] , A. Surzhykov[2,3], and S. Fritzsche[1,4]

[1]Helmholtz-Institut Jena, Germany; [2]Physikalisch-Technische Bundesanstalt, Braunschweig, Germany; [3]Technische Universität Braunschweig, Germany; [4]Friedrich-Schiller-Universität Jena, Germany

The elastic scattering of photons by the bound electrons of atoms or ions, commonly known as Rayleigh scattering, has been intensively explored over the past decades. From a theoretical viewpoint, the Rayleigh scattering has attracted much interest as one of the simplest second-order quantum electrodynamical (QED) process. In the past, a large number of experimental and theoretical studies have been performed in order to understand how the electronic structure of atoms affects the polarization of the Rayleigh-scattered photons. In particular, the linear polarization of the elastically scattered light has been measured directly by Blumenhagen et al. at the PETRA III synchrotron at DESY [1]. This experiment was performed for a gold target with a highly linearly polarized incident plane-wave radiation. Until the present, however, very little has been known about the Rayleigh scattering of twisted (or vortex) light beams. When compared to plane-wave radiation, such twisted photons have a helical wave front and carry a well-defined projection of the orbital angular momentum upon their propagation direction. In addition, the transverse intensity profile of the twisted beams exhibits a ringlike pattern with a dark spot (vortex) at the center. In experiments, twisted (Bessel) beams can nowadays be readily produced by means of spatial light modulators or axicons.

In the present work, we analyze theoretically the behavior of the polarization Stokes parameters of scattered photons for the elastic scattering of twisted Bessel light. Here we restrict ourselves to the nonresonant Rayleigh scattering of light by hydrogenlike ions in their ground state, and especially by hydrogenlike carbon. We consider and derive the Stokes parameters within the framework of second-order perturbation theory and the density-matrix approach. Three different possible experimental scenarios are considered here for the scattering of the incident Bessel beam at a single atom, a mesoscopic (atoms in a trap), or a macroscopic (foil) atomic target, and which are all assumed to be centered on the beam axis. We show that the linear and circular polarization of scattered light depends generally on the helicity and the opening angle of Bessel beams, leading to Stokes parameters that differ quite significantly from the scattering of incident plane-wave photons. Moreover, results of our calculations indicate that the polarization of the scattered photons is very sensitive to the projection of the total angular momentum (TAM) of twisted light for single atoms and mesoscopic atomic targets of a few tens of nm in size, while it remains unaffected by the TAM in the case of a larger macroscopic target. In particular, Figure 1 illustrates the first Stokes parameter, which characterizes the degree of linear polarization of outgoing photons, as a function of the scattering angle for mesoscopic target. As seen from this figure, the outgoing photons are completely linearly polarized at the scattering angle 90 degrees for incoming plane waves. However, the scattering of a Bessel beam by mesoscopic target with the width of 10 nm, for example, leads to a significant decrease of the polarization at this angle, depending on the TAM projection of twisted light.

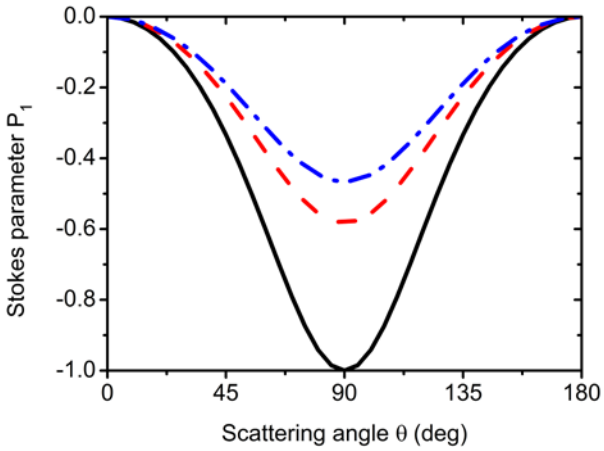


Figure 1: Stokes parameter of Rayleigh scattered light on hydrogenlike carbon ions in their ground state as a function of the emission angle. Results for incident plane waves (black solid lines) are compared with those for Bessel beams with TAM +1 (red dashed lines) and -1 (blue dash-dotted lines), respectively. Relativistic calculations were performed for mesoscopic atomic target of size 10 nm. Results are shown for the helicity +1, opening angle 30 degrees, and photon energy 100 eV of a Bessel beam.

Although our study was restricted to the scattering by hydrogenlike ions in their ground 1s state, similar polarization properties can also be observed in the scattering of twisted light by electrons in other s shells. In view of this, Rayleigh scattering may serve as an accurate technique for measuring the properties of twisted beams in a wide range of photon energies, and in particular at rather high energies.

References

[1] K.-H. Blumenhagen S. Fritzsche, T. Gassner, A. Gumberidze, R. Märtin, N. Schell, D. Seipt, U. Spillmann, A. Surzhykov, S. Trotsenko, G. Weber, V. A. Yerokhin, and T. Stöhlker, New J. Phys. 18 (2016) 103034.

[2] A. A. Peshkov A. V. Volotka, A. Surzhykov, and S. Fritzsche, Phys. Rev. A 97 (2018) 023802.

*Also part of the Annual Report 2017, Helmholtz Institute Jena.

 DOI:10.15120/GR-2018-1

The spin-polarised electron target PEGASUS

D. Schury[1,2],M. Lestinsky[1],A. Kalinin[1],S. Schippers[2],S. Hagmann[1],C. Kozhuharov[1],T. Stöhlker[1,3,4]

[1]GSI, Darmstadt, Germany; [2]JLU Gießen, Gießen, Germany; [3]HI Jena, Jena, Germany; [4]FSU Jena, Jena, Germany

A source for spin-polarised electrons for experiments on (highly charged) ions at storage rings has been built. Its performance is presently being characterized.

Chirality is a prominent characteristic of the molecular building blocks of life. It refers to the mirror symmetry of the spatial structure of a molecule. The influence of the differences in the positions of the nuclei in the molecule on chemical reactions has been widely studied in chemistry. In contrast, effects of molecular chirality on the electronic structure and dynamics have received much less attention. The ELCH collaboration (Electrodynamics of chiral systems) was formed with partners from different hessian universities to conduct research on chirality and related symmetries covering a wide range of topics from the molecular domain to strong field processes in highly charged ions. Within this collaboration, a source for spin-polarised electrons has been built at GSI [1].

In this source (see Figure 1), the spin-polarised electrons are extracted from a bulk GaAs semiconductor photocathode by polarised laser radiation [2]. The vacuum setup is divided into three sections. In the first section, the cathode is heat-cleaned and prepared into a state of negative electron-affinity [3]. By an alternating inlet of molecular oxygen and caesium into the preparation chamber, approximately one monolayer of oxidized caesium is produced on the cathode, which dramatically enhances its quantum efficiency. After preparation, the cathode is transferred to the adjacent section where it is irradiated by a near-infrared solid-state laser to generate a beam of spin-polarized electrons. In the same section, the electrons are accelerated to an energy of up to 10 keV. After acceleration, the beam is deflected by a 90° electrostatic bender to separate the electron beam from the laser beam and to achieve a transversal polarization with respect to the beam propagation direction. The third section is used for the analysis of the electron-beam properties and for providing a connection to experiments. Currently, we can measure intensity, lateral profile, energy distribution, and the degree of the transversal polarisation of the electron-beam. For the determination of the latter quantity a mini-MOTT detector is attached. Already our first beams exhibited a polarization degree of about 25%. The compact setup with a footprint of only 2 m^2 is mobile and can be easily used at different storage rings, as well as at other facilities.

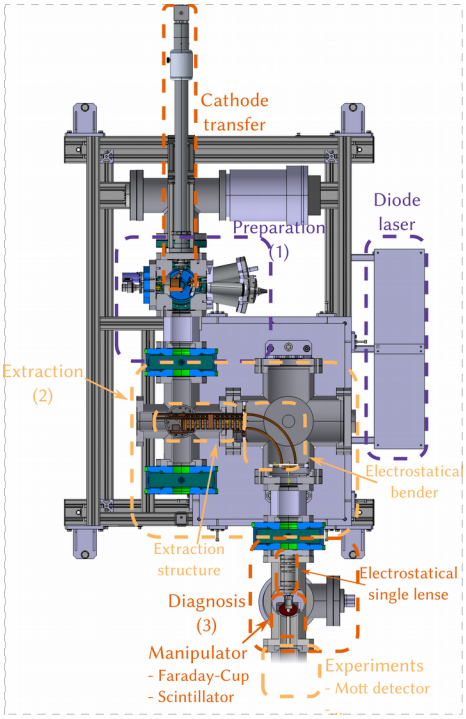


Figure 1: Schematic overview of the setup.

A number of technical improvements are foreseen: In the future, strained superlattice cathodes[4] will deliver polarization degrees of up to 90 %. The cathode handling shall be improved to keep more than one sample prepared simultaneously. Additionally, atomic hydrogen is planned for improved in-vacuum reconditioning of the cathode surface.

The only element manipulating the electron spin so far is the electrostatic bender which turns the polarisation from longitudinal to transversal. By adding two adjacent Wien-filters it will become possible to deliberately select the spin-orientation according to the experimental requirements.

References

[1] D. Schury, Construction and characterization of a spin-polarized electron source for future experiments with chiral molecules, PhD Thesis, Justus-Liebig University Gießen, 2017.
[2] D. Pierce, F. Meier and P. Zürcher, Appl. Phys. Lett. (26), 1975
[3] H. Sonnenberg, Appl. Phys. Lett. (14), 1969
[4] T. Nishitani, et al., J. Appl. Phys. (97), 2005

Experiment beamline: none
Experiment collaboration: APPA-SPARC
Experiment proposal: none
Accelerator infrastructure: none
PSP codes: none
Grants: H2020 ERC-2015-CoG/LOEWE-ELCH 05E12CD2
Strategic university co-operation with: Gießen

A third amplifier stage in the pulse system for laser cooling of relativistic ion beams at SIS100

D. Kiefer[1] and Th. Walther[1]

[1]Institute of Applied Physics, TU-Darmstadt, Darmstadt, Germany

Laser cooling has been demonstrated in the ESR and is planned for SIS100 as well as for HESR. With the aim of achieving white light cooling [1] of relativistic heavy ion beams, a pulsed laser system with adjustable repetition rate and spectral width is under development.

The principle of the laser system has been presented elsewhere [2] and the Fourier limited character of the laser pulses has been investigated [3]. A first test of the second harmonic generation [4] has been reported. In brief, the system consists of an external cavity diode laser (ECDL), whose radiation at 1028 nm is amplified, followed by a fast electro-optic modulator stage producing the laser pulses between 70 and 740 ps. Finally, two fiber based amplifier stages are used to increase the available average power. In the final system there will be nonlinear frequency conversion to the 4th harmonic. However, the results discussed here were achieved at 1028 nm. In order to achieve pulse energies high enough for cooling of even the heaviest elements [5], we installed an additional third amplifier stage to the pulse laser system. This amplifier stage consists of a backward pumped air-clad fiber. The 80 cm long fiber rod has a core diameter of 85 microns, resulting in a mode field area over 40 times larger than that of the second amplifier stage. This helps to avoid nonlinear effects as well as intensity induced damage. The pump cladding diameter is 260 microns and the rod is temperature stabilized by a water chiller. The fiber allows polarization-maintaining single-mode operation. Due to the currently available maximum cw pump power of 27 W at 976 nm, the amplification is limited. An even further increase of the pulse energies should be possible with a stronger pump laser source.

For laser cooling with short laser pulses, the pulse energy has to be adjusted to each different ion species, preferably with the repetition rate scalable to the ion velocity and the number of buckets. Therefore, the laser system is developed to provide flexibility in both energy and repetition rate. Table 1 shows the achieved pulse energies and average powers dependent on repetition rate and pulse duration. The pulse energies increase with pulse duration. The average power is independent of repetition rate, indicating that there is no saturation at our pump levels. Thus, more pump power will significantly increase the output power and pulse energies providing a fairly straightforward way to reach even higher energies.

Table 1: Pulse energies in J and average power in W observed after three ampli er stages

Rep.Rate	Pulse Duration		
	250 ps	500 ps	735 ps
1 MHz	11 J, 11 W	13 J, 13 W	15 J, 15 W
5 MHz	2.2 J, 11 W	2.6 J, 13 W	3 J, 15 W

The sinc^2-shaped frequency spectrum of the output measured with a slowly scanning Fabry-Pérot interferometer (FPI, Free Spectral Range (FSR) 10 GHz) with a FWHM of 1.86 GHz is shown in figure 1. The inset shows the corresponding rectangular timing signal. The time bandwidth product equals 0.93 suggesting Fourier transform limited pulses.

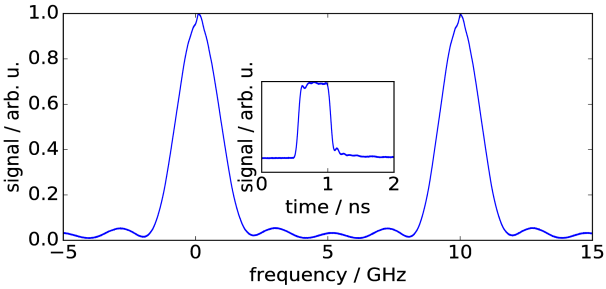


Figure 1: Spectrum and corresponding temporal shape (inset) of a rectangular pulse of 500 ps duration after the third amplifier stage. The spectrum was observed with a slowly scanning FPI (FSR 10 GHz). These results are independent of the repetition rate.

References

[1] R. Calabrese, V. Guidi, P. Lenisa et al.,"White-light laser cooling of ions in a storage ring" Hyperfine Interact 99: 259, 1996

[2] T. Beck and Th. Walther, "A flexible pulsed ps/ns laser system for ion beam cooling at ESR/SIS100", GSI Scientific Report 2014

[3] D. Kiefer, T. Beck and Th. Walther, "Flexible Picosecond Master Oscillator Fiber Amplifier System for Ion Beam Laser Cooling at ESR/SIS100", GSI Scientific Report 2015

[4] D. Kiefer, S. Klammes, B. Rein and Th. Walther, "Recent Work on the Darmstadt laser systems for laser cooling of relativistic ion beams at SIS100", GSI Scientific Report 2016

[5] L. Eidam, O. Boine-Frankenheim, D. Winters, "Cooling rates and intensity limitations for laser-cooled ions at relativistic energies", Nuclear Instruments and Methods in Physics Research Section A: Accelerators, Spectrometers, Detectors and Associated Equipment, Volume 887, Pages 102-113, 2018

Experiment beamline: ESR
Experiment collaboration: APPA-SPARC
Experiment proposal: E136
Accelerator infrastructure: ESR / SIS100 / HESR
PSP codes: none
Grants: funded by BMBF, grant number 05P15RDFA1.

 DOI:10.15120/GR-2018-1

Auger cascade calculations in krypton supporting pump–probe experiments*

S. O. Stock[1,2], R. Beerwerth[1,2], and S. Fritzsche[1,2]

[1]Helmholtz Institute Jena, Germany; [2]Theoretisch-Physikalisches Institut, Friedrich Schiller University Jena, Germany

Recent advances in experimental techniques such as ultrafast time-resolved spectroscopy and modern UV and X-ray sources have enabled detailed studies of ionization processes. In order to interpret the results of these experiments, large-scale atomic structure computations are an important tool. Here, we report our theoretical results in support of a recent experimental study of the ionization dynamics in inner-shell excited krypton [1].

The experiment employs a pump–probe scheme and for the first time combines absorption spectroscopy and photoion spectroscopy to give a detailed picture of the ionization dynamics. The pump pulse, an attosecond XUV beam centered around 90 eV, excites the $3d^{-1}np$ resonances in neutral krypton while an intense few-cycle near-infrared (NIR) pulse acts as probe by (doubly) ionizing different groups of Kr^+ ions to Kr^{3+}. Through variation of the NIR intensity, different groups of levels can be "reached" by the probe pulse which allows a detailed view into the ionization dynamics (see Ref. [1] for details). By varying the delay between XUV and NIR pulse, one gains access to the lifetimes of the levels which are ionized by the NIR pulse.

In order to support the experiment, we performed extensive multiconfiguration Dirac–Fock calculations using the GRASP [2] and RATIP [3] packages. After excitation by the XUV pulse, the $3d^{-1}np$ excited atoms decay predominantly by a two-step Auger cascade. We model this decay cascade by considering all possible normal Auger decays as well as shake processes of the *np* valence electron, in an approach similar to our recent theoretical studies [4,5]. All calculations are performed at a fine-structure level in order to obtain a comprehensive view of the autoionization paths.

An overview of the Auger cascade following the resonant $3d^{-1}np$ excitation is given in Fig. 1. In the first step of the cascade, the inner-shell excited krypton atoms decay predominantly via spectator Auger decays to the $4p^{-2}np$, $4s^{-1}4p^{-1}np$, $4p^{-3}4dnp$, and $4s^{-2}np$ levels, while participator processes can be neglected. In the second step of the cascade, the $4s^{-1}4p^{-1}np/4p^{-3}4dnp$ levels autoionize further to the ground configuration of Kr^{2+} while the $4s^{-2}np$ levels autoionize to the Kr^{2+} $4s^{-1}4p^{-1}$ and $4p^{-3}4d$ configurations.

Even though only a few of the autoionizing Kr^+ levels (marked with the numbers 1–12 in Fig. 1) are predominantly populated during the first step of the cascade, their lifetimes range from a few femtoseconds to several hundred femtoseconds. Since the experiment cannot access the decay curves of individual levels, but instead rather large groups of levels within an energy range, we calculate *effective* lifetimes, as a weighted average of the individual lifetimes, for different level groups. While the $4s^{-2}np$ levels have an effective lifetime of only 6 fs, the $4s^{-1}4p^{-1}np/4p^{-3}4dnp$ levels decay considerably slower, with an effective lifetime of 49 fs. This difference in effective lifetimes is consistent with the experimental findings where a higher NIR intensity leads to a longer apparent lifetime, since lower-lying levels are being addressed by the probe pulse.

In conclusion, comprehensive theoretical studies of Auger cascades are important to support new kinds of experiments with modern UV and X-ray sources.

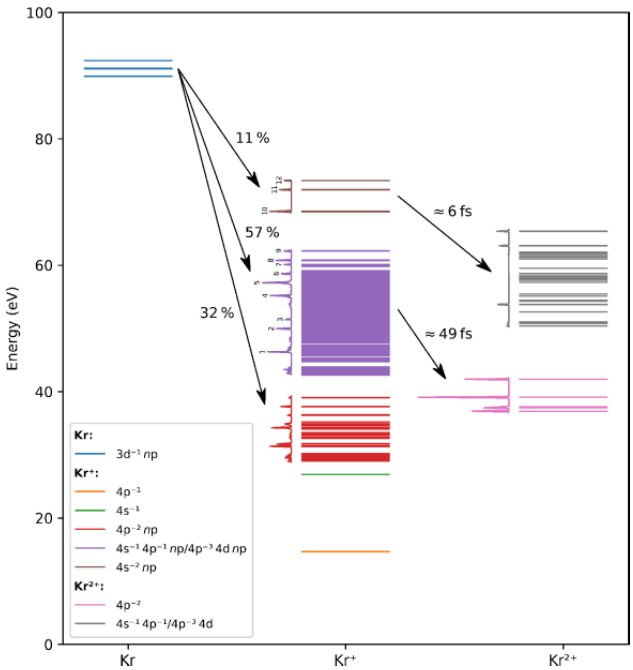


Figure 1: Diagram of the levels involved in the two-step Auger cascade after resonant $3d^{-1}np$ excitation of Kr. The spectra to the left of each group of levels show the relative population of the respective levels. Energies are given relative to the ground level of neutral krypton. The $4s^{-1}4p^{-1}np$ and $4p^{-3}4dnp$ configurations of Kr^+ as well as the $4s^{-1}4p^{-1}$ and $4p^{-3}4d$ configurations of Kr^{2+} are mixing heavily and are therefore not clearly distinguishable.

References

[1] K. Hütten et al., Nat. Commun. 9 (2018), 719
[2] P. Jönsson et al., Comput. Phys. Commun. 177 (2007), 597–622
[3] S. Fritzsche, Comput. Phys. Commun. 183 (2012), 1525–1559
[4] S. Schippers et al., Phys. Rev. A 94 (2016), 41401
[5] S. Stock, R. Beerwerth, and S. Fritzsche, Phys. Rev. A 95 (2017), 53407

*Also part of the Annual Report 2017, Helmholtz Institute Jena

Elliptical dichroism in two-photon atomic ionization

J. Hofbrucker[1,2], A. V. Volotka[1], S. Fritzsche[1,2]

[1] Helmholtz Institute Jena [2]Friedrich-Schiller Universität Jena

Dichroic behavior is usually associated with an interaction of polarized atomic or chiral molecular target and circularly polarized light. Since the observations of asymmetries in above-threshold ionization of nobel gases by elliptically polarized light [1], it became apparent that a dichroic behavior is not a unique characteristic of a chiral target, but can also arise from a non-linear light-matter interaction. In contrast to circular dichroism, it arises from the interference of the dominant ionization channels. It is solely the interference between the different ionization channels which carries the information about the sign of the elliptical polarization. Since the elliptical dichroism is system specific, it gives us an opportunity to study many-electron effects as well as fundamentals of non-linear light-matter interaction.

In our recent work, we studied the intriguing phenomenon of elliptical dichroism in two-photon ionization of a *K*-shell electron of neutral atoms by elliptically polarized light [2, 3]. It was found that a strong effect can be found at threshold energies for two-photon ionization of light elements. However, for inner-shell ionization, high energy photons are required, but the polarization control at current free-electron laser facilities is scarce. In cooperation with our experimental colleagues from the European XFEL project, we decided to find an experimental system for verification of inner-shell elliptical dichroism within the limits of current technologies (proposal 20174073 at FERMI). Out of rare gas atoms, electrons from the krypton *3p* shell were chosen as the most convenient showcase to detect a strong two-photon ionization elliptical dichroism (see Figure 1). Since the cross section for a direct two-photon ionization of Kr *3p* is relatively low and two-photon absorption requires comparably long acquisition times for obtaining statistically valid spectra, we proposed to study the elliptical dichroism in the vicinity of the Kr *3p-3d* resonance in order to facilitate the feasibility of the experiment. The photoelectron spectra will be measured for five photon energies, covering the dynamical energy dependence of the elliptical dichroism, including measurements of both strong and zero dichroism.The proposed experiment of two-photon ionization of Kr will be the first confirmation of elliptical dichroism in inner-shell ionization and it will give us the opportunity to accurately extract atomic parameters relevant for the ionization process.

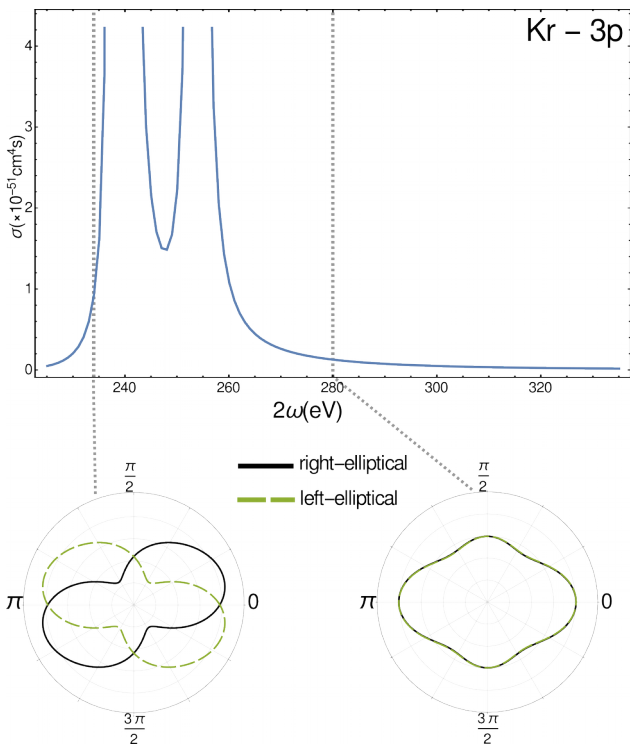


Figure 1: (Upper): Total two-photon cross section in the range of the Kr *3p-3d* resonance as a function of two-photon energy (energy transferred to the initially bound electron). (Lower): Electron distributions in the plane perpendicular to the photon propagation (dipole plane) are shown for two energy points. These distributions represent the maximal and minimal elliptical dichroism for the two-photon ionization of Kr *3p*. From the figures, it is apparent that the dichroism is highly sensitive to the photon (or photoelectron) energy. It is worth noting that the resonance itself only plays a secondary role in the process.

References

[1] M. Bashkansky, P. H. Bucksbaum, and D. W. Schumacher, Phys. Rev. Lett. 60, 2458 (1988).

[2] J. Hofbrucker, A. V. Volotka, and S. Fritzsche, Phys. Rev. A 94, 063412 (2016).

[3] J. Hofbrucker, A. V. Volotka, and S. Fritzsche, Phys. Rev. A 96, 013409 (2017).

Also part of the Annual Report 2017, Helmholtz Institute Jena

 DOI:10.15120/GR-2018-1

Towards a quantum standard for high voltage measurements

K. König[1], J. Krämer[1], C. Geppert[2], P. Imgram[1], B. Maaß[1], J. Meisner[3], E. W. Otten[4], S. Passon[3], T. Ratajczyk[1], J. Ullmann[1] and W. Nörtershäuser[1]

[1]Institut für Kernphysik, TU Darmstadt, Germany, [2]Institut für Kernchemie, JGU Mainz, Germany, [3]Physikalisch Technische Bundesanstalt, Germany, [4]Institut für Physik, JGU Mainz, Germany

Many experiments, e.g. at the ESR or at KATRIN rely on accurate high voltage measurements. These are usually carried out with high voltage dividers which are limited to an accuracy of up to 1 ppm [1] due to an intricate, step-wise calibration tracing back to low-voltage Josephson standards [2]. The susceptibility of the resistors to thermal changes and aging effects is the main source of systematic uncertainties and prohibits a long-term stability [3].

On the contrary, a stable quantum standard for high voltage measurements could be defined with collinear laser spectroscopy: If an atom or ion beam is superposed collinearly by a laser beam, the laboratory-frame laser frequency ν_L will be Doppler-shifted according to

$$\nu_L = \nu_0 \, \gamma \, (1 \pm \beta) \qquad (1)$$

for co-/counter-propagating beams in the rest frame of the moving particles. For an electrostatically accelerated ion with the charge q and mass m, the velocity β is defined by the potential difference U since

$$qU = mc^2(\gamma - 1)\,. \qquad (2)$$

Solving Eq. 1 and 2 for the acceleration potential, the applied voltage is linked to the measurement of a laser frequency only by fundamental constants

$$U = \frac{mc^2}{2q} \frac{(\nu_L - \nu_0)^2}{\nu_L \nu_0}. \qquad (3)$$

Hence, for ions with well-known mass and transition frequency ν_0 the applied voltage can be determined, if the laser frequency in the laboratory frame is identified. This can be realized e.g., with a laser scan while observing the fluorescence light emitted by the excited ions.

Earlier attempts with this technique were limited by the uncertainty of the optical frequency measurement [4] or the uncertainty of the real starting potential of the ions in the ion source [5]. In the ALIVE (Accurate Laser Involved Voltage Evaluation) experiment a two-stage laser interaction for a pump and probe approach is combined with a highly accurate frequency determination with a frequency comb [6] to overcome these limitations.

In this first stage of the experiment we used calcium ions produced in a surface ion source and compared the achieved results with a Julie Research Laboratory HVA100 and the PT20 high voltage divider from the Physikalisch-Technische Bundesanstalt (PTB) which both have a 5 ppm relative uncertainty.

We have performed a measurement series with voltages between -5 kV and -19 kV. The deviation of the laser spectroscopic measurement from the simultaneous measurement with the voltage dividers is shown in Fig. 1. The black error bars indicate the statistical uncertainty whereas the green error bars represent a systematic uncertainty due to a possible misalignment of the post acceleration stage which was identified as the main source of systematic uncertainty and always shifts the measured voltage to smaller values. Within the uncertainty of the voltage dividers of 5 ppm our results are in good agreement.

In the next phase of the experiment we will use indium ions produced with very low transverse emittance in a liquid metal ion source. This will allow smaller apertures leading to a better overlap and hence a higher accuracy by better ion beam collimation. Furthermore, the transition will be very narrow, allowing higher precision in the determination of the resonance position. With these improvements we think that we will be able to reach an accuracy better than 1 ppm.

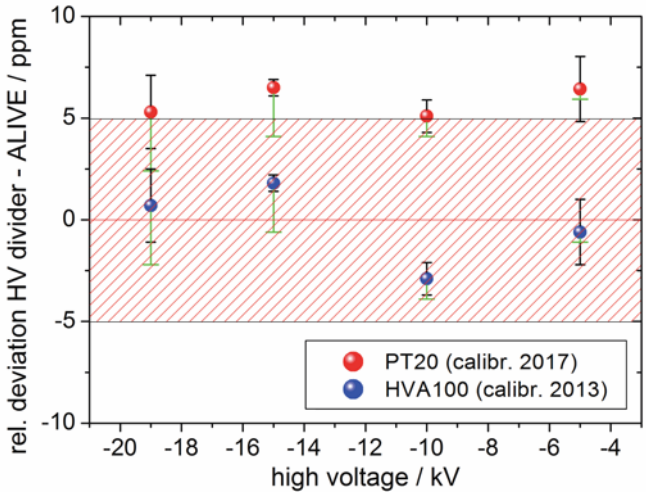


Figure 1: Results of the high voltage measurement [7]. The relative deviation of the laser spectroscopic from the electronic measurement is shown as a function of the voltage for the two high voltage dividers. The shaded area marks the uncertainty of the voltage dividers used in this experiment. For more details see text.

References

[1] T. Thümmler, et. al., New J. Phys., 11 (2009) 103007
[2] B. Josephson, Phys. Lett., 1 (1962) 251
[3] K. Kim, et. al, IEEE Trans. Instr. Meas.,52 (2007) 469
[4] O. Poulsen, E.Riis, Metrologia, 25 (1988) 147
[5] S. Götte, et.al., Rev. Sci. Instr., 75 (2004) 1039
[6] T. Udem, et. al., Nature, 416 (2002) 233
[7] J. Krämer, K. König, et. al., Metrologia (2018) https://doi.org/10.1088/1681-7575/aaabe0

Experiment beamline: CRYRING / ESR
Experiment collaboration: APPA-SPARC
Experiment proposal: none
Accelerator infrastructure: ESR / CRYRING
PSP codes: none
Grants: HIC for FAIR, DFG INST 163/392-1 FUGG, HGS-HIRE
Strategic university co-operation with: Darmstadt

Towards a solution of the hyperfine puzzle of strong-field bound-state QED

J. Ullmann[1,2], S. Schmidt[1,3] and W. Nörtershäuser[1]
L. Skripnikov[4], A. Volotka[4,5], and V. Shabaev[4]

[1] TU Darmstadt, Institut für Kernphysik, Darmstadt, Germany; [2]Westfälische Wilhelms-Universität Münster, Institut für Kernphysik, Münster, Germany; [3]Johannes Gutenberg-Universität Mainz, Institut für Physik, Mainz Germany; [4]St. Petersburg State University, Department of Physics, St. Petersburg, Russia; [5]Helmholtz-Institut Jena, Jena, Germany

The first high-precision measurement of the so-called specific difference $\Delta' E = \Delta E_{2s} - \xi \Delta E_{1s}$ of the hyperfine structure splitting in hydrogen-like $^{209}Bi^{82+}$ and lithium-like $^{209}Bi^{80+}$ was reported in [1] and analysed as a test of bound-state quantum electrodynamics (BS-QED) in strong fields, where a pertubative description of QED is no longer possible. It was found that the experimental value deviates by more than 7σ from the theoretical prediction, giving rise to the so-called hyperfine puzzle of BS-QED. The result has triggered many discussions in the community, as it has the potential to challenge BS-QED.

Here, we summarize the efforts to provide a solution of this hyperfine puzzle. As already pointed out in [1], there are three possible explanations for the observed discrepancy: (1) new physical effects not considered in current QED calculations, (2) a wrong nuclear magnetic moment of bismuth, as this experimentally determined value enters linearly into the specific difference, or (3) an unexpected deficiency in the specific difference. In the following we will concentrate on points (2) and (3), which both have to be clarified before (1) can be considered.

To examine the nuclear magnetic moment of ^{209}Bi, we have performed NMR measurements in collaboration with the group of Prof. M. Vogel (TU Darmstadt) on $Bi(NO_3)_3$ dissolved in concentrated and diluted nitric acid to study effects of the chemical environment. In parallel, state-of-the-art calculations of the diamagnetic correction and the chemical shift were carried out. The NMR measurements were performed at an 8.4-T magnet using the same temperature stabilized double resonance probe for ^{209}Bi NMR and ^{1}H NMR calibration with tetramethylsilane (TMS). The observed effects of temperature and acidity in the $Bi(NO_3)_3$ solution could hardly be explained by model calculations, due to the unknown quantity of water molecules involved in the hydration of the Bi^{3+} ions. A much cleaner system concerning the chemical shift, yet experimentally harder to handle, turned out to be the hexafluoridobismuthate(V) (BiF_6^-) anion, which has a high spatial symmetry. The sample was prepared in an elaborate process by the fluoride specialist group of Prof. F. Kraus (University of Marburg). During the NMR measurement of this sample, the typical septet structure in the spectrum was observed, which uniquely assures the chemical environment. Moreover, the temperature dependency was insignificant in this case. The knowledge of the chemical environment in this sample strongly reduced the uncertainty of the chemical shift correction, which previously has been the dominant uncertainty. The specific difference based on this new nuclear magnetic moment agrees within uncertainties with the experimental value in [1]. This indicates an explanation for a large part of the deviation [2]. Clear evidence requires a correction-free measurement, e.g., at the ARTEMIS trap experiment.

Possibility (3) from above can be examined by extending the measurement of the specific difference to the isotopic sequence in bismuth, in particular ^{208}Bi and ^{207}Bi. The results will give new insights into nuclear structure theory, specially our understanding of the magnetic distribution inside the nucleus (Bohr-Weisskopf effect). The proposed studies are foreseen to be carried out at the experimental storage ring at GSI.

As a prerequisite towards laser spectroscopy of H-like and Li-like ^{208}Bi, a more precise value of its nuclear magnetic moment is mandatory. Moreover, a new value will lead to better predictions of the transition wavelength under investigation, which is important for spectroscopy experiments of this kind. Therefore, the hyperfine structure (hfs) splitting (hyperfine *A* and *B* factors) of this isotope were measured at the collinear laser spectroscopy experiment (COLLAPS) at ISOLDE, CERN, with improved accuracy. By combining these results with theoretical calculations of the hfs anomaly, we have provided a new value for the nuclear magnetic moment of ^{208}Bi based on the magnetic moment of ^{209}Bi that was determined from the ESR experiments reported in [1] under the assumption that QED is correct [3]. In addition, we have obtained theoretical predictions of the ground-state hyperfine transition energies, which are 5600(4) meV and 878.1(5) meV for H-like and Li-like ^{208}Bi, respectively [3].

The results present an important step towards a first measurement of the specific difference using a radioactive isotope. Hereby, a major challenge will be the reduced fluorescence rate due to the lower beam intensity in the storage ring. For H-like ^{208}Bi the production rate will be sufficient to follow an optical detection scheme. In contrast, for lithium-like ^{208}Bi and for ^{207}Bi ions, more dedicated detection methods are necessary, which are currently being developed (see [4]).

References

[1] J. Ullmann et al., Nature Comm. 8, 15484 (2017)
[2] L. Skripnikov et al., PRL **120**, 093001 (2018)
[3] S. Schmidt et al., Phys. Lett. B **779**, 324 (2018)
[4] M. Lestinsky, et al., Eur. Phys. J. **225** 797 (2016)

Experiment beamline: ESR
Experiment collaboration: APPA-SPARC
Experiment proposal: E128
Grants: BMBF 05P15RDFAA; HIC for FAIR; SPbSU-DFG (Grants No. 11.65.41.2017 and No. STO 346/5-1); DFG VO 1707/1-3
Strategic university co-operation with: Darmstadt

 DOI:10.15120/GR-2018-1

Highly Charged Ions at the HILITE Penning trap experiment

N. Stallkamp[1,2,3], S. Ringleb[3], M. Kiffer[3], S. Kumar[4], T. Morgenroth[1,3], G. Paulus[2,3], W. Quint[1,5], Th. Stöhlker[1,2,3] and M. Vogel[1]

[1]GSI, Darmstadt, Germany; [2]Helmholtz-Institut Jena; [3]Friedrich Schiller Universität Jena; [4]Inter-University Accelerator Centre, New Delhi, [5]Ruprecht Karls-Universität Heidelberg

High-sensitivity measurements of reaction educts and products of laser-particle interactions benefit from a preparation of the target ensemble in a well-defined way. Therefore, we have conceived, designed and built the HILITE Penning trap experiment. It employs ion-cloud formation techniques as well as destructive and non-destructive techniques to analyse the trap content for all species and charge states individually and simultaneously [1]. This facilitates reconstruction of non-linear interactions of stored particle species with high-energy and/or high-intensity lasers.

In order to be independent from external ion sources and to be able to perform experiments at different laser facilities, a dedicated ion source is needed, which fulfils the key requirement of the complete setup, namely to be easily transportable. For that purpose, a compact electron beam ion source (EBIS) together with a dedicated control and readout system (see Fig.1) has been implemented and brought into operation [2].

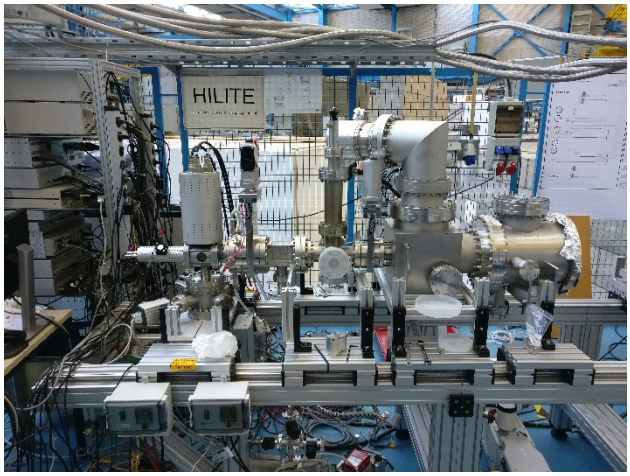


Figure 1: Ion source setup (EBIS, left) with attached diagnostic chamber (right).

We have measured the voltage switching times for ion deceleration and ion capture to verify the performance when slowing down ions extracted from the EBIS for subsequent storage in the HILITE trap. After capture, the ions will initially have kinetic energies of the order of 200 eV. For fast and efficient ion slowing, we have developed a novel implementation of 'active ion slowing', where the ion-signal induced in one trap electrode segment is used for negative feedback. Consequently, the ions experience a repulsive force when approaching the electrode and an attractive when leaving it. Obviously, feeding the slowing signal back to the pick-up electrode causes a strong overlap between ion signal and the slowing signal itself. To overcome this issue, we have implemented a balanced Wheatstone bridge consisting of four capacitors, one of which is the trap electrode itself. The voltages applied to both branches are subtracted from each other. In consequence, the difference is the pure ion signal, as this is only induced in one of the branches. The circuit diagram and the manufactured electronics board used in our trap is shown in figure 2. First tests show, that both branches can be balanced out well.

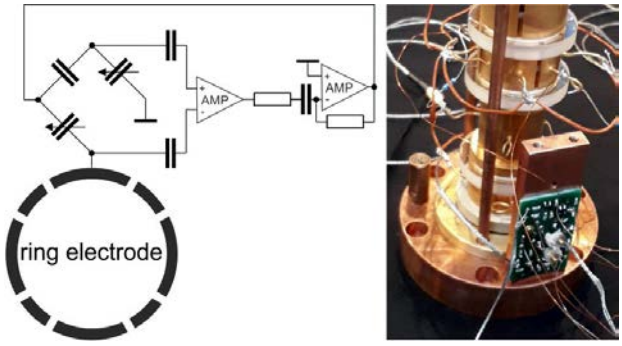


Figure 2: Feedback ion-cooling circuit and photo of the electronics board attached to the trap.

Following this active feedback slowing, we will apply cooling techniques to further cool the ion ensemble down to the environmental temperature of about 4K. This will be done by the well-known 'resistive cooling' technique, where the ions lose energy by dissipating power to a cryogenic resonance resistance. Such cooling facilitates the application of various ion manipulation techniques for control over ion density, position and the overall composition of the target ion ensemble confined in the trap.

*Also part of the annual report 2017, Helmholtz-Institut Jena

References

[1] S. Ringleb, M. Vogel, S. Kumar, W. Quint, G. Paulus, Th. Stöhlker, Journal of Physics Conference Series 635 (2015) 092124

[2] T. Morgenroth, Master thesis, Uni Jena 2017

Experiment beamline: none
Experiment collaboration: APPA-SPARC
Experiment proposal: none
Accelerator infrastructure: none
PSP codes: none
Grants: none

First online applications of the LASPEC DAQ system

S. Kaufmann[1], K. König[1], I. Metzler[1], F. Sommer[1] and W. Nörtershäuser[1]

[1]TU Darmstadt, Darmstadt, Germany;

Bunched-beam collinear laser spectroscopy (CLS) has become very popular in the recent years, due to the impressive background suppression in the order of 10^4 which results from the temporal control of the ions. This allows to perform experiments with exotic isotopes that are produced at rates of only a few 100 ions/s and will also be used in the LASPEC experiment at FAIR.

In order to match these experimental conditions, a new time resolved data acquisition (DAQ) system was developed during the last years at the LASPEC collinear ion beamline TRIGA-LASER [1]. It is called TILDA (**TRI**GA **L**ASER **D**ata **A**cquisition) and its real-time operations are realised by two FPGAs located in a PXI-crate. The flexibility of the FPGAs ensures that the system can be adapted to various experimental conditions required for collinear laser spectroscopy since a variety of detection techniques can be applied. Thanks to the high-level programming languages python and LabVIEW in combination with a sophisticated layer architecture, new developers can adapt TILDA to their needs in short time.

One of the first tests for TILDA was the offline commissioning campaign of the radio frequency cooler and buncher (RFQCB) at the MATS-LASPEC-prototype TRIGA-SPEC [1,2]. The next step in development was then its first passive online usage at the COLLAPS experiment at ISOLDE-CERN in parallel to a well-established data acquisition that lacks photon-timing capabilities. The benefits of TILDA's time resolution became quickly obvious during this measurement campaign, since it provides important information about the proper operation of the RFQCB that cannot be easily obtained by other means. In 2017, TILDA became the main data acquisition system for COLLAPS and was successfully used during two online measurement campaigns. In the upper part of Figure 1, a typical spectrum of this campaign is shown for ^{61}Ni.

Furthermore, TILDA is now implemented also at the COALA beamline (**Co**llinear **A**pparatus for **L**aser Spectroscopy and **A**pplied Physics) in Darmstadt, which serves now as the German development platform for LASPEC, while the TRIGA-laser beamline is operated at Argonne (USA) within FAIR phase 0. Here, TILDA has been adapted to implement also the possibility of fast laser switching using acousto-optical modulators (AOM). The advantage of laser-beam switching for example to avoid hyperfine pumping of the small components in a spectrum was demonstrated at TRIUMF previously and will also be of advantage at LASPEC.

At GSI it is planned to implement TILDA as the DAQ system for laser spectroscopy experiments at CRYRING.

References

[1] S. Kaufmann, et al., Journal of Physics: Conference Series 599-1-012033 (2015)

[2] Ch. Gorges, S. Kaufmann, Hyperfine Interactions **238**, 26 (2017)

[3] I. Metzler, Bachelor Thesis, TU Darmstadt (2017)

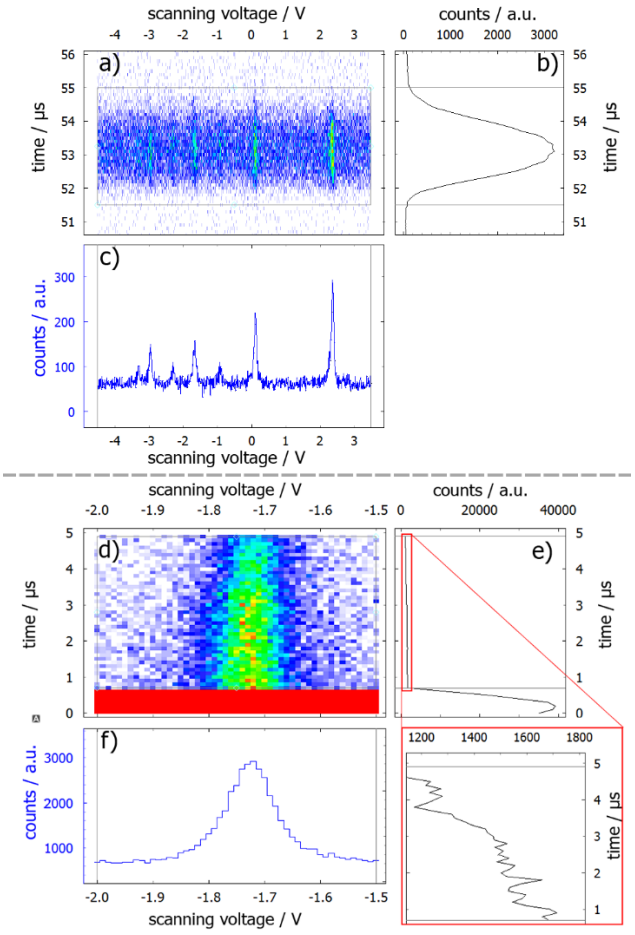


Figure 1: The application of TILDA's timing resolution with a pulsed ion beam of ^{61}Ni (a-c) and a "pulsed" laser beam (d-f) (switched off by an AOM at 0.7 µs) to visualize the versatility of the time-resolved DAQ. Graphs a,d: color coded fluorescence count rate as a function of the Doppler-tuning voltage (*x*-axis) and the time of flight (*y*-axis) relative to a timing trigger (in (a) the time after the extraction of the ions from ISCOOL, in (d) 0.7 µs before the pump laser is turned off). Graphs b,e: temporal projection of the number of counts within the marked region of interest (ROI) onto the time axis from which information on the bunch structure (c) or the excitation profile along the ion beam (e) can be extracted. Graphs e,f: resonance lineshape as a function of the Doppler-tuning voltage. For more details see [2,3].

Experiment beamline: none
Experiment collaboration: NUSTAR-LASPEC
Experiment proposal: none
Accelerator infrastructure: none
Grants: BMBF contract 05P15RDFN
Strategic university co-operation with: Darmstadt

 DOI:10.15120/GR-2018-1

Cooling time constant of ions stored in Penning traps

A. Henkel[1,2,3], F. Herfurth[1], R. Pinnau[2] and T.-K. Strempel[3,]

[1]GSI, Darmstadt, Germany; [2]Technische Universität Kaiserslautern, Germany; [3]University of Applied Sciences, Darmstadt, Germany

The HITRAP (Highly Charged Ions Trap) facility at GSI allows to investigate slow highly charged ions up to U^{92+}. The most important part of the facility is the Penning trap, which allows the trapping of ions.

A microscopic simulation of the ion cloud is only possible to a limited extent [1]. For this reason, based on [2] we derive two new models, the *global* and *local cooling model*. The global cooling model describes the cooling constant of the center-of-mass motion. While the local cooling model describes the cooling constant of the internal motion.

The cooling model

In contrast to [2] the starting point of both cooling models is the differential equation of the resonant circuit for the voltage

$$\frac{d^2u(t)}{dt^2}+\frac{R}{L}\frac{du(t)}{dt}+\frac{1}{LC}u(t)=\frac{R}{LC}\left(i(t)+\frac{L}{R}\frac{di(t)}{dt}\right) \qquad (1)$$

with resistor R, inductor L, capacitor C and current *i(t)*. The electrical power

$$P(t)=\frac{energy}{time}=\frac{dE_{kin}(t)}{dt}=-u(t)i(t) \qquad (2)$$

can be used to link the kinetic energy $E_{kin}(t)$ of the system with the resonant circuit equation (1). The minus sign in (2) is due to the fact that the energy in the resonant circuit is dissipated and will not be returned to the system.

The global cooling constant

For the global current $i_G(t)$ we choose the approach

$$i_G(t)=\frac{1}{\sqrt{12}}q\kappa\sqrt{N}\sqrt{\frac{2E_{kin}^G(t)}{m}}\cos(\omega_{res}t)$$

with the kinetic center-of-mass energy E_{kin}^G, mass *m*, number of particles *N*, charge *q*, resonance frequency ω_{res} and a constant of proportionality κ. Now (1) and (2) can be solved numerically. The results are shown in Figure 1.

An analytical solution of the system (1) and (2) can not be given. But if we assume that the kinetic energy is almost not changed compared to the current over an oscillation period, the system can be reduced to a driven harmonic oscillator whose solution is known. Assuming the center-of-mass is in resonance with the resonant circuit, we get the global cooling time constant

$$\tau_G=\frac{12m}{q^2N\kappa^2R_{res}} \qquad (3)$$

with the resonance resistance R_{res}.

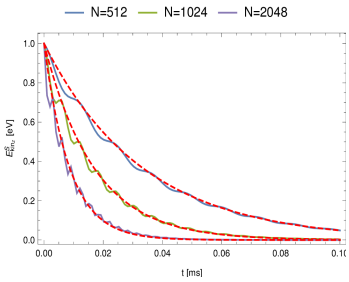


Figure 1: The red dashed lines are the solutions of the global cooling model and the others are the solutions of the microscopic model.

The local cooling constant

For the local current $i_L(t)$ we choose the approach

$$i_L(t)=q\kappa\frac{\sqrt{N}}{N}\sqrt{\frac{k_BT(t)}{m}}\cos(\omega_{res}t)$$

with the BOLTZMANN constant k_B, the temparatur T und use the relationship between mean kinetic energy and temperature.

Analogous to the global model, if we assume that the temperature hardly changes compared to the current over an oscillation period, the system of differential equations can be solved.

We get the local cooling time constant

$$\tau_L=\frac{3mN}{q^2\kappa^2R_{res}}. \qquad (4)$$

If we compare both cooling time constants (3) and (4), it is noticeable that with τ_G the numer of particles N appears in the denominator and by τ_L in the numerator. If we increase the number of particles, more particles contribute to the current during the center-of-mass motion, which results in rapid global cooling. Instead, the local cooling slows down. This is because the velocities are cancelled out.

References

[1] Henkel, A. et al. GSI Scientific Report 146, 2015.

[2] VOGEL, M., et al. Resistive and sympathetic cooling of highly-charged-ion clouds in a Penning trap. *Physical Review A*, 2014, 90. Jg., Nr. 4, S. 043412.

Precision spectroscopy using a maXs microcalorimeter

M. O. Herdrich[1,2,3], G. Weber[1,2], A. Fleischmann[4], D. Hengstler[4], and Th. Stöhlker[1,2,3]

[1]HI Jena; [2]IOQ, FSU Jena, [3]GSI, Darmstadt, [4]KIP, RKU Heidelberg

Introduction

A new generation of cryogenic microcalorimeters for usage as high precision X-ray spectrometers is currently under development for the SPARC collaboration. The maXs-30 of the maXs (microcalorimeter array for X-ray spectroscopy) detector design developed by the group of Prof. Enss at KIP, Heidelberg features 64 pixels and a theoretical energy resolution of 5 eV FWHM at 6 keV photon energy with an accessible energy range from several 100 eV up to 100 keV [1]. A fast signal rise time (≈100 ns) enables coincidence measurements with time resolutions in the order of 10 ns. Combined with a high linearity [2] and a good long-term stability, the maXs detector system is well suited for high precision measurements at storage rings such as the ESR or CRYRING at GSI/FAIR. First experiments have already been conducted using a prototype detector in the beginning of 2016 and preliminary results were obtained using a new signal processing algorithm based on finite response filters. The new method is more stable and due to much a faster execution time allows for an online analysis of the detector signals.

Preliminary Results

The experiment was conducted at the ESR using U^{89+} ions with a beam energy of 80 MeV/u in collision with a N_2 gas target. A maXs-30 detector was positioned at 90° with respect to the beam axis, with a ≈10 cm air gap to the interaction chamber. Preliminary results (see fig. 1) show that an energy resolution of approx. 80 eV is achieved throughout the whole energy range of the detector using the newly designed finite response filter for data analysis. This is only 10 eV worse compared to the commonly used optimal filter algorithm [3] which is too computational expensive for online analysis of the measured data. Insufficient temperature control of the detector and noise induced by the ESR might explain the divergence from the theoretical optimal resolution. Nevertheless, a comparison with results from experiments with He-like Uranium conducted by X. Ma et. al in 2000 [4] shows that the achieved energy resolution already surpasses the one of standard semiconductor-based X-ray detectors be a factor of 5. Further improvements can be expected with a better temperature correction. The rather small ratio between the intra-shell transition Δn=0 and the Balmer lines compared to theory is explainable by the absorption of the photons in the air gap and two Beryllium windows which act like a high pass filter for X-rays. A detailed simulation of the collision system is planned to determine the spectral lines as well as to separate radiation stemming from capture and excitation processes.

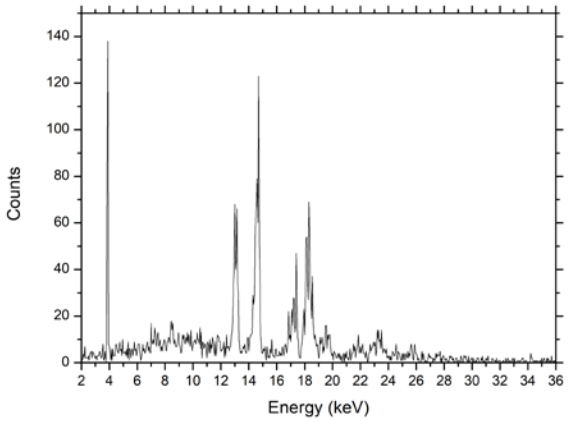


Figure 1: Preliminary results showing an X-ray spectrum recorded at the ESR for U^{89+} collisions with N_2 at 80 MeV/u. Visible are the inner shell transition Δn=0 in the L-shell ($1s_2\ 2p_{3/2} \rightarrow 1s_2\ 2s_{1/2}$) of the projectile as well as several Balmer ($n > 2 \rightarrow L$) and Paschen ($n > 3 \rightarrow M$) transitions. Radiation resulting from both capture and excitation of the projectile can be seen.

Conclusion and Outlook

The analysis of first experimental data recorded by the maXs-30 detector shows that results generated with the new algorithm are comparable to the results of the optimal filter. Planned improvements include a recently updated version of the maXs-30 detector, which contains a temperature sensitive pixel. Every global temperature change of the detectors shifts its operating point and thereby changes the baseline of the detector signals. By reading out the baseline of the temperature sensitive pixel for every read-out cycle, a correlation between energy and working point can be found. A simple bilinear correction is applied to compensate temperature induced shifts of the read-out energy. First tests show, that this method is highly effective in resolving artificial multipeak structures arising from an unstable operation point.

References

[1] D. Hengstler et al., Phys. Scr. T166, 2015
[2] C. Enss et al., J. Low Temp. Phys., Vol. 121, 2000
[3] A. Fleischmann, Dissertation, RKU Heidelberg, 2003
[4] X. Ma et al., Phys. Rev. A, Vol. 64, 2001

Experiment beamline: ESR

Experiment collaboration: APPA-SPARC
Accelerator infrastructure: ESR
Grants: This work is supported by the European Union and the federal state of Thuringia via Thüringer Aufbaubank within the ESF program (2015 FGR 0094).
Strategic university co-operation with: Friedrich-Schiller-University Jena

This report is also part of the HIJ Annual Report 2017

 DOI:10.15120/GR-2018-1

The Transverse Electron Target for CRYRING@ESR

C. Brandau[1,2], A. Borovik, Jr.[1], B.M. Döhring[1], B. Ebinger[1], M. Lestinsky[2], T. Molkentin[1], A. Müller[1], S. Schippers[1] for the SPARC working group 'Electron Targets'

[1]Justus-Liebig-Universität Gießen, Germany; [2]GSI, Darmstadt, Germany

As outlined in the CRYRING@ESR Physics Book of the SPARC collaboration and the CRYRING Instrumentation TDR [1, 2] it is planned to install a ribbon-shaped free-electron target in the experimental section YR09 of CRYRING@ESR [3]. The target will be mainly used for atomic electron-ion collision studies and is optimized for operation in the storage ring environment of CRYRING. The target can be fully retracted from the storage ring behind a gate valve. The target will be concurrently installed in the experimental section YR09 with the gas-jet target allowing for an optimal use of beam time. The electron beam interacts with the ion beam under a collision angle of 90° with a free sight field to the interaction zone for photon spectroscopy (Fig. 1).

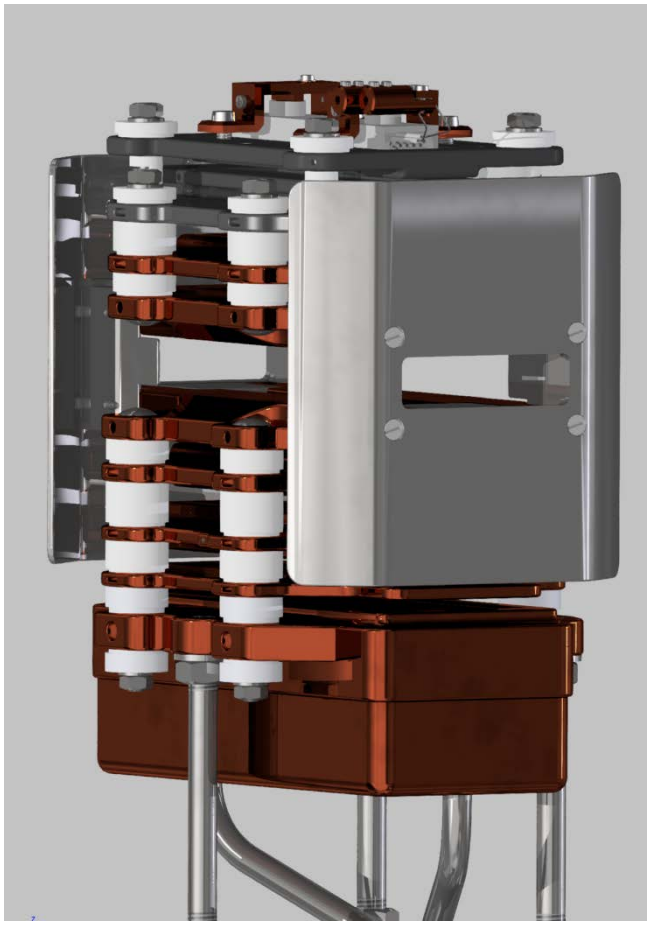


Figure 1: CAD model of the electron gun for the CRYRING@ESR transverse electron target. The electron beam is directed from top to bottom. Behind the interaction region, the beam is decelerated and dumped in the collector. The ion beam passes the gun through the shielding apertures at the front and at the back. The geometrical overlap of electron and ion beam can be controlled and quantified by moving the gun in the horizontal direction. The interaction volume is open from both sides providing a large solid angle for photon spectroscopy.

The electron gun features a high-energy mode up to 12.5 keV electron energy, and a high-density mode with electron densities surpassing $n_e = 1 \cdot 10^9$ cm^{-3}. Further details of the target and the envisaged set-up in the CRYRING experimental section are given in [4, 5].

During the last year, further options were added to the gun and the design of the gun-electrodes was finalized (Fig. 1). It is now foreseen to pulse the voltage of the first anode that controls the electron emission from the cathode. This feature allows the electron beam to be swiftly switched off during phases with no ion beam in the ring, thus substantially reducing the heat-load on the collector and, hence, the gas-load to the ring-vacuum. In addition, it will be investigated whether the switching can also be used for timing purposes. Four electrodes at the side of the interaction zone enable the shaping of the potential, e.g., to flatten the space charge potential of the electron beam for a more precise energy definition of the electrons and higher experimental resolution as well as to avoid trapping of slow ions from the residual gas. Like the anode, the clearing/shaping electrodes' voltages can be pulsed to swiftly switch between different modes (e.g., flat potential, trapping, non-trapping).

The electrodes and other parts of the gun are presently being manufactured. Vacuum recipients, pumps, the main manipulator and a first set of power supplies have been ordered and are partially already delivered. We expect to assemble the target and to perform first offline tests by the end of 2018. Depending on additional funding, the target will be available in CRYRING@ESR in 2021.

References

[1] M. Lestinsky et al., Eur. Phys. J Spec. Top. **225** (2016), 797.
[2] Z. Andelkovic et al., Technical Design Report: Experimental Instrumentation of CRYRING@ESR, 2015, http://www.fair-center.eu/en/en/for-users/experiments/appa/documents.html.
[3] M. Lestinsky et al., Phys. Scr. T**166** (2015), 014075.
[4] C. Brandau et al., GSI Scientific Report 2015, p. 143.
[5] C. Brandau et al., GSI Scientific Report 2016, p. 240.

Experiment beamline: CRYRING
Experiment collaboration: APPA-SPARC
Experiment proposal: none
Accelerator infrastructure: CRYRING
PSP codes: 1.3.1.5.9
Grants: BMBF contract No. 05P15RGFAA and HIC for FAIR
Strategic university co-operation with: Gießen

Status of a new laser ablation ion beam source for LASPEC

T. Ratajczyk[1], V. Varentsov[2,3] and W. Nörtershäuser[1]

[1]Institut für Kernphysik, TU Darmstadt, Germany, [2]Facility for Antiproton and Ion Research in Europe (FAIR GmbH), Darmstadt, Germany, [3]Institute for Theoretical and Experimental Physics, Moscow, Russia

Continuous and pulsed ion beams having low emittances are required for many high precision laser spectroscopy experiments. A high quality and compact source of various stable ions is for example needed for the LASPEC project [1]. A multi-purpose collinear beamline has been installed at TU Darmstadt [2] and will serve as the German development platform for LASPEC. An ion source that can provide high quality beams in a wide range of stable isotopes is an ideal tool to be used for further improvement of the system performance, for precision laser spectroscopy and to test the whole setup to ensure efficient operation during online measurements of the radioactive isotopes at FAIR. The ion source might also be used at CRYRING to provide additional ion species.

The laser ablation ion source of a new type that is under construction at TU Darmstadt is based on the proposal described in details in [3]. It combines the ion production by laser ablation in presence of helium gas, ion extraction via a supersonic gas jet into an RF-only ion funnel and then into original RF-buncher placed downstream in high vacuum conditions. The schematics of this ion source together with results of a gas dynamics simulation for the gas velocity flow field is shown in Figure 1.

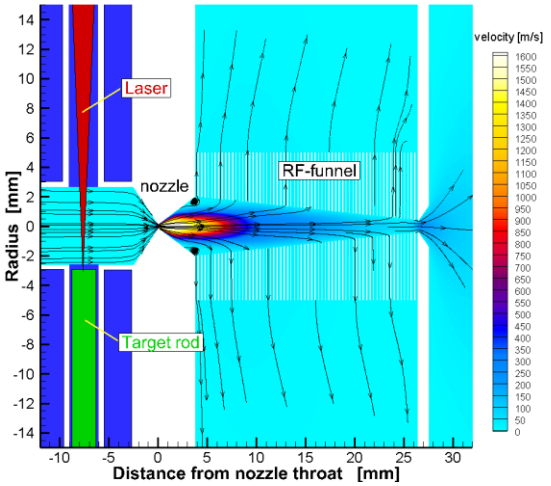


Figure 1. Schematics of the new laser ablation ion source together with the results of gas dynamics simulation of its operation. The Rf-buncher behind the RF-only funnel is not shown.

The CAD-rendering of the setup design is shown in Fig. 2. This ion source system has been manufactured, assembled (see Fig. 3) and first gas dynamic measurements were recently performed. These measurements are in a good agreement with full Navier-Stokes gas dynamics simulations (flow fields of gas temperatures, densities and velocity components), which have been used for detailed ion trajectory Monte Carlo simulations.

The main calculated parameters of the extracted ion beam (ablated from the aluminium target at He stagnation pressure of 200 mbar) are as follows: Beam energy - 92.6 eV, longitudinal energy spread (90% level) - 0.018 eV, beam radius (90% level) - 0.74 mm, transverse emittance - 16.3 π mm mrad, time of bunching - 1 ms, extracted bunch width - 5 µs, longitudinal emittance (90% level) - 0.09 eV µs.

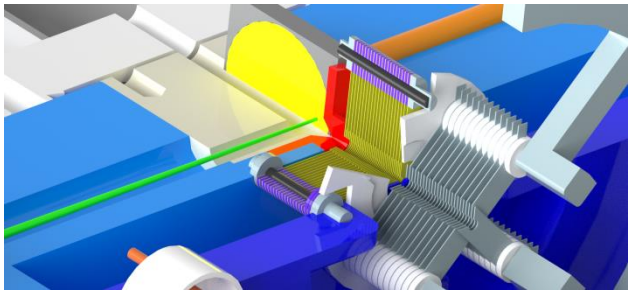


Figure 2. CAD-rendering of the setup design. Green: laser, yellow: target, red: nozzle, yellow and violet: RF-only funnel, grey and white: RF-buncher

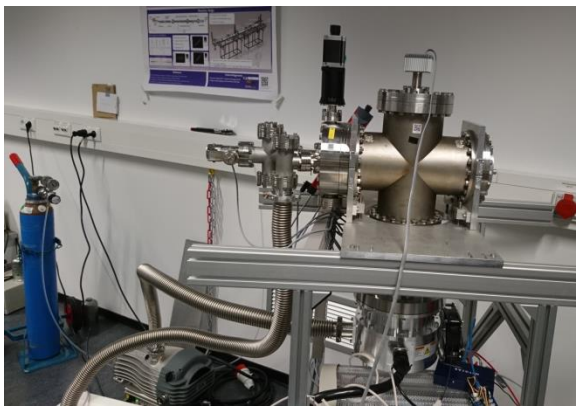


Figure 3. Current assembly connected to a CF 160 cross with a 900 l/s TMP and an 11 l/s Dry Piston Pump.

References

[1] D. Rodríguez, K. Blaum, W. Nörtershäuser et. al, MATS and LaSpec: High-precision experiments using ion traps and lasers at FAIR, Eur. Phys. J. Special Topics **183**, 1–123 (2010), DOI: 10.1140/epjst/e2010-01231-2.

[2] J. Krämer, K. König, et. al., Metrologia **55**, 268 (2018)

[3] Victor Varentsov, Proposal of a new Laser ablation ion source for LaSpec and MATS testing, NUSTAR Collaboration Meeting, 1 March, 2016, DOI: 10.13140/RG.2.2.10904.39686

Experiment beamline: none
Experiment collaboration: APPA-SPARC, NUSTAR-LASPEC
Experiment proposal: none
Accelerator infrastructure: CRYRING
PSP codes: none
Grants: HIC for FAIR, HGS-HIRE, BMBF 05P15RDFN1
Strategic university co-operation with: Darmstadt

 DOI:10.15120/GR-2018-1

Experimental determination of electron capture cross sections into excited states of decelerated xenon projectiles

F. M. Kröger[1,2,*], G. Weber[2,3], J. Glorius[3], Y. Litvinov[3,4], M. O. Herdrich[1,2], U. Spillmann[3], M. Vockert[1,2], Th. Stöhlker[1,2,3]

[1]FSU Jena, Germany; [2]HI Jena, Germany; [3]GSI, Germany; [4]RKU Heidelberg, Germany

Currently only very few data exists for electron-capture cross sections of highly-charged ions colliding with atoms/molecules at energies well below the respective projectile ionization threshold. However, such conditions will be common for beams of decelerated highly-charged heavy ions in the recently commissioned CRYRING@ESR of GSI/FAIR, Darmstadt, where the capture rate with residual gas atoms/molecules will determine the ion beam lifetimes. Thus, the knowledge of electron capture cross sections is of particular importance for the planning of experiments in this storage ring.

Here we report on the evaluation of experimental cross-section data obtained for Xe^{54+} ions colliding with H_2 molecules [1]. The experiment was performed at the internal gas target of the ESR storage ring at GSI, Darmstadt using collision energies between 5.5 MeV/u and 30.93 MeV/u. An array of Ge(i) X-ray detectors was placed at various observation angles around the interaction zone. These detectors allowed to record the X-ray emission arising from the ion-atom collisions, in particular those resulting from radiative capture of target electrons into bound states of the projectile ions and also characteristic K radiation due to subsequent transitions from excited states to the ground state, see fig. 1. Note that for a H-like high-Z system two-photon transition rates are negligibly small compared to single-photon transitions. Therefore, as all electron-capture events into excited states will lead to K transitions, the K-shell emission cross-section is a measure of the total electron capture cross-section into projectile states with $n > 1$. By normalizing the observed intensity of the characteristic K radiation to the K-REC (meaning Radiative Electron Capture into the projectile K-shell) intensity (similar to [2]) we related the characteristic K emission cross-section to the well-known K-REC angular differential cross-section.

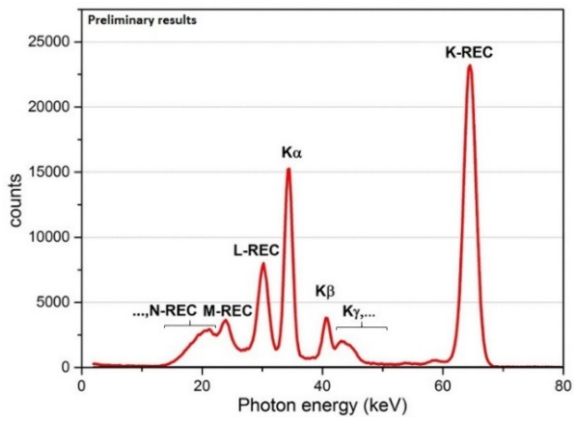


Figure 1: X-ray spectrum of bare xenon ions colliding with H_2 molecules at 30.93 MeV/u, recorded with a photon detector at 60°.

*felix.kroeger@uni-jena.de

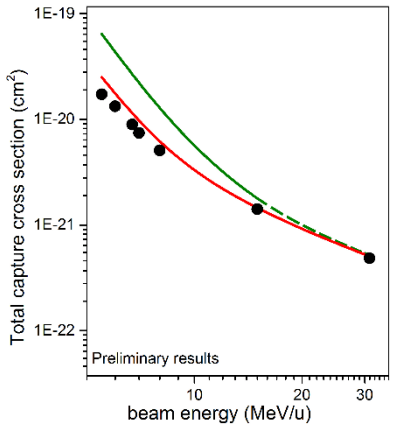


Figure 2: Comparison of total electron-capture cross-sections resulting as the sum of the REC cross sections from [3] and the NRC cross sections calculated with the Schlachter formula (green line) and with the eikonal theory (red line) to the experimental data (full circles) as function of the ion beam energy. In order to present total capture cross sections into all projectile states the experimental cross sections were complemented by theoretical K-REC cross sections.

In figure 2, a comparison of the commonly used empirical Schlachter formula (green line) [4] and of the eikonal theory [5] for non-radiative electron capture (NRC) plus the REC to the preliminary experimental data (full circles) is shown. For the particular collision system under discussion, the range of validity of the Schlachter formula is limited to $E_{kin} < 16$ MeV/u. A dashed line is used for beam energies that lie beyond this range. Note that for the operation of the CRYRING the most important parameters are the total electron capture cross-sections into all projectile states. Therefore, in order to compare the resulting experimental and the theoretical total electron capture cross-sections, theoretical K-REC cross-sections [3,6] were added to the experimental and theoretical capture cross sections into projectile states with $n > 1$. For completion also theoretical K-shell NRC cross-sections should be included, which however are negligibly small compared the K-REC cross-sections.

As can been seen in figure 2, the results of the Schlachter formula deviate markedly from the experimental data in contrast to the eikonal theory, which is in reasonable agreement with the experimental data.

[1] J. Glorius et al., JPCS 875, 092015 (2017).
[2] Th. Stöhlker et al., Phys. Rev. A 58(3), 2043 (1998).
[3] M. O. Herdrich et al., NIM B 408, 294 (2017).
[4] A. S. Schlachter et al. Phys. Rev. A, 27, 3372 (1983).
[5] J. K. M. Eichler, Phys. Rev. A 23, 498 (1981).
[6] G. Weber et al., JPCS 599, 012040 (2015).
[7] J. Eichler and Th. Stöhlker, Phys. Rep. 439, 1 (2007).

Towards laser spectroscopy of Mg^+ ions at CRYRING

K. Mohr[1], A.W. Barasa[1], Z. Andelkovic[2], A. Buß[3], V. Hannen[3], W. Nörtershäuser[1], T. Ratajczyk[1], R. Sánchez[2]

[1]Institut für Kernphysik, TU Darmstadt, Germany; [2]GSI, Darmstadt, Germany; [3]Institut für Kernphysik, WWU Münster, Germany

Storage ring experiments would tremendously benefit from polarized beams of stable and exotic nuclei, e. g. for experiments on parity violation. Therefore it has been suggested to polarize beams by optical pumping, which can be used to polarize the electron shell as well as the nucleus in the case of odd isotopes. However, it is not clear yet whether the induced polarization will persist during the revolution in the storage ring without additional means. On the round trip, the ions have to pass rapidly changing fields through the dipole and quadrupole magnets for deflection and focusing.

First evidence of the preservation of the polarization of an ion beam was found in our group during an experiment at the Experimental Storage Ring (ESR) to test special relativity [1]. A resonance signal was observed when irradiating the ion bunch by linearly polarized light. The resonance disappeared as soon as circularly polarized light (either σ^+ or σ^-) was used. In this case, the state with the highest magnetic quantum number m_F by using σ^+-light was occupied. Because there was no excited state with a magnetic quantum number $m_F' = m_F + 1$, no further excitation was possible and thus the fluorescence signal disappeared. However, systematic investigations are mandatory to prove the preservation of polarization carried in the electron shell during the round-trip.

Due to the vanishing nuclear spin there is no hyperfine splitting in $^{24}Mg^+$. This introduces $^{24}Mg^+$ as an ideal two-level candidate for these investigations. The $3\,^2S_{1/2} \leftrightarrow 3\,^2P_{1/2}$ transition at 280.35 nm could be used to populate the $m_s=+1/2$ sub-state, which is a dark state for further excitation with σ^+ light and thus realizing a polarization of the electron shell. The setup for such an experiment is ongoing.

To create $^{24}Mg^+$-ions, the local Nielsen-type ion source of CRYRING will be used. This local ion source was modified to accommodate an oven from which solids can be vaporized and fed into the plasma for ionization. From first tests we have observed $^{24}Mg^+$-ions with energies of 40keV and currents of about 10 µA before the injection into CRYRING. In the upcoming beam time at this storage ring it is planned to store and accelerate the Mg-ions up to 173 keV/u. Acceleration is mandatory to yield sufficient lifetimes of $^{24}Mg^+$-ions for the laser spectroscopy experiment.

One further experimental requirement is the efficient detection of the fluorescence light emitted by the excited ions. Fluorescence photons will be collected by using a combination of a mirror system mounted in vacuum together with sensitive photomultipliers (PMTs) [2]. The signal from the PMTs will be processed using photon tagging, a technique successfully used in previous laser experiments at ESR and TRIGA-LASER [3].

To ensure the common propagation direction of the laser beam and the ion beam, a scraper system has been installed in section YR07 (fig. 1). It will be used to check the ion beam's position in the horizontal and vertical direction and to superpose the ion and laser beams.



Figure 1: Scraper installation at section YR07.

Piezo-driven mirror-mounts positioned on turrets close to the coupling windows will be used to stabilize the laser beam in position. In addition, it can be used to adapt the position of the laser beam to the ion beam.

The laser laboratory has been completed and equipped with the required infrastructure including optical tables and laminar flow boxes. The laser transport from the lab to the coupling towers in section YR07 has been designed. The CRYRING cave is connected by a borehole to the laser lab. Breadboards for installation of optics like mirrors and some parts of the stabilization system have been mounted in the cave.

We will use a bunched beam to improve the signal-to-noise ratio. For data acquisition, TILDA [3] will be used. It is a time-resolved DAQ, which has been developed at the TRIGA-LASER setup [4] for laser spectroscopy on bunched and continuous beams. [3]. First tests of TILDA at the CRYRING facility will happen in 2018, to investigate and optimize scattered light background.

References

[1] M. Lestinsky et al., European Physical Journal: Special Topics 225, 797 (2016).
[2] see A. Buß *et al.*, this Annual Report.
[3] see S. Kaufmann *et al.*, this Annual Report
[4] C. Gorges, S. Kaufmann et al., Hyperfine Interactions 238, 1 (2017);

Experiment beamline: CRYRING
Experiment collaboration: APPA-SPARC
Experiment proposal: none
Accelerator infrastructure: CRYRING
PSP codes: 1.3.1.5.8.1.1
Grants: BMBF contract 05P15RDFAA, HIC4FAIR
Strategic university co-operation with: Darmstadt

 DOI:10.15120/GR-2018-1

Detectors and drives for UHV particle detection in CRYRING

A. Kalinin[1, 2], J. Glorius[1], C. Brandau[1,3], C. Langer[4], M. Lestinsky[1], Yu. A. Litvinov[1], S. Schippers[3], R. Reifarth[4], L. Varga[1], Y. Xing[1] and T. Stöhlker[1,2]

[1]GSI, Darmstadt, Germany; [2] HI Jena, Germany; [3] Justus-Liebig-Universität Gießen, Germany;
[4] Goethe Universität Frankfurt am Main, Germany;

Versatile detector drives for CRYRING

The design of new detector drives for the CRYRING@ESR facility based on the most recent detector drive installations in the ESR [1] has been finalized. The main concept behind the design is to have an ultra-high vacuum compatible detector chamber, which is separated from the ring vacuum by a gate valve. Thus, installation and bake-out of detectors is possible without disturbing the ring vacuum. A large variety of detection systems can be installed, as long as it can be adapted to the CF100 flange at the far end of the welded bellow. The system allows flexible positioning of the detectors with two types of drives: a stepping motor, used for slow and precise positioning and a pneumatic actuator that can be used for fast and automated movement.

The drives come in two different lengths as shown in Fig.1. The long version provides a stepping motor travel of 70 cm, which is needed to cover the full acceptance inside the dipole chambers. A shorter version with a travel of 35 cm is sufficient for direct connection to the beam pipe.

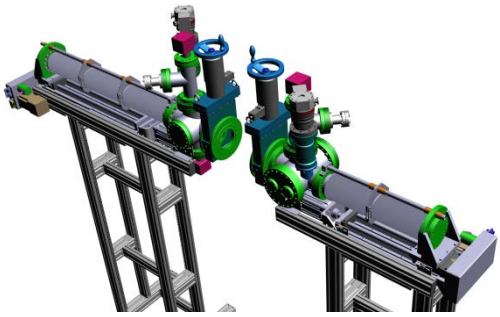


Figure 1: CAD drawing of the long version (left side) and the short version (right side) of the new detector drives.

A new dipole chamber for section YR09/10

In order to register ions from ionization and electron capture (or equivalent) processes for low charge states at the internal target of CRYRING, a large acceptance directly behind the next dipole is needed. The dipole chamber installed behind the electron cooler served as a basis for a new design of a similar chamber. The new chamber has been already built (Fig. 2) and vacuum tested at GSI.



Figure 2: The new dipole chamber at first inspection in the UHV lab of GSI before the vacuum tests.

A fast particle detector for UHV environment

To fulfil the experimental demands of the CRYRING and to meet the technical design requirements of the detector drives, a suitable detector system has been designed, manufactured and tested. The detection scheme is based on surface secondary-electron emission with subsequent multiplication in an channel electron multiplier (CEM) [2]. The detector head is mounted on a > 1m long supporting holder arm with appropriate electrical connections.

Implementation of an extended dynamic range channel electron multiplier, in the current design, improves the performance of the detector for count rates up to 15 MHz, as it was verified with up to 2 MeV singly charged argon ions from the Van-de-Graaff accelerator at IKF, Frankfurt.

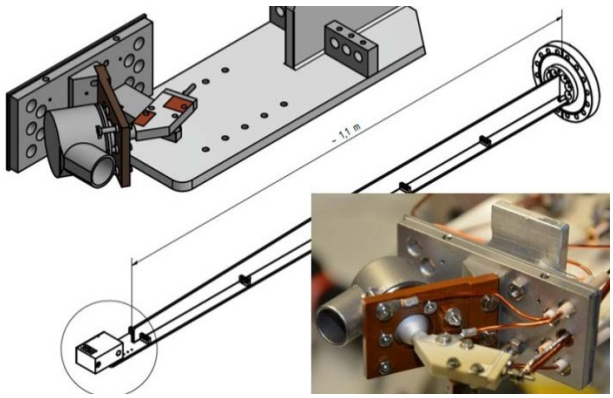


Figure 3: CAD drawings of the detector construction (top left), detector's holder arm (middle) and photo of the detector assembly without protection housing (bottom right).

References

[1] Brandau et al., GSI scientific report 2013, p. 160.
[2] Rinn et al., Rev. Sci. Instr. 53 (1982) p. 829.

Experiment beamline: CRYRING
Experiment collaboration: APPA-SPARC
Experiment proposal: none
Accelerator infrastructure: CRYRING
PSP codes: 1.3.1.5.7.1
Grants:
- BMBF 05P15RFFAA
- EU H2020 contract No. 682841 "ASTRUm"
Strategic university co-operation with:
- Goethe Universität Frankfurt am Main;
- Justus-Liebig-Universität Gießen;

Measurements of linear polarization of radiative electron capture*

M. Vockert[1,2], G. Weber[2,3], U. Spillmann[3], T. Krings[4] and Th. Stöhlker[1,2,3]
for the SPARC Collaboration

[1]Friedrich Schiller University, Jena, Germany; [2]HI Jena, Germany; [3]GSI, Darmstadt, Germany; [4]FZ Jülich, Germany

In recent years, substantial efforts of the SPARC collaboration went into the development of Compton polarimeters to address the linear polarization properties of hard x-rays emitted by relativistic highly-charged ions interacting with matter. By applying this technique, subtle effects could already be revealed such as the E1/M2 multipole mixing for the linear polarization of the Lyman transitions in H-like uranium [1] or the polarization transfer of bremsstrahlung arising from spin-polarized electrons [2]. Moreover, recently the polarization transfer in Rayleigh scattering was studied using the aforementioned polarimeter systems [3]. To further improve and to widen the range for future applications, a new 2D position-sensitive demonstrator system has been developed based on a ≈9 mm thick Li-drifted silicon detector (for details see Ref. [4]). The unique feature of this new demonstrator is cooled preamplifiers, enabling a strong noise reduction and consequently a substantial improvement of the energy resolution.

The superior performance of the new polarimeter system was demonstrated in a test experiment at the internal gas target of the ESR storage ring. For the measurement, bare xenon ions at an energy of 31 MeV/u have been used, colliding with a molecular hydrogen target [5]. The x-ray emission associated with electron capture into the projectile ions has been observed at 90° with respect to the beam axis in coincidence with a particle detector located behind the next dipole magnet. The resulting well-resolved x-ray spectrum is displayed in figure 1, showing radiative electron capture (REC) as well as characteristic transitions of the projectile.

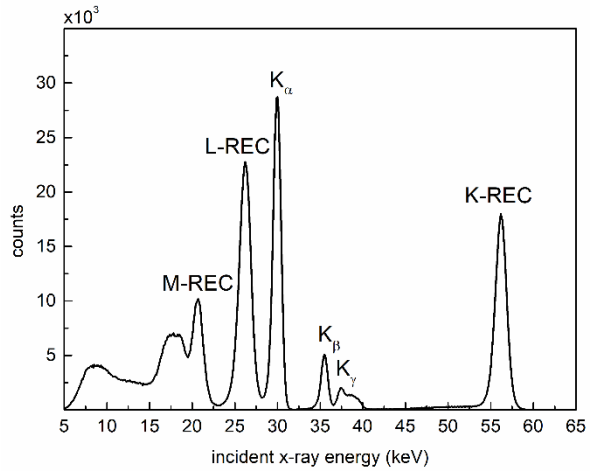


Figure 1: Spectrum obtained at the internal gas target of the ESR storage ring at 90° observation angle using a beam of bare xenon ions at a kinetic energy of 31 MeV/u and a hydrogen target.

Due to the improved detector performance, Compton polarimetry could be applied to the K-REC radiation with an energy of about 56 keV. Note that when using the previous Compton polarimeters with preamplifiers at room temperature, this technique could only be applied at energies above 80 keV.

The preliminary analysis indicates an almost complete linear polarization (close to 100%, see Fig. 2). This finding is in agreement with rigorous relativistic calculations which for the specific collision system and observation angle yield similar results as the non-relativistic dipole approximation [6]. This observation indicates that for medium-Z ions and at such low collision energies, relativistic effects are quite small. Note, in comparison with the data previously obtained at higher energies [7,8], the obtained accuracy of the improved polarimeter is significantly higher, leading to an uncertainty in the degree of linear polarization of only about 1.5%. In addition, we would like to note that by utilizing the characteristics of the REC radiation, we realize an energy-tunable, monochromatic source of almost fully polarized x-rays for a broad energy range.

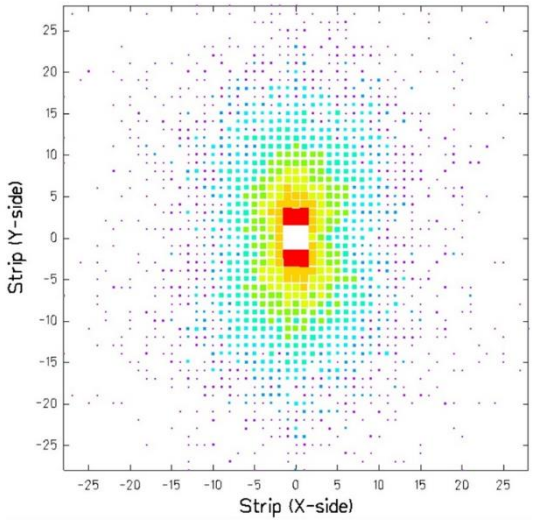


Figure 2: Position distribution of the scattered Compton photons with respect to the point where the scattering took place for the K-REC peak restricted to polar scattering angles of $\vartheta = (90 \pm 15)°$.

[1] G. Weber et al., Phys. Rev. Lett. 105, 2010, 243002
[2] R. Märtin et al., Phys. Rev. Lett 108, 2012, 264801
[3] K.-H. Blumenhagen et al., New J. Phys. 18, 2016, 103034
[4] M. Vockert et al., Nucl. Instr. Meth. B 408, 2017, 313
[5] J. Glorius et al., J. Phys. Conf. Ser. 875, 2017, 092015
[6] J. Eichler and Th. Stöhlker, Phys. Reports 439, 2007, 1-99
[7] S. Tashenov et al., Phys. Rev. Lett. 97, 2006, 223202
[8] S. Hess et al., J. Phys. Conf. Ser. 194, 2009, 012205

* Work supported by BMBF Verbundprojekt 05P15SJFAA. This report is also part of the HI Jena Scientific Report 2017.

 DOI:10.15120/GR-2018-1

Ground-state ionization energies of boronlike ions

A. V. Malyshev[1,2], D. A. Glazov[1,3], A. V. Volotka[1,4], I. I. Tupitsyn[1,5], V. M. Shabaev[1], G. Plunien[6], and Th. Stöhlker[4,7,8]

[1]St. Petersburg State University, St. Petersburg, Russia; [2]ITMO University, St. Petersburg, Russia; [3]SSC RF ITEP of NRC „Kurchatov Institute“, Moscow, Russia; [4]Helmholtz-Institut Jena, Jena, Germany; [5]Peter the Great St. Petersburg Polytechnic University, St. Petersburg, Russia; [6]Technische Universität Dresden, Dresden, Germany; [7]GSI, Darmstadt, Germany; [8]Friedrich-Schiller-Universität, Jena, Germany

State-of-the-art quantum electrodynamics (QED) calculations of the energy levels in highly charged ions include all relevant contributions up to the second order in α, see, e.g., Refs. [1,2] for theory concerning H- and He-like heavy ions. High-precision measurements of the binding and transition energies which are sensitive to the second-order corrections [3-6] con rm predictions made by QED theory to a high level of accuracy and allow one to test bound-state QED in the strong- eld regime. Nevertheless, the precision currently reached in the strong eld domain of high-Z ions is still much less as compared to the one for light atoms and thus a further extension and improvement of *ab initio* QED calculations are of great importance.

The present investigation [7] is focused on ve-electron (boronlike) ions. Namely, we perform high-precision QED calculations of the ground-state ionization energies for all boronlike ions with the nuclear charge numbers in the range $16 \le Z \le 96$. The developed rigorous QED approach includes all many-electron QED e ects up to the second order of the perturbation theory. The contributions of the third- and higher-order electron-correlation e ects are accounted for within the Breit approximation by means of the con guration-interaction Dirac-Fock-Sturm method [8] and alternatively employing the recursive formulation of the perturbation theory [9]. The nuclear recoil and nuclear polarization e ects are taken into account as well. All the calculations are carried out in the framework of the extended Furry picture starting with several di erent types of the screening potential. The deviations of the nal results obtained with the use of di erent zeroth-order approximations are employed in order to estimate the uncalculated higher-order QED contributions.

The results obtained are presented in Table 1 for selected boronlike ions. Our theoretical predictions for the ionization energies are compared with the results obtained by other groups [10-13]. One can see, that our results are in good agreement with the results of the previous relativistic calculations. However, the accuracy of the theoretical predictions is improved signi cantly.

Finally, we note, that taking into account the results of [14] one can easily obtain the ionization energies for the rst excited state of boronlike ions; for this one needs to add the transition energies presented in [14] to the ground-state ionization energies evaluated in this work.

Nucleus	This work [7]	Other works	Ref.
^{40}Ca	-973.7863(53)	-973.70(33)	[10]
		-973.83	[11]
		-973.84(29)	[12]
^{56}Fe	-1798.7978(63)	-1798.43(78)	[10]
		-1798.8	[11]
^{132}Xe	-9238.499(20)	-9238.2	[11]
		-9243(4)	[13]

Table 1: Ionization energies (in eV) for boronlike ions.

References

[1] V. A. Yerokhin and V. M. Shabaev, J. Phys. Chem. Ref. Data 44 (2015) 033103.
[2] A. N. Artemyev *et al.*, and G. Soff, Phys. Rev. A 71 (2005) 062104.
[3] A. Gumberidze *et al.*, Phys. Rev. Lett. 92 (2004) 203004.
[4] C. Brandau *et al.*, Phys. Rev. Lett. 91 (2003) 073202.
[5] P. Beiersdorfer *et al.*, Phys. Rev. Lett. 95 (2005) 233003.
[6] K. Kubiček *et al.*, Phys. Rev. A 90 (2014) 032508.
[7] A. V. Malyshev *et al.*, Phys. Rev. A 96 (2017) 022512.
[8] I. I. Tupitsyn *et al.*, Phys. Rev. A 68 (2003) 022511.
[9] D. A. Glazov, Nucl. Instr. Meth. Phys. Res. B 408 (2017) 46.
[10] E. Biémont *et al.*, At. Data Nucl. Data Tables 71 (1999) 117.
[11] M. F. Gu, At. Data Nucl. Data Tables 89 (2005) 267.
[12] N. N. Dutta and S. Majumder, Phys. Rev. A 85 (2012) 032512.
[13] G. C. Rodrigues *et al.*, At. Data Nucl. Data Tables 86 (2004) 117.
[14] A. N. Artemyev *et al.*, Phys. Rev. A 88 (2013) 032518.

Experiment collaboration: APPA-SPARC

Grants: SPSU-DFG (No. 11.65.41.2017 and No. STO 346/5-1)

Strategic university co-operation with: St. Petersburg State University

The spectral shape of the atomic two-photon transition in He-like ions

S. Trotsenko[1], A. Volotka[2,3], A. Surzhykov[4,5], A. Kumar[6], D. Banas[7], A. Gumberidze[8], H.F. Beyer[8], H. Bräuning[8], S. Fritzsche[1,2], S. Hagmann[8,9], S. Hess[8], P. Jagodzinski[7], C. Kozhuharov[8], R. Hess[8], S. Salem[8], A. Simon[10], U. Spillmann[8], M. Trassinelli[11], L.C. Tribedi[12], G. Weber[2,8], D. Winters[8], and Th. Stöhlker[1,2,8]

[1]Friedrich-Schiller-Universität, Jena, Germany; [2]Helmholtz Institute Jena, Jena, Germany; [3]Department of Physics, St. Petersburg State University, St. Petersburg 198504, Russia; [4]Physikalisch-Technische Bundesanstalt Braunschweig Germany; [5]Technische Universität Braunschweig Braunschweig Germany; [6]NPD, Bhabha Atomic Research Centre, Mumbai, India; [7]IP, Jan Kochanowski University, Kielce, Poland; [8]Helmholtzzentrum GSI, Darmstadt, Germany; [9]IKF, University of Frankfurt, Frankfurt, Germany; [10]Department of Physics, University of Notre Dame, Notre Dame, IN 46556, USA; [11]Institut des NanoSciences de Paris, CNRS, Sorbonne Universités, UPMC Univ Paris 06, F-75005 Paris, France; [12]Tata Institute of Fundamental Research, Homi Bhabha Road, Coloba, Mumbai 400005, India

Two-photon decay has been an interesting topic since its prediction in 1930's by M. Göppert-Mayer [1]. In this process, two correlated photons are emitted simultaneously under the boundary condition that the sum of their energies equals to the total transition energy, i.e.

$$\hbar\omega_1 + \hbar\omega_2 = E_I - E_F = E_0 \qquad (1)$$

Here, $\hbar\omega_1$ and $\hbar\omega_2$ are the energies of the photons, E_0 is the total transition energy, and E_I and E_F are the energies of initial and final atomic states, respectively. The energies of individual photons form a continuum spectrum which, for the case of decay from $2s$ state, has a maximum intensity at half of the transition energy and gradually falls to zero at both endpoints. This continuum shape is determined by the summation over all intermediate bound- and continuum-states for calculating the transition probabilities which requires knowledge of their energies and wave functions. Hence, the spectral distribution of the two-photon emission is sensitive to the entire atomic structure.

Measurements of the two-photon spectral shape in He-like ions have been significantly improved by the method involving a selective ionisation of a K-shell electron from the initially Li-like ion [2]. Using this method a very clean spectral distribution of the 2E1 decay of $2\,^1S_0$ in He-like tin has been measured. From the measured distribution, a reduced full width at half maximum (FWHM) was obtained. For this, the experimental distribution was fitted with a polynomial distribution. The reduced FWHM was calculated as the width of the distribution divided by the maximum possible photon energy (the energy difference between the $1s2s\ ^1S_0$ and $1s^2\ ^1S_0$ states).

Our preliminary result for the reduced FWHM is compared with theoretical values in figure 1. The comparison shows a clear deviation from the non-relativistic prediction and a very good agreement with our relativistic calculations based on the method developed in [3]. This unambiguously confirms the importance of the relativistic effects for the 2E1 two-photon decay energy distribution. Here, we would like to add that the relativistic values for FWHM obtained by Derevianko and Johnson [4] were found to be in good agreement with the results of our relativistic calculations [2]. The current experimental value for He-like tin can be considered to favor the fully relativistic treatment against the frozen Dirac-Fock result, thus emphasising the importance of accurate treatment of the electron-electron interaction in the mid-Z regime.

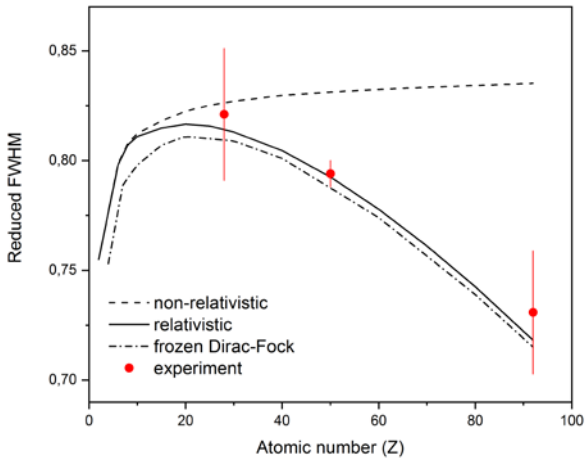


Figure 1: Preliminary results: Comparison of the measured reduced FWHM of the 2E1 two-photon spectral shape for He-like tin with the nonrelativistic calculations (dashed line), the frozen Dirac-Fock method (dashed-dotted line) and the relativistic calculations (solid line). In addition, the experimental values for He-like nickel [5] and uranium [6] are shown.

References

[1] M. Göppert-Mayer, Naturwissenschaften 17, 932 (1929)
[2] S. Trotsenko et al., Phys. Rev. Lett. 104, 033001 (2010).
[3] A. V. Volotka, A. Surzhykov, V.M. Shabaev, and G. Plunien, Phys. Rev. A 83, 062508 (2011).
[4] A. Derevianko, W. R. Johnson, Phys. Rev. A 56, 1288 (1997).
[5] H. W. Schäffer et al., Phys. Scr. T80, 469 (1999).
[6] D. Banas et al, Phys. Rev. A 87, 062510 (2013).

Experiment beamline: ESR
Experiment collaboration: APPA-SPARC
Accelerator infrastructure: ESR
Strategic university co-operation with: FSU Jena

*Also part of the HI-Jena scientific report 2017

 DOI:10.15120/GR-2018-1

First tests of x-ray crystal optics at the S-EBIT facilities

S.Wipf,[1,2], S.Trotsenko[1], Robert Lötzsch[1], R. Schuch[3], Th. Stöhlker[1,2]

[1]Friedrich-Schiller-Universität Jena, Germany; [2]HI Jena, Germany; [3]University of Stockholm

Studies at Electron Beam Ion Traps (EBIT) have gained large interest in particular in the domain of atomic physics and astrophysics. Here, majority of experiments are based on x-ray spectroscopy of the trapped ions. Thereby one can acquire detailed knowledge about transitions in partially ionized atomic systems and also gain information on the physical processes in EBITs to make statements particularly concerning the ion charge-state distributions. In such x-ray spectroscopic studies, the energy resolution plays certainly a very important role.

The S-EBIT facility of the Helmholtz Institute Jena, apart from other activities, provides a tool for further steps in the improvement of x-ray spectroscopy in terms of resolving power and collection efficiency. Our previous x-ray diagnostics at the S-EBIT was so far based on a silicon (or germanium) pin-diode detectors with a resolution of a few 100 eV in the energy region of interest [1].

Magnetic metallic microcalorimeters possess new very promising x-ray detection technology that combines the excellent spectral resolution being typical for crystal spectrometers with the high stopping power of solid-state detectors. With this detector technology, the resolution for photon energies in keV range can be as good as a few eV [2]. But, such microcalorimeters usually provide only a small active area and, consequently, can cover only a small solid angle, in particular if the high magnetic field of the EBIT limits the geometry. Here, the application of focussing x-ray crystal optics becomes handy and the effective surface of the detector can be increased by at least an order of magnitude (Fig. 1). The incident and the outgoing x-rays should fulfil the Bragg condition for the x-ray energies that are subject to enhanced detection efficiency. For the details of this technology we refer to [3].

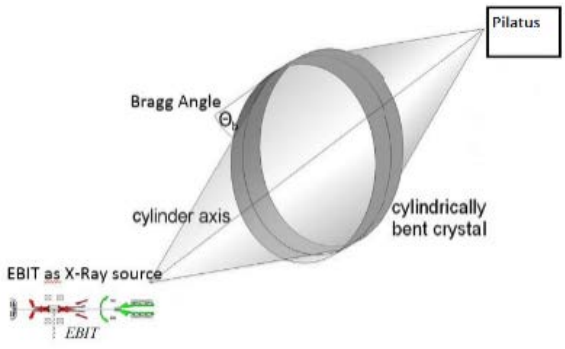
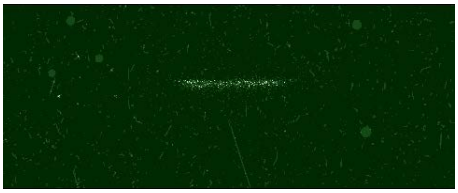


Figure 1: A sketch of the set up and crystal optics mounted in front of the EBIT together with a position sensitive Pilatus detector.

Here we present a first proof of principle measurement with the aforementioned method. The K_α-line of iron ions was observed at around 6.75 keV. The crystal optics we used is made of Highly Annealed Pyrolitic Graphite (HAPG) and modified for reflection in the energy range from 7 keV to 12.5 keV. We used a spatial resolving silicon pixel detector PILATUS behind the toroidal shaped x-ray optics and obtained an image of the ion cloud inside the trap. A motorized steering with dedicated LabView software was used to align the x-ray optics to match the focussing conditions, given by the energy-dependent Bragg angle and the distance between source, optics and the detector. The threshold of the Pilatus detector was set to 1.5 keV and frames with 100 s exposure time were taken. Figure 2 (top) shows an image of the ion trap in the x-ray wavelength- range with the presented set up and a corresponding energy spectrum measured with a Si-pin diode on the opposite view port of the trap (bottom). The EBIT-I operated with 25mA (10keV) electron beam.



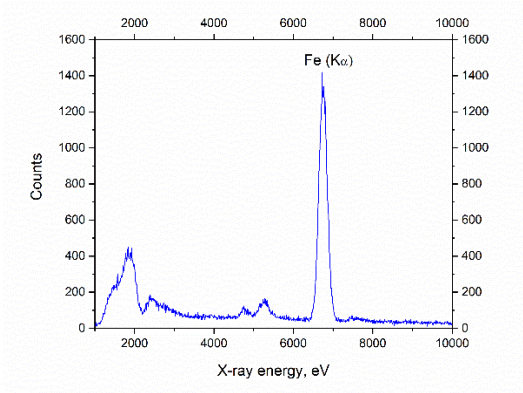


Figure 2: Image of the EBIT x-rays formed by the x-ray optics (top) and a spectrum measured in parallel with the Si-pin diode (bottom).

The further steps are currently in progress and will involve measurements with a position and energy resolving CCD detector. Ultimately, a combination of the magnetic metallic microcalorimeter detectors with the crystal optics at the S-EBIT should reveal the full power of the invented method for x-ray spectroscopy of highly charged ions.

References

[1] S. Trotsenko, HI Jena Scientific Report 2016, p.76
[2] C. Pies et al., 2012, J Low Temp Phys (2012) 167:269–279
[3] R. Lötzsch, HI Jena Scientific Report 2015, p. 49

Experiment collaboration: APPA-SPARC
PSP codes: [none]
Strategic university co-operation with: FSU Jena

*Also a part of the HI-Jena scientific report 2017

Status of the data analysis from proton capture reaction measurement with a UHV compatible DSSSD

L. Varga[1], T. Davinson[2], J. Glorius[1], C. Langer[3], Yu. A. Litvinov[1], R. Reifarth[3], Z.Slavkovska[1], T. Stöhlker[1,2], P. J. Woods[2], Y. Xing[1] and NuCAR Collaboration

[1]GSI, Darmstadt, Germany; [2]University of Edinburgh, UK; [3]Goethe Universität Frankfurt am Main, Germany

In 2016, the very first measurement of the ^{124}Xe(p,γ)^{125}Cs proton capture reaction was performed at Experimental Storage Ring (ESR) at GSI. A beam of stable fully-stripped $^{124}Xe^{54+}$ ions was stored at five different energies, from 10 MeV/u to 5.5 MeV/u. The aim was to measure the absolute cross section [1].

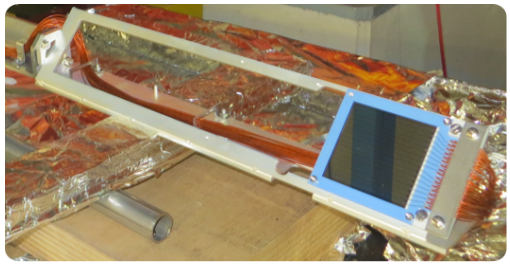


Figure 1: A photo of the UHV compatible DSSSD used in the experiment.

For the measurement at such low energies, the use of Ultra High Vacuum (UHV) proof detectors due to the excellent vacuum conditions of the ESR (10^{-11} mbar) was indispensable. The required UHV compatibility was ensured by the special design of a double sided silicon strip detector (DSSSD) with nearly 100% particle detection efficiency for heavy ions at ESR energies (see Fig. 1).

Due to the x and y segmentation of the DSSSD realized by 16 silicon strips on both, the front and back side of the detector (perpendicularly aligned), spacial resolution of the reaction products can be achieved. The proton capture products can be recognized as a narrow cluster of events on the top of the background signal due to the elastically scattered ions as shown in Figure 2. In order to determine the absolute cross section of the (p,γ) reaction, the number of hits in the proton capture cluster should be identified. However, to achieve high detection efficiency for Highly Charged Ions (HCI) a clear separation between the ion and the noise events is essential. For this, the excellent energy resolution of the silicon detector can be utilized. In Figure 3 the energy spectrum of one strip of the DSSSD is visible. In the energy distribution, three different types of events can be distinguished: close to 0 energies is the noise peak, at the higher-end of the distribution is the ion peak, and between these two peaks are the so-called interstrip (IS) events. In case of IS events, the charge produced by an ion hit is shared between two adjacent Si strips. In order to provide a better separation between the noise and the ion peak, the energy of the IS hits should be reconstructed by summing up the energies of the neighboring strips event by event. After the reconstruction, a narrow acceptance window close to the ion-peak energy can be applied to select the events of interest.

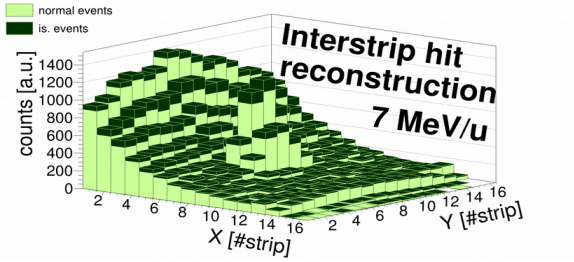


Figure 2: Spacial distribution before and after IS hit reconstruction

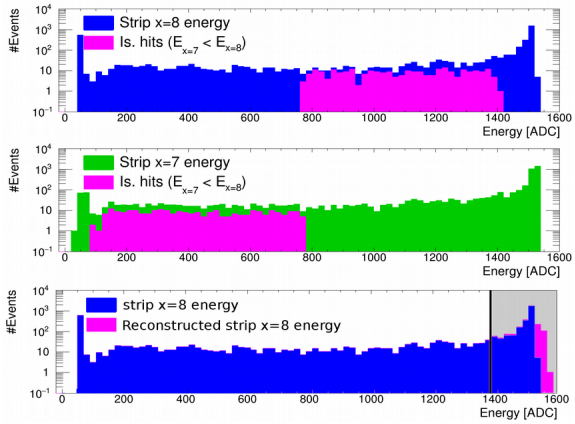


Figure 3: Top and middle panels: energy spectra of two adjacent strips. Bottom figure: energy spectrum of a strip before and after IS hit reconstruction

In Figure 2 the spatial distribution of the DSSSD hits at 7 MeV/u is visible before and after the interstrip hit reconstruction. In case of a narrow acceptance window, the reconstructed interstrip hits have considerable impact on the total number of events. The average ratio between the single-strip events (light green) and the interstrip events (dark green) reaches ~15%.

References

[1] J.Glorius et. al., J. Phys: Conf. Ser 875 (2017)092015.

Experiment beamline: ESR
Experiment collaboration: APPA-SPARC
Experimental proposal: E108
Accelerator infrastructure: ESR

Grant: EU H2020 contract No. 682841 "ASTRUm"

 DOI:10.15120/GR-2018-1

Progress of a variable sensitivity resonant Schottky pick-up cavity

M. S. Sanjari[1], O. Gumenyuk[1], D. Dmytriiev[1,2], Ch. Kozhuharov[1], Yu. A. Litvinov[1,2] and Th. Stöhlker[1,3]

[1]GSI, Darmstadt; [2]Universität Heidelberg; [3]Helmholtz-Institut Jena

Schottky pickups are indispensable at accelerators. They can as well be designed to meet specific needs for performing precision atomic and nuclear physics experiments with stored highly-charged ions (HCI) in storage rings. In this work, we report on the progress of our latest developments at GSI.

The passage of particles through non-destructive electromagnetic detectors in storage rings induces a periodic signal that can be related to the particle's mass through its revolution frequency. Additionally, the recorded signal can deliver information on the lifetime of the unstable nuclei if the data is processed through short time Fourier analysis. Furthermore, these so called Schottky signals deliver information on general properties of the particle beam such as momentum spread [1] and can even be used to observe stability of other elements in the storage ring such as the electron cooler [2] and magnet power supplies.

Electromagnetic detectors designed for the detection of Schottky signals are based on a variety of geometries with their respective advantages and disadvantages for each application [3]. Of particular interest for precise determination of particle frequencies and intensities in storage rings are resonant cavities. Due to their high Q value, they can achieve high sensitivities, albeit at the cost of lower operation bandwidth. The usually large eigenmode frequency also allows for higher frequency and hence higher mass resolution power. One such detector has been developed for the ESR storage ring at GSI facility [4] and its single ion sensitivity has been demonstrated [5].

An R&D prototype of a longitudinally sensitive resonant Schottky cavity has been constructed and delivered to GSI. It is designed for the Collector Ring (CR) and High Energy Storage Ring (HESR) of the future FAIR project as a part of ILIMA and SPARC collaborations. The technical design report (TDR) has been prepared [6].

The new detector will allow for on-line variation of its sensitivity during the operation. This is achieved by means of mode dependent loading and by inserting dispersive material. This feature would extend the scope of application of resonant cavity detectors in future storage ring experiments.

All frequency tuner drives are controlled by standard FAIR components and hence compatible with FAIR control system. It is planned to test the prototype in the ESR. To this end, the cavity is currently undergoing various electromagnetic and vacuum tests. Further studies regarding the Data acquisition will employ Software Defined Radio (SDR).

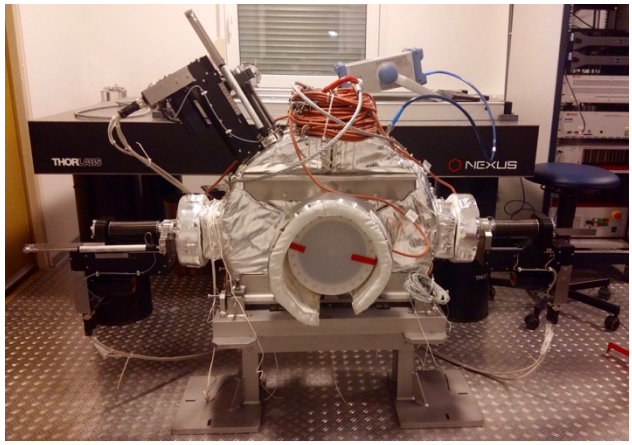


Figure 1: The prototype Schottky detector under test.

Acknowledgements

M. S. S. Would like to thank many colleagues involved in the preparation and construction of this prototype: J. Häuser, (Kress GmbH), H. E. Durand-Paredes, E. Keller, I. Schurig, W. Sturm, O. Zurkan (mechanical integration, K. Dermati, J. Holluba, M. Rosan, M. Romig, S. Teich, T. Schneider, (mechanical construction), D. Acker, M. Bevcic (Infrastructure), M. C. Bellachioma, J. Cavaco Da Silva, Ch. Kolligs, J. Kurdal, E. Renz, G. Savino, M. P. Suherman, L. Urban (vacuum systems) and Z. Fekete, R. Vincelli (IT) and M. Steck (ESR) and the ILIMA and SPARC collaboration members.

References

[1] F. Caspers 2009 CERN-2009-005.407
[2] S. Sanjari et al. GSI Sci. Rep. 2015 p 335
[3] G. R. Lambertson 1989 ISBN 978-3662137116
[4] F. Nolden et al. 2011 NIM A v 659 pp 69-77
[5] F. Bosch et al. 2013 Phys.Lett.B v1726 pp638-645
[6] S. Sanjari et al. 2017 TDR Schottky Detector System

Experiment beamline: ESR
Experiment collaboration: APPA-SPARC / NUSTAR-ILIMA
Experiment proposal: none
Accelerator infrastructure: ESR, CR, HESR
PSP codes: 1.2.6.3 and 1.3.1.3.12
Grants: ERC-2015-CoG (ASTRUm - 682841)
Strategic university co-operation with: Heidelberg

Excitation of helium-like uranium in relativistic collisions

A. Gumberidze[1], D.B. Thorn[2,], A. Surzhykov[3,4], C.J. Fontes[5], H.L. Zhang[5], B. Najjari[6], A. Voitkiv[7] , S. Fritzsche[8,9], D. Banas[10], H.F. Beyer[11], W. Chen[12], R. E. Grisenti[11,13], S. Hagmann[11,13], R. Hess[11,], P.-M. Hillenbrand[14,], P. Indelicato[15,], C. Kozhuharov[11], M. Lestinsky[11,], R. Märtin[8,11,], N. Petridis[11,], R. Popov[16,], R. Schuch[17], U. Spillmann[11], S. Tashenov[18], S. Trotsenko[8,9], A. Warczak[19], G. Weber[8,11], W. Wen[20], D.F.A. Winters[11], N. Winters[11], Z. Yin[21] and Th. Stöhlker[8,9,11]

[1]ExtreMe Matter Institute EMMI and Research Division, GSI Darmstadt, Germany; [2]LLNL, Livermore, California, USA; [3]Physikalisch-Technische Bundesanstalt, Braunschweig, Germany; [4]Technische Universität Braunschweig, Germany; [5]Computational Physics Division, LANL, Los Alamos, USA; [6]Institut Pluridisciplinaire Hubert-Curien, Strasbourg, France; [7]Heinrich-Heine-University of Düsseldorf, Germany; [8]Helmholtz-Institut Jena, Germany; [9]Friedrich-Schiller-Universität Jena, Germany; [10]Jan Kochanowski University, Kielce, Poland; [11]GSI Darmstadt, Germany; [12]Chinese Academy of Sciences, Institute of High Energy Physics, Dongguan, China; [13]Goethe-Universität, Frankfurt am Main, Germany; [14]Columbia University, New York City, USA; [15]Laboratoire Kastler Brossel, UPMC, CNRS, ENS-PSL Research University, College de France, Paris, France; [16]St. Petersburg State University, Russia; [17]Stockholm University, Sweden; [18]Ruprecht-Karls-Universität Heidelberg, Germany; [19]Jagiellonian University, Krakow, Poland; [20]Institute of Modern Physics, Chinese Academy of Sciences, Lanzhou, China; [21] DESY, Hamburg, Germany

In this contribution, we present an experimental and theoretical study of the K-shell excitation in helium-like uranium in relativistic collisions with different gaseous targets. The experiment was conducted at the experimental storage ring ESR. Around 10^8 U^{90+} ions produced by successive acceleration and stripping were stored and cooled in the ESR. For the measurement, the internal supersonic jet target was used crossing the beam in a perpendicular direction. The used target areal densities were between 10^{13} and 10^{14} particles/cm^2 and the interaction zone was defined by an overlap of the cooled ion beam (diameter ~2 mm) with the jet target (diameter ~6 mm). The projectile excitation process was explored by looking at characteristic X-rays emitted during the decay of the excited L-shell levels. For this purpose, we used the atomic physics experimental chamber at the internal target of the ESR. More details concerning the experimental setup and data analysis can be found in [1,2]

The experiment was performed with H_2 and Ar targets and two different beam energies of 218 MeV/u and 300 MeV/u. By performing measurements with different targets as well as with different collision energies, we were able to gain access to both; proton (nucleus) impact excitation (PIE) and electron impact excitation (EIE) processes in the relativistic collisions [1,2]. These beam energies have been chosen to be near and well above the EIE threshold. The cross sections for the two processes scale as Z^2_T and Z_T , respectively (Z_T being the target atomic number). Therefore, the relative contribution of the EIE is largest for hydrogen target.

In table 1, we present a comparison of our experimental results for intensity ratios of the characteristic Kα lines with state-of-the-art theoretical predictions based on the methods outlined in [3,4]. From the comparison it can be stated that the experimental results can be reproduced well by the fully relativistic calculations taking into account both PIE and EIE processes. Only PIE calculations significantly deviate from the experimental results even for the Argon target. It should be noted that the comparison is still preliminary because the possible influence of cascade contributions due to the excitation to higher levels as well as the possible role of the Compton profile of the bound target electrons have still to be assessed.

	218 MeV/u		**300 MeV/u**	
	H_2	Ar	H_2	Ar
Experiment	0.92 ± 0.02	1.33 ± 0.03	1.03 ± 0.03	1.39 ± 0.02
PIE+EIE	0.89	1.38	1.08	1.41
PIE	1.47	1.47	1.46	1.46

Table 1. Experimental results in comparison with theoretical predictions for $K\alpha_1/K\alpha_2$ intensity ratios for the K-shell excitation of U^{90+} in collision with H_2 and Ar targets at 218 MeV/u and 300 MeV/u.

References

[1] A. Gumberidze at al., Phys. Rev. Lett. 112, 213201 (2013).

[2] A. Gumberidze et al., J. Phys. B: At. Mol. Opt. Phys. 48, 144006 (2015)

[3] A. Surzhykov at al., Phys. Rev. A 77, 042722 (2008).

[4] C. J. Fontes, D. H. Sampson, and H. L. Zhang, Phys. Rev. A 47, 1009 (1993).

Experiment beamline: ESR
Experiment collaboration: APPA-SPARC
Experiment proposal: E101
Accelerator infrastructure: ESR
PSP codes: [none]
Grants: [This work was supported by the Helmholtz Alliance Program of the Helmholtz Association, Contract No. HA216/EMMI ‘‘Extremes of Density and Temperature: Cosmic Matter in the Laboratory.’’]
Strategic university co-operation with: Frankfurt-M / Jena]

 DOI:10.15120/GR-2018-1

Mode-dependent loading of resonant pick-up cavities

D. Dmytriiev[1,2], M. S. Sanjari[1], Yu. A. Litvinov[1,2], Th. Stöhlker[1,3]

[1]GSI, Darmstadt; [2] Universität Heidelberg; [3]Helmholtz Institut Jena

Non-destructive Schottky spectroscopy is a widely used technique in experiments at storage rings. While passing through the cavity, beam induces mirror charges on the inner surface of the cavity and one can use oscillations of the excited electromagnetic field inside the cavity as a signal source. Due to losses in materials, oscillations of the electromagnetic field inside the cavity will be damped. Therefore, one can imagine the resonant cavity as a parallel RLC circuit (Figure 1) where M_1 is the coupling between the beam and the electromagnetic field inside the cavity, R – real part of the cavity impedance, L – inductivity of the cavity, C – electrical capacitance of the cavity. M_2 and M_3 are the couplings related to the coupler of the external read-out circuit and additional loading.

The main subject of this work is to investigate the influence of external loading on the loaded quality factor of the cavity. The reason is that the cavity should have a negligible influence on the ion beam while other experiments are running in the storage ring but also work as a detector when it is needed. To change intensity of interaction between the cavity and the beam, one can use mode-dependent loading.

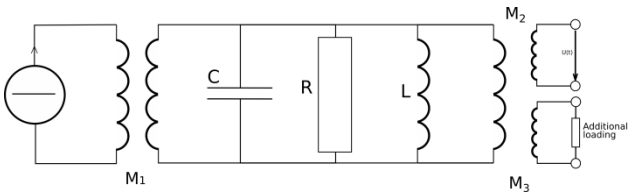


Figure 1: Equivalent circuit of the resonant cavity.

Cavities have large quality factors, usually several thousands and this means that oscillations of the electromagnetic field fade very slowly. The electromagnetic field induced in the cavity can influence the beam. To decrease the effect of the cavity on the beam its quality factor should be decreased.

Electromagnetic field excited by the beam has an infinite amount of modes with different geometries in the volume of the cavity. The larger the flux into the coupling loop, the larger is its interaction with the magnetic field. Position and size of the coupler which is connected to the external circuit will define which modes of the magnetic field will interact with a coupler. Choosing the position of the coupler will increase influence of the external circuit on the overall loaded quality factor.

Loaded quality factor depends on external quality factor and quality factor Q_0 (see Eq. 1) which is defined only by materials and geometry of the cavity. On the other hand, Q_l is a quality factor of the system when connected to generator and measurement circuits [1]. The relation between them is as follows

$$\frac{1}{Q_l} = \frac{1}{Q_{ext}} + \frac{1}{Q_0} \qquad (1)$$

where Q_{ext} is a quality factor of the external loading circuit. Loaded quality factor can be calculated using frequencies, where the imaginary of the one port scattering parameter is at its maximum and minimum, while phase of the central frequency is normalized [1] (see Eq. 2). This information can be obtained using a vector network analyser.

$$Q_l = \frac{f_{resonant}}{|f(Im(S_{11})_{\max}) - f(Im(S_{11})_{\min})|} \qquad (2)$$

where S_{11} is the reflection S-parameter. In order to check dependency of the loaded quality factor on the external resistivity, several important values of loading were measured.

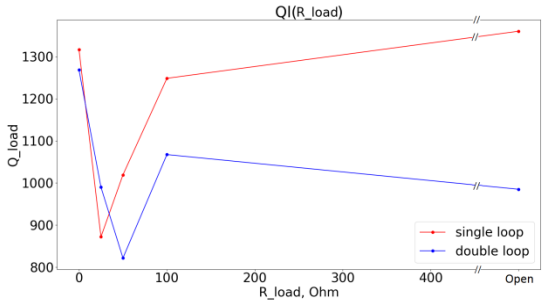


Figure 2: Dependency of the loaded quality factor of the cavity on external resistance for magnetic couplers with single and double loop.

For these measurements different resistances were connected to the single and double loop magnetic couplers. Measurements on a prototype show that mode-dependent loading can decrease loaded quality factor by 30% (Figure 2). Efficiency of this method is limited by the position, orientation and size of the coupler.

It is planned to apply this method in a prototype resonant Schottky cavity [2] in ESR.

References

[1] F. Caspers, “RF engineering basic concepts the Smith chart”, CERN, Geneva, Switzerland, 2010.

[2] S. Sanjari et. al. Current scientific report.

Experiment beamline: ESR
Experiment collaboration: APPA-SPARC / NUSTAR-ILIMA
Accelerator infrastructure: ESR, CR, HESR
PSP codes: 1.2.6.3 and 1.3.1.3.12
Grants: ERC-2015-CoG (ASTRUm - 682841)
Strategic university co-operation with: Heidelberg

Excitation cross sections of hydrogenlike uranium in collisions with hydrogen and nitrogen targets

G. Weber[1], A. Gumberidze[2], A. Surzhykov[3,4], C. J. Fontes[5], and Th. Stöhlker[1,2,6]

[1]Helmholtz Institute Jena, Germany; [2]GSI, Germany; [3]PTB, Germany; [4]TU Braunschweig, Germany; [5]Los Alamos National Laboratory, USA; [6]FSU Jena, Germany;

Electron impact excitation (EIE) and proton impact excitation (PIE) of bound electrons belong to the most fundamental atomic physics interaction processes. Compared to ionization, excitation is mediated by the same interaction mechanism, but the bound electron is excited into a bound state of the ion and not into the continuum. Therefore, the final state of the electron after the collision can be determined by measurements of the deexcitation photons, which allows for a rigorous testing of corresponding theories. While in particular EIE excitation of few electron ions, such as hydrogenlike argon, titanium and iron, has been thoroughly studied in electron beam ions traps [1], for probing of relativistic effects, i. e. the generalized Breit interaction (GBI) [2,3], high-Z ions that are available at GSI provide the best conditions.

Indeed, a recent study of the Lyman radiation emitted by hydrogenlike uranium in collisions with hydrogen and nitrogen gas targets allowed the first identification of the GBI contribution in EIE of a high-Z system [4,5]. The measurement was performed at the internal gas target of the experimental storage ring of GSI, Darmstadt where an array of standard Ge(i) detectors were recording the x-ray emission from the interaction zone of the ion beam and the gas jet target. After capturing a target electron the down-charged projectiles were recorded by a MWPC detector located downstream after the next dipole magnet. Applying a coincidence condition between x-rays and down-charged ions allows identifying those spectral features that are associated with the capture of target electrons into bound projectile states. This is illustrated in Fig. 1 where the photon spectrum coincident with electron capture is contrasted to the one which is not associated to a change of the projectile charge and that contains Lyman emission subsequent to the excitation of the projectile in collisions with target atoms. The previous study of projectile excitation [4,5] concentrated on the intensity ratio of the Ly-a_1 line ($2p_{3/2}$ to $1s_{1/2}$) to the Ly-a_2 ($2s_{1/2}$, $2p_{1/2}$ to $1s_{1/2}$) line that reflects a significant enhancement of the EIE cross section due to the GBI which populates preferentially the j=1/2 orbitals.

In a follow-up study we now aim to determine not only relative excitation cross sections (ground state to the L shell) but absolute ones by normalizing the observed Lyman radiation intensity to the intensity of the radiation emitted in the capture of target electrons into the K and L shell of projectile (K- and L-REC). Since in light targets the electrons are only loosely bound, they can be treated as quasi-free, making REC similar to the radiative recombination (RR), which is the time-inverse of the well-understood photoelectric effect.

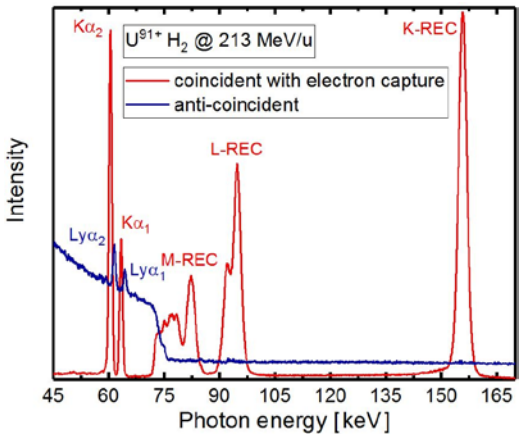


Figure 1: X-ray spectrum recorded by a Ge(i) detector located at 120° with respect to the ion beam axis.

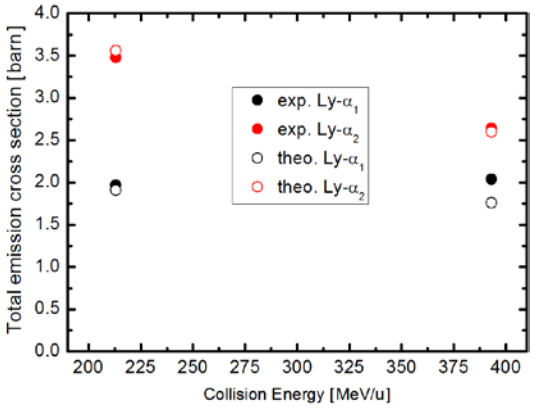


Figure 2: Preliminary results for K-L excitation cross sections for U^{91+} in collision with hydrogen atoms.

Preliminary results of this analysis are shown in Fig. 2 for the collision of hydrogenlike uranium with hydrogen atoms. Theoretical predictions combine both PIE as well as EIE, the latter including the GBI. Note that the population of n=2 states by cascades from higher lying states is not included yet in the theoretical values.

[1] D. L. Robbins et al., Phys. Rev. A 74, 022713 (2006).
[2] C. J. Bostock et al., Phys. Rev. A 80, 052708 (2009).
[3] C. J. Fontes et al., Phys. Rev. A 49, 3704 (1994).
[4] A. Gumberidze et al., Phys. Rev. Lett. 110, 213201 (2013).
[5] A. Gumberidze et al., J. Phys. B 48, 144006 (2015).

Experiment collaboration: APPA-SPARC
Accelerator infrastructure: ESR

 DOI:10.15120/GR-2018-1

A status report on 2D Compton polarimeter development

U. Spillmann[1], T. Krings[2], M. Vockert[3,4], G. Weber[3], and Th. Stöhlker[1,3,4] on behalf of the SPARC collaboration

[1]GSI, Darmstadt, Germany; [2]IKP, FZ-Jülich, Germany; [3]HI Jena, Germany; [4]IOQ, Friedrich Schiller Universität Jena, Germany

For the experimental program of the SPARC collaboration [1] at GSI and FAIR, x-ray spectroscopy and x-ray polarimetry are essential tools.

Polarization of x-rays coming from recombination processes induced by collisions of heavy and highly charged ions at relativistic energies with electrons or low-density gaseous targets provides a unique insight into the dynamics of charged particles in extremely strong and temporally short electromagnetic fields. Detailed knowledge of these processes has, besides atomic physics itself, a great relevance for plasma- and astrophysics.

During the last years we continuously strengthened the instrumentation portfolio of SPARC with dedicated Si(Li)-and Ge(i)-Compton polarimeters which we employed very successfully in experiments at GSI and other research labs, like DESY and ESRF. This technology is based on LN_2-cooled planar double-sided structured detectors (Li-drifted silicon or high purity germanium bulk) with thicknesses in the range of 10 mm. The optimization of such systems for different energy regimes is an ongoing effort.

In this context we designed two test systems where the discrete preamplifier stage was replaced by ASICs to study the pros and cons with focus on a multi-channel readout solution. A 16-pixel HPGe(i) detector was equipped with Cube-ASICs which were run in the transistor-reset as well as in the resistor-reset mode [2]. With this chip we measured the best spectroscopic resolution for our systems up to now. Unfortunately the very high price per channel will only allow for the implementation in very special cases.

In the second study we built a system based on the PIXIE-ASIC[3], developed by Rutherford Appleton Laboratory (RAL), bonded to a linear Si(Li) pixel detector and later to a linear Ge(i) pixel detector. The PIXIE ASIC was developed by RAL to study the properties of CdTl and CdZnTe detectors with small pixel structures at room temperature.

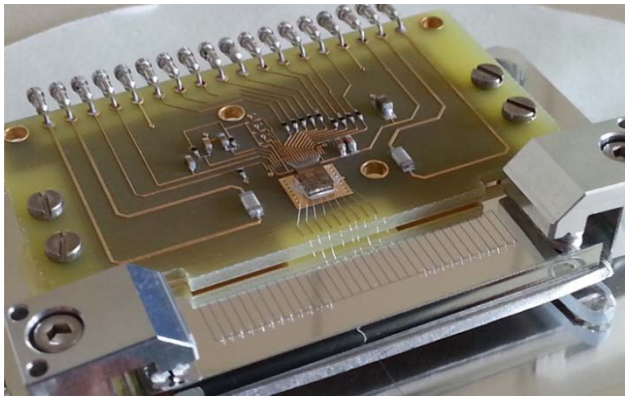


Figure 1: The test pcb with the PIXIE ASIC bonded to a test detector.

Finally we were able to show that this chip, although cooled down to 200 K and operated with higher detector capacitance than allowed by the specs, was able to produce nice results. With pixel structures of 1x5mm^2 we achieved 1.5 keV resolution at 60 keV x-ray energy. This is comparable with discrete preamps run at room temperature. The ASIC pcb is at least by a factor 5 more compact compared to discrete preamps. This test has proven the usability of this technology for a multi-channel readout ASIC for Si(Li)- and Ge(i)-detectors. With minor modifications, to adapt the ASIC especially for these semiconductors, the spectroscopic performance could even be more optimized.

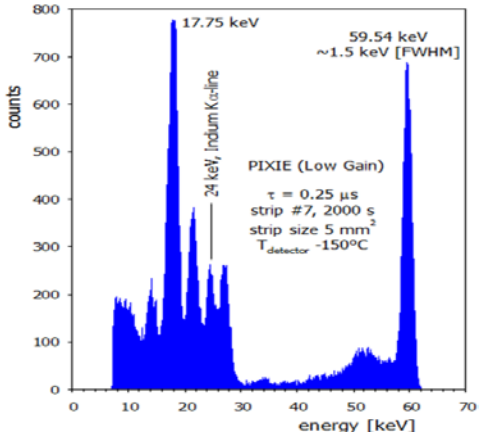


Figure 2: Spectroscopic results of the PIXIE ASICs with Si(Li) pixel detector irradiated with a Am-241 x-ray source.

We like to thank P. Seller, M. French, M.C. Veale, J. Lipp, L.L. Jones, A. Hardie from STFC, RAL(United Kingdom).

This report is also part of the HI Jena Scientific Report 2017.

References

[1] Technical Report of the SPARC collaboration https://www.gsi.de/work/forschung/appamml/atomphysik/ap_und_fair/sparc/dokumente.htm

[2] T. Krings et al., 2015 JINST 10 C02043

[3] M.C. Veale et al., IEEE Trans. Nucl. Sci., vol. 58, no. 5, October 2011, pp. 2357-2362

Experiment beamline: none

Experiment collaboration: APPA-SPARC

Experiment proposal: none

Accelerator infrastructure: none

PSP codes: none

Grants: supported by BMBF Verbundprojekt 05P15SJFAA

Strategic university co-operation with: FSU Jena

Electron capture decay of hydrogen-like ^{142}Pm ions: status of data analysis

F. C. Ozturk[1,2], F. Bosch[1,], P. Bühler[3], R. B. Cakirli[2], T. Faestermann[4], H. Geissel[1], P. Kienle[4,**], C. Kozhuharov[1], Yu. A. Litvinov[1], F. Nolden[1], Y. Oktem[2], N. Winckler[1], M. S. Sanjari[1], C. Scheidenberger[1], M. Steck[1], Th. Stöhlker[1,5,6], and the TBWD Collaboration*

[1]GSI Darmstadt; [2]Istanbul University; [3]SMI Vienna; [4]TU Munich; [5]HI Jena; [6]University Jena

Observation of the modulated behavior of electron capture (EC) decays in hydrogen-like 140Pr and 142Pm [1] caused an extensive controversial discussion in literature which called urgently for a confirmation or disproof of the effect. Therefore, significant efforts have been devoted to the improvement of the non-destructive detection of stored highly-charged ions in the ESR. A resonant cavity-based Schottky detector has been successfully designed, built and installed into the ESR [2]. Owing to the highly increased sensitivity, this novel detector has greatly contributed to numerous nuclear-, atomic- and astrophysics experiments at the ESR [3]. Furthermore, other storage ring facilities are now equipped with such detectors.

However, the largest boost has been given to the Single-Ion Decay Spectroscopy. The experiment mentioned at the beginning has been repeated with hydrogen-like 142Pm ions. Compared to the first experiment, about eight times larger statistics, namely 8665 EC decays, were recorded. The entire set of new decay data did not show any significant modulation [4]. However, one long series of about 4000 consecutive EC decays indicated some oscillatory behavior at the same frequency but with about two times smaller amplitude and a slightly different phase than in the first experiment [4]. A possible explanation could be a failure to remove the “old” ions before the injection of the new ions into the ESR. In such case the start time of the modulation would be smeared out.

A dedicated EMMI Rapid Reaction Task Force took place in July 2014 in Jena. In an open discussion a clear recommendation has been formulated that the experiment has to be repeated under conditions as close to the ones in the first experiment as possible. In the new experiment, which was carried out in fall 2014, more than 10000 EC decays of 142Pm ions have been precisely measured. Attention has been given to the monitoring of all relevant accelerator parameters. Special efforts were made to achieve the reliable emptying of the ESR (from the “old” ions) before every new injection.

The data were analyzed manually and with an automated procedure [5] leading to consistent results. New data can well be described by an exponential decay curve with the decay constant λ=0.0140(6) s-1. No significant modulation is observed. In order to explain the contradiction with the first experiment further studies would be required, probably addressing the hydrogen-like 140Pr ions which have a longer half-life. The corresponding publication is in preparation [6].

* deceased
** deceased

References

[1] Yu. A. Litvinov et al., Phys. Lett. B 664 (2008) 162.
[2] F. Nolden et al., Nucl. Instr. Meth. A 659 (2011) 69.
[3] F. Bosch et al., Prog. Part. Nucl. Phys. 73 (2013) 84.
[4] P. Kienle et al., Phys. Lett. B 726 (2013) 638.
[5] P. Buehler, Nucl. Instr. Meth. A 819 (2016) 167.
[6] F. C. Ozturk et al., Nucl. Phys. A, in preparation (2018).

Experiment beamline: ESR / FRS
Experiment collaboration: APPA-SPARC / NUSTAR-ILIMA / TWBD
Experiment proposal: E077 / E082
Accelerator infrastructure: SIS18 / ESR / FRS
PSP codes: none
Grants:
Scientific Research Project Coordination Unit of Istanbul University. Project numbers: 48110, 54135 and 53864;
European Research Council (ERC) under the European Union's Horizon 2020 research and innovation programme (grant agreement No 682841 "ASTRUm");
Helmholtz Chinese Academy of Sciences Joint Research Group HCJRG-108
Strategic university co-operation with:
Technical University Munich;
JL University Giessen;
RK University Heidelberg;
FS University Jena;
Istanbul University;
North-West Normal University Lanzhou

 DOI:10.15120/GR-2018-1

Grain size effects on irradiated CeO_2, ThO_2, and UO_2

W. Cureton[1,2], R. Palomares[1], J. Walters[1], C. Tracy[2], C. Chen[2], R. Ewing[2], G. Baldinozzi[3], J.°Lian[4], C. Trautmann[5,6], M. Lang[1]

[1]University of Tennessee, Knoxville, U.S.A; [2]Stanford University, Stanford, U.S.A; [3]CNRS, Centrale Supélec, Université Paris-Saclay, France; [4]Rensselaer Polytechnic Institute, Troy, U.S.A.; [5]GSI Helmholtzzentrum and Technische Universität Darmstadt, Darmstadt, Germany

Actinide oxides and analogue materials have many energy-related applications such as nuclear fuel and electrolytes for solid oxide fuel cells. Swift heavy ion irradiation experiments can give insight into defect formation processes and implications such as those encountered in a nuclear reactor by the slowing down of energetic fission fragments. Recently, it has been shown that the redox response of cations in fluorite-structured actinide oxides plays a crucial role in the accumulation of defects and associated volumetric swelling [1]. In this study, we have expanded this approach with a focus of understanding how grain size affects redox behavior under swift heavy ion irradiation [2].

CeO_2, ThO_2, and UO_2 in micro- and nanocrystalline form (~2 µm and ~20 nm particle size, respectively) were irradiated with 946 MeV Au ions at the M3 beamline of the GSI UNILAC. Subsequent analysis included synchrotron X-ray diffraction (XRD), Raman spectroscopy, and transmission electron microscopy. All materials retain crystallinity up to the maximum fluence of 3×10^{13} ions/cm^2 and show a unit-cell expansion following a single-impact model, Eq. 1, except microcrystalline UO_2, which shows a small unit cell contraction (Fig. 1).

$$\frac{\Delta a}{a_0} = \frac{a(\phi) - a_0}{a_0} = \frac{a_{sat} - a_0}{a_0}\,(1 - e^{-\sigma\phi}) \quad (1)$$

In Eq. 1, a is the unit cell parameter, a_0 is the unit cell parameter of the unirradiated reference sample, a_{sat} is the unit cell parameter at saturation, σ is the cross-sectional ion track area, and ϕ is the ion fluence.

As observed previously [1], nanocrystalline CeO_2 exhibits a significantly higher degree of swelling than its microcrystalline counterpart (Fig. 1). This effect can be explained by a more efficient redox process in the presence of a high grain-boundary density.

ThO_2 exhibits the least difference in swelling between the micro- and nanocrystalline materials possibly due to the lack of accessible redox states of the thorium cation which retains tetravalent under most conditions. Thus, defect formation related to changes in the redox behavior, which are greatly enhanced in nanomaterials, are absent in ThO_2 leading to an overall reduced swelling.

The most dramatic difference in swelling between different grain sizes occurs in UO_2. Microcrystalline UO_2 exhibits a small contraction whereas the nanocrystalline counterpart shows the largest degree of swelling for all materials. Raman spectroscopy measurements elucidated the underlying local defect structure of both samples. Swift heavy ion irradiation causes oxidation in micro UO_2 while nano UO_2, already oxidized prior to irradiation, is reduced under ion irradiation. This is in agreement with the XRD results and previous studies on the behavior of the unit cell parameter of UO_{2+x} for varying x.

In summary, the cation redox behavior is critical in understanding the differences in response between nano- and microcrystalline actinide oxide materials under swift heavy ion irradiation. This study successfully utilized a recently developed sample-holder system, which allowed for safe encapsulation of microscopic actinide oxide materials for swift heavy ion irradiation at GSI and subsequent synchrotron X-ray characterization at the Advanced Photon Source.

*This work was supported by the Energy Frontier Research Center Materials Science of Actinides funded by the US DOE, Office of Science, Office of Basic Energy Sciences (DE-SC0001089).

References

[1] C. Tracy, et al.; "Redox Response of actinide materials to highly ionizing radiation", Nat. Mater. 5 (2015) 6133.

[2] W. Cureton, et al., to be published (2018).

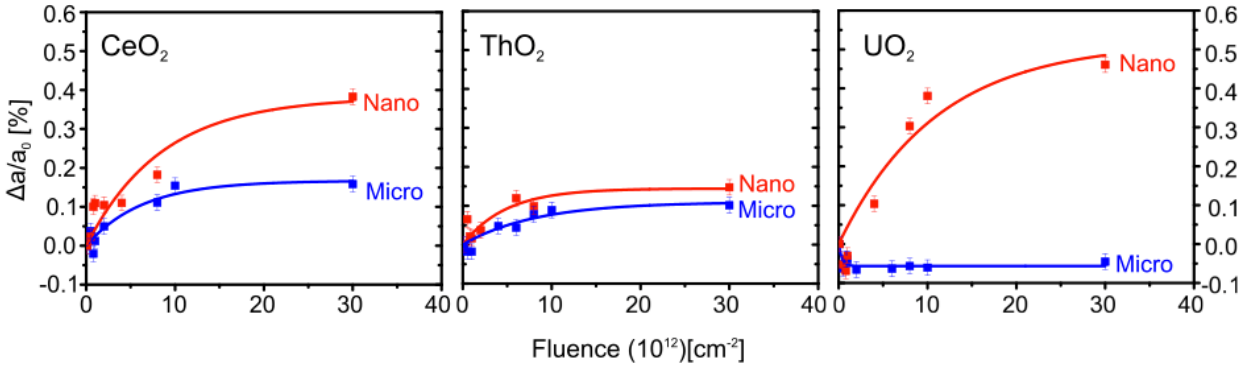


Figure 1: Relative unit cell parameter change induced by 946 MeV Au ions for mico- and nanocrystalline CeO_2, ThO_2, and UO_2 based on refinement of X-ray diffraction patterns. The curves represent fits to Eq. 1

Radiation-induced disordering in compressed $A_2Zr_2O_7$ (A = Nd, Sm, & Er)

S. Park[1], C. L.Tracy[1], F. Zhang[2], C. Park[4], S. Tkachev[5], C. Trautmann[6], M. Lang[3], W.L. Mao[1,7], R.°C. Ewing[1]

[1]Department of Geological Sciences, Stanford Univ., Stanford, USA; [2]Materials Science and Technology Division, Oak Ridge Nat. Lab., Oak Ridge, USA; [3]Department of Nuclear Engineering, Univ. of Tennessee, Knoxville, , USA; [4]HPCAT, Geophysical Lab., Carnegie Institution of Washington, Argonne, USA; [5]Center for Advanced Radiation Sources, Univ. of Chicago, USA; [6]GSI Helmholtzzentrum and Techn. Univ. Darmstadt, Germany; [7]Stanford Inst. for Materials & Energy Sciences, SLAC Nat. Accelerator Lab., Menlo Park, USA

Both pressure and irradiation-induced ionization offer a means for modifying the materials in this system by perturbing their electronic structures. Swift heavy ion (SHI) irradiation-induced disordering alters the energy landscapes associated with the collective atomic motion necessary for high pressure phase transformations. This can dramatically alter the high pressure phase space, making this successive exposure to different extreme environments a potentially useful tool for synthesizing new phases. This study investigates the manner in which ion irradiation and subsequent exposure to high pressure affects the structural behaviour of $A_2Zr_2O_7$ (where A = Nd, Sm, and Er) pyrochlore-type materials (Figure 1).

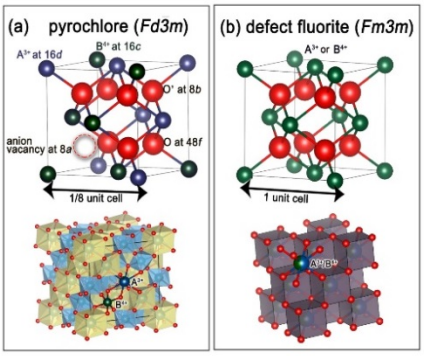


Figure 1: Schematic diagrams of (a) the pyrochlore structure showing both 1/8 of a unit cell (top) and an entire unit cell (bottom) and (b) the defect-fluorite structure.

With increasing fluence, $Er_2Zr_2O_7$ exhibits no substantial change in its long-range periodicity, and the defect-fluorite structure is retained. In contrast, $Sm_2Zr_2O_7$ and $Nd_2Zr_2O_7$, which initially exhibit the pyrochlore structure, disorder into defect-fluorite structures. This is evidenced by the disappearance of the less intense maxima of the pyrochlore, attributed to the mixing of A- and B-site cations onto a single sublattice, as well as mixing of anion 8a vacancies on the other anion sublattice sites [1].

Upon compression, all unirradiated samples exhibit a cubic-to-defect-cotunnite-like phase transformation, with the critical pressures for the transformations dependent on the initial structure. Interestingly, this formation of the cotunnite-like phase (Pnma) at high pressure is inhibited for all compositions that have been irradiated with SHIs. Instead, the only phase transformation that occurs in the irradiated materials is evidenced by the appearance of significant asymmetry in the (111) diffraction maxima. This asymmetry grows into a diffuse scattering band, which evidences the presence of an amorphous phase. Since the more stable cotunnite-like phase is rendered inaccessible by irradiation-induced structural changes, amorphization of all three compositions occurs gradually upon compression. The inaccessibility of the cotunnite-like phase suggests that SHI irradiation-induced electronic excitation yields defects and disorderings that alter the energy landscape at high pressure.

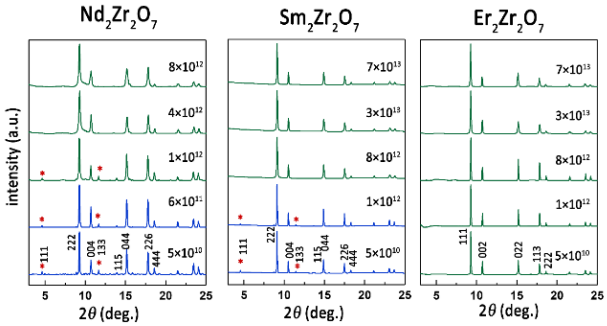


Figure 2: XRD patterns of $A_2Zr_2O_7$ compounds irradiated with 2.2 GeV Au ions at various fluences (X-ray wavelength λ = 0.496 Å).

This phenomenon can be understood as an extension of the high pressure metastability field of the amorphous phase to lower pressures after irradiation (Figure 3). Upon the release of pressure, any compound with a defect-fluorite structure recovers this initial structure, regardless of the disordering or defects induced by SHI irradiation. The irradiation-induced modification of the phase stability fields of pyrochlore compounds at high pressures results from the interplay between nanoscale defects induced by dense electronic excitation, changes in bonding that accompany electron orbital overlap at high pressure, and the collective atomic motions associated with high pressure phase transformations. The study demonstrates that SHI irradiation makes accessible, at a given pressure, phases that cannot be achieved without the combination of these extreme environments.

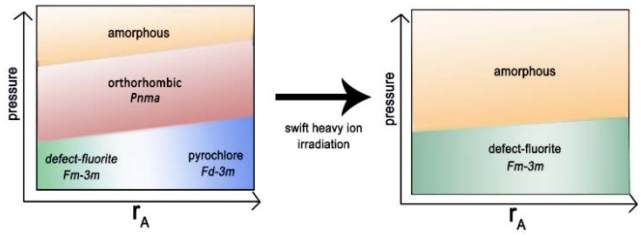


Figure 3: Schematic representation of the stability field of lanthanide zirconates at high pressure.

[1] M. Lang, F.X. Zhang, J. Lian, C. Trautmann, Z. Wang, R.C. Ewing, J. Mater. Res. 24 (2009) 1322

 DOI:10.15120/GR-2018-1

Similar local order in disordered fluorite and aperiodic pyrochlore structures*

J. Shamblin[1,2], C.L. Tracy[3], R.I. Palomares[2], E.C. O'Quinn[2], R.C. Ewing[3], J. Neuefeind[4], M. Feygenson[4], J. Behrens[2], C. Trautmann[5], M. Lang[2]

[1]Department of Physics and Astronomy, University of Tennessee, Knoxville, USA; [2]Department of Nuclear Engineering, University of Tennessee, Knoxville, USA; [3]Department of Geological Sciences, Stanford University, Stanford, USA; [4]Chemical and Engineering Materials Division, Spallation Neutron Source, Oak Ridge National Laboratory, Oak Ridge, USA; [5]GSI Helmholtzzentrum and TU Darmstadt, Darmstadt, Germany

A major challenge to understanding the response of materials to extreme environments is to unravel the processes by which a material can incorporate atomic-scale disorder, and at the same time, remain crystalline. Such conditions are unavoidable for many technological applications, (e.g., nuclear waste-storage, high-power lasers, fission/fusion reactors, and spacecraft materials); thus, there is general interest in gaining a more fundamental understanding in the underlying structure of order-disorder transformations [1].

Two pyrochlore compositions, one of which is known to disorder ($Er_2Sn_2O_7$) and the other to amorphize ($Dy_2Sn_2O_7$) under radiation, were irradiated with 2.2 GeV Au ions of fluence 8×10^{12} /cm^2 at the X0 beamline of the GSI UNILAC. The ions passed completely through the polycrystalline samples and lost energy exclusively *via* electronic excitation. For characterization, the irradiated samples were transferred to quartz capillaries for analysis by neutron total scattering experiments at the NOMAD beamline at the Spallation Neutron Source at Oak Ridge National Laboratory [2].

Neutron total scattering analysis confirmed that ion irradiation induced different long-range structures in the two samples with $Er_2Sn_2O_7$ disordering to defect fluorite and $Dy_2Sn_2O_7$ becoming amorphous. Despite their very different long-range behaviors, pair distribution function (PDF) analysis revealed striking similarities in their local structures with nearly identical atomic configurations (Fig. 1).

Based on the comparison of neutron diffraction data with PDF results, we have shown that locally ordered structural "units", which are best modelled with a weberite-type arrangement, exist in both the amorphous and disordered pyrochlore oxides. The existence of a locally ordered structure within both the amorphous and disordered domains was previously also suggested by Electron Energy Loss and Raman spectroscopy results [3]. While these spectroscopic studies indirectly indicated the existence of similar local order, the PDF results of the present study provide a direct description of the atomic arrangement as being of weberite-type character. The final long-range radiation response depends then on the pyrochlore composition as to whether the local weberite-type arrangement modulates into the long-range defect-fluorite type arrangement ($Er_2Sn_2O_7$), maintaining overall crystallinity, or into a long-range aperiodic phase ($Dy_2Sn_2O_7$).

Thus, the presence of similar local order in disordered vs. amorphous pyrochlores suggests that the dominating factor determining radiation tolerance is not simply a material's ability to incorporate local disorder, but rather its ability to adopt pseudo-periodic modulations of this local order in such a way that long-range crystallinity is maintained. Locally-ordered weberite units appear to be a universal phenomenon in pyrochlore oxides based on the present and previous work and it may also exist as local order within the "molten" phase induced within swift heavy ion tracks.

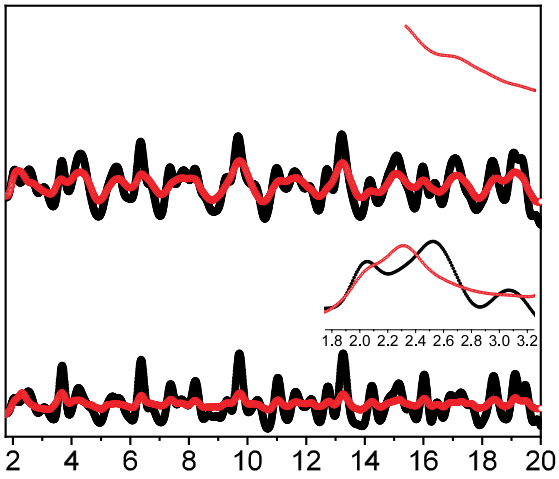


Figure 1: Neutron PDFs (G(r)) of pyrochlores before (black) and after (red) being irradiated with 2.2 GeV Au ions to a fluence of 8×10^{12} ions/cm^2. Despite vastly different behaviors over longer length scales ($Er_2Sn_2O_7$: disordering, $Dy_2Sn_2O_7$: amorphization), both compositions exhibit nearly identical local atomic arrangements.

*Work was supported as part of the Materials Science of Actinides, an Energy Frontier Research Center funded by the U.S. DOE, Office of Science, Office of Basic Energy Sciences under Award Number DE-SC0001089.

References

[1] Shamblin, J.; Tracy, C. L.; Palomares, R. I.; O'Quinn, E. C.; Ewing, R. C.; Neuefeind, J.; Feygenson, M.; Behrens, J.; Trautmann, C.; Lang, M.; Acta Mater. 144 (2018) 60.

[2] Neuefeind, J.; Feygenson, M.; Carruth, J.; Hoffmann, R.; Chipley, K. K.; Nucl. Instr. Meth. B 287 (2012) 68.

[3] Tracy, C. L.; Shamblin, J.; Park, S.; Zhang, F.X.; Trautmann, C.; Lang, M.; Ewing, R. C. Phys. Rev. B 94 (2016) 064102.

Effects of single swift heavy ions on H/Si(001) studied by means of STM

C. Länger[1], P. Ernst[2], M. Bender[3], D. Severin[3], C. Trautmann[3,4], M. Schleberger[2], and M. Dürr[1]

[1]Justus Liebig University Giessen, Germany; [2]University Duisburg-Essen, Germany; [3]GSI Helmholtzzentrum, Darmstadt, Germany; [4]TU Darmstadt, Darmstadt, Germany

Material modifications by swift heavy ions (SHI) have been successfully obtained in insulators as the electronic stopping causes sufficient energy density in the material that can be transferred, e.g., via electron-phonon-coupling, to the lattice [1]. This holds also for many semiconductors, but the two crystalline semiconductors silicon and germanium are notable exceptions. Neither in the bulk nor on the surface could any swift heavy ion induced changes be detected up to stopping powers of 21 keV/nm [2,3]. This is in clear disagreement with the standard model to describe track formation due to SHI irradiation, i.e., the inelastic thermal spike model [4], which predicts lower thresholds down to 8 – 10 keV/nm [3,5].

In order to enhance the sensitivity for ion-induced damage on a silicon surface, we used hydrogen-terminated single crystal Si(001) surfaces (Fig. 1) in combination with scanning tunnelling microscopy (STM). Desorption of single hydrogen atoms or molecules leads to a clear signature in the STM images [6] and thus damage could be resolved on the atomic scale.

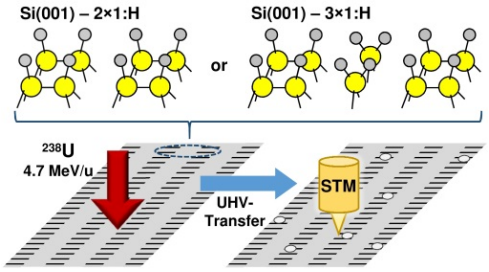


Figure 1: Top: Schematic representation of the H/Si(001) 2×1 (left) and 3×1 reconstruction (right). Bottom: Scheme of experiment: After preparation of the H/Si(001) surfaces and sample transfer in UHV to the M1-beamline at the UNILAC, the samples were irradiated with $^{238}U^{28+}$ ions. After UHV-transfer to the analysis chamber, the samples were investigated by means of STM.

In Figs. 2(a) and (b), a H/Si(001) surface before and after irradiation with $^{238}U^{28+}$ ions (4.7 MeV/u) is shown. In both images, the dimer row reconstruction of Si(001) is clearly observed. After irradiation, additional bright features are detected. As the number density of the bright features is significantly higher than the applied ion fluence and as the bright features are statistically distributed over the whole area, we conclude that most of the features are not directly caused by ion impacts on the surface. In any case, the size of the features observed after SHI impact are compared with isolated dangling bonds created by means of laser-induced thermal desorption of hydrogen in Figs. 2(c) and (d). The comparison indicates that the features observed after SHI irradiation, as shown in Figs. 2(b) and (c), are restricted to one or two silicon surface atoms if caused by hydrogen desorption. We thus conclude that the detectable impact of the SHI on crystalline silicon is, if at all, very localized and cannot be described within the thermal spike model.

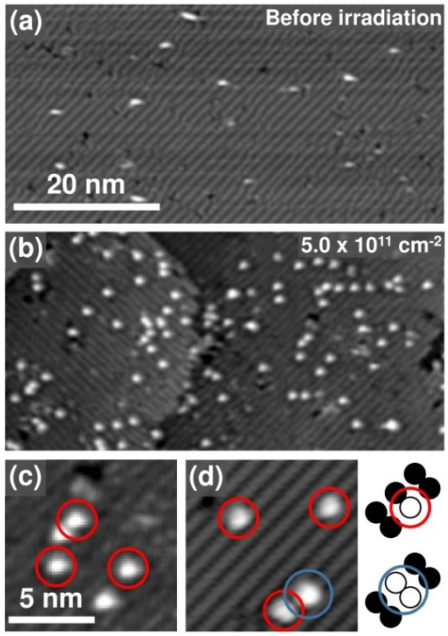


Figure 2: Filled state STM images (U_t = -2 V; I_t = 0.5 nA) of hydrogen-terminated Si(001) surfaces, before and after irradiation with $^{238}U^{28+}$ ions (4.7 MeV/u). (a) Before irradiation, the H/Si(001)3×1 surface shows few dark and bright features, which correspond to defects, adsorbates, or dangling bonds after desorption of hydrogen originating from sample preparation. (b) After irradiation with the highest ion fluence used in the experiments, a distinct increase of bright features is observed. (c) A magnified part of (b) shows the size of the bright features. When compared to laser-induced desorption experiments on H/Si(001) [6] shown in (d), the observed features are of similar size in both experiments.

References

[1] F. Aumayr, S. Facsko, A.S. El-Said, C. Trautmann, M. Schleberger, J. Phys. Cond. Matt. 23 (2011) 393001.

[2] A. Kamarou, W. Wesch, E. Wendler, A. Undisz, M. Rettenmayr, Phys. Rev. B 78 (2008) 054111.

[3] O. Osmani, I. Alzaher, T. Peters, B. Ban d'Etat, A. Cassimi, H. Lebius, I. Monnet, N. Medvedev, B. Rethfeld, M. Schleberger, Nucl. Instr. and Meth. B 282 (2012) 43.

[4] M. Toulemonde, C. Dufour, C. Paumier, Phys. Rev. B 46 (1992) 14362.

[5] S.L. Daraszewicz, D.M. Duffy, Nucl. Instr. Meth. B 269 (2011) 1646.

[6] M. Dürr, A. Biedermann, Z. Hu, U. Höfer, and T. F. Heinz, Science 296 (2002) 1838.

 DOI:10.15120/GR-2018-1

Effect of high-energy heavy ion irradiation on the nanoscale state of promising titanium alloys and ODS steel*

S. Rogozhkin[1,2], A. Bogachev[1,2], A. Nikitin[1,2], A. Vasiliev[3], M. Presnyakov[3], V. Skuratov[4], M. Tomut[5], C. Trautmann[5,,]

[1]NRC «Kurchatov Institute» - ITEP, Moscow, Russia; [2]National Research Nuclear University MEPhI, Moscow, Russia; [3]NRC "Kurchatov Institute", Moscow, Russia; [4]Joint Institute for Nuclear Research, Dubna, Russia; [5]GSI Helmholtzzentrum, Darmstadt, Germany; [6]Technische Universität Darmstadt, Darmstadt, Germany

The most promising functional materials for operation under high-energy and high intensity particle beams are complex heterogeneous systems strengthened by nanoscale inclusions and phases. Energy losses in such structures are nontrivial and can contribute to local changes in the structural-phase state of the material. Objects of this study are two titanium alloys (Ti-5Al-4V-2Zr and Ti-6Al-4V) and oxide dispersion strengthened steel ODS Eurofer steel.

The effect of room temperature irradiation on the microstructure was studied by high-resolution transmission electron microscopy (TEM) with energy-dispersive spectroscopy. Cross-section and usual TEM samples of the pristine and irradiated state of the materials were produced by means of focused ion beam and electrochemical thinning.

Irradiation of titanium alloys

Two types of titanium alloys were irradiated at the GSI UNILAC with Au ions (4.8 MeV/nucleon, up to 1×10^{13} ions/cm^{-2}). The microstructure of this widely used Ti-6Al-4V is formed by large (~30 μm) nearly equiaxial α-phase grains enriched with Al and decorated at their boundaries with V-rich β-phase inclusions. Ti-5Al-4V-2Zr alloy shows a bimodal grain distribution: packets of elongated α-phase grains separated by β-phase columns (so called basket-wave microstructure).

Irradiations with swift Au ions led to the formation of structural defects observed as a black dots aligned along the irradiation direction. Their average size is estimated to be 2±1 nm (Figure 1). These features seem to be partially coherent with the matrix. It is assumed that they may serve as nucleation sites of intra-granular β-phase precipitates. TEM EDXS analysis showed that the chemical composition of both α and β phases, as well as the spatial distribution of the grains remain stable under irradiation.

An earlier investigation of the microstructure of the Ti-5Al-4V-2Zr alloy after irradiation with low-energy (101 keV/nucleon) titanium ions at 260 °C revealed a high concentration of dislocation loops in the irradiated region of the sample. Tomographic atom probe analysis (APT) of the local chemical composition of the irradiated sample showed the formation of nanoscale vanadium pre-precipitates in the α-phase of the alloy.

Irradiation of ODS Eurofer

Irradiations of ODS Eurofer with 4.8 MeV/nucleon Au ions (1×10^{11} and 5×10^{12} cm^{-2}) and 1.2 MeV/nucleon Xe ions (1×10^{13} and 1×10^{14} cm^{-2}) led to the formation of amorphous areas within large (>8 nm) oxide particles. These features are probably tracks produced along the ion paths. Our finding is consistent with the results of previous studies of the effect of high-energy radiation on the nanostructure of ODS steel [2]. The average size of the observed tracks is 3±1 nm. Their number density correlates with the applied ion fluence. An amorphous transition layer was observed at the interface of large oxide particles after irradiation with 4.8 MeV/nucleon Au ions.

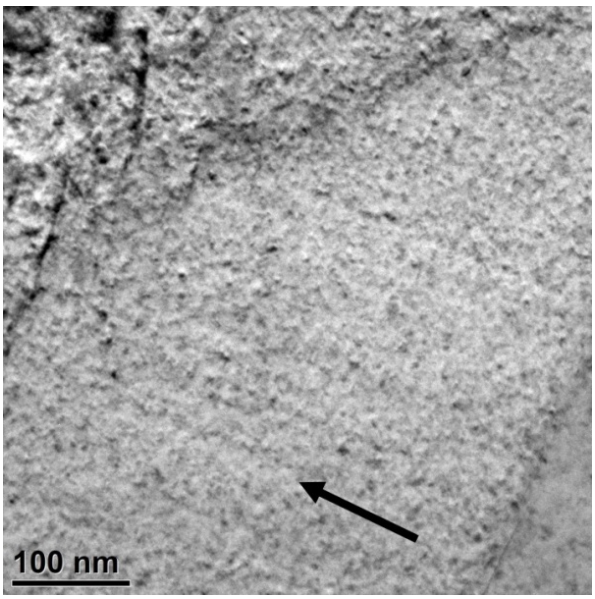


Figure 1: Representative bright-field TEM image of Ti-6Al-4V alloy irradiated with Au ions (4.8 MeV/nucleon) up to 5×10^{12} cm^{-2} at room temperature. Arrow shows irradiation direction

It has been shown that after the irradiation with low energy Fe ions (100 keV/nucleon), the number density of oxide particles increased. Also, an increase in the fraction of small-size oxides (less than 5 nm) was observed. APT analysis showed that the composition of the nanoclusters changes under irradiation. There is an exchange of chemical elements between clusters, matrix and oxide particles.

Our results provide evidence of the instability of strengthening nanoscale phases and inclusions in promising titanium alloys and ODS steels under ion irradiation.

*The work is carried out with financial support of the FAIR-Russia Research Center.

References

[1] S.V. Rogozhkin et al., Inorganic Materials: Applied Research 8 (2017) 279–285.

[2] V.A. Skuratov et al., Journal of Nuclear Materials 442 (2013) 449-457.

Online monitoring of stress waves induced by short-pulsed 4.8 MeV/u ^{238}U°beam in polycrystalline graphite

P. Bolz[1,2], A. Prosvetov[1,2], P. Simon[1,2], C. Trautmann[1,2], M.Tomut[1]

[1]GSI, Darmstadt, Germany; [2]TU Darmstadt, Germany;

The short pulse-structure and the high intensity of ion beams at FAIR might result in failure of graphite components like the production target of the Super Fragment Separator due to high-amplitude cyclic thermal loads. Experiments at the UNILAC allow an efficient monitoring of the response of target materials to high-intensity short beam pulses due to the large energy-loss around the Bragg maximum combined with low sample activation. For this purpose, a 500 µm thick disc made of a fine-grain isotropic graphite (SGL R6650) was clamped in a ring shaped sample holder (Fig. 1) and exposed to 100 µs long U ions pulses with an energy of 4.8 MeV/u and a frequency of 0.5 Hz. at a pulse intensity of 1.2-1.6×10^{10} ions/cm². The energy deposited by the ion beam leads to materials heating within the volume penetrated by the ions resulting in thermal expansion. This excites flexural waves of the thin target and stress waves traveling along radial and transversal direction and reflecting at the target edges (Fig. 2).With help of a Laser Doppler Vibrometer (LDV) aligned at 45° with respect to the back surface of the sample, the surface velocity caused by bending modes or stress waves can be measured.

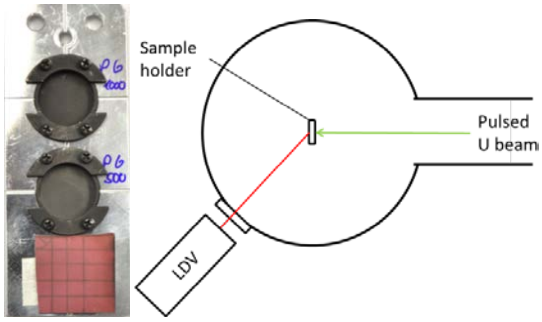


Figure 1: Sample holder (left) and schematic set-up for online monitoring of stress waves using a Laser Doppler Vibrometer at the M3 beamline at UNILAC (right).

The expected bending frequency f_{b1} is calculated using equation (1) assuming a clamped circular plate [1] with a thickness, t = 500 µm, diameter, d = 2 cm, Young's modulus, E = 12.5 GPa, Poisson's ratio, ν = 0.18, and density, ρ = 1.84 g/cm³. The frequency f_{tr} of the transversal stress wave is calculated using equation (2) with the velocity of sound in graphite, v, and the length, s, equalling twice the thickness of the plate

$$f_{b1} = \frac{39.771}{2\pi \cdot d^2} \cdot \sqrt{\frac{E \cdot t^2}{12 \cdot (1-\nu^2) \cdot \rho}} = 7.5 \text{ kHz} \quad (1)$$

$$f_{tr} = \frac{v}{s} = \sqrt{\frac{E}{\rho}} \cdot \frac{1}{2 \cdot t} = 2.6 \text{ MHz} \quad (2)$$

The LDV recorded velocity signal shows a damped harmonic oscillation with a frequency of about 5.4 kHz, corresponding to the bending of the sample (Fig. 2).

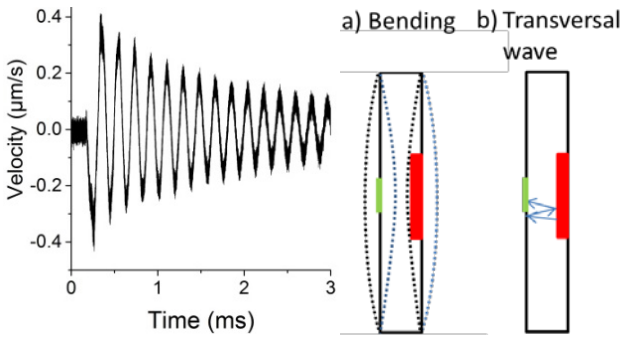


Figure 2: Time dependence of velocity measured at rear surface of target, after impact of a 100 µs U ions pulse (left), schematic drawing of excited first bending mode (centre), and transversal stress wave (right).

The velocity signal was further investigated by continuous wavelet analysis, allowing the extraction of the time and frequency resolved harmonic component, corresponding to stress wave propagation and reflections. A high absolute value of the wavelet coefficient C represents high velocity for this time and frequency. The beam arrives 163 µs after the triggered start of the measurement. Afterwards the target material in the beam spot is heated for the pulse length of 100 µs resulting in the highest stress at the end of the pulse. This can be observed with the highest wavelet coefficient at 261 µs and a frequency of 2.6 MHz for transversal propagation of stress waves, as calculated in equation (2).

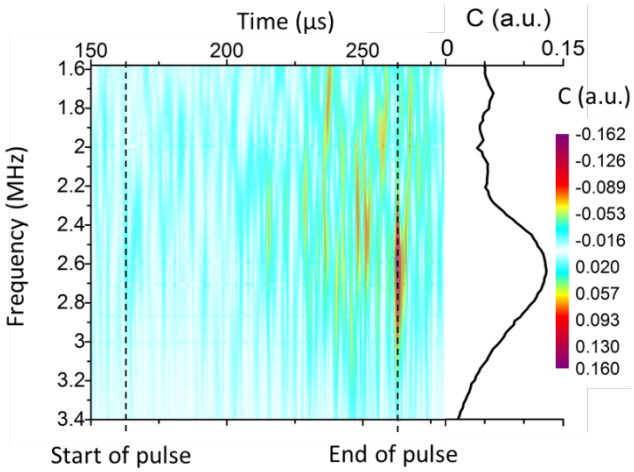


Figure 3: Contour plot of the wavelet coefficient C as a function of time and frequency (left) and maximum wavelet coefficient depending on the frequency (right). The time window covers one beam pulse starting at 163 µs.

[1] C. Hubert, NIM B365 (2015) 509-514
[2] A. Leissa (1969), Vibration of plates, NASA SP-160, Columbus, Ohio

 DOI:10.15120/GR-2018-1

Impact response of high-performance carbon-based materials

D. Schmitt[1,2], P. Bolz[1,3], P. Simon[1,3], C. Trautmann[1,3], M. Tomut[1]

[1]GSI, Darmstadt, Germany;[2]University of Stuttgart, Germany;[3]TU Darmstadt, Germany;

Within the next few years, future accelerator facilities such as HL-LHC at CERN or FAIR will provide primary beams of orders of magnitude higher intensities. Higher intensities result in higher thermal loads, requiring new high-performance materials for beam intercepting devices such as collimators, beam windows or production targets that withstand such extreme conditions. Particularly short beam pulses lead to fast thermo-mechanical solicitations that need to be tested dynamically to characterize the materials response at high strain rates.

Because of its excellent thermal conductivity, thermal shock resistance and radiation hardness [1] graphite-based materials are most suitable for application in extreme environments e.g. in high power accelerators and nuclear reactors as well as in aerospace applications like solid rocket motor throats, nozzle exit cones or aircraft brakes. This work investigates the response to several dynamic impact tests of polycrystalline graphite (PG), 2D- and 3D-carbon-fibre reinforced carbon composites (CFC), graphitic foams, and pyrolytic graphite (TPG).

Nanoindentation allows to precisely estimate mechanical properties of a material including hardness, Young's modulus or creep behaviour using the principle developed by Oliver and Pharr [2]. To determine dynamic properties, a sharp diamond cube corner indenter tip is mounted on the indentation platform and is accelerated from a distance of 2 µm, with a force of 15 mN towards the sample surface. The movement of the indenter tip and thereby the penetration depth is monitored as a function of time. The materials dynamic hardness is estimated by the ratio of load to projected contact area.

$$H_{dyn} = \frac{3m(v_{in}^2 - v_{out}^2)}{2c\, h_{res}^3} \qquad (1)$$

where m is the pendulum mass, v_{in} the contact velocity, v_{out} the outgoing velocity at the moment the tip detaches from the sample, the tip geometry is considered by the constant c and h_{res} denotes the residual plastic depth.

The studied composite materials are orthotropic, having different mechanical properties depending on the loading direction. Investigations are performed in two directions. Figure 1 shows that CFC materials and pyrolytic graphite exibit a higher dynamic hardness when fibres are normal to the indented surface. The polycrystalline graphite grades differ in their average grain size (1µm and 20µm). Their dynamic hardness increases for the finer structure.

Beside the dynamic hardness, the materials damping is determined based on the decrease of the amplitudes of indentation tip re-bouncings after a single impact. The damping constant is defined by the reciprocal of the time until the tips bouncing is damped to 1/e.

To investigate the materials susceptibility to fatigue failure, series of 75 consecutive impact tests are performed at the same spot, monitoring the evolution of the penetration depth. An abrupt increase in penetration depth is indicative of material failure resulting into a permanent deformation.

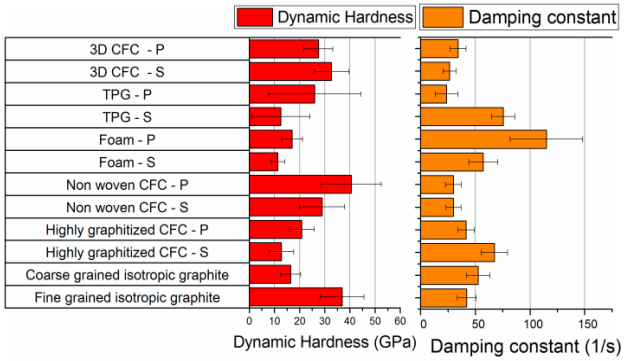


Figure 1: Estimated dynamic hardness and damping constant for the investigated carbon materials. S-fibre plains normal to surface, P-fibre plains parallel to surface

For a reliable conclusion about fatigue resistance, a fracture probability was estimated by ranking the number of impact-to-fracture events and then assigning a probability of fracture P(f) to the nth-ranked fracture event in a total number of N [3].

$$P(f) = \frac{n}{N+1} \qquad (2)$$

No fracture events were observed in polycrystalline graphite grades. For the foam, depending on the measured spot, the indenter tip depth signal saturates from the first impacts. Figure 2 shows a higher failure probability in the fibre direction. The 3D CFC has a very good fatigue behaviour in both loading directions due to additional vertical strengthening fibres which connect the layers and avoid delamination.

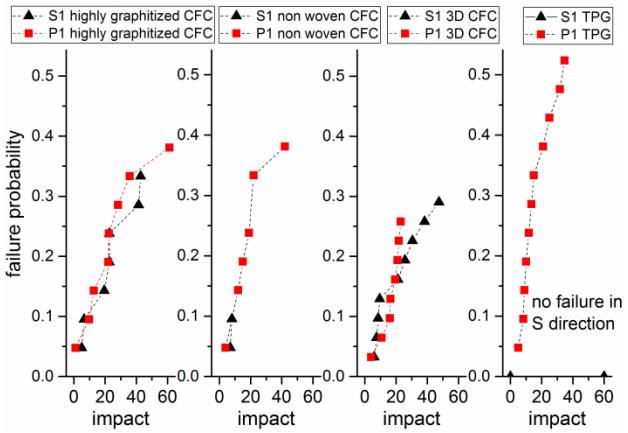


Figure 2: Failure probabilities as a function of the number of impacts in nanoindentation fatigue tests

[1] C.Hubert et al, Nucl. Instr. Meth B 365 (2015) 509–514

[2] W.Oliver and G.M.Pharr, J.Mater. Res. 7 (1992) 1564-1583

[3] B.Beake and J.Smith, "Nano-impact testing". Surf. Coat. Techn. 188-189 (2004) 594-598

Figures of merit of carbon materials for high power beam intercepting devices

F. Jäger[1,2], P. Simon[1,2], C. Trautmann[1,2], M. Tomut[1]

[1]GSI, Darmstadt, Germany; [2]TU, Darmstadt, Germany

Increasing beam intensities at the next-generation of particle accelerator facilities such as FAIR lead to increasing transient thermo-mechanical loads in targets, beam dumps and collimators. Currently graphitic materials are used for beam intercepting devices (BID) as they exhibit low activation, high radiation hardness and thermal stability combined with improved strength at high temperatures.

The goal of this work is to develop a suitable figure of merit (FoM) in order to qualitatively predict which candidate materials have enough resilience for applications at the next generation of high power accelerators. This approach uses easily accessible material properties to predict how a given material would respond to a high-energy particle beam impact [1]. The deposited energy of the incident particle beam is proportional to the mass density ρ of the carbon target. For the figure of merit, the beam-induced stress is compared with the flexural strength, σ_f. The thermal stress is the product of the linear coefficient of thermal expansion (CTE), α, Young's modulus, E, and the temperature variation. The increase in temperature is inverse proportional to the heat capacity, c_p

$$FoM = \frac{\sigma_f c_p}{E\alpha\rho} \qquad (1)$$

In the current project, the flexural strength σ_f was determined by the three point bending method (TPB) using a universal testing machine with a maximum force of 2 kN. All samples had rectangular cross-sections. The measured flexural strengths of different carbon materials are shown in fig. 1.

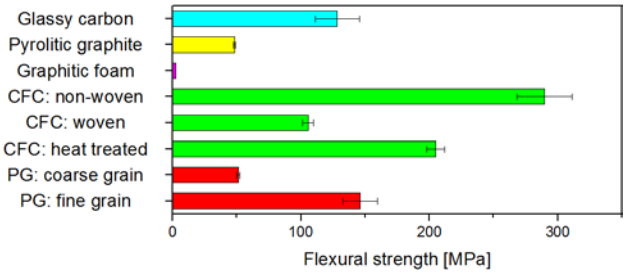


Figure 1: Measured flexural strength of different graphitic materials: polycrystalline isotropic graphite (PG) grades with different grain sizes (red), 2D carbon fibre composites (CFC) (green), graphitic foam (magenta), pyrolytic graphite (yellow), and glassy carbon (cyan).

The materials shown in fig. 1 are sorted in different classes using colour codes. Two isotropic polycrystalline graphite (PGs) grades with different grain sizes are represented in red. The production process ensures random orientation of the grains, leading to isotropic properties. 2D carbon-fibre reinforced carbon composites (CFC) are represented in green. Carbon-fibres, which can be woven in 2D sheets, are used to reinforce a graphite matrix, which results in orthotropic material properties. It is possible to increase the degree of graphitization of the fibres using heat treatment. Thermal pyrolytic graphite (TPG) is made of highly oriented graphene layers. The graphitic foam has a high degree of porosity which causes a low density. Glassy carbon (GC) is an insulating, hard and non-graphitizing carbon material with nanometric closed porosity. The PG grade with the smaller average grain size of 1 µm exhibits a higher flexural strength than the one with a grain size of 20 µm. In CFC materials, the flexural strength is enhanced up to a factor of 2 using fibre reinforcement. The strength of TPG is comparable to that of the coarse grained graphite. For GC it reaches similar values to those of the fine grained graphite and woven CFC.

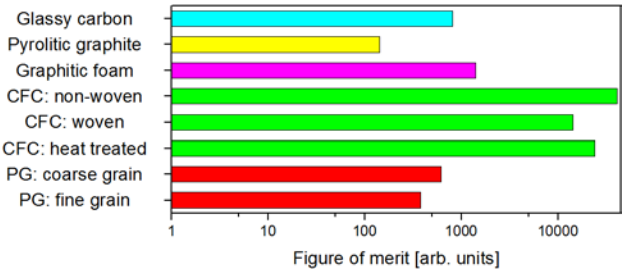


Figure 2: Logarithmic representation of FoM's calculated for the same set of materials like in fig. 1, using the measured flexural strength

The calculated figures of merit, based on the measured flexural strength, for the investigated set of carbon materials are shown in fig. 2. All other material properties are taken from data sheets. For anisotropic materials the properties along the fibre and basal planes have been incorporated.

Due to the highest value of the flexural strength and the nearly zero CTE, CFCs have the highest FoM, exceeding the values for other materials by an order of magnitude. Unexpectedly, the low strength foam comes on the second place in the ranking due to its low density and low CTE. The large grain size isotropic polycrystalline graphite has a FoM comparable to that of the fine grain size grade. This can be explained by the much smaller CTE (~25% of the fine grained). GC performance ranks between that of foam and PG. The material with the lowest FoM is TPG, due to a combination of high density, large value of elastic modulus, and moderate flexural strength.

The presented FoM is a first indicator of the performance of different carbon materials for BIDs. Complete thermo-mechanical characterizations of materials as well as online monitoring of their response to high-power particle beams are ongoing and will be used to benchmark the materials ranking based on calculated FoMs.

References

[1] A Bertarelli et al. Research and development of novel advanced materials for next-generation collimators. Tech. rep. CERN (2011).

 DOI:10.15120/GR-2018-1

Non-homogeneous ion beam induced modification of flexible graphite along the ion range*

A. Prosvetov[1,2], *C. Trautmann*[1,2], *M. Tomut*[1]

[1]GSI, Darmstadt, Germany; [2]TU Darmstadt, Germany;

Flexible graphite (FG) is a well oriented carbon material obtained by exfoliation of natural graphite flakes and subsequent compaction into soft sheets. Like highly oriented pyrolytic graphite (HOPG), FG has pronounced anisotropic properties. Due to high in-plane thermal conductivity and a mass density lower than normal graphite grades, FG might be of interest for applications in beam dumps and beam catchers for diluting the energy deposition by the primary beam and passive cooling. Moreover, the initial well-ordered structure, with little amount of defects makes this material a good model system for studying beam induced defect formation in ideal graphite.

A series of ~22 µm thick FG samples were irradiated in stacks of 3 samples with 5.9 MeV/u Au ions at the UNILAC. According to SRIM calculation, the ion range for these conditions is about 65.8 µm, which almost equals the total thickness of the 3 samples in the irradiated stack. Analysing the individual samples of each stack, it is possible to study the radiation damage at several depth positions along the ion range. The structural analysis of beam induced disorder was performed by Raman spectroscopy on the sample surfaces [1]. The in-plane thermal diffusivity was measured using a Netzsch Laser Flash Apparatus.

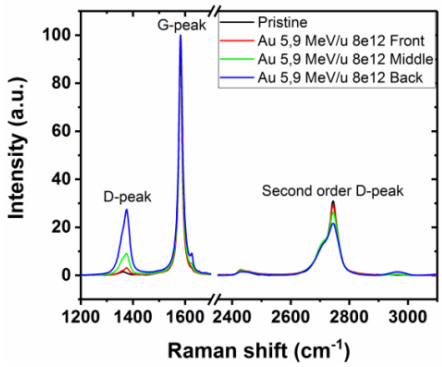


Figure 1: Raman spectra measured on on the front surface of a pristine sample and of the 3 stacked samples irradiated with 5.9 MeV/u Au ions (8×10^{12} ions/cm^2).

For samples exposed to the same fluence in a stack, the intensity of the normalized defect band (D peak) increases with depth (Fig. 1) demonstrating the increasing beam induced defects concentration along the ion range. For all applied fluences the intensity ratio of the D and G peak, I(D)/I(G), grows with penetration depth of the ions, following the trend of the nuclear energy loss of Au ions in flexible graphite (Fig. 2).

Another evidence of non-homogeneous radiation damage along the ion range comes from the degradation of in-plane thermal diffusivity of the irradiated FG samples (Fig. 3). The values measured for the middle samples in a stack are lower in comparison with the respective front sample. This is consistent with the results of Raman spectroscopy and SRIM calculations. For back samples, the thermal diffusivity values are larger showing also a lower decrease with fluence. This effect is due to the fact that the beam was stopped in these samples. As a result, an undamaged layer remains contributing to the measured effective thermal diffusivity.

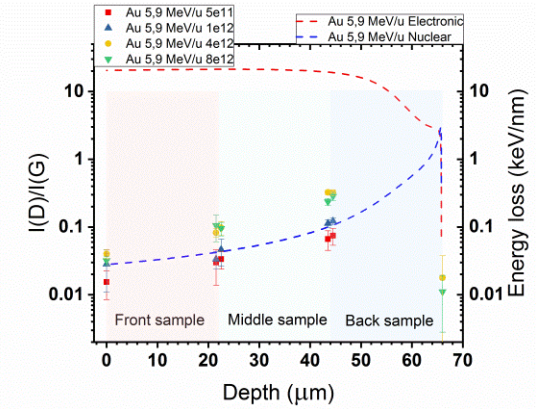


Figure 2: Intensity ratio of D- over G-bands measured on front and back surfaces of FG samples as a function of ion penetration depth. Dashed lines show the corresponding electronic (red) and nuclear (blue) energy loss.

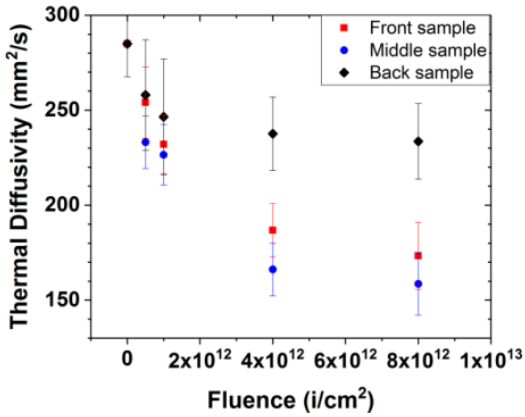


Figure 3: In-plane thermal diffusivity of FG samples as a function of fluence for 5.9 MeV/u Au ions.

The well-ordered crystalline structure of FG makes it sensitive to point defects, produced by elastic collisions of projectile ions with target atoms. Even small amounts of defects lead to significant changes in material properties. This can explain observed non-homogeneous damage along the ion range, following the evolution of the nuclear energy loss with sample depth. Further structural analysis and electron microscopy are required for better understanding the nature of the defects.

*This work has received funding from the European Union's Horizon 2020 Research and Innovation program under Grant Agreement No 730871.

[1] A.C. Ferrari, D.M. Basko, Nat. Nanotechnol. 8 (2013) 235–246.

Ion-induced desorption and sputtering from frozen CO layers

L. Kirsch[1,2], A. Warth[2], V. Velthaus[1,2], C. Trautmann[2,3], and M. Bender[2]

[1]Hochschule RheinMain, Rüsselsheim, Germany; [2]GSI, Darmstadt, Germany; [3]TU Darmstadt, Germany

In heavy ion accelerators, beam losses can stimulate extensive release of gas, e.g. from the wall of the beam tube or vacuum chamber. This so-called ion-induced desorption can put a stable accelerator operation at risk. Systematic research and development has led to a simple mitigation technique to overcome high desorption yields and significantly improve the problematic dynamic vacuum conditions. New accelerators more often use superconducting cryogenic structures. As the sticking probability of gas on cold surfaces is high, a significant surface coverage can be accumulated over time and could act as a source of desorbing gas.

Experimental

Heavy ion-induced desorption yields from frozen gas layers were measured as a function of layer thickness. CO as prominent gas within heavy ion-induced desorption was frozen onto a gold-coated copper plate at 7.5 K. Desorption yields were measured in terms of pressure increase during irradiation for growing CO layer thicknesses. The complete cryostat is shown in figure 1. CO gas was introduced into the setup at increasing pressure levels and for increasing time spans, resulting in a growing surface coverage of CO ice between one and 300 monolayers. The layer growth was controlled by pressure and time and complimentary by a quartz microbalance.

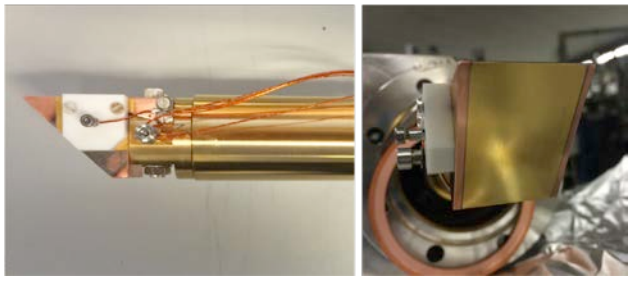


Figure 1: Left: Cryostat assembly with view onto the quartz microbalance. Right: view on sample region that is irradiated by the ion beam.

The gold-coated surface including the ice layer was irradiated under normal incidence by 4.8 MeV/u Au ions delivered by the UNILAC. In the past, similar experiments were conducted at CERN LINAC 3 with 4.2 MeV/u Pb ions [1] and at GSI HLI with 1.4 MeV/u Xe ions [2]. In this work, we also varied the charge state of the ions (Au^{27+} and Au^{54+}) with otherwise constant parameters by inserting a stripper foil at the entrance to the M-branch. To select a certain charge state, the M1 beam line to the irradiation chamber was used as mass-to-charge-filter.

Results

The measured pressure increase was normalized to the ion current. This value is noted as desorption yield in arbitrary units and is plotted versus surface coverage (gas load) in Fig. 2. Note that 10^{19} CO molecules per m^2 correspond to roughly one monolayer.

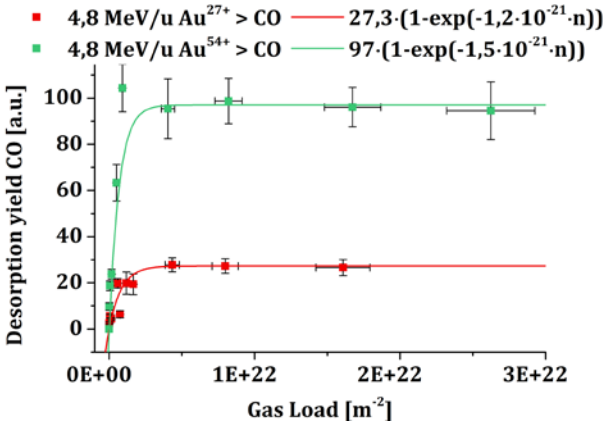


Figure 2: CO desorption yield as a function of the gas load for two different charge states of the projectile ions.

The desorption yield steeply increases with the first few ice layers, followed by a saturation of the yield at about 30-50 CO layers. This behavior was also observed in the experiments at CERN LINAC 3 [1] and GSI HLI [2]. The experimental values were fitted by an asymptotic equation as

$$\eta = \eta_0 \left(1 - e^{-(n_{sat} - n)}\right) \quad (1)$$

n_{sat} is the saturation value. The saturation implies that the desorption originates from surface-close regions, with a maximum contributing depth that is exceeded at 30-50 monolayers.

The value of η_0 is approximately a factor of 4 higher for Au^{54+} ions as compared to Au^{27+} ions. This indicates a linear energy loss scaling of the desorption yield because the charge state of the two projectiles differs by a factor of two and the energy loss depends on the square of the charge state. Our finding is another evidence that desorption occurs at surface-close regions of the target as the charge state of the projectile ion changes rapidly when penetrating into the target.

At present, the cryostat is being modified to meet the requirements of the ToF-SIMS setup at the M1 beam line. Future ToF-SIMS experiments will clarify whether CO is desorbed as molecule or as larger cluster.

References

[1] E. Mahner et al., Phys. Rev. ST Accel. Beams 14, 050102 (2011)

[2] D.P. Holzer et al., Phys. Rev. ST Accel. Beams 16, 083201 (2013)

 DOI:10.15120/GR-2018-1

Outgassing of gold-coated copper samples

B. Tietz[1,3], V. Velthaus[2,3], L. Bozyk[3], B. Lommel[3], B. Kindler[3], C. Trautmann[3,4], and M. Bender[3]

[1]THM, Friedberg, Germany; [2]Hochschule RheinMain, Rüsselsheim, Germany; [3]GSI Helmholtzzentrum, Darmstadt, Germany, [4]Technische Universität Darmstadt, Germany

Heavy ion ring accelerators suffer from dynamic vacuum increase due to ion-induced desorption. Lost beam ions collide with the vacuum vessel and trigger the release of gas. The resulting pressure rise leads to more beam losses. This self-amplifying effect is a severe intensity limitation and affects the design and operation of next generation heavy ion accelerators.

A common mitigation of dynamic vacuum deterioration is the installation of ion-catcher systems in beam-loss regions. These so-called collimators ensure beam losses in a controlled manner by providing increased pumping speed and perpendicular beam impact. In addition, the collimator block has to be made of low-desorbing material. Gold-coated copper was established as material with the lowest desorption yield under different beam parameters. The low desorption can be explained by the high thermal conductivity of copper. The gold coating prevents the surface from oxidation. As gold and copper diffuse into each other, a barrier layer of chromium, nickel or silver is applied. Presently, it is still under investigation which material is best as diffusion barrier.

Technically there are three methods available for coating the copper blocks: (i) electroplating, (ii) thermal evaporation coating, and (iii) sputter coating. The latter two methods use high vacuum environments, with an applied process-gas pressure in case of sputtering. This leads to the risk of process-gas inclusions in sputter coatings. Sputter coatings have higher adhesive forces on the substrate compared to evaporation-coated layers. Electro-deposition on the other hand uses a rather undefined environment with a high probability of impurity inclusions. The aim of this work is to investigate the content of volatile species (such as C, N, and O) released from the coatings produced by different methods and of various layer thicknesses. Volatile species are suspected candidates that degrade the dynamic vacuum and therefore have to be minimized.

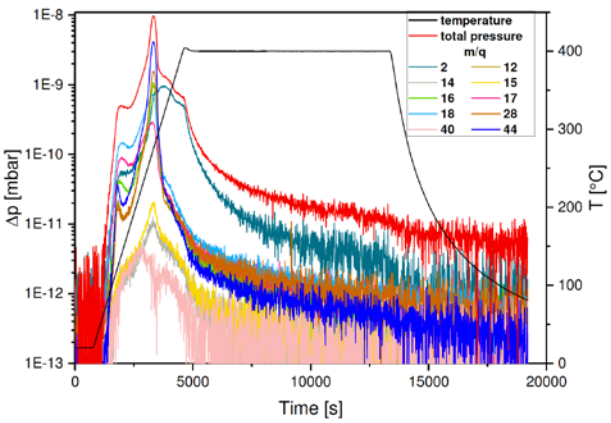


Figure 1: Temperature and evolution of pressure increase as a function of time for different gas species.

A recent measurement campaign is dedicated to determine the amount of volatile species in the layers by thermal desorption spectroscopy performed in a newly designed setup [1]. The samples are introduced into the vacuum chamber by a load lock. The temperature ramp was chosen to be 0.1 K/s with a maximum temperature of 400° C. After heating up, the ultimate temperature was kept for roughly 2 hours to test if the outgassing reduces at high temperature over time. The desorbed gas from the heated surface is introduced into an analyzing vessel where the amount and species of thermally desorbed gas is determined with a quadrupole mass spectrometer. Figure 1 shows the temperature ramp and pressure evolution for different gas species as a function of time. The base pressure was approximately 4e-11 mbar.

The integral of the pressure curve (example shown in figure 1) results in the total amount of gas desorbed during the heating cycle. Figure 2 presents this number as a function of the layer thickness for coated and uncoated copper samples. The different barrier materials (Ni, Cr and Ag) and the Au layer were sputter coated with the same thickness of both layers. In addition, samples with barrier material only, i.e., without the Au layer, were investigated (not shown). Their outgassing is almost the same as for gold-coated samples.

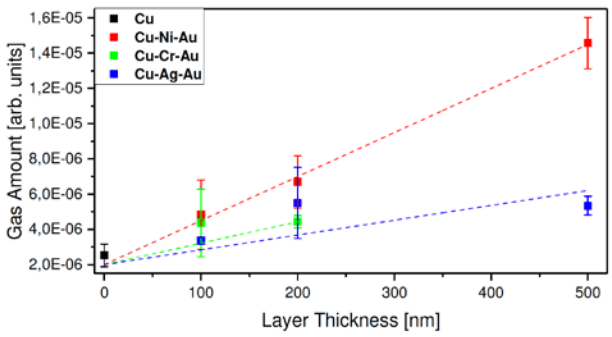


Figure 2: Outgassing amount as a function of layer thickness (barrier and gold) for different samples.

Comparing the different barrier materials, the relative outgassing of Ni rises stronger with increasing layer thickness than the value of Ag and Cr. This means that Ag provides the least outgassing barrier layer among the investigated materials. We found out that the gold layer itself does not contribute notably to the outgassing, whereas pure copper shows notable outgassing, emphasizing the importance of the cleanliness of the interface between Cu and any coating.

References

[1] V. Velthaus et al., “A new setup for the investigation of stimulated desorption”, GSI Scientific Report 2015

Radiolysis of polymers: temperature effect

M. Ferry[1], S. Esnouf[1], M. Cornaton[1], O. Okamba-Diogo[1], J.M. Ramillon[2], D. Severin[3]

[1] Den-Service d'Étude du Comportement des Radionucléides (SECR), CEA, Université Paris-Saclay, Gif-sur-Yvette, France; [2] CIMAP (CEA/CNRS/ENSICaen/UCN), Caen, France; [3] GSI, Darmstadt, Germany

Polymers are components of nuclear waste in intermediate level waste packages because of their use in active handling facilities (glove box operations for instance). In these packages, these materials are in contact with actinides and are thus degraded upon gamma but also alpha irradiation. Among other defects, gas such as hydrogen will be released and the accumulation of these gases can affect the integrity of the waste container. For safety purpose, it is thus necessary to predict the quantity of gases released by the different organic materials. Prior to model this process, the influence of the following parameters has to be taken into account: dose rate, dose, atmosphere, LET (Linear Energy Transfer) and temperature.

This last parameter is essentially relevant to transportation. The temperature inside the packaging is supposed to be above room temperature (generally close to 50°C) during standard conditions. Nevertheless, safety scenario during transportation of nuclear waste packages takes into account, e.g., a road accident with fire with a temperature increase in the container up to 150°C during a short time.

The effect of temperature on the radiolysis of polymers is the subject of only few studies [1-3]. Moreover, there is no information about the influence of temperature on the radiolysis of polymers at high LET irradiation, which has been the topic of this work.

The polymer samples were irradiated in a dedicated chamber (CHIMERE, Figure 1) designed by the CIMAP team (Caen, France). Two valves enable gas sampling after irradiation and flushing the chamber. Gases were collected and analysed by µ-GC gas chromatography.

The range of temperature investigated was between room temperature and 120°C. The GSI facility has the advantage to deliver beams at high dose rates yielding short enough irradiation times to prevent a significant contribution of the thermolysis to gas release.

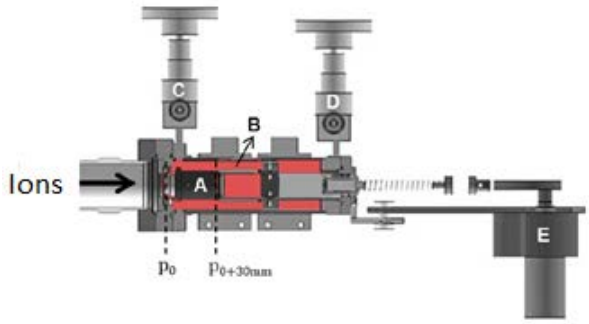


Figure 1: CHIMERE chamber attached at the end of M3-beamline at the UNILAC. The setup includes (A) sample holder, (B) the irradiation chamber, (C and D) valves for gas conditioning of the chamber and gas sampling after irradiation, (E) system that allows sample displacement during irradiation (not used in this experiment).

Polymer chosen was HDPE (High Density Polyethylene) provided by Goodfellow. Samples were irradiated with carbon ions of 5.9 MeV/u. The objective was to be as close as possible to the LET of alpha rays. In this first experiment, all the irradiations were realized under inert atmosphere.

Figure 2 presents the hydrogen radiation chemical yields, extrapolated at zero dose, from our irradiation experiment with carbon ions under nitrogen atmosphere (black rectangles). The plot also shows data from Seguchi et al. [2], who used gamma rays under vacuum (red circles).

This first series of results indicates that the response of HDPE is similar at low LET (gamma) and high LET (GSI ions). From room temperature to about 80°C, the hydrogen radiation chemical yield remains almost constant. Above 80°C, it increases with temperature, and this increase seems to be more pronounced at high LET.

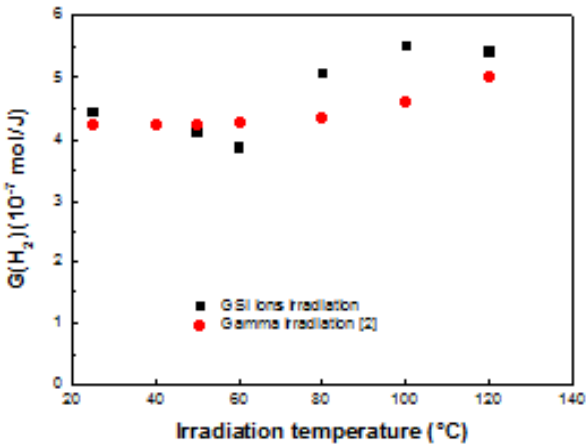


Figure 2: Hydrogen radiation chemical yields, extrapolated at zero dose, as a function of the irradiation temperature. Irradiations were performed with gamma rays under vacuum (red circles) [2] and with carbon ions under nitrogen atmosphere (this work, black squares).

References

[1] T. Okada and L. Mandelkern, "Radiation Chemistry of Linear polyethylene", in "The Radiation Chemistry of Macromolecules", Vol. I, Academic Press, New York, ed. M. Dole (1972) 322

[2] T. Seguchi, Y. Haruyama and M. Sugimoto, "Temperature dependence of gas evolution from polyolefins on irradiation under vacuum", Radiat. Phys. Chem. 85 (2013) 124

[3] A.A. Miller, "Radiation Chemistry of Polyvinyl Chloride", J. Phys. Chem. 63 (1959) 1755

 DOI:10.15120/GR-2018-1

In situ small angle x-ray scattering measurements of ion tracks in poly-carbonate*

P. Kluth[1,#], A. Hadley[1], C. Notthoff[1], M. Grigg[1], P. Mota-Santiago[1], U. H. Hossain[1], N. Kirby[2], M. E. Toimil-Molares[3], C. Trautmann[3,4]

[1]Australian National University (ANU), ACT, Australia; [2]Australian Synchrotron, ANSTO, VIC, Australia; [3]GSI, Darmstadt, Germany; [4]Technische Universität, Darmstadt, Germany.

Membranes containing nano-sized pores have many important applications in the areas of ultra-filtration, bio- and medical sensing, nano-fluidics, and nano-electronic devices. These applications require pores to be nano-engineered with controlled shapes and uniform sizes. Nano-pore membranes with extremely narrow pore size distributions can be fabricated in a variety of polymers by irradiation with high-energy heavy ions followed by chemical track etching, yielding so called 'track-etched membranes'. The crucial step for the fabrication of these membranes is the etching process in particular during the initial stage. While the technique is commercially used for the fabrication of nano- and micro-pore membranes, a detailed understanding of the track etching process is still lacking, predominantly due to challenges for characterisation of the high aspect ratio pore morphologies. Here, we present our recently developed method for measuring the nanopores during etching in situ using synchrotron based small angle x-ray scattering (SAXS).

Experimental

30 μm thick films of polycarbonate (PC) were irradiated with 2.1 GeV Au ions (10^9 cm^{-2}) at the GSI UNILAC accelerator. In situ SAXS measurements were conducted at the SAXS/WAXS beamline of the Australian Synchrotron using 3M NaOH at different temperatures. A custom-built sample cell was used that allows temperature control and injection of chemicals from both sides of the membrane with controlled flow rate. Measurements were done in transmission configuration and scattering intensity patterns were recorded on a 2-dimensional Pilatus 1M hybrid pixel detector with a time resolution of ~10s.

Figure 1 (a) shows a SAXS detector image of the PC membrane after etching for 20.5 min at 55°C and (b) the 1D scattering intensities extracted along the narrow streak of high intensity (dark contrast) in (a) for different etching times.

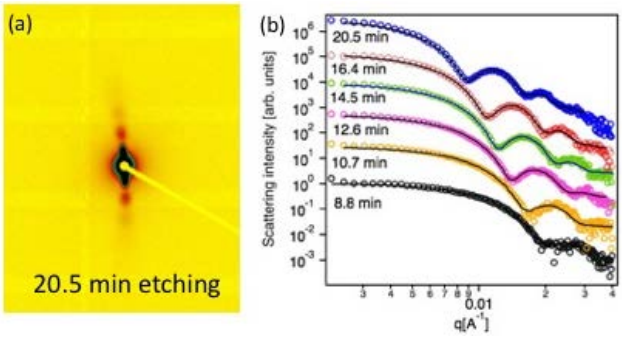


Figure 1: (a) SAXS image for pores etched in situ after 20.5 min; (b) Extracted scattering intensities (symbols) and cylinder fits (solid lines) for different etching times (offset for clarity).

Results and Discussion

The data is best reproduced by a simple cylinder model where the main fitting parameter is the cylinder radius. This is consistent with the formation of largely cylindrical pores [1]. Figure 2 (a) shows the pore radii as a function of etching time for etching at different temperatures. The track radius grows linearly with time for all temperatures above a radius of about 20 nm. An Arrhenius plot of the etching rates extracted from the linear fits to the plots in Fig. (a) is shown in (b). An activation of 0.56±0.03 eV for the track etching process has been extracted from the plot.

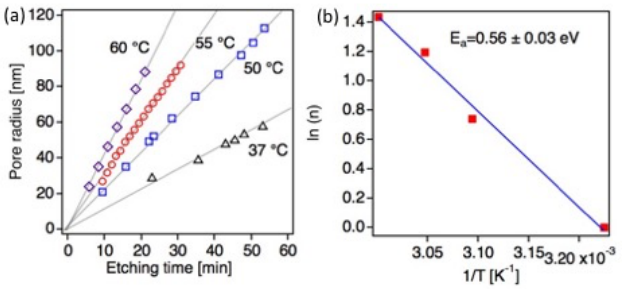


Figure 2: (a) Pore radius as a function of etching time for etching at different temperatures; (b) Arrhenius plot for the etching rate n.

In the early stages of etching, the data evaluation is more complex as the process is dominated by the etching along the ion damaged zone, but first estimates show a longitudinal etching rate of > 5 μm/min, i.e. more than 3 orders of magnitude higher than the radial etching rate. The results clearly demonstrate that the in situ characterisation using SAXS can yield new and more accurate results on the track etching process than previously achieved and opens up the opportunity for an in depth study of the track etching process in many materials. Improvements to the method that are currently being implemented include electrodes that enable monitoring trans-membrane currents while applying a bias between the cells as well as reducing the time resolution to about 1 s. The setup also allows us to study the pore morphology of membranes in liquid environments under working conditions such as during molecular transport.

* Work supported by the Australian Research Council (ARC) and the Australian Synchrotron).

patrick.kluth@anu.edu.au

References

[1] M.-E. Toimil-Molares, Beilstein J. Nanotechnol. 2012, 3, 860–883

Ion sieving using nanoporous polymeric membranes

M. Wang[1], P. Wang[1], F. Liu[1,2], P. Apel[3], P. Kluth[4], C. Traumann[5] and Y. Wang[1]

[1]State Key Laboratory of Nuclear Physics and Technology, Peking University, China; [2]Center for Quantitative Biology, Peking University, China; [3]Flerov Laboratory of Nuclear Reactions, Joint Institute for Nuclear Research, Dubna, Russian Federation; [4]Department of Electronic Materials Engineering, Research School of Physics and Engineering, Australian National University, Canberra, Australia; [5]GSI Helmholtzzentrum and TU Darmstadt, Darmstadt, Germany

The great potential of nanoporous membranes for water filtration and chemical separation has been challenged by the trade-off between selectivity and permeability. High ionic selectivity through nanopores can be achieved as the pore diameters approach the subnanometer scale. In this project, we are interested in using ion-track membranes with parallel oriented subnanometer pores produced without chemical etching but solely by exposing ion-irradiated polymer foils to sufficient UV radiation. 12-µm thick polyethylene terephthalate (PET, Hostaphan®) films were irradiated at the UNILAC with GeV heavy ions and subsequently exposed to UV radiation for 3 h.

The resulting nanopores show ionic transport selectivity spanning more than 6 orders of magnitude for different ion species (Fig. 1a). The order of the transport rate is $Li^+ > Na^+ > K^+ > Cs^+ \gg Mg^{2+} > Ca^{2+} > Ba^{2+}$. Heavy metal ions such as Cd^{2+} and anions are blocked (Fig. 1a). The transport can be switched off with a sharp transition by decreasing the pH value of the electrolyte (Fig. 1b). Structural measurements and molecular dynamics simulations suggest that the ionic transport is attributed to negatively charged nanopores with pore radii of ~0.3 nm. The selectivity is suggested to be associated with the dehydration effect which leads to different width of the hydration shell (Fig. 1c).

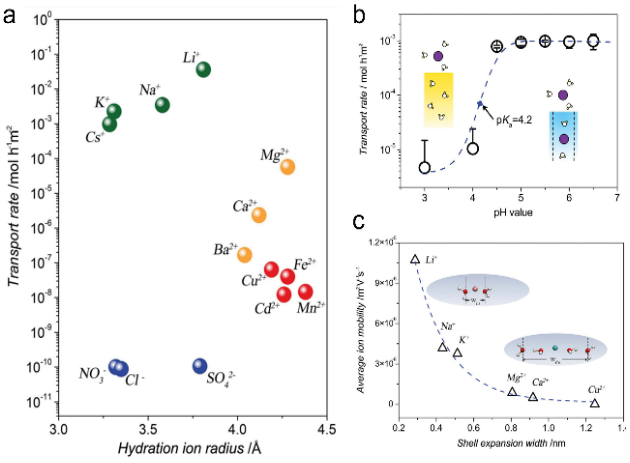


Figure 1: Transport of the electrolyte ions in nanoporous PET Hostaphan® membranes. (a) Ionic transport rates of cations as a function of corresponding hydration radius. (b) Average transport rate of Na^+ ions through membranes as a function of pH value. (c) The average ion mobility of the cations as a function of the width of the hydration shell, w (see illustration in the insets).

Despite the excellent selectivity, the application of the PET Hostaphan® films seems to be limited because their transport rates for K^+ ions are only $2 \times 10^{-3}\ mol\ h^{-1}\ m^{-2}$. By selecting 2-µm-thick PET Lumirror® films, we further generated nanoporous polymer membranes with an excellent balance between selectivity and permeability of ions.

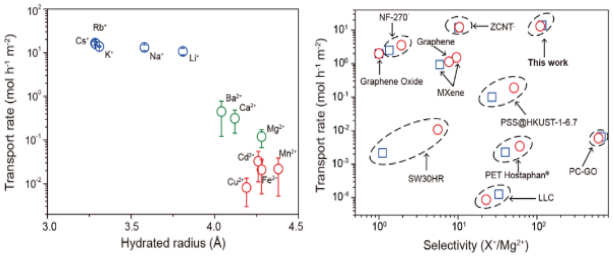


Figure 2: Transport rates and selectivity of nanoporous PET Lumirror® membranes. (left) Transport rates of alkali metal ions (blue), alkaline earth metal ions (green), and transition metal and heavy metal ions (red) measured with ICP, as a function of the hydration radius of the ions. (right) Transport rates versus selectivity of various nanoporous membranes; the ionic sieving membrane tested in this study excels in both transport rates and ionic selectivity of K^+/Mg^{2+} (blue) and Na^+/Mg^{2+} (red)

These nanoporous PET Lumirror® membranes show a high transport rate of K^+ ions of up to 14 $mol\ h^{-1}\ m^{-2}$ and a selectivity of alkali metal ions over heavy metal ions of >500 (Fig. 2, left). Combining transport experiments and molecular dynamics simulations with a polymeric nanopore model, we demonstrated that the high permeability is attributable to the presence of nanopores with a radius of ~0.5 nm and a density of up to $5 \times 10^{10}\ cm^{-2}$. The nanoporous PET Lumirror® film simultaneously excels in both permeability and selectivity, demonstrating great application potential for ion separation (Fig. 2, right). This artificial nanopore system shows great potential for industrial applications where ultrafast ionic sieves are required.

References

[1] Wen, Qi, Dongxiao Yan, Feng Liu, Yugang Wang, et al. Adv. Funct. Mater. 26 (2016) 5796–5803

[2] Wang, Pengfei, Mao Wang, Feng Liu, Yugang Wang, et al. Nature Communications. 9 (2018) 569

 DOI:10.15120/GR-2018-1

Etched ion tracks in SiO_2: dependence on ion energy and etching parameters*

A. Hadley[1,#], C. Notthoff[1], P. Mota-Santiago[1], U.H. Hossain[1], N. Kirby[2], M.E. Toimil-Molares[3], C.°Trautmann[3,4], and P. Kluth[1]

[1]Australian National University (ANU), ACT, Australia; [2]Australian Synchrotron, VIC, Australia; [3]GSI, Darmstadt, Germany; [4]Technische Universität, Darmstadt, Germany.

Nanopores in Silicon dioxide (SiO_2) have promising applications as sensors and in novel electronic devices due to their chemical and thermal stability [1], and their compatibility with existing electronic device processing tools. The ion track etching method offers a controllable way to produce highly uniform and parallel pores with minimum diameters of just several nanometres. In order to reliably produce pores for specific applications more needs to be understood about the relationship between the un-etched track structure and the resulting etched pores.

A systematic study of the morphology of etched ion tracks in SiO_2 was conducted using synchrotron based small angle x-ray scattering (SAXS) measurements. This method enables us to determine the etch rates in both the radial and axial directions with unprecedented precision.

Experimental

2 µm thick films of SiO_2 were irradiated with 1.1 GeV Au ions (10^8 cm^{-2}) at the GSI UNILAC accelerator and with 185 and 89 MeV Au ions at the ANU Heavy Ion Accelerator Facility. Samples were then etched using 2.5% and 5% aqueous hydrofluoric acid (HF) at room temperature for etch times between 2 and 12 minutes.

SAXS measurements in transmission configuration were conducted at the SAXS/WAXS beamline of the Australian Synchrotron. Scattering intensity patterns were recorded on a 2-dimensional Pilatus 1M hybrid pixel detector. The etched pores were first aligned parallel to the x-ray beam and then a series of measurements was performed with the etched ion tracks tilted by an angle γ with respect to the x-ray beam.

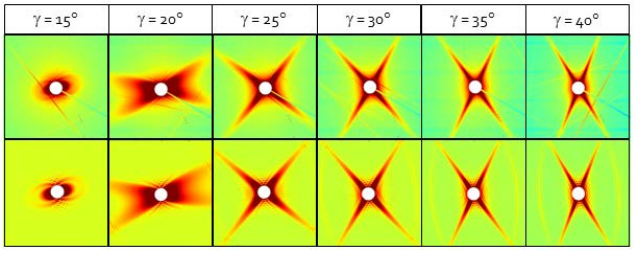


Fig. 1: Tilt sequence of SAXS measurements with the experimentally obtained images on the top row, and fits of the data shown in the bottom row.

Figure 1 shows a tilt sequence of SAXS measurements, with the experimental images shown the top row, and the calculated fits to each image shown on the bottom row. Each data point is an average of the complete tilt sequence for that sample.

Results and Discussion

To analyse the data, we developed a routine to numerically fit the 2D detector images using a conical pore model. The form factor for this model is given in Equation 1, where the Z direction is parallel to the x-ray beam, H is the height of the cone, J_1 is the Bessel function of the first order, and $\Delta\rho_0$ is the density contrast.

$$f(\vec{q}) \propto \Delta\rho_0 \int_0^H J_1(q_r R_z) \frac{R_z}{q_z} exp^{(izq_z)} dz \quad (1)$$

The model fit reproduces the experimental scattering images very well and yields the length (or height H) of the cone and the half cone opening angle β. The base radii may then be deduced geometrically. Figure 2 shows the half cone opening angles obtained for samples irradiated with the three irradiation conditions described earlier and then etched with etchant concentrations of 2.5% (left) and 5% (right).

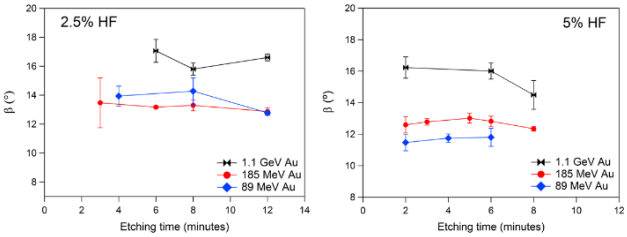


Fig. 2: Measured half cone opening angles for two etchant concentrations plotted as a function of etching time.

The measured cone angles plotted in Fig. 2 highlight the differences observed in etched track morphology for the different irradiation conditions. Tracks generated under higher energy irradiation conditions have a significantly larger cone opening angle. Beyond the region of the irradiation damage of the latent track in the radial direction (not shown), the etch rates can be assumed to resemble the bulk etch rate of SiO_2. In the axial direction, the etch rates are reduced at the higher irradiation energy, consistent with the larger cone angles observed, despite the higher energy loss. For 1.1 GeV, the energy loss is 23 keV/nm, compared with 18 and 12 keV/nm for 185 MeV and 89 MeV Au ions, respectively. Clearly the nature of the irradiation damage differs with the energy, which may be related to the velocity effect. We plan to investigate this further by continued detailed analysis of our results.

* Work supported by the Australian Research Council (ARC) and the Australian Synchrotron.
# andrea.hadley@anu.edu.au

References

[1] D. Fink, A. V. Petrov, K. Hoppe, W. R. Fahrner, R. M. Papaleo, A. S. Berdinsky, A. Chandra, A. Chemseddine, A. Zrineh, A. Biswas, F. Faupel and L. T. Chadderton, NIM B 218 (2004) p. 355-361.

The iNAPO-project: Ion-track etched nanostructures in polymers as a base for ion conducting nanochannels for molecular sensing*

W. Ensinger[1], A. Andrieu-Brunsen[1], M. Biesalski[1], G. Buntkowsky[1], M. Gallei[1], K. Hamacher[1], B. Laube[1], M. Mikosch-Wersching[1], H. F. Schlaak[1], V. Stein[1], G. Thiel[1], A. Tietze[1], M.E. Toimil-Molares[2], C. Trautmann[1,2], N. Van der Vegt[1], M. Vogel[1,]

[1]Technische Universität Darmstadt, Germany, [1]GSI Helmholtzzentrum, Darmstadt, Germany

The LOEWE Research Cluster iNAPO – ion conducting nanopores –deals with the development of nature inspired sensors. The vision is to develop a new generation of nanostructure-based sensor devices, which combine synthetic and biological nanopores[1,2].

The synthesis of solid-state nanopores is conducted by applying the ion track nanotechnology which is based on the irradiation of polymers foils (e.g., 10-30 µm thick polycarbonate PC or polyethylene terephthalate PET) with swift heavy ions (e.g. 2 GeV Au ions) from the GSI UNILAC. When penetrating through the polymer each individual ion produces a cylindrical damage zone of a few nm in diameter. By selective chemical etching the damage tracks are converted into open nanochannels. Suitable irradiation conditions allow us to expose a given sample to one individual ion resulting in a single-pore membrane. Under asymmetric etching conditions (etching solution on one side and etch-stopping solution on the other side), a conical nanopore is generated, with its small aperture being in the few nm range (Fig. 1).

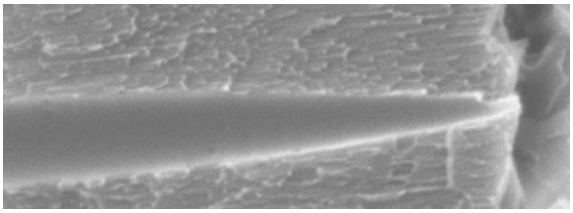


Figure 1: Scanning electron micrograph of cross-section of ion-track etched conical nanopore in a polymer foil.

The iNAPO cluster consists of ten sub-projects covering expertise in synthesis, characterization, simulation and lab-on-chip integration (Fig. 2).

Regarding the synthesis of solid state nanopores, one focus is the chemical modification of the nanopore walls, e.g., by click chemistry or atomic layer deposition. The attached molecules can specifically react with counterpart molecules in a key-lock type reaction. The resulting pore-diameter reduction and the ionic conductivity of the pore is monitored via current measurements in an electrochemical conductivity cell [3,4]. Recording I-V curves allows us to identify current rectification of the nanopores.

One of the iNAPO aims is mimicking structural and functional principles of biological pores [5] and combining their sensitivity and selectivity with synthetic pores for a new generation of sensing devices [6]. Moreover, genetic and protein engineering is used for fabricating proteins and use them as building blocks with specific sensing and switching characteristics [7,8]. High resolution nuclear magnetic resonance spectroscopy and theoretical and computer simulation tools are used to study physico-chemical processes of ion transport in pores and their interaction [9].

Micro-Nano Integration, the incorporation of the pore-containing polymer foils into microfluidic/microelectronic systems is in progress [6]. Planned applications of our nanopore-based sensing devices are for medical diagnostics as well as environmental and process analysis.

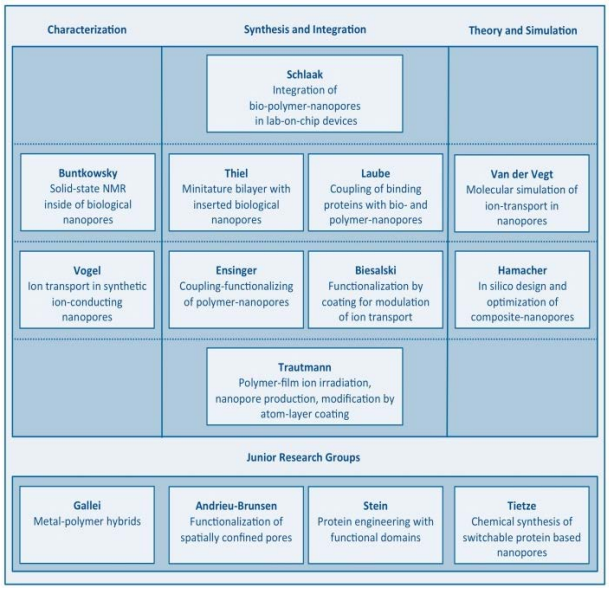


Figure 2: The iNAPO research cluster has three pillars with ten base projects and four junior research projects [1]

*This work has been supported within the frame of the LOEWE project iNAPO by the Hessen State Ministry of Higher Education, Research and the Arts.

References

[1] http://www.inapo.tu-darmstadt.de/inapo/index.en.jsp
[2] W. Ensinger et al., GSI Sci. Rep. 2016 (2017) 261.
[3] G. Perez-Mitta et al.; Small (2018) 1702131; doi: 10.1002/smll.201703144
[4] M. Ali et al.; Langmuir 33 (2017) 9170-9177
[5] S. Smeazzetto et al.; Journal of Electroanalytical Chemistry 812 (2018) 244.
[6] W. Ensinger et al., "The iNAPO Project: Biomimetic Nanopores for a New Generation of Lab-on-Chip Micro Sensors", Proceedings of RAN'17, Barcelona (2017); doi: 10.11159/icnnfc17.141
[7] A.C. Baumruck et al.; Chem. Sci. 9 (2018) 2365; doi: 10.1039/C8SC00004B
[8] V. Stein, V.; Methods Mol Biol. 1596 (2017) 3-25.
[9] N.F.A. van der Vegt et al.; Chem. Rev. 116 (2016) 7626

 DOI:10.15120/GR-2018-1

Integration of ion-track etched membranes modified by atomic layer deposition in microfluidic systems for biochemical sensing*

M. EL Khoury[1], G.R. Distefano[2,3], M.E. Toimil-Molares[2], C. Trautmann[2,4], H.F. Schlaak[1]

Technische Universität Darmstadt, Microtechnology and Electromechanical Systems Laboratory, Darmstadt, Germany; [2] GSI Helmholtzzentrum, Darmstadt, Germany; [3] Technische Universität Darmstadt, Membranbiophysik der Pflanzen, Darmstadt, Germany; [4] Technische Universität Darmstadt, Material- und Geowissenschaften, Darmstadt, Germany

Biological cell membranes consist of proteins and carbohydrates embedded in a phospholipid bilayer in accordance with the fluid mosaic model. This structural organization ensures selective permeability of cell membranes. Thanks to their highly selective and sensitive nature, channel proteins regulate the transport of ions and chemicals as well as the cell-to-cell communication. However, the fragility and long-term instability of biological membranes impede their application as sensors. Solid-state nanochannels, emerged as a valid alternative to fabricate long-lasting stable sensors. In particular, etched ion-track membranes with nanochannels of controlled geometry and size have been developed and characterized as nanofluidic diodes. Currently, efforts are being devoted to develop surface modification techniques that confer specific surface functionalities to these nanochannels [1-3]. These techniques include, e.g., wet chemistry, sputtering, and atomic layer deposition (ALD) [4-5].

We fabricate etched ion-track membranes ALD-coated with Al_2O_3. Applying different thicknesses of the ALD layer, the channel diameter and surface isoelectric point of the membranes are tailored in a systematic manner. Both unmodified and ALD-coated membranes are integrated into a microfluidic system specifically designed to record ion conductivity while enabling optical monitoring of the fluid transport towards and across the membranes.

In a first step, 30 µm thick polycarbonate foils (Makrofol N, Bayer) are irradiated with 2-GeV Au ions at the GSI UNILAC. The irradiated foils are subsequently immersed in a 6 mol/L NaOH solution at 50 °C to selectively dissolve the ion tracks and convert them into open cylindrical channels. In a second step, some of the membranes are ALD coated with Al_2O_3 of defined thickness. The ALD process uses trimethylaluminium ($(CH_3)_3Al_2$, electronic grade, SAFC Hitech) and deionised water as precursors during sequential gas-phase reactions taking place at 110 °C [4]. The deposition process is homogeneous along the entire length of the nanochannels allowing a precise and controllable decrease of the diameter.

To produce the microsystem [6], a 20 nm thick chrome and 150 nm thick gold layer are deposited on a borosilicate glass substrate (BOROFLOAT® 33) by thermal evaporation. Both metal layers are etched chemically to form the electrodes and electrical lines. To fabricate the first microfluidic channel, a thin layer of the adhesion promoter (TI Prime) and a 5 µm layer of the photoresist SU-8 are applied on the substrate. A 200 µm thick dry film epoxy photoresist (DJ MicroLaminates' SUEX) is laminated on the SU-8 layer. Both SU-8 and SUEX are patterned by UV lithography. A 25 µm thin dry film of photoresist (DJ MicroLaminates' ADEX) is laminated and structured on the microfluidic channels. Two etched ion-track membranes (one ALD-modified and one unmodified) are positioned between the microfluidic channels and laminated at 65 °C. The fabricated microfluidic system is shown in figure. 1.

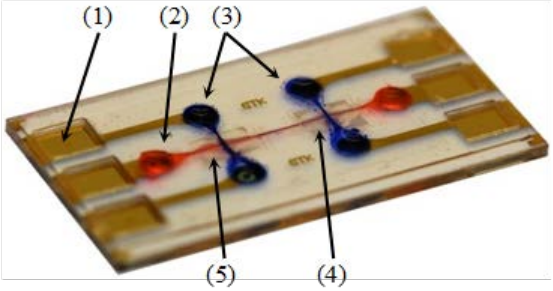


Figure 1: Photo of microfluidic system: (1) measuring electrodes, (2) lower microfluidic channel filled with KCl and red ink, (3) upper microfluidic channel filled with KCl and blue ink; (4) ALD-coated nanopore membrane, (5) unmodified nanopore-membrane.

* Work supported by the Hessen State Ministry of Higher Education, Research and the Arts in the frame of the LOEWE project iNAPO.

References

[1] N. Sobel, C. Hess, M. Lukas, A. Spende, B. Stühn, M. E. Toimil-Molares, C. Trautmann, Beilstein J. of Nanotechnol. Vol. 6, 472–479 (2015). DOI:10.3762/bjnano.6.48.

[2] W. Ensinger, M. Ali, S. Nasir, I. Duznovic, C. Trautmann, M. E. Toimil-Molares, G. R. Distefano, B. Laube, M. Bernhard, M. Mikosch-Wersching, H. F. Schlaak, M. El Khoury, 2nd World Congress on Recent Advances in Nanotechnology (RAN'17), Barcelona, Spain (2017). DOI: 10.11159/icnnfc17.141.

[3] G. Pérez-Mitta, A. G. Albesa, C. Trautmann, M. E. Toimil-Molares, O. Azzaroni, Chemical Science, Vol. 8, pp. 890-913, (2017).

[4] A. Spende, N. Sobel, M. Lukas, R. Zierold, J. C. Riedl, L. Gura, I. Schubert, J. M. Montero Moreno, K. Nielsch, B. Stühn, C. Hess, C. Trautmann, M. E. Toimil-Molares, Vol. 26, p. 335301, (2015).

[5] P. Chen, T. Mitsui, D. B. Farmer, J. Golovchenko, R. G. Gordon, D. Branton, Nano letters, Vol 4, Nr. 7, p. 1333, (2004)

[6] M. E. Khoury, I. Duznovic, M. Ali, W. Ensinger, and H. F. Schlaak, MikroSystemTechnik Kongress 2017, München (2017), VDE-Verlag, pp. 175-178

Selective recognition of histamine with single nanofluidic pores*

M. Ali[1,2], I. Duznovic[2], S. Nasir[2], W. Ensinger[2]

[1]GSI, Darmstadt, Germany; [2]TU Darmstadt, Germany

Neurotransmitters in living organisms are considered as chemical messengers that transmit neurological information in the form of electrical signals within the cellular system. Histamine (Hm) is an important neurotransmitter which exists in human body in trace amounts and plays a key role in physiological functions controlled by the brain. An excess of Hm level in the body can cause Alzheimer's disease, abnormal arousal, asthma, allergies and some other neuropsychiatric disorders [1].

Different methods have already been developed for the detection of this biologically important amine. However, most of them need expensive instrumentation and are time consuming. It is of interest to design simple and low-cost detection techniques with fast response times. In this context, here we describe a new label-free Hm detection method using a nanofluidic device. Recently, asymmetric nanopores have been widely used for the miniaturization of (bio)chemical sensing devices because of their unique transport properties [2].

The proposed sensor is based on single conical nanopores fabricated in polyethylene terephthalate (PET) membranes through asymmetric track-etching technique [3]. For this purpose, first the inner pore surface is decorated with nitrilotriacetic (NTA) moieties followed by Ni2+ ion complexation to form NTA–Ni2+ chelates. These metal chelates act as recognition sites for the specific recognition of Hm analyte. The modification process resulted in the changes of pore surface charge density which in turn affects the rectification of the pore.

Then, the modified pore is successfully employed as a sensing device for the selective recognition of neurotransmitters [4]. To this end, Hm is chosen as a model neurotransmitter. Hm contains a primary amino group, a secondary imidazole nitrogen and a tertiary imidazole nitrogen atom. The secondary nitrogen does not take part in coordination reaction. Hm is then considered as a bidentate ligand and makes a six membered ring with metal ion (Figure 1A). For the control experiment, various neurotransmitters including glycine (Gly), serotonin (5-HT), gamma-aminobutyric acid (GABA) and dopamine (DA) are employed. An aqueous KCl (100 mM, pH 7.1) solution is used to prepare the analyte concentrations.

Figure 1B (left panel) shows the changes observed in the I–V curves when the modified nanopore is exposed to electrolyte solutions having different Hm concentrations. On increasing Hm concentration, the displacement rate of Ni^{2+} ions from the NTA moieties was increased. This leads to a successive increase in the pore surface charges, thus enhancing the pore permselectivity and rectification characteristics.

Figure 1B (right panel) shows the changes in the I–V curves on exposing the sensor to the various neurotransmitters, separately. The Gly and 5-HT hardly induce any change in the ion transport characteristics. With GABA and DA, the pore slightly rectifies the ion current, suggesting a partial removal of chelated Ni^{2+} ions. In contrast, Hm almost completely removes the metal ions from the NTA–Ni^{2+} chelates, leading to well defined current rectification.

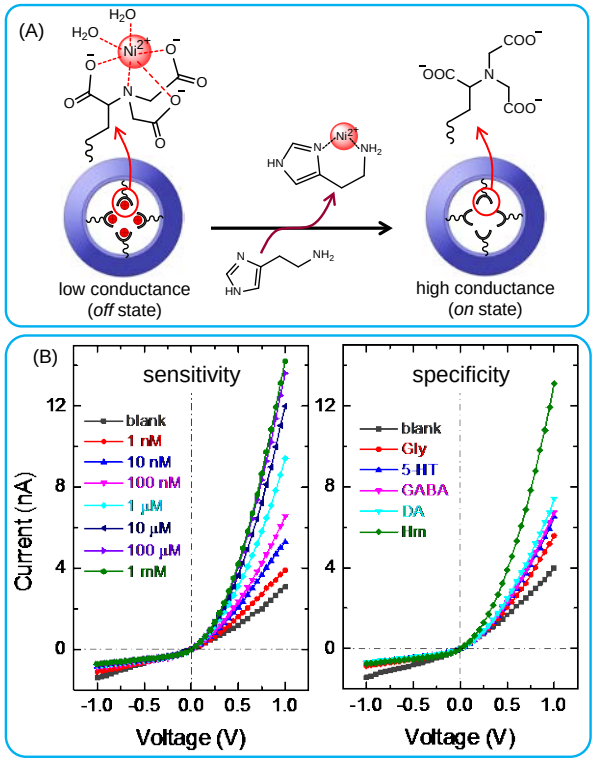


Figure 1: (A) Scheme representing the changes in surface chemistry of the nanopore having Ni(II)–NTA complexes, and the NTA regeneration on exposure to Hm solution. (B) I–V curves of modified pore (d ~ 45 nm) on exposure to different Hm concentrations (left panel) and various analytes (1 mM) in the electrolyte solution: Gly, 5-HT, GABA, DA and Hm (right panel).

In summary, we have demonstrated the miniaturization of a nanofluidic sensor for Hm recognition based on the metal ion displacement mechanism. The sensor exhibited high sensitivity, specificity, and reusability towards Hm detection. It has the potential to be clinically used for monitoring the concentration of biologically relevant neurotransmitters.

* Work supported by the Hessen State Ministry of Higher Education, Research and the Arts in the frame of the LOEWE project iNAPO.

References

[1] B. Webster, Neurotransmitter Systems and Function: Overview, John Wiley & Sons, Ltd. 2002.
[2] Perez-Mitta et al. Chem. Sci. 8 (2017) 890.
[3] P.Y. Apel et al. Nucl. Instr. Meth. Phys.B 184 (2001) 337.
[4] M. Ali et al. Colloids Surf. B; 150 (2017) 201.

 DOI:10.15120/GR-2018-1

Translocation of polystyrene nanoparticles through track-etched nanopores*

N. Goethals[1,2], G. Distefano[1,3], C. Trautmann[1,3], M. E. Toimil-Molares[1]

[1]GSI, Darmstadt, Germany; [2]THM, Gießen, Germany; [3] TU Darmstadt, Germany

The idea of using nanopores as sensors for biomolecules and DNA was developed in the 1990s by Deamer and Akeson [1]. Biological pores are transmembrane protein channels that are typically embedded in a lipid bilayer of cell membranes. Solid-state nanopores, in turn, are produced from various materials (e.g. silicon, graphene, polymers). Their geometry and size can be tailored, and their surface can be easily modified to change their chemical and physical properties. They are robust and more stable, making them excellent and promising platforms for DNA and protein sequencing. [2]

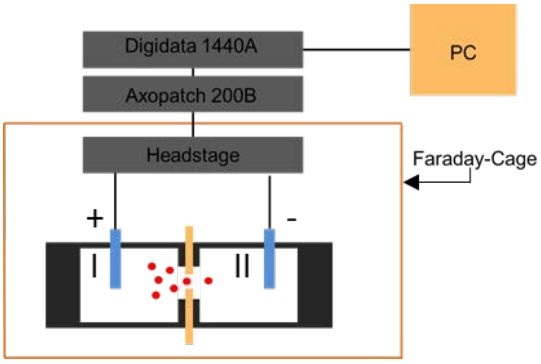


Figure 1: Schematic of experimental setup to measure translocation of nanoparticles (shown in red).

Foils of 12 µm thick polyethylene teraphthalate (PET) (Hostaphan, RN12, Hoechst) were irradiated with single 11.4 MeV/u Au ions at the linear accelerator UNILAC. For better echability, the irradiated foils were exposed to UV-light (1 h each side). Track etching was performed in a 2 M NaOH solution at 60°C. To obtain channels with various diameters, the foils were etched in groups of 4 for different times. To determine the diameter of each single nanochannel, the membrane was placed in an electrochemical cell separating two chambers filled with 1 M KCl solution (specific conductivity δ = 113.5 mS/cm). Two Ag/AgCl electrodes are immersed in the compartments, and connected to an Axopatch 200B amplifier (Molecular Devices) (Fig. 1). Assuming cylindrical geometry, the diameter of each nanopore was determined by

$$d = 2 * \sqrt{\frac{L*I}{\delta 2\pi*V}} \quad (1)$$

where d and L are diameter and length of the nanopore, respectively. The diameter of the single channels was adjusted between 13 ± 2 nm and 235 ± 5 nm by varying the etching time from 2 to 20 min.

During translocation experiments, the potential applied across the membrane leads to a force that drags positively charged amine modified polyestyrene (PS) nanoparticles (red) through the nanopore from chamber I to chamber II. The whole cell is placed in a Faraday-cage to minimize noise. Previously, experiments reported the transport of larger PS nanoparticles through a µm-size channel [3].

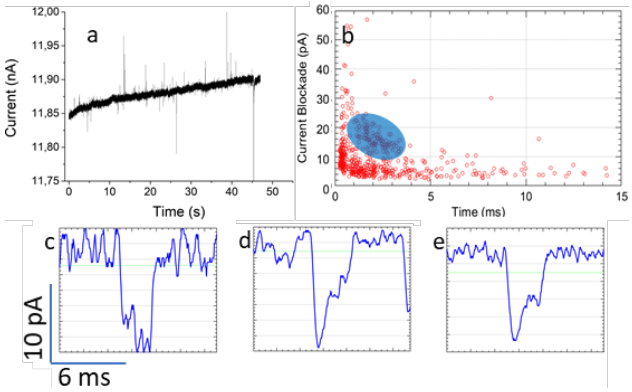


Figure 2: (a) Current-time trace. (b) Scatter plot of 100 nm amine functionalized PS nanoparticles that translocate through a 235 nm PET single nanopore in 0.01 M KCL electrolyte at pH 3. The events in the group marked in the blue area are identified as translocation events through the pore. (c-e) examples of 3 different events of this group.

Each interaction of a nanoparticle with the nanopore leads to an event in the current-time trace (Fig. 2a). We observe different events regarding time and current change. Drops in current are caused by a particle translocating through the pore due to the temporary blockage of the nanopore. Increases in current have been attributed to the movement of counter ions [4]. Transient nanoparticles in front of the pore produce much shorter events. It is also possible that more than one particle enters the pore leading to a convolution of the different event curves. The events were analysed using a custom written Matlab plugin called Transalyzer [5], and are presented in Fig. 2b as a function of current blockage and duration. Identified translocation events are marked by a blue circle. Representative events of this group are shown in Fig. 2 c-e.

In the future, we will investigate translocation events as a function of nanoparticle/nanochannel size ratios and surface charge. These experiments with well-defined channel systems will contribute to achieve a better understanding of the influence of channel geometry and surface charge on the translocation dynamics.

* Work supported by the Hessen State Ministry of Higher Education, Research and the Arts in the frame of the LOEWE project iNAPO.

References

[1] Deamer et al. 2016. Nature biotechn. 34, 5, 518.
[2] Magi et al. 2017. Briefings in bioinformatics. DOI: 10.1093/bib/bbx062.
[3] Pevarnik et al. 2012. ACS nano 6, 8, 7295–7302.
[4] Smeets et al. 2006. Nano letters 6, 1, 89.
[5] Plesa et al. 2015. Nanotechnology 26, 8, 84003

Cu_2O nanowire arrays photocathodes synthesized by electrodeposition and ion-track technology*

F. Yang[1], C. Schröck[1,2], S. Zhang[3], C. Trautmann[1,2], C. Scheu[3], and M. E. Toimil-Molares[1]

[1]GSI, Darmstadt, Germany; [2]Technische Universität Darmstadt, Germany; [3]Max-Planck-Institut für Eisenforschung, Düsseldorf, Germany

Semiconductor-based nanostructures provide an excellent platform for fundamental research as well as for potential applications in various fields such as nanofluidics, nanophotonics, or sustainable energy conversion. A challenging topic is the carbon-free energy conversion by solar water splitting [1]. Hydrogen, a clean energy carrier and chemical fuel can be produced by splitting water molecules under sun light using a semiconductor material.

Among available photocathode materials, Cu_2O is a promising semiconductor because its electronic and optical properties favour water splitting reactions. Moreover, this metal oxide is non-toxic, cheap and suitable for low fabrication cost. However, since Cu_2O has limited stability in aqueous solutions, Cu_2O must be protected with a passivation layer.

In this work, we present the synthesis and characterization of TiO_2-coated Cu_2O nanowire arrays as photocathodes for solar hydrogen production. The Cu_2O nanowire arrays were fabricated by ion-track technology and electrodeposition. Polycarbonate (PC) foils were irradiated with 11.1 MeV/u Au ions at the GSI UNILAC accelerator. The applied fluence was 10^8 ions/cm^2. Each irradiated foil was exposed to UV light, and subsequently immersed in 6M NaOH solution at 50°C to convert the ion tracks into nanochannels. For electro-deosition, a conductive electrode was prepared by sputtering a thin Au layer on one side of the PC film. This layer was reinforced electrochemically by applying U = -0.7 V vs a Au rod using a commercial gold sulfite solution (Metakem). The electrodeposition in the nanochannels was performed at 60 °C, applying U = -0.4 V vs. Ag/AgCl (sat. KCl) in a 0.02 M $CuSO_4$ solution with 0.4 M lactic acid (adjusted to pH 12) using a three-electrode configuration. After the Cu_2O electrodeposition, the polymer membrane was dissolved in dichloromethane. A thin and conformal TiO_2 layer was deposited on the Cu2O nanowire array by atomic layer deposition (ALD). The ALD deposition was performed at 110°C, applying sequential pulses of titanium isopropoxide and water as precursors. The growth rate was estimated to be 0.11 Å/cycle.

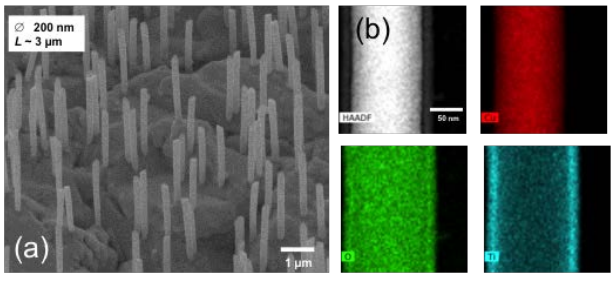


Figure 1: (a) SEM image of a representative Cu_2O /TiO_2 nanowire array (b) HAADF HR-STEM image, and EDX elemental mapping of Cu, O, Ti, of a nanowire section.

Morphology, crystallinity, and composition of the Cu_2O nanowires was investigated by scanning electron microscopy (SEM), high-resolution scanning transmission electron microscopy (HR-STEM), and energy dispersive x-ray analysis, respectively. Fig. 1 (a) shows a SEM image of a representative array of Cu_2O /TiO_2 core-shell nanowires (length ~ 3 µm, diameter ~200 nm). The HAADF HR-STEM and EDX elemental mapping images of thinner single Cu_2O /TiO_2 nanowires reveals the homogeneous distribution of Cu (red) and O (green) on the nanowire (Fig. 1b). EELS measurements also confirmed that the electrodeposited material is Cu_2O (not shown) without the presence of either Cu or CuO. Ti mapping (light blue) shows a conformal and homogeneous TiO_2 layer surrounding the Cu_2O nanowire. Additional high magnification HR-STEM images (not shown) revealed that the Cu_2O nanowires are single crystalline with (111) planes perpendicular to the wire axis, while TiO_2 is amorphous.

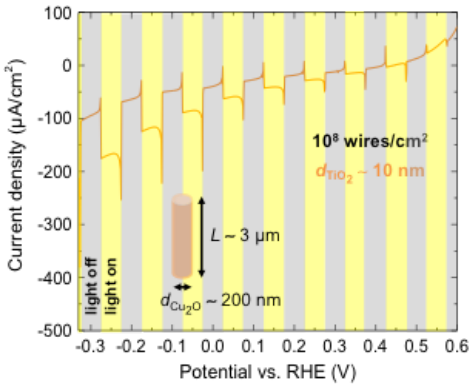


Figure 2: Voltammogram recorded under chopped light illumination with 100 mW/cm² simulated (AM1.5) sunlight. The scan rate was 10 mV/s.

The performance of Cu_2O /TiO_2 nanowire based photocathodes was characterized by linear sweep voltammetry (LSV) (fig. 2). As expected, a negative photocurrent is observed upon light illumination, confirming the p-type character of the photocathode. Switching the light on and off alternatively every 5 s leads to pronounced transients, especially when the light is switched on. Such transients indicate recombination of the photo-generated charge carriers, which can be due to accumulation of electrons near the surface, accumulation of holes in the bulk, or electrons/holes trapping at surface states.

*Work supported by the priority program of the Deutsche Forschungsgemeinschaft (DFG SPP1619).

References

[1] M.G. Walter et al., Chem. Rev. 110 (2010) 6446.

 DOI:10.15120/GR-2018-1

Micro-probing of electronic components for space and high energy physics

V. Ferlet-Cavrois[1], M. Tali[1,2,3], M. Muschitiello[1], R. Garcia Alia[2], S. Buchner[4], A. Khachatri[4], N. Roche[4], A. Javanainen[3], Z. Fleetwood[5], A. Ildefonso[5], M. Wachter[5], J. Cressler[5], P. Kupsc[1] , A. Barnes[1], A. Zadeh[1], J. Calcutt[1], C. Poivey[1], E. Daly[1], K-O. Voss[6]

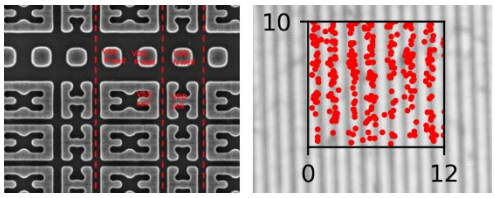
[1]European Space Agency, ESA ESTEC, Noordwijk, Netherlands; [2]CERN, Geneva, Switzerland; [3]University of Jyväskylä, Finland; [4]NRL, Naval Research Laboratory, Washington DC, USA; [5]Georgia Tech, Georgia, USA; [6]GSI Helmholtzzentrum, Darmstadt, Germany

The microprobe facility at GSI allows for charge deposition with a uniquely precise spatial control. This experiment gathered several groups, each one with specific devices, illustrating the diversity of radiation hardening needs for space and high energy physics: CERN with SRAM memories, University of Jyväskyla with SiC diodes, Georgia Tech with SiGe bipolar transistors (HBTs), NRL with GaN high electron mobility transistor (HEMT) and ESA with capacitors for GaN ampifiers.

Sensitive volume topology for SRAM

The main purpose of the study was to analyse the dimensions of the sensitive volume in order to implement a Monte Carlo tool to predict single event latch-up (SEL). The test was done using Ca ions (LET ~15-18 MeVcm²/mg) from the UNILAC in combination with the micro-probe beam focused on memory dies. This LET value is just above the SEL threshold, therefore only a relatively small fraction of the active surface of the component is expected to be SEL sensitive. The results show the well direction in the tested SRAMs. The Samsung clearly displays a vertical well structure, while the Alliance has a horizontal structure (Fig. 1).

a) Samsung SRAM, K6R4016V1D



b) Alliance SRAM, AS7C34098A

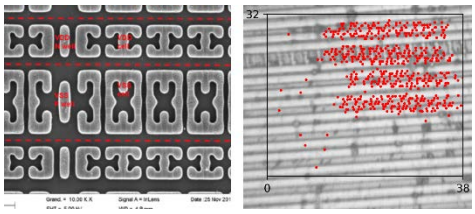


Figure 1: Scanning electron micrographs of two different SRAMs compared to SEL test mapping at the microprobe using 4.8 MeV/u Ca ions.

This confirms the assumption of a sensitive volume consisting of two cells in the direction perpendicular to the doping wells (~4 µm) and 16 or 32 cells (in the studied SRAMs) in the direction parallel to the wells, corresponding to the distance between well contacts. The geometry and dimensions of the sensitive volume have a strong impact on the respective simulated SEL response, especially for indirect ionization, dominating the SEE rate in a high-energy accelerator environment.

SiC diode studies by using the microprobe

The beam of the GSI microprobe was used to test high-voltage SiC Schottky diodes from three different manufacturers (STMicroelectronics, Infineon and Cree). Two types of beam were used: Ca and Au, both at 4.8 MeV/u. The goal of these tests was to learn more about the stochastic behaviour of ion energy deposition due to the scattering from the auxiliary structures (i.e. bonding wires) of the tested devices, and also the physical mechanisms involved in the ion-induced damage.

The tests successfully proved the hypothesis proposed in Ref. [1] that says that ion scattering from the bonding wires has a strong influence on the device response. This has important implications on the error rate prediction for space applications, made from heavy-ion tests that typically consider the energy deposition only from the average LET values.

The next step in these studies is to investigate the heavy-ion response of SiC MOSFETs by using the microprobe beam. It is of interest to learn how the ions hitting different areas of a more complicated (with source and gate regions) SiC device result in different device response and damage.

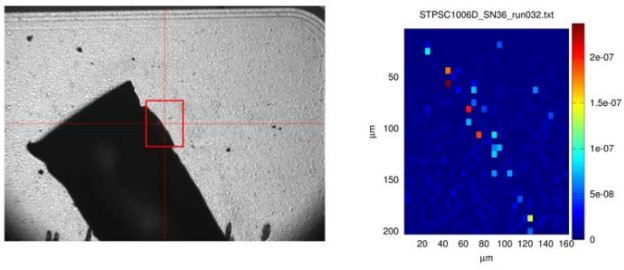


Figure 2: Micrograph (left) of STPSC1006D SiC Schottky diode, showing the bonding wire and the area scanned with Ca-ion. The corresponding "heat map" of the observed damage (right), showing higher damage (i.e. leakage current, red dots) next to the edge of the bonding wire. Here a single ion induced up to 250 nA increase, compared to about 8 nA for the other ions.

SETs in SiGe HBTs

The primary aim was to investigate single-event transients (SETs) in SiGe HBTs. SETs are time-based perturbations at the transistor level of the voltage or current operating condition. Results for a 0.5 × 10 µm² npn SiGe HBT response to Ca ions is shown in Fig. 3.

A major goal of the radiation effect community is to correlate the response of electronics from a heavy ion source to that of a pulsed-laser photon source, in order to improve testing procedures for electronics intended for space or radiation intense environments. The SiGe HBT results from GSI are directly comparable to laser test campaigns with the same structure, in which charge deposition is induced via a two-photon absorption (TPA) pulsed-laser source.

Recent endeavours involve combining both these sources in simulation. A physics-based, meshed model using a hydrodynamic transport code can accurately create both the heavy ion and the laser event in the calibrated transistor structure. The model is in the final stages of development and publication comparing the two methods is expected in the near future.

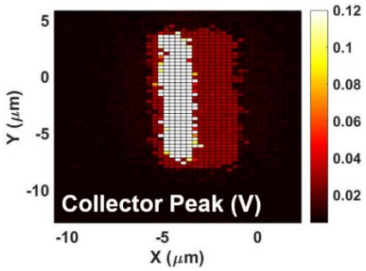


Figure 3: Peak voltage response for SiGe HBT exposed to Ca ions at the GSI microprobe.

SETs in GaN HEMTs [2, 3]

A promising material for power devices in space applications is GaN configured as a high electron mobility transistor (HEMT). Because its electronic bandgap is much larger than that of silicon, GaN can operate under higher voltages and at higher temperatures, making it significantly more power efficient. GaN-based devices have a reliability problem in radiation environment because ionizing particles traveling through the device can cause voltage glitches that temporarily disrupt the normal operation, or can even cause destructive failure. We are investigating focused pulsed X-rays at a synchrotron source (Argonne National Laboratory), focused pulsed laser light, UV by single-photon absorption (SPA) or via two-photon absorption (TPA) (both at NRL), and ion beams at the microprobe (GSI).

Fig. 4 shows a comparison of the transients obtained using the four different radiation sources. It is clearly evident that, whereas the transients generated by pulsed visible light, X-rays and heavy ions are fairly similar in shape, the transients obtained using UV light are very different, being much broader with long trailing edges.

These results demonstrate that the UV light, which has a penetration depth of only 300 nm, much smaller than the penetration depths of the other radiation sources (tens of microns) is responsible for the difference in shape. The structure of the HEMT consists of an AlGaN layer on top of the GaN layer. We attribute the difference to the large stress in the AlGaN layer, which can lead to the formation of trapping charge defects, facilitating current flows between gate and drain. This does not happen to the same extent with the other sources because only a small fraction of the deposited charge is near the surface where the traps are located. These results demonstrate the role of charge track range relative to charge collection depth in the single event transient shapes in GaN HEMTs.

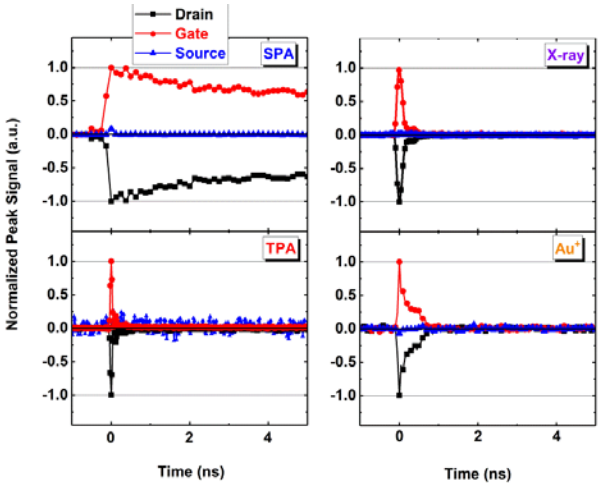


Figure 4: Transients, positive at the gate and negative at the drain, obtained using four different radiation sources: pulsed UV laser light via SPA, pulsed visible laser light via TPA, pulsed X-rays and Au ions at GSI microprobe.

MIM Capacitors for GaN Amplifiers

Testing single event effects (SEE) of metal–insulator–metal (MIM) capacitors is part of an ESA initiative (GREAT2) to develop European GaN technology for space applications [4]. Microbeam test has permitted to identify the intersection of the air bridge and metal line as a location where heavy-ion induced dielectric breakdown occurs at lower voltage than expected [5]. This will support technology modifications for future GaN amplifiers developed for space.

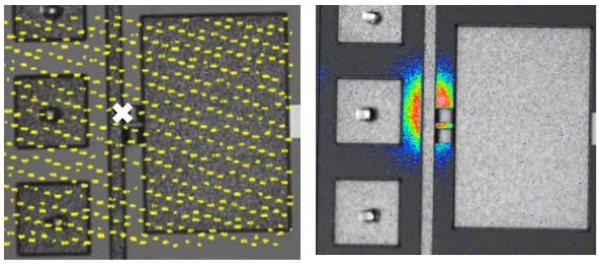


Figure 5: Ion hit locations (yellow dots) with Ca microbeam of a capacitor (left). The white cross shows the ion hit location causing breakdown. The current leakage was verified with NIR (near infrared) microscopy (right) [5].

References

[1] A. Javanainen, et. al.; IEEE Trans. Nucl. Sci. 64 (2017) 415.
[2] A. Khachatrian, et al.; IEEE Trans. Nucl. Sci. 6 (2018) 369.
[3] A. Khachatrian, et al.; IEEE Trans. Nucl. Sci. 64 (2017) 106.
[4] K. Hirche et al.; (2014). GaN Reliability Enhancement and Technology Transfer Initiative (GREAT2). https://escies.org/
[5] P. Kupsc, et. al.; IEEE Trans. Nucl. Sci. 65 (2018) 732.

 DOI:10.15120/GR-2018-1

Activity report of the Plasma Physics department

V. Bagnoud[1,2], A. Blaževi[1,2], B. Borm[3], C. Brabetz[1], C. Bruske[1], U. Eisenbarth[1], S. Götte[1], D. Khaghani[4], A. Kleinschmidt[2], S. Kunzer[1], T. Kühl[1], P. Neumayer[1], D. Reemts[1], O. Rosmej[1], V. Schanz[5], D.Schumacher[1], N. A. Tahir[1], A. Tauschwitz[1], L. Tymura[1], D. Varentsov[1], K. Weyrich[1], S. Zaehter[3], and B. Zielbauer[1]

[1]GSI, Darmstadt, Germany; [2]HI Jena, Jena, Germany; [3]JWG University, Frankfurt Germany; [4]FS University, Jena, Germany; [5]TU Darmstadt, Darmstadt, Germany

The plasma physics department of GSI is responsible for the operation at three experimental facilities on the GSI campus, namely the Z6 experimental area at the UNILAC, the High Energy cave HHT at the SIS18 and the PHELIX laser facility. In addition, the department is strongly involved in the preparation of the FAIR experiments. Below is a summary of the highlights for 2017.

Highlights from the Plasma Physics Program

In 2017, the study of the interaction of short laser pulses with matter was at the center of the research of the plasma physics department because of the direct applications of laser-driven diagnostics for FAIR.

In a series of experiments conducted with PHELIX, our group has shown that optical diagnostics can be employed to study the relativistic laser-plasma interaction at the femtosecond time-scale when the part of the pulse reflected [1] or transmitted [2] through thin targets is analysed. In particular, a method based on spectral interferometry has been used for the first time for the characterization of the relativistic laser-plasma interaction, showing evidence of interaction in the relativistic transparency regime.

In a second laser-plasma experiment at the Ti:sapphire laser JETI40 of the FSU Jena conducted by our group, ultra-high energy density plasma states with a keV bulk electron temperature, near-solid electron density and GBar pressure were diagnosed using x-ray spectroscopy tools. The generation of 150-nm thick plasma layers by irradiation of metallic foils at high laser temporal contrast and at the second harmonic laser frequency was explained by the collisional mechanism of the laser pulse absorption in a thin skin layer of plasma with a step-like electron density profile, followed by the electron heat transport. This scenario is opposite to the usually considered volumetric heating by supra-thermal electrons, which production was strongly suppressed [3].

In laser-plasma interaction, one of the central issues is the coupling efficiency of the laser energy into secondary particle or radiation. Using foam targets developing into plasmas at near critical plasma density is a way toward higher conversion efficiency of the laser energy into MeV electron beams. Such an experiment has been performed at the PHELIX, where preliminary results show dramatic increase of the supra-thermal electron energy far beyond ponderomotive one (16 MeV compared to 2 MeV) and strong increase of the total number of electrons with energies above 10 MeV (tens of nC). This was confirmed by measuring the gamma dose caused by bremsstrahlung. Both energetic electrons and gamma-rays are excellent candidates for radiographic applications in HED experiments [4].

Another route to enhance the yield of secondary radiation produced by intense laser pulses is the use of structured target surfaces. Thin metal foil targets covered with dense arrays of aligned high aspect ratio nano- and micro-wires have been produced at GSI in collaboration with the material science department and subjected to high-energy laser pulses from the PHELIX facility. Significant enhancement in both x-ray emission and proton acceleration has been demonstrated [5]. Irradiation of such delicate targets with the high-energy picosecond laser pulses has become feasible at the PHELIX facility due to the significant improvement of the laser pulse contrast over the past years.

Backlighting of mm-scale high-Z targets as foreseen in the FAIR plasma physics program will require hard x-ray radiation with photon energies above 100 keV, which can be produced by high-energy short-pulse laser systems. An experiment to extensively characterize the emission characteristics of such sources (conversion efficiency, angular and spectral distribution) over a wide range of laser parameters has been carried out at PHELIX [6], which provides important data towards the requirements for a future "Helmholtz beamline at FAIR". Also in this experiment, x-ray emission source sizes down to 5 µm could be achieved using thin tungsten wires as generation target. Such small source sizes provide the necessary spatial coherence to realize x-ray phase contrast radiography. This was demonstrated in a subsequent campaign, where x-ray phase contrast imaging was used to diagnose laser-driven shock waves [7].

The LIGHT (Laser Ion Generation, Handling and Transport) experiments concerns the capture of laser accelerated ions by a conventional solenoid, their phase rotation in a rf-cavity, followed by their transport over longer distances before being refocused again for applications. Here, the focus of the investigations in 2017 was set to prepare the ion beam for an energy loss experiment in plasma [8]. In two experimental campaigns done at the Z6 target area, the proton beam at the end of the LIGHT beamline was further characterized, after the 6-m-long beam transport that includes a time-compression stage of the ion pulse and its spatial focusing with a pulse solenoid. At a proton energy of 8.1 MeV, the beam was focused down to 1.3 x 2 mm² with a peak current of 121 mA and a pulse duration of 500 ps, which is an improvement compared to the results obtained previously.

As the stopping power of protons is small, heavier ions would be preferable to employ the LIGHT beamline for heavy-ion energy-loss measurement experiments. Therefore, some time was dedicated to the generation and characterization of TNSA-driven carbon ions by heating tungsten foils evaporated with carbon to temperatures of

above 1000°C to remove the protons. The experiments showed that above an energy of 0.5 MeV/u C 4+ is dominating the spectrum and can be transported efficiently over longer distances by conventional accelerator components. The results are very promising when regarding these short (<500 ps) pulses as probe for energy loss experiments of heavy ions in laser generated plasma.

Operation and Improvements of PHELIX

PHELIX has continuously delivered beam time to the international user community for the last nine years. In 2017, its operation profile was, as in previous years, distributed between maintenance and upgrade phases and beam-time operation (52%) as shown in Figure 1. The operation plan has been impacted in summer when a mandatory fire-safety-relevant building rehabilitation had to be made. During this time however, a long-standing survey and upgrade of the control system has taken place such that the shut-down time could be as efficiently used as possible.

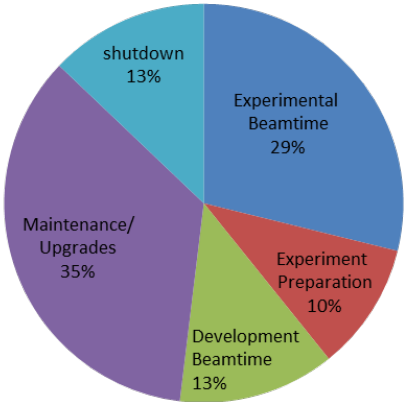


Figure 1: Operation profile of PHELIX in 2017.

In total 10 experiments have been conducted at PHELIX, which can be separated in 150 shifts dedicated to external users and 46 shifts used for the internal program of the LIGHT experiment at the Z6 experimental place [8]. The topics of the experiments vary from the first demonstration of x-ray phase-contrast imaging with the small spatially limited keV secondary sources generated by our group to the test of new liquid-crystal targets. Again, laser-driven acceleration has been at the topic of many of the experiments. PHELIX has been during this time, as in the past, very reliable with less than 5% of the shots as failed shots registered, thereof only 1.7% of the shots failed because of hardware-related issues.

Improvements to the facility have been performed on many of its sub-systems in 2017. A major on-going project is the upgrade of the PHELIX pre-amplifier to an architecture allowing for a 10-fold increase of its repetition rate. In 2017, the upgrade of the amplifier was completed during one of the maintenance phase early in the year, such that all the short-comings found during the commissioning done in 2016 could be fixed. Together with work done on the beam quality control, PHELIX could deliver in 2017 the nominal beam size of 28 cm as standard aperture which corresponds to an energy of 200 J at the end of the amplifier chain for short pulse experiments and 300 J for nanosecond pulses used at the Z6 experimental area before frequency conversion. Note that this energy is limited right now for the short-pulse option by the diffraction gratings of the compressor that show some sign of ageing and are therefore run at a maximum laser fluence of 0.85 J/cm^2.

Another major on-going project for the facility is the development of a VISAR system at the Z6 experimental place that turns the existing preliminary device developed in collaboration with the Technical University of Darmstadt to a reliable and versatile system that can be offered as a standard diagnostics tool to the users community, as recommended by the PHELIX committee. In 2017, the system has undergone the necessary upgrade that includes work on the laser source (better temporal coherence) and its interferometer (improved setup stability). Already in 2018, users will employ this diagnostic tool as their main diagnostic.

Developments on optical temporal diagnostics went on. Here the detection system of the short-pulse 3ω-cross-correlator named EICHEL[9] was improved further to make it more insensitive to pulse-to-pulse energy fluctuations. First tests were conducted at the Polaris laser at HI Jena. In addition, EICHEL was used to characterize the temporal contrast of PHELIX when its linear regenerative amplifier is by-passed, showing an important reduction of the number of pre-pulses in the -1 to -.2 ns time window before the peak of the pulse. An upgrade of PHELIX to include this by-pass should happen in the next months to exploit this new finding.

PHELIX Committee 12, 2017

In spring 2017, a call for proposals synchronized to the general call for proposals of the GSI accelerator was made. This call is embedded in the strategy of GSI to offer beam time to the FAIR collaborations at GSI's facilities during the build-up phase of the new accelerator: the so-called phase 0 program. The PHELIX committee met during the summer and granted 11 laser-only proposals with beam time plus one combined laser-ion experiment. At the HHT and Z6 caves, 4 additional experiments have been granted access to the ion facility. In total, this amounts to a 42% success rate for applicants. The high demand on GSI's plasma physics facilities illustrates the vitality of the field and their attractiveness

Progress on the FAIR Ion Facility for Plasma Physics

During the workshop on high-energy-density physics in Hirschegg, the community has decided to found a new collaboration called HED@FAIR, which aims at overtaking the responsibilities of the two previous collaborations involved in the FAIR project. One of the consequences of this move has been to raise interest in the planned experiments from further groups, e.g. the Chinese community that increased its contacts with our group. Negotiations to give Chinese groups a leading role in the plasma physics program at FAIR took place along the year, for instance during the EMMI workshop at GSI and the 1st Workshop for International Collaboration on High Energy Density

 DOI:10.15120/GR-2018-1

Science at FAIR and HIAF. The latter was held with about 70 participants from China and Germany in Xi'An, China. Participants from the Institute of Physics (Beijing), Peking University (Beijing), Laser Fusion Research Center (Mianyang), Xi'an Jiaotang University (Xi'an) and Shanghai Jiaotong University (Shanghai) showed interest to be part of the collaborative effort. The workshop resulted finally in a memorandum of understanding between the University of Xi'An and GSI.

The preparation for the FAIR phase 0 program, that will be conducted from 2018 on at the existing plasma physics experimental areas at GSI is well ongoing. Four experimental proposals dealing with the proton microscopy set up PRIOR have been submitted and all of them granted with beam time. To gather experience on proton microscopy technology and get a head-start with experiments, the proton microscope will be set up at HHT using part of the GSI contribution to FAIR. The in-kind contract with FAIR for financing the magnets and power supplies has been signed and the detailed specification written, so that the magnets can be ordered in 2018. Later on, the PRIOR system will be transferred to the FAIR building for HED@FAIR experiments, called APPA cave, where the plasma physics experiments at FAIR will be performed.

A second experiment platform to be made available at GSI for the phase-0 period is a target chamber for the HIHEX (Heavy Ion Heating and Expansion) scheme. This target chamber should be complemented with an arm of the PHELIX laser sent to HHT to volumetrically diagnose the samples generated by the ion beam already during the upcoming years. For this purpose, preliminary conceptual work has been performed and discussions on the various possible experiments took place during the EMMI workshop on plasma physics at FAIR that took place in the summer of 2017 at GSI. In particular, this target station could exploit the 10^{11} Ni ions per bunch at an energy of 200-400 MeV/u available from the SIS-18 for the HIHEX scheme. With the existing HHT-focusing system, one can reach a Ni-beam specific energy deposition in to Al - Pb from 4 up to 16 kJ/g (cooled ion beam), which should be enough to start the scientific program of the plasma physics community at FAIR.

The planning of the APPA cave is progressing well and should be finalized in 2018. Concerning the experimental equipment in the APPA cave the last Technical Design Report relevant for the day-1 experiments is approved and the technical board of HED@FAIR is now concentrating more and more to the definition of the detailed specifications and ordering of the components, while the final focussing system, consisting of 4 super conduction large aperture quadrupoles, has been contracted with the Institute of High Energy Physics in Protvinov, Russia, and is now in the final design phase.

Concerning the science program for plasma physics at FAIR, hydrodynamical simulations using the code BIG2 have shown that the ion parameters expected at FAIR in the APPA cave, namely uranium ion intensities from 10^{11} to 5×10^{11} ions/pulses, are very appropriate to realize low-temperature compression of iron using the LAPLAS (LAboratory PLAnetray Science) scheme to conditions relevant to earth and super-earth core conditions [10]. In this proposed experiment, an annular ion beam quickly heats a tungsten temper that compresses a cold iron inner core. The maximum pressure accessible using FAIR by varying the number of ions in the pulse is in the range of 2 to 7 Mbar. In addition, the temperature of the iron pay load is independently tuned by changing the amount of ions leaking on axis. In such conditions, the temperature achievable during compression can be as low as 0.1 eV (no ions on axis) and continuously increased to 2 eV when the ion density on axis reaches 20% of the ring density. All-in-all, these parameters cover the range of pressures and temperatures necessary to study earth core and super-earth core conditions in the laboratory. This type of experiments could extend the current data obtained by diamond anvil cells on iron to the WDM region relevant to planetary science.

References

[1] J. Hornung et al., this report
[2] V. Bagnoud et al., PRL **118,** 255003 (2017)
[3] O. Rosmej et al., submitted to PoP
[4] S. Zaether at al., this report
[5] D. Khaghani et al., Scientific Reports 7, 11366 (2017)
[6] B. Borm et al., this report
[7] L. Antonelli et al., this report; L. Antonelli et al., submitted to PRL
[8] D. Jahn et al., this report and J. Ding et al, R. Leonhard et al, this report
[9] V. A. Schanz et al., Opt. Express **25**, 8 (2017)
[10] N. A. Tahir et al., this report; N. A. Tahir et al., The Astrophysical Journal Supplement Series **232**, 1 (2017)

X-ray Phase-Contrast Imaging for Laser-induced shock-wave

L. Antonelli[1,2], F. Barbato[3], J. Trela[4], D. Mancelli[4], G. Zeraouli[5], A. Atzeni[1], A. Schiavi[1], G. Boutoux[4], L. Volpe[5], P. Bradford[2], N. Woolsey[2], V. Bagnoud[6], C. Brabetz[6], P. Neumayer[6], B. Zielbauer[6], B. Borm[6] and D. Batani[4]

[1]University of Rome „La Sapienza“, Rome, Italy; [2]University of York, York, UK; [3]EMPA, Zurich, Swisserland; [4]University of Bordeaux, Talence, France; [5]CLPU, Salamanca, Spain; [6]GSI, Darmstadt, Germany; [4]Goethe University, Frankfurt-M, Germany

X-ray Phase-Contrast Imaging (XPCI) is a technique where the phase-shift induced by a density gradient is used to enhance a diffraction pattern in an X-ray image. This well-known technique is normally applied in biology and medicine because it is ideal to make visible any interface where a change of density is present. In high energy density science experiments the sensitivity to density gradients is ideal to probe hydrodynamic instabilities as well as shock front degradation [1,2] which could be caused by the presence of hot electrons which could cause a non-uniform target temperature.

In our experiment at GSI we used the laser PHELIX to generate X-ray pulses with a limited source size. The aim of our experiment was to demonstrate the feasibility of single-shot XPCI using short-pulse (picosecond) laser-driven X-ray bremsstrahlung emission sources. The necessary small source size if achieved using tungsten wires with a diameter of 5 μm as targets to produce the x-ray source [3], which were developed in a previous beamtime at the PHELIX laser. We used this X-ray flash to obtain XPCI of static objects as well as to probe a laser-induced shock-wave propagating in a polystyrene cylinder irradiated with long-pulse (nanosecond) beam.

Figure 1 shows experimental XPCI images obtained in the experiment. Nylon wires with a range of diameters were used as static test objects. The presence of phase contrast enhancement in these images is clearly visible where interface surface are located. Because we are using an incoherent broadband spectrum light source the phase contrast is given by the so called lateral coherence defined as:

$$l_t \approx \frac{R_0 \lambda}{s}$$

where R_0 is the source-target distance, λ the incidence X-ray wavelength and s the source size. In our case an average value of the lateral coherence was 10 μm which guarantees the possibility to probe steep density gradient in our target. Using the double-pulse option of the PHELIX laser we have also demonstrated XPCI in a pump-probe scheme, using one of the laser pulses to drive a strong shock into a sample (Fig. 1, right). The radiographic image shows the shock-front at a time of 6 ns after the end of the drive laser pulse. The presence of phase contrast is evident at the target-vacuum interface, as well as at the shock-front. In addition, we observe phase contrast in the central part of the shock-wave. This is attributed to the rarefaction wave propagating inside the shock lowering the pressure.

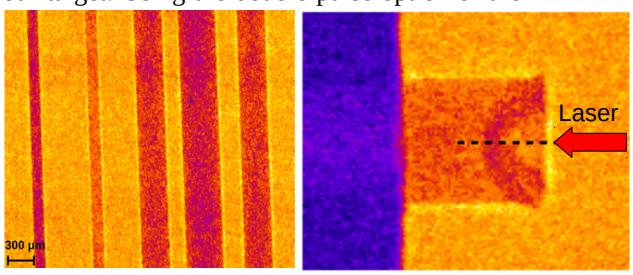


Figure 1: XPCI images taken with the laser-generated x-ray source of (left) Nylon wires and (right) a laser-driven shock propagating into a cylindrical target.

This first proof-of-principle experiment shows how this technique can provide a deeper insight in the shock physics underline details which would not be present with a conventional X-ray absorption radiography. Moreover, this experiment validate the feasibility of the technique on intermediate-scale laser facilities, but can also be applied on larger scale facility like OMEGA or NIF.

What is required is the capability to control the source dimension and this can be successfully achieved using mass limited target or pin-hole.

XPCI due to its intrinsically sensibility to density gradient is the ideal diagnostic to probe hydrodynamic instability as well as shock front degradation which could be caused by the presence of hot electron which could cause a non-uniform target temperature.

References

[1] A. Schropp et al., SCI REP-UK 5, 11089 (2015).
[2] J. Workman et al., Rev. Sci. Instrum. 81, 10E520 (2010).
[3] B. Borm *et al.*, GSI Scientific Report 2017

Experiment beamline: PHELIX
Experiment collaboration: none
Experiment proposal: P133
Accelerator infrastructure: none
PSP codes: none
Grants: This work benefited from the support of COST Action MP1208 ’Developing the physics and the Scientific Community for Inertial Fusion’ and by the EUROfusion project ”Preparation and Realization of European Shock Ignition Experiments”. The research leading to these results has received funding from LASERLAB-EUROPE (grant agreement no. 654148, European Union’s Horizon 2020 research and innovation programme).

 DOI:10.15120/GR-2018-1

Ultra-high magnetic field generation in curved targets: A novel approach to laboratory astrophysics and laser-based applications

P. Korneev[1,2], J.J. Santos[3], M. Ehret[3,5], Y. Abe[6], F. Law[6], Y. Kochetkov[1], V. Stepanishchev[1], S. Fujioka[6], E. d'Humieres[3], V. Bagnoud[4], B. Zielbauer[4], G. Schaumann[5], M. Roth[5], V. Tikhonchuk[3]

[1]NRNU MEPhI, Russian Federation; [2]Lebedev Institute, Russian Federation;
[3]CELIA, Université de Bordeaux, France; [4]GSI, Darmstadt, Germany; [5]IKP TU-Darmstadt, Germany,
[6]ILE, Osaka University, Japan;

Optical-based magnetic field generation is a convenient tool for applications, including particle guiding, laboratory based astrophysical-related studies and studies of matter behaviour in magnetic fields. The goal of this experimental campaign was a detailed study of a novel recently proposed scheme of such generation, in which a relativistic laser pulse interacts with a cylindrically shaped target [1], performing multiple reflections along the internal target surface (see Fig.1). In these conditions, the laser pulse generates relativistic electrons, propagating along the surface, and, consequently, return currents in the target bulk, which are responsible for the magnetic field generation.

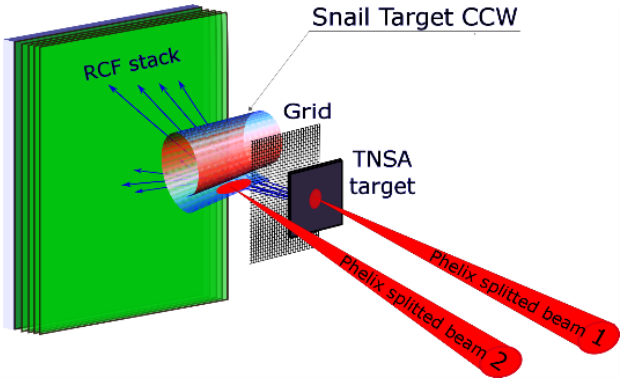


Figure 1: Principal experimental setup for generation of magnetic fields in snail-shaped target. Proton deflectometry diagnostic is shown; optical (polarimetry and interferometry) and Kα diagnostics are not shown.

In the experimental campaign, the PHELIX laser beam was splitted in two, one used as a target driver (CP1), and another (CP2) as a TNSA proton generator when interacting with a gold foil with 4 μm thickness. Besides the main target and the foil, a fine mesh was aligned on the way of TNSA protons for better resolution of proton deflection in the diagnosed fields. Optical diagnostics (polarimetry and interferometry) was also performed.

About twenty successful shots gave the information about the generated field structure, its time-dependence, and strength. A sample RCF image with a preliminary analysis is presented in Fig. 2. The observed shape of detected diagnostic protons is in a good agreement with the test-particle modelling of deflected TNSA protons, assuming a ~500T magnetic field in the target generated by solenoidal-like currents. Preliminary analysis of the experimental data for different time delays between CP1 and CP2 shows that the magnetostatic structure is stable for ~ 80 ps, which is of the hydrodynamic scale of the target expansion.

The obtained experimental data are being processed yet, but already we can state several important results: the snail-shaped targets are efficient quasi-static magnetic field generators with the time-of-life of the magnetized structures being of the hydrodynamic time scale. The experimental study opens new perspectives for optical-based magnetic field generation and applications.

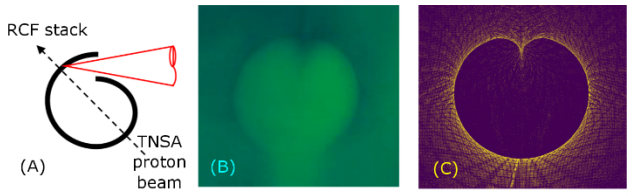


Figure 2: (A) a sketch of the principal experimental setup, (B) an example RCF image (from preliminary experimental results), (C) test-particle modelling of proton deflectometry image, assuming a solenoidal generated magnetic field of ~500T in the target.

References

[1] Ph. Korneev et.al., Phys.Rev. E 91, 043107 (2015)

Experiment beamline: PHELIX
Experiment collaboration: none
Experiment proposal: P136
Accelerator infrastructure: none
PSP codes: none

Grants: 2015-2019 grant of the Institut Universitaire de France obtained by CELIA, Russian Foundation for Basic Research (# 16-52-50019 ЯФ), Excellence program NRNU MEPhI (contract No. 02.a03.21.0005, 27.08.2013), Program of Increase in the Competitiveness of the National Research Nuclear University MEPhI. The EUROfusion Consortium and the Euratom research and training programmes 2014-2018 under grant agreement No 633053 and 2017-2018 under grant agreement No CfP-AWP17-IFE-CEA-02. The views and opinions expressed herein do not necessarily reflect those of the European Commission.
Strategic university co-operation with: Darmstadt

Fourier transform spectral interferometry as plasma diagnostics

V. Bagnoud[1,2], J. Hornung[1,2], T. Schlegel[1,2], B. Zielbauer[1], C. Brabetz[1], M. Roth[3,4], P. Hilz[5], M. Haug[5], J. Schreiber[5], and F. Wagner[1,2]

[1]GSI, Darmstadt, Germany; [2]HI Jena, Jena, Germany; [3]Technische Universität Darmstadt, Darmstadt, Germany; [4]FAIR, Darmstadt, Germany; [5]Ludwig-Maximilians-Universität, Garching, Germany

The interaction of short laser pulses of the highest intensities with thin sub-micrometer foils has received lots of attention in the last years because of its potential applications to laser-driven particle acceleration and the generation of hard x-rays that could be prime diagnostics for the FAIR facility for instance. In the last years, these studies were made possible by the ever-increasing temporal qualities of short laser pulses delivered by the most modern laser systems. While thin sub-micrometer foils used to be fully blown off many 10's of picosecond before the interaction with the main part of the pulse had begun, the latest generation of lasers with ultra-high temporal contrast like PHELIX enables such an interaction to happen. Yet, the exact status of the foil at the time of the interaction remains unclear and should be studied in details. Here, we have shown that the use of a second pulse that interrogates the plasma after the interaction with the first one is possible using standard spectroscopic methods [1]. It is possible to analyse the signal S(ω) by Fourier transformation with a technique known as Fourier-transform spectral interferometry (FTSI) that was proposed and demonstrated more than 20 years ago [2]. To understand the underlying mathematics, let us define the electric field of laser pulse as:

$$E(t) = A(t)e^{i\omega_0 t} \quad (1)$$

where A is the complex amplitude of the field and ω_0 the carrier angular frequency of the pulse. After propagation through the plasma, the field is modulated by a complex function T(t) whose modulus describes the time-dependent transmission through the foil and its argument temporal phase effects, like relativistic self-phase modulation or electron blow-out. When two pulses delayed by τ, of fields E_1 and E_2, cross a plasma and their amplitude is modulated by T_1 and T_2, the total field after the plasma can be described as:

$$E(t) = A_1(t)T_1(t)e^{i\omega_0 t} + A_2(t)T_2(t)e^{i\omega_0(t-\tau)} \quad (2)$$

A spectrometer that analyses the resulting pulses shows a signal S exhibiting an interference that is given by:

$$S(\omega) = |E(\omega)|^2 \quad (3)$$
$$= \left|FT(A_1(t)T_1(t)e^{i\omega_0 t}) + FT(A_2(t)T_2(t)e^{i\omega_0 t})e^{-i\omega_0\tau}\right|^2$$
$$= |E_1(\omega)|^2 + |E_2(\omega)|^2 + 2\cos(\omega\tau + \Delta\varphi)\,|E_1(\omega)E_2(\omega)|$$

where $E_{1,2}(\omega)$ is the complex spectral amplitude of the pulses after transmission through the plasma and Δφ the spectral phase difference between both pulses with:

$$E_{1,2}(\omega) = FT\left(A_{1,2}(t)T_{1,2}(t)e^{i\omega_0 t}\right) \quad (4)$$

In eq. 3, the information about the amplitude |E(ω)| and spectral phase difference Δφ is somehow entangled. However, when τ is chosen such that the fringes are still resolved by the spectrometer but fine enough so that the interference resolves the spectrum modulations, an analysis in the Fourier domains yields three peaks that can be numerically isolated and inverse Fourier-transformed to yield $|E_1(\omega)|$, $|E_2(\omega)|$ and Δφ at once.

The experimental demonstration was done during the beamtime P126 granted at the PHELIX facility with the setup shown in fig. 1. More details can be found in [1].

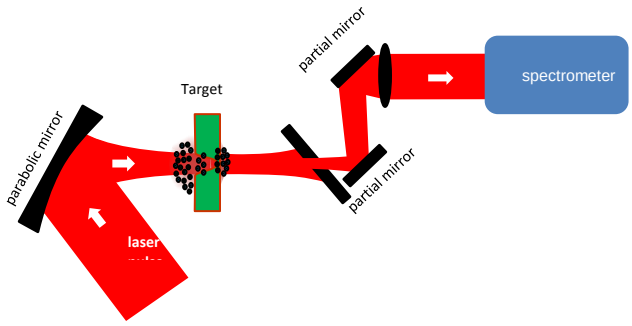


Figure 1: Experimental setup of experiment P126 that enables measuring the spectral interference for FTSI.

In our implementation the second pulse has an intensity ratio of a few percent to the main pulse and it was generated in the front end of PHELIX. Our analysis has shown that one can easily retrieve the difference in transit delay through the plasma, showing that for the thinnest targets, the plasma is relativistically transparent [1]. In addition, coupled to a FROG [3], the full temporal structure of the pulses $E_1(t)$ and $E_2(t)$ after the interaction can be reconstructed.

Further experiments could be planned in the near future to study the plasma dynamics by varying the delay τ for instance.

References

[1] V. Bagnoud, J. Hornung, T. Schlegel, et al. "Studying the Dynamics of Relativistic Laser-Plasma Interaction on Thin Foils by Means of Fourier-Transform Spectral Interferometry" Phys. Rev. Lett. **118** 255003 (2017)

[2] L. Lepetit, G. Chériaux, and M. Joffre. " Linear techniques of phase measurement by femtosecond spectral interferometry for applications in spectroscopy" JOSA B **12**, 2467 (1995)

[3] F. Wagner, J. Hornung, C. Schmidt, et al. "Backreflection diagnostics for ultra-intense laser plasma experiments based on frequency resolved optical gating" Review of Scientific Instruments **88** (2017) 023503

 DOI:10.15120/GR-2018-1

Experiment beamline: PHELIX
Experiment collaboration: APPA-HED@FAIR
Experiment proposal: P126
Accelerator infrastructure: none
PSP codes: none
Grants: Transregio 18
Strategic university co-operation with: Darmstadt

Relativistic interaction of mid-infrared laser pulses with nanowire targets: towards a novel laser-plasma interaction regime

Z. Samsonova[1,2], S. Höfer[1], V. Kaymak[3], S. Ališauskas[4], V. Shumakova[4], A. Pugžlys[4], A. Baltuška[4], T. Siefke[1], S. Kroker[5], O. Rosmej[6], A. Pukhov[3], I. Uschmann[1], C. Spielmann[1,2], and D. Kartashov[1]

[1]IOQ & IAP, Friedrich-Schiller-University Jena, Germany; [2]Helmholtz Institute Jena, Germany; [3]Heinrich-Heine-University Düsseldorf, Germany; [4]Vienna University of Technology, Austria; [5]LENA, Technical University Braunschweig, PTB, Germany; [6]GSI, Darmstadt, Germany.

In this report we present the results of the investigation of the relativistic mid-infrared laser pulses with silicon targets. The novelty of this regime lies in the scaling of the interaction parameters such as plasma critical density and normalized vector potential with the wavelength [1]. It also means that for mid-IR pulses the ionization happens in the tunnel regime, which in contrast to one/multiphoton ionization allows sharp plasma density gradients. These new features strongly influence the parameters of created plasmas, thus, generated X-ray emission. The use of nanostructured targets may additionally enhance the effect due to the high laser energy absorption shown in earlier works [2-4]. In order to investigate the possibility to generate extreme plasma states we compare the line emission spectra and bremsstrahlung emission generated from different targets, and apply PIC simulations together with kinetic FLYCHK code to match our experimental findings and the theoretical predictions.

Experiment & Results

The p-polarized idler beam of OPCPA laser system (TU Vienna) with energy of 25 mJ is focused under 45° onto the samples resulting in the peak intensity of nearly 10^{17} W/cm^2 with a pulse duration of 90 fs. The generated X-ray emission is then detected with the crystal spectrometer and the Timepix detector in a single shot. It is shown, that the intensity of the K-shell emission from neutral atoms as well as the hard X-ray bremsstrahlung are comparable for polished and nanowire (NW) targets. However, the efficiency of the line emission from highly charged ion states differs dramatically. In case of the polished sample there is essentially no emission from the transitions in He- and H-like Si observed (Fig. 1). This means that the electron density and bulk electron temperature are higher for the NW target.

Simulations & Discussions

To estimate the achieved plasma parameters we attempted to fit the experimental X-ray spectra with the synthesized ones using the temporal evolution of the parameters predicted by the PIC code. In case of NWs, the bulk electron temperature reaches its maximum value in the keV range by the end of the laser pulse, while the electron density exceeds solid density in the whole volume of nanowires. Corresponding X-ray line emission spectrum matches well to the hot part of the experimental spectra (Si^{12+}-Si^{13+}). The PIC simulations for the polished target are more troublesome requiring an inclusion of the spatial distribution of the laser intensity and higher resolution. However, assuming similar time scale for plasma cooling and its recombination and introducing a two-parameter search over the maximum bulk electron temperature and density we achieve a good agreement between the simulations and the experimental results for the maximum electron density about 10^{23} cm^{-3} and the bulk temperature of several hundred eV. The severe difference may arise from the larger penetration depth and higher absorption of the laser pulse within the NWs. Remarkably, the predicted electron density exceeds the critical density calculated for the used mid-infrared pump by 3 orders of magnitude.

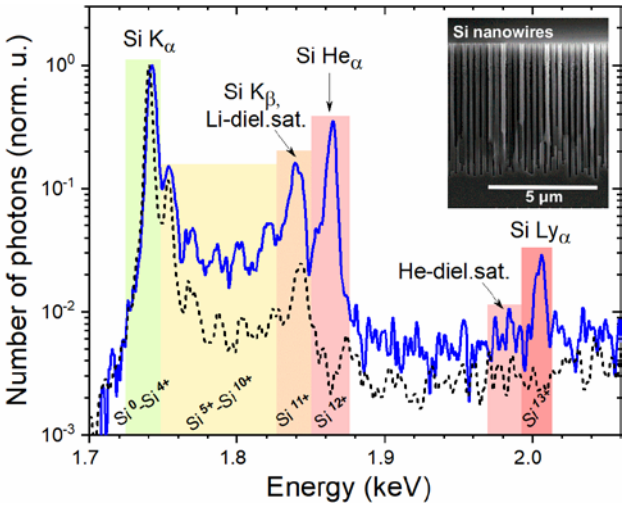


Figure 1: K-shell emission spectra for the polished (black dashed) and the NW (blue solid) Si targets. Inset: SEM image of the NW array.

Our studies demonstrate that relativistically intense ultrashort laser pulses in mid-IR spectral range are capable to generate solid density and keV-temperature plasmas and using NW targets may significantly increase the efficiency of the impact ionization and plasma heating.

References

[1] J. Weisshaupt et. al., Nat. Phot. 8, 927-930 (2014).
[2] T. Nishikawa et. al., Appl. Phys. B 78, 885 (2004).
[3] S. Mondal et. al., Phys. Rev. B 83, 035408 (2011).
[4] M. A. Purvis et. al., Nat. Phot. 7, 796-800 (2013).

Experiment beamline: none
Experiment collaboration: none
Experiment proposal: none
Accelerator infrastructure: none
Strategic university co-operation with: Vienna, Austria
*This report is also submitted to the HI Jena Annual Reports 2017

 DOI:10.15120/GR-2018-1

X-ray generation by laser hole boring and channelling in dense plasma

R. Wilson[1], B. Gonzalez-Izquierdo[1], M.J. Duff[1], C. Armstrong[1,2], R.J. Gray[1], M. King[1], C. Brabetz[3], B. Zielbauer[3], V. Bagnoud[3], D. Neely[2,1] and P. McKenna[1]

[1]SUPA, Department of Physics, Universtiy of Strathclyde, Glasgow, G4 0NG, United Kingdom; [2]Central Laser Facility, STFC Rutherford Appleton Laboratory, Didcot, Oxfordshire, OX11 0QX, United Kingdom; [3]PHELIX Department, GSI Helmholtz Center for Heavy Ion Research, Planckstrasse 1, D-64291, Germany

Introduction

We report on an experiment which aimed to investigate the sensitivity of X-ray radiation generation to the degree of laser channelling occurring in overdense plasma. Channelling is driven by the processes of relativistic self-induced transparency (RSIT) [1] and radiation pressure hole boring (HB) [2] and enables the laser to interact with the target plasma volumetrically. X-rays are produced by electron acceleration in the fields generated, or via Bremsstrahlung due to interaction with the fields of the target atoms, and provide a useful diagnostic due to their penetration through the dense target, enabling the channelling dynamics to be probed. Investigation of laser hole-boring and channelling physics in dense plasma at the upper limits of intensities achievable today (~10^{21} Wcm^{-2}) benchmarks models used to design future experiments at multi-petawatt lasers, for which radiation pressure driven effects will dominate the physics.

Experiment

The experiment was conducted using the PHELIX laser. This system is one of few capable of routinely achieving peak intensities up to mid-10^{20} Wcm^{-2}, which are required to probe radiation pressure-driven phenomena. This system can deliver 200 J pulses (~155 J on-target) with a duration of 700 fs (FWHM). The high temporal intensity contrast delivered (~10^{11} [3]) is also critical for experimentation using ultra-thin (nanometre scale) and low density foam type targets, to prevent significant target expansion prior to the arrival of the peak laser energy.

To investigate X-ray generation, a complementary suite of diagnostics were implemented to characterise both the spectral and spatial distributions, and source size. These included a crystal spectrometer operating in the range 17-200 keV, a scintillator-based array diagnostic, which provides low resolution spatial and spectral measurements extending to the hard X-ray range, and a high resolution (μm) penumbral imaging system to quantify the X-ray source size.

Additionally, a curved stacked detector [4], consisting of image plate and steel filters, was placed around the interaction region. This provides a high resolution angular and low resolution energy measurement of the distribution of electrons which 'escape' the target foil. Furthermore, the degree of laser light both reflected from and transmitted through the target was measured. This not only enables the plasma absorption dynamics to be probed, but additionally enables the conditions for the onset of transparency to be determined. Pictures of the experimental set-up in the PHELIX target chamber are shown in Fig. 1.

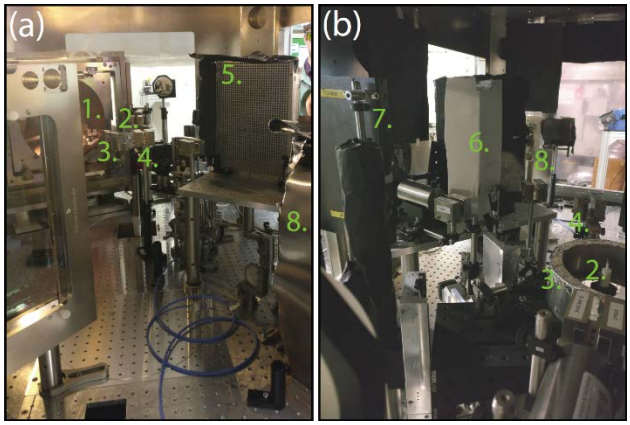


Figure 1: (a) and (b) Photographs of the experimental set-up, where the labels identify the main components as follows; 1. off-axis parabola, 2. target, 3. curved stacked detector, 4. penumbral imager, 5. scintillator array, 6. laser transmission screen, 7. electron spectrometer and 8. X-ray crystal spectrometer.

The targets selected for exploring X-ray generation were relatively thin (40-1000 nm) foils (Al, Au and CH) and low density plastic based foam targets (25-500 mg/cm^3), in order to investigate the transition from surface-dominated physics to volumetric interaction induced by HB and RSIT.

Analysis of the data measured on the experiment is currently underway, and results will be reported in future publications.

References

[1] V.A. Vshivkov et al. Phys. Plasmas 5, 2727 (1998).
[2] S.C. Wilks et al Phys. Rev. Lett. 69, 1383 (1992).
[3] F. Wagner et al. Appl. Phys. B 116, 429 (2014).
[4] R.J. Gray et al. Appl. Phys. Lett. 99, 171502 (2011).

Experiment beamline: none
Experiment collaboration: other: PHELIX
Experiment proposal: P124
Accelerator infrastructure: other: PHELIX
PSP codes: none
Grants: EP/J003832/1, EP/L001357/1 and EP/K022415/1
Strategic university co-operation with: none

A pump-probe technique for laser-driven proton beam heating to warm, dense states with the PHELIX laser

C. McGuffey[1], C. Brabetz[2], M. Dozieres[1], J. Kim[1], M. Bailly-Grandvaux[1], P. Forestier-Colleoni[1], F. N. Beg[1], M. Roth[3], V. Bagnoud[2]

[1]University of California San Diego, La Jolla, CA, 92071, U.S.A.; [2]GSI Helmholtzzentrum für Schwerionenforschung, Plasma Physik/PHELIX, Darmstadt, Germany; [3]Institut für Kernphysik, Technische Universität Darmstadt, Darmstadt, Germany

Conceptual technique for warm dense matter creation and characterization

Warm Dense Matter (WDM) is a scientifically interesting thermodynamic state falling in between the descriptions of condensed matter and plasma. WDM samples can be produced, for example, by rapid isochoric heating by an intense proton beam driven by a short pulse laser. We used the double short pulse beam capability of the PHELIX facility (<=100 J, >=0.5 picosecond) to begin developing a pump/probe method.

The main split of the laser (35 J, 1x10^19 W/cm^2) was delivered to curved 10 µm thick diamond-like carbon foils to generate protons through the target normal sheath acceleration mechanism [1]. The protons heated a tamped sheet of Cu edge-on. The second split of the laser (20 J, 6x10^18 W/cm^2) was delivered to a backlighter target using an independent parabolic mirror and delay stage. This produced a broadband x-ray strobe, face-on to the Cu foil, allowing x-ray absorption spectroscopy through the thin dimension (100 nm). The conceptual configuration is shown in Figure 1.

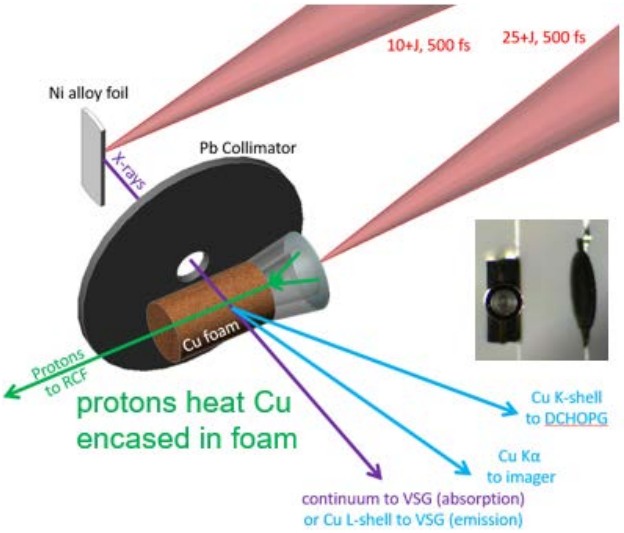


Figure 1: Conceptual setup with a Cu foam target variation. The baseline target used an upright solid Cu foil with plastic tamp walls and built-in aperture in place of the Cu foam (inset shows a real target as seen from the laser).

The probing technique was a variant of x-ray absorption near edge spectroscopy (XANES) as in [2] but using the laser-driven backlighter. As the sample is heated, a range of increasing charge states evolves. According to Non-LTE calculations with the PrismSPECT code, the simple L-edge of Cu turns into a multi-step edge when heated to 10 eV, and new bound-bound absorption features appear; both feature types are temperature-sensitive.

Demonstration of a proton-heated WDM sample and measurement of its temperature history would represent a major step in our ability to create characterized WDM samples for future experiments such as ion stopping measurements with FAIR ion beams.

Results

Proton source

The proton spectrum from the main pulse, shown in Figure 2, was measured with a Thomson parabola ion spectrometer and found to extend with a broad distribution typical of TNSA extending up to 7 MeV, corresponding to a range of 350 µm in solid Cu.

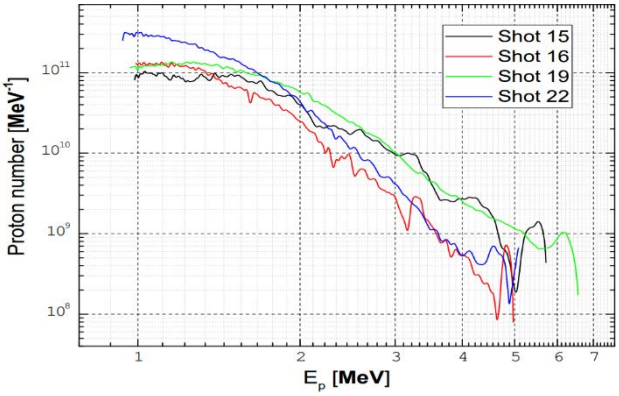


Figure 2: proton spectrum generated by the main split.

XANES (VSG grating spectrometer)

The spectrometer was calibrated and absorption measurements were made around the Cu L edge and Al K edge at a few delays.

K-shell emission (HOPG spectrometer)

Ni K-α and K-β were observed on all backlighter shots as a monitor. Cu K-α was observed in pump-only and pump + probe shots, while Cu K-β was not observed. Further analysis is necessary to derive a temperature minimum value from this fact.

References

[1] R. A. Snavely, M. H. Key, S. P. Hatchett, T. E. Cowan, M. Roth, et al., Phys. Rev. Lett. 85, 2945 (2000).

[2] B. I. Cho, K. Engelhorn, A. A. Correa, T. Ogitsu, C. P. Weber, et al., Phys. Rev. Lett. 106, 167601 (2011).

 DOI:10.15120/GR-2018-1

Experiment beamline: none
Experiment collaboration: none
Experiment proposal: p131
Accelerator infrastructure: none
PSP codes: none
Grants: U.S. Department of Energy Fusion Energy Sciences, High Energy Density Laboratory Plasmas grant DE-SC0014600
Strategic university co-operation with: none

Upgrade of back-reflection diagnostic based on frequency-resolved optical gating at PHELIX*

J. Hornung[1,2], V. Bagnoud[1,2], M. Zepf[2,3,4]

[1]GSI, Darmstadt, Germany, [2]Helmholtz-Institut Jena, Germany, [3]Institut für Optik und Quantenelektronik, Friedrich-Schiller-Universität Jena, Germany, [4]School of Mathematics and Physics, Queens University Belfast, UK

Motivation

During the interaction of an ultra-intense laser pulse with sub-micrometer thin foils, complex effects on the femtosecond timescale take place. During this interaction, a part of the laser pulse is transmitted via hole boring/relativistic transparency and another is reflected back at the position of the critical plasma density. Both the reflected and transmitted pulse are spectrally modulated due to effects like relativistic self-phase-modulation, while the spectrum of the reflected pulse is additionally Doppler-shifted by the moving critical plasma density happening during hole boring. To study these effects and timescales a diagnostic for back-reflected light based on frequency resolved optical gating (FROG) [1] has been developed and implemented at the PHELIX facility [2]. The FROG consists of a single-shot autocorrelator and an imaging spectrometer which spectrally and temporally resolves the incoming laser pulse. To achieve more reliable results the existing diagnostics has been upgraded.

Upgrade

One part of the upgrade is the change of the spectrometer setup. To keep the device as small as possible, a crossed Czerny-Turner-spectrometer was used in the first setup. Short focal-length mirrors and large reflection angles inside the spectrometer lead to strong aberrations, mostly astigmatism, that strongly influence the spectral resolution and spatial homogeneity of the two-dimensional spectrometer. To reduce the aberrations the focal length of the mirrors has been doubled, from 100 mm to 200 mm and the reflection angles could be reduced from 25 and 20 degree to roughly 16 and 12 degrees. The result of this change can be seen in figure 1. which shows the spectral lines of a calibration lamp.

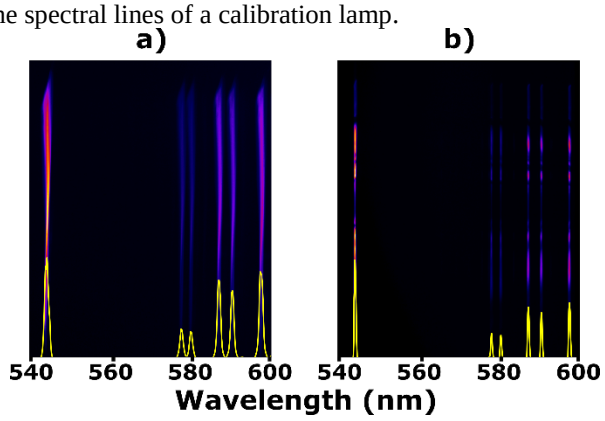


Figure 1: Spectrum of a calibration lamp and the corresponding sum over the complete image in yellow for the old (a) and new (b) spectrometer setup.

The corresponding sum of the spectrum in yellow, for the previous (a) and new (b) configuration, shows narrower lines. This changes the resolution from roughly 1 nm to below 0.5 nm with a much more homogeneous resolution over the whole image.

A further problem, detected during the commissioning of the device, was a slightly asymmetric FROG-trace in the delay axis, shown in figure 2 a), which was due to the misalignment of the autocorrelator and a beamsplitter with a non-equal transmission and reflection ratio. After changing the beamsplitter and realigning the autocorrelator the FROG-trace symmetry in the delay axis could be improved, as shown in figure 2b).

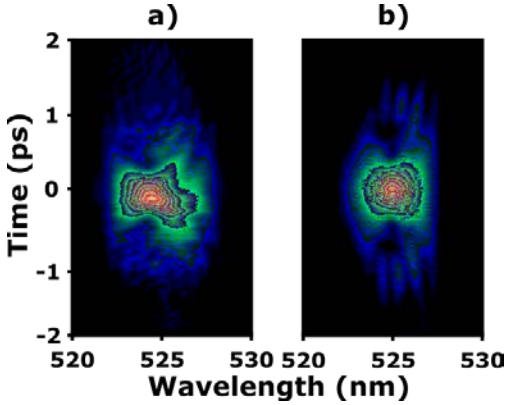


Figure 2: FROG-trace before (a) and after (b) the change of the beamsplitter and realignment of the autocorrelator.

This symmetry improvement increases the accuracy of the pulse-reconstruction algorithm [3] which therefore leads to more reliable measurements.

Conclusion

The upgrade of the back-reflection diagnostic lead to a more symmetric and spectrally better resolved FROG-trace which will produce more reliable data in upcoming experiments.

References

[1] D. J. Kane and R. Trebino, IEEE Journal of Quantum Electronics **29**, Issue 2 (1993) 199311

[2] F. Wagner, J. Hornung, C. Schmidt, et al., Review of Scientific Instruments **88** (2017) 023503

[3] K. W. DeLong, R. Trebino, J. Hunter, et al., Journal of the Optical Society of America B, **11** (1994) 002206

* This report has also been published in "HI-Jena Scientific Report 2017".

 DOI:10.15120/GR-2018-1

Experiment beamline: PHELIX
Experiment collaboration: none
Experiment proposal: none
Accelerator infrastructure: none
PSP codes: none
Grants: none
Strategic university co-operation with: Darmstadt

Generation and transport of heavy ion beams at LIGHT

J. Ding[1], D. Schumacher[2], D. Jahn[1], C. Brabetz[2], F.E. Brack[3,4], F. Kroll[3,4], R. Leonhard[1], I. Semmler[1], U. Schramm[3,4], T.E. Cowan[3,4], A. Blazevic[2], V. Bagnoud[2], M. Roth[1,6]

[1]TU Darmstadt, Darmstadt, Germany; [2]GSI, Darmstadt, Germany; [3]TU Dresden, Dresden, Germany; [4]HZDR, Dresden, Germany; [5]HI Jena, Jena, Germany; [6]FAIR, Darmstadt, Germany

The LIGHT collaboration has been founded to provide a testbed for Laser Ion Generation, Handling and Transport [1]. The laser ion generation is based on the Target Normal Sheath Acceleration (TNSA) mechanism and is driven by the PHELIX 100 TW beam line at GSI. A pulsed solenoid captures and collimates a divergent ion beam coming from the TNSA-driven ion source. By means of chromatic focusing one can cut out a part of the exponentially decaying energy spectrum. The resulting collimated beam can be compressed in phase or energy in a radiofrequency (rf) cavity which is situated two meters behind the ion source. The resulting ion beam is then diagnosed with a diamond detector for a temporal analysis of the achieved phase focus at a distance of six metres from the target.

After a successful first demonstration of the generation, handling and transport of fluorine ions in 2015 [2] and a subsequent campaign in 2016 [3] with small optimizations for the resulting ion beam, two campaigns in 2017 were dedicated to the generation and characterization of a TNSA-driven carbon ion source and the transport and bunching of the resulting ion beam. Figure 1 depicts the energy spectrum of the central part of the carbon ion beam, measured with a Thomson Parabola 0.6 m behind the target.

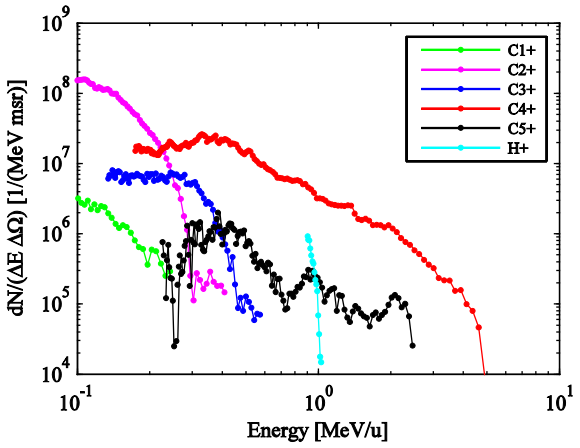


Figure 1: Energy spectrum of TNSA-driven carbon ion source. C4+ dominates the spectrum from 0.5 MeV/u on.

By heating the target up to around 1000 °C one successfully removed most of the hydrogen contaminations on the target surface and enabled efficient acceleration of heavy ions. In the process carbon ions of all charge states, barring 6+, were accelerated together with the remaining hydrogen. From figure 1 it is obvious, that carbon ions with charge state 4+ dominated the beam, from 0.2 MeV/u up to the cut-off energy at around 3.5 MeV/u.

Collimation and transport of the carbon ion beam was achieved with a pulsed solenoid, capable of delivering up to 10 T. From the thin lens approximation in equation (1) one can derive, that all generated charge states are transported through the beamline at varying energies. With future applications such as energy loss measurements of heavy ions in hot and dense plasmas in mind, the transport energy was set to around 1.2 MeV/u. For this purpose the solenoid was pulsed with 8.92 kA, leading to a maximum magnetic field on axis of 6.72 T.

$$\frac{1}{f} = \frac{q^2}{m^2}\frac{1}{4\gamma^2 v^2}\cdot\int B^2 dz \qquad (1)$$

The ion beam was diagnosed with a fast diamond detector. The result is shown in figure 2, where the Time-of-Flight (ToF) data was converted to kinetic energy and the signal has been rescaled due to the related change of bin widths. This also causes a significant rise of the noise level at low ion energies. Simulations with TraceWin, taking space charge into account, show that mainly C4+ was transported with the previously described solenoid configuration and beamline setup. In the simulations the solenoid was modelled as a current-carrying coil. The good agreement of TraceWin simulations with ToF data serves as benchmark for future simulations.

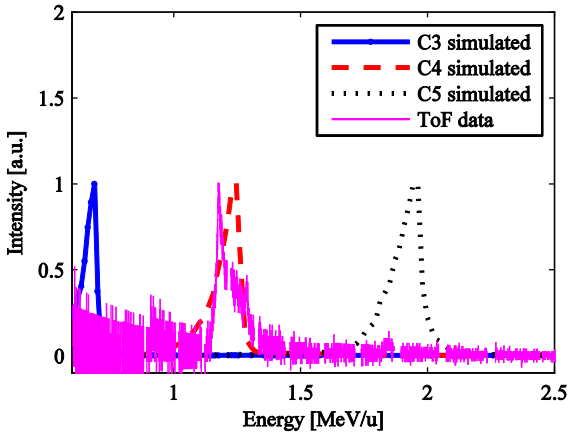


Figure 2: ToF data of diamond detector converted to energy spectrum of transported carbon beam at a solenoid current of 8.92 kA. For decreasing energy the noise per bin increases.

In two successful beam times in 2017, we were able to characterize an efficient TNSA-driven carbon ion source and demonstrate transport and energy collimation of carbon ions in our LIGHT beamline.

References

[1] S. Busold et al., NIMA 740, 94-98 (2014).
[2] J. Ding et al., HEDgeHOB annual report 2015.
[3] J. Ding et al., HEDgeHOB annual report 2016.

 DOI:10.15120/GR-2018-1

Experiment beamline: Z6
Experiment collaboration: APPA-HED@FAIR
Experiment proposal: I012
Accelerator infrastructure: UNILAC other: PHELIX
PSP codes:
Grants:
Strategic university co-operation with: Darmstadt

Final focussing of collimated proton beams with the laser-driven LIGHT beamline *

D. Jahn[1], D. Schumacher[2], C. Brabetz[2], J. Ding[1], R. Leonhardt[1], F. Kroll[3,4], F. E. Brack[3,4], U. Schramm[3,4], A. Blazevic[2,5] and M. Roth[1]

[1]Technische Universität Darmstadt, Darmstadt, Germany; [2]GSI, Darmstadt, Germany; [3]Technische Universität Dresden, Dresden, Germany; [4]HZDR, Dresden, Germany; [5]HI Jena, Jena, Germany.

Laser-driven ion sources offer excellent beam properties (high particle numbers, low emittance) and have been intensely investigated in the past two decades. These sources deliver an exponentially decaying spectrum with a ≤30 deg divergence. As many applications require a monoenergetic, collimated beam the LIGHT collaboration was founded to combine the advantages of laser-driven ion acceleration with conventional acceleration technology. A prototype beamline has been realized at the Z6 experimental area at GSI [1]. The target normal sheath acceleration source is driven by the Petawatt High-Energy Laser for Heavy Ion Experiments (PHELIX) 100 TW beam and delivers an exponential spectrum up to several tens of MeV. In the next step, a high-pulsed solenoid selects protons of (8±1) MeV via chromatic focussing directly 10 cm behind the thin target foil. In 2 m distance, the protons pass a radiofrequency cavity and are phase-rotated. Through the phase rotation the proton bunch can be energy-compressed to $\Delta E/E_0$ = (2.7±1.7) % or time-compressed into the subnanosecond regime [2]. Behind the cavity, a transport line leads the collimated proton beam to a second target chamber where diagnostics and applications can be placed. Inside this second chamber, a new final focussing system has been installed (6 m behind the target) for steep focussing. This part is necessary to prepare the beam for applications requiring a high intensity beam, e.g. for energy-loss measurements inside plasmas or to study fast processes inside materials. As a final focusing system a second high-field solenoid was placed in the second target chamber and operated at 7 T. As a detector a radiochromic film stack (RCF) was placed 10 cm behind the solenoid. The protons penetrate deeper into the RCF stack, if they have a higher energy according to their characteristic Bragg peak behaviour. The protons deposit their energy inside the RCF films leading to a change in their colour which is analysed. The RCF films of the focus are shown in figure 1. The solenoid parameters haven been chosen in this way that 8.3 MeV protons are focussed in a 460 ps bunch length, shown in the 4th RCF film (figure 1). The focal spot size is 1.3 mm x 2 mm with $3x10^8$ protons resulting in a current of 7.5 x 10^8 1/ns ~ 121 mA. The focus profile is shown in figure 2. In 2015, we measured a focal spot size of 2.3 mm x 2.3 mm [3]. In the next experimental campaign in 2018, these focussed proton bunches will be used for first application studies, e.g. precise energy loss measurements in plasma.

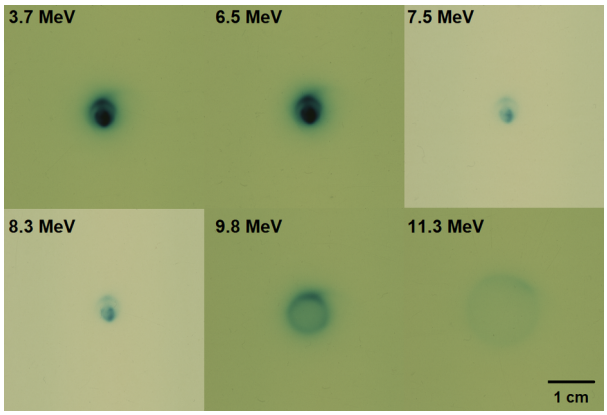


Figure 1: RCF stack detecting the final proton focus: The Bragg peak energy is shown. The 3rd and 4th RCF films are of the type HD-V2, the others are type EBT3. The solenoid´s setting focusses 8.3 MeV protons which is clearly seen in the 4th RCF film. On the other RCF films, the particular particle trajectories at the specific energies are shown.

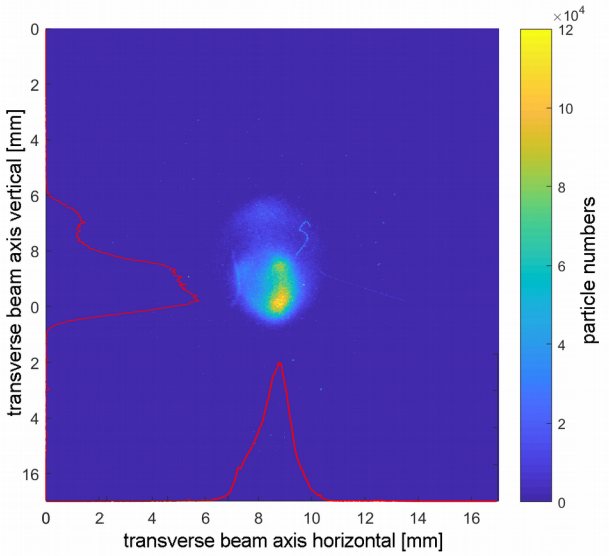


Figure 2: Proton beam profile measured with the 4th RCF film: The focal spot size is 1.3 mm x 2 mm at an energy of 8.3 MeV. The deposited energy is converted into particle numbers per pixel and shown.

References

*[1] S. Busold et al., NIMA **740**, 94-98 (2014)*
*[2] S. Busold et al., Scientific Reports **5**,12459 (2015)*
[3] D. Jahn et al., GSI Scientific Report 2015 (2015)

* This report is also published in *News and Reports from High Energy Density generated by Heavy iOn and Laser Beams 2017.*

 DOI:10.15120/GR-2018-1

Experiment beamline: Z6
Experiment collaboration: APPA-HED@FAIR
Experiment proposal: none
Accelerator infrastructure: UNILAC
PSP codes: none
Grants: none
Strategic university co-operation with: Darmstadt

Emittance measurement with the pepperpot measuring method at the LIGHT beamline

R. Leonhardt[1], D. Jahn[1], J. Ding[1], D. Schumacher[2], C. Brabetz[2], F. E. Brack[3,4], F. Kroll[3,4], U. Schramm[3,4], A.Blazevic[2,5], V.Bagnoud[2,5], and M. Roth[1]

[1]Technische Universität Darmstadt, Darmstadt, Germany; [2]GSI Helmholzzentrum für Schwerionenforschung, Darmstadt, Germany; [3]Technische Universität Dresden, Dresden, Germany; [4]Helmholz-Zentrum Dresden-Rossenddorf, Dresden, Germany; [5]Helmhilz-Institut Jena, Jena, Germany

The laser-driven LIGHT (Laser Ion Generation, Handling and Transport) beamline at the Z6 experimental area is build to shape ion beams based on the TNSA-source which delivers an exponential spectrum [3]. The ion beam is captured with a solenoid. The solenoid focuses the beam chromatically. The collimated energy is 7.8 MeV with an energy spread of 1.7 MeV. A following rf-cavity enables a phase rotation of the incoming particle beam. The resulting particle pulse length of the particle bunch is 462 ps ± 40 ps [1].

Accordingly, the emittance is the central value for the focusablity and the divergence of the beam [2]. The used method to measure the emittance is the pepperpot method because it allows the transverse emittance measurement with only one single shot. The pepperpot plate is placed 42.5 cm behind the solenoid. To image the beam behind the pepperpot device radiochromatic ms (RCF) are used to image the transported particles which allows to analyze the r-r' transverse phase space [3]. To analyze the diferent energies of the particles, the RCF layers are stacked so that the particles with diferent energies are stopped in diferent layers of the stack.

In September 2017, latest emittance measurement of a proton beam were performed. First, the solenoid was turned of to measure the emittance of the TNSA-source (fg. 1). Figure 1 shows the RCF image of the TNSA-source at a energy of 3.8 MeV. The picture has the typical pepperpot symmetry. The protons are clustered at specifc areas at regular intervals in a two-dimensional array which is seen at the regular dark dots. The transverse emittance of the 3.8 MeV domain is in the x-direction 2.7 mm mrad and in the y-direction 1.5 mm mrad. Fgure 2 shows the tranverse phase space of the x-direction. The phase space is calculated out of the measured image of fgure 1. The tranverse phase space of the y-direction is analogous to the phase space of the x-direction.

The next step was to measure the emittance of the focused beam. The solenoid was turned on at di erent voltages so that the in uence of the solenoid voltage on the emittance was measured and will be evaluated in the future.

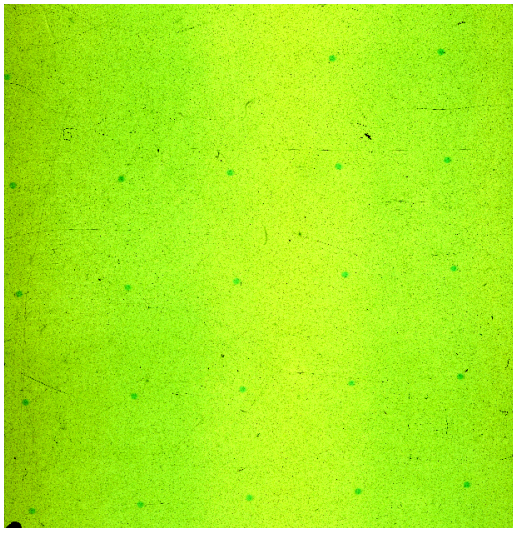


Figure 1: RCF layer at 3.8 MeV showing the TNSA-source emittance. The protons have the beamlet symmetry of the pepperpot, which allows the calculation of each transverse direction of the emittance.

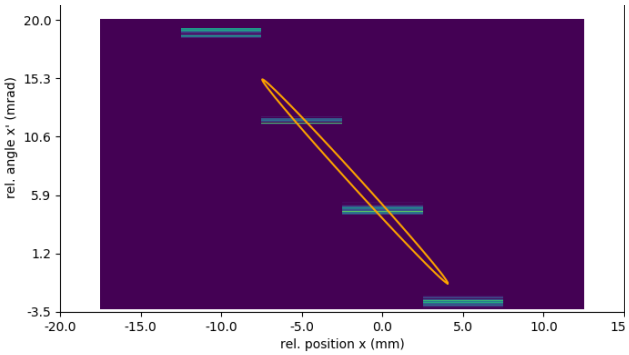


Figure 2: The tranverse phase space of the x-direction of the 3.8 MeV domain. The phase space is calculated out of the beamlets in fgure 1. The width of the horizontal lines are the angle-distributions of the columns.

References

[1] S. Busold et al., Scientific Reports 5, 12459 (2015)
[2] S. Fritzler et al., Phys. Rev. Lett. 92, 165006 (2004)
[3] S. Busold et al., Phys. Rev. special topics 16, 101302 (2013)

 DOI:10.15120/GR-2018-1

Ion acceleration with high laser energy using variable thickness liquid crystal

P. L. Poole[1], G. E. Cochran[2], J. Hornung[3], V. Schanz[3], M. Zimmer[3], V. Bagnoud[4], M. Roth[3], B. Zielbauer[4]

[1]LLNL, Livermore, CA 94551, U.S.A, [2]OSU, Columbus, OH 43210, U.S.A., [3]TU-D, Darmstadt, Germany, [4]GSI, Darmstadt, Germany

Laser-based ion acceleration is an area of significant interest due wide-ranging applications from laboratory astrophysics to radiography to hadron cancer therapy [1]. Several mechanisms have been studied that enable 10s of MeV/nucleon accelerated energies, but the optimization of these depends strongly on both laser parameters (contrast, energy, pulse duration) and target conditions (thickness, density, geometry), requiring multiple campaigns preferably with identical targets.

Experimental setup

An experimental campaign (Fig. 1) was carried out on the PHELIX laser (180 J, 500 fs, focused intensity > $1x10^{20}$ W/cm^2) to observe changes in accelerated protons due to target thickness variations, achieved with liquid crystal films tunable from 10 nm to over 50 µm [2] (inset in Fig. 1). A confocal positioner was used to align the films with µm-scale accuracy, and proton energy was recorded using a stack of RadioChromic Film (RCF). Transmitted light was observed using a Frequency Resolved Optical Gating (FROG) autocorrelator and scatter screen, where enhanced transparency indicates the onset of volumetric acceleration mechanisms.

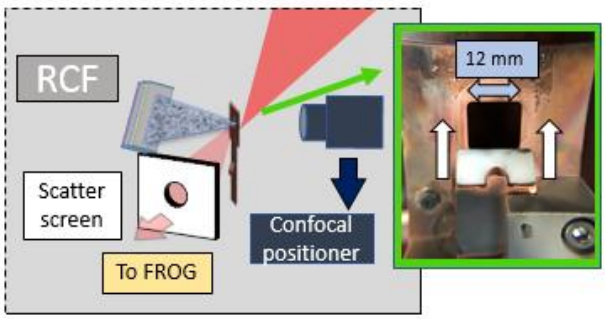


Figure 1: Experimental schematic including target formation device (detail in inset) and several alignment/experimental diagnostics.

Results and discussion

Though laser fluctuations can significantly impact proton acceleration, the highest RCF dose was observed near 400 nm target thickness for a range of pulse energies (Fig. 2), with a decrease in dose consistently observed for thinner targets. This indicates the onset of laser pre-pulse affecting film morphology prior to main pulse arrival. This data completes a series of liquid crystal ion acceleration experiments [3] taken across 4 facilities with a wide range of laser energies (1-200 J), pulse durations (30-500 fs), and intensity contrasts, and is the first to be done over this range of parameters using one target material for the full scan.

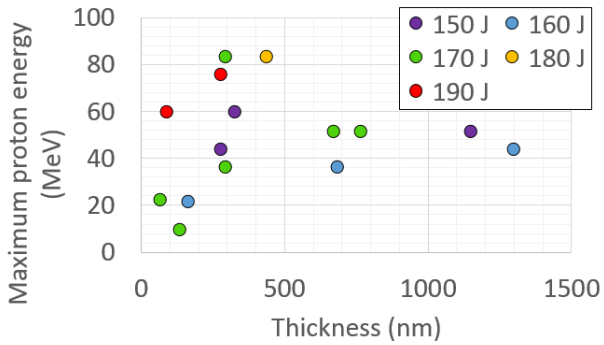


Figure 2: Proton energy observed for changing target thicknesses at different incident laser energies, showing maximum acceleration around 400 nm (error bars ±3 MeV).

Properly identifying RCF signal as high energy protons or low energy electrons/x-rays requires a sophisticated stack unfold analysis that is ongoing using data from the set of campaigns. Additionally, 2D Particle-in-cell (PIC) simulations are underway to further understand the intra-target physics inherent to thin target ion acceleration and corroborate the experimental ion data. Figure 3 shows the accelerated proton spectrum from two different intensities on a 250 nm liquid crystal target (implicit solver, energy conserving interpolation, fully ionized target, 12 x 96 nm cell size).

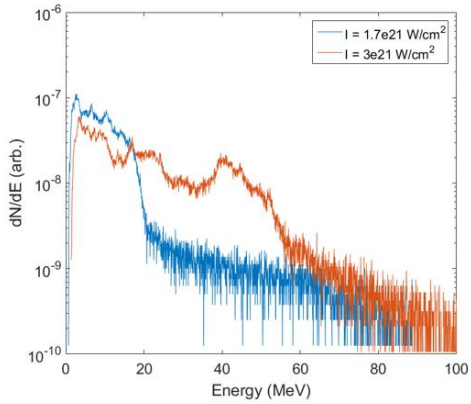


Figure 3: 2D PIC simulation showing proton energy distribution for two different intensities. These simulated spectra can be compared to RCF data to validate proton signal.

References

[1] A. Macchi et al., Rev. Mod. Phys. 85, 751 (2013).
[2] P. L. Poole et al., App. Phys. Lett. 109, 151109 (2016).
[3] P. L. Poole et al., New J. Phys. 20, (2018).

Experiment beamline: none
Experiment collaboration: none
Experiment proposal: P141
Accelerator infrastructure: none
PSP codes: none
Grants: **E**uratom research and training programme 2014 - 2018 under grant agreement No 633053; Deutsche Forschungsgemeinschaft through the Munich-Centre for Advanced Photonics cluster of excellence and the program Transregio 18 (TR18)
Strategic university co-operation with: Darmstadt

 DOI:10.15120/GR-2018-1

Ion acceleration using a flattop laser beam

M. Afshari[1], *V. Bagnoud*[1]

[1]GSI, Darmstadt, Germany;

Laser ion acceleration [1] is of particular interest for Helmholtz Association and for applications driven by upcoming FAIR facilities specifically for warm dense matter studies.

The most widely accepted mechanism for the laser ion acceleration is Target Normal Sheath Acceleration (TNSA) [2]. According to the TNSA model, the shape of the accelerated ions strongly depends on the structure of the hot electron cloud in the backside of the target which itself follows the laser beam profile. Accordingly, a Gaussian laser beam produces a Gaussian hot electron sheath which accelerates ions non-uniformly in all directions. Such high angular distribution is not suitable for most applications due to severe energy loss after passing few micrometers.

In a novel approach we propose a scheme using a phase plate to generate a uniform laser beam which generates a concentrated ion beam with much lower angular divergence. In the following, we present the results of EPOCH [3] simulation for two different laser profiles: first a Gaussian laser profile and second a flattop laser profile to check the differences.

Gaussian laser profile

To benchmark our simulation, we considered a Gaussian laser profile and simulated its interaction with a 10 µm plastic layer. The laser beam propagates in the x direction and has a peak intensity I = 1 × 10^{21} W/cm^2, its wavelength equals 1.053 µm and its temporal and spatial lengths equal 575 fs and 8 µm (FWHM) respectively.

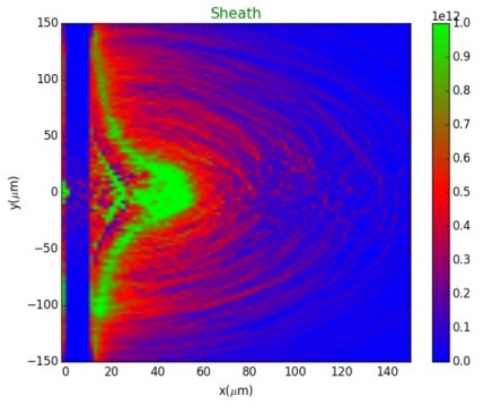


Fig.1: Electrostatic field strength distribution due to the interaction of a Gaussian laser beam with 10 µm plastic.

The interaction of the Gaussian laser profile with the plastic layer creates a Gaussian like sheath, as it is shown in Fig.1 at t = 1100 fs. Such sheath is resulting from not only the laser intensity distribution but also the electron dynamics at the rear side of the target. For these simulation parameters, the angular distribution of the protons found to be a typical TNSA angular distribution with a divergence angle with the FWHM of 50°.

Flattop laser profile

The novel idea of this study is to work with a distribution of the laser focus that is spatially top hat. A way to come around this difficulty is to employ a random phase plate (RPP) that creates a speckle pattern of high spatial frequency over the desired spot size. The laser propagates in the x direction and has peak intensity I = 1× 10^{19} W/cm^2, wavelength equals to λ= 1.053 µm with temporal and spatial lengths equal to 1000 fs and 104 µm (FWHM) respectively. The electric field distribution at the input of the simulation box is calculated using Matlab such as to obtain the desired intensity distribution at x = 0 and fed as numerical input into EPOCH. Using the same laser parameters, energy and duration, as for the Gaussian beam yields reduced electrostatic field strength, as it can be seen in Fig.2, but the resulting electric field distribution is much more favourable. Indeed, the interaction of the flattop laser profile with the 10 µm plastic target creates a smooth and uniform flattop sheath which propagates in the direction normal to the target. The most important result is that the angular distribution of ions now is much more peaked around the target normal direction. At this instant, the particles are propagating in a total divergence angle of 12° with the FWHM of 2°.

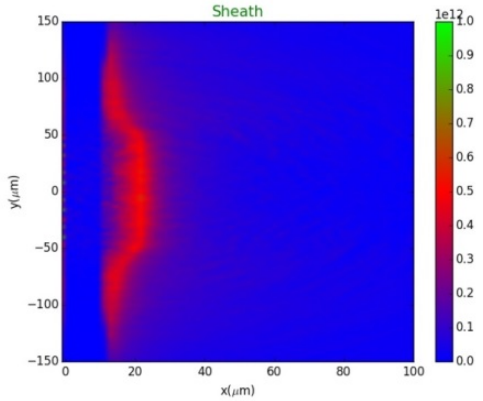


Fig.2: Electrostatic field strength distribution due to the interaction of a flattop laser beam with 10 µm plastic.

References

[1] M. Roth et al., The generation of high-quality, intense ion beams by ultra-intense lasers, Plasma Phys. Control. Fusion, 44 (2002).

[2] S. C. Wilks et al., Energetic proton generation in ultra-intense laser–solid interactions, Physics of Plasmas, 8, 542 (2001).

[3] T. D. Arber et al., A particle-in-cell code for laser-plasma interactions: test problems, convergence and accuracy, J. Comp. Phys., 2014.

Experiment beamline: none
Experiment collaboration: APPA-HED@FAIR
Experiment proposal: P152
Accelerator infrastructure: other: PHELIX
PSP codes: none
Grants: Euratom EUROfusion-ER-ToIFE(19040)
Strategic university co-operation with: none

 DOI:10.15120/GR-2018-1

Progress on the development of an actively cooled glass amplifier at PHELIX

M. Patrizio[1], V. Bagnoud[2,3], B. Zielbauer[2], M. Roth[1,4]

[1]TU Darmstadt, Darmstadt, Germany; [2]GSI, Darmstadt, Germany;
[3]Helmholtz-Institute Jena, Jena, Germany; [4]FAIR, Darmstadt, Germany;

As contribution to FAIR, PHELIX, in cooperation with the Technical University of Darmstadt and funded by the Bundesministerium für Bildung und Forschung (BMBF), is developing an actively cooled glass amplifier for a PHELIX-like laser system planned as a diagnostic tool at the APPA Cave at FAIR. This new amplifier design seeks to improve on the repetition rate of glass disc laser systems to enable more elaborate experimental campaigns [1].

Simulated wave front deformation

Building on the simulations discussed in [2], a mesh containing the temperature distribution in the glass discs can be exported. Taking into account the temperature induced change in refractive index and expansion of the glass this temperature mesh can be converted into a 2D map of the optical path length. From this map the deformation of a plane wave transmitted through the amplifier glass can be calculated (Fig. 1). The simulation results show very low phase deformations after 300 s of cooling. This further encourages development of the concept.

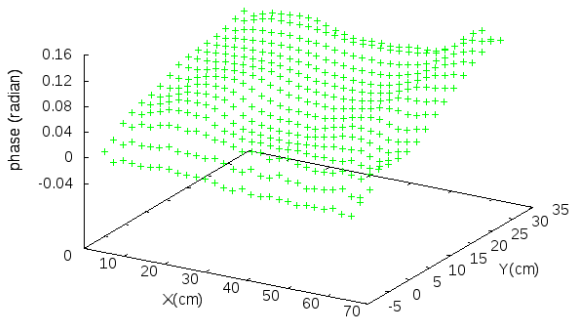


Figure 1: Simulated wave front behind the amplifier after a cooling time of 300 seconds.

Cooling liquids

Extensive research was conducted to find a suitable cooling liquid for our amplifier. During this research several key parameters of the potential coolants have been identified. Refractive index, absorption coefficient, viscosity and chemical compatibility are the most important factors to be taken into account. The heat capacity is negligible due to the low thermal conductivity of the glass. Since the absorption coefficient for liquids at certain wavelengths is not readily available for many liquids, help was acquired from the department of Surface chemistry and spectroscopy at the Technical University of Darmstadt. Their Photo-Spectrometer was used to measure the absorption coefficients for several potential cooling liquids. This was done to assess the viability a perfluorinated hydrocarbons (F2 PP-series). The results are shown in Fig. 2.

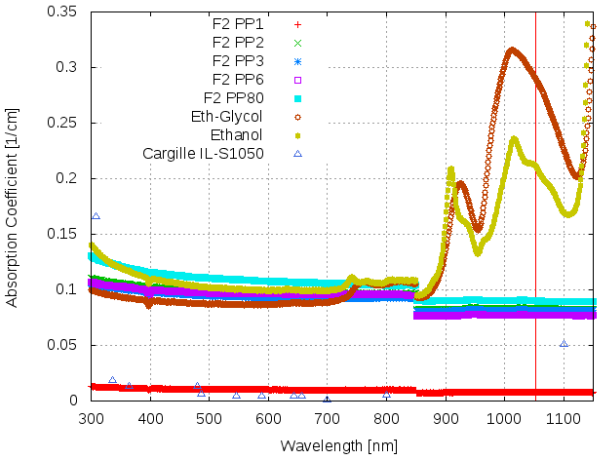


Figure 2: Absorption coefficients of several potential cooling liquids as function of their wavelength (laser wavelength as red vertical line). Measurements conducted at TU Darmstadt, Workgroup Prof. Dr. Hess. Data for Cargille IL-S1050 extracted from data sheet for reference.

Concept Design

Parallel to the search for a suitable cooling liquid the design phase for a concept of the amplifier prototype was started. The concept calls for a modular design for various configurations of the prototype, compatibility with the PHELIX infrastructure for potential Phase-0 use, no contact between glass and metal parts to avoid damaging the glass and no bending forces on the glass especially in the direction of the laser beam to avoid additional distortions of the wave front.

References

[1] V. Bagnoud *et al.*, Laser-based pump-probe equipment for the APPA Cave at FAIR, Revision 2.2 (2014) (TDR for the HEDgeHOB/WDM collaborations at FAIR)

[2] M. Patrizio *et al.*, Development of an actively cooled glass amplifier at PHELIX, GSI Scientific Report 2016 (DOI:10.15120/GR-2017-1)

Stretcher simulation for temporal laser pulse profile optimization

V.A. Schanz[1,2], V. Bagnoud[1], M. Roth[2]

[1]GSI, Darmstadt, Germany; [2]TU Darmstadt, Darmstadt, Germany

The temporal pulse profile of a high-intensity laser pulse is very relevant for laser-plasma experiments. Parts of the pulse interacting with a target are already intense enough to create a pre-plasma prior to the arrival of the main peak. The rising slope of the laser pulse, which persists hundreds of picoseconds, influence the pre-plasma conditions the most. Several publications in the past conclude noise in the CPA-systems stretcher as the prime reason for this slow rising slope. For further investigation, we developed a MATLAB based ray tracing code, simulating stretcher geometry with the possibility to generate noise at the optics of the stretcher. In this report, we present the status quo of this ray tracing simulation.

Temporal pulse contrast

Up to the present day, all short-pulse high-intensity laser systems have one issue in common: the need to improve and understand their temporal contrast, which is defined as the ratio of the maximum intensity to the intensity of the pulse at a certain time before the maximum. Especially, the rise time at the leading edge of the main peak, which is depicted in Figure 1, is much longer than a Fourier-transform limited pulse dictates.

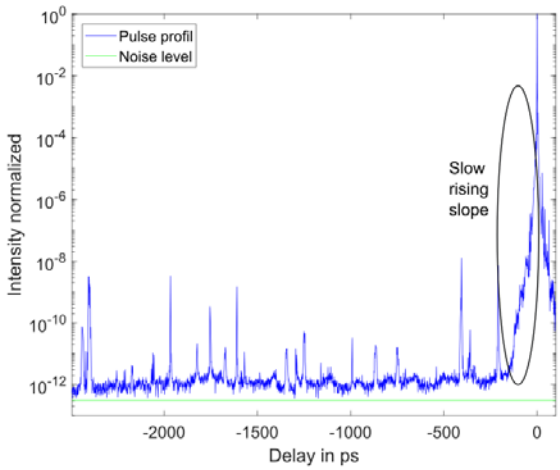


Figure 1: Temporal pulse profile of the PHELIX laser, measured with a specially designed detector [1,2]. The detection limit is shown in green and the leading edge, which will be improved with the development presented in this report, is highlighted in black.

Almost all high-intensity short-pulse laser systems are based on the chirped pulse amplification (CPA), where the pulse is temporally stretched, amplified and afterwards recompressed. Stretching and compression are done by the arrangement of dispersive optics, e.g. gratings, whereby a wavelength dependent optical path is achieved. Today's conventional wisdom expects the main reason for the shape of the leading slope in amplitude and phase modulations, occuring in the stretcher.

Ray tracing CPA system analysis

To investigate this topic, we created a MATLAB based ray tracing code and simulated the propagation of a beam through a stretcher- compressor setup (Fig. 2), resulting in zero dispersion after propagation through the whole system.

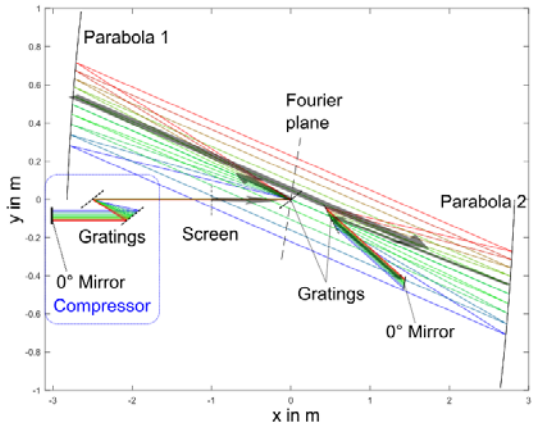


Figure 2: Visualization of a simulated beam path, generated with a self-written ray tracing code. Different colours represent beams with different wavelength. Positions of simulated optics and for calculation needed planes (Screen and Fourier plane) are shown in black. Rays start at the screen, propagating to the right, following the indicated grey arrows. After hitting the 0° mirror, they propagate back on the same path, passing the screen and entering the compressor. For clarity reasons, no arrows are shown for the second pass (back) in the stretcher and the passes in the compressor.

Randomly distributed scattering objects, with densities corresponding to clean room definitions, are defined on the gratings and the Fourier plane. When hit, such an object will attenuate the intensity of an incoming ray and apply an additional phase. At a defined screen the spectrum and spectral phase of the resulting pulse after propagation through the system is determined. This allows the calculation of the resulting temporal pulse profile.

Parameter studies will be carried out this year to investigate the influence of different distortions at different optics, followed by experimental verification.

References

[1] V.A. Schanz et al., “Noise reduction in third order cross-correlation by angle optimization of the interacting beams”, Opt. Express 25, 9252-9261 (2017)

[2] V.A. Schanz et al. EP 16 188 142.0, EPO, patent pending

Strategic university co-operation with: Darmstadt

 DOI:10.15120/GR-2018-1

Characterization of hard X-ray sources for radiographic purposes at the PHELIX laser

B. Borm[1], J. Hornung[2], D. Khaghani[2,3], P. Neumayer[4]

[1]Goethe-Universität Frankfurt, Germany; [2]Helmholtz-Institut Jena, Germany; [3]Friedrich-Schiller-Universität Jena, Germany; [4]GSI, Darmstadt, Germany

High-energy high-intensity lasers – like the Petawatt Laser for Heavy Ion Experiemnts (PHELIX) at GSI – are a formidable tool to create hard X-ray sources with extraordinary properties. These are mainly the short emission duration, which is in the same order of magnitude as the laser pulse duration, the small source size, which is defined by both the target geometry and the laser focus size, and the spectral distribution which extends into the several 100 keV range [1]. All of these properties make laser-based hard X-ray sources very suitable for radiography of hydrodynamically evolving high-Z high-density plasmas, like they will be produced in the future plasma physics experiments at FAIR (e.g. LAPLAS). Since the emitted X-ray spectrum depends on a variety of experimental parameters, particularly the laser intensity and the target geometry, a full characterization of the source properties is an appropriate step to reliably predict radiographic imaging performance.

We have performed an experiment at the PHELIX laser with the goal to determine the emission characteristics of bremsstrahlung X-ray sources regarding spectral and angular distribution, depending on the laser intensity and contrast and on the target geometry. Furthermore, the source sizes were measured. The laser intensity was varied between 4.1×10^{16} and 1.1×10^{20} W/cm², the contrast between the "low" of 10^{-6} and the high of $<10^{-10}$. Two target types were used: gold foils of 5 µm thickness and tungsten wires of 5 µm diameter. Bremsstrahlung was detected by a set of 12 hard x-ray spectrometers, placed in the horizontal and vertical around the target (white tubes in Fig. 1). Using imaging plate detectors and a set of tantalum filters, the spectrometer working range is 20-400 keV. The attenuated signal was fitted by a Maxwellian energy distribution with two effective temperatures to retrieve conversion efficiencies (CEs) from laser energy to

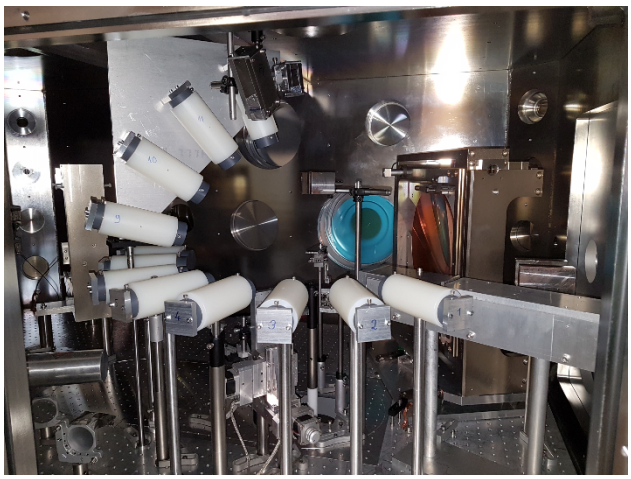


Figure 1: Hard x-ray spectrometer array to determine the emission distributrion of the laser-driven x-ray source.

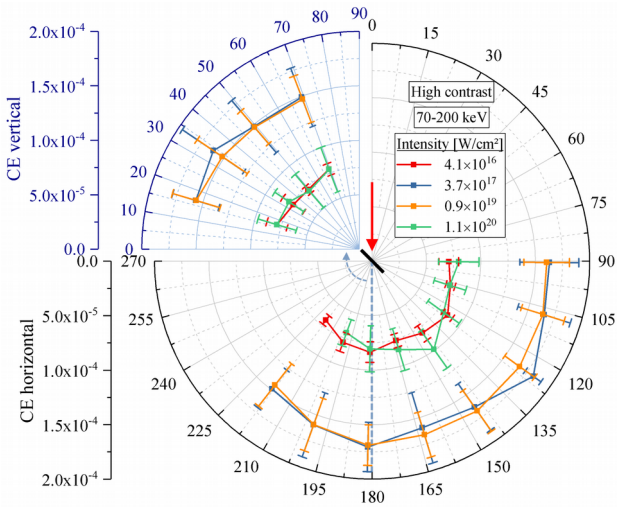


Figure 2: Angular dependency of the CE

x-ray emission into the 70-200 keV range. Source sizes were determined using a gold knife-edge imaging setup with 1 µm spatial resolution.

We find that bremsstrahlung up to 400 keV is emitted isotropically, independent of laser intensity and contrast (see Fig. 2) and target type. The CE however rises between the lower two intensities used, then drops again for the highest by a factor of around 2. The CE is systematically higher for the low contrast laser pulses by up to a factor of 2. On average, we determined a CE into the 70-200 keV interval of $(1.5\pm0.2)\times10^{-4}$ at 0.9×10^{19} W/cm² and high contrast using gold foil targets.

The source sizes measured in the thin direction of the foil targets varied between 3.7-12.0 µm. On average, wire targets at high contrast showed 5 µm source size, exactly their diameter. In a follow-up experiment, this laser-generated x-ray source has enabled x-ray phase contrast imaging of laser-driven shock waves.

References

[1] R. Tommasini *et al.*, Physics of Plasmas. **18**, 056309 (2011)

[2] L. Antonelli *et al.*, GSI Scientific Report 2017

Experiment beamline: PHELIX
Experiment collaboration: none
Experiment proposal: P134
Accelerator infrastructure: none
PSP codes: none
Grants: none
Strategic university co-operation with: Frankfurt-M

Application of a TLD-based ten channel system for the spectrometry of bremsstrahlung generated by laser-matter interaction

N. Zahn[1], O. Rosmej[1,2], F. Horst[2], S. Zähter[1], A. Sokolov[2], N. Borisenko[3], L. Borisenko[3], N. Pimenov[4] and J. Jacoby[1]

[1]Goethe University, Frankfurt, Germany; [2]GSI, Darmstadt, Germany; [3]P. N. Lebedev Physical Institute (RAS), Moscow, Russia ; [4]Zelinsky Institute of Organic Chemistry (RAS), Moscow, Russia

The interaction of relativistically intense laser pulses produced by the PHELIX-system with near critical plasmas has been investigated in order to optimize the energy and the total charge of the laser-accelerated electron bunch for FAIR-relevant applications. The enormous increase of total charge and energy of the laser-accelerated electrons was predicted by the theory [1], that is much higher than defined by Wilks law [2]. In described experiments, electrons were accelerated in plasma of near critical density. The electron energy distribution was directly analysed by applying a static magnetic field and indirectly by measuring the bremsstrahlung radiation produced when MeV electrons were passing through the 17 mm-thick steel flange placed 87 cm distant from the target in the laser propagation direction. For measurements of the gamma bremsstrahlung spectra 10 channels TLD detector-based thermoluminescence dosimetry method was applied.

The schematic drawing of the ten channel spectrometer is shown in Fig. 1. The TLD-spectrometer has a cylindrical shape with a default incident direction of the radiation. Ten TLD-cards are placed between absorbers of different material and thickness inside a shielding from lower to higher Z materials with a collimator window in the front. The incident x-rays penetrate the TLD's. The absorbers cause a different response of every TLD, which can be used as information about the spectrum of the incident x-rays. The spectrometer is designed for an energy range from 30 keV to 100 MeV [3].

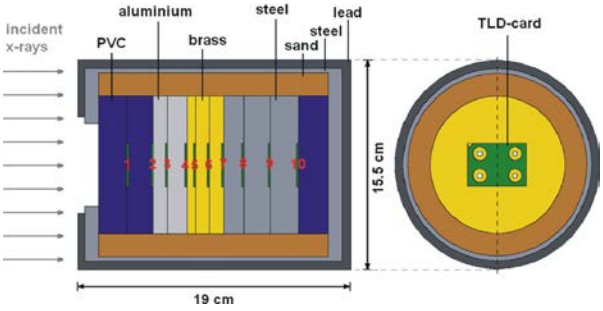


Figure 1: Schematic view of the TLD-spectrometer [3].

The materials of the TLD cards used in these measurements are pieces of doped lithium fluoride in two variations - Harshaw TLD 700 (^{7}LiF: Mg, Ti) and TLD 700H (^{7}LiF: Mg, Cu, P). TLDs absorb radiation and emit photons proportionally to the deposited dose when heated to a few hundred degrees Celsius.

In the experiment (P138, Oktober 2017) electrons were accelerated in the interactions of the PHELIX-laser pulse of $3\cdot10^{19}$ W/cm^2 intensity with different foil-targets (Ti, Cu, Ta) of 5-20 µm thickness and with low density foams. Additionally, foil-targets were combined with the CHO foam layer (2mg/cc Triacetate-Cellulose $C_{12}H_{16}O_8$) with thickness of 300 and 500 µm. The laser energy was 100 J, with pulse duration of 750± 250 fs. Supplementary to the shots with a single laser pulse, a double pulse configuration was used where a 1.5 ns prepulse with a time delay of 0.5-3 ns before the main pulse and energies of 1-3 J was applied in order to drive a super-sonic ionization in the low density CHO-foams and create a homogeneous channel of near critical plasma. Using pre-ionized by the ns-prepulse low-density CHO-plasma with a mean density near to the PHELIX-laser critical density ($n_e=10^{21}\cdot$cm^{-3}) it was possible to increase by 2-3 orders of magnitude the fraction of 20-100 MeV electrons compared to the case of the laser interaction with planar foils and thus to gain 2-3 orders of magnitude increase of the gamma-rays. Preliminary results for the spectrometer response to different laser shots are shown in Fig. 2. The experiments have shown the effective generation of electrons with tens of MeV-energy if the relativistic laser pulse interacts with extended plasmas of the near critical density.

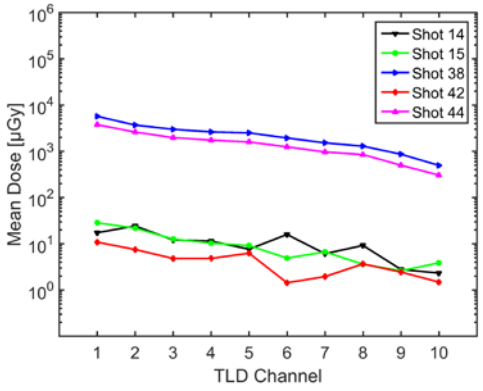


Figure 2: Preliminary results for five different shots. Shots 14, 15 and 42: contrast 10^{-10}, no prepulse, target – 25 µm Cu-foil. Shots 38 and 44: contrast 10^{-10}, prepulse – 1 J, t = 1.5 ns, dt = 5 ns, target – CHO-Foam 500 µm.

The main mechanisms leading to extreme high electron energies are the laser beam self-focusing in the preplasma and a betatron mechanism of the electron acceleration. TLD measurements of the radiation dose are consistent with results of the electron spectrometers. Using the Monte Carlo code FLUKA [4] the electron spectra will be evaluated from the photon radiation doses measured by the TLDs.

References

[1] L. P. Pugachev et al., NIM A **829** (2016) 88-93.
[2] S. C. Wilks et al., Phys. Rev. Lett. **69** (1992) 1383.
[3] F. Horst et al., NIM A **782** (2015) p. 69-76.
[4] http://www.fluka.org.

 DOI:10.15120/GR-2018-1

Optimisation of laser based sources of electrons and gammas for backlighting of high areal density targets at FAIR*

Ş. Zähter[1], O. Rosmej[2], N. Andreev[3], L. Borisenko[4], N. Borisenko[4], B. Borm[1,2], P. Christ[1], F. Horst[2,5], P. Neumayer[2], D. Khaghani[2,6], V. Pimenov[7], L. Pugachev[3], K. Schmal[1], C. Wagner[1], N. Zahn[1], K. Zerbe[1], J. Jacoby[1], APPA-HED@FAIR, Plasmaphysics/PHELIX

[1]Institute for Applied Physics (IAP), Goethe University, Frankfurt am Main, Germany; [2]GSI, Darmstadt, Germany; [3]Joint Institute for High Temperatures (JIHT), Russian Academy of Sciences (RAS), Moscow, Russia; [4]Lebedev Physical Institute (LPI), RAS, Moscow, Russia; [5]Justus-Liebig-University, Giessen, Germany; [6]Friedrich Schiller University, Jena, Germany; [7]Zelinsky Institute of Organic Chemistry (ZIOC), RAS, Moscow, Russia

The development of laser based intense and well directed beams of MeV electrons and Gamma-rays for backlighting states of matter with high areal density is of great importance for the planned experiments at FAIR. If the laser parameters cannot be changed, one will be able to optimise the properties of the secondary laser sources using custom made structured targets of near critical density. A significant increase of the electron number at tens of MeV energy makes such type of laser-based electron source very prospective for the diagnostic of high areal density high energy density states. Simulations demonstrate that the interaction of relativistic laser pulses ($2-4\cdot10^{19}\,\mathrm{W/cm^2}$) with a near critical plasma layer ($10^{21}\,\mathrm{cm^{-3}}$) leads to an effective generation of highly energetic electrons (>10-20 MeV), carrying a charge that at least 2 orders of magnitude exceeds prediction by ponderomotive scaling for the incident laser amplitude [1]. Electrons accelerated from the by a ns-prepulse preionised low density foam target (triacetatecellulose, $C_{12}H_{16}O_8$) with a thickness of 500 µm and $2\,\mathrm{mg/cm^3}$ density have the highest energies and the highest charge (ca. 25 nC for electrons with energies higher than 30 MeV). In this work we present first pilot experiments on the characterization of MeV electron beams generated by the interaction of the PHELIX-laser pulse with low density CHO-foams (P138, October 2017).

Electron spectra up to 100 MeV were measured by the application of dipole magnets as dispersive elements. The electrons follow a certain path in the spectrometer according to their kinetic energy and the radius of gyration. That leads to a calculated dispersion. FUJI Film BAS-TR imaging plates were used as detectors. The response function of the imaging plates is known for photons, electrons and several types of heavier particles [2]. The schematic of this electron spectrometer is shown in Figure 1.

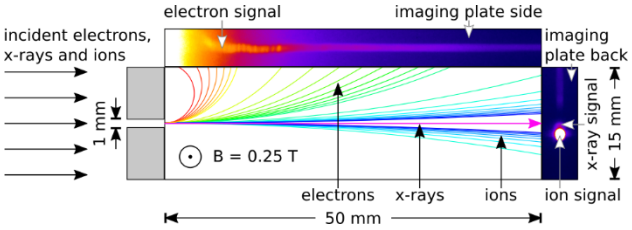
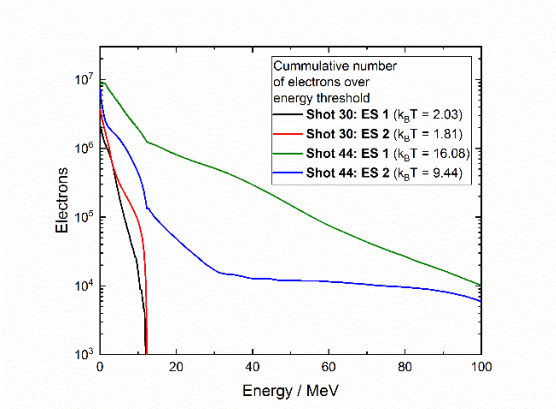


Figure 1: Schematic view of the electron spectrometer. Data shown in false colour images.

The interaction of the high power laser pulse of relativistic intensities with different target materials allow for the generation of MeV electrons. The Ponderomotive law predicts an electron temperature of 2.1 MeV for the used laser intensity. In the mentioned experiments with near critical plasmas the production of intense MeV electron beams is demonstrated. Figure 2 shows the cumulative number of electrons above an energy threshold up to 100 MeV. The usual way for laser-based particle acceleration is to shoot onto Cu-foils (shot 30, black and red solid lines). In comparison the interaction of relativistic laser pulses with pre-ionized low density plasmas of near critical density leads to a strong increase of the number of



electrons with energies above 10 MeV (green solid line, shot 44).

Figure 2: Cumulative number of electrons above energy threshold.

Electrons are mostly accelerated in laser direction reaching a mean energy/temperature of 16 MeV. Hot MeV electrons interacted with a 17 mm thick Fe-flange and created hard bremsstrahlung radiation measured by means of a 10 channel TLD-spectrometer [3]. The radiation dose on the TLD-cards showed the same result as the electron spectrometers: 2-3 orders of magnitude increase in the bremsstrahlung dose for the direction of laser propagation. The experiments have demonstrated the stability of the effect.

References

[1] L.P. Pugachev et al., “Acceleration of electrons under the action of petawatt-class laser pulses onto foam targets”, NIM A 829 (2016), pp. 88-93.

[2] T. Bonnet et al., “Response functions of imaging plates to photons, electrons and 4He particles”, RSI 84 (2013), pp. 103510-1-103510-7.

[3] F. Horst et al., “A TLD-based ten channel system for the spectrometry of bremsstrahlung generated by laser-matter interaction”, NIM A (2015), p. 1.

Experiment beamline: PHELIX
Experiment collaboration: APPA-HED@FAIR
Experiment proposal: P138
Accelerator infrastructure: none
Grants: BMBF-Project: 05P15RGFAA, HGS-Hire
Strategic university co-operation with: Frankfurt-M / Gießen

* Work supported by BMBF-Project: 05P15RGFAA, HGS-Hire;
This report is also submitted to "News and Reports from High Energy Density generated by Heavy Ion and Laser Beams 2017"

 DOI:10.15120/GR-2018-1

Investigation of proton induced demagnetisation effects in Permanent Magnet Quadrupoles*

M. Endres[2], *M. Schanz*[1,2]

[1]GSI, Darmstadt, Germany; [2]TU Darmstadt

The PRIOR-I (Proton Microscope for FAIR) proton microscope at the GSI experimental area HHT employs a system of permanent magnet quadrupoles (PMQs) for imaging using protons from the SIS-18 accelerator [1]. After the first tests with this particular prototype, the demagnetisation of these PMQs due to primary and secondary radiation was investigated. Therefore, a spare module consisting of several magnetic wedges forming a Halbach Array-type Quadrupole [2] was deliberately irradiated.

Measuring the magnetization direction

In order to measure the hysteresis loops of the irradiated material, samples were cut out of the single wedges. The measurement itself was carried out with a pulsed field magnetometer (Metis HyMPulse)† where the magnetization direction of the outer applied field of the magnetometer has to be parallel to the internal field of the sample. This means the surface of the cut sample and the direction of the magnetization α have to be parallel. A misalignment could lead to a steep inclination in the flat top region of the loop. The first measurements showed exactly this behaviour. To improve the results, a method for the determination of α was developed.

A measurement was set up to determine the inclination of the magnetic field at the surface of the wedges. The wedges were scanned with a 1D Hall sensor by the magnet department of GSI. On a path of 30 mm first the Bx component was measured then the sensor was turned by 90° to measure the By component. This was done on the upper and the lower side of the Wedge.

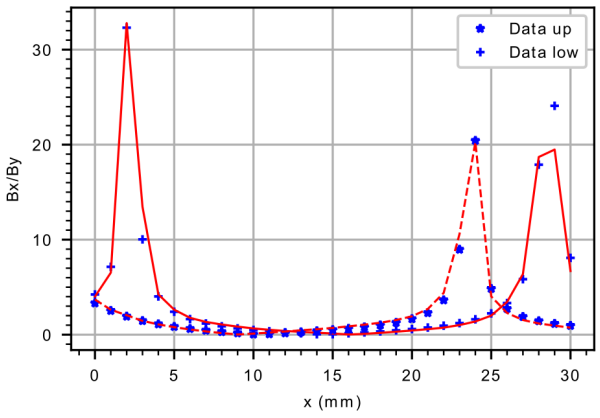


Figure 1: The inclination of the magnetic flux on the lower (full) and upper (dashed) surface of wedge 10 with the best fitting simulation.

This data was compared to simulations [3] of the field of the wedges for different directions of the magnetisation. A fitting routine selected the best fitting pattern of inclinations. With this procedure the magnetisation direction could be determined. For example the magnetization angle of wedge 10 (see Figure 1) was found to be α≈82.5°. According to the specification it should be 75°. The measured direction differed approximately 7.5 degrees from the specified angles.

Degradation of the HD5 value

Using the known deviations of the magnetization directions the hysteresis loops of different irradiated wedges were measured again. The HD5 value was chosen as a benchmark for the amount of demagnetization. It is given by the intersection of the hysteresis loop itself with 90\% of a straight line fitted to the flat top part of the loop. A degradation of the material due to radiation leads to a decreased stability towards a demagnetizing field. This in turn leads to a larger bending of the left section of the loop which also results in a lower HD5 value.

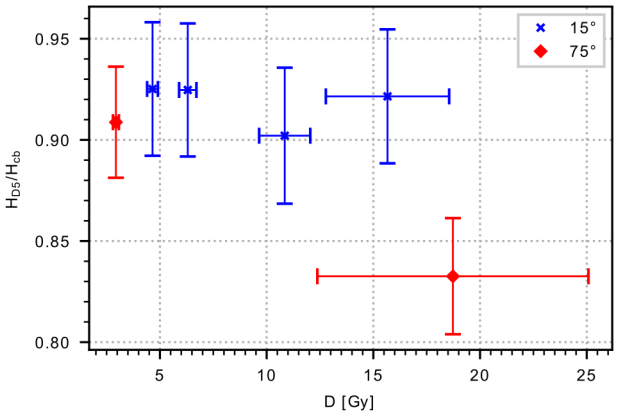


Figure 2: The HD5 values versus the applied dose recorded with Gafchromic films for different segments [4]

The analysis of the hysteresis loops for different wedges revealed that wedges containing a higher internal demagnetization field (type 75°) showed a significantly larger degradation of the HD5 value than the wedges from regions with a lower internal demagnetization field (type 15°). These results and further investigations on the origin of the observed damage were already published [4].

* Work supported by BMBF (05K13RDB). This report is also submitted to “News and Reports from High Energy Density generated by Heavy Ion and Laser Beams 2017”

† Measurements by K. Löwe (Group Functional Materials, TU Darmstadt)

Reference

[1] D. Varentsov et al, Rev. Sci. Instrum. 87, 023303 (2016)
[2] K. Halbach, Nucl. Instru. Methods 169,1 (1980)
[3] Finite Elements Methods Magnetics (FEMM), Version 4.2, www.femm.info (October 2010)
[4] M. Schanz et al, Rev. Sci. Instrum. 88, 125103 (2017)

Experiment beamline: SIS18-other: HHT
Experiment collaboration: APPA-HED@FAIR
Accelerator infrastructure: SIS18
Grants: BMBF (05K13RDB)
Strategic university co-operation with: Darmstadt

 DOI:10.15120/GR-2018-1

On equation-of-state measurements at the binodal in ion-beam heated matter

An. Tauschwitz[1], O. Rosmej[2], A. Tauschwitz[2] and J. Jacoby[1]

[1]Institute for Applied Physics, Goethe University Frankfurt, Germany; [2]GSI , Darmstadt, Germany

Modern particle accelerators provide intense beams of energetic charged particles which are able to create extended samples of matter at high energy density. The experimental area HHT at the SIS-18 heavy ion synchrotron allows to use focused ion beams of moderate intensities which means that a careful choice of beam-target configuration is essential to obtain meaningful experimental data. In the past it was proposed to heat isobarically a low density foam with energetic heavy ions to investigate the phase diagram and critical point parameters of selected materials [1]. Later on, the behaviour of a single foil heated initially at constant pressure and then undergoing a transition to the liquid-gas equilibrium state was described in [2].

In this second approach, shown schematically in Fig. 1, the expansion starts at the point O at the cold curve and follows the metastable EOS along an isobar. If the condition of quasi-static isobaric expansion is fulfilled, i.e. the foil is thin enough for a given heating rate, then, to a good accuracy, all thermodynamic quantities are constant in space and the entire foil is represented by a point on the phase plane. The expanding foil crosses the binodal in the liquid state at point B_0 and, before approaching the spinodal, undergoes a practically instantaneous transition into a gas-liquid equilibrium: $B_1 \rightarrow B_2$. The exact moment of vaporization of the metastable liquid inside the binodal curve is determined by the criteria of explosive boiling [2]. For sufficient beam power deposition the expansion after the transition is no longer isobaric. The reason for this is the lower sound speed in the liquid-gas mixture compared to the pure liquid. Hence, the different fluid elements follow different phase trajectories after the transition. At figure 1 the lower curve starting at point B_2 corresponds to the foils surface relaxing quickly to ambient pressure p_0 . The upper curve represents the foil center and the middle one an element in between.

Provided the ion beam is still heating the foil after the transition, its center stays very close to the binodal until the rarefaction waves from the foil surface approach the center. The reason for that is the discontinuity in the sound speed on the liquid-vapour coexistence curve. This extraordinary hydrodynamic situation offers a unique possibility to investigate states of matter directly on the binodal. In the calculations presented in [2] an energy deposition of 10 kJ/g for a foil made of SiO_2 is assumed which cannot be realized with ion beam at HHT. For moderate beam intensities high-Z low-melting-temperature targets would be preferable. According to the simulations done with the EOS provided by the FEOS-code [3], an energy deposition of 1 kJ/g would be enough for e.g. a Bi target to perform an experiment. In first experiments it is essential to verify the assumption of explosive boiling, the nearly instantaneous transition from metastable liquid into the stable liquid-gas mixture. This can be done by detection of the predicted jump in the expansion velocity due to transition to the phase equilibrium accompanied by a rapid increase of pressure $p_0 \rightarrow p_2$ [2].

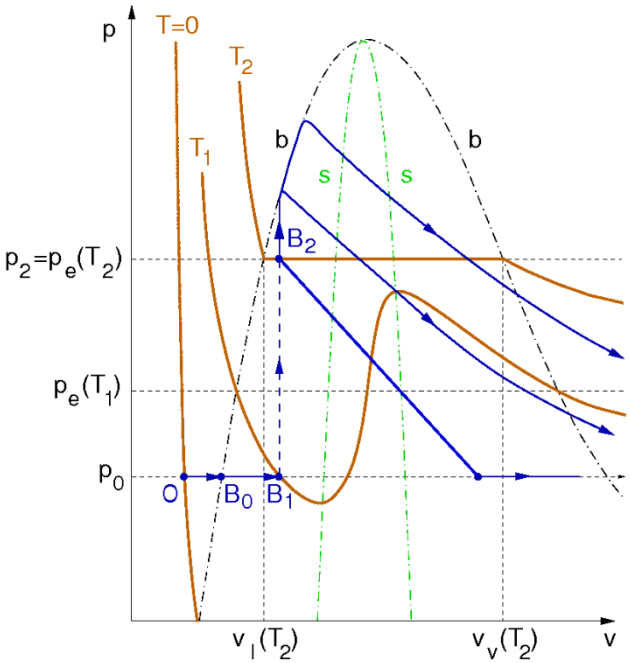


Figure 1: Temporal evolution of the thermodynamic state of ion-beam heated matter (schematic view).

The material properties of a metastable liquid before the transition can be diagnosed without temporal resolution since all thermodynamic variables in the foil are distributed uniformly in the direction of beam propagation. Furthermore, the knowledge of the beam parameters together with the energy deposition by the ions would immediately provide the internal energy because the kinetic energy for quasi-static isobaric expansion is negligible. Once the transition to equilibrium took place, temporally and spatially resolved measurements are necessary. Since the center of the target remains virtually on the binodal as long as release waves from the target surface don't arrive, the knowledge of only two (and not three) thermodynamic variables is sufficient to obtain a point on the binodal. The calculations show that the beam-target configuration can be optimized to ensure a low fraction of kinetic energy in the target center (below 3 %). Hence, to this accuracy, the energy deposited by the ion beam corresponds to the internal energy on the binodal and it would be sufficient to measure only one thermodynamic variable.

References

[1] I. Iosilevskiy, GSI Report GSI-2007-2, May 2007.
[2] S. Faik, M. Basko, An. Tauschwitz, I. Iosilevskiy, J. Maruhn, High Energy Dens. Phys. 8 (2012) 349.
[3] S. Faik, An. Tauschwitz, I. Iosilevskiy, Comput. Phys. Commun. 227 (2018) 117.

Experiment beamline: SIS18-HHT
Experiment collaboration: APPA-HED@FAIR
Experiment proposal: none
Accelerator infrastructure: SIS 18
PSP codes: none
Grants: BMBF-Projekt 05P15RGFAA
Strategic university co-operation with: Frankfurt

 DOI:10.15120/GR-2018-1

Prospects of planetary physics research using intense ion beams at FAIR

N.A. Tahir[1], A. Shutov[2], I.V. Lomonosov[2], A.R. Piriz[3], P. Neumayer[1], V. Bagnoud[1], and S.A. Piriz[3]

[1]GSI Darmstadt, Germany; [2]IPCP Chernogolovka, Russia; [3]UCLM Ciudad Real, Spain; [4]HI Jena, Jena, Germany

In this contribution we present a summary of simulation studies that were performed to explore the possibility of employing intense uranium beam to be generated at FAIR to produce planetary core conditions in the laboratory. A dedicated experiment named LAPLAS (Laboratory Planetary Sciences) has been proposed as part of the FAIR High Energy Density (HED) physics program. The beam-target geometry is shown in Figure 1.

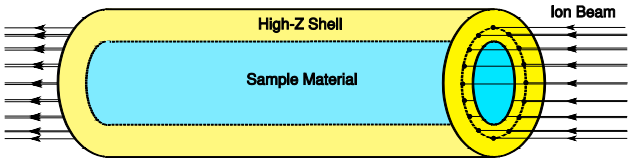


Figure 1: Beam-target geometry of LAPLAS experiment.

The target is comprised of a sample enclosed in a high-Z cylindrical shell. In the present calculations, Fe sample and a W shell have been used. One face of the cylinder is irradiated with a uranium beam with particle energy of 1.5 GeV/u having an annular focal spot that avoids direct heating of the sample by the beam. A 2D hydrodynamic code has been used to study the thermodynamic and the hydrodynamic response of the target. It has been shown that this configuration leads to a multiple shock reflection scheme which generates a low-entropy compression. This means the sample is imploded to ultra-high pressures, super-solid densities but relatively low temperatures. These simulations have shown that using the FAIR uranium beam, one can generate the Earth core conditions as well as those of more massive extrasolar rocky planets, the Super-Earths [1].

These calculations have been thoroughly extended by systematically varying the beam and the target parameters. It has been found that the results are rather insensitive to these changes over a wide parameter range which indicates the stability and robustness of the experimental scheme.

In the present studies the cylinder length is 4 mm while the sample radius is considered to be 0.2 mm and 0.3 mm, respectively. The inner radius of the focal spot ring is assumed to be 0.2 mm, 0.3 mm and 0.4 mm, respectively in the former case. In the latter case, it is considered to be 0.3 mm, 0.4 mm and 0.5 mm, respectively. The width of the focal spot ring is 1 mm.

It is to be noted that an annular focal spot will be generated by using an rf-wobbler that will rotate the beam with high frequency. Since the natural transverse intensity distribution in the focal spot is Gaussian, there always will be some intensity inside the ring that will preheat the sample. To take into account this effect in our studies, we include a linear intensity foot (0, 5, 10, 15 and 20 %) together with parabolic intensity profile in the ring.

Figure 2 shows pressure vs temperature for a particular set of parameters. It is seen that using an intensity of 2.5×10^{11} ions per bunch and a foot level of 5 %, one can generate Earth core conditions with a temperature of 5000 K and a pressure of around 4 Mbar.

Assuming an intensity of 5×10^{11} ions per bunch, one can generate a temperature of about 8000 K and a pressure of 8.5 Mbar, which represent the core conditions of Super-Earth which is few times more massive than the Earth.

It is also seen that considering an intensity of 10^{12} ions per bunch, a temperature of 10000 K and a pressure of 15 Mbar is generated which represents the core conditions of a rocky planet 10 times more massive than the Earth. Further details can be found in [2].

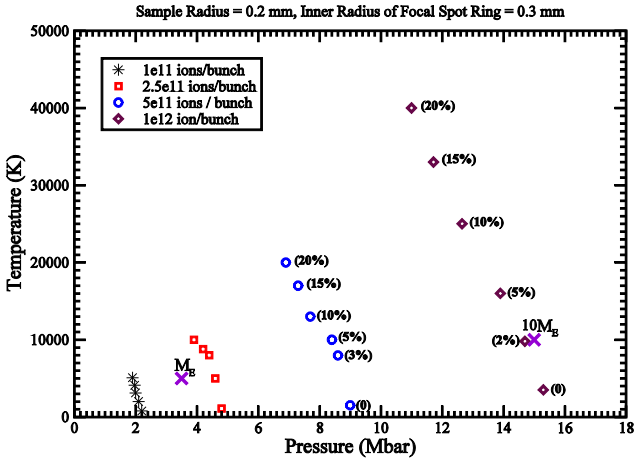


Figure 2: Pressure vs temperature in Fe for different intensities and different foot level, sample radius = 0.2 mm, inner radius of focal spot ring = 0.3 mm and bunch length = 75 ns.

References

[1] N.A. Tahir et al., "Studies of core conditions of the Earth and Super-Earths using intense ion beams at FAIR", Astrophysical J. Supplement Series 232:1, 2017 September.

[2] N.A. Tahir et al, Ion beam driven planetary physics research at FAIR, Astrophysical J. Suppl. Series (2018) submitted.

Experiment beamline: none
Experiment collaboration: APPA-HED@FAIR
Experiment proposal: LAPLAS
Accelerator infrastructure: none
PSP codes: none
Grants: BMBF
Strategic university co-operation with: none

Investigations on laser-based neutron sources for possible applications*

M. Zimmer[1] , A. Kleinschmidt[2,3], S. Aumüller[1], V. A. Schanz[1], D. Jahn[1], J. Hornung[2], M. Roth[1,4]

[1]Institut für Kernphysik, TU Darmstadt, Germany, [2]Helmholtz-Institut Jena, Germany
[3]GSI Helmholtzzentrum für Schwerionenforschung, Darmstadt, Germany
[4]FAIR -Facility for Antiproton and Ion Research, Darmstadt, Germany

Introduction

The demand for compact neutron sources is rapidly growing in the last years. To meet this growing need, laser-based neutron sources will play a major role in the upcoming development. These sources can provide neutron beams with maximum energies of several 10s of MeV depending on laser intensity and energy. For many applications, like Neutron Resonance Spectroscopy (NRS) or Neutron Resonance Imaging (NRI), the neutron energy needs to be decreased into the regime of a few eV. This can be done with multiple scattering inside a moderating material. The moderator must be composed of elements that have a low mass for rapid slowing down, while at the same time must have a low neutron absorption cross section. Hydrogen has the lowest mass, but a high absorption cross section, carbon on the other hand has a high mass but a low absorption. Therefore, a moderator out of High Density PolyEthylene (HDPE) is used which consist of C and H atoms in a ratio 1:2.

Experiment

To test the capabilities of a laser-based neutron source for NRS and NRI, an experiment was designed and conducted at the PHELIX laser as a succession of a beamtime at the Trident laser facility at the Los Alamos National Laboratory, USA[1]. The intended goal was to test a new moderator design and two new neutron detectors.

New moderator design

Fluka Monte Carlo simulations have shown that a new moderator design could enable a gain of up to 30% more epithermal neutrons into the direction of the detector. This gain is achieved by two modifications to the previous moderator design of earlier experiments [1]. The width of the rear part in the direction of the detector, was decreased by two centimetres to 5 cm as seen in Figure 1. This reduces absorption by hydrogen during moderation and minimizes the neutron Time of Flight (ToF) pulse width which is mainly limited by the time neutrons diffuse inside the moderator before they reach the HDPE surface. The second modification is the addition of two HDPE wings at the front of the moderator. These wings are able to capture and moderate neutrons, that are emitted with an angle between 90° and 146° towards the TNSA axis, which otherwise would have been lost for experimental purposes.

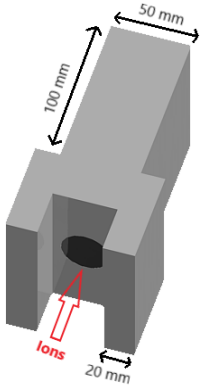


Figure 1: New moderator design with rear part reduced to 50 mm width and including two wings at the front side for moderating additional neutrons.

Testing of new neutron-ToF detector

The ToF detector is made of two 100x100mm borated Multi Channel Plates (MCP) in chevron configuration and an anode. Boron has a high cross section for (n,α) reactions. The emitted α-particles produce electrons in the MCP which are amplified and can be detected as a current on the anode. With this detector it was possible to distinguish between single neutron absorption events with a 10 ns temporal resolution. For higher neutron fluxes, the current can be seen as proportional to the amount of counted neutrons. Experiments have shown, that a high amount of neutron shielding around the detector is necessary to prevent scattered neutrons from the camber walls from interfering with the ToF measurement.

NRI detector

In addition to the NRS detector, a NRI detector consisting of a lithium glass scintillator and a fast gateable camera system was tested. The detector was placed in a distance of 1.1 m from the moderator in 90° towards laser forward direction. Scattered neutrons in this direction were shielded by a collimator made out of borated HDPE. In front of the scintillator several materials with high neutron absorption cross sections and absorption resonances were placed with the intent to distinguish between different samples in the image. As a result of this beamtime, it is possible to say that the detector can distinguish between a blocked and a free neutron flight path but for neutron resonance imaging, the signal to noise ratio has to be advanced and the neutron flux improved. For instance this can be done by using a larger light capturing system, decreasing the distance between scintillator and camera or by cooling the imaging system to reduce the camera noise.

References

[1] GSI Scientific Report 2016, DOI: 10.15120/GR-2017-1 RESEARCH-APPA-PP-11 P281

* This report is also submitted to “High Energy Density Physics Report 2017”

 DOI:10.15120/GR-2018-1

Experiment beamline: PHELIX
Experiment collaboration: APPA-PP
Experiment proposal: [P151]
Accelerator infrastructure: other: PHELIX
PSP codes: [none]
Grants: [none]
Strategic university co-operation with: Darmstadt

***** This report is also submitted to "High Energy Density Physics Report 2017"

Moderation of laser-driven neutrons for Neutron Resonance Spectroscopy

A. Kleinschmidt[1,2], A. Favalli[3], A. Tebartz[4], G.A. Wurden[3], V.A. Schanz[4], and M. Roth[4]

[1]GSI, Darmstadt, Germany; [2]HI Jena, Jena, Germany; [3]LANL, Los Alamos, NM, USA; [4]Institut für Kernphysik, TU Darmstadt, Germany

Introduction

The interaction of neutrons with matter is highly different from that of charged particles or electromagnetic waves. Therefore, they are an interesting research and diagnostic instrument for various applications. One of these is Neutron Resonance Spectroscopy (NRS) which, amongst other things, allows the identification of materials and their elemental composition as well as material-selective imaging of objects. The technique is based on the resonance structure of neutron capture and scattering reactions with matter, which is unique for every element and isotope.

A laser-driven neutron source is based on a high-intensity short-pulse laser irradiating a deuterated polymer foil with a thickness in the range of several 100 nm. The subsequently accelerated ions impinge a beryllium converter (so-called catcher) and generate neutrons via nuclear reactions. The resulting neutron spectrum shows an exponential decay with cutoff energies of a few 10 MeV [1].

However, to apply laser-generated neutrons to NRS, a moderating material has to be used, as a high number of isotopes have pronounced resonances in the epithermal energy range (0.1 eV to 100 keV). The material and geometry of the moderator are designed to maximize the neutron yield in the desired energy range and at the same time minimize the temporal spread of the neutron pulse caused by the additional material.

Neutron moderation for NRS at Trident

During the experiment at the Trident laser facility at Los Alamos National Laboratory, a polyethylene moderator was used to slow down neutrons emitted by the beryllium catcher. The Trident short-pulse laser had an energy of 80 J and was focused on thin polystyrene foils via a f/1.5 off-axis parabola leading to intensities above 10^{20} W/cm^2 on target.

To maximize the emitted neutron yield, the cylindrical beryllium catcher had a 15×15 mm hole drilled into it facing the incoming ion beam. As can be seen in Figure 1, the catcher was placed inside a high-density polyethylene (HDPE) moderator with a length of 13.8 cm in laser-forward direction and a width of 7 cm in line of sight to the time of flight (ToF) detector, which was set up perpendicular to the laser axis. In addition, a collimator consisting of steel disks and boronated polyethylene blocks was placed in line of sight to the detector to limit the field of view to the neutron source.

The neutrons were detected by a boron- and gadolinium-doped microchannel plate (MCP) with a sensitive area of 28 mm in diameter [2], which was placed inside a metal box and surrounded by thick boronated polyethylene blocks to shield it from electromagnetic pulses and scattered neutrons. The MCP was set up at a distance of 1.67 m to the neutron source.

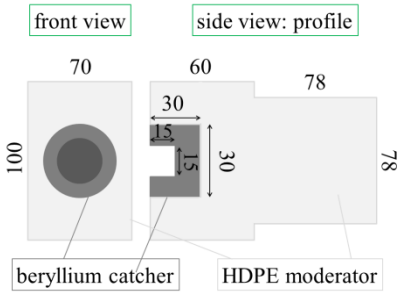


Figure 1: Sketch of the catcher-moderator setup. The accelerated ion beam is impinging the center of the hole. Dimensions are given in mm.

The chosen material for the NRS measurement was indium, which has a pronounced resonance at 1.46 eV. Thus, the neutron yield had to be maximized around this energy. A comparison of neutron energy spectra measured with and without a moderator is shown in Figure 2. The energy range of the plot was chosen around the indium resonance at 1.5 eV. At this specific energy, the moderator causes an increased neutron yield of a factor 3. The difference of both setups is even more pronounced for smaller energies, resulting in an order of magnitude more neutrons at the thermal energy of 25 meV.

These results enable the application of laser-driven neutrons to NRS measurements in the epithermal energy range. During the experiment, the above given indium resonance could successfully be measured [3].

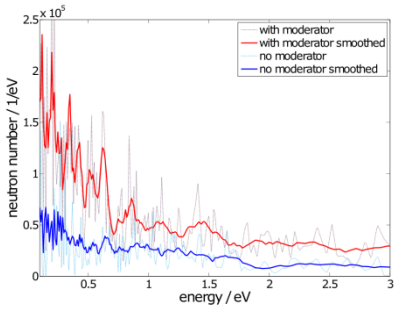


Figure 2: Comparison of neutron spectra obtained from a single laser shot with (red) and without (blue) a moderator around the catcher.

References

[1] J.C. Fernández et al., Phys. Plasmas 24, 056702 (2017)

[2] A.S. Tremsin et al., Nucl. Instrum. Methods Phys. Res. A 539, 287 (2005)

[3] A. Kleinschmidt, GSI scientific report 2016, p. 281 (2017)

 DOI:10.15120/GR-2018-1

Experiment beamline: none
Experiment collaboration: none
Experiment proposal: none
Accelerator infrastructure: none
PSP codes: [none]
Grants:
Strategic university co-operation with: Darmstadt

Construction, characterization and optimization of a plasma window for FAIR, status update

B. F. Bohlender[1#], A. Michel[1], M. Dehmer[1], M. Iberler[1], J. Jacoby[1]

[1]IAP, Goethe University, Frankfurt, Germany

Introduction

The Plasma window is a membrane free beam transition between a region of higher pressure (e.g. Target chamber, gas stripper) and the vacuum of an accelerator. For details on the working principle, the reader is referred to [1], [2], [3].

Constructional remarks

As described within the last report [1], the thermal stress on all parts of the window, especially the stress on the cathode, proved to be a real challenge. Nearly all parts showed thermal caused damage, the cathode being nearly completely devastated after 15min of operation.

New constructed Cooling plate design and the usage of WIG-welding needles as cathode tips allow to increase the lifetime of the window to at least 5h.

Experimental results

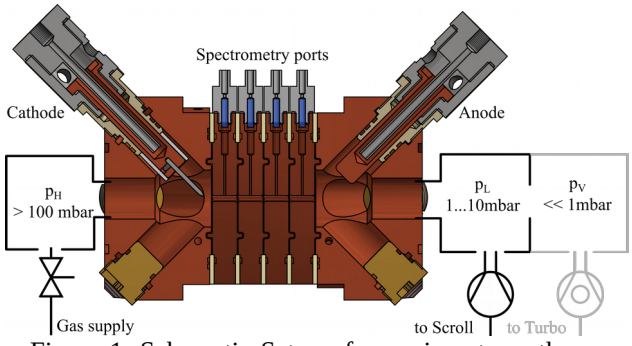


Figure 1: Schematic Setup of pumping stage, the gray turbo-stage has not yet been set up but is due this year.

The data presented herein has been collected with a residual gas composed of Ar with 2% H_2. Currents between 40A and 60A have been used, while the pressure on the high pressure side ranges from 280mbar to 450mbar, on the low pressure side from 4mbar to 7mbar. The aperture of the discharge channel is 3.3mm.

Figure 1 shows a schematic view of the setup including a cross-section of the current window. High pressure side is to the left, as is the cathode.

Plasma parameters

First tests of a radial spectrometry setup along the discharge axis enabled the simultaneous determination of (radial integrated) plasma parameters. In comparison to last years data, the electron temperature increased significantly from around 0.5eV to 1.2eV, this is mainly due to the improved cathode construction where now less energy is being deposited into the melting of the material.

In addition, first measurements of the electron density were carried out, showing a strong dependence on the current, pressure and the position inside the discharge channel. Values of n_e vary from $0.2{*}10^{16}cm^{-3}$ up to $4{*}10^{16}cm^{-3}$.

Pressure parameters

The pressure measurements were carried out while holding the pressure on the low pressure side (i.e. pumping side) constant, thus keeping a constant volume flow through the experiment.

The measurements show that the pressure quotient, that is the pressure on the high side divided by the pressure on the low side, is clearly dependent on the discharge current, and seems to depend on the volume flow. This quotient ranges from almost 60 to over 70, see Fig. 2.

Compared to the quotient measured when no plasma is burning, it's plain to see that the plasma increases the quotient by a factor around 10, resulting in the same possible reduction in length over a differential pumping system.

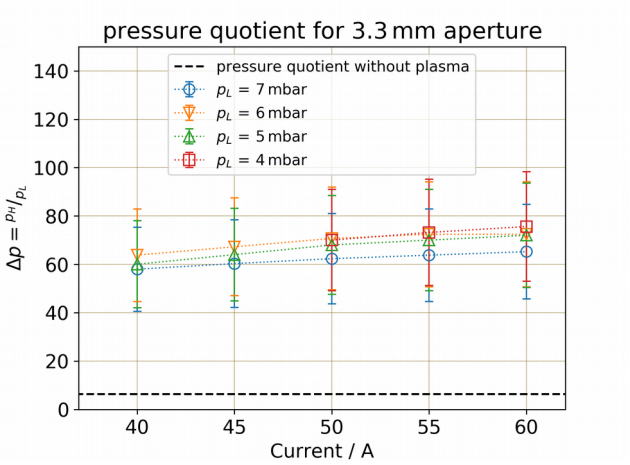


Figure 2: Pressure quotient for different p_L and currents. Quotient without plasma is around 6-7

Conclusion and outlook

The plasma window is operational for well over 5h now and realizing an improvement in the pressure quotient by a factor of 10 when compared to a differential pumping system.

In the near future, the complete differential pumping system, including the turbo-stage, will be build and tested. Additional tests with a larger aperture will be performed.

References

[1] B. Bohlender et al GSI HED report 2017

[2] B. Bohlender et al GSI HED report 2016

[3] A. Hershcovitch, J. Appl. Phys, 1995

bohlender@iap.uni-frankfurt.de

 DOI:10.15120/GR-2018-1

Experiment beamline: none
Experiment collaboration: Hadronenlinacs
Experiment proposal: Neu- und Weiterentwicklungen von Beschleunigeranlagen, Detektorsystemen, Verfahren der Physikanalyse
Accelerator infrastructure: UNILAC / SIS18
PSP codes: none
Grants: BMBF: 05P15 RFRBA
Strategic university co-operation with: Darmstadt

bohlender@iap.uni-frankfurt.de

Study on a dense and high ionized plasma for ion beam stripping*

P. Christ[1], K. Cistakov[1], T. Ackermann[1], A. Blazevic[2], A. Fedjuschenko[1], R. Gavrilin[3], M. Iberler[1], T. Manegold[1], L. Manganelli[1], O. Rosmej[2], S. Savin[3], K. Weyrich[2], G. Xu[1] and J. Jacoby[1]

[1]Goethe University, Frankfurt, Germany; [2]GSI, Darmstadt, Germany; [3]ITEP, Moscow, Russia

After a positive "proof of concept" with the screw-pinch and the spherical theta-pinch at a beam time at GSI in 2014 [1,2], a revised version of the theta-pinch has been developed and built for future research [3].

First spectroscopic diagnostics on this revised design have shown a time-averaged peak electron density of about $1.8 \cdot 10^{16}$ cm^{-3} at 60 Pa and 20 kV (see fig. 1), from which a maximum momentary electron density of $1 \cdot 10^{17}$ cm^{-3} is inferable. To gain an even higher electron density, the charging voltage will be increased up to 35 kV. According to a linear behaviour of the maximum electron density and the discharge energy [4], a maximum momentary electron density of approximately $5 \cdot 10^{17}$ cm^{-3} and an advance of the electron temperature from 1 eV up to 4 eV is expected from the increased discharge energy.

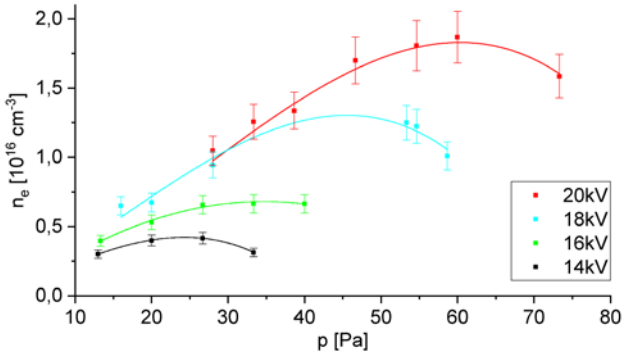


Figure 1: Time-averaged electron density at different pressures and load voltages.

Additionally, the spiral cylindrical shape of the new coil offers two basic advantages. On one hand, the ion beam transmission through the plasma cell is enhanced due to a more symmetrical magnetic field and on the other hand, the axial plasma exhalation displaces undesired residual gas between the vessel and the differential pumping system, extending the plasma ion beam interaction zone. The new design has been tested for its serviceability at GSI in 2016 and will be applied at a beam time at GSI in 2018. Besides researchers form Goethe University, Frankfurt, this beam time will be conducted by scientists from other facilities such as ITEP, Moscow, IMP, Lanzhou and IUAC, New Delhi, who are studying on the same topic.

For a better understanding of the internal plasma processes, multiple time-resolved spectroscopic diagnostics as well as a laser interferometry are intended. The interferometric diagnostic will be based on previous investigations, which have focused on finding a suitable basic scheme and pre-setting main operation parameters such as wavelength and time resolution [5]. Since a high electron density of the order 10^{17} cm^{-3} is expected, to restrict the all over phase shift to lower the standards for the scope, to have a simpler alignment and to limit the influence of a potentially existing density gradient, short wavelengths in the visible range are favoured.

During interferometric test measurements on a small-scale z-pinch, a suspected disturbing influence of electromagnetic noise has occurred. Consequently, a sufficient metallic shielding of the interferometer and its vulnerable electric components in a separate set-up as well as an improvement of the signal-to-noise ratio by a raised laser power are designated. To transfer the laser beam towards and back from the plasma experiment, a fibre connection will be investigated.

Figure 2 shows a first draft of the interferometer for future time-resolved measurements of the electron density.

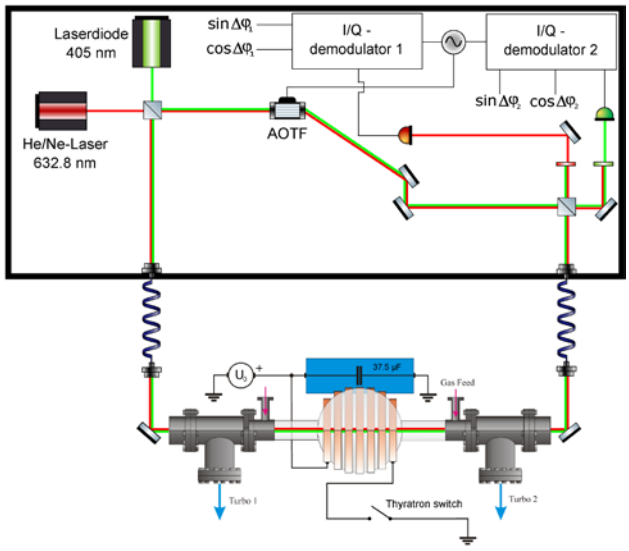


Figure 2: First draft of the future interferometer set-up.

A novel combination of an acousto-optic heterodyne technique and a two-colour vibration compensation with wide separated wavelengths is illustrated. If the vibrational contribution is negligible to the plasma contribution, the second wavelength could be utilized to estimate the ionization degree, which would lead to a precise measurement of the electron temperature. In addition, an acousto-optic tuneable filter (AOTF) will be tested as a solution for maintaining the required collinearity of the wavelengths.

References

[1] G. Xu *et al.*, Phys. Rev. Lett. **119**, 204801 (2017).
[2] G. Xu *et al.*, GSI SCIENTIFIC REPORT 2014, AP-PA-MML-PP-16.
[3] K. Cistakov *et al.*, GSI SCIENTIFIC REPORT 2016, RESEARCH-APPA-PP-22.

* This report is also submitted to the report `News and Report from High Energy Density generated by Ion and Laser beams 2017`.

 DOI:10.15120/GR-2018-1

[4] C. Teske *et al.*, Physics of Plasmas **19**, 033505 (2012).
[5] P. Christ, Master thesis, 2017

Experiment beamline: Z6
Experiment collaboration: APPA-HED@FAIR, Research group "Hadron Accelerators"
Experiment proposal: U275, U306, U317
Accelerator infrastructure: UNILAC
PSP codes: none
Grants: BMBF No.: 05P15RGFAA and 05P15RFRBA, HGS-HIRe
Strategic university co-operation with: Darmstadt

Cone compression of a pulsed plasma sheath

T. Manegold[1], S. Faik[1], C. Benzing[1], P. Tavana[1], J. Wiechula[1], M. Iberler[1] and J. Jacoby[1]

[1]Goethe University of Frankfurt, Frankfurt am Main, Germany.

Introduction

Coaxial plasma accelerators (CPA's) have been investigated in different experimental configurations in the past, with applications to space propulsion [1], plasma refuelling for fusion reactors [2] and as a high voltage switch [3]. The purpose of the presented project is the application as an intense UV/VUV back lighter source. The wavelength spectrum of the emitted light depends on the excited states, whereas the intensity is in correlation to the electron density. The plasma sheath of the utilized CPA has been characterized in [4]. To increase electron density and to extend the emitted spectrum to lower wavelengths, the plasma is compressed by a glass cone after acceleration phase.

Experiment and Results

The experiment is driven by a CPA, whose pulse forming network has a total capacitance of 27µF with a maximum voltage of 10kV. Due to the high current of up to 150 kA, the Lorentz force accelerates the plasma to velocities in the 10 km/s range.

The electron density determination of the uncompressed plasma has been performed time and spatially integrated by the common method of linear Stark-broadening of the H_β line. This method is however only applicable at the beginning of the compression. Then, due to the high electron densities, this line is broadened too widely to be utilized. As an alternative, the broadening according to the quadratic Stark-effect of a copper line at 479.40nm was applied. It was possible to cross calibrate this line with the H_β line at lower densities. Doing so, we obtain

$$n_e\left[\mathrm{cm}^{-3}\right] = C \cdot \Delta\lambda_s\left[\mathrm{nm}\right] \qquad (1)$$

with the calibration factor of $C=(3.07\pm0.475)\cdot10^{18}$.

In a first cone, which is characterized by an opening at the end of 5mm and a tapering angle of 26.5°, the electron density could be increased from initially several $10^{15}\mathrm{cm}^{-3}$ in the uncompressed plasma cloud to about $10^{18}\mathrm{cm}^{-3}$ at the tip of the cone at a charging voltage of 9kV and a Helium gas pressure of 15mbar. Two-dimensional hydrodynamic simulations of the compression have been performed with the RALEF-2D code. According to these simulations (Fig. 1), the electron density can even be increased by changing the cone parameters to a tiny opening of 0.5mm and a tapering angle of 12°. The discrepancy of the density values between simulation and experiment is assumed to be unobserved by the highly time dependant changes and additional radiation losses, not taken into account in the code.

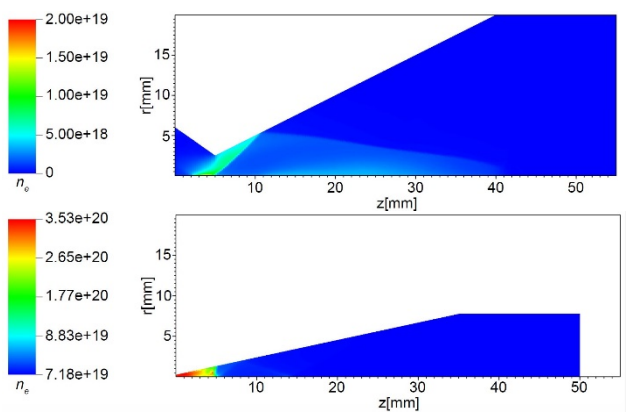


Figure 1: Simulation of the electron densities in different cone shapes at the time of maximum value with first cone (top) and optimized cone (bottom).

The experimental results of the electron density at U=5kV and p=5mbar are depicted in Fig. 2 in dependence of the position z. As can be seen, although voltage and gas pressure are reduced, an optimized cone compressed the plasma to electron densities comparable to the values of the first cone at 9kV and 15mbar. Compared to the uncompressed values, the compression increases the electron density by about a factor of 630.

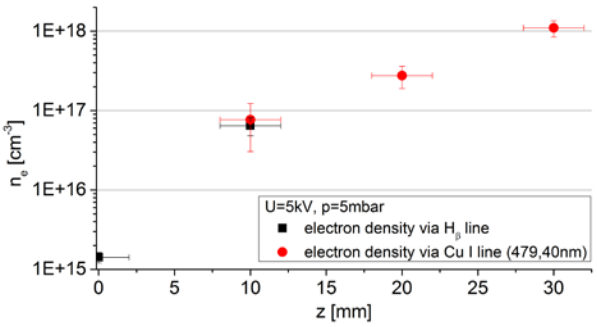


Figure 2: Electron densities in the optimized cone

Additionally, the observed emitted wavelength has expanded at higher densities from wavelengths above 97.25nm to a wavelength range starting already at approximately 53.70nm. Our next step is to replace the fragile glass by a different material to be able to perform the compression at higher voltages and pressures to increase electron density even more. According to the RALEF-2D simulations, this could increase the compressed density by a further order of magnitude.

References

[1] D. Y. Cheng, “Application of a deflagration plasma gun as a space propulsion thruster,” AIAA Journal, vol. 9, no. 9, pp. 1681–1685, Sep. 1971.

[2] D. Witherspoon, et al., “A contoured gap coaxial plasma gun with injected plasma armature,” Review of Scientific Instruments, vol. 80, no. 8, 2009

 DOI:10.15120/GR-2018-1

[3] M. Iberler, et al., “Optical and electrical investigations of a high power Lorentz drift based gas discharge switch,” IEEE ICOPS, June 2008, pp. 1–1.
[4] T. Manegold, et al., “Generation and characterization of a pulsed dense plasma with helium,” IPMHVC, pp. 580–584, July 2016.

Experiment beamline: none
Experiment collaboration: APPA-HED@FAIR
Experiment proposal: none
Accelerator infrastructure: none
PSP codes: none
Grants: none
Strategic university co-operation with: Frankfurt-M

Acceleration of plasma-propelled flyer plates*

S. Sander[1], J. H. Hanten[1], M. M. Basko[2], An. Tauschwitz[3], G. Schaumann[1], D. Schumacher[4], A. Blazevic[4] and M. Roth[1],

[1]Technische Universität Darmstadt, Institut für Kernphysik, Darmstadt, Germany; [2]Keldysh Institute of Applied Mathematics RAS, Moscow, Russia; [3]Goethe Universität, Frankfurt, Germany; [4]GSI Helmholtzzentrum für Schwerionenforschung GmbH, Darmstadt, Germany

* This report is also submitted to "News and Reports from High Energy Density generated by Heavy Ion and Las

Introduction

Man-made space debris is exponentially increasing in the low earth orbit, posting a big threat on current and future space missions [1]. To remove this space debris, high velocity impacts (v > 10 km/s) of tungsten balls with a presumed momentum transfer factor of ~10-15 are proposed to slow down space debris [2]. Thereby, it will decrease in orbit und burn up in the atmosphere sooner.

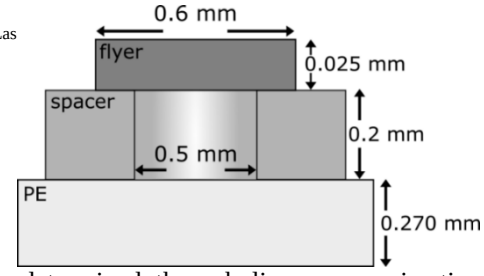
Experiment

For preliminary experiments in this area of high velocity impacts, a special target design has been developed as seen in figure 1. The objective is the acceleration of a high velocity, solid state tungsten flyer plate for future impact experiments.

Previous experiments, using different target designs, failed to show an acceleration of the flyer but suggested an evaporation of the tungsten disk. Therefore, a target design which allows for a completely free flyer is developed. The target consists of three layers. The bottom layer is a 270 µm thick polyethylene (PE) sample. A steel spacer of 200 µm thickness and with a 500 µm diameter hole is glued on top of the PE. The hole is covered with a tungsten disk with a diameter of 600 µm and 25 µm thickness. In this setup, the to be accelerated disk is completely free and not glued to any structure.

The experiments are performed at the target area Z6 at GSI, where the nhelix laser system is used to drive a shock wave into the PE. After the shock breakout, the material expands through the hole and hits the disk. This is supposed to accelerate the tungsten to high velocities, while retaining its solid state. As the target is driven from below, a completely new beam path is put in place. The beam is guided through the bottom flange and focused with a lens and random phase plate onto the PE. A laser energy of 2 J is used to ensure the integrity of the accelerated disk.

The targets rear side is observed with two DICAM Pro in a side view configuration with a relative angle of 90° between them. In figure 2, the recorded images can be seen. A background is subtracted to enhance the visibility of the disk for one of the cameras (figure 2a). The disk is observed in flight in both images. The disk clearly rotates, which is thought to originate from a non-uniform plasma expansion inside of the steel spacer. From the two different images and the time delay a velocity of about 110 ± 4 m/s is deduced. With a streak camera the disk movement is observed over a time window of 1000 ns around the expected time of acceleration. The movement



speed was determined through linear approximation to 100 ± 30 m/s.

Figure 1: Schematic of the layered target design. A steel spacer is glued on top of a polyethylene foil (PE). The flyer is made of tungsten and placed without fixation. The target is driven from below, accelerating the plasma and flyer upwards.

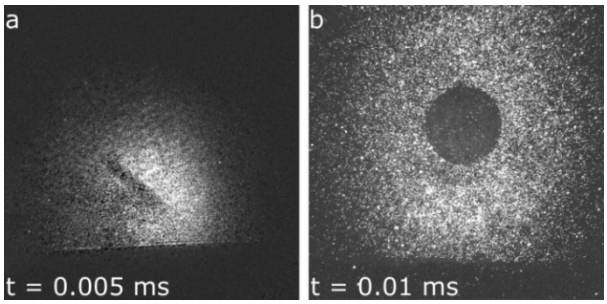


Figure 2: Recorded images of the two DICAM Pro. A background image is subtracted from image (a) to increase visibility. The flyer is clearly seen in both images, rotating rather than flying straight up.

Simulation

Simultaneously, hydrodynamic fluid simulations in two dimensions are performed with the RALEF code [3,4], to further study the target. These simulations with a laser energy of 2 J are in good agreement with the measured velocities, calculating the flyer velocity to 101 m/s. In addition, the simulations suggest a fluid pressure of 19 kbar inside the tungsten. This value closely corresponds to the tensile strength of tungsten, explaining previous failures of the targets driven with higher intensities.

References

[1] D. McKnight, D. Kessler, IEEE Spectrum, Retrieved (2012).
[2] G. Ganguli et al., Aerospace Conference, 2012 IEEE (2012).
[3] M. M. Basko, J. Maruhn, A. Tauschwitz, J. Comp. Physics, 228, (2009)
[4] M. M. Basko, J. Maruhn, A. Tauschwitz, GSI-Report 2010-1, PLASMA-PHYSICS-25 (2010)

 DOI:10.15120/GR-2018-1

Experiment beamline: Z6
Experiment collaboration: none
Experiment proposal: none
Accelerator infrastructure: none
PSP code: none
Grants: none
Strategic university co-operation with: Darmstadt

 DOI:10.15120/GR-2018-1

Use of TC-Tag and ReAsH as a DNA DSB Marker in CLEM

S. Tonnemacher[1,2], G. Becker[1], A. Heselich[1], G. Taucher-Scholz[1,3] and B. Jakob[1]

[1]GSI, Darmstadt, Germany; [2]Goethe-Univerity, Frankfurt/Main, Germany; [3]TU, Darmstadt, Germany.

Introduction

Correlative light and electron microscopy (CLEM) can combine the advantages of fluorescence microscopy (FM) and electron microscopy (EM). In radiation biology we are applying this method for FM imaging of radiation-induced dynamic processes of DNA repair proteins followed by subsequent imaging of structural chromatin changes at the DNA double-strand break (DSB) sites using high resolution in the EM. For the identification of damage sites, a marker is needed that can be detected in both microscope types. For this purpose we choose and generated a Tetracysteine (TC)-tagged version of the DSB marker 53BP1. The small tag (4kDa including an additional V5-epitope) [1] should not interfere with the functionality of 53BP1. In FM, the TC-Tag can be imaged by binding to membrane permeable ReAsH-EDT_2 which becomes fluorescent (Resorufin Arsenical Hairpin Binder, Em608nm) upon binding [1, 2]. In EM the TC tagged 53BP1 can be detected by ReAsH mediated photoconversion of diaminobenzidine (DAB) - causing polymerization of DAB, which can subsequently be contrasted by electron dense osmium tetroxide (OsO_4).

Materials and Methods

Murine NIH/3T3 cells were seeded in glass bottom petri dishes on day zero. On day one, cells were transfected with pcDNA6.2/nTC-Tag-DEST_53BP1 (plasmid backbone from Invitrogen). On day two, cells were stained with ReAsH-EDT_2, irradiated with 1 Gy X-ray at 250kV and fixed using 2% buffered paraformaldehyde 30 minutes after irradiation. For immunocytochemical staining the cells were additionally permeabilised with 0.5% Triton X-100 and blocked with 0.4% BSA. Anti-V5-epitope (Invitrogen) and Anti-53BP1 (Abcam) primary, and Alexa488 and Alexa647 coupled secondary antibodies (both Life Technologies) were used.

Results

We first checked the transfection and expression of the TC-tagged 53BP1 in NIH3T3 cells (not shown). The functionality of the tagged protein was evaluated by the accumulation at induced DSB, either by immunocytochemistry (Fig.1) or, after adding ReAsH-EDT_2 to the living cells, by binding of ReAsH to the TC-tag (Fig. 2). In both cases cells were irradiated (1 Gy of X-rays) and subsequently fixed. Radiation-induced foci were clearly observed (Fig. 1 and 2) for the V5 epitope and antibodies against 53BP1 (Fig 1 a, b) as well as for ReAsH binding to the TC-tag (Fig. 2a). This typical accumulation at radiation induced foci colocalising with the DSB marker γH2AX (Fig. 2b) provides evidence for the functionality of the TC-tagged 53BP1.

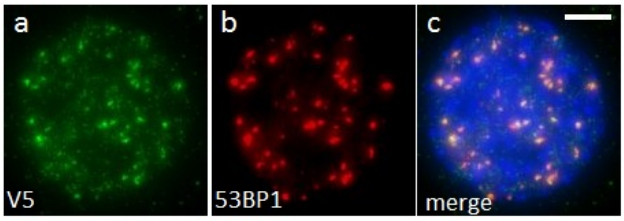


Figure 1: NIH/3T3 cell transiently transfected with TC-tagged 53BP1 and irradiated with 1 Gy X-rays. Both stainings of V5-epitope (a) and 53BP1 (b) show clear radiation-induced foci which colocalise. (c) Merged image with DNA stain (DAPI, blue). Scale bar: 5µm.

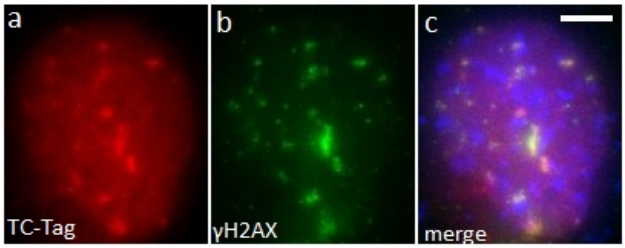


Figure 2: NIH/3T3 cell transiently transfected with TC-tagged 53BP1 and irradiated with 1 Gy X-rays after ReAsH staining. After fixation the sample was additional stained against γH2AX as DSB marker (b) showing the colocalisation (c, merged together with DAPI, blue). Scale bar 5µm.

Outlook

After proving the functionality of the 53BP1 construct, the DAB polymerisation as a staining for the EM will be next. We will also produce a stable cell line to achieve a more homogeneous marker protein expression level for future work. This cell line will then be used to study the radiation effect of charged particles on chromatin structure using high resolution EM.

References

[1] Molecular Probes™. MAN00002400. (2016).
[2] Gaietta, Guido, *et al*. Science 296.5567 (2002).

Experiment beamline: none
Experiment collaboration: APPA-BIOMAT
Experiment proposal: none
Accelerator infrastructure: none
PSP codes: none
Grants: HGS-HIRe and the German federal ministry of education and research (BMBF), Grant # 02NUK037A.
Strategic university co-operation with: none

Upgrade of the fluorescence lifetime imaging microscope for the measurement of metabolic changes linked to radiation damage and repair

E. Janiel[1,2], G. Becker[1], G. Taucher-Scholz[1,2], B. Jakob[1]

[1]GSI, Darmstadt, Germany; [2]Technical University Darmstadt, Germany.

Introduction

Normal, terminally differentiated cells rely on oxidative phosphorylation (OXPHOS) for efficient ATP production inside mitochondria. For this metabolic pathway oxygen is essential as terminal electron acceptor. Only under conditions of low oxygen tension the cells switch to anaerobic glycolysis, a less resourceful pathway to produce ATP. Otto Warburg was the first to describe the ability of highly proliferative or tumour cells to maintain a high glycolytic rate even in conditions of sufficient oxygen. This so-called aerobic glycolysis, also termed the Warburg effect, is based on a metabolic reorganization with augmented anabolic reactions linked to cell growth and proliferation[1]. Interestingly, this metabolic shift is associated with several types of cancers and is described to impact on the sensitivity to DNA damaging agents and radiation[2, 3, 4].

Among various cellular cofactors, NADH and NADPH (NAD(P)H) have been identified as indicators of OXPHOS efficiency. Their fluorescence intensity and lifetimes are tightly related to the redox status of the cell[5]. Monitoring NAD(P)H fluorescence intensity and lifetime is a promising approach in order to address the interplay between irradiation and energy metabolism. We describe here the upgrade of the FLIM (fluorescence lifetime imaging microscopy) setup with a two-photon TiSa laser system to establish lifetime measurements of NAD(P)H for future studies of the influence of the energy metabolism on the radiation response in living cells.

Methods

The Becker&Hickl DCS-120 FLIM Scanner was upgraded with a coherent chameleon ultra II TiSa laser and an acousto-optical modulator (AOM) for multi-photon excitation of NAD(P)H (Fig. 1 A). For detection a non-descanned fast hybrid-detector HPM-100-07 (Becker&Hickl) equipped with a blocking (FSP-680) and a band-pass filter (Semrock 458/64) were installed. AG1522-D cells were plated on glass bottom petri dishes and colourless imaging medium used during measurements. With two-photon excitation of NAD(P)H at 720 nm TCSPC (time-correlated single photon counting) was done over a period of 120s at 80MHz laser repetition rate. The acquired fluorescence decays (Fig 1B) were analysed according to the protocol by Blacker at al. 2017[5].

Results and Outlook

Analysis of FLIM data obtained with this new setup allowed for successful detection of NAD(P)H autofluorescence and fluorescence lifetime with decay times τ1 and τ2 comparable to literature data[4, 6]. Ongoing experiments will include targeted manipulation of energy metabolism pathways to confirm the sensitivity of NAD(P)H FLIM to changes in OXPHOS balance. Based on these experiments, cells will be irradiated by an integrated x-ray source (Fig 1A, 4) and the impact of irradiation on OXPHOS efficiency will be monitored. In addition the influence of the energy metabolism status on DNA repair efficiency after irradiation will be addressed both after x-rays and ion irradiation.

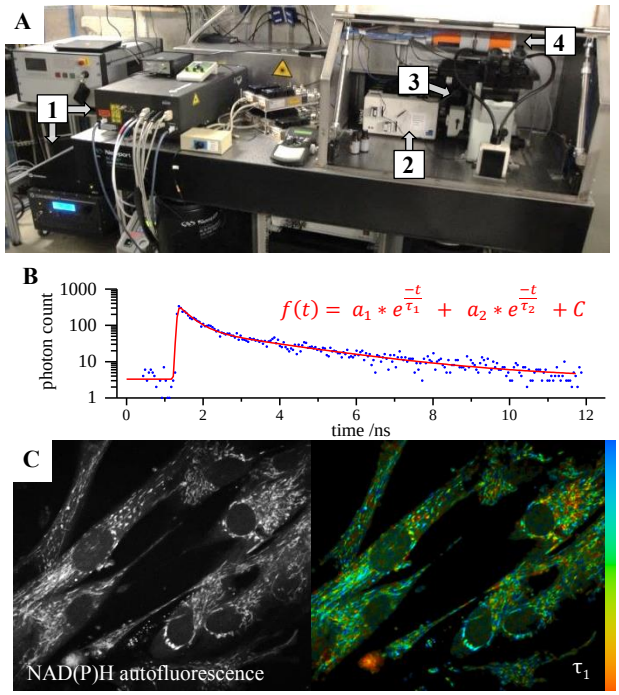


Fig. 1: A: Two-photon FLIM setup. 1 TiSa laser 2 DCS-120 scan head, 3 Non-descanned detector, 4 X-ray tube. B: Typical fluorescence decay curve with bi-exponential fit. C: NAD(P)H autofluorescence in AG1522-D cells (left: photon count image; right: overlay with colour coded lifetime image for τ1 = 228ps (red) - 437ps (blue)).

References

[1] Warburg Science 1956, 123, 309-314
[2] Sameni et al. Sci Rep 2016, 6, 34755
[3] Liu et al. Oncotarget 2015, 6, 4214-4225
[4] Bhatt et al. BMC Cancer 2015, 15, 335
[5] Blacker et al. Bio Protoc 2017, 7
[6] Blacker et al. Free Radic Biol Med 2016, 100, 53-65

Experiment beamline: none
Experiment collaboration: APPA-BIOMAT
Experiment proposal: none
Accelerator infrastructure: none
PSP codes: none
Grants: This work is supported by the DFG GRK1657 and the BMBF, Grant#: 02NUK037A
Strategic university co-operation with: none

 DOI:10.15120/GR-2018-1

Influence of sirtuin inhibitor nicotinamide on radiation-induced DNA damage repair

A. Heselich[1], L. Pack[1], G. Taucher-Scholz[1,2] and B. Jakob[1]

[1]GSI, Darmstadt, Germany; [2]TU Darmstadt, Darmstadt, Germany

Motivation

DNA damage induced e.g. by ionizing irradiation needs to be accessible to allow recruitment of repair factors and efficient DNA double-strand break (DSB) rejoining. Radiation induced chromatin alterations not only promote access of repair factors to the lesion, but play an essential role in mediating and regulating the damage response machinery [1]. Especially clustered DSBs induced after high-LET irradiation might demand extended alterations of the surrounding chromatin as indicated by local chromatin depletion at traversal sites [2]. Aim of our project is the identification of chromatin and repair protein modifying factors influencing the DNA damage response at heavy ion induced clustered lesions. Here we analyzed the influence of the deacetylase and mono-(ADP)-ribosylase sirtuin 6 (Sirt6), shown to play a role in DNA repair [3, 4] and chromatin alterations [5, 6], on DSB repair using α-irradiation.

Materials & Methods

Murine fibroblasts (NIH/3T3) were treated 16h w/wo 10mM SIRTi (Nicotinamide, NAM). Cells were then either irradiated with α-irradiation (^{241}Am, LET ~150 keV/µm) or X-rays (250kV, 16mA). DSB rejoining was analysed in immunofluorescence stained samples via γH2AX foci formation and loss over time (Fig. 1, 2).

Results

Whereas after photon irradiation we couldn't detect an influence of sirtuin inhibition in our repair studies in NIH/3T3 fibroblasts, an influence of sirtuin activity on DNA DSB rejoining after alpha irradiation was revealed (Fig. 2) indicated by impaired loss of γH2AX foci, becoming evident after longer incubation times (>8h, Fig. 2 A). Elevated levels of γH2AX foci compared to control cells could still be observed at 24hrs after irradiation.

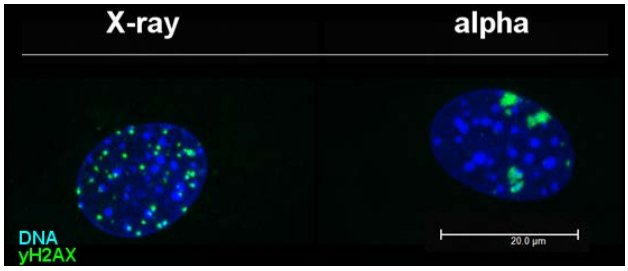


Figure 1: Differences in γH2AX-foci formation 1h after X-ray and α-irradiation. NIH/3T3 fibroblasts immunostained against phosphorylated H2AX (γH2AX, green). DNA counterstained with DAPI (blue).

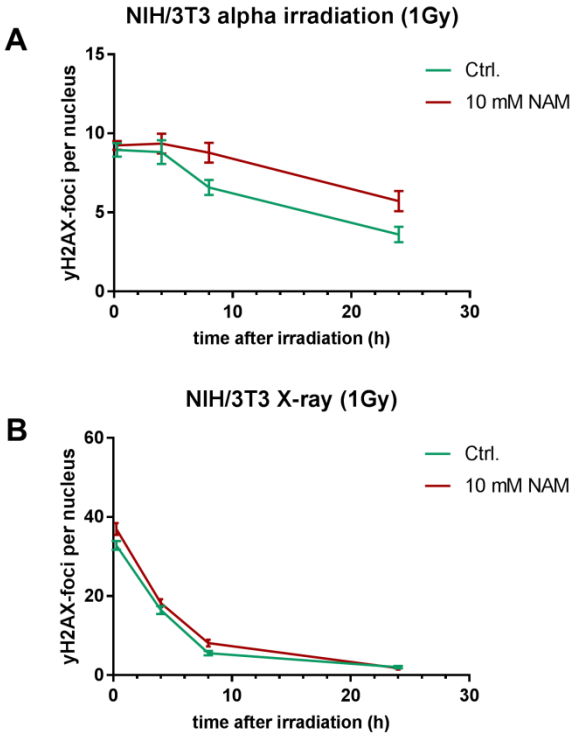


Figure 2: SIRTi-treatment (10 mM NAM) resulted in impaired DNA DSB rejoining after alpha (A) but not after X-ray irradiation (B) in NIH/3T3 fibroblasts. Data represent mean ± SEM (n=50 nuclei per time point), endogenous foci were subtracted.

Summary

Sirtuin inhibition shows an impact on late DNA repair after alpha irradiation, but not after X-rays. Up to now it remains unclear if impaired DNA DSB rejoining after SIRTi is connected to chromatin alterations or rather based on a direct influence on repair factors. Therefore we are now focusing on the underlying mechanisms.

References

[1] Peterson CL, Almouzni G. CSHPerspectBiol, 5, 2013.
[2] Jakob et al. NAR 39, 2011.
[2] Kaidi, A., et al. Science 329, 2010.
[3] Van Meter, M., et al. Aging (Albany NY) 3, 2011.
[4] Atsumi, Y., et al. Cell Rep 13, 2015.
[5] Toiber, D., et al. Mol Cell 51, 2013.

Experiment beamline: none
Experiment collaboration: APPA-BIOMAT
Experiment proposal: none
Accelerator infrastructure: none
PSP codes: none
Grants: BMBF-Grant #02NUK037A.
Strategic university co-operation with: none

DNA end resection is decreased in RNF138 knockout cells upon irradiation

C. Barent[1,2], L. Pack[1], A. Heselich[1], B. Jakob[1], G. Taucher-Scholz[1,2], and N. B. Averbeck[1]

[1]GSI Helmholtzzentrum für Schwerionenforschung, Darmstadt, Germany; [2]Technische Universität Darmstadt, Germany;

Motivation

DNA double-strand breaks (DSB) represent a lethal risk to living cells. Cells developed a DNA damage response that efficiently detects and repairs these breaks. Simple DSBs are repaired resection dependent only in the S/G2 cell-cycle phase, whereas complex, ion-induced DSBs are partially repaired resection dependent also in G1-phase cells [1]. It was shown that the ubiquitin ligase RNF138 plays an important role in DNA end resection in S/G2 phase by removing the resection antagonist Ku80 from DSBs [2] and facilitating the recruitment of the resection factor CtIP [3]. Previous data suggest that RNF138 stimulates resection of complex, ion-induced DSBs in G1-phase cells as well [4]. In order to study the role of RNF138 in future experiments in more detail we generated an RNF138 deficient human cell line.

Material and Methods

Human osteosarcoma cells (U2OS) were used to generate a knockout cell line of RNF138 using pSpCas9(BB)-2A-Puro (PX459) V2.0 [5], which was a gift from Feng Zhang (Addgene plasmid # 62988). Obtained clones were screened for a successful biallelic knockout by sequencing, immuno-blot analysis of RNF138, and the Cas9 cleavage assay. The functionality of the knockout was tested in an immuno-blot against pRPA of X-ray irradiated cells (30 Gy, ISOVOLT 320 M1; Seifert/GE; 250 kV; 16 mA).

Results

First we verified that the obtained RNF138 knockout (RNF138-KO) clones are lacking RNF138. We checked the protein expression level of RNF138 in several knockout clones compared to the wildtype (WT) host cell line. All examined clones showed no RNF138 expression compared to the WT cells (Figure 1).

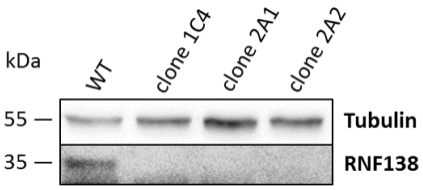


Figure 1: RNF138 expression level of several RNF138-KO clones is reduced compared to WT cells. Several RNF138-KO clones were generated in human osteosarcoma cells (U2OS cells) using the CRISPR/Cas9 system. The protein expression of RNF138 was verified by western blot analysis.

Sequence analyses and a Cas9 cleavage assay confirmed the successful biallelic knockout in all clones (data not shown).

To find out whether the RNF138-KO in the clones is functional we studied the resection marker RPA. Within the resection process this ssDNA protecting protein is phosphorylated and in cells lacking RNF138 less phospho-RPA (pRPA) is detected [2]. Upon irradiation with 30 Gy X-rays (X-IR) we found less pRPA in RNF138-KO clones than in WT cells (Figure 2; one representative clone is shown).

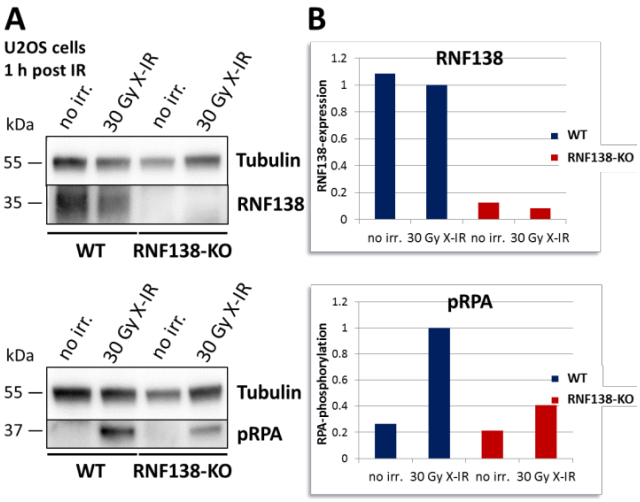


Figure 2: The level of phosphorylated RPA is decreased in RNF138-KO cells after X-ray irradiation. (A) Asynchronous WT and RNF138-KO human osteosarcoma cells (U2OS) were irradiated with 30 Gy X-rays (X-IR). Cells were harvested 1 h post irradiation and the protein level of RNF138 and pRPA was analysed in a western blot analysis. Tubulin served as a loading control. (B) The quantitative evaluation was carried out with the ImageJ software. The expression level of RNF138 and pRPA were normalized to the values of the irradiated WT sample and the loading control Tubulin.

References

[1] Averbeck, N. B. *et al.* Cell Cycle, 2014. **13**: 2509 ff.
[2] Ismail, I. H. *et al.* Nat Cell Biol, 2015. **17**: 1446 ff.
[3] Schmidt, C. K. *et al.* Nat Cell Biol, 2015.**17**:1458 ff.
[4] Barent, C. *et al.* GSI Scientific Report, 2016.
[5] Ran, F.A., et al., Nat Protoc, 2013. **8**: p. 2281 ff.

Experiment beamline: none
Experiment collaboration: APPA-BIOMAT
Experiment proposal: none
Accelerator infrastructure: none
PSP codes: none
Grants: This work is supported by the DFG GRK1657 and the German federal ministry of education and research (BMBF), Grant # 02NUK037A.
Strategic university co-operation with: none

 DOI:10.15120/GR-2018-1

Early response of human neural stem cells to ionizing radiation

O. Arrizabalaga[1], S. Sadeghi[1], J. Kunz[1], E. Nasonova[1,2], I.S. Schroeder[1], S. Ritter[1]

[1]GSI, Darmstadt, Germany; [1]JINR, Dubna, Russia.

Human embryonic stem cell-derived neural stem cells (hNSCs) are a useful model system to study the effect of ionizing radiation on the (re-)generation of the brain. hNSCs are able to self-renew and to differentiate into the three neural cell types (neurons, astrocytes and oligodendrocytes). They can be expanded as adherent cultures or as three-dimensional aggregates named neurospheres, which resemble more closely the physiological conditions of the stem-niche in the brain.

Recently we have shown that exposure to X-rays affects the ability of hNSCs to form neurospheres [1]. In the present work, we studied the radiation response of hNSCs grown as adherent cultures. Cells were exposed to 1 or 2 Gy X-rays (250 kV, 16 mA) or sham-irradiated; and cell proliferation, cell cycle progression, apoptosis and the induction of cytogenetic damage were examined up to 96 hours post-irradiation. As an indicator of chromosome damage, the formation of micronuclei was measured, which originate from chromosome breakage or lagging chromosomes and are considered to be lethal.

The exposure to X-rays resulted in a pronounced dose-dependent growth delay (Figure 1). This effect was attributable, at least in part, to a transient cell cycle arrest. As shown in Figure 2, hNSCs started to accumulate in G2/M phase about 6 hours after exposure; 10 and 14 hours later a release from the block was observed for cells exposed to 1 and 2 Gy X-rays, respectively.

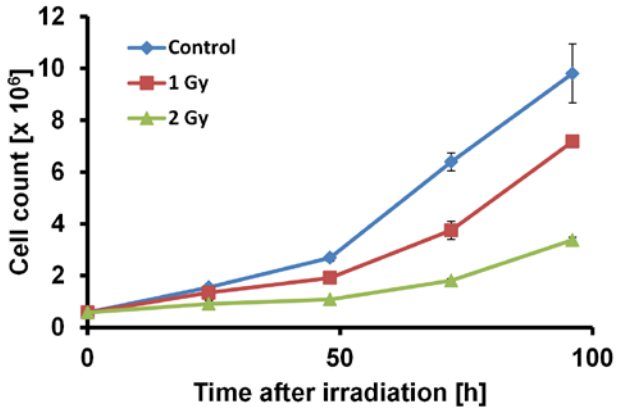


Figure 1: Growth curve of hNSC after X-ray exposure. The number of viable hNSCs was determined by means of Trypan Blue dye exclusion.

Likewise, in irradiated samples the proportion of apoptotic cells was higher than in control cultures and this effect increased with dose (data not shown) demonstrating that cell death contributes to the observed growth delay. As can be inferred from Figure 3, 72 hours after exposure to 1 Gy the micronucleated cells were successfully removed from the population, while even 96 hours after exposure to 2 Gy the proportion of damaged cells was significantly higher than in the control.

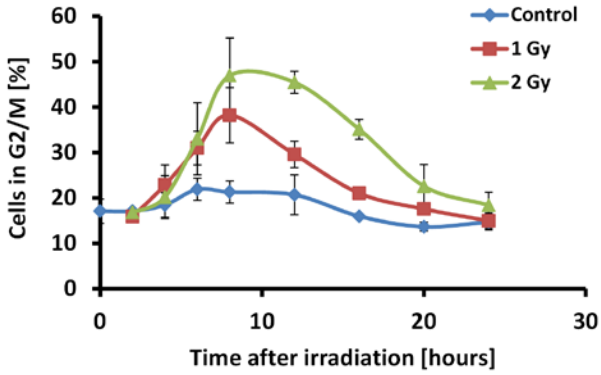


Figure 2: Percentage of cells in G2/M phase determined by flow cytometry at the indicated times.

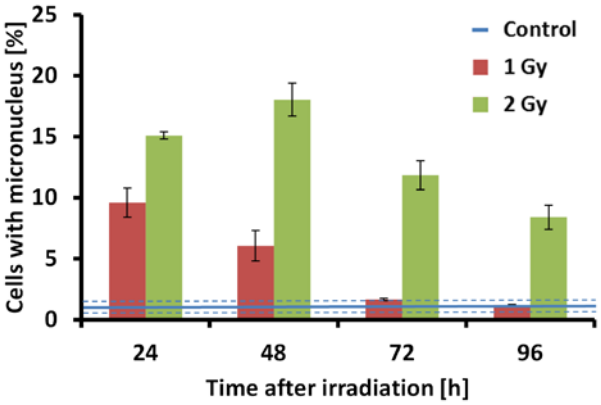


Figure 3: Percentage of micronucleus-containing cells. The frequency ($mean \pm SD$) measured in control cultures ($0.9 \pm 0.5\%$) is indicated by the blue lines.

Altogether our results indicate that ionizing radiation has a long-lasting effect on hNSCs and their progeny. In particular after the exposure to 2 Gy X-rays, the cells did not recover from radiation damage within 96 hours as reflected in an elevated frequency of both apoptotic and micronucleus-bearing cells, while a recovery process was visible after 1 Gy exposure. Whether the progeny of irradiated hNSC maintain the ability to differentiate into the three neural cell types will be examined in future studies.

Reference

[1] Arrizabalaga et al, GSI Report 2017-1, p. 328

Experiment beamline: none
Experiment collaboration: APPA-BIOMAT
Experiment proposal: SBio_Ritter
Accelerator infrastructure: none
PSP codes: none
Grants: BMBF (02NUK034C, 02NUK049)
Strategic university co-operation with: none

Generation of neural stem cells for the analysis of radiation-induced impairment of neurogenesis and neuroregeneration - BrainRadiationAssay

C. Schielke[1], O. Arrizabalaga[1], M. Mayer[2], C. Thielemann[2], S. Ritter[1] and I. Schroeder[1]

[1]GSI, Darmstadt, Germany; [2]University of Applied Sciences, Aschaffenburg, Germany

Tumors of the brain and central nervous system represent the biggest group of pediatric cancers. Improved treatment regimens including radiation therapy, often combined with chemotherapy, have significantly increased the overall survival. However, this positive effect is dampened by the occurrence of severe long term side effects such as cognitive impairment and neurological dysfunctions comparable to those seen in Alzheimers patients. Damage to neural stem and progenitor cells causing impaired or dysregulated neurogenesis/regeneration, especially when combination therapies are used, are discussed as a possible cause even though the underlying mechanisms and the contribution of the treatment components have yet to be determined in detail. In a joint effort between the University of Applied Sciences, Aschaffenburg, and GSI, a project called BrainRadiationAssay was initiated to study the effects of combination therapies on neurogenesis and neuroregeneration using brain-like 3D organoids.

As a prerequisite for the formation of brain-like organoids neural stem cells (NSCs) have to be generated from human embryonic stem cells (hESCs) and two protocols have been compared: The generation of NSCs using a commercially available Neural Induction Medium (NIM) according to Yan et al. [1], with and without addition of a rho kinase inhibitor (RI) and an improved version of the same protocol according to Zhang et al. [2], which uses the stromal cell-derived factor 1 (SDF1) to promote NSC proliferation. The ability to generate early/intermediate NSCs, marked by the expression of SOX2 and nestin, or late NSCs (characterized by the expression of PAX6) was determined in both protocols.

While the expression of nestin was similar in all NSCs generated, SOX2 mRNA expression was more pronounced in the NSCs using the Yan protocol with the RI having no effect (Fig 1).

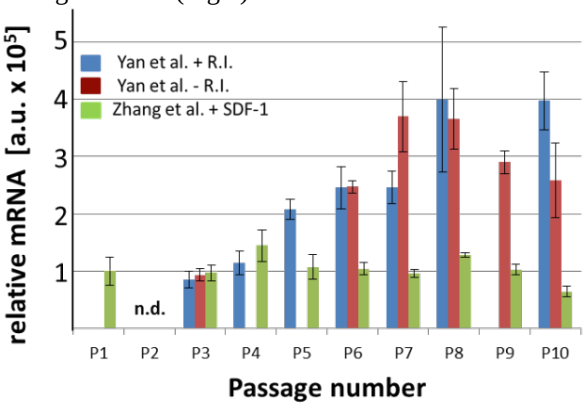


Figure 1: relative mRNA level of SOX2 in NSCs derived using the Yan or Zhang protocol, RI: Rho kinase inhibitor, SD of three technical replicates of a representative experiment

As SOX2 is not only a marker for NSCs but also for pluripotent cells such as the hESCs used as a source, it can be speculated that many of the hESCs either escaped the differentiation process or that the Yan protocol results in rather early NSCs. The latter hypothesis was supported by the findings that protein expression of the late NSC marker PAX6 was only observed in the NSCs generated using the Zhang protocol but not in the Yan protocol (Fig. 2).

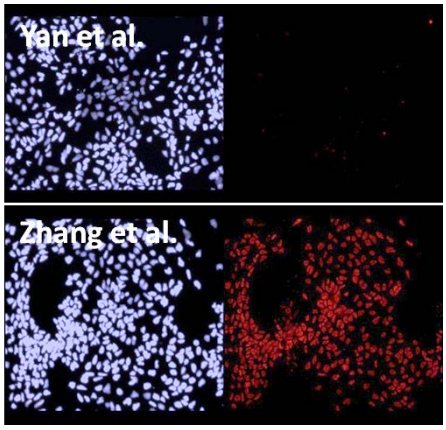


Fig. 2: PAX 6 protein expression (red, right side), nuclei stained with Hoechst 33342 (left side), magnification: 200x

Despite their immaturity, even NSCs generated according to the Yan protocol were able to form 3D neurospheres with electrophysiological function as measured by microelectrode arrays (MEAs, in collaboration with the University of Applied Sciences, Aschaffenburg, [3]). However, the NSCs generated according to the Zhang protocol appear to be more suitable for further differentiation strategies as PAX6 expression is imperative for the formation of neuronal rosettes, structures that ensure the polarized spreading of neurons and their proper assembly in complex neuronal circuits within in vitro brain-like organoids.

References

[1] Yan, Y. et al., Stem Cell Translational Medicine, 2013, 2: p. 862-870

[2] Zhang, L. et al., Neuroscience, 2016, 337: 88-97

[3] Mayer, M. et al., Biosens. Bioelectron., 2018, 100: p.462-468

Experiment beamline: none
Experiment collaboration: APPA-BIOMAT
Experiment proposal: SBIO_RITTER
Accelerator infrastructure: none
PSP codes: none
Grants: BMBF 02NUK049 and 02NUK034C
Strategic university co-operation with: none

 DOI:10.15120/GR-2018-1

Characterization of the cardiac cultures generated from human embryonic stem cells with distinct differentiation protocols

S. Nitsch[1,2], F. Braun[1,3], J. Kunz[1], M. Scholz[1], G. Taucher-Scholz[1,2], S. Ritter[1], I. Schroeder[1]

[1]GSI, Darmstadt, Germany; [2]Technical University, Darmstadt, Germany; [3]Hochschule Darmstadt, Germany

Human embryonic stem cells (hESCs) are a versatile *in vitro* model to investigate human embryonic development not only under normal conditions but also upon exposure to various noxae. Since ionizing radiation (IR) is increasingly used for medical treatments and diagnostics, the likelihood increases that women are exposed to IR during the earliest stages of pregnancy. Therefore, there is a need for risk assessment for those women. The heart is the first functional organ in human embryos and its correct development is crucial for all subsequently developing organs. To study cardiogenesis, several protocols for directed cardiac differentiation of hESCs were developed, leading to atrial, ventricular or nodal cells. In first experiments, we used the hESC line H9 grown on a MEF-feeder layer and compared the protocols published by Lian et al., 2013 [1] and Kadari et al., 2015 [2] to characterize the resulting cardiac derivatives.

*C*ells progressed *in vitro* through all the developmental stages that also occur during *in vivo* cardiac development. Around day 8 the cardiac clusters started to beat spontaneously. Marker gene and protein expression analyses were performed at multiple stages during cardiac differentiation. Additionally, we developed a software called cBRA (cardiac Beat Rate Analyzer) for functional analyses of the beating clusters (for details see Nitsch et al., 2018).

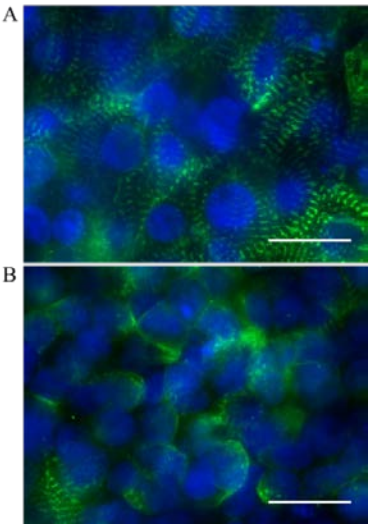


Figure 1: Immunocytochemical staining of alpha-Actinin in cardiomyocytes. Cardiomyocytes generated according to Kadari et al. (A) and Lian et al. (B) were stained for alpha-Actinin (green) at day 15 of differentiation; blue, DNA. Exemplary images of one marker protein.

Marker gene expression analyses revealed that the cardiomyocytes (CM) expressed atrial genes and the pacemaker marker HCN4 (data not shown) independent on the culture protocol. However, cardiac cultures resulting from the Kadari protocol expressed more mature and ventricular markers than the ones generated with the Lian protocol (data not shown). These results could be confirmed by protein expression analyses via immunocytochemistry. Compared to the Lian protocol (Fig. 1B) a more pronounced sarcomeric organization level in the CM resulting from the Kadari protocol (Fig. 1A) was observed.

The two protocols lead to similar beat rates at an early stage of cardiac differentiation (day 8). However, the clusters resulting from the Kadari protocol tended to beat faster at day 15 of differentiation (Fig. 2, n = 1).

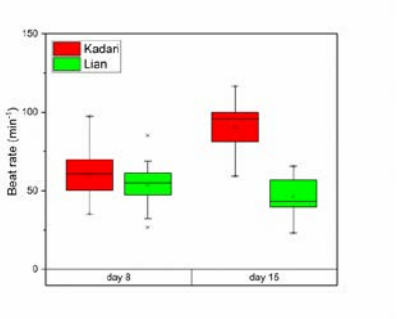


Figure 2: Beat rates of the hESC-derived cardiac clusters analyzed with cBRA. Videos of 25 beating clusters were taken at day 8 and 15 of differentiation. Exemplary results from one out of three independent experiments.

In conclusion, the hESC-derived CM resulting from the Kadari protocol display a more mature phenotype than those generated with the Lian protocol. Thus, they are more similar to human fetal CM, even though, compared to adult CM, they are still immature. Therefore, we chose the Kadari protocol to perform all subsequent analyses concerning the impact of IR on the cardiac differentiation capability of hESCs.

References

[1] Lian et al., Nature Protocols 8 (2013), p. 162-175
[2] Kadari et al., Stem Cell Rev and Rep (2015), p. 560-569
[3] Nitsch et al., in press, Stem Cell Res (2018)

Experiment beamline: none
Experiment collaboration: APPA-BIOMAT
Experiment proposal: BIO-05-003
Accelerator infrastructure: none
PSP codes: none
Grants: HGS Hire
Strategic university co-operation with: Technical University of Darmstadt

Persistence of translocations versus dicentrics after radiotherapy

C. Hartel[1], M.C. Fuss[1], M. Kraemer[1], E. Nasonova[1,2], D. Oetzel[3] and S. Ritter[1]

[1]GSI, Darmstadt, Germany; [2] JINR, Dubna, Russia; [3]Heidelberg University Hospital, Heidelberg, Germany.

Chromosomal aberrations in peripheral blood lymphocytes (PBLs) are a widely used biomarker for radiation exposure. To gain insight into the cytotoxic effects of the therapy to the normal tissue, represented by the PBLs, we analysed aberrations in PBLs from prostate cancer patients undergoing radiotherapy using multiplex-fluorescence in situ hybridization (mFISH, see Figure 1). Comparing different treatment techniques showed a pronounced influence of the target volume, but no difference between treatment with a Carbon-ion boost followed by IMRT and IMRT alone [1].

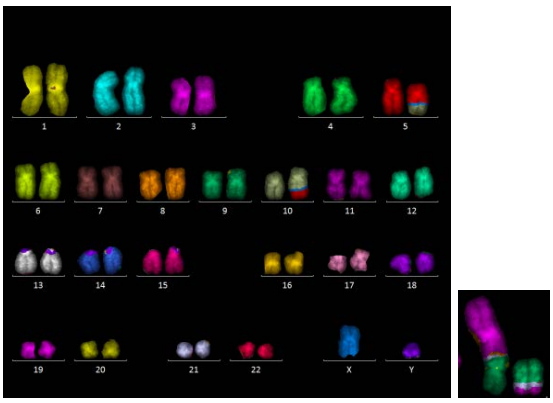


Figure 1. Left: Human karyogram with a translocation between chromosomes 5 and 10. Right: dicentric chromosome with acentric fragment (originating from Chromosomes 3 and 9).

Radiation exposure leads to several types of chromosomal aberrations, including translocations (transmissible to daughter cells during cell-division) and dicentric chromosomes (non-transmissible) (Examples shown in Figure 1). Translocations and dicentrics were induced by the therapy with similar frequencies. In the year after therapy, the yield of dicentric chromosomes declined significantly, while the yield of translocations remained unchanged. The ratio of (non-transmissible) dicentrics to (transmissible) translocations changed from 0.92±0.09 to 0.55±0.07. Mature PBLs are normally not undergoing cell divisions; changes in the ratio between non-transmissible and transmissible aberrations can therefore be considered an indicator for aberrant hematopoietic stem/progenitor cells. To further follow the persistence of aberrations, we analyzed samples collected 2.5 years after therapy, which confirmed the decline in the dicentrics/translocation ratio. To relate this finding to the exposure of hematopoietic stem/progenitor cells, we reviewed the treatment plans for bone marrow (BM) exposure. The patients receiving a combined radiotherapy were treated with a scanned C-ion boost (18 GyE of biologically effective dose to gross tumour volume) followed by step-and-shoot-IMRT consisting of 5-7-fields (60 Gy to clinical target volume). The corresponding dose-volume histograms for both modalities are presented in Figure 2. The C-ion boost caused ~240 cm³ of pelvic BM (femoral heads and part of acetabula) to be irradiated with a relatively homogeneous dose distribution as depicted in Figure 2a. During photon IMRT, a much more substantial amount of BM -the entire lower pelvis and femoral heads and necks- received a highly inhomogeneous dose including hot spots > 50 Gy. Details can be seen in the dose-volume-relationship of the normal tissue enclosing the irradiated BM ("lower pelvis NT incl. BM") in Figure 2b.

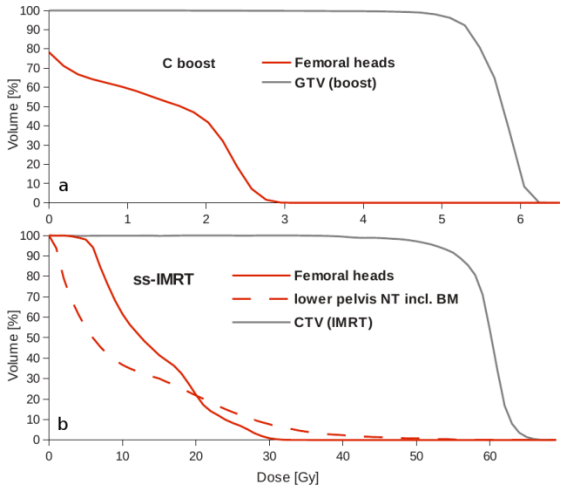


Figure 2. Dose-volume histograms for (a) C-ion boost (referred to physical dose) and (b) IMRT including the respective target volumes and normal tissue volumes/OARs representative for irradiated bone marrow. DVH data are averages over (a) 13 patients (26 femoral heads) and (b) two patients, one for each field configuration.

The observed change in the aberration ratio can be explained by the dose deposition in the bone marrow during radiotherapy. The detectable influence of the radiotherapy on hematopoietic stem/progenitor cells underlines the importance of optimal normal tissue sparing to avoid detrimental late effects.

References

[1] Hartel C et al., Radiother Oncol 95(1) 73-78 (2010).

Experiment beamline: SIS18-CaveM
Experiment collaboration: APPA-BIOMAT
Experiment proposal: none
Accelerator infrastructure: SIS18
PSP codes: none
Grants: BMBF 02S8203 and 02S8497
Strategic university co-operation with: none

 DOI:10.15120/GR-2018-1

A new approach for spike detection in a low signal-to-noise environment

M. Mayer[1], O. Arrizabalaga[2], F. Lieb[1], M. Ciba[1], S. Ritter[2] and C. Thielemann[1]

[1]University of Applied Sciences, Aschaffenburg, Germany; [2]GSI, Darmstadt, Germany

In previous studies, we analyzed the effect of ionizing radiation (IR) on the electrophysiological properties of human embryonic stem cell (hESC) derived neurospheres (NS) using microelectrode array (MEA) chips [1].

During this study, it was found that the analysis of spikes derived from neuronal 3D cultures is challenging due to a low signal to noise ratio (SNR), see Fig. 2A. To analyse the character of the background noise, hESC derived NS were cultivated on MEA chips as previously described [2]. One day after plating, cells as well as neurites migrated radially out of the NS. After spontaneous spikes were observed, noise was recorded from electrodes covered by the NS (black electrodes in Fig. 1A) as well as from electrodes covered by a monolayer of outgrowing cells (white electrodes in Fig. 1A). To analyze differences in the noise level, the root mean square (RMS) was calculated for a time frame of 2 seconds containing exclusively noise [3], resulting in a value of 3,03 µV for electrodes in contact with outgrowing cells and 3,68 µV for electrodes below the NS (Fig. 1B). This significant increase is most likely caused by low amplitude spikes originating from neurons in the NS. The number of cells within the detection range of a single electrode is clearly much higher in 3D than in 2D cell models leading to an enhanced level of background noise due to an overlay of unavoidable electrical and biological noise.

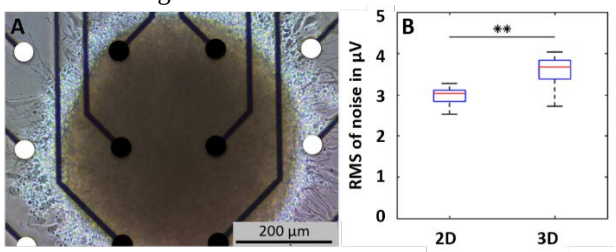


Fig. 1: Analysis of background noise. (A) NS were cultured on MEA chips. (B) Boxplot showing RMS of electrodes in quartiles, whiskers show minimum and maximum values (n=10 for 2D, n= 13 for 3D, Mann-Whitney U test, **P ≤ 0,01).

Furthermore, spikes recorded from NS as well as from outgrowing cells possess very small amplitudes with a mean value of 19,71 ± 3,93 as compared for example to 2D primary rat neurons where amplitudes of 57,68 µV± 28,25 µV were found. In combination with the above mentioned high level of background noise, the SNR of NS measurements is very low and detection of neuronal spike events with a simple threshold-based algorithm [3] is hampered. To address this issue, we combined the well-known threshold-based spike detection with a new algorithm named stationary wavelet transform based teager energy operator (SWTTEO), which has already shown superior performance to other commonly used algorithms by using simulated data [4]. Due to this combination, spike detection takes into account not only the amplitudes but also the time-frequency behavior of signals. The analysis procedure of a typical neuronal measurement (Fig. 2A) using threshold based spike detection and SWTTEO is shown in Fig. 2. First, potential spikes are preselected by a threshold-based algorithm. The threshold was determined by multiplying the estimated standard deviation of the noise by ± 4.5. Subsequently, SWTTEO verifies their authenticity by evaluating the time-frequency behavior of each spike. This approach allows for the distinction between background noise (Fig. 2B) and neuronal signals (Fig. 2C) leading to a profound reduction in the number of false positive signals.
For further details see Lieb et al. [4] and Mayer et al. [2].

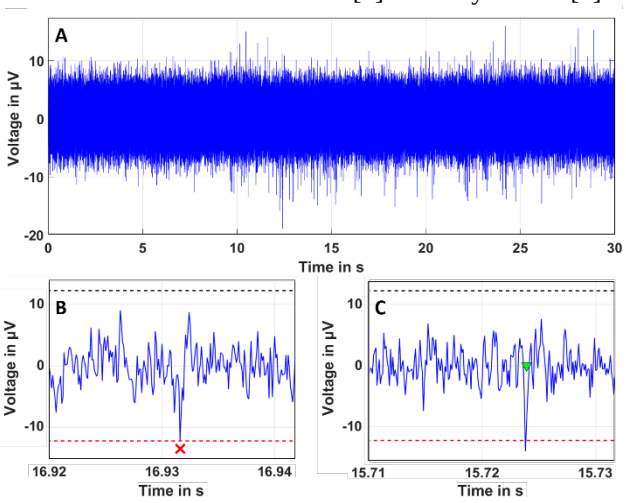


Fig. 2: Analysis procedure using threshold-based algorithm and SWTTEO. (A) Typical neuronal measurement of a NS recorded by a single electrode. (B) Background-noise. (C) Neuronal signal.

We conclude that the combination of threshold-based spike detection and SWTTEO is highly suitable to analyze neuronal signals derived from 3D cultures leading to more accurate results compared to threshold-based spike detection. In further studies, this new approach will be used to assess the impact of antiepileptic drugs and IR on electrophysiological properties of 3D neuronal networks.

References

[1] Mayer, M. et al., GSI Scientific Report 2015, p. 205
[2] Mayer, M. et al., Biosens.Bioelectron., 2018, 100: p. 462-468
[3] Nick, C. et al., SPIJ 2013, 7 (2): p. 96-109
[4] Lieb, F. et al., Neural Eng. 2017, 14 (3): 036013

Experiment beamline: none
Experiment collaboration: APPA-BIOMAT
Experiment proposal: SBio_Ritter
Accelerator infrastructure: none
PSP codes: none
Grants: BMBF 02NUK049 and 02NUK034C
Strategic university co-operation with: Hochschule Aschaffenburg

Characterization of glioblastoma stem-like cells

N. B. Averbeck[1], Y. Knies[1], S. Lehnung[1,2], S. Ritter[1], C. Hartel[1]

[1]GSI, Darmstadt, Germany; [2]Fachbereich für Chemie- und Biotechnologie, Hochschule Darmstadt, Germany.

Glioblastoma multiforme is a very aggressive cancer and represents the most common brain tumour in adults. Routine treatment of this cancer involves surgery and subsequent radiotherapy. Yet, recurrences are the rule and the recurrent tumours are frequently more radioresistant than the primary tumour. The mechanism of the tumour radioresistance is not well understood. Hence, we aim to elucidate its underlying molecular mechanisms by studying a patient derived primary glioblastoma cell line (#10) [1] and its radioselected daughter cell-line (#10-IR), which both were kindly provided by A. Giese, Uniklinikum Mainz, Germany. For comparison, the widely used glioblastoma cell-line U-87 MG was used (ATCC, Manassas, VA, USA). All cells were cultured in serum-free stem cell culture medium supplemented with growth factors [2]. These conditions promote the growth of tumour-stem-like cells – the cell type that is believed to be responsible for the tumour relapse and therapy resistance. In contrast to standard culture conditions, where the cells grow as a monolayer, the cells form floating tumourspheres in serum-free medium. The formation of tumourspheres from single cells can be used (in analogy to the colony forming assay for adherent cells) to establish dose-effect curves.

The radioselected #10-IR cells showed a radioresistant subpopulation in the tumoursphere-formation assay after X-ray exposure [3]. A similar shape of the dose-effect curve hinting at a radioresistant subpopulation was also observed for the parental cell line #10.

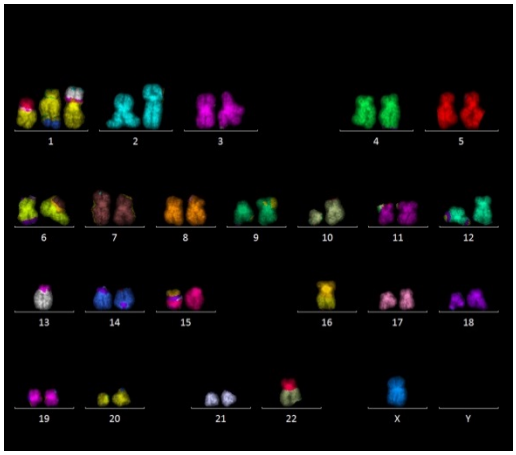


Figure 1: Example of an mFISH stained karyotype of the U-87 MG cell line cultured in serum-free conditions.

To better understand their radiation response, all three cell lines were further characterized by cytogenetics and the expression of p53, a biomarker for cancer which can influence the radiosensitivity [4]. The cytogenetic analysis by the mFISH technique revealed several characteristic numerical and structural aberrations in all three cell lines. An mFISH karyogram of the cell line U-87 MG showed several aberrations, including (1'-13), (9`)T, (16'-1), and (22'-10) (Figure 1). The #10-IR cells carried aberrations that are present in the parental line #10 [e.g. (13'-2)], as well as additional ones.

On the level of the cancer biomarker p53 we found that both, the #10-IR cells and their more radiosensitive parental line #10, expressed p53 to a similar extend as the p53 wild-type glioblastoma cell line U-87 MG [5] (Figure 2) supporting the notion that the observed radioresistance of #10-IR is not based on p53 deficiency.

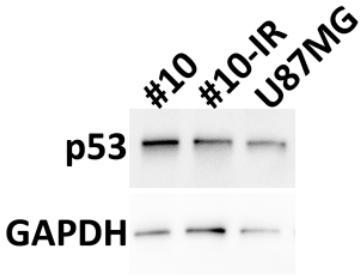


Figure 2: The radioresistant gliomablastoma cell line #10-IR expresses p53 to a similar extend as its more radiosensitive counterpart #10. Western analysis of cells grown in serum-free culture. GAPDH served as a loading control.

Future experiments will include DNA-repair kinetics, cell-cycle analyses, and gene-expression studies to further elucidate the mechanisms of radiation resistance in glioblastoma stem-like cells after sparsely and densely ionising radiation.

References

[1] Barrantes-Freer A., et al., J Neuropathol Exp Neurol, 2013, 72(4): p. 307-24.
[2] Hartel, C., et al., GSI Scientific Report 2012, p. 443.
[3] Hartel C., et al., GSI Scientific Report 2013, p 225.
[4] Rubner Y., et al., Radiation Oncol 2014, 9:89.
[5] Ferrandon, S., et al., Cancer Lett, 2015, 360(1): p. 10-16.

Experiment beamline: none
Experiment collaboration: APPA-BIOMAT
Experiment proposal: SBio_Ritter
Accelerator infrastructure: none
PSP codes: none
Grants: BMUB / BfS contract no. 3616S32262
Strategic university co-operation with: none

 DOI:10.15120/GR-2018-1

Effect of extrusion-based bioprinting on neurospheres

S. Allig[1], M. Mayer[1], O. Arrizabalaga[2], S. Ritter[2], I. Schröder[2] and C. Thielemann[1]

[1]University of Applied Sciences, BioMEMS Lab, Aschaffenburg, Germany, [2]GSI, Biophysics, Darmstadt, Germany

Bioprinting is a promising new approach which applies additive manufacturing technologies in the field of tissue engineering to create well-defined cell formations or artificial tissues. The resulting structure can be used for in vitro drug screening and disease modelling, or the regeneration of tissues and organs [1].

According to Zhuang et al. [2] three-dimensional (3D) cell cultures can be categorized into cell biology-based and engineering-based systems. In this work, both systems were combined to generate a controlled 3D neural tissue model high in complexity and consistency, i.e. neurospheres (NS) were embedded in a hydrogel scaffold.

For the experiments human embryonic stem cell (hESC, line WA09) derived NS were used, as described in [3]. Briefly, after 32 days in culture, NS were mixed with commercially available bioink (Cellink Bioink RGD) consisting of alginate, nanofibrillated cellulose and RGD peptides. In a next step, the cell-laden bioink was extruded pneumatically through a 25 gauge precision needle (250 µm inner diameter) by means of the bioprinter 3D Discovery™ (regenHU, Switzerland) at different pressure levels (90 kPa, 75 kPa and 60 kPa). The printing speed was 400 mm/min. Once a meandering structure was printed, calcium chloride solution was applied for 5 min to crosslink the structure providing long sustainability. Structures were printed on multiwell plates coated with polyethyleneimine and laminin to guarantee adhesion between the bioink and the plate. To examine the effect of the printing process on the viability of NS, the fluorescence dyes CellTracker™ Green and DAPI were used to distinguish live and dead cells, respectively.

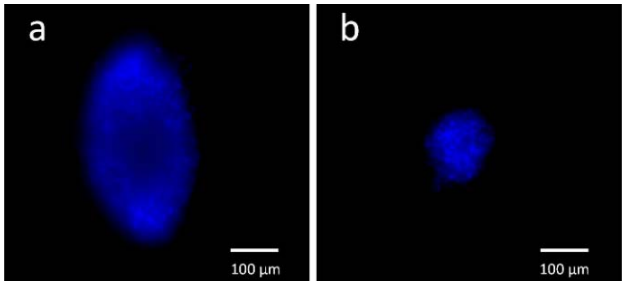


Figure 1: Elongation was detected at NS larger than 200 µm (a) while smaller ones remained circular (b). Cell nuclei of dead cells were marked with DAPI.

Our microscopy studies showed that most cells were labelled with DAPI. Thus, the extrusion-based bioprinting process reduced the cell viability significantly. Furthermore, elongation of NS was detected throughout all pressure levels. In general, shapes of NS range from circular to elliptical, but after printing the proportion of elliptical NS increased (Figure 1a). Notably, this effect was not observed for NS significantly smaller than 200 µm (Figure 1b).

Additionally, single cells were detected in the printed structure indicating a disruption of the NS architecture by shear stress. Blaeser et al. have proven that this exposure to shear stress during the bioprinting process reduces cell viability and thus proliferation potential if shear forces exceed a specific threshold [4]. Nevertheless, in our study living cells were found three days after printing within NS smaller than 200 µm (Figure 2) demonstrating that the chosen bioink was porous enough to allow nutrients and gas to diffuse through the scaffold.

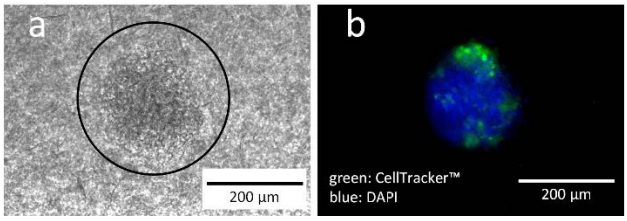


Figure 2: Single NS embedded in bioink. (a) Analysis by means of transmitted-light microscopy. The dark circle indicates the position of the NS in the hydrogel scaffold. (b) Life/dead staining of the same NS three days after printing. Green labelling indicates living cells via CellTracker™ probe; blue labelling indicates dead cells via DAPI staining.

In summary, our first data show that bioprinting of NS is feasible if the diameter of the NS is significantly smaller than the nozzle diameter. Future experiments on the interactions between NS and artificial ECM are planned; as well as experiments with smaller NS, to obtain more information about the effect of extrusion-based bioprinting on NS. This knowledge will be valuable as bioprinting enables engineering of complex 3D model systems, e.g. organoids with controlled cell-cell and cell-matrix interactions. The resulting cell systems provide an excellent model to investigate effects of ionizing radiation on neuronal networks, e.g. functionality and neural differentiation while being more representative of the situation in vivo than conventionally used cell models.

References

[1] Murphy S.V. et al., Nature Biotechnology 2014, 32: 773–785.
[2] Zhuang P. et al., Biomaterials 2017, 154: 113–133.
[3] Mayer M. et al., Biosensors and Bioelectronics 2018, 100: 462-468.
[4] Blaeser A. et al., Advanced Healthcare Materials, 2015, 5: 326-333.

Experiment beamline: none
Experiment collaboration: APPA-BIOMAT
Experiment proposal: SBio_Ritter
Accelerator infrastructure: none
PSP codes: none
Grants: BMBF 02NUK049 and 02NUK034C
Strategic university co-operation: none

Effect of reduced gravity on hematopoietic stem and progenitor cells and peripheral blood lymphocytes – a pilot study

K. Shreder[1], D. Kraft[1], M. Rall-Scharpf[2], L. Wiesmüller[2], O.Ullrich[3], C. Fournier[1]

[1]GSI, Darmstadt, Germany; [2] Division of Gynecological Oncology, Department of Obstetrics and Gynecology of the University of Ulm, Ulm, Germany, [3] Institute of Anatomy, University of Zurich, Zurich, Switzerland

Introduction

The influence of space conditions on the health of astronauts is a limiting factor for human spaceflight. Both microgravity and radiation exposure induce a variety of degenerative effects in different organs and tissues [1]. The aim of the project is to investigate the combined effect of microgravity and radiation exposure on human hematopoietic cells (stem and progenitor cells, HSPC, and peripheral blood lymphocytes, PBL) with respect to DNA damage and repair. Here we present results obtained from the pilot experiment on board of an Airbus A300 Zero.

Experiment set up and results

The pilot test for the cultivation of both cell types (HSPC and PBL) under conditions of reduced gravity was performed as a part of experiment EPICON (Prof. O. Ullrich, University of Zurich) during the 28th DLR parabolic flight campaign on board Airbus A300 Zero. The microgravity is achieved by following a flight profile which alternates in several phases between ascent and descent maneuvers. These parabolas result in 22 seconds of microgravity (Fig. 1A). The aircraft is equipped with experimental racks for performing life science experiments (Fig. 1B).

Prior to the experiment on board of the aircraft, cultivation of HSPC and PBL in special blood bags without temperature regulation and supply of CO2 was established. Importantly, we observed in both cell types in the presence of growth factors a similar cell cycle distribution and a percentage of programmed cell death (apoptosis) below 10%. This indicates that the cells proliferate in the blood bags and survive the stress of transport.

For the experiment, HSPC and PBL were isolated from healthy donors and cultivated under standard conditions (37ºC, 5% CO2, 95% RH) for 24h. Cells were then transferred in the blood bags for the transport and experiments on board the aircraft (approx. 48h). Fixation of the cells with 2% paraformaldehyde (PFA) was performed in the lab (ground control), on board before start (inflight control) and on board before the last parable (inflight µg). For the analysis of DNA damage and repair, the cells were immunolabeled for detection of γH2AX and analysed using a fluorescence microscope according to [2]. The obtained results suggest that under changing gravity conditions the formation of γH2AX is reduced compared to ground control. This accounts for both cell types but is more pronounced in HSPC (Fig. 2), pointing to an altered DNA damage signalling under changing gravity conditions.

Based on the establishment of the experimental conditions, combined effects of radiation and reduced gravity on HSPC and PBL will be investigated.

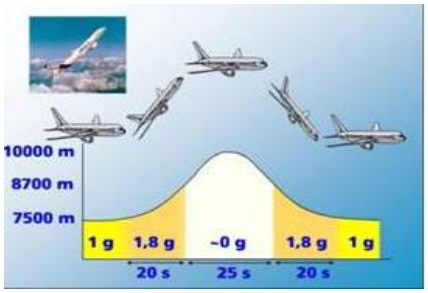


Fig.1 Trajectory for zero gravity maneuver (www.dlr.de)

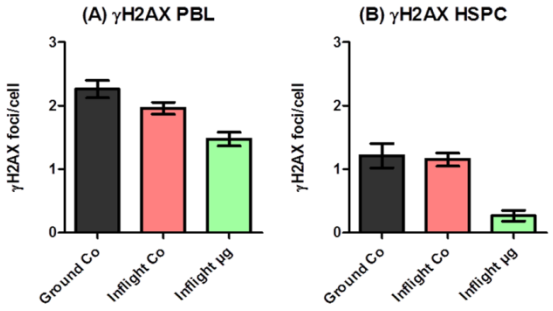


Fig.2 Induction of γH2AX in PBL (A) and HSPC (B) under changing gravity conditions. Microscopic analysis and quantification of γH2AX foci. N=1, n=2

References

[1] F.A. Cucinotta and M. Durante, The Lancet. Oncology 2006, 7(5):431-35

[2] Kraft et al., Leukemia 2015, 29 (7): 1543–54.

Experiment beamline: none
Experiment collaboration: none
Experiment proposal: none
Accelerator infrastructure: none
PSP codes: none
Grants: Work supported by BMWI (50WB1716)
Strategic university co-operation with: none

 DOI:10.15120/GR-2018-1

Pharmacological augmentation of heavy ion cancer therapy

Norman Reppingen[1], Susanne Wolf[2], Claudia Fournier[1]

[1]GSI, Darmstadt, Germany; [2]University Frankfurt

Our efforts towards an efficient pharmacological optimization of heavy ion cancer therapy are currently devoted to the elucidation of the underlying mechanisms of this treatment modality which involves the broad spectrum tyrosine kinase inhibitor XL-184 [3] and to the design of further optimization steps of the approach by combination with radiotherapy. We reported a strongly reduced tumor growth in the 4T1 model of metastatic breast cancer in our last report[3].

We here report data suggesting an involvement of reactive oxygen species (ROS) in the mechanism of activity of the pharmacological entity, irradiation and the combination of both treatment modalities. ROS have an established role as effector molecules in drug treatments[1]. Further, there are hints to an immune mediated mechanism in the literature and in our preliminary histological analysis, which needs further exploration (see figure 2).

In vitro ROS measurements

For the tyrosine kinase inhibitor axitinib, an influence on metabolic ROS levels and cellular senescence was reported, which is closely reflected by our results concerning the ROS levels (see figure 1)[1]. This is pointing us to characterize the efficacy of our approach in inducing cellular senescence, which was reported in conjunction with a selective inhibitor of c-Met[2]. c-Met is a highly relevant molecule for targeted cancer drugs, correlated with advanced stag3, poor prognosis, and also a key drug target of XL-184[2].

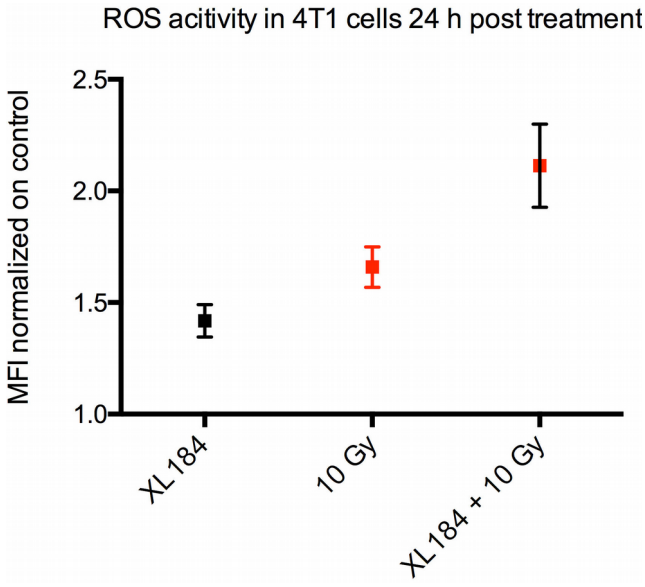


Figure 1: Analysis via flow cytometry: Cells were treated with our pharmacological entity after irradiation with 10 Gy of x-ray and were incubated with dehydroethidium (DHE) in serum free medium for 2 h to assess metabolic activity of reactive oxygen species (ROS). Both irradiation and pharmacological treatment revealed an increase in ROS activity, with an additional effect upon combination.

In vivo analysis – histology

Tumor samples from the *in vivo* experiments using XL-184, which were subject in our last scientific report revealed CD11b positive immune cells (figure 2). These are possibly tumoricidal Natural Killer (NK) cells, because in the frame of another experiment we detected CD11b expression on cells, which were also positive for a marker for NK cells (NK1.1). For XL-184, immune activating properties were reported[4]. Therefore, we are headed to find out if NK cells or other immune cells are involved in the mechanism of activity, or if the tumor shrinkage furnished by XL-184 is caused by more direct effects.

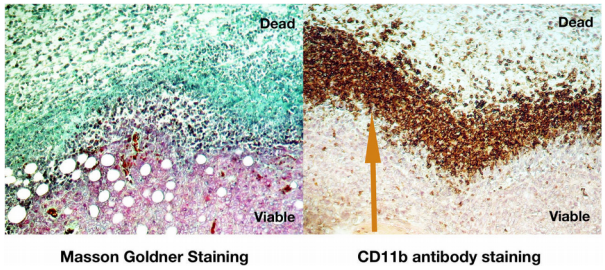


Figure 2: Histological analysis: The picture shows the border region between dead and viable regions in a tumor treated with XL-184. This zone showed a positivity of the marker CD11b, a marker present on myeloid cells and NK cells.

References

[1] Morelli, Maria Beatrice, et al. "Axitinib induces senescence-associated cell death and necrosis in glioma cell lines: The proteasome inhibitor, bortezomib, potentiates axitinib-induced cytotoxicity in a p21 (Waf/Cip1) dependent manner." *Oncotarget* 8.2 (2017): 3380.

[2] Francica, Paola, et al. "Depletion of FOXM1 via MET Targeting Underlies Establishment of a DNA

Damage–Induced Senescence Program in Gastric Cancer." *Clinical cancer research* 22.21 (2016): 5322-5336.
[3] N. Reppingen, M. Durante, C. Fournier, Scientific Reports 2016
[4] Patnaik, Akash, et al. "Cabozantinib eradicates advanced murine prostate cancer by activating antit mor innate immunity." Cancer discovery 7.7 (2017): 750-765. 10.1158/2159-8290.CD-16-0778

Experiment beamline: none

Experiment collaboration: APPA-BIOMAT

Experiment proposal: none

Accelerator infrastructure: none

Strategic university co-operation with: none

 DOI:10.15120/GR-2018-1

Substrate specific differentiation of osteoclasts in irradiation experiments

Rapp F[1], Schott K[1], Tsoukala I[1], Hassan S[1], Kraft D[1], Benzer A[1], Lutter AH[2], Anderer U[2], Richter S[3], Teuscher N[3], Fournier C[1]

[1]GSI, Darmstadt, Germany; [2]Brandenburgische Technische Universität Cottbus-Senftenberg ; [3]Fraunhofer IMWS, Halle/Germany

Introduction

Low doses of ionizing radiation, such as α-particles emitted during Radon decay or low dose X-ray therapy (LD-RT, [1]) are used for treatment of chronic-inflammatory musculoskeletal diseases [2]. However, the molecular and cellular effects remain mostly unclear. We investigate effects of low dose irradiation on bone metabolism, since bone degradation by bone resorbing cells, osteoclasts (OC), is often seen in chronic inflammatory diseases [3]. For functional analysis of these cells, the culture substrate has to be as physiological as possible. Therefore we used standard cell culture plastic, an osteosarcoma-derived matrix [4], and bone slices. To investigate Radon effects, an α-particle source has to be used, which requires special culture conditions.

Methods

Human OC precursors (monocytes) were isolated from buffy coats of healthy donors (German Red Cross blood donor service Frankfurt/Main). Differentiation of OC was initiated by adding RANKL and M-CSF. The differentiation state was assessed by staining of TRAP, F-actin and number of cell nuclei. Irradiation was performed with X-rays or with an α-particle source. Cultivation of OC was performed either on regular cell culture plastic, extracellular matrix produced by osteosarcoma cells (Saos-2), bovine bone slices, or plasma-treated Mylar foil.

Results

Cultivation of OC on bone slices is the most physiological ex vivo method to date, but growth and differentiation is not well reproducible. After 7 days on bone slices, mainly spindle-shaped pro-OC can be detected, whereas on plastic, mature OC are present in non-irradiated controls (Fig. 1).

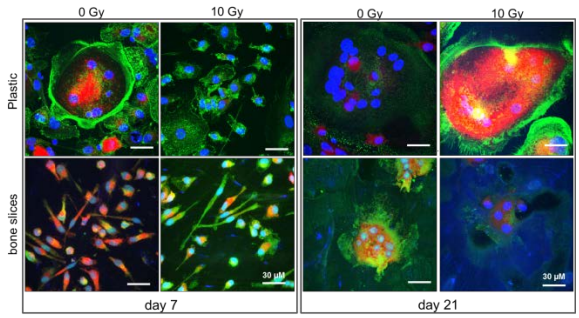


Figure 1: Confocal microscopy of OC grown on plastic or bone slices. OC differentiation was initiated directly after irradiation with 10 Gy of X-rays and imaged after 7 and 21 days. Staining: F-actin (FITC-Phalloidin, green), cell nuclei (DAPI, blue) and TRAP (red). Maximum intensity projections from z-stacks (630x, scale bar= 30µm).

Differentiation of OC precursors on an extracellular matrix is a less complex alternative, but cell-cell interactions seem to play a role in differentiation (Fig. 2). Irradiation effects, measured by the amount of resorption pits, were dependent on individual donors (data not shown).

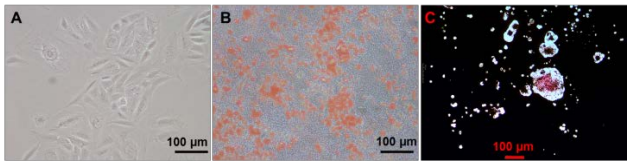


Figure 2: Saos-2 cells before differentiation (A) and after 24 d of differentiation and matrix production (B). Monocytes are seeded on the matrix and produce resorption pits, if active (C). A and B: light microscopy pictures, C: van Kossa staining. Scale bars= 100µm.

For experiments using α-particle irradiation, cells have to be grown on a thin Mylar foil (3 µm). Here we used a novel plasma-treated foil, which enhances cell adhesion and growth. Monocytes adhere well on the foil, but do not differentiate over time in a similar way as on plastic or bone substrates (Fig. 3). We therefore established a method to shortly let monocytes adhere to the foil, irradiate and immediately detach them to further cultivate on more suitable substrates for long-term experiments.

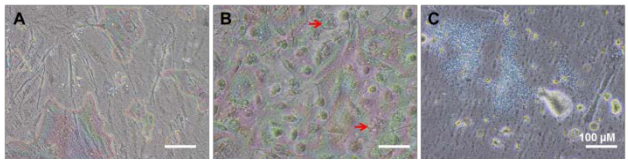


Figure 3: OC were cultured and differentiated on plasma-treated Mylar foil for 21 days. Some samples exhibit a spindle-shaped form of Pro-Osteoclasts (A) whereas others are more differentiated (B, arrows) or did not grow at all (C). Light microscopy, 100x; scale bar= 100 µm.

Discussion

For irradiation experiments and the analysis of a physiological response of OC, suitable cultivation substrates are needed. X-irradiation decreases differentiation level and prohibits fusion of pro-osteoclasts to mature OC. We currently establish a method to irradiate monocyte cultures with alpha particles to mimic effects of Radon, but the differentiation level and radiation response of OC is donor dependent.

References

[1] A Cucu et al, Front Immunol. 2017 25;8:882
[2] PF Rühle et al, Autoimmunity. 2017 50(2):133-140.
[3] SM Jung et al, J Immunol Res. 2014;2014:263625.
[4] AH Lutter et al, J. Cell. Biochem., 2010, 109: 1025-1032

Experiment beamline: none
Experiment collaboration: APPA-BIOMAT
Experiment proposal: none
Accelerator infrastructure: none
PSP codes: [none]
Grants: BMBF (GREWIS 02NUK017A and 02NUK17D)
Strategic university co-operation with: h_da Darmstadt other: Fraunhofer IMWS, Halle/ Germany; Brandenburgische Technische Universität Cottbus-Senftenberg]

 DOI:10.15120/GR-2018-1

Senescence and inflammation in human endothelial cells

F. Rapp[1], S. Schmidke[1,2], P. Wendel[1,2], S. Ktitareva[1], C. Fournier[1]

[1]GSI, Darmstadt, Germany; [2]h_da Hochschule Darmstadt, Germany

Introduction

Human primary cells undergo ageing processes during cultivation such as senescence [1]. In endothelial cells (EC) building the inner layer of blood vessels, this could lead to an increase in inflammatory signalling and therefore increased peripheral blood lymphocytes (PBL) adhesion. In chronic inflammatory diseases such as rheumatoid arthritis, immune cells are recruited to the joints via the endothelium [2]. Treatment options, besides standard drugs, include low dose radiation therapies with photons or α-particle emitters (Radon spas) [3]. In our previous work, we showed that low doses of irradiation can reduce inflammatory reactions in EC, resulting in a reduced adhesion of PBL [4]. Here, we wanted to identify reliable markers to detect senescent cells *in vitro* and investigate effects of cellular senescence on EC-PBL interactions.

Methods

Primary human microvascular cells (HMVEC) of the same donor were cultivated up to passage 18. Senescent cells were detected by staining for senescence-associated β-galactosidase (SA-β-Gal, [5]) or with immunofluorescent stainings for p16. PBL were isolated from buffy coats (German Red Cross blood donor service Frankfurt/Main), and the adhesion assay was performed as described previously [2].

Results

HMVEC cultures were examined for SA- β-Gal positive cells at early and later passages (Fig. 1). The ratio of senescent cells increased more than 6-fold from passage 5 to passage 15.

To investigate whether an increased amount of senescent cells has an impact on PBL adhesion, we measured adhesion on an early passage (P5) HMVEC culture parallel to a late passage (P18) of the same donor (Fig. 3). The number of adherent PBL was not changed in the older HMVEC culture compared to the younger culture.

Discussion

During cultivation, primary cells naturally undergo senescence. We investigated the occurrence of senescence in HMVEC cultures at early and late passages and established methods to stain for senescence markers (SA-β-Gal and p16). The combined staining allows for a reliable identification of senescent cells. Since inflammatory processes in the endothelium *in vivo* could be enhanced by senescent cells, as described for established cell lines [7], we tested if PBL adhesion is increased when the ratio of senescent cells is higher. This was not confirmed in first experiments under static culture conditions, which will be extended to laminar conditions.

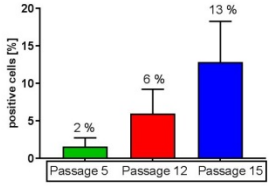


Figure 1: HMVEC at different cultivation stages were stained for SA-galactosidase (Gal). The amount of SA-Gal positive cells increases over cultivation time (N=1, n= 2, mean + SD) (modified after [6]).

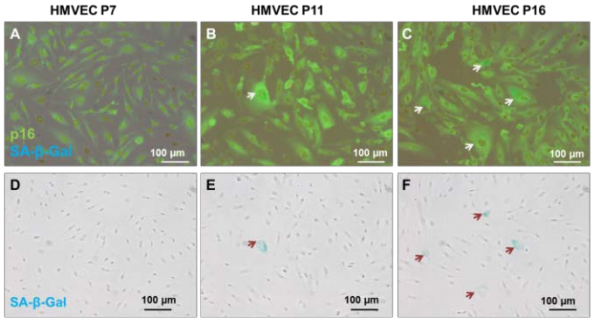


Figure 2: HMVEC cultures at different passages (A, D P7, B, E P11, C, F P16) were stained for senescence markers (p16, green; SA-β-Gal, blue) to identify senescent cells. A-C: merge of fluorescent and light microscopic pictures, D-F: light microscopy. Scale bars= 100µm.

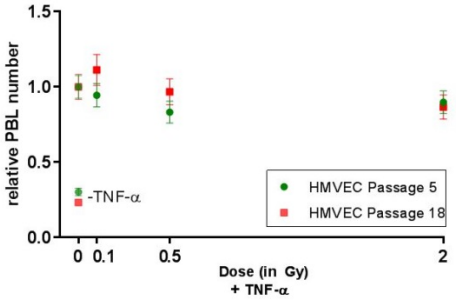


Figure 3: HMVEC of two different passages (P5, early and P18, late) were stimulated with TNF-α, irradiated with photons and co-incubated with PBL. Relative adherent PBL numbers were then determined. (N=1, n=3) (modified after [6]).

References

[1] A.J. Donato et al, JMolCellCardiol 2015 89 (Pt B):122-35.
[2] A. Al-Soudi et al, AutoimmunRev 2017 16(9):951-962
[3] P.F. Rühle et al, Autoimmunity 2017 50(2):133-140
[4] N. Erbeldinger et al, Front Immunol 2017 1;8:627
[5] G.P. Dimri et al, ProcNatlAcadSci USA 1995 26; 92(20):9363-7
[6] P. Wendel, Bachelor thesis, 2017
[7] D. Lowe, K. Raj JVisExp. 2015 18;(100):e52924.

Experiment beamline: none
Experiment collaboration: APPA-BIOMAT
Experiment proposal: none
Accelerator infrastructure: none
PSP codes: [none]
Grants: BMBF (GREWIS 02NUK017A and 02NUK17D)
Strategic university co-operation with: none

 DOI:10.15120/GR-2018-1

Exposition of a mechanical lung model to radon gas

A. Maier[1], J. Jones[1,2], H. Schmidt-Böcking[2], G. Kraft[1], C. Fournier[1]

[1]GSI, Darmstadt, Germany; [2]Goethe Universität Frankfurt a. M., Germany

Introduction

The radioactive noble gas radon is used for the therapy of inflammatory diseases but is also associated with an increased risk for lung cancer [1]. To better quantify the risk, the knowledge of the dose deposited in the lung is of great interest. The main contributors to the lung dose are the radon decay products, which can attach to aerosols (attached progenies). The formation of those aerosols is shown in fig. 1. In this work we want to analyse if there is a saturation effect of the attached progenies with increasing radon activity concentration.

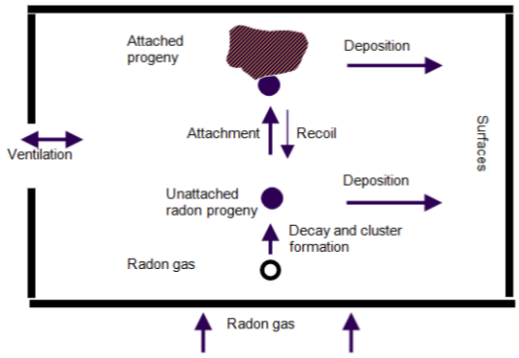


Fig. 1: Formation of radioactive aerosols

Material and Method

For the experiments a mechanical lung model was developed (see fig. 2) [3]. The radon progenies are deposited on a glas- wool filter inside a tube. A small pump regulates the air flow through the model, which is measured by a flowmeter. The tube is placed inside the smaller version of the radon chamber which allows radon activity concentrations up to some MBq/m³. The filters were exposed at various ^{222}Rn concentrations for one hour at a flowrate of around 200 ml/min.

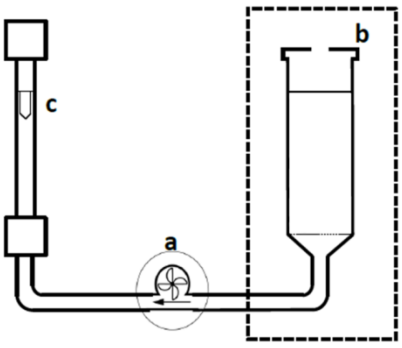


Figure 2: Schematic drawing of the mechanical lung model with the glass wool filter for the radon progenies (in b), a small pump (a) and a flowmeter (c). The airflow is generated from right to left.

After exposure the activities of the radon decay products ^{214}Pb and ^{214}Bi were measured by γ-spectroscopic measurements for around two hours and the results plotted in a semi logarithmic scale. By adapting a linear fit to the data points, the initial activities of those isotopes could be determined by the intersection with the y-axis.

Result

In fig. 3 we plotted the initial activity of the adsorbed radon progeny on the filter over the radon activity concentration during exposure. From these results, there seem to be no saturation effect even at high radon activity concentrations of up to 6 MBq/m³.

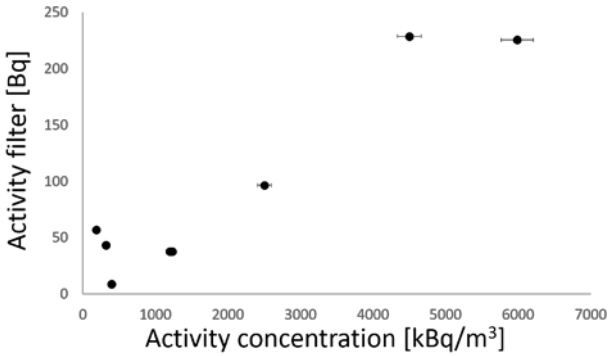


Fig. 3: Activity of adsorbed radon progenies on the filter with increasing activity concentration inside the radon chamber [4].

Outlook

For future experiments, more data are needed to confirm the obtained results. Additionally, the variation of other parameters like aerosol concentration or size distribution must be investigated to get a general idea of the deposition mechanism of aerosols in the lung. Moreover, a more anatomical correct lung model will be constructed.

References

[1] S. Darby et al. Residential radon and lung cancer – detailed results of a collaborative analysis of individual data on 7148 persons with lung cancer and 14208 persons without lung cancer from 13 epidemiologic studies in Europe, Scand. J. Work Environ. Health, 32, 1-84, 2006

[2] Committee on Health Risks of Exposure to Radon, National Research Council, Health Effects of Exposure to Radon (BEIR VI), National Academy Press, 1999

[3] S. Sternkopf, Dosisbeitrag von Radonzerfallsprodukten in der Lunge, Bachelor Thesis, Goethe University, Frankfurt, 2016

[4] J. Jones, Exposition of a mechanical lung model to high concentration radon gas, Bachelor Thesis, Goethe University, Frankfurt, 2018

Experiment beamline: none
Experiment collaboration: APPA-BIOMAT
Experiment proposal: none
Accelerator infrastructure: none
PSP codes: none
Grants: Work is supported by BMBF project funding reference number 02NUK050A
Strategic university co-operation with: Goethe Universität Frankfurt am Main

 DOI:10.15120/GR-2018-1

Characterisation of a psoriasis model system using cells grown on plasma treated boPET-foil

J. Wiedemann[1], V. Grünebaum[1], A. Maier[1], M. Dornhecker[1], C. Fournier [1,2]

[1]GSI, Darmstadt, Germany; [2]Hochschule Darmstadt, Germany

Introduction

Psoriasis is a common chronic inflammatory skin disease [1] which is on the indication list for therapy in galleries where patients are exposed to the α-particle emitter radon [2]. It is characterized by red plaques with white scales at elbows, knees and scalp. This phenotype is caused by an overshooting and persisting activation of the immune system, mainly driven by an amplifying feedback loop due to IL-17, IL-22 and IFN-γ release [3, 4].

As the access to skin biopsies from psoriasis patients and patients treated in radon galleries is limited, we established a psoriasis model system based on monolayer keratinocytes induced with cytokines. In order to allow irradiation with α-particles, the cells have to be cultured on a special plasma treated boPET-foil, which allows attachment and proliferation of the cells and α-particle penetration. To exclude inflammatory effects due to the cultivation on the foil we compare here the expression of psoriasis-relevant markers by induced and non-induced keratinocytes cultured in cell culture dishes and on boPET-foil.

Material and Methods

NHEK (normal human epidermal keratinocytes) were cultured under standard conditions and treated with IL-17 (200 ng/ml), IL-22 (20 ng/ml) and TNF-α (10 ng/ml) in petri dishes or on plasma treated boPET-foil in special stainless steel rings fitting into the irradiation setup. Supernatants were collected 24 hours after cytokine treatment and mRNA extraction was performed. A gene expression study was conducted to show specific psoriatic marker and cytokines in the supernatant were measured with ELISA.

Results

Results of qPCR analysis (figure 1) show a significant enhancement of the psoriasis-relevant markers IL-19 and ß-defensin (BDEF2) after the treatment with the cytokine combination. This shows the onset of the characteristic pathologic feedback mechanism in psoriasis. No significant differences between the cells cultured on the boPET foil compared to cell culture dishes were observed.

ELISA measurements of the inflammatory cytokine IL-6 show a clear induction after cytokine treatment (figure 2). The basal expression level in the controls is slightly higher in cells cultured on boPET foil but compared to the IL-6 release of induced NHEK still very low.

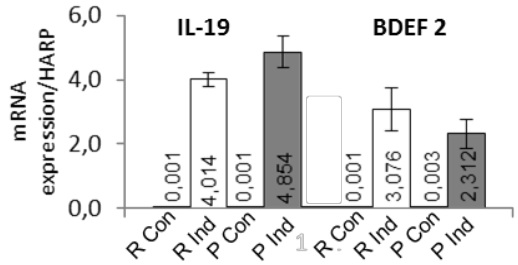


Figure 1: qPCR measurements of induced and non- induced cells grown in cell culture dishes (P) or on boPET foil(R)

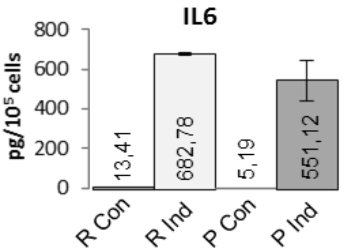


Figure 2: Cytokine measurements in supernatants of induced and non-induced cells grown in cell culture dishes (P) or on boPET foil(R)

Conclusion

The results shown here demonstrate that the culture of NHEK cells on the plasma-treated boPET foil is not inducing any inflammatory reactions by itself. The induction of a psoriasis-like phenotype is comparable to the induction observed in cell culture dishes. This shows that the psoriatic model system cultured on the boPET-foil can be used in future for irradiation experiments with alpha irradiation.

References

[1] Lowes MA, Bowcock AM, Krueger JG; Nature (2007); doi:10.1038/nature05663

[2] Gasteiner Kur- Reha- und Heilstollen Betriebsges.m.b.H. www.gasteiner-heilstollen.com

[3] Johnson-Huang LM, Lowes MA, Krueger JG; (2012); Dis Model Mech; doi:10.1242/dmm.009092

[4] Kim, J. & Krueger, J. (2016), Annu Rev Med., pp. 255 – 269; doi: 10.1146/annurev-med-042915-103905

Experiment beamline: none
Experiment collaboration: APPA-BIOMAT
Experiment proposal: [e.g. S339] none
Accelerator infrastructure: none
PSP codes: none

Grants: Forschungsinstitut Bad Gastein (FOI-15/08-031WIE), EURADON, the Radon Gallery of Bad Gastein and GREWIS (02NUK017A)
Strategic university co-operation with: none]

Influence of the LET distribution on the reliability of the dose-averaged LET as predictor for relative biological effectiveness

R. Grün[1], T. Friedrich[1] and M. Scholz[1]

[1]GSI, Darmstadt, Germany

Introduction

The dose-averaged linear energy transfer (LET_D) is frequently used as first order surrogate for the relative biological effectiveness (RBE) of a radiation type [1, 2]. In the case of a non-linear RBE(LET)-relationship under track segment condition we observe deviations in the RBE calculated directly from the LET distribution at a given point in a mixed radiation field compared to the RBE for the LET_D value of the exact same distribution. The following equations will explain the observed deviations and further demonstrate why the RBEMix is sometimes higher than the RBE based on a LET_D reference value and sometimes lower.

Methods & Results

LETD at position z in the radiation field is defined by

$$\overline{LET_D}(z)=\frac{\sum_i \int LET_i^2(E)\cdot\Phi_i(E,z)\,dE}{\sum_i \int LET_i(E)\cdot\Phi_i(E,z)\,dE}=\frac{\sum_i \int LET_i(E)\cdot D_i(E,z)\,dE}{\sum_i \int D_i(E,z)\,dE}$$

with dose is $D = C * LET \cdot \phi$ where ϕ describes the particle fluence and C is used for unit conversion. The non-linear RBE(LET) relationship under track segment conditions shall be defined by

$$RBE_\alpha = c_0 + c_1 \cdot LET + c_2 \cdot LET^2$$

with the constant coefficientsc_0, c_1 and c_2. If LET_D of the distribution is used as reference for the RBE calculation, the RBEα of a mixed radiation field is thus calculated with:

$$RBE_{\alpha,Ref}(LET_D) = c_0 + c_1 \cdot LET_D + c_2 \cdot {LET_D}^2$$

However, the proper way to calculate RBE_α is to use the underlying LET distribution with

$$\begin{aligned} RBE_{\alpha,\mathrm{Mix}} &= \frac{\sum_i RBE_{\alpha i}\cdot D_i}{\sum_i D_i} = \frac{\sum_i (c_0+c_1\cdot LET_i+c_2\cdot {LET_i}^2)\cdot D_i}{\sum_i D_i} \\ &= c_0 + c_1 \cdot LET_D + c_2 \cdot \frac{\sum_i {LET_i}^2\cdot D_i}{\sum_i D_i} \\ &= c_0 + c_1 \cdot LET_D + c_2 \cdot \frac{\sum_i {LET_i}^3\cdot \phi_i}{\sum_i LET_i\cdot \phi_i} \end{aligned}$$

Comparing the two terms we get:

$$RBE_{\alpha,\mathrm{Ref}} - RBE_{\alpha,\mathrm{Mix}} = c_2 \cdot \left({LET_D}^2 - \frac{\sum_i {LET_i}^3\cdot\phi}{\sum_i LET_i\cdot\phi}\right)$$

As only parameter c2 appears in this equation, it becomes clear that the non-linear component of the $RBE_{\mathrm{Ref}}(LET_D)$-dependence is responsible for the observed deviations.

Impact of the width of the underlying LET distribution

To simplify matters we assume a log-normal distribution of LET with parameters μ and σ

$$\phi(LET) = \frac{1}{\sigma LET\sqrt{2\pi}} e^{-\frac{1}{2}\left(\frac{\log(LET)-\mu}{\sigma}\right)^2}.$$

The dose-mean LET is then given by

$$LET_D = \frac{\int_{-\infty}^{\infty} LET^2\cdot\phi(LET)\,\mathrm{d}LET}{\int_{-\infty}^{\infty} LET\cdot\phi(LET)\,\mathrm{d}LET} = e^{\mu+\frac{3}{2}\sigma^2} = \overline{LET} + \frac{V}{\overline{LET}}$$

with variance V and the mean $\overline{LET}$ of the distribution.

The corresponding RBE for the mixed field is obtained as

$$\begin{aligned} RBE_{\alpha,\mathrm{Mix}} &= \frac{\int_{-\infty}^{\infty} RBE_\alpha(LET)\cdot LET\cdot\phi(LET)\,\mathrm{d}LET}{\int_{-\infty}^{\infty} LET\cdot\phi(LET)\,\mathrm{d}LET} \\ &= \frac{\int_{-\infty}^{\infty} (c_0+c_1\cdot LET+c_2\cdot LET^2)\cdot LET\cdot\phi(LET)\,\mathrm{d}LET}{\int_{-\infty}^{\infty} LET\cdot\phi(LET)\,\mathrm{d}LET} \\ &= c_0 + c_1 LET_D + c_2\overline{LET}^2\left(1+\frac{V}{\overline{LET}^2}\right)^3 \end{aligned}$$

Comparing the two terms we get:

$$\begin{aligned} &RBE_{\alpha,Ref}(LET_D) - RBE_{\alpha,Mix} \\ &\quad = c_2\cdot {LET_D}^2 - c_2\overline{LET}^2\left(1+\frac{V}{\overline{LET}^2}\right)^3 \\ &\quad = -c_2 V\left(1+\frac{V}{\overline{LET}^2}\right)^2 \end{aligned}$$

This result reflects that both the curvature of the monoenergetic RBE(LET) relationship as well as the width of the LET distribution lead to a deviation between the correct, mixed RBE and the surrogate obtained by employing the LET_D.

Conclusion

The equations demonstrated that LET_D can be used as predictor for RBE if and only if a linear relationship for RBE and LET under track segment conditions holds true. Since the linear nature of this relationship is questionable LET_D is a sufficiently accurate predictor for RBE only in regions with comparably narrow LET distribution, but not in regions with broad LET distribution as e.g. in the spread out Bragg peak. The deviations are caused by the non-linearity of the RBE(LET)-relationship in the case of track-segment conditions. Thus, generally, LET_D is not an adequate predictor for RBE.

References

[1] A. McNamara et al., Phys Med Biol (2015)
[2] R. Grün et al., Phys Med Biol (2017)

 DOI:10.15120/GR-2018-1

Towards modelling secondary cancer induction with the local effect model

A. Hufnagl[1,2], T. Friedrich[1] and M. Scholz[1]

[1]GSI, Darmstadt, Germany; [2] TU Darmstadt, Germany

Introduction

Neoplastic cell transformation arises from genetic mutations and is characterized amongst others by cell growth that is not contact inhibited by surrounding cells and does not need to be attached to a solid surface. Neoplastic cells may attain the ability to keep dividing indefinitely and thereby become a tumor cell. Genetic mutations can be induced by ionizing radiation. The probability of an initial mutation which leads to transformation scales with the absorbed dose of the radiation.

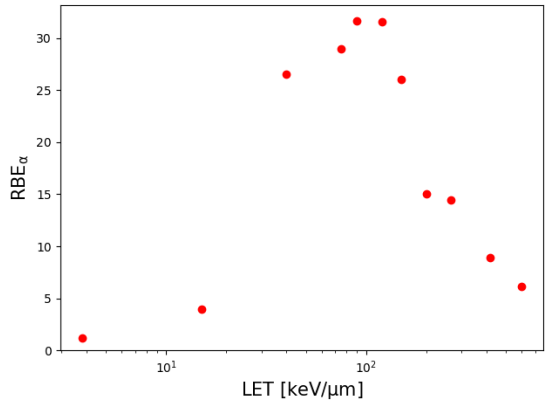


Figure 1: Simulation of RBE□ for transformants per survivor for different LET values and different ions from Miller et al. [2].

Modelling neoplastic cell transformation

To model neoplastic cell transformation we make use of the local effect model (LEM), which has been shown to be able to simulate cell survival [1]. This computational model derives the response of a cell to ion radiation from the response to photon radiation. The assumption is that equal local doses, and especially equal local damage complexities, should lead to equal local effects.

We assume that cell transformation and cell survival are not independent processes. It is impossible to measure cell transformation without the influence of cell survival. Only cells that survive can become transformed. Therefore the number of observable transformed cells per surviving cell is used to illustrate cell transformation in vitro. Since the basic assumptions are the same, namely genetic mutations, we can use the same mechanism we used for simulating cell survival. However, LEM simulates only cell transformation or cell survival, so in order to simulate the number of transformants per survivor some we use the following equation:

$$TperS(D) = \frac{\sum_k p\,(k,D) S_k T_k}{\sum_k p\,(k,D) S_k}$$

where p(k,D) is the poisson distribution for k hits and a given dose D, S_k is the survival after k hits and T_k is the transformation after k hits. TperS(D) is the dose-response curve for transformation per survival and gives us the LQ parameters α and β for transformation per survivor. With these we can calculate the RBE$_\alpha$ (see Figure 1).

Modelling tumor induction

Neoplastic cells become tumor cells which can lead to cancer. The radiation which is applied to the healthy tissue in radiotherapy can lead to secondary tumours. It is of great interest for treatment planning to get an estimation of how big this risk is and how it changes with radiation quality. The aim is to model the risks for secondary cancer after radiotherapy with the LEM and to assess whether carbon ion therapy could lead to a lower risk than proton or photon therapy.

Tumor induction can be written as T*S, where T is the probabilty of a cell becoming a tumor cell and S being the probability of a cell to survive. For lower doses T*S will increase with dose, since the survival is high for lower doses. For higher doses the survival becomes important and T*S decreases.

Outlook

The longterm goal of our work is to implement LEM based predictions of secondary cancer induction in the treatment planning environment TRiP in order to allow for treatment plan comparisons and the corresponding assessment of relative risks for different treatment scenarios, e.g. different ion beams etc.

References

[1] Scholz M, Kellerer A, Kraft-Weyrather W, and Kraft, G. (1997). Computation of cell survival in heavy ion beams for therapy. the model and its approximation. Radiat Environ Biophys, 36:59–66.

[2] Miller RC et al. (1995). The Biological Effectiveness of Radon-Progeny Alpha Particles. II. Oncogenic Transformation as a Function of Linear Energy Transfer. Radiation Research, 142:54-60.

Experiment beamline: none
Experiment collaboration: APPA-BIOMAT
PSP codes: none
Grants: DFG, GrK 1657
Strategic university co-operation with: Darmstadt

Effect enhancement induced by micrometer focused particle beams

T. Friedrich[1], *M. Scholz*[1]

[1]GSI, Darmstadt, Germany

It is well accepted in radiobiology that the key lesions by which radiation damage is inferred into cells and tissues are double strand breaks (DSB) to the DNA. However, it is also known that even DSB are repaired with high fidelity. There are experimental indications that composite damage like the clustering of DSB in close neighborhood may serve for an enhanced biological effect. The interaction range of DSB to form such more complex damage is on the order of a micrometer. Such clustering is included in the mathematical framework of the Local Effect Model (LEM) aiming to describe the effectiveness of ion radiation for any ion type and energy. Furthermore, recent experiments with microbeam focused ion spot irradiation of cells [1] impressively supported the underlying hypotheses [2]. Here we investigate the dependence of the ion effects on the average distance of DSB induced to cells.

DSB interaction in the Local Effect Model

The LEM employs the concept of chromatin loop domains in which DSB can accumulate. While a single DSB within can be repaired quite effectively, more than one DSB represent a more harmful lesion [3]. Considering a typical DNA length segment of 2 Mbp per chromatin loop a physical size of about half a micrometer can be estimated for typical cell nuclear sizes. For nuclei with 500 μm^3 an interaction length of 0.54 µm is used.

The LEM had been adapted before to describe the effect ions focused to Gaussian beam spots [4]. Such spot foster the concentration of DSB within chromatin loops, hence leading to an enhanced effect. Using this model adaption the effect in spot irradiated cells could be adequately described [2]. While in these experiments the mutual distance between ions was varied by means of particle number, a complementary question is how the effect varies with changing spot size.

DSB induction for high energetic ions

The most interesting case to study the effect of varying spot size is for ions with a sufficiently large kinetic energy so that the physical interaction with the biological target and thus the linear energy transfer (LET) is low. In that case one expects that per track hitting the cell nucleus on average much less than one DSB is induced. We study this scenario here at hand of model cells with hypothetical photon dose response parameters (see Fig. 1) which are used as model input.

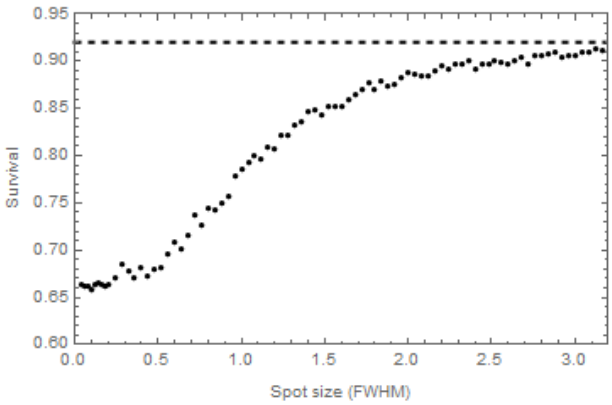


Figure 1: Cell survival plotted after irradiation of cells irradiated with Gaussian beam spots consisting of 100 protons with 20 MeV kinetic energy. The photon dose response parameters of the hypothetic cells have been chosen as $\alpha = 0.1\ Gy^{-1}$, $\beta = 0.05\ Gy^{-2}$ and Dt = 8 Gy. The DSB interaction is allowed within chromatin loops of 0.54 µm size. The dashed line shows the limit survival for random irradiation with on average 100 protons.

In Fig. 1 a clear predicted effect increase with decreasing spot size is predicted. The steepest gradient of effect change with spot size is found at roughly the double of the interaction range. For faint spots smaller than the interaction range, survival saturates. Roughly, simply by focusing protons to spots the survival can be reduced by a factor of 2. The quantitative understanding of this tremendous effect as predicted by LEM is of importance: The density of particles hitting the nuclei is increased also with dose, thus facilitating DSB interaction as well. Hence the considered spot irradiation is a key tool to also understand the entire dose response characteristics as predicted in [5]. Based on these preliminary considerations now dedicated experiments are under way.

Grants: This work was funded by the German Ministry of Education and Research within research grant 02NUK031D.

References

[1] C. Greubel et al., Nucl. Instr. Meth. Phys. Res. B. 404, 155 (2017).
[2] T. Friedrich et al., submitted to Scientific Reports (2018).
[3] Elsässer et al., IJROBP 78, 177 (2010).
[4] T. Friedrich, M. Scholz, GSI Scientific Report 2015
[5] T. Friedrich, Radiat. Res. 178, 385 (2012).

 DOI:10.15120/GR-2018-1

Physical dose enhancement by Au nanoparticles under ion beam irradiation

M.C. Fuss[1], D. Boscolo[1], E. Scifoni[1,2], and M. Krämer[1]

[1]GSI, Darmstadt, Germany; [2]TIFPA-INFN, Trento, Italy

High-Z nanoparticles (NPs) are under discussion for use as localized dose enhancers in radiotherapeutic applications. Effective radioenhancement has been shown for photon beams, whereas the sensitization effect for ion irradiation is under investigation more recently [1]. Here we investigate the physical dose enhancement produced in the vicinity of Au NPs.

The present simulations are carried out with TRAX [2], a track structure Monte Carlo simulation for charged particles. The simulated geometry is a cylindrical water volume (2 µm long, radius 1µm) including one Au NP in the centre and being penetrated along the central axis with protons, carbon and oxygen ions at clinically relevant energies. Interaction processes include: ionization, electronic excitation, Auger electron emission, volume plasmon excitation (for gold), subelectronic excitations (for water), and elastic electron scattering.

The resulting 2D dose distributions reveal a highly local, slightly forward-oriented additional dose due to the presence of the NP. For protons, C and O with energies ranging from 19 to 204 MeV/u, the dose enhancement factor (DEF) reaches a maximum value between 1.9 and 4.6, depending on the NP size. Smaller NPs enhance the high-dose region at the NP surface, whereas larger NPs act upon a larger lower-dose volume. In fact, for NP sizes in excess of a few nm (radius), partial reabsorption of the additional secondary electrons is found. No enhancement is observed for the most frequent scenario where an ion passes closely but does not directly traverse the NP.

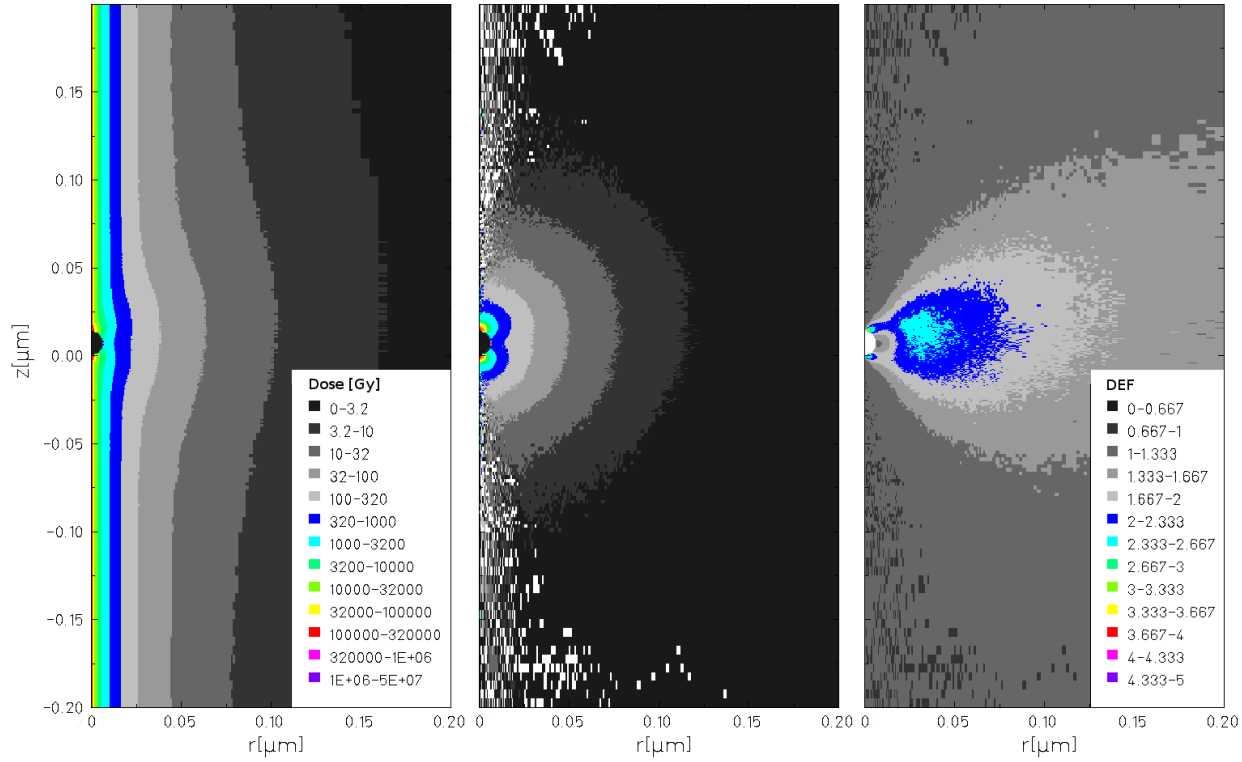


Figure 1: Dose distribution around a 7 nm (radius) Au NP hit by a C ion at 44 MeV/u. Left panel: absolute dose distribution, centre: net NP dose, right panel: ratio between doses deposited in presence of / without a Au NP in the water volume (DEF).

References

[1] S. Lacombe, E. Porcel and E. Scifoni, Cancer Nanotechnology 8 (2017) 9.

[2] C. Wälzlein, E. Scifoni, M. Krämer and M. Durante, Phys. Med. Biol. 59 (2014) 1441.

Experiment beamline: none
Experiment collaboration: APPA-BIOMAT
Experiment proposal: none
Accelerator infrastructure: none
PSP codes: none
Grants: EU FP7 grant agreement No. 608163
Strategic university co-operation with: none

Contribution of dissolved molecular oxygen to the chemical ion track evolution

D. Boscolo[1], M. Krämer[1], M.C.Fuss[1], M.Durante[2], E.Scifoni[2]

[1]GSI, Darmstadt, Germany; 2TIFPA, Trento, Italy.

The effect of radiation on well oxygenated tissues results to be up to three times larger than under respective hypoxic conditions. On the microscopic scale, this effect is assumed to be related to the indirect effect of radiation and, thus, to the action of radical species [1].

In order to study this effect, the TRAX-CHEM code [2] has been extended, and is now able to handle the interactions of a particle chemical track with the molecular oxygen, O_2, dissolved in the water target.

O_2 is a strong scavenger for e_{aq}^- and $H^\bullet$ radical and, when scavenging occurs, the interaction leads to the production of the two highly toxic species: superoxide anion O_2^- and its protonated form HO_2, which are both supposed to have a role in the oxygenation effect [3].

The impact of the oxygenation level on the temporal evolution of the radical yield is shown in figure 1 for a 500 keV electron radiation impinging on a water target with an atmospheric oxygen pressure at the surface of the 0% and 21%. The effect of intermediate oxygenation levels in the final yield of the different radical species is, instead, shown in figure 2.

With the increase of the LET, the particle track becomes denser increasing the probability of radical recombination. This will reduce the interactions with the O_2 dissolved in the water target and leads to a decreased yield of the two toxic species O_2^- and HO_2. The yield as a function of the LET for e_{aq}^- and O_2^- is shown for a partial oxygen pressure of 0% and 21% in figure 3.

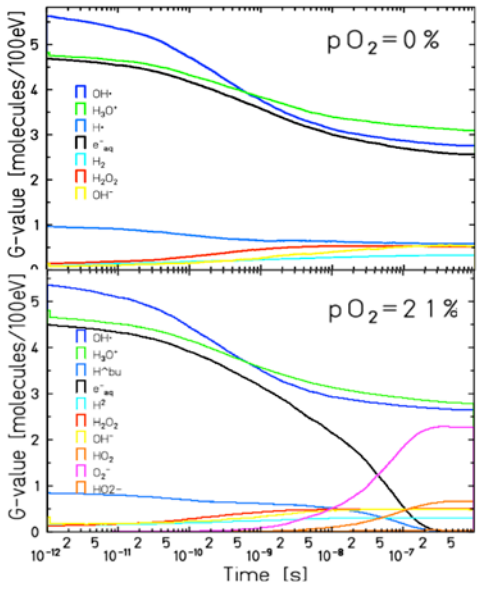


Figure1: Time-dependent yield of the chemical species generated by 500 keV electrons in an anoxic water target (upper panel) and in an oxygenated water target (lower panel).

The decreased yield of production of O_2^- and HO_2 is consistent with the LET dependence of the oxygen effect on the macroscopic level. This observation seems to confirm the hypothesis of a direct involvement of the O_2^- and HO_2 in the increased radioresistance of hypoxic tissues.

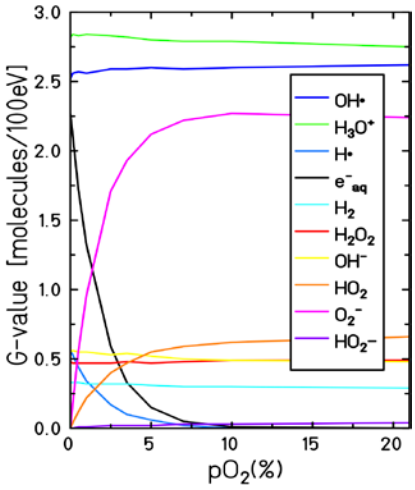


Figure 2: Radiolytic yields, at 1 µs, for all the chemical species generated by 500 keV electron irradiation at different oxygen concentrations.

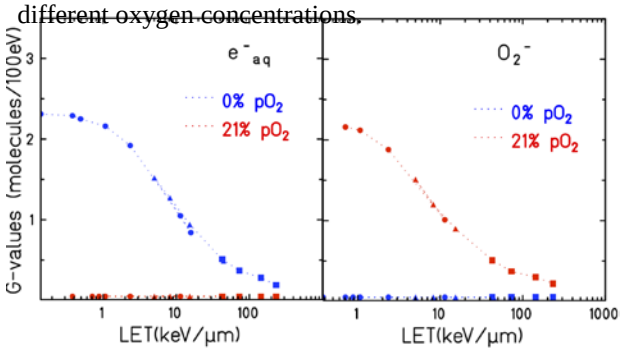


Figure 3: Radiolytic yields for e_{aq}^-, $H^\bullet$, O_2^- and HO_2 in hypoxic (blue curves) and oxygenated (red curves) conditions, as a function of the LET.

References

[1] W.Tinganelli et al,Sci. Rep. (2005)
[2] D.Boscolo et al. Chem. Phys. Lett. (2018)
[3] M.Beuve, M., J. Phys. Conf. Ser. (2015)

Experiment beamline: none
Experiment collaboration: APPA-BIOMAT
Experiment proposal: none
Accelerator infrastructure: none
PSP codes: none
Grants: EU FP7 grant agreement No. 608163
Strategic university co-operation with: none

 DOI:10.15120/GR-2018-1

Towards a Space-TRiP: a space radiation version of the TRiP98 code

M. Krämer[1], E. Scifoni[2], M. Giraudo[3], and M. Durante[2]

[1]GSI, Darmstadt, Germany; [2]TIFPA-INFN, Trento, Italy; [3]Thales Alenia Space, Turin, Italy.

Introduction

TRiP98, the GSI in-house treatment planning system for particles [1] was suggested to be extended for space radiation protection studies already several years ago [2]. The main rationale was the advantage of its fully modular structure, its table driven design, the computational efficiency of an analytical code and last but not the least the possibility to include radiobiological effects for risk studies. The task was started in the context of the ESA ROSSINI-2 project.

Methods

The code was modified in order to allow radiation shielding tests with different radiation sources and materials. For that, the internal transport code of TRiP98, normally used for beam model generation in particle therapy, was extended to handle different materials as well as compound multi-layers of them. Preliminary results were presented in the previous GSI report [3]. Since then, the transport model and associated cross sections were improved to yield reasonable agreement with both experimental data [4] and other simulations with Monte Carlo codes.

Results

We report preliminary results for the shielding of Solar Particle Event (SPE) proton spectra in tables 1 and 2. Full results are available in Ref. [5].

Material	Aeric Density (g/cm^2)	Dose deposited (MeV) TRiP98	Dose deposited (MeV) PHITS	DR (%) TRiP98	DR (%) PHITS
No Target	0	1.40	1.27	100	100
Water	3.49	0.039	0.036	97.21	97.18
PMMA	3.57	0.037	0.036	97.33	97.19
LiH	5.82	0.017	0.018	98.79	98.60
Alu2024	8.47	0.016	0.015	98.86	98.83

Table 1: Comparison of TRiP98 and PHITS for dose deposited in 2cm thick detectors and dose reduction (DR) with different shielding of an ESP spectrum.

Material	Aeric Density (g/cm^2)	Dose deposited (MeV) TRiP98	Dose deposited (MeV) PHITS	DR (%) TRiP98	DR (%) PHITS
No Target	0	15.6	15.9	100	100
Water	3.49	1.60	1.66	89.74	89.57
PMMA	3.57	1.62	1.65	89.62	89.62
LiH	5.82	0.80	0.87	94.87	94.52
Alu2024	8.47	0.74	0.75	95.26	95.28

Table 2: Comparison of TRiP98 and PHITS for dose deposited in 2cm thick detectors and dose reduction (DR) with different shielding of a “worst hour” spectrum.

Summary and Outlook

TRiP98 can efficiently be used for radiation shielding analysis in different materials for both monochromatic and spectral radiation sources with an accuracy comparable to MC codes. This encourages further extensions towards the higher energies found in Galactic Cosmic Ray regime.

References

[1] M. Krämer and M. Durante, Ion beam transport calculations and treatment plans in particle therapy, Eur. Phys. J. D **60**, 195 (2010).

[2] M. Krämer, TRiP98 (TReatment PlannIng for Particles), THREE - Heal. Risk Extraterr. Explor. 2012, 1 (2012).

[3] M. Krämer et al., Space shielding simulations with TRiP98 for the ROSSINI-2 project, GSI Sci-Rep 2016, Research-APPA-Health-33, p. 331 (2017).

[4] U. Weber et al., Dose attenuation measurements in the ROSSINI-2 project for space research, GSI Sci-Rep 2015, Biophysics-46, p. 234 (2016).

[5] M. Krämer, et al., TRiP98 Simulations, ESA ROSSINI2 Technical Note (2017) accepted

Experiment beamline: none
Experiment collaboration: none
Experiment proposal: none
Accelerator infrastructure: none
PSP codes: none
Grants: ESA Contr. No.4000112525/14/NL/LF
Strategic university co-operation with: none

Applications for proton radiography in radiation oncology

M. Schanz[1], N. Peters[2], M. Kraemer[1]

[1]GSI, 64291 Darmstadt, Germany; [2]Oncoray, 01062 Dresden, Germany

Ion radiotherapy — as it was developed at GSI during the 1990s — requires exact knowledge of the patient geometry and tissue composition in order to create a treatment plan. It depends on the patient tissue's individual spatial stopping power distribution for the respective type of heavy ion used for the therapy. This is currently achieved by using X-ray CT scans, which, however, only reflect the attenuation properties of the target with regard to photon interactions. Therefore, a conversion into ion stopping power is mandatory, which is presently realised by using a Hounsfield Lookup Table (HLUT). This table is in turn calibrated against tissue samples and phantom materials with known geometry and properties prior to the actual patient scan. The overall accuracy of the HLUT obtained this way is about a few percent. In order to overcome the inherent uncertainties of the HLUT, several novel methods are currently investigated.

Recalibration of X-ray CT Data

One new approach is to use patient information gathered with the exact same type of particle – in this case protons – that is later used for the treatment procedure. Here we propose to use flash proton radiography, which can offer multiple advantages compared to other methods like single particle tracking such as fast data acquisition and even faster data processing.

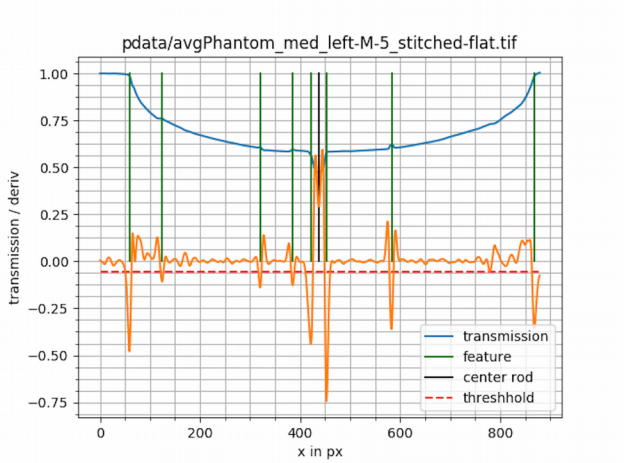


Figure 1: Example output of the feature detection software showing also the transmission profile of the investigated plastic phantom. The software detects the sides and the central orientation rod made from stainless steel inside the object and automatically selects the corresponding xCT projection. Additional detected features do improve the result.

Instead of using a conversion table, the spatial density distribution of the patient can be accessed directly. The transmission through the used imaging system can be described as a function of the scattering inside the target, thereby information on the material properties such as the radiation length X_0 and the nuclear collision length become available by using Moliere's theory and its approximations [1].

Flash proton radiography can be used to directly capture full CT scans of the object investigated, but – due to the complexity and size of the setup – currently requires the target object (i.e. a patient) to be rotated. Therefore one promising field of application is to use single images captured during the treatment process for a live verification of the target region. This can be essential especially for small or moving tumours, which can easily be visualized due to the superior spatial resolution capabilities in the micrometer range.

A different approach for obtaining data for treatment planning was newly developed at GSI in 2017 [2]. By using xCT base data instead which is then recalibrated by single proton images, the rotation of the object investigated can be completely omitted. This however requires a minimum of a least two independent proton images from different angles to take into account the convolution of several materials with different properties. In addition, it is not suitable to compensate for the errors of the initial X-ray measurement itself. In order to simplify the procedure for a proof of concept, only single projections of a plastic head phantom were captured for a recalibration attempt, resulting in a minor loss of accuracy of the density reconstruction due to the convolution of different materials. For the recalibration itself, the corresponding target images were overlapped resulting in a correlation between X-ray attenuation coefficients and proton transmission through the lens system. As multiple target images were recorded, the overlapping was performed with an algorithm searching for characteristic features such as the border of the 3 used insets in the target images (see Fig. 1). The calibration curve was then fitted using a spline and applied to the full dataset before reconstructing the relative densities with the transmission equation through the proton microscope. Having obtained now the areal density map the we were able to calculate a "pCT" in density values using the inverse Radon transformation.

Results and Discussion

Within the framework of the performed work the feasibility of recalibrating xCT base data using flash proton radiography was proven. However, in order to overcome the presently included convolution errors, more proton projections are needed for practical applications to achieve the best results for material compositions. Further experiments in the framework of this project are planned for 2019 using the new PRIOR-II setup for proton radiography at FAIR.

 DOI:10.15120/GR-2018-1

References

[1] B. Gottschalk et al., Nucl. Instr. and Meth. B, Vol. 74 (1993), p. 467-490
[2] N. Peters, "X-Ray CT Recalibration for Particle Therapy using 2D Flash Proton Radiography", Master Thesis (2017), Martin Luther University of Halle-Wittenberg

Experiment beamline: HHT (2019)
Experiment collaboration: APPA-BIOMAT
Experiment proposal: SBio_Krämer
Accelerator infrastructure: SIS18 / SIS100

Treatment planning studies with ^{16}O beams for hypoxic tumors

O. Sokol[1], A. Myronenko[2], E. Scifoni[3], S. Hild[3], M. Krämer[1]

[1]GSI, Darmstadt, Germany; [2]V. N. Karazin Kharkiv National University, Kharkiv, Ukraine;
[3]TIFPA Trento Institute for Fundamental Physics and Applications, Trento, Italy

According to the statistics provided by the Particle Therapy Cooperation Group [1], by the end of 2015 more than 150 000 patients received the treatment with ion beams. At the moment the facilities in operation offer the treatment only with protons and carbon ions. However, there is a growing interest in introducing other modalities into clinical practice. In particular, due to their increased LET ^{16}O ions are considered to be a good candidate for the treatment of hypoxic tumors. In [2] it has been revealed, that the damage to the cells in the entrance channel can be reduced when irradiating hypoxic tumors with ^{16}O beams rather than with lighter modalities.

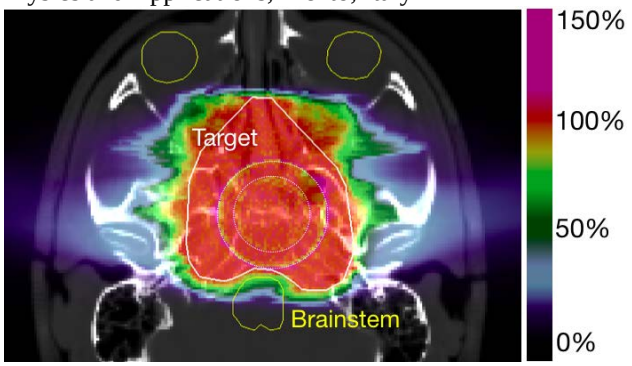
To proceed with more realistic studies, the TRiP98 treatment planning system was upgraded by adding the option of processing externally supplied oxygenation (hypoxia) maps, similar to the handling of CT data. A series of treatment planning studies, using the patient data from the GSI pilot project, was carried out.

An example is given in Fig. 1. A simulated partially hypoxic (24% of the total volume was assumed to have the oxygenation of 0.15% pO_2 and 16% was assumed to be anoxic) skull base chordoma was irradiated with two fields entering at 100 and -100 degrees, respectively. Using the kill-painting approach [3], the plan was optimized for a uniform RBE- and OER-weighted dose of 2 Gy. Apart from the damage to the residual tissue, the dose received by the brainstem, which was considered as an organ at risk, was analyzed. The X-ray response parameters were chosen as $\alpha = 0.003$ Gy^{-1}, $\beta = 0.0015$ Gy^{-2}, and transitional dose $D_t = 22$ Gy as in [4].

The resulting dose-volume histograms (DVHs) for the plans for normoxic (dashed lines) and hypoxic (solid lines) tumors for ^{1}H, ^{4}He, ^{12}C, and ^{16}O beams are given in Fig. 2. In both cases, the plan with ^{16}O results in a mean dose to the brainstem between the outcome of the ^{12}C and ^{4}He plans. However, for serial organs, a more crucial parameter can be the maximum received dose, indicating the presence of the 'hotspots', mainly in the proximity of the target. In the demonstrated case, for hypoxic target the lowest maximal dose, received by the brainstem, is observed for the ^{16}O plan. The corresponding hotspot has a ≈ 6% and ≈ 17% lower dose than those for ^{12}C and ^{4}He plans, respectively. This and the following studies involving other patient geometries, demonstrated the similar quality of treatment plans with ^{12}C and ^{16}O, however, in the latter case the maximal doses to the critical structures and the doses to the residual tissues are expected to be reduced when the tumors are highly hypoxic.

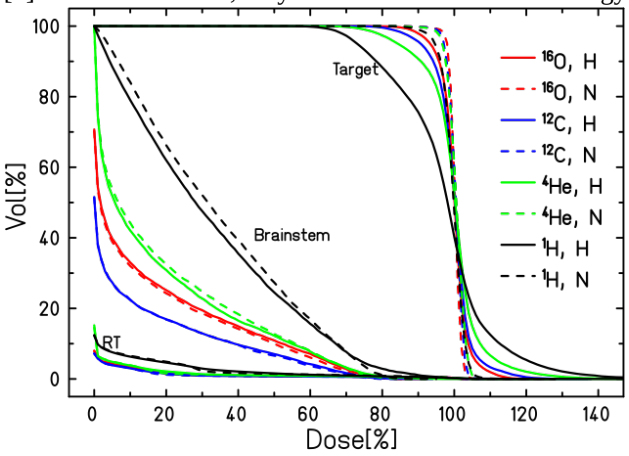
Figure 1. RBE- and OER-weighted dose distribution for a skull base chordoma. The dashed lines mark the borders of the hypoxic regions.

Figure 2. Resulting DVHs for the target, brainstem and residual tissue (RT) for the ^{1}H, ^{4}He, ^{12}C, and ^{16}O plans.



References

[1] Jermann, M., PTCOG (2016).
[2] O. Sokol et. al., Physics in Medicine and Biology 62(19) (2017)
[3] W. Tinganelli et. al., Scientific reports (2015).
[4] R. Grün et. al., Medical Physics 42(2) (2015) 1043-47.



Experiment beamline: none
Experiment collaboration: APPA-BIOMAT / other: MoVe IT
Experiment proposal: none
Accelerator infrastructure: none
PSP codes: [none]
Grants: []
Strategic university co-operation with: none

 DOI:10.15120/GR-2018-1

Robust treatment planning with 4D intensity modulated particle therapy for multiple targets in stage IV non-small cell lung cancer

M. Wolf [1], *K. Anderle*[1], *C. Graeff* [1]

[1]GSI, Darmstadt, Germany

Recently, we introduced a 4D IMPT optimization approach handling multiple targets and including all motion states of a 4DCT. This method was expanded by a robust non-linear biological optimizer for carbon ions – accounting for setup and range uncertainties – to explore its potential in improving plan robustness and sparing of critical organs in patients with stage IV non-small cell lung cancer.

Methods

The 4D IMPT method optimizes a treatment plan for all CTVs in all motion states of a 4DCT, i.e. during the optimization voxel from all affected target and OAR voxel in each motion phase are considered in the calculation. Slice by slice rescanning with up to 10 rescans is used for motion mitigation [1].

The implemented worst-case scenario method considers 9 different scenarios: nominal scenario, under- and overestimation of particle ranges (±3.5%) and isotropic shifts of patient's isocenter (±3 mm in the 6 major anatomical directions) [2].

Within the 4D IMPT optimization approach, robust IMPT on the CTV is compared to conventional IMPT with 3 mm isotropic margins. For each patient case, the two resulting plans are assessed by performing a robustness analysis consisting of 84 different 4D dose calculations (4 respiratory motions combined with 21 uncertainty scenarios).

The main focus of plan optimization is on meeting strict constraints for critical structures.

Results

Both optimization methods are compared in two lung cancer cases with multiple lesions in proximity to the smaller airways (SA) with a target dose of 1 x 24 Gy. By using robust IMPT the given constraints for SA could be fulfilled in 98.2% of all regarded cases compared to just 47.6% with conventional IMPT. This was enabled by a decrease in target coverage. For example D99 was reduced from 88.7±16.0% to 81.8±20.1% in average which decreased the critical dose constraint (D0.5cc) for SA from 102.3±10.7% to 85.7±7.6%. Additionally, the D50 spread could be reduced from 3.8 to 1.0 Gy in average. Especially for P1 this means a significant reduction of the uncertainty band in the areas of the D50 value (compare Fig. 1 (a) and (b)).

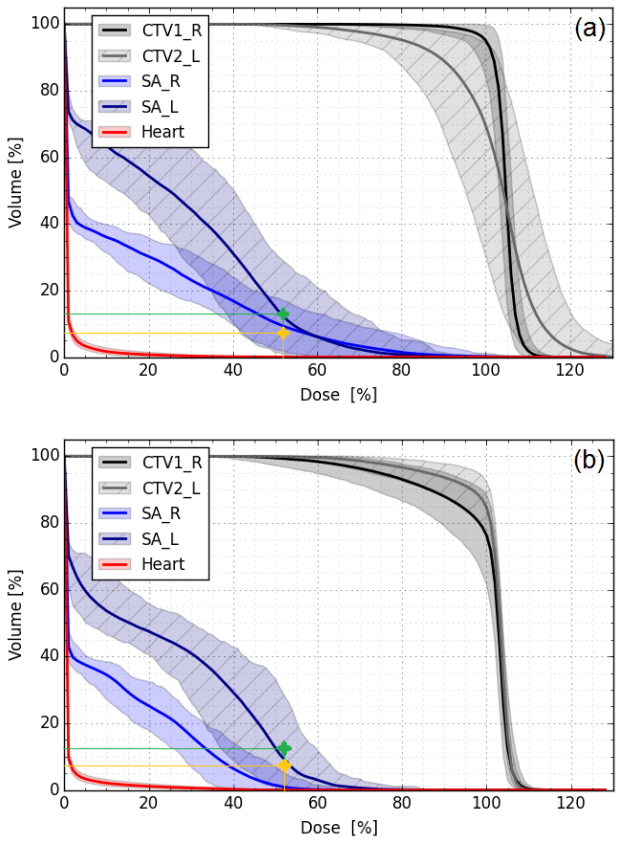


Figure 1: DVH with uncertainty bands for P1 with conventional IMPT (a) and robust IMPT (b). The green points indicate the dose volume constraint for SA left the orange ones for SA right.

Conclusion

The study showed that by using robust optimization in 4D IMPT plan robustness could be significantly improved, especially for critical structures. However, focusing on improved OAR sparing implicates a decrease in target coverage in the majority of the regarded uncertainty scenarios.

References

[1] K. Anderle et al., "Treatment planning with intensity modulated particle therapy for multiple targets in stage IV non-small cell lung cancer", Phys. Med. Biol. 63(2), 2018

[2] W. Liu et al., "Robust optimization of intensity modulated proton therapy", Phys. Med. 39(2), 2012

Experiment beamline: none
Experiment collaboration: APPA-BIOMAT
Accelerator infrastructure: none
Strategic university co-operation with: none

Measurement of cross section data relevant for PET range verification in proton therapy.

F. Horst[1,2], C. Schuy[1], M. Rovituso[3], W. Adi[4], L. Nies[4], H.-G. Zaunick[4], K.-T. Brinkmann[4], K. Zink[2,5,6], U.Weber[1]

[1]GSI, Darmstadt, Germany; [2]THM, IMPS, Gießen, Germany; [3]INFN-TIFPA, Trento, Italy; [4]JLU, II. Phys. Inst., Gießen, Germany; [5]UKGM, Klinik f. Strahlentherapie, Marburg, Germany; [6]FIAS, Frankfurt, Germany

Introduction

The analysis of PET activation distribution induced by the therapeutic beam is an established technique for in-vivo range verification in proton and heavy ion therapy [1]. For this method, the distribution of the positron emitters within the irradiated tissue needs to be calculated for each individual treatment plan. Such transport calculations require a precise knowledge of the underlying nuclear reactions, i.e. the production cross sections for the isotopes of interest (mainly ^{10}C, ^{11}C and ^{15}O).

Methods and Materials

A detector system (Fig. 1) to measure such cross sections, consisting of three BaF_2 scintillators for the detection of the 511 keV annihilation photons in coincidence, was developed and characterized. A short proton or heavy ion pulse impinges on a target (e.g. graphite or beryllium oxide) and activates the material. Two scintillators measure the rate of 511 keV photons emitted in 180° and the third scintillator is used to measure the random coincidence rate. The initial activities of the generated isotopes (^{10}C, ^{11}C, ^{15}O) can be obtained by fitting the measured decay curve with a superposition of multiple exponential functions with different half-lives corresponding to the different isotopes. Finally, the production cross sections can be calculated from these initial activities.

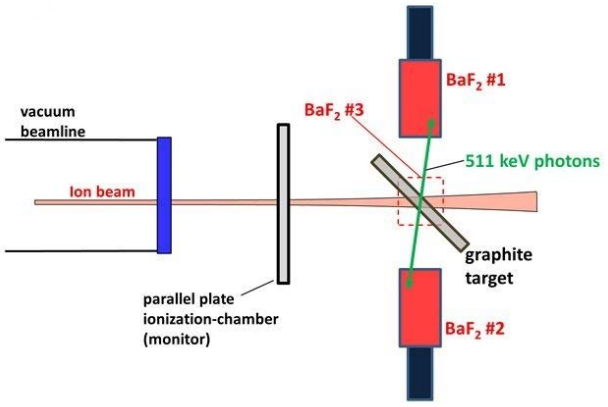


Figure 1: Experimental setup applied in Trento. Two BaF_2 scintillators in 180° measures the decay rate of the generated positron emitting target fragments and a third in 90° is used to monitor the random coincidence rate. An ionization chamber measures the number of primary ions.

The developed setup was used in a first experiment with protons conducted at the Trento proton therapy center (Italy) to measure ^{12}C(p,pn)^{11}C- und ^{12}C(p,p2n)^{10}C cross sections in the energy range 50 – 230 MeV.

Results and Discussion

The obtained cross sections are in good agreement with literature data and complement them well.
As a result of the variation of the beam spot size for different energies, the detection efficiency of the setup for 511 keV photons had to be calculated for each individual proton energy.
Possible improvements include the suppression of the data acquisition system during the time when the beam is on as well as using a more precise beam monitor.

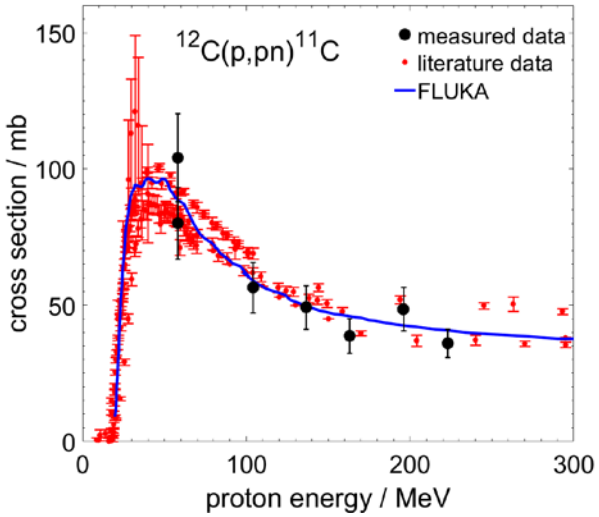


Figure 2: Preliminary experimental cross sections obtained at the proton experiment conducted at Trento in comparison with data from the literature [2] and with the prediction by the Monte Carlo code FLUKA [3].

The use of beryllium oxide targets will allow the measurement of PET isotope production cross sections on oxygen targets since nuclear reactions on beryllium do not generate any positron emitting target fragments. Moreover, experiments with heavier projectiles where the data are more sparse than for protons (e.g. ^{4}He and ^{12}C) are planned.

References

[1] W. Enghardt et al. “Positron emission tomography for quality assurance of cancer therapy with light ion beams”, Nuclear Physics A 654 (1999).
[2] Experimental Nuclear Reaction Database (EXFOR), URL: https://www-nds.iaea.org/exfor/
[3] G. Battistoni et al., “The FLUKA Code: An Accurate Simulation Tool for Particle Therapy”, Frontiers in Oncology 6 (2016).

 DOI:10.15120/GR-2018-1

Experiment collaboration: APPA-BIOMAT
Strategic university co-operation with: Gießen

Beam profile measurements with the MIMOSA28 pixel detector

C.-A. Reidel[1,2], C. Schuy[1], Ch. Finck[2] and U. Weber[1,]

[1]GSI, Darmstadt, Germany; [2]IPHC, Strasbourg, France

Introduction

Nuclear physics experiments with low particle rates of typ. 10^3-10^4 particles/s often require the precise information of the beam position, the beam width and its angular distribution (after a target). The MIMOSA28 sensor [1] was tested for this purpose at the Proton Therapy Center in Trento. This vertex detector can reach a spatial resolution < 5µm. In order to reach this resolution, an alignment procedure has to be done beforehand. A new alignment algorithm with the minimization of a complex least square function based on a linear regression analysis has been developed and implemented in the QAPIVI software [2] data analysis.

Experiment description

A total of 6 sensors were placed along the beam axis in the region of interest without a target in front (Figure 1). The proton beam energy was in the range of 80-220 MeV.



Figure 1: Setup for the beam profile experiment with 6 sensors placed along the beam axis.

Results

The beam profiles were computed by projecting the cluster map of the sensors in x and y directions (Figure 2).

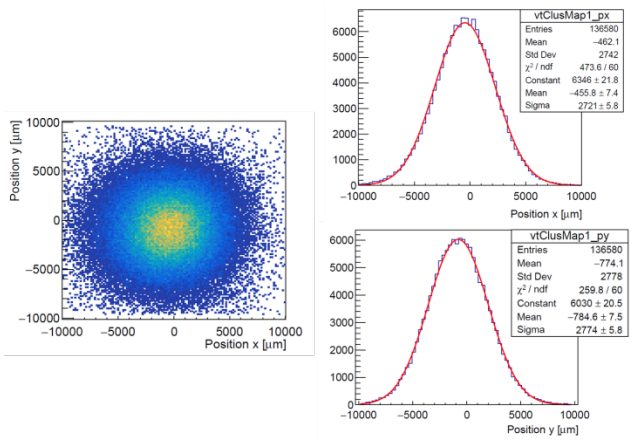


Figure 2: Cluster map of the first sensor and its projection in x (top right) and y (bottom right) for 220 MeV protons.

The alignment procedure was done for each run and has shown a good robustness. In Figure 3, the position of the center-of-mass of the beam profile in y is shown before and after the alignment procedure.

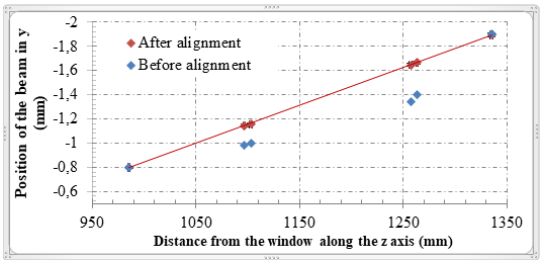


Figure 3: Center-of-mass of the beam profile in x along the beam axis before (blue diamond) and after (red diamond) the alignment procedure for 220 MeV protons.

Thus, the beam width at different positions from the vacuum window is measured as the half-width of the fitted Gaussian profile for each sensor. The evolution of the beam envelope is calculated in parallel by a deterministic transportation code based on multiple coulomb scattering defined by the Highland formula (Figure 4). The ion optical parameters of the beam (initial angular distribution, initial width beam focussing, etc.) can be extracted from the measured points and give valuable information for the analysis of the experiment (e.g. for MC benchmarking).

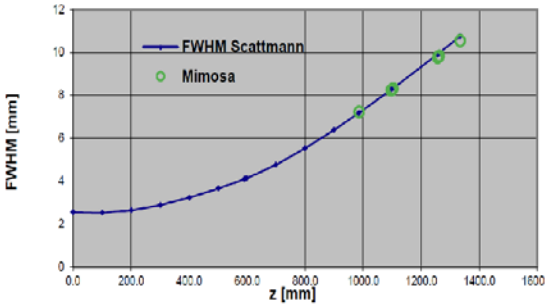


Figure 4: Measured beam width (FWHM) with the MIMOSA28 sensor fitted with Scattmann for 220 MeV protons.

Conclusion

The new alignment algorithm has shown promising results better than with the standard algorithm originally implemented in the analysis software. The MIMOSA28 sensor allows a precise measurement of the profile of low intensity proton beams. By fitting the measured profile data with a simulated beam envelope for the used setup, the ion optical parameters of the beam (as beam divergence or focussing) from the beam line can be determined.

References

[1] I. Valin et al., A reticle size cmos pixel sensor dedicated to the start hft, Journal of Instrumentation 7 (2012).

[2] Ch. Finck et al., Study for online range monitoring with the interaction vertex imaging method, Phys. Med. Biol. (2017).

 DOI:10.15120/GR-2018-1

Experiment beamline: Proton Therapy Center in Trento
Experiment collaboration: APPA-BIOMAT
Experiment proposal: none
Accelerator infrastructure: none

PSP codes: none
Grants: none
Strategic university co-operation with: none

Dose build-up effects in clinical proton Bragg curves

T. Pfuhl[1,2], F. Horst[1,3], C. Schuy[1], J. Stroth[1,2], U. Weber[1]

[1]GSI, Darmstadt, Germany; [2]Goethe University, Frankfurt, Germany; [3]THM, Gießen, Germany

Introduction

The precise knowledge of the dose deposition of ions in matter is essential for an accurate treatment planning for cancer patients. Therefore, the dose build-up effects in 220 MeV proton Bragg curves were investigated in detail [1]. There are two dose build-up effects to be considered. The δ-electron build-up effect takes place in the first few millimeters of the target until an equilibrium state of the forwards scattered δ-electrons is reached. The target fragment build-up effect covers the first centimeters in the target and is a result of forwards-emitted target fragments created in inelastic interactions of the beam particles with target nuclei. As these fragments have an increased LET they are of great interest in current radiobiology research.

Materials and Methods

The measurements of 220 MeV proton Bragg curves with the focus set to their build-up regions were performed at the proton therapy center in Trento, Italy, in November 2017. In the experiment two parallel plate ionization chambers were positioned around a series of solid polyethylene targets (e.g. foils) of different thicknesses. The ratio of the accumulated charge in the second ionisation chamber (IC2) to the accumulated charge in the first ionisation chamber (IC1) was measured. Consequently, the measurements were independent from the primary proton number.

In a second experimental setup a magnetic field was introduced to filter out the δ-electrons emitted from the target in order to separate the δ-electron build-up effect from the target fragment build-up effect (see figure 1). A magnetic dipole (permanent magnets of NdFeB) was used to obtain the necessary magnetic field strength.

The exact geometry of both setups (distances of the targets, magnetic field size, and collimator size) was optimized in advance with FLUKA [2, 3, 4] Monte Carlo simulations to enable a measurement of optimal pronounced build-up effects.

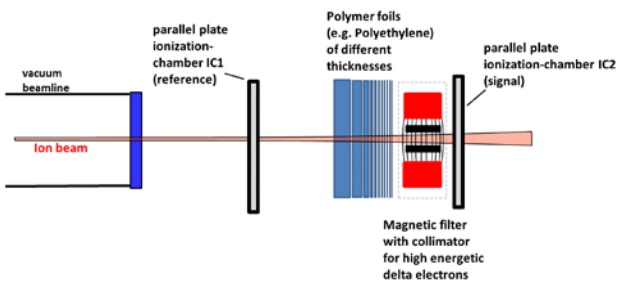


Figure 1: Schematic setup for the measurement of Bragg curves at low penetration depths. The optional magnetic filter enabled the separation of the δ-electron build-up effect from the target fragment build-up effect.

The direct measurement of target fragments is extremely difficult. However, with this approach, the target fragment production could be examined indirectly.

Results

Figure 2 shows the results of the Bragg curve measurements with/without the magnetic filter. The δ-electron build-up effect takes place in the first two millimeters of the target. It could be suppressed by the magnetic field, so that the plain target fragment build-up region could be measured. The target fragment build-up effect is mainly relevant in the first centimeters of the target.

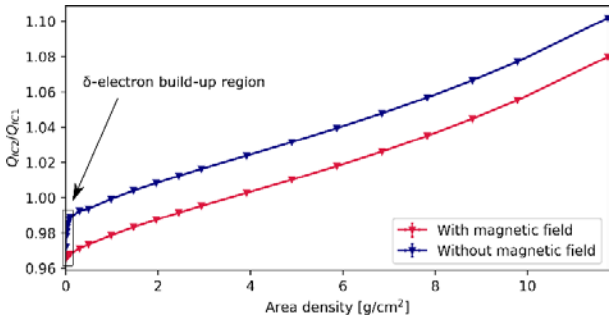


Figure 2: Results of the measurements of the 220 MeV proton Bragg curve. By introducing the magnetic field, the δ-electron build-up effect could be suppressed.

Conclusions

The experimental setup enabled a precise measurement of the build-up regions in a 220 MeV Bragg curve with a very low noise. The strength of the magnetic field was sufficient to suppress the δ-electron build-up effect.

References

[1] "Dose build-up effects in clinical proton Bragg curves" (master's thesis), T. Pfuhl (2018)

[2] "FLUKA: a multi-particle transport code", A. Ferrari et al., CERN-2005-10 (2005), INFN/TC_05/11, SLAC-R-773

[3] "Overview of the FLUKA code", G. Battistoni et al., Annals of Nuclear Energy 82, 10-18 (2015)

[4] "The FLUKA code: An accurate simulation tool for particle therapy", G. Battistoni et al., Frontiers in Oncology, Radiation Onc. Section, 00116 (24 p.) (2016)

Experiment beamline: Proton therapy center, Trento (Italy)
Experiment collaboration: APPA-BIOMAT
Experiment proposal: none
Accelerator infrastructure: none
PSP codes: none
Grants: none
Strategic university co-operation with: Frankfurt-M

 DOI:10.15120/GR-2018-1

Programme Report on IBER18

U. Weber[1], C. Kausch[1], TJ. Ngo-Anh[2]

[1]GSI, Darmstadt, Germany; [2]European Space Agency, Noordwijk, The Netherlands

GSI has been considered by the European Space Agency (ESA) as ideally suited to investigate the biological effects of space radiation. Cosmic radiation poses a major threat to the health of astronauts exploring outer space. In order to study in more detail the biological effects of cosmic radiation and identify possible countermeasures for effective radiation protection measures in space, the ESA and GSI Helmholtzzentrum für Schwerionenforschung have been cooperating on the research project IBER (Investigations into Biological Effects of Radiation) for almost ten years. Through this cooperation, many groups of researchers have been able to make use of the GSI's unique accelerator facilities to study the biological effects of cosmic radiation. The last two IBER campaigns were implemented in 2008 and 2010, and now, within the third IBER-cycle of activities, 11 European science teams will have again the opportunity to study this topic at GSI and utilize GSI's beam time.

Preparation for IBER 18

In 2016 a group of experts, the so-called 'ESA Topical Team' investigating the biological effects of space radiation using ground-based facilities, was put in place. The group provided recommendations to ESA on how to establish European space and ground-based radiation competence and knowledge within a multi-year strategy and highlighted the unique and complementary capabilities of GSI to support ESA for their goals. Based on these recommendations, the GSI directorate agreed to provide 20 shift of beam time for European research groups in the field of space radiation research. Therefore, an extension (until 2020) of the existing framework contract for IBER activities between ESA and GSI was put in place in April 2017.

As a result of the contract renewal, ESA published an 'Announcement of Opportunity', soliciting for proposals for radiation experiments with space relevance making use of beam time available at GSI. The beam times are scheduled in the second half of the both years 2018 and 2019. In September 2017 a workshop with ca. 30 scientist was held at GSI in order to inform the interested research groups about the scientific programme and to discuss the usage of beam time at GSI, various project ideas and their feasibility.

ESA received 11 proposals from European research groups (6 Germany, 2 Italy, 2 Belgium, 1 Romania) by the submission deadline of 29th of September 2017. The proposals were reviewed for scientific merit, space relevance and technical feasibility by a group of 8 independent experts, culminating in peer panel meetings in January 2018 at ESTEC/ESA (Noordwijk, The Netherlands): Of the 11 proposals recommended for selection, 1 was rated 'Outstanding', 7 were rated 'Excellent' and 3 were rated 'Very Good'. The outcome of the scientific review process was then approved by the ESA Life Sciences Working Group (LSWG). In February all applicants were informed about the outcome of the peer review and feasibility assessment; since then the GSI biophysics group is responsible for hosting the experiments during the ESA beam times in 2018/2019.

Scientific goals of IBER 18

The selected experiments contribute to improved risk assessments or will study countermeasure concepts on cells or animals to allow future safe and stable human space exploration with acceptable risk from exposure to space radiation. Currently, the radiation risk is characterized by a high uncertainty and lack of simple countermeasures. Most of the uncertainty on space radiation risk is associated with the poor knowledge of the biological effects of cosmic rays. This includes interaction of radiation damage with the effects of other space environment stressors, relative biological effectiveness (RBE) factors for energetic heavy ions for late effects, errors in human data including statistical, dosimetry and transfer between populations in application to space risks, effects of exposure to mixed high and low LET space radiation and the dose response curve at low radiation doses. Therefore, the objectives stated in the ESA roadmap for Radiation research [1] (developed together with the European science community during the Research Community Consultation Workshop in January 2016) will address these points through experimental studies at accelerator beams. The data to be obtained shall improve the models, which are necessary for a correct radiation risk assessment. The following table provides more detail on each of these topics.

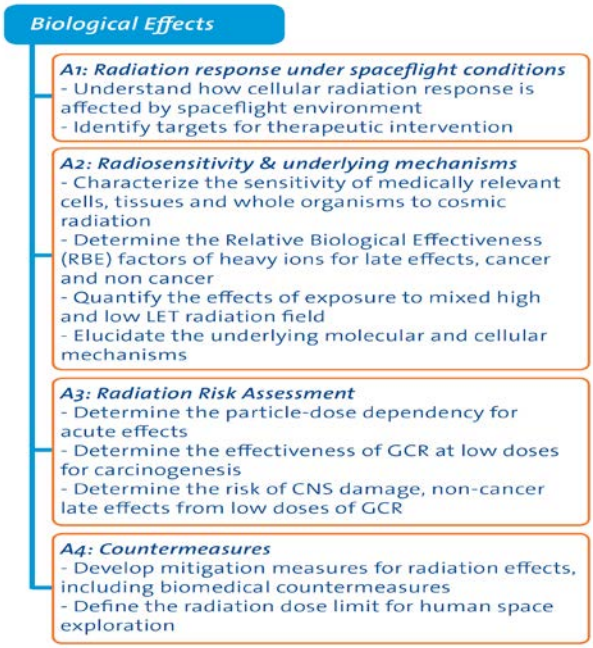


Figure 1: Specific biological objectives in Cosmic Radiation Risks for Human Exploration of the Solar System.

DOI:10.15120/GR-2018-1

Reference [1]: ESA brochure, ROADMAPS FOR FUTURE RESEARCH, A redefinition of strategic goals for future space research on the ISS and supporting research platforms, https://indico.gsi.de/event/6401/picture /10.pdf, 2016.

Experiment beamline: none
Experiment collaboration: APPA-BIOMAT
Experiment proposal: none
Accelerator infrastructure: SIS100
PSP codes: none
Grants: none
Strategic university co-operation with: other: ESA (European Space Agency)

 DOI:10.15120/GR-2018-1

Flood fill segmentation for images from time-varying computed tomography

B. R. Schlei[1]

[1]GSI, Darmstadt, Germany

For questions: b.schlei@gsi.de

Abstract

In this report, we propose to apply a region-growing based segmentation technique for the processing of images from time-varying computed tomography. The particular challenge is the selection of all voxels that represent a contrast fluid in a beating human heart. First results are presented, which will allow for further numerical processing of the quantitatively characterized shapes.

Introduction

In the field of medical image processing for computed tomography (CT), the field values of the three-dimensional (3D) voxel data are often encoded while using the so-called material density related Hounsfield scale (*cf.*, e.g., Ref. [1]). For instance, distilled water at standard pressure and temperature corresponds to zero Hounsfield units (HU), whereas air corresponds to -1000 HU.

The input data for the following processing consist of a set of eight 3D images, each having 9,830,400 = 256 x 256 x 150 voxels in the x-, y-, and z-directions, respectively. Here, the Hounsfield values range between the extremes of -1024 HU and 3067 HU for the provided (2-byte valued) data [2]. These data contain—among many other things—a CT reconstructed contrast fluid in a beating human heart. The contrast fluid is believed here to take on density values of about 250 HU and above.

The perhaps most simple way to select volumetric picture elements is based on a so-called grey-level segmentation (*cf.*, e.g., Ref. [3]). However, by simply selecting a fixed grey-level (range) for collecting voxels that may represent the sought-after contrast fluid, one may often pick up also undesired material contained in the data.

Approach and Results

Here, we propose to use a region-growing based segmentation technique for the data under consideration. For the first 3D image of the data set we select a seed voxel that is believed to represent the contrast fluid. For each nearest six-connected neighbourhood, further voxels, which have a Hounsfield value ≥ 250 HU, are iteratively collected until a single-connected contrast fluid region has been identified (via so-called flood fill). The found voxels of a given 3D image are then used as seed voxels for the next (temporal successor) 3D image.

Fig.1 shows a temporal sequence of the fully processed set of the here considered image data, where a seed voxel at position x = 145, y = 120, and z = 40 has been selected in the first 3D image. In order to visualize the generated shapes for each single 3D image, we enclose segmented voxels with a shifted, high-resolution mixed-mode VESTA surface [4, 5]. The segmented voxels qualify for a further spacetime based processing with STEVE [5, 6].

References

[1] T. M. Buzug, Einführung in die Computertomographie: Mathematisch-physikalische Grundlagen der Bildrekonstruktion, Springer, 2005.

[2] Courtesy of C. Graeff, GSI.

[3] J. R. Parker, Algorithms for Image Processing and Computer Vision, John Wiley & Sons, 1997.

[4] B. R. Schlei, "Volume-Enclosing Surface Extraction", Computers & Graphics 36 (2012) p. 111, doi: 10.1016/j.cag.2011.12.008.

[5] B. R. Schlei, "Method for Hypersurface Construction in N Dimensions", U.S. patent 9,607,431, Mar. 28, 2017; E.P. patent 2,715,673, Nov. 22, 2017.

[6] B. R. Schlei, "STEVE – Space-Time-Enclosing Volume Extraction", (2013) arXiv:1302.5683 [cs.CG].

Experiment beamline: none
Experiment collaboration: none
Experiment proposal: none
Accelerator infrastructure: none
PSP codes: none
Strategic university co-operation with: none

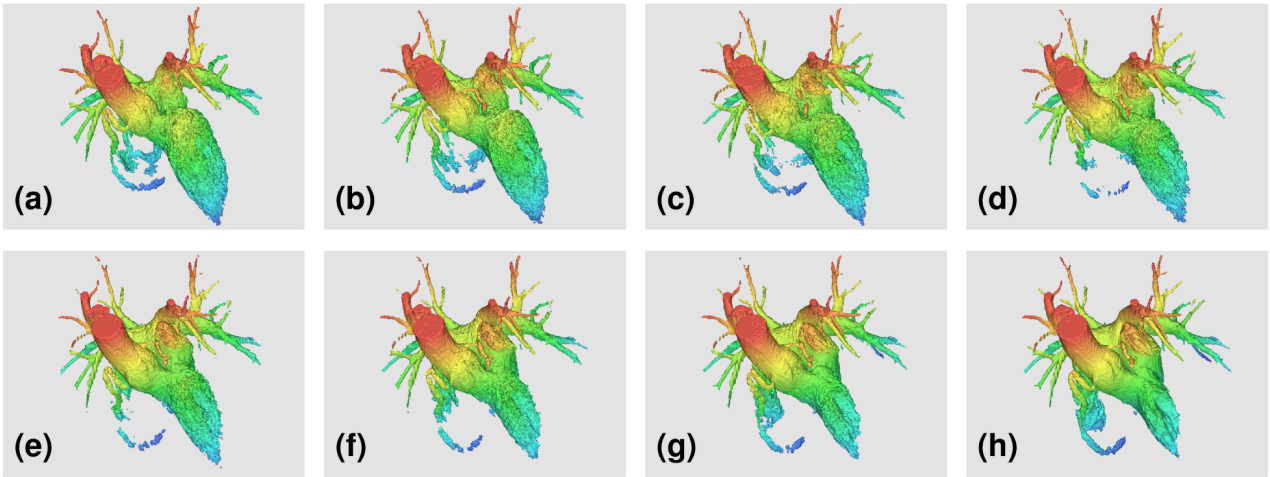


Figure 1: (a) – (h) Temporal sequence of eight 3D shapes that have been obtained from the application of the here proposed segmentation technique to the tomographically reconstructed image data, and a subsequent surface extraction with VESTA [4, 5]. Note that the colours refer to the different z-positions of the individual VESTA surface triangles.

 DOI:10.15120/GR-2018-1

Low mass dileptons as fireball thermometer at HADES energies

F. Seck[2], T. Galatyuk[1,2], R. Rapp[3] and J. Stroth[4,2]

[1]TU Darmstadt, Darmstadt, Germany; [2]GSI, Darmstadt, Germany; [3]Texas A&M University, College Station (TX), USA; [4]Goethe Universität, Frankfurt, Germany;

The systematic study of dilepton production in heavy-ion collisions across a large range of collision energies makes it possible to link experimental observables like yields and slopes of the spectra to features (phase transition(s) and possible critical point) in the QCD phase diagram. As dileptons are emitted during the whole space-time evolution of the collision, the resulting spectra comprise several contributions from first-chance NN collisions, the hadronic freeze-out cocktail, but also thermal radiation which serves as messenger of the QCD matter properties inside the hot and dense medium.

We couple in-medium thermal dilepton rates with a coarse-graining method of hadronic transport simulations to compute dilepton spectra at SIS18 beam energies, where hydrodynamic simulations may be less reliable. After checking the degree of thermalization of the system, local temperature, baryon and pion densities can be extracted in the nearly equilibrated parts of the fireball. This allows for the convolution of thermal rates with the space-time evolution of the medium.

The slope of the invariant-mass spectrum of thermal dilepton radiation in the intermediate mass region (IMR) between the ϕ and the J/Ψ mesons can be utilized as a thermometer of the fireball. If the electromagnetic spectral function $\mathrm{Im}\Pi_{\mathrm{em}}/\mathrm{M}^2$ is constant, the shape of the spectrum is given by $\frac{\mathrm{dN}}{\mathrm{dM}} \sim (\mathrm{MT})^{3/2} \exp(-\mathrm{M}/\mathrm{T})$. To good approximation, this is true for the IMR [1, 2]. The observed temperature necessarily represents an average over the space-time evolution of the fireball. It is however dominated by the radiation emanating from the hottest stage reached during the collision.

Since the invariant-mass is Lorentz-invariant, the extracted temperature is not affected by a blue shift caused by the radial expansion of the medium.

In heavy-ion collisions at beam energies in the SIS18 range the conditions reached during the evolution comprise high baryon densities of several times normal nuclear matter density and temperatures up to 85 MeV.

Under those environments there are strong medium modifications to the spectral function of the ρ meson [3]. This leads to an almost structureless spectrum [4] as shown in figure 1.

At energies accessible to the HADES experiment at SIS18, the IMR is hard to access. The statistics collected during the Au+Au beamtime with 1.23A GeV collision energy in the year 2012 was not enough to populate the spectrum above the ϕ meson with sufficient yield. Theoretical modelling predicts T ~ 85 MeV, corresponding to the hottest space-time cells in the evolution [4, 5].

Due to the strong medium effects, $\mathrm{Im}\Pi_{\mathrm{em}}/\mathrm{M}^2$ is also reasonably flat in the mass range 0.3-0.7 GeV/c^2 as shown in figure 2.

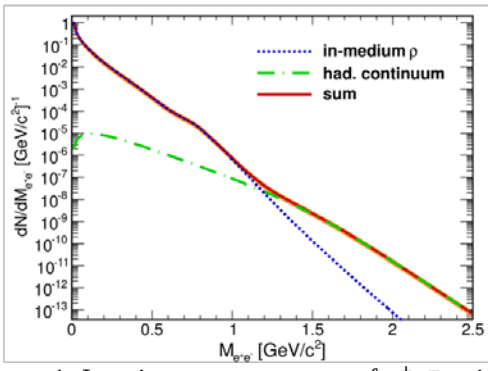


Figure 1: Invariant-mass spectrum of e^+e^- pairs radiated from a central Au+Au collision at 1.23A GeV [4].

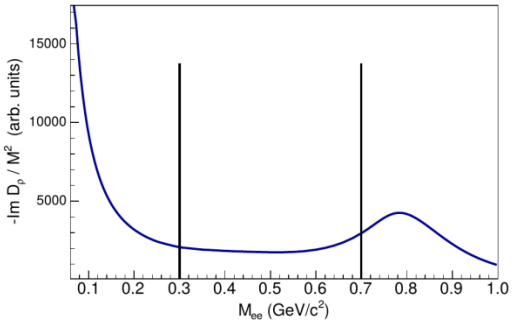


Figure 2: In-medium ρ spectral function $\mathrm{Im}\,\mathrm{D}_\rho/\mathrm{M}^2$ averaged over different temperatures and baryon densities as they occur during the space-time evolution.

This allows the use of the low mass region (LMR) for the temperature measurement instead.

As the suppression from the thermal Boltzmann factor is weaker at lower masses, the radiation in this mass region is not restricted to the hottest stage and more cells with different conditions can contribute. This leads to an extracted temperature which is ~ 20MeV lower, indicating that the measurement integrates over a longer time interval in the space-time evolution of the medium.

The upcoming Ag+Ag beamtime of HADES at a slightly higher collision energy will make it possible to test this relation between the temperatures extracted from the IMR and the LMR in experiment.

References

[1] R. Rapp and H. van Hees, PLB 753 (2016) 586
[2] H. Specht (NA60), AIP Conf. Proc. 1322 (2010) 1
[3] R. Rapp and J. Wambach, EPJ A 6 (1999) 415
[4] T. Galatyuk et. al, EPJ A 52 (2016) 131
[5] F. Seck et. al, arXiv: 1710.06256

Grants: VH-NG-823, DFG through grant CRC-TR 211
Strategic university co-operation with: Darmstadt

The dark matter axion mass

G. D. Moore[1], *V. B. Klaer*

[1]IKP, TU Darmstadt, Germany

Introduction

A major potential link between particle physics and cosmology is the nature of dark matter. One of the most interesting dark matter candidates is the axion, a pseudo-Goldstone boson whose existence would explain the observed time-reversal symmetry of QCD.

Highly coherent, nearly-at-rest axions can be created in the early Universe, and they make an ideal dark matter candidate. If we can establish how efficient this process is, we can relate the axion mass to the axion's role as dark matter. If we assume that:

1) the axion exists;
2) PQ symmetry is restored in the early Universe or the axion field otherwise starts out randomly different through space;
3) the axion makes up all of the dark matter,

then we are able to make a unique prediction for the axion mass.

Methodology

The axion Lagrangian in terms of a complex scalar field

$$\mathcal{L} = g^{\mu\nu}\partial_\mu\varphi\partial_\nu\varphi + \frac{m^2}{8f_a^2}\left(2\varphi^*\varphi - f_a^2\right)^2 + \chi(T)(1-\cos\theta_a) \quad (1)$$

can be solved directly as a real-time classical field theory, with random initial conditions for the scalar field, via lattice methods. The dynamics is rich because the scalar field can contain topological structures called axionic strings; close to such a string, in cylindrical coordinates, the field obeys

$$\varphi = f(r)f_a e^{i\theta_a}, \quad \theta_a = \pm\phi \quad (2)$$

such that the scalar changes by plus or minus 2pi in winding one time around in azimuth. The energy associated with such a string diverges at short distances as the logarithm of distance, cut off by the inverse of the mass in the Lagrangian. This distance is of order 30 orders of magnitude shorter than the inter-string separation, giving rise to a logarithmically large string tension for such strings. But numerical simulations cannot reproduce this, because both scales must be resolved on the lattice which cannot be much larger than 2000 points across. Therefore simulations feature strings with approximately 10 times too small a tension.

We resolve this problem, and thereby present reliable simulations of axion production in the early Universe, by proposing a model with additional massive degrees of freedom, which are only active in the string core and which give rise to a much higher value for the string tension, with otherwise the same long-distance axionic dynamics. We do this by studying a theory with two complex scalars with different charges, and a single U(1) gauge field; one linear combination of fields is the axion, the other couples to the gauge field and forms abelian-Higgs strings. Each string has both an axionic and an abelian-Higgs character, with the abelian Higgs component contributing only to its tension, which we can therefore tune. Details of the method are presented in [1] and the cosmological results are presented in [2].

The most significant result is that the axion production is *smaller* than it would be, under the approximation that each region of space has a different starting angle and evolves independently (the misalignment approximation). The axion number increases as one increases the string tension, but quite weakly, as shown in Figure 1.

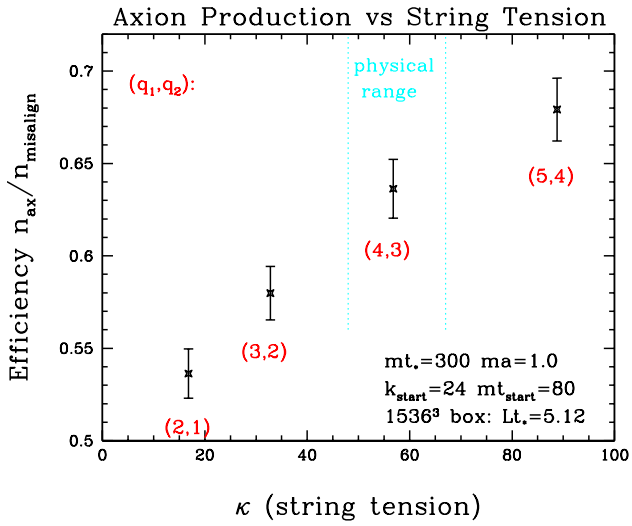


Figure 1: Axion production efficiency (relative to the misalignment approximation) as a function of the extra contribution to the string tension (the log of the scale separation we want to simulate).

Based on these results, we are able to establish the axion decay constant, and axion mass, for which the axions would make up 100% of the dark matter. Specifically, with the assumptions mentioned in the introduction, we find that the axion mass should be 26.2 plus or minus 3.4 micro-electron volts. This prediction narrows the frequency range experiments must explore.

References

[1] V. B. Klaer and G. D. Moore, "How to simulate global cosmic strings with large string tension," JCAP 1710, Oct. 2017, article 043.

[2] V. B. Klaer and G. D. Moore, "The dark-matter axion mass," JCAP 1711, Oct. 2017, article 049.

Strategic university co-operation with Darmstadt

 DOI:10.15120/GR-2018-1

Transport coefficients of quark matter from the Kubo formalism

A. Harutyunyan[1], D. H. Rischke[1], and A. Sedrakian[2]

[1]ITP, D-60438 Frankfurt-Main, Germany, [2]FIAS, D-60438 Frankfurt-Main, Germany

The transport coefficients of quark plasma are important input parameters for the hydrodynamical simulations of heavy-ion collision experiments. In this context, we have computed all first order transport coefficients of two-flavor quark plasma close to the critical temperature of chiral phase transition. The quark matter is described within the two-flavor Nambu Jona-Lasinio model which is well-suited for studies of chiral phase transitions [1, 2].

The transport coefficients are extracted from the Kubo type formulas by evaluating the specific correlation functions required for the electrical and thermal conductivities as well as shear and bulk viscosities. We apply the $1/N_c$ expansion in order to truncate the infinite series of Feynman diagrams contributing to the correlation functions and find that the conductivities and the shear viscosity can be described by a single-loop skeleton diagram with full quark propagator. In contrary, the bulk viscosity requires a resummation of a full series of multi-loop diagrams. Close to the critical temperature of chiral phase transition the dispersive effects that lead to nonzero transport coefficients arise from quark-meson fluctuations above the Mott-temperature T_M for meson dissociation.

We find that the conductivities and the shear viscosity are decreasing functions of temperature and density for $T>T_M$, see Fig. 1. These coefficients show a universal behavior as functions of the scaled temperature T/T_M.

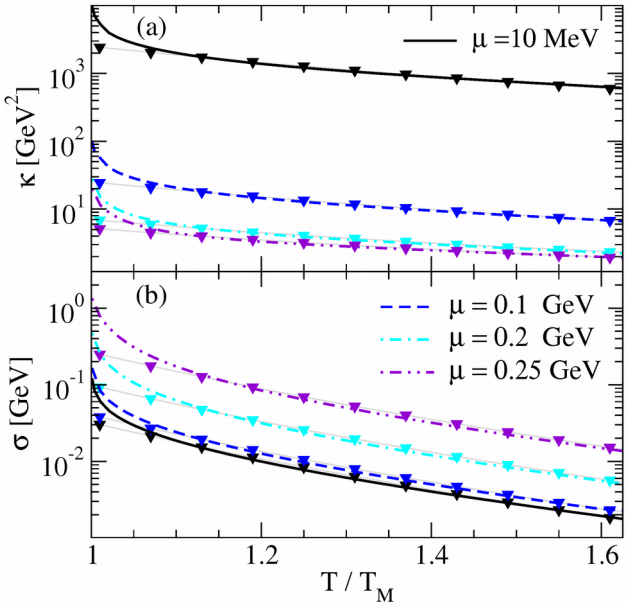
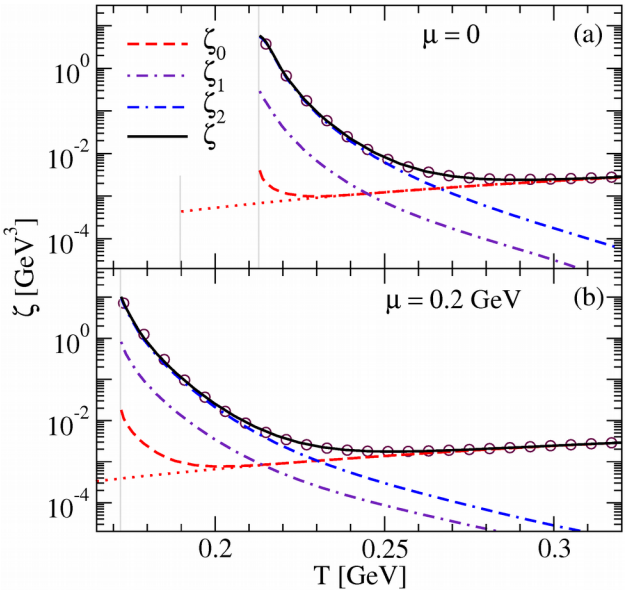


Figure 1: The thermal conductivity κ (a) and the electrical conductivity σ (b) as functions of the scaled temperature T/T_M at several values of the chemical potential. The triangles reproduce the results of the fit formulas.

The case of the bulk viscosity turns out to be special, because the multi-loop contributions ζ_1 and ζ_2 dominate the single-loop contribution ζ_0 close to the Mott line in the case where the chiral symmetry is explicitly broken, see Fig. 2. We find that in this case only at high temperatures the one-loop contribution becomes dominant. The resulting bulk viscosity has a mild minimum as a function of temperature and exceeds the shear viscosity close to the Mott temperature by factors 5 ÷ 20 when multi-loop contributions are included. In the high-temperature domain



the bulk viscosity is negligible compared to the shear viscosity.

For practical applications we provide simple fits to the transport coefficients, which can facilitate the implementation of our results in hydrodynamic simulations.

Figure 2: Three components of the bulk viscosity and their sum as functions of temperature for two values of the chemical potential. The dotted lines correspond to the chiral limit. The results of the fits are shown by circles.

References

[1] A. Harutyunyan, D. H. Rischke and A. Sedrakian, Transport coefficients of two-flavor quark matter from the Kubo formalism, Phys. Rev. D 95 (2017) 114021, [1702.04291].

[2] A. Harutyunyan and A. Sedrakian, Bulk viscosity of two-flavor quark matter from the Kubo formalism, Phys. Rev. D 96 (2017) 034006, [1705.09825].

Strategic university co-operation with: Frankfurt-M

Influence of the axial anomaly on the decay $N(1535) \to N\eta$

L. Olbrich[1], M. Zétényi[1,2,3], F. Giacosa[1,4], and D. H. Rischke[1,5]

[1]Goethe University, Frankfurt am Main, Germany; [2]Wigner Research Center for Physics, Budapest, Hungary; [3]GSI, Darmstadt, Germany; [4]Jan Kochanowski University, Kielce, Poland; [5]University of Science and Technology of China, Hefei, Anhui, China.

The decay width of $N(1535) \to N\eta$ is as large as that of $N(1535) \to N\pi$. This is surprising, because considering flavor symmetry we would expect that

$$\frac{\Gamma_{\mathrm{N}(1535)\to N\eta}}{\Gamma_{\mathrm{N}(1535)\to N\pi}} \simeq \frac{\cos^2\theta_P}{3} \simeq 0.17\,, \qquad (1)$$

where the factor 3 takes the pion triplet into account and $\theta_P \simeq -44.6°$ [1] is the strange−non-strange mixing angle of the isoscalar-pseudoscalars. [Phase space reduces the ratio in Eq. (1) even further.]

We propose that the axial $U(1)_A$ anomaly is responsible for the enhanced coupling of $N(1535)$ to the η meson. To test this idea, we consider the so-called extended linear sigma model (eLSM). It includes (pseudo)scalar and axial(-vector) mesons [1] as well as glueballs [2] and features the explicit, spontaneous, and anomalous breaking of chiral symmetry. In Refs. [3,4], chirally symmetric Lagrangians describing baryons and their chiral partners in the mirror assignment were constructed for the cases $N_f = 2$ and $N_f = 3$, respectively. Both models cannot reproduce the decay width of $N(1535) \to N\eta$ [as expected because flavor symmetry holds in any chirally symmetric model, and thus Eq. (1) follows].
However, treating baryons in the mirror assignment allows to construct a further term in the baryonic sector, which preserves the chiral $SU(N_f)_L \times SU(N_f)_R$ symmetry but explicitly breaks the axial $U(1)_A$ symmetry, see Ref. [5]. Such anomalous terms induce additional interactions of some baryons and their chiral partners with the η meson.

The eLSM parametrizes (pseudo)scalar mesons via the field $\Phi(x)$, which behaves under chiral transformations as $\Phi \to U_L \Phi\, U_R^\dagger$, where $U_{L(R)} \in U(N_f)_{L(R)}$. Thus, terms involving $\det\Phi$ can be embodied to model the axial anomaly. We consider the following negative-parity term:

$$\det\Phi - \det\Phi^\dagger\ . \qquad (2)$$

Coupling this term to a baryonic field combination (equal to the one of the chirally invariant mass term, which exists only in the mirror assignment), yields a parity-even chiral invariant, see Ref. [5].

For the case $N_f = 2$ [and in the absence of (axial-)vector degrees of freedom], we obtain

$$\det\Phi - \det\Phi^\dagger = -i\,(\sigma_N + \phi_N)\eta_N + i\,a_0\cdot\pi\ , \qquad (3)$$

where we shifted the isoscalar-scalar field σ_N by its non-zero vacuum expectation value ($\sigma_N \to \sigma_N + \phi_N$), which arises from the spontaneous breaking of chiral symmetry. From Eq. (3) it is visible that the coupling of Eq. (2) to a baryonic combination induces a direct coupling of the η meson to some baryons. Indeed, incorporating such an anomalous term into the two-flavor eLSM of Ref. [3], an enhanced decay $N(1535) \to N\eta$ can be obtained by adjusting the respective coupling constant, see Ref. [5].

For the case $N_f = 3$, we consider the eLSM as investigated in Ref. [4], where four baryonic multiplets are present. One can introduce analogous anomalous terms, which enhance the decay of chiral partners into baryons and an η meson. Then, upon identifying $N(1535)$ as the chiral partner of the nucleon and $\Lambda(1670)$ as chiral partner of $\Lambda(1116)$, after fixing the decay width of $N(1535) \to N\eta$, the decay $\Lambda(1670) \to N\eta$ can be correctly described, see Ref. [5]. This approach predicts also a strong $N(1535)N\eta'$ coupling, which is important for studies of η' production processes.

Finally, the developed formalism can be used to couple a pseudoscalar glueball to baryons. We have found that it couples strongly to $N(1535)N$ and possibly to $N(1440)N$, see Ref. [5]. Thus, we expect that the pseudoscalar glueball can be seen in the future PANDA experiment by investigating the process $p + \bar{p} \to p + \bar{p}(1535) + \text{h.c.}$.

References

[1] D. Parganlija, P. Kovacs, G. Wolf, F. Giacosa and D. H. Rischke, Phys. Rev. D 87, 014011 (2013).
[2] W. I. Eshraim, S. Janowski, A. Peters, K. Neuschwander and F. Giacosa, Acta Phys. Polon. Supp. 5, 1101 (2012).
[3] S. Gallas, F. Giacosa and D. H. Rischke, Phys. Rev. D 82 (2010) 014004.
[4] L. Olbrich, M. Zétényi, F. Giacosa and D. H. Rischke, Phys. Rev. D 93 no. 3, 034021 (2016).
[5] L. Olbrich, M. Zétényi, F. Giacosa and D. H. Rischke, Phys. Rev. D 97 (2018) no.1, 014007.

Experiment beamline: none
Experiment collaboration: none
Experiment proposal: none
Accelerator infrastructure: none
PSP codes: none
Grants: HGS-HIRe/HQM, Hungarian OTKA Fund No. K109462, HIC for FAIR, OPUS project no. 2015/17/B/ST2/01625, High-End Visiting Expert project GDW20167100136 (SAFEA), DFG grant no. RI1181/6-1
Strategic university co-operation with: Frankfurt-M, Kielce, Budapest

 DOI:10.15120/GR-2018-1

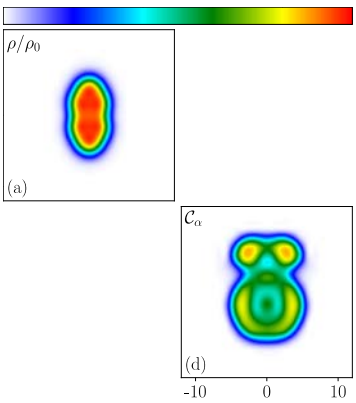
Clustering in pre-compound nuclei in the TDDFT framework

B. Schuetrumpf [1,2] W.Nazarewicz [3]

[1]GSI, Darmstadt, Germany; [2]Institut für Kerphysik, Technische Universität Darmstadt; [3]FRIB Laboratory, Michigan State University

Clustering in atomic nuclei is a ubiquitous phenomenon. Although it is commonly accepted to be very important for many aspects, it is hard to describe and detect in numerical simulations. Earlier works showed, that clustering can be revealed in nuclear mean-field calculations by the nucleonic localization function (NLF), which was adapted from quantum chemistry. In this work the NLF is applied to time-dependent density functional theory (TDDFT) calculations of collisions of intermediate mass nuclei. A special focus is put on the early stage of the collision, where -in contrast to the equilibrated compound nucleus- the freshly fused system (or pre-compound nucleus) still carries a strong imprint of the entrance channel of the collision.

Usually TDDFT calculations are analyzed using predominantly the nucleon density distribution. Examples of snapshots of the time evolution are shown in Fig. 1 left panels. However, the density contains only little information of the internal structure of the nucleus. On the other hand, the NLF, which is based on the inverse probability of finding two nucleons with same spin and isospin in the vicinity of each other (Fig. 1 right panels), reveal distinct regions with localizations close to 1, signaling the presence of clusters. Regions of high localizations at the tips as in Fig. 1 (b) mark alpha clusters, since for an alpha particle the probability of finding two nucleons with same spin and isospin close to each other vanishes. Other clusters like carbon clusters containing 6 neutrons and 6 protons manifest in ring structures. That can be easily verified by analyzing the nucleon content of the cluster regions. In our study it was found that the collision of two oxygen nuclei at a center of mass energy of around 20 MeV results in a pre-compound system where two alpha particles oscillate against two carbon clusters



[1].Figure 1: Snapshots of oxygen + oxygen (top) and calcium + oxygen (bottom) TDDFT simulations of central collisions. Total densities normalized to nuclear saturation density ((a) and (c)) and nucleon localization ((b) and (d)). Collisions is cylindrically symmetric w.r.t. the z=0 axis. Taken from [1].

Not only central collisions, but also collisions with a non-zero impact parameter were carried out. The alpha-C-C-alpha structure displayed in Fig. 1 (b) is shown in Fig. 2 for different impact parameters. While for the central collision the system conserves axial symmetry, for b > 0 the alpha clusters shift slightly into the direction of rotation thus creating more overlap with the carbon clusters, resulting in a lower localization. However, the overall structure of the state remains up to high impact parameters.

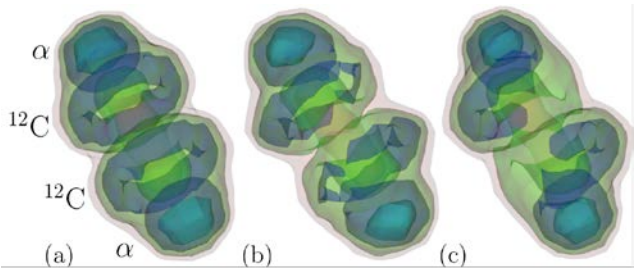


Figure 2: Alpha-C-C-alpha structure in oxygen + oxygen for the central collision (a), with b=2 fm (b), and b=4 fm (c). Taken from [1].

A study of oxygen + carbon collisions around the Coulomb barrier reveals extreme alpha clustering for all impact parameters where (intermediate) fusion occurs [1]. This supports experimental studies [2], which have detected enhanced alpha emission in those reactions. The authors of [2] find that statistical models underestimate the alpha emission strongly for those reactions. The results suggest, that the cluster structure of the initial fragment nuclei gives rise to strong entrance channel effects, neglected by the statistical models. This influences the alpha emissions following fusion.

In summary it has been shown that the NLF provides a useful measure to reveal clustering also in the time-dependent formalism. The assumption of a fully equilibrated compound nucleus in such reactions is incomplete and entrance channel effects play an important role, especially in reactions with short contact time. With the help of the NLF clusters can be traced and, with significant modifications and beyond mean-field techniques the emission probabilities could be extracted in future works.

References

[1] B. Schuetrumpf and W. Nazarewicz, Phys. Rev. C **96**, 064608 (2017)

[2] J. Vadas, T. K. Steinbach, J. Schmidt, V. Singh, C. Haycraft, S. Hudan, R. T. deSouza, L. T. Baby, S. A. Kuvin, and I. Wiedenhöver, Phys. Rev. C **92**, 064610 (2015).

Strategic university co-operation with: TU Darmstadt

Dilepton production in carbon-carbon collision in comparison to HADES measurements

J. Staudenmaier[1,2] and H. Petersen[1,2,3]

[1]GSI, Darmstadt, Germany; [2]Johann Wolfgang Goethe-Universität, Frankfurt am Main, Germany; [3]Frankfurt Instiute for Advanced Studies (FIAS), Frankfurt am Main, Germany

Electromagnetic probes offer the unique possibility to gain undisturbed insights into strongly interacting matter produced by nucleus-nucleus collisions. This includes lepton pairs (dileptons) that are, for the here discussed low energy reactions, predominantly produced by decays of resonances. Therefore, they offer the possibility to study resonance properties within a hadronic medium. In-medium changes to these properties e.g. the spectral function have been discussed to reveal features of the theory of the strong interaction (QCD) such as chiral symmetry restoration [1].

However, before probing in-medium properties, a solid baseline description for di-lepton production in absence of a medium needs to be established. This is possible in the context of the rich experimental data set from HADES with elementary reactions and small nucleus-nucleus reaction, which represent a superposition of elementary reactions.

The approach chosen for this work is a new hadronic transport model: SMASH (=Simulating Many Accelerated Strongly-interacting Hadrons) [2]. As a transport model, it is based on the relativistic Boltzmann equation. The collision term is emulated by decays and binary collisions using a geometric collision criterion. All well-known resonance from the PDG [3] up to a mass of 2.3 GeV are included. Di-leptons are produced by decays of various resonance. This work focuses on di-electron production, for which mesonic decays of $\pi, \eta, \rho, \omega, \phi$ and baryonic decays from the Δ resonance are included. New in this approach are contributions to the direct vector meson decay channels below the hadronic thresholds, which equals the combined mass of the lightest hadronic decay products [4].

Results for the di-electron production in carbon-carbon collisions at E_{Kin} = *2.0A* GeV are shown in Figure 1. In the invariant mass spectrum the dominant contribution for masses below 500 MeV are the pseudo-scalar meson π and η decays. Above 500 MeV the vector meson channels are dominant. ρ and ω contributions below the hadronic threshold, which for the ρ is at two π masses, are observed. The ρ contribution is the second largest contribution around 250 MeV. The agreement with experimental data [5] is excellent. Only around the ω pole a slight overestimation is seen.

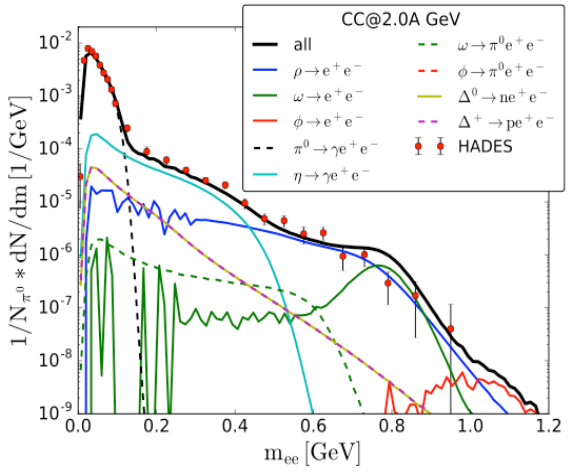


Figure 1: Invariant mass spectrum of di-electrons produced by carbon-carbon collisions at E_{Kin} = *2.0A* GeV compared to HADES data from [5].

On this solid description of smaller systems, the dilation production for larger systems can be studied. The vector meson contributions are sensitive to modification to the spectral function, since they decay directly into a lepton pair. With HADES data available also for larger system it is possible to probe for which systems the assumption of vacuum properties remains valid and for which the invariant mass spectrum of di-leptons is senstive to medium modifications.

References

[1] R. Rapp, J. Wambach, and H. van Hees, Landolt-Bornstein 23, 134 (2010), arXiv:0901.3289 [hep-ph].

[2] J. Weil et al, Phys.Rev. C94 (2016) no.5, 054905

 DOI:10.15120/GR-2018-1

[3] K. A. Olive et al. (Particle Data Group), Chin. Phys. C38, 090001 (2014).
[4] J. Staudenmaier et al, J.Phys.Conf.Ser. 832 (2017) no.1, 012037
[5] G. Agakishiev et al. (HADES), Eur. Phys. J. A40, 45 (2009), arXiv:0902.4377 [nucl-ex].

Experiment beamline: HADES
Experiment collaboration: CBM / HADES
Experiment proposal: [e.g. S339] none
Accelerator infrastructure: SIS18 / SIS100 / CERN-LHC
PSP codes: [none]
Grants: Work supported by Helmholtz Nachwuchsgruppe VH-NG-822, by the LOEWE Initiative HIC for FAIR of the State of Hesse and GSI. Computational resources have been provided by the Center for Scientific Computing (CSC) at the Goethe-University of Frankfurt and the GreenCube at GSI. J.S. acknowledges support by the Deutsche Forschungsgemeinschaft (DFG) through the grant CRC-TR 211 “Strong-interaction matter under extreme conditions”.
Strategic university co-operation with: Frankfurt-M / FIAS

Lattice QCD investigation of the structure of the $a_0(980)$ meson

J. Berlin[1], M. Wagner[1] in collaboration with *C. Alexandrou[2,3], M. Dalla Brida[4], J. Finkenrath[3], T. Leontiou[5]*

[1]Goethe-Universität Frankfurt am Main, Institut für Theoretische Physik, Max-von-Laue-Straße 1, D-60438 Frankfurt am Main, Germany
[2]Department of Physics, University of Cyprus, P.O. Box 20537, 1678 Nicosia, Cyprus
[3]Computation-based Science and Technology Research Center, The Cyprus Institute, 20 Kavafi Street, 2121 Nicosia, Cyprus
[4]Dipartimento di Fisica, Universita di Milano-Bicocca and INFN, Sezione di Milano-Bicocca, Piazza della Scienza 3, I-20126 Milano, Italy
[5]Department of Mechanical Engineering, Frederick University, 1036 Nicosia, Cyprus

We have investigated the quark content of the low-lying states in the $I(J^P) = 1(0^+)$ sector, which are the quantum numbers of the $a_0(980)$ meson, using lattice QCD (for details cf. our recent publication [1]).

We have considered correlation functions of six different two- and four-quark interpolating fields:

$$\mathcal{O}^1 = \mathcal{O}^{q\bar{q}} = N_1 \sum_{\mathbf{x}} \left(\bar{d}(\mathbf{x})u(\mathbf{x})\right)$$

$$\mathcal{O}^2 = \mathcal{O}^{K\bar{K},\ \text{point}} = N_2 \sum_{\mathbf{x}} \left(\bar{s}(\mathbf{x})\gamma_5 u(\mathbf{x})\right)\left(\bar{d}(\mathbf{x})\gamma_5 s(\mathbf{x})\right)$$

$$\mathcal{O}^3 = \mathcal{O}^{\eta_s\pi,\ \text{point}} = N_3 \sum_{\mathbf{x}} \left(\bar{s}(\mathbf{x})\gamma_5 s(\mathbf{x})\right)\left(\bar{d}(\mathbf{x})\gamma_5 u(\mathbf{x})\right)$$

$$\mathcal{O}^4 = \mathcal{O}^{Q\bar{Q}} = N_4 \sum_{\mathbf{x}} \epsilon_{abc}\left(\bar{s}_b(\mathbf{x})(C\gamma_5)\bar{d}_c^T(\mathbf{x})\right) \epsilon_{ade}\left(u_d^T(\mathbf{x})(C\gamma_5)s_e(\mathbf{x})\right)$$

$$\mathcal{O}^5 = \mathcal{O}^{K\bar{K},\ \text{2part}} = N_5 \sum_{\mathbf{x},\mathbf{y}} \left(\bar{s}(\mathbf{x})\gamma_5 u(\mathbf{x})\right)\left(\bar{d}(\mathbf{y})\gamma_5 s(\mathbf{y})\right)$$

$$\mathcal{O}^6 = \mathcal{O}^{\eta_s\pi,\ \text{2part}} = N_6 \sum_{\mathbf{x},\mathbf{y}} \left(\bar{s}(\mathbf{x})\gamma_5 s(\mathbf{x})\right)\left(\bar{d}(\mathbf{y})\gamma_5 u(\mathbf{y})\right)$$

We have evaluated all diagrams, including diagrams, where quarks propagate within a timeslice, e.g. with closed quark loops. A necessary preparatory step was the comparison of the efficiency of various methods to compute two-point correlation functions of two-quark and four-quark interpolating fields of different structure, including combinations of point-to-all propagators, stochastic timeslice-to-all propagators, the one-end trick and sequential propagators (cf. Ref. [2]).

We have demonstrated that diagrams containing such closed quark loops have a drastic effect on the final results and, thus, may not be neglected. Our analysis, which has been carried out at unphysically heavy u and d quark mass corresponding to m_{pion} = 296(3) MeV and in a single spatial volume of extent 2.9 fm, shows that in addition to the expected spectrum of two-meson scattering states there is an additional energy level around the two-particle thresholds of K + K and eta + pion. This state in the energy region of 1100 MeV to 1200 MeV is a candidate for the $a_0(980)$ meson. It is predominantly generated by the quark-antiquark interpolating field O^1, but also receives sizable contributions from the diquark-antidiquark interpolating field O^4, i.e. a likely interpretation is that it is mainly a quark-antiquark state with a minor tetraquark component. To some extent this is supported by a previous computation, where we have neglected quark propagation within a timeslice [3]. Then the quark-antiquark interpolating field decouples from the four-quark interpolating fields and an analysis of the four-quark correlation matrix only yields the expected two-meson scattering states.

Our analysis has been performed using AMIAS, a novel statistical method based on the sampling of all possible spectral decompositions of the considered correlation functions, as well as solving standard generalized eigenvalue problems.

References

[1] C. Alexandrou, J. Berlin, M. Dalla Brida, J. Finkenrath, T. Leontiou and M. Wagner, "Lattice QCD investigation of the structure of the $a_0(980)$ meson," Phys. Rev. D **97**, 034506 (2018) [arXiv:1711.09815 [hep-lat]].

[2] A. Abdel-Rehim, C. Alexandrou, J. Berlin, M. Dalla Brida, J. Finkenrath and M. Wagner, "Investigating efficient methods for computing four-quark correlation functions," Comput. Phys. Commun. **220**, 97 (2017) [arXiv:1701.07228 [hep-lat]].

[3] C. Alexandrou, J. O. Daldrop, M. Dalla Brida, M. Gravina, L. Scorzato, C. Urbach and M. Wagner, "Lattice investigation of the scalar mesons $a_0(980)$ and kappa using four-quark operators," JHEP **1304**, 137 (2013) [arXiv:1212.1418 [hep-lat]].

 DOI:10.15120/GR-2018-1

Nucleosynthesis in neutrino-driven supernova ejecta: Influence of variations in the astrophysical conditions and of (α,n) reaction rates

J. Bliss[1], A. Arcones[1,2], F. Montes[3,4], J. Pereira[3,4], M. Witt[1]

[1]TU Darmstadt, Darmstadt, Germany;[2]GSI, Darmstadt, Germany;[3]NSCL, Michigan State University, MI 48824, USA;[4]Joint Institute for Nuclear Astrophysics, Michigan State University, MI 48824, USA

Core-collapse supernovae synthesize lighter heavy elements between Fe up to possibly Ag depending on the properties of the ejected matter. Despite the fast progress in supernova simulations and experimental astrophysics, the astrophysical and nuclear physics uncertainties are still large and can critically influence the nucleosynthesis. Therefore, we address both sources of uncertainty and study their impact on the nucleosynthesis in neutron-rich neutrino-driven supernova ejecta.

To explore the variations in the astrophysical conditions we rely on a steady-state model [1] because a systematic study based only on trajectories from hydrodynamic simulations is computationally expensive. Steady-state models allow to investigate all possible conditions found in current and future supernova simulations. We vary the mass and radius of the proto-neutron star as well as the total luminosity and energy of the neutrinos, which are input parameters in the wind equations, to cover a wide range of astrophysical conditions and calculate the nucleosynthesis [2]. In the final abundances, we identify four abundance patterns (NSE1, NSE2, CPR1, CPR2) by different neutron, alpha, and seed abundances at T = 3 GK. The different nucleosynthesis groups distinguish in the evolution of the nucleosynthesis path and each groups exhibits characteristic abundance patterns and peaks. The abundance patterns of the groups NSE1 and NSE2 are mainly determined during the nuclear statistical equilibrium (NSE) phase and thus rather depend on binding energies and partition functions. The group CPR1 describes the transition between NSE1 or NSE2 to CPR2. After the breakdown of NSE, charged-particle reactions still redistribute the abundances but the nucleosynthesis path cannot overcomes the neutron shell closure at N = 50. Thus, the final abundances are given by Q-values of (α,n) reactions. Within the groups NSE1, NSE2, and CPR1 the nucleosynthesis evolution is similar. In contrary, we find a lot of variations in the final abundances of the nucleosynthesis group CPR2 (see Fig.1) and especially the heaviest synthesized elements vary. Individual charged particle reactions can critically affect the abundance evolution and nuclei heavier than Z~40 are produced.

For neutron-rich conditions, matter mainly evolves towards heavy nuclei by charged-particles reactions, especially (α,n) reactions [3]. None of the relevant (α,n) reactions has been measured in the energy range that is significant for astrophysical conditions in neutrino-driven supernova ejecta. Therefore, the reaction rates included in our nucleosynthesis studies are calculated with theoretical reaction codes based on the statistical Hauser-Feshbach model. The reaction rates contain some uncertainty due to intrinsic technical aspects in the reaction codes and nuclear physics input [4]. To estimate the uncertainty in the (α,n) rates we calculate them using different alpha optical potentials which are the main contribution to the uncertainty for the relevant astrophysical conditions [5]. Moreover, we compare the theoretical reaction rates with the few available measurements of stable nuclei in the absence of relevant experiments. We conclude that the reliability of the theoretical (α,n) rates is not better than a factor of 10.

We investigate the influence of the rate uncertainties on the nucleosynthesis for different astrophysical conditions by varying all (α,n) reaction rates for nuclei between Fe and Rh by factors of 5, 10, and 50 up and down. When the (α,n) rates are reduced (increased) less (more) matter moves towards nuclei beyond Z=38 compared to the case where no rates are varied. This result is robust for different astrophysical conditions unless the nucleosynthesis evolution is close to the valley of stability. We conclude that (α,n) rate uncertainties are crucial for the nucleosynthesis in neutrino-driven supernova ejecta. Thus, more studies are required to identify the individual important reactions whose measurements will contribute to further reduce the nuclear physics uncertainties.

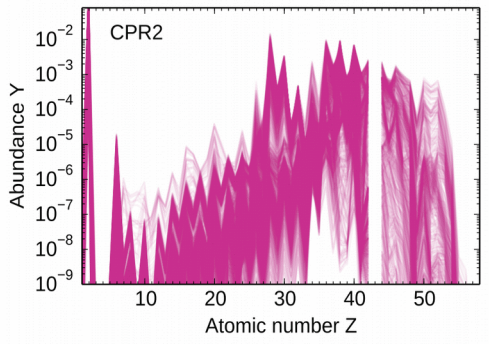


Figure 1: Final abundances of the group CPR2.

Grants: Helmholtz Young Investigator Grant No. VH-NG-825

References

[1] K. Otsuki et al., ApJ 533 (2000) 424.

[2] J. Bliss et al., accepted by ApJ (2018).

[3] S.E. Woosley & R.D. Hoffman, ApJ 395 (1992) 202.

[4] J. Pereira & F. Montes, Phys. Rev. C 93 (2016) 034611.

[5] J. Bliss et al., J. Phys. G: Nucl. Phys. 44 (2017) 054003

Impact of spatial correlations among the proton constituents at LHC energies

J.L. Albacete[1], H.Petersen[2,3,4] and A.Soto-Ontoso[1,2]

[1]Universidad de Granada, Granada, Spain.; [2] FIAS, Frankfurt am Main, Germany, [3] GSI, Darmstadt, Germany, [4] Goethe University, Frankfurt am Main, Germany.

Introduction

The first discovery at the Large Hadron Collider (LHC) occurred in 2010 when two-particle correlations at small relative azimuth angle extending over several units of rapidity were measured in high multiplicity proton-proton (p+p) collisions. This phenomenon, dubbed the ridge, had been previously measured in heavy-ion (A+A) collisions and considered to be a golden probe of quark-gluon plasma (QGP) formation. In addition to the ridge, other QGP-sensitive observables such as the flow harmonic coefficients and their correlations in terms of symmetric cumulants have shown a similar behavior in p+p and in the A+A case [1]. At this point, a natural question arises: are small droplets of QGP being formed in p+p collisions at the TeV regime?

An indispensable ingredient in any theoretical model attempting to describe the striking experimental results is the parametrization of the geometry of the collision.

The model

We propose a description of the proton geometry based on three main ingredients. First, the fundamental constituents of the proton are considered to be gluonic hot spots, by default we consider 3, that can be interpreted in a radiative picture as a valence quark surrounded by a gluonic cloud. Next, the positions of these hot spots in the transverse plane are subjected to short-range repulsive correlations that effectively enlarge the mean transverse separation between them (see Eq.2 in [2]). The inclusion of this effect is the main novelty of this work with respect to others in the literature. Finally, the radius of the hot spot grows with increasing energy of the collision. The theoretical justification for the last two assumptions is given in [3].

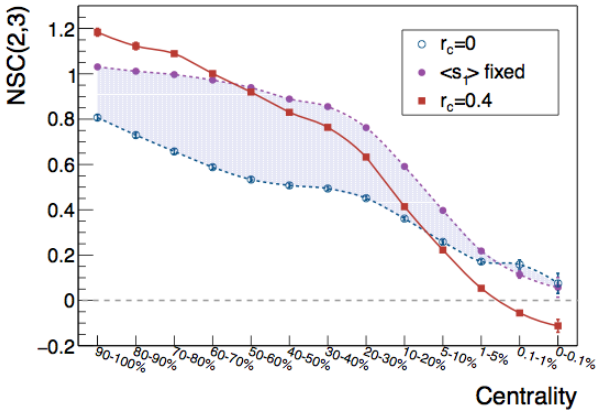
We implement this geometry in a Monte Carlo event generator à la Glauber including fluctuations in the hot spots positions and their entropy deposition. The entropy deposition is considered a proxy of particle production and, therefore, is constrained by the experimental data on the charged particle multiplicity distributions. Further, it is the quantity that defines the centrality classes.

Symmetric cumulants

In Fig.1 the correlation between the eccentricity and the triangularity, NSC(2,3) (see Eq.2 in [4]), of p+p collisions at 13 TeV is shown. The most remarkable feature is that the negative sign of NSC(2,3) in the highest centrality bins is only achieved in the correlated scenario [4]. This is the first result in the literature that is, at least, in qualitative agreement with the experimental measurement where the correlation is measured in terms of elliptic and triangular flow.

Together with their drastic impact on the description of the hollowness effect [3] and the absolute values of the eccentricities [2], the symmetric cumulant study adds evidence to the fact that the inclusion of spatial correlations between the sub nucleonic degrees of freedom of the proton modifies the initial state properties of proton-proton interactions at LHC energies.

Figure 1: Normalized symmetric cumulant as a function of the centrality. The light purple band contains the uncorrelated results while the red line corresponds to the correlated scenario.



References

[1] CMS Collaboration, “Evidence for collectivity in pp collisions at the LHC”, Phys. Lett. B765 (2017) 193–220 .

[2] J.L.Albacete, H.Petersen and A.Soto-Ontoso, “Correlated wounded hot spots in proton-proton interactions”, Phys.Rev. C95 (2017) no.6, 064909.

[3] J.L.Albacete and A.Soto-Ontoso, “Hot spots and the hollowness of proton-proton interactions”, Phys.Rev. C95 (2017) no.6, 064909.

[4] J.L.Albacete, H.Petersen and A.Soto-Ontoso,“Symmetric cumulants as a probe of the proton substructure at LHC energies”, Phys.Lett. B778 (2018) 128-136.

Grants: Helmholtz Young Investigator Group VH-NG-822, FP7-PEOPLE-2013-CIG Grant of the European Commission QCDense/631558, RYC-2011-09010 and FPA2013-47836.

 DOI:10.15120/GR-2018-1

Baryon number fluctuations in chiral effective models and their phenomenological implications

G. A. Almasi[1], B. Friman[1], and K. Redlich[2,3]

[1]GSI, Darmstadt, Germany; [2]ExtreMe Matter Institute (EMMI), D-64291 Darmstadt, Germany;
[3]University of Wroclaw - Faculty of Physics and Astronomy, PL-50-204 Wroclaw, Poland.

In this work we study the influence of the chiral phase transition on fluctuation observables in strongly interacting matter at non-zero temperature and net baryon density [1]. We focus on the properties of net-baryon-number fluctuations, which are quantified by the baryon number cumulants. These are directly influenced by the chiral phase transition, owing to the coupling of the quarks to the scalar order parameter. Furthermore, since the cumulants can be related to the fluctuations of the net proton number, which are accessible experimentally, they are ideal observables for identifying the phase boundary and critical structures in the QCD phase diagram.

We model chiral dynamics with the Polyakov-loop extended Quark-Meson (PQM) model. To correctly account for the critical behaviour at the chiral symmetry restoration transition in the O(4) and Z(2) universality classes, we employ the Functional Renormalization Group (FRG) [2]. We formulate the FRG equations in the presence of repulsive interactions and derived the flow equations for derivatives of the thermodynamic pressure.

The main focus of our studies is the analysis of the STAR data on proton number fluctuations and the comparison with model predictions. To reduce the influence of the non-critical characteristics of the model, like e.g. the mass spectrum or the kinematical cuts on particle momentum distributions, we compute ratios of susceptibilities. We fix the freeze-out line in our model using the skewness data measured by STAR. By doing so, we qualitatively reproduce the behaviour of all cumulant ratios with multiple parameter sets, except for the rise of the kurtosis at low energies (Fig. 1). We conclude that, since our model calculations do not reproduce this behaviour, this rise cannot be solely attributed to chiral criticality in equilibrium.

We also computed the baryon number cumulants of fifth and sixth order along the freeze-out line. Figure 2 shows that the sixth to second and fifth to first cumulant ratios agree at high beam energies. Since non-equilibrium effects are expected to spoil this relation, we propose to use the ratios of cumulants as probes of equilibration.

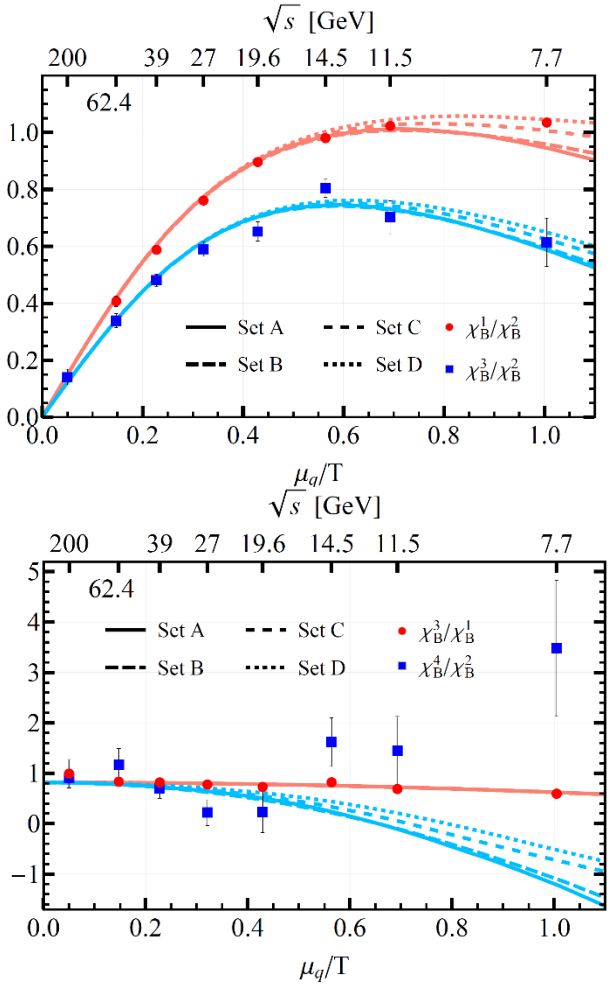


Figure 1: Baryon number cumulant ratios in the PQM model on the freeze-out line fitted to STAR data.

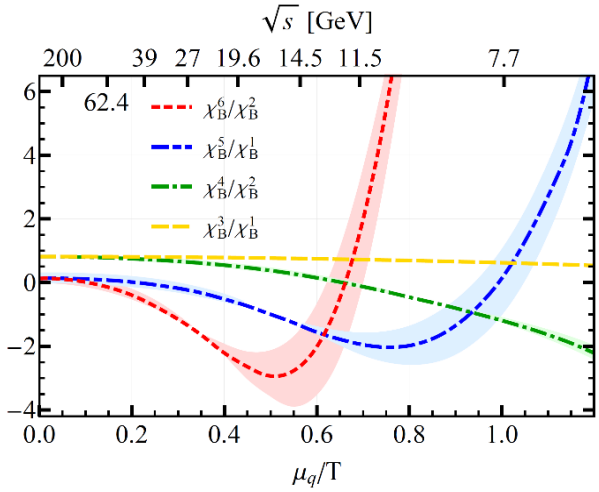


Figure 2: Higher order cumulant ratios in the PQM model along the freeze-out line.

References

[1] G. A. Almasi, B. Friman and K. Redlich, Phys. Rev. D 96, 014027 (2017)
[2] B. Friman, F. Karsch, K. Redlich and V. Skokov, Eur. Phys. J. C 71, 1694 (2011)

Experiment beamline: none
Experiment collaboration: none
Experiment proposal: none
Accelerator infrastructure: none
PSP codes: none
Grants: none
Strategic university co-operation with: Darmstadt

S-matrix approach to thermodynamics with structureless N-body scatterings

P. M. Lo[1,2]

[1]University of Wroclaw, PL-50204, Wroclaw, Poland; [2]GSI, Darmstadt, Germany

Structureless N-body scattering

According to the S-matrix formulation of statistical mechanics, the contribution to the thermodynamic pressure due to interactions takes the following form:

$$(\Delta \ln Z) = V \int \frac{d^3P}{(2\pi)^3} \frac{dM}{2\pi} e^{-\beta\sqrt{P^2+M^2}} B(M)$$
$$B(M) \equiv 2 \frac{\partial}{\partial M} Q(M).$$

Here B(M) is an effective spectral function and Q(M) is the corresponding phase shift function. For the case of elastic 2 -> 2 scattering processes, Q(M) can be formally identified with the usual scattering phase shift. In terms of quantum field theory amplitudes, we can write

$$Q(M) = \frac{1}{2} \mathrm{Im} \ln \left[1 + i \int d\phi_2 \, \mathcal{M} \right].$$

The amplitude can be constructed using the standard Feynman rules. The integration over the 2-body phase space means

$$\int d\phi_2 \, (\cdots) \to \int \frac{d^3p_1}{(2\pi)^3} \frac{1}{2E_1} \frac{d^3p_2}{(2\pi)^3} \frac{1}{2E_2} \times (2\pi)^4 \delta^4(P_I - \sum_i p_i) \, (\cdots).$$

The general N-body phase shift function Q(M) is difficult to obtain. However, if we restrict our attention to processes involving only structureless scatterings, that is, replacing the ampltidue with a (dimensionful) coupling constant

$$i\mathcal{M} = i \lambda_N,$$

the problem reduces to that of calculating the N-body phase space function. An efficient way to accomplish this task is to employ the Kallen expansion, which provides a recursive definition of the N-body phase space function via

$$\phi_N(s) = \frac{1}{16\pi^2 s} \int_{s'_-}^{s'_+} ds' \sqrt{\lambda(s, s', m_N^2)} \times \phi_{N-1}(s', m_1^2, m_2^2, ..., m_{N-1}^2),$$

To demonstrate how the N-body phase space function increases with s=M^2, we compute them numerically for a system of pions. The result is shown in Fig. [1].

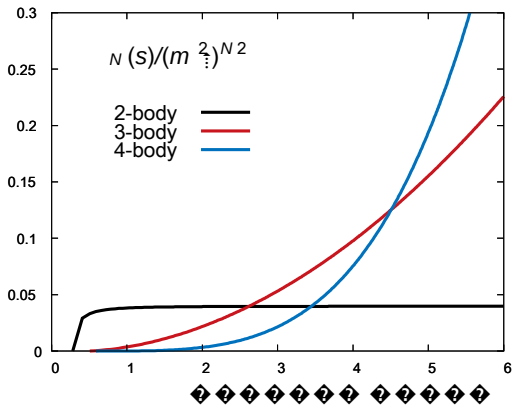


Figure 1: (N=2,3,4)-body phase space functions, scaled by the appropriate powers of pion mass, versus the center of mass energy sqrt(s).

From a purely kinematical point of view, effects from higher N-body phase space are generally suppressed compared to the lower ones at low invariant mass. However, their effects will show up and will eventually be dominating at high invariant masses in the manner dictated. In case of finite density or chemical potential, the takeover by higher N-body phase spaces can occur more rapidly due to the fugacity factor associated with an N-body state.

The phase space dominance model discussed here may be of interest to phenomenological studies. Performing modelling on the level of S-matrix elements or amplitudes, e.g. the invariant mass dependence of the coupling, can establish closer connection between observables and model parameters. Moreover, symmetries and physical conditions can be imposed on the S-matrix elements to constrain their functional form. Finally, we note that the purely kinematical consideration presented here can be non-trivially modified by interaction dynamics. [1]

References

[1] P. M. Lo, “S-matrix formulation of thermodynamics with N-body scatterings”, EPJC 77, 8, 533 (2017)

 DOI:10.15120/GR-2018-1

Experiment beamline: none
Experiment collaboration: none
Experiment proposal: none
Accelerator infrastructure: none
PSP codes: none
Grants: Maestro grant DEC-2013/10/A/ST2/00106
Strategic university co-operation with: none

Single electrons from open heavy-flavors in relativistic heavy-ion collisions

T. Song[1], H. Berrehrah[2], J. Torres-Rincon[2], L. Tolos[3], D. Cabrera[4], W. Cassing[1], and E. Bratkovskaya[2,5],

[1]Universität Gießen, Gießen, Germany; [2]Johann Wolfgang Goethe Universität, Frankfurt am Main, Germany;
[3]Campus Universitat Autonoma de Barcelona, Bellaterra, Spain;
[4]Centro Mixto Universidad de Valencia, Valencia, Spain; [5]GSI, Darmstadt, Germany.

We have studied the single electron spectra from D- and B-meson semileptonic decays in Au+Au collisions at $\sqrt{s_{NN}} = 200$, 62.4, and 19.2 GeV by employing the parton-hadron-string dynamics (PHSD) transport approach that has been shown to reasonably describe the charm dynamics at Relativistic-Heavy-Ion-Collider (RHIC) and Large-Hadron-Collider (LHC) energies on a microscopic level. In this approach the initial charm and bottom quarks are produced by using the PYTHIA event generator which is tuned to reproduce the fixed-order next-to-leading logarithm (FONLL) calculations for charm and bottom production. The produced charm and bottom quarks interact with off-shell (massive) partons in the quark-gluon plasma with scattering cross sections which are calculated in the dynamical quasi-particle model (DQPM) that is matched to reproduce the equation of state of the partonic system above the deconfinement temperature Tc. At energy densities close to the critical energy density ($\approx 0.5\ GeV/fm^3$) the charm and bottom quarks are hadronized into D- and B-mesons through either coalescence or fragmentation. After hadronization the D- and B-mesons interact with the light hadrons by employing the scattering cross sections from an effective Lagrangian. The final D- and B-mesons then produce single electrons through semileptonic decay.

Figures 1 and 2 show, respectively, the R_{AA} and v_2 of single electrons from D-meson and B-meson semileptonic decays in Au+Au collisions at $\sqrt{s_{NN}} = 200$ GeV. The shadowing effect enhances the bottom production and suppresses the charm production at low transverse momentum. The single electrons from B decay have a larger contribution than that from D decay above $p_T \approx 2.7 - 2.8\ GeV/c$. The dotted lines are the R_{AA} of single electrons including both shadowing and Cronin effects. Although the Cronin effect enhances the R_{AA}, it is not significant.

We have found that the PHSD approach well describes the nuclear modification factor R_{AA} and elliptic flow v_2 of single electrons in d+Au and Au+Au collisions at $\sqrt{s_{NN}}$ =200 GeV and the elliptic flow in Au+Au reactions at $\sqrt{s_{NN}} = 62.4$ GeV from the PHENIX collaboration, however, the large R_{AA} at $\sqrt{s_{NN}} = 62.4$ GeV is not described at all. Furthermore, we have made predictions for the R_{AA} of D-mesons and of single electrons at the lower energy of $\sqrt{s_{NN}} = 19.2$ GeV. Additionally, the medium modification of the azimuthal angle ϕ between a heavy quark and a heavy antiquark has been studied. We have found that the transverse flow enhances the azimuthal angular distributions close to $\phi = 0$ because the heavy flavors strongly interact with the medium in relativistic heavy-ion collisions and almost flow with the bulk matter.

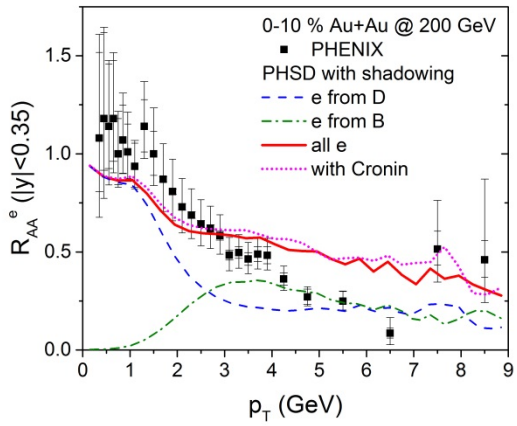


Figure 1: R_{AA} of single electrons from the semi-leptonic decay of D-mesons (dashed) and of B-mesons (dot-dashed) and the sum of them (solid) with shadowing effect in 0-10 % central Au+Au collisions at $\sqrt{s_{NN}} = 200$ GeV in comparison to the experimental data from the PHENIX collaboration. The dotted line is the R_{AA} including both shadowing and Cronin effects.

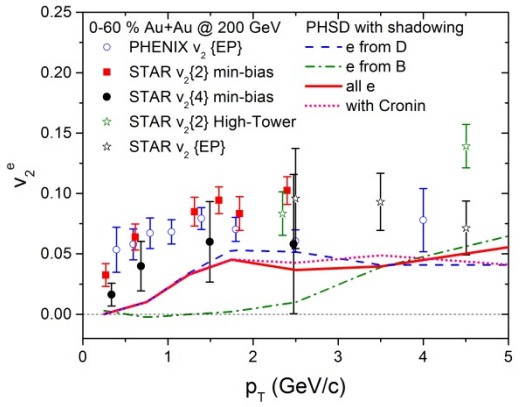


Figure 2: The elliptic flow v_2 of single electrons from the semi-leptonic decay of D-mesons (dashed) and of B-mesons (dot-dashed) and of both of them (solid) with shadowing effect in 0-60 % central Au+Au collisions at $\sqrt{s_{NN}} = 200$ GeV in comparison to the experimental data from the PHENIX and STAR collaborations. The dotted line is the v_2 of single electrons including both shadowing and Cronin effects.

References

[1] T. Song, H. Berrehrah, J. Torres-Rincon, L. Tolos, D. Cabrera, W. Cassing, E. Bratkovskaya, Phys. Rev. C96 (2017) 014905.

 DOI:10.15120/GR-2018-1

Foundations of the Trojan-Horse method

S. Typel[1,2]

[1]IKP, Technische Universität, Darmstadt, Germany; [2]GSI, Darmstadt, Germany

The Trojan-Horse (TH) method has been proposed by G. Baur in 1986 as an indirect approach to extract low-energy cross sections of a rearrangement reaction

$$A + x \rightarrow C + c \quad (1)$$

of astrophysical interest by studying the breakup reaction

$$A + a \rightarrow C + c + b \quad (2)$$

in the laboratory at much higher energies [1]. The TH nucleus a is assumed to be well described by a two-cluster system b+x where x is the transferred particle and b acts as a spectator. The connection of the cross section of reaction (1) with that of the surrogate reaction (2) was established with the help of direct reaction theory. This concept was already suggested in G. Baur's talk at the 1985 Varna International Summer School on Nuclear Physics [2]. The direct measurement of cross sections of reaction (1) at astrophysical energies is extremely difficult because of low-reaction rates and thus many experimental challenges arise. In contrast, reaction (2) is performed at energies above the Coulomb barrier without the strong suppression of the cross section caused by the Coulomb repulsion at very low energies. In addition, reaction (2) does not suffer from electron screening effects.

In the original proposal [1], G. Baur argued that the Fermi motion of x inside a would compensate the relative motion of A and x making small energies accessible in this system. However it was realized by Claudio Spitaleri and his group in Catania that the surrogate reaction (2) has to be studied at quasi-free scattering conditions, corresponding to a small momentum transfer to the spectator b, to exploit the virtues of the TH method, see, e.g., reference [3] and publications cited therein.

In first experimental attempts to apply the TH method it remained unclear how to establish the connection between the cross sections of reactions (1) and (2). Using detailed theoretical considerations [4,5] the cross section of reaction (2) could be factorized by employing a modified plane-wave impulse approximation (PWIA). The product contains a kinematic factor, the momentum distribution of relative motion $|\Phi_a(p_{bx})|^2$ of b and x inside a, and the half-off-shell cross section $d\sigma^{HOES}/d\Omega$ of reaction (1). The latter is related to the on-shell cross section by a simple penetrability factor. Applying this formulation, extensive applications of the TH method followed and low-energy cross sections of astrophysical reactions were determined with success, see, e.g., reference [6].

The conventional formulation of direct reaction theory for reaction (2) can be derived from the post form of the transition matrix element in distorted wave Born approximation (DWBA) with additional assumptions, in particular the so-called surface approximation. Formally, the matrix element is a first-order amplitude in reaction theory. The factors $|\Phi_a(p_{bx})|^2$ and $d\sigma^{HOES}/d\Omega$ can be related to two processes: the breakup of the Trojan horse a and reaction (1) as a subprocess of (2). Hence, the TH reaction can also be viewed as a two-step process with an intermediate off-shell propagation of the transferred particle x.

The connection between the one-step and two-step descriptions of the TH reaction was recently established in reference [7]. It was observed that the TH cross section is the direct part of the inclusive non-elastic breakup cross section. The corresponding transition matrix element contains the source function ρ with the exact three-body wave function. In the post representation within DWBA it has the Ichimura-Austern-Vincent form $\rho^{IAV}=\rho^{UT}+\rho^{HM}$ with two contributions. The Udagawa-Tamura term ρ^{UT} describes the elastic breakup of a and the fusion of x with A remaining in the ground state. The Hussein-McVoy term ρ^{HM} contains all other processes where A is excited or other channels in the A+x system are reached. The new formulation can be used for improvements in the analysis of experiments in order to access the validity of the approximations in the standard approach to the TH method.

References

[1] G. Baur. Phys. Lett. B 178 (1986) 135.
[2] G. Baur. Nuclear Energy 25 (1987) 183.
[3] S. Typel, EPJ Web Conf 165 (2017) 02008.
[4] S. Typel and H.H. Wolter, Few-Body Systems 29 (2000) 75.
[5] S. Typel and G. Baur, Annals Phys. 305 (2003) 228.
[6] C. Spitaleri et al., Eur. Phys. J. A 52 (2016) 77.
[7] C. A. Bertulani, M. S. Hussein, and S. Typel, Phys. Lett. B 776 (2018) 217.

Experiment beamline: none
Experiment collaboration: none
Experiment proposal: none
Accelerator infrastructure: none
PSP codes: none

Grants: DFG, SFB 1245
Strategic university co-operation with: none

Visualizing velocity field strengths with hyper-surfaces in spacetime

B. R. Schlei[1]

[1]GSI, Darmstadt, Germany

For questions: b.schlei@gsi.de

Abstract

One-dimensional (1D) time sequences of spatial, three-dimensional (3D) simulation or image data may implicitly carry dynamical information of their embedded subregions. Continuous hyper-surfaces can be constructed for the full 3+1D data that enclose certain spacetime regions. Here, we demonstrate that such hyper-surfaces may be viewed as 3D velocity vector fields, which explicitly characterize dynamically evolving 3D shapes contained in 4D.

Introduction

In this report, we consider the special case of 4D spacetime, where three dimensions refer to space, and a fourth dimension refers to time (i.e., 3+1D). E.g., relativistic hydrodynamical models that simulate relativistic heavy ion collisions may require the extraction of a so-called freeze-out hyper-surface (FOHS) from the 3+1D simulation data (*cf.*, e.g., Ref. [1] and Ref.s therein). The STEVE algorithm [2, 3] generates iso-valued hyper-surfaces that may implicitly be contained in four-dimensional (4D) data sets. A FOHS generated by STEVE consist of a finite set of tetrahedrons, which are embedded in 4D. For each tetrahedron (3-simplex), a covariant 4-normal, $d\sigma_\mu(x^\mu)=(d\sigma_x,d\sigma_y,d\sigma_z,d\sigma_t)$, at the contravariant event, $x^\mu=(x,y,z,t)$, with the three spatial cartesian coordinates x, y, and z, and the time t, respectively, can be calculated due to Ref. [2].

Approach and Results

Using the components of the 4-normals, let us define a 3-velocity

$$\vec{v}=(v_x,v_y,v_z)\equiv\frac{-d\sigma_t}{d\sigma_x^2+d\sigma_y^2+d\sigma_z^2}(d\sigma_x,d\sigma_y,d\sigma_z) \quad (1)$$

for each 3-simplex of a given hyper-surface that is embedded in 4D spacetime.

The magnitude $v=\sqrt{v_x^2+v_y^2+v_z^2}$ of each single 3-velocity, (*cf.*, Eq. (1)) can be encoded with a colour, which may then be assigned to its corresponding tetrahedron.

Fig.1 shows an example (*cf.*, also Ref. [2]) of a temporal sequence of intersections of a FOHS. The resulting 3D isothermes consist of triangles, which have inherited their colour from an intersected tetrahedron. In the figure, the colour red refers to regions of high speed, whereas the colour purple refers to zero and/or very low speeds.

We conclude our presentation with the notion that such processing may be useful also for medical applications [4], e.g., in the field of time-varying computed tomography [5].

References

[1] Yun Cheng, L. P. Csernai, V. K. Magas, B. R. Schlei, and D. Strottman, "Matching Stages of Heavy-Ion Collision Models," Phys. Rev. C81, 064910 (2010), doi: 10.1103/PhysRevC.81.064910.

[2] B. R. Schlei, "STEVE – Space-Time-Enclosing Volume Extraction", (2013) arXiv:1302.5683 [cs.CG].

[3] B. R. Schlei, "Method for Hypersurface Construction in N Dimensions", U.S. patent 9,607,431, Mar. 28, 2017; E.P. patent 2,715,673, Nov. 22, 2017.

[4] Private communication, C. Graeff, GSI.

[5] B. R. Schlei, "Flood fill segmentation for images from time-varying computed tomography", this GSI Scientific Report.

Experiment beamline: none
Experiment collaboration: none
Experiment proposal: none
Accelerator infrastructure: none
PSP codes: none
Strategic university co-operation with: none

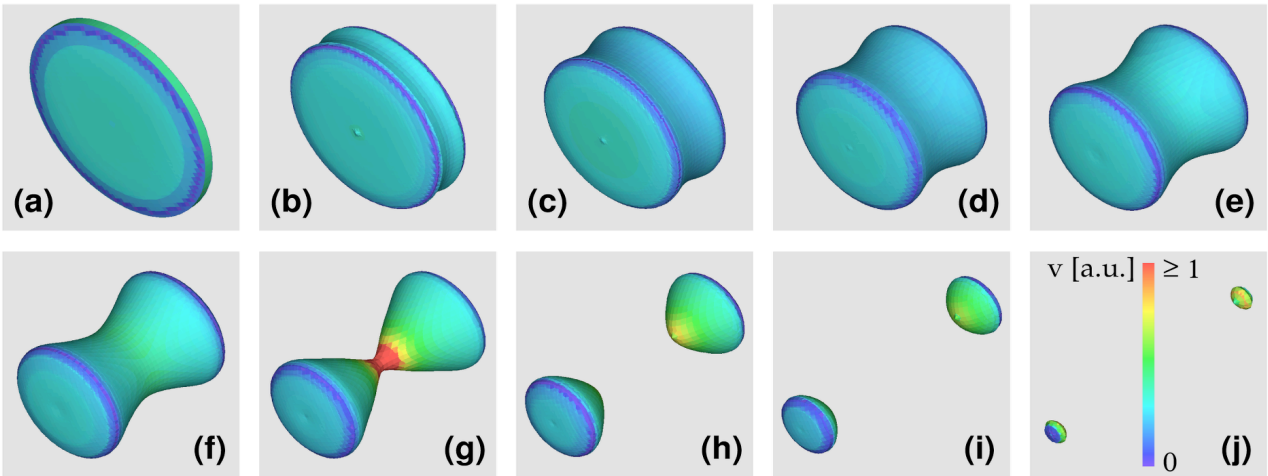


Figure 1: (a) – (j) Chronologically developing isothermes as a result of spatial hyper-surface intersections at equidistant times; (j) shows in addition a colour bar which decodes the relative velocity magnitudes of all images, (a) – (j). Note that the colour red refers to relative velocity magnitudes in the range of $[1.0,+\infty)$.

 DOI:10.15120/GR-2018-1

Parton-Hadron-Quantum-Molecular Dynamics (PHQMD) - a novel microscopic N-body transport approach for heavy-ion dynamics and hypernuclei production

E. Bratkovskaya[1,2], J. Aichelin[3] , A. LeFevre[1], V. Kireyev[4] , Y. Leifels[1]

[1]GSI, Darmstadt, Germany, [2]Johann Wolfgang Goethe Universität, Frankfurt am Main, Germany, [3]SUBATECH, Universite de Nantes, France, [4]Joint Institute for Nuclear Research, Russia

The formation of hypernuclei clusters in heavy-ion reactions has been a subject of many theoretical studies. Recent experimental results have shown that the hypernuclei and anti-hypernuclei can be produced in relativistic heavy-ion collisions (HIC) from SIS to LHC energies. Detailed investigations of the theoretical predictions have identified two sources of hypernuclei in these reactions:

a) In the overlap region of projectile and target, called participant region, strange baryons are produced in initial collisions between projectile and target nucleons. These strange baryons can migrate into the cold spectator matter where they can be absorbed and form heavy hypernuclei which have a rapidity close to projectile or target rapidity.

b) The Λ's may stay in the participant region, which expands and their interaction with the surrounding nucleons allows forming light clusters and hence lighting hypernuclei. In view of their small binding energy and their hot environment, this is like the creation of “ice in a fire”. Nevertheless, such hypernuclei have been found around mid-rapidity in RHIC and LHC experiments, a phenomenon which awaits an explanation.

In addition, the production of both types of hypernuclei may shed light on our theoretical understanding of the dynamics of heavy-ion reactions, which cannot be addressed by other probes. In particular, the formation of heavy projectile/target like hypernuclei elucidates the physics at the interface between spectator and projectile matter. Since the strange baryon comes necessarily from the overlap region the multiplicity as well as the rapidity distribution of the hypernuclei is related to the probability that strange baryons of a given rapidity are absorbed by the spectator matter by means of their potential interaction with the cold spectator matter. On the other hand, mid-rapidity hypernuclei test the phase space distribution of baryons in the expanding participant matter, especially whether strange and non strange baryons are in thermal equilibrium and whether their space time distribution is similar. This may contribute to clarifying the origin of their formation.

We have developed the novel microscopic n-body dynamical transport approach PHQMD (Parton-Hadron-Quantum-Molecular-Dynamics) for the description of particle production and cluster formation in heavy-ion reactions at relativistic energies. The PHQMD extends the established PHSD (Parton-Hadron-String-Dynamics) transport approach by introducing n-body quantum molecular dynamic type propagation of hadrons. This allows for a dynamical description of cluster formation based on the FRIGA (‘Fragment Recognition In General Application’) model. It keeps the collision integral (which describes the particle collisions) of the PHSD. This allows to use the PHQMD transport approach in different modes: the mean-field based PHSD mode and the QMD mode based on two and three-body potential interactions between the nucleons and, thus, to study the sensitivity of observables for the different ways of the description of the heavy-ion dynamics.

The PHQMD includes the following features for the dynamical fragment identification: the final fragment yield can either be determined with a minimum spanning tree (MST) procedure [2] or with cluster finding algorithms based on the Simulated Annealing Clusterization Algorithm (FRIGA) [3]. First results from combining the PHSD with the FRIGA code have been reported in [4].

In Figure 1 we validate our approach by showing that we can reproduce the complex fragment pattern observed by the ALADIN collaboration at the highest energies where experimental data for heavy fragments are available. These heavy fragments have a rapidity close to beam and target rapidity and with increasing energy also hyperfragments can be formed in this kinematical region.

Within the PHQMD we have obtained the first results for hadronic 'bulk' observables - as clusters production at SIS and FAIR/NICA energies, rapidity distributions and transverse mass spectra [5].

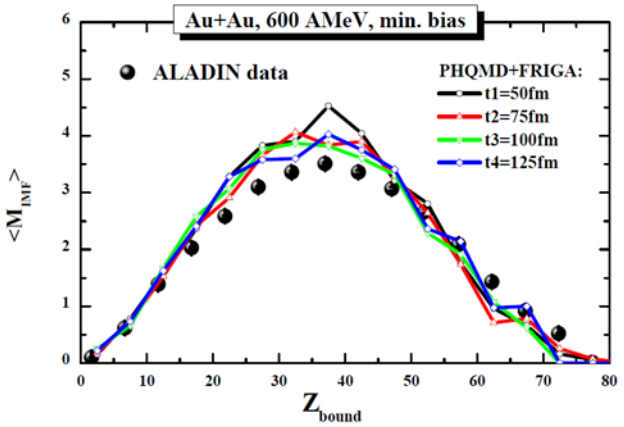


Figure 1: Rise and fall of the multiplicity of intermediate mass fragments as a function of the total bound charge. Both quantities are measured for forward emitted fragments. We compare the results of PHQMD for different times to identify fragments with the experimental data [1].

References

[1] A. Schuttauf et al., Nucl. Phys. A 607 (1996) 457.
[2] J. Aichelin, Phys. Rept. 202 (1991) 233.
[3] R. K. Puri, J. Aichelin, J. Comput. Phys. 162, 245 (2000).
[4] A. Le Fevre et al., J. Phys. Conf. Ser. 668, 012021 (2016).
[5] E.Bratkovskaya eta al., in preparation.

Production of light r-process elements in blue kilonova

S. Nikas[1,2], G. Martinez-Pinedo[1,2], A. Sieverding[1,2]

[1]GSI, Darmstadt, Germany; [2]TU Darmstadt, Darmstadt, Germany;

The r-process is responsible for the production of about half of the heavy elements observed in the solar abundances. The site of the r-process was unknown until recent observations. The gravitational wave event GW170817, which was identified as a binary Neutron Star Merger (NSM), was followed by the detection of an electromagnetic counterpart (EM170817) that is consistent with predictions for a kilonova/macronova associated with r-process nucleosynthesis [1,2]. In particular the observation of a bright fast fading UV component.

Since the complicated atomic structure of lanthanides implies high opacity ejecta, this indicates the presence of material with relatively high electron fractions and consequently low lanthanide production[3,4,5]. While the distinction between s and r-process produced elements is well defined for heavy elements, this is not the case for lighter elements. This is also partly due to the impact of other proposed processes like the i-process and the νp-process that are thought to have a contribution in this region. We study the nucleosynthesis for the conditions of high Ye outflows from NSMs to try to see if this could be the site for the production of the r-process abundance pattern for A <100.

Calculations-Results

We use a range of Ye (0.35, 0.36, 0.37, 0.38) which we average with ejecta velocity v/c = 0.2 and entropy 15 k_B per baryon following the presciption of [7]. Figure 1 shows that we can reproduce the peaks seen A=80 and A=84 in the r-process abundance pattern and have an overall agreement in the region. The details of the r-process abundance pattern are very sensitive to the nuclear physics underlying this process. Nuclear information (namely: masses, beta decay rates, and neutron capture rates) in this region are not known for all the neutron rich nuclei participating in the r-process. As a result of ongoing experimental campaigns more and more data becomes available. With the current knowledge of nuclear physics underlying this process we can conclude that we can not exclude NSM as the source of light r-process elements but a final conclusion require a better understanding of the properties of n-rich nuclei.

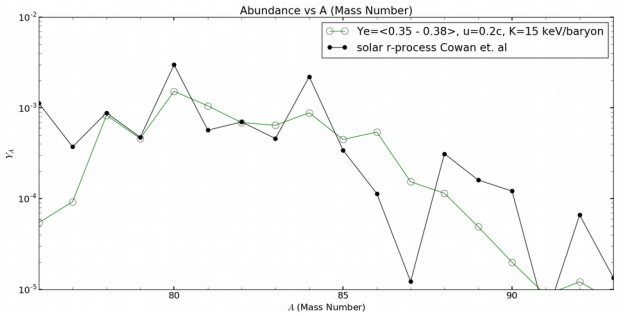


Figure 1: Filled black circles represent the r-process abundances as presented in the paper of Cowan et al. [6] Green open circles represent the average abundance for Ye between 0.35 and 0.38, ejecta velocity of 0.2c and entropy of 15 keV per baryon.

References

[1] Metzger, B. D., et al. "Electromagnetic counterparts of compact object mergers powered by the radioactive decay of r-process nuclei." Monthly Notices of the Royal Astronomical Society 406.4 (2010): 2650-2662.

[2] Kasliwal, M. M., et al. "Illuminating gravitational waves: a concordant picture of photons from a neutron star merger."Science 358.6370 (2017): 1559-1565.

[3] Evans, P. A., et al. "Swift and NuSTAR observations of GW170817: Detection of a blue kilonova."Science 358.6370 (2017): 1565-1570.

[4] Metzger, Brian D., and Edo Berger. "What is the most promising electromagnetic counterpart of a neutron star binary merger?." The Astrophysical Journal 746.1 (2012): 48.

[5] Joel de Jesús Mendoza-Temis, Joel, et al. "Nuclear robustness of the r process in neutron-star mergers." Physical Review C 92.5 (2015): 055805.

[6] Cowan, John J., et al. "R-process abundances and chronometers in metal-poor stars." The Astrophysical Journal 521.1 (1999): 194.

[7] S Rosswog et al 2017 "Detectability of compact binary merger macronovae" Class. Quantum Grav. 34 104001

Experiment beamline: none
Experiment collaboration:other: / none
Experiment proposal: none
Accelerator infrastructure:other: / none
PSP codes: none
Grants:
Strategic university co-operation with: Darmstadt

 DOI:10.15120/GR-2018-1

Short-range and tensor correlations in back-to-back nucleon pairs

T. Neff[1], and H. Feldmeier[1,2]

[1]GSI, Darmstadt, Germany; [2]FIAS, Frankfurt, Germany

Short-range correlations (SRC) in nuclei reflect the repulsive core and the strong tensor component of the nucleon-nucleon interaction. To study SRC in nuclei we combine many-body calculations in the ab-initio no-core shell model with unitarily transformed interactions and operators using the similarity renormalization group (SRG). The SRG transformation softens the interaction and makes solving the many-body problem possible. It is important to note that a consistent approach requires that not only the Hamiltonian but also all operators are transformed. Due to the short-range nature of the transformation long-range observables like radii or electromagnetic transition strengths are only weakly sensitive to the transformation. The situation is totally different for observables that are sensitive to the short-range behaviour of the wave function.

This is the case for the high-momentum components that are also studied in great detail experimentally. Up to now one of the clearest approaches have been (e,e'NN) reactions, i.e. the knockout of nucleon pairs by electrons. The experimental information has to be compared to theoretical predictions and it is important to identify as clearly as possible the experimental and theoretical observables. In the knockout process nucleon-nucleon pairs are observed as a function of relative momentum. However there are experimental cuts that restrict the total pair momenta. That the relative momentum distributions depend very strongly on the pair momentum is shown in Fig. 1 where we show the contributions to the total relative momentum distributions from nucleon pairs with total spin S and total isospin T in the alpha particle as a function of relative momentum. The first observation is that the momentum distributions are very different from what would be expected in a mean-field description. In this simple picture the contributions of the two even channels (S,T)=(1,0) and (S,T)=(0,1) would be both 0.5 independent from relative momentum. The contributions from the odd channels would be zero. What we observe is quite different. The situation is very clear for back-to-back pairs shown on the bottom. Here we find a situation close to what would be expected in the mean-field for pairs with relative momentum well below Fermi momentum. Around Fermi momentum however almost all pairs found are deuteron-like (S,T)=(1,0). This is caused by tensor correlations that dominate in that momentum region. We observe similar but not identical results for the different interactions. The situation is much more complicated when we do not restrict the total momentum as shown on top. Whereas back-to-back pairs only show two-body correlations we find significant contributions from many-body correlations if we look at all pairs. These are especially visible in the significant contribution of (S,T)=(1,1) pairs that can be traced backed to three-body correlations induced by the tensor force. In Fig. 2 we show the same information in a different way that allows to compare with experimental data from JLAB measuring the ratio of proton-proton to proton-neutron pairs as a function of relative momentum.

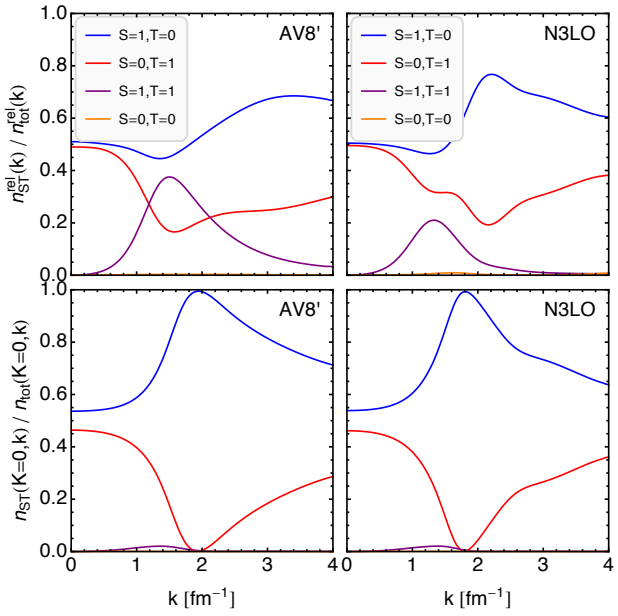


Figure 1: Contribution of the different spin-isospin channels to the total relative momentum distribution as a function of relative momentum. On top for all pair momenta, on the bottom for back-to-back pairs only. On the left for the AV8' interaction on the right for the N3LO interaction.

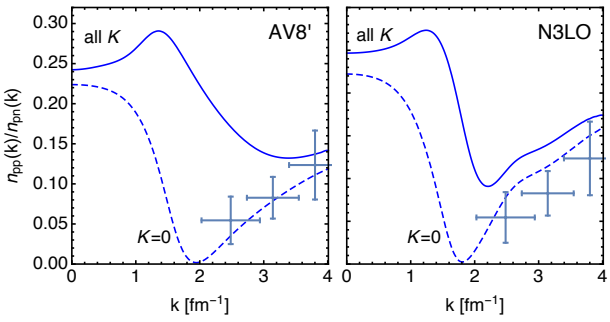


Figure 2: Ratio of proton-proton pairs to proton-neutron pairs for the AV8' interaction on the left and the N3LO interaction on the right. Full curves show the ratio for all pairs, dashed curves show the ratio for the back-to-back pairs. Experimental data are from [2]

References

[1] T. Neff, H. Feldmeier, W. Horiuchi, Phys. Rev. C 92, 024003 (2015)

[2] I. Korover et al. (Jefferson Lab Hall A Collaboration), Phys. Rev. Lett. 113, 022501 (2014).

Implementation of conservation laws at transition from hydrodynamics to microscopic transport in heavy ion collisions

C. Schwarz [1,2], D. Oliinychenko [1], L.-G. Pang[1], S. Ryu[1] and H. Petersen[1,2,3]

[1]Frankfurt Institute for Advanced Studies, Ruth-Moufang-Straße 1, 60438 Frankfurt am Main, Germany
[2]Institut für Theoretische Physik, Goethe-Universität, Max-von-Laue-Straße 1, 60438 Frankfurt am Main, Germany
[3]GSI Helmholtzzentrum für Schwerionenforschung GmbH, Planckstraße 1, 64291 Darmstadt, Germany

Heavy ion collisions, at the Relativistic Heavy Ion Collider (RHIC) and the Large Hadron Collider (LHC), are experimental tools to explore high-temperature QCD matter. Realistic dynamical models are indispensable to connect the experimental results with the properties (equation of state and transport coefficients) of hot QCD matter.

The current state-of-the-art are so called hybrid approaches, which combine viscous hydrodynamics and microscopic transport to take increasing mean free path into account. The transition from hydrodynamics to microscopic transport (dubbed 'particlization') is based on the Cooper-Frye formalism [1], which provides a connection between Boltzmann distribution function and momentum-space distribution emerging from specific 3-dimensional hypersurface such that energy and momentum are conserved.

$$\frac{dN}{d^3p} = \frac{d}{(2\pi)^3}\int_\Sigma f(x,p)\frac{p^\mu d^3\Sigma_\mu}{E_p} \quad (1)$$

where d and Σ are respectively degeneracy and hypersurface.

The simplest way to implement this formalism, which is also used in Ref. [2], is to sample each species at each space-time point independently, assuming grand canonical ensemble. Conservation of charges, energy and momentum is achieved only on average over events. This so-called “conventional” sampling starts by multiplicity sampling from Poisson distribution with average

$$\langle N_i\rangle_{1-cell} = d_i\left[\int \frac{d^3k}{(2\pi)^3} f_i(k)\right] u^\mu \Delta\Sigma_\mu \quad (2)$$

where u^μ and $\Delta\Sigma_\mu$ are the flow velocity and normal vector of the hypersurface, respectively. Then, the momenta of particles are sampled from the distribution function $f(x,p)$ near thermal equilibrium.

Even though the conventional way of particlization, in conjunction with oversampling, can be used to study single-particle distribution, the event-by-event conservation must be ensured to investigate fluctuations and correlations. It is shown in [3] that charge and energy can be globally conserved in each event by the Single Particle Rejection with Exponential Weights (SPREW) method.

To implement global charge conservation in the SPREW sampling, the average of conserved charge X (baryon number B, strangeness S and electric charge Q) is evaluated according to

$$X_{surface} = \sum_i X_i d_i \int_\Sigma n_i(x)\, u^\mu d^3\Sigma_\mu \quad (3)$$

where the summation goes over all particles species. If the newly sampled particle would result in larger deviations of the total charge from its average value (i.e., $X_{new\ particle}$ and $X_{sample} - X_{surface}$ have the same sign), it is rejected with the following probability.

$$P_{reject} = 1 - e^{-|X_{sample} - X_{surface}|} \quad (4)$$

After momenta are sampled in the same way as the conventional sampling, they are rescaled for energy conservation.

$$E_{surface} = \sum_n \sqrt{(1+a)^2 p_n^2 + m_n^2} \quad (5)$$

In the case of Au-Au collisions, the typical value of a is very small ($|a| \simeq 3$ %). Therefore, one finds that charge conservation does not lead to significant deformation of momentum-space distribution. Figure 1 shows global baryon number conservation in the SPREW sampling algorithm. These conservation laws are important for the fluctuation observables to measure the phase transition as it will be done at FAIR.

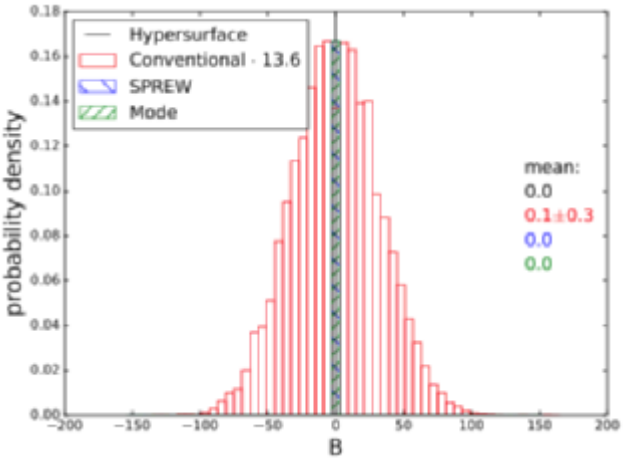


Figure 1: Probability distribution of net baryon number in Au-Au collisions with $\sqrt{s_{NN}} = 200$ GeV. Taken from Ref. [3].

References

[1] F. Cooper and G. Frye, Phys. Rev. D 10, 186 (1974).
[2] S. Ryu, J.-F. Paquet, C. Shen, G. S. Denicol, B. Schenke, S. Jeon and C. Gale, Phys. Rev. Lett. 115, no. 13, 132301 (2015) [arXiv:1502.01675 [nucl-th]].
[3] C. Schwarz, D. Oliinychenko, L.-G. Pang, S. Ryu and H. Petersen, J. Phys. G 45, no. 1, 015001 (2018) [arXiv:1707.07026 [hep-ph]].

Grants: Helmholtz Young Investigator Group VH-NG-822 from the Helmholtz Association and GSI

 DOI:10.15120/GR-2018-1

DDS: The Dynamic Deployment System

A. Lebedev[1] *and A. Manafov*[1]

[1]GSI, Darmstadt, Germany

The Dynamic Deployment System (DDS) [1] is a tool-set that automates and significantly simplifies a deployment of user-defined processes and their dependencies on any resource management system (RMS) using a given topology.

During 2017 we focused on shared memory channels, lobby-based deployment and DDS session feature.

Shared memory channels

In the initial implementation DDS agents used to have only a network connection transport for communication with user tasks. This introduced certain implications, for instance, there was no guarantee that all key-value updates or custom command messages will be delivered to the user. As a fallback solution a shared memory was used to cache messages coming from network channels, to make sure that all messages are actually delivered to the user tasks. In order to improve and simplify this algorithm we have implemented a generic shared memory channel. The channel has similar API as DDS network channel, it supports two way communication, asynchronous read and write operations. Its implementation is based on the boost::message_queue library [2], on the DDS protocol which is used for message encoding and decoding and on the boost::asio library [2] for thread pooling and implementation of the proactor design pattern. The shared memory channel is used for communication between DDS agents from the same lobby and between DDS agents and user tasks, which significantly simplifies and secures the implementation. There is no need to cache messages any more as we now can guarantee the delivery. All messages are stored directly in the shared memory and managed by the message queue.

Lobby-based deployment

The main goal of the DDS is to be able to handle hundreds of thousands user processes. In DDS world each user process is controlled by a DDS agent (watchdog). Having all agents connecting back to a central DDS server (commander) is extremely resource consuming. We therefore implemented a so-called lobby-based deployment feature.

DDS agents of a given user on one host represent a lobby. A lobby leader is the only agent, which has a direct network connection to commander. A lobby leader is elected locally on each host. The election process is a local negotiation between agents and no connection to the commander is required. All other agents are lobby members communicating with the commander via the leader. Agents of a given lobby communicate with each other via shared memory channels.

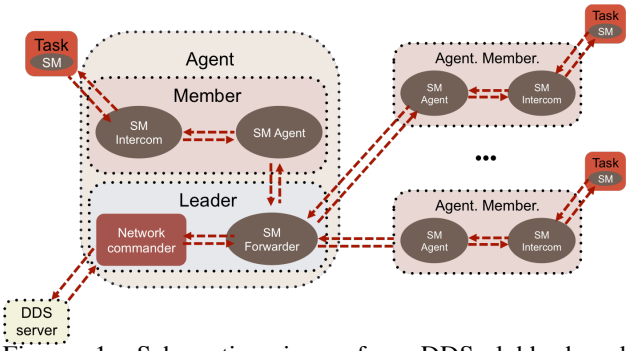


Figure 1: Schematic view of a DDS lobby-based deployment.

DDS session

We used to have only one main use case, which is Alice Online. For such a case it was enough to run one DDS session per user per host. Now other uses cases coming into the game. In offline analysis there are use cases, when a single user needs to run multiple different topologies hosting DDS commander on the same host. For the Grid and different RMS it might be useful to run DDS in a batch mode. For all these new use cases it is necessary to support multiple runtime topologies per user per host.

In order to cover these use cases a DDS session feature has been introduced. This new feature offers users a possibility to run multiple commanders on the same host. Each new commander instance creates a DDS session. Sessions are sandboxed and isolated, therefore can't disturb each other. Sessions can be operated (listed, cleaned, sorted, etc) using the new dds-session command.

References

[1] The Dynamic Deployment System (DDS), http://dds.gsi.de

[2] The BOOST C++ Libraries, http://boost.org

New release v6.3 of data acquisition framework MBS

J. Adamczewski-Musch[1], Nikolaus Kurz[1], Sergei Linev[1,]

[1]GSI, Darmstadt, Germany.

Since November 1, 2017, the MBS version 6.3 has become the new production version [1]. MBS version 6.3 replaces the old production version 6.2. The new MBS and its commands can be used as before.

New features

MBS version 6.3 provides several new features and improvements at the GSI installations. These are described in the following.

New GSI servers for MBS with dedicated VLAN

At GSI a pair of new servers for the MBS systems is in operation since May 2017. It will provide the DHCP, TFTP and NFS services for the diskless MBS nodes. In addition to the NFS mount point of the MBS installation ("/mbs") and various user partitions, the server will also provide NFS nodes with software installations of dabc ("/dabc"), Go4 ("/analysis"), and of EPICS ("/epics") frameworks for suitable platforms. Together with the new server, all MBS nodes moved from GSI LAN into the Virtual Local Area Networks (VLAN) MBS-NETZ (mbs nodes for experiments) or MBS-NETZ-ACC (nodes for accelerator tasks).

Support of 64 bit Linux

The complete source code of the MBS framework has been remanufactured to work also on 64 bit Linux systems. This has been tested on several X86 PC nodes running with Debian 7 and Debian 9. As a benefit from the enhanced address space, a larger pipe memory can be set up on such systems.

Linux device driver software

The driver software for the PCIe optical receiver boards PEXOR and KINPEX has been newly implemented for x86 Linux platforms [2]. This consists in a new kernel module "mbspex" with corresponding C library. Additionally, a command line tool" gosipcmd" allows front-end configuration and controls from the system shell.

Front-end control GUIs

Several Graphical User Interfaces (GUI) applications have been developed to monitor and control the properties of different kinds of front-end boards at the GOSIP readout chain. They are based on the Qt graphical library and are executed locally on the MBS readout nodes hosting the KINPEX board. Communication between such GUIs and the read-out slaves is provided by the mbspex device driver library safely concurrent to the MBS read-out. Currently GUIs are available for the proprietary GSI front-ends POLAND, NYXOR, FEBEX2 (TUM-addon), APFEL, and TAMEX2 (with PADI).

Remote control via DABC

In addition to the existing MBS status server socket, two new socket channels have been introduced to MBS for control with the software framework DABC [3]. They can be started optionally. Firstly they allow a remote steering of the MBS console from external scripts using the DABC "mbscmd" executable. Moreover, a DABC session connected to MBS in this way offers an HTTP server with a web browser GUI designed for generic MBS monitoring and control. Such DABC web server for MBS has been installed at all GSI MBS Linux nodes, and can be started by alias command "webmbs" [1].

White Rabbit support

The future FAIR general machine timing distribution will be based on the White Rabbit system [4]. The White Rabbit timing receiver (WRT) hardware PEXARIA (PCIe), EXPLODER5A (PCIe, USB), and VETAR2A (VME) is supported by MBS. WRTs provide a special "Time Latch Unit" (TLU) that can record the time stamp when an input signal changes, e.g. by the trigger signal. Driver software release "Cherry v4" of GSI-CSCO has been deployed on all MBS Linux platforms. Additionally, dedicated drivers for VMEbus on RIO4 and IPV systems have been developed. Especially for MBS, a "direct TLU access" mode is being tested to speed up the timestamp read-out compared with regular etherbone cycles.

New mass storage interface LTSM

A new API Lightweight Tivoli Storage Manager (LTSM) [5] is going to replace the RFIO interface to directly write DAQ data into the tape robot at GSI. MBS v6.3 still supports the RFIO protocol for local disk servers and for any existing GSI RFIO tape servers. Additionally, a special local RFIO server has been developed as a gateway to the LTSM archive [1]. This gateway application will be further tested and deployed at GSI in 2018.

References

[1] J. Adamczewski-Musch, N. Kurz, S. Linev: “GSI Data Acquisition System MBS Release Notes V6.3”, GSI, November 2017, https://www.gsi.de/mbs

[2] J.Adamczewski-Musch, N.Kurz, S.Linev: "MBSPEX and PEXORNET - Linux device drivers for PCIe Optical Receiver DAQ and control", IEEE TNS Vol 6-2 (February 2018), https://doi.org/10.1109/TNS.2017.2783043

[3] The DABC framework, http://dabc.gsi.de

[4] General Machine Timing System at FAIR wiki, https://www-acc.gsi.de/wiki/Timing/WebHome

[5] T. Stibor et al, LTSM source code, available: https://github.com/tstibor/ltsm/

 DOI:10.15120/GR-2018-1

Progress in FairDB development

D.Bertini[1] and Evgeny Lavrik[2]

[1]GSI, Darmstadt, Germany; [2]Universität Tübingen, Germany.

Introduction

FairDB[1] is a ROOT[2] based virtual database which allows to communicate and store data in different database management systems, such as PostgresSQL, MySQL, SQLite, based on the configuration. One of the primary use for it is FairROOT[3][parameter storage. FairDb is an insert only database, meaning there is no need to update the single entries and the whole history of the entries is available.

Data serialization

The base FairDb parameter classes have been expanded to support the data serialization in the JSON format. This allows the data exchange with non-ROOT environments such as LabVIEW[7] and web services. In addition to the existing data aggregation mechanism the introduction of the relational mechanism allows to establish one-to-one and one-to-many links between stored entries.

Database ROOT class generation

To improve the user experience, reduce the number of errors and further enhance the feature set of the FairDB the database class generation mechanism have been added [5]. It provides a web application based user interface to define the data format, which needs to be stored. Here, the user defines the classes, their properties and relations between classes. The classes are organized in projects, which can be loaded to and from the disk (Fig. 1).

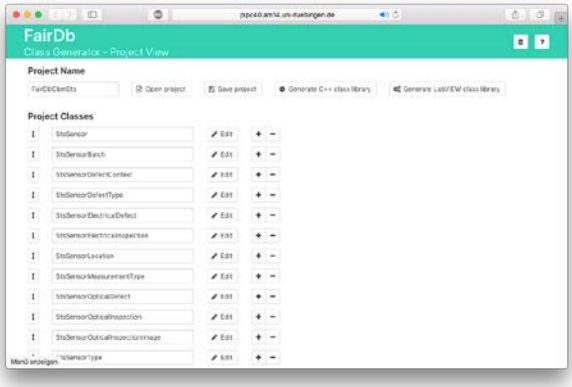


Figure 1: Graphical user interface to define the database classes organized together in projects.

Precise configuration of the properties such as their C++ type, database type, JSON type, default value etc. is available (Fig.2).

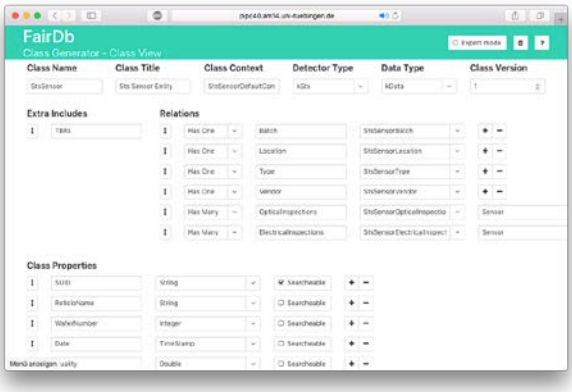


Figure 2: Graphical user interface to define the database class properties and relations.

After defining the class data, the user is offered to generate the class library, which is ready to be included into the FairROOT framework. Additionally the database configuration file and a template database data priming macro are included into the generated library.

For the detector groups using LabVIEW in their work, the generation of the LabVIEW class library is available.

Database content management system

Based on the user input for the class generation the content management system for the user data can be generated. This includes the RESTful web service, which communicates to the FairDB and serves the data in the JSON format for the consuming web application. The service provides the role-based data access control, requiring the user to authenticate before accessing the data. The secure HTTPS protocol is enforced for the data exchange between web service and web application. The web application itself allows the user to view, edit and add data to the database. The administrator's workplace allows managing users, who have access to the database, define their role and permissions to view and edit data. The content management system is generated based on the template and can be further expanded for functionality such as plotting the graphs based on the stored data. Visualization of the ROOT-native data such as TGeoVolume is available with JSROOT [6] framework.

Using FairDB: QA Data Scheme

The usage of the FairDB was covered in [4] and since then has been expanded to support the recent developments.

In a framework of the STS sensor optical inspection project the relational database schema have been developed and used for the data export (Fig. 3). The data gathered for 25 sensors inspected have been exported into FairDB which resulted in more than 49000 records inserted and the SQLite database file size of 18,9 MB.

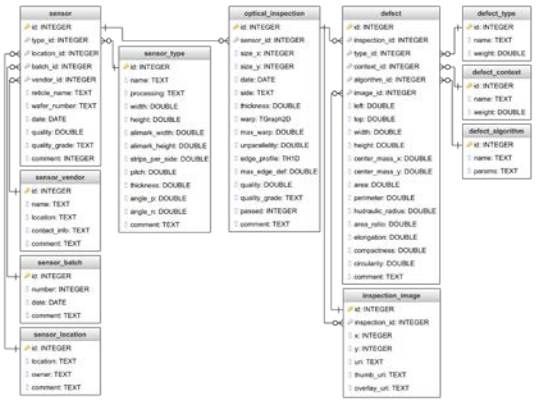


Figure 3: The database schema for the optical QA of the STS silicon sensors

The class generation described above was used to create the ROOT classes for data storage. The primary measurement data is obtained from LabVIEW program and stored in JSON format. A ROOT export macro was used to read the JSON data, deserialize it and store in the FairDB.

Using the generation of the database content management system the exported data was made available for the external users to be visualized and edited if allowed. The figure 4 (Fig. 4) shows the user workspace to view and edit the information about the sensor vendor.

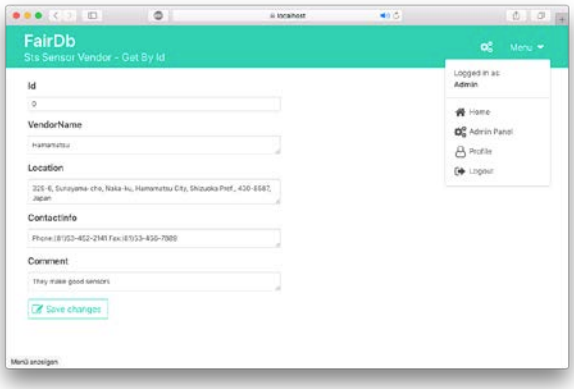


Figure 4: The generated graphical user interface to view the data of a data

Conclusion

FairDB virtual database provides flexible way to store and access detector specific data. The recent developments were targeted to enhance the user experience when defining the data to be stored. The generation of ROOT classes in a standard way not only simplifies the process but further improves the stability of the code as well.

The generation of the content management systems allows the ease of visualization and manipulation.

References

[1] D. Bertini. FairRoot Virtual Database (User Manual)
[2] R. Brun, F. Rademakers, P. Canal, I. Antcheva, D. Buskulic, O. Couet, A. and M. Gheata {\it ROOT User Guide} CERN, Geneva 2005
[3] The FAIR simulation and analysis framework 2008 J. Phys.: Conf. Ser. 119 032011
[4] D. Bertini {\em et al.}, CBM Progress Report 2015
[5] https://cbmgsi.githost.io/evgeny.lavrik/dbClassGen
[6] https://github.com/root-project/jsroot
[7] http://ni.com/labview

 DOI:10.15120/GR-2018-1

Status of the ALICE Tier2 Centre at GSI and first prototype of an ALICE Analysis Facility

K. Schwarz[1], S.Fleischer[1], R.Grosso[1], J.Knedlik[1], P. Kramp[1], T.Kollegger[1,]

[1]GSI, Darmstadt, Germany

This article describes the improvements implemented in 2017 in order to increase the reliability and performance of the ALICE Tier2 Centre at GSI as well as the setup of a first prototype of an ALICE Analysis Facility.

ALICE Tier2 centre at GSI and ALICE Grid in Germany

The ALICE Tier2 centre and the National Analysis Facility at GSI provide a computing infrastructure for the ALICE Grid and for the local usage of the German ALICE groups. The storage resources pledged to the global ALICE community (2300 TB) are provided via a Grid Storage Element which consists of a set of xrootd daemons in a redundant setup mode running on top of the Lustre file system. The main elements are two xrootd redirectors with a DNS alias as single point of entry in combination with three xrootd data servers as well as two xrootd forward proxy servers. The redirector of the GSI storage element is using the split directive of xrootd and redirects external clients to the external interfaces of the xrootd data server machines and internal clients to the internal interfaces which are directly connected to the local Infiniband Cluster. The xrootd forward proxy servers provide the possibility to Grid jobs running inside the protected HPC environment to read and write data from and to external data sources using the proxy interface. All ALICE Grid jobs running at GSI make use of the container technology Singularity. In this way the jobs can run smoothly in their standard Scientific Linux environment on top of the Debian based host system of the GSI HPC cluster. The complete setup is shown in fig. 1.

Throughout the year GSI participates in centrally managed ALICE Grid productions and data analysis activities, but also analysis jobs of individual users are running on the ALICE Tier2 centre. The overall share of successfully computed jobs in 2017 contributed by the German Grid sites, the GSI Tier2 centre and Forschungszentrum Karlsruhe (ALICE Tier1 centre) has been 10% of all ALICE Grid jobs worldwide. This corresponds well with the promised CPU resources for 2017: 28000 HEP-SPEC06 for GSI Tier2 (7% of the global Tier2 requirements) and 60500 HEP-SPEC06 for FZK (25% of the global Tier1 requirements).

References

[1] K. Schwarz et. al. First Challenges for the ALICE Tier2 Centre at GSI (PS05-4-466) Journal of Physics: Conference Series 331 (2011) 052018

[2] J. Knedlik, P. Kramp, Site specific XRootD related development, this Scientific Report

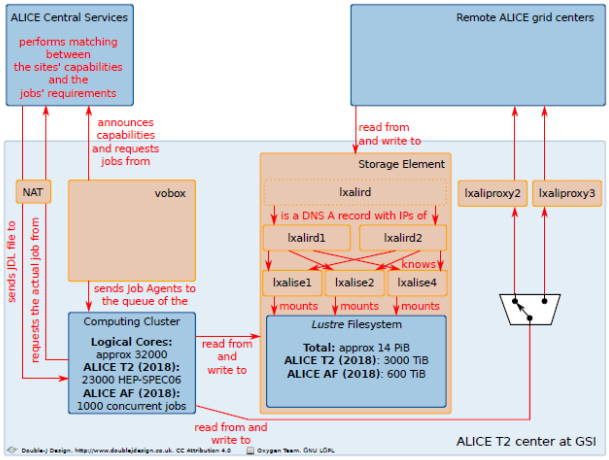


Figure 1: Setup of the ALICE tier centre at GSI

Prototype of an ALICE Analysis Facility

In LHC Run 3 ALICE data analysis will take place on a few dedicated Analysis Facilities of which GSI will become one of the first. On the storage element only analysis data sets (AODs) will be stored. A first prototype of an ALICE Analysis Facility has been set up at GSI based on the design of the current ALICE Tier2 centre, but optimised for I/O performance. Initial resources are 600 TB disk space and 1000 concurrent job slots taken from the Tier2 allocation. A first complete data set has been transferred and a first analysis train ran successfully.

XRootD Plugins

In order to optimise the current storage infrastructure, namely the access to Lustre through XRootD data servers, several XRootD Plugins have been developed. One solution provided is a server based Plugin which is able to redirect XRootD file operations directly to Lustre thus bypassing the need for Grid jobs running at GSI to double the network traffic by first communicating with the XrootD data servers. A second Plugin creates symlinks for data stored on Lustre providing logical file names as they are used in the ALICE Grid File Catalogue. A third solution provided is a Plugin which reports to the central ALICE Grid Monitoring the ALICE Grid quota on Lustre instead of the full Lustre capacity at GSI as it did before. All three Plugins described above are in operational mode at the ALICE Analysis Facility prototype at GSI.

Status of the R3BRoot framework

D. Kresan[1], M. Al-Turany[1], V. Wagner[2], M. Heil[1], B. Löher[1,2], the R³B collaboration, and the FairRoot group

[1]GSI, Darmstadt, Germany; [2]TU, Darmstadt, Germany

Reactions with Relativistic Radioactive Beams (R³B) is an international collaboration [1] which will perform nuclear physics experiments at the future FAIR facility. The focus of these experimental studies is put on nuclear structure and dynamics of exotic nuclei far off stability, as well as astrophysical aspects and technical applications. Combination of different detection sub-systems and a sophisticated data acquisition require a dedicated software package to allow physicists both to simulate an experiment and to analyze experimental data. The R3BRoot software framework [2] was created for this purpose. It is based on FairRoot [3] – common software for FAIR experiments. A group of 17 developers is currently working on extending features of R3BRoot and including support for all planned R³B detectors. The framework is written in C++, is ROOT based, compiled of approximately 35000 lines of code and can be deployed on Linux and macOS. The C++11 standard is supported. The code is stored and distributed via GitHub [4] with continuous integration workflow. Close to 40% code coverage with quantitative automatic tests allow to immediately detect possible violations of the program functionality and to results of numeric algorithms.

Data analysis

Several experiments, including the commissioning run of R³B, will be performed fall of 2018 using beam from SIS18 at GSI. The largest effort is put into the development of algorithms for detector calibration up to so-called HIT-level: measurement of coordinates in cm (local frame), energy-loss in MeV and time in ns. Following detectors are currently calibrated in R3BRoot: start detector LOS, proton and gamma calorimeter CALIFA, neutron detector NeuLAND, heavy fragment tracker arm PSPx, TOFd, and proton ToF wall. The later analysis stage, which is called fragment tracker, should combine the single measurements and fit an ion trajectory in a non-homogeneous dipole field in order to determine mass and momentum of a reaction fragment. This measurement in combination with data from proton ToF wall and NeuLAND will give the possibility to calculate properties of incident reaction.

Another important tool, which is also being developed, is an online event-display to support near-line analysis during data taking. The online event display of R3BRoot will be a tool for monitoring of the detectors and for an immediate decision about the quality of the data. Several successful tests were already performed with cosmic rays.

Simulation

Simulation of the upcoming R³B experiments is required for:

- detailed design of a setup,
- feasibility study of a measurement of an observable,
- development and testing of physics analysis algorithms,
- a better understanding of background effects, present in experimental data.

In order to develop an algorithm for fragment tracking and to compare simulated and experimental data on the HIT level, digitizer tasks have been implemented for TOFd and 3 tracking fiber detectors. A digitizer is an algorithm, which simulates the response of a detector and converts Monte Carlo results into detector-like signals. Mainly effects from geometry granularity, read-out scheme, and non-perfect resolution were included.

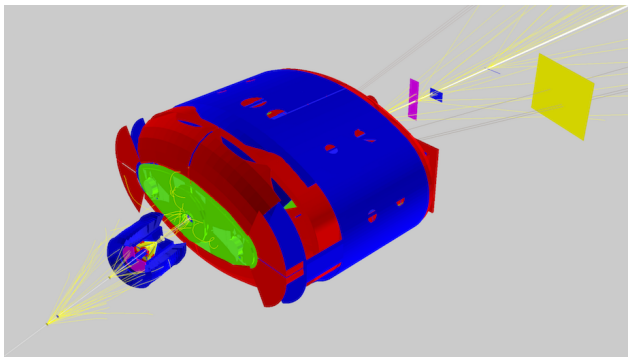


Figure 1: Visualisation of the R³B detector geometry and particle trajectories using the simulation event display of FairRoot. Large volume in the middle – GLAD magnet. Beam direction from the bottom left corner.

Concerning the neutron measurement, a new algorithm based on statistical scoring is being developed and tested with simulated data. This new technique should have better performance with respect to separating classes of multi-neutron events.

The simulation code for CALIFA spectrometer is under construction to match detector response of the real-size prototype, which will be also tested during experiments end of 2018.

The development of the fragment tracker is ongoing. Currently, we have the tool for propagating a charged particle in the magnetic field of GLAD through the detector geometry and a machinery for the fitting of ideal measurements without taking into account energy-loss in a material. The first realistic version of the algorithm is expected mid of 2018.

Summary

Current status of software development in R³B, presented in this report, is the result of coordination of activities within the international community, representing different detector working groups. R3BRoot is on a good track towards supporting experimental runs fall of 2018 / 2019

 DOI:10.15120/GR-2018-1

and towards performing high-level physics analysis of accumulated data. Preliminary tests of the fragment tracker show feasibility of momentum reconstruction with resolution in the order of 10^{-3}.

References

[1] R^3B, https./www.gsi.de/r3b
[2] R3BRoot, http./www.r3broot.gsi.de
[3] M. Al-Turany et al., J. of Phys. Conf. Ser. 396 (2012) 022001
[4] R3BRoot code repository, https./github.com/R3B-RootGroup/R3BRoot.git

Ongoing site specific XRootD related development

J. Knedlik[1], P. Kramp[1]

[1]GSI, Darmstadt, Germany

1.1 Abstract

Operating an XRootD service, the established software standard for WAN data access in HEP and HENP. Accessing the scientific data, stored on-top of the HPC infrastructure at the ALICE Tier 2 centre and the ALICE Analysis Facility prototype at GSI, revealed multiple challenges and requirements. This article describes the current state of development for XRootD based solutions, especially XRootD client & server plug-ins.

1.2 ALICE Analysis Facility & XRootD

GSI is operating the only German ALICE Tier 2 centre and will operate one of the first ALICE Analysis Facilities(ALICE AF) for which a prototype is currently being set up. In this context, GSI will provide computing and storage resources to the ALICE community. In ALICE's AliEn Grid framework data is accessed through the XRootD protocol. XRootD enables the use of this data through a scalable federated storage system. At GSI, instead of operating XRootD servers with local storage, the shared HPC Lustre filesystem is used as storage backend of the XRootD servers. In AliEn, Grid jobs requiring the same data are preferably scheduled on the same site to lower the need for traffic between sites. This means, that local data is reused many times and therefore it is essential to optimize the I/O performance.

1.2.1 Improving the I/O performance at GSI using XRootD plug-ins

With the current storage infrastructure at GSI, namely the access to Lustre through the XRootD data servers, the following room for improvement has been identified: The three XRootD dataservers can provide limited I/O bandwidth and all data read locally via XRootD from Lustre needs to be sent over the network twice (Lustre to XrootD server & XrootD server to client), effectively doubling the network traffic for an I/O operation.

In addition, the need for additional XRootD dataservers to handle data is eliminated.

As an improvement to last years solution[1], an XRootD client plug-in, which had to be loaded by all clients running on the GSI hpc cluster, an XRootD redirector plug-in was developed.

A redirector server may load this plug-in in order to redirect clients to locally available files, if both client and redirection target are inside a private network, as this guarantees local availability of the required file at the Lustre filesystem. In order to allow redirection to a local file, additional changes needed to be implemented into the XRootD base code.

The cooperation with the XRootD core development team resulted in the integration of necessary client and server side changes in the XRootD base code. Since XRootD Version 4.8.0, a local redirection of a client by a redirector is possible with the use of the cms plug-in we developed. In addition, the plug-in is able to distinguish between new and old clients and will only redirect newer clients that have the capability to handle such a redirection to a local file.

1.3 XRootD Disk Caching Proxy for opportunistic resources

In cooperation with KIT, an infrastructure for the utilization of opportunistic resources such as clouds, has been developed for CMS. The idea is to build a virtual site inside the opportunistic resource. In order to minimize external I/O and to provide high data locality, an XRootD disk-caching-proxy is used.
In this setup, all clients access data through a redirector, which tells the client the location of the desired data. The redirector either directs the client towards the locally available shared filesystem, in case the data exists on it, or to the disk-caching-proxy. The disk-caching-proxy forwards the request to external sites and retrieves the data. In the meantime, the data is being cached on the shared filesystem for later use.
In case jobs working with the same data are bundled together, this infrastructure minimizes I/O and speeds up data accesses inside the virtual site.
This infrastructure relies on XRootD-plug-ins developed at GSI. One plug-in handles the referral to the redirector2 while the second plug-in handles the redirection to the proxy or shared file system3. A test setup has been deployed on the bwhpc4 cluster NEMO at Freiburg

1.4 Conclusion

In conclusion we have implemented XRootD plug-ins redirecting clients to data on Lustre which significantly improves the I/O performance. Last years proposed changes have been integrated into the XRootD main base by the XRootD development team. In addition, an XRootD infrastructure to utilize opportunistic resources has been developed.

References

[1] "GSI Scientific Report 2016", doi = 10.15120/GR-2017-1, http://dx.doi.org/10.15120/GR-2017-1
[2] https://github.com/pkramp/RedirPlugin/tree/kit-proj
[3] https://github.com/jknedlik/XrdProxyPrefix/tree/kit-proj
[4] http://www.bwhpc-c5.de/en/

 DOI:10.15120/GR-2018-1

Annealing studies of avalanche photodiodes irradiated with different γ-doses

R. Ganai[1], A. Wilms[1], D. Scharnberg[1], J. Bailey[1], A. El Mosleh[1], P. Wicke[1], H. Al-Turany[1], C. Warneke[1].

[1]GSI, Darmstadt, Germany.

Introduction

Avalanche **P**hoto**D**iodes (APDs) used in **H**igh **E**nergy **P**hysics (HEP) experiments are supposed to operate at very hard environmental conditions like high magnetic elds and high radiation doses for a long period of time. Hence the long term annealing behavior needs to be investigated. Preliminary results of an annealing period of ~7 days under applied bias voltage are presented in this report.

Annealing studies of APDs

Sixteen APDs were irradiated with di erent γ-doses of 37 Gy, 100 Gy, 200 Gy, 500 Gy, 1000 Gy, 1500 Gy, 2200 Gy and 2680 Gy. Eight of them were operated with bias voltage applied during irradiation and the others had no electrical contacts during irradiation. After irradiation, the APDs were annealed with a reverse bias voltage of 100 V applied for ~7 days at the Photo Sensor Laboratory (PSL), GSI. During annealing, the temperature was raised from room temperature to 80° C and was then kept constant. The current values for biased and unbiased APDs during irradiation were monitored during the whole annealing period and are shown in Figure 1 and Figure 2 respectively. The applied γ-dose values are stated in the included legends.

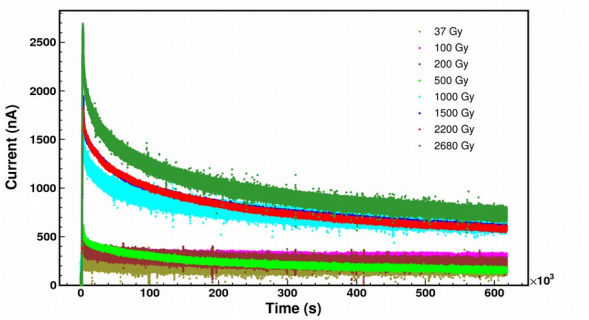


Figure 1: Annealing curves of eight di erent APDs irradiated with di erent γ-dose under the condition of applied bias voltage during irradiation.

In order to investigate the long term annealing behaviour of the APD current, the tail parts of the curves shown in Figure 1 and Figure 2 (in the time interval of $200*10^3$ s – $620*10^3$ s) were tted with a linear function. A comparison of the decrease in the rate of change of the leakage current values for all sixteen APDs is shown in Figure 3.

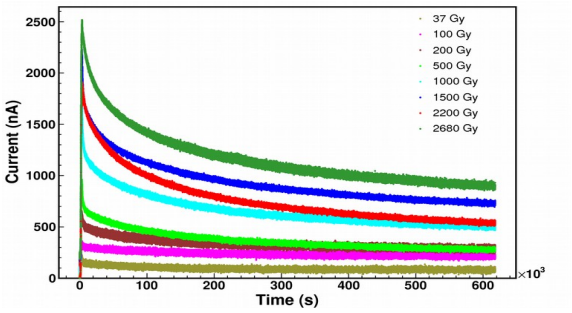


Figure 2: Annealing curves of eight di erent APDs irradiated with di erent γ-doses with no electrical connections during irradiation.

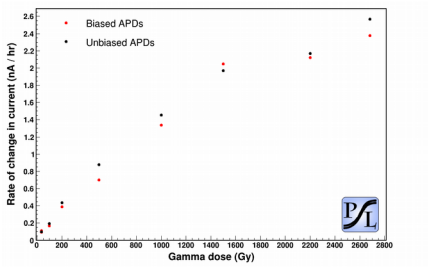


Figure 3: Comparison of the decrease in the rate of change of the leakage current for APDs irradiated under biased and unbiased conditions. The error bars are within the marker size.

Results and conclusion

A set of 16 APDs was annealed with a reverse bias voltage of 100 V after irradiation with di erent γ-doses. The annealing temperature was increased from room temperature to 80° C and was then kept constant. The decrease of the APD leakage current was studied, regarding the in uence of long term annealing e ects. The higher the γ-radiation dose was, the faster the leakage current decreases. This is consistent with the assumption of an exponential time dependence of trap recovery with a large time constant (~10^5 s). The unbiased APDs showed higher rate of decrease in current with respect to biased APDs except for a γ-dose of 1500 Gy which needs to be tested in more detail.

Acknowledgment

We sincerely acknowledge the help rendered by our colleagues at UGC-DAE Consortium for Scienti c Research, Kolkata Centre and Mr. Vinod Singh Negi, for their sincere e orts to irradiate the APDs with di erent γ-doses.

Development of a 128 channel ≤ 500 ps RMS TDC system for MBS DAQ

H. Heggen[1], S. Minami[1] and N. Kurz[1]

[1]Experimentelektronik – GSI, Darmstadt, Germany

Introduction

The precise measurement of time has become one of if not the most important tool in particle identification experiments which usually rely on time-of-flight, drift time and/or pulse-width measurements. Most of the in-house time-to-digital converter (TDC) developments of recent years were aimed at achieving highest precision (down to 7 ps) [1,2]. However, there are many applications that do not require such high precision and which would benefit from a system with moderate precision but higher channel density and lower channel price. Here we report on the development of a TDC system with 128 channels and a precision better than 500 ps for the MBS (Multi Branch System) data acquisition framework [3,4,5].

Prototype hardware

The prototype hardware (see figure 1) features 128 differential input channels for LVDS signals. The channels are distributed over 8 board-to-cable connectors to allow the connection of 16-channel front-end cards via flexible flat cables. A first 16-channel analog front-end based on the PADI (preamplifier-discriminator) ASIC [6] has also been developed (see figure 1). The front-end features a standard 2.54 mm square socket for signal input making it easy to adapt to various detector systems. The PADI front-end is designed for input signals between a few mV and ~200 mV. Larger signals can be accommodated by equipping an attenuator network at every input.

Results & Outlook

Laboratory tests with the described prototype system already yield an average precision well below 400 ps RMS for both, channel-to-channel and pulse-width measurements. The TDC is dead-time free and currently has a double-pulse resolution of ~10 ns. However, development of the FPGA circuit implementation is still ongoing [7] and these figures are not final yet.

The prototype system has also just been deployed in a first beam time at KVI-CART, reading out a total of 1024 channels of multi-anode photomultiplier tubes to test various fibre detector prototypes for the NUSTAR-R3B experiment. The tests were very successful for both, detectors and electronics and preparations have been started to equip the R3B experiment with 2048 readout channels for the 2018 beam time.

For the coming years, more than 6000 readout channels are foreseen at the R3B experiment and the development of dedicated hardware has been started. Various other NUSTAR experiments and Super-FRS particle identification are also considering the use of this new TDC system, potentially adding up to another 25 000 channels in the long-term.

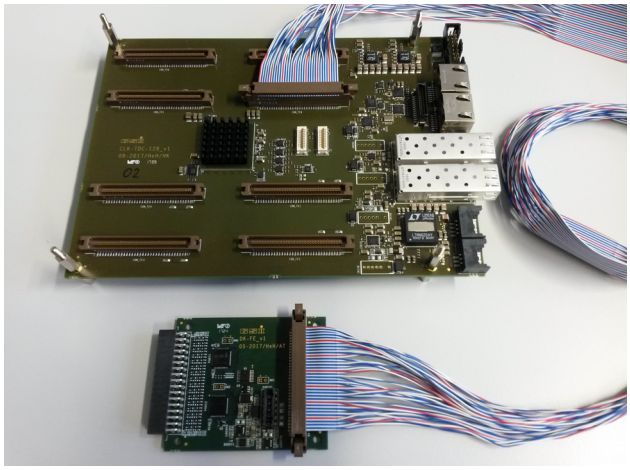


Figure 1: The prototype hardware consists of the CLK-TDC-128 motherboard with 128 channels (LVDS inputs) tailored to read out up to eight 16-channel analog front-ends based on the PADI ASIC [3].

References

[1] C. Ugur et al., "264 Channel TDC Platform applying 65 channel high precision (7.2 psRMS) FPGA based TDCs", IEEE Nordic Mediterranean Workshop on FPGA based TDCs (NoMe TDC), 2013, p. 1-5;

[2] C. Ugur et al., "A novel approach for pulse width measurements with a high precision (8 ps RMS) TDC in an FPGA", Topical Workshop on Electronics for Particle Physics (TWEPP), 2016.

[3] H.G. Essel and N. Kurz, "The General Purpose Data Acquisition System MBS", IEEE Trans. Nucl. Sci., vol. 47, no. 2, 2000, p. 337-339, www.gsi.de/mbs;

[4] J. Adamczewski-Musch et al., "MBSPEX and PEXORNET-Linux Device Drivers for PCIe Optical Receiver DAQ and Control", IEEE Trans. Nucl. Sci., vol.65, no. 2, 2018, p. 788-794;

[5] S. Minami et al., "Design and Implementation of a Data Transfer Protocol Via Optical Fiber", IEEE Trans. Nucl. Sci., vol. 58, no. 4, 2011, p. 1815-1819.

[6] M. Ciobanu, "PADI, an Ultrafast Preamplifier-Discriminator ASIC for Time-of-Flight Measurements", IEEE Transactions on Nuclear Science, vol. 61, no. 2, 2014, p. 1015-1023.

[7] S. Minami et al., "An FPGA implementation of a 128-channel sub-nanosecond time-to-digital converter", in this report.

Experiment beamline: FRS / R3B
Experiment collaboration: NUSTAR-R3B / NUSTAR-SuperFRS-Experiments
Accelerator infrastructure: Super-FRS

 DOI:10.15120/GR-2018-1

An FPGA implementation of a 128-channel sub-nanosecond time-to-digital converter

S. Minami[1], H. Heggen[1] and N. Kurz[1]

[1]GSI, Darmstadt, Germany

There has been demand for the development of a time-to-digital converter (TDC) which has moderate time resolution, better than 500 ps, but has high channel density to be cost effective. The technique to realize field programmable gate array (FPGA) based TDCs have long been studied by many former works [1-3]. The easiest way to implement a TDC in a FPGA is to sample an input signal with a flip-flop operated by a clock with period $T_{clk.}$, resulting in a TDC bin width of T_{clk}. In order to achieve better precision than the method limited by maximum clock frequency of FPGAs typically around 500 MHz, we have adopted a method sampling the input signal with a set of several phase-shifted clocks of the same frequency. In the ideal case that all clocks are distributed without delay and skew, this results in a TDC bin width of T_{clk}/N_{clk} where N_{clk} is the number of shifted clocks. The method consumes low amount of logic resources, allowing the integration of more channels per FPGA [3].

In recent years, various front-end electronics with FPGAs and the small form-factor pluggable (SFP) transceivers have been developed to coop with our data acquisition (DAQ) framework, the multi-branch-system (MBS), supporting readout by a standard PC equipped with a PCIe card via our custom data transfer protocol GOSIP [4]. We started the implementation of a TDC on one of those existing devices with an XC7K160T, the second smallest FPGA in Kintex-7 family, classified as the best price/performance/watt at 28 nm[5].

The maximum frequency of the FPGA is 400 MHz, however we started with a clock frequency of 250 MHz and 8 phase-shifted clocks created by one Mixed-Mode Clock Manager (MMCM) module just to achieve the targeted precision of ≤500 ps [5]. As to the number of input channels, 128 differential channels were implemented since that is close to the limitation imposed by the number of IOs of the FPGA. A 12-bit coarse time counter operated by 250 MHz clock enables a maximum trigger window of 16 μs. Ones among the 8 flip-flops for fine time determination are summed and converted into 4-bit-wide data. A fine time and a coarse time for leading edges and trailing edges of a single input are combined and stored in a ring-buffer with a depth of 1024. At the very moment a pre-set trigger delay time has passed after accepting a trigger signal, the data in the ring-buffer are examined on whether they are within a pre-set time window relative to the trigger time. Only valid data are recorded in the second buffer of the same size. After parallel processing of 129 channels including the trigger signal, the data are merged into one of two output buffers with a size of 16 Kbytes connected to the GOSIP readout module. The implemented TDC utilized only 24 % of the FPGA logic resources as listed in Table 1.

Resource	Used	Available	Utilization
Slice LUT	24324	101400	24 %
Slice Flip-Flop	46664	202800	23 %
Block RAM	275	325	85 %
MMCM	2	8	25 %
IO	384	400	96 %

Table 1: Resource utilization of the FPGA TDC[5]

A new electronics dedicated TDC applications, CLK-TDC-128, has been designed and produced [6]. The precision of the FPGA TDC on the new electronics was evaluated by measuring time differences between 2 channels using a LVDS fan-out board. The single channel RMS resolutions were demonstrated to be better than 400 ps for all the channels.

References

[1] J. Kalisz, “Review of methods for time interval measurements with picosecond resolution”, Metrologia 41, 2004, p.17-32

[2] C. Ugur et al. "264 Channel TDC Platform applying 65 channel high precision (7.2 psRMS) FPGA based TDCs," IEEE Nordic Mediterranean Workshop on FPGA based TDCs, (NoMe TDC) 2013 pp.1-5

[3] M. Büchele et al., “The GANDALF 128-Channel Time-to-Digital Converter”, Physics Procedia 37, 2012, p. 1827-1834; A. Balla et al., “The characterization and application of a low resource FPGA-based time to digital converter”, Nucl. Instr. Meth. Phys. Res. A 739, 2014, p. 75-82

[4] H.G. Essel and N. Kurz, “The General Purpose Data Acquisition System MBS,” IEEE Trans. Nucl. Sci., vol. 47, no. 2, 2000, p. 337-339; J. Adamczewski-Musch et al., “MBSPEX and PEXORNET-Linux Device Drivers for PCIe Optical Receiver DAQ and Control” IEEE Trans. Nucl. Sci., vol.65, no. 2, 2018 p. 788-794; S. Minami et al., “Design and Implementation of a Data Transfer Protocol Via Optical Fiber” IEEE Trans. Nucl. Sci., vol. 58, no. 4, 2011, p. 1815-1819

[5] Xlinx Inc. 7-Series FPGAs Data Sheet: Overview DS180 2018; 7-Series FPGAs Cloking Resources User Guide UG472 2017

[6] H. Heggen et al., “'Development of a 128 channel ≤ 500 ps RMS TDC system for MBS DAQ” in these reports

Monte Carlo simulations in FairMQ

R. Karabowicz[1], M. Al-Turany[1], D.Klein[1], T.Kolleger[1], D.Kresan[1], A.Lebedev[1], A. Manafov[1], A. Rybalchenko[1], F. Uhlig[1]

[1]GSI, Darmstadt, Germany

The FairMQ framework developed currently by the FairRoot group allows users reliable and transparent data exchange between devices – computer processes created by the user. The following paper summarizes our effort to run Monte Carlo simulations in separate devices parallelly and store or analyse created data.

Simulation parallelization

The Monte Carlo simulations are arguably one of the most time and resource consuming parts of the computing aspects of the modern experiments. Many efforts are committed to facilitate the costly simulations, and these can be grouped by the level of parallelization applied. The most general strategy uses multi-processor computer farms to run individual simulations that store output data in separate output files. Similar approach was adopted by the GEANT4 group, that uses multithreading to delegate simulation of individual events to different threads. Another level of parallelism is to assign transport of single particles to separate threads within one process. In this report the first of the described approaches has been applied.

FairMQ simulation example

As a base for this work a running FairMQ example described in [1] has been used. There, a set of devices to read, analyse and store FairRoot compliant data has been described. Two of these devices could be reused in the simulation example, namely the FairMQEx9TaskProcessor to process data, and the FairMQEx9Sink to store the output data in a ROOT file. The ParameterMQServer had to be greatly extended, its purpose to read parameter files and to provide parameters needed to reconstruct the data has been extended by the ability to receive parameters and to store them in output files. A completely new device has been introduced, a FairMQSimDevice, to perform Monte Carlo simulations using standard FairRunSim class, with user's set of detectors specified in the running executable.

The example topology is presented in the Figure 1. Each box in the figure represents a running device. The data flows from left to right through channels, drawn as lines. The leftmost devices, the FairMQSimDevices, run separate simulations of the same detector set. It should be stressed that it is possible to start any number (limited by the available resources) of these devices, thus increasing the simulation event rate. In the shown example, the data is sent straight to one of the FairMQEx9Sinks, where it is stored directly in the ROOT file. Furthermore, the same data is sent over to FairMQEx9TaskProcessor, which processes the data in the way specified by the user task attached to the processor. Such processed data is subsequently stored in the ROOT file by the second FairMQEx9Sink. To perform more complicated tasks, the user may create any other path for the data to be processed, implementing layers of desired TaskProcessors.

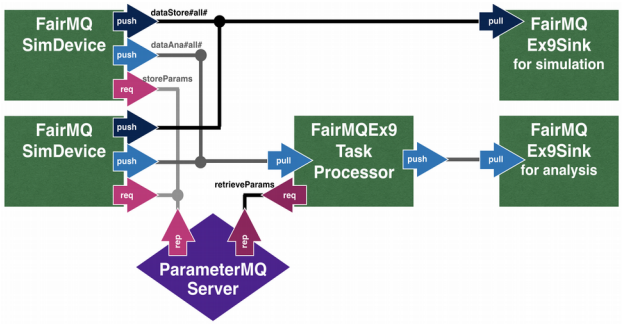


Figure 1: Schematic view of the running topology.

In the bottom of the figure the ParameterMQServer device is presented. It connects to the simulation devices, which use the server to store the simulation parameters. After receiving any of the parameters, the server automatically saves them in a file specified by the user. The other connection is reserved for the processing devices, which need simulation parameters to process data. Besides, the ParameterMQServer may read and distribute parameters stored in ASCII or ROOT files.

FairSink

It is worthwhile to mention, that the FairMQSimDevices do not themselves write any data to disk. To allow this, the FairRootManager has been redesigned in a way similar to that presented in [2]. Namely, the data storing functionality has been moved to a separate abstract class, called FairSink. The default FairRoot macros store data in the output ROOT files using FairRootFileSink implementation. In the case of FairMQ, the produced date is sent via FairMQSimDevice, which as well derives from FairSink.

Summary

This paper presents the example of running the Monte Carlo simulations in the FairMQ framework. The data from simulations running parallelly on different processes (even on different computers) may be sent to a device capable of either storing the data or processing it. These building blocks may be used by users as a base for creating more sophisticated topologies.

References

[1] R. Karabowicz et al, "Message based reconstruction example in FairRoot", GSI Scientific Report 2016.

[2] R. Karabowicz et al, "Redesign of the FairRootManager", GSI Scientific Report 2014.

 DOI:10.15120/GR-2018-1

Advancing shared memory transport in ALFA

A. Rybalchenko[1], M. Al-Turany[1], D. Klein[1],

[1]GSI, Darmstadt, Germany;

The ALFA framework [1] is a common ALICE/FAIR software layer that offers a platform for simulation, reconstruction and analysis for particle physics experiments. In addition to standard services provided for simulation and reconstruction, such as event generation, magnetic field and so on, ALFA also provides tools for inter-node and inter-process data transport, configuration and deployment. The FairMQ component of ALFA [2] provides building blocks for creating processes that communicate between each other via message passing. It offers an abstract interface with different implementations of different transport technologies. This report presents the most recent developments and improvements to the FairMQ transport layer with the focus on the shared memory transport.

Shared memory transport in FairMQ

The original implementation of FairMQ used ZeroMQ library [3] for transport of the data via network or inter-process communication. It was quickly realized that in order to stay future-proof, the transport details need to be hidden from the user behind an abstract interface. Since then two new transports have been introduced (and fourth is under development) that the user can switch to via a simple configuration change, without having to modify any code. The new shared memory transport [4] builds upon Boost.Interprocess library [5] in connection with ZeroMQ to offer an efficient and zero-copy transport implementation between processes on the same node.

Unmanaged region

The shared memory transport, as all other transports in FairMQ, hides all memory allocation details from the user, with the aim of ease of use. The user can simply request memory of certain size, which, after filling, will be transferred to further processes. However, in some special cases the user needs to control the memory layout and allocation in much greater detail. Example for this is a detector readout that requires certain memory layout restrictions and optimizations. Ideally, in such a use case the data from this carefully controlled memory should reach all of its receivers with no or minimal copies. This becomes particularly important for shared memory, where no copy is the main goal of the transport.

To support this a feature called Unmanaged Region has been introduced to FairMQ. It allows to define a custom memory region, which is under full control of the user. The region is created using the transport methods provided by FairMQ, therefore ensuring maximum efficiency and no unnecessary copies. The user can then give FairMQ subsets of this region, which will be sent as messages to interested processes. In case of shared memory, no copy of the data is involved. The receiver will see the message as a regular message and does not need any special knowledge of the region layout. Furthermore, the sender is notified whenever a message has been processed by the receivers and the transport, so that it can then cleanup and reuse the parts of the region.

Automated cleanup

All the shared memory creation and destruction in FairMQ is done behind the scenes. Because shared memory can outlive the process, a proper cleanup needs to be done to avoid polluting the system with unused memory. This is done automatically by the transport implementation by monitoring shared memory usage and cleaning up when all users have finished their work. Even for the cases when processes crash, the memory will be cleaned up by an automated and independent monitor process. The cleanup tools also offer monitoring information on the shared memory.

Flexible message creation

The most efficient way to prepare messages for transfer in FairMQ is by requesting messages of certain size and filling them with data. This avoid unnecessary copies of user buffers to transport buffers. However, certain algorithms, such as compression or reconstruction may not know the size of their data in advance. To make sure they also can be handled in an efficient way, FairMQ now provides a mechanism to request an upper bound size buffer from the transport, which can be efficiently shrinked after filling by giving the framework the used size. For shared memory this allows rapid reuse of unused memory, and for other transports this reduces the size of the transfers and reduces the amount of meta information to include with each message.

References

[1] M. Al-Turany et al., “ALFA: A new Framework for ALICE and FAIR experiments”, GSI Scientific Report 2013

[2] A. Rybalchenko, and M. Al-Turany, “Streaming data processing with FairMQ”, GSI Scientific Report 2013

[3] ZeroMQ: http://zeromq.org/. Last visit 15.03.2018

[4] A. Rybalchenko, and M. Al-Turany, “FairMQ status”, GSI Scientific Report 2016

[5] Boost.Interprocess: http://www.boost.org/doc/libs/1_66_0/doc/html/interprocess.html Last visit 15.03.2018

Experiment beamline: none
Experiment collaboration: none
Experiment proposal: none
Accelerator infrastructure: none
PSP codes: none
Grants: none
Strategic university co-operation with: none

 DOI:10.15120/GR-2018-1

A prototype for a new 108 MHz CW RFQ for the HLI

D. Koser[1], P. Gerhard[2], O. Kester[3], and H. Podlech[1]

[1]IAP, University of Frankfurt, Germany; [2]GSI, Darmstadt, Germany; [3]TRIUMF, Vancouver, BC, Canada

With the aim of developing a completely newly revised cw capable 4-rod RFQ structure for the HLI, a 108 MHz prototype with six stems was designed at IAP based on the already approved concepts from the RFQs for FRANZ and MYRRHA [1, 2]. The structure was manufactured by NTG [3] and has been delivered to IAP in November 2017. Besides for the required cooling capabilities regarding cw operation, the prototype was optimized for the prevention of mechanical vibrations of the electrodes. This was taken into consideration because the currently operated HLI-RFQ suffers from severe modulated power reflections, which evidently originate from rf affecting mechanical electrode oscillations [4, 5] and impose restrictions to stable operation as well as limit the achievable performance. The simulated properties of the prototype design shall be validated by measurements investigating the mechanical behaviour and rf performance.

RF & Mechanical Design

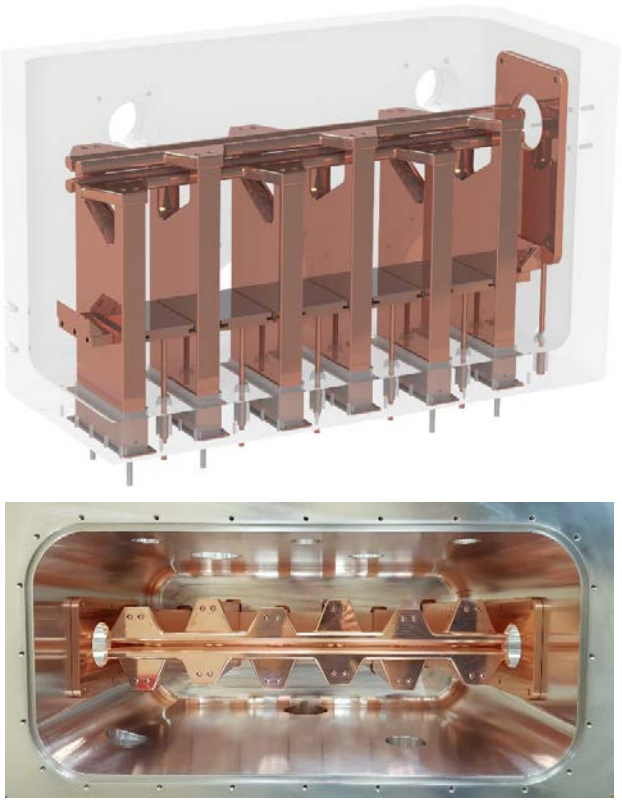


Figure 1: Rendered sectional view of the 6-stem RFQ prototype with transparent tank (above) and top view (below).

Figure 1 depicts the mechanical design of the prototype structure, which features six stems with a height of 283 mm at a distance of 120 mm. The stem arms of the lower electrode have a sideways offset of 15.9 mm (see top view) for dipole compensation. The electrode profile is non-modulated with an aperture radius of 4 mm and an electrode radius of 3 mm. The overall electrode length (including the overhang) is 702 mm. The tank is fitted with four diagnostic vacuum windows facing the electrodes for the purpose of vibrometer measurements.

Prototype Properties

The expected shunt impedance is 115 kΩm, corresponding to a power loss of 31.3 kW/m at a reference electrode voltage of 60 kV. The electric dipole component is expected to be compensated entirely. According to first estimations considering the simulated mechanical resonance response (see Figure 2) the rf affecting electrode vibration amplitudes are decreased by a factor of 20 compared to the existing HLI-RFQ.

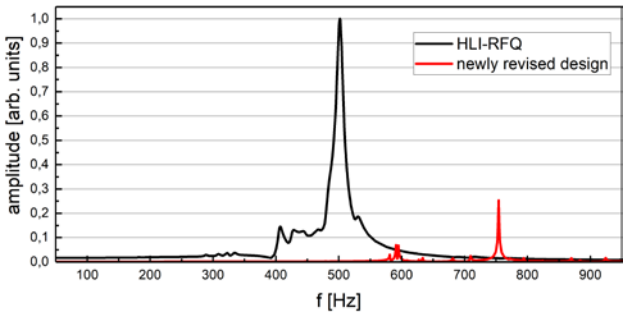


Figure 2: Comparison of the simulated mechanical resonance response for the existing HLI-RFQ and the newly revised (prototype) design (with 1 % damping ratio).

References

[1] D. Koser et al., “Prototype Design of a Newly Revised CW RFQ for the High Charge State Injector at GSI”, Proc. of IPAC2016, pp. 889-891.

[2] D. Koser et al., “Advanced Design Optimizations of a Prototype for a Newly Revised 4-Rod CW RFQ for the HLI at GSI”, Proc. of LINAC2016, pp. 586-588.

[3] Neue Technologien GmbH & Co. KG (www.ntg.de)

[4] P. Gerhard et al., “In Situ Measurements of Mechanical Vibrations of a 4-Rod RFQ at GSI”, Proc. of LINAC2014, pp. 553-555.

[5] D. Koser et al., “Structural Mechanical Analysis of 4-Rod RFQ Structures in View of a Newly Revised CW RFQ for the HLI at GSI”, Proc. of IPAC2017, pp. 4142-414

Upgrade of the HITRAP ion trap and charge breeding system

Z. Andelkovic[1], J. Fischer[2], F. Herfurth[1], W. Nörtershäuser[2], M. Shroff[2], J. Viering[2], G. Vorobyev[1]

[1]GSI, Darmstadt, Germany; [2]TU Darmstadt, Germany

Production of a new cooling trap

A new design for the HITRAP cooling trap was proposed in order to improve its stability and voltage rigidity [1]. Based on this design, new electrodes were machined, gold plated and prepared for installation in 2017. The biggest challenge was the appropriate choice of insulating material between the electrodes, which needed to be thermally conductive at the same time. The very limited choices were put down to:

Material	*Conductivity*	*Hardness*	*Price*
Sapphire	40 W/mK	very high	high
Shapal ™	220 W/mK	medium	high
BIN77 ™	80 W/mK	medium	medium

Finally BIN77 was chosen as the most suitable candidate due to acceptable thermal conductivity, machinability into complex forms and moderate price.

Short-circuits, broken cables or discharges were so far the biggest issue, causing repeated opening and closing of the trap. A way to circumvent that problem is to reduce the number of cables, provided by a smaller number of electrodes in the new trap design, as well as to keep all trap components on a similar HV. As a consequence, the voltage in the trap is not higher than 8 kV for the outer electrodes and 1 kV for all other with respect to neighbouring electrodes. Besides, the cables also do not have large potential differences between each other, so that standard cables can be used, eliminating the existing sensitive cable connection system. The chosen cables are listed in the table below:

Type	*HV*	*Heat load*	*coax.*
UT-141B-SS Stainless steel	9600 V	10 mW/m	yes
312-KAP-MAN-025 Manganine	6000 V	0.2 mW/m	no
TFCC-020 Konstantan	500 V	0.1 mW/m	no

The finished electrode assembly of the new trap can be seen in the figure below. Assembly inside the superconducting magnet and first tests are planned for 2018.



Figure 1: New electrode stack of the HITRAP cooling trap, Photograph by J. Viering, Master thesis in preparation, TU Darmstadt

Charge breeding of metallic ions in an EBIT

The SPARC-EBIT (Electron Beam Ion Trap) has been successfully in operation as a test ion source for HITRAP for already 10 years [2]. It can routinely perform charge breeding and deliver up to 10^6 highly charged ions produced either from inert gasses or from externally injected singly charged ions [3]. The gas-based procedure is by far favourable because of its simplicity and higher yields. However, many elements, especially metals, are difficult to find in gaseous form and thus difficult to produce.

A solution to that problem was investigated with the so-called MIVOC (Metal Ions from VOlatile Compounds) method [4]. It takes advantage of a relatively large vapour pressure of organic compounds with weakly bound metallic ions to produce sufficient quantities of gaseous material for injection into the EBIT. Iron, Antimony and Boron compounds were chosen for the first studies [5], listed in the table below:

Compound	*Formula*	*vap. pressure*
Ferrocene	$Fe(C_5H_5)_2$	10^{-2} mbar
Triphenylantimon	$Sb(C_6H_5)_3$	10^{-5} mbar
Trimethylborat	$B(OCH_3)_3$	10^{2} mbar

Applying vapours of these gasses inside the EBIT, the trapping, i.e. charge breeding time was varied for different gas pressures. The charge state composition of the ejected ions was analysed with a dipole magnet and by the time-of-flight method. Results have shown that production of various charge states of all three test candidates was successful. With an electron energy of about 5 keV it was possible to produce Fe^{21+}, Sb^{35+} and B^{5+}. For TOF analysis the ions were transported some 10 m along the HITRAP low-energy beamline [3] with efficiency close to 100%. The limiting factor turned out to be the dipole magnet, which was not able to separate all antimony charge states and isotopes. Nevertheless, the results show the feasibility of the MIVOC method which significantly increases the number of elements and charge states possible to produce and deliver to experiments at the HITRAP EBIT facility.

References

[1] Z. Andelkovic, et al., GSI Scientific Report (2015)
[2] Z. Andelkovic, et. al., NIM-A 795, 109 (2015)
[3] G. Vorobjev, et. al., Rev. Sci. Inst. 83, 053302 (2012)
[4] T. Werner, et. al., Rev. Sci. Inst. 71, 2038 (2000)
[5] J. Fischer, Bachelor Thesis, TU Darmstadt (2017)

Experiment collaboration: APPA-SPARC
Experiment proposal: E130
Accelerator infrastructure: none
PSP codes: none
Grants: BMBF, contract 05P15RDFAA
Strategic university co-operation with: TU Darmstadt

 DOI:10.15120/GR-2018-1

First beam acceleration at the heavy ion cw-Linac Demonstrator

M. Miski-Oglu[1], W. Barth[1,2], K. Aulenbacher[3], M. Basten[4], M. Busch[4], F. Dziuba[1], V. Gettmann[1], M. Heilmann[1], T. Kürzeder[1], H. Podlech[4], A. Rubin[2], A. Schnase[2], M. Schwarz[4], S. Yaramyshev[2]

[1]HIM, Mainz, Germany; [2]GSI, Darmstadt, Germany; [3]Johannes Gutenberg-Universität, Mainz, Germany; [4]Goethe-Universität, Frankfurt, Germany

A standalone superconducting (sc) cw-Linac is assumed to meet the demands of GSI users on high duty factor beams at its best. Additionally, with significantly higher beam intensity the SHE production rate will be increased as well. The cw-Linac layout is based on sc Crossbar H-Mode (CH) cavities, efficient multi-cell structures combining the advantages of sc and long room temperature cavities [1]. Recently, the first Linac section (financed by HIM and GSI) as a demonstration of the capability of 217 MHz multi gap CH structures has been commissioned and extensively tested with argon and helium beams from the GSI High Charge State Injector HLI at the test demonstrator test cave.

Demonstrator test setup

The demonstrator setup, embedded in a new radiation protection cave, is located in straightforward direction of the HLI. The liquid helium (LHe) supply is covered by a 3000 l tank, while the consumed helium gas is collected in a 25 m^3 recovery balloon and bottled by a compressor. The demonstrator comprises a 15 gap sc CH-cavity embedded by two superconducting solenoids; all three components are mounted on a common support frame. The support frame, as well as the accelerator components, are suspended each by eight tie rods in a cross-like configuration balancing the mechanical stress during the cool down and warm up. The beam focusing solenoids provide maximum fields of 9.3 T, the free beam aperture is 30 mm. The solenoids are connected to LHe ports inside the cryostat by copper tapes allowing dry cooling. The sc CH-cavity (Fig. 1) is the key component and offers a variety of research and development opportunities.

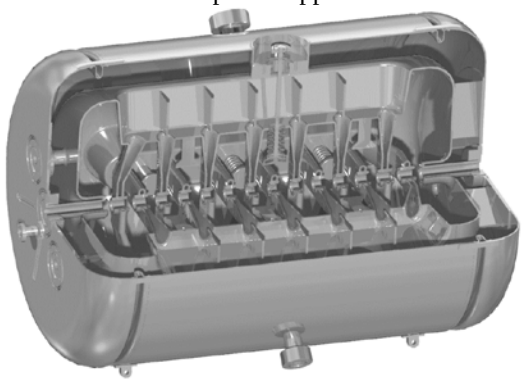


Figure 1: Sectional drawing of the 15-gap demonstrator CH-cavity.

First beam acceleration

At June 28th of 2017, after successful rf-testing of the superconducting rf-cavity in 2016, setting up the matching line to the demonstrator and short commissioning and ramp up time of some days, the CH-cavity accelerated Ar^{11+} ions with full transmission for the first time up to the design beam energy of 1.866 MeV/u (ΔW_{kin} = 0.5 MeV/u). For the first beam test the sc cavity was powered with 10 Watt of net rf-power providing an accelerating voltage of more than 1.6 MV within a length of 69 cm. Further on the design acceleration voltage of 3.5 MV has been verified and even exceeded by acceleration of beams with high rigidity (A/q = 6.7). Argon and helium ion beams with different charge states from an ECR ion source ($^4He^{2+}$, $^{40}Ar^{6+, 9+, 11+}$) were accelerated at the HLI for further beam tests with the demonstrator. For longitudinal beam matching the re-buncher settings were adapted according to the mass to charge ratio, as well as the acceleration voltage.

Systematic beam measurements

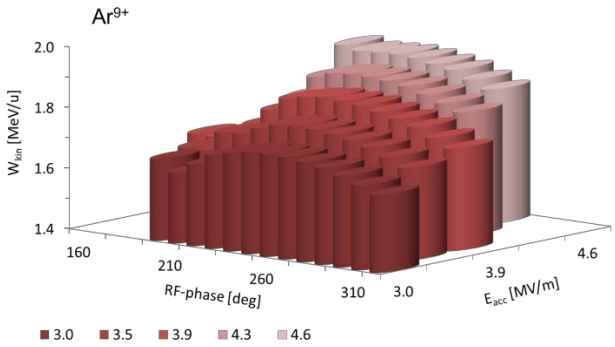


Figure 2: 3D-scan of Ar^{9+}-beam energy versus accelerating gradient and RF-phase.

In Fig. 2 a full measured 3D-scan of beam energy for a wide range of different accelerating fields and rf-phases is depicted. A linear increase of beam energy with ramped accelerating gradient could be observed for different rf-phase settings, while the beam transmission is kept high. To gain for the maximum beam energy at a given accelerating gradient the rf-phase has to be adapted slightly. In general these measurements confirm impressively the EQUUS beam dynamics, featuring effectively the non-resonant beam acceleration up to different beam energies without particle loss and without significant beam quality degradation. As measured with helium beam and recently confirmed by beam dynamics simulations, for lighter ions maximum beam energy of up to 2.2 MeV/u could be reached with the demonstrator cavity.

References

[1] W. Barth, et al., “First heavy Ion Beam Test eith a superconducting multi gap CH-cavity, Phys. Rev. Accel. Beams 21, 020102 (2018).

New results on development of 2.7 Hz operation for heavy elements from high current ion sources

A. Adonin[1] and R. Hollinger[2]

[1]GSI, Darmstadt, Germany

To produce high intensity heavy ion beams with SIS100 for the future FAIR experiments such as NUSTAR, CBM and APPA a special operation mode of UNILAC is required. It will be necessary to provide four beam pulses of 100 µs length each within 1.1 s and inject them into SIS18 [1]. That corresponds to operation of the ion sources with 2.7 Hz repetition rate. For light and intermediate-mass elements (with ion charge state $q_{ion} \leq 3^+$ required for injection into the RFQ) there should be no difficulties, but for heavy elements ($Q_{ion} = 4^+$) as Au, Pb, Bi and U this is challenging. Operation of heavy elements from high current vacuum arc ion source VARIS [2] is well established with 0.5 Hz / 0.5 ms for Au, Pb and Bi using the composite materials in the cathodes [3,4], as well as with 1 Hz / 0.5 ms for U using pure material in cathodes. Thus, the operation repetition rate has to be increased almost by a factor of 6 for Au, Pb and Bi and by a factor of 3 for U.

Tests with bismuth

As shown earlier [3,4], the production of 4^+ ion beams with a flat top of more than 100 µs in temporary profile for Au, Pb and Bi is not a trivial task, and it does not work with pure materials due to their physical properties. As solution, the composite materials with modified physical properties have been used in the cathodes. Stable operation of high current 4^+ ion beam has been achieved for all three elements by using the following compositions: Au-Cr (50% Wt.), Pb-Cu (40% Wt.) and Bi-Cu (40% Wt.). However, stable operation was only possible with a low repetition rate (0.5 Hz) and long conditioning time (up to 2 hours) was noted generally for all cathodes. Further investigation of used cathodes with SEM (scanning electron microscope) have shown that the material structure plays an important role in cathode performance. In order to keep an optimal material ratio (desired/admixed) on the working surface of the cathode during the whole operation lifetime, a special production procedure has been applied: Cu formed in a "litz wire" structure was heated up and homogeneously filled with liquid Bi. As the result, a particular material structure has been achieved for Bi-Cu (40% Wt. or 69% At.) cathodes.

Two cathodes of a new type have been manufactured for tests. The tests were performed in Sep. 2017 at terminal North with VARIS. Various operation modes have been tested: 1 Hz / 2 Hz / 2.8 Hz with beam pulse lengths between 0.3 and 0.4 ms. The test results were very successful: is was possible to get stable Bi-operation even with 2.8 Hz repetition rate achieving up to 10 mA of Bi^{4+} ion beam current in UH1-section (in front of the HSI-RFQ). The new type cathodes require much shorter conditioning time: 5 mA of Bi^{4+} beam current was reached after 15 min. operation with 1 Hz, and a full performance − after 30-40 min. The operation lifetime of the cathodes was estimated to about 20 hours by 1 Hz / 0.35 ms and about 8 hours by 2 Hz / 0.4 ms.

Tests with uranium

Increasing the repetition rate from 1 Hz to 2.8 Hz at U-operation with VARIS leads to an increasing of a surface temperature of the cathode, growth of the neutrals flux from the surface during the beam pulse, as well as an increasing of a temperature of extraction electrodes. That causes a number of inhibiting factors for operation, such as arc ignition failures, shifting the ion spectrum to the lower charge states and sparking in the extraction system of the ion source. These factors result in the loss of operation stability and general performance drop of the ion source. One of the possible solution of this problem is modifying the physical properties of the cathode material, improving the thermal characteristics and refractoriness by admixing a more refractory metal. Tungsten has been chosen as the admixed material to uranium. After study of the production possibilities of U-W composition a set of the test cathodes with U-W (5% Wt.) and U-W (12% Wt.) has been manufactured by Framatome company (formal AREVA GmbH) for the tests at GSI.

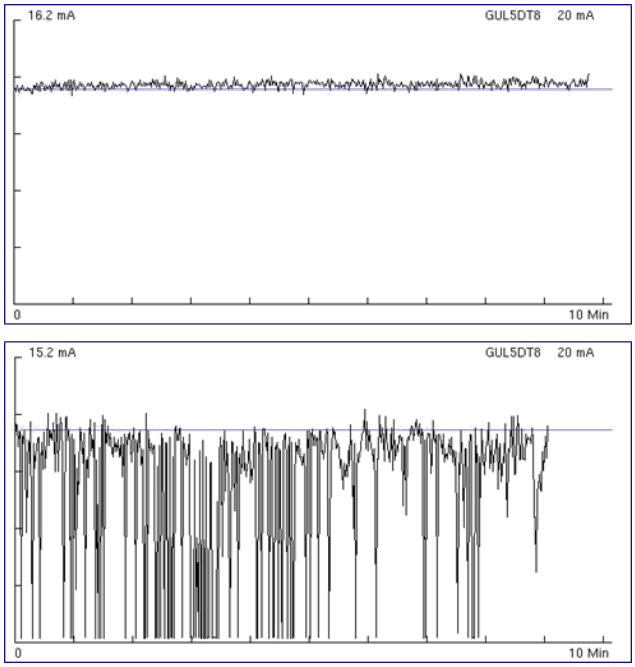


Figure 1: Operation stability of U-W composite cathode at repetition rate of 2.8 Hz recorded over 10 min. during the stable (upper) and unstable (lower) phases.

The tests were performed in the period from Sep. 2017 to Feb. 2018 at terminal North and have shown quite promising results: it was possible to get a stable operation by 2.8 Hz / 0.4 ms (total beam pulse length) with up to 18 mA of U^{4+} beam current in UH1-section (Fig.1). The pulse shape of U^{4+} beam had an appropriate temporal

 DOI:10.15120/GR-2018-1

structure with over 120 µs flat top and very low (for vacuum arc ion sources) intensity fluctuations: <10%. Taking into account also excellent pulse-to-pulse repetition stability with fluctuations below 10% (Fig.1) all this represents the perfect conditions for tuning the ion beam in the UNILAC and further injection into SIS18. The conditioning times of the cathodes were pretty short: 10-15 min. at 2.8 Hz.



Figure 2: Shrinkage cavities in U-W alloy, formed during the production process.

Nevertheless, there was one notable disturbing factor observed generally for all test-cathodes: so called "unstable phases" in cathode operation. These are the operation phases with extremely unstable burning of the arc discharge leading to beam intensity fluctuation up to 70% during the pulse as well as with very high rate of arc ignition failures: more than 50% of the beam pulses were missing. Figure 1 demonstrates the operation stability of U^{4+} ion beam during both stable (upper) and unstable (lower) phases. It was noted, that during the first hours of cathode operation the bad phases were short (5-10 min.) and appeared seldom (in average one per hour). While closer to the end of the cathode lifetime these phases were longer (up to 30 min.) and appeared more often. The average operation lifetime of one U-W cathode reached up to 7 hours by 2.8 Hz repetition rate. The total time of unstable phases was ~1.5 hours per cathode. The origin of unstable phases in cathode operation is not clear at the moment and has to be further investigated. A possible reason could be shrinkage cavities inside the U-W composition material, formed conceivably during the cooling phase of the production process. Figure 2 shows one of such cavities located on side surface of the cathode.

Conclusions and outlook

The use of particular "litz wire" Cu-structure in Bi-Cu composite cathodes has allowed to increase the repetition rate for Bi-operation to 2.8 Hz (requested by FAIR) and to reduce the conditioning time of cathodes by a factor of three. It is planned to implement and test this new structure with Pb-Cu cathodes. In the case of successful tests the new type composite cathodes with enriched Pb-isotopes (^{206}Pb and ^{208}Pb) will be used in the beamtime in 2018. The use of U-W composition in the cathodes could be the possible solution to reach the FAIR requirements for the operation duty cycle for U^{4+} ion beam if the factor of unstable phases will be excluded. To understand the origin of the unstable phases it is planned to investigate the material and the surface structure of used U-W cathodes under the scanning electron microscope (SEM) in cooperation with Framatome GmbH (Erlangen).

The recent development status for all four heavy elements with respect to the future FAIR requirements is summarize in the Table 1.

Table 1: Currently achieved ion beam parameters for heavy elements in UH1-section (in front of the HSI-RFQ)

Ion sort	Achieved parameters		Efforts w.r.t. FAIR requirements
	Beam current	Rep. rate	
Au^{4+}	4 mA	1 Hz	intermediate
Pb^{4+}	6 mA	0.5 Hz	intermediate
Bi^{4+}	10 mA	2.7 Hz	few
U^{4+}	15 mA	< 2 Hz	large

The last column introduces the future efforts to achieve the requirements of FAIR experiments. For Bi the required ion beam parameters are already achieved, however manufacturing procedure of composite cathodes with particular structure has to be routinized. For Au and Pb the operation repetition rate has to be increased that could require further development on composition materials for cathodes. The biggest efforts are expected for U: not only the operation repetition rate has to be increased, but also a beam brilliance. It will be required to achieve 23 mA of U^{4+} ions inside an emittance of 260π mm·mrad in front of the HSI-RFQ [5].

References

[1] P. Schütt, O. Geithner, and P. Forck, FAIR operation modes, EDMS: 1688183.

[2] R. Hollinger and M. Galonska, "*Status of vacuum arc ion source development for injection of high current uranium ion beams into the GSI accelerator facility*", Nucl. Instr. and Meth. in Phys. Res. B 239 (2005).

[3] A. Adonin and R. Hollinger, "*Development of high current Bi and Au beams for the synchrotron operation at the GSI accelerator facility*", Rev. Sci. Instrum. 83, 02A505 (2012).

[4] A. Adonin and R. Hollinger, "*Challenges of Production of High Current four-fold Bi and Au Beams from Vacuum Arc Ion Sources at GSI*", Accelerator Facility Proc. of ISDEIV, Tomk, Russia, 6412599 (2012).

[5] Ch. Xiao, "*Consistent front to end simulations for the upgraded UNILAC*", Operations Beam Physics and Techniques Salon, (https://www.gsi.de/fileadmin/user_upload/Xiao_salon_20180314.pdf).

CW LINAC Advanced Demonstrator beam dynamics investigations

M. Schwarz[1], K. Aulenbacher[2], W. Barth[3,4], M. Basten[1], M. Busch[1], F. Dziuba[4], V. Gettmann[4], M. Heilmann[3], T. Kürzeder[4], M. Miski-Oglu[4], H. Podlech[1], A. Rubin[3], A. Schnase[3], S. Yaramyshev[3]

[1]IAP, Goethe-Universität, Frankfurt, Germany, [2]Johannes Gutenberg-Universität, Mainz, Germany,
[3]GSI, Darmstadt, Germany, [4]HIM, Mainz, Germany

For future experiments with heavy ions near the coulomb barrier within the super-heavy element (SHE) research project a multi-stage R&D program of GSI/HIM and IAP is currently in progress. It aims for developing a superconducting (sc) continuous wave (CW) LINAC with multiple CH cavities as key components downstream the High Charge State Injector (HLI) at GSI. The LINAC design is challenging due to the requirement of intense beams in CW mode up to a mass-to-charge ratio of 6 while covering a broad output energy range from 3.5 to 7.3 MeV/u with minimum energy spread. After successful tests with the first CH-cavity in 2016 demonstrated a promising maximum accelerating gradient of 9.6 MV/m, the worldwide first beam test with this sc multi-gap CH cavity in 2017 was a milestone in the R&D work of GSI/HIM and IAP [1]. In the light of experience gained in this research so far, the beam dynamics layout for the entire LINAC is recently being updated and optimized.

Beam Dynamics Simulations

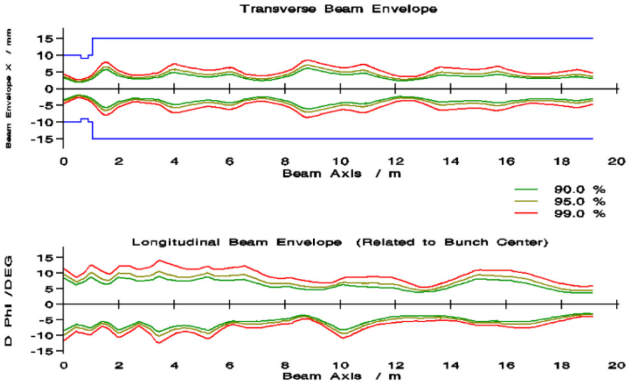


Figure 1: Transv. (x) and long. (phase) envelopes for a LINAC setup as shown in Fig. 3; LORASR-simulations with A/q = 6, 100001 particles and I = 0 mA.

Up to now, the reference design for the CW LINAC dates back to the proposal of Minaev et al. in 2009 [2]. Meanwhile, significant expertise has been gained in design, fabrication and operation of superconducting CH-cavities and the associated components. In this context, a revision of the beam dynamics layout was recommended. Optimized cavity layouts resulted in modified voltage distributions. Furthermore, the cryomodule layout and intertank sections were specified in a more detailed way. Promising RF- and beam testing with the 15-gap CH0 showed, that higher accelerating gradients can be achieved, thus leading to a more efficient design approach. Consequently, extensive beam dynamics studies are carried out to determine the best layout with respect to the beam and all other RF and mechanical requirements. Figures 1-3 show an exemplary layout, which has been currently studied. Applying an accelerating gradient of up to E_a = 7.1 MV/m for the CH-cavities results in acceleration from 1.4 MeV/u up to 8.0 MeV/u (thus exceeding the required 7.3 MeV/u of final energy). For further details please refer to [3].

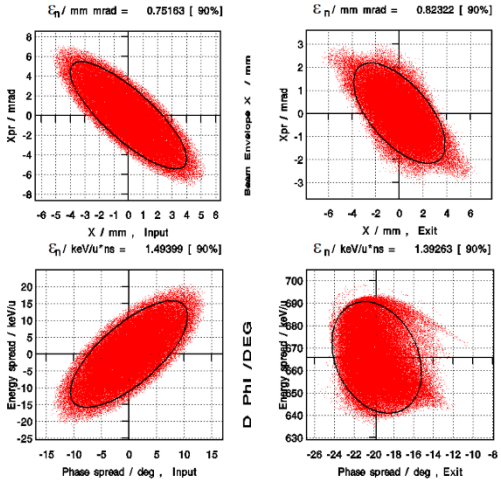


Figure 3: Phase space distributions for the recent beam dynamics layout; top: x - x', bottom: $\Delta\varphi$ - ΔW, left: Input for first cryomodule, right: Output of fourth cryomodule.

References

[1] W. Barth et al., "First heavy Ion Beam Test with a superconducting multi gap CH-cavity", Physical Review Accelerators and Beams 21, 020102 (2018), doi: 10.1103/PhysRevAccelBeams.21.020102

[2] S. Minaev et al., "Superconducting, energy variable heavy ion linac with constant β, multicell cavities of CH-type", Phys. Rev. ST AB 12, 120101 (2009), doi: 10.1103/PhysRevSTAB.12.120101

[3] M. Schwarz et al., “Beam Dynamics Simulations for the New Superconducting CW Heavy Ion LINAC at GSI”, in Proc. IPAC’18, Vancouver, BC, Kanada, May 2018, paper TUPAK003

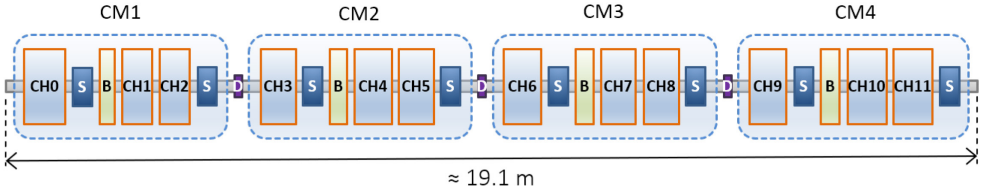


Figure 2: Exemplary LINAC layout with twelve superconducting CH-DTLs in four cryomodules. Captions: CM = Cryomodule, S = Solenoid, B = 2-Gap-Buncher, D = Diagnostics.

 DOI:10.15120/GR-2018-1

Development and upgrade of the ECRIS facility

K. Tinschert, F. Maimone, J. Mäder, R. Lang, P. T. Patchakui, and D. van Rooyen

GSI, Darmstadt, Germany

Double Frequency Heating

Experimental investigations at the ECRIS (Electron Cyclotron Resonance Ion Source) test bench were carried out with the aim to enhance the extracted ion currents in pulsed mode. In the so called afterglow mode an increase of pulse current of highly charged ions is obtained by pulsing the microwaves feeding the plasma [1]. The current of the highly charged ions can also be significantly raised by applying microwave based techniques like frequency tuning or double frequency heating. Recent experimental results proved that the combination of microwave frequency tuning and afterglow operation mode allows to further enhance the intensity of pulsed highly charged ion beams [2]. In order to analyse the effect of superimposing different frequencies in pulsed mode and in CW mode the experimental set-up at the CAPRICE-ECRIS shown in Fig. 1 has been used. A coaxial power combiner is installed to connect the two microwave generators to the TWTA (Traveling Wave Tube Amplifier). A waveform generator modulates the amplitude of a microwave generator to provide for the microwave pulses for the afterglow mode. For the present investigations argon was used as main gas with helium as support gas.

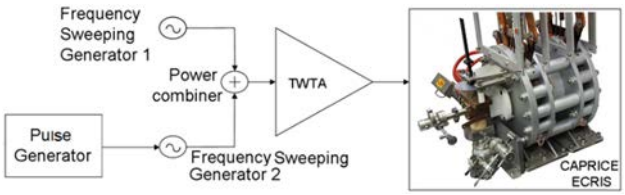


Figure 1: Block diagram of the experimental set-up.

After tuning the ECRIS parameters with a single microwave generator set at 14.5 GHz in cw mode for optimized production of Ar^{12+}, frequency sweeps were performed to identify frequencies showing enhanced intensities with respect to 14.5 GHz. The highest intensity of Ar^{12+} was measured at 13.125 GHz. Therefore 14.5 GHz and 13.125 GHz were chosen for the multiple frequency injection. In pulsed mode different duty cycles were investigated for a pulse period of T_p = 100 ms. The highest afterglow intensity is obtained for a duty cycle of 40% (pulse length of 40 ms). So this combination was used for the experiments. When setting the two microwave generators to the same optimized frequency no enhancement of the afterglow current is observed. A current intensity enhancement, both for the steady state current and for the afterglow peak is observed only when the pulsed power is provided at 14.5 GHz and the CW power is provided at the optimized frequency of 13.125 GHz (see Figure 2). Figure 3 shows a comparison of argon spectra obtained in pulsed mode with single frequency and in double frequency operation (pulsed power + CW power). For each setting the maximum intensity of the afterglow peak (AG) and in the steady state range (StSt) is presented. It appears that the superposition of cw power and pulsed power for optimising the afterglow intensity is sensitive to the selected frequencies. However, the single frequency tuning combined with the afterglow mode turned out to provide the highest and widest afterglow peaks of high charge state ion beams from the ECRIS [3].

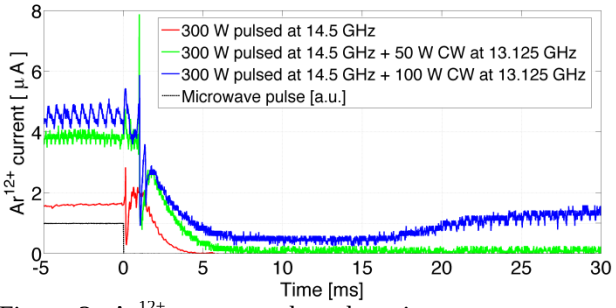


Figure 2: Ar^{12+} currents when the microwave generators are set at different frequencies.

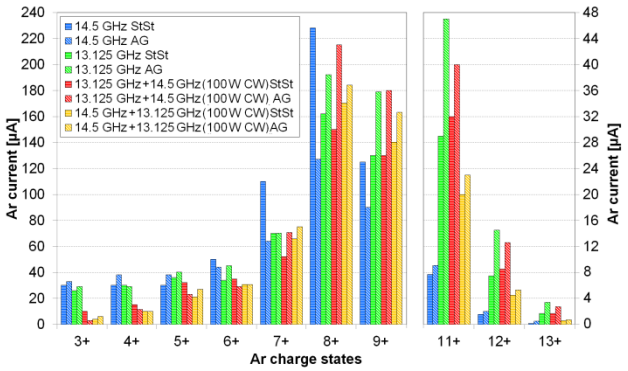


Figure 3: Ar spectra for different single frequencies and for the combination of two microwave frequencies in pulsed mode (AG: AfterGlow) and cw mode (StSt: Steady State). (Different scale for Ar^{11+} to Ar^{13+}; right)

Collaboration on ECRIS technologies

The EU-ENSAR2-MIDAS networking activity (NA) is a collaboration of teams developing ECRIS and beams for the needs of the ENSAR2 facilities [4]. The ECRIS team of GSI is participating together with corresponding teams from Finland (JYFL), France (GANIL, LPSC), The Netherlands (RUG-KVI-CART), Hungary (ATOMKI), Spain (UCLM) and CERN. The objective of the MIDAS-NA is to enhance the networking and dissemination of best practices between the partner teams.

In the framework of this collaboration a first training workshop on microwave technologies for ECRIS was organized at GSI. During the workshop theoretical and practical knowledge about the handling of microwave devices and components was imparted and the main issues about microwave generators, resonance cavities and coaxial/waveguide components for the implementation of microwave lines for plasma generation were handled. Operation methods of the ECRIS like frequency tuning by sweeping the microwave frequency and double frequency

heating by combining two microwave generators were experimentally executed. Active discussion sessions provided a good dissemination and exchange of knowledge.

Upgrade of ECRIS Injector at the HLI

At the High Charge State Injector (Hochladungsinjektor HLI) of GSI the CAPRICE ECRIS is in operation since 1992. The total number of its operating hours delivering beam to the accelerator exceeded more than 5000 hours per year. Even though upgraded repeatedly the ion source and its ancillary equipment show age related deterioration. In order to maintain the availability and reliability of the machine a program has been started to upgrade and improve the infrastructure equipment of the ECRIS. In 2017 this comprised the reconditioning of the high pressure water cooling system of the ECRIS including the replacement of thermal sensors and flowmeters to achieve a contemporary standard. In addition a reconditioning of the current leads and connectors was performed. The interlock system of the ion source and the supply units is subject to an extensive renewal by replacing the former relay technique by a modern PLC based system. The development and implementation of this system is ongoing and will be performed stepwise. It will provide a detailed fault memory which facilitates an easy fault analysis during operating periods.

Performance upgrade of ECR Ion Sources

Besides the degradation of the infrastructure equipment the technical standard of the CAPRICE ECRIS itself is outdated nowadays and implies the replacement by adequate technologies.

Future user defined ion beam requests comprise FAIR science (APPA, CBM, NUSTAR) as well as UNILAC science (SHE physics & chemistry, materials research, biophysics, plasma physics). Main requests concern the increase of available intensities of established ion beams, but also the availability of novel ECRIS ion beams to be developed, both including beams of rare isotopes.

In order to follow these raised requirements an evaluation was performed, as to which strategy is to be pursued to provide enhanced performance and availability of ion beams from ECRISs for GSI/FAIR.

For ECRISs a well-established and proven semi-empirical scaling law indicates the proportional dependence of the achievable ion beam intensity of a given ion species A^{q+} on the square of the ECR-frequency. This directly implies the increase of the microwave operating frequency which in turn requires the proportional increase of the B-field of the magnetic confinement. For highest magnetic fields superconducting magnet systems are indispensable.

Generally cw operation of the ECRIS perfectly fulfils the requirements of a cw-LINAC, while pulsed afterglow operation is fully compatible with synchrotron requirements (up to 10 pulses per second from the ion source).

Finally, the following two-step approach is proposed as upgrade strategy. At a first stage a moderate upgrade with a conventional ECRIS operating at 18 GHz as replacement of the 14.5 GHz CAPRICE ECRIS is intended. A full performance upgrade with a Superconducting-ECRIS operating at frequencies beyond 22 GHz, installed at a separate injection beam line, is planned as second stage. Two redundant injection lines are foreseen in order to provide high flexibility for utilizing the appropriate ion source depending on the demands of the requested ion beam. Furthermore it would greatly improve the availability of ion beam in case of a failure of one of the ion sources.

Presently promising projects on 18 GHz ECRISs utilizing new technologies and new materials are pursued based on well-established techniques:

HIISI (University of Jyväskylä, Finland) utilizes a permanent magnet hexapole and conventional room temperature (RT) solenoid coils [5], while AISHA (INFN-LNS Catania, Italy) applies a hybrid concept with a permanent magnet hexapole and LHe-free SC solenoid coils [6].

28 GHz SCECRISs have already proven to be capable of providing considerably increased intensities of highly charged ions beyond those of an 18 GHz ECRIS. Utilizing established cryogenic technology adjustable axial and radial magnetic fields are provided for optimum adaptation of the working point for medium and high charge states. During the past decade several projects have been realized like VENUS-SCECRIS at LBNL (USA) [7], RIKEN-SCECRIS at RIKEN (Japan) [8] and SECRAL-SCECRIS at IMP-Lanzhou (China) [9].

References

[1] K. Tinschert et al, Rev. Sci. Instrum. 75, 1407 (2004).
[2] F. Maimone, et al, Rev. Sci. Instrum. 87, 02A712, (2016).
[3] F. Maimone et al, Proc of ICIS17, 15-20 Oct 2017, Geneva, Switzerland, accepted for publication.
[4] https://wiki.jyu.fi/display/ensar2
[5] H. Koivisto et al., Rev. Sci. Instrum., 87, 02A725 (2016).
[6] L. Celona et al., Proceedings of IPAC2017, Copenhagen, Denmark, 570 (2017).
[7] D. Z. Xie et al., Proceedings of ECRIS2016, Busan, Korea, 141 (2017).
[8] Y. Higurashi et al., Proceedings of ECRIS2016, Busan, Korea, 10 (2017).
[9] L. Sun et al., Proceedings of LINAC2016, East Lansing, MI, USA, 1027 (2017).

Accelerator infrastructure: UNILAC
PSP codes: none
Grants: EU-H2020 contract No. 654002 - WP3 - NA3

 DOI:10.15120/GR-2018-1

Shutdown report 2017

P.Schütt, M.Vossberg, S.Reimann

GSI, Darmstadt, Germany

This report is a follow up of the shutdown report 2016 [1] and describes the further development of the main service and upgrade measures of the GSI accelerator facilities, which were started in 2016 and will be continued until mid-2018. The presented information is based on the work of the shutdown coordination and the corresponding MS-Project shutdown schedules.

General Overview

In July 2016 began the longest shutdown GSI has ever seen. It is expected to end in May 2018. The bulk of the workload was finished in 2017.

The coordination process was continued as described in the last report: In weekly meetings with the machine coordinators and representatives of all involved departments, including civil construction and infrastructure, the actual progress is monitored, pending work and critical incidents are discussed and the overall schedule is adapted accordingly.

Work Packages

Civil construction

The largest work package is the civil construction project GAF (GSI Anbindung an FAIR, Link of GSI to FAIR), which comprises additional shielding of SIS18, fire protection measures, as well as the connection of the new beam line tunnel towards FAIR to the existing TR hall. In 2017, it was complemented by the project WTK (Westwand TransferKanal, west wall of the transfer line building), which comprises a beam dump for the planned proton linac and preparation works for the p-linac building at the west side of the transfer channel.

GAF and WTK works are ongoing, tasks inside the SIS18 ring tunnel must be stopped end of April, forcing some rest work to be postponed until after beam time 2018.

One issue of these construction works was water penetrating into the SIS18 tunnel and in an electronics room: extensive cleaning works caused interruptions of other tasks for several weeks. Another issue was the shift of the transfer channel building during WTK. This forced us to break the vacuum and open the beam pipe.

UNILAC

The modernization of post-stripper RF systems at the UNILAC, which started in 2015, was continued. This project comprises a prototype Thales power amplifier for Alvarez 4, refurbishment of control racks and new high voltage power supplies.

This project was severely impaired by two issues:

• During a test of the emergency switches, a main power switch was damaged, and left the RF gallery without electricity for nearly 3 months.

• The refurbishment of the Heating, Ventilation and Air Conditioning (HVAC) system of the UNILAC tunnel was scheduled to interrupt the RF works from September until December 2017. Instead, stable conditions of the air cooling could only be reached mid-March 2018.

Thus, three of the 5 Alvarez power amplifiers are left unchanged and need to be refurbished in the next shutdown period. Several tasks for the refurbishment need to be finished and all renewed systems still need to be tested.

Remaining issues with the ventilation of the RF systems need to be solved urgently to ensure enough test time for the RF systems and stable operation during the beam time 2018.

The refurbishment of UNILAC vacuum controls had to be postponed, beam time 2018 has to be operated with the old vacuum control system (age of component ~40years). Therefore higher failure rates must be tolerated, causing extra effort for remedial maintenance. We expect several issues per month, taking 3 hours each for repair.

Cooling water leaked into the beam pipe in the transfer channel, in the TK3 stripper section. This issue caused a lot of effort for repair: The TK3 section has been opened and about 400 l of water were removed. All profile grids in the section TK3 were removed and had to be replaced. Faraday cups, phase probes and transformers were removed and had to be cleaned.

Control system

The retrofitting of the FAIR control system to SIS18, ESR and HEST is progressing well. To ensure a smooth commissioning several Dry Runs were scheduled beginning October 2017 to test all devices with the new control system. The control system refurbishment also implies beam diagnostics upgrades and the implementation of modern consoles for SIS18 and ESR in the main control room. These consoles are the first of series for the new FAIR control room consoles and are already used during the Dry Runs.

ESR

The vacuum refurbishment of the ESR northern arc is progressing well. Bake-out is scheduled for June 2018.

Repair of a short-circuit fault in the electron cooler of the ESR was aborted. During the preparation, asbestos-containing heating jackets were found. They will be disposed according to official directives and afterwards, the section will be closed and baked out.

HEST

The shutdown work in the HEST concentrates on the upgrade of the HADES beam line with respect to the aperture and beam diagnostics. The new vacuum chamber is installed and the installation of the new beam diagnostics will be ready for beam time 2018.

For the HEST vacuum we expect a more reliable operation due to replacement of old ion getter pump controllers and of old total pressure gauges.

The preparation for the Mini CBM is ongoing and should be finished in time.

SIS18

The new transformer station North (SIS18/SIS100 pulse power) was successfully commissioned and power tests of the new dipole power converter with maximum ramp rates and pulse power started in March 2018.

All three modules of the new h=2 RF cavities have been installed. A new high frequency cavity for smoothing of the spill structure is under construction and sector 11 is prepared for the installation.

The magnet GTS1MU1 will be replaced by a new one, which will steer the extracted beam from SIS18 either to the fragment separator, to the experimental hall or to the upcoming SIS100. The new magnet has been delivered. However, the corresponding beam pipe is delayed. Hence, the old magnet will be used in 2018.

Alignment

Due to civil construction not only in GAF but also for the new FAIR buildings, the accelerator tunnel floors moved significantly and the corresponding accelerator components accordingly. In the transfer channel, there are significant displacements in horizontal and vertical direction (~1cm). Vertically the SIS18 is moving down significantly in the east-northeast direction. Re-adjustment in a tilted plane is planned to minimize general adjustment and offset towards HEST. Nevertheless, survey and alignment is estimated to take 2-3 months.

Others

Development of the cw-demonstrator is completed. The first tests with beam are completed and showed good results.

The commissioning of CRYRing is proceeding well. Many features of the new control system were tested there during the implementation work for the retrofitting to SIS18.

Shifted Tasks

Several tasks had to be shifted to the next shutdown period after beam time 2018:

The electrostatic acceleration section of terminal north has not been renewed. However, development of high current sources proceeded well.

The refurbishment of UNILAC vacuum controls had to be postponed.

A major part or the refurbishment of the UNILAC RF systems needed to be rescheduled in the next shutdown.

The beam pipe for the new magnet TS1MU1 will not be delivered in time, therefore, the old magnet will be reinstalled.

The budget for the new chopper in the transfer channel was late, thus the old one is used and higher failure rates are expected.

The new IPM (profile measurement) in SIS18 is not yet ready.

The beamline from FRS to ESR will be refurbished later.

The repair of the short-circuit fault in the ESR electron cooler was postponed.

Status and Outlook

In March 2018, preparation of the beam time is under way. Many tasks have to be fulfilled timely in order to start the user beam time as scheduled. The main risks are:

The air cooling of the UNILAC RF systems may not run reliably.

The commissioning of the RF systems, new and legacy, may reveal unexpected problems.

The new power connection together with the new main magnet power supplies of SIS18 must be commissioned successfully (AEG-Tests).

Bake-out of SIS18 and ESR bears an intrinsic risk of resulting in a vacuum leak. This would delay commissioning by 2-3 weeks.

Survey may reveal an ongoing movement of the accelerator buildings. This would increase the effort for the alignment and might compromise the performance of the accelerators and/or the beam quality.

References

[1] P. Schütt, M. Vossberg, S. Reimann, Shutdown Report in GSI Jahresbericht 2016

Experiment beamline: none
Experiment collaboration: none
Experiment proposal: none
Accelerator infrastructure: UNILAC / SIS18 / ESR / FRS / CRYRING / HEST
PSP codes: none
Grants: none
Strategic university co-operation: none

 DOI:10.15120/GR-2018-1

UNILAC Upgrade Activities

L. Groening[1], X. Du[1], P. Gerhard[1], M. Heilmann[1], M.S. Kaiser[1], S. Mickat[1], A. Rubin[1], A. Seibel[1], P. Scharrer[1], H. Vormann[1], C. Xiao[1],

[1]GSI, Darmstadt, Germany

The motivation of the upgrade project for the more than 40 year old UNILAC is twofold. First, as stated by a dedicated report on the status of availability and reliability of the existing post-stripper drift tube linac (ps-DTL), this section is not expected to cover the life time of FAIR [1]. Second, the layout of the whole UNILAC, even if fully refurbished, cannot meet the requirements imposed by FAIR [2]. In response to this, several upgrade activities where defined. They are listed in Tab.1 together with their current status.

Table 1: UNILAC Upgrade Activities.

Activity	Status	Duration [mos]
CompactLEBT	not approved	44
RFQ-matching	80% finished	12
RFQ electrodes	20% finished	27
MEBT	not approved	44
H2-Stripper	10% finished	36
new ps-DTL FoS	5% finished	39
new ps-DTL	not approved	96
UHV controls	15% finished	36
p-DTH HF FoS	90% finished	48
ps-DTL HF	not approved	48

The CompactLEBT comprises a dedicated uranium source terminal and beam line that does not use any bending magnet thus avoiding higher order field components and dispersion. It shall be installed between the existing northern and southern source terminals. Its design is finished but the project is not yet approved.

Final beam matching into the Radio Frequency Quadrupole (RFQ) is accomplished by a quadrupole quartet. The latter has been replaced by a new device including its power converters. The installation has been finished and commissioning without beam has been completed [3]. Commissioning with beam will be within the re-start of operation in 2018.

For the subsequent HSI-RFQ a new beam dynamics layout has been worked out, which in connection with the new matching allows for more beam intensity [4]. The electrodes will be fabricated in-house in order to install them in 2019.

The section between the RFQ and the subsequent prestripper DTL does not allow for optimized beam transport into the DTL. A new layout offering the required operational flexibility has been designed and components are ready for procurement. However, the activity has not been approved yet.

A systematic campaign on investigating stripper media and technologies to enhance the stripping efficiency of ions behind the pre-stripper DTL was conducted in the years 2013-2016 [5]. To transfer this successful prototyping into regular operation a dedicated test stand has been constructed and commissioned [6]. The layout of the new gas supply, vacuum-, and ventilation system has been started.

The aged post-stripper DTL causes an increasing amount of down time and its design does not allow for reaching the FAIR requirements. The conceptual design of a new Alvarez-type DTL has been elaborated, evaluated by an external committee [7], and summarized into a CDR [8,9,10]. The design and construction of a first-of-series (FoS) cavity section has been started and the order for the production of its cavity mantle has been placed. Significant progress has been made in the design of the drift tubes including pulsed quadrupoles [11]. With the exception of the FoS construction, the post-stripper DTL replacement has not been approved yet.

Last year the adaption of the control system of the UNILAC UHV control system to FAIR standards has been launched. Electronic components procurement and recabling inside the tunnel started.

The post-stripper DTL rf-power alimentation is based on technology of the 1970s. Its upgrade has been planned and a new FoS unit was commissioned successfully onsite [12]. Except for this FoS unit the upgrade of the full system has not been approved so far.

Figure 1 summarizes the horizontal beam brilliance (current per emittance) achieved most recently, together with the FAIR requirement. Results from fully consistent front-to-end simulations based on measured beam properties at the source exit are plotted for comparison. These simulations assume that all upgrade activities were implemented.

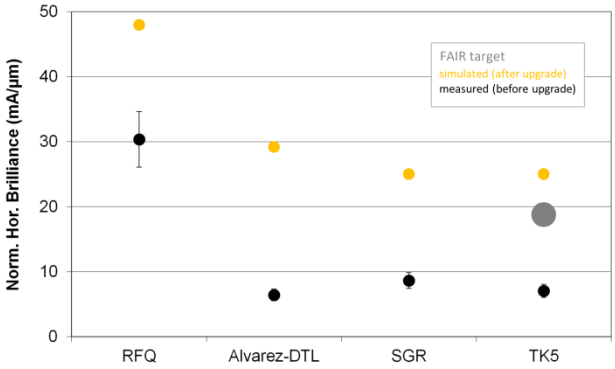


Figure 1: Horizontal beam brilliance along the UNILAC as measured in 2016 and as simulated under the assumption that all upgrade activities were accomplished.

References

[1] S. Mickat, H. Vormann et al. "Die UNILAC Post-Stripper Sektion - Zustandsaufnahme und Betriebsrisiko", internal report, (2013).

[2] "GSI FAIR Injector Review", edited by F. Gerick (CERN), internal report, (2014).

[3] H.Vormann et al. "Installation of the new HSI-LEBT quadruplet", this report.
[4] A. Lombardi et al. (CERN), "Beam dynamics design for the upgrade for the RFQ of GSI's high current injector", CERN report, (2017).
[5] P. Scharrer et al., Phys. Rev. Accel. Beams 20 043503, (2017).
[6] P. Scharrer et al., "The gas stripper test stand", this report.
[7] "Expert Review on Alvarez Replacement", edited by F. Gerick (CERN), internal report, (2017).
[8] S. Mickat et al., "Concept towards a new Alvarez type post-stripper DTL for the UNILAC", internal report, (2017).
[9] S. Mickat et al., "Status of new post-stripper DTL proposal", this report.
[10] A. Rubin et al., "Brilliance and error studies for the new post-stripper DTL", this report.
[11] M. Heilmann et al., "Prototyping for the new post-stripper DTL", this report.
[12] B. Schlitt et al., "Site acceptance tests of the new 108 MHz, 1.8 MW power amplifier protoype & status of the RF system modernisation at the UNILAC", this report.

Experiment beamline: UNILAC-Other
Experiment collaboration: none
Experiment proposal: none
Accelerator infrastructure: UNILAC
PSP codes: none
Grants:
Strategic university co-operation with: Frankfurt-M

 DOI:10.15120/GR-2018-1

UNILAC status report

P. Gerhard[1]

[1]GSI, Darmstadt, Germany

This status report overviews maintenance and refurbishment activities, upgrade measures and the preparation for the beam time 2018 at the UNILAC. Due to the general shutdown there was no beam operation in 2017.

Shutdown activities

The preparation of the GSI facility for FAIR (GaF), especially the preliminary works for the connection of the proton linac (pLinac) to the transfer channel (TK) and the construction of the pLinac building, had a major impact on the UNILAC. The TK beamline had to be completely covered with rugged plastic foils for several months to protect it from dirt and water running through the ceiling. Due to the earthmoving outside the TK building, certain sections of the building moved. Three bellows along the beamline were damaged. Alignment of the TK beamline will be necessary before the beam time 2018 starts.

Both large rotary pumps of the gas stripper pumping station suffered from degeneration of the oil and subsequent wear out. They had to undergo a general overhaul by the manufacturer. It has to be investigated if this was caused by overheating and/or extensive operation with hydrogen as stripper gas in the beam time 2016.

In July approx. 400 l of water were found in the TK foil stripper and charge state separator section TK3. A small leak in a water cooled baffle in the chamber of the first dipole TK3MV1 was identified as the cause. This leak had presumably opened some months earlier, but was not discovered, because the vacuum control system of this section was out of order. The dipole chamber was exchanged with a spare. Many beam diagnostic devices were polluted by foil residues and had to be refurbished or exchanged. The foil ladder and its drive have to be refurbished as well. This work was not finished in 2017.

The exchange of the HSI IH drift tube, with the defective quadrupole magnet triplet UH3QT5 inside, was already started in July 2016 [1]. The installation of the spare drift tube was delayed because a necessary shim was damaged during its copper plating. A new shim was ordered in February and ready for installation after copper plating in July. The installation was finished in November, but re-establishing of the vacuum is delayed to 2018 due to the damage of the stripper pumping station.

A new RF coupling loop was assembled and mounted on the 108 MHz buncher TK4BB11. This was the last action of refurbishment after a water leak of the coupling occurred in 2016 [1]. The commissioning will take place in 2018.

As a consequence of the severe breakdown of a kicker magnet power converter during the last beam time [1], a strategic refurbishment programme was developed by the EPS department. Several magnet power converters were already refurbished by exchanging aged capacitors and thyristor modules, ventilators and hoses. It was found, that capacitors are prone to aging during long shutdowns. This will be mitigated by powering all converters regularly. Additionally, direct current link voltage circuits were improved.

The cooling circuits of the single gap resonators UE1BE2 and UE1BE4 had to be rinsed. The foil stripper for the material science branch UM was revised, and SEM grids, beam current transformers and other beam diagnostic devices were checked. The data supply for the HSI magnets was adapted to allow for individual limits for low rigidity operation.

Beam time preparation

The modernisation of the UNILAC vacuum control system was delayed to 2019 due to difficult resource allocation; therefore the existing system had to be refurbished, including maintenance of the vacuum system. Defective devices (gate valves, IG and turbo pumps) were exchanged and vacuum leaks in the Alvarez cavities A2A (RF probe) and A3 (stop valve) were resolved. The pressure gauge of the gas stripper jet was fixed as well.

The UNILAC accelerator control system will remain unchanged for the time being, while all other accelerators will be controlled via the new LSA based FAIR control system from now on, including the timing system. Therefore, the synchronization between UNILAC and SIS has to be re-established. This will be tested during the dry runs.

Alignment of several sections was carried out due to the installation of new equipment (HSI LEBT) or maintenance activities (gas stripper section and HLI MEBT).

Upgrade measures

The main upgrade measure during this shutdown at the UNILAC was the installation of the new quadrupole quartet UH1QQ1 in the HSI LEBT, which started in March 2017 [2]. It required partial dismounting of the radiation shielding wall between the UNILAC tunnel and the ion source area, thereby interfering with RF tests. The installation of the magnets took much more effort than expected, mostly due to the 64 water cooled power lines, which had to be mounted properly. During commissioning of the new power converters in November, perturbing eddy currents induced in the beam pipe were discovered. Remedy has to be provided before the beam time 2018.

The upgrade of the RF gallery was continued [3] until the renewal of the air conditioning started in September. The main activities are the new high power amplifier for the Alvarez A4 transmitter and the modernisation of the Alvarez A3 transmitter and several power converters. During construction of the new ventilation building, rain water entered into the UNILAC tunnel through the roof.

The development for the replacement of the post-stripper DTL was continued, the procurement of a First-of-Series cavity section has been started [4, 5]. Testing of the new pulsed gas stripper using new low pressure gas valves was continued at a test bench [6]. As a first major

DOI:10.15120/GR-2018-1

part of the new vacuum control system, about 35 km of new cables were laid along the UNILAC and the TK. All upgrade measures are summarised in [7].

References

[1] P. Gerhard, "UNILAC Status report", GSI Scientific Report 2016, p. 389
[2] H. Vormann, "Installation of the new HSI-LEBT quadruplet", this report
[3] B. Schlitt et al., "Site acceptance tests of the new 108 MHz, 1.8 MW power amplifier prototype & status of the RF system modernisation at the UNILAC", this report
[4] S. Mickat, "Status of new post-stripper DTL proposal", this report
[5] M. Heilmann, "Prototyping for the new post-stripper DTL", this report
[6] P. Scharrer, "The gas stripper test stand", this report
[7] L. Groening, "UNILAC upgrade activities", this report

Experiment beamline: UNILAC-Other
Experiment collaboration: none
Experiment proposal: none
Accelerator infrastructure: UNILAC
PSP codes: none
Grants: none
Strategic university co-operation with: Frankfurt-M

 DOI:10.15120/GR-2018-1

Installation of the new HSI-LEBT Quadruplet

H. Vormann, P. Gerhard, L. Groening, M. Maier, S. Mickat, C. Xiao

GSI, Darmstadt, Germany

To improve the conditions for beam operation at the High Current Injector HSI a new quadrupole quartet with larger aperture has been installed. It will increase the degree of freedom for tuning of the LEBT matching, including both existing ion source branches and the proposed third branch [1, 2].

Quadrupole Quartet Design

The quadrupole quartet (QQ) is located at the end of the HSI-LEBT (where the two ion source branches are merged), right in front of the chopper followed by the RFQ (Fig. 1).

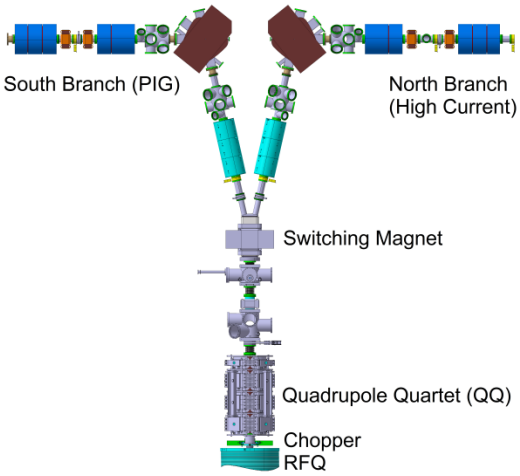


Figure 1: Sketch of the HSI-LEBT.

Based on operation experiences, the new QQ was designed with a large aperture (new: 150 mm; old: 100 mm), and optimised lengths of the single quadrupoles. The larger aperture requires high pole tip flux density (new: 0.92 T; old: 0.70 T), achieved through higher coil currents (new: 1100 A; old: 400 A), provided by high performance power supplies for pulsed operation (50 Hz, i.e. 20 ms cycles, incl. max. 15 ms ramping time and 5 ms flat top).

Power Supplies

The four new power supplies SVE25m were procured in 2015 and delivered in September 2017 (Fig. 2). They provide for a voltage of 1200 V, to ramp up to 1100 A nominal coil current within less than 15 ms.

Assembly

The procurement for the new QQ started in 2010, it was delivered to GSI in 2012 and field mapped in 2013. At that time installation did not yet start because power supplies were not available, and could not be procured soon, due to the work load for FAIR. Assembly of the QQ started in March 2017: after disassembly of the LEBT the old QQ was removed from its place in the concrete shielding wall. The new connection boxes were produced in house and installed until end of April. The new QQ was installed and provisionally aligned by the end of May. Most time consuming was the bending and brazing of the 64 coil supply tubes (copper 9x9 mm, length up to 5 m), with additional fixations. Modifications of the door lock system, the radiation protection switchboard, the cooling water supply circuits, the venting system of the ion source north terminal, and the electric mains supply were performed for the QQ assembly, as well as the installation of a new electricity sub-distribution. The LEBT beam diagnostics and steerer magnets were re-assembled with shorter distances, using space-saving vacuum tubes with integrated bellows. At the end of 2017 the assembly was almost finished (except alignment and re-cabling of peripheral devices, Fig. 3). Commissioning and SAT of the power supplies have been performed successfully in December. The tests revealed increased eddy currents on the chamber surface. Impact and counter measures are under investigation. However, the beam time 2018 can be served as foreseen.



Figure 2: Power supplies (each 2.8 m x 0.8 m x 2m) installed in the basement.

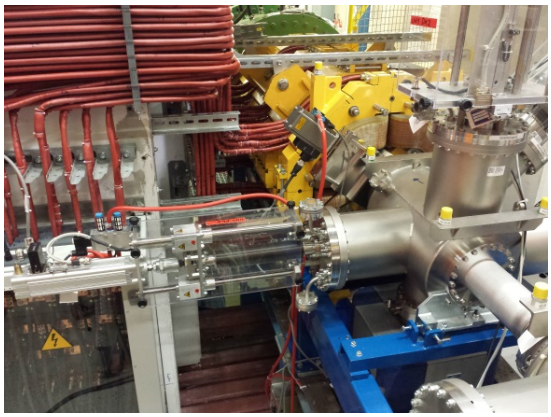


Figure 3: New QQ (yellow) installed, insulated coil supply tubes, connection boxes, beam diagnostic chambers.

References

[1] L. Dahl et al., Proc. of LINAC 2006 Conf., MOP060 (2006)

[2] L. Groening et al., this report

Experiment beamline: none
Experiment collaboration: none
Experiment proposal: none
Accelerator infrastructure: UNILAC
PSP codes: none
Grants: none
Strategic university co-operation with: none

 DOI:10.15120/GR-2018-1

Site acceptance tests of the new 108 MHz, 1.8 MW power amplifier prototype and status of the RF system modernisation at the UNILAC

B. Schlitt, M. Hörr, G. Schreiber, J. Catta, T. Eiben, G. Eichler, S. Hermann, F. Lorenz, S. Petit, M. Pilz, J. Salvatore, R. Scholz, A. Windolf, and J. Zappai

GSI, Darmstadt, Germany

A substantial modernisation of the 108 MHz RF systems at the Alvarez post-stripper linac at the UNILAC is in progress to prepare the existing facility for the future FAIR operation [1, 2].

New 1.8 MW cavity amplifier prototype

The new 1.8 MW cavity amplifier prototype delivered by Thales Electron Devices [1–3] was commissioned successfully at GSI in 2017. The existing 1 MVA, 24 kV anode power supply of the Alvarez tank 4 (A4) RF system is used to provide the required DC power. Commercial grid power supplies are installed in a separate control rack which comprises also a fast measurement and interlock unit as well as further control elements (Fig. 1). A manual control unit developed by GSI was used for commissioning and tests. A new PLC system is currently being installed for routine operation and to allow remote control by the accelerator control system [1]. The input RF power is provided by the existing A4 driver amplifier. An existing huge coaxial transmission line switch in the output RF line is used to switch between a water dummy load and Alvarez tank 4.



Figure 1: New 1.8 MW cavity amplifier prototype during site acceptance tests at the UNILAC RF gallery plus control rack equipped with grid power supplies and control elements.

During site acceptance tests (SAT) of the new amplifier at GSI in July and August 2017 an RF pulse output power ≥ 1.8 MW and a gain factor of about 12.8 dB were reached successfully at the specified pulse length of 2 ms and a pulse repetition rate of 10 pps (Fig. 2). Tests were conducted on water dummy load as well as on Alvarez tank 4 (closed-loop operation controlling RF amplitude and phase in the accelerating cavity). The levels of harmonic and non-harmonic frequencies were well below the specified limits (< –24 dBc and < –60 dBc, respectively). Further tests were performed at a certain cavity mismatch and at intermediate pulse power levels with different pulse schemes, as well as a 2 hour test run without any trips of the amplifier. Routine operation of the new amplifier is planned on A4 tank from beam time 2018 on.

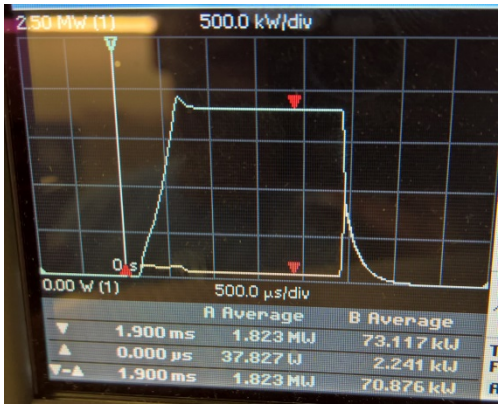


Figure 2: Forward (upper trace) and reflected RF power during closed-loop operation on Alvarez tank 4.

Modernisation of existing RF systems

The newly developed PLC system for control of the high power amplifiers [1] was installed and tested at the Alvarez 3 RF system in 2017. After successful operation of this prototype during beam time 2018 similar PLC systems will be installed at Alvarez 1 and 2. In parallel, new PLC systems to control the 1 MVA power supplies [4] were installed and tested at A1 – A3.

A new versatile microcontroller based system for resonance frequency control of the accelerating structures [4] was operated successfully at the HLI RFQ during beam time 2016. It was developed further and tested at the Alvarez tanks in 2017 and will be applied during routine operation at the Alvarez linac in 2018. Besides, first RF tests of a new digital low-level RF system (LLRF) for amplitude and phase control based on the MicroTCA.4 standard [5, 2] were conducted successfully at a laboratory test setup [6].

In parallel to the modernisation of the RF systems, a new forced-air cooling system providing air cooling for > 60 devices at the UNILAC RF gallery was installed and commissioned by external companies and by the GSI Plant & Facility Engineering department.

References

[1] B. Schlitt et al., GSI Scientific Report 2016, p. 392.
[2] B. Schlitt et al., LINAC2016, THPLR025.
[3] Thales Electron Devices, Thonon-les-Bains, France.
[4] B. Schlitt et al., GSI Scientific Report 2015, p. 310.
[5] J. Zappai et al., GSI Scientific Report 2015, p. 309.
[6] J. Zappai et al., LLRF2017, Barcelona, Poster P-12.

Experiment beamline: none
Experiment collaboration: none
Experiment proposal: none
Accelerator infrastructure: UNILAC
PSP codes: none
Grants:
Strategic university co-operation with: none

 DOI:10.15120/GR-2018-1

Status of the new post-stripper DTL

S. Mickat, L. Groening

GSI, Darmstadt, Germany

In February 2017 the GSI/FAIR directorate decided that for the new post-stripper DTL the Alvarez option will be followed exclusively. The decision towards a new Alvarez type DTL against three competitive DTL concepts was made mainly for its robust beam dynamics concept. The applied periodic particle beam dynamics provides best beam qualities for FAIR along the DTL even in case of beam fluctuations, alignment tolerances, and multi-beam operation [1].

The beam dynamics advanced in interaction with optimisations of the RF cavity design [2, 3]. A detailed error study has been worked out. The UNILAC was modelled for front-to-end simulations - from the sources to the SIS18 entrance - taking the new post-stripper DTL design and the planned UNILAC upgrade measures into account. The results confirm former predictions, that the new post-stripper DTL together with the UNILAC upgrades [4] meets the FAIR requirements.

An important milestone towards the realisation of the new post-stripper DTL was the funding of the first section of the new first Alvarez cavity as a First-of-Series (FoS) in August 2017 [5] (Fig. 1). A budget of 1.5 MEUR until 2020 was allocated for the cavity, technical subsystems and infrastructure measures. For instance, a cavity test stand for high power RF tests will be installed, which needs common media supplies for cooling water, air-pressure, electrical connections, an adequate x-ray shielding, and an RF-power supply itself. An existing 200 kW RF-amplifier can be used initially. For finalising the tests at nominal RF-power the regular amplifier of the existing Alvarez IV cavity can be used temporarily in accordance with the UNILAC beam time schedule. Negotiations on an adequate location for the test stand at the UNILAC experimental hall are ongoing.

Regarding the procurement of the FoS three main components are distinguished: the tank shell, the two end-plates, and the eleven drift tubes with integrated quadrupoles. The order for the tank section was placed in November 2017. Currently the specification of the two cooled end plates is in progress. Adaptions of the drift tube design in favour of RF-efficiency and beam dynamics were applied implying changes to the integrated quadrupole design and to the established fabrication sequence of the existing AIII and AIV drift tubes. Currently a modified fabrication and assembly sequence is tested at the on-site workshop.

These and further aspects in detail as well as the current planning towards a new post-stripper DTL are presented in a CDR, which has been published in December 2017 [6].

References

[1] S. Mickat et al., “Benchmarking of four post-stripper DTL options”, GSI Scientific Report 2016, p. 395.
[2] A. Rubin et al., “Brilliance and error studies for the new post-stripper DTL”, this report.
[3] X. Du et al., “Cavity design activities for the UNILAC”, this report.
[4] L. Groening et al., "Upgrade of the UNILAC for FAIR", Proceedings IPAC2016, MOPOY017, Busan, Korea.
[5] M. Heilmann et al., “Prototyping for the new post-stripper DTL”, this report.
[6] S. Mickat et al., "Concept towards a new Alvarez type post-stripper DTL for the UNILAC", internal report (2017).

Experiment beamline: none
Experiment collaboration: none
Experiment proposal: none
Accelerator infrastructure: UNILAC
PSP codes: none
Grants: none
Strategic university co-operation with: none

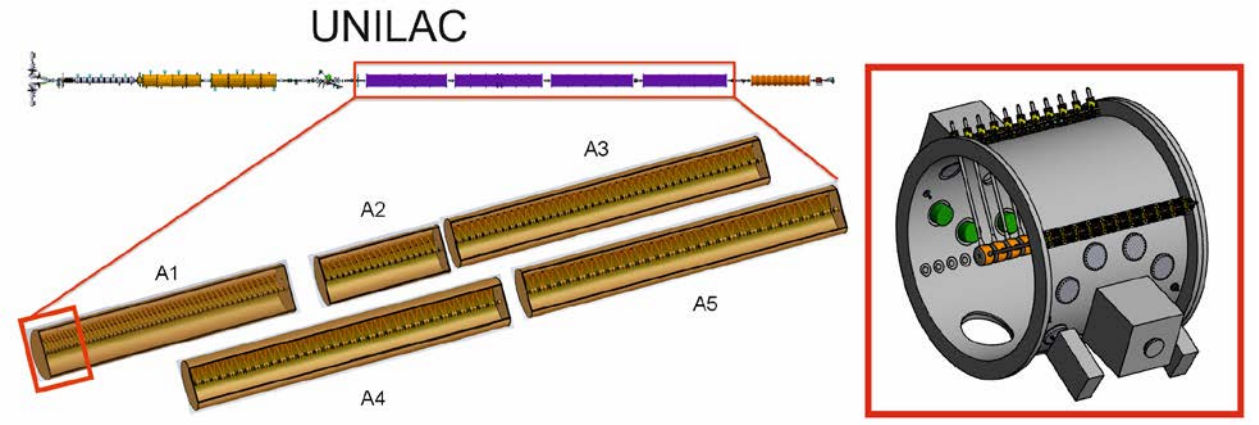


Figure 1: The new DTL design consists of five cavities (A1-A5like the existing post-stripper DTL. The first section of cavity A1 is the First-of-Series (FoS): a nearly two meters long tank section containing 11 drift tubes (right).

Cavity design activities for the UNILAC

X. Du[1], P. Gerhard[1], L. Groening[1], and S. Mickat[1]

[1]GSI, Darmstadt, Germany

Post-stripper DTL

The design of a completely new post-stripper DTL is part of the UNILAC upgrade program for FAIR[1]. Acceleration from 1.4 MeV/u to 11.4 MeV/u is achieved by five tanks. The new design features a homogenous surface field at the drift tube surfaces thus improving the shunt-impedance. Additionally, a new RF-field stabilization method has been developed and experimentally confirmed [2].

In 2017 the beta profile design of the DTL has been updated and improved w.r.t. further reduction of the betatron amplitude and hence the longitudinal beam quality. The results were used for the design of the transverse beam dynamics [3]. The beta profile design process has been improved by an advanced tuning algorithm for the cell lengths and by optimization of the synchronous particle energy gains per cell. The inadequate beam dynamics description caused by the generally uniform particle speed approximation was considerably updated.

According to recent simulations and measurements the design input energy was lowered from 1.393 MeV/u to 1.358 MeV/u [4]. The actual beta profile design includes this change.

Re-bunchers

The existing re-bunchers US4BB3 and US4BB4 in front of the post-stripper DTL shall provide for accurate longitudinal beam matching. For their crucial relevance of operation spare cavities need to be made available.

The RF design of the re-bunchers starts with geometric parameters adapted from existing cavities BB3. In order to match the existing pillow, the new designs use the existing outer tank radii. Table 1 lists the geometric parameters of the two re-bunchers.

Table 1: Geometric parameters of the new re-bunchers US4BB3 and US4BB4.

Parameter	BB3	BB4
Cell number	3	2
Tank inner radius	250 mm	175 mm
Tank inner length	520 mm	201 mm
Tube inner radius	27.5 mm	20 mm
Tube outer radius	32.5 mm	25 mm
Gap length	26.4 mm	16.14 mm

The spiral stems were re-designed for sufficient mechanical stability and shunt impedance. US4BB3 has two stems fixing one drift tube each. Their winded total lengths are 2.5 m thus causing the inductivity to provide for low resonant frequency using a small tank radius. These lengths together with their appropriate widths feature sufficient rigidity to prevent detuning from Lorentz forces.

In fact, the existing re-buncher US4BB3 has mechanical stability issues and the stems were reinforced by 40 mm. For the new layout, the estimated Lorentz force on the drift tube and stems is about 1.2 N, which shall be confirmed by simulations using mechanics solver [5].

Simulations with CST-MWS were performed to determine free geometric parameters to be used for further optimization of the RF-parameters. Table 2 presents the achieved RF-parameters.

Table 2: RF-parameters of re-buncher US4BB3 and US4BB4 from CST-MWS simulations.

Rf-parameters	US4BB3	US4BB4
Frequency	36.136 MHz	108.408 MHz
Total gap voltage	875 kV	350 kV
Total power loss	74 kW	13 kW
Shunt impedance	12 MOhm/m	9 MOhm/m
E_peak	49 MV/m, 6 Kilp.	22 MV/m, 2 Kilp.
Tuning range	0.5 MHz	2 MHz

Mechanical error studies on US4BB3 investigated frequency shifts due to alignment errors and fabrication imperfections. The most sensitive part in the whole cavity is the volume between the drift tubes, where the electric energy density and the surface gradients are at maximum. Simulations show that the frequency shift induced by transverse (longitudinal) drift tube shifts is 0.0175MHz/mm (0.045MHz/mm). For the drift tube thickness it is 0.11 MHz/mm. Considering the anticipated machining precision, the tuning range is much larger w.r.t. to these frequency shifts. The orders for the production of both re-bunchers have been placed, delivery is expected end of 2018.

References

[1] L. Groening et al., Upgrade of the Universal Linear Accelerator UNILAC for FAIR, Proc. of IPAC 2016, MOPOY017, (2016).
[2] X. Du et al., Phys. Rev. Accel. Beams, 20 032001 (2017).
[3] A. Rubin et al., this report.
[4] L. Groening, "Design input energy for the new UNILAC post stripper DTL", internal report (2017).
[5] https://www.cst.com/Applications/MWandRF.

Experiment beamline: UNILAC-Other
Experiment collaboration: none
Experiment proposal: none
Accelerator infrastructure: UNILAC
PSP codes: none

 DOI:10.15120/GR-2018-1

First measurements of the short CH-Cavities for the cw heavy Ion LINAC@GSI

M. Basten[1], K. Aulenbache4[3], W. Barth[2,3], M. Busch[1], F. Dziuba[2], V. Gettmann[2], M. Heilmann[3], T. Kürzeder[2], M. Miski-Oglu[2], H. Podlech[1], A. Rubin[3], M. Schwarz[1], S. Yaramyshev[3]

[1]Goethe-Universität, Frankfurt, Germany, [2]HIM, Mainz, Germany; [3]GSI, Darmstadt, Germany; [4]Johannes Gutenberg-Universität, Mainz, Germany

The upcoming FAIR project (Facility for Antiproton and Ion Research) at GSI will use the existing UNILAC (UNIversal Linear Accelerator) as an injector to provide high intensity heavy ion beams at low repetition rates. As a consequence a new superconducting (sc) continous wave (cw) high intensity heavy ion Linac is required to provide ion beams above the coulomb barrier to keep the Super Heavy Element (SHE) physics program at GSI competitive on an international level [1]. The cw Linac design comprises a high performance ion source (ECR), the High Charge State Injector (HLI) upgraded for cw-operation, and a matching line (1.4 MeV/u) followed by a sc Drift Tube Linac (DTL). Presently two sc eight gap CH-cavities are under construction at Research Instruments (RI). Several intermediate RF measurements have been performed during the construction phase.

Pressure sensitivity measurements

The design of the cavity is based on eight equidistant gaps without girders and with stiffening brackets at the front and end cap to reduce pressure sensitivity. To verify the simulated pressure sensitivity with the simulations, the deformation of the cavity as well as the frequency change (Fig. 1) have been measured.

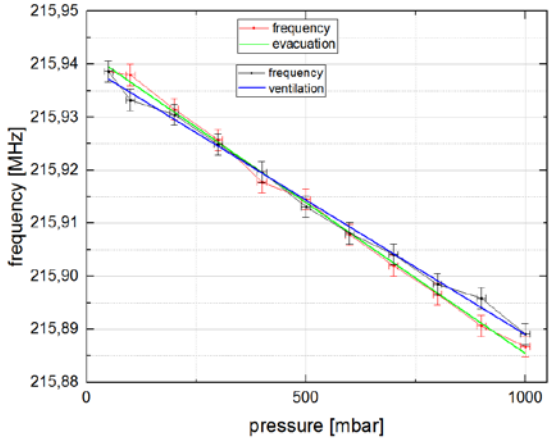


Figure 1: Measured pressure sensitivity during evacuation and ventilation of the cavity

Taking the change in ε_r into account we measured a pressure sensitivity of approx. $\Delta f = (-6.74 \pm 1)$ Hz/mbar during evacuation and approx. $\Delta f = (-12.87 \pm 1.1)$ Hz/mbar during ventilation. The simulated pressure sensitivity was approx. $\Delta f = +4.61$ Hz/mbar. In contrast to the simulation the frequency goes down during the evacuation process. This means we have more deformation in regions with high electric fields that in regions with high magnetic fields. The measured deformation however was lower than simulated. We measured the deformation on three different spots with fine dial indicators and all of them showed less deformation than expected from the simulations with CST. Nevertheless the pressure sensitivity is significantly lower compared to the first CH-structure of the demonstrator. As a consequence stable operation at the resonance frequency can be confirmed.

Frequency measurements during thermal shrinking

The frequency change induced by thermal shrinking of the cavity has been compared with CST simulations. The cavity was positioned in a metal tub and cooled with liquid nitrogen. 6 temperature sensors were placed along the cavity to evaluate the average temperature of the cavity. The frequency change depending on the average temperature (Fig. 2) have been evaluated.

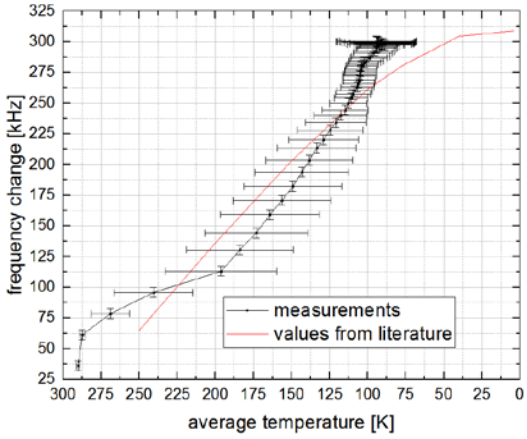


Figure 2: Measured frequency change depending on the average temperature of the cavity

The measured frequency change at an average temperature of 95 K was approx. 14% more than expected by deformation values from literature. It seems that the gradient in the average temperature along the cavity is mainly responsible for this discrepancy. We covered roughly half of the cavity with liquid helium while the top of the cavity became more than 20 K warmer than the bottom of the cavity. To provide high acceleration gradients a well prepared surface is indispensable. The BCP-treatment etches several µm from the inner surface of the cavity. As a consequence the frequency increases. Taking all influences on the resonance frequency into account, we can now perform the final BCP to reach the design frequency of 216.816 MHz. BCP is scheduled for February 2018, the first cavity will be delivered in March 2018, the delivery of the second cavity may follow approx. 2 months later.

[1] W. Barth et al., "Further investigations for a superconducting cw-Linac at GSI", in Proc. IPAC'17, Copenhagen, Denmark, May 2017, paper TUPVA055, pp. 2197-2200

Prototyping for the new post-stripper DTL

M. Heilmann, X. Du, L. Groening, M. Kaiser, S. Mickat, C. Mühle, V. Srinivasan*

[1]GSI, Darmstadt, Germany

The final design describes the First-of-Series (FoS) Alvarez-Cavity-section of the first tank being part of the new post-stripper DTL of the UNILAC [1]. The FAIR experiments have new requirements to the linac and a high availability is important for the new main operational injector [2]. In the first step the FoS-cavity (Table 1) has an input energy of 1.36 MeV/u with 11 drift tubes (including quadrupole singlets) in a total length of 1.9 m and a diameter of 2 m with an operation frequency of 108.4 MHz [3,4]. The drift tubes will have a new shape profile at the end plates. The single layered quadrupole singlets inside the drift tubes are pulsed with 10 Hz and will have a maximum field gradient of 51 T/m. The new drift tube design combines the new shape profile with the transverse and longitudinal installation space of the magnet. The FoS Alvarez-cavity will be part of the first section of the new Alvarez DTL. It shall be operated at nominal RF- and magnetic fields prior to procurement of the series. After low level measurements at the test stand the Alvarez-prototype will be conditioned and operated with high RF power.

Mechanical Integration

The tank is under construction at the company VA-TEC. The next tendering for the main components is planned for the two end plates and after that for the drift tubes (including magnets). For RF coupling a well-established coupler-type will be used. The RF-power test stand is planned to be ready at the end of 2018 (Fig. 1).

The drift tube prototype is under technical development together with the GSI-mechanical workshop (MeWe) and the magnetic design is being finalized by the GSI-department "Normal Conducting Magnets" (Fig. 2).

Table 1: Parameters of the Alvarez-Prototype

Parameter	Unit	Value
Frequency	MHz	108.408
A/q		≤8.5
Max. beam current	mA	16.5
Synchronous phase	deg.	-30
RF-pulse length	ms	2
RF pulse repetition rate	Hz	10
Input energy	MeV/u	1.36
Output energy	MeV/u	1.67
Gaps	#	12
Gap length	mm	40.5-44.6
Drift tubes	#	11
Drift tube length	mm	109.9-121.0
Drift tube diameter	mm	180.0
Aperture	mm	30.0
Tank diameter	mm	1952.6
Tank length	mm	1880.5
Q-Factor		82000

* m.heilmann@gsi.de

The drift tube design was simplified so that all components can be built at GSI and just the magnets must be stocked as spare parts.

The pulsed quadrupole singlet lens design is based on a single layer winding concept. The new Alvarez-DTL (A1-A5) will have seven different groups of quadrupole magnets; each of them has its own aperture, effective length, and gradient.

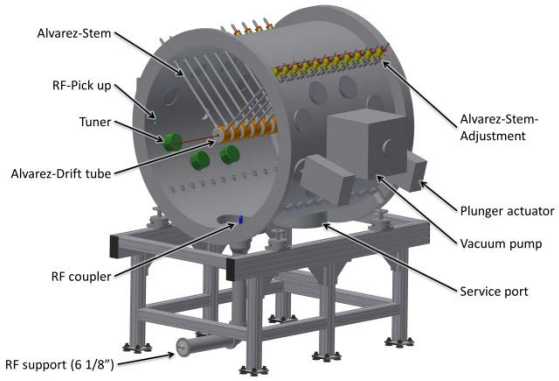


Figure 1: CAD-model of the post-stripper DTL. The FoS-tank has a length of 1.9 m and 11 drift tubes. The adjustment concept will be the same as in the existing Alvarez. The plunger actuator will have a range of 250 mm at the FoS-Alvarez-Cavity-section and the tuners are of 100 mm in length with a diameter of 180 mm.

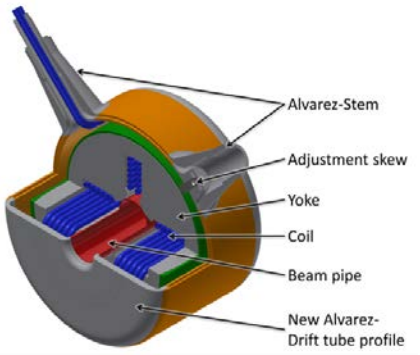


Figure 2: Alvarez-drift tube prototype with the new shape profile and an aperture of 30 mm. Inside of each drift tube is a pulsed quadrupole singlet magnet with a gradient of 51 T/m and an effective length of 99.5 mm.

References

[1] M. Mickat et al., "Concept towards a new Alvarez type post-stripper DTL for the UNILAC ", Technical Note, Internal Report, December 2017.

[2] L. Groening et al., "Upgrade of the Universal Linear Accelerator UNILAC for FAIR", IPAC'16, May 2016, Busan, Korea, p. 880, http://www.jacow.org.

[3] X. Du et al. (this report).

[4] A. Rubin et al. (this report).

 DOI:10.15120/GR-2018-1

Experiment beamline: none
Experiment collaboration: none
Experiment proposal: none
Accelerator infrastructure: UNILAC
PSP codes: none
Grants: none
Strategic university co-operation with: none

Brilliance and error study for the new post-stripper DTL

A. Rubin[1], X. Du[1], P. Gerhard[1], L. Groening[1], S.Mickat[1]

[1]GSI, Darmstadt, Germany

The GSI UNILAC has served as injector for all ion species since 40 years. Its 108 MHz Alvarez DTL providing acceleration from 1.4 MeV/u to 11.4 MeV/u. It has suffered from material fatigue and has to be replaced by a new section [1]. The design of the new post-stripper DTL is developed at GSI [2]. The beam dynamics simulations for the new model were done for 238U28+ using the TraceWin code. Five Alvarez tanks with four inter-tank sections provide 100% transmission and low emittance growth (about 5% transverse and 7% longitudinal rms emittance growth for the FAIR case) [3].

Error study for the new Alvarez DTL

Error studies for the new Alvarez DTL were done taking into account machine and beam errors (Tab. 1), which are independent and uniformly distributed within given intervals. All cases revealed 100% transmission.

Table 1: Machine and beam errors:

Quadrupole x,y displacement	± 0.15mm
Quadrupole x,y,z rotation	± 1°
Gap voltage	± 1%
Gap phase	± 1°
Initial energy	± 0.5%
Input emittances	± 15%
Input beam mismatch	± 10%
Input current	± 15%

The average additional rms emittance growth caused by machine and beam errors is about 26%. The detailed investigation shows that the 1st tank is the most sensitive to the errors. The main reason for additional emittance growth is quadrupole rotation around the beam axis (Fig.1). Limiting the quadrupole rotation in tank A1 to ±0.5° while keeping it at ±1° in A2-A5 leads to 13% of mean emittance growth for the whole machine.

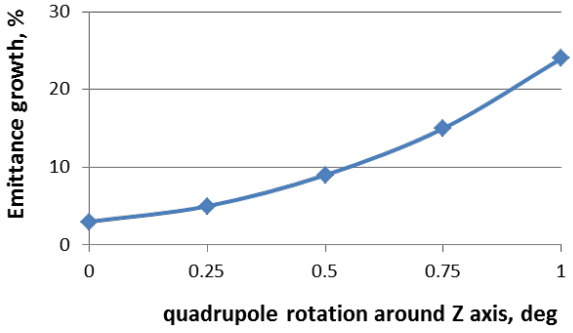


Figure 1: Mean additional emittance growth as a function of the quadrupole rotation around beam axis.

Brilliance analysis at SIS18 input

In order to estimate the beam brilliance behind the DTL a virtual collimator line was constructed. After four quadrupole triplets and four collimators the beam has a well defined total emittance. The horizontal acceptance of the synchrotron SIS18 to be filled by the DTL is 0.8 mm mrad (total, normalized). The collimators width is chosen such that the beam emittance behind the virtual collimator line leaves a margin for additional growth until injection into the SIS18 of 10% or 30%. The transmission through the collimators line allows to estimate the expectes current into the SIS18 acceptance. This investigation was done without machine (DTL) and beam errors as well as with errors. The position of the data on the 3D Pareto front [4] assuming emittance growth along the transport channel is shown in Fig. 2. The current in case of no DTL errors (13.2 mA) corresponds to suitable injection losses below 5%. With DTL errors it drops to 12.2 mA. Reduction of the assumed emittance growth along TK to 10% shifts the corresponding point for the case with DTL errors (13.2 mA again) towards the preferable region.

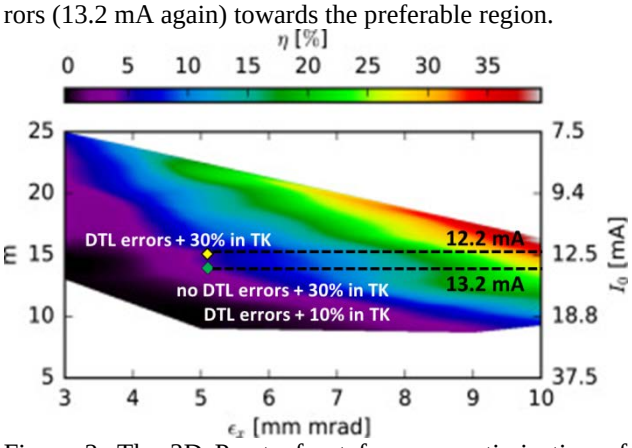


Figure 2: The 3D Pareto front from an optimization of multiplication factor, loss, and emittance with the data achieved behind new DTL assuming emittance growth in the transport channel to SIS18 [4].

References

[1] L. Groening, et al. ”Upgrade of the Universal Linear Accelerator UNILAC for FAIR”, IPAC 2016, Busan, Korea, Mar. 2016, MOPOY017, pp. 880-882

[2] X. Du, et al. ”Alvarez DTL Cavity Design for the UNILAC Upgrade”, IPAC 2015, USA

[3] A. Rubin, et al. ” Status of beam dynamics design of the new post-stripper DTL”, annual report 2016, GSI

[4] S. Appel, et al. ” Injection optimization in a heavy-ion synchrotron using genetic algorithms”, Nuclear Instruments and Methods in Physics Research Section A, Volume 852, 21 April 2017, pp. 73–79

Experiment beamline: UNILAC-Other
Experiment collaboration: none
Experiment proposal: none
Accelerator infrastructure: UNILAC
PSP codes: none
Grants: none
Strategic university co-operation with: none

 DOI:10.15120/GR-2018-1

First results at the pulsed gas stripper test stand

P. Scharrer[1], M. Maier[1], W. Foosang[2], P. Gerhard[1], K.P. Horn[1], M. Schweda[1,]

[1]GSI, Darmstadt, Germany; [2]Faculty of Science, Chiang Mai University Chiang Mai 50200, Thailand.

The pulsed gas stripper for the UNILAC was developed and tested in beam times 2013 to 2016 [1]. An increase of the stripping efficiency into the FAIR design charge state of U^{28+} of up to 65% has been achieved using a H_2 target (instead of a N_2 target). Injector valves, commonly used for liquid fuel in combustion engines, were used for the gas injection (liquid valve).

In recent beam times in 2016, this valve type showed a serious flaw in prolonged operation, resulting in frequently arising interlocks from the pumping system. Therefore, a new valve type, designed to be used with gaseous media, was chosen to allow for using the pulsed H_2 gas stripper for UNILAC standard operation. Before commissioning of the new valve type with beam during the upcoming beam time, an offline test stand was built to characterize the new valves (gas valve) and compare their performance with the previously used liquid valve type.

Valve test stand

One of the most important parameters for the pulsed H_2 gas stripper is the applied target thickness, as it defines the resulting charge state distribution [2]. The optimal back-pressure for U^{28+} operation in previous beam times using liquid valves was 7.5 MPa. The gas valves can only be operated with back-pressures below 1.2 MPa, but have an increased opening aperture. The main question being addressed was, if the required target thickness can be achieved using the new gas valve type.

A simplified design was chosen for the test stand setup. At the UNILAC, the target thickness is usually determined as an effective value using the measured energy loss of the beam [1]. At the test stand, the pressure in the chamber behind the gas valve as well as the gas flow through the valve, are measured to evaluate the valve performance.

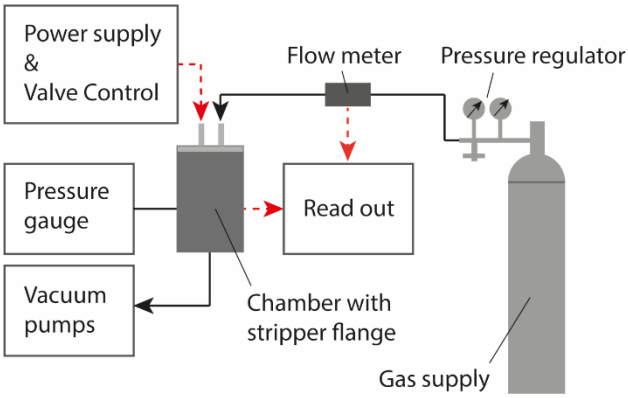


Figure 1: Scheme of the current test stand setup.

The setup of the test stand is shown in Fig. 1. The valves are mounted on the original flange of the pulsed gas stripper [1] on top of the chamber. To mount the smaller gas valves, the valve adapter was redesigned and built in-house. The vacuum chamber is connected to a pumping system, featuring two roots vacuum pumps and a rotary pump. Due to safety reasons, the operation with H_2 gas is not possible at the test stand. Instead, He and N_2 gas are used for test purposes. Additionally, a new valve control system was commissioned, which allows for more flexibility in adjusting the valve parameters and provides better compatibility with the UNILAC control system. The main assembly of the setup and first measurements were done in the framework of the summer student program.

Measurements

In Fig. 2, the measured pressure in the chamber is shown as a function of the back-pressure using He gas for both valve types at 1 ms opening time. Both valves reach similar gas pressures inside the chamber, operating in their respective range of back-pressure. This behavior is confirmed by measurements of the gas flow and suggests that a similar target thickness can be obtained in the UNILAC gas stripper using the new gas valves.

However, the gas flow measurements at varying opening times also show that the conductance of the gas supply system is insufficient to feed the gas valves. This results in unreliable flow measurements at longer opening times, which are important to determine the optimal opening sequence of the valves when synchronizing the gas injection with the beam pulse timing. A new stripper flange with a higher conductance has been designed and is currently manufactured. Together with an improved gas supply system it will be tested in 2018.

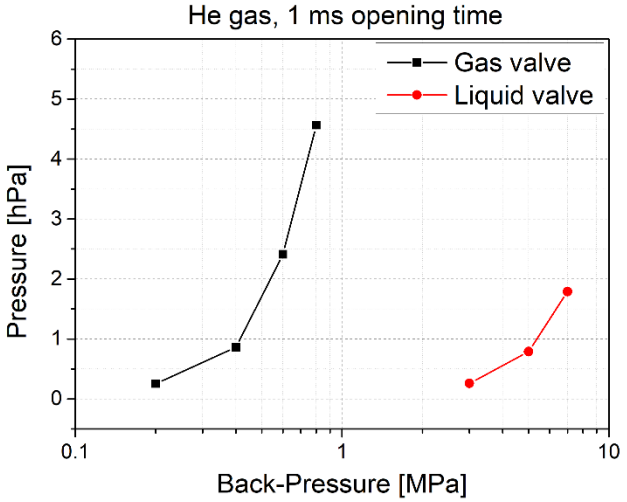


Figure 2: First measurements comparing the pressure inside the chamber with both valve types.

References

[1] P. Scharrer et al., Phys. Rev. Accel. Beams 20 043503 (2017).

[2] H. D. Betz, Rev. Mod. Phys. 44 3, p. 465-539 (1972).

Experiment beamline: none
Experiment collaboration: none
Experiment proposal: none
Accelerator infrastructure: UNILAC
PSP codes: 170100312
Grants: none

 DOI:10.15120/GR-2018-1

Development of an IH-type linac for the acceleration of high current heavy ion beams

H. Hähnel, U. Ratzinger, R. Tiede*

Institut für Angewandte Physik, Goethe Universität, Frankfurt, Germany

* Contact: haehnel@iap.uni-frankfurt.de

An efficient and compact linac design proposal for the UNILAC poststripper based on H-mode cavities and KONUS beam dynamics has been developed at IAP Frankfurt in the last few years [1, 2]. It features five RF-cavities with high shunt impedances of $Z_{eff} = 90 - 152\ M\Omega/m$. In combination with the short period length of $L_p = \beta\lambda/2$, another main benefit of H-mode linacs, the total length of the proposed poststripper linac is 22.8 m.

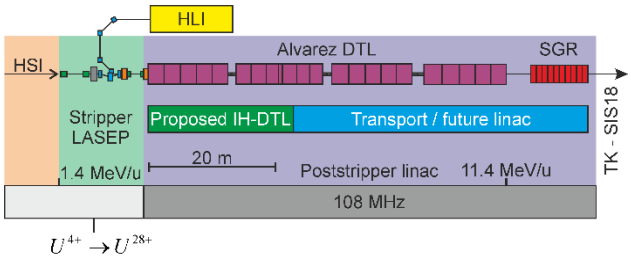


Figure 1: Sketch of the existing UNILAC poststripper section with the dimenstions of the proposed IH-DTL linac.

Beam Dynamics / Focusing

By utilising the KONUS beam dynamics concept, a linac design with long IH-type cavities and a total of only seven quadrupole triplet lenses for the whole linac was possible. Based on a two-stage constant phase advance approach, the emittance growth of the linac was minimized to just above 25 % in the transverse planes. The careful design of the longitudinal beam motion in the KONUS lattice resulted in high longitudinal beam quality with only 10 % emittance growth (as shown in Figure 2). Design simulations were performed with a waterbag input distribution. For the reference beam ($15\ mA\ U^{28+}$), full beam transmission is achieved.

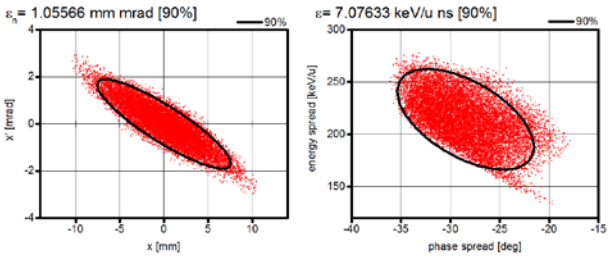


Figure 2: Particle distribution at the exit of the IH-DTL poststripper linac from LORASR simulations with $5 \cdot 10^6$ macroparticles. Transverse (left) and longitudinal (right) planes are shown.

Error Studies

To judge the real-world performance of the proposed linac, extensive error studies were performed. In these studies, realistic and even excessive machine errors ranging from misalignment of components to fluctuations of machine settings were investigated [1]. For realistic tolerance values, the linac performance was almost unchanged with additional emittance growth for all cases in the range of only 1-2 %. In combination with a developed steering strategy, the total beam losses of even the worst case could be reduced to 0.03 %. Beam losses in the case of realistic tolerance almost vanished to only $6 \cdot 10^{-8}$.

Fieldmap Calculations

Recent beam dynamics calculations using realistic 3D-fieldmaps of the electromagnetic field in the first two cavities (= four KONUS sections) were performed using the TraceWin code (see Figure 3). The results are in good agreement with LORASR simulations. With TraceWin, an even lower transverse emittance growth is predicted.

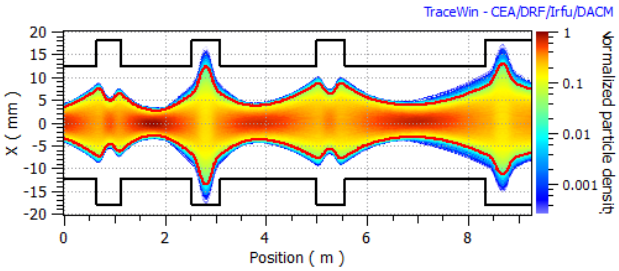


Figure 3: Transverse beam envelope from beam dynamics calculations with cavity fieldmaps calculated from the CST cavity models.

These results in combination with the aforementioned error studies clearly hint towards satisfying real-world performance of the proposed poststripper linac design.

Acknowledgements

We appreciate the collaboration within the UNILAC upgrade program at GSI (W. Barth, L. Groening, et al.).

References

[1] H. Hähnel, Dissertation, Goethe University, Frankfurt, 2017, URN: urn:nbn:de:hebis:30:3-439833 http://tinygu.de/HaehnelDiss

[2] H. Hähnel et al., 2017 J. Phys.: Conf. Ser. 874 012047

Accelerator infrastructure: UNILAC
Grants: BMBF 05P15RFRBA
Strategic university co-operation with: Frankfurt-M

Investigations on KONUS beam dynamics using the pre-stripper drift tube linac at GSI

C. Xiao, X.N. Du, and L. Groening

GSI, Darmstadt, Germany.

Interdigital H-mode (IH) drift tube linacs (DTLs) based on KONUS beam dynamics are very sensitive to the rf-phases and voltages at the gaps between tubes. In order to design these DTLs, a deep understanding of the underlying longitudinal beam dynamics is mandatory. The report presents tracking simulations along an IH-DTL using the PARTRAN and BEAMPATH codes together with MATHCAD and CST. Applying the existing geometrical design, rf-voltages, and rf-phases of the DTL were re-adjusted. In simulations this re-optimized design can provide for more than 90% of transmission of an intense 15 emA beam of $^{238}U^{4+}$ keeping the reduction of beam brilliance below 25%. Details can be found in [1].

Single particle tracking

In the MATHCAD code the electric field on axis (r = 0) of each cell is solved using:

$$E_z(z,r,t) = -\cos(\omega t + \varphi_0)\sum_{m=1}^{M} E_m I_0(\mu_m r)\sin\left(\frac{2\pi m z}{\Gamma}\right),$$

where I_0 is the Bessel functions of zero and first order, ω is the angular frequency of the field, r is the radial coordinate, and φ_0 is the phase at the gap at t = 0. Typically the number of Fourier harmonics is M = 30.

$$\mu_m = \frac{2\pi}{\lambda}\sqrt{\left(\frac{m\lambda}{\Gamma}\right)^2 - 1},\ \Gamma = l + 2g + d,\ E_0 = \frac{U}{g}.$$

Each DTL cell comprises a front half tube, gap, and end half tube. Lengths of front tube, gap, and end tube are defined as l, g, and d, respectively. The inner radius of the tube is a and the electric field along the gap is obtained from

$$E_m = \frac{4E_0}{I_0(\mu_m a)}\frac{\pi m(l+g)}{\Gamma}\frac{g}{\Gamma}\frac{\sin\left[\frac{\pi m(l+g)}{\Gamma}\right]}{\frac{\pi m(l+g)}{\Gamma}}\frac{\sin(\frac{\pi m g}{\Gamma})}{\frac{\pi m g}{\Gamma}},$$

U is the integral voltage along the whole cell. The single particle starts moving at z = 0.

The reference particle vector function is defined as:

$$Z(t,z) = \begin{bmatrix} z \\ \frac{dz}{dt} \end{bmatrix} = \begin{bmatrix} z \\ \beta c \end{bmatrix},$$

with βc as velocity. Starting at t=0 and z=0

$$Z(0,0) = \begin{bmatrix} 0 \\ \beta_0 c \end{bmatrix}.$$

The derivative DZ is

$$DZ(t,z) = \frac{dZ(t,z)}{dt} = \begin{bmatrix} \beta c \\ \frac{q}{\frac{m_0}{\sqrt{1-\beta^2}}} E_z(z)\cos(\omega t + \varphi_0) \end{bmatrix}.$$

$E_z(z,t) = E_z(z)\cos(\omega t + \varphi_0)$. This differential equation is non-linear and cannot be solved analytically. MATHCAD provides several routines to solve systems of ordinary differential equations. Each one uses a different integration algorithm and takes the same arguments. The Bulirsch–Stoer method (a very robust method which some prefer over Runge–Kutta) is applied solving derivative DZ and the results are written as matrix F.

$$F = Bulstoer\left[Z(0,0), t_i, t_f, s, Dz(t,z)\right],$$

where $Z(0,0)$ is the vector with initial conditions, t_i and t_f are the starting and ending points of the integration, s is the number of integration steps, and $DZ(t, z)$ is the vector containing the differential equations. At each step

$$F_1 = t_n, F_2 = z_n, F_3 = \beta_n c,\quad n = 1,2,\cdots s,$$

$F^{1,2,3}$ indicates column 1, 2, and 3 of matrix F. The parameters of effective voltage, time transition factor, and rf-phase of each gap can be calculated according to the above MATHCAD routine and imported into BEAMPATH and PARTRAN codes to perform the beam dynamics simulations with space-charge effects.

Multi-particle tracking

A realistic particle distribution at the exit of the HSI-RFQ (radio frequency quadrupole) is imported and non-linear space-charge forces are considered in the tracking simulations.

A more accurate method for calculation of rf-phases, effective voltage, and time transition factor parameters has been developed basing on the single particle tracking through the one-dimensional electric field-map, and these parameters were imported into PARTRAN code. On the other hand, BEAMPATH code has been applied to simulate the IH-DTL. Corresponding twofold particle distributions at the exit of the IH-DTL are shown in Fig. 1

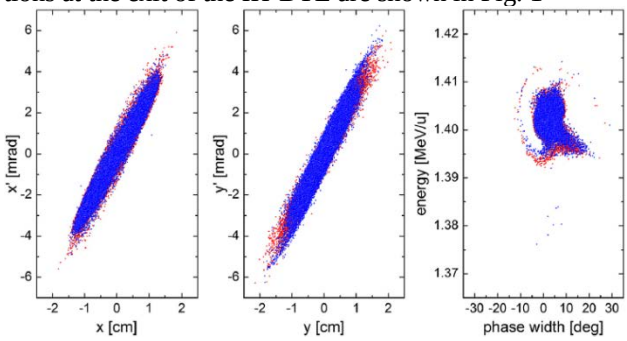


Figure 1: Particle distributions at the exit of the DTL simulated with PARTRAN (blue) and BEAMPATH (red).

Self-consistent beam dynamics of this IH-DTL optimized with the t-code BEAMPATH can provide for more than 90% of transmission of the $^{238}U^{4+}$ beam with 15 emA at the design energy of 1.4 MeV/u. These results could be reproduced very well with PARTRAN using realistic TTF parameters, measured gap voltages, and upgraded rf-phases taking into account unequal lengths of front and end half tubes.

Reference

[1] C. Xiao et al., Nuclear Inst. and Methods in Physics Research, A 887 (2018) 40–49.

 DOI:10.15120/GR-2018-1

Experiment beamline: UNILAC-Other
Experiment collaboration: none
Experiment proposal: none
Accelerator infrastructure: UNILAC
PSP codes: none
Grants:
Strategic university co-operation with: Frankfurt-M

 DOI:10.15120/GR-2018-1

Low-Level RF for the ESR Barrier-Bucket System

J. Harzheim[2], D. Domont-Yankulova[2], M. Frey[1], K. Groß[2], H. Klingbeil[1,2], D. Lens[1]

[1]GSI, Darmstadt, Germany; [2]TU Darmstadt, Germany.

Introduction

For sophisticated longitudinal beam manipulations, the Experimental Storage Ring (ESR) at GSI, Darmstadt, is to be equipped with a Barrier-Bucket (BB) RF System. This system will consist of two broadband RF cavities, each driven by a solid state amplifier, with the purpose to produce two voltage pulses per beam revolution to longitudinally capture the beam. By shifting the pulses towards each other, the beam can be compressed or decompressed which can be used for particle accumulation. For the generation of the BB pulses, two cavity systems will be installed in the ESR, providing one pulse per revolution each. In stacking mode [1], the desired pulses are clean (ringing <2.5%) single sine pulses of 5 MHz with a repetition frequency of 900 kHz - 2 MHz. To reach the high quality requirements, a mathematical model of the cavity system has been developed in order to generate predistorted input signals [2].

Low-Level RF topology

The planned Low-Level RF (LLRF) for the Barrier Bucket operation is shown in Figure 1. The predistortion of the signals is performed by the Industrial PC. To determine the predistortion, appropriate test signals generated by the Tabor 3362 signal generators are applied to the ESR BB system. The gap signal is measured and transmitted to the PC by an oscilloscope. Based on this measurement, a predistorted input signal is generated and stored inside the signal generators. Repetition frequency will vary during pulse shifts which might lead to conditions, where a new pulse sequence has to be started while the former sequence is still running. Therefore, two signal generators need to be triggered alternately by the TRG-Module. Amplitude and phase ramps are loaded in the Scalable Control Unit (SCU). While the phase information will influence the signal trigger generated by direct digital synthesis (DDS), the amplitude is directly manipulated inside the signal generators.

Measurement results

The functionality of the ESR BB LLRF system is currently tested. Figure 2 shows the phase shift between two LLRF topologies, one providing a stationary pulse while the other system performs a trapezoidal phase shift. The ripple is an artifact caused by the low time resolution.

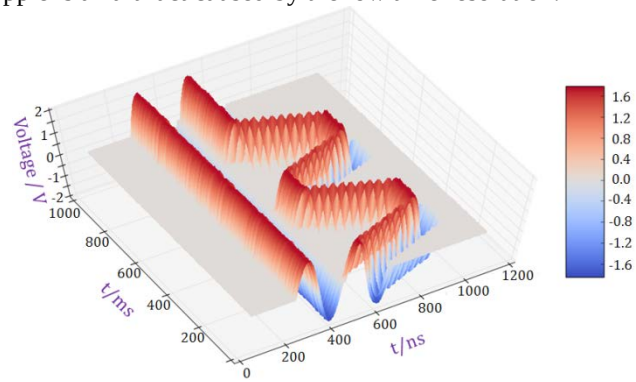


Figure 2: Measured pulse shift at the LLRF prototype system

Currently, amplitude control and linear and nonlinear predistortion with the full system are tested. Furthermore, online signal optimization will be tested. After this, the system will be prepared for standard operation and installed in the ESR tunnel.

References

[1] M. Steck et al., "Demonstration of Longitudinal Stacking in the ESR with Barrier Buckets and Stochastic Cooling". Cool'11, Alushta, Ukraine, 2011.

[2] J. Harzheim, D. Domont-Yankulova, M. Frey, K. Groß, H. Klingbeil, "Input Signal Generation for Barrier-Bucket RF Systems at GSI". Proc. of IPAC'17, Copenhagen, Denmark, 2017.

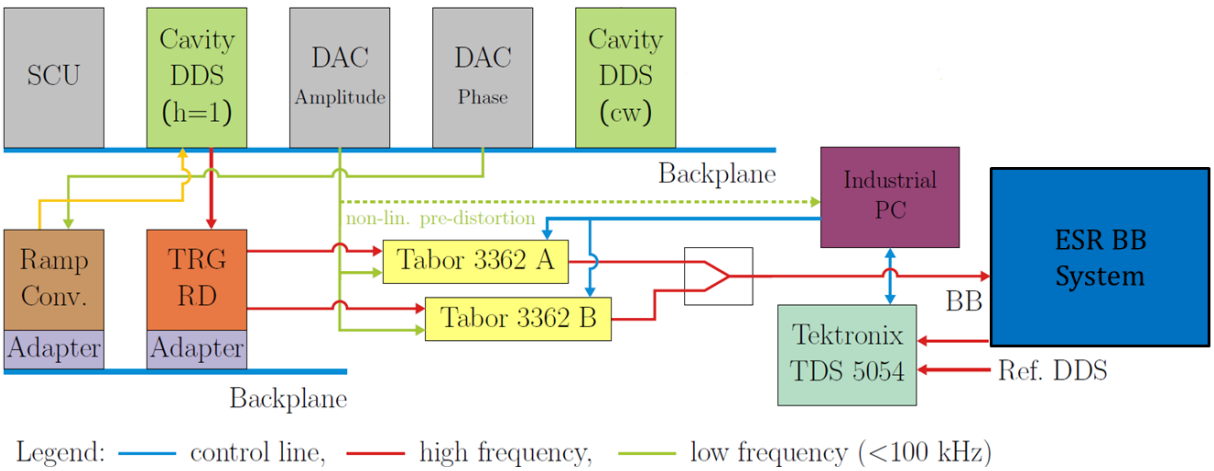


Figure 1: Planned Low Level RF topology for one ESR Barrier-Bucket system.

Selection of β-decay daughters in the ESR

S. Litvinov[1], J. Glorius[1], Yu. A. Litvinov[1], R.Reifarth[2], S. Sanjari[1], Z.Slavkovská[2], M. Steck,[1] T. Stöhlker[1]
[1]GSI, Darmstadt, Germany; [2]Goethe Universität Frankfurt, Germany

The ESR is a powerful instrument for precise β - decay experiments with exotic highly-charged ions.
β - decay daughters can only be stored and detected if the decays occur in the two straight sections of the ESR. The daughters with same *m/q* appearing in different straight sections will have different trajectories in the ring and therefore, come on different positions in the detector. Thus, we can select the nuclei of interest, scraping unwanted daughters and other same *m/q* species, for an example, electron capture by mother ion in the cooler section. Here the experimental demonstration of the proper daughter selection and its ion-optical explanation will be presented.

During the proton capture reaction *(p,γ)* experiment at the ESR in 2016 [1], the bare $^{124}Xe^{54+}$ primary beam with energy of 100 MeV/u was injected into the ESR, cooled, decelerated to 15 MeV/u, moved and stored on the inner orbit (black dashed curve in Fig. 1), which was centred at the hydrogen target, by a special horizontal target bump of 16 mm (black solid curve in Fig. 1). For detection of $^{124}Xe^{53+}$ daughters which can capture an electron in the target, a MWPC detector was installed in the northern arc of the ESR in a special moveable pocket (see yellow box in Fig. 1). The detector calibration has been performed by moving the pocket out stepwise from its inner position, corresponding to the central orbit of the ring. At each step of 20 mm the corresponding spectrum was recorded.

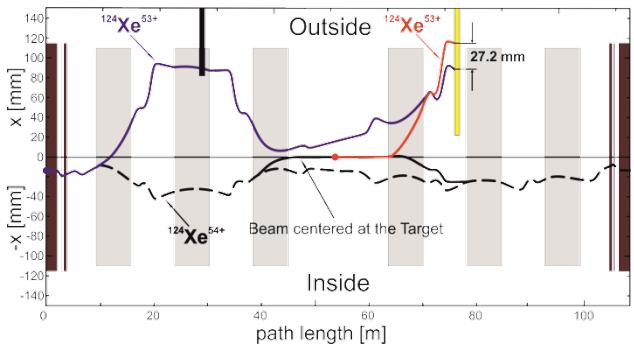


Figure 1: Calculated beam trajectories for one turn in the ESR, started at the electron cooler (brown boxes). The primary $^{124}Xe^{54+}$ beam stored at the inner orbit is marked by the dashed black curve. The target bump is marked by the solid black curve. The $^{124}Xe^{53+}$ ions coming from the cooler and the target are marked by blue and red curves, respectively. The dipole apertures are shown as grey boxes.

However, instead of one peak of $^{124}Xe^{53+}$ daughter coming from the target (red curve in Fig. 1) we observed two peaks with a distance of 27 mm. The second peak can be attributed to the daughter starting in the cooler section, capturing there an electron (blue curve in Fig. 1). It has been proved by using a fast scraper installed in the southern dipole of the ESR and moving from the outside (see black box in Fig. 1), which cut only one peak, but that one which appeared in the inner side of the detector, as can be seen in Fig. 2. In order to understand these results, a dedicated ion-optical simulation has been performed (see Fig.1) which explains the peaks positions at the detector and calculates their distance in a good agreement with the experiment. Therefore, the presented method can be used as an additional separation technique of selected daughters at certain positions. It could be a solution for the experiments which cannot be performed up to now because of background contamination. For example, the experiment for finding yet unobserved decay mode bound state $e^- - e^+$ pair decay in $^{194}Pb^{82+}$, where one of the biggest problem is the background from atomic electron capture in the electron cooler of the ESR [2].

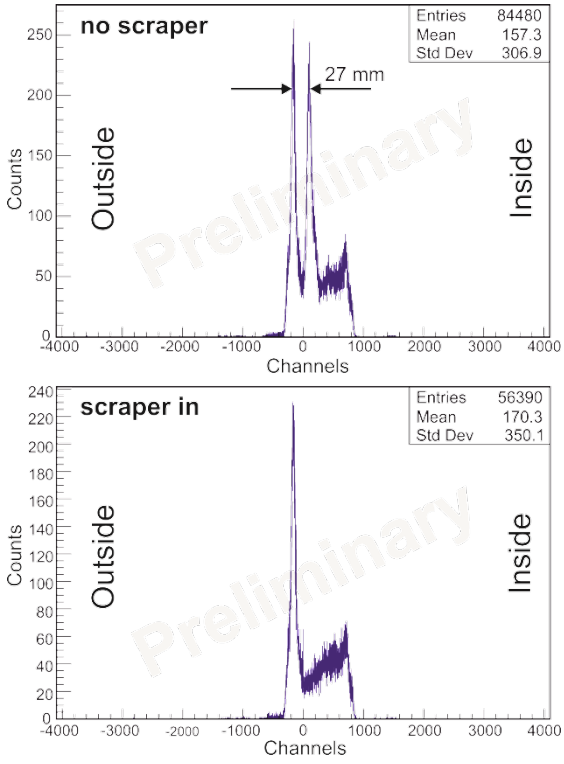


Figure 2: Experimental horizontal distribution of MWPC detector at the radial position of 20 mm out of the central orbit of the ESR, without and with scrapping, respectively.

References

[1] J. Glorius et al., et al 2017 J. Phys.: Conf. Ser. 875 092015
[2] F. Bosch et al., EPJ Web of Conferences 123, 04003 (2016)

Experiment beamline: ESR
Experiment collaboration: APPA-SPARC / NUSTAR-ILIMA
Grants: ERC-2015 CoG (682841-ASTRUM)
Strategic university co-operation with: Frankfurt-M

 DOI:10.15120/GR-2018-1

Resonant dynamics of particles in presence of space charge

G.Franchetti[1]

[1]GSI, Darmstadt, Germany

The theory of the resonances in absence of space charge allows a clear discussion of the properties of particle dynamics subject to one-dimensional resonance (type $n_x Q_x = m$). The effect of space charge on one-dimensional resonances is difficult to assess, especially for the dynamics of particles in a bunched beam where the time scale of the effects happens over "long" storage, that is over "many" synchrotron oscillations. Machine experiments have explored the effect of space charge on the storage of bunched beams when the space charge tune-spread ($\Delta Q_x \sim 0.05$) overlaps one-dimensional resonances as $4Q_x = 25$, $3Q_x = 13$. The associated studies have explained emittance growth and beam loss with the mechanism of the periodic resonance crossing. The understanding of the dynamics created by coupled resonances $n_x Q_x + n_y Q_y = m$ is instead more elusive even neglecting the effect of space charge. A recent analytical investigation of the simplest coupled nonlinear resonance $Q_x + 2\,Q_y = m$ [1] evidenced that the resonant dynamics creates on a Poincare' section a special topological structure called "fixed line". This structure is a closed curve that extends in the four-dimensional phase space. In Fig. 1 left is shown an example of fixed line and the typical correlation in the planes x-y otherwise decoupled; the usual x-x' and y-y' planes exhibit instead the standard Courant-Snyder ellipses: hence usual emittances a_x, a_y allow a complete determination of a fixed line size.

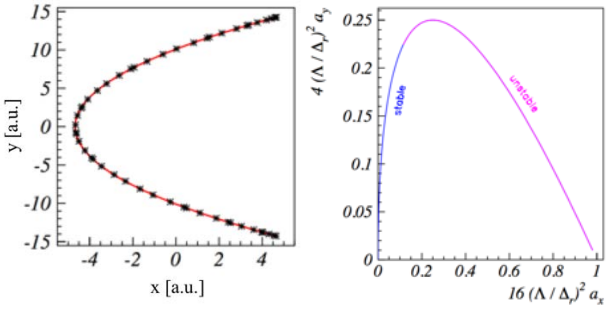


Figure 1: The left picture shows the x-y projection of an example of fixed line on a Poincare' section. Right: set of stable fixed lines in terms of a_x, a_y. The pink dots identify unstable fixed lines whereas the blue dots are for stable one.

The amplitude of the fixed lines (i.e. the emittances of the oscillating amplitudes) is determined by the distance from the resonance $\Delta_r = Q_x + 2\,Q_y - m$, and by the strength of the harmonics excited by the distributed sextupolar errors Λ (driving term). A substantial difference with respect to the one-dimensional resonances is that the resonant dynamics creates infinite fixed lines. Fig. 1 left shows all fixed lines (stable and unstable) plotted in terms of scaled a_x, a_y.

When space charge in not negligible the situation is very complicated, and the interpretation used for the case of one dimensional resonances (scattering and trapping generated by islands) is not helpful. The problem was clarified by the numerical studies of an experimental campaign performed at the CERN-PS. Simulations have highlighted that space charge does not destroy the fixed lines, but even determines their sizes. An example of this finding is shown in Fig. 2 left from Ref. [2].

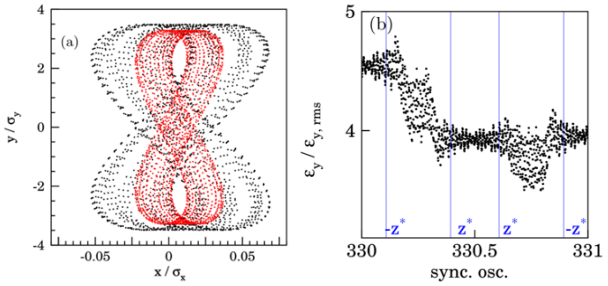


Figure 2: Left: two resonant tori obtained in the simulation of the PS experiment. Right: "kicks" of the invariant of one test particle due to the four crossings of $Q_x + 2\,Q_y = m$ during one synchrotron oscillation.

This picture shows that the "fixed line" is asymmetric and the simulation studies evidenced that the amplitude of the instantaneous fixed line along the bunch changes according to the local transverse space charge tune-spread. This allows to conclude that the periodic crossing of the fixed lines is responsible for a slow diffusion altering the beam distribution. Fig. 2 right shows the particle invariant "jump" when one test particle crossed the resonance (four times per synchrotron oscillation). This study allows to conclude that by computing the maximum extension of the fixed lines (including space charge), it is possible to predict the amplitude of the halo formation.

Accelerator infrastructure: SIS18, CERN-SPS, CERN-PS
Grants: EuCARD2, ARIES
Strategic co-operation with: CERN

References

[1] G. Franchetti and F. Schmidt Phys. Rev. Lett. 114, 234801 (2015).

[2] G. Franchetti, S. Gilardoni, A. Huschauer, F. Schmidt, R. Wasef, Phys. Rev. Accel. Beams 20, 081006 (2017).

 DOI:10.15120/GR-2018-1

HEST upgrade towards beam time 2018

M. Sapinski, B. R. Schlei, S. Reimann, GSI division: Accelerator Operations

During the 2-year shutdown from July 2016 till May 2018, GSI machines went through a series of modifications in order to renovate the accelerator chain and prepare it for operation with FAIR machines [1]. The High Energy Transfer Lines (Hochenergie-Strahlführung, HEST) transport the beams from the SIS18 synchrotron to experimental caves and storage rings. The schematic of HEST is shown in Fig. 1. The main shutdown works were: preparation of HADES beam line to high intensity operation [2], modification of HTD beam line and Cave C to accomodate mini-CBM [3], modernisation of ion getter pump controllers with the goal to improve performance of the vacuum system and change of the accelerator control system, which is described here.

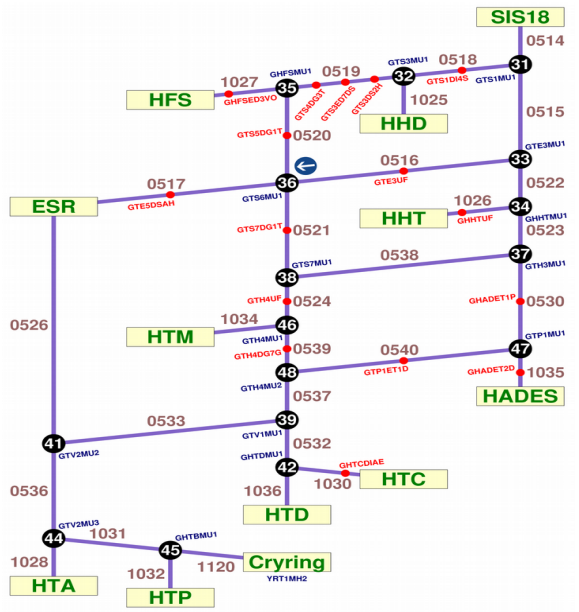


Figure 1: Diagram of HEST "accelerator zones" from control system perspective.

The old accelerator control system contained magnet settings generated by MIRKO beam optics program. For HEST about 20 of such "theory" optics were prepared. During the operation, corrections to those settings are applied in order to optimize beam properties. Those corrected settings were stored in special files (called IBHS files, from the name of the old program). Several thousands of these files were generated over the decades of operation of GSI machines.

The old control system was based on OpenVMS system and suffered from limitations which had to be overcome for FAIR operation. As a successor, the LHC Software Architecture (LSA) setting management system has been chosen [4]. LSA has a hierarchical structure, it is flexible, modular and uses modern technologies (OO, Oracle DB, Java). In addition, also equipment control layer (FESA), timing system and electronic control units have been replaced.

Hierarchy generation is an essential task of the HEST machine modelling. It is realized by generic coding strategies, based both on Python and JSON. The implemented hierarchies allow for propagation of physics parameters (e.g., dipole and/or quadrupole field strengths) to hardware parameters (e.g., currents for power supply units).

LSA stores the setting of device parameters in database tables. In order to reproduce the old system functionality, the information about beam optics setting must be transferred to LSA. The import functions require specific type of text files to be generated. Those files contain integrated strengths of the optical elements as well as Twiss parameters along the beamline.

The strategy adapted to fulfil this task is the following:

1. Execute MIRKO for each optics, generate Twiss files.
2. Convert MIRKO optics to MAD-X, run MAD-X, assure its agreement with MIRKO results.
3. Use Twiss files and information about accelerator zones to generate input for LSA using Python scripts.
4. Import files to LSA verifying consistency of the data. Resulting LSA setting were tested during Dry Runs.

The second task is to provide data from IBHS files for trimming the optics. A Python script has been prepared which converts the IBHS format to format of the files which can be imported into trim application.

References

[1] P. Schuett et al., "Shutdown report 2017", this report

[2] M. Sapinski and al., "Upgrade of GSI HADES beam line in preparation for high-intensity run", IPAC'17, Copenhagen, May 2017, TUPVA060

[3] C.Sturm et al. for the CBM Collaboration, CBM Progress Report 2017, DOI 10.15120/GSI-2018-00485

[4] G. Kruk et al.,"LHC Software Architecture LSA – Evolution Toward LHC Beam Commissioning", ICALEPCS'07.

Experiment beamline: SIS18-CaveA / SIS18-CaveM / mCBM@SIS18 / FRS / HADES / R3B / SIS18-other
Accelerator infrastructure: HEST

 DOI:10.15120/GR-2018-1

Beam profile measurements and observation of beam cooling at CRYRING@ESR

A. Reiter, H. Bräuning, T. Milosic, H. Reeg, T. Sieber

GSI, Darmstadt, Germany

Abstract

We report on the first measurements of beam profiles at CRYRING@ESR with cooled and with un-cooled beams. The measurements were performed with ionisation profile monitors that detect interaction vertices of the beam with the residual gas. The storage ring is equipped with two devices, one for each transverse plane. Their main task is the monitoring of the beam cooling process.

Ionisation Profile Monitor and Readout

The ionisation profile monitors (IPM) [1] were originally operated in CRYRING at the Manne-Siegbahn laboratory in Sweden. The entire storage ring has been transferred to GSI as part of the Swedish in-kind contribution to the FAIR facility. The square opening area of the IPM field cage is 100 mm^2, its length 80 mm. When a residual gas molecule is ionised by the beam, the positive reaction product is accelerated towards a stack of two 40 mm multi-channel plates (MCP) in Chevron configuration. The MCP generates a fast timing pulse, while the following resistive-anode encoder splits the electron cloud into four separate signals. These allow for calculation of the interaction vertex by the method of charge division [2]. In order to verify the IPM response, vertex distributions were acquired with a preliminary test setup and an alpha emitter on a linear drive.

A new VME data acquisition system integrates the IPMs into the FAIR-style accelerator control system. It operates under the front-end software architecture (FESA) framework. The output signals of fixed-gain charge-sensitive amplifiers are post processed after ~35 m coaxial transmission by a 16 channel NIM spectroscopy amplifier CAEN N586E with network interface for remote control. Positive semi-Gaussian pulses of total length < 2 µs are generated with a shaping time of 200 ns. A 12 bit peak-sensing ADC CAEN V785N converts all signals within about 6 µs into a set of amplitudes and stores the events for further processing by the FESA software. A satisfactory readout rate of 20 kHz has been observed with a Men A20 2eSST VME controller. The position resolution of 0.3 mm (FWHM) that has been achieved in Sweden is yet to be confirmed at CRYRING@ESR.

Due to the moderate interaction rates, both IPMs are joined in an OR logic and digitised by the same ADC board. Leading edge discrimination of the fast MCP pulses triggers the event latch, i.e. generation of the 2 µs ADC gate pulse and discriminator inhibit signals via the ADC busy signal. For identification of the active IPM in the analysis the discriminator outputs are recorded together with the analogue signals. There is also a possibility to include the MCP output pulses in the readout.

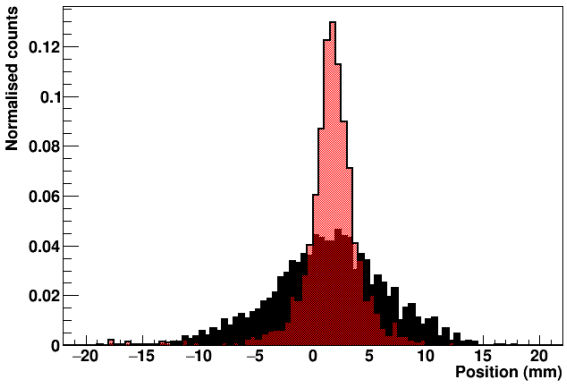


Figure 1: Beam profiles with 0.5 mm bin size at the start of cooling process (black) and at the cycle end (red).

First Operational Experience

During electron cooler commissioning in November 2017 both IPMs were operated together for the first time. The RFQ injector provided a molecular 300 keV/u H_2^+ beam. About $2x10^8$ particles were stored at the start of the 5 s long machine cycle, and the resulting MCP count rate reached 50 kHz with a low discriminator threshold. The rates will drop as vacuum conditions are still improving and, at higher energies, due to a smaller specific energy loss dE/dx that drives the ionisation process.

Both IPMs were operated at a field value exceeding 40 kV/m, and the beam was deflected by a few mrad. The resulting orbit shift was not compensated during this beam time.

Figure 1 shows two vertical beam profiles of 0.5 mm bin size and normalised area. The acquisition window was 300 ms long for each profile. The broad distribution represents the beam prior to the cooling process (black) and the narrow one the beam at the end of the cycle (red). At that time the beam was still cooling down. Noteworthy are the quite clean areas outside the beam spot, an indication of the achieved quality of beam and detector setup.

The IPM operational parameters are the high voltage values, discriminator threshold, and spectroscopy amplifier gains to match the signals to the ADC input range. Their optimisation will be studied when longer cycle, and hence cooling, times will produce beam spot sizes in the ~1 mm range.

References

[1] A. Källberg et al., Proc. of DIPAC'97, Frascati, Italy
[2] M. Lampton and C.W. Carlson, Rev. Sci. Instrum. 50, 1093 (1979)

Experiment beamline: CRYRING
Experiment collaboration: CRYRING@ESR
Experiment proposal: [none]
Accelerator infrastructure: [CRYRING]
PSP codes: [none]
Grants: [none]
Strategic university co-operation with: [none]

 DOI:10.15120/GR-2018-1

CRYRING@ESR commissioning – ions stored, cooled, accelerated

F. Herfurth[1], M. Lestinsky[1], Z. Andelkovic[1], A. Bräuning-Demian[1], S. Fedotova[1], W. Geithner[1], A. Källberg[2], G. Vorobjev[1] and the CRYRING@ESR team

[1]GSI, Darmstadt, Germany; 2ANL, Argonne, IL 60439, U.S.A.

Commissioning of CRYRING@ESR, the low energy storage ring now located at GSI/FAIR has been started in 2016. The commissioning went on during 2017 with establishing stored ion beam, testing beam cooling using the installed electron cooler and first attempts to accelerate.

CRYRING@ESR is the early installation of the low-energy storage ring LSR [1], a Swedish in kind contribution to FAIR, which was proposed as the central decelerator ring for antiprotons at the FLAIR facility.

Status of Commissioning

A local ion source in combination with a radio frequency quadrupole structure is available to provide light ion beams at 300 keV/nucleon for injection into the storage ring. For commissioning this hot cathode type ion source produces singly charged hydrogen molecules. In 2017, the anode voltage was pulsed to prolong the typical operation time until interventions necessary to replace the cathode or the insulators. Now the anode is supplied with voltage for just 1 ms. This shortened considerably the time the ion source plasma burns and led to improved up-times of several weeks. Additionally, a treatment of the Ta cathode wire with triple carbonate spray coating increased the electron emission and hence the ion output. The source is now capable of delivering 1 ms pulses of more than 100 µA peak current of H_2^+ ions for at least a week of continuous operation.

In 2017 three commissioning runs were conducted of about three weeks each. The first run was used mostly for detailed debugging of control system issues. The results from 2016, a first turn, have been reproduced in the remaining three days. Careful analysis of the collected information, a detailed alignment check of all components and the completed bake out of the ring were followed by the second run. In this second run stored ion beam was achieved. The third run ended with successful acceleration and the demonstration of electron cooling.

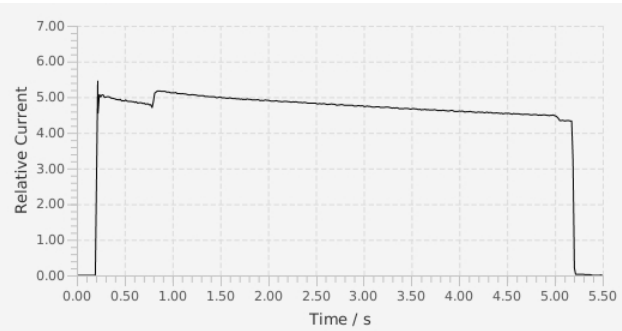


Figure 1: Intensity of stored ion beam versus time during acceleration from injection energy, i.e. 300 keV/nucleon, to 2 MeV/nucleon. Acceleration starts at about 1 s and ends at 5 s.

To test the multi turn efficiency of the local injection, the time between injection and start of the bumper ramp down has been varied. It was found that about 3 turns could be injected [2]. Simulations show that up to ten turns should be achievable. For this the power supply for ramping down the bumpers (orbit distortion) has to be adapted to have more flexibility in choosing the slope.

The storage time strongly depends on the vacuum conditions. Hence, the ring's vacuum system is completely bakeable. The system to heat and bake the ring is at the same time the first large scale installation of the industrial control environment developed for FAIR installations. Several smaller bugs and a serious performance limitation have been identified and solved. Eventually, all ring segments and the last meters of the injection beam line have been heated for about seven days to about 200 degree C. This results an average pressure of $1 \cdot 10^{-10}$ mbar along the ring directly after the bake out procedure.

During the most recent beam test in November 2017, the exponential decay time constant τ of H_2^+ ions at 300 keV/nucleon has been measured to be about 5 s.

Finally, the ion beam, injected locally at 300 keV/nucleon, has been accelerated to 3 MeV/nucleon. Figure 1 plots the relative intensity during the complete cycle of injection, bunching, and acceleration. This has been recorded by picking up the ion bunch signal on a capacitive pickup during acceleration. While the small increase during the bunching sequence is probably an artefact, the overall decrease is almost entirely due to collisions with the residual gas that limit storage time.

The last part of the commissioning run was dedicated to cooling. The electron cooler has demonstrated its functionality and first cooling has been observed both at injection energy and after acceleration to 1.5 MeV/nucleon [3].

References

[1] H. Danared et al. (2011), "LSR - Low Energy Storage Ring, Technical Design Report", MSL, Stockholm University, v 1.3.

[2] F. Herfurth et al., “Commissioning of the Low Energy Storage Ring Facility CRYRING@ESR”, in Proc. 11th Workshop on Beam Cooling and Related Topics (COOL'17), https://doi.org/10.18429/JACoW-COOL2017-THM13 (2018)

[3] R. Hess at al., "Commissioning of the CRYRING electron cooler", GSI Report 2018-1, (2018).

Experiment beamline: CRYRING
Experiment collaboration: APPA-SPARC
Experiment proposal: none
Accelerator infrastructure: CRYRING
PSP codes: 1.3.4.2
Grants: none
Strategic university co-operation with: none

Investigations of different types of current coupling for the new Cryogenic Current Comparator with eXtended Dimensions (CCC-XD)*

V. Tymppel[1], R. Neubert[2], Jessica Golm[2], and the FAIR@GSI Beam Instrumentation R&D group

[1]Helmholtz Institute, Jena, Germany; [2]Institute of Solid State Physics, Jena, Germany

The FAIR project triggers the development of CCCs with larger diameters for the non-destructive, highly-sensitive measurement of charged particle beam intensities. Before the final acceptance test in May 2017 [Fig. 1] different types of current coupling were investigated.



Figure 1: CCC-XD in a wide neck cryostat in front of the magnetic shielded chamber in Jena (l. to r: R. Neubert, T. Sieber, F. Kurian, V. Tympel).

Different types of current coupling

Inside the so-called SQUID-Cartridge the low inductance of the SQUID (Superconducting Quantum Interference Device) has to be coupled with the high inductance of the pickup coil capturing the magnetic field of the charged particle beam. As shown in Fig. 2 three types of coupling were simulated: direct (black), balanced (red) and enhanced (blue). Using the measured inductance values from [1] the simulation shows that the parasitic capacity of the CCC meander shielding leads to resonance peaks above 100 kHz [Fig. 3]. Especially the direct version which is without any matching transformer has a strong peak. A transformer dimensioned with higher inductance values (balanced, enhanced) can generate an additional current magnification at the expense of the bandwidth.

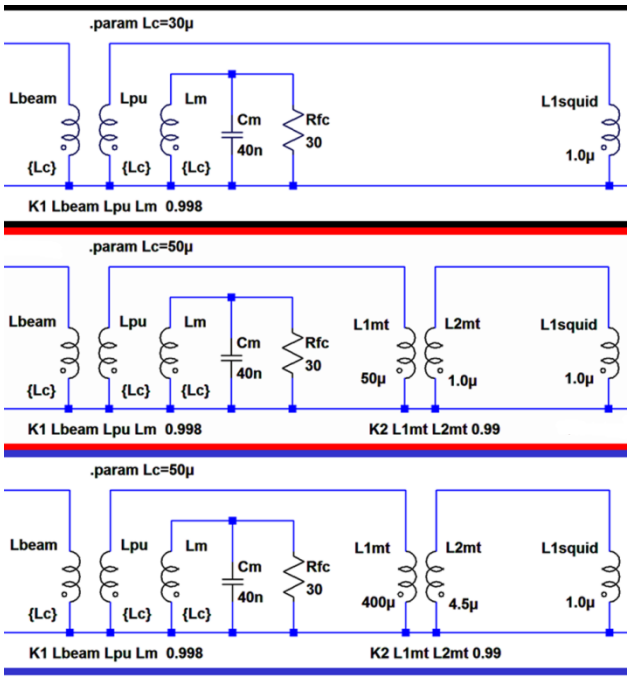


Figure 2: Circuit diagrams of the three coupling types.

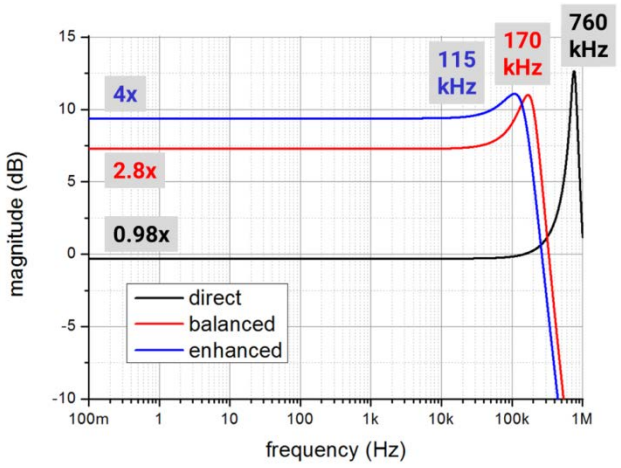


Figure 3: LTspice simulation of the coupling types [2].

Measurement results

The CCC-XD measurements, done in Jena, established that the flux concentrator core surrounded by the pickup coil is the dominant source of current noise. An additional current magnification in front of the SQUID is not necessary. The calculated bandwidths und resonances could be measured. To realize a stable flux-locked-loop working mode with the SQUID the high resonance peak of the direct version has to be damped. Therefor the balanced version was used at the end. This research is supported by the BMBF (project# 05P15SJRBA), the TU Darmstadt and the Leibniz Institute of Photonic Technology.

References

[1] V. Tympel et al., “The next generation of cryogenic current comparators for beam monitoring.”, proceedings of IBIC’16, Barcelona, Spain, pp. 441-444, ISBN 978-3-95450-177-9

[2] V. Tympel et al., “Cryogenic Current Comparators for 150 mm Beamline Diameter,” IBIC’17, Grand Rapids, MI, USA, Aug. 2017, paper WEPCF07, in press.

* also published in annual HI Jena report 2017

 DOI:10.15120/GR-2018-1

A fluorescence detection system for laser-spectroscopy experiments at CRYRING@ESR

A. Bußˆ[1,2], V. Hannen[1], C. Huhmann[1], K. Mohr[3], Z. Andelkovic[2], C. Weinheimer[1]

[1]Institut für Kernphysik, WWU Münster, Germany, [2]GSI, Darmstadt, Germany, [3]TU Darmstadt, Germany

The low energy storage ring CRYRING is being set up as the first storage ring of the upcoming accelerator facility FAIR at GSI. In order to enable laser spectroscopy experiments with stored ions, a fluorescence detection system has been developed at the Institut für Kernphysik in Münster. Earlier this year, the detector has been set up in section 7 of CRYRING. The detector is designed to measure in a broad wavelength regime between 250 nm to 850 nm.

Several ions of interest have transitions in this wavelength regime. For instance Mg^+ (at 280 nm, see [1]) and Be^+ (at 313 nm). The latter is a relevant candidate for studying laser induced dielectronic recombination (LIDR).

Status

Initial test and construction of the detector chamber was completed in January 2018 (see fig. 1 and 2). In February 2018, the scrapers were installed and the setup was checked in the vacuum facility of GSI. After baking, a leakage rate of less than $1x10^{-10}$ mbar l s^{-1} and an outgassing rate of $2x10^{-12}$ mbar l s^{-1} cm^{-2} were measured.

Also, vertical and horizontal scrapers have been installed. These allow measurement of the beam position directly in front of the detector chamber. As explained in [2] and [3], this is of importance for the detector's working principle. Proper alignment of the beam can be achieved with magnetic steerers. However, the chamber itself also is adjustable, as it is mounted into the CRYRING with metal bellows.

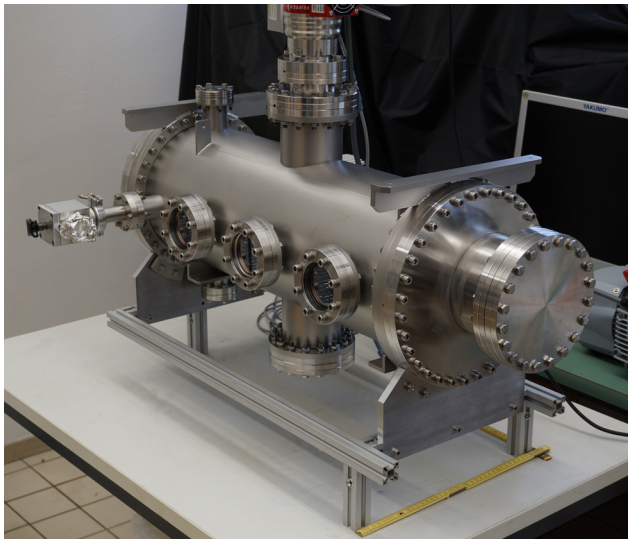


Figure 1: Detector chamber during vacuum test in Münster. At CRYRING site, turbo molecular pump will be substituted by an absorption pump.

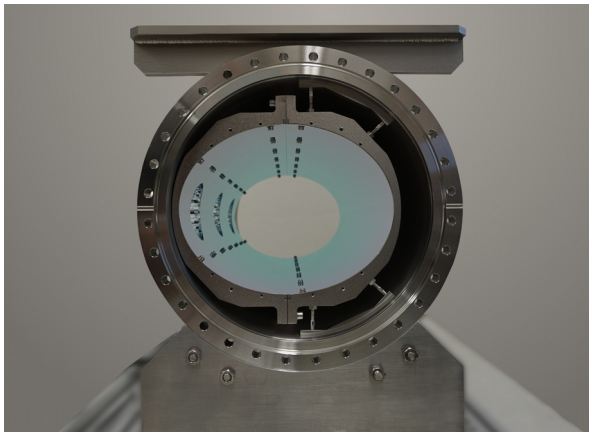


Figure 2: Elliptical mirror chamber. For better visibility, front and end mirror caps are not mounted. The beam will be aligned along the right focus point of the ellipse.

The fluorescence light will be detected by two sets of three PMTs each, one for UV and visible wavelengths (Type 9235QBA by Electron Tubes) and one red-sensitive set (Type 9658BA). In order to allow for single photon counting, air-cooled housings will be used to reduce the dark count rate, especially for the IR-sensitive PMTs. The 2-inch PMTs and cooling housings will be delivered in early April.

References

[1] see Z. Andelkovic *et al.*, this Annual Report

[2] A. Buß, "A Fluorescence Detection System for Laser-Spectroscopy Experiments at CRYRING@ESR", GSI scientific report 2016

[3] D. Thomas, bachelor thesis, Institut für Kernphysik Münster, 2016

Experiment beamline: CRYRING / ESR
Experiment collaboration: APPA-SPARC
Experiment proposal: none
Accelerator infrastructure: ESR / CRYRING
PSP codes: 1.3.1.5.8.1.2
Grants: BMBF contract number: 05P15PMFAA
Strategic university co-operation with:
other: University Münster

First electron cooled beam in CRYRING after electron cooler commissioning

R. Heß[1], C. Dimopoulou[1], J. Roßbach[1], M. Bräscher[1], M. Kelnhofer[1], and J. Krieg[1]

[1]GSI, Darmstadt, Germany

In 2017 the activities at the CRYRING electron cooler focussed on commissioning the device and investigating the proper operation parameters. The cooler was operated remotely in DC mode, via newly developed application software, embedded into the new FAIR control system.

Standalone commissioning

After a short bake-out of the cooler vacuum system, a first electron beam was guided from the gun to the collector, confirming the function of all hardware and controls. After a longer bake-out 10^{-10} mbar without electron beam (< 9 10^{-9} mbar with 12 mA electron current in the collector) was reached. The newly mounted cathode, heated according to the supplier instructions at 1200 K (measured with a pyrometer), was fully activated for electron emission. Following the data from former operation in Sweden, the electrode voltages, the guiding magnetic fields and the electron steerers were quickly set so as to extract and guide an electron beam from the gun to the collector. All optimizations were carried out by minimizing the electron beam loss to the ground (and on all anode electrodes) and maximizing the electron current reaching the collector. Operation settings were systematically studied, for cooler voltages ranging from 100 V up to 5 kV and magnetic expansion factors between 30 and 100, as relevant for CRYRING operation with beams from the local injector and from the ESR. Finally, the cooler was ready to be brought into operation with ion beam during the CRYRING beam time in November/December 2017.

Commissioning with ion beam

From the local injector, a molecular hydrogen H_2^+ beam was injected and stored into the CRYRING at a kinetic energy of 300 keV/u (β=0.025, revolution frequency= 140 kHz). The operation cycle was about 8.5 s, limited by the ion beam lifetime under the given vacuum residual gas pressure in the ring. This was sufficient to demonstrate the reduction of the phase space volume of the ion beam under electron cooling. Figure 1 shows the evolution of the vertical ion beam size during cooling. The profiles were recorded with an ionization profile monitor (IPM) after optimization of the x and y electron cooler steerers in the cooling section, to provide fastest cooling (best alignment to the ion beam). In figure 2 the corresponding longitudinal cooling is shown. This waterfall Schottky spectrum was recorded for a coasting ion beam of $2{\cdot}10^8$ ions (5µA current) at the 20th harmonic (2.8 MHz). The settings of the electron cooler were: cooler voltage 168 V, electron density $1.3{\cdot}10^6$ cm^{-3}, adiabatic magnetic expansion factor 100 (gun at 2 T, cooling solenoid at 0.02 T). Thus, the electron beam expands from the cathode (4 mm diameter) to a diameter of 40 mm in the cooling section. This electron beam fully overlaps the ion beam in the cooling section. This was confirmed by the measured ion beam spots on the IPMs and the known lattice functions. Partial horizontal overlap between electrons and ions was seen for smaller electron beam diameter (28.3 mm, for expansion factor 50).

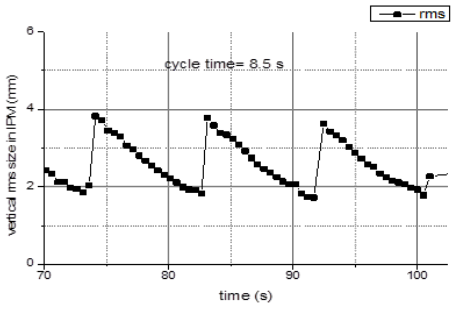


Figure 1: Due to electron cooling the transverse ion beam size (i.e. the transverse emittance) decreases with time. Vertical rms beam size as recorded with an IPM. Simultaneous reduction of the horizontal beam size was observed with a separate IPM in a similar way.

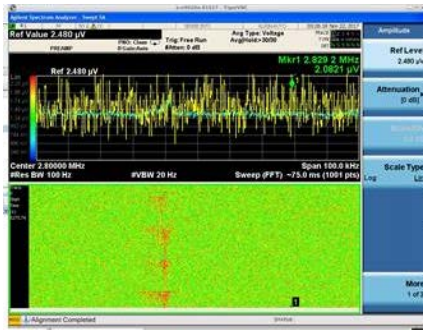


Figure 2: Schottky spectrum showing the evolution of the frequency distribution i.e. of the momentum distribution of the stored ion beam (horizontal axis) with time (vertical axis) under the action of electron cooling.

The cooling effect was further verified by slightly varying the cooler voltage (i.e. velocity mismatch between the electron and the ion beam) and observing in the Schottky spectrum that the ion beam distribution was pulled towards the velocity of the electrons.

The superconducting gun solenoid worked at the required fields (up to 3 T) but its Helium consumption was extremely high, so that the cryostat had to be filled every 30 hours. This indicates a thermal leak inside the cryostat system which is presently under investigation.

In summary, the CRYRING electron cooler and its dedicated control software were successfully put into operation with stored ion beams at fixed energy. In 2018, the ramped operation mode will be implemented so as to apply cooling at variable beam energies within the machine cycle (i.e. accelerated/decelerated ion beams), as requested by physics experiments. In general, the cooler needs further runs with stored ion beams of sufficient lifetime compared to the expected cooling times.

 DOI:10.15120/GR-2018-1

Experiment beamline: CRYRING
Experiment collaboration: none
Experiment proposal: none
Accelerator infrastructure: CRYRING
PSP codes: none
Grants: none
Strategic university co-operation with: none

Progress on the construction of the precision high voltage divider for the electron cooler at CRYRING

D. Winzen[1], I. Denesjuk[1], T. Dirkes[1], V. Hannen[1], W. Nörtershäuser[2], H.-W. Ortjohann[1], O. Rest[1], Ch. Weinheimer[1]

[1]Institut für Kernphysik, WWU Münster; [2]Institut für Kernphysik, TU Darmstadt

In high precision experiments at ion storage rings the velocity of the ions is a critical quantity. For measurements at CRYRING the electron cooler determines the ion velocity and momentum spread of the ions by superimposing the ion beam with a monoenergetic electron beam. Consequently, a precise knowledge of the acceleration voltage of the electron beam is essential for the accuracy of the experiments. Therefore, we construct a high-precision voltage divider for voltages up to 35 kV which will be similar to the ultrahigh-precision voltage dividers which have been constructed in Münster in cooperation with PTB for use at the KATRIN experiment [1, 2]. The precision of the divider will be in the low ppm range.

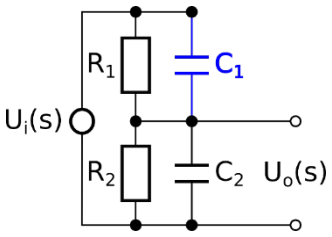


Figure 1: Compensation of a capacitance C_2 by introducing a capacitance C_1 that fulfils the compensation condition $R_1C_1 = R_2C_2$.

Besides static electron cooler voltage measurements, periodic detuning of the electron cooler voltage on time scales of several ms is necessary for electron-ion merged-beam experiments [3]. Hence the voltage at the voltage taps of the HV-divider has to settle in an appropriate timing window to be able to measure the applied voltage with the desired precision. Since the divider is not an ideal ohmic divider (Vishay precision resistors have a capacitance of approximately 0.5 pF [4], stray capacitances, etc.), the settling time of the voltage at the voltage taps is frequency-dependent. A method to optimize the timing behaviour of the high voltage divider has been developed based on the all-pass filter principle. The principle is illustrated for a simple ohmic-capacitive divider as shown in Fig. 1 with a transfer function of:

$$\frac{U_o(s)}{U_i(s)} = \left(\frac{R_2}{R_1 + R_2}\right) \cdot \frac{sR_1C_1 + 1}{s(R_1 \parallel R_2)(C_1 + C_2) + 1}$$

By dimensioning the capacitance C_1 according to the all-pass compensation condition $R_1C_1 = R_2C_2$, the system becomes frequency independent. By applying this method, the transient response of the HV-divider could be optimized in simulations as shown in Fig. 2. For the real setup this method is limited by unknown stray capacitances which have to be determined experimentally.

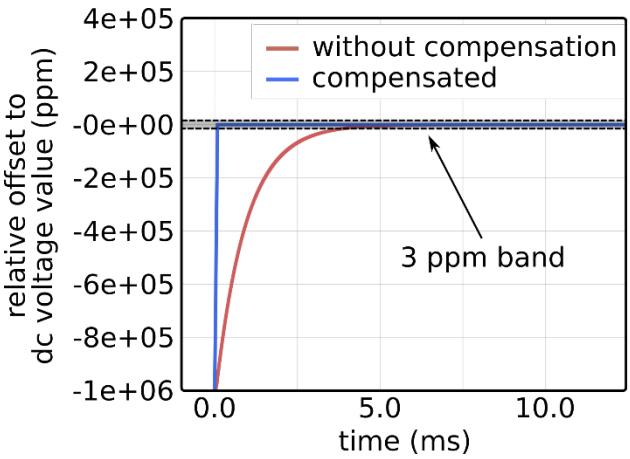


Figure 2: LTspice XVII transient response simulation to 1 kV amplitude ramp with 12µV/s ramping speed for 100:1 voltage tap of the HV-divider [5].

The construction of the high voltage divider has started end of 2017 (see Fig. 3) and is expected to be finished in February/March 2018. Subsequently calibration and characterization measurements will be conducted before integration of the HV-divider into the CRYRING framework.

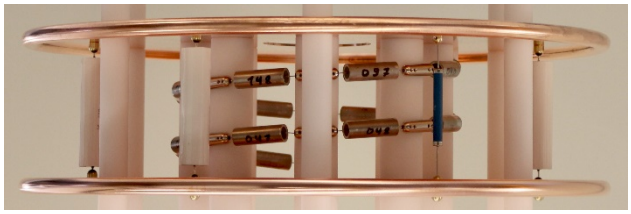


Figure 3: Setup of one of the precision resistor planes of the new HV-divider.

References

[1] T. Thümmler *et al.*, New J. Phys. 11 (2009) 103007
[2] S. Bauer *et al.*, JINST 8 (2013) P10026
[3] Andelkovic Z *et. al.*, Technical Design Report: Experimental Instrumentation of CRYRING@ESR FAIR Facility for Antiproton and Ion Research, p. 19.
[4] Vishay H-series foil resistors, Data sheet, www.vishaypg.com/docs/63006/hmetlab.pdf
[5] T. Dirkes, Bachelor Thesis, Münster 2017.

Experiment beamline: CRYRING
Experiment collaboration: APPA-SPARC
Experiment proposal: none
Accelerator infrastructure: CRYRING
PSP codes: 1.3.1.5.8.2
Grants: BMBF contract No. 05P15PMFAA
Strategic university co-operation with: WWU Münster

 DOI:10.15120/GR-2018-1

Overview of the status of the FAIR project

J. Blaurock, FAIR Technical Managing Director; E. Rosi, FAIR Project Management Office; M. Raponi, FAIR PMO Reporting & Processes; P. Spiller, SPL SIS 100; H. Simon, SPL SFRS; K. Knie, SPL PLinac; I. Koop, SPL CR; D. Prasuhn, SPL HESR; S. Menke, SPL Commons; A. Braeuning-Demian, APPA; J. Gerl, NUSTAR; W. Mueller, CBM; L. Schmitt, PANDA

GSI, Darmstadt, Germany

The remarkable progress in the FAIR project reached its preliminary highlight on July 4th, 2017, when the ground breaking ceremony for the Area North took place with a wide internal and external audience (Figure 1). Immediately after the ceremony the site works for the excavation of the tunnel 110 have started. All preparatory works for the Area North (SIS100 tunnel and CBM cave) are on target schedule.

Parallel to the work on the FAIR civil construction, all connection tasks between the GSI premises and the FAIR site (Gebäude Anbindung FAIR, GAF), as well as the enhancement of the SIS18 shielding and the construction of the main transformer stations North and South were under execution by end of 2017.

The rework of the project planning was finished late 2016 resulting in an integrated master time schedule with all three areas, Accelerator, Civil construction and Experiments integrated. The progress of the project is continuously monitored against this newly defined baseline. In addition, a new risk management was established, which will be common for GSI and FAIR.

The status of the accelerator and experiment projects is detailed in the following sections. Progress on accelerator design and procurement is described first, followed by short reports on civil construction works for the FAIR project and on the major experimental projects.

FAIR accelerator subprojects

The status of the subprojects SIS18,SIS100, Super Fragment, Separator, Proton-Linac and p-bar Target, Collector Ring, High Energy Storage Ring and the cross functional topic Commons is descried in the following overview.

SIS18

The goal of this subproject is enabling the existing synchrotron SIS18 to function as injector of the FAIR accelerators, which requires a major upgrade of SIS18 and civil construction measures to connect the GSI facilities with the future FAIR buildings, GAF.

The completion of the latter is an important precondition for SIS18 recommissioning and operation in 2018. The major part of the construction works serve the purpose to enhance the shielding of the SIS18 tunnel. For this purpose a table construction over SIS 18 has been designed, which finally will carry the additional shielding material. The table pillars are installed, and the outer



Figure 1 : From the left: Paula Eerola (Finland), Catarina Sahlberg (Sweden), Albin Kralj (Slovenia), Fanny Farget (France), Pascal Debu (France), Beatrix Vierkorn-Rudolph (Germany), Viacheslav Pershukov (Russia), Dr. Georg Schütte (Federal Ministry of Research, Germany), Rakesh Bhandari (India), Zbigniew Majka (Poland), Ionel Andrei (Romania), Eric Seng (Hessian Ministry of Science), Sibaji Raha, Chairman of the FAIR Joint Scientific Council, Professor Sebastian Schmidt (Management Board member of Forschungszentrum Jülich), Ursula Weyrich, Paolo Giubellino, Jörg Blaurock (all: FAIR Management Board)



Figure 2: Construction works for the interface of the Proton Linac building

reinforcement wall, supporting the mound on the Northern side next to the public walkway „Prinzenschneise“ are completed.

The original scope of the GAF project was extended during the start-up phase in order to include the construction of the SIS18 interface to the FAIR Proton Linac building. A cost effective solution was developed which facilitated the earlier construction. Therefore, the SIS18 ground works have been extended to the UNILAC-SIS18 transfer tunnel. Until March 2018 the Proton Linac beam dump on the eastern side of the transfer tunnel and the modification of its western wall to allow for the tunnel into the FAIR Proton Linac building (Figure 2) will be finalized.

The power converters which will provide the power grid and power supplies of SIS18 are placed on "Freifläche Nord". It is essential that the new transformer station is completed before the start of the recommissioning of SIS18. The manufacturing of the big new pulse transformers, which will be installed in this area, is finalized and the transformers have been delivered end of 2017. The site preparation and the groundworks for the transformer station are progressing well. The set-up of the underground cable duct between the new transformer station and the GSI campus, guiding the new 20kV cables has been completed.

On the Eastern side of the GSI campus the interface to the new FAIR accelerator complex has been set-up. The outer concrete wall of the experimental hall has been opened and the link to the FAIR tunnel 101, which will contain the extraction beam line out of SIS18 towards SIS100, has been built (Figure 3).



Figure 3: Construction works for the interface to the FAIR tunnel 101.

It is expected that all activities within the GAF project and the FAIR construction relevant for SIS18 operation in 2018 will be finished in time for the planned beam time. In parallel to the civil construction activities, the upgrade of the SIS18 accelerator has been continued. Major new components are in the final phase of manufacturing. The new large bipolar dipole magnet, deflecting the SIS18 beam towards the FAIR tunnel 101, has been manufactured by the company Danfysik and was delivered. The production of the dipole magnet chamber has just been awarded and the IPM (ionization beam profile monitor) magnet system was built and approved by a factory acceptance tests (FAT), before being delivered.

Due to the building displacements generated by the ongoing construction, the accelerator facility needs to be realigned beginning of 2018. Already in 2017, first dry runs with the new control and timing system has been performed.

SIS100

The series production of the SIS100 superconducting dipole magnets has started (Figure 4). The first of series magnet was delivered in September/October 2017. First acceptance tests, especially addressing the precision of the geometry of the internal magnet aperture, indicate a very high manufacturing accuracy which lies within the specified limits. The preparatory works for the series testing at the Series Test Facility (STF) at GSI are continuing. In collaboration with CERN, the set-up of a cold rotating field probe has been completed. All high temperature super-conducting current leads for the Series Test Facility have been delivered and accepted. While carrying out the site acceptance tests, three dipole magnets will be tested in parallel. The cold testing process for each dipole will last four weeks.



Figure 4: Yoke manufacturing for the series dipole magnets

 DOI:10.15120/GR-2018-1



Figure 5: First-of-Series radiofrequency accelerator cavity at external company site.

The first two FOS (First-of-Series) quadrupole doublet units, comprising two superconducting quadrupole magnets, a superconducting steerer- and a sextupole magnet have been tested successfully at JINR Russia.

A dedicated test facility for superconducting magnets of FAIR and NICA has been set-up at JINR and was taken into operation with an official ceremony in November 2016.

One of the largest procurements of the subproject SIS100/SIS18 is the integration of the quadrupole modules, which comprises the design and production of the cryostat system. A producer was found and the contract is signed.

The major design initiative for the quadrupole modules and the so-called missing dipole modules (MDP) is almost finalized. The design of these modules has been performed by an industrial partner. There are still changes in the design of some subcomponents; therefore, the overall set of manufacturing drawings for the modules will be finalized in the GSI design office.

A First-of-Series acceleration radiofrequency (RF) cavity has been manufactured and commissioned. The cavity has reached the specified gap voltage over the complete frequency range. The formal factory acceptance tests are in preparation.

The production of the series of bunch compression cavities could be launched. A delay at the company, which produces the power converters for the cavities, could be mitigated. It has been agreed that the First-of-Series power converters will be directly installed and commissioned on site of the provider of the cavities. The installation of the first power converter is scheduled for January 2018.

One still unresolved technical issue is the insulation of the cooling pipes of the cryogenic vacuum chambers. To investigate the cooling properties achieved by using different bonding technologies, a number of model chambers have been manufactured by a company. The chambers have been installed in the First-of-Series dipole magnet, where temperature and pressure measurements have been conducted. The temperature measurements have shown that the desired surface temperatures below 15 K can be reached. However, the ceramics insulation still cracks after the thermal cycle. Therefore, new tests are planned with cooling pipes equipped with an enamel coating.

The procurement and production of several other components of the SIS100 UHV system is progressing well. Among others, the order for the cryogenics adsorption pumps has been placed and after successful First-of-Series production, the series production has been launched.

Design and tests of beam instrumentation components are converging. Several items of the beam instrumentation system could be ordered and have been delivered already, e.g. the ring cores for the beam transformers, beam loss monitors and other items. The tendering process for the cryogenic beam position monitors has been completed and the contract was awarded.

The components of the local cryogenic system of SIS100 which will distribute liquid helium to the different accelerator components, are designed in WrUST (Wrozlaw University of Science and Technology), Poland. The cryogenic system contains one of the most critical parts with respect to engineering demands: the cryogenic bypass line. A first part of the bypass line, containing the He transfer system and the superconducting bus bar system, has been manufactured and delivered to GSI. In a site acceptance test, which has been conducted at the Series Test Facility, this First-of-Series device was verified (Figure 6). In parallel, the design of the current lead box has been developed up to a full 3D model.



Figure 6: First-of-Series cryogenic bypass line of the local cryogenic system of SIS100 installed at the GSI Series Test Facility

Super Fragment Separator

In 2017 the Production Readiness for the short superconducting multiplets (July 2017) as well as for the long SC multiplets (December 2017) was achieved. The production of the First-of-Series (FoS) short SC multiplet was started. All major subcomponents are produced. The Factory Acceptance Test (FAT) of this multiplet is foreseen before summer 2018. Afterwards the multiplet will be shipped to the test facility at CERN.

The tendering process to procure the required 21 standard superconducting dipole magnets for Super-FRS was initiated in April 2017. After a company qualifying round and two rounds of negotiations the Spanish company ELYTT was awarded with the contract. ELYTT will first verify the already existing magnet design and then produce a First-of-Series (FoS) magnet (Figure 7) which is expected to be ready in autumn next year.

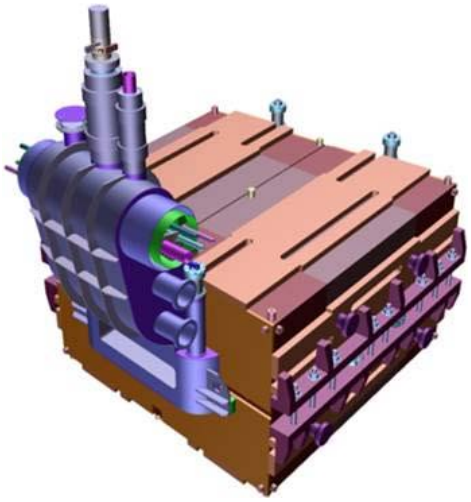


Figure 7: Design of a standard super-conducting dipole for the Super FRS by CEA Saclay as part of the documents for the tendering process

As part of technical collaboration agreement with CEA Saclay a design study for three branching super-conducting dipoles is performed. Compared to the standard dipoles these magnets require an adapted yoke and cryostat design in order to provide an additional straight beam exit to connect the different branches of Super-FRS. The kick-off for this project was in June 2017 and a preliminary design (see dedicated contribution to this report) was already presented in December 2017. It is expected that the design will be completed until summer 2018.

The specifications for the normal-conducting dipoles in the target area have been approved. Currently it is investigated whether the package can be carried out by BINP in Novosibirsk as potential in-kind. The First-of-Series prototype has been developed and built there. In parallel FAIR tendering documents are being prepared and the start of the construction of the remaining two dipoles is expected latest beginning 2019.

The conceptual design of the target chamber is ongoing together with our collaboration partner KVI-CART. The remote guidance of the up to 4.5 tons heavy plug inserts into the chamber was identified as a crucial operation. Thus a full scale mock-up of the target wheel plug was built and the operation could be successfully verified.

Late April 2017 CDR draft documents for the beam catcher, including the recommendations by the 16th MAC, have been received by CMERI Durgapur, India. This was followed by an exchange of information on the necessary remote handling methods this summer.

For the shielding flasks we aim at a combined procurement (tender and in-kind via HIP Finland) with the p-bar subproject in a common working group. The specifications for the Super-FRS transport flask are progressing. In collaboration with the Paul Scherrer Institute (PSI) in Switzerland, a potential subcontractor for HIP has been identified as KVI-CART. The specifications and documents for both packages will be finalized within 2018.

The interfaces to the hot-cell as far as construction planning for the building shell is concerned have been completed, and a study together with Siempelkamp Nukleartechnik GmbH on inserts (doors, lead window frames, crane supports, etc.) to the concrete shell has been carried out. This study will be followed up by another one specifying the details of the installations in the hot-cell.

Proton Linac

Previously, the finalization and commissioning of the p-Linac was not expected to be earlier than 2025, which might have put at risk the HESR and PANDA commissioning. Therefore, the construction of the p-Linac building was re-evaluated and subsequently rescheduled to an earlier date. The p-Linac will deliver beam already in 2023. The extended design documentation and costing has been finished in August 2017.

The proton source built at CEA is close to completion. Commissioning has been started; a current of 70 mA has been achieved, which is close to the design value of 100 mA already. The construction of the low energy beam transport (LEBT) is in progress. Additional power supplies procured by GSI are sent to CEA.

The contract with French collaborators from CNRS is signed. All seven klystrons provided by CNRS passed the Factory-Acceptance-Tests successfully and are delivered to GSI. The production of the First-of-Series modulator is in progress. This is done in-house, which has proven to be the most cost effective approach.

After the very successful power radiofrequency tests of the ladder RFQ prototype, the design of the full size RFQ, which is done at IAP Frankfurt by the group of Ratzinger, is completed and the production has started. A part of the RFQ tank has been successfully copper plated at GSI.

The layout of the CH and CCH cavities is finished. The production of the internal quadrupole triplets is ongoing.

P-bar target

Simulations for target, collimators and beam dumps (for HEBT and APPA as well) are in progress. For this purpose, an ANSYS (Multiphysics finite elements code) working group has been established in collaboration with the Technical University of Warsaw. An experiment at the HiRadMat facility at CERN is in preparation. It is planned to test the mechanical stability of different potential materials for the pbar target and to perform a benchmarking of the simulations. The work on the target station and the alignment system for the beam, a magnetic horn, is progressing.

Together with the Super-FRS team a working group for transport of the highly activated targets to hot cells has been established in order to use synergies for the construction of the shielding flasks and target handling systems.

Collector ring CR

A contract with BINP on the production of the last unassigned CR components is under preparation. Work on the remaining specifications is ongoing.

A prototype vacuum chamber will be constructed and tested at BINP' in order to check the feasibility of the technical concept for the vacuum system according to the MAC recommendations. The technical design of the pro-

 DOI:10.15120/GR-2018-1

totype chamber is finished. The production started already.

Facility-Acceptance and Site-Acceptance-Tests of the First-of-Series of the CR debuncher have been successfully completed. The device fulfils the specifications and was formally accepted. The series production was started already.

The acceptance tests of the First-of-Series of the CR stochastic cooling power amplifier failed. The RF module was redesigned and a new Facility Acceptance Test has taken place, while engineering activities for the pick-up tank and RF signal processing of the stochastic cooling system are ongoing.

High Energy Storage Ring HESR

The components with the longest delivery times for the HESR, dipoles and quadrupoles were delivered completely to Jülich and were technically approved. Half of the dipole magnets were pre-assembled with vacuum chambers in Jülich and delivered to Darmstadt for interim storage.

All other essential components are in production or series production and will be delivered to Jülich by the end of 2018. After pre-assembly, these components will also be transported to Darmstadt by mid-2019.

Commons

The status report for the subproject Commons follows the major technical systems used in the other subprojects:

Magnets

After the pre-series of batch1 (51 dipole magnets) was successfully completed in February 2017 (one dipole magnet of type dip1s_0 and one of type dip13_0), the series production of the rest of the dipole magnet is under way. After having passed the Factory-Acceptance-Test (FAT) at Efremov Institute of Electrophysical Apparatus in St. Petersburg, Russia (NIIEFA) the magnets are shipped to GSI. Shipment of the series magnets started in August 2017 (Figure 8). In total 7 series magnets of type dip1f_0 and 5 series magnets of type dip13_0 underwent successful FAT at NIIEFA and were delivered to GSI until December 2017.



Figure 8: Dipole magnet type dip13_0 (S/N FAIR-023, left) and type dip1f_0 (S/N FAIR-004, right) packed for shipment to FAIR/GSI

The magnets of batch2 and 3 (22 dipole, 166 quadrupole, 92 steerer magnets) will be built by the Budker Institute of Nuclear Physics (BINP), Novosibirsk, Russia. While most of the magnet types are currently in the final design phase, production of yokes and coils of the standard 18Tm quadrupole magnet quad2 and the 100Tm steering magnet s100 has already started, see (Figure 9 and Figure 10). The FATs of the pre-series magnets of these types are re-scheduled for March 2018.



Figure 9: Yoke (left) and coil of the quadrupole magnet quad2 (right)



Figure 10: Yoke halves (left) and coils (right) of the steering magnet s100

Efremov Institute launched stamping of the laminations for dipole magnets of batch2 and 3 having identical yoke cross section like the dipole magnets of batch1 in March 2017. Initially 11400 laminations were stamped and were delivered to BINP, see Figure 11. The first magnet to be built from these laminations is the pre-series magnet of type dip15_0. Stamping of another 8000 lamination of the same type is currently in progress.



Figure 11: Lamination for dipole magnet dip15_0 at BINP

Power converters

The power converters for High Energy Beam Transport quadrupole and steering magnets will be mainly built by the Indian company ECIL (Electronics Corporation of India Limited). Up to now two contracts between FAIR, the Indian shareholder BOSE institute and the provider ECIL comprising in total 196 power converters for HEBT (152 for quadrupole and 44 for steering magnets) have been signed. The Factory Acceptance Test (FAT) for the first series of power converters is scheduled for March 2018 after solving problems in the manufacturing process.

Beam instrumentation

The day zero beam instrumentation of the HEBT lines foresees resonant transformers (RT), fast current transformers (FCT), and particle detector combinations (PDC) for intensity measurements and secondary electron emission grids (SEM-Grid), multi-wire proportional chambers (MWPC) and scintillator screens (SCR) for the determination of the transverse beam profile. After prototypes of all these instruments were tested successfully during the GSI beamtime 2016 and passed all tests, procurement, production and assembly of many components of the series were started.

During a visit at Bergoz Instrumentation in France on May 3rd – 5th 2017, the FAT (Factory Acceptance Test) of all current transformers for the FCTs was successfully completed (Figure 12) and all detectors were delivered to GSI on May 16th, 2017.



Figure 12: Current transformer of FCT

The order to produce 25 vacuum chambers with a ceramic gap for RT/FCT (Figure 13) was awarded to the German company FMB Feinwerk- und Meßtechnik GmbH. The First-of-Series (FoS) chamber was produced in February 2018. Production and Tests of the complete series will be completed in 2018.

Data acquisition and expert control applications were implemented, which are based on the FESA framework developed at CERN (Front-End Software Architecture). Progress was especially achieved with the integration of data acquisition modules into the White Rabbit Timing Network, resulting in precise triggers and timestamps for data acquisition and analysis. A major part of the data acquisition has already been tested in a production environment using the CRYRING accelerator.

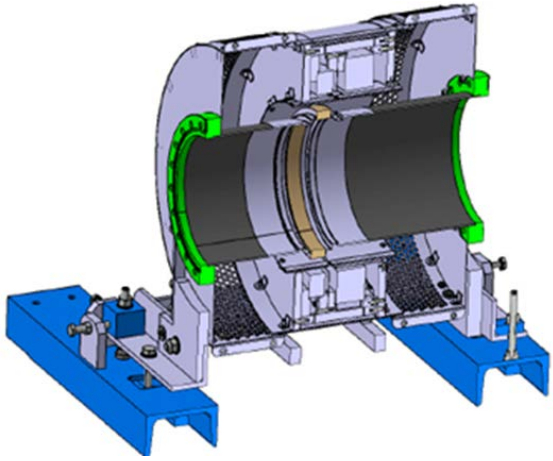


Figure 13: 3D-model of resonant transformers combined with FCT (cut view including both toroids).

Several subprojects which are carried out with the Slovenian in-kind partner Instrumentation Technologies: the DAQ for the beam position monitors BPM of the high energy beam transport system HEBT was delivered in January 2018 and the design of the BPM pre-amplifier are finished and Final Design Reviews (FDR) took place. The board layout for pre-amplifiers was approved, prototype and series were produced, and delivery to FAIR already took place.

Moreover, the Slovenian in-kind partner VacuTech will start the production of the pneumatic drives in this year.

Vaccuum chambers

The vacuum chambers for the dipole magnets of batch1 will be built by BINP. The Factory Acceptance Test (FAT) of the first two pre-series vacuum chambers took place in May 2017 (Figure 14). After giving the allowance for the delivery, the two chambers were shipped to FAIR/GSI on 7th of August 2017 for the Site Acceptance Test (SAT).

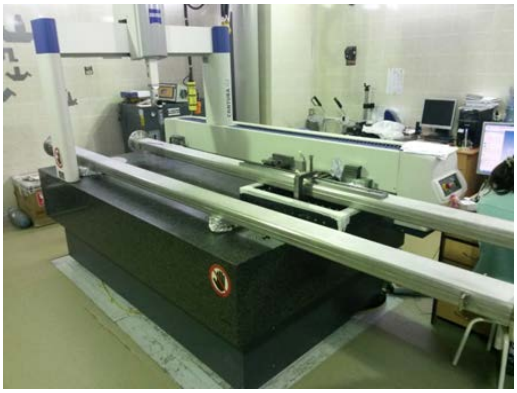


Figure 14: Geometrical inspection of pre-series chambers during FAT at BINP in May 2017

The material for all five branching chambers arrived at BINP in March 2017. In the meanwhile the production of the five chambers has started, with FAT being concluded for two already.

Power connection to FAIR

An intensive collaboration between the technical department EPS, FAIR S&B and the energy provider e-netz took place in order to design and construct new transformer station for the FAIR and GSI accelerators. The orders of four main items (buildings, transformers, high voltage cables and 20 kV switchgear) were placed in April 2017. The construction of the new FAIR transformer stations North and South are progressing within plans. Shell construction works on the FAIR transformer station North for the witch gear-building, the transformer foundations with oil pits, and the foundations for the HV-circuit breaker are completed (Figure 15).

 DOI:10.15120/GR-2018-1



Figure 15: FAIR transformer field North



Figure 16: New Transformer in test field



Figure 17: Transformers ready for transport

Factory-acceptance-tests of the new transformers took place successfully in Balikesir/Turkey (see Figure 16 and Figure 17). The delivery of the new transformers has started. The work on the transformer field north base started in February 2017 and has been finished beginning of 2018.

Power converters Cables and Machine cable management

The new work package (2.14.1.10) “Machine cable management” will provide the best possible cable data quality to the planners, using the cable database for the collection of this information. Later on, this information will be used for the cable routing and the procurement processes. A first complete list of cables (total numbers of cables: 43.400) was given to FAIR S&B in November 2017.

Together with FAIR Site & Buildings, the specifications for the procurement and cable-laying were developed so that a specification of services will be compiled end of 2018.

Cryogenics:

The technical department Commons Cryogenics (CRY) is responsible for the GSI and FAIR wide cryogenic helium cooling of superconducting magnets. CRY is presently operating a prototype test facility (PTF), a series test facility (STF), a helium supply unit (HeSu) and two more cryo plants for the R3B GLAD magnet testing and for the cooling of the CRYRING electron cooler solenoid. The main customers at FAIR are the SIS100 and the Super-FRS with a total helium inventory of about eight tons. Additionally CRY serves small consumers like the final focusing system of APPA and the large scale experiments CBM/HADES and Panda. Furthermore the department is responsible for the so-called local cryogenics belonging to SIS100 and Super-FRS respectively.

Helium Supply Unit (HeSu)

The HeSu is a liquefier with a decant station, a mobile Dewar parking station and a warm gas recovery system with campus wide helium return lines. The HeSu was taken into operation in 2015 and has delivered more than 49,000 l of LHe to users onside the campus so far. The

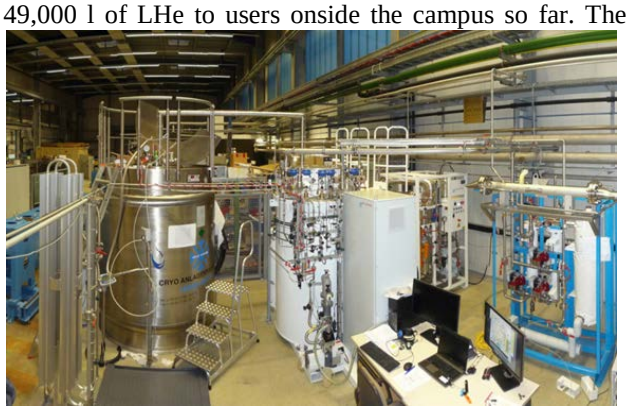


Figure 18: Helium supply unit for FAIR prototype testing



Figure 19: Universal cryostat for FAIR prototype testing

main purpose is the cryogenic testing of FAIR prototypes. It has a liquefaction capacity of approximately 25 l/h for pure helium gas and 17 l/h in purification mode. A picture of the installation is shown in Figure 18. The warm gas storage capacity was upgraded by additional 30 m³. Part of the HeSu project was a universal cryostat for the testing of FAIR components, in particular SIS100 beam pipe vacuum chambers. The universal cryostat has a more than 4 m long cold testing area with an actively cooled table. A picture of the universal cryostat is shown in Figure 19. The big side flanges can be operated by one single person crane support. Several different cooling techniques are realized: (a) LN2 shield cooling and LHe 4 K cooling with Dewars (using the HeSu), (b) LHe cooling only, with a boil-off cooling of the shield using again Dewars, or (c) connection to the universal connection box of the STF, see below in Figure 19.

Cryogenic Infrastructure for the Series Test Facility (STF)

The series test facility for SIS100 dipole serial magnet testing was taken into operation in 2015 and continuously running in 2016 and 2017 for the testing of the first of series (FoS) dipole magnet, but additionally for the test of the SIS100 main current leads, for the SIS100 local current leads, for SIS100 cryo adsorption pumps and for the site acceptance test (SAT) of the first parts of the local cryogenics for SIS100 arrived at GSI in summer 2016. The serial testing of the dipole magnets was started in 2017. The STF has an overall cooling capacity of 1.5 kW @4K equivalent and is equipped with four test benches for magnet testing and one universal connection box. Up to now the plant has about 15,000 h of operation. A picture of the STF cryogenic infrastructure is shown in Figure 20.



Figure 20: The GSI series test facility

Procurement of the FAIR Cryo Plant CRYO2:

For FAIR one central cryo plant will be installed serving a helium cooling capacity for SIS100, Super-FRS, CBM and HADES. In the first step a 19 kW @ 4 K equivalent cryo plant will be installed, including a campus wide 1.6 km long distribution system. Two industrial studies concerning the cryo plant layout were performed in 2014 and afterwards the specification was continuously adapted to future user requirements. The procurement phase is currently ongoing: After specification was approved, the budget was released and the official announcement has taken place in October 2017. According to the present time schedule the contract with the manufacturer will be signed in September 2018 and the plant installation will take place in the second half of 2021 followed by the commissioning performed until the end of 2022.

Cryogenic Infrastructure for the GLAD Magnet:

For the testing of the GSI GLAD magnet, which will be later a central component of the high energy branch of the SuperFRS, the cryogenic department has refurbished an existing cryo plant. The refurbishment comprises a complete check of the hardware, the replacement of a large number of actors and sensors, a complete new electronic cabinet and state of the art control software using the CERN industrial control software environment UNICOS in combination with Siemens WinnCC OA. The GLAD magnet was cooled down for the first time in 2017.

Control Systems (CO)

The activities of the accelerator Controls Department is fully focused on the development and implementation of the accelerator control system for FAIR.

During the past months significant progress has been made in all control system subprojects. The design of the standard equipment controllers (SCU) for FAIR power converters and many other systems, of which more than 1200 units will be needed, has been successfully completed and production and assembly of the first batch (100 units) has been completed. Several components of the newly developed White Rabbit protocol-based high-precision time and event distribution system, backbone of real-time control in the control system for the full facility, has been further developed and is already installed and under production test for the CRYRING machine.

Electronic timing receiver boards (FTRN) in several form factors (PCe, VME, PMC, uTCA), both GSI in-house developments as well as Slovenian in-kind contribution projects are under development. Schematics design and board layout has been checked and prototypes have been produced or are presently under evaluation. Significant progress has also been made in development of the fundamental underlying control system software frameworks for accelerator equipment control (FESA), communication middleware, databases, physics modelling of the machines and beam lines (LSA) as well on user interfaces graphical control room applications. Development on the accelerator measurement and data archive system has started; an early prototype version is presently being evaluated in the controls lab to confirm the technologies and products. On the industrial controls side, vacuum control with the industrial control SCADA-based UNICOS framework has been developed, installed, commissioned and is presently under testing as a collaboration project of GSI and a Slovenian in-kind provider at the CRYRING. The vacuum bake-out control of all sections of the CRYRING has been already successfully implemented and tested, shortcomings and problems have al-

 DOI:10.15120/GR-2018-1

ready being identified and are presently being addressed. In respect of cryogenic controls, several cryogenic sensors and actuators have been tested as a sound base for the cryogenic controls system design. Technical and functional specification documents for the control system of the upcoming tendering of the FAIR central cryo-plant have been worked out and are formally approved.

Following the agreed project strategy of the control system subproject, the full control system architecture was implemented at the CRYRING machine, being used as test-bench for FAIR. During the last months numerous tests have been performed in order to identify bugs and limits and apply. Finally the control system was already used for commissioning the CRYRING local injector and ring with beam. Presently a new release of the control system stack is being prepared for beam operation in August/September. In parallel, the control system team is fully engaged in providing the FAIR control system already for the upcoming beam time of the existing GSI machines in 2018 and 2019. These two applications to existing machines will greatly reduce the time and risk during commissioning of the FAIR machines

Transport and Installation

Numerous workshops on the topic of accelerator installation have been carried out since 2016, resulting in the creation of dedicated additional work packages and corresponding detailed installation plans.

An overall concept for the intermediate storage of FAIR components is currently in progress.

Measures have been taken to use existing Campus Facilities according to increasing requests for adequate component testing and storage. The overall need for intermediate storage leads to leasing of external storehouse areas. Presently the storage of HESR components delivered by Forschungszentrum Jülich (FZJ) is ongoing (see Figure 21 and Figure 22).



Figure 21: Unloading of one of the HESR dipole magnets

Engineering /Mechanical Integration

For visualization of beam lines, buildings and technical building services and for facilitation of coordination tasks and test processes in a web-based tool, the Kisters 3D viewer, was implemented. This tool allows work package leaders, subproject leaders and management to receive a general overview. Independently of CAD tools the configuration of the beam lines will be shown together with their position in the buildings. This view can be used on any web-connected unit like computers or mobiles independently of any license structure. The content will be



Figure 22: Remote positioning of an HESR dipole magnet

updated regularly once in a month by the person in charge of DMU group.

Figure 23 shows the screenshot of the Kisters 3D viewer with the detail of the HEBT beam lines and buildings.

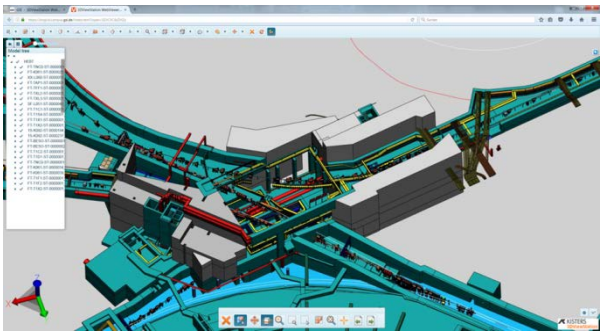


Figure 23: Screen shot of Kisters 3D viewer with HEBT

FAIR Site & Buildings

The approval for the tendering and awarding of civil works for the construction area North by the BMBF is given mid-September 2016. The reorganization of the FSB department was completed in 2017. The development of a staffing plan of FSB department is also finalized.

The civil works execution plan for the FAIR project is divided into construction area North and construction area South. The contractual schedules with the civil design companies will be adapted accordingly. Detailed scheduling of civil work packages is currently progressing in cooperation with the civil designers.

An overall time schedule including defined periods for installation of machine components was developed as part of the integrated project master time schedule.

The ZBAU reapplication, which is required by German law for building measures financed by the federal government, was submitted to the Landesbetrieb Bau und Immobilien Hessen, LBIH, on time in December 2016.

The tenders for groundwater lowering, trench sheeting and excavation in the construction area North was contracted on schedule in Mai 2017. Official ground breaking ceremony has been performed on July 4th, 2017. Site works have been started in July 2017 and are progressing as planned.

The overall project civil construction permission is issued since 2014 for the entire facility. Some construction permissions for the buildings have to be revised as part of the design process (e.g. for the north and south electrical substations). The revised applications are scheduled in line with the civil construction schedule.

FAIR Experimental Areas

Major developments for the experimental areas of CBM, APPA, NUSTAR & PANDA are described in the following chapters.

APPA

Work on design and construction of the experiment components proceeds as planned. Special efforts have been made to complete the installation and continue the commissioning of the CRYRING. In May 2017, a new test with beam has been performed, which served as a test of the FAIR control system. With this new FAIR-like control system, the operation status as of 2016 could be re-achieved. Also tests of the beam diagnosis elements (PBMs) and the first training for the operators' team to get used to the new control system were done. For these activities, we acknowledge the strong support from the on-site specialist as well as from our collaboration members from the Jagiellonian University, in Krakow, Poland.

With high enthusiasm, the completion of components which will be used in the FAIR Phase-0 for experiments was pushed ahead. The APPA collaborations submitted over 70 experiment proposals for the FAIR Phase-0 program, and currently prepare the new equipment needed for carrying them out.

In July 2017, the Expert Committee ECE recommended two TDRs for key components of the APPA plasma physics to be accepted. A third one is still in the evaluation process and three new ones are in preparation.

The Plasma workshop organized in July at GSI concluded the reorganization process and program update of the HEDgeHOB/WDM collaboration. The new collaboration, HED@FAIR (High Energy Density physics at FAIR) strengthened the scientific goals of the plasma physics program at FAIR and gained new collaboration members interested in contributing to the realization of the experiments.

CBM

CBM experiment: The CBM magnet has been contracted to BINP, the review of the planning status was completed in April 2017; the magnet is currently in the conceptual design phase. The silicon tracker (STS), RICH, time-of-flight (TOF), and muon (MUCH) detector systems have approved TDRs, are in the engineering design phase, and full-sized pre-series chambers are verified in test beam campaigns. The STS, as most complex detector project, will structure the production readiness reviews in three parts (sensor, electronics, integration) planned for 2017 and 2018. A co-operation has been established with JINR, which builds 4 silicon tracker planes using the same technology as CBM to augment the BM@N tracking system, the fixed target experiment at the Nuclotron in Dubna. The photon detector of the Ring Imaging Cherenkov Detector, RICH, is in an advanced stage, all of the photo multipliers are tested.

The RICH readout is a joint CBM, HADES, and PANDA development. The RICH photon detector component has a modular design and is planned to be used in the context of the HADES experiment at SIS-18 starting 2018. The production readiness review for the first batch of Time-of-Flight ToF chambers was completed in March 2017, the production has started. The Projectile Spectator Detector, PSD, also has an approved TDR; all modules have been produced and will be tested at CERN and JINR. The STS, RICH, TOF, and PSD activities at BM@N/JINR, STAR/RHIC and HADES/SIS-18 constitute the CBM FAIR Phase-0 activities which will produce early operational experience for these detector systems and generate valuable physics data. The feasibility of the whole data-acquisition chain with high rates is proposed to be demonstrated using mini-CBM within Phase-0.

In total 7 out of 12 planned TDRs are approved, they describe in terms of financial volume about 80% of the components which require a TDR and are mandatory for the day-1 setup. One of the remaining TDRs was submitted in 2017 and the last ones in 2018. The final TDR describing the Online/Offline Software including the online event selection will be prepared in close coordination with the FAIR Computing TDR.

HADES experiment: HADES is a running experiment which will be moved from its current place in the SIS-18 experimental hall to the CBM cave. The work structure is therefore very different from the one of the CBM experiment and consists of the construction of an ECAL, a major upgrade of the RICH, the addition of tracking and time-of-flight detectors covering the very forward hemisphere, and several other upgrades. The HADES ECAL mainframe was delivered and installed in the current HADES cave by end of August 2017. It is largely funded by Polish contributions. The RICH upgrade is done in collaboration with CBM, using identical photon detector technology and actually sharing high cost components. Both ECAL and RICH will be ready in mid-2018 in time for the FAIR Phase-0 program at SIS-18. The forward tracking stations are based on PANDA straw technology and the geometry of the PANDA forward tracker.

NUSTAR

For all experimental set-ups of the NUSTAR pillar, the list of components and associated Work Breakdown Structure code (PSP Code) was refined and re-confirmed. An intense activity was devoted to the improvement of the time scheduling of the planned NUSTAR experiments, which was matched to the Integrated Master Schedule of the FAIR project. For each experiment, the milestone defining the completeness of each component

 DOI:10.15120/GR-2018-1

necessary for the installation of the experimental set-up was mirrored in an overview plan. This allowed also the creation of an installation plan. The time range available for installation is established in the plan of the Civil Construction.

Two time windows define the time range available for the assembly of components. The allocated time slot for the installation of NUSTAR experiments is in some cases too early with respect to the foreseen beam availability. The beam availability is scheduled in only one plan (Commissioning plan) for the whole FAIR project. For this reason, it is foreseen to reschedule the experiment installation starting backwards from the Commissioning plan. This would be advantageous for some of the experimental groups which could profit from experimental activities at the upgraded GSI facility and other laboratories.

Work has continued on the detailed technical specifications for several In-Kind and Collaboration Contracts. Three previously submitted TDRs have been accepted by ECE.

Work on NUSTAR detection systems, electronics, data acquisition is proceeding according to the internal planning. Focus is on readiness for FAIR Phase-0 experiments from 2018 onwards. In total 39 Phase-0 proposals have been submitted to the GSI PAC. The CDR for the LEB magnets has been reworked and has very recently been accepted.

PANDA

Electromagnetic Calorimeter (EMC): The first-of-series of 16 modules of the Target Spectrometer Barrel EMC is under construction at University of Gießen (D) in collaboration with IHEP Protvino (RU). All sub-modules have been assembled with crystals and APDs. But the final assembly of the module planned for summer 2017 is further postponed due to the much delayed delivery of the PCBs needed for the mounting of readout chips, reducing the margin on the schedule by half a year. The delivery of the high-purity PWO base material funded by Russia was completed in May 2017. The samples showed very good quality and are stored for further processing. The crystal producer CRYTUR in Czech Republic has by now produced 75 crystals of a pilot series, which show very good quality. The mass production should resume as soon as possible preventing delays. The Forward Endcap EMC is currently under construction in Bonn and Bochum and will be fully assembled at FZ Jülich until mid-2018. The module design of the Backward Endcap EMC has been revised and is complete now. A full readout chain was tested successfully with beam.

Superconducting Solenoid Magnet: The PANDA solenoid magnet was assigned to BINP Novosibirsk (RU) and a collaboration contract for the construction of the complete magnet was signed in March 2017. It is planned to perform technical follow-up of the contract with help from CERN. Work has started and a plan review was performed in summer 2017. The yoke production was subcontracted in November 2017 and the yoke FDR was started.

Barrel DIRC: The TDR of the Barrel DIRC, a German in-kind contribution to FAIR, was submitted in September 2016 and updated in May 2017 with results from a test- beam in fall 2016. The TDR has meanwhile been approved by FAIR ECE.

Luminosity Detector: The Luminosity Detector TDR was submitted in March 2017 and is currently under review by FAIR ECE.

Time-of-Flight (ToF) Detectors: The technical design of the Barrel ToF Detector is based on Silicon Photomultipliers and thin scintillator tiles. Its TDR – submitted in April 2017 - will be approved beginning of 2018 by FAIR ECE. The Forward ToF consists of more conventional large area scintillator bars read out by photomultiplier tubes. This TDR was revised and will be submitted to FAIR.

Forward Tracker: The technical design of the forward tracking detectors was completed with the missing piece of the required simulation of track pattern recognition and was reviewed internally. It is currently revised for submission to FAIR ECE.

Endcap Disc DIRC: After a first technical report in 2014 a review team had recommended a list of studies and improvements, which were completed by the beginning of 2017. A TDR for a full-size prototype was compiled on the basis of these experiences.

Infrastructure: The planning of electrical supplies for the experiment was coordinated with the electrical planning of the building to save cost in the infrastructure of the experiment.

Further service planning for cooling and routing of experiment cables and supplies is ongoing.

The technical service planning of the hall led to a revision of the architecture of rooms and dimensions requiring a re-planning of parts of the layout of the experiment infrastructure.

The FAIR Sequencer
Semi-automation in view of accelerator commissioning and operation

R. J. Steinhagen, H. Hüther, R. Müller, GSI, Darmstadt, Germany;

Abstract

FAIR extends and supersedes GSI's existing accelerator infrastructure both in complexity as well as in number of devices that required to safely inject, accelerate, and extract particle beams to the experiments.

In order to perform the initial accelerator hardware- and beam-commissioning, quality assurance, as well as subsequent system re-validation tests in a most efficient and reliable fashion with the limited resources at hand, a high-level Java-based sequencer frame-work has been developed as a core part of the control system to aid the semi-automated testing, validation of the devices' system responses, and control of the accelerator facility (e.g. processing of SAT check-lists, generation of QA documentation. 'as-good-as-new' machine protection tests, etc.).

Introduction

For many sub-systems the number of involved devices increases ten-fold with respect to what exists in the present facility (notably power-converters, magnets, RF systems, beam instrumentation, cryo- and quench protection systems). At the same time, a much higher level of detail and more stringent testing of the system function and accelerator setup is required at FAIR to provide a safe and reliably accelerator control, necessary while operating at the highest beam intensities and energies.

Thus, the validation of the systems' function is not only required during the initial Site-Acceptance-Tests (SAT) but also as part of an 'as-good-as-new' testing policy during regular routine operation in view of validating the machine protection and ALARA (ie. As-Low-As-Reasonably-Achievable) loss minimisation targets, as well as for an early detection and identification of non-conformities and faults. The gathered information can be used to schedule planned preventative maintenance during routine day-to-day operation before these non-conformities become beam-inhibiting faults.

Architecture and Design

The FAIR Sequencer is based on earlier concepts, developments, and experience at CERN [1]. It is conceptually divided into three parts: the middle-tier 'sequencer' service, i.e. the software system capable of running the sequences, the 'sequences' themselves, and a graphical user interface that provides a more ergonomic and user-friendly interaction with these test procedures.

Each sequence consists of a subset of tasks that contain the individual testing steps (ie. SAT checklist items) as described, for example, by the individual device SAT criteria, commissioning or test procedures outlined in [2].

Sequences are typically defined per device, can be further nested, executed in parallel for a group of devices with the possibility to 'start', 'stop', 'pause', 'step', or 'repeat' individual tasks as required.

At the same time, the execution result of each task ('pass', 'failure', 'warning', 'skipped', etc.) is documented alongside the applicable detailed testing meta information in the FAIR Archiving System out of which an automatic PDF-based test report can be generated.

While keeping the same user-level functionality, it was decided, to re-implement the Sequencer core due to the obsolescence of some of the used software library components, unavailability of the required controls infrastructure services at GSI, and also to deploy more modern Java development concepts that since became available [3].

The Sequencer interacts with all FAIR sub-systems, controls interfaces and databases, and provides a generic abstraction interface that moves large parts of the complexity of interacting with the accelerator control system towards the frame-work itself rather than the user-level testing code that can be kept simple, short and functional.

The Sequencer is being tested and already used during the early Dry-Runs in 2017, and equipment specialists, operation and others are encouraged to consider using it if semi-automated testing and/or other procedures interacting with the FAIR control system are required that are not covered by the other available tools.

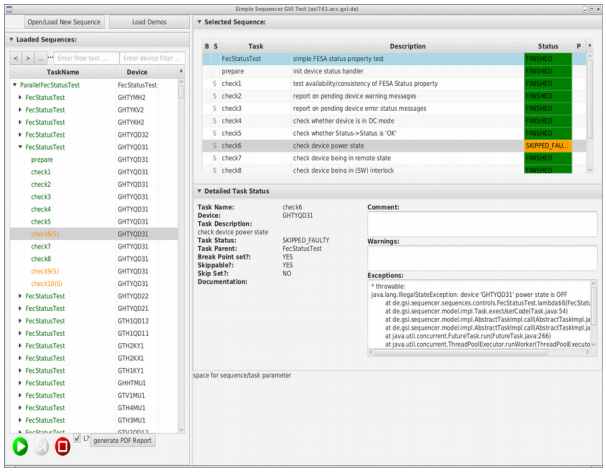


Figure 1: Sequencer GUI impression.

Acknowledgements

The valuable contributions, advice and recommendations that guided the re-implementation of the new FAIR Sequencer from our CERN colleagues V. Baggiolini and R. Gorbonosov are greatly acknowledged.

References

[1] V. Baggiolini et al. "A Sequencer for the LHC era", ICALEPCS'09, Kobe, Japan, 2009

[2] Commissioning: https://fair-wiki.gsi.de/FC2WG

[3] https://www-acc.gsi.de/svn/applications/sequencer/

 DOI:10.15120/GR-2018-1

Accelerator infrastructure: UNILAC / SIS18 / ESR / FRS / CRYRING / pbar-Separator / SIS100 / p-Linac / CR / Super-FRS / HEBT / HEST / CERN-LHC
PSP codes: 2.14.17, 2.14.10.1
Strategic co-operation with: CERN

Development of optical beam profile monitors

P. Forck[1], R. Hampf[2], A. Himpsl[2], S. Udrea[1], A. Ulrich[2], J. Wieser[3]

[1]GSI, Darmstadt, Germany; [2]TU-München, Germany; [3]Excitech GmbH, Schortens, Germany

Optical beam diagnostics is planned for intense ion beams which would destroy conventional beam diagnostic devices. The concept is to measure beam-induced light emission from a gas target, space-resolved, and to deduce beam profiles from these data. A more detailed description of the concept is given in Ref. [1] and references therein. More results are also presented in the annual report of the plasma physics group at GSI for the year 2017.

An important issue is to study, if the concept can be used at the low pressure conditions within the beam-lines. Model experiments at the Munich Tandem accelerator using a DC-beam of 87 MeV ^{32}S ions (2.72 MeV/u) exciting various gases over a wide pressure range were performed in 2017. Both spectroscopic studies and preliminary profile measurements have been performed. The spectroscopic studies are used to identify appropriate optical transitions. Based on the results transmission filters were used to take pictures of the beam in various wavelength regions. Differential pumping was installed at the beam entrance for pressures below 1mbar. A f=30cm vacuum monochromator (McPherson 218) was used to record beam induced spectra of Ne, Ar, Kr, Xe, and N_2. An example is given in Fig. 1. It shows mainly lines (and in the case of nitrogen molecular bands) of neutral and singly ionized target species.

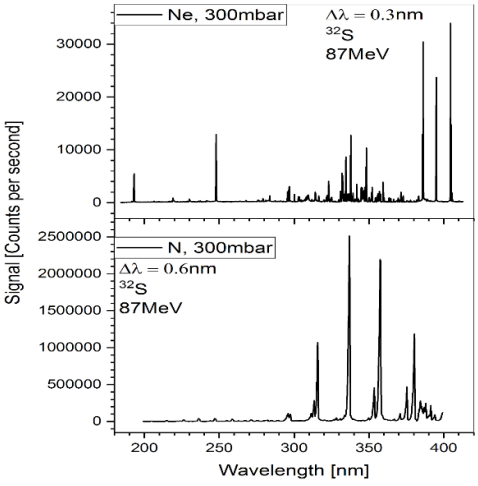


Figure 1: Overview spectra for neon and nitrogen recorded at an elevated target gas pressure of 300mbar.

Beam profile measurements were performed with a sensitive, cooled CCD camera (ATIK 383L+) combined with a f=60mm broadband (315 to 1100nm) apochromatic lens. Appropriate bandpass filters were used to select various emission regions for the emission from neutral and ionized species. The ion beam was sent through a 1mm diameter aperture into the target gas. A general result is that secondary electrons can strongly excite neutral species, which leads to pronounced wings in the beam profiles for target densities around 1mbar (see Ref. [1]).

At low pressure, the range of the secondary electrons is so large that they do not lead to the formation of visible "wings" and rather hit the walls of the cell (Fig. 2). In Fig. 3 it is shown that the beam profile is well represented for both low pressure and high pressure. At high pressure it is due to the fact that the range of the secondary electrons is short compared to the diameter of the ion beam.

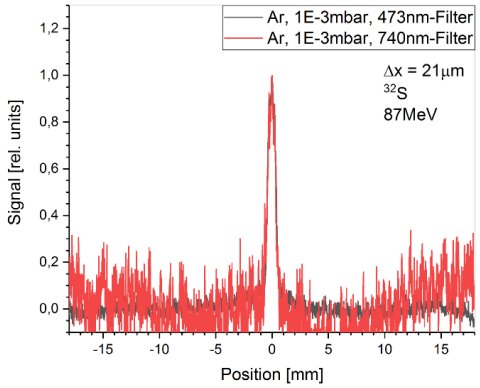


Figure 2: Example of a beam profile measurement at relatively low pressure. The "wings" which appear for measurements using neutral lines (red) are not pronounced under these conditions.

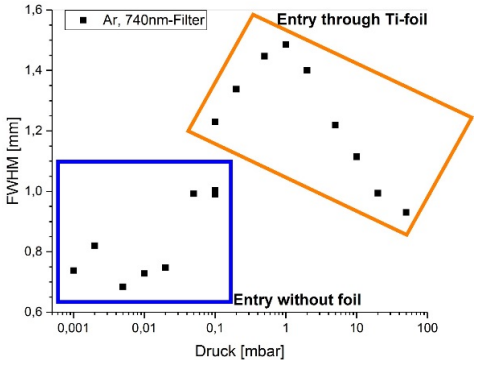


Figure 3: Beam diameters (FWHM) measured for a wide range of target gas pressures using the emission from an atomic line.

Acknowledgements

This work has been funded by the BMBF project APPA R&D, FKZ 05P15WOFA1, GSI Vorhaben TUM ULRI1719, and Maier Leibnitz Labor München (MLL).

References

[1] A. Ulrich et al., High Energy Density generated by Heavy Ions and Laser Beams Report 2016 (GSI-2016-2), page 31 and the analogue report for 20174.

 DOI:10.15120/GR-2018-1

Prototype development of a Multipurpose Hardware Unit for deterministic bunch-to-bucket transfers between synchrotrons

O. Bachmann[1], T. Ferrand[2], K. Hofmann[1]

Technische Universität Darmstadt, Germany, [1]IES; [2]TEMF

Introduction

In the context of the FAIR project, a new concept for a fully-deterministic bunch-to-bucket transfer (B2B) between sending and receiving synchrotrons (e.g. SIS18 and SIS100) is currently under development. Developing dedicated electronic solutions for each technological task represents an invest in terms of costs and time. Hence, it is intended to develop a new multipurpose hardware unit (MHU) to minimize this invest. The MHU has to fit in a large spectrum of current and future applications with sufficient performance. As a result, it has to be at least compatible with all kinds of signal formats currently being used in the low-level radio frequency (LLRF) environment at GSI.

MHU Application Areas

The MHU is based on a programmable unit which covers the actual application concerning the most general functions on parallel input signal conversion and processing. An FPGA-based solution is planned. Several currently defined functional blocks, e.g. Phase Advance Prediction or Phase Shift Module, are foreseen and based on the requirements document [1].

MHU Prototype Realization

A wide range of the required hardware components can be based on commercial-off-the-shelf (COTS) devices, but for special interface requirements of GSI there is a need for the development of new modular interface modules. The Achilles Arria 10 System on Module (SoM) constitutes the processing unit of the MHU which enables high modularity and interchangeability in case of future designs. A carrier board is connected to the SoM and a customized backplane, which enables the interfacing of modular extension boards and GSI inherent boards like the DIOB (Digital Input Output Board) [2] and MMD (Maintenance Module for External Devices) [3] module connected to the SCU backplane [4]. Regarding current Use Cases described in [5] several customized interface boards shown in figure 1 have to be developed. They are depicted as an optical interface board for ODL (Optical Direct Link) and OTR (Optical Token Ring), a PC interface board providing debugging and access points via Ethernet, or UART and a peripheral interface Board providing BuTiS clock reference, analog TTL based IOs and status LEDs. As depicted in figure 1, one of the carrier board FMC ports is connected to the customized backplane, the other one is foreseen as modular FMC interface for the extension with standardized COTS FMC daughter boards; e.g. ADC/DAC daughter board.

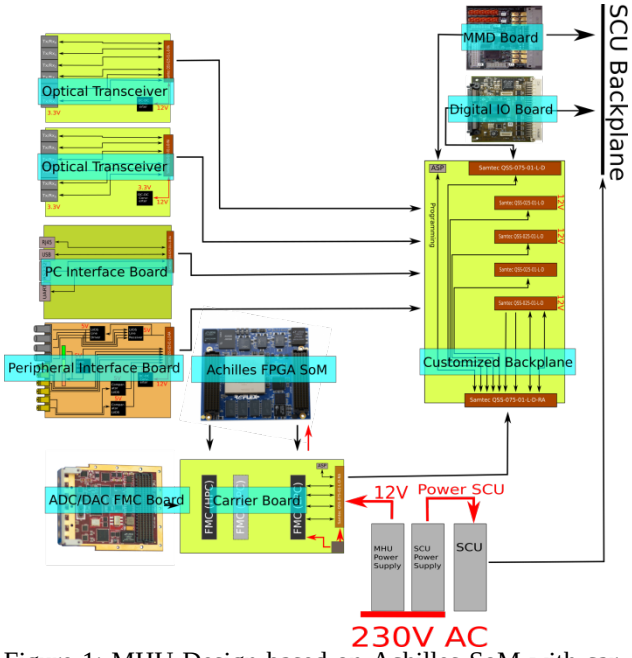


Figure 1: MHU Design based on Achilles SoM with carrier board, customized extension boards, customized backplane and GSI system interfaces.

Outlook

The first prototype designs have been started with the availability of the SoM, the ADC/DAC FMC daughter board, the DIOB, MMD, SCU-Backplane and the development of the ODL interface board, that was successfully tested. Further prototype development will be necessary to implement the entire MHU, which concerns the development of the carrier board, the customized backplane, the peripheral interface board and the PC interface board.

References

[1] T. Ferrand, D. Lens and H. Klingbeil, “Multipurpose Hardware Unit for Deterministic Bunch-to-Bucket Transfers between Synchrotrons, Requirements Specification”, rev. 1.94, 2016.

[2] GSIPBRF, "Digital/Analog IO-FPGA Part, FG900.50xn", 2016.

[3] K.-P. Ningel, "HW Maintenance and Diagnostics Specification", 2012.

[4] K. Kaiser, “Detailed Documentation of the Scalable Control Unit SCU3 FG 900.112, FAIR Technical Concept, F-TN-C-008e”, rev. 1.1, 2014.

[5] T. Ferrand, H. Klingbeil, J. Bai and O. Bachmann, “Development of a topology for the bunch-to-bucket Transfer for FAIR”, GSI SCIENTIFIC REPORT 2015, 2016.

Characterization of the Cryogenic Current Comparator for FAIR*

D. Haider[1#], F. Kurian[1], M. Schwickert[1], T. Sieber[1],V. Tympel[2], R. Neubert[3], T. Stöhlker[1,2]

[1]GSI, Darmstadt, Germany; [2]Helmholtz Institute Jena, Germany; [3]Friedrich-Schiller-University, Jena

The design of the Cryogenic Current Comparator (CCC) has been adapted to offer an optimal performance when it is used for nA beam current measurements in the FAIR facilities. Following this preparation, in 2017 the FAIR prototype, also called CCC-eXtended-Dimension (CCC-XD), was manufactured from niobium and assembled into an optimized superconducting shielding geometry, surrounding an enhanced flux-concentrating core made from NANOPERM© material [1]. Extended tests on the new system have been performed, which showed that the transition to the large FAIR beamline diameter was a success [1, 2].

Performance of the CCC-XD

The primary challenge of the new design for the CCC at FAIR was to increase the radius to accommodate for the beamline diameter of 150 mm while maintaining the performance of the predecessors. After its assembly the CCC-XD (shown in fig. 1) was characterized in a controlled environment inside a wide-neck cryostat. A magnetically shielded room is available at Friedrich-Schiller-University Jena to exclude external magnetic influences. With this setup a white noise level of <3 pA/Sqrt(Hz) [2] can be achieved which is regarded as an improvement compared to earlier values of 11 pA/Sqrt(Hz), measured in the accelerator environment [3].

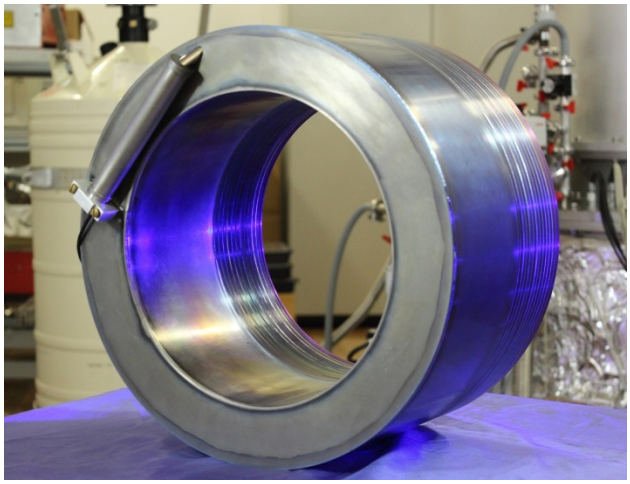


Figure 1: The FAIR prototype CCC-XD. The cartridge holding the SQUID electronics is mounted to the front. In the back the welding of the meander structure is visible.

In order to determine the current resolution, a calibration wire passes through the CCC and allows to apply a test current to simulate an ion beam. Figure 2 shows the response of the CCC-XD (red) to a 1.65 nA current pulse (green). In the laboratory, these intensities can easily be detected without any additional data processing.

The sensitivity of the SQUID can be tuned by adjusting the coupling of the pick-up coil around the flux concentrator to the sensing coil of the SQUID. Here the signal gain and the frequency bandwidth can be balanced depending on the requirements. The present configuration achieves a slew rate of 0.16 µA/µs using the full bandwidth of 200 kHz [2]. For some applications in which time resolution is less important (e.g. in storage rings) a 10 kHz low-pass filter is used to suppress high frequency noise which limits the slew rate at the same time (fig. 2).

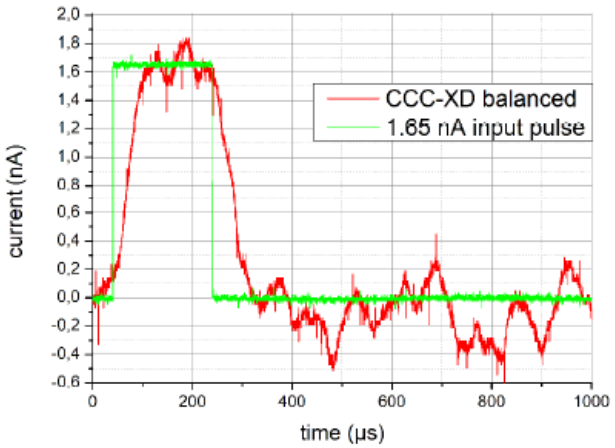


Figure 2: Response of the CCC-XD (red) to a 1.65 nA (200 µs) current pulse (green), measured with a 10 kHz low pass filter [4].

Specification of the CCC cryostat for FAIR

The specification for the FAIR beamline cryostat was finalized and the construction is finished until the end of 2018. The mechanical design has been supported by ANSYS calculations in the frame of the collaboration with TU Darmstadt. Throughout the measurement campaigns it has become apparent that mechanical oscillations of the cryostat are a source of noise for the sensitive SQUID system. Thus the cryostat is designed in a way to avoid mechanical resonances and to provide sufficient damping of external vibrations. Further tests on noise sources and alternative shielding geometries are ongoing [1]. With the CCC-XD tested and ready to measure currents, the focus is currently on the preparation for the setup in CRYRING.

References

[1] T. Sieber, F. Kurian, M. Schwickert et al., “Optimization of the Cryogenic Current Comparator (CCC) for beam intensity measurement”, Proceedings of IBIC 2017, Grand Rapids, MI, USA

[2] P. Seidel, V. Tympel, R. Neubert et al., "Cryogenic Current Comparators for large beamlines", Proceedings of EUCAS 2017, Geneva, CH

[3] F. Kurian, “Cryogenic Current Comparator for Precise Ion Beam Current Measurements”, PhD thesis, Goethe University, Frankfurt am Main, 2015

[4] V. Tympel, T. Stöhlker et al., "Cryogenic Current Comparators for 150 mm beamline diameter", Proceedings of IBIC 2017, Grand Rapids, MI, USA

D.Haider@gsi.de

* Work supported by the EU H2020 Marie-Curie Action No. 721559 and by the BMBF under contract No. 05P15SJRBA

 DOI:10.15120/GR-2018-1

Bunch Shape Measurements at the GSI cw-Linac prototype

T. Sieber[1,#], P. Forck[1], S. Udrea[1]

[1]GSI, Darmstadt, Germany

The existing GSI accelerator will become the injector for FAIR. To preserve and enhance the current experimental program at UNILAC, a dedicated new Linac is under development, which shall run in parallel to the FAIR injector, providing cw-beams of ions at energies from 3.5 – 7.3 MeV/u.

For this cw-Linac a superconducting prototype cavity (demonstrator) has been developed and was first operated with beam in summer 2017 [1]. The resonator is a Crossbar H-structure (CH) of 0.7 m length, with a resonant frequency of 216.8 MHz. It has been installed behind the GSI High Charge State Injector (HLI), which provided 108 MHz bunches of 1.4 MeV/u Ar6+/9+/11+ ions at a duty cycle of 25%. Due to the frequency jump and small longitudinal acceptance of the CH, proper matching of the HLI beam to the prototype was required. The bunch properties of the injected beam as well as the effect of different phase- and amplitude-settings of the cavity were measured in detail with a bunch shape monitor (BSM) fabricated at INR, Moscow, while the mean energy was analyzed by time of flight method. Figure 1 shows the experimental setup at the cw-Linac test stand.

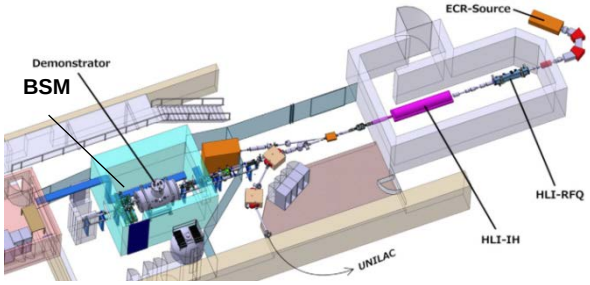


Figure 1: Setup for cw-Linac test measurements at the HLI beamline.

Figure 2 shows the basic principle of the BSM. The device was developed at by A. Feschenko at the INR Moscow and is therefore often referred to as “Feschenko Monitor” [2]. The beam is longitudinally scanned with a tungsten wire, placed at the beam axis on negative potential (–10 kV). By interaction of the ions with the metal surface secondary electrons are generated, which are extracted towards ground potential. The electrons pass through an rf-deflector (operating at the frequency of the accelerating cavity) and are swept over a vertical slit before they get deflected by magnetic field for energy separation. The counts at the SEM detector are plotted as a function of rf-phase. In this way, the spatial information of the particle distribution inside the bunch is transformed into phase information, relative to the rf-period of the accelerator (deflector field). It is obvious that the BSM can - as a matter of principle - not be considered as non-destructive. Besides reduction of intensity, slight deviations in particle position and energy have been observed. However, with a phase accuracy of ~1°, high stability, reproducibility and good handling, the device was found to be an excellent tool for Linac commissioning.

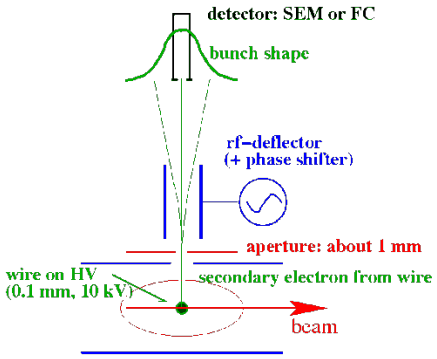


Figure 2: Principle of the BSM.

After optimization of the buncher settings for injection, the injection parameters and rf-power and phase in the demonstrator were varied to check the effect on output current, bunch structure, particle energy and transverse emittance. In this way, the characteristics and design values of the prototype could be verified in very detail. Representative for the numerous measurements, which have been carried out, figure 3 shows a scan of the bunch width as a function of the demonstrator rf-phase. The resolution of the system, basically dependent on the aperture shown in fig. 2, is better than 1°.

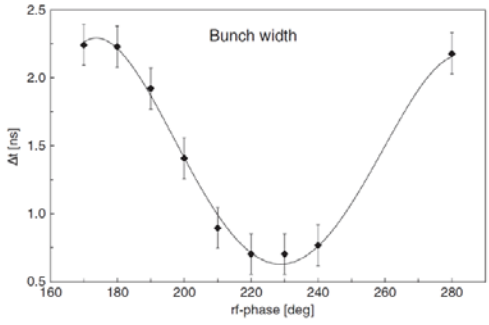


Figure 3: Phase scan of the output bunch length.

References

[1] W. Barth et al. Phys. Rev. Accel. Beams 21, 020102 (2018) ion UNILAC as an injector for FAIR, Nucl. Instrum. Methods Phys. Res., Sect. A 577, 211 (2007)

[2] A. V. Feschenko, Technique and instrumentation for bunch shape measurements, in Proc.RuPAC’12 Conference, St-Petersburg, Russia (2012), pp. 181–185

#T.Sieber@gsi.de

RADHARD: a program for radiation damage to materials for FAIR

A. Evdokimov[1], *R. Lang*[1], *T. Radon*[1]

[1]GSI, Darmstadt, Germany

Introduction

FAIR will consists of at least 20 radiation protection areas at the accelerators and connected beam lines where a lot of different complex devices will be exposed to high neutron radiation fields in quasi-continuous operation. It is crucial to maintain a stable operation of all devices and mechanisms in in these areas. To achieve this one key aspect is to take into account the radiation hardness of materials. The radiation hardness of a material depends on its type; e.g. metals in comparison to most polymers can stay longer under irradiation until certain damage occurs. More details can be found in the work previously done at GSI [1].

Description

In order to obtain an estimate of the lifetime of materials located in high radiation field areas of FAIR the RADHARD program was created at GSI. The program uses a collection of data which has been taken mostly from CERN radiation damage test data [2].

This program is written in Python programming language [3] and a remote access to the program is available under Linux at GSI (/u/aevdokim/codes/radhard), access under Windows is still under development.

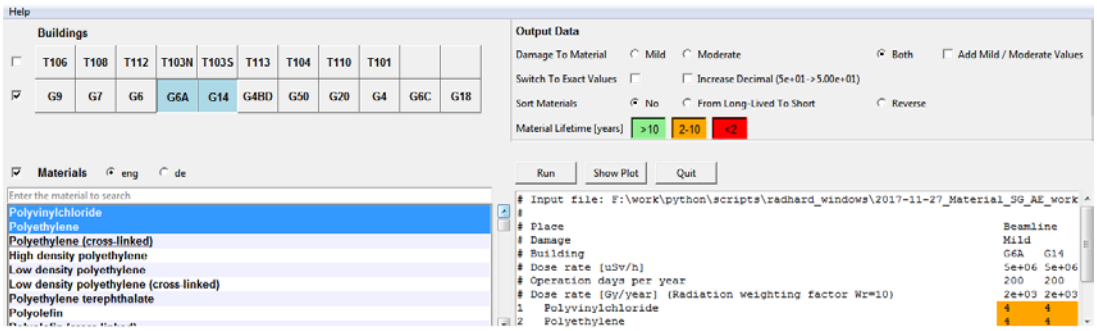


Figure 1: Example of the graphical user interface of the program. On the left side is input; on the right side are toolbar (up) and output data (down).

Purpose of the program was to have a convenient and user-friendly possibility to get a quick result on the lower limit of the expected lifetime of materials of interest for selected buildings for a broad spectrum of users at GSI and FAIR, e.g. architects, planners, scientists etc.

The program includes data on radiation damage for more than 70 materials (polymers, metals, ceramics etc.).

Features

The user interface of the program is divided into three sections: input, output, toolbar (see Fig. 1).

The Input section includes a selection of FAIR buildings and materials, the possibility of switching between English and German names for materials, and a search for materials by pattern. The Output section includes a window for displaying data.

The Toolbar section allows to fine-tune the output with the following options: sort materials by their lifetime, highlighting lifetime of selected materials and show their exact values, show result of Mild/Moderate/Both damage to materials and add the column with their values respectively.

The program allows the user to automatically create a bar plot with data on relative radiation effects for selected materials (see Fig. 2).

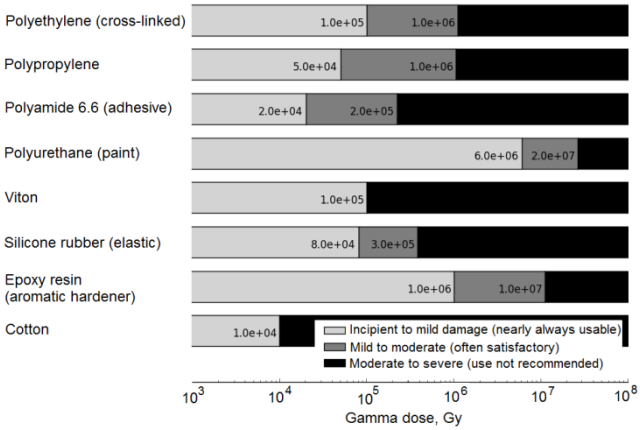


Figure 2: Plot example of general relative radiation effects for selected materials. The scale shows how much radiation in Gy each material can resist keeping its functionality.

Development

The work to improve the program continues, and in future some other features as well as new materials will be included as follows: group materials by class (thermoplastic and thermosetting polymers, natural polymers, metals and alloys, ceramics, oils etc.), add flexibility to work with input and output data. We encourage all GSI and FAIR Users to submit requests for new materials to evaluate and include into this Database.

References

[1] A. Belousov, G. Fehrenbacher, R. Lang, T. Radon, GSI Scientific Report 2014 (2015), 388-389 p

[2] P. Beynel, P. Maier and H. Schönbacher, CERN (1982), 82–10, DOI: 10.5170/CERN-1982-010

[3] Python Software Foundation. Python Language Reference, version 3.6, http://www.python.org.

 DOI:10.15120/GR-2018-1

The SIS100 laser cooling facility*

D. Winters[1], T. Beck[2], G. Birkl[‡2], O. Boine-Frankenheim[‡1,2], M. Bussmann[3], L. Eidam[2], V. Hannen[‡4], D. Kiefer[2], S. Klammes[1,2], Th. Kühl[1,5], M. Löser[3,7], X. Ma[§6], U. Schramm[‡3,7], M. Siebold[3], Th. Stöhlker[1,5,8], J. Ullmann[4], Th. Walther[‡2], W. Wen[6], P. Spiller[1]

[1]GSI Helmholtzzentrum, Darmstadt, Germany; [2]Technical University Darmstadt, Germany; [3]Helmholtz-Zentrum Dresden-Rossendorf, Germany; [4]Münster University, Germany; [5]Helmholtz Institute Jena, Germany; [6]Institute of Modern Physics-CAS, Lanzhou, China; [7]Technical University Dresden, Germany; [8]Jena University, Germany

The project group 'SIS100 laser cooling' is setting up a laser cooling facility at the FAIR heavy-ion synchrotron SIS100, being supported by POFIII ARD 'Matter and Technologies'. With the aid of this facility, intense relativistic heavy-ion beams will be laser-cooled to lowest temperatures [1,2]. The project group consists of scientists from GSI and the collaborating partner universities and research centers in Dresden-Rossendorf, Darmstadt, Jena, Münster, and Lanzhou (China).

The laser systems are being developed by the HZDR/TU-Dresden and the TU-Darmstadt, with strong support from the BMBF. These laser systems can be operated at 257 nm or 514 nm, and produce about 100 mW of coherent radiation. The TU-Darmstadt will provide a fast scanning cw-laser system [3], and a pulsed laser system with long (up to 1 ns) pulses and a high repetition rate (up to 1.5 MHz) [4]. The HZDR will provide a pulsed laser system with short pulses (~ps) and a high repetition rate up to 1 MHz [5]. The Münster group will provide an XUV/X-ray detector for the SIS100, again supported by the BMBF [6]. (*Note:* These groups have all applied for a continuation of their funding for the next BMBF period (2018-2021), which shows how committed they are.)



Figure 1: Collage showing a selection of the components purchased in 2017. Upper row: vacuum chamber `mirror box´, rotary fore-pump. Lower row: high-precision wavelength meter, multichannel switch (for 4 laser systems).

In 2017, the design for the laser-detector chamber (LDC) has been completed and a company was selected to manufacture this UHV chamber, the bake-out jackets, and the frame. The chamber is a crucial part of the project: it will be used to couple the laser light into the SIS100 accelerator, and to couple out the fluorescence emitted from the laser-excited ions. The chamber is currently being built by a vacuum company and should be ready in 2018. Also, the design for the first `mirror box´ (vacuum chamber), which an important component of the future SIS100 laser beam line, has been completed. A vacuum company could be found to build and deliver the chamber still in 2017.

In order to be able to test these vacuum chambers (and components inside them), but also for operation later on, vacuum pumps (rotary pump, turbo pump, NEG pump) have been ordered. These pumps are especially quiet and almost without vibrations, so as to prevent for mechanical and acoustical influences on the laser beamline. Since the laser light has to travel via several mirrors over a long distance, small variations in the positions of these mirrors could already lead to noticeable deviations of the laser beam position inside the SIS100 accelerator and modify the overlap between laser and ion beam somewhat.

Since we will have to combine different laser systems at the same time for our experiments at the SIS100, and require very reliable knowledge of the exact wavelengths of these laser systems, a high-precision wavelength meter with a 4-channel switch box is now available for tests and experiments. This way, all laser wavelengths can be measured and monitored as required.

During the year, we have also performed necessary tests of the optical components that are available for the SIS100 laser beam line, such as mirror holders and piezo-actuators. These tests will continue in 2018.

Finally, it seems that it might be possible to perform a laser cooling experiment at the CSRe of the IMP in Lanzhou China in 2018. We are very much looking forward to this important and exciting event. (*Note:* Since the CSRe is rather similar to the ESR, it is very well suited for complementary tests and new experiments.)

References

[1] D. Winters et al., Phys. Scr. **T166** (2015) 014048.
[2] L. Eidam et al., Nucl. Instr. Meth. Phys. Res. A **887** (2018) 102.
[3] T. Beck et al., Opt. Lett. **41** (18) (2016) 4186.
[4] D. Kiefer et al., GSI scientific report 2017.
[5] M. Siebold et al., Opt. Expr. **20** (2012) 21992.
[6] J. Ullmann et al., GSI scientific report 2017.
[7] D. Winters et al., GSI scientific report 2016.

Experiment beamline: none
Experiment collaboration: APPA-SPARC
Experiment proposal: none
Accelerator infrastructure: SIS100
PSP codes: 2.8.10
Grants: *Work supported by HGF POFIII ARD-ST2. ‡Work supported by BMBF. §Work supported by BMBF-WTZ.
Strategic university co-operation with: Darmstadt

Current status of the phase calibration of synchrotron RF reference signals

A. Andreev[1], D. Lens[2], S. Schäfer[2], B. Zipfel[2], D. Domont-Yankulova[1], and H. Klingbeil[1,2]

[1]TEMF, TU Darmstadt, Germany; [2]GSI, Darmstadt, Germany

Introduction

For the successful operation of the FAIR complex it is important to maintain the desired accuracy of the accelerating voltage [1]. The deviation of the phase of the reference signals must not exceed ±1 degree in the whole frequency range from 100 kHz to 6 MHz and a maximum difference of ±3 degrees for the complete system is acceptable. Although closed cavity field control loops stabilize amplitude and phase of the generated RF gap voltages, imperfections of components lead to errors in the signal transmission. Also errors in the detection of the gap voltage affect the accuracy. As a result the actual accelerating voltage interacting with the beam can be different from the target values provided by the Central Control System (CCS). This could compromise reaching the desired beam quality if the above mentioned accuracy requirements are not met. In order to overcome the undesirable errors countermeasures to calibrate synchrotron RF signals are performed.

Group DDS calibration

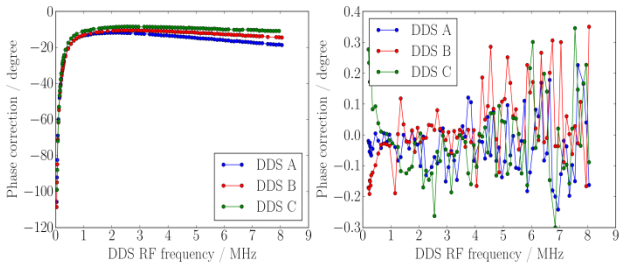


Figure 1: Example for calibration curves of 3 DDS modules before calibration (left) and after calibration (right).

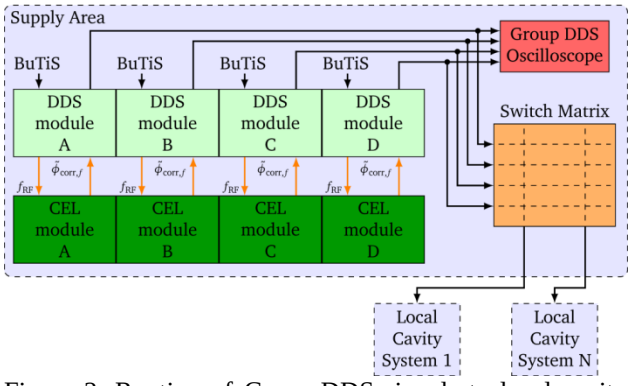


Figure 2: Routing of Group-DDS signals to local cavity systems.

An automated Group DDS phase calibration procedure with respect to the absolute phases of DDS modules defined with BuTiS is described in [2]. Figure 1 shows an example for the calibration curves of modules before and after calibration. It can be seen that the remaining phase response of Group DDS modules is far below 1 degree for the whole frequency range (please note the different scales in the diagrams on the left and on the right), which is within the margins of the phase accuracy requirements. This allows us to conclude that in a supply area it is possible to achieve an in-phase generation of reference RF signals which can later be used for local cavity RF systems (Fig. 2). This also includes the in-phase generation of different harmonics of the revolution frequency, which is needed for example for dual-harmonic operation and bunch merging.

The long term stability of the calibration is important to minimize interruptions needed for accelerator maintenance. First results show that changes of the phase difference between the modules after 3 weeks are within ±1 degree.

Optimisation of parameters

The DDS RF signals' phase accuracy estimation depends on measurement parameters. In order to decrease the deviation of estimated values and increase the precision of the calibration it is important to perform optimisations.

Among the parameters to be optimised are the number of samples per each sinewave and the number of signal periods which are then used to perform a sine wave fit algorithm [3]. Figure 3 shows the first preliminary results for the required number of samples. The next step is the detailed analysis of further parameters and finding their optimal values.

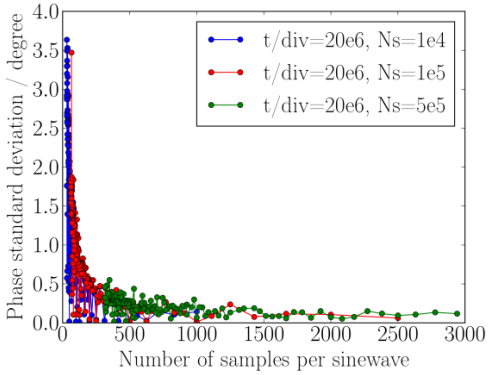


Figure 3: Example for the dependence of the estimated phases' standard deviation on the number of samples per sinewave.

References

[1] H. Klingbeil et al., “New digital low-level rf system for heavy-ion synchrotrons”, Phys. Rev. ST Accel. Beams, vol. 14, p. 102802, 2011.

[2] A. Andreev, H. Klingbeil and D. Lens, “Phase calibration of synchrotron RF signals”, IPAC’17, Copenhagen, May 2017, p. 3945.

[3] P. Händel, “Properties of the IEEE-STD-1057 four-parameter sine wave fit algorithm”, IEEE Trans. on Instr. and Meas., vol. 49, no. 6, pp. 1189-1193, 2000.

 DOI:10.15120/GR-2018-1

Fluorescence detector concept for laser cooling at the SIS100

J. Ullmann[1], V. Hannen[1], D. Winters[2], C. Weinheimer[1]
[1] Westfälische Wilhelms-Universität Münster, Institut für Kernphysik, Münster, Germany
[2]GSI Helmholtzzentrum für Schwerionenforschung Darmstadt, Germany

The acceleration of high intensity ion beams up to the mass range of uranium to highest energies will be possile in the future heavy ion synchrotron SIS100. At Lorentz factors of up to $\gamma = 12$, ion cooling becomes a challenging task and the only feasible option here is laser cooling [1,2]. It requires a fast optical transition in a wavelength region which is accessible to a laser system.

The feasibility of this technique has been demonstrated at lower velocities on C^{3+} ions at the ESR in past beam times [3]. At the high ion velocities expected at SIS100, the energies of the fine structure transition in, e.g., Li-like ions, are blue-shifted by the Doppler effect and allow the application of state-of-the-art UV-laser systems in an anti-collinear setup.

The required counterforce to reduce the momentum spread can not be applied by a co-propagating laser beam, since a laser system producing photon energies in the soft x-ray region is not available yet. The counterforce is therefore exerted by the bucket potential of the bunched ion beam.

To overlap ion and laser beam at one of the six straight sections of the synchrotron, the ion beam is tilted by 2.3 mrad relative to the design orbit and two sets of horizontal and vertical scrapers are used to align both beams. This is schematically shown in Fig. 1.

When the laser frequency is in resonance with the fine structure transition, fluorescence light is emitted isotropically in the ions' rest frame. In the laboratory frame, the emission is transformed by the Lorentz boost to a strongly forward directed cone. Since the cooling takes place at a distance between 12 and 24 meters away from the detector chamber, the angle between ion propagation and detected fluorescence is in the range of 4 to 9 mrad. Here, photon energies in the XUV- and soft x-ray region are expected. A suitable detector requires a sufficient quantum efficiency in this energy range and a high temporal resolution to gain insight to the dynamics of the ion bunch during the cooling process. The spectral resolution of the fluorescence would be even more interesting, since it would allow for spectroscopic measurements of transitions. For many of the medium-heavy Li-like ions, measurements of their fine structure transitions could be performed for the first time here.

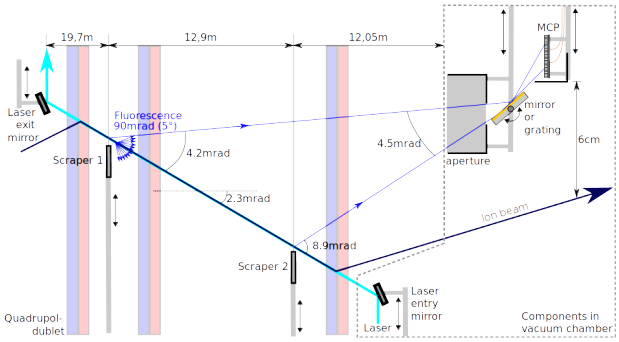


Figure 1: Schematic overview of the proposed detection setup. Ion beam (dark blue) and laser beam (light blue) are overlapped by the use of two scrapers. The fluorescence light (blue arrows) enters the detector chamber at a small angle of few mrad.

The proposed detection setup is schematically shown in Fig. 1 and will be developed in two stages. In the first stage, the timing and the sensitivity of the detector will be optimized. Therefore, a multichannel plate (MCP) detector [4] with a high temporal resolution will be installed. Typical quantum efficiencies of 10% are expected. Estimations of the fluorescence detection rate by a Geant4-simulation are currently ongoing. Enhancements of the efficiency are possible by using a CsI-coated front MCP. An aperture in front of the MCP is used to reduce background light or particles. All parts will be mounted on linear feedthroughs and can be placed at a safe distance from the ion beam during injection and acceleration. Prototypes will be built and tested at Insitut für Kernphysik in Münster.

As a preparation for the second stage, a gold mirror at grazing incidence will be installed on a rotational feedthrough to test the reflection of the fluorescence. Subsequently, the gold mirror will be replaced by a gold coated, laminar flat-field reflection grating with a line density of 2400 lines/mm to diffract the fluorescence light onto the MCP. The planned geometry corresponds to commercially available spectrometers for photon energies of up to 2 keV. Here, a resolving power of 500 is achieved. To detect the spectrum, the MCP will be equipped with a delay-line anode to achieve a spatially resolved detection [4]. An MCP detector with delay-line anode available from the former WITCH experiment at ISOLDE is currently used to equip a new detector test stand in Münster. The data acquisition has been set up and first tests of the read out electronics have been performed.

References

[1] L. Eidam et al., NIM A 887, 102 (2018)
[2] D. Winters et al., this report
[3] D. Winters et al., Phys. Scr. T166, 014048 (2015)
[4] A. Czasch et al., NIM A 580, 1066 (2007)

Experiment beamline: SIS100
Experiment collaboration: APPA-SPARC
Experiment proposal: none
Accelerator infrastructure: SIS100
PSP codes: none
Grants: BMBF 05P15PMFAA
Strategic university co-operation with: none

Tuning rules for the digital filters of the SIS 100 longitudinal feedback system

B. Reichardt[1], J. Adamy[1], D.E.M. Lens[3], D. Domont-Yankulova[1,2], H. Klingbeil[2,3]

[1]TU Darmstadt RMR, Germany; [2]TU Darmstadt TEMF, Germany; [3]GSI, Darmstadt, Germany

Damping of longitudinal coherent bunched-beam oscillations is needed in SIS100 to stabilize the beam, prevent emittance growth and keep beam loss low during acceleration. An FIR (finite impulse response) filter approach with 3 taps, cf. [1], which has already been successfully used at GSI in several machine experiments for beam-phase control in a longitudinal feedback system has further been investigated. The dissertations [2] and [3] deal with an analytical way of how to apply the tuning rules for this approach for stationary, single and dualharmonic operation. In last year's work, extensive tracking simulations were performed to investigate the performance of the feedback system in terms of emittance-growth and settling-time numerically regarding the two tunable parameters of the FIR-filter.

Feedback system

The feedback system can be separated into two parts. One is a bandpass filter, implemented as a symmetric, biasfree bandpass filter. The bandpass frequency, which scales with the linear synchrotron frequency can be detuned by the frequency modificator χ, which is one of the tunable parameters.

The bandpass filtered bunch-phase is integrated and multiplied with a gain factor, to obtain a phase-shift in the gap voltage. The gain-factor also scales with the linear synchrotron frequency. It can further be modified by the gain factor modificator k.

Simulation settings

The tracking simulations have been performed to get a tuning rule for the feedback system, especially for the case of different bunch lengths, synchrotron frequencies and particle energies. Therefore typical synchrotron frequencies for SIS18 (below 2 kHz) and SIS100 (below 1.5 kHz), as well as bunch lengths reaching from 115° to 200° have been tested. The bunch length is the smallest phase range within a bucket, which contains 85% of its particles.

For testing the performance of the filter, the phase of the gap voltage was shifted by 10° to induce a longitudinal dipole oscillation.

Results

In stationary operation constant tuning rules are sufficient. For single harmonic operation the frequency modification factor χ is between 0.95 and 1.0, the gain factor modificator at 0.25. This is comparable to the results for linear buckets in [2].

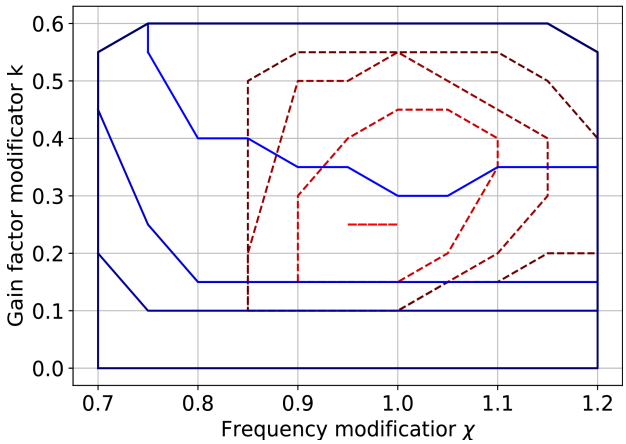


Figure 1: Parameter scan for single-harmonic operation with a bunch-length of 115°. In dashed red are the areas for 2, 3, 4 and 5 oscillations (light to dark) settling time. In solid blue are the areas for 10%, 30%, 50% and 100% (light to dark) relative emittance-growth compared to system without feedback.

For dual-harmonic operation the frequency modification factor is at 0.8 and the gain factor between 0.2 and 0.25. For both parameters, this is about 80% of the parameters used in machine experiments in [3].

In both cases the system is tuned to fast settling times. Notable RMS-emittance-growth from longitudinal dipole oscillations only occurs when the amplitude reaches more than 3 degrees. High damping rates should prevent such critical states.

Outlook

As constant tuning rules for single- and dual-harmonic stationary operation for a large variety of longitudinal beam parameters are sufficient to obtain strong damping rates and decreased RMS-emittance-growth from longitudinal dipole oscillations, it has to be studied whether this also holds on acceleration ramps, due to the strong deformations of the separatrix.

References

[1] H. Klingbeil et al., "A digital beam-phase control system for heavy-ion synchrotrons", IEEE Transactions on Nuclear Science Vol. 54, No. 6, Dec 2007

[2] D. Lens, "Modeling and Control of Longitudinal Single-Bunch Oscillations in Heavy-Ion Synchrotrons", VDI Fortschrittsberichte Vol. 8, No.1209, Düsseldorf, 2012

[3] J. Grieser, “Beam Phase Feedback in a Heavy-Ion Synchrotron with Dual-Harmonic Cavity System”, Dissertation, Darmstadt, 2015

 DOI:10.15120/GR-2018-1

FLUKA/ANSYS study of the APPA beam bump for the BIO-MAT experiment

S. Damjanovic[1], M. Schwickert[1], and V. Venturi[1]

[1]GSI, Darmstadt, Germany

Four beam dumps are planned for the experimental APPA cave, one of which, XBM2SD, will be used for the BIO-MAT experiment (see Figure 1). Given a wide range of different beam parameters (kinetic energies, ion species, time structure) which will be provided for this experiment, multiple FLUKA-ANSYS simulations had to be performed in order to optimize the design of the inner

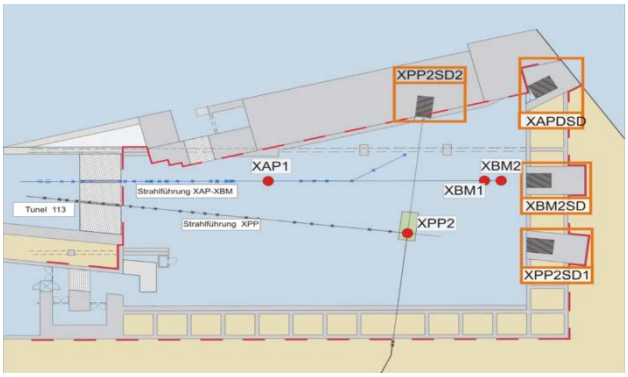


Figure 1: Position of the four beam dumps planned in the experimental APPA cave.

core of the dump as to the dimensions and materials for a safe operation. Another important goal of this study was to find out whether cooling would be required, and if so to propose a cooling design scheme. The starting proposal for the dump core was a composition of a 3m long iron with a 20cm long graphite part at the entrance phase to absorb the Bragg peak region associated with ion beams.

The beams considered for the dump optimization as well as their time structures are summarized in Table 1.

The analysis is based on the following steps. In the first the thermal load from the beam impact is calculated by FLUKA in terms of energy deposition. This is then used as an input into a thermo-mechanical analysis with ANSYS to calculate maximum temperatures and maximum thermal stresses reached by irradiation. After focusing the beam onto the target with a beam radius of 2σx/y=10 mm, the transverse size of the beam at the position of the XBM2SD dump is 2σx/y=30mm.

Table 1: beam parameters considered for the study

Experiment	Particle type	Energy [GeV/n]	Beam Intensity	Time structure
BIO	proton	10	5×1010 /s	Slow extraction
BIO	uranium	10	108 /s	Slow extraction
BIO	carbon	10	108 /s	Slow extraction
BIO	iron	10	108 /s	Slow extraction
MAT	uranium	2	109 /s	Slow extraction
MAT	uranium	0.7	5×1010 /pulse	Fast extraction

For the material risk assessment a thermal-structural analysis was performed. For the highest energy ion beams, the maximum temperatures reached were 29.4 °C for the higher energy uranium beam within the iron part (see Figure 2), and 23 °C for the proton beam within the graphite part, which is about 10 and 100 times lower than the maximum service temperature of iron (230 °C) and graphite (2600 °C), respectively.

The maximum values of the Von-Mises stress were found to be 4.2 MPa within iron part of the dump (see Figure 3) and 1.2 MPa within the graphite part of the dump for the highest energy uranium beam. All values are found to be well below the maximum tensile strengths which are 250 MPa for iron and 30 MPa for graphite of the type R4550.

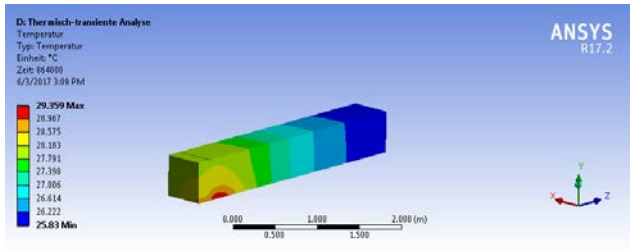


Figure 2: Temperature distribution in steady-state case for a uranium beam at E_k=10 GeV/n

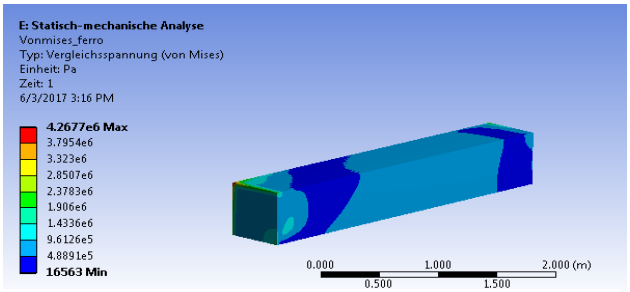


Figure 3: Von-Mises stress distributions for the 3m long iron part of the dump for U beam@E_k=10 GeV/n

Conclusions

The studies presented in this Report indicate that the proposed configuration for the XBM2SD dumps would provide safe operation during the planned running time of the BIO-MAT experiments without any need for active cooling.

FLUKA/ANSYS study of the beam dump for the plasma physics experiment

S. Damjanovic[1], *M. Schwickert*[1], *and V. Venturi*[1]

[1]GSI, Darmstadt, Germany

This report summarizes the concept study for the beam dump XPP2SD1, part of the experimental APPA cave and planned to be used for the Plasma-Physics Experiments. The goal of this study was to optimize the design of the inner cores of the dump as to the dimensions and material, based on coupled FLUKA-ANSYS simulations, which would assure a safe operation. Another important goal of the study was to find out whether cooling would be required. The complete geometry of the APPA cave with the surrounding shielding had already been modelled for the reasons of previous studies related to the optimization of the plasma physics target chamber.

The starting geometry of the XPP2SD1 beam dump was the same as used for the BIO-MAT experiment, i.e.

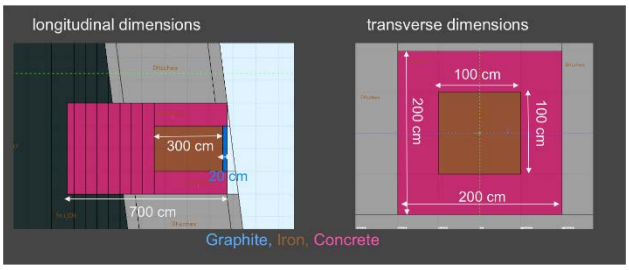


Figure 1: Geometry of the XPP2SD1 beam dump. Side view (left) and cut through the dump (right).

consisting of a 3m long iron core with a 20cm long graphite part at the entrance phase to absorb the Bragg peak region associated with uranium beams (see Figure 1).

The studies are based on an uranium beam intensity of 3×1011 ions/spill at Ek=1 and 2 GeV/n, and on a proton beam of intensity 2.5×1013 p/spill at Ek=5 GeV. A realistic irradiation profile of one pulse every 3 minutes for 10 days is assumed for the analysis. After a strong focusing of the beam onto the target, the beam is very wide at the entrance of the XPP2SD1 dump positioned about 12 m downstream of the target. The transverse beam size at the entrance to the dump is indicated in Table 1.

Beam energy	Beam radius 2σ horizontal size	Beam radius 2σ vertical size
U@2 GeV/n	314 mm	55 mm
U@1 GeV/n	218 mm	126 mm
p@5 GeV	320 mm	320 mm

The analysis steps are the same as used for the studies of the BIO-MAT beam dump. In the first the thermal load from the beam impact is calculated by FLUKA in terms of energy deposition. This is then used as an input into a thermo-mechanical analysis with ANSYS to calculate maximum temperatures and maximum thermal stresses reached by irradiation. The resulting distribution of energydeposition for one pulse of a uranium beam at 2 GeV/n, calculated with FLUKA, is shown in Figure 2 separately for the graphite and iron parts of the inner core of the beam dump.

After considering all three beam configurations, a uranium beam at Ek=2 GeV/n is shown to be the worst-case

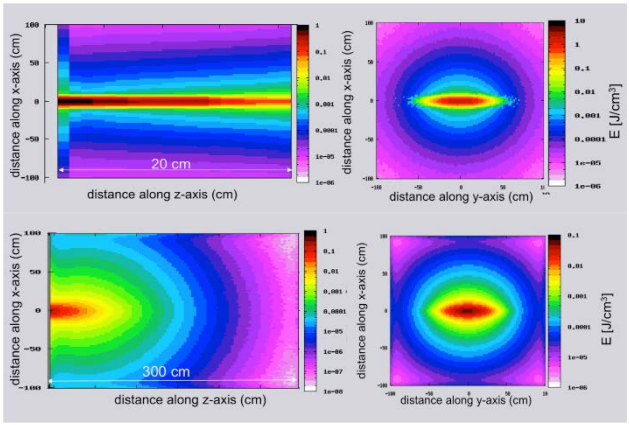


Figure 2: Edep within the core of the beam dump for the C- (upper) and the Fe part (lower) for U@2 GeV/n

scenario. The maximum temperature reached by imposing an average power after 10 days is only 24 ºC on the graphite part. If adding a pulse to the steady state condition, the max T will reach only 27 ºC, far below the maximum service temperature of 2600 ºC for graphite.

The maximum stress reached in each of the pulses is 9 Pa in tension and 0.16 MPa in compression as indicated in

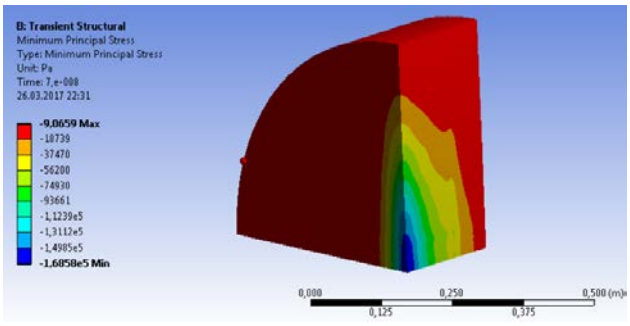


Figure 3: Stress in compression for each of a single uranium 2 GeV pulse.

Figure 3, far from any risk like rapture or yielding.

Conclusions

These results demonstrate that the present configuration of the beam dump will work in safe conditions even for the worst-case scenario and that no active cooling would be required during the whole planned operation including the other beams.

 DOI:10.15120/GR-2018-1

Exploitation of circulant symmetry in SIS18 orbit response matrix

S. H. Mirza[1, 2], H. Klingbeil[1,2], P. Forck[1], R. Singh[1]

[1]GSI, Darmstadt, Germany; [2]TEMF, TU Darmstadt, Germany

Introduction

A closed orbit feedback (COFB) system is under development for the SIS18 synchrotron [1]. This system consists of beam position monitors, a controller and dipolar magnets (correctors). The corrector strength θ_i of each i^{th} corrector (combined in a vector $\boldsymbol{\Theta}$) can be calculated for the position readings y_j of each j^{th} BPM (combined as a vector **Y**) through the inverse of the orbit response matrix (ORM) as given by

$$\Theta = \boldsymbol{R^{-1}Y}. \quad (1)$$

If **R** is not a square matrix, the pseudo-inverse can be used instead of the inverse.

SVD and its relationship with DFT

Singular value decomposition (SVD) is mostly used for the inversion of the ORM [2]. It decomposes a matrix into a product of three matrices, **U**, **S** and **V** where **U** and **V** are orthonormal matrices while **S** is a diagonal matrix of singular values:

$$\mathbf{R} = \mathbf{USV^T} \quad (2)$$

If the matrix is invertible, the inverse is given as

$$\mathbf{R^{-1}} = \mathbf{VS^{-1}U^T}. \quad (3)$$

SVD also helps to calculate the pseudo-inverse ($\mathbf{R^+}$) of non-invertible matrices by providing the liberty to remove smaller or zero singular values in the **S** matrix and their corresponding column of **U** and **V** matrices before inversion.

Decomposed matrices are inter-related with each other; e.g. a unique phase relationship between the columns of **U** and **V** exists. In case of lattice changes during the acceleration ramp, as executed in SIS18, all three matrices need to be recalculated.

Due to the symmetric placement of BPMs and steerers, the vertical ORM of the SIS18 has a special "circulant symmetry" [3]. A circulant matrix can be diagonalized with the help of the discrete Fourier transform (DFT) of only one row or column. The diagonal matrix consists of the complex Fourier coefficients with the standard Fourier matrix **F** as both right and left orthonormal matrix

$$\mathbf{R} = \mathbf{FHF}^*. \quad (4)$$

The DFT-based decomposition of an ORM gives a physical interpretation of SVD modes and a relationship between the two algorithms has been described in the proceeding of ICALEPCS'2017 [4].

Robustness against missing BPMs

Besides the computational benefits of DFT over SVD, sine/cosine DFT modes help to estimate the orbit position at the location of a malfunctioned BPM reading. The idea of modal decomposition is to decompose a perturbed orbit into discrete modes (either SVD or DFT modes) and the elimination of these modes results in a global correction of the orbit. DFT gives a more physical explanation of these modes in the form of pure sine/cosine Fourier modes. These modes can also be used to reconstruct the perturbed orbit by a general curve fitting method. This idea has been employed in this work in order to predict the orbit position at one or two missing BPM locations by fitting the orbit measured with the help of available BPMs over the dominant DFT modes. The CERN accelerator toolbox MAD-X [5] has been used to demonstrate the orbit correction.

Figure 1 shows the perturbed orbit in red and the corrected orbit (when all BPMs are functional) in magenta colours. The black curve shows the scenario when one BPM is missing and there is a significant residual global orbit in the vicinity of the missing BPM after correction using 11 BPMs and 12 correctors. The green curve represents the corrected orbit when the orbit position at the missing BPM location is predicted by DFT fitting (effectively using 12 BPMs with one BPM reading different from actual by the fitting uncertainty). An overall improved correction (lower residual error) is seen in the vicinity of the missing BPM in this case. The blue curve shows a special scenario for comparison when the orbit position is considered to be cantered (0 mm) at the missing BPM location.

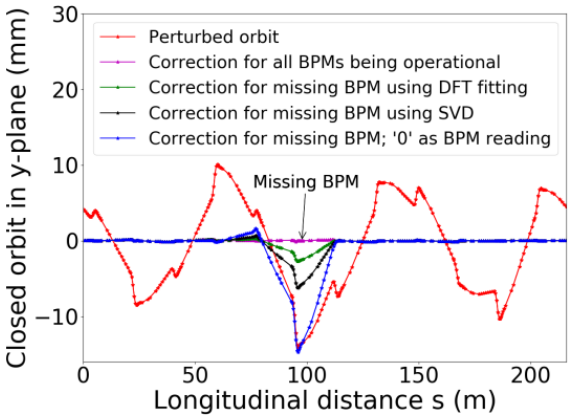


Figure 1: Demonstration of better global orbit correction for missing BPM scenario using estimated orbit position at the missing BPM location.

References

[1] S.H.Mirza, et al. GSI annual report 2017.
[2] Y. Chung *et al.* "Closed orbit correction using SVD of ORM", (Argonne National Laboratory, IL, 1993)
[3] P. J. Davis. "Circulant matrices", Chelsea, 1994.
[4] S.H. Mirza, *et al* Proceedings of ICALEPCS 2017.
[5] http://mad.web.cern.ch/mad/

SIS100 Inspection robot – lane keeping and curved pipes

N. Schweizer[1] and I. Pongrac[2]

[1]TU Darmstadt RMR, Darmstadt, Germany; [2]GSI, Darmstadt, Germany

Current status and steering capability

In previous work we presented a basic robot concept for visual inspection of the SIS100 vacuum system [1,2]. A 3D printed robot prototype was built and it was shown that the robot is able to traverse simple obstacles inside the beamline vacuum system like single steps and gaps. The general robot concept follows a modular design, consisting e.g. of joints between the modules to lift or lower specific parts of the robot. Each module has two driven wheels and all wheels are controlled synchronously. As a result, the robot would only be able to move in a straight direction which has two significant disadvantages.

On the one hand, the robot could leave the center of the beam pipe if initially it is not placed precisely straight or if there are any inaccuracies in the control or manufacturing of the motors. Without steering capabilities the robot would run onto the curved sides of a pipe and would get stuck if the pipe has an elliptical shape, and in cylindrical pipes it could tilt over, which is even worse. On the other hand, the SIS100 is a ring accelerator with curved pipe sections. A robot that moves exclusively straightforward cannot be used here, obviously. Thus, additional joints between the modules must be provided to enable the robot to bend in the horizontal plane.

Description of the new prototype

The problem of steering capabilities and climbing skills can be considered separately. In a first step the joints for vertical movement are neglected. Instead, solely small robot smart actuators are inserted between the modules as it is shown in Fig. 1 for a robot configuration with four modules. The size of these joints is very important because their axles are arranged vertically, and with respect to the dimensions of the SIS100 dipole vacuum chambers the total height of the robot is limited to 5 cm.

According to [3], the velocity of each module must now be controlled separately. To keep the amount of wires manageable, port expanders are placed next to the first and the third joint, respectively. An additional benefit is that only two pins of the microcontroller are needed for an I²C communication with the port expanders instead of 16 to directly control the stepper motors. The servos are interconnected and merely require one control pin. A half duplex asynchronous serial communication enables both write and read instructions. Each servo possesses a unique identification address and can be operated with an angle resolution of 0.29°.

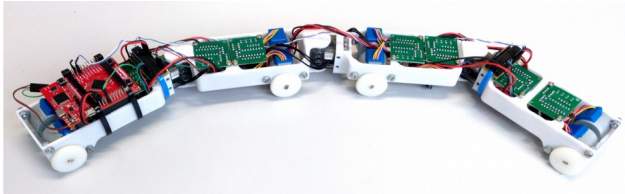


Figure 1: Prototype with four modules and three servos as steering joints.

Further development

Next, the prototype has to be tested and its dynamical parameters must be identified to derive a suitable model which can be used for concurrent simulations and to calculate the steering angles as well as the individual module velocities. With the help of an inertial measurement unit curved pipes or deviations of the robot from the pipe center will be detected and corrected by a dedicated controller.

Currently, a third prototype is under development which combines climbing and steering capabilities in one robot. This is achieved by a series connection of the two different joints between two modules.

Furthermore, the stepper motors will be replaced by robot smart servos, obviating the need for external motor drivers and saving space on the modules, e.g. for essential sensors or batteries. The servos can be set to wheel mode for endless turn. Additionally, the microcontroller board will be substituted with a more sophisticated controller board with smaller dimensions, therefore better fitting into a module.

A major modification will be done for the control concept. To use the same implemented programs as in the robot simulator Gazebo, the robot has to be operated within the Robot Operating System (ROS) framework. For this purpose, the robot will be equipped with a WiFi module to be able to communicate with an external control computer.

References

[1] N. Schweizer and I. Pongrac, IPAC'17, pp. 4528-4530.

[2] N. Schweizer and I. Pongrac, GSI Scientific Report 2016, September 2017.

[3] B. Murugendran et al., IROS'09, pp. 3643-3650.

 DOI:10.15120/GR-2018-1

Commissioning of the beam induced fluorescence monitor for the CERN e-lens

S. Udrea[1], P. Forck[1], M. Ady[2], E. Barrios Diaz[2], O.R. Jones[2], P. Magagnin[2], T. Marriott-Dodington[2], G. Schneider[2], R. Veness[2], A. Salehilashkajani[3], C. Welsch[3], H. Zhang[3]

[1]GSI, Darmstadt, Germany; [2]CERN, Geneva, Switzerland; [3]Cockcroft Institute, Warrington, UK

A hollow electron lens is presently under study as a possible addition to the collimation system for the high luminosity upgrade of the LHC [1], while an electron lens system is also proposed for space charge compensation in the SIS-18 synchrotron for the high intensities at the future FAIR facility. For a precise alignment between the hadron and electron beams a beam diagnostics set-up based on an intersecting gas sheet and the observation of beam-induced fluorescence (BIF) is under development. Its main components are a supersonic gas sheet generator and an intensified camera system. The electron lens will generate a hollow, 5 A, 10 keV electron beam stabilized around the axis of the high energy proton beam by a 4 T solenoidal field. Presently two BIF stations are foreseen, one at each end of the solenoid. There the electron beam is expected to have an outer diameter of ≈10 mm and an inner one of ≈7 mm, while the proton beam will have an rms radius of ≈0.3 mm. The gas sheet is planned to have a width of about 11 mm and a thickness of less than 1 mm. As working gases both N_2 and Ne are considered.

The new BIF monitor set-up

Cross-sections and integration times estimated for both N_2 and Ne [2,3] show that a camera system capable of detecting single photons is required.

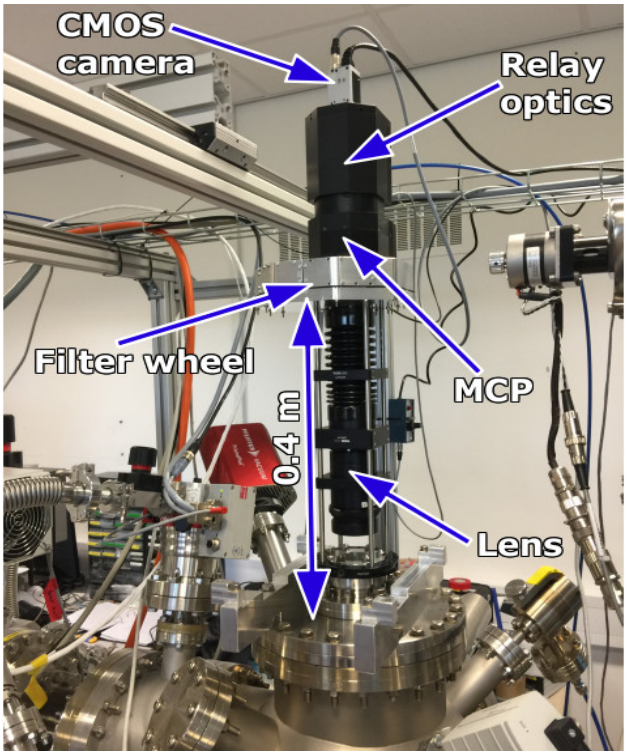


Figure 1: The new BIF set-up as installed at the present gas jet facility at the Cockcroft Institute.

Thus a ProxiKit PKS 2581 TZ-V image intensifier made by ProxiVision and using a Ø 1" double MCP in Chevron configuration has been acquired together with a BASLER acA1920-40gm CMOS camera. The MCP has a UV enhanced S20 photocathode with a quantum efficiency of 5-28% for 260 $< \lambda <$ 650 nm. It can be gated with a minimum gate time of 25 µs and a repetition rate up to 1 kHz. A Schneider Componon 12 35/2.8 lens is used as optical relay to image the phosphor screen on the camera sensor. Several image ratios are possible, e.g. 18:8, 18:11, 25:8, 25:11.

Imaging is achieved with an apochromat lens triplet manufactured by Bernhard Halle Nachfl. GmbH. It is optimised for unit magnification, has an aperture of 40 mm and a focal length of 160 mm. The overall resolution of the optical set-up is 20 lp/mm at magnification 1.2, as assessed with an USAF 1951 test chart. The set-up is shown in Fig. 1.

Results

The measurements at the gas jet facility at the Cockcroft Institute have been performed both with N_2 and Ne as background gases and with a N_2 gas jet. An electron beam generated by a commercial electron gun has been used to excite the gases. Fig. 2 shows the detected interaction between an 30 µA, 5 keV electron beam and an N_2 gas jet.

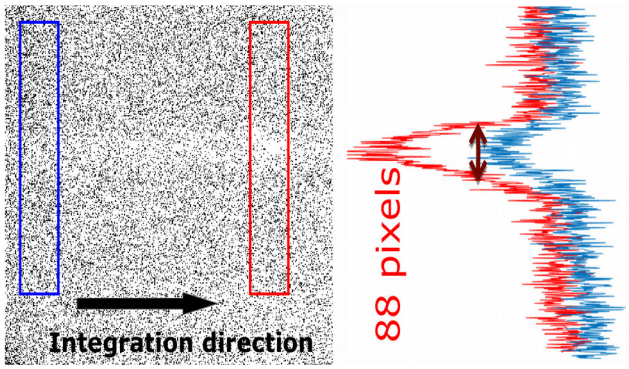


Figure 2: Detected interaction between electron beam and gas jet. The two profiles have been obtained by integration within the marked regions. The increased intensity is due to the gas jet. Images are not to scale.

References

[1] D. Perini and C. Zanoni, arXiv:1702.00234.
[2] S. Udrea et al., IBIC2016, p. 528.
[3] S. Udrea et al., IBIC2017, in press.

Closed orbit feedback system for GSI SIS18 synchrotron

S. H. Mirza[1, 2], A. Bardorfer[3], H. Klingbeil[1, 2], K. Lang, P. Forck[1], P. Kowina[1], R. Singh[1], W. Kaufmann[1]

[1]GSI, Darmstadt, Germany; [2]TEMF, TU Darmstadt, Germany; [3]I-tech Solutions, Slovenia

Introduction

The SIS18 synchrotron will serve as the booster ring for the SIS100 synchrotron of the upcoming FAIR facility to cope with higher beam intensities. One add-on to the existing SIS18 will be a closed orbit feedback (COFB) system for the preservation of the beam quality by stabilizing the beam orbit during the full acceleration cycle. A typical closed orbit feedback system consists of beam position monitors (to measure the orbit), corrector magnets to influence the orbit and a controller built alongside the position monitoring system. The type of controller depends upon many factors e.g. the stability requirements of the closed orbit, temporal responses of the hardware involved in the closed loop, correction bandwidth as well as the requirements on robustness.

The main challenges for the SIS18 COFB are:

1. The thin vacuum chambers (e.g. 0.3 mm for quadrupole chambers) make the beam vulnerable to the power supply ripples as can be seen in figure 1. Also, the fast reaction time during the acceleration ramp (typically lasting 100-500 ms) requires a higher bandwidth of the controller (up to 1 kHz).
2. The change of lattice from triplet to doublet during acceleration ramp resulting in a variable orbit response matrix.
3. Tune movements during the ramp and coherent tune shifts [1].
4. Momentum deviation contributes to the orbit modification during the ramp.

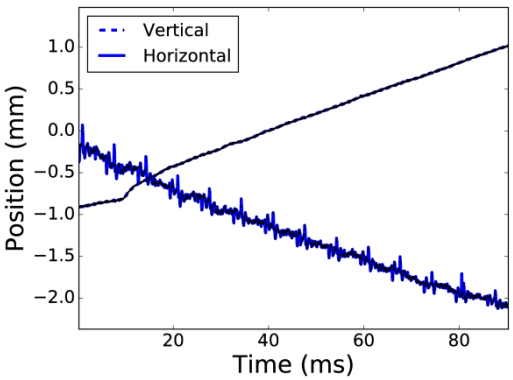


Figure 1: Position in both planes measured at the BPM in section 8 during first 90 ms in the acceleration ramp [2].

Based upon the challenges listed above, a study has been made for the mathematical algorithms used to calculate the corrector strengths in order to find faster and robust algorithms. The details are given in [3].

Hardware preparation

Libera Hadron Platform B is the Slovenian in-kind contribution for the SIS100 COFB which was delivered in January 2018 and is now under test. It will soon be installed at SIS18 and it will also be used as the base-hardware for the SIS18 COFB. It consists of a beam position measurement system based on 16-bit ADCs with a sampling rate of 250 MS/s. A real-time orbit is exchanged between all BPM modules by means of Gigabit data exchange modules (GDX). The GDX modules come inbuilt with a user programmable FPGA where the corrector settings are calculated from the orbit positions grouped from all BPMs at 10 kHz rate. An independent Proportional Integral (PI) controller with an anti-windup protection of each Eigen-mode of the orbit response matrix is also implemented. The magnet settings are then sent to the corrector magnet power supplies via serial interface modules (SER) to the magnet power converters.

The latency of this process is about 30 µs.

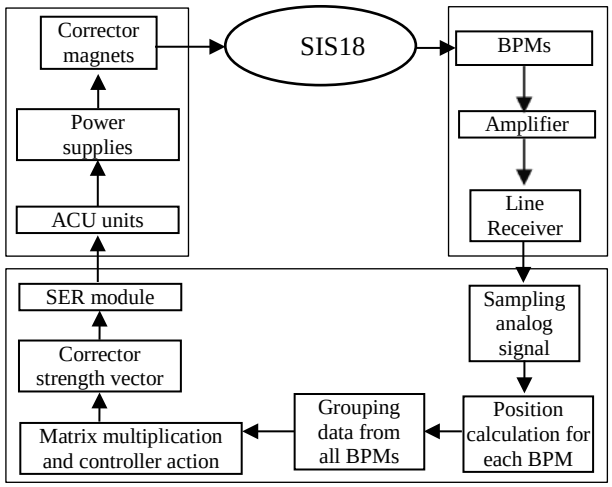


Figure 2: Block diagram of the SIS18 COFB loop

The system identification for the SIS18 COFB loop has been started to estimate the realizable bandwidth. This involves the measurement of transfer functions of corrector magnet power supplies, delay measurements in transmission lines etc. Along with this, the possible model errors and their effects on the closed orbit correction are also being studied through simulations in order to estimate the robustness requirements of the controller. Finally a robust model predictive controller will be implemented on the hardware described above.

References

[1] R. Singh, PhD Thesis, TU Darmstadt
[2] S. H. Mirza, *et al.*, Proceedings of ICALEPCS 2017
[3] S. H. Mirza, *et al.*, Exploitation of circulant symmetry in SIS18 orbit response matrix. In: GSI Scientific Report 2017

 DOI:10.15120/GR-2018-1

Beamloading effects and their influence on cavity detuning in multi-cavity operation in SIS100

D.Mihailescu-Stoica[1], J. Adamy[1], D. Domont-Yankulova[1,2,3], H. Klingbeil[2,3] and D. Lens[3]

[1]TU Darmstadt RMR, Darmstadt, Germany; [2]TU Darmstadt TEMF, Darmstadt, Germany; [3]GSI, Darmstadt, Germany

One possibility to reduce the beam impedance in SIS100 is to detune those cavities that are temporarily unused. Beamloading effects during this detuning are still an open topic. Especially the influence of empty buckets as arising in SIS100 scenarios has to be clarified. We show that the resulting side bands in the beam current limit the degrees of freedom for the impedance reduction strategies.

Critical points during the ramp

Previous results have demonstrated that empty buckets have only a small impact on the beam quality, if only one sum cavity is considered [1]. However, the planned SIS100 heavy ion synchrotron will possess 14 ferrite cavities (20 in the final configuration). Especially during injection and at flat top not all cavities will be active, e.g. during the planned $^{238}U^{28+}$ extreme cycle 18 cavities will be in idle mode during injection and are going to be switched on successively. Up to now the effect of the beam current (including empty buckets) on the induced gap voltage in these idle cavities has not been rigorously investigated. Especially it is an open question if the impedance reduction procedures from SIS18 can be applied unaltered while guaranteeing the desired beam quality.

One of the main approaches besides gap switches is the detuning of the idle cavities to some parking frequencies which are sufficiently separated from the exogenous beam loading disturbance. Anticipating that a single bunch may be sufficiently modelled by a Gaussian distribution during regular operation the corresponding Fourier transform of the beam current is:

$$I_B^{SB}(\omega) = \hat{I}_B \sigma \sqrt{2\pi} e^{\frac{-(\omega\sigma)^2}{2}}$$

The frequency components of the circulating bunch train can be obtained by sampling with a Dirac comb with the frequency $1/T_R$, with $T_R$being the period of revolution. The result is [2]

$$I_B(\omega) = \left(I_B^{SB}(\omega) \sum_{k=1}^{h} \epsilon_k e^{-j\omega k T_{RF}} \right) \sum_{k=-\infty}^{\infty} \delta(\omega - k\omega_R)$$

with σ being the variance of the normal distribution of the particles inside the bucket, h denotes the harmonic number and ϵ_k is parameter equal to 1 or 0 depending on whether the k-th bucket is filled or empty. Figure 1 shows the resulting Fourier coefficients in the cases that eight and ten out of ten buckets are filled with bunches. While in the case that all buckets are filled, only the harmonics appear, the existence of empty buckets leads to considerable sidebands. Consequently, the choice of suitable parking frequencies for the idle cavities is restricted due to the existence of these parasitic components.

Figure 1 shows that for the choice of the resonance frequency of

$$\omega_n = (1/2 + n)\omega_{RF}, \qquad n \in \mathbb{N}_0,$$

the amplitudes of the Fourier coefficients are zero. These frequencies represent natural candidates for detuning of the cavities via the resonance control loop. Due to symmetry, this result also holds during injection, when two buckets are perpetually injected in the synchrotron.

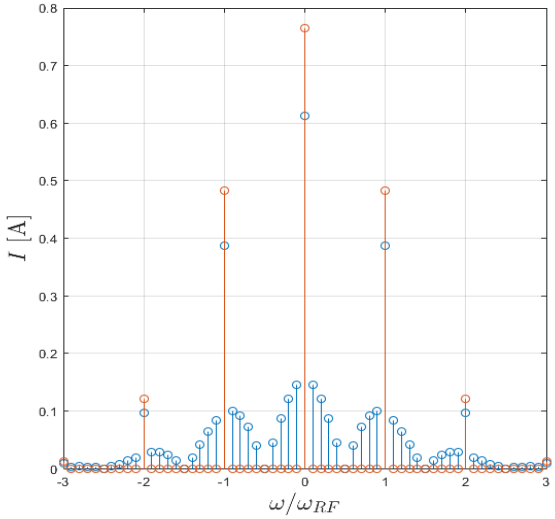


Figure 1: Fourier coefficients of the beam with eight out of ten filled buckets (blue) and Fourier coefficients of the beam with ten out of ten filled buckets (red).

Outlook

For the operation of the SIS100 accelerator with up to 20 ferrite cavities additional investigations are indispensable. Due to the existence of empty buckets, previous impedance reduction strategies from the predecessor SIS18 cannot be directly applied to SIS100. In the case that the cavities will be detuned, extensive simulations will be needed to specify the requirements on the transient detuning dynamics. The assumption underlying this analysis is the Gauss distribution of the particles in the beam. Especially during slow extraction this assumption is not justified. Thus, this case has to be treated separately towards clarifying the question, if impedance reduction via detuning alone suffices to guarantee successful operation.

References

[1] D. Mihailescu-Stoica, J. Adamy, D. Domont-Yankulova, H. Klingbeil and D. Lens, “Behaviour of the planned RF feedback loops under beam loading during a reference SIS100 Cycle”, GSI Scientific Report 2016

[2] D. Mihailescu-Stoica, D. Domont-Yankulova, D. Lens and H. Klingbeil, “On the impact of empty buckets on the ferrite cavity control loop dynamics in high intensity hadron synchrotrons”, IPAC’17, Copenhagen, May 2017.

Signal processing hardware for single-bunch manipulation*

M. Hardieck[†3] *, D. Lens*[‡1] *, K. Groß*[2] *, H. Klingbeil*[1,2] *, M. Kumm*[3] *, and P. Zipf*[3]

[1] GSI; [2] TU Darmstadt, TEMF; [3] University of Kassel, Digital Technology Group

Overview of the System

The bunch-by-bunch longitudinal feedback planned for SIS100 is a broad-band feedback system (BBFB) that will help to stabilize the beam, keeping longitudinal emittance blow-up low and minimizing beam losses [1]. The most components of the system are mainly based on hardware and software components that have already been successfully tested in several machine experiments at SIS18, e.g., [2, 3]. However, new components have to be developed such as a bunch signal de-multiplexer and multiplexer (MUX). The progress on the development of the digital MUX and an overview of its properties is reported in the following.

Multiplexer Prototype

The BBFB system separates the beam current into 10 channels. For each channel (each represents a single bunch) an analog preprocessing unit and a DSP System calculates phase and amplitude correction values and converts them into inphase and quadrature components (I/Q). These signals are used by the MUX to modulate the RF signal for the kicker cavities, which allows individual manipulation for each bunch. [4]

Currently, a system prototype is under test in a laboratory environment at GSI. An example MUX output for harmonic number h=4 is shown in Figure 1. The signals in the upper half are based on the beam (C1 ≙ h=1, C2 ≙ h=4). The lower signal (C3) is the output generated by the MUX. The output is synchronized with the RF signal (h=4) and modulates different outputs for each bunch. The first bunch is set to zero. The second one is not modulated. The third has triple amplitude and the last has twice the amplitude and a phase shift of -90°. The bunch numbering starts every rising edge of the h=1 sine signal (C1).

System Specifications

In Table 1, the primary parameters of the current implementation are shown. The total system latency is the time difference from the RF (sine) input signal which corresponds to the bunch frequency and the analog output of the system. The correction value consist of an I-part and a Q-part. Finally, the whole output signal can be scaled with a relative amplitude. The output signal is generated by a digital to analog converter (DAC) which has 14 bit resolution. It is planned to adapt the design to a newer hardware platform. This would allow a higher clock frequency which leads to smaller bunch transition jitter and less latency.

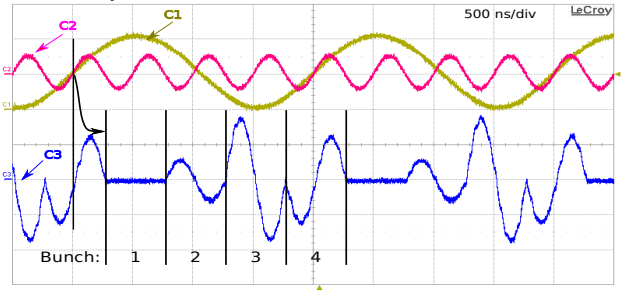


Figure 1: Example MUX output for h=4 (h=1 is 500 kHz)

Table 1: System properties

Parameter	Value
Sampling Frequency	80 MHz
Total System Latency	250 ns
ADC/DAC contribution	112.5 ns
Computation contribution	137.5 ns
Bunch Transition Jitter	25 ns
Q-Range	-3 to +3
Q-Resolution	2^{-13}
I-Range	-3 to +3
I-Resolution	2^{-13}
Relative Amplitude Range	0 to 255
Relative Amplitude Resolution	2^{-24}
Output Signal Resolution	14 bit
Max RF Frequency	5.5 MHz
Max Supported Bunches	16

Outlook

As a next step, a machine experiment with beam at SIS18 using one of the h=2 magnetic alloy cavities as dedicated kicker cavity is planned to evaluate the setup.

References

[1] K. Groß et al., GSI SR 2014, FG-SIS100-10 (2015).
[2] H. Klingbeil et al., “A digital beam-phase control system for heavy-ion synchrotrons”, IEEE Trans. Nucl. Sci. 54(6)2604:2610 (2007).
[3] D. Lens et al., GSI SR 2014, FG-GENERAL-29 (2015).
[4] D. Lens et al., GSI SR 2016, FAIRPROJECT-SIS100-SIS18-15 (2017)

∗ Work supported by GSI.
† hardieck@uni-kassel.de
‡ d.e.m.lens@gsi.de

 DOI:10.15120/GR-2018-1

Developments and results of Dry-Runs at the fragmentseparator FRS

J.P. Hucka[1,2], J. Enders[1], S. Pietri[2], R. Steinhagen[2], D. Ondreka[2], F. Ameil[2], H. Weick[2], K.H. Behr[2], R. Baer[2], H. Hüther[2], S. Reimann[2], C. Scheidenberger[2], B.R. Schlei[2], M. Sapinski[2],Y. Tanaka[2]

1 TU Darmstadt, Darmstadt, Germany; 2 GSI, Darmstadt, Germany

With the preparations for the upcoming beamtime of FAIR-phase 0, Dry-Runs [1] are being deployed to test the functionalities of the newly implemented control system framework LSA [2], to guarantee fail-safe working of the corresponding power converters, and minimize potential errors during the operation as much as possible. Respectively, the FRS [3] is being modelled in LSA as well. Within this modelling it has to be guaranteed that settings and values have to be reproduceable especially with the ion optical elements. Therefore a magnetic precycling sequence has been designed, implemented and tested successfully during the Dry-runs within the sequencer [4] framework.

Development

Motivation

The magnetic precycling is a procedure that was developed inside the sequencer framework to guarantee reproducibility of settings and values for the magnetic fields and magnetic rigidities of ion optical elements due to hysteresis. This has to be considered when operating magnets and changing currents by more than a factor of 1.01, as it can lead to unwanted different magnetization values varying by up to 0.5% [5], which leads to the selection of incorrect isotope fragments.

Precycle procedure

A solution to this problem has been a procedure named “magnetic washing”, which has been in use at the FRS since 2006 [5]. It has been renamed to magnetic precycling during current developments inside the sequencer. The procedure consists of the following steps:

1. Ramp the magnet up in 15 seconds to the maximum current to achieve saturation.
2. Wait 15 seconds.
3. Ramp the magnet down in 15 seconds to minimum current.
4. Wait 15 seconds.
5. Repeat steps 1 to 4 again once.
6. Ramp up to new value for the current.

Under the assumption of reproducibility, this procedure sets the magnetization always coming from the same side and should only take 2 minutes. It is supposed to be run on either single dipole magnets, all magnets of one particular zone or all magnets of several zones in parallel, while beam to the corresponding beamlines is being cut off by either slits or beam plugs.

Dry-run tests

It was possible to use the developed magnetic precycle procedure in the sequencer during Dry-Run testing of the GSI beamlines. At first it was possible to successfully run the procedure on a single magnet and afterwards on several magnets, both dipoles and quadrupoles, in parallel. The runtime of 2 minutes was achieved. The result of the precycling was monitored during the Dry-run by reading both current and hall probe values. The first iteration of the future parameter hierarchy used by the FRS machine model was tested and guaranteed a control of the machine. Additionally drives for targets, valves and detectors were tested separately either using higher applications utilising the JAPC framework or by directly interacting with the front-end devices.

Conclusion

A proof of principle was achieved with the successful test of the magnetic precycling procedure during the Dry-Runs. Intended use of the procedure as well as the degree of embedding into the control system framework of LSA is being implemented. The usage of currently generically developped Tools and applications for the control system, which tend to the needs of generic machines like rings or transfer lines, led to the conclusion that they could be used for during the Dry-Runs for the FRS but showed that further specialized applications for the control of the FRS need to be developped to guarantee a streamlined fluent operation of the FRS during experiments in FAIR-phase 0. Future Dry-Runs will test all required applications and developped concepts for the FRS from its own control room and layer.

References

[1] https://www.gsi.de/work/beschleunigerbetrieb/betrieb/dry_run.htm, Last visit. 07.02.2018
[2] M. Lamont et al., LHC Project Note 368
[3] H. Geissel et al., NIM B 70, 286 (1992)
[4] R. Steinhagen, “Dry-run procedures & 1st Sequencer iteration”, presentation 2017-10-04
[5] H. Weick, private communication

Experiment beamline: FRS
Experimentcollaboration:NUSTAR-Super-FRS-Experiments
Accelerator infrastructure: FRS
PSP: [2.4.19]
Grants: work supported by HIC for FAIR and BMBF (05P15RDFN1)
Strategic university co-operation with: Darmstadt

Recent developments for controls at the superconducting fragmentseparator S-FRS in the LHC software architecture LSA

J.P. Hucka[1,2], J. Enders[1], S. Pietri[2], B.R. Schlei[2], J. Fitzek[2], H. Hüther[2], H. Liebermann[2], D. Ondreka[2], H. Weick[2]

[1]TU Damrstadt, Darmstadt, Germany; [2]AGSI, Darmstadt, Germnay

The LSA [1] framework from CERN is used to implement a new control system for accelerators and beam transfers. The implementation at the SIS18 accelerator and CRYRING and ESR rings is currently being finalized. In addition, controls of the fragment separator FRS [2] and later also the superconducting fragment separator Super-FRS at FAIR will be provided by this framework. In an earlier work [3] the corresponding machine model has been benchmarked with experimental data and it was shown as a proof of principle that the control is possible. Following these results further developments were achieved. It was possible to model slits and the propagation of charge states through matter.

Motivation

The first iteration of the machine model was still lacking several types of matter and devices that are capable of changing beam properties, such as the magnetic rigidity or energy. In order to provide a complete machine model, slits and the propagation of charge states, elements and isotopes were modelled in the most recent developments for the FRS machine model in the control system framework LSA.

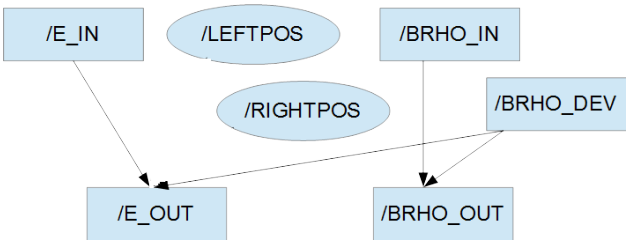


Figure 2: Hierarchy of a pair of horizontal slits. Position parameters are initial parameters and need to be set. Furthermore outgoing rigidity is determined by a deviation factor and incoming beam.

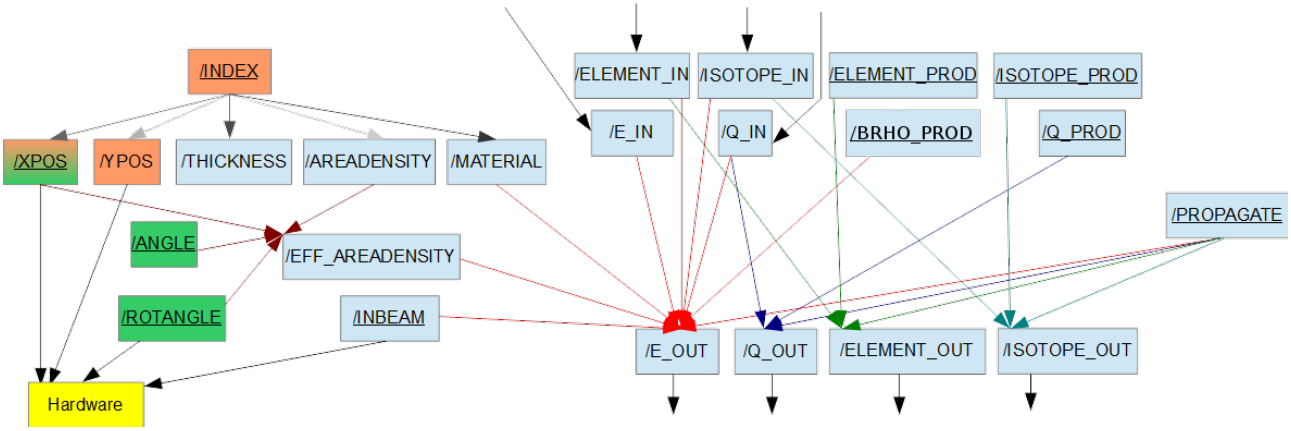


Figure 1: Updated Hierarchy for matter in FRS. Blue are parameters of the basic target hierarchy, which is further expanded depending on the type of matter being present. Orange representing targetladders and green degraders and degrader disks. Arrows of the same colour show relations between parameters and determine how a parameter is being calculated. After calculation, a parameter value is either propagated or sent to the Hardware.

Slit modelling

Slits are being distinguished in the following 5 groups:

- A group of slits consisting of a pair of horizontal and vertical slits
- Horizontal slits consisting of a pair of left and right slits
- vertical slits consisting of a pair of upper and lower slits
- left slits and right slits individually
- upper and lower slits individually

The group is mainly used for monitoring purposes, horizontal slits posses the ability of changing magnetic rigidity and beam energy. The individual separate slits and vertical slits are used to send set values to the hardware.

Propagation

Considering matter, there are 2 cases to be considered. Propagation of a beam through matter and production of secondary beam fragments inside matter. Only atomic energy-loss interaction has to be considered in the calculation of the energy of the beam after the matter, this is done via a solution using ATIMA [4] routines in LSA. In the case of production happening, the boolean parameter /PROPAGATE has to be toggled to FALSE, forcing the operator to put in a produced isotope with corresponding properties. Calculations for these properties are not being done inside LSA since they depend heavily on the nuclear physics models to be used, which operators will not be knowledgeable about, hence output from calculations from outside of the framework is pre-

 DOI:10.15120/GR-2018-1

ferred. Instead these values have to be provided by a physicist outside of the control system via LISE++ [5] for example.

Conclusion

Recent developments in the machine model lead to a more refined and realistic model of the FRS, taking into account slits as a new form of device with beam changing attributes. Furthermore the basic hierarchy of targets has been expanded by a modelling of propagation and production inside the matter. Tests have not yet been conducted but will be done during upcoming Dry-runs.

References

[1] M. Lamont et al., LHC Project Note 368
[2] H. Geissel et al., NIM B 70, 286 (1992)
[3] J.P. Hucka et al., DOI:10.15120/GR-2017-1
[4] H. Weick et al., NIM B 164/165 (2000) 168
[5] LISE++ home page, http://lise.nscl.msu.edu/lise.html

Experiment beamline: FRS
Experimentcollaboration:
NUSTAR-SuperFRS-Experiments
Experiment proposal: none
Accelerator infrastructure: FRS
PSP codes: 2.4.0.2.
Grants: work supported by HIC for FAIR and BMBF (05P15RDFN1)
Strategic university co-operation with: Darmstadt

Super-FRS design status report

M. Winkler[1], S. Althoff[1], F. Amjad[1], K.-H. Behr1, A. Bergmann[1], T. Blatz[1], E.J. Cho[1], W. Freisleben[1], H. Geissel[1,2], C. Karagiannis[1], R. Knöbel[1], A. Krämer[1], A. Kratz[1], J.Kurdal[1], H. Leibrock[1], H. Müller[1], I. Mukha[1], C. Nociforo[1], S. Pietri[1], A. Prochazka[1], S. Purushotaman[1], M.V. Ricciardi[1], P. Rottländer[1], C. Scheidenberger[1,2], F. Schirru[1], C. Schlör[1], M.M. Schmidt[1], H. Simon[1], P. Szwangruber[1], K. Sugita[1], F. Wamers[1], H. Weick[1], A. Wiest[1], J.S. Winfield[1], and Y. Xiang[1]

[1]GSI, Darmstadt, Germany; [2]JLU Giessen, Germany

System design

The wide range of magnetic rigidity (Bρ) between 2-20 T·m of the Super-FRS requires the variation of the magnetic field B0 of the dipoles in the range 0.16-1.6 T. The upper third of that range is situated in a non-linear saturation region of the magnetization curve B(H), which leads to shortening of the effective length of the dipole field and the change of the field distribution with increasing current I. We have analyzed these effects for one of the 11^0-bend normal-conducting dipoles of the Pre-Separator. At present, a 3D field distribution from finite-element calculations is used for different excitation currents and a resulting Bρ(I), but in the future the measured field will be used. From the fields the high order Taylor transfer maps for the particles are obtained using DA techniques (COSY-infinity).

Magnets

SC multiplets

In 2017 we accomplished the production readiness for the short SC multilets (PRR in July 2017) as well as for the long SC multiplets (PRR in December 2017) [1]. The production of the First-of-Series (FoS) short SC multiplet was started. All major subcomponents are produced (see Figure 1) and are at the manufacturer site (ASG; Genoa). The Factory Acceptance Test (FAT) of this multiplet is foreseen before summer 2018. Afterwards the multiplet will be shipped to our test facility at CERN, where the Site Acceptance Test (SAT) will be conducted.



Figure 1: FoS short multiplet manufacturing: quadrupole and sextupoe coils (upper left panel), sextupole yoke assembly (upper right pael), thermal shield (lower left pannel), and vacuum vessel (lower right panel).

SC dipoles

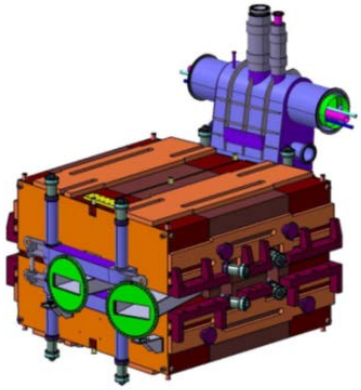


Figure 2: 3D model of the SC branching dipole magnet with additional straight beam exit.

The tendering process to procure the required 21 standard superconducting dipole magnets for Super-FRS was initiated in April 2017. After a company qualifying round and two rounds of negotiations we awarded the Spanish company ELYTT with the contract. The kick-off meeting took place at the company site in Bilbao, Spain, together with our collaborator from CEA Saclay, France, who will conduct the follow follow-up of the project. ELYTT will first verify the already existing magnet design and then produce a First-of-Series (FoS) magnet which is expected to be ready in autumn next year.

Under the frame of a technical collaboration agreement with CEA Saclay we are in parallel conducting a design study of the 3 branching SC dipoles [2]. Compared to the standard dipoles these magnets require an adapted yoke and cryostat design in order to provide an additional straight beam exit to connect the different branches of Super-FRS. The kick-off for this project was in June 2017 and a preliminary design (see Figure 2) was already presented in December 2017. It is expected that the design will be completed until summer this year, including a Conceptual Design report and the Detailed Specifications. Afterwards a dedicated tender for these magnets will be required since they are not within the scope of the above mentioned contract with ELYTT.

Magnet test facility

The assembly of the technical infrastructures of the testing facility for SC magnets at CERN is mostly finalised (Figure 3) and the commissioning of the cryogenic

 DOI:10.15120/GR-2018-1

system is under way. It is expected that the remaining work will be finalized until early summer 2018 to be ready for the cold test of the FoS short SC multiplet. As an important step also the contract amendment for the operating phase of the test facility has been closed.



Figure 3: SC magnet test facility at CERN building 180. The figure shows the 3 test benches coloured in white, blue, and green.

Local cryogenics

The reported change of structure and design [3] for the Super-FRS Local Cryogenics towards smaller numbers of component types and thus greater series-depths has been implemented. Components lists, nomenclature system, cost break-down, and of course the hydraulical and thermal system layout, have been updated. The main structure of the system in terms of 9 branches has been preserved. The ongoing activities are focused on:

- finalizing the interfaces to certain building sections (in particular to the LEB and HEB caves),
- working out a geometrical concept for the triplets of dipole feed boxes,
- summarising the Super-FRS Local Cryogenics requirements in several specification documents.

In parallel, large efforts have been made in order to define the requirements and strategy for fabrication, acceptance tests, installation, and commissioning of the Local Cryogenics components. For this goal, workshops with cryogenics colleagues from ESS and DESY have been organized and communication for experience exchange and knowledge transfer has been established.

Beam instrumentation

The production of the pre-series y-slit system was finalized at the site of our collaboration partner KVI-CART Groningen and the FAT was accomplished [4]. In parallel the production of the series x-slit system was prepared and is now under way.

Last year our first FAIR In-Kind Contract (IKC) with Finland on the MUSIC (Multi Sampling Ionization Chamber) detectors was closed. This detector measures the energy loss (ΔE) of particles in the detector material in order to determine their charge state Z. Altogether 4 systems are required along the separator. Our partner from Jyvaskyla intends to develop the first detector already for the second half of next year.

One more IKC on the TOF (Time-Of-Flight) detector is right now under negotiation with our assigned Russian in-kind partner from the IOFFE institute in St. Petersburg. Moreover detailed specification for most of the other important detector systems (e.g. GEM-TPC tracking detectors) could be finalized and IKCs are in preparation.

Target area / handling system

The conceptual design of the target chamber is ongoing together with our collaboration partner KVI-CART [3]. The remote guidance of the up to 4.5 ton heavy plug inserts into the chamber was identified as a crucial operation. Thus a 1:1 mock-up of the target wheel plug was built and the operation could be successfully verified.



Figure 4: 1:1 mock-up of the target wheel plug during insertion test in a dummy chamber.

Beam catcher

Our Indian in-kind partner CMERI, Durgapur finalized the conceptual design report for the beam catcher systems. Each catcher will be equipped with two absorber blocks, a Cu absorber for slow extracted beams and a C absorber for fast extracted beams. Next step will be to build an absorber mock-up and to verify the remote handling capability.

References

[1] E.J. Cho et al., “Magnetic Design for the Superferric Multipole Magnets of the Super-FRS”, IEEE transaction on Applied Superconductivity, vol. 28, no. 4, 2018
[2] A. Madur et al., “Preliminary Design of the FAIR Super-FRS Superferric Branched Dipoles”, IEEE transaction on Applied Superconductivity, vol. 28, no. 3, 2018
[3] M. Winkler et al., “Super-FRS Design Status Report”, GSI Scientific Report 2016
[4] C. Rigollet et al., “Design verification tests of the Super-FRS slit system”, this report

Accelerator infrastructure: Super-FRS
PSP codes: 2.4

Low cost interface for remote handling of insertions at the Super-FRS

C. Schlör[1], T. Blatz[1], C. Karagiannis[1], C. Nociforo[1], M. Winkler[1]

[1]GSI, Darmstadt, Germany

At the Super-FRS, many insertions devices (detector drives, degrader, slits, secondary target ladder, etc.) which are installed in the vacuum chambers at the various focal planes have to be remote handled due to the highly activated environment in these areas.

The remote handling system consists out of an industrial robot system KUKA KR 1000[1] adapted on a KUKA Omnimove[2] platform. It is a fully autonomous system capable to change the various experimental setups and to exchange and maintain the insertions.

In order to connect and disconnect automatically the insertions from their supply units (electrical power, electrical signals, cooling water, compressed air, etc.) a low cost mechanical interface, called "media board" was developed at GSI. In total, 19 insertions at the Pre-Separator of the Super-FRS have to be equipped with such a system. Two sizes of the media board are foreseen to cover the different amount of signal pins and feedthrough required by the different insertion types. The main task was to design a modular and scalable utilities device to supply each insertion.

The media board assembly is shown in (Figure 1). It consists of two plates equipped with modular configurable multi-pin connectors (CombiTac by Stäubli[3]) for electrical signals, optical fibres, high voltage, gas, fluids etc. The connectors are mounted floating on the carrier plates and allow a lateral displacement of ±1mm (X/Y plain) and an angular misalignment of ±3°.

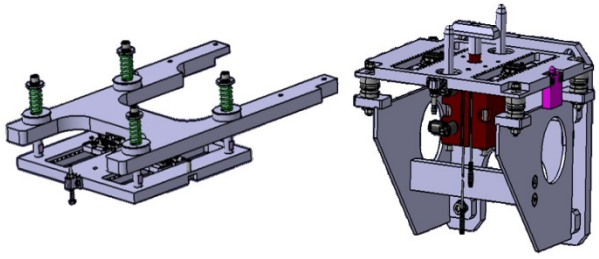


Figure 1: CAD drawings upper part (left) and lower part (right) of the media board including supports

One plate is mounted to the vacuum chamber and the other one to the insertion (drive flange). The plate which is fixed at the vacuum chamber includes the coupling actuator (pneumatic cylinder) and its connectors are wired to the DAQ equipment located in the supply-tunnel and niches of Super-FRS.

The robot delivers the new / repaired insertion and places it with high precision on the top of the vacuum chamber. Once the insertion is in place the plates are pre-aligned but not connected. The plate coupling is performed by a linear / rotary movement of a pneumatic cylinder. The coupling force depends on the media board configuration and can be adjusted by a compressed air regulator.

The trigger signal for the plate coupling is sent by the robot system and activates the cylinder which connects the two plates by pulling the upper one (mounted on the insertion) to the lower one (fixed at the vacuum chamber).

A PLC is monitoring the status of the cylinder (up or down position) and the relative position of the plates by means of reed sensors. The PLC communicates with the autonomous robot system and gives feedback (handshake) in order to trigger the coupling / decoupling procedure.

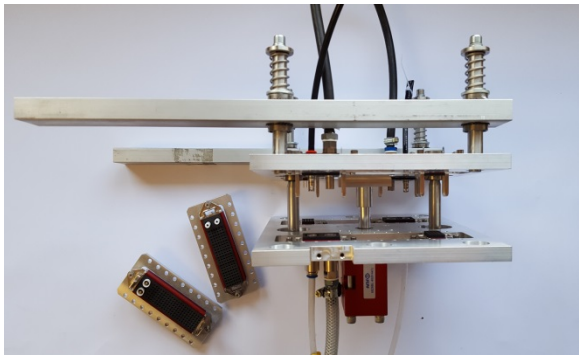


Figure 2: Media board prototype

In case of malfunctioning interlocks are sent to interrupt the connecting procedure.

References

[1] https://www.kuka.com/de-de/produkte-leistungen/robotersysteme/industrieroboter/kr-1000-titan
[2] https://www.kuka.com/de-de/produkte-leistungen/mobilität/mobile-plattformen/kuka-omnimove
[3] http://ec.staubli.com/products/combitac

Accelerator infrastructure: Super-FRS
PSP code: 2.4.6.
Grants: none
Strategic university co-operation with: none

 DOI:10.15120/GR-2018-1

Design verification tests of the Super-FRS slit system

C. Rigollet[1], M. Ali Najafi[1], B. Malheiros[1], N. Kalantar-Nayestanaki[1], S. Althoff[2], C. Karagiannis[2], O. J. Kuiken[1], M. F. Lindemulder[1], C. Nociforo[2], H. A. J. Smit[1], H. J. Timersma[1]

[1]KVI-CART, University of Groningen, The Netherlands ; [2]GSI, Darmstadt, Germany

A series of tests have been performed to demonstrate the fulfilment of the technical requirements of the Super-FRS slit system.

The Super-FRS slit system is used to cut and collimate the ion beams in one transversal direction (horizontal or vertical) to the beam axis. The slit system consists of 15 slit-pairs, 9 horizontal (X-slit) and 6 vertical (Y-slit). Each slit contains two identical stopping blocks made of DENSIMET® (96% tungsten, 3% nickel and 1% iron), moveable transversal to the beam direction and operated in vacuum. This block material was chosen especially because of its high stopping power and heat resistance. The block sizes match the beam envelopes and can stop up to ^{12}C ions at 18 Tm.

All X-slit pairs have a symmetrical opening (±190 mm), except the one to be designed for the mid-focus of the Main-Separator of the Super-FRS. The lifting structure on the slit allows robot handling. The prototypes of the X- and Y-slits (see Figure 1) were designed and manufactured at KVI-CART. In order to verify the design of the slit system, the factory acceptance tests (FAT) were performed at KVI-CART.

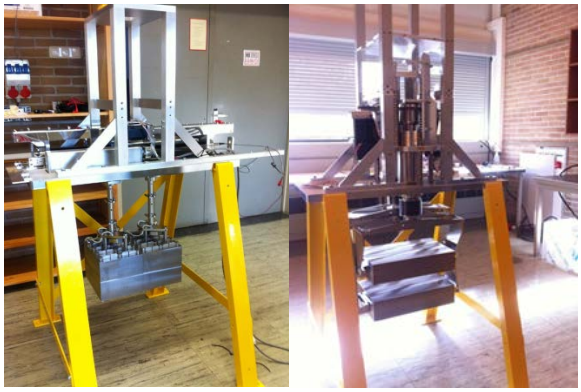


Figure 1: X-slit first of series of Super-FRS X- (left panel) and Y-slits (right panel).

Vacuum tests

Vacuum tests demonstrated that an ultimate pressure of 10^{-7} mbar could be obtained and that an integral leakage rate lower than10^{-9} mbar·l/s was achieved.

A test to measure the minimum gap between the blocks showed that they closed within 0.1 mm uniformly over the whole surface of the block.

Motion tests

An endurance test performed in vacuum demonstrated that the complete system was capable to open and close 5000 times, without any damages. After the test, the components subject to wear, such as the bellows, will be replaced.

A motion test demonstrated that all end switches (8 in total) were working with an accuracy of 0.1 mm and a block positioning precision within the specifications (± 0.1 mm) was achieved.

The stopping blocks are quickly released, e. g. they can be dismounted regardless of their positions. Their open to close speed of a full cycle is inferior to 120 s.

Beam absorption tests

The results of the beam absorption tests of the blocks and comparison with simulations showed that the slit were fully functional up to about 1.3 kW load. For this load the top plate temperature remains well below the safety margin of 80°C [1].

Hook test

In the PS area of the Super-FRS, human intervention is limited to a short time. Therefore, all actions (removal of a malfunctioning slit for example) are performed by a robot. The robot is equipped with a hook that will attach to the top structure of the slit and lift it. Tests showed that the slit can be safely lifted by the robot arm using the hook, irrespective of the position of the blocks.

Outlook

The FAT for both X- and Y-slits prototypes were successfully performed at KVI-CART. The manufacture of the series production for the X- and Y-slits is ongoing. The prototype of the ´asymmetric´ slit will be assembled and tested in the course of the year.

References

[1] B. Malheiros, BSc thesis, University of Groningen, 2016.

Accelerator infrastructure: Super-FRS
PSP codes: 2.4.6.2.3

Tests of a SEETRAM prototype for the Super-FRS

S. Schlemme[1,2], J. Enders[1], C. Karagiannis[2], M. Jastrzab[3], M. Kis[2], A. Kratz[2], N. Kurz[2], C. Nociforo[2], F. Schirru[2]

[1]TU Darmstadt, Darmstadt, Germany; [2]GSI, Darmstadt, Germany; [3]GSI, Kracow, Germany;

A series of tests have been performed to demonstrate the performance of a SEETRAM prototype of the Particle Detector Combination (PDC) of the Super-FRS.

Introduction

The Super-FRS PDC is a combination of three different detectors, a Secondary Electron Emission TRAnsmission Monitor (SEETRAM), an ionization chamber (IC) and a diamond detector. The PDCs are required at the entrance of the Super-FRS, i.e. FPF0 or target station, and at the end of the Pre-Separator, i.e. FPF4 station, to measure the intensity of slow-extracted ion beams for a broad range of energy (0.3 – 1.5 GeV/nucl.) and ion species, in addition to monitor and optimize the beam transmission. Diamond detectors will be reference detectors, which will serve to calibrate the SEETRAM and IC.

The tested SEETRAM prototype was designed and manufactured at GSI [1]. It consisted of three circular aluminum foils, with thicknesses of 24 µm and diameter of 107 mm, each placed 5 mm apart. In order to verify the functionality of the prototype a test experiment had been carried out at the LNS in Catania (Italy). For this purpose a cyclotron ^{12}C beam at 62 MeV/nucl. had been used. The test aimed at i) demonstrating the proportionality between the measured intensity recorded by SEETRAM and diamond detector and ii) verifying the precision of a direct calibration of the prototype using light ions at 10^5 – 10^6 ions/s.

Setup of the experiment

The ion beam entered the setup shown in Figure 1 from the right side. All detectors had been placed in a vacuum chamber. In front of the detectors a collimator – diameter 3 mm – had been placed.

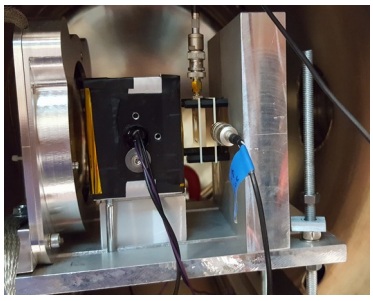


Figure 1: Setup, from right side: collimator, diamond detectors, plastic SCI and SEETRAM.

Next in line a single- (SC) and a poly-crystalline (PC) diamond detector were placed. Further a plastic scintillator (SCI) mounted downstream was used as reference detector, defining the absolute count rate. Last in line the SEETRAM was placed. The signals of the SC, PC and SCI detectors were sent to a scaler after discrimination. As for the SEETRAM, the signal was sent at first to a current digitizer [2] and then to a scaler module.

Results

A uniform response of all detectors with respect to the beam intensity was observed. Comparison between the SC and SCI showed a count efficiency of 100% of the SC. Hence the SC had been used as reference detector for all further measurements. Due to the low charge and intensity of the ion beam, the SEETRAM signal was so small, that it demanded a change in the sensitivity of the digitizer to the highest (10^{-14}A/count).

The calibration between SC and SEETRAM for different beam intensities is shown in Figure 2. Noise varying between 100-300 counts had been in the order of the SEETRAM current, leading to large relative errors in the fit. The result shows in the linear region a remarkable dependency of the fitting range on the calibration factor, which is found to be 6925±321 counts/10^{-14}A. An uncertainty of about 5% was achieved.

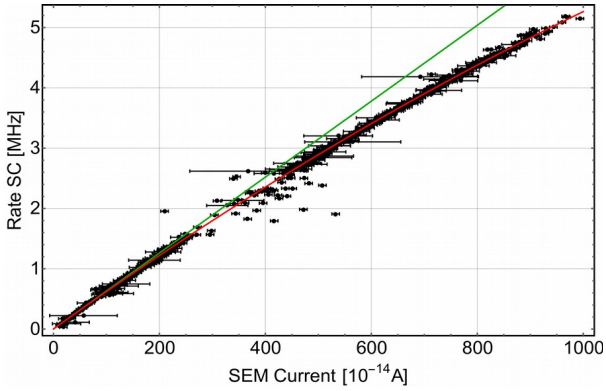


Figure 2: Calibration curve between SEETRAM and SC.

Outlook

Due to the higher intensity at FPF0, it is foreseen to equip the SEETRAM with different material (e.g. Ti-foils). The device will be mounted on a linear drive. The correct mounting/dismounting of the SEETRAM via manipulator will be verified in the current year.

References

[1] P. Boutachkov et al, GSI report 2016, p. 465.
[2] Current Digitizer CD101x Documentation, GSI.

Accelerator infrastructure: Super-FRS
PSP codes: 2.4.6.1.1
Grants: EU H2020 contract No. 654002 - ENSAR2
Strategic university co-operation with: Darmstadt

 DOI:10.15120/GR-2018-1

Status of the modulated 3 MeV 325 MHz Ladder-RFQ*

M. Schuett†, U. Ratzinger, M. Syha

IAP, Goethe-University, Frankfurt, Germany

* Work supported by BMBF 05P15RFRBA.
† schuett@iap.uni-frankfurt.de

Abstract

An unmodulated Ladder RFQ prototype with an electrode length of 63 cm was successfully designed, manufactured and tested during 2014 and 2015 [1]. The successful high power tests of the unmodulated prototype motivated the development of a new beam dynamics with an increased electrode voltage of 96 kV [2]. Consequently, a modulated prototype (s. fig. 1) with an electrode length of approx. 3:3m was designed to accelerate protons from 95 keV to 3:0MeV according to the design parameters of the p-Linac at FAIR. Manufacturing is expected to be completed in May 2018.

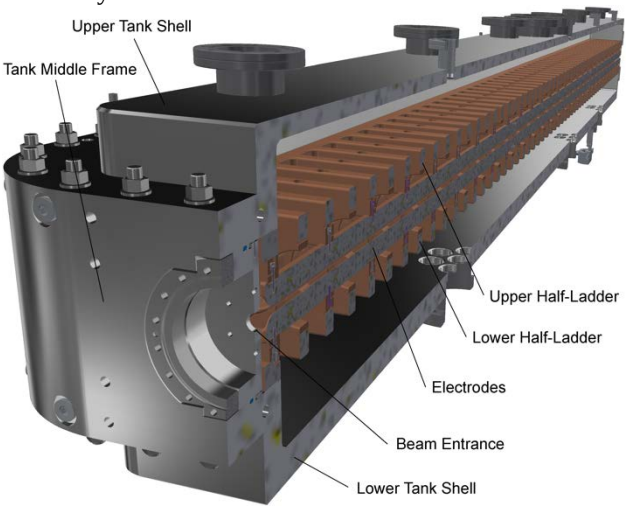


Figure 1: Isometric view of the 3.3 m modulated Ladder-RFQ prototype. Copper carrier-rings guarantee the electrode positioning as well as the RF contact. The ladder structure consists of bulk copper components. Any brazing or welding processes were avoided for the assembly of the main components.

Status of Manufacturing

Manufacturing of the tank components, consisting of an upper tank shell, middle frame and lower tank shell started in September 2017 and has been completed in February 2018. The middle frame has been copper-plated by GSI in 12/2017. The upper and lower tank shell will follow until March 2018. The copper structure is machined in parallel from 02-04/2018. The electrodes will also be completed in April. The whole assembly is scheduled for May 2018.

Compensation of Fringe Fields

The longitudinal electric field in the entrance gap of the RFQ will be beneficially exploited as a pre-buncher (s. fig. 2). Further details will be published separately.

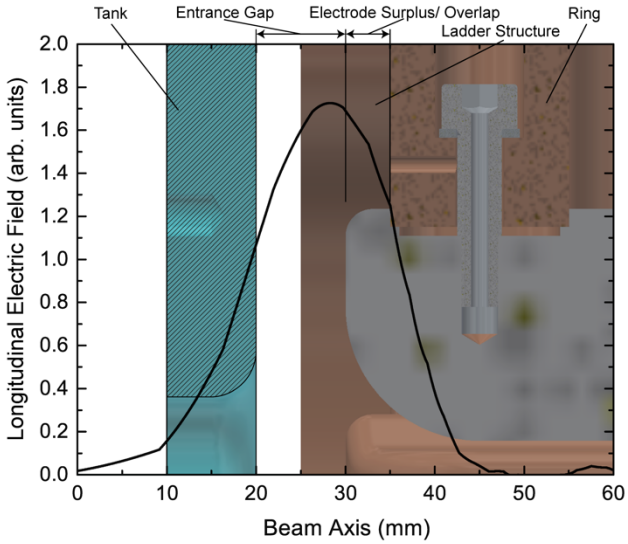


Figure 2: Fringe field in the entrance gap of the RFQ.

Conclusion and Outlook

As soon as manufacturing is completed first low level RF measurements such as frequency, spectra and flatness will be performed in Q2/2018. Accompanied by simulations, the heights of the ladder cells will then be machined to tune the longitudinal voltage distribution and frequency. Simultaneously, the frequency plunger and RF coupler will be designed and built. After the final assembly, the RFQ will be RF conditioned at the end of 2018 as well as high power RF tested at the GSI test bunker [3]. With completion of the p-Linac building, the RFQ can be installed together with the ion source and LEBT to be tested with beam.

References

[1] M. Schuett, M. Obermayer, U. Ratzinger, M. Syha “Status of the modulated 3MeV 325MHz Ladder-RFQ”, Proc. of IPAC2017.

[2] M. Syha, M. Obermayer, U. Ratzinger, M. Schuett, “Beam Dynamics for a high Current 3 MeV, 325 MHz Ladder-RFQ”, Proc. of IPAC2017.

[3] G. Schreiber, E. Plechov, J. Salvatore, B. Schlitt, A.Schnase, M. Vossberg, “First High Power Tests at the 325 MHz RF Test Stand at GSI”, Proc. of LINAC2016, East Lansing, USA, p. 3745.

Experiment beamline: none
Experiment collaboration: none
Experiment proposal: none
Accelerator infrastructure: p-Linac
PSP codes: none
Grants: none
Strategic university co-operation with: Frankfurt-M

Status of high power components for the FAIR Proton Linac RF systems

A. Schnase[1], G. Schreiber[1], S. Pütz[1], E. Plechov[1]

[1]GSI, Darmstadt, Germany

In middle of 2017 the In-kind contracts between GSI/FAIR and CNRS (France) related to radio frequency components for the GSI/FAIR pLinac were concluded.

We continued with the acceptance tests of the delivered components. Related to waveguide parts, we modified and calibrated in total 11 dual directional couplers and 7 six-port couplers. In the end of 2017 the next 6 Klystrons TH 2181 were delivered. Here we explain the test procedures.

In order to operate the Klystrons - at the test bench and later in the pLinac RF Gallery, we need high voltage Modulators. The in-house preparation of a prototype modulator is progressing.

RF system components at test bench

As described in [1], the modification and testing of waveguide directional couplers was continued. Now in total 64 ports are calibrated. The coupling is in the range 60 ±0.4 dB. Especially for the couplers detecting the reflected power, the isolation is better than 100 dB providing a directivity of better than 40 dB. Thus the upgraded dual directional couplers enable a reliable protection of the Klystrons against reflected power and the improved six-port couplers will deliver the signals for precise tuning of the acceleration cavities in the pLinac.

The RF power for the accelerating cavities is sent via WR 2300 waveguides to the tunnel - followed by transition elements to a short coaxial line, which connects to the cavity input couplers. Several variants of transitions and coaxial elements were specified and ordered. Testing these components at the test bench requires pulsed RF power up to 2.5 MW peak delivered by a Klystron, which in turn is powered by a high voltage modulator [2].

The power electronics and electromechanical design of the modulator is complete and component procurement is ongoing. The development of the electronic control system is progressing.

TH2181 Klystrons

The TH2181 Klystron prototype is installed at the test bench. The FAT of the Klystrons #2 - #7 was conducted successfully in two groups of three at the company Thales. Finally in December 2017 the Klystrons were delivered to a GSI storage facility (Betriebshof) as shown in figure 1. Each Klystron has a weight of 4.2 tons. Fortunately, GSI owns a strong fork lifter, which can handle this load. The SAT Aa testing is following a procedure prescribed by Thales, that the Klystron filament current will be applied in a slow ramp while observing the ion pump currents, which represent the vacuum state. This is shown as an example in figure 2. The filament current is increased until the design value of 18 A is reached. The ion-pump current should stay below 10 µA. Both ion-pump currents should be similar, because the ion pumps are connected to the same klystron vessel. All of the klystrons passed the filament test. However, for 3 of the klystrons only one of the ion pumps became active. Thus, these tests have to be repeated in 1 month intervals.



Figure 1: The Thales Klystrons #2-#7 are stored.

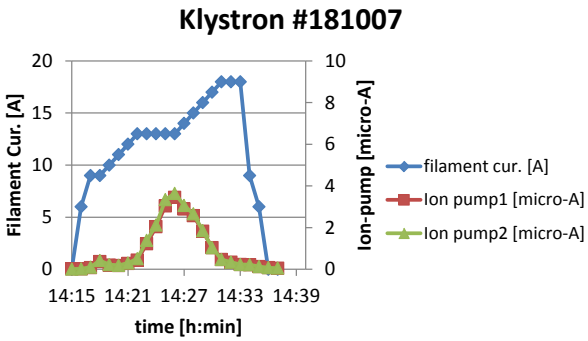


Figure 2: Ion-pump current during filament test.

Outlook

With the delivery of the Klystrons an important milestone towards the pLinac was reached. We will continue our efforts to prepare the RF systems for the pLinac.

References

[1] A. Schnase, M. Helmecke, E. Plechov, S. Pütz, G. Schreiber, "Preparation work at the 325 MHz test stand at GSI for Klystron FAT and SAT", GSI sci. report 2016, p. 383.

[2] S. Pütz, A. Schnase, G. Schreiber, "Design and Production of Klystron Modulators for the pLINAC", GSI sci. report 2016, p. 459.

Experiment beamline: none
Experiment collaboration: none
Experiment proposal: none
Accelerator infrastructure: p-Linac
PSP codes: 2.7.4.1
Grants: none
Strategic university co-operation with: none

 DOI:10.15120/GR-2018-1

Commissioning of the proton injector for FAIR at CEA/Saclay

R. Berezov[1], O. Delferriere[2], J. Fils[1], Y. Gauthier[2], R. Hollinger[1], K. Knie[1], C. Kleffner[1], O. Tuske[2], C. Ullmann[1].

[1]GSI, Darmstadt, Germany; [2]CEA, Saclay, France

The proton injector for Facility for Antiproton and Ion Research (FAIR) is designed and built at CEA/Saclay (France). It will provide primary proton beam at 95 keV energy and up to 100 mA current into compact proton linac, where it will be accelerated to 68 MeV for further injection into upgraded Heavy Ion Synchrotron (SIS18).

The proton injector itself consists from pulsed ion source operates with a frequency of 2.45 GHz based on electron cyclotron resonance (ECR) plasma production and Low Energy Beam Transport (LEBT) matching the proton beam to the radio-frequency quadrupole (RFQ) [1]. The designed value of emittance at the entrance of RFQ should be lower than 0.3π mm mrad (normalized, rms).

The commissioning of the proton injector is running now at CEA/Saclay and divided in several steps. The first commissioning phase includes beam characterisation direct after accelerated column shown in the Fig.1. The ion source is located at the high voltage platform inside the Faraday cage. The diagnostic chamber is mounted outside of the Faraday cage with different diagnostic tools as: Allison scanner (EMU) for emittance measurements, current transformer (ACCT) and faraday cup (FC) for current measurements and Wien filter (WF) for detection of different ion species.

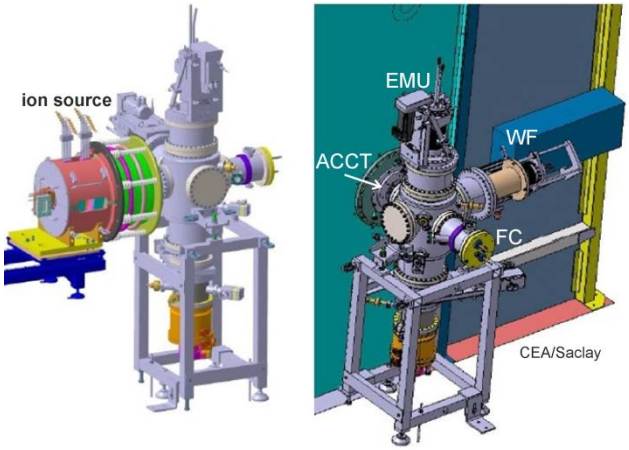


Figure 1: 3-D view of microwave ion source and diagnostic chamber for first commissioning phase.

This commissioning phase is on final stage at CEA. The maximum total extracted current from ion source measured with ACCT is near 150 mA. The measured beam composition with WF shows high proton value in the order of 82-85%. First emittance measurements show good results with emittance narrow to designed value for proton injector.

As a next step it is planned to install LEBT consisting of two solenoids including an iron shielding with two horizontal and vertical integrated magnetic steerers. A diagnostic chamber with different diagnostic tools is mounted between the solenoids. During this phase the measurements will be carried out between solenoids in diagnostic chamber and behind second solenoid. Similar beam characterisation including current, emittance and proton fraction measurements will be done [2].

In the last commissioning phase (Fig.2) chopper chamber with injection cone will be installed. In proton linac electrostatic chopper will be placed between the second solenoid and the RFQ entrance to cut the beam pulse current to 36 µs.

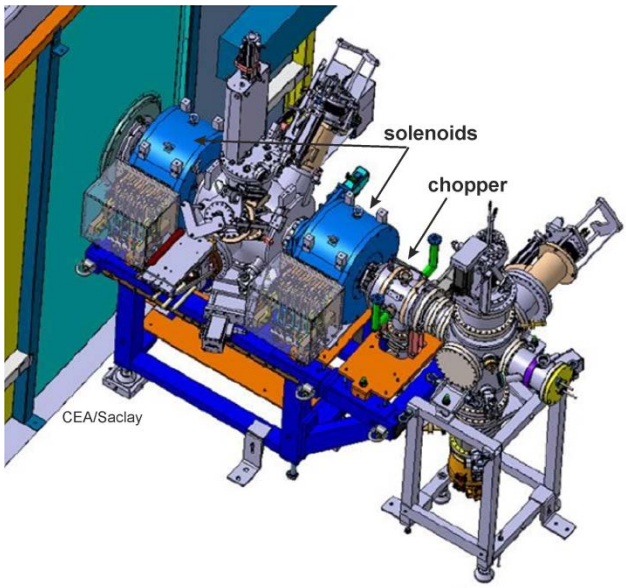


Figure 2: 3-D view of LEBT, chopper and diagnostic chamber.

In this phase the measurements of beam intensity will be done with ACCT behind the pentode extraction system, behind second solenoid and as additional in the diagnostic chamber and at the end of beam line with faraday cup. The emittance and beam composition measurements will be done in this case after the injection cone to feature the beam parameters produced from proton injector. The stability of the ion source including beam fluctuation and pulse-to-pulse repetition rate will be tested during the long time of operation.

After successful commissioning of the proton injector at CEA, it will be transported to GSI for final commissioning in the new proton linac building for FAIR.

References

[1] R. Berezov et. al., “High intensity proton injector for facility of antiproton and ion research”, Rev. Sci. Instrum. 87, 02A705, (2016).

[2] R. Berezov et. al., Proceeding of ICIS 2017, Geneva.

 DOI:10.15120/GR-2018-1

Publications and dissertations in 2017

Matter and universe – 610

259 publications listed in Web of Science or SCOPUS

G. Aarts et al.
Heavy-flavor production and medium properties in high-energy nuclear collisions - What next?
The European physical journal / A, A53(5):93.
doi: 10.1140/epja/i2017-12282-9.

M. Ablikim et al.
Amplitude analysis of the χ c 1 → η π + π − decays.
Physical review / D, 95(3):032002.
doi: 10.1103/PhysRevD.95.032002.

M. Ablikim et al.
Analysis of $D^+ \to \bar{K}^0 e^+ \nu_e$ and $D^+ \to \pi^0 e^+ \nu_e$ Semileptonic Decays.
Physical review / D, 96(1):012002.
doi: 10.1103/PhysRevD.96.012002.

M. Ablikim et al.
Branching fraction measurement of $J/\psi \to K_S K_L$ and search for $J/\psi \to K_S K_S$.
Physical review / D, 96(11):112001.
doi: 10.1103/PhysRevD.96.112001.

M. Ablikim et al.
Determination of the Spin and Parity of the $Z_c(3900)$.
Physical review letters, 119(7):072001.
doi: 10.1103/PhysRevLett.119.072001.

M. Ablikim et al.
Evidence of Two Resonant Structures in $e^+e^- \to \pi^+\pi^- h_c$.
Physical review letters, 118(9):092002.
doi: 10.1103/PhysRevLett.118.092002.

M. Ablikim et al.
Improved measurements of branching fractions for $\eta_c \to \phi\phi$ and $\omega\phi$.
Physical review / D, 95(9):092004.
doi: 10.1103/PhysRevD.95.092004.

M. Ablikim et al.
Improved measurements of two-photon widths of the χ_{cJ} states and helicity analysis for $\chi_{c2} \to \gamma\gamma$.
Physical review / D, 96(9):092007.
doi: 10.1103/PhysRevD.96.092007.

M. Ablikim et al.
Measurement of branching fractions for $\psi(3686) \to \gamma\eta', \gamma\eta,$ and $\gamma\pi^0$.
Physical review / D, 96(5):052003.
doi: 10.1103/PhysRevD.96.052003.

M. Ablikim et al.
Measurement of cross sections of the interactions $e^+e^- \to \phi\phi\omega$ and $e^+e^- \to \phi\phi\phi$ at center-of-mass energies from 4.008 to $4.600\ GeV$.
Physics letters / B, 774:78.
doi: 10.1016/j.physletb.2017.09.021.

M. Ablikim et al.
Measurement of $e^+e^- \to \pi^+\pi^-\psi(3686)$ from 4.008 to 4.600 GeV and observation of a charged structure in the $\pi^\pm\psi(3686)$ mass spectrum.
Physical review / D, 96(3):032004.
doi: 10.1103/PhysRevD.96.032004.

M. Ablikim et al.
Measurement of higher-order multipole amplitudes in $\psi(3686) \to \gamma\chi_{c1,2}$ with $\chi_{c1,2} \to \gamma J/\psi$ and search for the transition $\eta_c(2S) \to \gamma J/\psi$.
Physical review / D, 95(7):072004.
doi: 10.1103/PhysRevD.95.072004.

M. Ablikim et al.
Measurement of the absolute branching fraction for $\Lambda_c^+ \to \Lambda_{\mu^+\nu_\mu}$.
Physics letters / B, 767:42.
doi: 10.1016/j.physletb.2017.01.047.

M. Ablikim et al.
Measurements of cross section of $e^+e^- \to p\bar{p}\pi^0$ at center-of-mass energies between 4.008 and 4.600 GeV.
Physics letters / B, 771:45.
doi: 10.1016/j.physletb.2017.05.033.

M. Ablikim et al.
Measurements of the branching fractions for $D^+ \to K_S^0 K_S^0 K^+, K_S^0 K_S^0 \pi^+$ and $D^0 \to K_S^0 K_S^0, K_S^0 K_S^0 K_S^0$.
Physics letters / B, 765:231.
doi: 10.1016/j.physletb.2016.12.020.

M. Ablikim et al.
Observation of the decay $\Lambda_c^+ \to \Sigma^-\pi^+\pi^+\pi^0$.
Physics letters / B, 772:388.
doi: 10.1016/j.physletb.2017.06.065.

M. Ablikim et al.
Observation of the doubly radiative decay $\eta' \to \gamma\gamma\pi^0$.
Physical review / D, 96(1):012005.
doi: 10.1103/PhysRevD.96.012005.

M. Ablikim et al.
Observation of the helicity-selection-rule suppressed decay of the χ_{c2} charmonium state.
Physical review / D, 96(11):111102.
doi: 10.1103/PhysRevD.96.111102.

M. Ablikim et al.
Observation of $\Lambda_c^+ \to nK_S^0\pi^+$.
Physical review letters, 118(11):112001.
doi: 10.1103/PhysRevLett.118.112001.

M. Ablikim et al.
Observation of $\chi_{c2} \to \eta^{'}\eta^{'}$ and $\chi_{c0,2} \to \eta\eta'$.
Physical review / D, 96(11):112006.
doi: 10.1103/PhysRevD.96.112006.

M. Ablikim et al.
Precise Measurement of the $e^+e^- \to \pi^+\pi^- J/\psi$ Cross Section at Center-of-Mass Energies from 3.77 to 4.60 GeV.
Physical review letters, 118(9):092001.
doi: 10.1103/PhysRevLett.118.092001.

M. Ablikim et al.
Search for the radiative leptonic decay $D^+ \to \gamma e^+\nu_e$.
Physical review / D, 95(7):071102.
doi: 10.1103/PhysRevD.95.071102.

M. Ablikim et al.
Search for the rare decay $D^+ \to D^0 e^+\nu_e$.
Physical review / D, 96(9):092002.
doi: 10.1103/PhysRevD.96.092002.

M. Ablikim et al.
Search for the rare decays $J/\psi \to D^0 e^+e^- + c.c.$ and $\psi(3686) \to D^0 e^+e^- + c.c.$.
Physical review / D, 96(11):111101.
doi: 10.1103/PhysRevD.96.111101.

M. Ablikim et al.
Search for $\psi(3686) \to \gamma\eta_c(\eta(1405)) \to \gamma\pi^+\pi^-\pi^0$.
Physical review / D, 96(11):112008.
doi: 10.1103/PhysRevD.96.112008.

M. Ablikim et al.
Study of J/ψ and $\psi(3686)$ decay to $\Lambda\bar{\Lambda}$ and $\Sigma^0\bar{\Sigma}^0$ final states.
Physical review / D, 95(5):052003.
doi: 10.1103/PhysRevD.95.052003.

M. Ablikim et al.
Study of J/ψ and $\psi(3686)$ decays to $\pi^+\pi^-\eta^{'}$.
Physical review / D, 96(11):112012.
doi: 10.1103/PhysRevD.96.112012.

M. Ablikim et al.
Study of J/ψ and $\psi(3686) \to \Sigma(1385)^0\bar{\Sigma}(1385)^0$ and $\Xi^0\bar{\Xi}^0$.
Physics letters / B, 770:S0370269317303222.
doi: 10.1016/j.physletb.2017.04.048.

T. Ablyazimov, V. Friese and V. Ivanov.
Finding the needle in the haystack: a charmonium trigger for the CBM experiment.
22nd International Conference on Computing in High Energy and Nuclear Physics, San Francisco (USA), 10 Oct 2016 - 14 Oct 2016.
IOP Publ., Bristol, 10th Oct. 2016.
doi: 10.1088/1742-6596/898/3/032043.

T. Ablyazimov et al.
Challenges in QCD matter physics –The scientific programme of the Compressed Baryonic Matter experiment at FAIR.
The European physical journal / A, 53(3):60.
doi: 10.1140/epja/i2017-12248-y.

S. Acharya et al.
Energy dependence of forward-rapidity J/ψ and $\psi(2S)$ production in pp collisions at the LHC.
The European physical journal / C, C77(6):392.
doi: 10.1140/epjc/s10052-017-4940-4.

S. Acharya et al.
J/ψ elliptic flow in Pb-Pb collisions at $\sqrt{s_{\rm NN}} = 5.02$ TeV.
Physical review letters, 119(24):242301.
doi: 10.1103/PhysRevLett.119.242301.

S. Acharya et al.
Kaon femtoscopy in Pb-Pb collisions at $\sqrt{s_{\rm NN}}$ = 2.76 TeV.
Physical review / C, C96(6):064613.
doi: 10.1103/PhysRevC.96.064613.

S. Acharya et al.
Linear and non-linear flow modes in Pb-Pb collisions at $\sqrt{s_{\rm NN}} = 2.76$ TeV.
Physics letters / B, B773:68.
doi: 10.1016/j.physletb.2017.07.060.

S. Acharya et al.
Measurement of deuteron spectra and elliptic flow in Pb–Pb collisions at $\sqrt{s_{\rm NN}}$ = 2.76 TeV at the LHC.
The European physical journal / C, C77(10):658.
doi: 10.1140/epjc/s10052-017-5222-x.

S. Acharya et al.
Measurement of D-meson production at mid-rapidity in pp collisions at $\sqrt{s} = 7$ TeV.
The European physical journal / C, C77(8):550.
doi: 10.1140/epjc/s10052-017-5090-4.

S. Acharya et al.
Measuring $K^0_S K^{\pm}$ interactions using Pb-Pb collisions at $\sqrt{s_{\rm NN}} = 2.76$ TeV.
Physics letters / B, B774:64.
doi: 10.1016/j.physletb.2017.09.009.

S. Acharya et al.
Production of π^0 and η mesons up to high transverse momentum in pp collisions at 2.76 TeV.
The European physical journal / C, C77(5):339.
doi: 10.1140/epjc/s10052-017-4890-x.

S. Acharya et al.
Production of muons from heavy-flavour hadron decays in p-Pb collisions at $\sqrt{s_{\rm NN}} = 5.02$ TeV.
Physics letters / B, B770:459.
doi: 10.1016/j.physletb.2017.03.049.

S. Acharya et al.
Searches for transverse momentum dependent flow vector fluctuations in Pb-Pb and p-Pb collisions at the LHC.
Journal of high energy physics, 1709(9):32.
doi: 10.1007/JHEP09(2017)032.

S. Acharya et al.
Charged-particle multiplicity distributions over a wide pseudorapidity range in proton-proton collisions at $\sqrt{s} = 0.9$, 7, and 8 TeV.
The European physical journal / C, 77(12):852.
doi: 10.1140/epjc/s10052-017-5412-6.

S. Acharya et al.
Erratum to: Production of π^0 π 0 and η η mesons up to high transverse momentum in pp collisions at 2.76 TeV.
The European physical journal / C, 77(9):586.
doi: 10.1140/epjc/s10052-017-5144-7.

P. Achenbach et al.
Beam helicity asymmetries in $K^+\Lambda$ K + Λ electroproduction off the proton at low Q2.
The European physical journal / A, 53(10):198.
doi: 10.1140/epja/i2017-12395-1.

J. Adam et al.
Anomalous evolution of the near-side jet peak shape in Pb-Pb collisions at $\sqrt{s_{\rm NN}}$ = 2.76 TeV.
Physical review letters, 119(10):102301.
doi: 10.1103/PhysRevLett.119.102301.

J. Adam et al.
Centrality dependence of the pseudorapidity density distribution for charged particles in Pb-Pb collisions at $\sqrt{s_{\rm NN}} = 5.02$ TeV.
Physics letters / B, B772:567.
doi: 10.1016/j.physletb.2017.07.017.

J. Adam et al.
Determination of the event collision time with the ALICE detector at the LHC.
The European physical journal / Plus, 132(2):99.
doi: 10.1140/epjp/i2017-11279-1.

J. Adam et al.
Enhanced production of multi-strange hadrons in high-multiplicity proton-proton collisions.
Nature physics, 13(6):535.
doi: 10.1038/nphys4111.

J. Adam et al.
Evolution of the longitudinal and azimuthal structure of the near-side jet peak in Pb-Pb collisions at $\sqrt{s_{\rm NN}} = 2.76$ TeV.
Physical review / C, C96(3):034904.
doi: 10.1103/PhysRevC.96.034904.

J. Adam et al.
Flow dominance and factorization of transverse momentum correlations in Pb-Pb collisions at the LHC.
Physical review letters, 118(16):162302.
doi: 10.1103/PhysRevLett.118.162302.

J. Adam et al.
Insight into particle production mechanisms via angular correlations of identified particles in pp collisions at $\sqrt{s} = 7$ TeV.
The European physical journal / C, C77(8):569.
doi: 10.1140/epjc/s10052-017-5129-6.

J. Adam et al.
J/ψ suppression at forward rapidity in Pb-Pb collisions at $\sqrt{s_{\rm NN}} = 5.02$ TeV.
Physics letters / B, B766:212.
doi: 10.1016/j.physletb.2016.12.064.

J. Adam et al.
$K^*(892)^0$ and $\phi(1020)$ meson production at high transverse momentum in pp and Pb-Pb collisions at $\sqrt{s_{\rm NN}}$ = 2.76 TeV.
Physical review / C, C95(6):064606.
doi: 10.1103/PhysRevC.95.064606.

J. Adam et al.
Measurement of azimuthal correlations of D mesons and charged particles in pp collisions at $\sqrt{s} = 7$ TeV and p-Pb collisions at $\sqrt{s_{\rm NN}} = 5.02$ TeV.
The European physical journal / C, C77(4):245.
doi: 10.1140/epjc/s10052-017-4779-8.

J. Adam et al.
Measurement of electrons from beauty-hadron decays in p-Pb collisions at $\sqrt{s_{\rm NN}} = 5.02$ TeV and Pb-Pb collisions at $\sqrt{s_{\rm NN}} = 2.76$ TeV.
Journal of high energy physics, 1707(7):52.
doi: 10.1007/JHEP07(2017)052.

J. Adam et al.
Measurement of the production of high-$p_{\rm T}$ electrons from heavy-flavour hadron decays in Pb-Pb collisions at $\sqrt{s_{\rm NN}}$ = 2.76 TeV.
Physics letters / B, B771:467.
doi: 10.1016/j.physletb.2017.05.060.

J. Adam et al.
ϕ-meson production at forward rapidity in p-Pb collisions at $\sqrt{s_{\rm NN}}$ = 5.02 TeV and in pp collisions at $\sqrt{s}$ = 2.76 TeV.
Physics letters / B, B768:203.
doi: 10.1016/j.physletb.2017.01.074.

J. Adam et al.
Addendum to: Centrality dependence of high-pT D-meson suppression in Pb-Pb collisions at $\sqrt{s_{NN}}$=2.76 TeV.
Journal of high energy physics, 2017(6):32.
doi: 10.1007/JHEP06(2017)032.

J. Adamczewski-Musch et al.
A facility for pion-induced nuclear reaction studies with HADES.
The European physical journal / A, 53(9):188.
doi: 10.1140/epja/i2017-12365-7.

J. Adamczewski-Musch et al.
Analysis of the exclusive final state npe+e- in the quasi-free np reaction.
The European physical journal / A, 53(7):149.
doi: 10.1140/epja/i2017-12341-3.

J. Adamczewski-Musch et al.
Conception and design of a control and monitoring system for the mirror alignment of the CBM RICH detector.
9th International Workshop on Ring Imaging Cherenkov Detectors, Bled (Slovenia), 5 Sep 2016 - 9 Sep 2016.
North-Holland Publ. Co., Amsterdam, 5th Sept. 2016.
doi: 10.1016/j.nima.2017.02.033.

J. Adamczewski-Musch et al.
Event reconstruction for the CBM-RICH prototype beamtest data in 2014.
9th International Workshop on Ring Imaging Cherenkov Detectors, Bled (Slovenia), 5 Sep 2016 - 9 Sep 2016.
North-Holland Publ. Co., Amsterdam, 5th Sept. 2016.
doi: 10.1016/j.nima.2017.01.066.

J. Adamczewski-Musch et al.
Inclusive Λ production in proton-proton collisions at 3.5 GeV.
Physical review / C, 95(1):015207.
doi: 10.1103/PhysRevC.95.015207.

J. Adamczewski-Musch et al.
Single photon test bench for series tests of HAMAMATSU H12700 MAPMTs.
9th International Workshop on Ring Imaging Cherenkov Detectors, Bled (Slovenia), 5 Sep 2016 - 9 Sep 2016.
North-Holland Publ. Co., Amsterdam, 5th Sept. 2016.
doi: 10.1016/j.nima.2017.02.034.

D. Adamova et al.
Azimuthally differential pion femtoscopy in Pb-Pb collisions at $\sqrt{s_{\mathrm{NN}}} = 2.76$ TeV.
Physical review letters, 118(22):222301.
doi: 10.1103/PhysRevLett.118.222301.

D. Adamova et al.
Production of $\Sigma(1385)^{\pm}$ and $\Xi(1530)^{0}$ in p-Pb collisions at $\sqrt{s_{\mathrm{NN}}} = 5.02$ TeV.
The European physical journal / C, C77(6):389.
doi: 10.1140/epjc/s10052-017-4943-1.

D. Adamová et al.
Triangular flow of negative pions emitted in PbAu collisions at $\sqrt{s_{NN}}$ = 17.3 GeV.
Nuclear physics / A, 957:99.
doi: 10.1016/j.nuclphysa.2016.08.002.

R. Adhikari et al.
A White Paper on keV sterile neutrino Dark Matter.
Journal of cosmology and astroparticle physics, 2017(01):025.
doi: 10.1088/1475-7516/2017/01/025.

S. V. Akkelin.
Hot origin of the Little Bang.
The European physical journal / A, 53(12):232.
doi: 10.1140/epja/i2017-12432-1.

H. Al Ghoul et al.
Measurement of the beam asymmetry Σ for π^0 and η photoproduction on the proton at $E_\gamma = 9$ GeV.
Physical review / C, 95(4):042201.
doi: 10.1103/PhysRevC.95.042201.

P. Alba et al.
Excluded-volume effects for a hadron gas in Yang-Mills theory.
Physical review / D, 95(9):094511.
doi: 10.1103/PhysRevD.95.094511.

J. L. Albacete, H. Petersen and A. Soto-Ontoso.
Correlated wounded hot spots in proton-proton interactions.
Physical review / C, 95(6):064909.
doi: 10.1103/PhysRevC.95.064909.

J. L. Albacete, H. Petersen and A. Soto-Ontoso.
Gluonic hot spots and spatial correlations inside the proton.
Nuclear physics / A, 967:924.
doi: 10.1016/j.nuclphysa.2017.05.021.

ALICE Collaboration.
Charged-particle multiplicities in proton–proton collisions at $\sqrt{s} = 0.9$ to 8 TeV.
The European physical journal / C, C77(1):33.
doi: 10.1140/epjc/s10052-016-4571-1.

ALICE Collaboration.
W and Z boson production in p-Pb collisions at $\sqrt{s_{\mathrm{NN}}}$ = 5.02 TeV.
Journal of high energy physics, 1702(2):77.
doi: 10.1007/JHEP02(2017)077.

G. A. Almási, R. D. Pisarski and V. V. Skokov.
Volume dependence of baryon number cumulants and their ratios.
Physical review / D, 95(5):056015.
doi: 10.1103/PhysRevD.95.056015.

G. A. Almási, B. Friman and K. Redlich.
Baryon number fluctuations in chiral effective models and their phenomenological implications.
Physical review / D, 96(1):014027.
doi: 10.1103/PhysRevD.96.014027.

G. A. Almási et al.
Scaling violation and the magnetic equation of state in chiral models.
Physical review / D, 95(1):014007.
doi: 10.1103/PhysRevD.95.014007.

D. E. Alvarez-Castillo and D. B. Blaschke.
High-mass twin stars with a multipolytrope equation of state.
Physical review / C, 96(4):045809.
doi: 10.1103/PhysRevC.96.045809.

D. Alvarez-Castillo, D. Blaschke and S. Typel.
Mixed phase within the multi-polytrope approach to high-mass twins.
Astronomische Nachrichten, 338(9-10):1048.
doi: 10.1002/asna.201713433.

A. Andronic et al.
Hadron yields, the chemical freeze-out and the QCD phase diagram.
16th International Conference on Strangeness in Quark Matter, Berkeley, CA (USA), 27 Jun 2016 - 1 Jul 2016.
IOP Publ., Bristol, 27th June 2016.
doi: 10.1088/1742-6596/779/1/012012.

D. Antypas et al.
Towards improved measurements of parity violation in atomic ytterbium.
Hyperfine interactions, 238(1):21.
doi: 10.1007/s10751-017-1396-8.

S. Aoki et al.
Review of lattice results concerning low-energy particle physics.
The European physical journal / C, 77(2):112.
doi: 10.1140/epjc/s10052-016-4509-7.

A. Arcones Segovia et al.
White paper on nuclear astrophysics and low energy nuclear physics Part 1: Nuclear astrophysics.
Progress in particle and nuclear physics, 94:1.
doi: 10.1016/j.ppnp.2016.12.003.

ASY-EOS Collaboration.
Probing the nuclear symmetry energy at high densities with nuclear reactions.
Il nuovo cimento / C, 39(5):378.
doi: 10.1393/ncc/i2016-16378-6.

T. Aumann et al.
Peeling Off Neutron Skins from Neutron-Rich Nuclei: Constraints on the Symmetry Energy from Neutron-Removal Cross Sections.
Physical review letters, 119(26):262501.
doi: 10.1103/PhysRevLett.119.262501.

R. Baldini Ferroli et al.
New G -parity violating amplitude in the J / ψ decay?
Physical review / D, 95(3):034038.
doi: 10.1103/PhysRevD.95.034038.

F. Barbosa et al.
The GlueX DIRC detector.
Nuclear instruments & methods in physics research / A, 876:69.
doi: 10.1016/j.nima.2017.01.054.

T. Beck et al.
E2 decay strength of the M1 scissors mode of ^{156}Gd and its first excited rotational state.
Physical review letters, 118(21):212502.
doi: 10.1103/PhysRevLett.118.212502.

O. Beliuskina et al.
Pulse-height defect in single-crystal CVD diamond detectors.
The European physical journal / A, 53(2):32.
doi: 10.1140/epja/i2017-12223-8.

S. Benić et al.
Probing gluon saturation with next-to-leading order photon production at central rapidities in proton-nucleus collisions.
Journal of high energy physics, 2017(1):115.
doi: 10.1007/JHEP01(2017)115.

BESIII Collaboration.
Amplitude analysis of $D^0 \to K^-\pi^+\pi^+\pi^-$.
Physical review / D, 95(7):072010.
doi: 10.1103/PhysRevD.95.072010.

BESIII Collaboration.
Amplitude Analysis of the Decays $\eta' \to \pi^+\pi^-\pi^0$ and $\eta' \to \pi^0\pi^0\pi^0$.
Physical review letters, 118(1):012001.
doi: 10.1103/PhysRevLett.118.012001.

BESIII Collaboration.
Branching fraction measurements of $\psi(3686) \to \gamma\chi_{cJ}$.
Physical review / D, 96(3):032001.
doi: 10.1103/PhysRevD.96.032001.

BESIII Collaboration.
Dark Photon Search in the Mass Range Between 1.5 and 3.4 GeV/c^2.
Physics letters / B, 774:252.
doi: 10.1016/j.physletb.2017.09.067.

BESIII Collaboration.
Determination of the number of J/ψ events with inclusive J/ψ decays.
Chinese physics / C, 41(1):013001.
doi: 10.1088/1674-1137/41/1/013001.

BESIII Collaboration.
Evidence for $e^+e^- \to \gamma\eta_c(1S)$ at center-of-mass energies between 4.01 and 4.60 GeV.
Physical review / D, 96(5):051101.
doi: 10.1103/PhysRevD.96.051101.

BESIII Collaboration.
Evidence for the singly-Cabibbo-suppressed decay $\Lambda_c^+ \to p\eta$ and search for $\Lambda_c^+ \to p\pi^0$.
Physical review / D, 95(11):111102.
doi: 10.1103/PhysRevD.95.111102.

BESIII Collaboration.
Luminosity measurements for the R scan experiment at BESIII.
Chinese physics / C, 41(6):063001.
doi: 10.1088/1674-1137/41/6/063001.

BESIII Collaboration.
Measurement of integrated luminosity and center-of-mass energy of data taken by BESIII at.
Chinese physics / C, 41(11):113001.
doi: 10.1088/1674-1137/41/11/113001.

BESIII Collaboration.
Observation of $\psi(3686) \to e^+e^-\chi_{cJ}$ and $\chi_{cJ} \to e^+e^-J/\psi$.
Physical review letters, 118(22):221802.
doi: 10.1103/PhysRevLett.118.221802.

BESSIII Collaboration.
Observation of $e^+e^- \to \eta h_c$ at center-of-mass energies from 4.085 to 4.600 GeV.
Physical review / D, 96(1):012001.
doi: 10.1103/PhysRevD.96.012001.

M. Bleicher and J. Steinheimer.
Sub-threshold charm and strangeness production at GSI/FAIR energies.
Astronomische Nachrichten, 338(9-10):1101.
doi: 10.1002/asna.201713442.

J. Bliss et al.
Impact of (α , n) reactions on weak r-process in neutrino-driven winds.
Journal of physics / G, 44(5):054003.
doi: 10.1088/1361-6471/aa63bd.

M. Block.
Recent trends in precision measurements of atomic and nuclear properties with lasers and ion traps.
Hyperfine interactions, 238(1):40.
doi: 10.1007/s10751-017-1410-1.

R. Bollig et al.
Muon Creation in Supernova Matter Facilitates Neutrino-Driven Explosions.
Physical review letters, 119(24):242702.
doi: 10.1103/PhysRevLett.119.242702.

A. S. Botvina et al.
Formation of hypernuclei in heavy-ion collisions around the threshold energies.
Physical review / C, 95(1):014902.
doi: 10.1103/PhysRevC.95.014902.

L. Bovard et al.
r -process nucleosynthesis from matter ejected in binary neutron star mergers.
Physical review / D, 96(12):124005.
doi: 10.1103/PhysRevD.96.124005.

E. L. Bratkovskaya, W. Cassing and O. Linnyk.
Electromagnetic emissivity of hot and dense matter.
Astronomische Nachrichten, 338(9-10):1038.
doi: 10.1002/asna.201713431.

E. Bratkovskaya et al.
Chiral symmetry restoration versus deconfinement in heavy-ion collisions at high baryon density.
Journal of physics / Conference Series, 878:012018.
doi: 10.1088/1742-6596/878/1/012018.

P. Braun-Munzinger, A. Rustamov and J. Stachel.
Bridging the gap between event-by-event fluctuation measurements and theory predictions in relativistic nuclear collisions.
Nuclear physics / A, A960:114.
doi: 10.1016/j.nuclphysa.2017.01.011.

R. A. Briceño, M. T. Hansen and C. J. Monahan.
Role of the Euclidean signature in lattice calculations of quasidistributions and other nonlocal matrix elements.
Physical review / D, 96(1):014502.
doi: 10.1103/PhysRevD.96.014502.

R. A. Briceño, M. T. Hansen and S. R. Sharpe.
Relating the finite-volume spectrum and the two-and-three-particle S matrix for relativistic systems of identical scalar particles.
Physical review / D, 95(7):074510.
doi: 10.1103/PhysRevD.95.074510.

M. W. Bruker, S. Friederich and K. Aulenbacher.
A test set-up for electron collector efficiency measurements.
Nuclear instruments & methods in physics research / A, 872:169.
doi: 10.1016/j.nima.2017.08.025.

R. Caballero-Folch et al.
β -decay half-lives and β -delayed neutron emission probabilities for several isotopes of Au, Hg, Tl, Pb, and Bi, beyond N = 126.
Physical review / C, 95(6):064322.
doi: 10.1103/PhysRevC.95.064322.

L. C. Campo et al.
Investigating the γ decay of ^{65}Ni from particle- γ coincidence data.
Physical review / C, 96(1):014312.
doi: 10.1103/PhysRevC.96.014312.

Klochkov and I. Selyuzhenkov.
Centrality determination in heavy-ion collisions with the CBM experiment.
International Conference on Particle Physics and Astrophysics, Moscow (Russia), 10 Oct 2016 - 14 Oct 2016.
IOP Publ., Bristol, 10th Oct. 2016.
doi: 10.1088/1742-6596/798/1/012059.

S. Chakraborty et al.
Ground-state configuration of neutron-rich ^{35}Al via Coulomb breakup.
Physical review / C, 96(3):034301.
doi: 10.1103/PhysRevC.96.034301.

G. Chatzidrosos et al.
Miniature Cavity-Enhanced Diamond Magnetometer.
Physical review applied, 8(4):044019.
doi: 10.1103/PhysRevApplied.8.044019.

J. Chen et al.
Optical quenching and recovery of photoconductivity in single-crystal diamond.
Applied physics letters, 110(1):3.
doi: 10.1063/1.4973692.

P. Chhetri et al.
Impact of buffer gas quenching on the $^1S_0 \rightarrow {}^1P_1$ ground-state atomic transition in nobelium.
The European physical journal / D, 71(7):195.
doi: 10.1140/epjd/e2017-80122-x.

L. X. Chung et al.
The dominance of the ν (0 $d_{5/2}$)^2 configuration in the N = 8 shell in ^{12}Be from the breakup reaction on a proton target at intermediate energy.
Physics letters / B, 774:559.
doi: 10.1016/j.physletb.2017.09.068.

J. Cleymans et al.
Collisions of Small Nuclei in the Thermal Model.
3. Critical Point and Onset of Deconfinement 2016, Wroclaw (Poland), 30 May 2016 - 4 Jun 2016.
Inst. of Physics, Jagellonian Univ., Cracow, 30th May 2016.
doi: 10.5506/APhysPolBSupp.10.531.

M. A. Dehn et al.
Reducing the contribution of the photoemission process to the unwanted beam in photoelectron sources at accelerators.
Applied physics letters, 111(13):132105.
doi: 10.1063/1.4996977.

A. Deisting and C. Garabatos.
Discharge and stability studies for the new readout chambers of the upgraded ALICE TPC.
Journal of Instrumentation, 12(05):C05017.
doi: 10.1088/1748-0221/12/05/C05017.

A. Deisting et al.
Measurements of ion mobility in argon and neon based gas mixtures.
Nuclear instruments & methods in physics research / A, 845:215.
doi: 10.1016/j.nima.2016.06.093.

A. Del Dotto et al.
Design and $R\&D$ of RICH detectors for EIC experiments.
Nuclear instruments & methods in physics research / A, 876:237.
doi: 10.1016/j.nima.2017.03.032.

T. Dickel et al.
Dynamical time focus shift in multiple-reflection time-of-flight mass spectrometers.
International journal of mass spectrometry, 412:1.
doi: 10.1016/j.ijms.2016.11.005.

T. Dickel et al.
Isobar Separation in a Multiple-Reflection Time-of-Flight Mass Spectrometer by Mass-Selective Re-Trapping.
Journal of the American Society for Mass Spectrometry, 28(6):1079.
doi: 10.1007/s13361-017-1617-z.

C. E. Düllmann.
Studying Chemical Properties of the Heaviest Elements: One Atom at a Time.
Nuclear physics news, 27(2):14.
doi: 10.1080/10619127.2017.1280333.

M. Düren et al.
The Endcap Disc DIRC of PANDA.
Nuclear instruments & methods in physics research / A, 876:198.
doi: 10.1016/j.nima.2017.02.077.

V. A. Dzuba and V. V. Flambaum.
Limits on gravitational Einstein equivalence principle violation from monitoring atomic clock frequencies during a year.
Physical review / D, 95(1):015019.
doi: 10.1103/PhysRevD.95.015019.

V. A. Dzuba, V. V. Flambaum and J. K. Webb.
Isotope shift and search for metastable superheavy elements in astrophysical data.
Physical review / A, 95(6):062515.
doi: 10.1103/PhysRevA.95.062515.

S. Ebihara, K. Fukushima and K. Mameda.
Boundary effects and gapped dispersion in rotating fermionic matter.
Physics letters / B, 764:94.
doi: 10.1016/j.physletb.2016.11.010.

A. Echler et al.
Determination of electronic stopping powers of 0.05–1MeV/u ^{131}Xe ions in C-, Ni- and Au-absorbers with calorimetric low temperature detectors.
Nuclear instruments & methods in physics research / B, 391:38.
doi: 10.1016/j.nimb.2016.10.011.

J. Eills et al.
Measuring molecular parity nonconservation using nuclear-magnetic-resonance spectroscopy.
Physical review / A, 96(4):042119.
doi: 10.1103/PhysRevA.96.042119.

V. Eremin et al.
Beam tests of full-size prototypes of silicon detectors for TOF heavy-ions diagnostics in Super-FRS.
Journal of Instrumentation, 12(03):C03001.
doi: 10.1088/1748-0221/12/03/C03001.

R. Ferrer et al.
Towards high-resolution laser ionization spectroscopy of the heaviest elements in supersonic gas jet expansion.
Nature Communications, 8:14520.
doi: 10.1038/ncomms14520.

F. Ficek et al.
Constraints on exotic spin-dependent interactions between electrons from helium fine-structure spectroscopy.
Physical review / A, 95(3):032505.
doi: 10.1103/PhysRevA.95.032505.

T. Fischer et al.
The State of Matter in Simulations of Core-Collapse supernovae—Reflections and Recent Developments.
Publications of the Astronomical Society of Australia, 34:e067.
doi: 10.1017/pasa.2017.63.

V. V. Flambaum and M. V. Romalis.
Effects of the Lorentz Invariance Violation on Coulomb Interactions in Nuclei and Atoms.
Physical review letters, 118(14):142501.
doi: 10.1103/PhysRevLett.118.142501.

W. Florkowski et al.
Relativistic Hydrodynamics of Particles with Spin 1/2.
4. Excited QCD 2017, Lisbon (Portugal), 7 May 2017 - 13 May 2017.
Inst. of Physics, Jagellonian Univ., Cracow, 7th May 2017.
doi: 10.5506/APhysPolBSupp.10.1139.

V. Friese and CBM Collaboration.
The high-rate data challenge: computing for the CBM experiment.
22nd International Conference on Computing in High Energy and Nuclear Physics, San Francisco (USA), 10 Oct 2016 - 14 Oct 2016.
IOP Publ., Bristol, 10th Oct. 2016.
doi: 10.1088/1742-6596/898/11/112003.

B. Friman, G. A. Almási and K. Redlich.
Modeling Chiral Criticality.
3. Critical Point and Onset of Deconfinement 2016, Wroclaw (Poland), 30 May 2016 - 4 Jun 2016.
Inst. of Physics, Jagellonian Univ., Cracow, 30th May 2016.
doi: 10.5506/APhysPolBSupp.10.567.

L. Gamer et al.
Simulation and optimization of the implantation of holmium atoms into metallic magnetic microcalorimeters for neutrino mass determination experiments.
Nuclear instruments & methods in physics research / A, 854:139.
doi: 10.1016/j.nima.2017.02.056.

L. Gastaldo et al.
The electron capture in ^{163}Ho experiment – ECHo.
European physical journal special topics, 226(8):1623.
doi: 10.1140/epjst/e2017-70071-y.

F. Giacoppo et al.
Recent Upgrades of the SHIPTRAP Setup: On the Finish Line Towards Direct Mass Spectroscopy of Superheavy Elements.
Acta physica Polonica / B, 48(3):423.
doi: 10.5506/APhysPolB.48.423.

S. Giron et al.
Spectroscopy of Fe 61 via the neutron transfer reaction H 2 (Fe 60 , p) Fe * 61.
Physical review / C, 95(3):035806.
doi: 10.1103/PhysRevC.95.035806.

M. Götz et al.
Radiochemical study of the kinematics of multi-nucleon transfer reactions in ^{48}Ca + ^{248}Cm collisions 10% above the Coulomb barrier.
Nuclear physics / A, 961:1.
doi: 10.1016/j.nuclphysa.2017.02.006.

group, FCC-ions study.
Physics with ions at the Future Circular Collider.
Nuclear physics / A, 967:888.
doi: 10.1016/j.nuclphysa.2017.06.029.

R. Haas et al.
Development and characterization of a Drop-on-Demand inkjet printing system for nuclear target fabrication.
Nuclear instruments & methods in physics research / A, 874:43.
doi: 10.1016/j.nima.2017.08.027.

R. Han et al.
Is light narrowing possible with dense-vapor paraffin coated cells for atomic magnetometers?
AIP Advances, 7(12):125224.
doi: 10.1063/1.4997691.

M. Hanauske et al.
Rotational properties of hypermassive neutron stars from binary mergers.
Physical review / D, 96(4):043004.
doi: 10.1103/PhysRevD.96.043004.

M. T. Hansen, H. B. Meyer and D. Robaina.
From deep inelastic scattering to heavy-flavor semileptonic decays: Total rates into multihadron final states from lattice QCD.
Physical review / D, 96(9):094513.
doi: 10.1103/PhysRevD.96.094513.

M. T. Hansen and S. R. Sharpe.
Applying the relativistic quantization condition to a three-particle bound state in a periodic box.
Physical review / D, 95(3):034501.
doi: 10.1103/PhysRevD.95.034501.

C. Harabati et al.
Electron recombination with tungsten ions with open f -shells.
Journal of physics / B, 50(12):125004.
doi: 10.1088/1361-6455/aa6cd1.

C. Hebborn and P. Capel.
Analysis of corrections to the eikonal approximation.
Physical review / C, 96(5):054607.
doi: 10.1103/PhysRevC.96.054607.

R. Heinke et al.
High-resolution in-source laser spectroscopy in perpendicular geometry.
Hyperfine interactions, 238(1):6.
doi: 10.1007/s10751-016-1386-2.

F. Heßberger and D. Ackermann.
Some critical remarks on a sequence of events interpreted to possibly originate from a decay chain of an element 120 isotope.
The European physical journal / A, 53(6):123.
doi: 10.1140/epja/i2017-12307-5.

F.-P. Hessberger.
Spontaneous fission properties of superheavy elements.
The European physical journal / A, 53(4):75.
doi: 10.1140/epja/i2017-12260-3.

G. von Hippel et al.
Nucleon matrix elements from lattice QCD with all-mode-averaging and a domain-decomposed solver: An exploratory study.
Nuclear physics / B, 914:138.
doi: 10.1016/j.nuclphysb.2016.11.003.

F. Horst, G. Fehrenbacher and K. Zink.
On the neutron radiation field and air activation around a medical electron linac.
Radiation protection dosimetry, 174(2):147.
doi: 10.1093/rpd/ncw120.

P. Huovinen et al.
Effects of ρ -meson width on pion distributions in heavy-ion collisions.
Physics letters / B, 769:509.
doi: 10.1016/j.physletb.2017.03.060.

J. W. Hwang et al.
Corrigendum to "Single-neutron knockout from ^{20}C and the structure of ^{20}C" [Phys. Lett. B 769 (2017) 503–508].
Physics letters / B, 774:723.
doi: 10.1016/j.physletb.2017.08.072.

J. W. Hwang et al.
Single-neutron knockout from ^{20}C and the structure of ^{19}C.
Physics letters / B, 769:503.
doi: 10.1016/j.physletb.2017.04.019.

M. Iliaš and V. Pershina.
Hexacarbonyls of Mo, W, and Sg: Metal–CO Bonding Revisited.
Inorganic chemistry, 56(3):1638.
doi: 10.1021/acs.inorgchem.6b02759.

A. Ilner et al.
K * vector meson resonance dynamics in heavy-ion collisions.
Physical review / C, 95(1):014903.
doi: 10.1103/PhysRevC.95.014903.

A. Jaiswal and V. Koch.
A viscous blast-wave model for heavy-ion collisions.
16th International Conference on Strangeness in Quark Matter, Berkeley (USA), 27 Jun 2016 - 1 Jul 2016.
IOP Publ., Bristol, 27th June 2016.
doi: 10.1088/1742-6596/779/1/012065.

A. Jungclaus et al.
Observation of a γ -decaying millisecond isomeric state in 128 Cd 80.
Physics letters / B, 772:483.
doi: 10.1016/j.physletb.2017.07.006.

J. Kahlbow et al.
Neutron radioactivity—Lifetime measurements of neutron-unbound states.
Nuclear instruments & methods in physics research / A, 866:265.
doi: 10.1016/j.nima.2017.06.002.

D. Kaji et al.
Study of the Reaction ^{48}Ca + ^{248}Cm → ^{296} Lv* at RIKEN-GARIS.
Journal of the Physical Society of Japan, 86(3):034201.
doi: 10.7566/JPSJ.86.034201.

P. Kehayias et al.
Solution nuclear magnetic resonance spectroscopy on a nanostructured diamond chip.
Nature Communications, 8(1):188.
doi: 10.1038/s41467-017-00266-4.

J. P. King, T. F. Sjolander and J. W. Blanchard.
Antisymmetric Couplings Enable Direct Observation of Chirality in Nuclear Magnetic Resonance Spectroscopy.
The journal of physical chemistry letters, 8(4):710.
doi: 10.1021/acs.jpclett.6b02653.

N. Kivel and M. Vanderhaeghen.
Radiative decays χ c J → V γ within the QCD factorization framework.
Physical review / D, 96(5):054007.
doi: 10.1103/PhysRevD.96.054007.

S. König.
Second-order perturbation theory for ^{3}He and pd scattering in pionless EFT.
Journal of physics / G, 44(6):064007.
doi: 10.1088/1361-6471/aa60d6.

S. König et al.
Nuclear Physics Around the Unitarity Limit.
Physical review letters, 118(20):202501.
doi: 10.1103/PhysRevLett.118.202501.

J. Konki et al.
Towards saturation of the electron-capture delayed fission probability: The new isotopes ^{240}Es and ^{236}Bk.
Physics letters / B, 764:265.
doi: 10.1016/j.physletb.2016.11.038.

S. Kraft-Bermuth et al.
Precise determination of the 1s Lamb shift in hydrogen-like lead and gold using microcalorimeters.
Journal of physics / B, 50(5):055603.
doi: 10.1088/1361-6455/50/5/055603.

D. T. Kutzke et al.
Tailorable dispersion in a four-wave mixing laser.
Optics letters, 42(14):2846.
doi: 10.1364/OL.42.002846.

D. Lascar et al.
Precision mass measurements of $^{125–127}$ Cd isotopes and isomers approaching the N = 82 closed shell.
Physical review / C, 96(4):044323.
doi: 10.1103/PhysRevC.96.044323.

J. Lassen et al.
Current developments with TRIUMF's titanium-sapphire laser based resonance ionization laser ion source.
Hyperfine interactions, 238(1):33.
doi: 10.1007/s10751-017-1407-9.

N. Leefer et al.
Investigation of two-frequency Paul traps for antihydrogen production.
Hyperfine interactions, 238(1):12.
doi: 10.1007/s10751-016-1388-0.

A. Lehmann et al.
Recent developments with microchannel-plate PMTs.
Nuclear instruments & methods in physics research / A, 876:42.
doi: 10.1016/j.nima.2016.12.063.

A. Lehmann et al.
Tremendously increased lifetime of MCP-PMTs.
Nuclear instruments & methods in physics research / A, 845:570.
doi: 10.1016/j.nima.2016.05.017.

H. Li et al.
Local and global Λ polarization in a vortical fluid.
Nuclear physics / A, 967:772.
doi: 10.1016/j.nuclphysa.2017.04.008.

W. Li et al.
Characterization of high-temperature performance of cesium vapor cells with anti-relaxation coating.
Journal of applied physics, 121(6):063104.
doi: 10.1063/1.4976017.

W. Li et al.
Hybrid optical pumping of K and Rb atoms in a paraffin coated vapor cell.
Optics letters, 42(20):4163.
doi: 10.1364/OL.42.004163.

P. M. Lo.
S-matrix formulation of thermodynamics with N-body scatterings.
The European physical journal / C, 77(8):533.
doi: 10.1140/epjc/s10052-017-5106-0.

P. M. Lo et al.
Repulsive interactions and their effects on the thermodynamics of a hadron gas.
Physical review / C, 96(1):015207.
doi: 10.1103/PhysRevC.96.015207.

C. Lorenz et al.
Quantum-state-selective decay spectroscopy of ^{213}Ra.
Physical review / C, 96(3):034315.
doi: 10.1103/PhysRevC.96.034315.

F. Maas and K. D. Paschke.
Strange nucleon form-factors.
Progress in particle and nuclear physics, 95:209.
doi: 10.1016/j.ppnp.2016.11.001.

H. Malygina and V. Friese.
A precision device needs precise simulation: Software description of the CBM Silicon Tracking System.
22nd International Conference on Computing in High Energy and Nuclear Physics, San Francisco (USA), 10 Oct 2016 - 14 Oct 2016.
IOP Publ., Bristol, 10th Oct. 2016.
doi: 10.1088/1742-6596/898/4/042022.

T. Marketin et al.
Microscopic Calculations of β-decay Rates for r-process.
Acta physica Polonica / B, 48(3):641.
doi: 10.5506/APhysPolB.48.641.

L. D. Meder et al.
A Timing Synchronizer System for Beam Test Setups Requiring Galvanic Isolation.
IEEE transactions on nuclear science, 64(7):1975.
doi: 10.1109/TNS.2017.2713524.

H. B. Meyer.
Lorentz-covariant coordinate-space representation of the leading hadronic contribution to the anomalous magnetic moment of the muon.
The European physical journal / C, 77(9):616.
doi: 10.1140/epjc/s10052-017-5200-3.

J. Michel et al.
Electronics for the RICH detectors of the HADES and CBM experiments.
01. Topical Workshop on Electronics for Particle Physics, Karlsruhe (Germany), 26 Sep 2016 - 30 Sep 2016.
Inst. of Physics, London, 26th Sept. 2016.
doi: 10.1088/1748-0221/12/01/C01072.

P. Moreau et al.
Evidence for chiral symmetry restoration in heavy-ion collisions.
Nuclear physics / A, 967:836.
doi: 10.1016/j.nuclphysa.2017.05.030.

M. D. Morte et al.
The hadronic vacuum polarization contribution to the muon g − 2 from lattice QCD.
Journal of high energy physics, 2017(10):20.
doi: 10.1007/JHEP10(2017)020.

N. Nakatsuka et al.
Observation of isoscalar and isovector dipole excitations in neutron-rich ^{20}O.
Physics letters / B, 768:387.
doi: 10.1016/j.physletb.2017.03.017.

Y. Nara et al.
Equation of state dependence of directed flow in a microscopic transport model.
Physics letters / B, 769:543.
doi: 10.1016/j.physletb.2017.02.020.

D. A. Nesterenko et al.
High-precision mass measurements for the isobaric multiplet mass equation at A = 52.
Journal of physics / G, 44(6):065103.
doi: 10.1088/1361-6471/aa67ae.

M. Oertel et al.
Equations of state for supernovae and compact stars.
Reviews of modern physics, 89(1):015007.
doi: 10.1103/RevModPhys.89.015007.

H. Oeschler et al.
Ratios of strange hadrons to pions in collisions of large and small nuclei.
The European physical journal / C, 77(9):584.
doi: 10.1140/epjc/s10052-017-5177-y.

D. Oliinychenko and H. Petersen.
Effective dynamical coupling of hydrodynamics and transport for heavy-ion collisions.
Journal of physics / Conference Series, 832:012052.
doi: 10.1088/1742-6596/832/1/012052.

D. Oliinychenko and H. Petersen.
Forced canonical thermalization in a hadronic transport approach at high density.
Journal of physics / G, 44(3):034001.
doi: 10.1088/1361-6471/aa528c.

L.-G. Pang et al.
Vorticity and Λ polarization in event-by-event (3+1)D viscous hydrodynamics.
Journal of physics / Conference Series, 779:012069.
doi: 10.1088/1742-6596/779/1/012069.

C. Paradela et al.
Isotopic production cross sections of residual nuclei in the spallation reaction ^{136}Xe (200 A MeV) + p.
Physical review / C, 95(4):044606.
doi: 10.1103/PhysRevC.95.044606.

E. Pellereau et al.
Accurate isotopic fission yields of electromagnetically induced fission of ^{238}U measured in inverse kinematics at relativistic energies.
Physical review / C, 95(5):054603.
doi: 10.1103/PhysRevC.95.054603.

V. Pershina and M. Iliaš.
Penta- and tetracarbonyls of Ru, Os, and Hs: Electronic structure, bonding, and volatility.
The journal of chemical physics, 146(18):184306.
doi: 10.1063/1.4983125.

K. Peters et al.
PANDA: Strong Interaction Studies with Antiprotons.
Nuclear physics news, 27(3):24.
doi: 10.1080/10619127.2017.1351182.

H. Petersen.
Beam energy scan theory: Status and open questions.
Nuclear physics / A, 967:145.
doi: 10.1016/j.nuclphysa.2017.04.018.

H. Petersen.
Nuclear physics: The fastest-rotating fluid.
Nature, 548(7665):34.
doi: 10.1038/548034a.

M. Pfaffinger et al.
Recent results with lifetime enhanced microchannel-plate photomultipliers.
Nuclear instruments & methods in physics research / A, 876:S0168900217311713.
doi: 10.1016/j.nima.2017.10.084.

L. Piersanti et al.
SNe Ia Keep Memory of Their Progenitor Metallicity.
The astrophysical journal / 2, 836(1):L9.
doi: 10.3847/2041-8213/aa5c7e.

S. Purushothaman et al.
Hyper-EMG: A new probability distribution function composed of Exponentially Modified Gaussian distributions to analyze asymmetric peak shapes in high-resolution time-of-flight mass spectrometry.
International journal of mass spectrometry, 421:245.
doi: 10.1016/j.ijms.2017.07.014.

S. Raeder et al.
High resolution spectroscopy of the hyperfine structure splitting in 97,99Tc.
Hyperfine interactions, 238(1):15.
doi: 10.1007/s10751-016-1389-z.

D. Ralet et al.
Lifetime measurement of neutron-rich even-even molybdenum isotopes.
Physical review / C, 95(3):034320.
doi: 10.1103/PhysRevC.95.034320.

D. B. Ríos et al.
New Measurements of the Beam Normal Spin Asymmetries at Large Backward Angles with Hydrogen and Deuterium Targets.
Physical review letters, 119(1):012501.
doi: 10.1103/PhysRevLett.119.012501.

J. L. Rodríguez-Sánchez et al.
Fission dynamics at high excitation energies investigated in complete kinematics measurements.
Journal of physics / Conference Series, 863:012047.
doi: 10.1088/1742-6596/863/1/012047.

J. L. Rodríguez-Sánchez et al.
Knockout and fragmentation reactions using a broad range of tin isotopes.
Physical review / C, 96(3):034303.
doi: 10.1103/PhysRevC.96.034303.

S. Rosswog et al.
Detectability of compact binary merger macronovae.
Classical and quantum gravity, 34(10):104001.
doi: 10.1088/1361-6382/aa68a9.

P. Russotto et al.
Probing the Symmetry Term of the Nuclear Equation of State at High Baryonic Densities.
Journal of physics / Conference Series, 863:012059.
doi: 10.1088/1742-6596/863/1/012059.

L. M. Satarov et al.
Bose–Einstein condensation and liquid–gas phase transition in strongly interacting matter composed of α particle.
Journal of physics / G, 44(12):125102.
doi: 10.1088/1361-6471/aa8c5d.

L. M. Satarov et al.
New scenarios for hard-core interactions in a hadron resonance gas.
Physical review / C, 95(2):024902.
doi: 10.1103/PhysRevC.95.024902.

M. Schmidt et al.
Particle identification algorithms for the PANDA Endcap Disc DIRC.
Journal of Instrumentation, 12(12):C12051.
doi: 10.1088/1748-0221/12/12/C12051.

P. A. Scholz et al.
High-precision X-ray spectroscopy of highly-charged ions at the experimental storage ring using silicon microcalorimeters.
Nuclear instruments & methods in physics research / B, 408:323.
doi: 10.1016/j.nimb.2017.04.078.

B. Schuetrumpf and W. Nazarewicz.
Cluster formation in precompound nuclei in the time-dependent framework.
Physical review / C, 96(6):064608.
doi: 10.1103/PhysRevC.96.064608.

C. Schwarz et al.
The PANDA DIRC detectors at FAIR.
07. INSTR17: Instrumentation for Colliding Beam Physics, Novosibirsk (Russia), 27 Feb 2017 - 3 Mar 2017.
Inst. of Physics, London, 27th Feb. 2017.
doi: 10.1088/1748-0221/12/07/C07006.

K. Schweda.
Experimental Overview of Open Heavy Flavor.
Journal of physics / Conference Series, 779:012001.
doi: 10.1088/1742-6596/779/1/012001.

V. M. Shapoval, P. Braun-Munzinger and Y. M. Sinyukov.
$K^*(892)$ and $\phi(1020)$ production and their decay into the hadronic medium at the Large Hadron Collider.
Nuclear physics / A, 968:391.
doi: 10.1016/j.nuclphysa.2017.09.002.

B. Singh et al.
Feasibility study for the measurement of πN transition distribution amplitudes at PANDA in $\bar{p}p \to J/\psi\pi^0$.
Physical review / D, 95(3):032003.
doi: 10.1103/PhysRevD.95.032003.

T. F. Sjolander et al.
^{13}C-Decoupled J -Coupling Spectroscopy Using Two-Dimensional Nuclear Magnetic Resonance at Zero-Field2.
The journal of physical chemistry letters, 8(7):1512.
doi: 10.1021/acs.jpclett.7b00349.

T. Song, J. Aichelin and E. Bratkovskaya.
Production of primordial J / ψ in relativistic p + p and heavy-ion collisions.
Physical review / C, 96(1):014907.
doi: 10.1103/PhysRevC.96.014907.

T. Song et al.
Single electrons from heavy-flavor mesons in relativistic heavy-ion collisions.
Physical review / C, 96(1):014905.
doi: 10.1103/PhysRevC.96.014905.

V. Sonnenschein et al.
Characterization of a pulsed injection-locked Ti:sapphire laser and its application to high resolution resonance ionization spectroscopy of copper.
Laser physics, 27(8):085701.
doi: 10.1088/1555-6611/aa7834.

E. Speranza, M. Zétényi and B. Friman.
Polarization and dilepton anisotropy in pion–nucleon collisions.
Physics letters / B, 764:282.
doi: 10.1016/j.physletb.2016.11.015.

D. K. Srivastava, S. A. Bass and R. Chatterjee.
Production of charm quarks in a parton cascade model for relativistic heavy ion collisions at $\sqrt{s_{NN}}$ = 200 GeV.
Physical review / C, 96(6):064906.
doi: 10.1103/PhysRevC.96.064906.

J. Staudenmaier, J. Weil and H. Petersen.
Non-equilibrium dilepton production in hadronic transport approaches.
Journal of physics / Conference Series, 832:012037.
doi: 10.1088/1742-6596/832/1/012037.

J. Steinheimer et al.
Influence of the hadronic phase on observables in ultrarelativistic heavy ion collisions.
Physical review / C, 95(6):064902.
doi: 10.1103/PhysRevC.95.064902.

J. Struckmeier et al.
Canonical transformation path to gauge theories of gravity.
Physical review / D, 95(12):124048.
doi: 10.1103/PhysRevD.95.124048.

T. Suda and H. Simon.
Prospects for electron scattering on unstable, exotic nuclei.
Progress in particle and nuclear physics, 96:1.
doi: 10.1016/j.ppnp.2017.04.002.

Y. K. Tanaka et al.
First Results on the Experimental Search for η'-Mesic Nuclei with the ^{12}C(p, d) Reaction.
Acta physica Polonica / B, 48(10):1813.
doi: 10.5506/APhysPolB.48.1813.

M. C. D. Tayler et al.
Invited Review Article: Instrumentation for nuclear magnetic resonance in zero and ultralow magnetic field.
Review of scientific instruments, 88(9):091101.
doi: 10.1063/1.5003347.

F.-K. Thielemann et al.
Neutron Star Mergers and Nucleosynthesis of Heavy Elements.
Annual review of nuclear and particle science, 67(1):253.
doi: 10.1146/annurev-nucl-101916-123246.

J. Tindall et al.
Equilibration and freeze-out of an expanding gas in a transport approach in a Friedmann–Robertson–Walker metric.
Physics letters / B, 770:532.
doi: 10.1016/j.physletb.2017.04.080.

L. Tinti, A. Jaiswal and R. Ryblewski.
Quasiparticle second-order viscous hydrodynamics from kinetic theory.
Physical review / D, 95(5):054007.
doi: 10.1103/PhysRevD.95.054007.

E. Uberseder et al.
Stellar (n,γ) cross sections of ^{23}Na.
Physical review / C, 95(2):025803.
doi: 10.1103/PhysRevC.95.025803.

M. Vandebrouck et al.
Effective proton-neutron interaction near the drip line from unbound states in ^{25,26}F.
Physical review / C, 96(5):054305.
doi: 10.1103/PhysRevC.96.054305.

V. Vovchenko, M. I. Gorenstein and H. Stoecker.
van der Waals Interactions in Hadron Resonance Gas: From Nuclear Matter to Lattice QCD.
Physical review letters, 118(18):182301.
doi: 10.1103/PhysRevLett.118.182301.

V. Vovchenko and H. Stoecker.
Examination of the sensitivity of the thermal fits to heavy-ion hadron yield data to the modeling of the eigenvolume interactions.
Physical review / C, 95(4):044904.
doi: 10.1103/PhysRevC.95.044904.

V. Vovchenko and H. Stoecker.
Surprisingly large uncertainties in temperature extraction from thermal fits to hadron yield data at LHC.
Journal of physics / G, 44(5):055103.
doi: 10.1088/1361-6471/aa6409.

V. Vovchenko et al.
Multicomponent van der Waals equation of state: Applications in nuclear and hadronic physics.
Physical review / C, 96(4):045202.
doi: 10.1103/PhysRevC.96.045202.

V. Vovchenko et al.
Repulsive baryonic interactions and lattice QCD observables at imaginary chemical potential.
Physics letters / B, 775:71.
doi: 10.1016/j.physletb.2017.10.042.

G. L. Wilson et al.
β -delayed fission of ^{230}Am.
Physical review / C, 96(4):044315.
doi: 10.1103/PhysRevC.96.044315.

A. Wilzewski et al.
A method for measurement of spin-spin couplings with sub-mHz precision using zero- to ultralow-field nuclear magnetic resonance.
Journal of magnetic resonance, 284:66.
doi: 10.1016/j.jmr.2017.08.016.

C. P. Wong et al.
Modular focusing ring imaging Cherenkov detector for electron–ion collider experiments.
Nuclear instruments & methods in physics research / A, 871:13.
doi: 10.1016/j.nima.2017.07.001.

Y. Xu et al.
Traces of nonequilibrium dynamics in relativistic heavy-ion collisions.
Physical review / C, 96(2):024902.
doi: 10.1103/PhysRevC.96.024902.

J. C. Zamora et al.
Nuclear-matter radius studies from ^{58}Ni(α, α) experiments at the GSI Experimental Storage Ring with the EXL facility.
Physical review / C, 96(3):034617.
doi: 10.1103/PhysRevC.96.034617.

X.-Y. Zhou, Y.-D. Wang and L.-G. Xia.
Analytic forms for cross sections of di-lepton production from e^+ e^- collisions around the J/Ψ resonance.
Chinese physics / C, 41(8):083001.
doi: 10.1088/1674-1137/41/8/083001.

S. Zimmermann et al.
The PANDA Barrel-TOF Detector at FAIR.
Journal of Instrumentation, 12(08):C08017.
doi: 10.1088/1748-0221/12/08/C08017.

18 dissertations

G. A. Almasi.
Properties of hot and dense strongly interacting matter.
TU Darmstadt, Darmstadt, 2017.

O. Arnold.
Study of the hyperon-nucleon interaction via femtoscopy in elementary systems with HADES and ALICE.
Technische Universität München, 2017.

J. Berlin.
Scalar tetraquark candidates on the lattice.
JWGU Frankfurt, Frankfurt am Main, 2017.

V. Di Pietro.
A time-based front-end ASIC for the silicon micro strip sensors of the PANDA Micro Vertex Detector.
JLU Giessen, Giessen, 2017.

E. Etzelmueller.
Developments towards the technical design and prototype evaluation of the PANDA Endcap Disc DIRC.
JLU Giessen, 2017.

M. Heiko.
Evolution of Degenerate Oxygen-Neon Cores.
TU Darmstadt, Darmstadt, 2017.

P. Huck.
Beam energy dependence of dielectron production in Au+Au collisions from STAR at RHIC.
JWGU Frankfurt, Frankfurt am Main, 2017.

T. Kunz.
Σ0-Produktion in p+Nb-Reaktionen bei E = 3,5 GeV.
Technische Universität München, 2017.

D. Martin.
r-process nucleosynthesis: on the astrophysical conditions and the impact of nuclear physics input.
TU Darmstadt, Darmstadt, 2017.

L. D. Meder.
Timing Synchronization and Fast-Control for FPGA-based large-scale Readout and Processing Systems.
Karlsruher Institut für Technologie, 2017.

D. Oliinychenko.
Interfaces between relativistic hydrodynamics and transport for the dynamical description of heavy ion collisions.
JWGU Frankfurt, Frankfurt am Main, 2017.

A. Riccardi.
Low power integrated system for a simultaneous time and energy measurement in the PANDA micro-strip detector.
JLU Giessen, Giessen, 2017.

A.-K. Rink.
Mass and Life-Time Measurement of the 1.7 MS ^{215}Po Isotope A Crucial Test of the Novel Concept of the Cryogenic Ion Catcher for the Super-FRS at GSI-FAIR.
Justus-Liebig Universität Gießen, 2017.

T. Scheib.
Λ and K0s production in Au+Au collisions at 1.23A GeV.
JWGU Frankfurt, Frankfurt am Main, 2017.

M. Schramm.
Goldstone Bosons in a Crystalline Chiral Phase.
TU Darmstadt, Darmstadt, 2017.

P. Sellheim.
Reconstruction of the low-mass dielectron signal in 1.23A GeV Au+Au collisions.
JWGU Frankfurt, Frankfurt am Main, 2017.

A. Tichai.
Many-Body Perturbation Theory for Ab Initio Nuclear Structure.
TU Darmstadt, Darmstadt, 2017.

A. Zacchi.
Thermal evolution of massive compact strange objects in a SU(3) chiral Quark Meson Model.
JWGU Frankfurt, Frankfurt am Main, 2017.

From matter to materials and life – 620

183 publications listed in Web of Science or SCOPUS

J. Adamczewski-Musch et al.
Δ (1232) Dalitz decay in proton-proton collisions at T = 1.25 GeV measured with HADES at GSI.
Physical review / C, 95(6):065205.
doi: 10.1103/PhysRevC.95.065205.

D. Adolph et al.
Real-time, single-shot, carrier-envelope-phase measurement of a multi-terawatt laser.
Applied physics letters, 110(8):081105.
doi: 10.1063/1.4976695.

V. A. Agababaev et al.
Quadratic Zeeman effect in boronlike argon.
18th International Conference on the Physics of Highly Charged Ions, Kielce (Poland), 11 Sep 2016 - 16 Sep 2016.
Elsevier, Amsterdam [u.a.], 11th Sept. 2016.
doi: 10.1016/j.nimb.2017.03.130.

M. Ali et al.
A redox-sensitive nanofluidic diode based on nicotinamide-modified asymmetric nanopores.
Sensors and actuators / B, 240:895.
doi: 10.1016/j.snb.2016.09.061.

M. Ali et al.
Cesium-Induced Ionic Conduction through a Single Nanofluidic Pore Modified with Calixcrown Moieties.
Langmuir, 33(36):9170.
doi: 10.1021/acs.langmuir.7b02368.

M. Ali et al.
Label-free histamine detection with nanofluidic diodes through metal ion displacement mechanism.
Colloids and surfaces / B, 150:201.
doi: 10.1016/j.colsurfb.2016.11.038.

M. Ali et al.
Tetraalkylammonium Cations Conduction through a Single Nanofluidic Diode: Experimental and Theoretical Studies.
Electrochimica acta, 250:302.
doi: 10.1016/j.electacta.2017.08.078.

N. A. Althubiti et al.
Spectroscopy of the long-lived excited state in the neutron-deficient nuclides ^{195,197,199}Po by precision mass measurements.
Physical review / C, 96(4):044325.
doi: 10.1103/PhysRevC.96.044325.

J. Andersson et al.
Auger decay of 4 d inner-shell holes in atomic Hg leading to triple ionization.
Physical review / A, 96(1):012505.
doi: 10.1103/PhysRevA.96.012505.

W. Assmann et al.
Charge-state related effects in sputtering of LiF by swift heavy ions.
Nuclear instruments & methods in physics research / B, 392:94.
doi: 10.1016/j.nimb.2016.12.013.

D. Atanasov et al.
Precision mass measurements of cesium isotopes—new entries in the ISOLTRAP chronicles.
Journal of physics / G, 44(4):044004.
doi: 10.1088/1361-6471/aa5a20.

D. Atanasov et al.
Studies at the border between nuclear and atomic physics: Weak decays of highly charged ions.
Journal of physics / Conference Series, 875:012008.
doi: 10.1088/1742-6596/875/2/012008.

V. Bagnoud et al.
Studying the Dynamics of Relativistic Laser-Plasma Interaction on Thin Foils by Means of Fourier-Transform Spectral Interferometry.
Physical review letters, 118(25):255003.
doi: 10.1103/PhysRevLett.118.255003.

R. Beerwerth and S. Fritzsche.
MCDF calculations of Auger cascade processes.
The European physical journal / D, 71(10):253.
doi: 10.1140/epjd/e2017-80064-3.

M. Bilal et al.
Ab initio calculations of energy levels, transition rates and lifetimes in Ni xii.
Monthly notices of the Royal Astronomical Society, 469(4):4620.
doi: 10.1093/mnras/stx1203.

A. A. Bogdanov et al.
Beam polarimetry at the SPASCHARM experiment at IHEP U-70 accelerator.
Journal of physics / Conference Series, 798:012179.
doi: 10.1088/1742-6596/798/1/012179.

M. Bohman et al.
Sympathetic cooling of protons and antiprotons with a common endcap Penning trap.
Journal of modern optics, 65(5-6):568.
doi: 10.1080/09500340.2017.1404656.

B. Böning, W. Paufler and S. Fritzsche.
Attosecond streaking with twisted X waves and intense infrared pulses.
Physical review / A, 96(4):043423.
doi: 10.1103/PhysRevA.96.043423.

J. Buldt et al.
Temporal contrast enhancement of energetic laser pulses by filtered self-phase-modulation-broadened spectra.
Optics letters, 42(19):3761.
doi: 10.1364/OL.42.003761.

M. Cassinelli et al.
Influence of surface states and size effects on the Seebeck coefficient and electrical resistance of Bi 1−x Sb x nanowire arrays.
Nanoscale, 9(9):3169.
doi: 10.1039/C6NR09624G.

W. Cayzac et al.
Experimental discrimination of ion stopping models near the Bragg peak in highly ionized matter.
Nature Communications, 8:15693.
doi: 10.1038/ncomms15693.

M. Chemnitz et al.
Hybrid soliton dynamics in liquid-core fibres.
Nature Communications, 8(1):42.
doi: 10.1038/s41467-017-00033-5.

X. C. Chen et al.
Statistical approaches to lifetime measurements with restricted observation times.
Physical review / C, 96(3):034302.
doi: 10.1103/PhysRevC.96.034302.

A. B. Cusick et al.
Amorphization of Ta_2O_5 under swift heavy ion irradiation.
Nuclear instruments & methods in physics research / B, 407:25.
doi: 10.1016/j.nimb.2017.05.036.

A. B. Cusick et al.
Phase transformation and chemical decomposition of nanocrystalline SnO_2 under heavy ion irradiation.
Nuclear instruments & methods in physics research / B, 407:10.
doi: 10.1016/j.nimb.2017.05.037.

E. Dartois et al.
Swift heavy ion irradiation of interstellar dust analogues.
Astronomy and astrophysics, 599:A130.
doi: 10.1051/0004-6361/201629646.

L. Deák et al.
Realizing total reciprocity violation in the phase for photon scattering.
Scientific reports, 7:43114.
doi: 10.1038/srep43114.

J. Deprince et al.
Influence of plasma environment on K-line emission in highly ionized iron atoms evaluated using a Debye–Hückel model.
9. the 12th International Colloquium on Atomic Spectra, Oscillator Strengths for Astrophysical and Laboratory Plasmas, Sao Paulo (Brazil), 4 Jul 2016 - 7 Jul 2016.
NRC Research Press, Ottawa, Ontario, 4th July 2016.
doi: 10.1139/cjp-2016-0667.

T. Egenolf, O. Boine-Frankenheim and U. Niedermayer.
Simulation of DLA grating structures in the frequency domain.
Journal of physics / Conference Series, 874:012040.
doi: 10.1088/1742-6596/874/1/012040.

M. Fernandes et al.
Non-perturbative measurement of low-intensity charged particle beams.
Superconductor science and technology, 30(1):015001.
doi: 10.1088/0953-2048/30/1/015001.

P. Finetti et al.
Pulse Duration of Seeded Free-Electron Lasers.
Physical review / X, 7(2):021043.
doi: 10.1103/PhysRevX.7.021043.

E. Fischer et al.
Nuclotron-Type Cables: From Fast Ramped Sc. Magnets to Multipurpose Application.
IEEE transactions on applied superconductivity, 27(4):1.
doi: 10.1109/TASC.2017.2663840.

G. Franchetti et al.
Space charge effects on the third order coupled resonance.
Physical review accelerators and beams, 20(8):081006.
doi: 10.1103/PhysRevAccelBeams.20.081006.

S. Fuchs et al.
Optical coherence tomography with nanoscale axial resolution using a laser-driven high-harmonic source.
Optica, 4(8):903.
doi: 10.1364/OPTICA.4.000903.

S. N. Galyamin, A. V. Tyukhtin and A. A. Peshkov.
Transition radiation at the boundary of a chiral isotropic medium.
Physical review / E, 95(3):032142.
doi: 10.1103/PhysRevE.95.032142.

M. Gebhardt et al.
High average power nonlinear compression to 4GW, sub-50fs pulses at 2µm wavelength.
Optics letters, 42(4):747.
doi: 10.1364/OL.42.000747.

M. Gebhardt et al.
Nonlinear pulse compression to 43W GW-class few-cycle pulses at 2µm wavelength.
Optics letters, 42(20):4179.
doi: 10.1364/OL.42.004179.

W. Geithner et al.
Status and outlook of the CRYRING@ESR project.
1. 10th International Workshop on Application of Lasers, Storage Devices in Atomic Nuclei Research: “Recent Achievements and Future Prospects” (LASER 2016), Poznań (Poland), 16 May 2016 - 19 May 2016.
Springer Science + Business Media B.V, Dordrecht [u.a.], 16th May 2016.
doi: 10.1007/s10751-016-1383-5.

H. Gies and F. Karbstein.
An addendum to the Heisenberg-Euler effective action beyond one loop.
Journal of high energy physics, 2017(3):108.
doi: 10.1007/JHEP03(2017)108.

H. Gies, R. Sondenheimer and M. Warschinke.
Impact of generalized Yukawa interactions on the lower Higgs-mass bound.
The European physical journal / C, 77(11):743.
doi: 10.1140/epjc/s10052-017-5312-9.

H. Gies and G. Torgrimsson.
Critical Schwinger pair production. II. Universality in the deeply critical regime.
Physical review / D, 95(1):016001.
doi: 10.1103/PhysRevD.95.016001.

H. Gies and L. Zambelli.
Non-Abelian Higgs models: Paving the way for asymptotic freedom.
Physical review / D, 96(2):025003.
doi: 10.1103/PhysRevD.96.025003.

J. S. M. Ginges, A. V. Volotka and S. Fritzsche.
Ground-state hyperfine splitting for Rb, Cs, Fr, Ba^+ , and Ra^+.
Physical review / A, 96(6):062502.
doi: 10.1103/PhysRevA.96.062502.

D. A. Glazov et al.
Higher-order perturbative relativistic calculations for few-electron atoms and ions.
Proceedings of the 18th International Conference on the Physics of Highly Charged Ions, Kielce (Poland), 11 Sep 2016 - 16 Sep 2016.
Elsevier, Amsterdam [u.a.], 11th Sept. 2016.
doi: 10.1016/j.nimb.2017.04.089.

J. Glorius et al.
Proton and α capture studies for nuclear astrophysics at GSI storage rings.
Journal of physics / Conference Series, 875:092015.
doi: 10.1088/1742-6596/875/10/092015.

C. Gorges et al.
Status of the TRIGA-LASER experiment.
1. 10th International Workshop on Application of Lasers, Storage Devices in Atomic Nuclei Research: "Recent Achievements and Future Prospects", Poznań (Poland), 16 May 2016 - 19 May 2016.
Springer Science + Business Media B.V, Dordrecht [u.a.], 16th May 2016.
doi: 10.1007/s10751-017-1400-3.

B. Goswami, B. Antony and S. Fritzsche.
Electron impact scattering and calculated ionization cross sections for SF_x (x = 1–5) radicals.
International journal of mass spectrometry, 417:8.
doi: 10.1016/j.ijms.2017.04.014.

C. Granados et al.
In-gas laser ionization and spectroscopy of actinium isotopes near the N = 126 closed shell.
Physical review / C, 96(5):054331.
doi: 10.1103/PhysRevC.96.054331.

A. Gumberidze et al.
Impact parameter sensitive study of inner-shell atomic processes in the experimental storage ring.
18th International Conference on the Physics of Highly Charged Ions, Kielce (Poland), 11 Sep 2016 - 16 Sep 2016.
Elsevier, Amsterdam [u.a.], 11th Sept. 2016.
doi: 10.1016/j.nimb.2017.04.090.

M. Günther et al.
Refractive-index measurement of Si at γ -ray energies up to 2 MeV.
Physical review / A, 95(5):053864.
doi: 10.1103/PhysRevA.95.053864.

P. Hansinger et al.
Refractive index dispersion measurement using carrier-envelope phasemeters.
New journal of physics, 19(2):023040.
doi: 10.1088/1367-2630/aa5ca3.

F. Heiße et al.
High-Precision Measurement of the Proton's Atomic Mass.
Physical review letters, 119(3):033001.
doi: 10.1103/PhysRevLett.119.033001.

S. H. Hendi et al.
Dilatonic black holes in gravity's rainbow with a nonlinear source: the effects of thermal fluctuations.
The European physical journal / C, 77(9):647.
doi: 10.1140/epjc/s10052-017-5211-0.

S. H. Hendi et al.
Three dimensional magnetic solutions in massive gravity with (non)linear field.
Physics letters / B, 775:251.
doi: 10.1016/j.physletb.2017.10.053.

S. H. Hendi et al.
Magnetic brane solutions in Gauss–Bonnet–Maxwell massive gravity.
Physics letters / B, 772:43.
doi: 10.1016/j.physletb.2017.06.012.

M. O. Herdrich et al.
Fast calculator for X-ray emission due to Radiative Recombination and Radiative Electron Capture in relativistic heavy-ion atom collisions.
18th Conference on the Physics of Highly Charged Ions, Kielce (Poland), 11 Sep 2016 - 16 Sep 2016.
Elsevier, Amsterdam [u.a.], 11th Sept. 2016.
doi: 10.1016/j.nimb.2017.04.022.

D. P. Higginson et al.
Detailed characterization of laser-produced astrophysically-relevant jets formed via a poloidal magnetic nozzle.
High energy density physics, 23:48.
doi: 10.1016/j.hedp.2017.02.003.

D. P. Higginson et al.
Enhancement of Quasistationary Shocks and Heating via Temporal Staging in a Magnetized Laser-Plasma Jet.
Physical review letters, 119(25):255002.
doi: 10.1103/PhysRevLett.119.255002.

J. Hofbrucker, A. V. Volotka and S. Fritzsche.
Photoelectron distribution of nonresonant two-photon ionization of neutral atoms.
Physical review / A, 96(1):013409.
doi: 10.1103/PhysRevA.96.013409.

J. Hofbrucker, A. V. Volotka and S. Fritzsche.
Relativistic effects in the non-resonant two-photon K -shell ionization of neutral atoms.
18th International Conference on the Physics of Highly Charged Ions, Kielce (Poland), 11 Sep 2016 - 16 Sep 2016.
Elsevier, Amsterdam [u.a.], 11th Sept. 2016.
doi: 10.1016/j.nimb.2017.03.153.

D. Hoff et al.
Tracing the phase of focused broadband laser pulses.
Nature physics, 13(10):947.
doi: 10.1038/nphys4185.

D. Hoff et al.
Using the focal phase to control attosecond processes.
Journal of optics, 19(12):124007.
doi: 10.1088/2040-8986/aa9247.

A. Hoffmann et al.
Online Monitoring of Laser-Generated XUV Radiation Spectra by Surface Reflectivity Measurements with Particle Detectors.
Applied Sciences, 7(1):70.
doi: 10.3390/app7010070.

R. Hollinger et al.
Enhanced absorption and cavity effects of three-photon pumped ZnO nanowires.
Applied physics letters, 111(21):213106.
doi: 10.1063/1.4999690.

U. H. Hossain et al.
SAXS investigation of un-etched and etched ion tracks in polycarbonate.
Nuclear instruments & methods in physics research / B, 409:293.
doi: 10.1016/j.nimb.2017.04.023.

M. Kahle et al.
Performance of a quantum defect minimized disk laser based on cryogenically cooled Yb:CaF_2.
Optics & laser technology, 92:19.
doi: 10.1016/j.optlastec.2016.12.025.

F. Karbstein.
Heisenberg-Euler effective action in slowly varying electric field inhomogeneities of Lorentzian shape.
Physical review / D, 95(7):076015.
doi: 10.1103/PhysRevD.95.076015.

F. Karbstein.
Photon Propagation in Slowly Varying Electromagnetic Fields.
Russian physics journal, 59(11):1761.
doi: 10.1007/s11182-017-0974-1.

F. Karbstein.
Tadpole diagrams in constant electromagnetic fields.
Journal of high energy physics, 2017(10):75.
doi: 10.1007/JHEP10(2017)075.

F. Karbstein and E. A. Mosman.
Photon polarization tensor in pulsed Hermite- and Laguerre-Gaussian beams.
Physical review / D, 96(11):116004.
doi: 10.1103/PhysRevD.96.116004.

M. F. Kasim et al.
Quantitative shadowgraphy and proton radiography for large intensity modulations.
Physical review / E, 95(2):023306.
doi: 10.1103/PhysRevE.95.023306.

D. Khaghani et al.
Enhancing laser-driven proton acceleration by using micro-pillar arrays at high drive energy.
Scientific reports, 7(1):11366.
doi: 10.1038/s41598-017-11589-z.

M. Kozák et al.
Acceleration of sub-relativistic electrons with an evanescent optical wave at a planar interface.
Optics express, 25(16):19195.
doi: 10.1364/OE.25.019195.

Y. S. Kozhedub et al.
Intensities of K -X-ray satellite and hypersatellite target radiation in Bi^{83+} -Xe @70 MeV/u collisions.
18th International Conference on the Physics of Highly Charged Ions, Kielce (Poland), 11 Sep 2016 - 16 Sep 2016.
Elsevier, Amsterdam [u.a.], 11th Sept. 2016.
doi: 10.1016/j.nimb.2017.04.045.

M. Kübel et al.
Streak Camera for Strong-Field Ionization.
Physical review letters, 119(18):183201.
doi: 10.1103/PhysRevLett.119.183201.

G. M. Kurtzer, V. Sochat and M. W. Bauer.
Singularity: Scientific containers for mobility of compute.
PLoS one, 12(5):e0177459.
doi: 10.1371/journal.pone.0177459.

C. Leithold et al.
Characterization of two ultrashort laser pulses using interferometric imaging of self-diffraction.
Optics letters, 42(24):5246.
doi: 10.1364/OL.42.005246.

H. Liebetrau et al.
Intracavity stretcher for chirped-pulse amplification in high-power laser systems.
Optics letters, 42(2):326.
doi: 10.1364/OL.42.000326.

B. Maaß et al.
Towards laser spectroscopy of the proton-halo candidate boron-8.
1. 10th International Workshop on Application of Lasers, Storage Devices in Atomic Nuclei Research: “Recent Achievements and Future Prospects”, Poznań (Poland), 16 May 2016 - 19 May 2016.
Springer Science + Business Media B.V, Dordrecht [u.a.], 16th May 2016.
doi: 10.1007/s10751-017-1399-5.

L. Madauß et al.
Fabrication of nanoporous graphene/polymer composite membranes.
Nanoscale, 9(29):10487.
doi: 10.1039/C7NR02755A.

I. A. Maltsev et al.
Pair production in low-energy collisions of uranium nuclei beyond the monopole approximation.
18th International Conference on the Physics of Highly Charged Ions, Kielce (Poland), 11 Sep 2016 - 16 Sep 2016.
Elsevier, Amsterdam [u.a.], 11th Sept. 2016.
doi: 10.1016/j.nimb.2017.05.005.

A. V. Malyshev et al.
Binding energies of the $1s^2\ 2s^2\ 2p_j$ states in boronlike argon.
18th International Conference on the Physics of Highly Charged Ions, Kielce (Poland), 11 Sep 2016 - 16 Sep 2016.
Elsevier, Amsterdam [u.a.], 11th Sept. 2016.
doi: 10.1016/j.nimb.2017.04.097.

A. V. Malyshev et al.
Ground-state ionization energies of boronlike ions.
Physical review / A, 96(2):022512.
doi: 10.1103/PhysRevA.96.022512.

V. Manea et al.
Penning-trap mass spectrometry and mean-field study of nuclear shape coexistence in the neutron-deficient lead region.
Physical review / C, 95(5):054322.
doi: 10.1103/PhysRevC.95.054322.

A. J. Miller et al.
First determination of ground state electromagnetic moments of ^{53}Fe.
Physical review / C, 96(5):054314.
doi: 10.1103/PhysRevC.96.054314.

M. Müller et al.
High-average-power femtosecond laser at 258nm.
Optics letters, 42(14):2826.
doi: 10.1364/OL.42.002826.

R. A. Müller et al.
Theoretical analysis of the electron bridge process in $^{229}Th^{3+}$.
Nuclear instruments & methods in physics research / B, 408:84.
doi: 10.1016/j.nimb.2017.05.004.

A. Nadzri et al.
Composition and orientation dependent annealing of ion tracks in apatite - Implications for fission track thermochronology.
Chemical geology, 451:9.
doi: 10.1016/j.chemgeo.2016.12.039.

H. Nagahama et al.
Sixfold improved single particle measurement of the magnetic moment of the antiproton.
Nature Communications, 8:14084.
doi: 10.1038/ncomms14084.

R. I. Palomares et al.
Defect accumulation in swift heavy ion-irradiated CeO_2 and ThO_2.
Journal of materials chemistry / A, 2017:10.1039.C7TA02640D.
doi: 10.1039/C7TA02640D.

R. I. Palomares et al.
Thermal defect annealing of swift heavy ion irradiated ThO_2.
Nuclear instruments & methods in physics research / B, 405:15.
doi: 10.1016/j.nimb.2017.05.007.

M. K. Pavićević et al.
Geochemical Determination of the Solar pp-Neutrino Flux with LOREX: A Progress Report.
27th International Conference on Neutrino Physics and Astrophysics, London (England), 4 Jul 2016 - 9 Jul 2016.
IOP Publ., Bristol, 4th July 2016.
doi: 10.1088/1742-6596/888/1/012192.

G. Pérez-Mitta et al.
An All-Plastic Field-Effect Nanofluidic Diode Gated by a Conducting Polymer Layer.
Advanced materials, 29(28):1700972.
doi: 10.1002/adma.201700972.

G. Pérez-Mitta et al.
Bioinspired integrated nanosystems based on solid-state nanopores: "iontronic" transduction of biological, chemical and physical stimuli.
Chemical science, 8(2):890.
doi: 10.1039/C6SC04255D.

G. Pérez-Mitta et al.
Noncovalent Approach toward the Construction of Nanofluidic Diodes with pH-Reversible Rectifying Properties: Insights from Theory and Experiment.
The journal of physical chemistry / C, 121(16):9070.
doi: 10.1021/acs.jpcc.7b01639.

A. A. Peshkov et al.
Photoexcitation of atoms by Laguerre-Gaussian beams.
Physical review / A, 96(2):023407.
doi: 10.1103/PhysRevA.96.023407.

A. R. Piriz, Y. B. Sun and N. A. Tahir.
Rayleigh–Taylor instability in accelerated solid media.
European journal of physics, 38(1):015003.
doi: 10.1088/0143-0807/38/1/015003.

S. A. Piriz, A. R. Piriz and N. A. Tahir.
Finite-thickness effects on the Rayleigh-Taylor instability in accelerated elastic solids.
Physical review / E, 95(5):053108.
doi: 10.1103/PhysRevE.95.053108.

S. A. Piriz, A. R. Piriz and N. A. Tahir.
Rayleigh-Taylor instability in accelerated elastic-solid slabs.
Physical review / E, 96(6):063115.
doi: 10.1103/PhysRevE.96.063115.

P. Ramirez et al.
Optimizing Energy Transduction of Fluctuating Signals with Nanofluidic Diodes and Load Capacitors.
Small, 13:1702252.
doi: 10.1002/smll.201702252.

P. Ramirez et al.
Hybrid Circuits with Nanofluidic Diodes and Load Capacitors.
Physical review applied, 7(6):064035.
doi: 10.1103/PhysRevApplied.7.064035.

R. Reifarth et al.
Spallation-based neutron target for direct studies of neutron-induced reactions in inverse kinematics.
Physical review accelerators and beams, 20(4):044701.
doi: 10.1103/PhysRevAccelBeams.20.044701.

J. Rothhardt et al.
High Average Power Near-Infrared Few-Cycle Lasers.
Laser & photonics reviews, 11(4):1700043.
doi: 10.1002/lpor.201700043.

A. de Roubin et al.
Nuclear deformation in the A ≈ 100 region: Comparison between new masses and mean-field predictions.
Physical review / C, 96(1):014310.
doi: 10.1103/PhysRevC.96.014310.

R. Sachan et al.
Forging Fast Ion Conducting Nanochannels with Swift Heavy Ions: The Correlated Role of Local Electronic and Atomic Structure.
The journal of physical chemistry / C, 121(1):975.
doi: 10.1021/acs.jpcc.6b12522.

R. Sachan et al.
New insights on ion track morphology in pyrochlores by aberration corrected scanning transmission electron microscopy.
Journal of materials research, 32(05):928.
doi: 10.1557/jmr.2016.418.

G. M. Samarin, M. Zepf and G. Sarri.
Radiation reaction studies in an all-optical set-up: experimental limitations.
Journal of modern optics, 64(21):2281.
doi: 10.1080/09500340.2017.1353655.

R. M. Sanchez Alarcon et al.
Laser spectroscopy measurement of the 2 s -hyperfine splitting in lithium-like bismuth.
Journal of physics / B, 50(8):085004.
doi: 10.1088/1361-6455/aa63a0.

M. S. Sanjari, Y. Litvinov and T. Stöhlker.
Electromagnetic non-destructive detectors for storage rings.
Journal of physics / Conference Series, 875:092014.
doi: 10.1088/1742-6596/875/10/092014.

T. Saule et al.
Phase-stable, multi-µJ femtosecond pulses from a repetition-rate tunable Ti:Sa-oscillator-seeded Yb-fiber amplifier.
Applied physics / B, 123(1):17.
doi: 10.1007/s00340-016-6611-9.

M. Schanz et al.
High energy proton induced radiation damage of rare earth permanent magnet quadrupoles.
Review of scientific instruments, 88(12):125103.
doi: 10.1063/1.4997116.

V. A. Schanz et al.
Noise reduction in third order cross-correlation by angle optimization of the interacting beams.
Optics express, 25(8):9252.
doi: 10.1364/OE.25.009252.

P. Scharrer et al.
Applications of the pulsed gas stripper technique at the GSI UNILAC.
Nuclear instruments & methods in physics research / A, 863:20.
doi: 10.1016/j.nima.2017.05.015.

C. Scheuner et al.
Nanometer collimation enhancement of ion beams using channeling effects in track-etched mica capillaries.
Scientific reports, 7(1):17081.
doi: 10.1038/s41598-017-17005-w.

S. Schippers et al.
Near L -edge Single and Multiple Photoionization of Singly Charged Iron Ions.
The astrophysical journal / 1, 849(1):5.
doi: 10.3847/1538-4357/aa8fcc.

S. Schmidt et al.
Sympathetic cooling in two-species ion crystals in a Penning trap.
Journal of modern optics, 64:1.
doi: 10.1080/09500340.2017.1342877.

G. Schneider et al.
Double-trap measurement of the proton magnetic moment at 0.3 parts per billion precision.
Science, 358(6366):1081.
doi: 10.1126/science.aan0207.

D. Schumacher et al.
Temperature measurement of hohlraum radiation for energy loss experiments in indirectly laser heated carbon plasma.
Physical review / E, 96(4):043210.
doi: 10.1103/PhysRevE.96.043210.

G. G. Scott et al.
Diagnosis of Weibel instability evolution in the rear surface density scale lengths of laser solid interactions via proton acceleration.
New journal of physics, 19(4):043010.
doi: 10.1088/1367-2630/aa652c.

C. Scullion et al.
Polarization Dependence of Bulk Ion Acceleration from Ultrathin Foils Irradiated by High-Intensity Ultrashort Laser Pulses.
Physical review letters, 119(5):054801.
doi: 10.1103/PhysRevLett.119.054801.

D. Seipt et al.
Depletion of Intense Fields.
Physical review letters, 118(15):154803.
doi: 10.1103/PhysRevLett.118.154803.

S. Sellner et al.
Improved limit on the directly measured antiproton lifetime.
New journal of physics, 19(8):083023.
doi: 10.1088/1367-2630/aa7e73.

L. Senje et al.
Experimental investigation of picosecond dynamics following interactions between laser accelerated protons and water.
Applied physics letters, 110(10):104102.
doi: 10.1063/1.4977846.

P. Sergelius et al.
Intra-wire coupling in segmented Ni/Cu nanowires deposited by electrodeposition.
Nanotechnology, 28(6):065709.
doi: 10.1088/1361-6528/aa5118.

F. Siek et al.
Angular momentum–induced delays in solid-state photoemission enhanced by intra-atomic interactions.
Science, 357(6357):1274.
doi: 10.1126/science.aam9598.

C. Smorra et al.
A parts-per-billion measurement of the antiproton magnetic moment.
Nature, 550(7676):371.
doi: 10.1038/nature24048.

C. Smorra et al.
Observation of individual spin quantum transitions of a single antiproton.
Physics letters / B, 769:1.
doi: 10.1016/j.physletb.2017.03.024.

A. Sobiczewski, Y. Litvinov and M. Palczewski.
Detailed illustration of the accuracy of currently used nuclear-mass models.
Atomic data and nuclear data tables, 119:1.
doi: 10.1016/j.adt.2017.05.001.

R. Sollapur et al.
Resonance-enhanced multi-octave supercontinuum generation in antiresonant hollow-core fibers.
Light, 6(12):e17124.
doi: 10.1038/lsa.2017.124.

H. Stark et al.
Electro-optically controlled divided-pulse amplification.
Optics express, 25(12):13494.
doi: 10.1364/OE.25.013494.

S. Stock, R. Beerwerth and S. Fritzsche.
Auger cascades in resonantly excited neon.
Physical review / A, 95(5):053407.
doi: 10.1103/PhysRevA.95.053407.

N. A. Tahir et al.
High energy density matter issues related to Future Circular Collider: Simulations of full beam impact with a solid copper cylindrical target.
Contributions to plasma physics, 57(9):6.
doi: 10.1002/ctpp.201700075.

N. A. Tahir et al.
High energy density physics issues related to Future Circular Collider.
Physics of plasmas, 24(7):072712.
doi: 10.1063/1.4993185.

N. A. Tahir et al.
Planetary physics research programme at the Facility for Antiprotons and Ion Research at Darmstadt.
Contributions to plasma physics, 57(8):76.
doi: 10.1002/ctpp.201700076.

N. A. Tahir et al.
Studies of the Core Conditions of the Earth and Super-Earths Using Intense Ion Beams at FAIR.
The astrophysical journal / Supplement series, 232(1):15.
doi: 10.3847/1538-4365/aa813e.

F. Tavella et al.
Soft x-ray induced femtosecond solid-to-solid phase transition.
High energy density physics, 24:22.
doi: 10.1016/j.hedp.2017.06.001.

A. Tebartz et al.
Creation and characterization of free-standing cryogenic targets for laser-driven ion acceleration.
Review of scientific instruments, 88(9):093512.
doi: 10.1063/1.5001487.

J. Thomas, M. Günther and A. Pukhov.
Beam load structures in a basic relativistic interaction model.
Physics of plasmas, 24(1):013101.
doi: 10.1063/1.4973322.

M. Toulemonde et al.
Electronic sputtering of LiF, CaF_2, LaF_3 and UF_4 with 197 MeV Au ions. Is the stoichiometry of atom emission preserved?
Nuclear instruments & methods in physics research / B, 406:501.
doi: 10.1016/j.nimb.2016.11.034.

X. L. Tu et al.
Application of isochronous mass spectrometry for the study of angular momentum population in projectile fragmentation reactions.
Physical review / C, 95(1):014610.
doi: 10.1103/PhysRevC.95.014610.

J. Ullmann et al.
High precision hyperfine measurements in Bismuth challenge bound-state strong-field QED.
Nature Communications, 8:15484 (2017).
doi: 10.1038/ncomms15484.

A. S. Varentsova et al.
Third-order Zeeman effect in highly charged ions.
18th International Conference on the Physics of Highly Charged Ions, Kielce (Poland), 11 Sep 2016 - 16 Sep 2016.
Elsevier, Amsterdam [u.a.], 11th Sept. 2016.
doi: 10.1016/j.nimb.2017.05.040.

M. Vockert et al.
Commissioning of a Si(Li) Compton polarimeter with improved energy resolution.
Nuclear instruments & methods in physics research / B, 408:313.
doi: 10.1016/j.nimb.2017.05.035.

M. Vogel.
Atoms and molecules interacting with light, by Peter van der Straten and Harold Metcalf.
Contemporary physics, 58(1):116.
doi: 10.1080/00107514.2016.1259260.

M. Vogel.
Basic X-ray scattering for soft matter, by W. H. de Jeu.
Contemporary physics, 58(3):294.
doi: 10.1080/00107514.2017.1330286.

M. Vogel.
Cosmic rays and particle physics, 2nd edition, by Thomas K. Gaisser, Ralph Engel, and Elisa Resconi.
Contemporary physics, 58(3):288.
doi: 10.1080/00107514.2017.1311376.

M. Vogel.
From matter to life: information and causality, edited by S. I. Walker, P. C. W. Davies and G. F. R. Ellis.
Contemporary physics, 58(3):300.
doi: 10.1080/00107514.2017.1344307.

M. Vogel.
Light sources, second edition: basics of lighting technologies and applications, by Spyridon Kitsinelis.
Contemporary physics, 58(1):102.
doi: 10.1080/00107514.2016.1246482.

M. Vogel.
Stellar explosions: hydrodynamics and nucleosynthesis, by Jordi Jose.
Contemporary physics, 58(1):106.
doi: 10.1080/00107514.2016.1249520.

M. Vogel.
Strange glow: the story of radiation, by Timothy J. Jorgensen.
Contemporary physics, 58(3):285.
doi: 10.1080/00107514.2017.1308967.

M. Vogel.
The Earth's inner core: revealed by observational seismology, by H. Tkalcic.
Contemporary physics, 58(4):380.
doi: 10.1080/00107514.2017.1371244.

M. Vogel.
The structure and dynamics of cities, by M. Barthelemy.
Contemporary physics, 58(4):369.
doi: 10.1080/00107514.2017.1371228.

A. M. Volchkova et al.
Nuclear magnetic shielding in boronlike ions.
18th International Conference on the Physics of Highly Charged Ions, Kielce (Poland), 11 Sep 2016 - 16 Sep 2016.
Elsevier, Amsterdam [u.a.], 11th Sept. 2016.
doi: 10.1016/j.nimb.2017.04.086.

A. E. Volkov et al.
Effect of ion velocity on creation of point defects halos of latent tracks in LiF.
Nuclear instruments & methods in physics research / B, 407:80.
doi: 10.1016/j.nimb.2017.05.065.

F. Wagner et al.
Backreflection diagnostics for ultra-intense laser plasma experiments based on frequency resolved optical gating.
Review of scientific instruments, 88(2):023503.
doi: 10.1063/1.4975827.

P. A. Walker et al.
Horizon 2020 EuPRAXIA design study.
Journal of physics / Conference Series, 874:012029.
doi: 10.1088/1742-6596/874/1/012029.

H. B. Wang et al.
Measurement of the lifetime and the proportion of $^{12}C^{3+}$ ions in stored relativistic ion beams as a preparation for laser cooling experiments at the CSRe.
18th International Conference on the Physics of Highly Charged Ions, Kielce (Poland), 11 Sep 2016 - 16 Sep 2016.
Elsevier, Amsterdam [u.a.], 11th Sept. 2016.
doi: 10.1016/j.nimb.2017.03.096.

A. Welker et al.
Binding Energy of ^{79}Cu : Probing the Structure of the Doubly Magic ^{78}Ni from Only One Proton Away.
Physical review letters, 119(19):192502.
doi: 10.1103/PhysRevLett.119.192502.

A. Welker et al.
Precision electron-capture energy in ^{202}Pb and its relevance for neutrino mass determination.
The European physical journal / A, 53(7):153.
doi: 10.1140/epja/i2017-12345-y.

M. Wiesel et al.
Optically transparent solid electrodes for precision Penning traps.
Review of scientific instruments, 88(12):123101.
doi: 10.1063/1.5002180.

N. Winckler et al.
BREIT code: Analytical solution of the balance rate equations for charge-state evolutions of heavy-ion beams in matter.
Nuclear instruments & methods in physics research / B, 392:67.
doi: 10.1016/j.nimb.2016.11.035.

C. Wraith et al.
Evolution of nuclear structure in neutron-rich odd-Zn isotopes and isomers.
Physics letters / B, 771:385.
doi: 10.1016/j.physletb.2017.05.085.

D. Wu and J. W. Wang.
Magetostatic amplifier with tunable maximum by twisted-light plasma interactions.
Plasma physics and controlled fusion, 59(9):095010.
doi: 10.1088/1361-6587/aa77c5.

D. Wu et al.
Monte Carlo approach to calculate ionization dynamics of hot solid-density plasmas within particle-in-cell simulations.
Physical review / E, 95(2):023208.
doi: 10.1103/PhysRevE.95.023208.

D. Wu et al.
Monte Carlo approach to calculate proton stopping in warm dense matter within particle-in-cell simulations.
Physical review / E, 95(2):023207.
doi: 10.1103/PhysRevE.95.023207.

Z. W. Wu et al.
Angle-resolved x-ray spectroscopic scheme to determine overlapping hyperfine splittings in highly charged heliumlike ions.
Physical review / A, 96(1):012503.
doi: 10.1103/PhysRevA.96.012503.

Z. W. Wu et al.
Dielectronic recombination of highly charged ions with spin-polarized electrons.
18th International Conference on the Physics of Highly Charged Ions, Kielce (Poland), 11 Sep 2016 - 16 Sep 2016. Elsevier, Amsterdam [u.a.], 11th Sept. 2016.
doi: 10.1016/j.nimb.2017.04.076.

M. Wünsche et al.
Quasi-supercontinuum source in the extreme ultraviolet using multiple frequency combs from high-harmonic generation.
Optics express, 25(6):6936.
doi: 10.1364/OE.25.006936.

P. Wustelt et al.
Numerical investigation of the sequential-double-ionization dynamics of helium in different few-cycle-laser-field shapes.
Physical review / A, 95(2):023411.
doi: 10.1103/PhysRevA.95.023411.

G. Xu et al.
Determination of Hydrogen Density by Swift Heavy Ions.
Physical review letters, 119(20):204801.
doi: 10.1103/PhysRevLett.119.204801.

J. Xu et al.
Dynamics of electron injection in a laser-wakefield accelerator.
Physics of plasmas, 24(8):083106.
doi: 10.1063/1.4996906.

D. T. Yordanov et al.
Spin and magnetic moment of ^{23}Mg.
Journal of physics / G, 44(7):075104.
doi: 10.1088/1361-6471/aa718b.

Y. S. Yuan et al.
Dispersion-Induced Beam Instability in Circular Accelerators.
Physical review letters, 118(15):154801.
doi: 10.1103/PhysRevLett.118.154801.

Y.-S. Yuan, O. Boine-Frankenheim and I. Hofmann.
Modeling of second order space charge driven coherent sum and difference instabilities.
Physical review accelerators and beams, 20(10):104201.
doi: 10.1103/PhysRevAccelBeams.20.104201.

R. Zabels et al.
Formation of dislocations and hardening of LiF under high-dose irradiation with 5–21 MeV ^{12}C ions.
Applied physics / A, 123(5):320.
doi: 10.1007/s00339-017-0934-1.

V. A. Zaytsev et al.
Hyperfine induced effects on the angular distribution of the dielectronic hypersatellite line.
18th International Conference on the Physics of Highly Charged Ions, Kielce (Poland), 11 Sep 2016 - 16 Sep 2016. Elsevier, Amsterdam [u.a.], 11th Sept. 2016.
doi: 10.1016/j.nimb.2017.04.081.

Q. Zeng et al.
Half-life measurement of short-lived $^{94m}_{44}$Ru^{44+} using isochronous mass spectrometry.
Physical review / C, 96(3):031303.
doi: 10.1103/PhysRevC.96.031303.

H. Q. Zhang et al.
Transmission profiles of ions through nano-capillaries of rectangular cross-section in mica.
Nuclear instruments & methods in physics research / B, 406:421.
doi: 10.1016/j.nimb.2017.01.039.

P. Zhang et al.
High-precision Q_{EC} values of superallowed $0^+ \rightarrow 0^+$ β-emitters ^{46}Cr, ^{50}Fe and ^{54}Ni.
Physics letters / B, 767:20.
doi: 10.1016/j.physletb.2017.01.039.

Y. Zhang et al.
Single-shot, real-time carrier-envelope phase measurement and tagging based on stereographic above-threshold ionization at short-wave infrared wavelengths.
Optics letters, 42(24):5150.
doi: 10.1364/OL.42.005150.

D. Zille et al.
Spin-dependent quantum theory of high-order above-threshold ionization.
Physical review / A, 95(6):063408.
doi: 10.1103/PhysRevA.95.063408.

D. Zille et al.
Spin-dependent rescattering in strong-field ionization of helium.
Journal of physics / B, 50(6):065001.
doi: 10.1088/1361-6455/aa5db1.

M. Zürch et al.
Transverse Coherence Limited Coherent Diffraction Imaging using a Molybdenum Soft X-ray Laser Pumped at Moderate Pump Energies.
Scientific reports, 7(1):5314.
doi: 10.1038/s41598-017-05789-w.

20 dissertations

A. K. Arunachalam.
Investigation of laser-plasma interactions at near-critical densities.
Friedrich-Schiller-Universität Jena, Jena, 2017.

J. Bai.
Development of the timing system for the Bunch-to-Bucket transfer between the FAIR accelerators.
JWGU Frankfurt, Frankfurt am Main, 2017.

F. Gärtner.
Investigation of Plasma-based Optical Parametric Amplifiers and High Power Seed Pulse Generation for Stimulated Raman Backscattering Experiments.
Goethe-Universität Frankfurt, 2017.

P. Katrik.
Activation analysis of heavy ion accelerator constructing materials and validation of beam-loss criteria.
TU Darmstadt, 2017.

M. Kienel.
Power Scaling of Ultrashort Pulses by Spatial and Temporal Coherent Combining.
Friedrich-Schiller-Universität Jena, Jena, 2017.

A. Kleinschmidt.
Investigation of a laser-driven neutron source with respect to different fields of application.
Technische Universität Darmstadt, Darmstadt, 2017.

J. Krieg.
Characterization of individual Bi_2Te_3 nanowires electrodeposited in etched ion-track membranes for nano-ARPES and electrical transport studies.
Technische Universität Darmstadt, Darmstadt, 2017.

B. Landgraf.
Stimulated Raman backscattering in transient laser generated plasmas with ultra-short seed pulses.
Friedrich-Schiller-Universität Jena, Jena, 2017.

T. Manegold.
Untersuchungen zur Kollision und Kompression von Plasmen koaxialer Beschleuniger.
Johann Wolfgang Goethe-Universität, Frankfurt am Main, 2017.

A. Martin and T. Walter.
Laser Spectroscopic Investigation of Exotic States in Noble Gases.
TU Darmstadt, 2017.

B. Marx-Glowna.
Hochauflösende Röntgenpolarimetrie.
Friedrich-Schiller-Universität Jena, Jena, 2017.

M. Möller.
Probing Strong-field Photoionization of Atoms and Diatomic Molecules with Short-wave Infrared Radiation.
Friedrich-Schiller Universität Jena, Jena, 2017.

F. C. Öztürk.
Investigation og the orbital electron-capture decay of hydrogen-like 142Pm60+ ions at the experimental storage ring (ESR).
University of Istanbul, Istanbul, 2017.

N. Schöppner.
Zerstörungsfreie Visualisierung von durch Schwerionen induzierten Kristalldefekten in natürlichen Mineralen mittels Ramanspektroskopie.
Ruprecht-Karls-Universität Heidelberg, Heidelberg, 2017.

D. Schury.
Aufbau und Charakterisierung einer Quellespinpolarisierter Elektronen für zukünftigeStoßexperimente mit chiralen Molekülen.
Justus-Liebig-Universität Gießen, Gießen, 2017.

N. Seegert.
Signatures of the quantum vacuum in inhomogeneous electromagnetic fields.
Friedrich-Schiller-Universität Jena, Jena, 2017.

J. Ullmann.
Laserspektroskopie an hochgeladenen Bismutionen zum Test der Quantenelektrodynamik.
Friedrich-Schiller-Universität Jena, Jena, 2017.

M. Wiesel.
Preparation and Investigation of Highly Charged Ions in a Penning Trap for the Determination of Atomic Magnetic Moments.
TU Darmstadt, 2017.

Z. Wu.
Angular Correlation and Polarization of X-rays Emitted from Highly Charged Ions.
Friedrich-Schiller-Universität Jena, Jena, 2017.

S. Zeller.
Das Heliumdimer.
Goethe Universität Frankfurt am Main, 2017.

Matter and technologies – 630

21 publications listed in Web of Science or SCOPUS

S. Appel, O. Boine-Frankenheim and F. Petrov.
Injection optimization in a heavy-ion synchrotron using genetic algorithms.
Nuclear instruments & methods in physics research / A, 852:73.
doi: 10.1016/j.nima.2016.11.069.

S. Appel et al.
Injection optimization through generation of flat ion beams.
Nuclear instruments & methods in physics research / A, 866:36.
doi: 10.1016/j.nima.2017.05.041.

W. Barth et al.
High brilliance uranium beams for the GSI FAIR.
Physical review accelerators and beams, 20(5):050101.
doi: 10.1103/PhysRevAccelBeams.20.050101.

J. Bortfeldt et al.
Low material budget floating strip Micromegas for ion transmission radiography.
Nuclear instruments & methods in physics research / A, 845:210.
doi: 10.1016/j.nima.2016.05.003.

X. Du et al.
Field stabilization of Alvarez-type cavities.
Physical review accelerators and beams, 20(3):032001.
doi: 10.1103/PhysRevAccelBeams.20.032001.

A. Evans et al.
Heavy-Ion Micro Beam and Simulation Study of a Flash-Based FPGA Microcontroller Implementation.
IEEE transactions on nuclear science, 64(1):504.
doi: 10.1109/TNS.2016.2633401.

G. Franchetti et al.
Studies and observations of beam dynamics near a sum resonance.
Journal of physics / Conference Series, 874:012075.
doi: 10.1088/1742-6596/874/1/012075.

I. Hofmann and O. Boine-Frankenheim.
Parametric instabilities in 3D periodically focused beams with space charge.
Physical review accelerators and beams, 20(1):014202.
doi: 10.1103/PhysRevAccelBeams.20.014202.

I. Hofmann and O. Boine-Frankenheim.
Revisiting the Longitudinal 90° Limit in High Intensity Linear Accelerators.
Physical review letters, 118(11):114803.
doi: 10.1103/PhysRevLett.118.114803.

J.-G. Hwang et al.
Development of high resolution linear-cut beam position monitor for heavy-ion synchrotron of KHIMA project.
Nuclear instruments & methods in physics research / A, 852:33.
doi: 10.1016/j.nima.2017.01.073.

K. Kasinski et al.
System-level considerations for the front-end readout ASIC in the CBM experiment from the power supply perspective.
Journal of Instrumentation, 12(03):C03023.
doi: 10.1088/1748-0221/12/03/C03023.

S. Levasseur et al.
Development of a rest gas ionisation profile monitor for the CERN Proton Synchrotron based on a Timepix3 pixel detector.
Journal of Instrumentation, 12(02):C02050.
doi: 10.1088/1748-0221/12/02/C02050.

B. Mei.
Improved empirical parameterization for projectile fragmentation cross sections.
Physical review / C, 95(3):034608.
doi: 10.1103/PhysRevC.95.034608.

S. Meyer et al.
Comparative Monte Carlo study on the performance of integration- and list-mode detector configurations for carbon ion computed tomography.
Physics in medicine and biology, 62(3):1096.
doi: 10.1088/1361-6560/aa5602.

M. Mitrovic et al.
A DC-to-8.5 GHz 32:1 Analog Multiplexer for On-Chip Continuous-Time Probing of Single-Event Transients in a 65-nm CMOS.
IEEE transactions on circuits and systems / 2, 64(4):377.
doi: 10.1109/TCSII.2016.2567781.

Y. Nie et al.
Numerical simulations of energy deposition caused by 50 MeV—50 TeV proton beams in copper and graphite targets.
Physical review accelerators and beams, 20(8):081001.
doi: 10.1103/PhysRevAccelBeams.20.081001.

P. Scharrer et al.
Measurements of charge state distributions of 0.74 and 1.4 MeV / u heavy ions passing through dilute gases.
Physical review accelerators and beams, 20(4):043503.
doi: 10.1103/PhysRevAccelBeams.20.043503.

M. Schuett et al.
Status of the modulated 3 MeV 325 MHz Ladder-RFQ.
Journal of physics / Conference Series, 874:012048.
doi: 10.1088/1742-6596/874/1/012048.

S. Swain et al.
A quad-GEM detector prototype operated at very low gas gain.
Journal of Instrumentation, 12(07):T07002.
doi: 10.1088/1748-0221/12/07/T07002.

E. Verbitskaya et al.
Development of silicon detectors for Beam Loss Monitoring at HL-LHC.
Journal of Instrumentation, 12(03):C03036.
doi: 10.1088/1748-0221/12/03/C03036.

J. W. Wang et al.
Plasma channel undulator excited by high-order laser modes.
Scientific reports, 7(1):16884.
doi: 10.1038/s41598-017-16971-5.

4 dissertations

I. Karpov.
Damping of Coherent Oscillations in Intense Ion Beams.
Technische Universität Darmstadt, 2017.

F. Nesting.
Numerical noise in particle-in-cell tracking : generation and propagation.
Johann Wolfgang Goethe-Universität Frankfurt, 2017.

P. Scharrer.
Charge state distributions of low-energy heavy ions passing through dilute gases.
Johannes-Gutenberg-Universität Mainz, 2017.

A. Seibel.
Untersuchungen zu einer neuen Alvarez-Struktur für den GSI Post-Stripper.
Johann Wolfgang Goethe-Universität Frankfurt, Frankfurt/M, 2017.

Cancer Research – 310

30 publications listed in Web of Science or SCOPUS

. **Live Cell Imaging to Study Real-Time ATM-Mediated Recruitment of DNA Repair Complexes to Sites of Ionizing Radiation-Induced DNA Damage**.
ATM Kinase / Kozlov, Sergei V. (Editor) ; New York, NY : Springer New York, 2017, Chapter 21 ; ISSN: 1064-3745=1940-6029 ; ISBN: 978-1-4939-6953-1=978-1-4939-6955-5 ; doi:10.1007/978-1-4939-6955-5.
Springer New York, New York, NY, 2017.
doi: 10.1007/978-1-4939-6955-5_21.

O. Arrizabalaga et al.
Electrophysiological investigation of human embryonic stem cell derived neurospheres using a novel spike detection algorithm.
Biosensors and bioelectronics, 100:462.
doi: 10.1016/j.bios.2017.09.034.

O. Azimzadeh et al.
Differential Impact of Single-Dose Fe Ion and X-Ray Irradiation on Endothelial Cell Transcriptomic and Proteomic Responses.
Frontiers in pharmacology, 8:570.
doi: 10.3389/fphar.2017.00570.

O. Azimzadeh et al.
Radiation-Induced Endothelial Inflammation Is Transferred via the Secretome to Recipient Cells in a STAT-Mediated Process.
Journal of proteome research, 16(10):3903.
doi: 10.1021/acs.jproteome.7b00536.

G. Battistoni et al.
Addendum: Measurement of charged particle yields from PMMA irradiated by a 220 MeV/u ^{12}C beam.
Physics in medicine and biology, 62(21):8483.
doi: 10.1088/1361-6560/aa8b35.

H. Crezee et al.
Quality assurance guidelines for superficial hyperthermia clinical trials: I. Clinical requirements.
International journal of hyperthermia, 33(4):471.
doi: 10.1080/02656736.2016.1277791.

A. Cucu, D. Kraft and S. Lehrian.
06.03Ionising radiation inhibits adipokine induced inflammation in synovial fibroblasts and differentiation of osteoclasts.
Annals of the rheumatic diseases, 76(Suppl 1):06.03.
doi: 10.1136/annrheumdis-2016-211053.3.

D. Czarnecki and D. Harder.
The absorbed doses to water and the TLD-100 signal contributions associated with the neutron contamination of a clinical 18 MV photon beam.
Radiation measurements, 106:331.
doi: 10.1016/j.radmeas.2017.02.007.

A. Eichhorn et al.
Immobilization for carbon ion beam ablation of cardiac structures in a porcine model.
Physica medica, 43:134.
doi: 10.1016/j.ejmp.2017.10.016.

C. Fournier et al.
Basics of Radiation Biology When Treating Hyperproliferative Benign Diseases.
Frontiers in immunology, 8:519.
doi: 10.3389/fimmu.2017.00519.

T. Friedrich and M. Krämer.
Systematics of relative biological effectiveness measurements for proton radiation along the spread out Bragg peak: experimental validation of the local effect model.
Physics in medicine and biology, 62(3):890.
doi: 10.1088/1361-6560/62/3/890.

C. Graeff.
How should we manage internal margins in four-dimensional dose assessments?
Radiological physics and technology, 10(4):535.
doi: 10.1007/s12194-017-0426-1.

A. Heselich et al.
Evaluation of the radiation-induced stress response in a human full thickness skin model.
44th Annual Meeting of the Arbeitsgemeinschaft-Dermatologische-Forschung, Göttingen (Germany), 9 Mar 2017 - 11 Mar 2017.
9th Mar. 2017.
doi: 10.1111/exd.13280.

A. C. Heuskin, E. Scifoni and M. Kraemer.
Backscattered electron emission after proton impact on carbon and gold films: Experiments and simulations.
Nuclear instruments & methods in physics research / B, 401:8.
doi: 10.1016/j.nimb.2017.04.032.

H. I. Lehmann et al.
ECG-based 4D-dose reconstruction of cardiac arrhythmia ablation with carbon ion beams: application in a porcine model.
Physics in medicine and biology, 62(17):6869.
doi: 10.1088/1361-6560/aa7b67.

I. Mattei et al.
Benchmarking Geant4 hadronic models for prompt- γ monitoring in carbon ion therapy.
Medical physics, 44(8):4276.
doi: 10.1002/mp.12348.

W. D. Newhauser et al.
A descriptive and broadly applicable model of therapeutic and stray absorbed dose from 6 to 25 MV photon beams.
Medical physics, 44(7):3805.
doi: 10.1002/mp.12286.

R. Paramatti et al.
Secondary radiation measurements for particle therapy applications: nuclear fragmentation produced by ^{4}He ion beams in a PMMA target.
Physics in medicine and biology, 62(4):1291.
doi: 10.1088/1361-6560/aa5307.

A. Rapp et al.
Identification of the elementary structural units of the DNA damage response.
Nature Communications, 8:15760.
doi: 10.1038/ncomms15760.

F. Rapp et al.
Measuring Leukocyte Adhesion to (Primary) Endothelial Cells after Photon and Charged Particle Exposure with a Dedicated Laminar Flow Chamber.
Frontiers in immunology, 8:627.
doi: 10.3389/fimmu.2017.00627.

D. Richter and S. E. Combs.
Planning strategies for inter-fractional robustness in pancreatic patients treated with scanned carbon therapy.
Radiation oncology, 12(1):94.
doi: 10.1186/s13014-017-0832-x.

C. Schuy, U. Weber and K.-T. Brinkmann.
Measurement of charge- and mass-changing cross sections for $^{4}He+^{12}C$ collisions in the energy range 80–220 MeV/u for applications in ion beam therapy.
Physical review / C, 96(2):024624.
doi: 10.1103/PhysRevC.96.024624.

C. Schuy et al.
Fragmentation of 120 and 200 MeV u −1 4 He ions in water and PMMA targets.
Physics in medicine and biology, 62(4):1310.
doi: 10.1088/1361-6560/aa5302.

E. Scifoni et al.
Oxygen beams for therapy: advanced biological treatment planning and experimental verification.
Physics in medicine and biology, 62(19):7798.
doi: 10.1088/1361-6560/aa88a0.

K. Shreder et al.
Decrease of Markers Related to Bone Erosion in Serum of Patients with Musculoskeletal Disorders after Serial Low-Dose Radon Spa Therapy.
Frontiers in immunology, 8:882.
doi: 10.3389/fimmu.2017.00882.

Y. Simeonov et al.
Modulation power of porous materials and usage as ripple filter in particle therapy.
Physics in medicine and biology, 62(7):2892.
doi: 10.1088/1361-6560/aa5c28.

U. Weber et al.
3D range-modulator for scanned particle therapy: development, Monte Carlo simulations and experimental evaluation.
Physics in medicine and biology, 62(17):7075.
doi: 10.1088/1361-6560/aa81f4.

U. Weber et al.
Corrigendum: 3D range-modulator for scanned particle therapy: development, Monte Carlo simulations and experimental evaluation (2017 Phys. Med. Biol . 62 7075).
Physics in medicine and biology, 62(19):7923.
doi: 10.1088/1361-6560/aa87f5.

M. Witt, U. Weber and R. Engenhart-Cabillic.
An efficient method to predict and include Bragg curve degradation due to lung-equivalent materials in Monte Carlo codes by applying a density modulation.
Physics in medicine and biology, 62(10):3997.
doi: 10.1088/1361-6560/aa641f.

R. Wunderlich et al.
Modulation of the peripheral immune system after low-dose radon spa therapy: Detailed longitudinal immune monitoring of patients within the RAD-ON01 study.
Autoimmunity, -:1.
doi: 10.1080/08916934.2017.1284819.

6 dissertations

E. Abdollahi Mirzanagh.
Monitoring physiological changes in cells after ionizing radiation using fluorescence lifetime imaging by time resolved single photon counting.
Technische Universität Darmstadt, 2017.

A. Eichhorn.
In-vivo feasibility study and developments for cardiac arrhythmia ablation using scanned carbon ions.
Technische Universität Darmstadt, 2017.

N. Erbeldinger.
Microvascular Damage as Initial Event of Scar Formation after Carbon Ion Irradiation of Cardiac Substructures.
Technische Universität Darmstadt, 2017.

M. Mayer.
Einfluss ionisierender Strahlung auf die elektrophysiologischen Eigenschaften sich entwickelnder neuronaler Netzwerke.
Technische Universität Darmstadt, 2017.

G. Paul.
Modellierung der DNA-Schadenscluster-, Zellzyklus- und Reparaturweg-abhängigen Strahlenempfindlichkeit nach niedrig- und hoch-LET-Bestrahlung.
Technische Universität Darmstadt, 2017.

K. Shreder.
Impact of ionizing radiation on adipokine-induced inflammation in musculoskeletal diseases (MSD): Investigations in primary cells and MSD patients.
Technische Universität Darmstadt, 2017.

Statutory organs and scientific advisory committees (2017)

compiled by K. Füssel and I. Augustin

GSI and FAIR, Darmstadt, Germany

Supervisory Board / Aufsichtsrat (AR), GSI:

Staatssekretär Dr. Georg Schütte [chair],
Bundesministerium für Bildung und Forschung, Bonn/Berlin (Germany),
as representative of the Federal Republic of Germany

MinR Dr. Volkmar Dietz,
Bundesministerium für Bildung und Forschung, Bonn/Berlin (Germany),
as representative of the Federal Republic of Germany

Ministerialdirigent Dr. Rolf Bernhardt,
Hessisches Ministerium für Wissenschaft und Kunst, Wiesbaden (Germany),
as representative of the State of Hesse in Germany

Dr. Bernd Ebersold,
Thüringer Ministerium für Wirtschaft, Wissenschaft und digitale Gesellschaft, Erfurt (Germany),
as representative of the State of Thuringia in Germany

Dr. Carola Zimmermann,
Ministerium für Bildung, Wissenschaft, Weiterbildung und Kultur, Mainz (Germany),
as representative of the State of Rhineland-Palatinate in Germany

Prof. Dr. Cornelia Denz,
Westfälische Wilhelms-Universität Münster (Germany),
as representatives from the fields of science and economy

Prof. Dr. Thomas Glasmacher,
Facility for Rare Isotope Beams, East Lansing (USA)
as representatives from the fields of science and economy

Prof. Dr. Klaus Blaum,
Max-Planck-Institut für Kernphysik, Heidelberg (Germany),
Vice-Chair of the Joint Scientific Council GSI/FAIR

Dr. Bettina Lommel,
GSI Helmholtzzentrum für Schwerionenforschung,
as spokesperson of the Scientific-Technical Council of GSI

Director's Board / Geschäftsführung:

Prof. Dr. Paolo Giubellino, Ursula Weyrich, Jörg Blaurock

Joint Scientific Council of GSI and FAIR (JSC):

(www.gsi.de/work/organisation/wissenschaftliche_gremien/sc.htm)

S. Raha [chair], Bose Institute, Kolkata (India);
K. Blaum [vice-chair and Head of GSI-SC], MPI-K, Heidelberg (Germany);
F. Azaiez, National Research Foundation, iThemba LABS (South Africa); M. J. G. Borge, Institute for the Structure of Matter (IEM), CFMAC, Madrid (Spain); E. Lindroth, Stockholm University (Sweden); K. Redlich, Wroclaw University (Poland); P. Rossi, Jefferson Laboratory, Newport News (USA); Chr. Roy, CNRS, Strasbourg (France); N. Saito, J-PARC Center, Ibaraki (Japan); L. Sihver, Vienna University of Technology & MedAustron GmbH, Vienna (Austria); R. Tribble, Brookhaven National Laboratory (USA); G. V. Trubnikov, Joint Institute for Nuclear Research, Dubna (Russia);
Secretary: C. Ewerz

Scientific and Technical Council / Wissenschaftlich-Technischer Rat (WTR):

(www.gsi.de/work/organisation/wissenschaftliche_gremien/wtr.htm)

B. Lommel [Spokesperson]; M. Bai; R. Bär; W. Barth; P. Braun-Munzinger; A. Bräuning-Demian; R. Fuchs; M. Gorska; F. Herfurth; C. Kausch; Y. Leifels [Vice-Spokesperson]; V. Lindenstruth; Y. Litvinov; F. Maas; P. Malzacher; D. Ondreka; K. Peters; H. Reich-Sprenger; C. Scheidenberger; C.J. Schmidt; L. Schmitt; M. Schwickert; P. Senger; H. Simon; P. Spiller; J. Stadlmann; T. Stöhlker; J. Stroth; C. Trautmann; U. Weinrich;

Scientific Programme Advisory Committees:

General Programme Advisory Committee (G-PAC)

(www.gsi.de/g-pac)

S. Galès [chair], IN2P, Paris (France);
Y. Blumenfeld, IPN Orsay (France); J. Bielcikova, The Czech Academy of Sciences, Rez (Czech Republic); P. Greenlees, Univ. of Jyväskylä (Finland); P. Indelicato, CNRS, Lab. Kastler Brossel (France); A. Mischke, Utrecht Univ. (The Netherlands); W. Nazarewicz, FRIB/MSU (USA); G. Neyens, KU Leuven (Belgium); M. Pajek, Jan Kochanowski Univ., Kielce (Poland); T. Pfeifer, Max-Planck-Instiute for Nucl. Physics, Heidelberg (Germany); A. Schwenk, Techn. Univ. Darmstadt (Germany); T. Uesaka, RIKEN (Japan); E. Widmann, Stefan Meyer Inst. for Subatomic Physics, Vienna (Austria);

Secretary: K. Füssel

PHELIX Committee

(www.gsi.de/phelix_committee)
P. Thirolf [chair], LMU, München (Germany);
B. Cros, CNRS, LPGP, Université Paris-Sud, Orsay (France); D. Gericke, Univ. Warwick, Coventry (UK); A. Golubev, ITEP, Moscow (Russia); V. Tikhonchuk, Univ. Bordeaux, Talence (France);
Secretary: K. Füssel

Programme Advisory Committee for Materials Research (Mat-PAC)

T. Cornelius, CNRS, IM2NP, Aix-Marseille Univ. (France); Y. Dai, PSI, Villingen (Switzerland); S. Klaumünzer, (formerly HZB), Berlin (Germany); Z. Siwy, Univ. of California, Irvine (USA);
Secretary: I. Schubert

Programme Advisory Committee for Biophysics and Radiobiology (Bio-PAC)

L. Sabatier, CEA, Paris (France); O. Jäkel, DKFZ, Heidelberg, (Germany);
Secretary: K. Füssel

Council / Gesellschafterversammlung, FAIR

Georg Schütte [chair],
Bundesministerium für Bildung und Forschung, Bonn/Berlin (Germany),

Thomas Nilsson [vice chair],
Chalmers University of Technology,
Gothenburg (Sweden)

Volkmar Dietz,
Bundesministerium für Bildung und Forschung,
Bonn (Germany),
as representative of the Federal Republic of Germany

Viacheslav Pershukov
Rosatom Nuclear Energy State Corporation,
Moscow (Russia),
as representative of the Russian Federation

Vladimir E. Fortov,
Russian Academy of Sciences,
Moscow (Russia),
as representative of the Russian Federation

Bikash Sinha,
Variable Energy Cyclotron Center,
Kolkata (India),
as representative of the Republic of India

Sibaji Raha,
Bose Institute,
Kolkata (India)
as representative of the Republic of India

Catarina Sahlberg,
Swedish Research Council (Vetenkapsrådet),
Stockholm (Sweden),
as representative of the Swedish - Finnish Shareholder

Paula Eerola,
Helsinki Institute of Physics,
Helsinki (Finland)

Anca Ghinescu,
Ministry of Research and Innovation,
Bucharest (Romania),
as representative of Romania

Ruxandra Popescu,
Ministry of Research and Innovation,
Bucharest (Romania),
as representative of Romania

Zbigniew Majka,
Jagellonian University Kraków,
Kraków (Poland)
as representative of the Republic of Poland

Mateusz Gaczynski,
Department of Innovation and Development of the Ministry of Science and High Education,
Warsaw (Poland,)
as representative of the Republic of Poland

Albin Kralj,
Ministry of Education, Science and Sports,
Ljubljana (Slovenia),
as representative of the Republic of Slovenia

Patricia Roussel-Chomaz,
Commissariat à l' Énergie Atomique et aux Energies Alternatives (CEA),
Gif-sur-Yvette (France),
as representative of the French Republic shareholder CEA

Fanny Farget,
Centre National de la Recherche Scientifique (CNRS),
Paris (France),
as representative of the French Republic shareholder CNRS

Janet Seed
Science and Technology Facilities Council (STFC),
Swindon (United Kingdom),
as representative of the Associate Partner United Kingdom
Secretary: Th. Beier

 DOI:10.15120/GR-2018-1

AFC - Administrative and Finance Committee (FAIR)

(https://fair-center.eu/fair-gmbh/organisation/administrative-and-finance-committee-afc.html)

Bernard Dormy,
Ministry of Education, Higher Education and Research, France [Chair]

Catalin Borcea
Horia Hulubei National Institute for R&D in Physics and Nuclear Engineering,
Romania [Vice Chair]

Finland / Sweden:

Jaana Aalto - Academy of Finland
Catarina Sahlberg - Swedish Research Council

France:

Stéphanie Dupuis - National Center for Scientific Research (CNRS)
Salah Dib - Alternative Energies and Atomic Energy Commission (CEA)

Germany:

Oda Keppler - Bundesministerium für Bildung und Forschung (BMBF)

India:

Praveer Asthana - Ministry of Science & Technology (MST)

Poland:

Alicja Nowakowska - Jagiellonian University Krakow
Gabriela Nowicka - Jagiellonian University Krakow

Romania:

Lucia Moise - Ministry of Research and Innovation
Raluca Stoicea - Horia Hulubei National Institute of Physics and Nuclear Engineering (NIPNE/IFIN-HH)

Russia:

Peter V. Bogdanov - State Atomic Energy Corporation (ROSATOM)
Vladimir I. Savosin - ROSATOM

Slovenia:

Albin Kralj - Ministry of Education, Science, Culture and Sport (MIZKS)

United Kingdom:

Jenny Hiscock - Science & Technology Facilities Council (STFC)

IKRB - In-Kind Review Board (FAIR)

(https://fair-center.eu/fair-gmbh/organisation/in-kind-review-board-ikrb.html)

Horst Wenninger - European Organization for Nuclear Research (CERN) [Chair]

Finland / Sweden:

Håkan Danared - European Spallation Source (ESS), Lund

France:

Nicolas Alamanos - Commissariat à l'énergie atomique et aux énergies alternatives (CEA)
Alex C. Mueller - Centre National de la Recherche Scientifique (CNRS)

Germany:

FAIR Project Leader
Dieter Prasuhn - Forschungszentrum Jülich

India:

Rakesh K. Bhandari - Variable Energy Cyclotron Centre (VECC), Kolkata

Poland:

Tomasz Matulewicz - University of Warsaw

Romania:

Livius Trache - Horia Hulubei National Institute of Physics and Nuclear Engineering (IFIN-HH)

Russia:

Yuri M. Shatunov - Budker Institute of Nuclear Physics

Slovenia:

Matej Lipoglavšek - Jožef Stefan Institute

MAC - Machine Advisory Committee (FAIR)

Thomas Roser, Brookhaven National Laboratory, USA [Chair]

Rakesh Bhandari, Inter University Accelerator Centre, India

Wolfram Fischer, Brookhaven National Laboratory, USA

Stephen Gourlay, Lawrence Berkeley National Laboratory, USA

Kazuo Hasegawa, Japan Atomic Energy Agency, (J-PARC), Japan

Sergey Ivanov, Institute for High Energy Physics (IHEP) of NRC KI, Russia

Philippe Lebrun, European Scientific Institute, France

Sergei Nagaitsev, Fermi National Accelerator Laboratory, USA

Suitbert Ramberger, CERN, Switzerland

Stephan Russenschuck, CERN, Switzerland

Rüdiger Schmidt, CERN, Switzerland

Kay Wittenburg; DESY, Germany

ECE - FAIR Expert Committee Experiments

Derek Lowenstein, Brookhaven National Laboratory (BNL), USA [Chair]

Volker Burkert, Jefferson Lab, Newport News, USA

Richard Casten, Yale University, USA

Jens Dilling, TRIUMF, Vancouver, Canada

Alexandra Gade, Michigan State University, USA

Thomas Hemmick, Stony Brook University, USA

Tohru Motobayashi, Rikagaku Kenkyūjo (RIKEN), Japan

Eugenio Nappi, Istituto Nazionale di Fisica Nucleare (INFN), Bari, Italy [Deputy Chair]

David Neely, Rutherford Appleton Laboratory, United Kingdom

Hans Georg Ritter, Lawrence Berkeley National Laboratory (LBNL), USA

Ewa Rondio, National Centre for Nuclear Research (NCBJ), Poland / CERN, Switzerland

Horst Schmidt-Boecking, University of Frankfurt, Germany

Peter Seyboth, Max Planck Institute for Physics (MPI), Munich, Germany

Peter Thirolf, University of Munich (LMU), Germany

Crispin Williams, Istituto Nazionale di Fisica Nucleare (INFN), Bologna, Italy / CERN, Switzerland

Craig L. Woody, Brookhaven National Laboratory (BNL), USA

 DOI:10.15120/GR-2018-1

DOI:10.15120/GR-2018-1

Facility for Antiproton and Ion Research in Europe GmbH
GSI Helmholtzzentrum für Schwerionenforschung GmbH

Organigramm

HELMHOLTZ
SPITZENFORSCHUNG FÜR GROSSE HERAUSFORDERUNGEN

FAIR Council
Vorsitz G. Schütte
Stellv. T. Nilsson

GSI Gesellschafterversammlung
Bund / Hessen / Rheinland-Pfalz / Thüringen

GSI Aufsichtsrat
Vorsitz G. Schütte
Stellv. Vorsitz R. Bernhardt

Scientific Council — S. Raha / K. Blaum
Administrative and Finance Committee (AFC) — B. Dorny
Machine Advisory Committee (MAC) — T. Roser
Board of FAIR Collaborations (BFC) — C. Trautmann
Program Advisory Committee (PAC) — S. Gales
In-Kind Review Board (IKRB) — H. Wenninger
Expert Committee Experiments (ECE) — D. Lowenstein
Resource Review Board (RRB) — P. Giubellino

Wissenschaftlich-Technischer Rat — B. Lommel
Betriebsrat — J. Regler
Schwerbehinderten-vertretung — K. Brinck
Gleichstellungs-gremium — C. Will

Stab der Geschäftsführung — K. D. Groß

Geschäftsführung
- **Wissenschaftliche Geschäftsführung FAIR & GSI** — Paolo Giubellino
- **Technische Geschäftsführung FAIR & GSI** — Jörg Blaurock
- **Kaufmännische Geschäftsführung FAIR & GSI** — Ursula Weyrich

Ausfuhrkontrolle — J. Shirotskiy
Presse- & Öffent-lichkeitsarbeit — I. Peter
Council Issues — T. Beier
Stab Wiss. Geschäfts-führung FAIR — I. Augustin
Innenrevision & Compliance FAIR & GSI — K. Scheller
QM, RM & Organisation — D. Wieczorek-Berg
IT-Sicherheit — W. Schön
Datenschutz — M. Schuldt
Technologietransfer — T. Engert

Strahlenschutz-bevollmächtigter — T. Radon
Leitende SiFa — N. Dausend
Sicherheit & Strahlenschutz — T. Radon

Forschungsdirektor FAIR — K. Langanke
Forschung — K. Langanke
Drittmittelberatung — D. Müller

HI Jena — T. Stöhlker
HI Mainz — F. Maas
ExtreMe Matter Institute (EMMI) — P. Braun-Munzinger
HGS-HIRe — H. Büsching

FAIR Forschungs-koordination — I. Lehmann

APPA / MML Koordination — T. Stöhlker
- **Atomphysik** — T. Stöhlker
  - **SPARC Detektoren** — Y. Litvinov
  - **Decelerator Experimente** — W. Quint / M. Lestinsky
- **Plasmaphysik / PHELIX** — V. Bagnoud
  - **Plasmaphysik-detektoren** — A. Blazevic
- **Material-forschung** — C. Trautmann
  - **BIOMAT**[1] — D. Severin

APPA / Gesundheit Koordination — M. Scholz
- **Biophysik** — M. Scholz / C. Kausch (acting)

CBM / MU Koordination — J. Stroth
- **ALICE** — S. Masciocchi
- **HADES** — J. Stroth
- **CBM** — P. Senger
  - **CBM Detektoren** — C. Sturm

NUSTAR / MU Koordination — C. Scheidenberger
- **FRS / SFRS Experimente** — C. Scheidenberger
- **Kernreaktionen** — T. Aumann
  - **R3B** — T. Aumann
- **Kern-spektroskopie** — J. Gerl
  - **HISPEC / DESPEC** — J. Gerl
- **SHE Chemie** — C. E. Düllmann
- **SHE Physik** — M. Block

PANDA Hadronen / MU Koordination — K. Peters
- **Hadronen-spektroskopie** — K. Peters
- **Hadronen-struktur** — F. Maas
- **PANDA Detektoren** — J. Schwiening

Theorie / MU Koordination — B. Friman
- **Hadronen & QCD** — B. Friman
- **Nukleare Astrophysik & Struktur** — G. Martinez Pinedo
- **Experiment-simulationen** — H. Stöcker

Wissenschaftliche IT & HL-Rechnen — V. Lindenstruth
- **Wissenschaftliche IT** — T. Kollegger
- **Hochleistungs-rechnen** — W. Schön
  - **Detektorlabor** — C. J. Schmidt
  - **Experiment-elektronik** — K. Koch
  - **Targetlabor** — B. Lommel
  - **Bibliothek & Dokumentation** — K. Große

Technical Integration — R. Fuchs / O. Boine-Frankenheim / T. Burkhard

Gesamtprojekt-leitung FAIR — J. Henschel
- **SIS 100 / SIS 18** — P. Spiller
  - **Ring RF** — H. Klingbeil
  - **System Design SIS 100 / SIS 18** — D. Ondreka
  - **SC Magnets & Testing** — C. Roux
  - **Ring HV** — U. Blell
  - **Super Fragment Separator** — H. Simon
    - **System Planning SFRS** — M. Winkler
  - **P-Linac / P-Bar-Target** — K. Knie
- **Commons** — S. Menke
  - **Control Systems** — R. Bär
  - **Vacuum Systems** — A. Krämer
  - **Cryogenics** — H. Kollmus
  - **Transport & Installation** — M. Bevcic
  - **Beam Diagnostics** — M. Schwickert
  - **Electric Power Systems** — K. Trumm
  - **HEBT** — F. Hagenbuck
  - **Engineering** — R. Fuchs
- **Collector Ring**** — I. Koop
  - **High-Energy Storage Ring**** — D. Prasuhn
  - **CBM Experiment Area***** — W. Müller
  - **NUSTAR Experiment Area***** — J. Gerl
  - **APPA Experiment Area***** — A. Bräuning-Demian
  - **PANDA Experiment Area***** — L. Schmitt

Project Management Office — E. Rosi

FAIR Site & Buildings**
- **Projektleitung ext., Bauleitung******** — T. Burkhard (acting)

Site Management**
- **Projektleitung ext.******** — H. Hagelskamp

Beschleunigerbetrieb — M. Bai
- **Betrieb** — S. Reimann
- **Beschleuniger-physik** — O. Boine-Frankenheim
- **Ionenquellen** — R. Hollinger
- **Linac** — L. Groening
- **Linac HF** — G. Schreiber
- **Speicherringe** — M. Steck
- **Deceleratoren** — F. Herfurth
- **Strahlkühlung** — C. Dimopoulou
- **Technologie-labor** — K. Dermati
- **cw-Linac** — W. Barth
- **Mechanische Werkstatt & Schlosserei** — M. Romig

Campus-entwicklung — G. Stephan
- **Gebäude- & Anlagentechnik** — R. Becker
- **Zentrale Dienste** — T. May

Personal — D. Sommer
- **Recht & Patente** — W. Dahlem
- **Controlling** — M. Jaeger
- **Basis-IT** — K. Miers

Einkauf & Material-wirtschaft — M. Spatar
- **Finanzen** — M. Fuhr
- **Finanzen FAIR*** — M. Fuhr

* bis zum Merger von FAIR und GSI

**In das Projekt funktional delegierter Vertreter des In-Kind-Partners.

***In das Projekt funktional delegierter Vertreter der Experiment-Kollaboration.

****Funktionale Berichtslinie zu FAIR-Projekt

Legende:
FAIR | FAIR & GSI | GSI | Stabsabteilung | Helmholtz-Institut der GSI

[1] Fachlich angebunden an Biophysik und Materialforschung

Personelle und organisatorische Einzelmaßnahmen befinden sich in der Umsetzung

Stand: 01.12.2017

 DOI:10.15120/GR-2018-1